symmetry

Special Issue Reprint

Symmetry in Nonlinear Dynamics and Chaos II

Edited by
Sergio Elaskar

mdpi.com/journal/symmetry

MDPI

Symmetry in Nonlinear Dynamics and Chaos II

Symmetry in Nonlinear Dynamics and Chaos II

Guest Editor

Sergio Elaskar

MDPI

Basel • Beijing • Wuhan • Barcelona • Belgrade • Novi Sad • Cluj • Manchester

Guest Editor
Sergio Elaskar
Aerospace Department
National University
of Cordoba
Córdoba
Argentina

Editorial Office
MDPI AG
Grosspeteranlage 5
4052 Basel, Switzerland

This is a reprint of the Special Issue, published open access by the journal *Symmetry* (ISSN 2073-8994), freely accessible at: https://www.mdpi.com/journal/symmetry/special_issues/U14FZ979TL.

For citation purposes, cite each article independently as indicated on the article page online and as indicated below:

Lastname, A.A.; Lastname, B.B. Article Title. *Journal Name* **Year**, *Volume Number*, Page Range.

ISBN 978-3-7258-4444-9 (Hbk)
ISBN 978-3-7258-4443-2 (PDF)
https://doi.org/10.3390/books978-3-7258-4443-2

© 2025 by the authors. Articles in this book are Open Access and distributed under the Creative Commons Attribution (CC BY) license. The book as a whole is distributed by MDPI under the terms and conditions of the Creative Commons Attribution-NonCommercial-NoDerivs (CC BY-NC-ND) license (https://creativecommons.org/licenses/by-nc-nd/4.0/).

Contents

About the Editor . . . . . **ix**

Preface . . . . . **xi**

Sergio Elaskar
Symmetry in Nonlinear Dynamics and Chaos II
Reprinted from: *Symmetry* **2025**, *17*, 846, https://doi.org/10.3390/sym17060846 . . . . . **1**

Sergio Elaskar and Ezequiel del Río
Review of Chaotic Intermittency
Reprinted from: *Symmetry* **2023**, *15*, 1195, https://doi.org/10.3390/sym15061195 . . . . . **7**

Alina Bogoi, Sergiu Strătilă, Grigore Cican, Daniel-Eugeniu Crunțeanu and Constatin Levențiu
Impact of Stochastic Atmospheric Density on Satellite Orbit Stability
Reprinted from: *Symmetry* **2025**, *17*, 402, https://doi.org/10.3390/sym17030402 . . . . . **61**

Junjie Tang, Huafei Wang, Mingyue Zhao, Ping Sun, Yutao Hao and Zhiyuan Zhu
Weed Detection in Lily Fields Using YOLOv7 Optimized by Chaotic Harris Hawks Algorithm for Underground Resource Competition
Reprinted from: *Symmetry* **2025**, *17*, 370, https://doi.org/10.3390/sym17030370 . . . . . **86**

Anatolij K. Prykarpatski, Radosław A. Kycia and Volodymyr M. Dilnyi
On Superization of Nonlinear Integrable Dynamical Systems
Reprinted from: *Symmetry* **2025**, *17*, 125, https://doi.org/10.3390/sym17010125 . . . . . **116**

Mudassir Shams and Bruno Carpentieri
A New High-Order Fractional Parallel Iterative Scheme for Solving Nonlinear Equations
Reprinted from: *Symmetry* **2024**, *16*, 1452, https://doi.org/10.3390/sym16111452 . . . . . **132**

Muhammed Salih Sarıkaya, Yusuf Hamida El Naser, Sezgin Kaçar, İrfan Yazıcı and Adnan Derdiyok
Chaotic-Based Improved Henry Gas Solubility Optimization Algorithm: Application to Electric Motor Control
Reprinted from: *Symmetry* **2024**, *16*, 1435, https://doi.org/10.3390/sym16111435 . . . . . **158**

Vasile Dragan and Ioan-Lucian Popa
The Linear Quadratic Optimal Control Problem for Stochastic Systems Controlled by Impulses
Reprinted from: *Symmetry* **2024**, *16*, 1170, https://doi.org/10.3390/sym16091170 . . . . . **191**

Othman Abdullah Almatroud, Ma'mon Abu Hammad, Amer Dababneh, Louiza Diabi, Adel Ouannas, Amina Aicha Khennaoui and Saleh Alshammari
Multistability, Chaos, and Synchronization in Novel Symmetric Difference Equation
Reprinted from: *Symmetry* **2024**, *16*, 1093, https://doi.org/10.3390/sym16081093 . . . . . **210**

Rui Yang, Huaigu Tian, Zhen Wang, Wei Wang and Yang Zhang
Dynamical Analysis and Synchronization of Complex Network Dynamic Systems under Continuous-Time
Reprinted from: *Symmetry* **2024**, *16*, 687, https://doi.org/10.3390/sym16060687 . . . . . **223**

María A. Navascués and Ram N. Mohapatra
Fixed Point Dynamics in a New Type of Contraction in b-Metric Spaces
Reprinted from: *Symmetry* **2024**, *16*, 506, https://doi.org/10.3390/sym16040506 . . . . . **239**

Juan Carlos Vielma-Quintero, Edgar Giovanny Diaz-Segura and Juan Carlos Vielma
Influence of the Plan Structural Symmetry on the Non-Linear Seismic Response of Framed Reinforced Concrete Buildings
Reprinted from: *Symmetry* **2024**, *16*, 370, https://doi.org/10.3390/sym16030370 . . . . . **261**

S. A. Lurie, P. A. Belov and H. A. Matevossian
Symmetry Properties of Models for Reversible and Irreversible Thermodynamic Processes
Reprinted from: *Symmetry* **2023**, *15*, 2173, https://doi.org/10.3390/sym15122173 . . . . . **283**

Lazaros Moysis, Marcin Lawnik, Christos Volos, Murilo S. Baptista and Sotirios K. Goudos
Chaotic Maps with Tunable Mean Value—Application to a UAV Surveillance Mission †
Reprinted from: *Symmetry* **2023**, *15*, 2138, https://doi.org/10.3390/sym15122138 . . . . . **304**

Alina Bogoi, Cătălina-Ilinca Dan, Sergiu Strătilă, Grigore Cican and Daniel-Eugeniu Crunteanu
Assessment of Stochastic Numerical Schemes for Stochastic Differential Equations with "White Noise" Using Itô's Integral
Reprinted from: *Symmetry* **2023**, *15*, 2038, https://doi.org/10.3390/sym15112038 . . . . . **324**

Akanksha Verma, Wojciech Sumelka and Pramod Kumar Yadav
The Numerical Solution of Nonlinear Fractional Lienard and Duffing Equations Using Orthogonal Perceptron
Reprinted from: *Symmetry* **2023**, *15*, 1753, https://doi.org/10.3390/sym15091753 . . . . . **337**

A. E. Matouk, D. K. Almutairi, M. A. E. Herzallah, M. A. Abdelkawy and T. N. Abdelhameed
Symmetry in a Fractional-Order Multi-Scroll Chaotic System Using the Extended Caputo Operator
Reprinted from: *Symmetry* **2023**, *15*, 1582, https://doi.org/10.3390/sym15081582 . . . . . **356**

Stelios M. Potirakis, Pericles Papadopoulos, Niki-Lina Matiadou, Michael P. Hanias, Stavros G. Stavrinides, Georgios Balasis and Yiannis Contoyiannis
Spontaneous Symmetry Breaking in Systems Obeying the Dynamics of On–Off Intermittency and Presenting Bimodal Amplitude Distributions
Reprinted from: *Symmetry* **2023**, *15*, 1448, https://doi.org/10.3390/sym15071448 . . . . . **370**

Hasib Khan, Jehad Alzabut, Wafa F Alfwzan and Haseena Gulzar
Nonlinear Dynamics of a Piecewise Modified ABC Fractional-Order Leukemia Model with Symmetric Numerical Simulations
Reprinted from: *Symmetry* **2023**, *15*, 1338, https://doi.org/10.3390/sym15071338 . . . . . **387**

Marcin Lawnik, Lazaros Moysis and Christos Volos
A Family of 1D Chaotic Maps without Equilibria
Reprinted from: *Symmetry* **2023**, *15*, 1311, https://doi.org/10.3390/sym15071311 . . . . . **406**

Lazaros Moysis, Marcin Lawnik, Ioannis P. Antoniades, Ioannis Kafetzis, Murilo S. Baptista and Christos Volos
Chaotification of 1D Maps by Multiple Remainder Operator Additions—Application to B-Spline Curve Encryption
Reprinted from: *Symmetry* **2023**, *15*, 726, https://doi.org/10.3390/sym15030726 . . . . . **420**

Ștefana Agop, Dumitru Filipeanu, Claudiu-Gabriel Țigănaș, Claudia-Elena Grigoraș-Ichim, Lucia Moroșan-Dănilă, Alina Gavriluț, et al.
Towards a Holographic-Type Perspective in the Analysis of Complex-System Dynamics
Reprinted from: *Symmetry* **2023**, *15*, 681, https://doi.org/10.3390/sym15030681 . . . . . **447**

Sergio Elaskar, Ezequiel del Rio and Walkiria Schulz
Analysis of the Type V Intermittency Using the Perron-Frobenius Operator
Reprinted from: *Symmetry* **2022**, *14*, 2519, https://doi.org/10.3390/sym14122519 . . . . . **460**

About the Editor

Sergio Elaskar

Sergio Elaskar has obtained degrees in Aeronautical and Mechanical Engineering and a Doctorate in Engineering Sciences at the National University of Cordoba (UNC). He has also completed a Ph.D. in Aerospace Engineering at the Polytechnic University of Madrid (UPM).

Elaskar is a Plenary Full Professor at UNC, a Principal Researcher at the National Council for Scientific and Technical Research (CONICET), and a Category I Researcher at the Ministry of Education of Argentina. He has been director of the Doctorate program in Engineering Sciences for 6 years; founder-organizer professor of the Master of Science program in Aerospace Engineering, and for 5 years its director; and director for 5 years of the Institute for Advanced Studies in Engineering and Technology (UNC and CONICET).

Elaskar has published more than 400 scientific papers and has written 5 books. He has been the advisor of around 30 undergraduate theses and 21 graduate theses. He has given more than 20 invited lectures. He owns 1 invention patent and has developed several scientific software programs. He has directed approximately 30 R&D projects in Argentina. Internationally, he has been the director of 6 research projects in cooperation with Brazil, Spain, and France. For his research work, he has received awards in Argentina and abroad.

Elaskar has participated as a researcher in five advisory activities for companies and industries. Also, he has participated as Principal Investigator in two advisory activities, one for the company "New Generation Space Vehicles" (VENG) and another for the National Commission for Space Activities (CONAE).

He has worked/works on different research topics: chaotic intermittency, nonlinear dynamics, the flow of granular materials, the flow of high enthalpy and chemically active gases, explosion simulations, magneto-hydrodynamics and plasma, space propulsion, solar physics, and turbulent flow simulation.

Preface

Nonlinear dynamics and chaos represent a vibrant and significant area of study and research, greatly enhancing our understanding of different phenomena in several branches of knowledge.

This compilation serves as a comprehensive review of recent advancements in nonlinear dynamical systems and chaotic behavior. It includes the editorial, one review article, and twenty-one research papers published recently in MDPI's journal, *Symmetry*, under the thematic title "Symmetry in Nonlinear Dynamics and Chaos II."

This volume elucidates recent developments related to chaotic systems and nonlinear dynamics across multiple scientific and engineering disciplines. It encompasses papers focusing on both discrete-time and continuous-time systems, alongside their applications in various modeling contexts.

The contents of this reprint are particularly relevant for graduate students and researchers across a diverse array of fields, including physics, chemistry, bio-medicine, social and economic sciences, engineering, etc.

Finally, I extend my sincere appreciation to all contributors for their valuable insights and efforts in this publication. My thanks to the National University of Cordoba and CONICET for funding my work during the time I spent editing this reprint. I also wish to express my gratitude to Ms. Ida Li, the Managing Editor. Without her invaluable support, this reprint would not have been possible.

Sergio Elaskar
Guest Editor

symmetry

MDPI

Editorial

Symmetry in Nonlinear Dynamics and Chaos II

Sergio Elaskar

Department of Aerospace Engineering, FCEFyN and Institute of Advanced Studies in Engineering and Technology (IDIT), National University of Cordoba and CONICET, Córdoba 5000, Argentina; selaskar@unc.edu.ar

Nonlinear dynamics and chaos are vibrant fields of physics that have enhanced our understanding of various phenomena. This Special Issue reviews recent advancements in nonlinear dynamical systems and chaotic behavior. It includes 22 papers recently published in MDPI's *Symmetry* under the thematic title "Symmetry in Nonlinear Dynamics and Chaos II". One of these papers is a review article [1], which provides a comprehensive overview of different types of intermittency. Additionally, it explains two recent formulations for evaluating reinjection processes. These new theoretical formulations have explained several previously termed pathological tests. The theoretical background also addresses the effects of noise on the reinjection mechanism [2].

In Ref. [3], Bogoi and coauthors examine a system of second-order stochastic ordinary differential equations (SDEs) related to satellite motion. This paper evaluates the accuracy and stability of five finite difference schemes for solving these SDEs. The authors discuss the uniformity of stabilization behavior in the stochastic trajectories of a dynamical system and analyze the impact of noise on the results. The graphical representations of the SDEs presented in this paper illustrate the symmetry of stochastic trajectories around the solution of the deterministic system.

Junjie Tang and coauthors analyze the decline in lily production caused by weed infestation [4]. They propose an advanced weed detection method that combines symmetry-based convolutional neural networks [5] with metaheuristic optimization. To improve detection efficiency, they introduce an optimized YOLOv7-Tiny model, which incorporates dynamic pruning and knowledge distillation. This approach reduces computational complexity while maintaining high accuracy. The study presents a high-performance, lightweight, and scalable solution for real-time precision weed management in lily fields, offering valuable insights for agricultural automation and smart farming applications.

In Ref. [6], Prykarpatski and coauthors investigate the superization problem in integrable nonlinear dynamical systems on functional manifolds. They focus on a quantum many-particle Schrödinger–Davydov model defined on an axis. The authors demonstrate that a broad class of classical Lax-type integrable nonlinear dynamical systems on axes exists, for which a superization scheme can be effectively developed. This scheme involves a reasonable superization of the related Lax-type representation by transitioning from the basic algebra of pseudo-differential operators on the axis to the corresponding super-algebra of super-pseudo-differential operators on the super-axis.

Following previous studies [7], Shams and Carpentieri present a new fractional parallel technique for solving nonlinear equations [8]. By employing a dynamical systems approach, they identify optimal parameter values. The symmetry observed in the dynamical planes for various fractional parameters demonstrates the stability of the method and its effectiveness in addressing nonlinear problems. This approach has been successfully applied to several engineering challenges.

Sarıkaya and coauthors present a novel metaheuristic optimization method that combines the Henry Gas Solubility Optimization (HGSO) technique with symmetric chaotic systems [9]. This new approach is called Chaotic Henry Gas Solubility Optimization (CHGSO), and its primary objective is to enhance the performance of the HGSO method. The authors applied CHGSO to 47 benchmark functions to optimize parameters for a PID controller used in the speed control of a DC motor. The results demonstrate that the proposed method achieved the best performance in 43 of the benchmark functions, surpassing other algorithms.

In Ref. [10], Dragan and Popa discuss the linear quadratic (LQ) optimal control problem for stochastic systems that are controlled by impulses over an infinite time horizon. They demonstrate that the well-posedness of the optimal control problem is assured by the existence of a maximal and bounded solution to the associated backward jump linear matrix difference equation (BJMLDE) that incorporates a Riccati-type jumping operator. Furthermore, the authors indicate that if the BJMLDE with a Riccati-type jumping operator has a maximal solution that meets a specific sign condition, then the optimal control problem is feasible. This feasibility is contingent on either having an optimal control in a state feedback form or the maximal solution of the BJMLDE being a stabilizing solution.

Almatroud and collaborators introduce a new third-order symmetric difference equation, which has been transformed into a 3D discrete symmetric map [11]. They demonstrate that this map exhibits several nonlinear characteristics, including multistability, chaos, and hyperchaos [12]. Additionally, they introduce a nonlinear controller designed to stabilize the symmetric map and synchronize two unified symmetric maps.

In Ref. [13], Yang and coauthors investigate the synchronization issue between complex dynamic networks [14] and chaotic systems [15]. They propose a state estimation scheme for multi-layer complex networks by using a state observer. The authors analyze a specific class of complex dynamic networks where the nodes correspond one-to-one. They assess the stability of the system by using the primary stability function analysis method and demonstrate the effectiveness of the network state observer in achieving synchronization between the target system and the complex dynamic network.

Navascués and Mohapatra introduce new forms of contractivity that extend the traditional concept of Banach contraction [16]. They also provide sufficient conditions for the existence of fixed points and common fixed points. The authors expand, to some degree, the modern theory of fixed points and common fixed points for self-maps defined on b-metric and quasi-normed spaces, along with their approximation methods.

The determination of the vulnerability of concrete buildings at slopes under the action of earthquakes is a topic of current research [17]. Vielma-Quintero and coauthors investigate buildings situated on slopes in densely populated urban areas, a common situation in Latin American cities that face high seismic risks [18]. They examine the asymmetry of medium-height reinforced concrete-frame buildings on variable inclines and how this affects their nonlinear response, evaluated through displacements, rotations, and damage. The study reveals the significant influence of structural asymmetry on nonlinear response parameters, such as ductility, transient inter-story drifts, and roof rotations. Additionally, it uncovers demand distributions for structural elements that exceed traditional analysis and expectations in earthquake-resistant design.

Coupled processes of deformation in media, considering heat and mass transfer, have been subjects of scientific interest in recent years [19,20]. Lurie and coauthors have developed a variational model for irreversible deformation processes that encompasses a broader range of coupled effects [21]. Their approach introduces non-integrable variational forms that clearly distinguish between dissipative processes and reversible deformation processes. They have established the fundamental nature of the symmetry and anti-symmetry proper-

ties of tensors related to multi-indices, which characterize independent arguments in the bi-linear forms used within the variational formulation of thermo-mechanical models. Additionally, an algorithm for creating variational models of dissipative irreversible processes has been proposed. This algorithm involves identifying the necessary number of dissipative channels and incorporating them into the established model of a reversible process.

In Ref. [22], Moysis and collaborators investigate the task of constructing maps, where statistical measures, such as the mean value, can be effectively controlled by adjusting the parameters of the map. They consider a family of piecewise maps, which include three control parameters that influence the endpoint interpolations. These maps can achieve a diverse range of values for their statistical mean. To illustrate this, the authors present chaotic path surveillance as a potential application for the maps they have designed. As an application case, the authors propose a strategy for the chaotic maneuvering of an unmanned aerial vehicle [23].

Bogoi and coauthors investigate the weak and strong convergence of six numerical schemes applied to multiplicative noise, additive noise, and a system of stochastic differential equations [24]. Among these methods, the Efficient Runge–Kutta technique [25] stands out as the top performer, demonstrating the best convergence properties across all scenarios, including the challenging case of multiplicative noise. The authors consider that this finding highlights the importance of developing advanced numerical techniques specifically tailored for stochastic systems.

Verma, Sumelka, and Yadav propose an approximation algorithm that utilizes Legendre and Chebyshev artificial neural networks to explore approximate solutions for fractional Lienard and Duffing equations involving a Caputo fractional derivative [26]. Their approach transforms the given nonlinear fractional differential equation into an unconstrained minimization problem. They also examine several non-integer order problems to verify their theoretical results. The numerical results demonstrate that the proposed strategies achieve superior outcomes compared to existing numerical techniques [27–29].

In Ref. [30], Matouk and collaborators explore the complex dynamics of a fractional-order multi-scroll chaotic system based on the extended Gamma function. They begin by introducing the extended left and right Caputo fractional differential operators. The authors propose a new operator that incorporates an additional fractional parameter, providing a higher degree of freedom. This enhancement allows the system to exhibit a greater variety of complex dynamics. The rich and complex dynamics observed include coexisting one-scroll chaotic attractors, two-scroll chaotic attractors, and approximate periodic cycles. These dynamics are shown to persist for a shorter duration compared to the corresponding states of the integer-order version of the multi-scroll system.

Potirakis and coauthors confirm that a recently introduced symbolic time-series-analysis method, known as the "PNA-based symbolic time-series analysis method" (PNA-STSM), can accurately obtain the exponent of the distribution of waiting times in the symbolic dynamics of two symbols generated by the 3D Ising model when it is in a critical state [31]. Following the numerical validation of PNA-STSM's reliability, three examples are presented to demonstrate its application to systems that exhibit on–off intermittency dynamics [32]. The findings suggest that identifying a system's proximity to spontaneous symmetry breaking offers a deeper understanding of its dynamics in terms of criticality.

Khan and collaborators introduce a nonlinear dynamical system for leukemia that utilizes a piecewise modified ABC fractional-order derivative [33]. They analyze this system through both theoretical and computational methods, focusing on the crossover effects of the model. The numerical analysis relies on a computational method developed by the authors, which has been implemented using Lagrange's interpolation polynomial. The newly constructed model is studied to determine the existence of solutions, its stability,

and to present computational results. The authors suggest expanding their research by integrating the stochastic version, using Ref. [34] as a guiding resource.

In Ref. [35], Lawnik and coauthors propose a family of piecewise chaotic maps. This family is characterized by the nonlinear functions used for each piece of the map, which can be either symmetric or asymmetric. By imposing constraints on the shape of each piece, the resulting maps do not have equilibria and can exhibit chaotic behavior. As such, this family falls under the category of systems with hidden attractors [36]. The authors provide several examples of chaotic maps that demonstrate fractal-like, symmetrical patterns at the transition between chaotic and non-chaotic behavior. The authors are working to extend the methodology to a broader range of multi-dimensional maps. The design constraint regarding the absence of fixed points must be met by every state of the map.

Moysis and collaborators introduce a chaotification technique designed to increase the complexity of chaotic maps [37]. This technique is an extension of those developed in Ref. [38]. It involves combining the results from multiple scaling of the map's value for the next iteration. The maps produced using this approach can attain a high Lyapunov exponent value, which can be adjusted through careful parameter tuning. As a potential application for these transformed maps, the encryption of B-spline curves and patches are explored.

Agop and coauthors provide a description of complex systems using a holographic perspective [39]. To achieve this, they utilize Scale Relativity Theory, applying Schrödinger- and Madelung-type scenarios to the dynamics of these systems. This approach reveals a Riccati-type gauge invariance that plays a crucial role in the dynamics of complex systems. As a result, it gives rise to conservation laws, simultaneity, and synchronization among the structural units' dynamics, as well as temporal patterns through harmonic mappings.

Elaskar and collaborators introduce a methodology to study the reinjection process in type V intermittency [40]. The authors implement the Perron–Frobenius operator technique [41]. Using this approach, they calculate the reinjection probability density function (RPD) and the probability density of the laminar lengths. They analyze a family of maps with both discontinuous and continuous RPDs. Several tests are conducted to compare the proposed technique with the classical theory of intermittency, the M function methodology, and numerical data. The new technique can accurately capturenumerical data. Thus, the scheme presented is a useful tool for theoretically evaluating the statistical variables related to type V intermittency.

Funding: This research received no external funding.

Conflicts of Interest: The author declares no conflicts of interest.

References

1. Elaskar, S.; del Rio, E. Review of Chaotic Intermittency. *Symmetry* **2023**, *15*, 1195. [CrossRef]
2. Elaskar, S.; del Rio, E. *New Advances on Chaotic Intermittency and Applications*; Springer: New York, NY, USA, 2017; ISBN 978-3-319-47836-4.
3. Bogoi, A.; Strătilă, S.; Cican, G.; Crunteanu, D.; Leventiu, C. Impact of Stochastic Atmospheric Density on Satellite Orbit Stability. *Symmetry* **2025**, *17*, 402. [CrossRef]
4. Tang, J.; Wang, H.; Zhao, M.; Sun, P.; Hao, Y.; Zhu, Z. Weed Detection in Lily Fields Using YOLOv7 Optimized by Chaotic Harris Hawks Algorithm for Underground Resource Competition. *Symmetry* **2025**, *17*, 370. [CrossRef]
5. Jiang, H.; Zhang, C.; Qiao, Y.; Zhang, Z.; Zhang, W.; Song, C. CNN Feature Based Graph Convolutional Network for Weed and Crop Recognition in Smart Farming. *Comput. Electron. Agric.* **2020**, *174*, 105450. [CrossRef]
6. Prykarpatski, A.K.; Kycia, R.A.; Dilnyi, V.M. On Superization of Nonlinear Integrable Dynamical Systems. *Symmetry* **2025**, *17*, 125. [CrossRef]
7. Shams, M.; Carpentieri, B. On Highly Efficient Fractional Numerical Method for Solving Nonlinear Engineering Models. *Mathematics* **2023**, *11*, 4914. [CrossRef]

8. Shams, M.; Carpentieri, B. A New High-Order Fractional Parallel Iterative Scheme for Solving Nonlinear Equations. *Symmetry* **2024**, *16*, 1452. [CrossRef]
9. Sarıkaya, M.S.; El Naser, Y.H.; Kaçar, S.; Yazıcı, I.; Derdiyok, A. Chaotic-Based Improved Henry Gas Solubility Optimization Algorithm: Application to Electric Motor Control. *Symmetry* **2024**, *16*, 1435. [CrossRef]
10. Dragan, V.; Popa, I. The Linear Quadratic Optimal Control Problem for Stochastic Systems Controlled by Impulses. *Symmetry* **2024**, *16*, 1170. [CrossRef]
11. Almatroud, O.A.; Hammad, M.A.; Dababneh, A.; Diabi, L.; Ouannas, A.; Khennaoui, A.A.; Alshammari, S. Multistability, Chaos, and Synchronization in Novel Symmetric Difference Equation. *Symmetry* **2024**, *16*, 1093. [CrossRef]
12. Zhou, X.; Sun, K.; Wang, H.; Yao, Z. Coexisting Hyperchaos and Multistability in a Discrete Memristor-Coupled Bi-Neuron Model. *Nonlinear Dyn.* **2024**, *112*, 9547–9561. [CrossRef]
13. Yang, R.; Tian, H.; Wang, Z.; Wang, W.; Zhang, Y. Dynamical Analysis and Synchronization of Complex Network Dynamic Systems under Continuous-Time. *Symmetry* **2024**, *16*, 687. [CrossRef]
14. Strogatz, S.H. Exploring Complex Networks. *Nature* **2001**, *410*, 268–276. [CrossRef]
15. Nayfeh, A.H.; Balachandran, B. *Applied Nonlinear Dynamics*; Wiley: New York, NY, USA, 1995; ISBN 0-471-59348-6.
16. Navascués, M.A.; Mohapatra, R.N. Fixed Point Dynamics in a New Type of Contraction in b-Metric Spaces. *Symmetry* **2024**, *16*, 506. [CrossRef]
17. Fotopoulou, S.D.; Pitilakis, K.D. Vulnerability Assessment of Reinforced Concrete Buildings at Precarious Slopes Subjected to Combined Ground Shaking and Earthquake Induced Landslide. *Soil Dyn. Earthq. Eng.* **2017**, *93*, 84–98. [CrossRef]
18. Vielma-Quintero, J.C.; Diaz-Segura, E.G.; Vielma, J.C. Influence of the Plan Structural Symmetry on the Non-Linear Seismic Response of Framed Reinforced Concrete Buildings. *Symmetry* **2024**, *16*, 370. [CrossRef]
19. Demirel, Y.; Gerbaud, V. Fundamentals of Nonequilibrium Thermodynamics. In *Nonequilibrium Thermodynamics*; Elsevier: Amsterdam, The Netherlands, 2019; pp. 135–186. [CrossRef]
20. Hütter, M.; Theo, A.; Tervoort, T.A. Coarse Graining in Elasto-viscoplasticity: Bridging the Gap from Microscopic Fluctuations to Dissipation. *Adv. Appl. Mech.* **2009**, *42*, 253–317. [CrossRef]
21. Lurie, S.A.; Belov, P.A.; Matevossian, H.A. Symmetry Properties of Models for Reversible and Irreversible Thermodynamic Processes. *Symmetry* **2023**, *15*, 2173. [CrossRef]
22. Moysis, L.; Lawnik, M.; Volos, C.; Baptista, M.; Goudos, S. Chaotic Maps with Tunable Mean Value—Application to a UAV Surveillance Mission. *Symmetry* **2023**, *15*, 2138. [CrossRef]
23. Curiac, D.I.; Volosencu, C. Path Planning Algorithm Based on Arnold Cat Map for Surveillance UAVs. *Def. Sci. J.* **2015**, *65*, 483–488. [CrossRef]
24. Bogoi, A.; Dan, C.; Strătilă, S.; Cican, G.; Crunteanu, D. Assessment of Stochastic Numerical Schemes for Stochastic Differential Equations with "White Noise" Using Itô's Integral. *Symmetry* **2023**, *15*, 2038. [CrossRef]
25. Newton, N.J. Asymptotically Efficient Runge-Kutta Methods for a Class of Ito and Stratonovich Equations. *SIAM J. Appl. Math.* **1991**, *51*, 542–567. [CrossRef]
26. Verma, A.; Sumelka, W.; Yadav, P. The Numerical Solution of Nonlinear Fractional Lienard and Duffing Equations Using Orthogonal Perceptron. *Symmetry* **2023**, *15*, 1753. [CrossRef]
27. Singh, H.; Srivastava, H.M. Numerical Investigation of the Fractional-Order Liénard and Duffing Equations Arising in Oscillating Circuit Theory. *Front. Phys.* **2020**, *8*, 120. [CrossRef]
28. Nourazar, S.; Mirzabeigy, A. Approximate Solution for Nonlinear Duffing Oscillator with Damping Effect Using the Modified Differential Transform Method. *Sci. Iran. B* **2013**, *20*, 364–368.
29. Ejikeme, C.L.; Oyesanya, M.O.; Agbebaku, D.F.; Okofu, M.B. Solution to Nonlinear Duffing Oscillator with Fractional Derivatives Using Homotopy Analysis Method (HAM). *Glob. J. Pure Appl. Math.* **2018**, *14*, 1363–1388.
30. Matouk, A.E.; Almutairi, D.K.; Herzallah, M.A.E.; Abdelkawy, M.A.; Abdelhameed, T.N. Symmetry in a Fractional-Order Multi-Scroll Chaotic System Using the Extended Caputo Operator. *Symmetry* **2023**, *15*, 1582. [CrossRef]
31. Potirakis, S.M.; Papadopoulos, P.; Matiadou, N.; Hanias, M.P.; Stavrinides, S.G.; Balasis, G.; Contoyiannis, Y. Spontaneous Symmetry Breaking in Systems Obeying the Dynamics of On–Off Intermittency and Presenting Bimodal Amplitude Distributions. *Symmetry* **2023**, *15*, 1448. [CrossRef]
32. Heagy, J.F.; Platt, N.; Hammel, S.M. Characterization of On-Off Intermittency. *Phys. Rev. E* **1994**, *49*, 1140–1150. [CrossRef]
33. Khan, H.; Alzabut, J.; Alfwzan, W.F.; Gulzar, H. Nonlinear Dynamics of a Piecewise Modified ABC Fractional-Order Leukemia Model with Symmetric Numerical Simulations. *Symmetry* **2023**, *15*, 1338. [CrossRef]
34. Ain, Q.T.; Nadeem, M.; Akgul, A.; De la Sen, M. Controllability of Impulsive Neutral Fractional Stochastic Systems. *Symmetry* **2022**, *14*, 2612. [CrossRef]
35. Lawnik, M.; Moysis, L.; Volos, C. A Family of 1D Chaotic Maps without Equilibria. *Symmetry* **2023**, *15*, 1311. [CrossRef]

36. Zhang, S.; Wang, X.; Zeng, Z. A simple no-equilibrium chaotic system with only one signum function for generating multi-directional variable hidden attractors and its hardware implementation. *Chaos Interdiscip. J. Nonlinear Sci.* **2020**, *30*, 053129. [CrossRef]
37. Moysis, L.; Lawnik, M.; Antoniades, I.P.; Kafetzis, I.; Baptista, M.; Volos, C. Chaotification of 1D Maps by Multiple Remainder Operator Additions—Application to B-Spline Curve Encryption. *Symmetry* **2023**, *15*, 726. [CrossRef]
38. Moysis, L.; Kafetzis, I.; Baptista, M.S.; Volos, C. Chaotification of One-Dimensional Maps Based on Remainder Operator Addition. *Mathematics* **2022**, *10*, 2801. [CrossRef]
39. Agop, S.; Filipeanu, D.; Tigănas, C.; Grigoras-Ichim, C.; Morosan-Dănilă, L.; Gavrilut, A.; Agop, M.; Stefan, G. Towards a Holographic-Type Perspective in the Analysis of Complex-System Dynamics. *Symmetry* **2023**, *15*, 681. [CrossRef]
40. Elaskar, S.; del Rio, E.; Schulz, W. Analysis of the Type V Intermittency Using the Perron-Frobenius Operator. *Symmetry* **2022**, *14*, 2519. [CrossRef]
41. Elaskar, S.; del Rio, E.; Zapico, E. Evaluation of the Statistical Properties for Type-II Intermittency Using the Perron-Frobenius Operator. *Nonlinear Dyn.* **2016**, *86*, 1107–1116. [CrossRef]

Disclaimer/Publisher's Note: The statements, opinions and data contained in all publications are solely those of the individual author(s) and contributor(s) and not of MDPI and/or the editor(s). MDPI and/or the editor(s) disclaim responsibility for any injury to people or property resulting from any ideas, methods, instructions or products referred to in the content.

symmetry

MDPI

Review

Review of Chaotic Intermittency

Sergio Elaskar [1,*,†] and Ezequiel del Río [2,†]

[1] Departamento de Aeronáutica, Instituto de Estudios Avanzados en Ingeniería y Tecnología (IDIT), FCEFyN, Universidad Nacional de Córdoba and CONICET, Córdoba 5000, Argentina
[2] Departamento de Física Aplicada, ETSI de Aeronáutica y Espacio, Universidad Politécnica de Madrid, 28040 Madrid, Spain; ezequiel.delrio@upm.es
* Correspondence: selaskar@unc.edu.ar
† These authors contributed equally to this work.

Abstract: Chaotic intermittency is characterized by a signal that alternates aleatory between long regular (pseudo-laminar) phases and irregular bursts (pseudo-turbulent or chaotic phases). This phenomenon has been found in physics, chemistry, engineering, medicine, neuroscience, economy, etc. As a control parameter increases, the number of chaotic phases also increases. Therefore, intermittency presents a continuous route from regular behavior to chaotic motion. In this paper, a review of different types of intermittency is carried out. In addition, the description of two recent formulations to evaluate the reinjection processes is developed. The new theoretical formulations have allowed us to explain several tests previously called pathological. The theoretical background also includes the noise effects in the reinjection mechanism.

Keywords: chaotic intermittency; review; types; maps; RPD; noise

1. Introduction

Chaos theory has many fields of investigation, such as the different routes to chaos. One route is chaotic intermittency, which has been observed in several subjects. Batchelor and Townsend, in the middle of the previous century, used the word intermittency to give an account of the fluctuating velocity in turbulent flows [1]. Subsequently, intermittency has been found in many and varied physical phenomena such as the nonlinear behavior of transient periodic plasma and conducting fluids [2–5], fluid mechanics and turbulent flows [6–10], Rayleigh–Benard convection [11], electronic digital oscillator [12], logistic map [13], Alfven wave-fronts and derivative nonlinear Schrodinger equation [14,15], premixed combustion [16], Lorenz system [17], coupled oscillators [18–21], catalytic reactors [22], Ginzburg Landau equation [23], solar cycles [24], spatiotemporal chaos [25,26], thermoacoustic instability [27], control chaos [28], etc. Furthermore, chaotic intermittency is also observed in systems in economics [29,30], medicine, [31,32], neuroscience [33,34], genetics [35], and marine biology [36,37]. Therefore, a more suitable understanding of chaotic intermittency can collaborate to describe these phenomena accurately. In addition, the correct description of chaotic intermittency possesses significance for systems whose precise equations are partially or totally unknown.

There are three classical routes by which continuous or discrete dynamical systems can evolve from regular functioning to chaotic behaviors: quasi-periodic route, period-doubling scenario, and intermittency [38]. In chaotic intermittency, the dynamical system solutions display alternation between regular or pseudo-laminar phases and chaotic bursts or non-regular phases. The laminar phases correspond to pseudo-equilibrium, pseudo-periodic solutions, and quasi-invariant objects close to them that the system may consume for a long time. On the other hand, the burst ones are consistent with chaotic evolution [39].

Approximately 50 years ago, chaotic intermittency was categorized into three different types, known as I, II, and III [17,40,41]. This classification was according to the fixed point

eigenvalues in the local Poincaré map or the Floquet multipliers of the continuous-system periodic solution [38,39,42]. Later works introduced other types of chaotic intermittency such as on–off, eyelet, ring, and in–out, type-X, and type-V [43–48].

The monodromy operator multipliers determine the type of intermittency [49]. Type-I intermittency happens if the periodic solution loses its stability by a cyclic-fold bifurcation [50], then a multiplier goes away from the unit circle by the real axis across +1. Type-II intermittency is born in a sub-critical Hopf bifurcation or a Neimark–Sacker bifurcation [38,51]. Accordingly, two complex-conjugate Floquet multipliers gets out the unit circle. Therefore, it is a consequence of a bifurcation scenario for T^2 torus breakdown. A sub-critical period-doubling bifurcation generates a type-III intermittency. In this bifurcation, an unstable period-2 orbit encounters and destabilizes a stable period-1 orbit. Type-III intermittency presents a progressive increase throughout the laminar phase of a period-2 component in the motion [52]. In addition, a one-dimensional map $F(x)$ showing a sub-critical period-doubling bifurcation possesses a positive Schwartzian derivative, $SF(x)$:

$$SF(x) = F'''(x)/F'(x) - 1.5\left(F''(x)/F'(x)\right)^2 > 0\,. \tag{1}$$

Chaotic intermittency may be investigated using one-dimensional maps (Poincaré maps) [38,39,42]. These maps have two main characteristics: a particular local map and a reinjection process or reinjection mechanism. The specific local map depicts the type of intermittency. The reinjection mechanism returns the trajectories from the chaotic regime to the laminar one. Therefore, the reinjection mechanism determines the reinjection probability density function (RPD). It considers only points in the laminar region, but in the preceding period they have not been there. Note that the RPD is used to describe the reinjection process and is defined by the chaotic dynamics of the system itself. The probability of the reinjection points being in a particular sub-interval inside the laminar interval equals the integral of the RPD in the sub-interval. The RPD function specifies the probability that trajectories are returned (reinjected) into the laminar zone around to the unstable or even the vanished fixed point, and together with the local map outline all the dynamical features of the system.

The precise determination of the RPD function is extremely significant in correctly describing the chaotic intermittency phenomenon. In addition, the evaluation of the RPD function from experimental or numerical is a hard task due to the large amount of data involved, and it is difficult to estimate the statistical fluctuations generated in the numerical result and experimental data. Several strategies were utilized to calculate the RPD function. Most results in the classical theory of chaotic intermittency were obtained considering uniform reinjection inside the laminar interval [41,42,53]. Other implemented RPD functions were constructed using specific characteristics of the nonlinear processes. For example, in type-I intermittency the reinjection was restricted to the fixed point [54], and for the intermittency of type-III the RPD function was assumed proportional to $(x-a)^{-1/2}$, with $a =$ constant [55]. Notwithstanding, these RPD functions cannot be generalized to other nonlinear systems.

Two new methodologies together with their theoretical background to obtain the RPD function were introduced in recent years. One of them is the M function methodology [56–64]. This methodology introduces a generalized power law for the RPD. It has been shown to be very accurate for a broad class of one-dimensional maps showing type-I, II, III, and V intermittencies. In addition, the M function methodology includes the classical approximation because it contains the uniform reinjection as a particular case. The second one is called the continuity technique. It utilizes the Perron–Frobenius operator to compute the reinjection probability density function. In the same way as the methodology of the M function, the continuity technique has been shown to be accurate for several maps displaying different types of intermittency [65–67].

To more precisely describe the intermittency phenomenon, other statistical functions are used, such as the probability density of the laminar lengths ($\psi(l)$), the average laminar length ($\bar{l}$), and the characteristic relation ($\bar{l} = \bar{l}(\varepsilon)$). Nonetheless, these functions depend on

the RPD. To calculate them, we previously have to know the reinjection probability density function [39,42].

The RPD and the other statistical functions used to describe the chaotic intermittency are affected by the noise and the lower boundary of reinjection (LBR). The M function methodology has been extended to incorporate both phenomena [68–70].

This paper presents a review of chaotic intermittency, with an emphasis on the evaluation of the RPD and other statistical functions.

2. Types of Chaotic Intermittency

Let us analyze a periodic solution of an autonomous continuous-time system. It is stable for some values of the control parameters. At that time, if a control parameter is modified until the periodic solution loses stability, the development of the solution shall depend on how the Floquet multipliers go away from the unit circle in the complex plane [38,42,53]. Note that the metamorphoses of a family of solutions around a closed orbit is a complex problem of bifurcation theory [71].

The existence of type-I, II, and III intermittency depends on the monodromy operator multiplier. Type-I intermittency occurs by a cyclic-fold bifurcation, then a multiplier goes away from the unit circle across +1. Type-II intermittency is born in a sub-critical Hopf bifurcation (or a Neimark–Sacker bifurcation), in which two complex-conjugate multipliers move away from the unit circle. Finally, type-III intermittency appears if a multiplier gets out the unit circle by -1, and a sub-critical period-doubling bifurcation happens [38,49,51].

2.1. Type-I Intermittency

Type-I intermittency is probably the most studied intermittency. Numerous books and papers describe it. When a control parameter surpasses the threshold value, type-I intermittency is born in a cyclic-fold bifurcation, then the fixed point of the Poincaré map vanishes.

To introduce the classic theoretical model for different types of intermittency, we use the following nonlinear system:

$$\frac{d\mathbf{x}}{dt} = \mathbf{f}(\mathbf{x}, \varepsilon) \tag{2}$$

where $\mathbf{x} \in \mathbf{R}^n$ is the variable vector, $\mathbf{f} \in \mathbf{R}^n$ is the vector field, and ε is a control parameter.

For $\varepsilon > \varepsilon_c$, a monodromy operator multiplier (or Floquet multiplier) related with a periodic solution of Equation (2) goes away the unit circle by +1, starting a discontinuous or catastrophic cyclic-fold bifurcation (bifurcation of codimension-one). The manifold of this multiplier possesses significant information related to intermittency—in other directions, there is dissipation [38]. Accordingly, to understand intermittency, we can study only a one-dimensional map associated with this manifold $x_{n+1} = F(x_n, \varepsilon)$, where $x_n, F \in \mathbf{R}$.

For type-I intermittency, the characteristic local map is [72]:

$$x_{n+1} = \varepsilon + x_n + a x_n^2 \tag{3}$$

The value of control parameter ε determines the number and stability of the fixed points of this map. For $\varepsilon < 0$, two fixed points exist. One is stable, and the other is unstable. When $\varepsilon = 0$, both fixed points collide and meet in only one fixed point. Finally, for $\varepsilon > 0$, the map does not have fixed points (tangent bifurcation).

When $\varepsilon > 0$, there is a narrow channel. The distance across the channel depends on ε. The trajectories spend a long time crossing the tunnel. The zone around the vanished fixed point determines the laminar interval. Accordingly, inside the laminar interval the trajectories are near to the disappeared fixed point. Nevertheless, they can not come to it.

To achieve type-I intermittency, in addition to the local map, a reinjection mechanism has to exist. The local map is given by Equation (3); however, the reinjection depends on the nonlinear map. Outside the channel, the trajectories show chaotic behavior. However, they return inside the narrow channel by the reinjection process. Usually, each trajectory returns to different points inside the laminar interval. The reinjection probability density

function, $\phi(x)$, determines the probability that trajectories are reinjected in the x-point. Therefore, it is the core of the statistical performance of chaotic intermittency.

In this subsection, we consider that the lower boundary reinjection point (LBR) coincides with the lower limit point of the laminar region. Consequently, the reinjection process occurs in the complete laminar interval [39].

We have previously established the significance of the RPD function in describing the chaotic intermittency phenomenon. The classical formulation for chaotic intermittency establishes a constant RPD. Consequently, reinjection probability is the same for all points in the laminar interval:

$$\phi(x) = k \tag{4}$$

where k is a constant value. Equation (4) implies uniform reinjection.

The laminar length or the length of the laminar interval is the number of iterations needed by the trajectory to cross the laminar interval. Accordingly, it is an integer number. We can describe the laminar length as the "time" utilized by each trajectory to move through the laminar zone. Note that reinjection point x determines the length of the laminar interval. For type-I intermittency, a reinjected trajectory progresses through the narrow channel until it moves away from the laminar interval. For $0 < \varepsilon \ll 1$, we can approximate the map (3) as a differential equation [42]:

$$\frac{dx}{dl} = \varepsilon + ax^2 \tag{5}$$

where we have considered $x_{n+1} - x_n \approx \frac{dx}{dl}$. Integrating this equation, we obtain the laminar length, l:

$$l(x,c) = \frac{1}{\sqrt{a\varepsilon}}\left[\arctan\left(\frac{c}{\sqrt{\varepsilon/a}}\right) - \arctan\left(\frac{x}{\sqrt{\varepsilon/a}}\right)\right] \tag{6}$$

where c is the upper limit of the laminar interval. Note that the laminar length does not depend on the reinjection mechanism; it only depends on the local map given by Equation (3).

The probability density of the laminar lengths, here called $\psi(l,c)$, outlines the probability of finding laminar lengths between l and $l + dl$ [42]:

$$\psi(l,c) = \phi[X(l,c)]\left|\frac{dX(l,c)}{dl}\right|; \tag{7}$$

in this last equation, $X(l,c)$ is the inverse of the laminar length given by Equation (6):

$$X(l,c) = \sqrt{\frac{\varepsilon}{a}}\tan\left[\tan^{-1}\left(\sqrt{\frac{a}{\varepsilon}}c\right) - \sqrt{a\varepsilon}\,l\right]. \tag{8}$$

The average laminar length, here called $\bar{l}$, is calculated as

$$\bar{l} = \int_0^{l_m} \psi(l,c)l(x,c)dl = \int_{-c}^{c} \phi(x)l(x,c)dx = \frac{1}{\sqrt{a\varepsilon}}\arctan\left(c\sqrt{\frac{a}{\varepsilon}}\right) \tag{9}$$

where l_m is the highest laminar length, which is obtained as $l_m = l(-c,c)$. Note that $l(c,c) = 0$.

The characteristic relation describes the dependence of average laminar length, $\bar{l}$, with the control parameter, ε. For type-I intermittency, if $c\frac{\sqrt{a}}{\sqrt{\varepsilon}} \gg 1$, it results in:

$$\bar{l} \propto \frac{1}{\sqrt{\varepsilon}}. \tag{10}$$

In general, the characteristic relation can be expressed as [39]:

$$\bar{l} \propto \varepsilon^{-\beta}. \tag{11}$$

From Equations (10) and (11), we can observe $\beta = 1/2$ for type-I intermittency.

2.2. Type-III Intermittency

Type-III intermittency starts in a sub-critical period-doubling bifurcation. Therefore, an unstable period-2 orbit collides with a stable period-1 orbit and destabilizes it. A Floquet multiplier moves away to the unit circle by -1, while the others multiplies are inside the unit circle. The information to describe type-III intermittency is in the manifold related to the unstable Floquet multiplier. Type-III intermittency can be analyzed using a map associated with this manifold, $F(x, \varepsilon)$ [38,39].

A local map can be written as

$$x_{n+1} = F(x_n) = -(1+\varepsilon)x_n + a_2\, x_n^2 + a_3\, x_n^3 + \dots \tag{12}$$

where $0 < \varepsilon \ll 1$ [52,58], and a_2 and a_3 depend on the dynamic process [38]. $x_0 = 0$ is a fixed point for all ε. It is stable for $\varepsilon < 0$ and unstable for $\varepsilon > 0$.

Note that the type-III intermittency behavior is different to that of type-I. The fixed point does not vanish; it only loses its stability. Furthermore, there is not a channel between the map and the bisector.

To examine type-III intermittency, the second iteration of Equation (12) is built:

$$\begin{aligned} x_{n+2} = F^2(x_n) = &-(1+\varepsilon)\left[-(1+\varepsilon)x_n + a_1\, x_n^2 + a_2\, x_n^3\right] + \\ &a_2\left[-(1+\varepsilon)x_n + a_1\, x_n^2 + a_2\, x_n^3\right]^2 + \\ &a_3\left[-(1+\varepsilon)x_n + a_1\, x_n^2 + a_2\, x_n^3\right]^3 + \dots \ . \end{aligned} \tag{13}$$

For small values of $|x|$ and ε, the second iteration of map (13) reduces to [39]:

$$x_{n+2} = F^2(x_n) = (1+2\varepsilon)x_n + a\, x_n^3 + \dots \tag{14}$$

where $a = -2(a_3 + a_2^2)$.

For $\varepsilon > 0$, the map (14) has two behaviors depending on the sign of the cubic term coefficient, a:

- $a < 0$. There are three fixed points: $x_0 = 0$ and $x_{1,2} = \pm(2\varepsilon/|a|)^{0.5}$. When x_0 loses its stability, the other two fixed points are stable and attract the trajectories. There is a supercritical pitchfork bifurcation, and intermittency does not occur.
- $a > 0$. For $\varepsilon > 0$, $x_0 = 0$ is the only real fixed point, which is unstable. If there is a reinjection mechanism, type-III intermittency occurs. It is related to a sub-critical pitchfork bifurcation of $F^2(x)$, or associated with a sub-critical period-doubling bifurcation of $F(x)$. Note that $a > 0$ implies $a_3 < -a_2^2$. For this reason, several studies utilize Equation (14) as a local map instead of Equations (12) or (13).

If $F(x)$ exhibits a subcritical period-doubling bifurcation, the Schwartzian derivatives have to be positive:

$$SF(x) = \frac{d^3F(x)/dx^3}{dF(x)/dx} - \frac{3}{2}\left[\frac{d^2F(x)/dx^2}{dF(x)/dx}\right]^2 > 0\,. \tag{15}$$

For $\varepsilon = 0$, this equation implies $a_3 < -a_2^2$. Accordingly, for one-dimensional maps, type-III intermittency occurs if $SF(x) > 0$.

For the classic formulation of chaotic intermittency, the RPD is constant, and it has to satisfy the normalization condition:

$$\int_{-c}^{c} k\, dx = 1 \tag{16}$$

then $\phi(x) = k = 0.5/c$.

Following the procedure used for type-I intermittency, the laminar length for a reinjected point x is:

$$l(x,c) = \int_x^c \frac{d\tau}{\tau(2\varepsilon + a\ \tau^2)} = \frac{1}{2\varepsilon} \ln\left(\frac{a + \varepsilon/x^2}{a + \varepsilon/c^2}\right) \tag{17}$$

where $l(x,c)$ is the laminar length for the $F^2(x)$ map. For simpleness we have used $2\varepsilon \to \varepsilon$. Consequently, the laminar length for the $F(x)$ map, given by Equation (12), results, $2\,l(x,c)$.

The probability of laminar lengths, $\psi(l)$, results (see Equation (7)).

$$\psi(l) = \left[\frac{\varepsilon}{\left(\frac{\varepsilon}{c^2} + a\right)e^{2\varepsilon l} - a}\right]^{3/2} \left(\frac{\varepsilon}{c^2} + a\right)\frac{e^{2\varepsilon l}}{2c}\,. \tag{18}$$

The average laminar length is [39]:

$$\bar{l} = \int_0^c \phi(x) 2l(x,c)dx = \frac{1}{c}\int_0^c l(x,c)dx = \frac{1}{c\sqrt{a\varepsilon}} \arctan\left(c\frac{\sqrt{a}}{\sqrt{\varepsilon}}\right). \tag{19}$$

The last equation verifies $\bar{l} \propto \varepsilon^{-1/2}$ when $c\frac{\sqrt{a}}{\sqrt{\varepsilon}} \gg 1$. Note that the characteristic relations for type-I and type-III intermittencies have the same form. The length of the laminar phases rises when ε decreases.

Note that Ref. [42] provides the following characteristic relation: $\bar{l} \propto \varepsilon^{-1}$. Consequently, two characteristic relations have been found for type-III intermittency, which originated debates on the subject [39]. There is no discrepancy in the present, as will be explained in the following sections.

2.3. Type-II Intermittency

Type-II intermittency happens in two or higher-dimensional maps. It occurs when two complex-conjugate eigenvalues of the fixed point go away from the unit circle, and a sub-critical Hopf bifurcation appears. A two-dimensional manifold is related to the two eigenvalues, which is spanned by the eigenvectors of the complex conjugate eigenvalues. We can study the dynamics of this manifold because the absolute values of other eigenvalues are less than 1. The complex monodromic eigenvalues can be expressed as $\nu = (1+\varepsilon)e^{i\theta}$, where θ is an angle. The local dynamic can be described by a two-dimensional map [38]

$$\begin{aligned} r_{n+1} &= (1+\varepsilon)r_n + a\ r_n^3; \\ \theta_{n+1} &= \theta_n + b + q\ r_n^2 \end{aligned} \tag{20}$$

where ε is the control parameter. a, b, and q are constants. For $\varepsilon > 0$, type-II intermittency can occur.

To explain type-II intermittency, the same statistical variables studied for type-I and type-III intermittencies are calculated. The classical formulation implements a constant RPD. Nevertheless, the other statistical variables are not constant. For $0 < \varepsilon \ll 1$, Equation (20) can be approximated as:

$$\frac{dr}{dl} = \varepsilon r + a\ r^3\,. \tag{21}$$

Hence, we have:

$$l(x,c) = \int_x^c \frac{dr}{\varepsilon r + ar^3} = \frac{1}{2\varepsilon} \ln\left(\frac{a + \varepsilon/x^2}{a + \varepsilon/c^2}\right) \tag{22}$$

where c is the upper limit of the laminar interval and x is the reinjection point. Note the laminar interval is $[0, c]$.

The probability density of the laminar lengths, $\psi(l)$, can be obtained from Equation (7):

$$\psi(l) = \left[\frac{\varepsilon}{\left(\frac{\varepsilon}{c^2}+a\right)e^{2\varepsilon l}-a}\right]^{3/2}\left(\frac{\varepsilon}{c^2}+a\right)\frac{e^{2\varepsilon l}}{c}\,. \tag{23}$$

The average laminar length is

$$\bar{l} = \int_0^c \phi(x) l(x) dx = (1/c)\int_0^c l(x)dx = \frac{1}{c\sqrt{a\varepsilon}}\arctan\left(c\frac{\sqrt{a}}{\sqrt{\varepsilon}}\right) \tag{24}$$

where the RPD is constant, $\phi(x) = k = 1/c$, where we have utilized the normalization condition given by Equation (16).

The characteristic relation is obtained from Equation (24) for $c\frac{\sqrt{a}}{\sqrt{\varepsilon}} \gg 1$; it results $\bar{l} \propto \varepsilon^{-1/2}$. Note that the characteristic relation for type-II intermittency is similar to those calculated for type-I and type-III.

2.4. Type-V Intermittency

Type-V intermittency occurs if a stable fixed point in a non-differentiable, even discontinuous, map meets with a non-differentiable or discontinuous point. Refs. [73–75] introduced this idea approximately 30 years ago.

Types-I, II, and III intermittencies occur on differentiable maps. Nevertheless, a different process can happen if the map has discontinuous or non-differentiable points. If a control parameter changes so that one non-differentiable point (NPD) moves in the direction of and meets with a stable fixed point, then a channel between the bisector and the map occurs.

Type-I intermittency occurs at a tangent bifurcation where the map is tangent to the bisector line at critical, and the eigenvalue associated with the critical point is +1. Notwithstanding, for a non-differentiable point, the map at this point is non-differentiable or discontinuous, so that there is no tangent. Then, a tangent bifurcation does not exist for a non-differentiable point. For some maps, there are two slopes around the non-differentiable point, one for the left part of the map and the other for the right one.

Let us to analyze the following map displaying type-V intermittency [73]:

$$F(x) = \begin{cases} F_1(x) = (x-a)^2 + b & \text{for} \quad x \geq x_d \\ F_2(x) = A\ rnd(x) + B & \text{for} \quad x < x_d \end{cases} \tag{25}$$

where $rnd(x)$ is a random number in the interval $[0,1]$ and x_d is the discontinuous point. A and B are settled on to satisfy that the reinjection happens below the intersection between the bisector line $x_{n+1} = x_n$ with the function $F_1(x)$. The parameters a and b govern the modification of the $F_1(x)$ function with the control parameter $\varepsilon = F_1(x_d) - x_d$. For decreasing ε, $F_1(x_d)$ moves toward the diagonal. For $\varepsilon = 0$, x_d is a fixed point: $F_1(x_d) = x_d$. At the discontinuity point, the slope of $F_1(x)$ is $dF_1(x_d)/dx = s$, which is assumed independent of ε. The parameters a and b can be written as function of s and ε:

$$a = \frac{4\,\varepsilon - s}{2}, \qquad b = \varepsilon - \frac{s^2}{4}\,. \tag{26}$$

If we consider that $s \neq 0$, $s \neq 1$, $\varepsilon \to 0$ and random reinjection, the average laminar length $\bar{l}$ results:

$$\bar{l} = \frac{\log(\varepsilon)}{\log(s)} + \beta(s) \tag{27}$$

where $\beta(s)$ is independent of ε. For $s = 0$:

$$\bar{l} = a\log[-\log(\varepsilon)] + \beta(s) \tag{28}$$

and for $s = 1$:

$$\bar{l} = \frac{a}{\varepsilon} + \beta(s)\,. \tag{29}$$

The scaling laws for other two maps were evaluated in [74]. The the right part of the first map is:

$$x_{n+1} = F_2(x_n) = x_n - a\sin(x_n) - \varepsilon \tag{30}$$

where a satisfies: $0 < a < 1$, and the control parameter is $\varepsilon \geq 0$. For $\varepsilon = 0$, there is a critical point.

The laminar length is:

$$l = \left| \int_x^{\frac{\varepsilon}{1-a}} \frac{d\tau}{a\sin(\tau) + \varepsilon} \right| = \frac{|\ln(\varepsilon)|}{a} + \frac{1}{a}\ln\left(\frac{2a(1-a)\sin(x)}{1+\cos(x)}\right). \tag{31}$$

If a random reinjection mechanism with probability $P(x)$ is considered. The average laminar length results:

$$\bar{l} = \int_{x_{out}}^{x} \frac{1}{a}\ln\left(\frac{2a(1-a)\sin(\tau)}{1+\cos(\tau)}\right) P(\tau)d\tau + \frac{1}{a}|\ln(\varepsilon)| \tag{32}$$

where x and x_{out} are the entrance and the exit points, respectively.

The second map is a generalization of Equation (25). Its right part can be written as [74]:

$$x_{n+1} = F_2(x_n) = \zeta x_n - \delta x_n^2 - \varepsilon\,. \tag{33}$$

The average laminar length results:

$$\bar{l} = \frac{|\ln(\varepsilon)|}{1-\zeta} + \int_0^c \frac{1}{1-\zeta}\ln\left(\frac{(1-\zeta)^2\zeta x}{|x\delta + \zeta - 1|}\right) P(x)dx\,. \tag{34}$$

Equations (27), (32), and (34) denote that a logarithmic scaling law, $\bar{l} = \bar{l}(\ln(\varepsilon))$, adapts for type-V intermittency.

2.5. Type-X Intermittency

Type-X intermittency was introduced in [44], and it is related to type-I intermittency. Notwithstanding that both intermittencies are different, each one possesses particular properties.

For type-I and type-X intermittencies, the local is:

$$x_{n+1} = \varepsilon + x_n + x_n^2 \tag{35}$$

where $x_0 = 0$ is an unstable fixed point, and ε is the control parameter.

Type-X intermittency displays a hysteresis mechanism together with a regular reinjection process where the trajectories are returned at the same point. This behavior, close to the threshold where the chaotic phase vanishes, is different to type-I intermittency. For type-X, there is no channel. Consequently, the laminar length is determined by the distance between the reinjection point and the unstable fixed point, and by the gradient of the map near this zone [39].

To investigate the local behavior of trajectories close to the unstable fixed point, the local map around the fixed point can be approximated by a straight line. In that case, the bisector line and the local map determine an X-shape. Accordingly, it is possible to use this assumption to evaluate the average laminar length and its dependence on the control parameter ε. Remember that all trajectories are reinjected at the same point after each chaotic interval; ρ is the distance separating the reinjected point from the unstable fixed point. For small ρ, it depends linearly on ε [44]:

$$\rho = k\,\varepsilon\,. \tag{36}$$

The linearized map around the unstable fixed point can be written as:

$$x_{n+1} = (1 + \mu)x_n \tag{37}$$

for $\varepsilon \ll 1$, we can approximate it as:

$$\frac{dx}{dl} = \mu x_n \,. \tag{38}$$

If the iterates advance from the reinjection point—defined by ρ—to the laminar interval upper limit c, the laminar length results:

$$l = \frac{\ln(c/\rho)}{\mu} \,. \tag{39}$$

Because the trajectories return at the same point, the laminar length and the average laminar length are equal, $l = \bar{l}$. Accordingly, for small ρ, the characteristic relation is given by:

$$\bar{l} \propto \ln\left(\frac{1}{\rho}\right) \propto \ln\left(\frac{1}{\varepsilon}\right) \tag{40}$$

Note that to obtain Equations (40), we have used Equation (36).

2.6. On–Off Intermittency

On–off intermittency presents sudden changes between approximately constant periods or static states and bursts of large-intensity irregular oscillations. The "off" states correspond to nearly constant periods. The "on" states show oscillations of large-intensity. These burst periods depart and return suddenly to the "off" states [45,76].

For the previously analyzed intermittency types, a trajectory of the map spends large periods of time near an unstable or vanished fixed point. This fixed point of the Poincaré map is consistent with a periodic orbit for the continuous system. However, the system states can spend a long time close to other unstable quasi-invariant or invariant objects. Accordingly, intermittency can happen nearby the quasi-invariant or even invariant objects where fixed points are solely singular cases. On–off intermittency has been observed in coupled chaotic oscillators [77]. Moreover, in Ref. [78], coupled oscillators exhibiting the coexistence of chaotic attractors having on–off and Type-I intermittencies among other chaotic scenarios has been reported.

We consider a state space of dimension $S \leq \infty$. In this space, there is an unstable object inside the hyper-surface, $x_1 = x_2 = \cdots = x_N$, with $N < S$. Near this object, on–off intermittency can happen. In addition, the co-dimension $K = S - N$ can be large, and on–off intermittency could occur for both deterministic and random development in the complementary state space [45].

The simpler version of on–off intermittency necessitates two components: an invariant object and orbits going inside and departing every small neighborhood of the invariant object. A dynamical system possessing these elements can be written in the following form:

$$\begin{aligned} \frac{d\mathbf{X}(t)}{dt} &= \mathbf{f}_1(\mathbf{X}(t), \nu(\mathbf{Y}(t))) \\ \frac{d\mathbf{Y}(t)}{dt} &= \mathbf{f}_2(\mathbf{Y}(t)) \end{aligned} \tag{41}$$

where $\mathbf{X}(t) = (x_1, x_2, \ldots, x_N)^T$ and $\mathbf{Y}(t) = (x_N + 1, x_N + 2, \ldots, x_S)^T$. Note in Equation (41) the derivative of $\mathbf{Y}(t)$ is independent of $\mathbf{X}(t)$; nevertheless, the $\mathbf{X}(t)$ evolution depends on $\mathbf{Y}(t)$. Subsequently, the dynamical system display a skew product structure.

Additionally, the hyper-plane $\mathbf{X}(t) = 0$ is an invariant object, which is unstable when the control parameter $\nu(\mathbf{Y}(t))$ goes beyond a critical value ν_c: $\nu(\mathbf{Y}(t)) > \nu_c$. If the trajectory evolves in such a way that $\mathbf{Y}(t)$ visits two zones, such as $\nu(\mathbf{Y}(t))$ moving above and below

the critical control parameter ν_c, and if the spent time by the trajectory in both regions is proper, then on–off intermittency can occur. Note that when $N = S$ and $\nu > \nu_c$, the classical intermittency mechanism can be recovered.

The process supporting on–off intermittency is the reiterated change of a dynamical variable across a bifurcation point of another dynamical variable. The first variable adjusts a time-dependent control parameter, which affects the second variable adopting the intermittent signal.

The possibility to control on–off intermittent dynamics, that is to stabilize a trajectory in a desirable state, has been investigated previously (see [77] and references therein). The control of the on–off intermittent dynamics by using a closed-loop algorithm requires full knowledge of the system. However, to avoid this issue, an open-loop control of a chaotic dynamical system that exhibits on–off intermittency has also been proposed [79].

2.7. Eyelet Intermittency

The eyelet intermittency occurs close to the phase synchronization boundary of chaotic coupled systems. It can be described by the phase synchronization of unstable periodic saddle orbits embedded in chaotic attractors [80].

Additionally, eyelet intermittency can arise nearby the phase synchronization boundary of a periodically forced chaotic system. This was introduced through the investigation of the phase synchronization onset, which corresponds with a collision between an attractor and a repeller.

Let us study the following two-dimensional map:

$$\begin{aligned} x(t+1) &= 1 - a|x| + k\,\rho\,\sin(2\pi\theta(t)) \\ \theta(t+1) &= \theta(t) + \Omega + k\cos(2\pi\,\theta(t)) + g(x)\,. \end{aligned} \tag{42}$$

Physically, the map is the stroboscopic characterization of a continuous-time chaotic oscillator externally excited by a periodic force. The system given by Equation (42) is composed of the perturbed tent map coupled with the circle map.

The variables x and θ are the amplitude and phase of the oscillator, respectively. The parameter $k < 0.5/\pi$ is related to the force amplitude. For autonomous systems, it verifies $k = 0$. The detuning between the periods of oscillations and external force is described by the terms $g(x)$ and Ω. In addition, Ω is proportional to the external force frequency. The chaotic modulation of the phase motion is described by $g(x) = \delta\,x(t)$.

The analysis of the characteristics of unstable periodic orbits embedded in chaotic attractors is an approximation to studying the phase synchronization of chaotic oscillators [81–83]. For the system (42), a phase-locked zone with zero rotation or winding number arises for each trajectory (Arnold's tongues).

In the phase-locked region, there are two orbits for phase θ for each orbit of the tent map. These two orbits are unstable in the x direction. However, in the θ direction, one is stable and the other is unstable. At the synchronization boundary, a saddle-node bifurcation happens. These orbits disappear, and a state with a nonzero rotation number arises.

A zone where all the phase-locked regions overlap is named the region of full-phase synchronization. It is limited by the phase-locked regions of the periodic orbits possessing the minimal and maximal average period.

Near the boundary of the full-phase synchronization region, the repeller and attractor approach each other. At the transition point, a saddle-node bifurcation of one of the unstable periodic orbits happens, and a attractor–repeller collision occurs. A few cycles miss the phase locking, permitting the phase to slip (most cycles continue phase-locked).

The dynamic in the θ direction, which is a weakly unstable direction, is driven by the saddle-node bifurcation. Consequently, the characteristic time of phase slip is:

$$t_s \propto \sqrt{\frac{1}{\Omega - \Omega_c}} \tag{43}$$

where Ω_c is at the bifurcation point.

For a phase slip to appear, a chaotic trajectory has to stay at least a time t_s near the vicinity of the ϕ direction (weakly unstable direction). However, the x direction is strongly unstable, and the distance to the weakly unstable direction is:

$$D(t) \approx D(0)|\nu|^t \tag{44}$$

where $\nu > 1$ is the multiplier in the strongly unstable direction.

For at least one phase slip to emerge, the initial distance should be small:

$$D(0) < \frac{C}{|\nu|^{t_s}} \tag{45}$$

where collision C is a constant. This region is called the eyelet and is exponentially small.

Nearby the border of the phase synchronization region, the phase difference $\Delta\theta(t)$ possesses time intervals of phase synchronized behavior, which are intermittently interrupted by abrupt phase slips.

Near the boundary of the phase synchronization, two intermittency types may emerge when the natural frequency of the system and the external signal frequency are moderately detuned: type-I and eyelet intermittencies. Then, two critical values exist [84].

There are two coupling strengths, κ_1 and κ_2 ($\kappa_1 < \kappa_2$), for two coupled chaotic systems. These strength values are the boundaries of different dynamical behaviors. Type-I intermittency appears for values of κ less than κ_1, i.e., $\kappa < \kappa_1$. For κ values satisfying $\kappa_1 < \kappa < \kappa_2$, there is eyelet intermittency, and for $\kappa > \kappa_2$ the phase synchronization region happens [84].

The equation relating to the mean length of the laminar phases, $\bar{l}$, with the control parameter κ is:

$$\bar{l} \sim e^{(\zeta\,(\sqrt{\kappa_2 - \kappa})^{-1/2})} \tag{46}$$

where ζ is constant.

The eyelet intermittency has been found in nonlinear systems by numerical calculations and experimental investigations [85].

A more recent investigation observed that noisy type-I and eyelet intermittencies can display the same type of dynamic. Nevertheless, these intermittencies can be found under different conditions [84].

For a deeper analysis of eyelet intermittency and synchronization, the readers can utilize the following references [47,81,83–85].

Another type of intermittency, called ring, also occurs near the boundary of the phase synchronization zone. Nevertheless, it happens for high initial frequency mismatches of two coupled systems [48].

2.8. Spatiotemporal Intermittency

A brief description of spatiotemporal intermittency is carried out. Spatially extended systems—systems with spatial extension—may generate intermittency. Nonlinear partial differential equations (PDEs) represent these types of systems. In consequence, it is a very vast research subject.

The dynamics of the viscous fluid flow is described by the Navier–Stokes equations [86–89]. These equations are an example of a spatially extended system:

$$\rho\left(\frac{\partial \mathbf{v}}{\partial t} + \mathbf{v}\nabla\mathbf{v}\right) = -\nabla p + \mu\triangle\mathbf{v} \tag{47}$$

where $\mathbf{v} = (v_1, v_2, v_3)$ is the velocity vector, p is the pressure, ρ is the density, μ is the viscosity, and t is the time.

For incompressible flow, we coupled the Navier–Stokes equations with the incompressible continuity equation:

$$\nabla.\mathbf{v} = 0\,. \tag{48}$$

On the other hand, for compressible flow the continuity equation results:

$$\frac{\partial \rho}{\partial t} + \mathbf{v}\nabla\rho = 0\,. \tag{49}$$

If the evolution of the variables of a system such as Equation (47) coupled with Equations (48) or (49) are random in time, it is possible to speak about spatio-temporal chaos. Additionally, spatio-temporal chaos could be considered a kind of temporally chaotic pattern-forming mechanism. In addition, if these variables show a spatially irregular behavior, the process can be called fully developed spatio-temporal chaos.

Spatiotemporal intermittency is an indication of spatiotemporal chaos and full spatiotemporal chaos. It has been observed in several experimental works [90,91]. In addition, spatiotemporal intermittency can occur in spatially extended dynamical systems. Each space-time point of these systems can show pseudo-laminar and pseudo-turbulent states. For pseudo-laminar states, the spatial behavior is regular. Despite this, the temporal dynamics could be both chaotic and regular. On the other hand, pseudo-turbulent states exhibit no recognizable regularity either in space or in time [92].

Spatiotemporal intermittency alternates in both time and space pseudo-laminar and pseudo-turbulent states. In addition, this type of intermittency can be understood as a transition state between regular and chaotic behaviors, where the domains of each phases possess well-defined contours.

Long-time averages of spatial variables are implemented to calculate the distribution amplitudes of pseudo-laminar and pseudo-turbulent states. Both distributions exhibit an exponential decay, which is connected with the average extension of the pseudo-laminar and pseudo-turbulent phases [93].

Furthermore, long transient behaviors for spatially extended systems can be described by spatiotemporal intermittency [94,95]. Additionally, some of these states have suitable long lifetimes to evaluate steady statistical variables. Consequently, spatiotemporal chaos can exhibit this type of intermittency. Then, spatiotemporal intermittency could contribute to a spatiotemporal chaotic attractor [92].

There are several works to develop a broad and deeper analysis of spatiotemporal intermittency [90–98].

2.9. Crisis-Induced Intermittency

In dynamical systems, Ref. [99] introduced the world crises. A crisis takes place through a collision between an unstable periodic solution with a chaotic attractor. During a crisis, as a control parameter is varied, the chaotic behavior of dissipative dynamical systems experiences sudden qualitative modifications

According to Ref. [100], there are three different types of crisis: exterior or boundary, interior, and attractor merging. The three types of crisis depend on how the chaotic attractor is abruptly modified (discontinuity of the chaotic attractor).

The chaotic attractor is suddenly destroyed by a boundary crisis. It occurs when a control parameter ε moves across a critical value ε_c. The boundary crisis is also called an exterior crisis [38]. For an interior crisis, the size of the attractor suddenly expands when the control parameter passes through the critical value ε_c. Finally, for an attractor merging crisis, if the control parameter goes through the critical value, two or more chaotic attractors of the system merge in only one chaotic attractor. The new attractor can acquire a larger size than the union of the previous chaotic attractors for $\varepsilon < \varepsilon_c$. The last two crises, interior and merging, are called explosive bifurcations [38].

To analyze crisis-induced intermittency, let us introduce the following map: [38,100]

$$x_{n+1} = -x_n^2 + a\,. \tag{50}$$

It is a quadratic map (one-dimensional). This map, for $a \geq -1/4$, possesses two fixed points :

$$x_s = -\frac{1}{2} + \sqrt{\frac{1}{4} + a}\,, \qquad x_u = -\frac{1}{2} - \sqrt{\frac{1}{4} + a}\,. \tag{51}$$

For $a = -1/4$, a tangent bifurcation appears, which generates stable and unstable fixed points, x_s and x_u. The stable fixed point misses stability at $a = 3/4$ by a period-doubling bifurcation. For larger values of a, a cascade of period-doubling bifurcations occurs with an accumulation point at $a_\infty = 1.40095$. For $a_\infty < a < 2$, there is a chaotic attractor that shows many tiny windows of periodic solutions. At $a = 2$, the chaotic attractor merges with the unstable fixed point, and it vanishes by an exterior crisis or blue sky catastrophe [38].

For $1.74 < a < 1.8$, there is an interior crisis. At $a = 1.75$, the chaotic attractor vanishes, and three tangent bifurcations appear. For each one of these bifurcations, stable and unstable fixed points start. At $a > 1.7692$, the stable period-three orbit sustains a period-doubling bifurcations sequence. At $a^c = 1.790327492$, the three chaotic bands and the unstable period-three orbit merge (an interior crisis occurs). Therefore, the chaotic attractor modifies from three chaotic bands to a one-band chaotic attractor [39].

For a slightly larger than a^c, the chaotic attractor trajectory spends long time intervals around the attractor before the interior crisis (pseudo-laminar region). These intervals are interrupted by bursts, where the trajectory departs to an extended region (chaotic region). Following that, the trajectory comes back to the zone around the chaotic attractor before the interior crisis, and this process continues. This behavior is called crisis-induced intermittency [99].

2.10. Fine Structure in Intermittency

Refs. [101,102] describe a fine structure in intermittency. These papers study numerically type-I intermittency. The Lyapunov exponent, the average laminar length, and the mean value of the dynamical variable, x, for several values of the control parameter ε, are calculated. The map analyzed in [101] is:

$$x_{n+1} = F(x_n) = \varepsilon + x_n + (x_n - 1)^z \mod 2 \tag{52}$$

where z takes the values 2 and 4. For this map, the characteristic relation is [101]:

$$\bar{l} \propto \varepsilon^{(1-z)/z}\,. \tag{53}$$

The Lyapunov exponent is calculated as:

$$\lambda = \lim_{N\to\infty} \frac{1}{N} \sum_{i=1}^{N} \ln(|F'(x)|_{x=x_i}) \tag{54}$$

where $F'(x) = \frac{d\,F(x)}{d\,x}$. The mean value (average) of the dynamical variable is:

$$\bar{x} = \lim_{N\to\infty} \frac{1}{N} \sum_{i=1}^{N} x_i \tag{55}$$

where the total number of iterations was $N = 3 \times 10^7$.

The three statistical variables, $\bar{l}$, λ, and $\bar{x}$, show oscillations. The oscillation amplitudes are larger for the Lyapunov exponent and the mean value of the dynamical variable.

If we do not consider the oscillations, the results display the traditionally known characteristic relation (see Equation (10)). The relation of the $\bar{x}$ with ε can be written as:

$$\begin{aligned} \bar{x} - 1 &\propto \varepsilon^{1/2} \ln \varepsilon, \qquad \text{for} \quad z = 2 \\ \bar{x} - 1 &\propto \varepsilon^{2/3} \ln \varepsilon, \qquad \text{for} \quad z = 4 \end{aligned} \tag{56}$$

The relation of the Lyapunov exponent with the control parameter results:

$$\lambda \propto \varepsilon^{3/4} \ln \varepsilon \,. \tag{57}$$

When the control parameter verifies $\varepsilon \to 0$, the oscillations scale as $\varepsilon^{-1/2}$ for $z = 2$, and $\varepsilon^{-3/2}$ for $z = 4$.

Ref. [102] introduced another map to analyze the fine structure in intermittency:

$$x_{n+1} = \begin{cases} a x_n + b & \text{for} \quad x_n < c \\ a^{-1}(x_n - 1 + b) + 1 & \text{for} \quad c < x_n \leq 1 - b \\ b^{-1}(x_n - 1) & \text{for} \quad x_n > 1 - b \end{cases} \tag{58}$$

where:

$$a = 1 - 2b + \varepsilon > 0, \quad c = (1 - b)/(1 + a) > 0, \quad 0 < b < 1/2 \,. \tag{59}$$

It is a piecewise linear map. This map, for $\varepsilon = 0$, possesses a fixed point $x = 1/2$, which vanishes for $\varepsilon > 0$.

The authors, using numerical simulations, found that the Lyapunov exponent, average laminar length, and the statistical moment of the chaotic variable display logarithmic periodic oscillations. Accordingly, the fine structure produced by the oscillations generates a signature of nonlinearity, which could be utilized to reach supplementary information about the characteristic exponents.

2.11. Two-Dimensional Intermittency

Some concepts to describe two-dimensional type-I intermittency are introduced in Ref. [103]. It occurs around a tangent bifurcation point similar to the one-dimensional type-I intermittency.

The first-order difference equations system, in m-dimensional space, can be written as:

$$\mathbf{x_{n+1}} = \mathbf{F}(\mathbf{x_n}) \tag{60}$$

where the vector $\mathbf{x_n} \in \mathbf{R}^m$, with $\mathbf{R}^m$ being the m-dimensional Euclidean vector space. For $m \geqslant 2$, high-dimensional intermittency can appear. For two-dimensional vector space, $m = 2$, the Equation (60) is reduced to:

$$\begin{aligned} x_{n+1} &= F(x_n, y_n) \\ y_{n+1} &= G(x_n, y_n) \,. \end{aligned} \tag{61}$$

In one-dimensional type-I intermittency, there is a channel where the trajectories spend a long time moving across it. The channel amplitude—the distance between the diagonal and the map—is determined by the control parameter ε.

To study high-dimensional intermittency, an m-dimensional diagonal hypersurface (DHS) has to be defined [103]. For two-dimensional vector space, $m = 2$; the DHS is the surface specified by $x_{n+1} = x_n$ and $y_{n+1} = y_n$. The map forms a channel between the DHS and the map. The pseudo-laminar behavior happens as long as the trajectory crosses this channel.

The local map for type-I intermittency in one-dimensional vector space is given by a quadratic equation (see Equation (3)). In two-dimensional intermittency, this map can be written as:

$$\begin{aligned} x_{n+1} &= a_1 x_n^2 + a_2 y_n^2 + a_3 x_n y_n + a_4 x_n + a_5 y_n + a_6 \\ y_{n+1} &= b_1 x_n^2 + b_2 y_n^2 + b_3 x_n y_n + b_4 x_n + b_5 y_n + b_6 \end{aligned} \tag{62}$$

where a_i and b_i are arbitrary coefficients. In an iterative process, given a point (x_n, y_n), the subsequent point (x_{n+1}, y_{n+1}) can be calculated as the addition of two vectors. The first one is in the x-direction, and the second is in the y-direction. As a consequence, the channel is not identical for all trajectories. To deal with this phenomenon of high-dimensional intermittency, a new parameter, named channel distribution function (CDF), has to be considered [103].

In two-dimensional intermittency, three trajectory categories can appear: limit cycle, quasiperiodic, and chaotic. The CDF depends on the trajectory, and it is distinct for each trajectory type. A limit cycle displays one trajectory in the $x_n - y_n$ plane. Then, the channel is unique. Its functioning is similar to that of one-dimensional intermittency. The quasiperiodic one generates a variable channel with a uniform CDF. Lastly, chaotic trajectories produce channels with fractal structures. Therefore, the conduit is not unique for quasiperiodic and chaotic trajectories. Consequently, a multichannel behavior happens, which is described by a probability distribution, $\xi(\varepsilon)$ or CDF. For this reason, the average laminar length depends on the CDF.

In Ref. [103], the authors calculated the average laminar length for the three trajectory types. For a limit cycle, the CDF verifies, $\xi(\varepsilon) = \delta(\varepsilon - \varepsilon_0)$, where delta is $\delta(i-j) = 1$ if $i = j$ and $\delta(i-j) = 0$ if $i \neq j$. The characteristic relation, connecting the average laminar length with the control parameter, results:

$$\bar{l} \sim \varepsilon^{-1/2}. \tag{63}$$

For a quasiperiodic trajectory, the CDF is uniform, $\xi(\varepsilon) = 1/k$, where $k =$ constant. In this case, the scaling law is:

$$\bar{l} \sim -\ln(\varepsilon_0) \tag{64}$$

where ε_0 is the nearest channel width.

For a chaotic trajectory, the channel exhibits a discrete fractal structure. Consequently, $\xi(\varepsilon)$ can be represented by a sum of delta functions. The higher delta function related to the nearest channel width governs the average laminar length, $\bar{l}$:

$$\bar{l} \sim \varepsilon_0^{-1/2}. \tag{65}$$

3. New Formulation of the Chaotic Intermittency

In Section 2, we have seen many approximations that have been used in the literature to describe the RPD function. A more extended approach is to consider RPD as uniform and thus independent of the reinjection point (see for instance [40,42,55,104–109]). For the uniform reinjection, the more important expressions as the probability density of the length of laminar phase, $\psi(l)$, was obtained , along with the characteristic exponent β, as we have shown in Section 2. Beside uniform reinjenciton, other investigations consider a limit approximation where the reinjection is only in a fixed point [54,107]. Previously, evidence was found on systems with intermittency whose statistical properties do not fit with the classical expected result derived for a uniform reinjection. An experimental Poincaré map with a gap around the fixed point was also reported. Note that this fact shows a non-uniform reinjection [56,104,110].

This demands a generalization of the RPD in order to include, in a generalized theory, every particular case that was not well explained by the classical intermittency theory.

This section is devoted to explaining this mentioned generalization and to extend the classical results on intermittencies.

3.1. The Reinjection Probability Density Function (RPD)

Let us consider the map described in Section 2, where

$$x_{n+1} = F(x_n), \qquad F : \mathbf{R} \to \mathbf{R} \tag{66}$$

is a general one-dimensional map having intermittency.

Firstly, let us generalize the local dynamics corresponding to the three types of intermittencies around the unstable fixed point, that is, for type-I intermittency, the local map determined by:

$$x_{n+1} = \varepsilon + x_n + a\, x_n^p \qquad \text{type-I} \tag{67}$$

where $a > 0$ represents the weight of the nonlinear component and ε is a small control parameter ($\varepsilon \ll 1$). The laminar behavior of type-II and type-III intermittencies around the fixed point are given by the following maps:

$$x_{n+1} = (1+\varepsilon)x_n + a\, x_n^p \qquad \text{type-II} \tag{68}$$

$$x_{n+1} = -(1+\varepsilon)x_n - a\, x_n^p \qquad \text{type-III}\,. \tag{69}$$

For $\varepsilon \gtrsim 0$, the fixed point $x_0 = 0$ becomes unstable; consequently, the trajectories slowly escape from the fixed point, preserving orientation for type-II and reversing orientation for type-III intermittency. Note that the nonlinear component in Equation (67) is not necessary quadratic, and for type-II and type-III it can be $p \neq 3$ in Equations (68) and (69). Note that this restriction corresponds only to classical local maps (see Equations (14) and (20)). In any case, for $\varepsilon > 0$, for type-II and type-III there is an unstable fixed point at $x = 0$, but for type-I there is not a fixed point and the trajectories move slowly along the narrow channel formed with the bisecting line.

To fix ideas, let us consider an illustrating model having type-II intermittency:

$$x_{n+1} = F(x_n) \equiv \begin{cases} F_1(x_n), & x_n < x_r \\ F_2(x_n), & x_n \geq x_r \end{cases} \tag{70}$$

where

$$F_1(x) = (1+\varepsilon)x + (1-\varepsilon)x^p \tag{71}$$

and x_r is the root of the equation $F_1(x_r) = 1$ (see Figure 1). Note that F_1 determines the laminar dynamics, whereas F_2 determines the reinjection mechanism from the chaotic region into the laminar one (see green arrow in Figure 1). The RPD, denoted by $\phi(x)$, drives the statistical distribution of the reinjected points and is determined by the shape of $F(x)$ in the chaotic region, that is $F_2(x)$. On the other hand, in the laminar region the origin is always the fixed point of F_1, and for $\varepsilon < 0$ it is stable; however, it is unstable for $\varepsilon > 0$, and the mapped points x_n of a starting point closed to the origin increases in a process determined by ε and p. A chaotic burst occurs when x_n becomes larger than x_r, which will be interrupted when x_n goes again into the laminar region mapped by $F_2(x)$, which determines the RPD. In the earlier paper [40], uniform reinjection was observed in the case of the map (70)–(71) for $F_2(x_n) = F_1(x_n) - 1$ and $p = 2$. In [57], the following generalization of the reinjection mechanism was proposed:

$$F_2(x_n) = (F_1(x_n) - 1)^\gamma, \tag{72}$$

where for $\gamma = 1$ the map studied in [40] is recovered. Let us estimate the behavior of $\phi(x)$ in a neighborhood of $x = 0$ for the case of $\gamma \neq 1$, but before embarking on a discussion

concerning RPD for $\gamma \neq 1$, it is interesting to note the relationship between the RPD and the probability measure of an interval $S \subset [0,1]$ given by:

$$P(S) = \lim_{N\to\infty} \frac{1}{N} \sum_{n=0}^{N} I_S(x_n) \tag{73}$$

where $I_S(x)$ denotes the characteristic function of the interval defined as:

$$I_S(x) = \begin{cases} 1, & \text{if} \quad x \in S \\ 0, & \text{if} \quad x \notin S\,. \end{cases} \tag{74}$$

Hence the probability measure gives the frequency of the signal in a specific interval of the attractor, and it depends on the invariant density, $\rho(x)$, by the follow integral:

$$P(S) = \int_S \rho(x)dx\,. \tag{75}$$

Note that in our scenario $P([0,1]) = 1$. Let L be the laminar region and s an subset in L, that is, $s \subset L$. In order to evaluate the probability, $P(s)$, according to definition (73), we split the whole data series into three subsets:

$$\{x_n\} = \{x_{n'}\} \cup \{x_{n''}\} \cup \{x_{n'''}\} \tag{76}$$

having an empty intersection between them:

$$\{x_{n'}\} \cap \{x_{n''}\} = \{x_{n''}\} \cap \{x_{n'''}\} = \{x_{n'''}\} \cap \{x_{n'}\} = \emptyset \tag{77}$$

with the following definitions. Firstly, we consider $x_{n'} \in s$, and in the preceding period it has already been there, that is $I_s(x_{n'}) = 1$ and $I_s(x_{n'-1}) = 1$. Now let us consider the following case, $x_{n''} \in s$, but in the preceding period it has not been there, hence $I_s(x_{n'}) = 1$ and $I_s(x_{n'-1}) = 0$. For the last case, we have $x_{n'''} \notin s$. Note that $P(s)$ is given by:

$$P(s) = \lim_{N\to\infty} \frac{1}{N} \sum_{n=0}^{N} I_s(x_{n'}) + \lim_{N\to\infty} \frac{1}{N} \sum_{n=0}^{N} I_s(x_{n''}) + \lim_{N\to\infty} \frac{1}{N} \sum_{n=0}^{N} I_s(x_{n'''}) \tag{78}$$

where the last term in Equation (78) is not necessary because, by definition, it is zero. The first term is just the probability of finding a point in s when, in the preceding period, it had already been there. Let us consider that $s = L$, then the second term in the RHS of Equation (78) is, by definition, the RPD, called here $\phi(x)$, and is determined by the following relation:

$$\lim_{N\to\infty} \frac{1}{N} \sum_{n=0}^{N} I_L(x_{n''}) = w \int_L \phi(x)dx \tag{79}$$

where the weight, w, is introduced to fit to one and normalize the function $\phi(x)$ over the whole laminar interval, L. We note that the fundamental characteristics of intermittency depends on $\phi(x)$, as for example, $\psi(l)$ and the characteristic exponent β, which are usually used to characterize the intermittency type, as will be seen below. Regarding the reinjection mechanism (72), for $\gamma \neq 1$ it is interesting to analyzed the behavior of of $\phi(x)$ in a neighbor of $x = 0$. Note that every point reinjected in the laminar region, that is in the interval $[0, c]$, are coming from the points near to x_r (see green arrow in Figure 1). Consequently for $x' \gtrsim x_r$, all points in the interval $(x', x' + dx')$ are mapped into the interval $(F_2(x'), F_2(x' + dx')) \approx (x, x + F_2'(x')dx')$, where $x = F_2(x')$. This means that the probability of finding a point in $(x', x' + dx')$ to be reinjected into the interval $(x, x + F_2'(x')dx')$ is equal, where we denote the derivative of the function $F_2(x)$ by $F_2'(x)$. Hence, we conclude that $k\rho(x')dx' = \phi(x)f_2'(x')dx'$, where we introduce the weight k to normalize $\rho(x)$ on the

whole interval $[0,1]$. Note that $\phi(x)$ is normalized only on the laminar interval; hence, we have $\int_0^c \phi(\tau)d\tau = 1$.

Finally, $\phi(x)$ can be approximated as follows:

$$\phi(x) = \rho(x') \frac{k}{\frac{dF_2(\tau)}{d\tau}\Big|_{\tau=x'}}. \tag{80}$$

For expression (80), evaluated for the function given by Equation (72), we have:

$$\phi(x) = \frac{K\rho(x')}{\gamma F_1'(x')} x^{\frac{1}{\gamma}-1}, \tag{81}$$

where $F_1'(x)$ is the derivative of function $F_1(x)$. In the first approximation of $F_1(x)$ in the interval $(x_r, F_2^{-1}(c))$, we can consider $F_1'(x)$ as a constant and the density $\rho(x')$ as uniform, and we get the following reinjection probability density:

$$\phi(x) = b\, x^{\alpha} \quad \text{where} \quad \alpha = \frac{1}{\gamma} - 1. \tag{82}$$

where b is a normalization constant given by Equation (159). Note that the function RPD strongly depends on parameter γ, which determines the curvature of the map in the colored region in Figure 1. Only the points in the colored region are mapped into the laminar region. In [57], a numerical verification of Equation (82) is presented. Moreover, the power law (82) was verified for many one-dimensional maps, including the so-called "pathological" cases that deviate significantly from the classical predictions [59,111]. Moreover, the power law (82) has been observed in the Poincaré map of an experimental 3-D system made by an electronic circuit [112].

Note that the classical uniform RPD holds for the map of Figure 1 only in the case of $\gamma = 1$, where ${x_r}^+$ is not an extreme point.

To evaluate the effect of LBR $\neq 0$, we consider the following map as having type-I intermittency (see Equation (70)):

$$x_{n+1} = G(x_n) = \begin{cases} \varepsilon + x_n + a\, x_n^p & \text{if} \quad x_n < x_r \\ (1-\hat{x})\left(\frac{x_n - x_r}{1-x_r}\right)^{\gamma} + \hat{x} & \text{otherwise} \end{cases} \tag{83}$$

where γ determines the nonlinear term of the reinjection mechanism, whereas x_r is the root of the equation $\varepsilon + x_n + x_n^p = 1$. The new parameter $\hat{x}$ is the so-called lower boundary reinjection point (LBR), defined by the limit value for the reinjected points from the chaotic region, as shown in Figure 2. Note that the statistical behavior of the intermittency strongly depends on the value of the LBR [63,69,106,113]. In the case of Equation (83), where $\hat{x} \neq 0$, the RPD includes the parameter $\hat{x}$ as follows:

$$\phi(x) = b\, (x - \hat{x})^{\alpha} \tag{84}$$

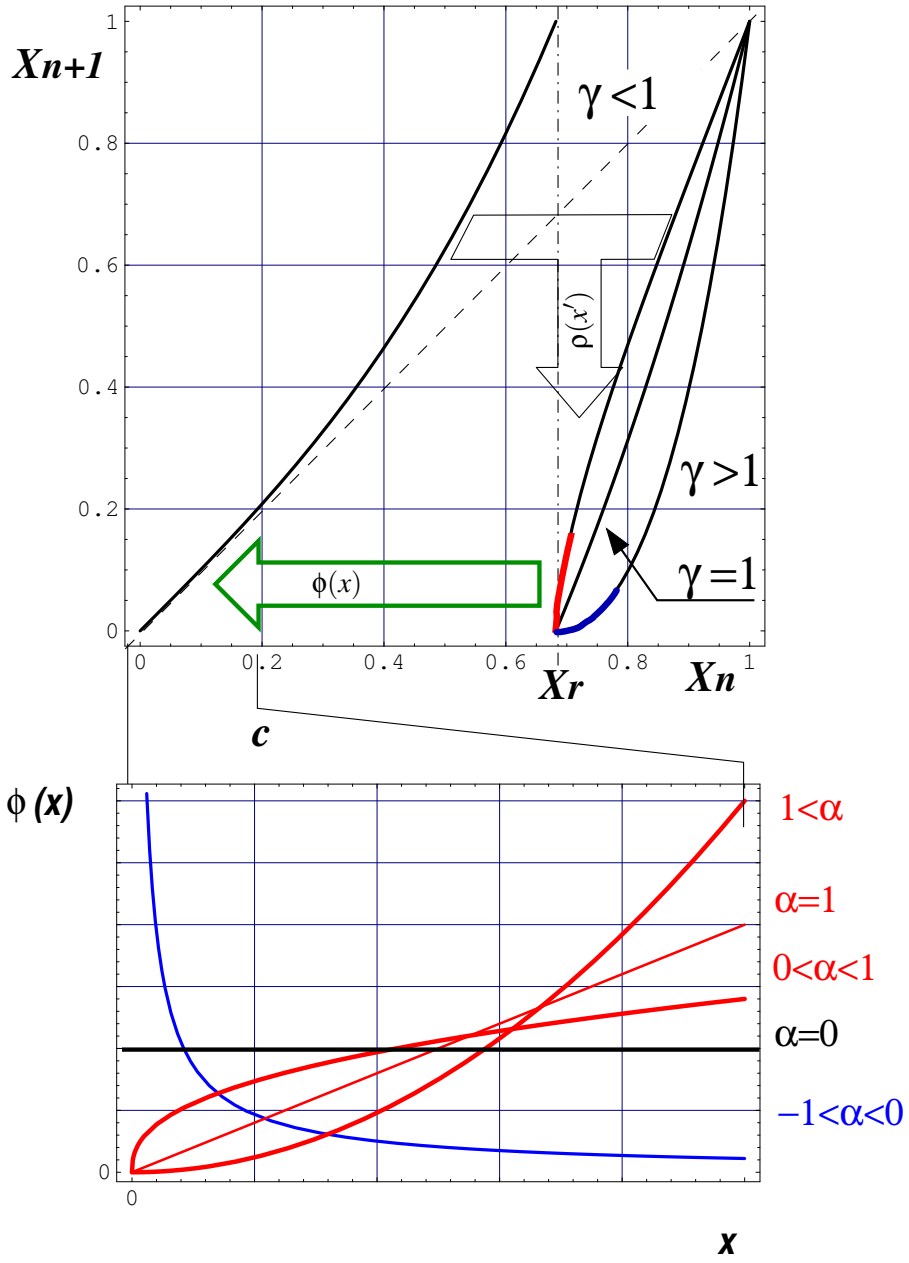

Figure 1. Top subplot: Maps given by Equations (70) and (71) having type-II intermittency. Three reinjected mechanisms (Equation (72) are drawn for three values of γ. Bottom subplot: RPDs of Equation (82) defined for the laminar interval $(0, c)$. For the RPDs, we have used the same color as the region where they were generated. Reprinted from the book "New Advances on Chaotic Intermittency and its Applications," authors Sergio Elaskar and Ezequiel del Rio, Copyright (2017) with permission from Springer Nature.

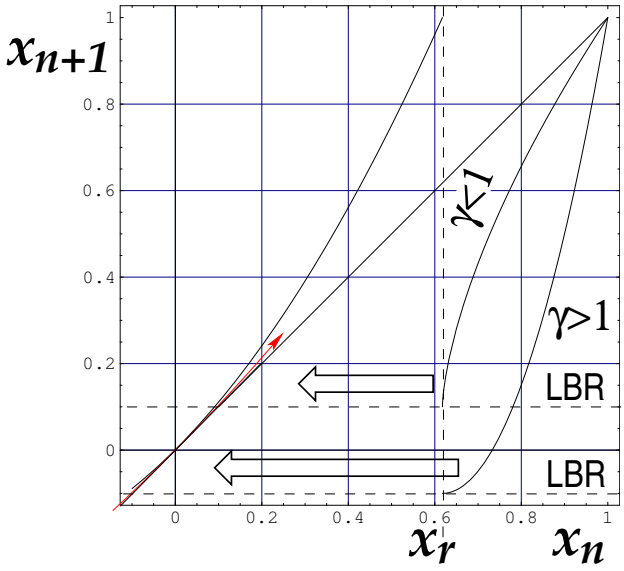

Figure 2. Map (83), with type-I intermittency. There are two LBRs (called $\hat{x}$ in the main text) indicated, corresponding to two reinjected mechanisms in Equation (83). The red arrow shows the corridor followed by the trajectories in the laminar region. Reprinted from the book "New Advances on Chaotic Intermittency and its Applications," authors Sergio Elaskar and Ezequiel del Rio, Copyright (2017) with permission from Springer Nature.

From Equation (84), it follows that if $\alpha < 0$, the RPD increases without boundary for $x \to \hat{x}$, as shown in Figure 1 for $\hat{x} = 0$. On the contrary, for $\alpha > 0$, the RPD decreases when $x \to \hat{x}$. Note that for $\alpha > 0$ we have two possibilities for the RPD, that is, convex or concave, which are separated by $\alpha = 1$ (see Figure 1).

The RPD (84) approaches to two limit cases:

$$\phi_0(x) = \lim_{\alpha \to -1} \phi(x) = \delta(x - \hat{x}) \tag{85}$$

$$\phi_1(x) = \lim_{\alpha \to \infty} \phi(x) = \delta(x - c)\,. \tag{86}$$

Note that in these cases we have $b(\alpha) \to 0$. In fact, for $\alpha < -1$, the integral (79) does not converge.

As a consequence of the power law (84), a hole can be observed in the local map around the fixed point $x = 0$. Behind this fact, two different phenomena can be identified. On one hand, if $\hat{x} > 0$ the endpoint of the holes should be $x = \hat{x}$, hence there are not reinjected points around $x = 0$. On the other hand, for $0 < \alpha$ a hole can be observed in the experimental or numerical realizations, even in the case of $\hat{x} = 0$, because we have $\lim_{x \to \hat{x}} \phi(x) = 0$. Note that, in this case, the gap length is not determined by $\hat{x} = 0$ and it decreases as the number of points increases, and for a long enough time, the gap can disappear [56,57]. The two free parameters determining the RPD (84), $\hat{x}$ and α, can be obtained from data series and also from the analytical definition of the map. This point will be explained in the following sections.

3.1.1. RPD from Data Series

In this case, we use the following integral characteristic [57]:

$$M(x) = \begin{cases} \frac{\int_{x_t}^{x} \tau\, \phi(\tau)\, d\tau}{\int_{x_t}^{x} \phi(\tau)\, d\tau} & \text{if } \int_{x_t}^{x} \phi(\tau) d\tau \neq 0 \\ 0 & \text{otherwise} \end{cases} \tag{87}$$

where x_t is a suitable "starting" point. The function $M(x)$ was used for the first time in a electronics circuit with intermittency [56], and it has been broadly extended due to $M(x)$

being a linear function for a RPD given by Equation (84); consequently, the function $M(x)$ is a useful tool to evaluate the parameters $\hat{x}$ and α.

Note that $M(x)$ is an integral characteristic, hence its numerical evaluation is more robust than the direct estimation of $\phi(x)$. This allows reducing statistical fluctuations produced by a relatively small data set or due to high levels of noise [57–59]. Because $M(x)$ is an average over reinjection points in the interval (x_t, x), we can write:

$$M(x) = M_j \equiv \frac{1}{j}\sum_{k=1}^{j} x_k, \qquad x_{j-1} < x \leq x_j \tag{88}$$

where the data set (N reinjection points) $\{x_j\}_{j=1}^{N}$ has been previously ordered, i.e., $x_j \leq x_{j+1}$. In the case of RPD given by Equation (84), the function $M(x)$ should follow the linear law:

$$M(x) = \begin{cases} m(x-\hat{x})+\hat{x} & \text{if} \quad x \geq \hat{x} \\ 0 & \text{otherwise} \end{cases} \tag{89}$$

where $m \in (0,1)$ and $\hat{x}$ can be approximated by $\hat{x} \approx \inf\{x_j\}$. Equation (87) determines the corresponding RPD:

$$\phi(x) = b(\alpha)(x-\hat{x})^{\alpha}, \quad \text{with} \quad \alpha = \frac{2m-1}{1-m}\,. \tag{90}$$

Note that by a simple least squares fitting we can estimate the parameters of the straight line (89) that determine the RPD given by Equation (90).

Figure 3 shows different RPD depending on exponent α for $\hat{x} = 0$ and $c = 0.5$. The corresponding function $M(x)$ depending on α according to Equation (90) is also shown.

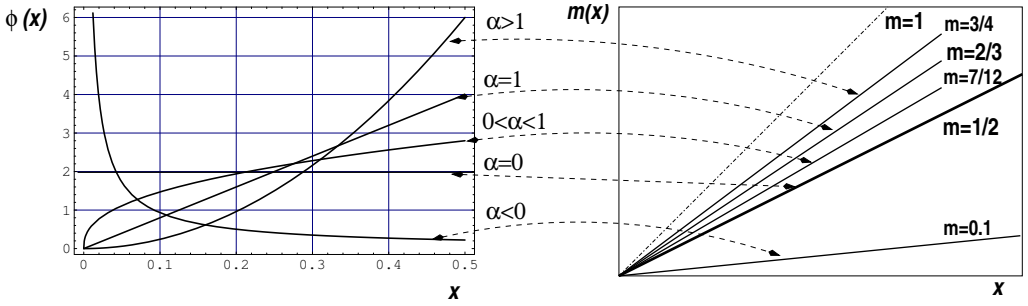

Figure 3. RPD for different values of α and the corresponding slope for the function $M(x)$. Dashed line represents the limit value $m = 1$. Reprinted from the book "New Advances on Chaotic Intermittency and its Applications," authors Sergio Elaskar and Ezequiel del Rio, Copyright (2017) with permission from Springer Nature.

For $m = 1/2$, we recover the classical approach of uniform RPD, that is, $\phi(x) = \text{cnst}$, whereas for RPD it goes to ∞ as $x \to 0$. On the contrary, when $m > 1/2$, we have $\phi(0) = 0$. Note that in this last case we have two possibilities for the RPD, concave or convex, split by the slope $m = 2/3$ (see Figure 3).

The evaluation of the function $M(x)$ allows a more reliable numerical and experimental access than the RPD, $\phi(x)$. We have numerically verified Equation (89) for a broad class of maps. We highlight that the slope, m, can be different from $1/2$. However, we always obtain $|m| < 1$.

In numerical or experimental data series there is a huge amount of data, which can include randomness. The M function methodology evaluates a mean value, reducing the randomness and allowing extraction of the physical information stored in the data series.

3.1.2. RPD from the Analytical Definition of the Map

Following the results of [111], let us analytically estimate the RPD by means of parameter γ of Equation (82). Let us consider a direct reinjection from the extreme point, which is the blue line on the minimum of the map in Figure 1. In this case, the map around the extreme point $x_m = x_r$ can be approached by $F(x) \approx F(x_m) + d(x - x_m)^\gamma$, where d is a suitable constant and the value of γ is given by the next indeterminate limit:

$$\gamma = \lim_{x \to x_m} \frac{\ln(F(x) - F(x_m)) - \ln d}{\ln(x - x_m)}. \tag{91}$$

To convert the limit (91) to an evaluated one, we can apply the L'Hopital rule. Note that usually we will get an indeterminate limit again. In general, when $x \to x_m$ we have $F^{(i)}(x) \to 0$ for $i \leq q$, where $F^{(i)}(x)$ indicates the i-derivative of $F(x)$; hence, by using the L'Hopital theorem $q + 1$ times, we obtain the following limit:

$$\gamma = q + \lim_{x \to x_m} F^{(q+1)}(x) \frac{x - x_m}{F^{(q)}(x)}. \tag{92}$$

Notice that if the derivative $F^{(q+1)}$ exists, the limit (92) gives $\gamma = q + 1$, and in the following Equation (82) we have:

$$\alpha = -\frac{q}{q+1} \tag{93}$$

where $\alpha < 1$, as corresponds with an RPD generated in a maximum or in a minimum.

Note that from Equation (93) two natural limits appear. For $q = 0$, the uniform reinjection is recovered, and on the other hand, for $q \to \infty$, $\alpha \to -1$ the RPD collapses into a δ-function. It is interesting to note that because of x_m being an extreme point, the values of q in Equation (93) are restricted to odd natural numbers.

Let us study an indirect reinjection given in maps such as (119), where to reinject into the laminar region points lying around the maximum, two or more iterations of the map are necessary.

A similar scenario can be observed for maps $F(x)$, defined by a composition of single ones $\{F_i\}$. See, for instance [41,82,106]. Hence, for a general case we consider the composed map:

$$x_{n+1} = F(x_n) \equiv F_r \circ F_{r-1} \circ \cdots \circ F_1(x_n), \tag{94}$$

where the function $F_1(x)$ has an extreme point at x_m that can be be mapped into the laminar region. In this case, points near x_m are mapped after successive application of the F_i functions, according to the composed map (94). In Ref. [111] we have shown that, even in this case, the RPD can be approximated by applying Equation (92) only to the function $F_1(x_n)$, instead of using the complete function, $F(x)$ Consequently, the estimation of γ in the case of a map defined like Equation (94) is given by:

$$\gamma = q + \lim_{x \to x_m} F_1^{(q+1)}(x) \frac{x - x_m}{F_1^{(q)}(x)}. \tag{95}$$

By this method, it is possible to estimate parameter α by evaluating the number of null derivatives that have only the map with extreme points. To show how this method works, let us apply it to three cases of pathological maps that produce an important deviation of the main result expected from the uniform distribution of the RPD [111]. These maps (see Figure 4) were considered in [113] and estimated the RPD by numerically solving the Shaw relation [114], but following our result it is very easy to use an analytical approach. The first map considered is a composition of logistic maps, as follows: $F(x) = f^{(A)}[f^{(B)}(x)]$ (we have used the notation of [113] and [111]), where $f^{(A)}(x) = 4Ax(1 - x)$ and $f^{(B)}(x) = 4Bx(1 - x)$. Note that, according to Equation (95), we only need to study the map $f^{(B)}(x)$ at its extreme point $x_m = 0.5$. As $f^{(B)}(x)$ is a second order polynomial, we conclude that its second derivative must be different from zero so we have $q = 1$, that is, the first odd natural

number, and from Equation (92) we have $\alpha = -1/2$, where, by using Equation (135), we get $\beta = 1/4$. In this simple way we get the result reported by ref. [113].

The second map considered in [113] was defined by a composed function in a similar that for first map but now $f^{(A)}(x) = A(1 - 16(x - 1/2)^4)$ and $f^{(B)}(x) = B(1 - 16(x - 1/2)^4)$. By using the same argument than before, we now have a fourth order polynomial for $f^{(B)}$, and we can then conclude that $q = 3$, the second odd natural number, hence we have $\alpha = -3/4$ and $\beta = 3/8$. Note that we recovered the same values reported by [113].

Finally, the third map shows a similar shape as the first one, but in the range $a < x < b$ the map is just a horizontal line at the level $x = x*$ (see Figure 4). Due to this fact, the derivative $F^{(q)}$ is zero for every value of q; consequently, in the limit $q \to \infty$ we get $\alpha \to -1$ and $\beta = 1/2$, that is, the value reported in [113].

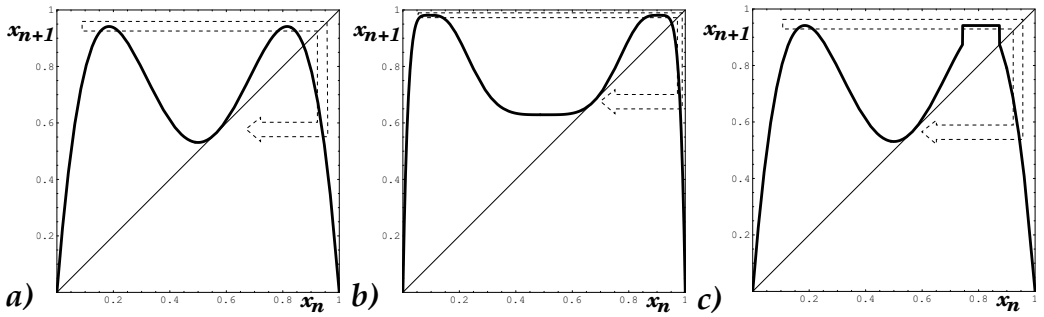

Figure 4. Maps investigated in [113] having type-I intermittency. The arrow draws a trajectory of a point from the chaotic region into the laminar one. We used the same set of parameter values as in [113], as follows: (**a**) $A = 0.9416195$; (**b**) $A = 0.98115325$; and (**c**) $A = 0.9416$, $B = 0.83023023$, $a = 0.743$, $b = 0.874$, and $x* = 0.9414793$.

Let us consider the case where x_m does not have zero derivative but has an unbounded derivative, as is the case of point x_∞ in Figure 5. Near that point, the map can be approximated as follows:

$$f(x') \approx f(x_\infty) + d(x' - x_\infty)^\gamma, \tag{96}$$

but now the previous result cannot be applied because $f'(x) \to -\infty$ as $x \to x_\infty$, hence it is necessary to consider the inverse function of $f(x)$, called here $g(x)$. Taking into account Equation (96) and by using the notation $y = f(x)$, hence $x = g(y)$, we obtain:

$$g(y') \approx g(y_\infty) + d'(y' - y_\infty)^{\gamma'}. \tag{97}$$

Note that now $g(x)$ has an extreme point in $y_\infty = f(x_\infty)$, hence we can apply Equations (92) and (93) to obtain:

$$\gamma' = q' + 1 \tag{98}$$

where q' is the number of non-zero derivatives of the inverse of map $g(y)$. Consequently, $\gamma' = \frac{1}{\gamma}$, and from Equation (84) we obtain:

$$\alpha = q'. \tag{99}$$

In the case of a map formed by composition of functions, such as Equation (94), the inverse will be a composition in reverse order, as follows:

$$y_{n+1} = g(y_n) \equiv g_1 \circ g_2 \circ \cdots \circ g_r(y_n). \tag{100}$$

If the function g_1 has an extreme point at y_∞, corresponding to x_∞, and the others the functions g_i with $i \neq 1$ having no extreme points, by applying the argument used in the composition in Equation (100), we can conclude that q' is determined only by the number of zero derivative of g_1. Consequently, Equation (99) can also be applied to the composition

of Equation (100), but considering only the derivatives of g_1. With this procedure, we can generalize the previous methodology to points with an infinite slope.

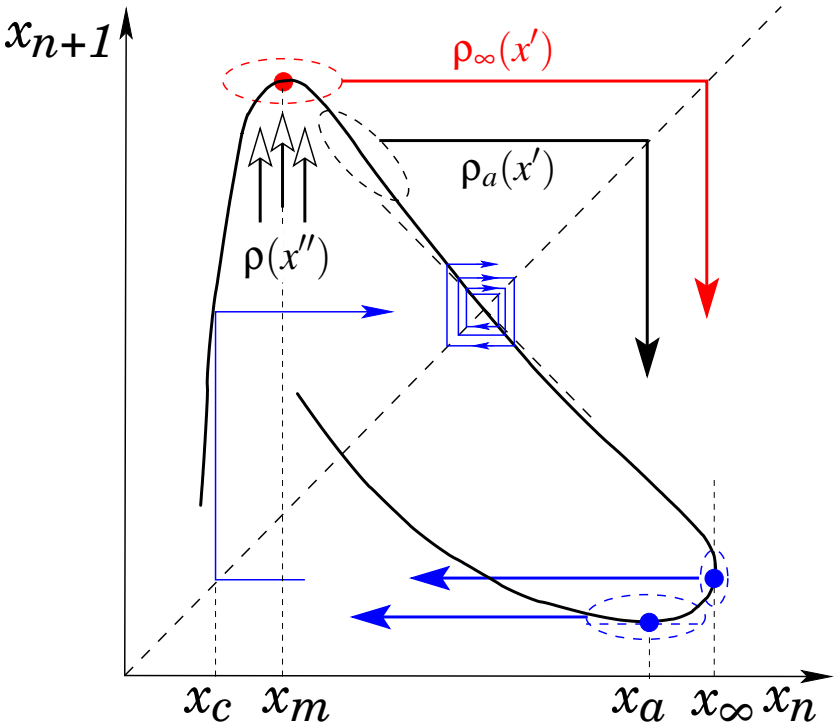

Figure 5. Map similar to the one reported in Ref. [56]. Blue arrow displays a typical trajectory of type-III intermittency in the laminar region. The two big blue arrows indicate trajectories going to the laminar region through the neighbor of x_c. $\rho_a(x')$, $\rho_\infty(x')$, and $\rho(x'')$ indicate the invariant densities around points x_a (minimum), x_∞, and x_m (maximum), respectively. The map has an infinite tangent at x_∞.

Where the function g_i is the inverse function of f_i. Note that, in previous analyzed cases, to obtain Equations (82) and (84), the assumption of uniform density $\rho_a(x')$ in Equation (81) was necessary. If that hypothesis is not true, we cannot apply Equations (93) and (99). This is the case displayed by the map of Figure 5 for the density $\rho_\infty(x')$ where the red point is mapped directly onto x_a or x_∞. The RPD in this case can be obtained by using the previous arguments, that is, assuming that $\rho(x'')$ in Figure 5 is uniform, hence we must conclude that the density $\rho(x')$ in Equation (81) should be given by:

$$\rho(x') = b'(x' - x_a)^{\alpha_a} \tag{101}$$

where the exponent α_a is determined by Equation (93) applied to the red point in Figure 5. Finally, by using a similar argument used to obtain Equation (82) and taking into account Equation (101), we obtain:

$$\phi(x) = b(x - \hat{x})^{\alpha_{equi}} \quad \text{where} \quad \alpha_{equi} = (\alpha_a + 1)(\alpha + 1) - 1\,. \tag{102}$$

The new α_{equi} brings information regarding the two points with zero or infinite derivatives [115]. Let us consider that an RPD generates by two points; one of them corresponds to an extreme point with α given by Equation (93) and the second one corresponds to an unbounded derivative, hence α is given by Equation (99). In this case, the equivalent value of α, following Equation (102), is given by:

$$\alpha_{equi} = \frac{q' + 1}{q + 1} - 1. \tag{103}$$

Consequently, if $q' = q$ we have in Equation (103) $\alpha = 0$ and we recover the classical uniform reinjection. In Ref. [115] a map was reported having a point like x_m with zero derivative, and other one like x_∞ with infinite derivatives. An important characteristic of this class of maps is that they can map x_m into x_∞. The topological position of these two critical points can produce a drastic change of the exponent α. that depends on a given control parameter. In Ref. [115] there are reported three cases; the RPD is driven by the neighbor of x_m, by the neighbor of x_∞, or finally by the neighbor of both points. In the last case, the parameter α is given by Equation (103). The RPD for the mentioned cases are $\phi_1(x) = bx^{-\frac{1}{2}}$, $\phi_2(x) = b|x|$, and $\phi_3(x)$ is the uniform reinjection.

Note from Figures 4 and 5 that the reinjection process can be controlled by the points with a derivative equal to zero or tending to infinite.

3.2. Type-II Intermittency

3.2.1. Length of Laminar Phase

Let us develop the new length of laminar phase for type-II intermittency. Let us introduce a continuous differential equation for the local map (68):

$$\frac{dx}{dl} = \varepsilon x + a\, x^p \tag{104}$$

where l representes the number of iterations in the laminar region, that is, the length of the laminar phase. Note that l depends, as in the classical case, on the reinjection point x, and from Equation (104) it is given by: [58]

$$l(x,c) = \int_x^c \frac{d\tau}{a\tau^p + \varepsilon\tau} \tag{105}$$

and by integration we obtain:

$$l(x,c) = \frac{1}{\varepsilon}\left[\ln\left(\frac{c}{x}\right) - \frac{1}{p-1}\ln\left(\frac{ac^{(p-1)} + \varepsilon}{ax^{(p-1)} + \varepsilon}\right)\right]. \tag{106}$$

We notice that Equations (104)–(106), referring to the local behavior in the laminar region, are similar to Equations (21) and (22), but now the local parameter p determines the evolution in the laminar region. Consequently, the probability density of the length of laminar phase $\psi(l)$ depends on $\phi(x)$, that is, a global property, as follows:

$$\psi(l) = \phi(X(l))\left|\frac{dX(l)}{dl}\right| = \phi(X(l))|\varepsilon X(l) + a\, X(l)^p| \tag{107}$$

where $X(l)$ is the inverse function of $l(x,c)$, and we have used Equation (104). Finally, after some algebraic manipulation we obtain:

$$\begin{aligned}\psi(l) =& b\left(\left(\frac{\varepsilon}{\left(a + \frac{\varepsilon}{c^{(p-1)}}\right)e^{(p-1)\varepsilon l} - a}\right)^{\frac{1}{p-1}} - \hat{x}\right)^{\alpha} \times \\ & \left(\frac{\varepsilon}{\left(a + \frac{\varepsilon}{c^{(p-1)}}\right)e^{(p-1)\varepsilon l} - a}\right)^{\frac{p}{p-1}} \left(a + \frac{\varepsilon}{c^{(p-1)}}\right)e^{(p-1)\varepsilon l}\end{aligned} \tag{108}$$

that in the case of $\hat{x} = 0$ takes a more compact form:

$$\psi(l) = b\left(\frac{\varepsilon}{\left(a + \frac{\varepsilon}{c^{(p-1)}}\right)e^{(p-1)\varepsilon l} - a}\right)^{\frac{p+\alpha}{p-1}} \left(a + \frac{\varepsilon}{c^{(p-1)}}\right)e^{(p-1)\varepsilon l} \tag{109}$$

which depends on the global parameter α that is determined by m, the slope function $M(x)$. In Ref. [57], the previous equations for $\psi(l)$ were verified.

3.2.2. Characteristic Relations

Let us consider the average laminar length $\bar{l}$ given by:

$$\bar{l} = \int_0^\infty s\psi(s)ds = \int_{\hat{x}}^c l(x,c)\phi(x)dx. \tag{110}$$

Note that Equation (110) depends on the LBR; consequently, we must split our analysis into different cases. Let us start with $\hat{x} = 0$. In this case, by using Equations (90), (106), and (105) we obtain:

$$\bar{l} = \lim_{x\to 0} \frac{b}{\alpha+1} l(x,c)x^{\alpha+1}\Big|_x^c + \frac{b}{\alpha+1}\int_{\hat{x}}^c \frac{x^\alpha}{\varepsilon + ax^{(p-1)}}dx\,. \tag{111}$$

Following a similar analysis that, in the classical case, we obtain for small values of ε

$$\bar{l} \approx \frac{1}{ac^{\alpha+1}}\left(\frac{a}{\varepsilon}\right)^{\frac{p-\alpha-2}{p-1}} \frac{\pi}{p-1}\sin^{-1}\left(\frac{\pi(1+\alpha)}{p-1}\right) \tag{112}$$

that in the limit $\varepsilon \to 0$ defines the the characteristic relation

$$\bar{l} \propto \varepsilon^{-\beta} \tag{113}$$

where the critical exponent β is given by (see [57]):

$$\beta = \frac{p-\alpha-2}{p-1} = \frac{p(1-m)-1}{(p-1)(1-m)}\,. \tag{114}$$

Note that now, contrary to the classical theory explained in Section 2, β does not take a single value. Now β depends on two things: p relates to the local map around the origin and m or α relate to the global dynamics of the map. Note also that, according to Equation (114) and taking into account that $-1 < \alpha < p-2$, the critical exponent, β, must be in the interval $(-1, 0)$ for any value of p.

Before we study the case of $\hat{x} < x_0$, let us show the necessary condition to obtain $\bar{l}$ as in the uniform reinjection case. Suppose that $\phi(x)$ satisfies the following conditions:

(i) $\phi(0) \neq 0$

(ii) $\left.\frac{\mathrm{d}\phi(x)}{\mathrm{dx}}\right|_0$ is bounded.

Then, for points close enough to $x = 0$, the slope of the function $M(x)$ can be approximated as $m \approx 1/2$, and consequently it produces the same value of β as in the case of uniform reinjection [58].

As a consequence, the characteristic exponent reported in classical theory for uniform reinjection can be obtained not only for this case but also by any RPD that satisfies the previous two conditions. We need the previous result so we can recover the estimation of the characteristic exponent β in the case of $\hat{x} < x_0$. Note that now the two previously mentioned conditions are satisfied by the RPD, the exponent β is given by Equation (114), with $\alpha = 0$ as in the uniform reinjection case. In conclusion, the average length, $\bar{l}$, can be classified into the following cases:

- Case A: $\hat{x} \approx x_0$
  - A1: $m \in (0, 1-\frac{1}{p})$ or equivalent $\alpha \in (-1, p-2)$.

$$\beta = \frac{\alpha+2-p}{1-p} = \frac{1+p(m-1)}{(1-p)(1-m)} \tag{115}$$

– A2: $m \in [1 - \frac{1}{p}, 1)$ or equivalent $p - 2 < \alpha$. We have, in this case:

$$\beta = 0 \tag{116}$$

- Case B: $\hat{x} > x_0$. There is an upper cut-off for l. In this case, with the limit $\varepsilon \to 0$, the value of $\bar{l}$ practically remains constant, hence:

$$\beta = 0 \tag{117}$$

- Case C: $\hat{x} < x_0$.

$$\beta = \frac{p-2}{p-1}. \tag{118}$$

as in the uniform reinjection.

3.3. Type-III Intermittency

Let us consider an illustrating model exhibiting type-III intermittency, as follows (see Figure 6):

$$x_{n+1} = F_{III}(x_n) = -(1+\varepsilon)\ x_n - a\ x_n^3 + d\ x_n^6\ \sin(x_n)\,. \tag{119}$$

The map shown in Figure 6 presents two important differences with respect to the previous one. On one hand, points in the neighbor of the maximum or minimum need two iterations of the map to reach the laminar reinjection, and on the other hand, it presents a symmetric reinjection mechanism into the laminar region.

Concerning the first difference, we must apply Equation (91), which refers to an indirect reinjection to recover the general power law for the RPD (84).

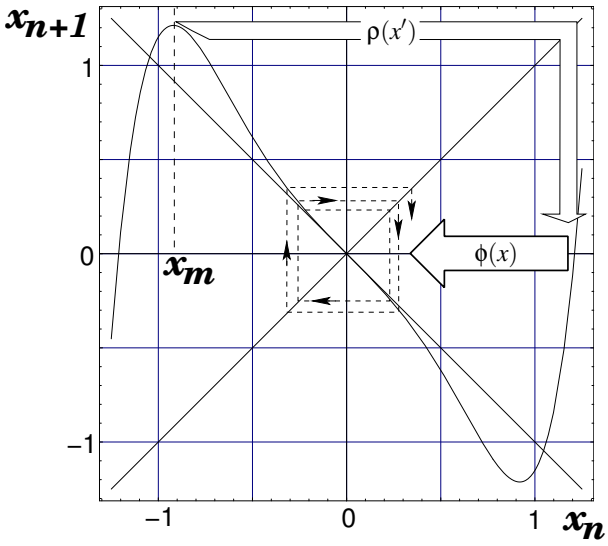

Figure 6. Map (119) with type-III intermittency. The reinjection mechanism is displayed by empty arrows. The dashed arrow shows the trajectory in the laminar region, and x_m indicates the maximum of the map. Reprinted from the book "New Advances on Chaotic Intermittency and its Applications," authors Sergio Elaskar and Ezequiel del Rio, Copyright (2017) with permission from Springer Nature.

Concerning the second characteristic of the map of Figure 6, that is, the two symmetric reinjection mechanisms, we must considered two cases. First, if $\hat{x} > 0$, then we recover the RPD given by Equation (84). In the second case, when $\hat{x} < 0$, the RPD must include

the overlapping effect of the two symmetry reinjections, which can be described by the following function:

$$\phi(x) = \begin{cases} b\left[(|\hat{x}| + x)^{\alpha} + (|\hat{x}| - x)^{\alpha}\right] & \text{if} \quad |x| \leqslant |\hat{x}| \\ b(|\hat{x}| + x)^{\alpha} & \text{if} \quad |\hat{x}| < x \leqslant c \\ b(|\hat{x}| - x)^{\alpha} & \text{if} \quad -c < x \leqslant -|\hat{x}| \end{cases} \tag{120}$$

where $b > 0$ is determined by the standard normalization condition. Note that the function $M(x)$ given by Equation (120) is not linear, but is still useful for finding the RPD from data series. To do this, we notice that $\phi(x)$, given by Equation (120), has two non-continuous points at $x = |\hat{x}|$; hence, $M(x)$ should be non-differentiable at these points, that is, $\hat{x}$ must appear as a vertex point. Following the definition of $M(x)$ given by Equation (87), we obtain, for the RPD of Equation (120), the following expression:

$$M(x) = \frac{1}{(2+\alpha)}\left[(1+\alpha)x - |\hat{x}| + 2\frac{|\hat{x}|(|\hat{x}| - x)^{1+\alpha} - |\hat{x}|^{2+\alpha}}{(|\hat{x}| - x)^{1+\alpha} - (|\hat{x}| + x)^{1+\alpha}}\right] \tag{121}$$

which, for the value $x = |\hat{x}|$, gives:

$$M(|\hat{x}|) = \frac{\alpha + 2^{-\alpha}}{\alpha + 2}|\hat{x}| \tag{122}$$

from which α can be obtained. More details regarding this method can be found in Ref. [58].

Length of Laminar Phase

In Section 2.3, it was shown that the length of the laminar phase of type-III can be obtained as in the type-II intermittency. This is because from Equation (69) we have:

$$|x_{n+1}| = (1+\varepsilon)|x_n| + a|x_n|^p \tag{123}$$

which can be approached by the following continuous differential equation:

$$\frac{d|x|}{dl} = \varepsilon|x| + a|x|^p \tag{124}$$

where l represents the number of iterations in the laminar region. As Equation (124) is similar to Equation (104), we can usel the results for type-II intermittency; hence, the functions determining the exponent β is the same as in the case of type-II intermittency.

3.4. Type-I Intermittency

3.4.1. Length of Laminar Phase

For type-I intermittency we obtain, from Equation (67), the continuous differential equation equivalent to Equation (5), as follows:

$$\frac{dx}{dl} = \varepsilon + a\,x^p, \tag{125}$$

from which we can obtain $l = l(x, c)$ as a function of x,

$$l(x,c) = \frac{c}{\varepsilon}\,{}_2F_1\left(\frac{1}{p}, 1; 1 + \frac{1}{p}; -\frac{a\,c}{\varepsilon}\right) - \frac{x}{\varepsilon}\,{}_2F_1\left(\frac{1}{p}, 1; 1 + \frac{1}{p}; -\frac{a\,x}{\varepsilon}\right), \tag{126}$$

in terms of the Gauss hypergeometric function ${}_2F_1(a, b; c; z)$ [116], which, for $p = 2$, $l(x, c)$, can be expressed by:

$$l(x,c) = \frac{1}{\sqrt{a\,\varepsilon}}\left[\tan^{-1}\left(\sqrt{\frac{a}{\varepsilon}}\,c\right) - \tan^{-1}\left(\sqrt{\frac{a}{\varepsilon}}\,x\right)\right]. \tag{127}$$

In the case of type-I intermittency, Equation (107) can be rewritten as follows

$$\psi(l) = \phi(X(l,c))\left|\frac{\mathrm{d}X(l,c)}{\mathrm{d}l}\right| = \phi(X(l,c))|aX(l,c)^p + \varepsilon| \tag{128}$$

where an explicit expression for $X(l,c)$ can be obtained from Equation (126) only for a few cases. However, following Ref. [60], we can plot the function, ψ, by using the parametrization suggested by Equation (128):

$$(l(x,c), \psi'(x)) = (l(x,c), \phi(x)|\varepsilon + ax^p|)\,, \tag{129}$$

where we have taken as the free parameter the coordinate of the reinjected points, x. Contrary to the classical theory, now we have different shapes for the probability density of laminar lengths $\psi(l)$ depending on α and $\hat{x}$. Note that the maximum length of $l = l_{max}$ is given for $x = \hat{x}$; it is then possible to obtain the value of $\psi(l_{max})$ by means of Equation (129) as:

$$\lim_{l\to l_{max}} \psi(l) = \lim_{x\to\hat{x}} \psi'(x) = \begin{cases} 0 & \text{if} \quad \alpha > 0 \\ b(\varepsilon + a\hat{x}^p) & \text{if} \quad \alpha = 0 \\ \infty & \text{if} \quad \alpha < 0 \end{cases} \tag{130}$$

which depends on α. Concerning the maximum and minimum of the function $\psi(l)$, and taking into account Equations (125) and (128), such points are given by the root of the following equation:

$$\frac{\mathrm{d}\psi(l)}{\mathrm{d}l} = \left((\varepsilon + ax^p)\frac{\mathrm{d}\phi(x)}{\mathrm{d}x} + a\,p\,\phi(x)\,x^{p-1}\right)\left|\frac{\mathrm{d}X(l)}{\mathrm{d}l}\right| = 0\,. \tag{131}$$

Because Equation (125) imposes $\mathrm{d}X(l)/\mathrm{d}l \neq 0$ for $\varepsilon \neq 0$, the expression inside the brackets in (131) must be zero for $x \in (\hat{x}, c)$ and $\varepsilon \approx 0$; consequently, the roots approach to

$$x_{r1} \approx 0 \quad \text{and} \quad x_{r2} \approx \frac{p\,\hat{x}}{\alpha + p}. \tag{132}$$

We conclude that the extreme points of $\psi(l)$ must occur at $L(x_{r1})$ and $L(x_{r2})$, only if x_{r1} and x_{r2} lie in $(\hat{x}, c)$.

Following previous arguments and the three cases splitting in Equation (130), we have six cases for the extreme points of $\psi(l)$. Equation (133) indicates the classification of the $\psi(l)$ according to its local extreme types, at $L(x_{r1})$ and $L(x_{r2})$, depending on the α and $\hat{x}$ values in the RPD; in addition, the limits $\lim_{l\to l_{max}} \psi(l)$ are given.

The corresponding different $\psi(l)$ profiles, depending on $\hat{x}$ and α, can be found in Ref. [60]. It is interesting to note that for $\alpha > 0$ we have $\psi(l_{max}) = 0$, and the shape of $\psi(l)$ has important differences from that obtained from classical theory, as can be seen in [41,42], for instance:

$$\begin{aligned}
&\alpha = 0,\ \hat{x} < 0 \Rightarrow\ L(x_{r1}) : \text{min},\ L(x_{r2}) : \nexists,\ \lim_{l\to l_{max}} \psi(l) \to \frac{\varepsilon + a\hat{x}^p}{|\hat{x} - c|} \\
&\alpha = 0,\ \hat{x} > 0 \Rightarrow\ L(x_{r1}) : \nexists,\ L(x_{r2}) : \nexists,\ \lim_{l\to l_{max}} \psi(l) \to \frac{\varepsilon + a\hat{x}^p}{|\hat{x} - c|} \\
&\alpha > 0,\ \hat{x} < 0 \Rightarrow\ L(x_{r1}) : \text{min},\ L(x_{r2}) : \text{MAX},\ \lim_{l\to l_{max}} \psi(l) \to 0 \\
&\alpha > 0,\ \hat{x} > 0 \Rightarrow\ L(x_{r1}) : \nexists,\ L(x_{r2}) : \nexists,\ \lim_{l\to l_{max}} \psi(l) \to 0 \\
&\alpha < 0,\ \hat{x} < 0 \Rightarrow\ L(x_{r1}) : \text{min},\ L(x_{r2}) : \nexists,\ \lim_{l\to l_{max}} \psi(l) \to \infty \\
&\alpha < 0,\ \hat{x} > 0 \Rightarrow\ L(x_{r1}) : \nexists,\ L(x_{r2}) : \text{min},\ \lim_{l\to l_{max}} \psi(l) \to \infty
\end{aligned} \tag{133}$$

3.4.2. Characteristic Relations

Let us describe how the characteristic exponent depends on the RPD of Equation (90). We remember that the characteristic relation Equation (113) defines the exponent β driven by the mean value of l given by Equation (110).

Taking into account the fact that the function ψ depends on $\hat{x}$ and α, to get the characteristic exponent β for type-I intermittency we can follow a similar analysis that has been carried out for type-II intermittency. We again found not a single value, and it is given as the following cases:

- Case D: $\hat{x} \approx x_0$
  - D1: $\alpha \in (-1, p-2)$. Equations (90), (128), and (110) give:

$$\beta = \frac{p-\alpha-2}{p} = 1 - \frac{1}{(1-m)p}. \tag{134}$$

    As in the type-II intermittency, assuming that the conditions given by Equation (93) holds, Equation (134) transforms into:

$$\beta = 1 - \frac{q+2}{p(q+1)} \tag{135}$$

  - D2: $p-2 < \alpha$. Now we have:

$$\beta = 0 \tag{136}$$

- Case E: $\hat{x} > x_0$.

$$\beta = 0 \tag{137}$$

- Case F: $\hat{x} < x_0$.
  - F1: $\alpha > 0$

$$\beta = \frac{p-2}{p}. \tag{138}$$

  - F2: $\alpha < 0$

$$\beta = \frac{p-1}{p}. \tag{139}$$

3.5. Remarks on the Characteristic Exponent β

Some comments can be related to the previous analysis. First of all, note that in Case C the value of β can also be given by setting $\alpha = 0$ in the expression of Case A1. In this way we obtain the same characteristic exponent as in the classical uniform RPD, but note that now we do not have a uniform RPD. This is because, in Case C, the RPD given by Equation (120) satisfies the conditions *i* and *ii* explained in Section 3.2.2. Accordingly, the value of β must correspond to the uniform reinjection case.

Note also that, for type-I intermittency, we can not apply the same argument, as we explain below.

While in type-II and III intermittencies the contribution to $\bar{l}$ of the points reinjected far from x_0 is neglected, in the type-I intermittency the reinjected points in the region $x < x_0$ must go across the narrow corridor extended along the laminar region, producing an important contribution to $\bar{l}$. A more complete discussion on this point can be found in [60].

Classically, the characteristic exponent β was used to identify the intermittency type, and at this time it is still used for such tasks. Note that after the previous discussion we obtain β as a function of α and $\hat{x}$; hence, we can question ourselves whether or not there is a parameter set that gives the same values of β, even in the case of different intermittent types. To answer this question, we studied two maps with type-I and II intermittencies and let β_I and β_{II} be their characteristic exponents, respectively, and let us

assume that $\beta_I = \beta_{II}$. Let us suppose that $\hat{x}_I = \hat{x}_{II} \approx x_0$; hence, from Cases A1 and D1 and Equations (115) and (134), respectively, we have α_I as follows:

$$\alpha_I = \frac{p_I(\alpha_{II}+1)}{p_{II}-1} - 2 \tag{140}$$

where I and II refer to the intermittency type. To fix this idea, we can consider only the case $p_I = p_{II} - 1$ as it happen in the classical nonlinearities for the local map. Remember that, classically, the folllowing were used: $p_{II} = 3$ and $p_I = 2$. To obtain the same values for the characteristic exponents for type-I and type-II and considering Equation (140), we get the simple relation, $\alpha_I = (\alpha_{II} - 1)$, which also works for type-III intermittency. A more complete discussion regarding this topic can be found in [39].

Finally, for maps with a point such as x_m with zero derivative and others such as x_∞ with infinite derivative, the value of β can strongly depend on the small variations of a control parameter [115]. In this cases, there is not a well defined characteristic relation.

4. Classical Theory about Noise Effects in Chaotic Intermittency

Because noise is always present in nature, it is very important to understand the effect of noise on systems. Previously, there has been a great effort to investigate noise effect in the chaotic intermittency phenomenon.

To study noise in the intermittent maps, several techniques have been proposed. The most popular are, on one hand, renormalization group analysis, and on the other hand, by using the Fokker–Plank equation. Note that these techniques are based on different mathematics fields, but in both case they have in common the fact that they consider only the noise effect in the laminar region on the map. It is clear that the noise affects the whole system, not just the local map; however, in most of the papers dedicated to the noise effect in chaotic intermittency, only noise in the laminar region is considered. Following these classic arguments, let us first consider the main results concerning noise in classical intermittency theory. In Section 4.1, noise effects using the Fokker–Plank approach are considered, whereas in Section 4.4 we deal with Renormalization Group Theory applied to study the noise effects in chaotic intermittency.

In Section 3, we introduced an RPD function that has been observed in a wide class of maps; consequently, in Section 5 we will consider the effect of noise on the RPD.

4.1. Noise Effect —Fokker–Plank Approach

In this subsection, we analyze the noise effects in classical types of intermittency by using the Fokker–Plank equation. Type-I intermittency is analyzed in the next subsection, while Type-II and III intermittencies perturbed by noise are studied in Section 4.3.

4.2. Type-I Intermittency

In the noiseless case, Equation (3) describes the local map for type-I intermittency in the laminar region. However, for $|\varepsilon| << 1$ we can approach the local map by the continuous Equation (5). Let us introduce an additive noise to Equation (3), as follows:

$$x_{n+1} = F(x_n) = \varepsilon + x_n + a\, x_n^2 + \sqrt{2D}\xi_n \tag{141}$$

where D is the spatial diffusion and ξ_n is taken to be a white Gaussian noise of zero mean and delta-correlated. The difference Equation (141) can be approached by a stochastic differential equation, as follows [42]:

$$\frac{\mathrm{d}x}{\mathrm{d}t} = -\frac{\mathrm{d}V(x)}{\mathrm{d}x} + \sqrt{2D}\xi(t) \tag{142}$$

where $\xi(t)$ is also a white Gaussian noise with zero mean and delta-correlated in time; hence, $< \xi(t) >= 0$ and $< \xi(t')\xi(t) >= \delta(t' - t)$, and the potential $V(x)$ is given by:

$$V(x) = -\frac{1}{3}ax^3 - \varepsilon x + c \tag{143}$$

Figure 7 represents the local map and the potential $V(x)$ for values of $\varepsilon < 0$. Note that for $\varepsilon < 0$ the map has two fixed points that meet in a single one for $\varepsilon = 0$. The stable point correspond to the minimum of the potential, whereas the unstable one correspond to the maximum. The extreme points are given by:

$$x_s = -\sqrt{-\varepsilon/a} \quad \text{and} \quad x_u = \sqrt{-\varepsilon/a}\,. \tag{144}$$

Note that in the noiseless map, this scenario does not show intermittency due to there being a stable fixed point. However, in the noisy scenario, the noise can move the trajectory outside onto the potential well, and then the trajectory can go through the laminar region, as in the noiseless intermittency case. The stochastic differential Equation (142) corresponds to the equation of motion of a massless particle in the potential $V(x)$ perturbed by an external noise; hence, by the standard methodology used in the stochastic theory [54], we can reach the corresponding backward Fokker–Plank equation (FPE), as follows:

$$\frac{\partial G(x,t)}{\partial t} = -\frac{\mathrm{d}V(x)}{\mathrm{d}x}\frac{\partial G(x,t)}{\partial x} + D\frac{\partial^2 G(x,t)}{\partial x^2} \tag{145}$$

where $G(x,t)$ is the probability density of finding a particle at the position x in the time t. To obtain the average laminar length in Equation (145), it is necessary to consider the mean first-passage time (MFPT) over the potential barrier $(V(x_s) - V(x_u))$. The MFPT is defined by the mean time escaping time $T(x)$, as follows:

$$T(x) = -\int_0^\infty \frac{\partial G(x,t)}{\partial t} t dt, \tag{146}$$

with the boundary conditions $G(x,0) = 1$ and $\lim_{t\to\infty} G(x,t) = 0$. Hence, we consider that all particles are placed in x at $t = 0$ and no particle can be found at x for a long enough time. By integrating Equation (145), we obtain a differential equation for the function $T(x)$, as follows:

$$0 = 1 - \frac{\mathrm{d}V(x)}{\mathrm{d}x} + D\frac{\mathrm{d}^2 T(x)}{\mathrm{d}x^2} \tag{147}$$

where the solution of Equation (147) can be written by means of integrals, as follows:

$$T(x) = k\int_{\hat{x}}^{x} \exp\left(\frac{1}{D}V(x')\right)dx' - \frac{1}{D}\int_{\hat{x}}^{x}\int_{\hat{x}}^{x'} \exp\left(\frac{1}{D}(V(x') - V(x''))\right)dx''\,dx'\,. \tag{148}$$

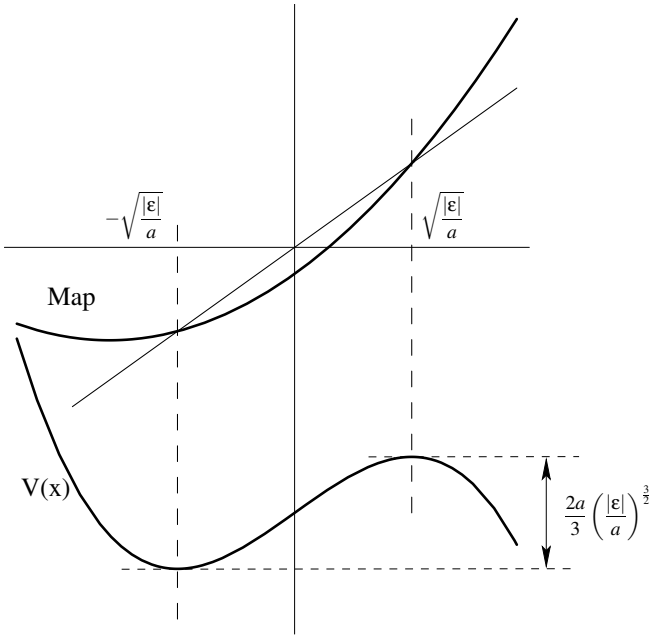

Figure 7. Local map of Equation (141) for $\varepsilon < 0$ and its associated potential Equation (143). The potential barrier is also indicated. Reprinted from the book "New Advances on Chaotic Intermittency and its Applications," authors Sergio Elaskar and Ezequiel del Rio, Copyright (2017) with permission from Springer Nature.

Notice that in Equation (148) the second term is dominant due to the factor $\frac{1}{D}$, but it is not integrable analytically so it is necessary to approach the potential by a second order Taylor expansion around the extreme point x_s, as follows:

$$V(x_s) \approx V(x_s) + \frac{1}{2}V''(x_s)(x - x_s)^2 + O((x - x_s)^3)\,, \tag{149}$$

where V'' indicates the second derivative of the function $V(x)$. In a similar way, we approach $V(x_u)$ around the point x_u. With this procedure, the solution to Equation (147) is given by:

$$\begin{aligned} T(x) \approx & -\frac{1}{D}\exp\left(\frac{1}{D}(V(x_u) - V(x_s))\right) \times \\ & \int_{\hat{x}}^{x}\int_{\hat{x}}^{x'} \exp\left(\frac{1}{2D}(V''(x_u)(x' - x_u)^2 - V''(x_s)(x'' - x_s)^2)\right) dx''\,dx'\,. \end{aligned} \tag{150}$$

To evaluate the integral in Equation (150), we need to introduce further approximation. Hence, we assume that $\hat{x} \ll x_s$, that is $\hat{x} \ll \sqrt{-\varepsilon}$; consequently, the reinjection takes place very close to $x = 0$, and finally we obtain an estimation for MFPT, as follows:

$$T = \frac{2\pi}{\sqrt{V''(x_s)V''(x_u)}}\exp\left(\frac{-B}{D}\right) \tag{151}$$

where B is the potential barrier height needed to jump the particle in the potential well. For the potential (143), we have (see Figure 7):

$$B = V(x_u) - V(x_s) = \frac{2a}{3}\left(\frac{|\varepsilon|}{a}\right)^{\frac{3}{2}} \tag{152}$$

and by using Equation (144), we obtain an estimation for the MFPT, which is for the average laminar length, $\bar{l}$, in the case of $\varepsilon < 0$, as:

$$\bar{l} \propto T = \frac{\pi}{\sqrt{a|\varepsilon|}} \exp\left(\frac{4}{3D\sqrt{a}}|\varepsilon|^{\frac{3}{2}}\right). \tag{153}$$

Equation (153) requires some comments. Note that as we approach the potential around the extreme points, Equation (153) can not be applied if there are no extreme points, that is, for $\varepsilon > 0$. Consequently, the particle will cross the laminar region in a similar way to that in the noiseless case, because the map iterations will be dominant over the small noise perturbation.

The solution given by Equation (153) is in agreement with the result obtained by the renormalization group technique, as we will see in Section 4.4. This approximation Equation (153) has been observed numerically in the two coupled Rössler oscillators [54].

4.3. Type-II and III Intermittency

For type-II and III intermittencies, the corresponding perturbed map by noise can be obtained from the pure deterministic map proposed in Section 2, as follows:

$$x_{n+1} = \mp(1+\varepsilon)x_n \mp a\, x_n^3 + \sqrt{2D}\xi_n \tag{154}$$

where the plus sign refers to type-II and the minus sign refers to type-III. As in the case of type-I, for very small values $(x_{n+1} - x_n)$, the difference Equation (154) can be approached by Equation (142), where the potential $V(x)$ is now a symmetric function, as follows:

$$V(x) = -\frac{1}{4}ax^4 - \frac{\varepsilon}{2}x^2 + c \tag{155}$$

having a single potential well at $(x = 0)$ between two maxima, as represented in Figure 8.

Hence, by applying Equations (151) and (152) to the potential Equation (155) and taking into account that

$$B = V(\sqrt{-\frac{\varepsilon}{a}}) - V(0) = \frac{\varepsilon^2}{4\,a}. \tag{156}$$

Equation (150) transforms into a new one:

$$\bar{l} \propto T = \frac{\sqrt{2}\pi}{|\varepsilon|} \exp\left(\frac{1}{3D\,a}|\varepsilon|^2\right). \tag{157}$$

The approximation Equation (157) has been observed in an electronic circuit [55].

Notice that Equation (151) remembers the Arrhenius formula regarding the chemical reaction theory.

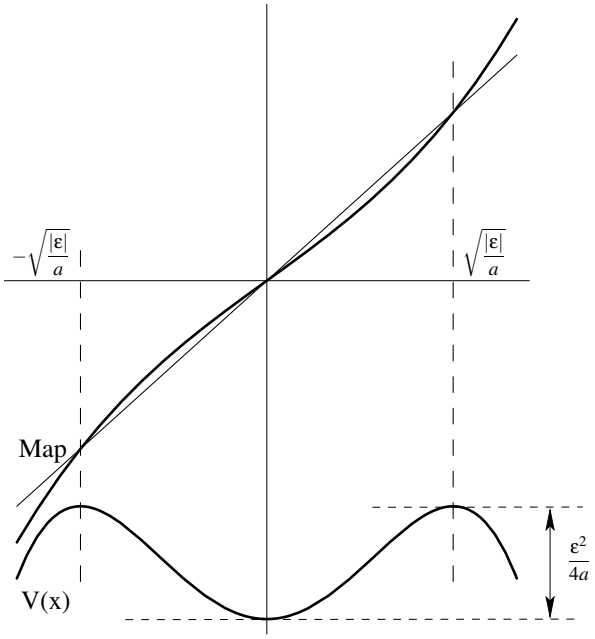

Figure 8. Local map of Equation (154) for $\varepsilon < 0$ and its associated potential Equation (155). The potential barrier is also indicated. Reprinted from the book "New Advances on Chaotic Intermittency and its Applications," authors Sergio Elaskar and Ezequiel del Rio, Copyright (2017) with permission from Springer Nature.

4.4. Renormalization Group and Scaling Theory

The renormalization group theory (RGT) applied to deterministic chaos was first used in the Feigenbaum cascade, because the period-doubling scenario provides a mathematical structure to be renormalized. A similar methodology has been applied to the map with chaotic intermittency, but it has only been applied to the laminar region of the map. This is an important difference with respect to the Feigenbaum cascade case, because in the intermittency case the general expression for the RPD is not considered to apply to the RGT; in particular, the roll played by the LBR is excluded [113]. Let us consider a generalization of the local map (3), as follows:

$$x_{n+1} = F(x_n) = \varepsilon + x_n + a\ |x_n|^p + \sigma\xi_n \tag{158}$$

where $\sigma = \sqrt{2D}$ is the diffusion term .

First, we consider the usual case $p = 2$ and the map $x'' = F^2(x') = F(F(x'))$. Let $L(\varepsilon, \sigma)$ be the number of iterations of map F that x' needs to leave the laminar region. Note that this number, referred to as map F^2, should be only a half with respect to F. Suppose also that we found a new set of parameters, ε' and σ', mapping x' into x'' in a single iteration, so we have:

$$L(\varepsilon', \sigma') = \frac{1}{2} L(\varepsilon, \sigma)\,. \tag{159}$$

A similar argument applied to l iterations provides:

$$L(\varepsilon', \sigma') = \frac{1}{l} L(\varepsilon, \sigma)\,. \tag{160}$$

Note that the mathematical function connecting the parameter sets (ε', σ') and (ε, σ) remains unknown, but it is still possible to formulate such function by means of two new scaling exponents, ρ and ν, as follows:

$$\varepsilon' = l^{\rho}\varepsilon \quad \text{and} \quad \sigma' = l^{\nu}\sigma\,. \tag{161}$$

Now Equation (160) can be rewritten in a new form:

$$L(\varepsilon, \sigma) = lL(l^{\rho}\varepsilon, l^{\nu}\sigma)\,. \tag{162}$$

If we multiply Equation (162) by a common factor, we can re-scale the "length" of the laminar region, as follows:

$$l^{\rho}\varepsilon = 1 \tag{163}$$

so Equation (162) becomes:

$$L(\varepsilon, \sigma) = \varepsilon^{\frac{-1}{\rho}} Z\left(\frac{\sigma}{\varepsilon^{\frac{\nu}{\rho}}}\right) \tag{164}$$

where we define the new function Z as $Z(\cdot) = L(1, \cdot)$.

Now the main task is to find the exponents ρ and ν. To do this, we must solve the renormalization group equation, as explained in the following subsection.

4.5. Exact Solution for Renormalization Group Equation

Before considering the noise effect, we need to find the fixed point in the functional space. By applying a similar argument used to develop the renormalization group in the period doubling scenario, a function, $g(x)$, satisfying the following equation, was postulated.

$$\frac{1}{\alpha} g(\alpha x) = g^{l}(x) \tag{165}$$

where α is the scaling factor for the function $g(x)$ after making l steps in the laminar corridor.

The boundary conditions used in this case can be obtained from the function $F(x)$, as defined by Equation (158). That is, for $\varepsilon = 0$, both functions and their derivatives must take the same values at the origin, hence:

$$g(0) = 0 \quad \text{and} \quad g'(0) = 1\,. \tag{166}$$

A solution of Equation (165) with the conditions (166) can be written in the form:

$$g(x) = \frac{x}{\left(1 - d\, x^{\frac{1}{x}}\right)^{q}} \tag{167}$$

where d is an arbitrary constant and we have made the identifications as follows:

$$\alpha = l^{q} \tag{168}$$

The boundary conditions (166) determine a single solution, so by expanding the general solution (167) around the origin and by comparison with the map $F(x)$ of Equation (141),

$$g(x) = x + q\, d\, x^{\frac{1}{q}+1} + \frac{q(q+1)}{2} d^2 x^{\frac{2}{q}+1} + \ldots, \tag{169}$$

by comparison with Equation (141), we obtain:

$$q = \frac{1}{p-1} \tag{170}$$

and by using the relation (168), we obtain the scaling factor as a function of p:

$$\alpha = l^{\frac{1}{p-1}}\,. \tag{171}$$

Now, the fixed point for the renormalization Equation (165) is obtained. The remaining task is to obtain the exponents ρ and ν. For this task, the perturbation theory was used, as

follows. In the case of exponent ρ, a small deterministic perturbation of the fixed point was used:

$$g_n(x) = g(x) + h_n(x) \tag{172}$$

Finally, it is necessary to postulate a convergence ratio, that is:

$$h_n(x) = \lambda^n h(x)\,. \tag{173}$$

By using Equation (165), an eigenvalue problem is defined that is generated by imposing $\lim_{n\to\infty} g_n(x) = g(x)$ and by linearization of Equation (165). Finally, the eigenvalues obtained are as follows [117]:

$$\lambda = l^{\rho}, \quad \text{with} \quad \rho = \frac{p}{p-1}\,. \tag{174}$$

Notice that the characteristic exponent β is defined in the limit $\varepsilon \to 0$, as follows:

$$\bar{l} \propto \varepsilon^{-\beta}, \tag{175}$$

hence we have from Equation (174):

$$\beta = -\frac{p-1}{p} \tag{176}$$

Let us perturb the fixed point $g(x)$ with a small noise:

$$g_n(x) = g(x) + \xi(t)D(x) \tag{177}$$

where $D(x)$ is a small function. By following a similar method to the noiseless case, we found the convergent ratio as follows:

$$\lambda = l^{\nu}, \quad \text{with} \quad \nu = \frac{p+1}{p-1}\,. \tag{178}$$

Hence Equation (164) is transformed into the new one:

$$L(\varepsilon,\sigma) = \varepsilon^{\frac{1-p}{p}} Z\left(\frac{\sigma}{\varepsilon^{\frac{p+1}{p}}}\right). \tag{179}$$

The renormalization group has a clear meaning in the chaotic route to chaos determined by the Feigenbaum cascade, but here in the intermittency scenario its real meaning is a little different. The most that we can find from Equation (164) in the nonperturbed case, that is, ($\sigma = 0$), is the function $L(\varepsilon, 0)$, which determine how fast L increases as ε decreases; hence we must have:

$$\beta = -\frac{p-1}{p}\,. \tag{180}$$

However, for $\sigma \neq 0$ it is difficult to determine β because the function Z in Equation (179) remains unknown.

Note also that in the case of $p = 2$, Equation (179) takes the specific form:

$$L(\varepsilon,\sigma) = \frac{1}{\sqrt{\varepsilon}} Z\left(\frac{\sigma}{\varepsilon^{\frac{3}{2}}}\right) \tag{181}$$

which is consistent with Equation (153). Note, however, that Equation (153) was derived for $\varepsilon < 0$, whereas this is not the case for Equation (181). Moreover, $\varepsilon \gg 0$ and $\sigma > 0$, as the scaling properties of the intermittency, are not in agreement with Equation (181) because the deterministic component of the map is dominant over the small noise [54].

The cases of type-II and III intermittencies have an additional difficulty due to Equation (164) for $\sigma = 0$ has the following form [118]:

$$L(\varepsilon, x_o, c) = 2^{-n} L(\lambda^n \varepsilon, \alpha^n x_o, \alpha^n c) \tag{182}$$

where x_0 is the starting point in the laminar region and c indicates the end of the laminar region. The important aspect of Equation (182) is that the laminar region shows three characteristic exponents, that is, $L(\lambda^n \varepsilon, \alpha^n x_o, \alpha^n c)$ remains constant under change of both $\alpha^n x_o$ and $\alpha^n c$. Unfortunately, the renormalization group theory cannot determine whether this is true or not.

Finally, we must remember that the classical noise theory applied to intermittencies only considers the noise effect on the local map. This is because classically it was considered that the RPD was uniform, and hence it was also assumed that the noise does not change this condition enough; however, as explained in Section 3, in the general case the RPD is not constant; hence, in Section 5, the noise on the RPD will be considered.

5. New Formulation of the Noise Effects in Chaotic Intermittency

In this subsection, we develop an analytical approach, the noisy reinjection probability density (NRPD) function, and examine its effect on type-II, III and I intermittencies.

5.1. Noisy Reinjection Probability Density Function (NRPD)

Let us introduce a noise perturbation into Equation (68), with type-II intermittency, as follows:

$$x'_{n+1} = \begin{cases} F(x_n) + \sigma\xi_n & x_n \leq x_r \\ (F(x_n) - 1)^\gamma + \sigma\xi_n & x_n > x_r, \end{cases} \tag{183}$$

where ξ_n is a uniform distributed noise, that is, $< \xi_m, \xi_n >= \delta(m-n)$ and $< \xi_n >= 0$, σ is the noise strength, and $F(x) = (1+\epsilon)x_n + (1-\epsilon)x_n^3$. As before, we denote by x_r the root of the equation $F(x_r) = 1$.

To obtain an analytical formulation for the NRPD, denoted by capital case $\Phi(x)$ to avoid confusion with the lower case $\phi(x)$ with is reserves for the noiseless RPD, we focus our attention on the effect of noise on the reinjection trajectories, as indicated in Figure 9. In such a figure, a noiseless trajectory drawn by a dashed line is sprayed by noise around the noiseless trajectory. Consequently, the reinjection point must be mapped inside an interval represented in Figure 9 by l_0. Note that the noiseless density $\phi'(x)$ must change due to the noise effect into a new density $\Phi(x)$, obtained by the following convolution:

$$\Phi(x) = \int \phi'(y) G(x-y, \sigma) dy, \tag{184}$$

where $G(x, \sigma)$ represents the probability density of the noise term $\sigma\xi_n$ in Equation (183). Note that the function $\phi'(x)$ is unknown because of the noise effect, but taking into account that the density $\rho(x')$ is generated in a region of the map without extreme points, we can approach $\phi'(x)$ as $\phi(x)$ given by Equation (84).

To evaluate the integral (184), we expand $\phi(x)$ to the first term, and integral (184) becomes as follows:

$$\Phi(x) \approx \phi(x) + \frac{\mathrm{d}\phi(x)}{\mathrm{d}x} \int (x-y) G(x-y, \sigma) dy \tag{185}$$

where we have used $\int G(x, \sigma) dx = 1$; consequently, we expect $\Phi(x) \approx \phi(x)$ in the regions for a small enough slope of $\phi(x)$. An important feature of the previous argument is that, for regions far from the LBR, that is $\hat{x}$, where $\Phi(x)$ is small enough, the slope, m, of the noisy function, $M(x)$, approaches the corresponding noiseless slope. This is useful in helping to determine the density, $\phi(x)$, corresponding to deterministic behavior. Note also that we need to know $\phi(x)$ to evaluate integral (184). In the following subsections, we will apply this result to some relevant cases of noisy intermittencies.

Note that the length of the laminar period in the noisy intermittency is determined by Equation (107), but now the function $\phi(x)$ should be changed by the corresponding RPD in the noisy scenario, that is $\Phi(x)$. We notice that this method, contrary to the classical analysis, takes into account, not the noise in the laminar region, but only the noise effect on the RPD. However, it provides a good approximation as it has been confirmed in a number of maps [39,62,63,68].

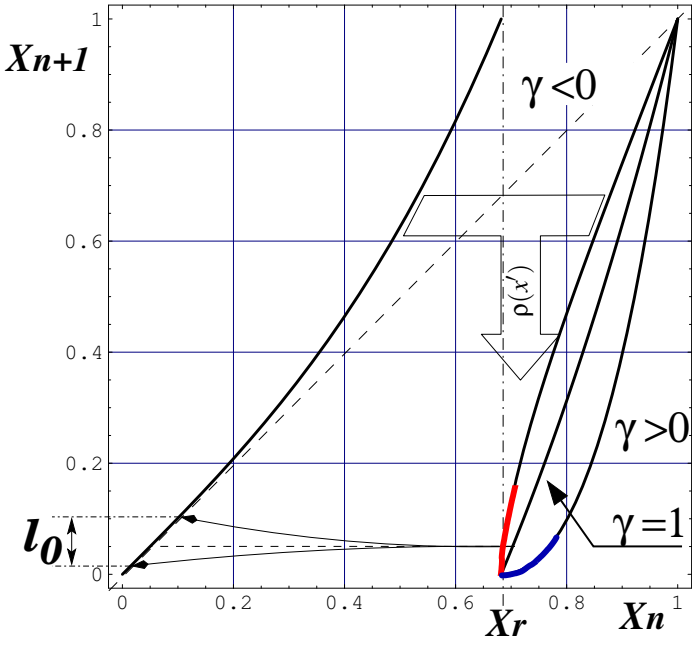

Figure 9. Noisy map (183). The horizontal dashed line indicates the noiseless trajectory going into the laminar region. The nosily trajectory should be expanded to end inside the interval l_0. Reprinted from the book "New Advances on Chaotic Intermittency and its Applications", authors Sergio Elaskar and Ezequiel del Rio, Copyright (2017) with permission from Springer Nature.

5.2. Noise Effect on Type-II Intermittency

Let us consider for this case the map (183) from the interval $[0,1]$ into itself. Note that, due to the noise, the value of x'_{n+1} may go out of the unit interval. To avoid this problem, we must define the following perturbed map:

$$x_{n+1} = \begin{cases} |x'_{n+1}| & x'_{n+1} \leq 1 \\ |x'_{n+1}| - 2 \bmod(|x'_{n+1}|, 1) & x'_{n+1} > 1. \end{cases} \tag{186}$$

As in the map (183), we have $\hat{x} = 0$, them we have $\phi'(x) \approx \phi(x) = b|x|^{\alpha}$ in Equation (184), where we assume that the probability density, G, in Equation (184) is given by:

$$G(x,\sigma) = \frac{\Theta(x+\sigma) - \Theta(x-\sigma)}{2\sigma}, \tag{187}$$

where $\Theta(x)$ is the Heaviside step function.

Finally, the integral in Equation (184) can be evaluated given the following NRPD:

$$\Phi(x) = \frac{1}{c^{1+\alpha}} \frac{(|x|+\sigma)^{1+\alpha} - Sg(|x|-\sigma)||x|-\sigma|^{1+\alpha}}{2\sigma}, \tag{188}$$

where we denote by $Sg(x)$ the sign function that extracts the sign from its argument. The result (188) is in good agreement with numerical evaluation of the NRPD function in a one-dimensional map [68].

We notice that different expressions should be obtained for NRPD (188) by considering in Equation (184) a different distributions of the noise. However, the noise distributions (187) provide good approaches in most cases.

Regarding noisy function $M(x)$, it must split into two cases. On one hand, for x close to $\hat{x}$, the slope of $M(x)$ approaches $\frac{1}{2}$, as in the case of uniform reinjection. On the other hand, considering that it is far from $\hat{x}$, the value of m for the slope of the noisy $M(x)$ approaches the value obtained for the noiseless case. This fact is very important for obtaining the parameter α of $\phi(x)$ by means of Equation (90). For a numerical simulation for the map Equations (183) and (186), see [39,68].

5.3. Noise Effect on Type-III Intermittency

The noise effect on the RPD of one-dimensional maps with type-III intermittency can be stronger than for type-II intermittency. This is due to the indirect reinjection, as we will see below. Let us consider the following composition of noiseless maps:

$$x'_n = F(x_n) = -(1+\varepsilon)\ x_n - a\ x_n^3 + d\ x_n^6\ \sin(x_n) \tag{189}$$

and the randomly perturbed map, that just adds a noise, defined as:

$$x_{n+1} = x'_n + \sigma\xi_n\,. \tag{190}$$

In Figure 10, the dashed line shows the noiseless trajectory corresponding to a point starting around the maximum of the map. This trajectory, due to the noise effect, may spread over a region of some width, say l_0. Note that l_0 will increase by a factor of K, up to $l_1 = K\,l_0$ on the graph of the map, as shown in Figure 10. Moreover, in Ref. [68], it has been proven that the NRPD for this case can be approximated as follows:

$$\Phi(x) = \frac{1}{c^{1+\alpha}}\frac{(|x|+K\sigma)^{1+\alpha} - Sg(|x|-K\sigma)||x|-K\sigma|^{1+\alpha}}{2K\sigma}. \tag{191}$$

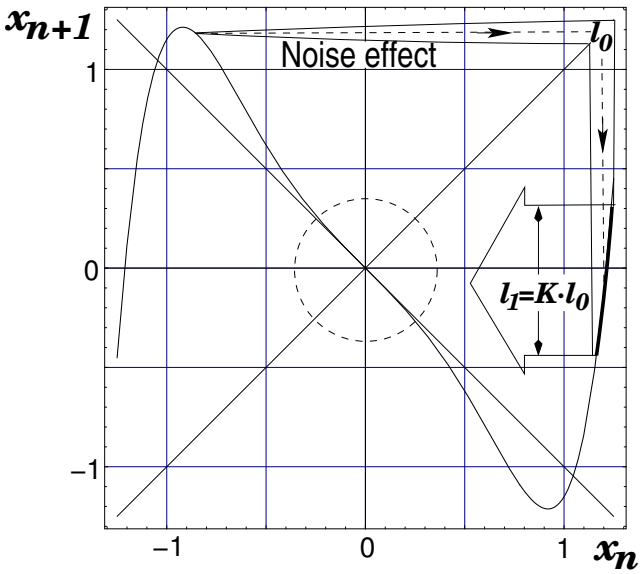

Figure 10. Map of Equation (189). Dashed arrows indicate the trajectory of a point near the maximum. Solid lines at both sides of the mentioned arrows indicate the effect of the noisy map on the same point, which will be mapped on the interval I over the graph of the map. Reprinted from the book "New Advances on Chaotic Intermittency and its Applications," authors Sergio Elaskar and Ezequiel del Rio, Copyright (2017) with permission from Springer Nature.

It is interesting to observe that the factor K in Equation (191), defined as $K = \frac{\mathrm{d}F}{\mathrm{d}x}$, introduces an amplification of the noise effect. Consequently, the whole analysis made

previously in the context of type-II intermittency can also be applied in this case. In particular, in spite of us having the factor K in Equation (191), it is possible to predict the RPD by using the noisy data. This is because the slope of the function $M(x)$, for points x far from $\hat{x}$, is robust against the noise. This technique was used in [68] for the map (189). We notice that, due to the factor k in Equation (191), the noise effect can be increased enough to make significant differences between the noisy slope of $M(x)$ and the noiseless one. However, even in this scenario it is possible to approach the function $M(x)$ for points $x > x_p$ far enough from $\hat{x}$, that is $x_p > \chi$. To do this, by using Equation (184) we can approach $\Phi(x)$ as $\Phi(x) \approx \phi'(x)$ for $x_p > x_0$, so by using the definition of $M(x)$ given by Equation (87), we have:

$$M_n(x) \approx M(x) + \frac{\int_0^{x_p} \tau(\Phi(\tau) - \Phi(\tau))\, d\tau}{\int_0^x \phi(\tau)\, d\tau} \quad \text{if} \quad x > x_0, \tag{192}$$

where $M(x)$ and $M_n(x)$ are the noiseless and noisy functions, respectively. By using Equation (88) to estimated $M(x)$, we get, for $x > x_p$:

$$M(x_l) \approx M_n(x_q) - \frac{C}{q} \approx \frac{\sum_{j=1}^{q} x_j}{q} - \frac{C}{q}. \tag{193}$$

As $M(\hat{x}) = \hat{x}$, the value C is given by the equation $M(\hat{x}) \approx \hat{x}$ to recover the noiseless function $M(x)$. This means that, even in a very high noise strength scenario, the value of α corresponding to the RPD $\phi(x)$ of the noiseless map can be recovered. This methodology has been used previously [68].

5.4. Noise Effect in Type-I Intermittency

To illustrate the effect of noise in type-I intermittency, let us consider a map with direct reinjection, as happened in the type-II case:

$$F(x) = \begin{cases} F_1(x) = \varepsilon + x + a\,x^2 + \sigma\xi_n, & \text{if } x < x_r, \\ F_2(x) = \hat{x} + \dfrac{1-\hat{x}}{(1-x_r)^\gamma}(x - x_r)^\gamma + \sigma\xi_n & \text{if } x > x_r \end{cases} \tag{194}$$

where x_r verifies $\varepsilon + x_r + a\,x_r^2 = 1$. The map (194) is represented in Figure 2 for $\sigma = 0$. Note that this map is similar to Figure 9, but now the boundary conditions should be different because the noisy reinjected point can be mapped out of the unity range.

In this case, the integral (184) gives us the NRPD as:

$$\Phi(x) = \frac{b}{2\sigma(\alpha+1)}\Big\{[x - (\hat{x} - \sigma)]^{\alpha+1} - \Theta[x - (\hat{x} + \sigma)][x - (\hat{x} + \sigma)]^{\alpha+1}\Big\}. \tag{195}$$

where Θ is the Heaviside step function. Let us compare the noisy Equation (195) with the corresponding noiseless RPD. Figure 11 shows both functions, the RPD and the NRPD.

Note that, for $x \to \hat{x}$, Equation (195) can be approached to:

$$\Phi(x) \approx \frac{b}{2\sigma(\alpha+1)}[x - (\hat{x} - \sigma)]^{\alpha+1} \tag{196}$$

as in the corresponding noiseless RPD but with two differences: exponent is now $\alpha + 1$ and the LBR is shifted to $\hat{x} + \sigma$. This effect can be observed in Figure 11, where $\Phi(x) \neq 0$ for points $x < \hat{x}$, whereas $\phi(x) = 0$ for such points. Note also that, due to the Heaviside step function, Equation (195) has a vertex point for $\alpha < 0$. The deterministic LBR should be in the middle of the mentioned vertex point and the noisy LBR, that is $\hat{x} + \sigma$, as shown in Figure 11. As a consequence, the function $M(x)$ can still be approximated by a piecewise

linear function, as in the case of type-II intermittency, but now the new slope is given by Equation (90) with $\alpha + 1$; hence, we have:

$$m_n = \frac{\alpha + 2}{\alpha + 3} \tag{197}$$

so the two slopes of function $M(x)$, the noisy one, m_n, and the one corresponding to the noiseless slope, m, are related by:

$$m_n = \frac{1}{2 - m}\,. \tag{198}$$

Note that, as $m > 0$, we have $m_n > 1/2$ and consequently for $x \to \hat{x}$ we have $\Phi(x) \to 0$.

The relations (195) and (198) are confirmed in one-dimensional noisy maps [62].

It is interesting to note an important consequence of Equation (195). As the value of $\hat{x}$ and α are changed by the noise effect, it is possible to select a set of noisy parameter values that correspond with a set of noiseless values. Moreover, as the noiseless and noisy values are given by $\alpha_n = \alpha + 1$, according to Equation (82), we obtain the following relation for γ_n and γ:

$$\frac{1}{\gamma_n} = \frac{1}{\gamma} + 1\,. \tag{199}$$

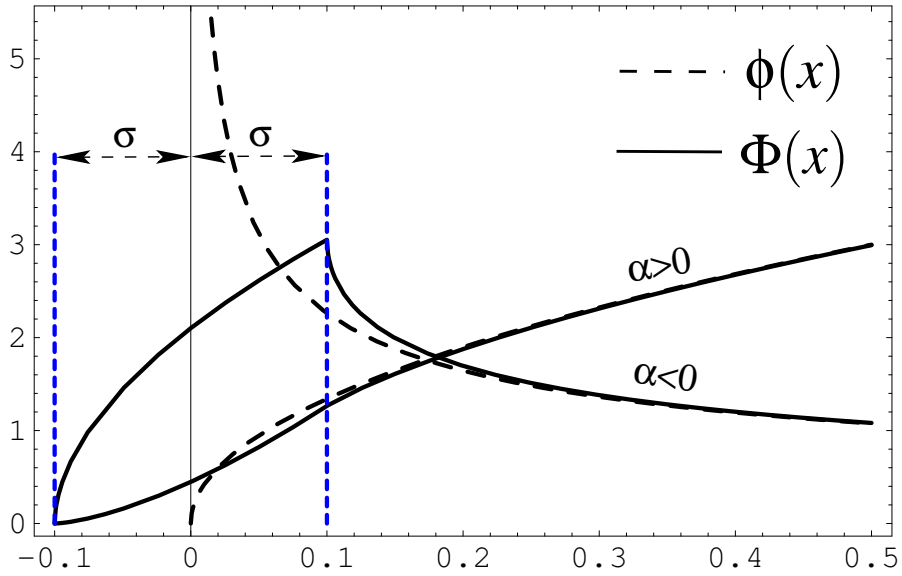

Figure 11. NRPD corresponding to Equation (195) with $\hat{x} = 0$. Dashed and solid lines show RPD and NRPD, respectively. Note that $\Phi(x) \neq 0$ for $x < \hat{x}$, where $\phi(x) = 0$.

6. Statistical Properties of Intermittency Using the Perron–Frobenius Operator

A new methodology to obtain analytical expressions for statistical functions describing chaotic intermittency is introduced here. This methodology implements the Perron–Frobenius operator, called the continuity technique [39,65–67]. This methodology has been successfully applied to type-II and V intermittencies [65,66]. It permits us to obtain very accurate $\phi(x)$ and $\psi(l)$ functions and can be applied when the M function is nonlinear. Nevertheless, to utilize the continuity technique we have to know explicitly the map and its inverse [65].

Let us start with a brief explanation of the evolution of densities [119,120]. We analyzed a family of evolution operators, $F^t(x) : D \to D$, which verified $F^{t_1+t_2} = F^{t_1} \circ F^{t_2}$ and $F^0 =$ identity, $x \in D$, t being the evolution variable, and D a compact manifold. When t is represented by real numbers ($t \in \mathbb{R}$), $F^t(x)$ is a continuous dynamical system. Notwithstanding, when t acquires only integer numbers, the operator $F^t(x)$ is a map. There are

at least two formulations to describe the behavior of $F^t(x)$. One formulation studies individual trajectories, and the other analyzes the density and the probability measure.

We introduce a generic map, $y = F(x)$, which maps some interval $\Delta \subset \mathbb{R}$ into another interval $\Delta_1 \subset \mathbb{R}$. Accordingly, $x \in \Delta$ and $y \in \Delta_1$. In Δ, the trajectories density is $\rho(x)$, although in Δ_1 it is $\rho_1(y)$. By the map application, the density ρ transforms in ρ_1, and we write $\rho_1 = \mathcal{L} \circ \rho$. If the interval $\Delta = [y_0, y]$ has a variable upper limit y, the density $\rho_1(y)$ in the interval Δ_1 results:

$$\rho_1(y) = \frac{d}{dy} \int_{F^{-1}[y_0,y]} \rho(x)\, dx = \rho(F^{-1}(y)) \left| \frac{dF^{-1}(y)}{dy} \right| . \tag{200}$$

Equation (200) assumes $F(x)$ is piecewise differentiable and invertible. In addition, the derivative $\frac{d\,F^{-1}(x)}{d\,x}$ is piecewise continuous [119].

To elaborate a broad study, we consider piecewise monotonic maps:

$$F(x) = \begin{cases} F_1(x), & a_0 \leq x < a_1, \\ F_2(x), & a_1 \leq x < a_2, \\ . & \\ . & \\ . & \\ F_n(x), & a_{n-1} \leq x \leq a_n, \end{cases} \tag{201}$$

where $a_0 = 0$, $a_n = 1$, $F_1(a_0) = 0$, and $F_n(a_n) = 1$. Note that $a_0 = 0$ is a fixed point of the system. The map also verifies $F_i(a_{i-1}) = 0$ for $i = 1, \ldots, n$. This map transforms the closed unit interval onto itself: $F(x) : [0, 1] \to [0, 1]$. Therefore, the state space of the system is $0 \leq x \leq 1$. In addition, Equation (201) shows that the unit interval is divided into n subintervals; and each $F_i(x)$ function is a C^1 function in $[a_{i-1}, a_i)$. For Equation (201), the Perron–Frobenius operator results [119]:

$$P \circ \rho(x) = \frac{d}{dx} \int_{F_i^{-1}[0,x]} \rho(u)\, du = \frac{d}{dx} \sum_{i=1}^{n} \int_{a_{i-1}}^{F_i^{-1}(x)} \rho(u)\, du = \sum_{i=1}^{n} \left| \frac{dF_i^{-1}(x)}{dx} \right| .\rho(F_i^{-1}(x)) \tag{202}$$

To acquire the RPD function, we take into consideration that the first term (first interval) in Equation (202) involves the laminar zone, and it has not to be included in the sum. Accordingly, the RPD function results:

$$\phi(x) = P_{int} \circ \rho(x) = \sum_{i=2}^{n} \frac{dF_i^{-1}(x)}{dx} \rho(x) \tag{203}$$

where $\rho(x)$ is the density in the preceding intervals to reinjection (pre-reinjection points).

$$[a_1, F_2^{-1}(x)), [a_2, F_3^{-1}(x)), \ldots [a_{n-1}, F_n^{-1}(x)] . \tag{204}$$

We assume $\rho(x) = k$, where k is a constant, and it verifies:

$$\sum_{i=1}^{n} \int_{a_{i-1}}^{F_i^{-1}(x)} k\, dx = 1 . \tag{205}$$

In Refs. [39,65,66], the behavior of several maps with intermittency was investigated. Here, we only analyze two maps displaying type-II intermittency and one family of maps with type-V intermittency. The first map with type-II intermittency is a piecewise monotonic map with three subintervals, and the second one shows a nonlinear function M. For type-V intermittency, we study a family of maps without symmetry around the fixed point. These maps can produce type-V intermittency, displaying continuous and discontinuous RPD functions [66].

6.1. Piecewise Monotonic Map with Three Subintervals

We study the following map: [39,65]

$$F(x) = \begin{cases} F_1(x) = (1+\varepsilon)x + (1-\varepsilon)x^p, & 0 \le x < a_1, \\ F_2(x) = [(1+\varepsilon)x + (1-\varepsilon)x^p - 1]^\gamma, & a_1 \le x < a_2, \\ F_3(x) = \left[1 + \ln(\frac{1}{x^{1/\ln(a_2)}})\right]^\theta, & a_2 \le x \le c, \end{cases} \tag{206}$$

where a_1 verifies $(1+\varepsilon)a_1 + (1-\varepsilon)a_1^p = 1$, and $0 < a_1 < a_2 < c$. The map has three subintervals, and the $F_2(x)$ function verifies: $F_2(a_2) < 1$. Note that this map is only an individual case of the map given in Equation (201).

To obtain the RPD, we use Equation (203):

$$\phi(x) = k\left[\frac{x^{\frac{1}{\gamma}-1}}{\gamma\left[(1+\varepsilon)^2 + 4(1-\varepsilon)(1+x^{1/\gamma})\right]^{1/2}} - \frac{\ln(x_z)x_z^{1-x^{1/\theta}}x^{\frac{1}{\theta}-1}}{\theta}\right] \tag{207}$$

where k satisfies

$$\int_{a_1}^{F_2^{-1}(c)} k\,dx + \int_{a_2}^{F_3^{-1}(c)} k\,dx = 1\,, \;\Rightarrow\; k = \frac{1}{F_2^{-1}(c) + F_3^{-1}(c) - a_1 - a_2} \tag{208}$$

where $F_2^{-1}(x)$ is the inverse function of $[(1+\varepsilon)x + (1-\varepsilon)x^p - 1]^\gamma$ and $F_3^{-1}(x)$ is the inverse of $\left[1 + \ln\left(\frac{1}{x^{1/\ln(a_2)}}\right)\right]^\theta$.

Several numerical test were performed (see [39]). For all tests, the theoretical equations very accurately verified the numerical results.

6.2. Map with Nonlinear Function $M(x)$

When the maps display a linear function $M(x)$, the RPD possesses a power law form, $\phi(x) = \Gamma x^\alpha$. For the $M(x)$ function methodology, Γ is a constant, and for the continuity technique, $\Gamma = \chi(x)$ [39].

In this subsection, we analyze a map showing type-II intermittency. This map has a distinctive characteristic: the function $M(x)$ is nonlinear for some range of the control parameters. The map is:

$$F(x) = \begin{cases} F_1(x) = (1+\varepsilon)x + (1-\varepsilon)x^p, & 0 \le x \le a_1, \\ F_2(x) = (e^{x^\nu} - e^{a_1^\nu})/(e - e^{a_1^\nu}), & a_1 < x \le 1, \end{cases} \tag{209}$$

where $x_0 = 0$ is a fixed point. It is unstable for $\varepsilon > 0$, and type-II intermittency occurs. In addition, a_1 verifies $(1+\varepsilon)a_1 + (1-\varepsilon)a_1^p = 1$.

To obtain the RPD function, we implement Equation (203):

$$\phi(x) = b\,\frac{(e - e^{a_1^\nu})\left[\ln\left(x(e - e^{a_1^\nu}) + e^{a_1^\nu}\right)\right]^{\frac{1}{\nu}-1}}{\nu\left[x(e - e^{a_1^\nu}) + e^{a_1^\nu}\right]} \tag{210}$$

where b is the normalization parameter, which satisfies:

$$b = \frac{1}{\left[\ln\left(c(e - e^{a_1^\nu}) + e^{a_1^\nu}\right)\right]^{1/\nu} - a_1}\,. \tag{211}$$

Note that the RPD function determined by Equation (210) does not possess a characteristic power law form as determined in Section 3.

Several numerical results have shown high accuracy with Equation (210) [65]. The continuity technique calculates the RPD function accurately, inclusive for this map with nonlinear $M(x)$. However, it requires knowing the equations ruling the system [39,65].

6.3. Type-V Intermittency

To apply the continuity technique in type-V intermittency, the following family of maps is studied:

$$F(x) = \begin{cases} F_1(x) = \lambda_1 x + \varepsilon & \hat{x} \leq x < 0, \\ F_2(x) = \varepsilon + x + \lambda_2 x^2 & 0 \leq x < x_m, \\ F_3(x) = \hat{x} + \frac{(y_m - \hat{x})(y_m - x)^\gamma}{(y_m - x_m)^\gamma} & x_m \leq x \leq y_m \,, \end{cases} \tag{212}$$

where the slope of the straight line is λ_1 ($0 < \lambda_1 < 1$), the coefficient of the quadratic term in $F_2(x)$ is λ_2, and γ is the exponent in $F_3(x)$. In addition, $y_m = F(x_m) = 1$, ε is the control parameter, and $\hat{x}$ is the lower boundary of reinjection [39].

For $\varepsilon = 0$, the point $x_0 = 0$ is a fixed point, and type-V intermittency appears for $0 < \varepsilon \ll 1$. To elaborate a broad study, this family of maps does not show symmetry around the fixed point. In addition, Equation (212) generates intermittency, displaying continuous and discontinuous RPD functions.

Applying Equation (200) on Equation (212), there are three sub-intervals. The first one is $[\hat{x}, F_1(\hat{x}))$, where:

$$\mathcal{L} \circ \rho\,(x) = \rho(F_3^{-1}(x)) \left| \frac{dF_3^{-1}(x)}{dx} \right|, \tag{213}$$

the second one is $[F_1(\hat{x}), 0)$, where we obtain:

$$\mathcal{L} \circ \rho\,(x) = \rho(F_1^{-1}(x)) \left| \frac{dF_1^{-1}(x)}{dx} \right| + \rho(F_3^{-1}(x)) \left| \frac{dF_3^{-1}(x)}{dx} \right|, \tag{214}$$

and for the third sub-interval $[0, y_m]$, we have:

$$\mathcal{L} \circ \rho\,(x) = \rho(F_2^{-1}(x)) \left| \frac{dF_2^{-1}(x)}{dx} \right| + \rho(F_3^{-1}(x)) \left| \frac{dF_3^{-1}(x)}{dx} \right|. \tag{215}$$

Figure 12 displays the three sub-intervals. Blue, red, and green arrows indicate where the intervals are transformed to obtain Equations (213)–(215), respectively.

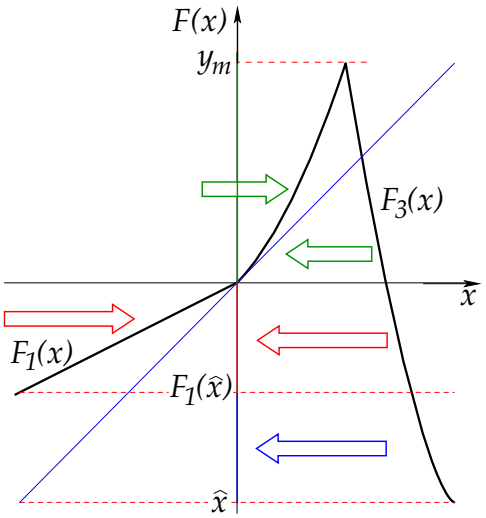

Figure 12. Density evolution. Green arrows: Equation (215). Red arrows: Equation (214). Blue arrow: Equation (213).

To determine the RPD function in Equations (213)–(215), we have to eliminate the terms that do not contribute to the reinjection process [39,65]:

$$\phi(x) = \sum_{j\neq l}^{n} \left| \frac{dF_j^{-1}(x)}{dx} \right| \rho(F_j^{-1}(x)) \,, \tag{216}$$

where l denotes the integrals that do not provide reinjection. In addition, the density in the previous iteration to reinjection is $\rho(F_j^{-1}(x))$. Therefore, the normalization condition results:

$$\sum_{j\neq l}^{n} \int_{F_j^{-1}(x_0-c)}^{F_j^{-1}(x_0+c)} \rho(F_j^{-1}(x))\, dx = 1 \,, \tag{217}$$

where x_0 is the fixed point and c is the laminar interval semi-amplitude, then the laminar interval results in $L = [x_0 - c, x_0 + c]$.

6.3.1. Continuous RPD

Let us assume for the family of maps (212) that the lower boundary of reinjection is the lower limit of the laminar interval, i.e., $\hat{x} = x_0 - c$, $x_0 = 0$, and $y_m = 1$. Accordingly, there is no reinjection from points $x < x_0 - c$. To reach an analytical expression for the RPD function, Equations (216) and (217) are used. We highlight that $F_1(x)$ and $F_2(x)$ do not generate reinjection, and the RPD function results:

$$\phi(x) = \rho(F_3^{-1}(x)) \left| \frac{dF_3^{-1}(x)}{dx} \right| , \tag{218}$$

where

$$\left| \frac{dF_3^{-1}(x)}{dx} \right| = \frac{(1 - x_m)\,(x + c)^{1/\gamma - 1}}{\gamma\,(1 + c)^{1/\gamma}} \,. \tag{219}$$

To be able to apply Equation (218), the density at the pre-reinjection points, $\rho(F_3^{-1}(x))$, has to be obtained. Therefore, we assume that ρ can be expanded by a Taylor series close to the pre-image of the lower boundary of the reinjection $F_3^{-1}(-c)$:

$$\rho(y) = \rho(y_{-c}) + \left. \frac{d\,\rho(y)}{d\,y} \right|_{y=y_{-c}} (y - y_{-c}) + \frac{1}{2} \left. \frac{d^2\,\rho(y)}{d\,y^2} \right|_{y=y_{-c}} (y - y_{-c})^2 + \dots \,. \tag{220}$$

To simplify the notation, we called $y = F_3^{-1}(x)$ and $y_{-c} = F_3^{-1}(-c)$. By the normalization condition:

$$\rho(y) \cong \frac{1}{\Delta y(c)} + \left. \frac{d\,\rho(y)}{d\,y} \right|_{y=y_{-c}} \left(\Delta y(x) - \frac{\Delta y(c)}{2} \right) + \left. \frac{d^2\,\rho(y)}{d\,y^2} \right|_{y=y_{-c}} \left(\frac{\Delta y^2(x) - \frac{\Delta y^2(c)}{3}}{2} \right) , \tag{221}$$

where $\Delta y(x) = F_3^{-1}(-c) - F_3^{-1}(x)$. Consequently, $\Delta y(c) = F_3^{-1}(-c) - F_3^{-1}(c)$.

From Equations (218) and (221), the RPD results [66]:

$$\begin{aligned} \phi(x) \cong \quad & \left(\tfrac{1}{\Delta y(c)} + \left. \tfrac{d\,\rho(y)}{d\,y} \right|_{y=y_{-c}} \left(\Delta y(x) - \tfrac{\Delta y(c)}{2} \right) \right) \left| \tfrac{dy}{dx} \right| \\ & + \left(\left. \tfrac{d^2\,\rho(y)}{d\,y^2} \right|_{y=y_{-c}} \left(\tfrac{\Delta y^2(x) - \frac{\Delta y^2(c)}{3}}{2} \right) \right) \left| \tfrac{dy}{dx} \right| . \end{aligned} \tag{222}$$

If the derivative $\left|\frac{dy}{dx}\right| = \left|\frac{dF_3^{-1}(x)}{dx}\right|$ is close to zero or acquires very high values and if $c \ll 1$, the variations produced by the linear and quadratic terms in Equation (221) can be not relevant in comparison with the first term, $\frac{1}{\Delta y(c)}$ [66]. Therefore, we can assume that

$$\rho(F_3^{-1}(x)) \cong \frac{1}{F_3^{-1}(-c) - F_3^{-1}(c)} = \frac{1}{1-x_m}\left(\frac{1+c}{2\,c}\right)^{1/\gamma}, \tag{223}$$

Accordingly, the RPD function can be written as:

$$\phi(x) = \frac{(x+c)^{1/\gamma-1}}{\gamma\,(2c)^{1/\gamma}}\,. \tag{224}$$

Note that the same result was obtained using the M function methodology, where $\alpha = \frac{1}{\gamma} - 1$ [70].

In Ref. [66], several numerical tests were performed. The accuracy between Equation (224) and the numerical results was very high.

6.3.2. Discontinuous RPD

When the lower boundary of reinjection satisfies $\hat{x} < x_0 - c$, the map shows type-V intermittency with discontinuous RPD functions. Two reinjection processes generate the RPD functions. One is developed by $F_1(x)$ and the other by $F_3(x)$. To obtain the RPDs, Equation (216) with $j \neq 2$ is utilized:

$$\phi(x) \quad = \phi_1(x) + \phi_3(x) = \left|\frac{dF_1^{-1}(x)}{dx}\right|\rho_1^1(F_1^{-1}(x)) + \left|\frac{dF_3^{-1}(x)}{dx}\right|\rho_3(F_3^{-1}(x))\,, \tag{225}$$

where $\rho_1^1(x)$ and $\rho_3(x)$ are the trajectory densities in the intervals $I_1^1 = [F_1^{-1}(x_0-c), x_0-c)$ and $I_3 = [F_3^{-1}(x_0-c), F_3^{-1}(x_0+c)]$, respectively. Henceforth:

$$\phi_1(x) = \left|\frac{dF_1^{-1}(x)}{dx}\right|\rho_1^1(F_1^{-1}(x))\,, \tag{226}$$

is defined only in the interval $[x_0-c, F_1(x_0-c))$. On the other had, $\phi_3(x)$ is defined inside the complete laminar interval $L = [x_0-c, x_0+c]$:

$$\phi_3(x) = \left|\frac{dF_3^{-1}(x)}{dx}\right|\rho_3(F_3^{-1}(x))\,. \tag{227}$$

Consequently, the RPD function can be written as:

$$\phi(x) = \begin{cases} \phi_I(x) = \phi_1(x) + \phi_3(x) & x < F_1(x_0-c), \\ \phi_{II}(x) = \phi_3(x) & x \geq F_1(x_0-c)\,. \end{cases} \tag{228}$$

Following the previous analysis, we assume that in the interval $I_3^s = [F_3^{-1}(\hat{x}), F_3^{-1}(x_0+c)]$, the density $\rho_3(x)$ verifies $\rho_3(x) = k =$ constant. As $I_3 \subset I_3^s$, the trajectories density $\rho_3(F_3^{-1}(x))$ is constant in Equations (225) and (227). On the other hand, $\rho_1^1(x)$ is defined inside the interval $I_1^1 = [F_1^{-1}(x_0-c), x_0-c)$ and depends on the density at the previous iteration. To evaluate this, we have to analyze the iteration procedure for the map (212).

Points in the interval $I_3^a = [F_3^{-1}(F_1^{-1}(x_0-c), F_3^{-1}(x_0-c)))$ map on the interval I_1^1.

$$I_3^a \;\longrightarrow\; I_1^1 : [F_3^{-1}(F_1^{-1}(x_0-c)), F_3^{-1}(x_0-c)) \to [F_1^{-1}(x_0-c), x_0-c)\,. \tag{229}$$

In addition, points in the interval $I_1^2 = [F_1^{-1}(F_1^{-1}(x_0 - c)), F_1^{-1}(x_0 - c))$ map on the interval $I_1^1 = [F_1^{-1}(x_0 - c), x_0 - c)$.

$$I_1^2 \;\longrightarrow\; I_1^1 : [F_1^{-1}(F_1^{-1}(x_0 - c)), F_1^{-1}(x_0 - c)) \to [F_1^{-1}(x_0 - c), x_0 - c)\,, \tag{230}$$

and as a consequence, the density $\rho_1^1(x)$ in the interval I_1^1 has two contributions (see Equations (229) and (230)); one is given by $\rho_3(x)$ from the interval I_3^a and the other one is produced by $\rho_1^2(x)$ from the interval I_1^2:

$$\rho_1^1(x) = \left|\frac{dF_1^{-1}(x)}{dx}\right| \rho_1^2(F_1^{-1}(x)) + \left|\frac{dF_3^{-1}(x)}{dx}\right| \rho_3(F_3^{-1}(x))\,. \tag{231}$$

As $\rho_3(x) = k$ inside $I_3^s = [F_3^{-1}(\hat{x}), F_3^{-1}(x_0 + c)]$, the Equation (231) reduces:

$$\rho_1^1(x) = \left|\frac{dF_1^{-1}(x)}{dx}\right| \rho_1^2(F_1^{-1}(x)) + \left|\frac{dF_3^{-1}(x)}{dx}\right| k\,, \tag{232}$$

where the constant k is calculated using the normalization condition:

$$\int_{F_3^{-1}(\hat{x})}^{F_3^{-1}(x_0+c)} -k\,dx = 1 \;\;\Rightarrow\;\; k = \frac{(y_m - \hat{x})^{1/\gamma}}{(x_m - y_m)\,(x_0 + c - \hat{x})^{1/\gamma}}\,. \tag{233}$$

We evaluate $\rho_1^2(x)$ in the interval I_1^2. We consider that points in the interval $I_1^n = [\hat{x}, F_1(\hat{x}))$ require n iterations to reinject in the laminar interval. The density ρ_1^n in I_1^n depends only on $\rho_3 = k$:

$$\rho_1^n(x) = k\left|\frac{dF_3^{-1}(x)}{dx}\right|. \tag{234}$$

Then, the density $\rho_1^{n-1}(x)$ in $I_1^{n-1} = [F_1(\hat{x}), F_1(F_1(\hat{x})))$ can be obtained as:

$$\rho_1^{n-1}(x) = \left|\frac{dF_1^{-1}(x)}{dx}\right| \rho_1^n(F_1^{-1}(x)) + k\left|\frac{dF_3^{-1}(x)}{dx}\right|. \tag{235}$$

In the interval $I_1^{n-2} = [F_1(F_1(\hat{x})), F_1(F_1(F_1(\hat{x}))))$, the density $\rho_1^{n-2}(x)$ results:

$$\rho_1^{n-2}(x) = \left|\frac{dF_1^{-1}(x)}{dx}\right| \rho_1^{n-1}(F_1^{-1}(x)) + k\left|\frac{dF_3^{-1}(x)}{dx}\right|, \tag{236}$$

where

$$F_1^{-1}(x) = \frac{x - \varepsilon}{a_1}; \qquad \frac{dF_1^{-1}(x)}{dx} = 1/a_1\,, \tag{237}$$

and

$$F_3^{-1}(x) = y_m - \frac{y_m - x_m}{(y_m - \hat{x})^{1/\gamma}}(x - \hat{x})^{1/\gamma}, \qquad \frac{dF_3^{-1}(x)}{dx} = \frac{x_m - y_m}{\gamma(y_m - \hat{x})^{1/\gamma}}(x - \hat{x})^{-1+1/\gamma}\,. \tag{238}$$

If Equations (233), (237), and (238) are introduced into Equations (234)–(236), we obtain:

$$\rho_1^n(x) = \frac{(x - \hat{x})^{-1+1/\gamma}}{\gamma\,(x_0 + c - \hat{x})^{1/\gamma}}\,, \tag{239}$$

$$\rho_1^{n-1}(x) = \frac{(x - \hat{x})^{-1+1/\gamma}}{\gamma\,(x_0 + c - \hat{x})^{1/\gamma}} + \frac{(F_1^{-1}(x) - \hat{x})^{-1+1/\gamma}}{a_1\,\gamma\,(x_0 + c - \hat{x})^{1/\gamma}}\,, \tag{240}$$

$$\rho_1^{n-2}(x) = \frac{(x-\hat{x})^{-1+1/\gamma}}{\gamma\,(x_0+c-\hat{x})^{1/\gamma}} + \frac{(F_1^{-1}(x)-\hat{x})^{-1+1/\gamma}}{a_1\,\gamma\,(x_0+c-\hat{x})^{1/\gamma}} + \frac{(F_1^{-2}(x)-\hat{x})^{-1+1/\gamma}}{a_1^2\,\gamma\,(x_0+c-\hat{x})^{1/\gamma}}\,. \tag{241}$$

Consequently, the last equations can be written as:

$$\rho_1^{n-h}(x) = \frac{\sum_{l=0}^{l=h} \frac{(F_1^{-l}(x)-\hat{x})^{-1+1/\gamma}}{a_1^l}}{\gamma\,(x_0+c-\hat{x})^{1/\gamma}}\,, \tag{242}$$

where $h = 0, 1, 2, \ldots, n$. For $h = n$, $\phi_I(x)$ is evaluated as (see Equation (228))

$$\phi_I(x) = \frac{\sum_{l=0}^{l=n} \frac{(F_1^{-l}(x)-\hat{x})^{-1+1/\gamma}}{a_1^l}}{\gamma\,(x_0+c-\hat{x})^{1/\gamma}}\,. \tag{243}$$

In Equation (228), the second RPD, $\phi_{II}(x)$, results:

$$\phi_{II}(x) = k\left|\frac{dF_3^{-1}(x)}{dx}\right| = \frac{(x-\hat{x})^{-1+1/\gamma}}{\gamma\,(x_0+c-\hat{x})^{1/\gamma}}\,. \tag{244}$$

Note that to obtain $\phi_{II}(x_n)$ we utilize points only coming from $F_3(x_{n-1})$, where $x_n = F_3(x_{n-1})$. Figure 13 displays the process of reinjection governed by $F_1(x)$ and $F_3(x)$. In the larger figure, the thick arrows show the evolution of the density produced by $F_3(x)$, and the red dashed lines exhibit the limits of the laminar interval. In the smaller box, thin blue arrows describe the evolution generated by $F_1(x)$. In this figure, a trajectory requires three iterations to displace it from $\hat{x}$ to $x_0 - c$.

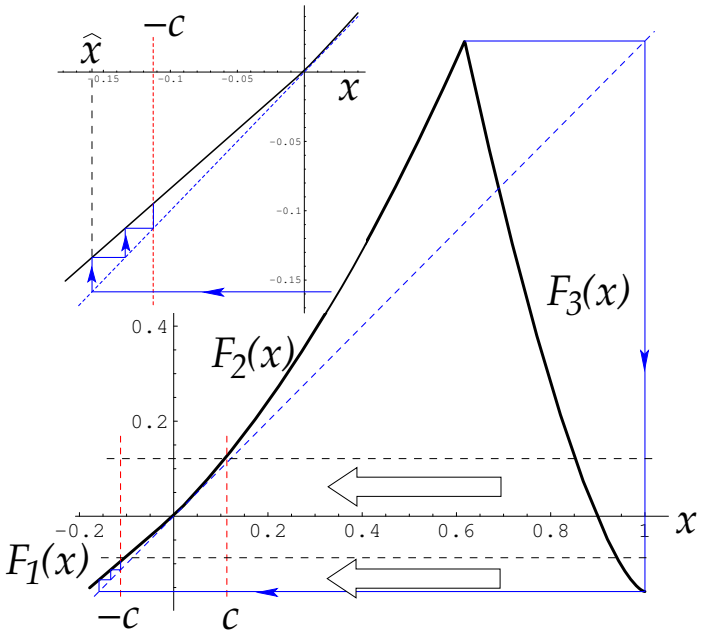

Figure 13. Reinjection process ruled by $F_1(x)$ and $F_3(x)$ functions.

7. Discussion and Conclusions

In this paper, a review of chaotic intermittency was developed. We started with the classical I, II, and III intermittency types. Later, other more recently introduced intermittency types were explained: V, X, on–off, eyelet, spatiotemporal, crisis-induced, two-dimensional, and the fine structure in intermittency. In addition, two new theoretical formulations of chaotic intermittency were presented. Both formulations evaluate the reinjection processes and the other statistical functions to describe the chaotic intermittency phenomenon. The first uses individual trajectories to determine the reinjection probability density function (RPD). It is a very general methodology and was verified for process with

and without noise. This formulation can also be applied to obtain the statistical properties of intermittency from data series, although the equations that govern the phenomenon are unknown. The second one, called the continuity technique, utilizes the density of trajectories and the Perron–Frobenius operator to evaluate the statistical variables. It has been shown to be a useful methodology for evaluating the RPD function and other statistical properties for type-II and V intermittencies. It works accurately, inclusive of nonlinear functions, M. However, we must know the map and its inverse function.

Note that there are some future research directions, such as:

- To extend the theory described in Sections 3, 5, and 6 to higher dimensional maps, starting with two-dimensional maps.
- To include noise in the mathematical model introduced in Section 6.
- To analyze the noisy theory due to the discrepancies between the experimental data in electronic circuits and the analytical results.
- To study the density evolution in maps with derivatives equal to zero or tending to infinity.

Author Contributions: Conceptualization, S.E. and E.d.R.; methodology, S.E. and E.d.R.; formal analysis, S.E. and E.d.R.; investigation, S.E. and E.d.R.; resources, S.E. and E.d.R.; writing—original draft preparation, S.E. and E.d.R.; writing—review and editing, S.E. and E.d.R.; supervision, S.E. and E.d.R.; project administration, S.E. and E.d.R.; funding acquisition, S.E. and E.d.R. All authors have read and agreed to the published version of the manuscript.

Funding: This work was supported by SECyT of Universidad Nacional de Córdoba, Universidad Politécnica de Madrid, and Ministerio de Ciencia, Innovación y Universidades of Spain under grand No RTI2018-094409-B-I00.

Data Availability Statement: The data presented in this study are available on request from the corresponding author.

Acknowledgments: The authors thank the Department of Aeronautics, FCEFyN of Universidad Nacional de Córdoba and Department of Applied Physics, ETSIAE of Universidad Politécnica de Madrid.

Conflicts of Interest: The authors declare no conflict of interest.

Abbreviations

The following abbreviations are used in this manuscript:

CDF	Channel Distribution Function
DHS	d-Dimensional Diagonal Hyper Surface
FPE	Backward Fokker–Plank Equation
LBR	Lower Boundary of Reinjection
MFPT	Mean First-Passage Time
NRPD	Noisy Reinjection Probability Density function
RGT	Renormalization Group Theory
RPD	Reinjection Probability Density function (form the chaotic region into the laminar one)

References

1. Batchelor, G.; Townsend, C. The nature of turbulent motion at large wave-number. *Proc. R. Soc. London Ser. A* **1949**, *199*, 238–255.
2. Irimiciuc, S.; Saviuc, A.; Tudose-Sandu-Ville, F.; Toma, S.; Nedeff, F.; Marcela Rusu, C.; Agop, M. Non-Linear Behaviors of Transient Periodic Plasma Dynamics in a Multifractal Paradigm. *Symmetry* **2020**, *12*, 1356. [CrossRef]
3. Chertovskih, R.; Rempel, E; Chimanski, E. Magnetic field generation by intermittent convection. *Phys. Lett.* **2017**, *381*, 3300–3306. [CrossRef]
4. Belyaev, I.; Biryukov, D.; Gerasimov, D.; Yurin, E. On-off intermittency and hard turbulence in the flow of fluid in the magnetic field. *Chaos Interdiscip. J. Nonlinear Sci.* **2019**, *29*, 083119. [CrossRef] [PubMed]
5. Goldman, M. *Plasma Wave Turbulence and Electromagnetic Radiation Caused by Electron Beams*; Grant 84-0007. AFOSR-TR-86-2062; Air Office Scientific Research: Arlington, Virginia, 1986.
6. Schmiegel, J.; Pons, F. Stochastic Intermittency Fields in a von Kármán Experiment. *Symmetry* **2021**, *13*, 1752. [CrossRef]
7. Manasseh, R. Breakdown regimes of inertia waves in a precessing cylinder. *J. Fluid Mech.* **1992**, *243*, 261–296. [CrossRef]

8. Loiseau, J.; Robinet, J.; Leriche, E. Intermittency and transition to chaos in the cubical lid-driven cavity flow. *Fluid Dyn. Res.* **2016**, *48*, 061421. [CrossRef]
9. Gao, J.; Zheng, Z.; Ma, J. Controlling turbulence via target waves generated by local phase space compression. *Int. J. Mod. Phys. B* **2008**, *22*, 3855–3863. [CrossRef]
10. Malm, A.; Waigh, T. Elastic turbulence in entangled semi-dilute DNA solutions measured with optical coherence tomography velocimetry. *Sci. Rep.* **2017**, *7*, 1186. [CrossRef]
11. Malasoma, J.; Werny, P.; Boiron, M. Multichannel type-I intermittency in two models of Rayleigh-Benard convection. *Phys. Rev. Lett.* **2004**, *51*, 487–500. [CrossRef]
12. Stavrinides, S.; Miliou, A.; Laopoulos, T.; Anagnostopoulos, A. The intermittency route to chaos of an electronic digital oscillator. *Int. J. Bifurc. Chaos* **2008**, *18*, 1561–1566. [CrossRef]
13. Elaskar, S.; del Rio, E.; Elaskar, S. Intermittency Reinjection in the Logistic Map. *Symmetry* **2022**, *14*, 281. [CrossRef]
14. Sanmartín, J.; López-Rebollal, O.; del Río, E.; Elaskar, S. Hard transition to chaotic dynamics in Alfven wave-fronts. *Phys. Plasmas* **2004**, *11*, 2026–2035. [CrossRef]
15. Sánchez-Arriaga, G.; Sanmartín, J.; Elaskar, S. Damping models in the truncated derivative nonlinear Schrödinger equation. *Phys. Plasmas* **2007**, *14*, 082108. [CrossRef]
16. Pizza, G.; Frouzakis, C.; Mantzaras, J. Chaotic dynamics in premixed Hydrogen/air channel flow combustion. *Combust. Theor. Model* **2012**, *16*, 275–299. [CrossRef]
17. Manneville, P.; Pomeau, Y. Intermittency and Lorenz model. *Phys. Lett. A* **1979**, *75*, 1–2. [CrossRef]
18. Casagrande, V.; Mikhailov, A. Birhythmicity, synchronization, and turbulence in an oscillatory system with nonlocal inertial coupling. *Phys. D Nonlinear Phenom.* **2005**, *205*, 154–169. [CrossRef]
19. Saha, A.; Feudel, U. Characteristics of in-out intermittency in delay-coupled FitzHugh–Nagumo oscillators. *Eur. Phys. J. Spec. Top.* **2018**, *227*, 1205–1219. [CrossRef]
20. Gil, S.; Mikhailov, A. Networks on the edge of chaos: Global feedback control of turbulence in oscillator networks. *Phys. Rev. E* **2009**, *79*, 026219. [CrossRef]
21. Hu, B.; Zheng, Z. Phase synchronizations: Transitions from high-to low-dimensional tori through chaos. *Int. J. Bifurc. Chaos* **2000**, *10*, 2399–2414. [CrossRef]
22. Elnashaie, S.; Abashar, M.; Teymour, F. Bifurcation, instability and chaos in fluidized bed catalytic reactors with consecutive exothermic chemical reactions. *Chaos Solitons Fractals* **1993**, *3*, 1–33. [CrossRef]
23. Li, H.-H.; Xiao, J.-H.; Hu, G.; Hu, B. Intermittencies in complex Ginzburg–Landau equation by varying system size. *Chin. Phys. B* **2010**, *19*, 050516.
24. Serre, T.; Nesme-Ribes, E. Nonlinear analysis of solar cycles. *Astron. Astrophys.* **2000**, *360*, 319–330.
25. Coulibaly, S.; Clerc, M.; Selmi, F.; Barbay, S. Extreme events following bifurcation to spatiotemporal chaos in a spatially extended microcavity laser. *Phys. Rev. A* **2017**, *95*, 023816. [CrossRef]
26. Pavlos, G.; Iliopoulos, A.; Tsoutsouras, V.; Karakatsanis, L.; Pavlos, E. Spatiotemporal chaos in distributed systems: Theory and practice. In *Chaotic Systems: Theory and Applications*; World Scientific: Singapore, 2010; pp. 268–283.
27. Sujith, R.; Unni, V. Complex system approach to investigate and mitigate thermoacoustic instability in turbulent combustors. *Phys. Fluids* **2020**, *32*, 061401. [CrossRef]
28. Zambrano, S.; Mariño, I.P.; Sanjuán, M. Controlling crisis-induced intermittency using its relation with a boundary crisis. *New J. Phys.* **2009**, *11*, 023025. [CrossRef]
29. Chian, A. *Complex System Approach to Economic Dynamics. Lecture Notes in Economics and Mathematical Systems*; Springer: Berlin, Germany, 2007.
30. Bhansali, R.; Holland, M.; Kokoszka, P. Intermittency, long-memory and financial returns. In *Long Memory in Economics*; Springer: Berlin, Germany, 2007; pp. 39–68.
31. Zebrowski, J.; Baranowski, R. Type-I intermittency in nonstationary systems: Models and human heart-rate variability. *Physics A* **2004**, *336*, 74–86. [CrossRef]
32. Velazquez, J.; Khosravani, H.; Lozano, A.; Bardakjian, B.; Carlen, P.; Wennberg, R. Type III intermittency in human partial epilepsy. *Eur. J. Neurosci.* **1999**, *11*, 2571–2576. [CrossRef]
33. Paradisi, P.; Allegrini, P.; Gemignani, A.; Laurino, M.; Menicucci, D.; Piarulli, A. Scaling and intermittency of brains events as a manifestation of consciousness. *AIP Conf. Proc.* **2012**, *1510*, 151–161.
34. Bashkirtseva, I.; Nasyrova, V.; Ryashko, L. Scaling and intermittency of brains events as a manifestation of consciousness. *Chaos Solitons Fractals* **2018**, *110*, 76–81. [CrossRef]
35. Suzuki, Y.; Lu, M.; Ben-Jacob, E.; Onuchic, J. Periodic, quasi-periodic and chaotic dynamics in simple gene elements with time delays. *Sci. Rep.* **2016**, *6*, 21037. [CrossRef] [PubMed]
36. Gardiner, J.; Atema, J. The function of bilateral odor arrival time differences in olfactory orientation of sharks. *Curr. Biol.* **2010**, *20*, 1187–1191. [CrossRef] [PubMed]
37. Atema, J.; Brönmark, C.; Hansson, L. Aquatic odor dispersal fields: Opportunities and limits of detection, communication and navigation. In *Chemical Ecology in Aquatic Systems*; Oxford University Press: New York, NY, USA, 2012; pp. 1–18.
38. Nayfeh, A.; Balachandran, B. *Applied Nonlinear Dynamics*; Wiley: New York, NY, USA, 1995.

39. Elaskar, S.; del Rio, E. *New Advances on Chaotic Intermittency and Applications*; Springer: New York, NY, USA, 2017; ISBN: 978–3-319-47836-4.
40. Manneville, P. Intermittency, self-similarity and $1/f$ spectrum in dissipative dynamical systems. *J. Phys.* **1980**, *41*, 1235–1243. [CrossRef]
41. Hirsch, J.; Huberman, B.; Scalapino, D. Theory of intermittency. *Phys. Rev. Lett.* **1982**, *25*, 519–532. [CrossRef]
42. Schuster, H.; Just, W. *Deterministic Chaos*; Wiley VCH: Mörlenbach, Germany, 2005.
43. Kaplan, H. Return to type-I intermittency. *Phys. Rev. Lett.* **1992**, *68*, 553–557. [CrossRef] [PubMed]
44. Price, T.; Mullin, P. An experimental observation of a new type of intermittency. *Phys. D* **1991**, *48*, 29–52. [CrossRef]
45. Platt, N.; Spiegel, E.; Tresser, C. On-off intermittency: A mechanism for bursting. *Phys. Rev. Lett.* **1993**, *70*, 279–282. [CrossRef]
46. Pikovsky, A.; Osipov, G.; Rosenblum, M.; Zaks, M.; Kurths, J. Attractor–repeller collision and eyelet intermittency at the transition to phase synchronization. *Phys. Rev. Lett.* **1997**, *79*, 47–50. [CrossRef]
47. Lee, K.; Kwak, Y.; Lim, T. Phase jumps near a phase synchronization transition in systems of two coupled chaotic oscillators. *Phys. Rev. Lett.* **1998**, *81*, 321–324. [CrossRef]
48. Hramov, A.; Koronovskii, A.; Kurovskaya, M.; Boccaletti, S. Ring intermittency in coupled chaotic oscillators at the boundary of phase synchronization. *Phys. Rev. Lett.* **2006**, *97*, 114101. [CrossRef]
49. Guckenheimer, J.; Holmes, P. *Nonlinear Oscillations, Dynamical Systems, and Bifurcations of Vector Field*; Springer: New York, NY, USA, 1983.
50. Bai-lin, H. *Elementary Simbolic Dynamics and Chaos in Dissipative Systems*; World Scientific: Singapure, 1989.
51. Wiggins, S. *Introduction to Applied Nonlinear Dynamical Systems and Chaos*; Springer: New York, NY, USA, 2003.
52. Laugesen, J.; Carlsson, N.; Mosckilde, E.; Bountis, T. Anomalous statistics for type-III intermittency. *Open Syst. Inf. Dyn.* **1998**, *4*, 393–405. [CrossRef]
53. Marek, M.; Schreiber, I. *Chaotic Behaviour of Deterministic Dissipative Systems*; Cambridge University Press: Cambridge, UK, 1995.
54. Kye, W.; Kim, C. Characteristic relations of type-I intermittency in presence of noise. *Phys. Rev. E* **2000**, *62*, 6304–6307. [CrossRef] [PubMed]
55. Kye, W.; Rim, S.; Kim, C.; Lee, J.; Ryu, J.; Yeom, B.; Park, Y. Experimental observation of characteristic relations of type-III intermittency in the presence of noise in a simple electronic circuit. *Phys. Rev. E* **2003**, *68*, 036203. [CrossRef]
56. del Rio, E.; Velarde, M.; Rodríguez-Lozano, A. Long time data series and difficulties with the characterization of chaotic attractors: A case with intermittency III. *Chaos Solitons Fractals* **1994**, *4*, 2169–2179. [CrossRef]
57. del Rio, E.; Elaskar, S. New characteristic relation in type-II intermittency. *Int. J. Bifurc. Chaos* **2010**, *20*, 1185–1191. [CrossRef]
58. Elaskar, S.; del Rio, E.; Donoso, J. Reinjection probability density in type-III intermittency. *Phys. A* **2011**, *390*, 2759–2768. [CrossRef]
59. del Rio, E.; Elaskar, S.; Makarov, S. Theory of intermittency applied to classical pathological cases. *Chaos* **2013**, *23*, 033112. [CrossRef]
60. del Rio, E.; Elaskar, S.; Donoso, J. Laminar length and characteristic relation in type-I intermittency. *Commun. Numer. Simul. Nonlinear Sci.* **2014**, *19*, 967–976. [CrossRef]
61. Krause, G.; Elaskar, S.; del Rio, E. Type-I intermittency with discontinuous reinjection probability density in a truncation model of the derivative nonlinear Schrödinger equation. *Nonlinear Dyn.* **2014**, *77*, 455–466. [CrossRef]
62. Krause, G.; Elaskar, S.; del Rio, E. Noise effect on statistical properties of type-I intermittency. *Phys. A* **2014**, *402*, 318–329. [CrossRef]
63. Elaskar, S.; del Rio, E.; Krause, G.; Costa, A. Effect of the lower boundary of reinjection and noise in type-II intermittency. *Nonlinear Dyn.* **2015**, *79*, 1411–1424. [CrossRef]
64. Elaskar, S.; del Rio, E.; Grioni, M. Chaotic intermittency with non-differentiable $M(x)$ function. *REDIM Rev. Fac. Ing.* **2023**, *in press*. [CrossRef]
65. Elaskar, S.; del Rio, E.; Zapico, E. Evaluation of the statistical properties for type-II intermittency using the Perron-Frobenius operator. *Nonlinear Dyn.* **2016**, *86*, 1107–1116. [CrossRef]
66. Elaskar, S.; del Rio, E.; Schulz, W. Analysis of the Type V Intermittency Using the Perron-Frobenius Operator. *Symmetry* **2022**, *14*, 2519. [CrossRef]
67. Elaskar, S.; del Rio, E.; Lorenzón, D. Calculation of the Statistical Properties in Intermittency Using the Natural Invariant Density. *Symmetry* **2021**, *13*, 935. [CrossRef]
68. del Rio, E.; Sanjuan, M.; Elaskar, S. Effect of noise on the reinjection probability density in intermittency. *Commun. Numer. Simul. Nonlinear Sci.* **2012**, *17*, 3587–3596. [CrossRef]
69. Elaskar, S.; del Rio, E.; Costa, A. Reinjection probability density for type-III intermittency with noise and lower boundary of reinjection. *J. Comput. Nonlinear Dyn. ASME* **2017**, *12*, 031020. [CrossRef]
70. Elaskar, S.; del Rio, E.; Gutiérrez Marcantoni, L. Non-uniform reinjection probability density function in type V intermittency. *Nonlinear Dyn.* **2018**, *92*, 683697. [CrossRef]
71. Arnold, V. *Geometrical Methods in the Theory of Differential Equations*; Springer: Berlin, Germany, 1988.
72. Rasband, S. *Chaotic Dynamics of Nonlinear Dynamics*; John Wiley & Sons: New York, NY, USA, 1990.
73. Bauer, M.; Habip, S.; He, D.; Martiessen, W. New type of intermittency in discontinuous maps. *Phys. Rev. Lett.* **1992**, *68*, 1625–1628. [CrossRef]

74. He, D.; Bauer, M.; Habip, S.; Kruger, U.; Martiessen, W.; Christiansen, B.; Wang, B. Type V intermittency. *Phys. Lett. A* **1992**, *171*, 61–65. [CrossRef]
75. Fan, J.; Ji, F.; Guan, S.; Wang, B.; He, D. The distribution of laminar lenghts in type V intermittency. *Phys. Lett. A* **1993**, *182*, 232–237. [CrossRef]
76. Heagy, J.; Platt, N.; Hammel, S. Characterization of on-off intermittency. *Phys. Rev. E* **1994**, *49*, 1140–1150. [CrossRef] [PubMed]
77. Pisarchik, A.N.; Feudel, U. Control of multistability. *Phys. Rep.* **2014**, *540*, 167–218. [CrossRef]
78. Pisarchik, A.N.; Jaimes-Reátegui, R.; Villalobos-Salazar, J.R.; Garcia-Lopez, J.H.; Boccaletti, S. Synchronization of chaotic systems with coexisting attractors. *Phys. Rev. Lett.* **2006**, *96*, 244102. [CrossRef] [PubMed]
79. Reategui, R.J.; Pisarchik, A.N. Control of on-off intermittency by slow parametric modulation. *Phys. Rev. E* **2004**, *69*, 067203. [CrossRef]
80. Kurovskaya, M. Distribution of laminar phases at eyelet-type intermittency. *Tech. Phys. Lett.* **2008**, *34*, 1063–1065. [CrossRef]
81. Pikovsky, A.; Rosenblum, M.; Kurths, J. *Synchronization—A universal concept in Nonlinear Sciences*; Cambridge University Press: Cambridge, UK, 2001.
82. Ott, E. *Chaos in Dynamical Systems*; Cambridge University Press: Cambridge, UK, 1994.
83. Osipov, G.; Kurths, J.; Zhou, C. *Synchronization in Oscillatory Networks*; Springer: Berlin, Germany, 2007.
84. Hramov, A.; Koronovskii, A.; Kurovskaya, M.; Moskalenko, O. Type-I intermittency with noise versus eyelet intermittency. *Phys. Lett. A* **2011**, *375*, 1646–1652. [CrossRef]
85. Boccaletti, S.; Allaria, E.; Meucci, R.; Arecchi, F. Experimental characterization of the transition to phase synchronization of chaotic CO_2 laser systems. *Phys. Rev. Lett.* **2002**, *89*, 194101. [CrossRef]
86. White, F. *Viscous Fluid Flow*; McGraw-Hill Inc.: New York, NY, USA, 1991.
87. Pope, S. *Turbulent Flows*; Cambridge University Press: Cambridge, UK, 2000.
88. Malvern, L. *Introduction to the Mechanics of A Continuous Medium*; Prentice-Hall Inc.: Hoboken, NJ, USA, 1969.
89. Aris, R. *Vectors, Tensors and the Basic Equations of Fluid Mechanics*; Dover Publications: New York, NY, USA, 1962.
90. Gollubm, J. Order and disorder in fluid motion. *Proc. Natl. Acad. Sci. USA* **1995**, *92*, 6705–6711. [CrossRef]
91. Lepiller, V.; Prigent, A.; Dumochel, F.; Mutabazi, I. Transition to turbulence in a tall annulus submitted to a radial temperature gradient. *Phys. Fluids* **2007**, *19*, 054101. [CrossRef]
92. Lai, Y.; Tei, T. *Transient Chaos*; Springer: New York, NY, USA, 2001.
93. Chaté, H.; Manneville, P. Transition to turbulence via spatiotemporal intermittency. *Phys. Rev. Lett.* **1987**, 58, 112–115. [CrossRef]
94. Kaneko, K. Pattern dynamics in spatiotemporal chaos. *Physics D* **1989**, *34*, 1–41. [CrossRef]
95. Qu, Z.; Hu, G. Spatiotemporal periodic states, periodic windows, and intermittency in coupled-map lattices. *Phys. Rev. E* **1994**, *49*, 1099–1108.
96. Keeler, J.; Farmer, J. Robust sapce-time intermittency and $1/f$ noise. *Phys. D* **1986**, *23*, 413–435. [CrossRef]
97. Kaneko, K.; Tsuda, I. *Complex System, Chaos and Beyond, a Constructive Approach with Applications om Life Sciences*; Springer: Berlin, Germany, 2000.
98. Rupp, P.; Richter, R.; Rehberg, I. Critical exponents of directed percolation measured in spatiotemporal intermittency. *Phys. Rev. E* **2003**, *67*, 036209. [CrossRef]
99. Grebogi, C.; Ott, E.; Yorke, J. Crisis, sudden changes in chaotic attractors and transient chaos. *Physics D* **1983**, *7*, 181–200. [CrossRef]
100. Grebogi, C.; Ott, E.; Romeiras, F.; Yorke, J. Critical exponents for crisis-induced intermittency. *Phys. Rev. E* **1987**, *36*, 5365–5380. [CrossRef]
101. Cavalcante, d.S.H.; Rios Leite, J. Fine structure in scaling of type-I intermittency bifurcation. *Physics A* **2004**, *342*, 356–362. [CrossRef]
102. Cavalcante, d.S.H.; Rios Leite, J. Logarithmic periodicities in the bifurcations of type-I intermittent chaos. *Phys. Rev. Lett.* **2004**, *92*, 254102. [CrossRef]
103. Kim, C.; Kye, W. Two-dimensional intermittency. *Phys. Rev. E* **2001**, *63*, 037202. [CrossRef] [PubMed]
104. Dubois, M.; Rubio, M.; Berge, P. Experimental evidence of intermittencies associated with a subharmonic bifurcation. *Phys. Rev. E* **1983**, *51*, 1446–1449.
105. Pikovsky, A. A new type of intermittent transition to chaos. *J. Phys. A* **1983**, *16*, L109–L112. [CrossRef]
106. Kim, C.; Kwon, O.; Lee, E.; Lee, H. New characteristic relations in type-I intermittency. *Phys. Rev. Lett.* **1994**, *73*, 525–528 [CrossRef]
107. Kim, C.; Yim, G.; Ryu, J.; Park, Y. Characteristic relations of type-III intermittency in an electronic circuit. *Phys. Rev. Lett.* **1998**, *80*, 5317–5320. [CrossRef]
108. Kim, C.; Yim, G.; Kim, Y.; Kim, J.; Lee, H. Experimental evidence of characteristic relations of type-I intermittency in an electronic circuit. *Phys. Rev. E* **1997**, *56*, 2573–2577. [CrossRef]
109. Cho, J.; Ko, M.; Park, Y.; Kim, C. Experimental observation of the characteristic relations of type-I intermittency in the presence of noise. *Phys. Rev. E* **2002**, *65*, 036222. [CrossRef]
110. Ono, Y.; Fukushima, K.; Yazaki, T. Critical behavior for the onset of type-III intermittency observed in an electronic circuit. *Phys. Rev. E* **1995**, *52*, 4520–4522. [CrossRef]
111. del Rio, E.; Elaskar, S. On the theory of intermittency in 1D maps. *Int. J. Bifurc. Chaos* **2016**, *26*, 1650228. [CrossRef]

112. del Rio, E.; Elaskar, S. Experimental evidence of power law reinjection in chaotic intermittency. *Commun. Numer. Simul. Nonlinear Sci.* **2018**, *64*, 122–134.
113. Kwon, O.; Kim, C.; Lee, E.; Lee, H. Effects of reinjection on the scaling property of intermittency. *Phys. Rev. E* **1996**, *53*, 1253–1256. [CrossRef] [PubMed]
114. Lichtenberg, A.; Lieberman, M. *Regular and Stochastic Motion*; Springer: New York, NY, USA, 1983.
115. del Rio, E.; Elaskar, S. Type III intermittency without characteristic relation. *Chaos* **2021**, *31*, 043127. [CrossRef] [PubMed]
116. Abramowitz, M.; Stegun, I. *Handbook of Mathematical Functions*; Dover: New York, NY, USA, 1970.
117. Hirsch, J.; Nauenberg, M.; Scalapino, D. Intermittency in presence of noise: A renormalization group formulation. *Phys. Lett. A* **1982**, *87*, 391–393. [CrossRef]
118. Kodama, H.; Sato, S.; Honda, K. Reconsideration of the renormalization-group theory on intermittent chaos. *Phys. Lett. A* **1991**, *157*, 354–356. [CrossRef]
119. Lasota, A.; Mackey, M. *Chaos, Fractals, and Noise: Stochastic Aspects of Dynamics*; Springer Science & Business Media: New York, NY, USA, 1998; Volume 97.
120. Beck, C.; Schogl, F. *Thermodynamics of Chaotic Systems*; Cambridge University Press: Cambridge, UK, 1993.

Disclaimer/Publisher's Note: The statements, opinions and data contained in all publications are solely those of the individual author(s) and contributor(s) and not of MDPI and/or the editor(s). MDPI and/or the editor(s) disclaim responsibility for any injury to people or property resulting from any ideas, methods, instructions or products referred to in the content.

symmetry

MDPI

Article

Impact of Stochastic Atmospheric Density on Satellite Orbit Stability

Alina Bogoi [1,2], Sergiu Strătilă [1,2,*], Grigore Cican [1,2], Daniel-Eugeniu Crunțeanu [1] and Constatin Levențiu [1]

[1] Faculty of Aerospace Engineering, National University of Science and Technology POLITEHNICA, 011061 Bucharest, Romania; alina.bogoi@upb.ro (A.B.); grigore.cican@upb.ro (G.C.)
[2] Romanian Research and Development Institute for Gas Turbines COMOTI, 061126 Bucharest, Romania
* Correspondence: sergiu.stratila@stud.aero.upb.ro

Abstract: The orbit stability of a satellite is a crucial aspect in its design and maintenance. Without an analysis of orbital trajectories, satellites, much like any small celestial objects, are prone to orbital decay, collision with other orbiting objects, or even variations in trajectory, leading to the impossibility of performing their tasks. Starting from an equation of angular momentum variation applied to a satellite in a circular orbit around Earth, the system of second-order ordinary differential equations of motion for the satellite can be determined. By introducing this term into the satellite's stochastic dynamic system, results much closer to reality are obtained. This paper analyses the accuracy and stability of five finite difference schemes in solving SDEs, applying them to a second-order stochastic differential equation. The uniformity of the stabilisation behaviour in the stochastic trajectories of the stochastic dynamical system is discussed, and the noise impact on the results is analysed by comparing cases with variations in the noise coefficient. The graphical results of the SDEs presented in this paper highlight the symmetry of the stochastic trajectories around the solution of the deterministic system.

Keywords: stochastic calculus; stochastic differential equations; Gaussian distribution; white noise; satellite orbit; orbit stability; pendulum

1. Introduction

The rotational dynamics of satellites, particularly in Low Earth Orbit (LEO), are significantly influenced by deterministic and stochastic forces. In such orbits, the gravity gradient torque, determined by the uneven distribution of Earth's gravitational field, plays a dominant deterministic role. However, aerodynamic torques caused by atmospheric drag and magnetic torques from interactions with the magnetic fields of the Earth and the moon are subject to stochastic variability due to fluctuations in atmospheric density and magnetic field strength. These effects are particularly pronounced in LEO, where atmospheric density is higher compared to higher altitudes, amplifying the stochastic influences. Additionally, external factors like solar radiation, meteorite impacts, and Earth's electric field further contribute to the stochastic nature of satellite motion.

For LEO satellites, moments of inertia are also subject to stochastic variation due to the dynamic effects of thermo-elastic deformations, crew activity, and fluid behaviour within tanks. These complexities make the orbital motion a highly stochastic process, best modelled using stochastic differential equations. This study builds upon foundational research in stochastic modelling and existing research in stochastic orbit analysis, offering insights into the influence of deterministic gravity gradient forces and stochastic aerodynamic

torques. By applying stochastic stability techniques, this research provides a comprehensive understanding of satellite dynamics in LEO, highlighting both the opportunities and challenges of operating in such an environment.

The analysis of the stability of an orbit is a calculation of great importance in the design of a satellite or in monitoring its operation, which is related to the field of aerospace engineering and the dynamics of celestial body systems [1]. The importance of maintaining a stable orbit is dictated by the vital role that satellites play in many areas: locating devices equipped with GPS technology and ensuring a safe ground and air navigation system, taking photographs of the Earth's surface, observing weather conditions and, above all, transmitting and retrieving information to and from Earth via telecommunications.

Deterministic methods of analysing the trajectory of satellites cannot take into account the unpredictable nature of the parameters of the atmosphere or their deviations from the standard model of the atmosphere, such as variations in temperature, pressure, and density (which has the greatest impact on the attitude of the satellites) [2]. Stochastic analysis using stochastic processes adds to the differential equations a probabilistic (or diffusion) term that allows for the integration of random variations [3,4] in the mentioned parameters—density, temperature, and pressure—taking into account the impact that these variations have on the results of the equations and thus obtaining results closer to reality.

Stochastic calculus, a domain that emerged in the early years of the twentieth century, was theorised by the Japanese mathematician Kiyosi Itô [5]. This domain has seen a great rise in interest from researchers in recent years and is greatly utilised in domains involving a certain degree of uncertainty or risk, such as in finance [6,7], meteorology, medicine, epidemiology [8], as well as in engineering, due to the underlying mathematical theory of associating a degree of probability, deviation from the mean, or even uncertainty to a differential equation.

The subject of interest of this paper is the study of the stability of the orbit of an artificial satellite of Earth using finite difference methods in solving the stochastic differential equations of the motion of the satellite and the comparison in stability of five stochastic finite difference schemes (Euler–Maruyama, Milshtein, Stochastic Heun, and two Runge–Kutta schemes).

2. Short Review of the Mechanical Aspects of the Satellite

Consider a rigid satellite occupying a spatial domain Λ, with local density ρ, which is orbiting Earth at a constant altitude on a circular equatorialLEO, with a constant angular velocity vector Ω parallel to the vertical axis of the Earth.

The axes system $O\xi\eta\zeta$ has the origin O positioned in the mass centre of the satellite (for which the position vector in relation to the centre of mass of Earth is $\mathbf{r}$), the $O\xi$ axis tangent to the circular trajectory, and the $O\eta$ axis radially positioned and the $O\zeta$ axis perpendicular to the trajectory plane. This axes system is, thus, an orbital one, and not a refence system completely "tied" to the satellite. Taking in consideration the fact that the satellite can spin around the mentioned axes, it is appropriate to describe a secondary system of axes, the Oxyz system, with the three axes aligned with the principal axes of the satellite (around which the tensor of inertia is a diagonal matrix [9]):

$$\mathbf{J} = \begin{pmatrix} A & 0 & 0 \\ 0 & B & 0 \\ 0 & 0 & C \end{pmatrix}, \tag{1}$$

in which A, B, and C are the principal moments of inertia. The transformation of coordinates between the two axes systems can be written using Euler transformations [9]:

$$\begin{pmatrix} x \\ y \\ z \end{pmatrix} = \mathbf{R}_{1,2,3}(\theta, \psi, \varphi) \begin{pmatrix} \xi \\ \eta \\ \zeta \end{pmatrix}, \tag{2}$$

in which the matrix of rotation is as follows:

$$\mathbf{R}_{1,2,3}(\theta, \psi, \varphi) = \begin{pmatrix} \cos\theta\cos\psi & \sin\theta\cos\psi & -\sin\psi \\ \cos\theta\sin\psi\sin\varphi - \sin\theta\cos\varphi & \sin\theta\sin\psi\sin\varphi + \cos\theta\cos\varphi & \cos\psi\sin\varphi \\ \cos\theta\sin\psi\cos\varphi + \sin\theta\sin\varphi & \sin\theta\sin\psi\cos\varphi - \cos\theta\sin\varphi & \cos\psi\cos\varphi \end{pmatrix}. \tag{3}$$

Due to the periodicity of the trigonometric functions, the angles are usually defined in the interval of [0,2π]. However, as we will see in the following sections of this paper, the stochastic stability of the mentioned satellite can be properly studied if the domain is extended to the real numbers set, $\mathbb{R}$, offering the ability to quantify either the instability trait of the motion differential equation or the number of full revolutions before stabilisation. The Euler angles and the position of the mass centre of the satellite are visualised in Figure 1, in which the intermediary reference systems are obtained as follows:

- Reference system $Ox_1y_1z_1$ is obtained by rotating $O\xi\eta\zeta$ around axis $O\zeta$ with the angular displacement θ.
- Reference system $Ox_2y_2z_2$ is obtained by further rotating $Ox_1y_1z_1$ around Oy_1 with the angular displacement ψ.
- Principal reference system $Oxyz$ is obtained by rotating Ox_2 around with the angular displacement φ; the final axis Ox is the symmetry axis of the satellite.

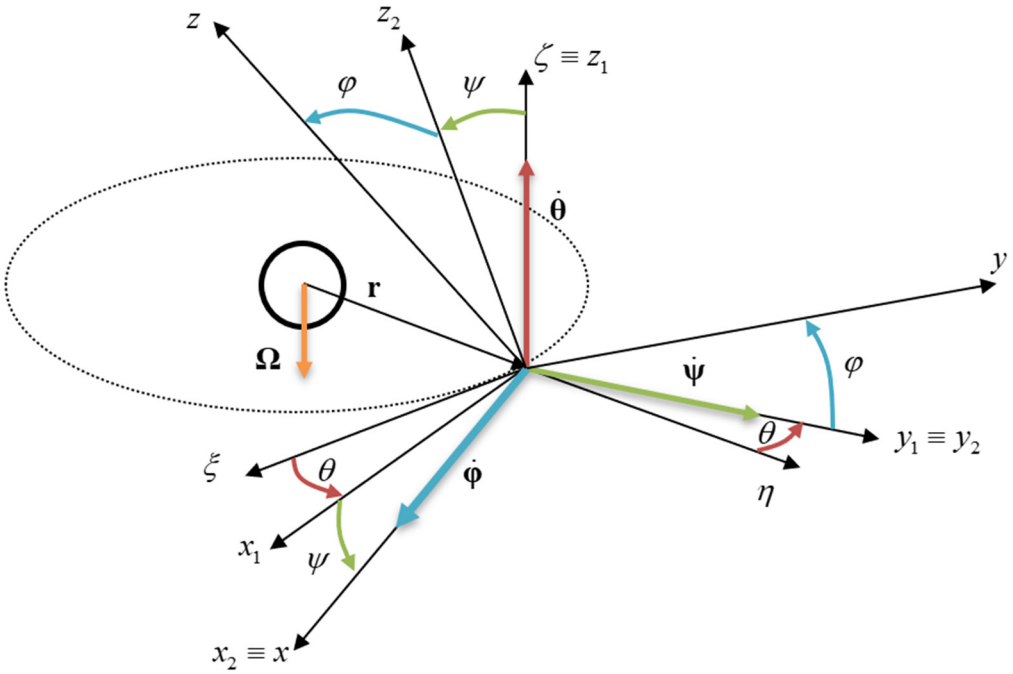

Figure 1. The Euler angles of the satellite and the angular speed vectors—the pitch angular velocity (red), the yaw angular velocity (green), the roll angular velocity (blue) and the angular velocity of the satellite mass centre around the centre of The Earth (orange).

Utilising the corresponding rotation matrices, the total angular velocity of the satellite can be evaluated by the following formulation:

$$\boldsymbol{\omega} = \begin{pmatrix} \omega_x \\ \omega_y \\ \omega_z \end{pmatrix} = \begin{pmatrix} \dot{\varphi} - \left(\dot{\theta} - \Omega\right) \sin\psi \\ \dot{\psi}\cos\varphi + \left(\dot{\theta} - \Omega\right)\cos\psi\sin\varphi \\ -\dot{\psi}\sin\varphi + \left(\dot{\theta} - \Omega\right)\cos\psi\cos\varphi \end{pmatrix}. \tag{4}$$

As previously mentioned, Ω is the angular speed of the mass centre of the satellite around the mass centre of the Earth. The angular momentum of the satellite can be written, according to the angular displacements and principal moments of inertia A, B, and C, in the absence of linear velocity (since the satellite is only exhibiting a rotational movement), as follows [10]:

$$\mathbf{K_O} = \begin{pmatrix} \mathrm{A}\left[\dot{\varphi} - \left(\dot{\theta} - \Omega\right)\sin\psi\right] \\ \mathrm{B}\left[\dot{\psi}\cos\varphi + \left(\dot{\theta} - \Omega\right)\cos\psi\sin\varphi\right] \\ \mathrm{C}\left[-\dot{\psi}\sin\varphi + \left(\dot{\theta} - \Omega\right)\cos\psi\cos\varphi\right] \end{pmatrix} = \mathbf{J}\boldsymbol{\omega}, \tag{5}$$

in which $\mathbf{J}$ is the tensor of inertia from (1) and $\boldsymbol{\omega}$ is the total angular velocity defined in (4). Due to the assumption that the satellite is axisymmetric around the *Ox* axis, we can write A < B = C. One can linearise this formulation (5) and the formulation in (4) considering small angle variations:

$$\sin\alpha_i \cong \alpha_i[\mathrm{rad}], \cos\alpha_i \cong 1[\mathrm{rad}],\ \alpha_i\alpha_j \cong 0, \alpha_i\dot{\alpha}_j \cong 0, \forall\alpha_i \in \{\varphi, \psi, \theta\}, \tag{6}$$

so that the total angular velocity and the angular momentum become the following:

$$\boldsymbol{\omega} \cong \begin{pmatrix} \dot{\varphi} + \Omega\psi \\ \dot{\psi} - \Omega\varphi \\ \dot{\theta} - \Omega \end{pmatrix}, \mathbf{K_O} \cong \begin{pmatrix} \mathrm{A}\left(\dot{\varphi} + \Omega\psi\right) \\ \mathrm{B}\left(\dot{\psi} - \Omega\varphi\right) \\ \mathrm{C}\left(\dot{\theta} - \Omega\right) \end{pmatrix} \tag{7}$$

The total derivative of the angular momentum in (7), considering the definition of the total derivative of a vector field [11], is equal to the sum of all the torques (moments of forces) which act on the satellite [1,9]:

$$\frac{\mathrm{d}\mathbf{K_O}}{\mathrm{dt}} = \frac{\partial\mathbf{K_O}}{\partial\mathrm{t}} + \boldsymbol{\omega} \times \mathbf{K_O} = \sum_i \mathbf{M_O}(\mathbf{F}_i). \tag{8}$$

Differentiating partially with respect to time and calculating the cross product between the total angular velocity and angular momentum, the differential of the angular momentum vector can be written as follows:

$$\frac{\mathrm{d}\mathbf{K_O}}{\mathrm{dt}} = \begin{pmatrix} \mathrm{A}\ddot{\varphi} + \Omega^2(\mathrm{C} - \mathrm{B})\varphi + \Omega(\mathrm{A} + \mathrm{B} - \mathrm{C})\dot{\psi} \\ \mathrm{B}\ddot{\psi} + \Omega^2(\mathrm{C} - \mathrm{A})\psi - \Omega(\mathrm{A} + \mathrm{B} - \mathrm{C})\dot{\varphi} \\ \mathrm{C}\ddot{\theta} \end{pmatrix}. \tag{9}$$

The moments of forces which act on the satellite are the gravity torque and the aerodynamic torque. The gravity torque has the following formulation:

$$\mathbf{M_G} = \mathrm{k}\frac{\mathrm{M}}{\mathrm{R}^3}\begin{pmatrix} -3\varphi(\mathrm{C}-\mathrm{B}) \\ 0 \\ -3\theta(\mathrm{A}-\mathrm{B}) \end{pmatrix}, \tag{10}$$

in which k is the universal gravitational constant (k = 6.6743 $\times$ 10^{-11} $\mathrm{m^3kg^{-1}s^{-2}}$ [12,13]), R is the orbit altitude, and M is the mass of the Earth. As a consequence to Binet's Equation [14] and to the circular orbit, the following equation stands:

$$\mathrm{kM} = \mathrm{R}^3\Omega^2. \tag{11}$$

In order to simplify the three-dimensional second-order differential equation, one can consider that the yaw and roll angles of the satellite remain constant and equal to zero [1]:

$$\psi(t) = \varphi(t) \cong 0. \tag{12}$$

According to the authors in [1,15,16], the aerodynamic torque has the following formulation:

$$\mathbf{M} = \frac{1}{2}\rho \mathrm{V}^2\left[\mathbf{f}(\phi,\psi,\theta) + \mathbf{K}\left(\dot{\phi},\dot{\psi},\dot{\theta}\right)\boldsymbol{\omega}\right], \tag{13}$$

where ρ is the local density of the atmosphere, V is the mass centre velocity of the satellite, and **f** is a vector function of the yaw, roll, and pitch angles, which depends on the satellite geometry and which determines the restoring aerodynamic torque. In the case of the constant roll and yaw angles [1], this vector has the following form:

$$\mathbf{f} = \begin{pmatrix} 0 \\ 0 \\ -\mathrm{S_0L_0c_1}\theta \end{pmatrix}. \tag{14}$$

Moreover, **K** is a matrix function of the angular velocities, which determines the dissipative term of the aerodynamic torque, and, for the same hypotheses, the product between **K** and the total angular velocity vector $\boldsymbol{\omega}$ takes the form [1]:

$$\mathbf{K}\boldsymbol{\omega} = \begin{pmatrix} 0 \\ 0 \\ -\mathrm{S_0L_0c_2}\frac{\mathrm{d}\theta}{\mathrm{dt}} \end{pmatrix}. \tag{15}$$

Finally, the aerodynamic torque for the case of constant roll and yaw angles [1] for an axisymmetric satellite that has only one component on the *Oz* axis (pitch axis) [1,15–17]:

$$\mathbf{M_A} \cong \frac{\rho \mathrm{V}^2}{2}\left[\begin{pmatrix} 0 \\ 0 \\ -\mathrm{S_0L_0c_1}\theta \end{pmatrix} + \begin{pmatrix} 0 \\ 0 \\ -\mathrm{S_0L_0c_2}\frac{\mathrm{d}\theta}{\mathrm{dt}} \end{pmatrix}\right], \tag{16}$$

where $\mathrm{S_0}$ and $\mathrm{L_0}$ are reference area and length of the satellite, $\mathrm{c_1}$ is a unitless coefficient, and $\mathrm{c_2}$ is a coefficient with the S.I. unit of seconds. To take into account the unpredictable external factors that can disturb the equilibrium of the satellite [1,2,18], in Equation (14), we introduced the Wiener process to the atmospheric density [1]:

$$\rho = \rho_0\left(1 + \varepsilon\frac{\mathrm{dW}}{\mathrm{dt}}\right). \tag{17}$$

In this case, ε is a real constant, with the S.I. unit of seconds and ρ_0 is the standard atmospheric density at altitude R. The second-order differential equation of the satellite is as follows:

$$C\frac{d^2\theta}{dt^2} = -\frac{3}{2}\Omega^2(A-B)\sin 2\theta + \frac{1}{2}\rho V^2\left[-S_0L_0c_1\sin\theta - S_0L_0c_2\frac{d\theta}{dt}\right]. \tag{18}$$

The next step is to make the pitch motion stochastic differential equation of the satellite non-dimensional before numerically solving the SDE. Thus, the equation becomes

$$\ddot{\theta} + b\dot{\theta} + \sin\theta = A_0\sin 2\theta - c\left(b\dot{\theta} + \sin\theta\right)\frac{dW}{d\tau}, \tag{19}$$

where τ is the dimensionless time and the constants are defined by

$$b = c_2\sqrt{\frac{S_0L_0\rho_0V^2}{2Cc_1}} \in \mathbb{R}_+, \tag{20}$$

$$A_0 = \frac{3\Omega^2C\left(1-\frac{A}{C}\right)}{c_1S_0L_0\rho_0V^2} \in \mathbb{R}_+, \tag{21}$$

$$c = \varepsilon\sqrt{\frac{S_0L_0\rho_0V^2}{2Cc_1}} \in \mathbb{R}. \tag{22}$$

3. Stochastic Numerical Methods

Let us consider the stochastic differential equation in Equation (20), in which $\mathbf{X}$ is the n-dimensional stochastic variable $\mathbf{X}(t) : \left[t^{(0)}, T\right] \to \mathbb{R}^n$, $\mathbf{F}$ is the vector function of the drift (or deterministic) term $\mathbf{F}\colon \mathbb{R}^n \times \left[t^{(0)}, T\right] \to \mathbb{R}^n$, $\mathbf{G}$ is the matrix function of the diffusion (or probabilistic, stochastic) term $\mathbf{G}\colon \mathbb{R}^n \times \left[t^{(0)}, T\right] \to \mathbb{R}^{n\times m}$, and $\mathbf{W}(t) \in \mathbb{R}^m$ is a Wiener process.

The general form of a stochastic n-dimensional differential equation system with m-dimensional noise (perturbation) is [19] (in which $t^{(0)}$ represents the initial moment of time):

$$\begin{gathered} d\mathbf{X}(t) = \mathbf{F}(\mathbf{X}, t)dt + \mathbf{G}(\mathbf{X}, t)d\mathbf{W}(t), \\ \mathbf{X}\left(t^{(0)}\right) = \mathbf{X}_0. \end{gathered} \tag{23}$$

A Wiener process is a stochastic process with independent and normally distributed variations [3,20] $W(t+\Delta t) - W(t) \sim N(0, \Delta t)$. This Wiener process represents the integral of a white noise with a Gaussian distribution, which is the cumulative function of a random disturbance with normal distribution with a mean of 0 and variance equal to the difference in the increments [4]. This white noise can be associated with an unpredictable and unwanted phenomenon, such as random vibrations occurring and affecting rigid bodies, random fluctuations of values considered constant (such as standard temperature, density and pressure), and the "white noise" that can be listened to with a radio, occurring because of multiple factors. In discrete time, the evolution of a white noise can be considered to be a sequence of random shocks (with a Gaussian distribution) [21].

The stochastic differential Equation (17) (for which n = 2 and m = 1) is transformed in a system of stochastic differential equations, utilising two function substitutions ($\theta = X_1$ and $d\theta/dt = X_2$):

$$d\mathbf{X} = \begin{pmatrix} X_2 \\ -bX_2 - \sin(X_1) + A_0\sin(2X_1) \end{pmatrix}dt + \begin{pmatrix} 0 \\ -c(bX_2 + \sin(X_1)) \end{pmatrix}dW. \tag{24}$$

The case of the present paper is that of a 2-dimensional system with scalar noise. An assessment of finite differences methods used in stochastic numerical methods has been performed by the authors [22], from which the best performing scheme was proven to be the **Efficient Runge–Kutta** method [23], when compared to the other schemes: **Euler-Maruyama** [3], **Milshtein** [24], **Stochastic Heun** [3], **First order Runge–Kutta involving the Itô coefficient** (FRKI) [23,25]. The formulation of the **Efficient Runge–Kutta** (**ERK**) scheme, extended for *n*-dimensional stochastic differential system with scalar noise, is the following:

$$\begin{aligned}\mathbf{X}^{(i+1)} = \mathbf{X}^{(i)} + \tfrac{1}{2}[\mathbf{F_1} + \mathbf{F_2}]\Delta t + \tfrac{1}{40}[37\mathbf{G_1} + 30\mathbf{G_3} - 27\mathbf{G_4}]\sqrt{\Delta t}u^{(i)} + \\ + \tfrac{1}{16}[8\mathbf{G_1} + \mathbf{G_2} - 9\mathbf{G_3}]\sqrt{3\Delta t},\end{aligned} \tag{25}$$

in which $u^{(i)}$ is a normally distributed variable of mean 0 and variance 1 which, when multiplied with the square root of the time step, represents the random increments of the white noise.

For easier understanding, the nondimensional time will be referred to, from now on, as simply t. The functions for the system are as follows:

$$\begin{aligned}\mathbf{F_1} = \mathbf{F}\left(\mathbf{X}^{(i)}\right), \qquad \mathbf{G_1} = \mathbf{G}\left(\mathbf{X}^{(i)}\right), \\ \mathbf{F_2} = \mathbf{F}\left(\mathbf{X}^{(i)} + \mathbf{F_1}\Delta t + \mathbf{G_1}\sqrt{\Delta t}\Delta u^{(i)}\right),\ \mathbf{G_2} = \mathbf{G}\left(\mathbf{X}^{(i)} - \tfrac{2}{3}\mathbf{G_1}\left(\sqrt{\Delta t}\Delta u^{(i)} + \sqrt{3\Delta t}\right)\right), \\ \mathbf{G_3} = \mathbf{G}\left(\mathbf{X}^{(i)} + \tfrac{2}{9}\mathbf{G_1}\left(3\sqrt{\Delta t}\Delta u^{(i)} + \sqrt{3\Delta t}\right)\right), \\ \mathbf{G_4} = \mathbf{G}\left(\mathbf{X}^{(i)} - \tfrac{20}{27}F_1\Delta t + \tfrac{10}{27}(\mathbf{G_2} - \mathbf{G_1})\sqrt{\Delta t}\Delta u^{(i)} - \tfrac{10}{27}\mathbf{G_2}\sqrt{3\Delta t}\right).\end{aligned} \tag{26}$$

The schemes utilised to solve the SDEs can be categorised by weak and strong convergence orders. Such a categorisation was presented in the assessments of numerical finite difference schemes performed by the authors in [22]. The **strong convergence** order for a discrete numerical approximation $X_{approx.}$ at time step $T = i\Delta t$ to the actual solution of the SDE, X(t), is defined by Kloeden and Platen [19] as the positive number γ, for which there is a constant C, which does not depend on the timestep size Δt, and for which the following relation exists:

$$E\left(\left|X(T) - X^{(i)}_{approx.}\right|\right) \leq C\Delta t^{\gamma}. \tag{27}$$

Similarly, the **weak convergence** order is the positive number β, for which there is another timestep-independent constant C which respects the following equation:

$$\left|\mathbb{E}(X(T)) - E\left(X^{(i)}_{approx.}\right)\right| \leq C\Delta t^{\beta}. \tag{28}$$

The previous definitions for the two types of convergence orders can be expressed in a discrete form:

- Strong convergence:

$$\frac{1}{N}\sum_{j=1}^{N}\left(X_j(T) - X^{(i)}_{j,approx.}\right) \leq C\Delta t^{\gamma}, \tag{29}$$

- Weak convergence:

$$\left|\frac{1}{N}\sum_{j=1}^{N}X_j(T) - \frac{1}{N}\sum_{j=1}^{N}X^{(i)}_{j,approx.}\right| \leq C\Delta t^{\beta}. \tag{30}$$

in which N is the number of stochastic trajectories, and, thus, the summation, is performed for all of the trajectories and the final timestep.

For accurately simulating individual trajectories, **strong numerical schemes** are necessary. These schemes closely approximate the true paths of the SDE for each realisation of the random process. On the other hand, **weak numerical schemes** are sufficient for tasks like computing frequency histograms or probability distributions, such as the invariant measure of a stationary solution, where precise individual trajectories are less critical than the overall statistical properties of the system.

A previous study on convergence order has been performed by the authors [20], and the results are displayed in Table 1:

Table 1. Converge order for all the schemes.

Name of the Scheme	Additive Noise		Multiplicative Noise	
	Weak Order	Strong Order	Weak Order	Strong Order
Euler–Maruyama	1	1	1	0.5
Milshtein	1	1	1	1
Stochastic Heun	2	2	1	1
FRKI	1	1	1	1
ERK	1	1	1.5	1.5

4. Numerical Simulations

4.1. Test 1. The SDE of a Forced Undamped Oscillator with Exterior Stochastic Disturbance

Starting from the differential equation of the pitch angle of the satellite described previously, considering the simplified case for b = c = 0 and for small pitch angles, and adding a free term with an oscillating function h(t) and a stochastic term described by the constant ε to the equation, the following equation is obtained:

$$\ddot{x} + \omega^2 x = \mathrm{h}(t) + \varepsilon \frac{\mathrm{dW}}{\mathrm{dt}}, x(0) = \frac{\pi}{180}, \dot{x}(0) = 0, \tag{31}$$

in which $\mathrm{h}(t) = \mathrm{F}_0 \cos(\omega_1 t)$, $\omega^2 = 1 - 2\mathrm{A}_0$, and $\varepsilon \in \mathbb{R}$. This equation was previously studied by the authors [22], without comparing the behaviour of the numerical schemes applied to this equation. This second-order stochastic differential equation of a forced undamped oscillator with exterior stochastic disturbance can be written as a two-dimensional system of first-order stochastic equation:

$$\mathrm{d}\mathbf{X}(t) = \mathrm{d}\begin{pmatrix} \mathrm{X}_1(t) \\ \mathrm{X}_2(t) \end{pmatrix} = \begin{pmatrix} \mathrm{X}_2(t) \\ -\omega^2 \mathrm{X}_1(t) + \mathrm{h}(t) \end{pmatrix} \mathrm{dt} + \begin{pmatrix} 0 \\ \varepsilon \end{pmatrix} \mathrm{dW}(t). \tag{32}$$

In the absence of an analytical solution for the stochastic differential system, the finite difference schemes can be compared, in the mean value, to the analytical solution of the "normal" differential equation (for $\varepsilon = 0$):

$$\ddot{x}(t) + \omega^2 x(t) = \mathrm{F}_0 \cos(\omega_1 t), \tag{33}$$

for which two cases can be distinguished:

A. Non-resonant case $\omega \neq \omega_1$.

In this case, the general solution determined by the summation of the homogenous and particular solutions [26–28] is as follows:

$$x(t) = \left(x(0) - \frac{F_0}{\omega^2 - \omega_1^2} \right) \cos(\omega t) + \frac{F_0}{\omega^2 - \omega_1^2} \cos(\omega_1 t). \tag{34}$$

B. Resonant case $\omega = \omega_1$.

For this case, the solution is as follows:

$$x(t) = x(0)\ \cos(\omega t) + t \frac{F_0}{2\omega_1} \sin(\omega_1 t). \tag{35}$$

The angular frequency of the perturbations and the amplitude for all the considered cases are $\omega_1 = 5$,$F_0 = 10$. The values of ε and ω were varied in order to see the impact of both white noise and the angular frequency of the stochastic pendulum on the results. The timestep considered for all of the following simulations results is $\Delta t = 0.02$, and the number of random paths considered is M = 5000. The time interval of integration is between $t^0 = 0$ and T = 4 for the simulations. The relation between the timestep size, integration time, and number of calculation points (N_p) on a uniform grid is as follows:

$$\Delta t = \frac{T}{N_p - 1}. \tag{36}$$

The mean value of all of the 5000 trajectories of the SDE results obtained with the **Efficient Runge–Kutta** (**ERK**) method is compared with the result of the ODE in order to highlight the zero-mean property of the white noise and to prove the mean stability of the ERK method compared to the other schemes—**Euler–Maruyama** (**EM**), **Milshtein** (**M**), **Stochastic Heun** (**H**), and **First order Runge–Kutta involving the Itô coefficient** (**FRKI**).

In the following test, we want to study the impact of the SDE coefficients on the pitch angle and pitch angular velocity.

A1. This case is for an angular frequency $\omega = 1$ and a small coefficient for the white noise $\varepsilon = 0.5$. Results can be seen in Figure 2.

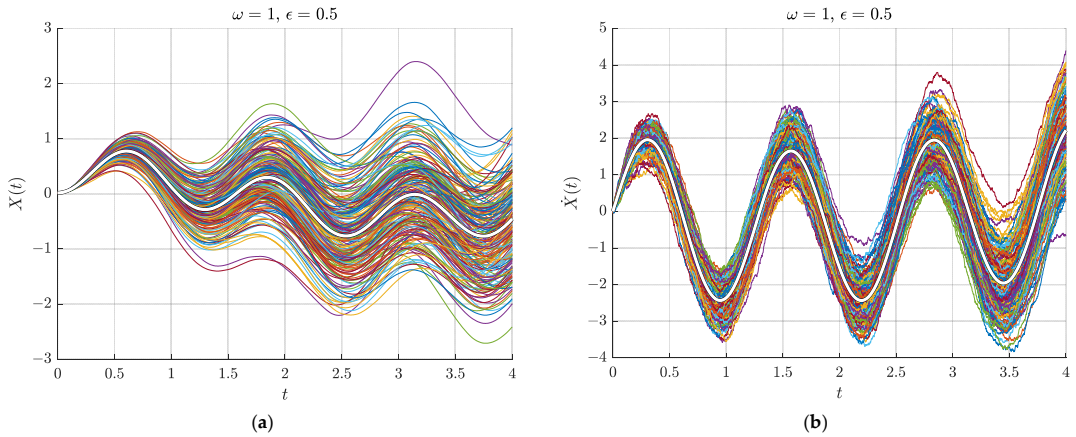

(**a**) (**b**)

Figure 2. *Cont.*

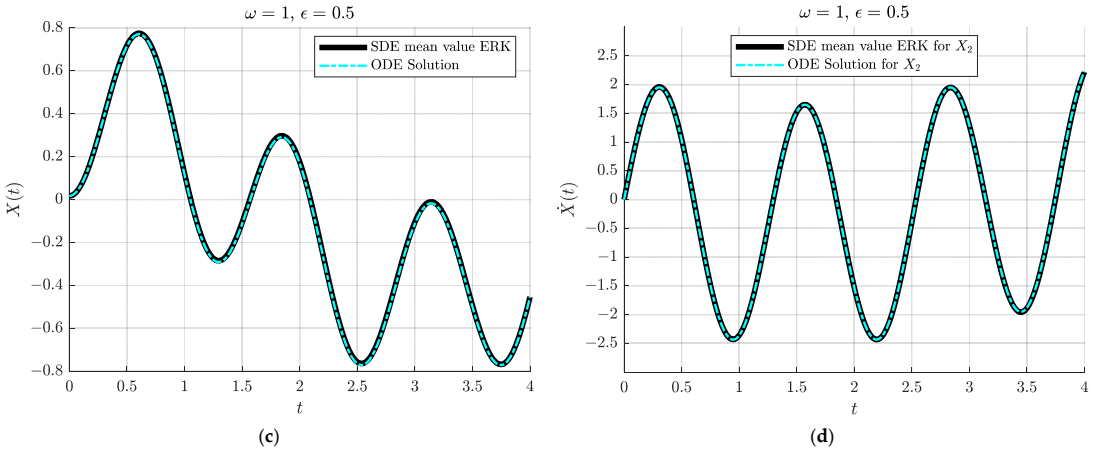

Figure 2. A1 test case (ω = 1, ε = 0.5), (**a**) mean value of X (white) and all trajectories (the coloured lines), (**b**) mean value of dX/dt (white) and all trajectories, and comparison between the ODE solution and the mean value of the ERK scheme for (**c**) X and (**d**) dX/dt.

Figure 2a shows the small disturbing effect of the white noise on both X and dX/dt. In the case of dX/dt (Figure 2b), the white noise has a more visible effect on the trajectories, causing them to look similar to a Wiener process, but maintaining the trend of the mean value (white trendline).

A2. This case is for an angular frequency ω = 1 and a larger coefficient for the white noise ε = 2. Results can be seen in Figure 3.

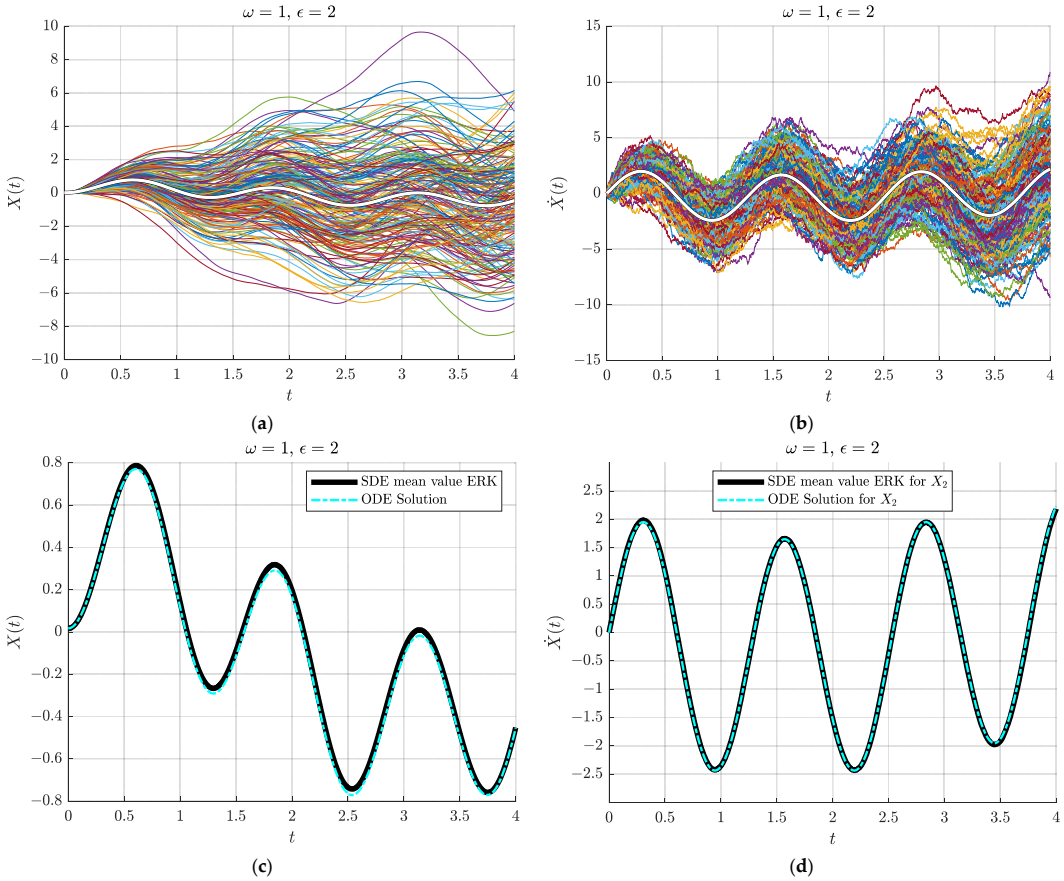

Figure 3. A2 test case (ω = 1, ε = 2), (**a**) mean value of X (white) and all trajectories (the coloured lines), (**b**) mean value of dX/dt (white) and all trajectories, and comparison between the ODE solution and the mean value of the ERK scheme for (**c**) X and (**d**) dX/dt.

The growth of the white noise coefficient ε is followed by the growth in amplitude of the trajectories (see the y-axis scale of Figure 3 compared to the scale of the y-axis in Figure 2); there are also trajectories for which X appears to maintain a constant value for short time intervals. However, just like in the previous case, the mean value of the SDE trajectories obtained with the **ERK** scheme follows the ODE solution closely.

B1. This case is for a resonant angular frequency $\omega = \omega_1 = 5$ and a small coefficient for the white noise $\varepsilon = 0.5$. Results can be seen in Figure 4.

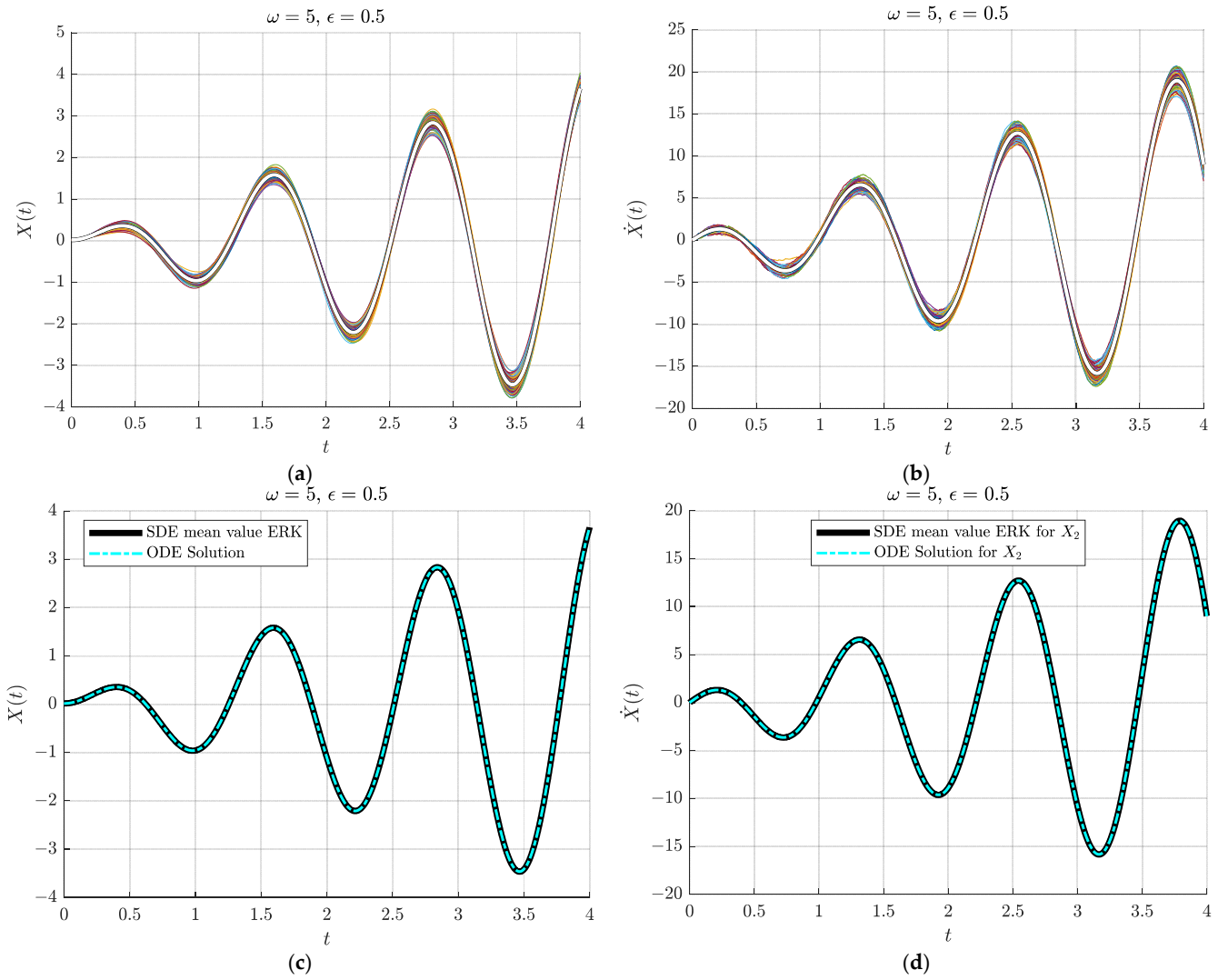

Figure 4. B1 resonant test case ($\omega = 5$, $\varepsilon = 0.5$), (**a**) mean value of X (white) and all trajectories (the coloured lines), (**b**) mean value of dX/dt (white) and all trajectories, and comparison between the ODE solution and the mean value of the ERK scheme for (**c**) X and (**d**) dX/dt.

For the resonant case, the impact of the white noise is not as visible, as in the previous case, Figure 4. The growth in amplitude caused by the equality between the angular frequency of the stochastic oscillator and the angular frequency of the exterior stochastic perturbing force, which shadows the impact of the white noise. However, in the case of a smaller stochastic coefficient, it can be seen that the 5000 paths are more evenly distributed around the mean path, suggesting the symmetry of the zero-mean Gaussian white noise.

B2. This case is for a resonant angular frequency $\omega = \omega_1 = 5$ and a larger coefficient for the white noise $\varepsilon = 2$. Results can be seen in Figure 5.

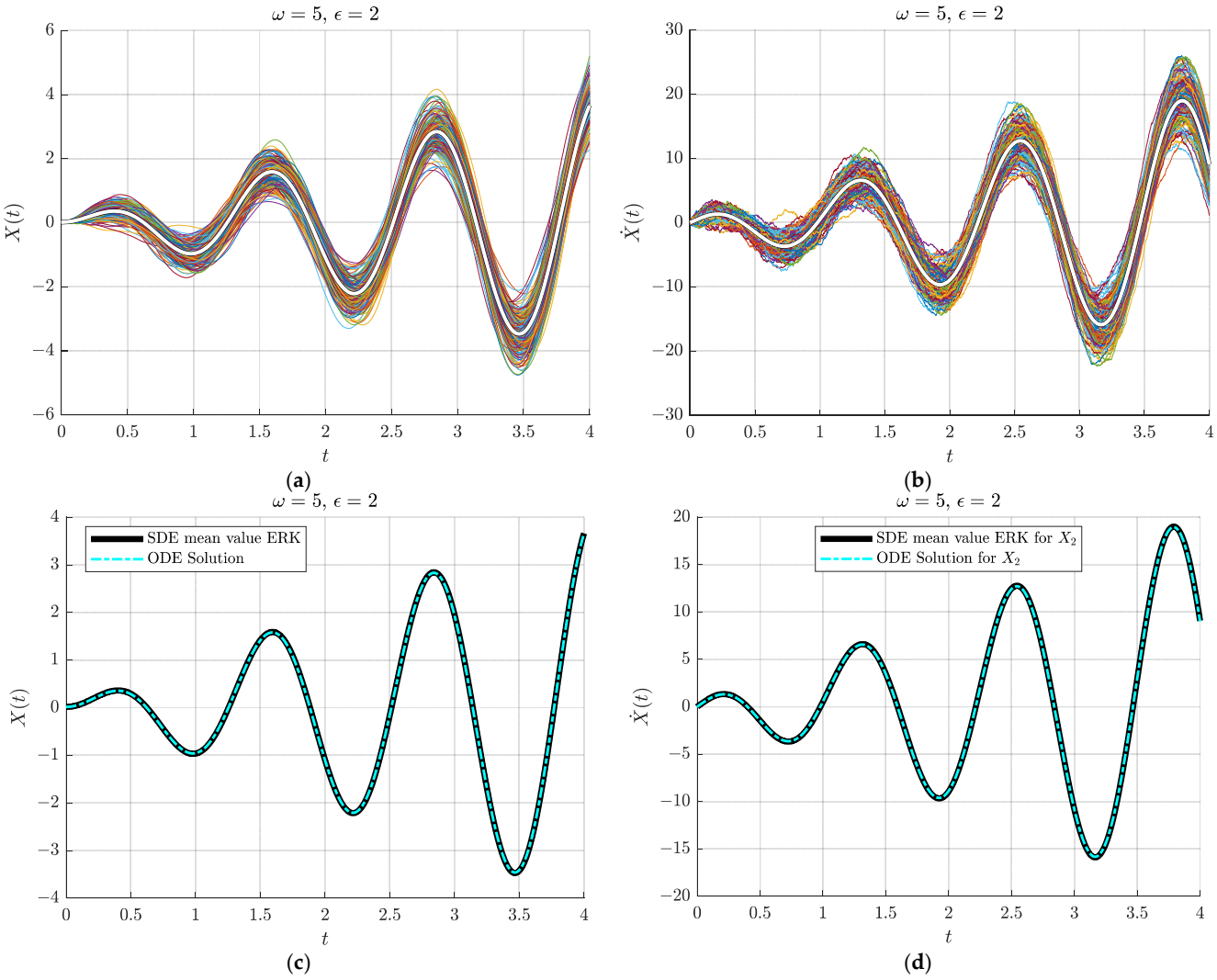

Figure 5. B2 resonant test case (ω = 5, ε = 2), (**a**) mean value of X (white) and all trajectories (the coloured lines), (**b**) mean value of dX/dt (white) and all trajectories, and comparison between the ODE solution and the mean value of the ERK scheme for (**c**) X and (**d**) dX/dt.

The smoothness of any of the stochastic trajectories of X function of time, compared to the stochastic trajectories of dX/dt function of time—which look similarly to the Wiener process, with "rough" edges in the curves—is due to the fact that integrating a derivative function (dX/dt) over time is averaging that function (X). Furthermore, in the stochastic differential equation, the white noise only affects the equation of dX/dt, and not that of X itself.

In both of the resonance cases, the mean value of the **ERK** results follows the ODE solution precisely (Figures 4 and 5).

A3. This case is for an angular frequency ω = 10 and a coefficient for the white noise ε = 2. Results can be seen in Figure 6.

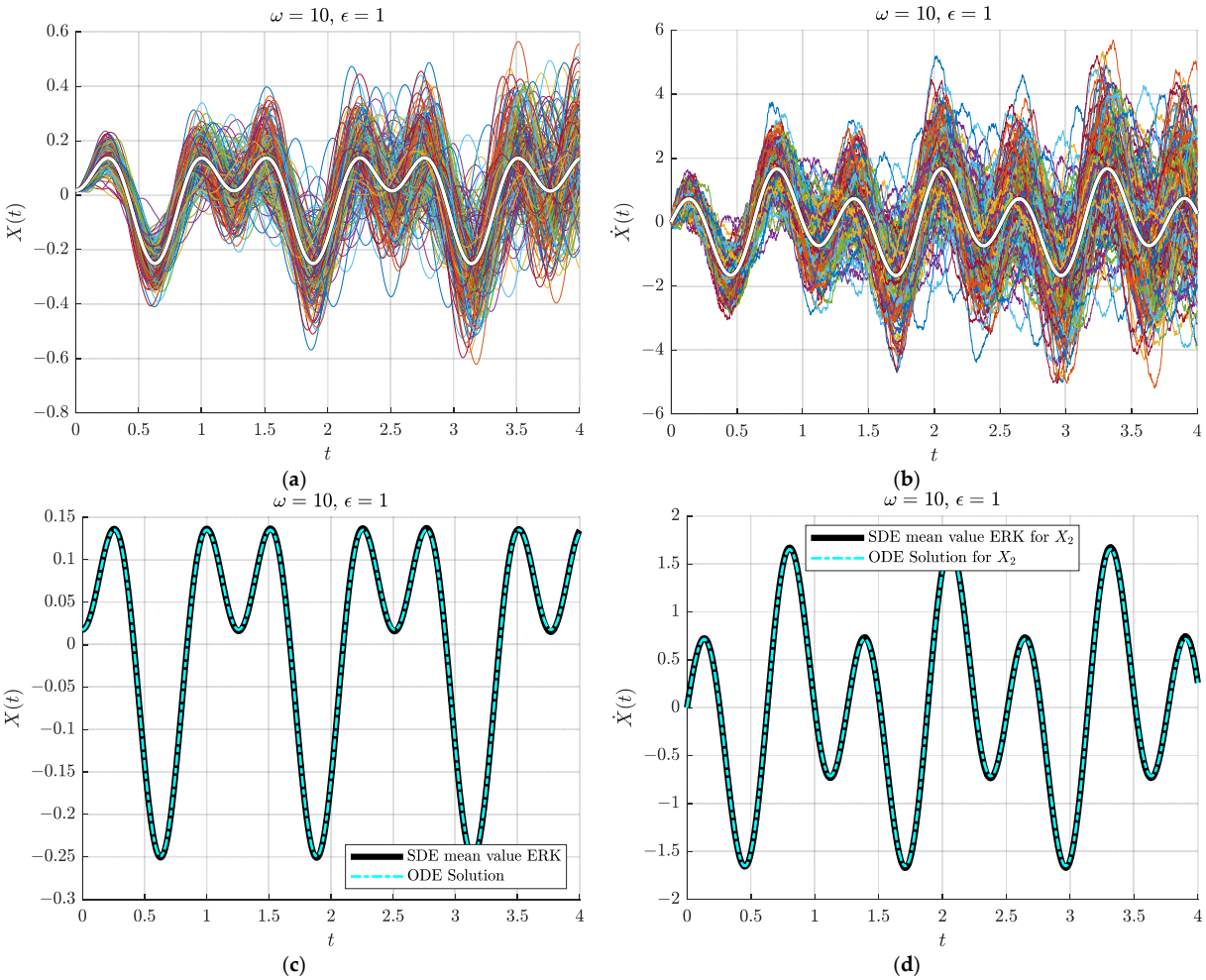

Figure 6. A3 test case (ω = 10, ε = 1), (**a**) mean value of X (white) and all trajectories (the coloured lines), (**b**) mean value of dX/dt (white) and all trajectories, and comparison between the ODE solution and the mean value of the ERK scheme for (**c**) X and (**d**) dX/dt.

A4. This case is for an angular frequency ω = 20 and a coefficient for the white noise ε = 1. Results can be seen in Figure 7.

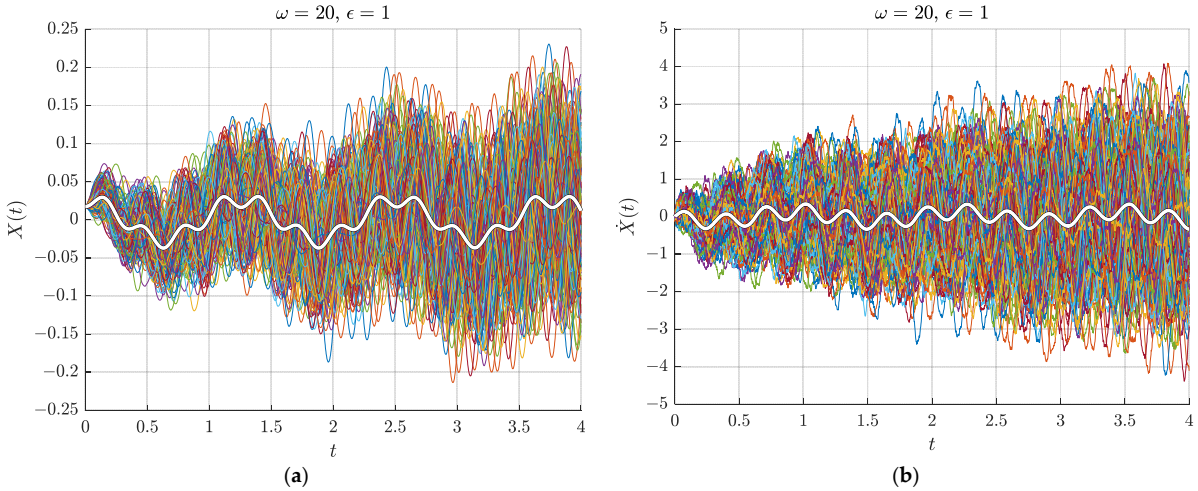

Figure 7. *Cont.*

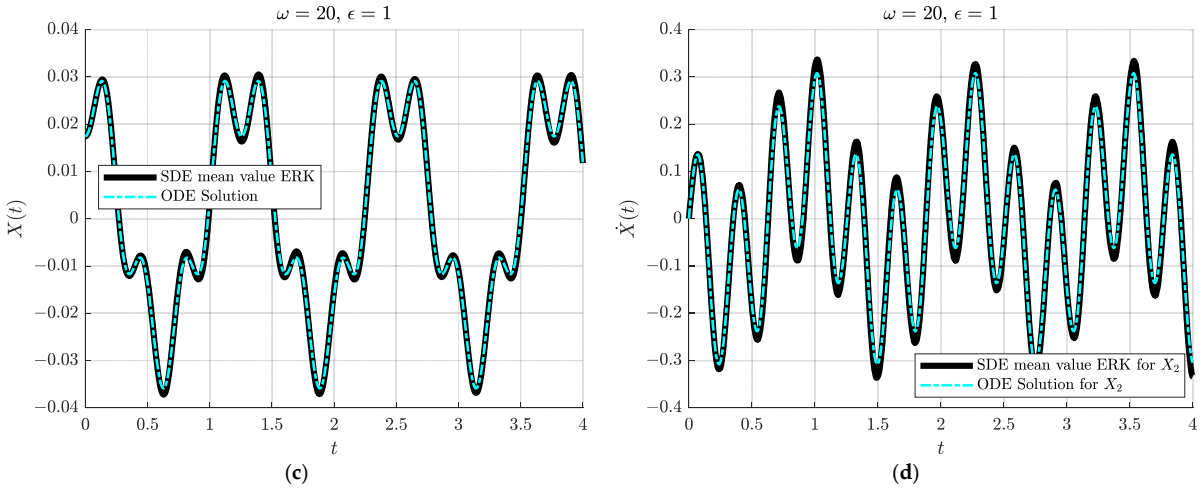

Figure 7. A4 test case (ω = 20, ε = 1), (**a**) mean value of X (white) and all trajectories (the coloured lines), (**b**) mean value of dX/dt (white) and all trajectories, and comparison between the ODE solution and the mean value of the ERK scheme for (**c**) X and (**d**) dX/dt.

All of the results for the different values of the constants are compared in the phase plane in the next figure, Figure 8.

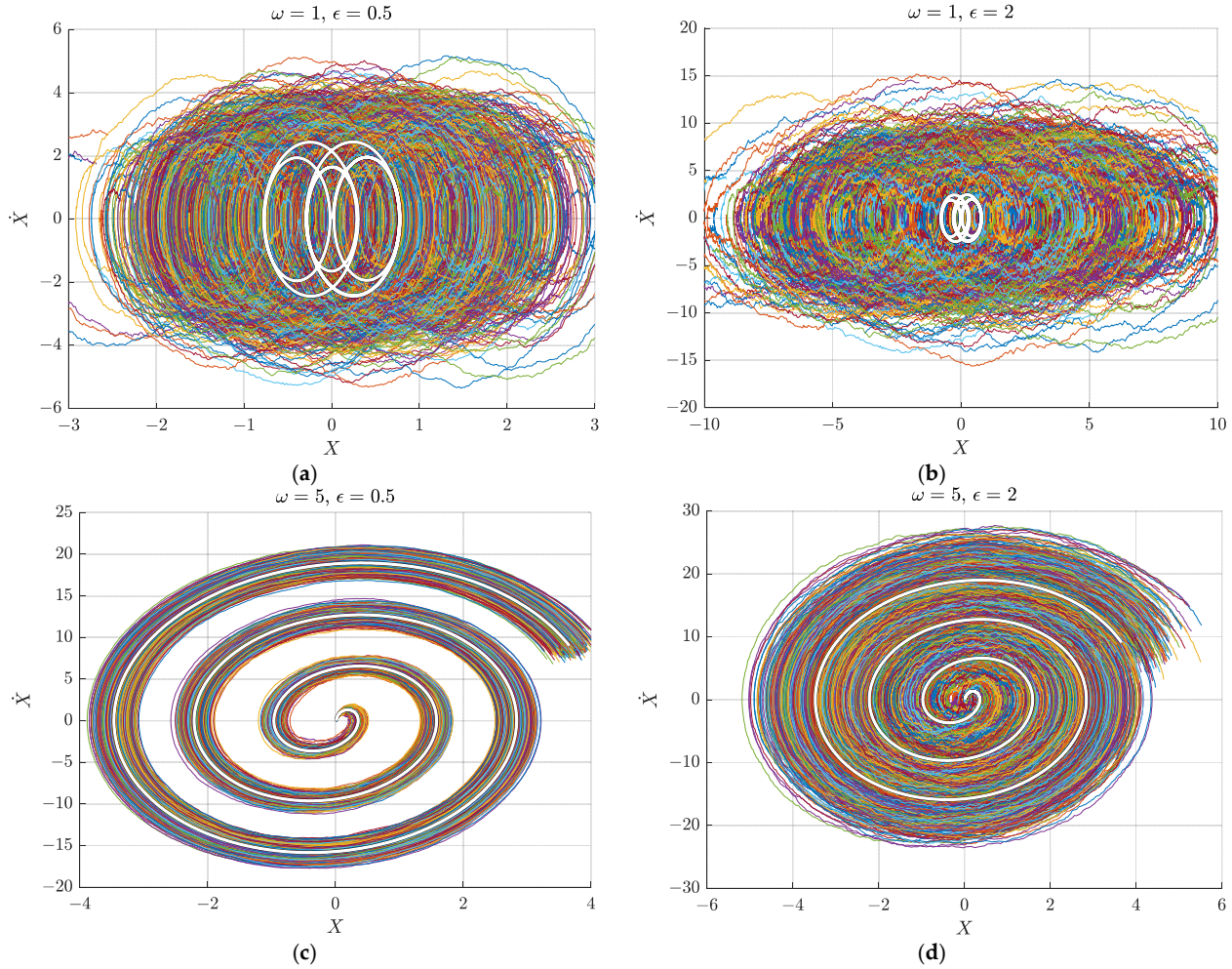

Figure 8. *Cont.*

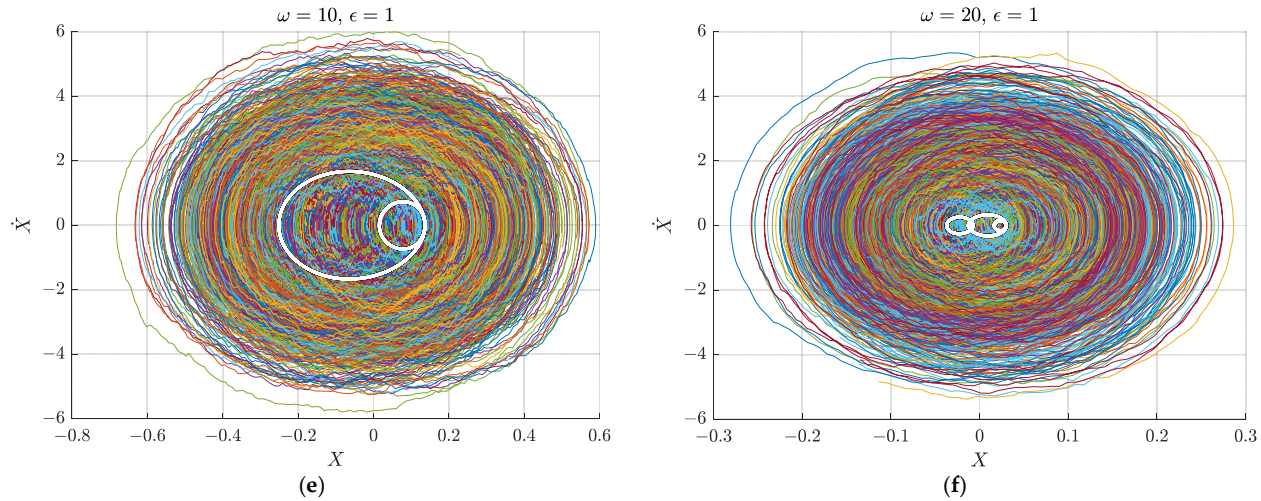

Figure 8. Result comparison for the **ERK Scheme** in the phase plane between the 5000 trajectories (the coloured lines) and the mean trajectory (white).

Due to the properties of the Wiener process (normally distributed variable with zero-mean), in the resonant case, the stochastic trajectories are symmetrically distributed around the values of the ODE deterministic solution. The resonant evolution for the stochastic dynamical system can be plotted in a 3D graph (Figure 9).

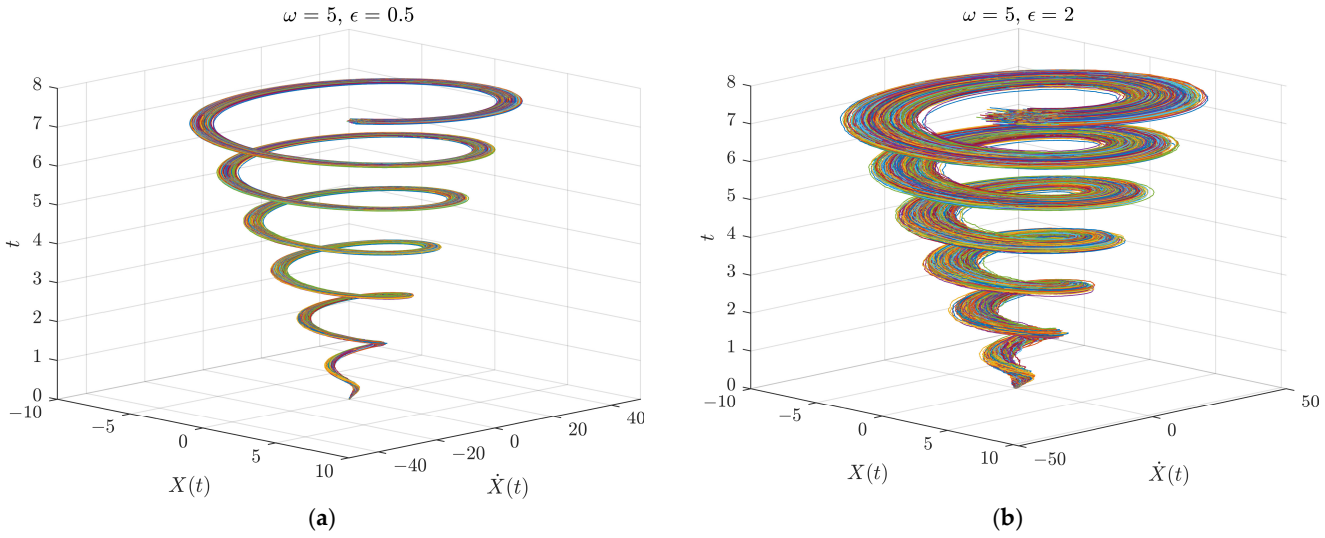

Figure 9. Results of the SDE for the 5000 trajectories (the coloured lines) obtained using the **ERK Scheme** for its evolution in dimensionless time for ω = 5, ε = 0.5 (**a**) and ω = 5, ε = 2 (**b**).

Considering the fact that the local minima and maxima of the SDE trajectories do not occur at the same locations as the corresponding extrema of the ODE, the roots of the derivative function have different locations for different paths. Thus, another level of symmetry is displayed by the SDE considered: the symmetry of the SDE instantaneous states in the phase plane.

In order to compare the stability of the scheme, a comparison between the mean values of the schemes and ODE solution (Figure 10) and a comparison between each schemes for a random path (Figure 11) are presented below.

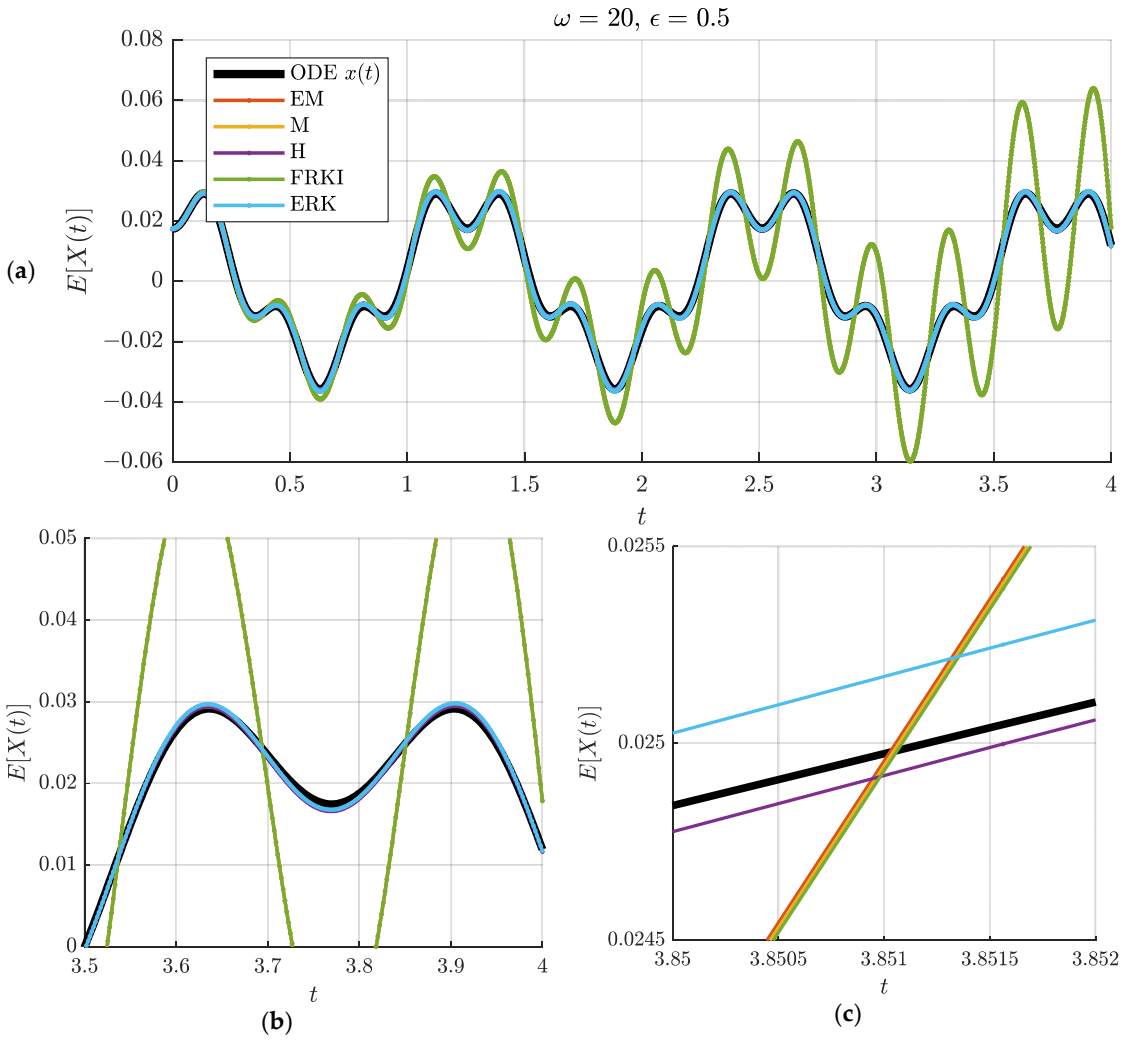

Figure 10. (**a**) Comparison between the schemes in the mean value and the ODE solution, (**b**,**c**) zoomed regions (the legend is shown in (**a**)).

It is obvious that, in the mean value, the schemes **EM**, **M**, and **FRKI** display an instability, which is seen in the deviation from the ODE solution (Figure 10). The best performing schemes are **Stochastic Heun** (**H**) and **Efficient Runge–Kutta** (**ERK**). The locations of the maxima and minima of the mean value of the function X are, however, predicted correctly by all of the schemes, even if their values are not.

In terms of stability in the weak sense (convergence of random trajectories), in the absence of an analytical solution, one can observe, in Figure 11, a similar result as before. The two best performing (**H** and **ERK**) schemes maintain a stable trendline, while the other three schemes display the same instability towards the final timestep. The amplitude displayed by the "unstable" schemes has a more rapid growth than the **H** and **ERK** schemes. The roots of X and the locations of the maxima and minima are also different between the two categories of schemes: stable and unstable.

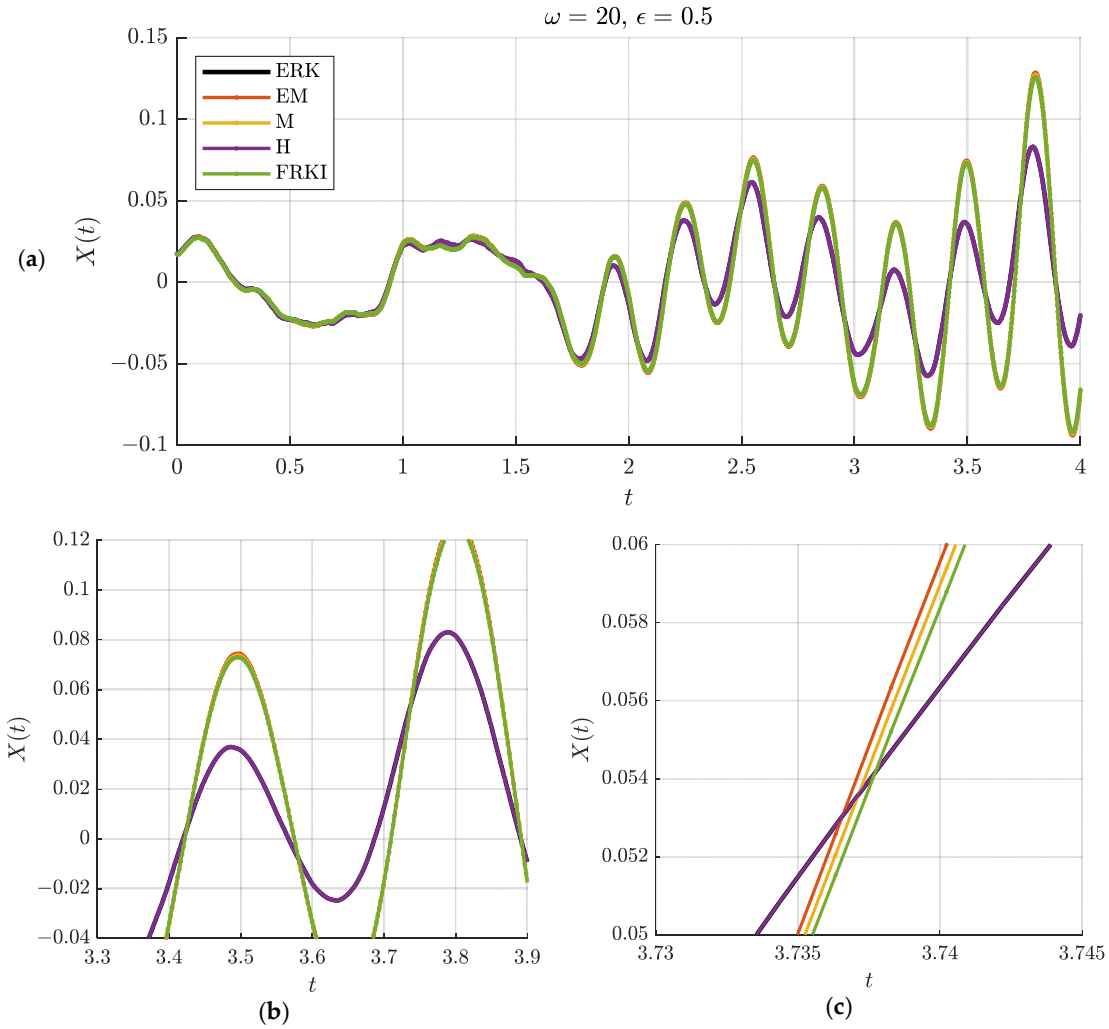

Figure 11. (**a**) Comparison between the schemes for a random path, (**b**,**c**) zoomed regions (the legend is shown in (**a**)).

4.2. The Dimensionless SDE of the Pitch Angle of the Satellite

The stability condition for the SDE without the white noise (deterministic stability) is determined by calculating the eigenvalues of the Jacobian matrix of the ODE around the critical points (the roots of the linearized system $\dot{\mathbf{X}} = \mathrm{JX}$). These points are as follows:

$$\left(\mathrm{X},\dot{\mathrm{X}}\right) = \left\{(\mathrm{k}\pi, 0) \cup \left(\pm\arccos\frac{1}{2\mathrm{A}_0} + 2\mathrm{k}\pi, 0\right)\right\}, \mathrm{k} \in \mathrm{Z}. \tag{37}$$

Out of these roots, the origin (0,0) is the most relevant in this case. To find the eigenvalues, we solve

$$\det(\mathbf{J} - \lambda \mathrm{I}_3) = 0, \tag{38}$$

in which the Jacobian matrix is evaluated at the origin:

$$\mathbf{J} = \begin{pmatrix} 0 & 1 \\ -\cos(\mathrm{X}_1) + 2\mathrm{A}_0\cos(2\mathrm{X}_1) & -\mathrm{b} \end{pmatrix}\Bigg|_{(\mathrm{X}_1,\mathrm{X}_2)=(0,0)} = \begin{pmatrix} 0 & 1 \\ 2\mathrm{A}_0 - 1 & -\mathrm{b} \end{pmatrix}. \tag{39}$$

The characteristic equation is given by the following:

$$\lambda^2 + \lambda b - (2A_0 - 1) = 0, \tag{40}$$

and the corresponding roots are as follows:

$$\lambda_{1,2} = \frac{-b \pm \sqrt{b^2 + 4(2A_0 - 1)}}{2}. \tag{41}$$

According to the Stability Criteria for Linearization of 2D Systems stability criterion [29], the critical point of an ODE is an attractor if and only if the eigenvalues of the linearised matrix **J** have negative real parts. As b is a real positive number, this leads to negative real eigenvalues with the following condition:

$$A_0 < \frac{1}{2}, \ \forall b \in \mathbb{R}_+, \tag{42}$$

and to complex eigenvalues with negative real parts:

$$A_0 < \frac{4 - b^2}{8}. \tag{43}$$

The stochastic stability of SDEs was previously studied, theorised, and formulated in various publications [30,31], and the stochastic stability of the pitch angle equation of motion was studied by Sagirow [1], and the relationship between the constants of the SDE which dictates the stability of the equation is the following:

$$A_0 \leq \frac{1}{2}\left(1 - \frac{c^2}{2b - c^2 b^2}\right). \tag{44}$$

We remark that, for c = 0, we re-obtain the same condition as discussed previously for the deterministic case.

4.2.1. Case 1

The proposed initial conditions are as follows:

$$X_0 = \dot{X}_0 = \pi/180, \tag{45}$$

which are very close from the stability point (0.0). Taking into consideration the previous conditions for stability, the constants considered for this SDE are as follows:

$$A_0 = 0.25, b = 2, c = 0.8. \tag{46}$$

The graphical results of this SDE are shown in the following figures.

In Figure 12, we represent the phase plane and the evolution in the dimensionless time of the 5000 trajectories. As was previously demonstrated, the pitch angle motion stabilises (or is asymptotically stable [26]) at the origin (0,0) after a short interval of time for all paths. A comparison between the results obtained with the schemes can be seen below in Figure 13.

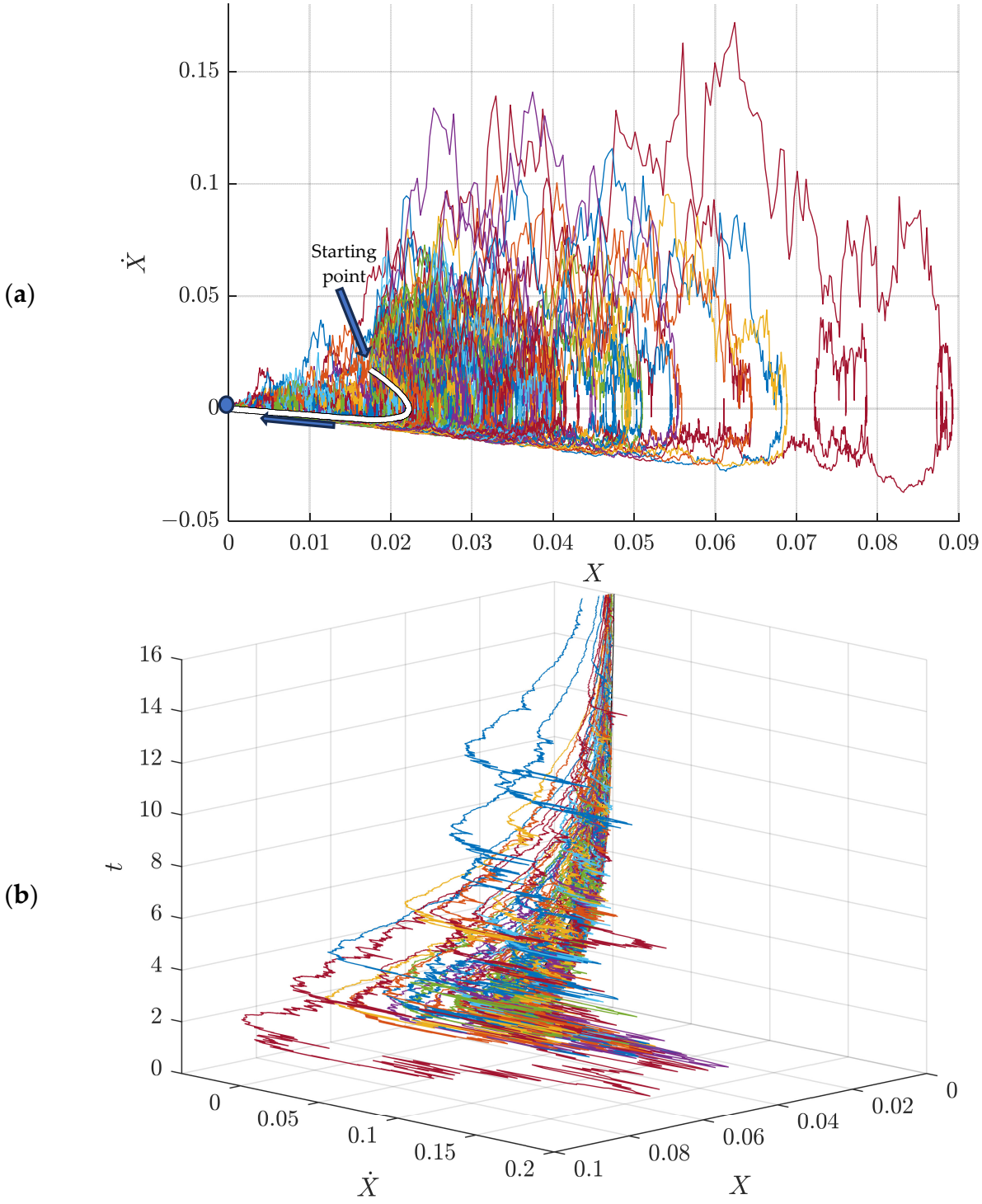

Figure 12. Results of the SDE for the 5000 trajectories (the coloured lines) and the mean value (white) obtained using the **ERK Scheme** for (**a**) the phase plane and (**b**) its evolution in dimensionless time.

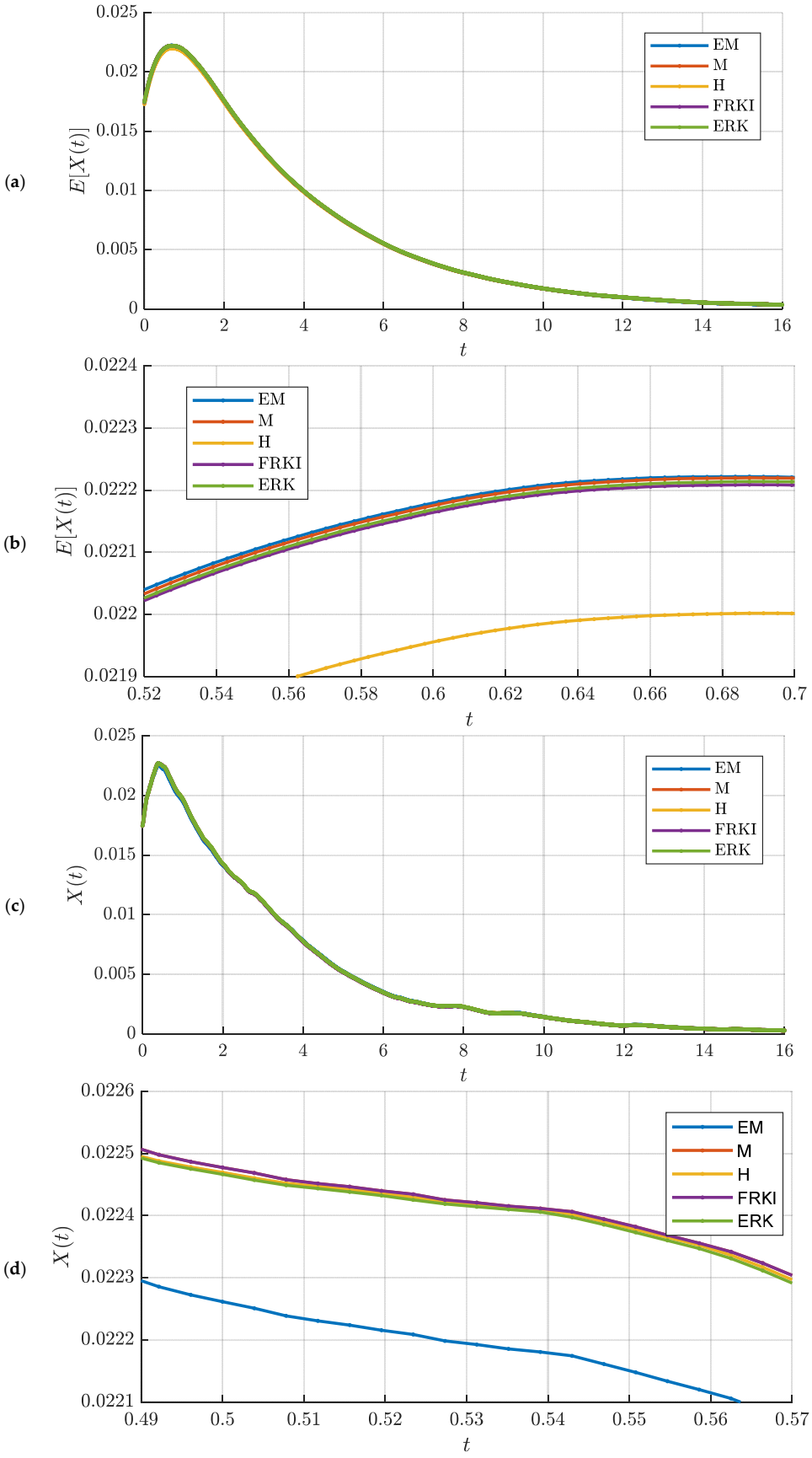

Figure 13. Comparison between the five schemes for (**a**) the evolution of mean value in time (**b**) zoomed region and (**c**) a random path of the pitch angle (**d**) zoomed region.

4.2.2. Case 2

In order to test the other stability points, we can consider the next initial values:

$$X_0 = \pi/2, \dot{X}_0 = -1/2, \tag{47}$$

for which the results can be seen below.

One can notice that, in Figure 14, although most of the trajectories stabilise at the origin, which is the globally equilibrium point, some of these 5000 cases stabilise at $X = 2\pi$. We are referring to the white noise that has a decisive effect on the stability of the dynamical system.

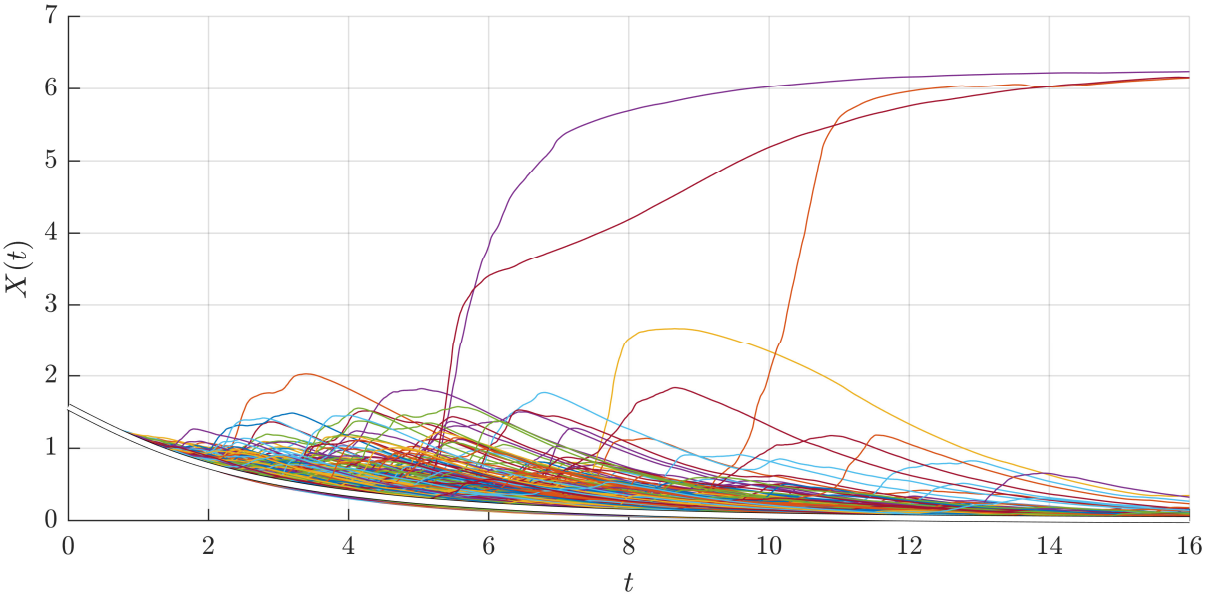

Figure 14. Stability analysis displaying two different stabilisation tendencies for the 5000 trajectories (the coloured lines) and the mean value (white).

4.2.3. Case 3

Let us consider another set of initial values:

$$X_0 = \pi/2, \dot{X}_0 = 1/2, \tag{48}$$

for which we obtain the results in Figure 15.

Although the noiseless differential equation will stabilise at the origin, there are certain paths for which stabilisation occurs at different points (for X = 2kπ), highlighting the uncertainty associated with SDEs and the importance of stability conditions.

It is obvious that, for the deterministic case (c = 0), for any initial condition, the trajectory evolution of the system will be stabilised on the closest point of equilibrium, which takes the form of (2kπ,0). One must remark that, although the initials are the same for all of the 5000 paths, there are three distinct points at which groups of these paths are asymptotically stable: (0,0), (2π,0), and (4π,0). In other words, if the system is asymptotically stable, in the present example, stability is achieved on any of the paths, but one cannot anticipate precisely on which of the equilibrium points each path will stabilise, nor can one tell the number of paths which will stabilise at a certain point.

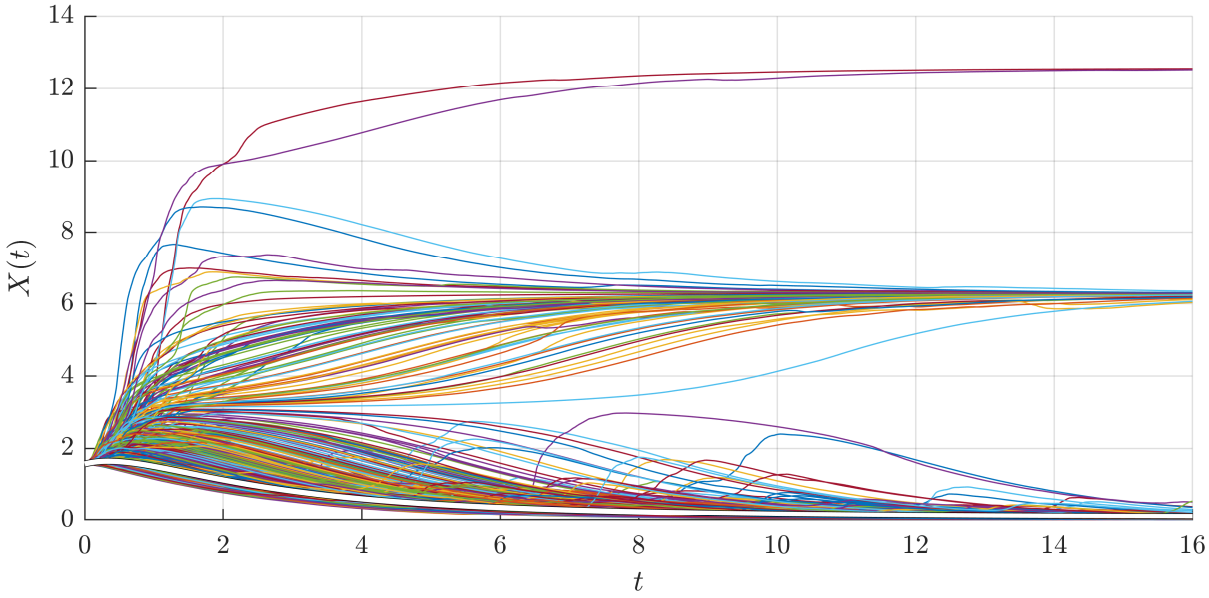

Figure 15. Stability analysis displaying two different stabilisation tendencies for the 5000 trajectories (the coloured lines) and the mean value (white).

4.2.4. Case 4

Let us consider another set of initial values:

$$X_0 = 20, \dot{X}_0 = 20. \tag{49}$$

This last case was considered to show that, depending on the initial conditions for the SDE system, the number of equilibrium points are increased as long as the point $(X_0, \dot{X}_0)$ is farther from the origin of the phase plane. Each of the trajectories is asymptotically stable (as time goes to infinity), as we can see in Figure 16, to numerous equilibrium points, which are multiples of 2π. The number of equilibrium points remains, for the moment, unclear, as we did not find any correlation between the position of the starting point and the points of the type ($2k\pi$,0). In this case, $k \leq 41$.

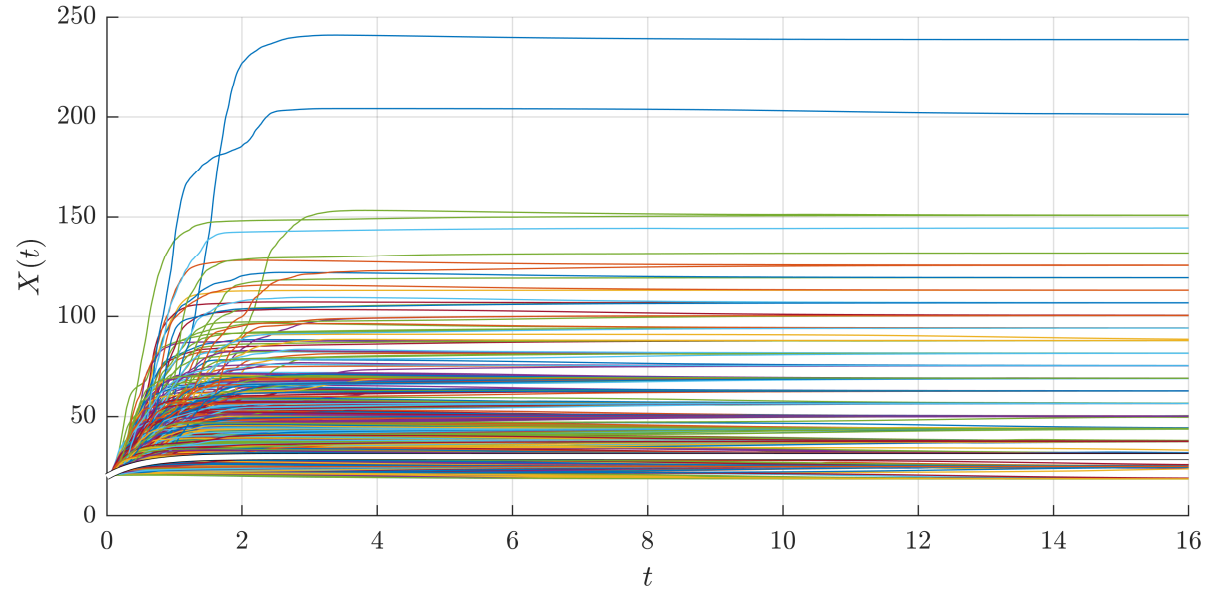

Figure 16. Stability analysis displaying many different stabilisation tendencies for the 5000 trajectories (the coloured lines) and the mean value (white).

The stabilisation of the stochastic paths in the numerous equilibrium points resembles the first level in a fractal tree. Considering the possibility of another external disturbance occurring on the satellite (such as a collision with a small object) having an effect on the system much like the initial values of the stochastic pitch angle, each of the previous equilibrium points of the system would generate another set of stabilisation points after the disturbance, thus creating another layer in this fractal tree.

5. Conclusions

This work aimed to analyse the stability of a satellite's orbit around the Earth in the case of a stochastic atmosphere density. Starting from the equations of motion (the equations of the angular momentum of a rigid) and applying simplifying assumptions, a nonlinear, non-homogenous, second-order stochastic differential equation (SDE); was derived.

To support this analysis, elements of probability theory, mathematical statistics, and stochastic calculus were briefly introduced. Five finite difference schemes used in solving the second-order stochastic differential equation were analysed and tested for differences. In total, 5000 random trajectories were considered, from which a path was randomly chosen, for which the results of the schemes were superimposed to estimate their accuracy and stability. From all of the schemes, the **ERK** (i.e., **Efficient Runge–Kutta**) gives the best results. The simplified case of the satellite stochastic system was studied starting from the differential equation of the pitch angle obtained from the analysis of the stability of the orbit of a satellite, a second-order system of stochastic differential equations. The stability of the ODE (without white noise) was studied and compared to the stability of the SDE. The behaviour of the stochastic dynamic system was analysed, and stabilisation was confirmed by the results.

The pitch angle stability SDE system is similar to the system one obtained in the case of an undamped forced oscillator with external stochastic disturbance. The analytical solution for the deterministic differential equation (in the absence of white noise) was compared to the average of the 5000 random trajectories. The conclusion reached from this comparison confirmed the convergence in the mean to the solution of the deterministic equation and the zero-mean property of the Wiener process, regardless of ε (the coefficient by which the stochastic noise is multiplied). However, if, in the case of the ideal oscillator with forced movements without a stochastic component, the oscillator is stable for any proper pulsation different from that of the forced movements, oscillating around the equilibrium position, in the case of stochastic (or "noisy") forced movements, the amplitude of the oscillations is amplified over time, no longer being able to reach stability.

The examples studied and the results obtained in this paper are a first step taken in a very important research direction—the study of the stability of the stochastic orbit of a satellite and, implicitly, also stochastic numerical methods, which, although being a field researched in the international literature, is still subject to scientific debate. The authors believe that there is a need for a greater deepening of theoretical knowledge in stochastic computing, and especially on stochastic systems with larger dimensions and more types of noise (i.e., vector Wiener processes). In the future, the authors intend to analyse physical phenomena that are reduced to stochastic systems with multidimensional noise, implementing other schemes with finite differences in the high-convergence-order Runge–Kutta type in solving them.

As a general conclusion, we can affirm that, if the stability condition is met, the stochastic pitch angle system will stabilise on any of the ($2k\pi$,0) points. Basically, being complete rotations, the satellite is brought to the equilibrium position (attitude).The solution paths of a stochastic differential equation (SDE) can be understood as the trajecto-

ries of a dynamical system influenced by stochastic processes. Visualising these trajectories can be achieved by plotting the numerical approximations of multiple sample paths. These visualisations offer a possibility to interpret the behaviour and the dynamics of a stochastic system.

Author Contributions: Conceptualization, A.B., S.S., D.-E.C. and C.L.; methodology, A.B., S.S. and C.L.; software, A.B. and S.S.; validation, A.B. and S.S.; formal analysis, A.B. and S.S.; investigation, A.B., S.S. and G.C.; resources, A.B.; data curation, A.B. and S.S.; writing—original draft preparation, S.S.; writing—review and editing, A.B.; visualisation, A.B.; supervision, G.C., D.-E.C. and C.L.; project administration, D.-E.C.; funding acquisition, D.-E.C. All authors have read and agreed to the published version of the manuscript.

Funding: This work was funded by The National University of Science and Technology POLITEHNICA Bucharest through the PubArt programme.

Data Availability Statement: Data are contained within the article.

Conflicts of Interest: The authors declare no conflicts of interest.

References

1. Sagirow, P. (Ed.) Stochastic Dynamical Systems. In *Stochastic Methods in the Dynamics of Satellites: Course Held at the Department for General Mechanics*; Springer: Vienna, Austria, 1970; pp. 8–47. [CrossRef]
2. Beletskii, V.V. Motion of an Artificial Satellite About Its Center of Mass. In *Mechanics of Space Flight*; Israel Program for Scientific Translation: Jerusalem, Israel, 1966.
3. Toral, R.; Colet, P. Introduction to Stochastic Processes. In *Stochastic Numerical Methods*; John Wiley & Sons, Ltd.: Hoboken, NJ, USA, 2014; pp. 167–190. [CrossRef]
4. Evans, L.C. *An Introduction to Stochastic Differential Equations*; American Mathematical Society: Providence, RI, USA, 2012; ISBN 1470410540.
5. Itô, K. Stochastic integral. *Proc. Jpn. Acad. Ser. Math. Sci.* **1944**, *20*, 519–524. [CrossRef]
6. Capasso, V.; Bakstein, D. An introduction to continuous-time stochastic processes: Theory, models, and applications to finance, biology, and medicine. In *Modeling and Simulation in Science, Engineering and Technology*; Birkhäuser: Boston, MA, USA; Basel, Switzerland; Berlin, Germany, 2005.
7. Dupačová, J.; Hurt, J.; Štěpán, J. Stochastic modeling in economics and finance. In *Applied Optimization*; No. 75; Kluwer Academic Publishers: Dordrecht, The Netherlands; Boston, MA, USA; New York, NY, USA; London, UK; Moscow, Russia, 2002.
8. Andersson, H.; Britton, T. Stochastic epidemic models and their statistical analysis. In *Lecture Notes in Statistics*; No. 151; Springer: New York, NY, USA; Berlin/Heidelberg, Germany, 2000.
9. Voinea, R.; Stroe, I.V.; Predoi, M.V. *Technical Mechanics*; Politehnica Press: Bucureşti, Romania, 2010.
10. Rao, A.V. *Dynamics of Particles and Rigid Bodies: A Systematic Approach*; Cambridge University Press: Cambridge, UK; New York, NY, USA, 2006.
11. Bogoi, A.; Dănăilă, S.; Isvoranu, D. *Ecuații Generale de Transport ale Dinamicii Fluidelor*; Monitorul Official: București, Romania, 2021.
12. Gillies, G.T. The Newtonian gravitational constant: Recent measurements and related studies. *Rep. Prog. Phys.* **1997**, *60*, 151–225. [CrossRef]
13. Li, Q.; Xue, C.; Liu, J.-P.; Wu, J.-F.; Yang, S.-Q.; Shao, C.-G.; Quan, L.-D.; Tan, W.-H.; Tu, L.-C.; Liu, Q.; et al. Measurements of the gravitational constant using two independent methods. *Nature* **2018**, *560*, 582–588. [CrossRef] [PubMed]
14. Goldstein, H. *Classical Mechanics*, 2nd ed.; Addison-Wesley Series in Physics; Addison-Wesley: Reading, MA, USA; Menlo Park, CA, USA; London, UK, 1981.
15. Schrello, D.M. Dynamic Stability of Aerodynamically Responsive Satellites. *J. Aerosp. Sci.* **1962**, *29*, 1145–1155. [CrossRef]
16. Sheporaitis, L.P. Stochastic stability of a satellite influenced by aerodynamic and gravity gradient torques. *AIAA J.* **1971**, *9*, 218–222. [CrossRef]
17. Mostaza-Prieto, D. Characterisation and Applications of Aerodynamic Torques on Satellites. Ph.D. Thesis, The University of Manchester, Manchester, UK, 2017.
18. Kutiev, I.; Tsagouri, I.; Perrone, L.; Pancheva, D.; Mukhtarov, P.; Mikhailov, A.; Lastovicka, J.; Jakowski, N.; Buresova, D.; Blanch, E.; et al. Solar activity impact on the Earth's upper atmosphere. *J. Space Weather Space Clim.* **2013**, *3*, A06. [CrossRef]
19. Kloeden, P.E.; Platen, E. *Numerical Solution of Stochastic Differential Equations*; Springer: Berlin/Heidelberg, Germany, 1992. [CrossRef]

20. Durrett, R. *Probability: Theory and Examples*, 5th ed.; Cambridge University Press: Cambridge, UK, 2019.
21. Mörters, P.; Peres, Y.; Schramm, O.; Werner, W. Brownian motion. In *Cambridge Series in Statistical and Probabilistic Mathematics*; No. 30; Cambridge University Press: Cambridge, UK, 2010.
22. Bogoi, A.; Dan, C.-I.; Strătilă, S.; Cican, G.; Crunteanu, D.-E. Assessment of Stochastic Numerical Schemes for Stochastic Differential Equations with "White Noise" Using Ito's Integral'. *Symmetry* **2023**, *15*, 2038. [CrossRef]
23. Saito, Y.; Mitsui, T. Stability Analysis of Numerical Schemes for Stochastic Differential Equations. *SIAM J. Numer. Anal.* **1996**, *33*, 2254–2267. [CrossRef]
24. Mil'shteĭn, G.N. *Numerical Integration of Stochastic Differential Equations*; Springer: Dordrecht, The Netherlands, 2011.
25. Saito, Y.; Mitsui, T. Discrete approximations for stochastic differential equations. *Trans. Jpn. SIAM* **1992**, *746*, 1–16.
26. Bogoi, A.; Cican, G.; Daniel-Eugeniu, C. *Fundamentals of Acoustics*; Lecture Notes for Engineers; Editura Monitorul Official: Bucureşti, Romania, 2024.
27. Bacalu, I.; Şerbănescu, C. *Ecuaţii Diferenţiale: Culegere de Probleme: Compendiu*; Printech: Bucureşti, Romania, 2013.
28. Boyce, W.E.; DiPrima, R.C. *Elementary Differential Equations and Boundary Value Problems*, 8th ed.; Wiley: Hoboken, NJ, USA, 2005.
29. Leipholz, H. *Stability Theory*, 2nd ed.; Vieweg+Teubner Verlag: Weisbaden, Germany, 1987.
30. Tunç, O.; Tunç, C. On the asymptotic stability of solutions of stochastic differential delay equations of second order. *J. Taibah Univ. Sci.* **2019**, *13*, 875–882. [CrossRef]
31. Zouine, A.; Imzegouan, C.; Bouzahir, H.; Tunç, C. General decay stability of nonlinear delayed hybrid stochastic system with switched noises. *Appl. Set-Valued Anal. Optim.* **2024**, *6*, 157–177. [CrossRef]

Disclaimer/Publisher's Note: The statements, opinions and data contained in all publications are solely those of the individual author(s) and contributor(s) and not of MDPI and/or the editor(s). MDPI and/or the editor(s) disclaim responsibility for any injury to people or property resulting from any ideas, methods, instructions or products referred to in the content.

symmetry

MDPI

Article

Weed Detection in Lily Fields Using YOLOv7 Optimized by Chaotic Harris Hawks Algorithm for Underground Resource Competition

Junjie Tang [1,2], Huafei Wang [3], Mingyue Zhao [4], Ping Sun [5], Yutao Hao [2] and Zhiyuan Zhu [2,*]

[1] Anhui Provincial Institute of Modern Coal Processing Technology, Anhui University of Science and Technology, Huainan 232001, China; qq1998@email.swu.edu.cn
[2] School of Electronic Information Engineering, Southwest University, Chongqing 400715, China; yutaohao22@email.swu.edu.cn
[3] Hubei Key Laboratory of Transportation Internet of Things, Wuhan University of Technology, Wuhan 430070, China; w3043066826@email.swu.edu.cn
[4] Qingdao Key Laboratory of Groundwater Resources Protection and Rehabilitation, Qingdao Geo-Engineering Surveying Institute, Qingdao 266101, China; myzhao@qddzgckc.com
[5] Key Laboratory of Geological Safety of Coastal Urban Underground Space, Ministry of Natural Resources, Qingdao 266101, China; sunping@qddzgckc.com
* Correspondence: zyuanzhu@swu.edu.cn

Abstract: Lilies, a key cash crop in Lanzhou, China, widely planted in coal-based fields, cultivated fields, and gardens, face significant yield and quality reduction due to weed infestation, which competes for essential nutrients, water, and light. To address this challenge, we propose an advanced weed detection method that combines symmetry-based convolutional neural networks with metaheuristic optimization. A dedicated weed detection dataset is constructed through extensive field investigation, data collection, and annotation. To enhance detection efficiency, we introduce an optimized YOLOv7-Tiny model, integrating dynamic pruning and knowledge distillation, which reduces computational complexity while maintaining high accuracy. Additionally, a novel Chaotic Harris Hawks Optimization (CHHO) algorithm, incorporating chaotic mapping initialization and differential evolution, is developed to fine-tune YOLOv7-Tiny parameters and activation functions. Experimental results demonstrate that the optimized YOLOv7-Tiny achieves a detection accuracy of 92.53% outperforming traditional models while maintaining efficiency. This study provides a high-performance, lightweight, and scalable solution for real-time precision weed management in lily fields, offering valuable insights for agricultural automation and smart farming applications.

Keywords: weed detection; convolutional neural network; YOLOv7; Harris hawks algorithm

1. Introduction

As a perennial herb of the *Lilium* genus, *Lilium davidii* var. unicolor, commonly known as Lanzhou lily [1], stands out in the botanical world due to its distinctive growth patterns and rich nutritional value. In addition to its high ornamental appeal, it holds significant economic importance, serving as a valuable agricultural product. However, one of the major challenges in lily cultivation is weed infestation, which competes with lilies for essential nutrients, water, and sunlight, ultimately affecting growth, reducing yield, and diminishing overall quality. Currently, weed control in lily fields primarily relies on manual labor, which is not only time-consuming and labor-intensive but also leads to increased production costs.

The inefficiency of manual weed removal underscores the urgent need for automated and intelligent solutions to improve precision and efficiency in weed management.

With the rapid advancement of artificial intelligence (AI) and deep learning technologies [2], intelligent identification and automated removal of weeds in agricultural fields have become viable solutions. By leveraging state-of-the-art object detection models, it is possible to enhance the efficiency and accuracy of weed recognition, reducing reliance on manual labor and promoting the sustainable and healthy development of the lily industry. However, the complexity of natural environments, including varying lighting conditions, occlusions, and diverse weed species, poses significant challenges for accurate and real-time weed detection. To address these issues, this study proposes a novel object detection algorithm optimized for weed identification in lily fields.

The proposed method addresses several key gaps in the field of weed detection. Unlike traditional CNN-based approaches, the lightweight YOLOv7-tiny model ensures real-time weed detection with reduced computational requirements. The integration of the Chaotic Harris Hawks Optimization (CHHO) algorithm enhances the hyperparameter tuning process, improving model performance. Furthermore, the incorporation of Tent Chaotic Initialization and Differential Evolution techniques boosts the accuracy and robustness of the model, enabling effective weed detection under diverse environmental conditions. Additionally, this study introduces a custom weed detection dataset for lily fields, distinguishing it from previous studies focused on crops like maize, soybean, or cotton, and ensuring better model performance in this specific context.

The choice of the Harris Hawks Optimization (HHO) [3] algorithm for optimizing YOLOv7-tiny in lily field weed detection is primarily based on its strong exploration–exploitation balance, convergence speed, and adaptability to complex search spaces. Unlike traditional optimization methods such as Genetic Algorithms (GAs) [4], Particle Swarm Optimization (PSO) [5], or Grey Wolf Optimizer (GWO) [6], HHO mimics the cooperative hunting strategy of Harris hawks, allowing it to dynamically switch between exploration and exploitation phases. This adaptive mechanism enhances its ability to fine-tune YOLOv7-tiny's hyperparameters, leading to improved detection accuracy and robustness in real agricultural environments. Furthermore, integrating chaotic mapping and differential evolution within HHO further improves its global search capability, preventing premature convergence and ensuring a more diverse set of optimal solutions. These enhancements are particularly beneficial in agricultural applications, where variations in lighting, occlusion, and complex backgrounds challenge detection performance. Given these advantages, HHO was selected as the optimization framework for this study to enhance YOLOv7-tiny's ability to detect weeds in lily fields more efficiently and accurately than existing approaches.

The main contributions of this work are summarized as follows:

- A specialized weed detection model for lily field images is proposed, significantly improving detection accuracy in complex field conditions, thereby advancing research in computer vision and precision agriculture.
- A lightweight YOLOv7-tiny model is developed, incorporating dynamic pruning and knowledge distillation to achieve efficient weed detection without compromising accuracy.
- An enhanced Harris Hawks Optimization (HHO) algorithm is introduced, integrating Tent Chaos and Differential Evolution mechanisms to fine-tune the parameters of the YOLOv7-tiny model, further boosting its performance.
- A dedicated dataset for lily field weed detection is constructed for the first time, providing a valuable benchmark for future research. Experimental results demonstrate the superior performance of the YOLOv7-tiny model on this dataset.

The remainder of this paper is structured as follows:

Section 2 provides an overview of related work, describing previous research on weed detection and deep learning-based approaches in agriculture. It also covers the materials and methods used in this study, including the construction of the lily field dataset, the fundamentals of the Harris Hawks Optimization algorithm, and the YOLOv7 framework. Section 3 describes the materials and methods, including the construction of the lily field dataset, the fundamentals of the Harris Hawks Optimization algorithm, and the YOLOv7 framework. Section 4 introduces the proposed approach, detailing the Chaotic Harris Hawks Optimization algorithm and the modifications made to the YOLOv7 model. Section 5 presents the experimental setup, evaluation metrics, and comparative analysis of different models. Finally, Section 6 discusses the main findings of this study, and Section 7 concludes the study with future research directions.

2. Related Works

In recent years, researchers have made stage-by-stage progress in adopting the use of deep learning to identify weeds for classification. For example, R. Punithavathi [7] proposed a weed classification model based on the combination of multi-scale Faster-RCNN-based and optimal limit learning machine (ELM)-based target detection, which resulted in a weed identification accuracy of 98.33%. Jiang et al. [8]designed a CNN-based graph neural network, which achieved 97.8%, 99.37%, and 98.93% accuracies on corn weed dataset, lettuce weed dataset, and radish weed dataset, respectively, which were higher than the values from a traditional CNN model, introducing a new breakthrough in the weed recognition field. Peng Mingxia [9] used a residual convolutional network to extract features and introduced the feature pyramid into the neural network to identify weeds in the cotton field; recognition rate reached 95.5%. Andrea et al. [10] studied the classification of maize and weeds by optimizing the CNN network, and the highest accuracy rate reached 97.26%, which provided strong technical support for the management of weeds in the maize field. Hu et al. [11] used the graph convolutional network structure based on convolutional features with Euclidean distance to construct the graph convolutional network and used semi-supervised learning to train the model and predict the target. On the other hand, they used a Graph Neural Network (GNN) to carry out a recognition study of eight weeds such as horse primrose tansy, silver gum daisy, and thorny acacia, with an accuracy of 98.1%, which shows the potential of GNNs in the field of weed recognition. Ahmad et al. [12] used VGG16 to carry out a recognition study of four weeds in maize and soybean fields with an accuracy of 98.90%, which further verified the applicability of VGG16 in weed recognition.

Moreover, significant progress has been made in optimizing deep learning models using metaheuristic methods. In natural orchard scenarios, complex environmental factors such as lighting and shadows increase the difficulty of accurately recognizing and locating apple fruits. To address this challenge, researchers proposed a heterogeneous image fusion model based on the Pulse Coupled Neural Network (PCNN) [13]. Notably, the PCNN model parameters were optimized using the Human Mental Search (HMS) [14] algorithm. Ahmet Karaman et al. [15] introduced a novel deep learning approach that differs from traditional systems. This method is fundamentally built on the YOLOv5 object detection algorithm integrated with the Artificial Bee Colony (ABC) optimization algorithm. The YOLOv5 model was employed for polyp detection, while the ABC algorithm was utilized to enhance the model's performance by identifying the optimal activation functions and hyperparameters—a concept that inspired this study. Similarly, Ishak Pacal et al. [16] replaced the entire structure with a Cross-Stage Partial Network (CSPNet), substituted the Leaky ReLU activation function with the Mish activation function, and replaced the Distance-IoU (DIoU) loss with the Complete-IoU (CIoU) loss. Furthermore, their work simultaneously optimized multiple hyperparameters to improve the model's

overall performance. To provide a clear and visual presentation of the gaps observed in the related works, we detail these differences in Table 1, where we list the contributions of previous studies alongside the identified gaps and how our method addresses them.

Table 1. Comparison of Methods and Observed Gaps in Weed Detection.

Reference	Method Used	Dataset	Performance Metrics	Gaps Observed
R. Punithavathi [7]	High computational complexity, not suitable for real-time detection	Weed dataset	Accuracy: 98.33%	High computational complexity, not suitable for real-time detection
Jiang et al. [8]	CNN-based Graph Neural Network	Corn, lettuce, radish weed datasets	Accuracy: 97.8%–99.37%	Model size and computational overhead not optimized
Peng Mingxia [9]	Residual CNN + Feature Pyramid	Cotton field dataset	Accuracy: 95.5%	Limited generalization across different weed species
Andrea et al. [10]	Optimized CNN for maize and weed classification	Maize dataset	Accuracy: 97.26%	No metaheuristic optimization applied
Hu et al. [11]	Graph Convolutional Network (GNN)	Weed dataset (8 species)	Accuracy: 98.1%	High computational cost, limited to specific weed types
Ahmad et al. [12]	VGG16-based classification	Maize/soybean dataset	Accuracy: 98.90%	No real-time capability, high inference time
Ahmet Karaman et al. [13]	YOLOv5 + Artificial Bee Colony (ABC) optimization	Medical polyp detection dataset	Improved performance with ABC tuning	No lightweight adaptation, high parameter count
Ishak Pacal et al. [14]	CSPNet-based YOLO optimization	General object detection dataset	Improved feature extraction with CSPNet	Lacks dataset-specific fine-tuning

3. Materials and Methods

3.1. Materials

The dataset used in this study was collected from the Yuzhong Experimental Base of the Institute of Plant Protection, Gansu Academy of Agricultural Sciences. Based on observations and statistics from the experimental base, the most detrimental field weeds to lilies during the early, middle, and late growth stages predominantly belong to the Amaranthaceae, Asteraceae, and Convolvulaceae families. Specifically, the Amaranthaceae family includes weeds such as Amaranthus retroflexus, Salsola collina, Amaranthus blitum, and Chenopodium hybridum; the Asteraceae family is represented by Lactuca indica; and the Convolvulaceae family includes Convolvulus arvensis. Images of the collected weeds are shown in Figure 1.

The dataset used in this study comprises images of lily plants and six types of weed plants. Specifically, the dataset includes 2233 images of lily plants, 427 images of Amaranthus retroflexus, 403 images of Salsola collina, 433 images of Amaranthus blitum, 660 images of Chenopodium hybridum, 1070 images of Lactuca indica, and 440 images of Convolvulus arvensis, resulting in a total of 5666 images. The dataset was divided into training, validation, and testing sets in a ratio of 8:1:1. Detailed information on the species is provided in Table 1.

Figure 1. Sample of lily-weed Image. (**a**) Lily. (**b**) Aotou amaranth. (**c**) *Teloxys aristata*. (**d**) *Amaranthus revolexus*. (**e**) *Dysphania schraderiana*. (**f**) *Lactuca indica*. (**g**) *Convolvulus arvensis*.

Based on the performance metrics in Table 2 and considering the number of images for each class in the dataset, it was observed that classes with larger quantities of images, such as lilies and Lactuca indica, demonstrated better recognition performance. In contrast, classes with fewer images exhibited poorer or more fluctuating evaluation metrics. To address the issue of insufficient images, a commonly used data augmentation strategy in the field of deep learning was employed. This strategy involved increasing the number of training images by applying data augmentation techniques, including horizontal flipping, rotation, and color jittering. Specifically, images were flipped horizontally, rotated by 20°, and adjusted in brightness and contrast. The brightness factor was randomly sampled from the range of [1.0, 2.0], while contrast adjustments varied within [1.0, 3.0], ensuring diverse

lighting conditions in the augmented dataset. The updated quantities of images for each class in the lily-weed dataset after data augmentation are shown in Table 3.

Table 2. Details of Lily-Weed Dataset.

Type	Original Quantity	Training Set	Validation Set	Testing Set
Lily	2233	1786	223	224
Aotou Amaranth	427	342	43	42
Teloxys aristata	403	322	41	40
Amaranthus retroflexus	433	346	43	44
Dysphania schraderiana	660	528	66	66
Lactuca indica	1070	856	107	107
Convolvulus arvensis	440	352	44	44
Total	**5666**	**4532**	**567**	**567**

Table 3. Updated Dataset Distribution.

Type	Current Quantity	Training Set	Validation Set	Testing Set
Lily	2233	1786	223	224
Aotou Amaranth	1281	1025	128	128
Teloxys aristata	1209	967	121	121
Amaranthus retroflexus	1299	1039	130	130
Dysphania schraderiana	1320	1056	132	132
Lactuca indica	1070	856	107	107
Convolvulus arvensis	1320	1056	132	132
Total	**9732**	**7785**	**973**	**974**

3.2. Harris Hawks Optimizer

The Harris Hawks Optimizer (HHO) [3] is a novel nature-inspired optimization algorithm proposed by Heidari et al. in 2019. This algorithm is inspired by the cooperative hunting strategies of Harris hawks (*Parabuteo unicinctus*), modeling their dynamic behaviors in the wild to hunt prey collaboratively. Harris hawks are renowned for their highly cooperative and adaptive hunting strategies, making them an excellent source of inspiration for addressing optimization problems.

As a metaheuristic algorithm, HHO has gained widespread application due to its simplicity, minimal parameter requirements, and ease of implementation. It has been successfully utilized in various fields, including function optimization, engineering design, image processing, and solving other complex problems. HHO is particularly noted for its efficiency and robustness, demonstrating exceptional performance in tackling multidimensional complex optimization problems.

HHO achieves global optimization by modeling the dynamic interactions between prey (the target in the solution space) and predators (candidate solutions). The algorithm integrates exploration and exploitation phases, which dynamically switch based on the fitness of current individuals and stochastic factors. This dynamic adjustment ensures a balance between global search (exploration) and local search (exploitation).

3.2.1. Exploration Phase

In HHO, a random value q within the range of $(0, 1)$ determines the behavior of individuals. When $q < 0.5$, individuals move based on the positions of other hawks; when $q \geq 0.5$, individuals randomly perch within the active range of the population.

During the exploration phase, Harris hawks simulate searching for prey across the environment. The mathematical model of this behavior is given by Equation (1).

$$X(t+1) = \begin{cases} (X_{\text{rabbit}}(t) - X_m(t)) - r_3 \cdot (LB + r_4 \cdot (UB - LB)), & \text{if } q < 0.5 \\ X_{\text{rand}}(t) - r_1 \cdot |X_{\text{rand}}(t) - 2r_2 \cdot X(t)|, & \text{if } q \geq 0.5 \end{cases} \tag{1}$$

$$X_m(t) = \frac{1}{N} \sum_{i=1}^{N} X_i(t) \tag{2}$$

where $X(t+1)$ represents the position of the individual after the $t+1$th iteration; $X(t)$ represents the position of the individual after the tth iteration; $X_{\text{rabbit}}(t)$ is the position of the rabbit, which is the optimal position in the population; $X_{\text{rand}}(t)$ is an individual randomly selected from the current population; $X_m(t)$ is the average value of population position; r_1, r_2, r_3, r_4 are random numbers in the range of $(0, 1)$; LB and UB are the lower and upper bounds of the population range, respectively; N represents the size of the population.

3.2.2. Transition from Exploration to Exploitation

In the Harris Hawks Optimizer (HHO), Escape energy (E)—see Equation (3)—is a dynamic parameter that simulates prey escape ability and guides the algorithm's search behavior at different stages. When the escape energy gradually changes through a mechanism greater than or equal to 1, the exploration phase is executed; otherwise, the development phase is executed. Dynamic switch an be performed between global search and local development to enhance the optimization performance of the algorithm.

$$E = 2E_0 \left(1 - \frac{t}{T}\right) \tag{3}$$

where E_0 represents a random number in the range of $[-1, 1]$ and T is the maximum number of iterations.

3.2.3. Exploitation Phase

During the development phase, the process of Harris hawks surrounding prey and hunting together is simulated. The development phase simulates the behavior of Harris hawks in capturing prey, utilizing the gradually depleted energy of the prey and adopting different strategies to approach the target individual. The process is based on the escape energy E value of the target individual, which determines whether to conduct contraction encirclement or capture prey. The escape energy E of the target individual is a dynamically changing parameter used to characterize their escape ability. Based on the energy level of the target individual, HHO mainly adopts two strategies during the development phase.

Soft besiege

When $r \geq 0.5$ and $|E| \geq 0.5$, the target individual still has a certain escape ability, and the population gradually shrinks and surrounds the prey to reduce its escape space. We update the formulas to Equations (4) and (5).

$$X(t+1) = \Delta X(t) - E|J(X_{\text{rabbit}}(t) - X(t))| \tag{4}$$

$$\Delta X(t) = X_{\text{rabbit}}(t) - X(t) \tag{5}$$

Here, $\Delta X(t)$ represents the distance between target individuals during the iteration process; J is the jump step size of the target individual, which is a random value with a range of $(0, 2)$.

Hard besiege

When $r \geq 0.5$ and $|E| < 0.5$, the escape ability of the target individual is weak, and the population quickly approaches the position of the target individual. We update the formula to Equation (6).

$$X(t+1) = X_{\text{rabbit}}(t) - E|\Delta X(t)| \tag{6}$$

Soft besiege with progressive rapid dives

During the development phase, HHO ensures the balance of search capabilities by combining the dynamic changes in the energy of target individuals, the updating of population positions, and random perturbations. In the later stage of the search (when the energy of the target individual is low), we focus on local fine search; in the early stage of search (when the energy of the target individual is high), we enhance global exploration ability to avoid falling into local optima.

When $r < 0.5$ and $|E| \geq 0.5$, the target individual has strong escape ability, and the population approaches the target individual's position using a soft surround mechanism. We update the formulas to Equations (7) and (8).

$$Y = X_{\text{rabbit}}(t) - E|JX_{\text{rabbit}}(t) - X(t)| \tag{7}$$

$$Z = Y + S^* \,\text{LF}(D) \tag{8}$$

$$\text{LF}(x) = 0.01 \times \frac{u \times \sigma}{|v|^{1/\beta}}, \sigma = \left(\frac{\Gamma(1+\beta)\sin\left(\frac{\pi\beta}{2}\right)}{\Gamma\left(\frac{1+\beta}{2}\right)\beta 2^{\frac{\beta-1}{2}}} \right)^{1/\beta} \tag{9}$$

$$X(t+1) = \begin{cases} Y & \text{if } F(Y) < F(X(t)) \\ Z & \text{if } F(Z) < F(X(t)) \end{cases} \tag{10}$$

Among them, D represents the dimension of the problem, S is a D-dimensional random vector, and $LF(x)$ in Equation (9) is the Levy flight formula. u, v are random numbers in the range of $(0, 1)$, and β is often set to 1.5.

Hard besiege with progressive rapid dives

When $r < 0.5$ and $|E| < 0.5$, the target individual has a lower ability to escape and there is a probability of escape. Therefore, a progressive soft surround strategy is adopted to shorten the gap with the target.

$$X(t+1) = \begin{cases} Y & \text{if } F(Y) < F(X(t)) \\ Z & \text{if } F(Z) < F(X(t)) \end{cases} \tag{11}$$

We update the formulas to Equations (12) and (13), $X_m(t)$ is the average value of population position as shown in Equation (2).

$$Y = X_{\text{rabbit}}(t) - E \cdot |J \cdot X_{\text{rabbit}}(t) - X_m(t)| \tag{12}$$

$$Z = Y + S^* \cdot LF(D) \tag{13}$$

In summary, the HHO pseudocode is shown in Algorithm 1.

Algorithm 1: Pseudo-code of HHO algorithm [3]

Input: Population size N and maximum number of iterations T

Output: The location of rabbit and its fitness value

Initialize the random population X_i $(i = 1, 2, \ldots, N)$ **while** *stopping condition is not met* **do**
  Calculate the fitness values of hawks;
  Set X_{rabbit} as the location of rabbit (best location);
  for *each hawk* X_i **do**
    Update the initial energy E_0 and jump strength J;
    $E_0 = 2 \cdot \text{rand}() - 1$;
    $J = 2 \cdot (1 - \text{rand}())$;
    Update the E using Equation (3);
    if $|E| \geq 1$ **then**
      Exploration phase;
      Update the location vector using Equation (1);
    if $|E| < 1$ **then**
      Exploitation phase;
      if $r \geq 0.5$ *and* $|E| \geq 0.5$ **then**
        Soft besiege;
        Update the location vector using Equation (4);
      else if $r \geq 0.5$ *and* $|E| < 0.5$ **then**
        Hard besiege;
        Update the location vector using Equation (6);
      else if $r < 0.5$ *and* $|E| \geq 0.5$ **then**
        Soft besiege with progressive rapid dives;
        Update the location vector using Equation (10);
      else if $r < 0.5$ *and* $|E| < 0.5$ **then**
        Hard besiege with progressive rapid dives;
        Update the location vector using Equation (11);
Return X_{rabbit}

3.3. YOLOv7

The YOLOv7 network [17] is an evolution of YOLOv5 [18], inheriting many hyperparameters from its predecessor. To enhance network performance, this study introduces improvements to the YOLOv7 algorithm in three aspects: loss function, Backbone feature extraction network, and attention mechanism. The architecture of the improved YOLOv7 algorithm is illustrated in Figure 2. The model consists of four layers, with input dimensions of 640 × 640 × 3, representing an image with a resolution of 640 pixels and three channels. The Backbone module serves as the core of the network, where each CBS block comprises a standard convolutional layer, a batch normalization (BN) layer, and an activation function layer using the SiLU function.

YOLOv7 is the foundational model in the YOLO series and demonstrates superior speed and accuracy compared to most known object detectors within the range of 5–160 frames per second. Among real-time object detectors achieving over 30 frames per second on the V100 GPU, YOLOv7 achieves the highest accuracy. The YOLOv7 series includes three primary models: YOLOv7-tiny [19], YOLOv7, and YOLOv7-W6 [20]. Com-

pared to other networks in the YOLO series, YOLOv7 adopts a detection strategy similar to YOLOv4 [21] and YOLOv5, with its network architecture depicted in Figure 2.

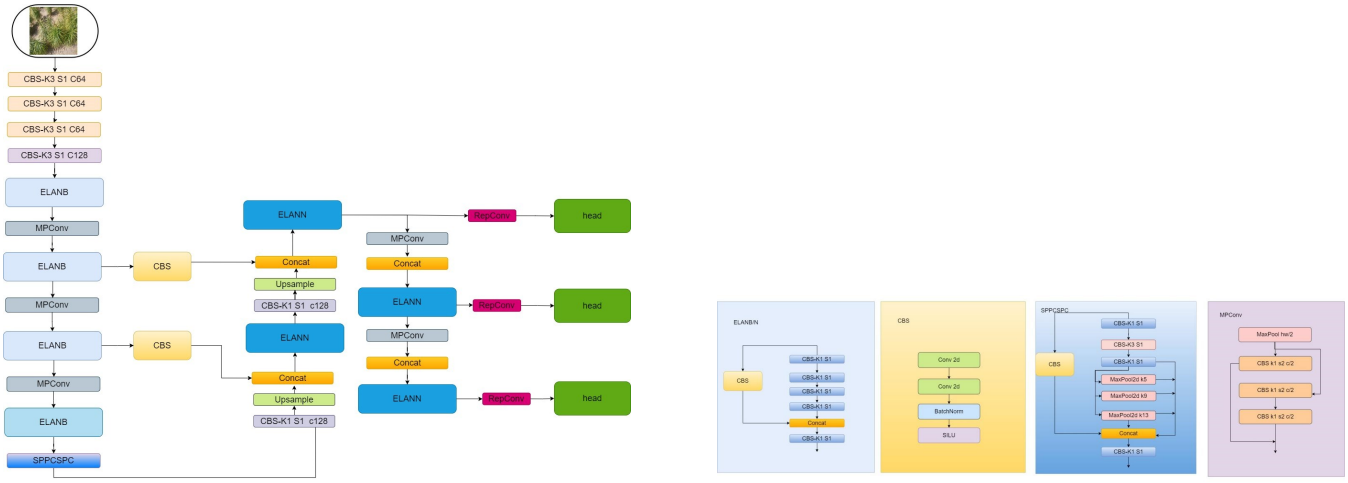

Figure 2. YOLOv7 Network model structure diagram: (**a**) YOLOv7 Network Architecture Backbone Network. (**b**) The specific structure of each network module in YOLOv7.

The YOLOv7 network model primarily consists of four components: Input, Backbone, Neck, and Head. First, the input images undergo preprocessing steps such as data augmentation in the Input module before being passed to the Backbone. The Backbone is responsible for extracting features from the preprocessed images. Subsequently, the extracted features are processed by the Neck module, which performs feature fusion to generate feature maps of three scales: large, medium, and small. Finally, the fused features are passed to the Head module, where detection results are produced.

The Backbone of the YOLOv7 model is composed of convolutional layers, the E-ELAN (Extended-ELAN) module, the MPConv module, and the SPPCSPC module. The E-ELAN module builds upon the original ELAN by modifying the computational blocks while retaining its transition layer structure. It enhances the network's learning capability through expand, shuffle, and merge cardinality operations without disrupting the original gradient pathways. The SPPCSPC module introduces parallel MaxPooling operations within a series of convolutions, addressing issues such as image distortion caused by processing operations and the challenge of extracting redundant features in convolutional neural networks.

In the MPConv module, the MaxPooling operation expands the receptive field of the current feature layer and fuses this information with the features processed by standard convolution, improving the network's generalization ability.

In summary, the YOLOv7 network model optimizes the structure and functionality of its components, achieving improved object detection performance while maintaining real-time processing capabilities. This makes YOLOv7 a robust performer across various practical application scenarios.

To address the challenges of complex field environments and low weed recognition rates, a weed detection method based on YOLOv7 is proposed for the identification of weeds in Lanzhou lily fields. This approach first applies dynamic pruning and knowledge distillation techniques to detect lily and weed images in complex environments. Experimental results demonstrate that compared to the YOLOv7 model, the proposed method significantly improves the classification accuracy of lilies and weeds.

4. Proposed Method

4.1. Chaotic-Based Harris Hawks Algorithm

4.1.1. Tent Chaotic System

In modern optimization algorithms, population initialization is one of the key steps influencing algorithm performance. A well-designed population initialization can enhance the diversity of solutions, improve the global search capability of the algorithm, and consequently elevate the quality of optimization results. To this end, chaos theory has gradually been incorporated into optimization algorithms to generate initial populations with favorable distribution characteristics. Chaotic systems [22], due to their randomness and ergodicity under deterministic conditions, have become an important tool in the design of optimization algorithms. Among them, the Tent map is a classical and simple chaotic map that demonstrates superior performance during population initialization.

The Tent map generates chaotic sequences through a simple recursive formula, and its mathematical expression is shown in (13):

$$x_{n+1} = \begin{cases} \mu x_n, & \text{if } x_n < 0.5, \\ \mu(1 - x_n), & \text{if } x_n \geq 0.5. \end{cases} \tag{14}$$

Here, $x_n \in (0, 1)$ is the state variable, and μ is the control parameter, usually taken as 2. In the case of $\mu = 2$, Tent mapping can generate a chaotic sequence that traverses the entire interval $(0, 1)$, providing a uniformly distributed initial solution for optimization algorithms.

Compared to traditional random initialization methods, the initialization approach based on Tent chaotic mapping can more effectively avoid the issue of concentrated distribution in the solution space, thereby improving the global search capability of the algorithm. This is particularly beneficial for complex optimization problems such as multi-modal function optimization and nonlinear constrained optimization, where the incorporation of Tent mapping significantly enhances the algorithm's performance.

This study explores the application principles of Tent chaotic mapping in population initialization and analyze its performance and advantages across various optimization algorithms.

In the Tent chaotic mapping process, the population is generated within a D-dimensional space as a chaotic sequence $s_i = \{s_{i,d} \mid d = 1, 2, \ldots, D\}$, where $i = 1, 2, \ldots, N$. This enables comprehensive coverage of the search space and enhances global search capabilities.

The initial values of the generated chaotic sequence are then mapped to the search space, resulting in a population matrix $X = \{X_i \mid i = 1, 2, \ldots, N\}$, where everyone is represented as $X_i = \{X_{i,d} \mid d = 1, 2, \ldots, D\}$. The mapping relationship is mathematically expressed as follows:

$$x_{i,d} = lbd + s_{i,d} \cdot (ubd - lbd) \tag{15}$$

Here, lbd and ubd denote the lower and upper bounds of the search space in the dth dimension, respectively, and $s_{i,d}$ represents the value of the chaotic sequence in the dth dimension.

This mapping transforms the nonlinear properties of the chaotic sequence into the spatial distribution of population individuals within the search space. As a result, the initial solutions gain diversity, significantly enhancing the algorithm's global search capabilities and laying a solid foundation for subsequent optimization processes.

4.1.2. Differential Evolution

Differential Evolution (DE) [23] is a population-based global optimization algorithm proposed by Storn and Price in 1995. As a classical evolutionary algorithm, DE has been

widely applied in optimization fields due to its simplicity, robustness, and efficiency. By simulating the "mutation, crossover, and selection" mechanisms found in biological evolution, DE progressively converges towards the optimal solution, making it particularly suitable for solving complex nonlinear, high-dimensional, and non-convex optimization problems.

The core concept of DE is to guide the search direction using the differential information between individuals in the population. The algorithm consists of four stages: initialization, mutation, crossover, and selection. In the mutation phase, DE introduces random differences between population individuals to generate new candidate solutions, enhancing diversity and the ability to explore the solution space. In the crossover phase, DE combines the mutated solutions with the current solutions to improve the algorithm's local exploitation ability. Finally, in the selection phase, individuals with higher fitness are retained to accelerate the convergence process. This unique mechanism enables DE to strike a balance between maintaining population diversity and accelerating convergence speed.

Compared to other optimization algorithms, DE has several notable advantages: its simple structure, ease of implementation, few parameters, and low dependency on parameter settings. Moreover, DE has demonstrated strong adaptability and competitiveness in high-dimensional problems, constrained optimization, and multi-objective optimization problems. As a result, it is widely applied in engineering optimization, machine learning, image processing, neural network training, and other scientific and engineering problems.

$$v = x_{\mathrm{r1}} + F \cdot (x_{\mathrm{r2}} - x_{\mathrm{r3}}) \tag{16}$$

$$v = x^* + F \cdot (x_{\mathrm{r2}} - x_{\mathrm{r3}}) \tag{17}$$

$$v = x_i + F \cdot (x^* - x_i) + F \cdot (x_{\mathrm{r1}} - x_{\mathrm{r2}}) \tag{18}$$

$$v = x^* + F \cdot (x_{\mathrm{r1}} - x_{\mathrm{r2}}) + F \cdot (x_{\mathrm{r3}} - x_{\mathrm{r4}}) \tag{19}$$

$$v = x_{\mathrm{rand1}} + F \cdot (x_{\mathrm{r2}} - x_{\mathrm{r3}}) + F \cdot (x_{\mathrm{r4}} - x_{\mathrm{r5}}) \tag{20}$$

In the formula, v_i is the position vector of the individual after mutation, F is the scaling factor, and x_{r1}, x_{r2}, and x_{r3} are the position vectors of random individuals $r1$, $r2$, and $r3$, respectively.

The core of differential evolution is to use the difference vectors between different individuals in the population to generate new solutions, thereby improving the diversity of search. In the improved HHO algorithm, the mutation operation is defined by the following Equation (21) to generate a new candidate solution:

$$v(t+1) = \begin{cases} (X_{\mathrm{rabbit}}(t) - X_m(t)) - r_3 \cdot (LB + r_4 \cdot (UB - LB)), & \text{if } q < 0.5 \\ X_{\mathrm{rand}}(t) - r_1 \cdot |X_k(t) - 2r_2 \cdot X(t)|, & \text{if } q \geq 0.5 \end{cases} \tag{21}$$

where X_k is the individual in the k-neighborhood, and the k-neighborhood consists of the 3/N individuals closest to the current individual x_i. This operation provides HHO with a stronger global exploration capability, helping it to jump out of local optima.

To increase the diversity of solutions and improve the robustness of the algorithm, the crossover operation in differential evolution is used to combine the variant individual $v_i(t)$ with the current individual $X_i(t)$ to generate the candidate solution:

$$X_{\text{new}}(t+1) = \begin{cases} v_i(t), & \text{if rand}_j \leq CR \text{ or } j = j_{\text{rand}} \\ X_i(t), & \text{otherwise} \end{cases} \tag{22}$$

where $v_i(t)$ is the mutated individual, rand_j is a random number between 0 and 1, CR is the crossover rate, and j_{rand} is the randomly selected index for the crossover operation.

The generated candidate solution is compared with the current individual, and the solution with the better fitness value is selected as the next generation individual. This is mathematically expressed as

$$X_i(t+1) = \begin{cases} X_{\text{new}}(t+1), & \text{if } F(X_{\text{new}}(t+1)) \leq F(X_i(t)) \\ X_i(t), & \text{otherwise} \end{cases} \tag{23}$$

where $X_{\text{new}}(t+1)$ is the candidate solution generated through mutation and crossover and $F(\cdot)$ represents the fitness function.

The selection mechanism maintains the diversity of CHHO populations while ensuring the gradual optimization of fitness values.

In summary, the CHHO pseudocode is shown in Algorithm 2.

Algorithm 2: Pseudo-code of CHHO algorithm

Input: The population size N and maximum number of iterations T
Output: The location of rabbit and its fitness value
Initialize the Tent population X_i $(i = 1, 2, \ldots, N)$ **while** *stopping condition is not met* **do**
  Calculate the fitness values of hawks;
  Set X_{rabbit} as the location of rabbit (best location);
  for *each hawk* X_i **do**
    Update the initial energy E_0 and jump strength J;
    $E_0 = 2 \cdot \text{rand}() - 1$;
    $J = 2 \cdot (1 - \text{rand}())$;
    Update the E using Equation (3);
    if $|E| > 1$ **then**
      Exploration phase;
      Update the location vector using Equations (20)–(22) ;
    if $|E| < 1$ **then**
      Exploitation phase;
      if $r \geq 0.5$ *and* $|E| \geq 0.5$ **then**
        Soft besiege;
        Update the location vector using Equation (4);
      else if $r \geq 0.5$ *and* $|E| < 0.5$ **then**
        Hard besiege;
        Update the location vector using Equation (6);
      else if $r < 0.5$ *and* $|E| \geq 0.5$ **then**
        Soft besiege with progressive rapid dives;
        Update the location vector using Equation (10);
      else if $r < 0.5$ *and* $|E| < 0.5$ **then**
        Hard besiege with progressive rapid dives;
        Update the location vector using Equation (11);
Return X_{rabbit}

4.2. YOLOv7-tiny

When using the YOLO model for object detection, especially in large-scale or complex scenes, the original YOLO model may face challenges due to high memory consumption and long processing times. To improve the efficiency of object detection algorithms, there has been continuous exploration of lightweight approaches aimed at reducing the model's parameter count and computational load while maintaining high recognition accuracy.

In the YOLOv7 algorithm, attempts have already been made to optimize the model by replacing some convolution modules with lightweight components. This approach reduces resource consumption while striving to maintain the model's performance. However, simply replacing convolution modules may not be sufficient to meet the stringent requirements for both efficiency and accuracy in demanding scenarios.

This study proposes a model optimization method that combines dynamic pruning and knowledge distillation. Dynamic pruning is a technique that dynamically removes unimportant connections or neurons during model training, effectively reducing the model's parameter count and computational complexity. Knowledge distillation, on the other hand, is a method that transfers knowledge from a large model (teacher model) to a smaller model (student model), enabling the smaller model to achieve performance close to that of the large model while maintaining a compact size.

By combining these two techniques, the proposed method enables efficient detection and recognition of weeds in lily fields without sacrificing accuracy. Specifically, dynamic pruning removes redundant connections and parameters in the model, reducing its complexity and memory usage, while knowledge distillation helps recover or enhance the performance that may be lost due to pruning by transferring knowledge from the large model. This approach holds promise for providing efficient and accurate object detection solutions in resource-constrained real-world applications.

4.2.1. Pruning

Pruning [24] is a commonly used model compression technique in deep learning neural networks aimed at improving the model's efficiency and inference speed by reducing redundant parameters and connections while also decreasing the risk of overfitting. The pruning rate, which is typically chosen through manual selection of hyperparameters, not only affects the degree of pruning but can also have adverse consequences if improperly selected, leading to serious issues in subsequent retraining.

To address this problem, this paper proposes the integration of dynamic pruning into the model training process. Unlike traditional pruning methods that rely on a fixed standard to evaluate the relationship between input images and convolution kernels or randomly discard connections, dynamic pruning adopts a more adaptive approach. The method involves pruning certain redundant channels in the neural network model, thereby reducing its complexity. Dynamic pruning operates through sparse training, where the parameters from the Batch Normalization (BN) layers are used to identify channels with smaller weights. These channels are then removed to achieve the desired pruning effect.

The dynamic pruning approach introduces a scarification parameter, which controls the sparsity of the model. The higher the scarification parameter, the sparser the model becomes, allowing for a higher pruning ratio. This parameter must be carefully tuned to ensure that the model's performance does not degrade significantly while also maintaining an adequate pruning rate. After pruning, the model performance typically drops, and further fine-tuning is required to restore its performance to a level comparable to the pre-pruned model.

4.2.2. Knowledge Distillation

Knowledge distillation [25] was first introduced by Bucila et al. [26]. It utilizes transfer learning to guide the training of a smaller and more compact student network using the outputs from a larger and more complex teacher network with superior performance. The compressed student network aims to retain the high performance of the teacher network by relying not only on the network's output but also on the intermediate feature information. Vasileios et al. introduced the concept of Generative Adversarial Networks (GANs) [27] using a discriminator to distinguish whether the output feature map comes from the teacher or the student network. This helps align the feature information from both networks as closely as possible. Similarly, GANs are used to learn the objective function from the teacher network and guide the training of the student network.

Knowledge distillation is applied to both the feature extraction layer and the feature fusion layer, allowing the student network to benefit from both the feature extraction knowledge and the feature fusion knowledge of the teacher network. In the YOLOv3 detection model, applying knowledge distillation resulted in a 9.3% improvement in mAP [28]. Typically, knowledge distillation-based compression methods transfer the feature information from the teacher network to the student network, with the compressed network outperforming the original. However, challenges arise in terms of feature space transformation, and this approach tends to deliver superior performance mainly in tasks involving the Softmax classification function. Its generalization ability in other tasks is often less effective. A flowchart of the knowledge distillation process is shown in Figure 3.

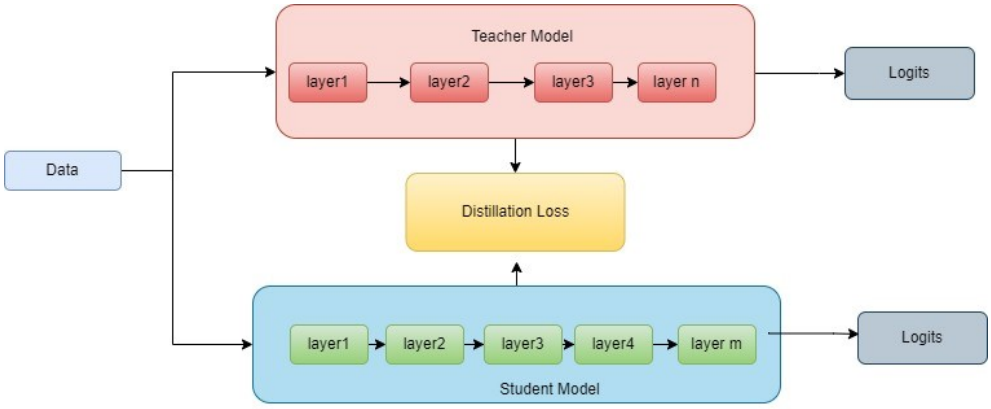

Figure 3. Knowledge distillation diagram.

As shown in Figure 3, logits refer to the part where the student directly mimics the final prediction of the teacher. Distillation loss refers to the component that learns the soft targets. The teacher model contains n layers, while the student model consists of m layers.

4.2.3. Parameter Optimization

In the CHHO framework, we optimized nearly super parameters (such as learning rate, momentum, data enhancement parameters, etc.) and a variety of activation functions (including Silu, Selu, swish, etc.) of YOLOv7-tiny. Through optimization, not only the accuracy of weed detection is improved, but also the robustness of the model to different weed species is enhanced.

The datasets of the weed detection task in the lily field usually have problems of distribution difference and occlusion diversity. CHHO provides flexible configuration of fitness function (such as map, F1, precision, or recall rate) and supports dynamic adjustment of population size and search range according to the size of dataset. For small datasets, smaller population size and evaluation quantity can be selected to reduce optimization time.

For large datasets, the larger search space ensures the comprehensiveness and robustness of optimization.

The optimized YOLOv7-tiny model has lightweight characteristics and is suitable for real-time weed detection in resource-constrained environments, such as embedded devices and mobile terminals. Through the optimization process of CHHO, the model training time can be effectively shortened and the deployment efficiency can be improved.

Figure 4 shows how this integration occurs. As shown in Figure 4, the proposed method has a very simple structure. Like all object detection algorithms, there are three basic operations, such as a dataset unit, a model unit, and an optimization unit. First, with the help of agricultural experts, the weeds in the lily field are marked, and then the dataset is obtained after using the image preprocessing method to clean these images. The last operation in the dataset unit is to appropriately divide the dataset into training data, validation data, and test data. Therefore, we can measure the generalization ability of the model on the validation set and its ability on invisible test data.

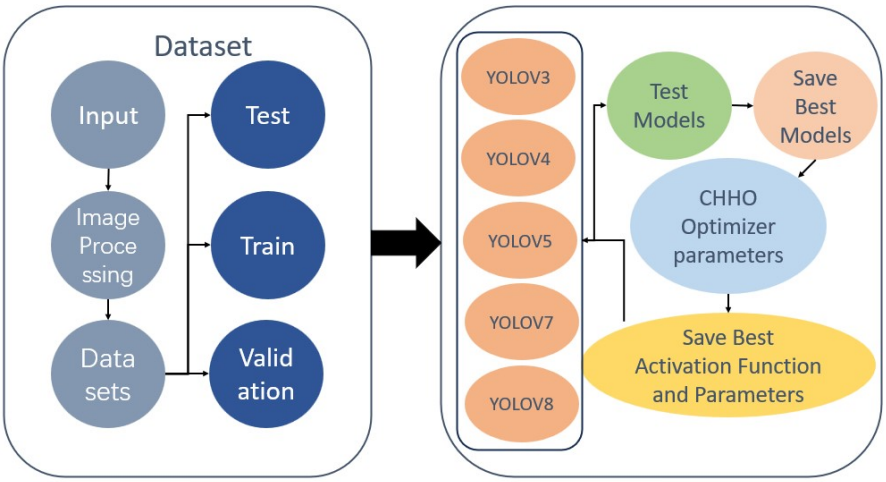

Figure 4. Parameter optimization of YOLO v7-tiny model for CHHO.

First, the dataset is preprocessed and divided into training, validation, and testing sets. This ensures that the YOLOv7-tiny model can effectively generalize and perform well on unseen data. The fitness function design uses the Mean Average Precision (mAP) as the fitness function to evaluate the performance of the YOLOv7-tiny model during the optimization process. The mAP score reflects the model's ability to accurately detect targets and minimize false positives and false negatives.

Initial training on the YOLOv7-tiny model is performed using default hyperparameters such as learning rate, momentum, activation function, etc. By using pre-trained weights through transfer learning, the model can achieve reasonable performance without the need for extensive initial training. If the mAP score does not improve after several epochs, an early stopping strategy is adopted.

The CHHO algorithm is introduced to optimize the hyperparameters and activation function of YOLOv7-tiny. The optimization scope includes hyperparameters such as learning rate, momentum, and batch size. For example, the initial learning rate is selected within the range of [10-5,10-1]. CHHO improves global search capability by introducing chaotic maps (such as Tent) to avoid becoming stuck in local optima. When initializing the CHHO algorithm, the population size is set to 50 and the number of iterations is 30 epochs to balance computational efficiency and optimization quality. In each iteration, CHHO dynamically adjusts hyperparameters and activation functions and updates them to improve the fitness (mAP) of YOLOv7-tiny. Meanwhile, the new activation functions

are evaluated against the existing SiLU activation function. Integer values are assigned to each activation function. The CHHO algorithm is enabled to select the optimal activation function. At the end of optimization, the optimal combination of hyperparameters and activation functions is selected based on the highest mAP score achieved by the model. This optimized configuration is used to further fine tune YOLOv7-tiny. The optimized YOLOv7-tiny model exhibits higher detection accuracy and faster convergence speed. The entire process ensures that the model is more adaptable to specific datasets and task requirements.

By combining the global search capability of the CHHO algorithm with the excellent detection performance of YOLOv7-tiny, this method effectively balances model accuracy and computational cost, providing an efficient and reliable solution for object detection tasks.

5. Experimental Results

The model training experiments in this study were conducted on a Linux system, using an NVIDIA GeForce GTX 3080 GPU, a 12 vCPU Intel(R) Xeon(R) Platinum 8255C CPU @ 2.50 GHz, 40 GB of RAM, and 80 GB of memory, which meet the requirements of this experiment.

For the model training hyperparameters, the initial learning rate was set to 0.001, and a dynamic learning rate strategy was employed, where the learning rate is reduced by a factor of ten every 30 epochs. This strategy helps the model converge faster and avoids being misled by local optima. The most used cross-entropy loss function was utilized to calculate the model's loss value, and the SGD optimizer was used to iteratively train the parameters. Detailed parameter information can be found in Table 4.

Table 4. Experimental parameters and configuration.

Name	Parameter
Operating System	Ubuntu 20.04
CPU	12 vCPU Intel(R) Xeon(R) Platinum 8255C CPU @ 2.50 GHz
GPU	NVIDIA GeForce GTX 3080
Video Memory	80 GB
Deep Learning Framework	PyTorch 1.11.0
Learning Rate	CHHO optimized
Batch Size	CHHO optimized
Epoch	100
Loss Function	Cross Entropy Loss
Optimization Algorithm	SGD

Through the lightweight optimization of YOLOv7, the efficiency of weed identification has been further improved, reducing the impact of precision on the model's classification performance. When the network model is large, convolutional neural networks become difficult to train. Therefore, we propose a method for identifying weeds in lily fields using a combination of pruning and distillation. Knowledge distillation allows the large model to transfer the knowledge it has learned to guide the training of the smaller model, significantly reducing the number of parameters and further achieving model compression and acceleration. Meanwhile, model pruning removes components that have minimal impact on the results, reduces the number of heads, and shares parameters, among other techniques. Together, knowledge distillation improves the model's accuracy, reduces its latency, and compresses its network parameters. Dynamic pruning further reduces the model's parameters, ultimately achieving a lightweight YOLOv7 network model.

The weed images in the lily fields were manually annotated using the Label Image rectangular annotation tool to ensure accurate labeling of the weed and lily contours. To

enhance the distinction between lilies and weeds under complex environmental interference, only the lily leaves were labeled, enabling the model to be highly sensitive to the overall structure of the lily. As shown in Figure 5, the annotated image environment was displayed. After annotation, the images were converted to the YOLO standard dataset format for subsequent training, validation, and testing. In cases of overlapping objects, the bounding boxes were carefully adjusted, further increasing the difficulty of extracting features from the lilies and weeds.

Figure 5. Weed marking diagram.

5.1. Comparative Results and Discussion of CHHO

The chaotic system [29] is a classical optimization strategy known for its diverse types and dynamic characteristics, which enable robust global search capabilities. Different chaotic systems exhibit varying performance in global exploration, local search, and space traversal. In this study, we selected 21 representative chaotic systems for comparative experiments to evaluate their optimization performance.

The experimental results indicate that the Tent chaotic system significantly outperforms other systems, particularly in terms of diverse search capabilities and approximating the global optimum. Consequently, we selected Tent as the core mechanism for chaotic initialization and search.

To further validate the superiority of Tent, we selected three types of classical test functions [30,31]: unimodal functions, multimodal functions, and fixed-dimensional functions. From these, six classical functions (see Table 5) with distinct characteristics were chosen for comparative experiments, covering simple convex optimization problems and complex nonlinear high-dimensional optimization challenges.

Table 5. Benchmark functions used in the experiment.

Type	Function	Name	Dimensionality	Search Space	Theoretical Optimal Value
Unimodal	F1	Sphere	30	$[-100, 100]$	0
	F3	Schwefel 1.2	30	$[-100, 100]$	0
Multimodal	F10	Ackley	30	$[-32, 32]$	0
	F12	Penalized1	30	$[-50, 50]$	0
Fixed-Dimensional	F15	Kowalk	4	$[-5, 5]$	0.0003075
	F21	Sheke_5	4	$[0, 10]$	-10.1532

In Table 5, the comparison metric is the final objective (fitness) value achieved on each test function, with results expressed in scientific notation. The test functions are denoted as F1, F3, F10, F12, F15, and F21, which represent standard benchmark functions

commonly used in the optimization literature to evaluate algorithm performance (e.g., unimodal, multimodal, and non-convex functions; see references [30,31]). For instance, F1 might correspond to a simple unimodal function like the Sphere function, while the other functions are designed to assess different aspects such as landscape ruggedness and scalability. Lower (or in some cases higher) final objective values indicate better optimization performance depending on the formulation of each test function. Table 6 also compares various chaotic mapping algorithms employed to generate initial populations or chaotic sequences, including methods such as Random, Chebyshev, Circle, Gauss, Iterative, Logistic, Piecewise, Sine, Singer, Sinusoidal, Kent, Fuch, SPM, ICMIC, Tent–Logistic–Cosine, Sine–Tent–Cosine, Logistic–Sine–Cosine, Henon, Cubic, Logistic–Tent, Bernoulli, and Tent. These algorithms are referenced in the literature (see references [29,32,33]) and serve as alternative approaches to facilitate global exploration in optimization problems.

Table 6. Comparison of algorithms on different test functions.

Algorithm	F1	F3	F10	F12	F15	F21
Random	2.17×10^{-19}	4.09×10^{-11}	6.38×10^{-09}	4.10×10^{-04}	4.56×10^{-04}	-4.96×10^{0}
Chebyshev	1.47×10^{-18}	1.27×10^{-10}	8.15×10^{-09}	5.50×10^{-04}	3.36×10^{-04}	-4.96×10^{0}
Circle	2.46×10^{-16}	3.32×10^{-07}	2.36×10^{-10}	1.18×10^{-04}	4.02×10^{-04}	-2.56×10^{0}
Gauss	5.72×10^{-17}	4.87×10^{-11}	2.99×10^{-09}	7.00×10^{-04}	4.09×10^{-04}	-4.92×10^{0}
Iterative	3.16×10^{-17}	3.12×10^{-09}	2.54×10^{-09}	1.68×10^{-03}	5.59×10^{-04}	-4.91×10^{0}
Logistic	1.20×10^{-14}	5.93×10^{-07}	9.90×10^{-10}	4.75×10^{-05}	4.57×10^{-04}	-5.05×10^{0}
Piecewise	5.96×10^{-16}	8.37×10^{-09}	6.24×10^{-09}	2.00×10^{-04}	3.38×10^{-04}	-4.76×10^{0}
Sine	1.01×10^{-19}	1.34×10^{-09}	5.06×10^{-10}	1.16×10^{-05}	4.48×10^{-04}	-4.99×10^{0}
Singer	8.25×10^{-15}	3.16×10^{-13}	1.83×10^{-08}	6.28×10^{08}	4.38×10^{-04}	-5.00×10^{0}
Sinusoidal	5.09×10^{-12}	3.18×10^{-13}	3.30×10^{-09}	1.28×10^{-04}	5.67×10^{-04}	-4.96×10^{0}
Kent	4.02×10^{-14}	1.02×10^{-12}	1.70×10^{-09}	1.69×10^{-04}	3.33×10^{-04}	-9.64×10^{0}
Fuch	2.38×10^{-14}	3.22×10^{-09}	1.77×10^{-09}	2.89×10^{-04}	1.41×10^{-03}	-5.01×10^{0}
SPM	4.33×10^{-15}	7.43×10^{-08}	1.10×10^{-07}	3.62×10^{-05}	4.32×10^{-04}	-5.04×10^{0}
ICMIC	2.48×10^{-16}	1.90×10^{-10}	1.09×10^{-09}	3.00×10^{-04}	5.63×10^{-04}	-5.04×10^{0}
Tent–Logistic–Cosine	3.07×10^{-17}	6.64×10^{-14}	4.18×10^{-09}	3.67×10^{-04}	3.59×10^{-04}	-4.85×10^{0}
Sine–Tent–Cosine	8.32×10^{-18}	2.73×10^{-10}	4.42×10^{-10}	2.85×10^{-05}	1.98×10^{-03}	-4.89×10^{0}
Logistic–Sine–Cosine	1.78×10^{-17}	8.32×10^{-09}	3.07×10^{-09}	2.01×10^{-03}	1.72×10^{-03}	-4.84×10^{0}
Henon	1.90×10^{03}	2.04×10^{05}	2.01×10^{01}	2.40×10^{00}	3.16×10^{-04}	-3.00×10^{-01}
Cubic	1.42×10^{-18}	4.30×10^{-08}	5.98×10^{-10}	1.53×10^{-04}	4.68×10^{-04}	-4.94×10^{0}
Logistic–Tent	1.47×10^{-14}	2.41×10^{-13}	5.13×10^{-08}	7.49×10^{-04}	8.00×10^{-04}	-4.89×10^{0}
Bernoulli	1.03×10^{-15}	2.84×10^{-12}	1.30×10^{-09}	4.58×10^{-04}	3.17×10^{-04}	-5.02×10^{0}
Tent	1.14×10^{-21}	3.55×10^{-17}	1.12×10^{-10}	5.52×10^{-06}	3.17×10^{-04}	-5.03×10^{0}

Experimental results in Table 6 demonstrate that the Tent system performs [34–36] exceptionally well across the selected test functions. Among 23 classical test functions, Tent exhibits outstanding performance in both unimodal and multimodal functions. It not only converges rapidly to the global optimal solution but also shows higher convergence stability and stronger resistance to interference.

To present the experimental results more intuitively, the following figures were plotted: Figure 6 illustrates the chaotic curve of the Tent system [32,33], representing its traversal performance across the search space. The curve indicates that Tent effectively covers the search space, avoiding local optima.

Figure 7 shows the performance histogram, displaying the fitness value distributions of different chaotic systems on the test functions. The histogram highlights Tent-stable performance across various functions.

Figure 8 is a chaotic scatter plot, representing Tent exploration and exploitation distribution in the high-dimensional search space. The plot showcases Tent-efficient exploration and robust global search characteristics.

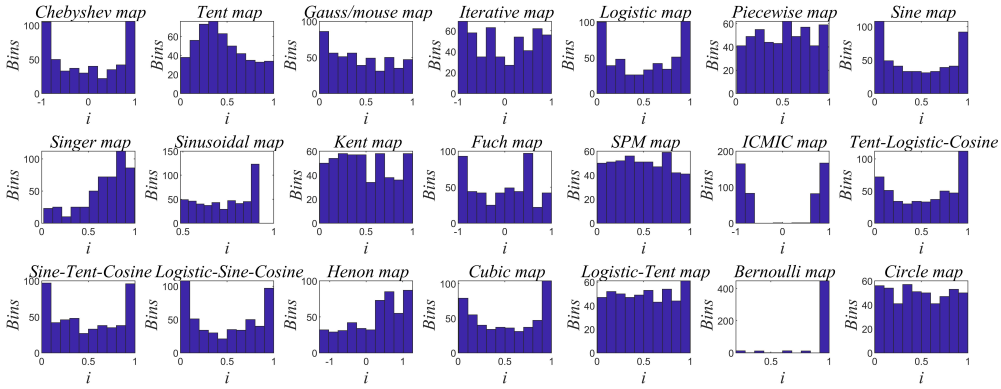

Figure 6. Chaotic curve of the Tent system.

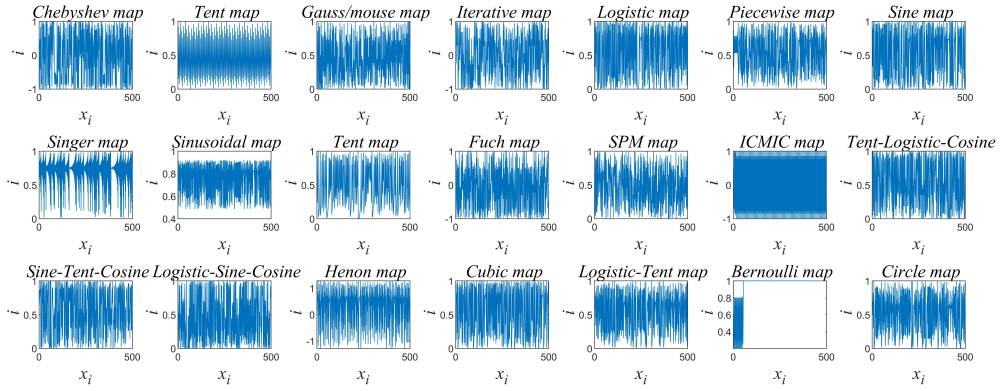

Figure 7. Performance histogram.

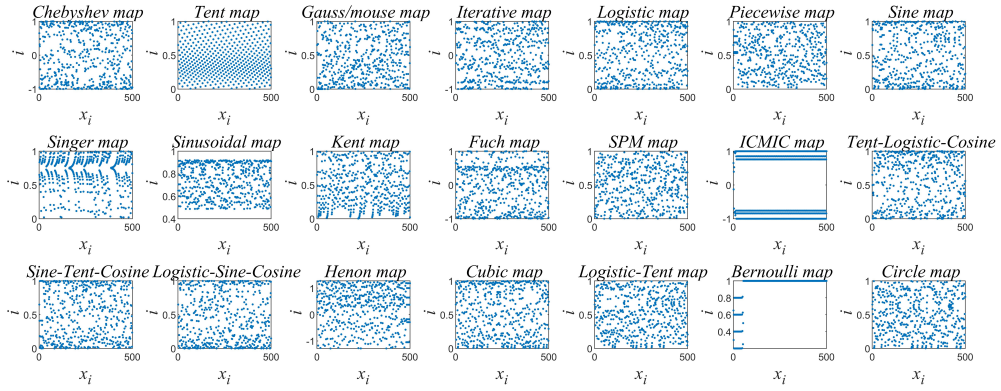

Figure 8. Chaotic scatter plot.

Figure 9 shows the comparison diagram of iteration curves, which are compared among 21 kinds of chaotic systems to select the optimal system.

To ensure the fairness and objectivity of the experiments, identical experimental parameters were applied across all algorithms, specifically the following: Population size N = 50, ensuring each chaotic system performs searches with the same number of individuals; Dimensionality D = 30 (excluding fixed-dimensional functions), standardizing the search space scale for optimization problems; Maximum number of iterations set to 50, balancing algorithm runtime and ensuring comparable results.

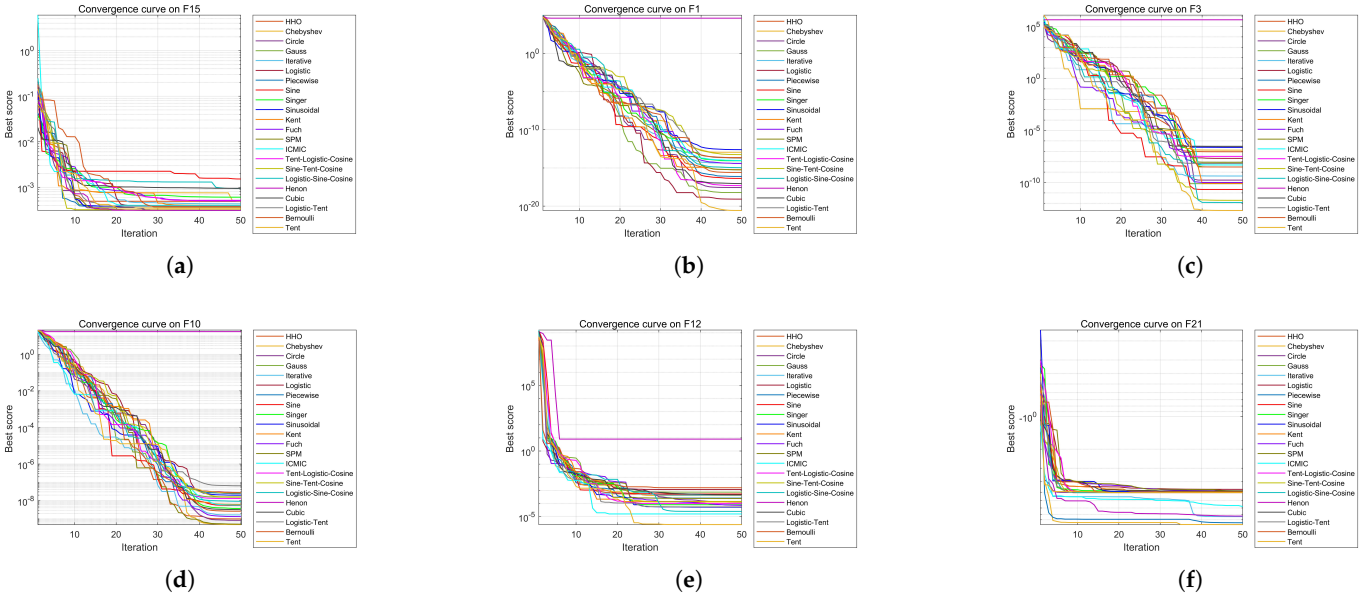

Figure 9. Convergence curves of some unimodal, multimodal, and fixed dimensional functions. (**a**) Convergence curve of function F15. (**b**) Convergence curve of function F1. (**c**) Convergence curve of function F3. (**d**) Convergence curve of function F10. (**e**) Convergence curve of function F12. (**f**) Convergence curve of function F21.

Overall, the experimental findings confirm that the Tent chaotic system consistently outperforms others across various optimization problems, particularly in global search capability and convergence accuracy. This discovery provides strong support for the practical application of chaotic optimization strategies.

For the lily field dataset, using the improved Chaotic Harris Hawks Optimization (CHHO) algorithm to optimize the YOLOv7-tiny algorithm significantly enhanced its performance in detecting lily field weeds. As shown in subsequent sections, the YOLOv7-tiny parameters optimized by CHHO exhibit stronger competitiveness in detection tasks.

Through iterative optimization with the CHHO algorithm, the optimal activation functions and hyperparameter combinations for the lily field dataset were identified. During the optimization process, weights trained using 11 activation functions for the YOLOv7-tiny model were accumulated into a weight pool, from which one weight was randomly selected as the starting point for optimization. The optimization was performed in the form of fine-tuning, requiring at least 20 epochs to ensure effectiveness. In this process, besides optimizing the activation functions, hyperparameters can also be adjusted, or both activation functions and hyperparameters can be optimized simultaneously.

This study employed a simultaneous optimization approach, leveraging ample computational resources and time. Table 7 compares the default hyperparameters and activation functions of the YOLOv7-tiny algorithm with the optimized values obtained through different optimization algorithms, including CHHO, HHO, SCA [37], WOA [38], and PSO [39]. The table highlights CHHO's superior tuning capabilities, demonstrating its effectiveness in refining key parameters such as activation functions, momentum, weight decay, and learning rate. This CHHO-based optimization method not only enhances model performance but also provides a comparative analysis of various metaheuristic approaches, offering practical insights for improving YOLO parameter tuning.

Table 7. Comparison of optimized YOLO parameters using different optimization algorithms.

Parameter	CHHO (Proposed)	HHO	SCA [37]	WOA [38]	PSO [39]
Activation Function	Swish	LeakyReLU	ReLU	LeakyReLU	ReLU
Momentum	**0.937**	0.90	0.92	0.91	0.89
Weight Decay	**0.0001**	0.0004	0.0032	0.0002	0.0004
Batch Size	**64**	32	24	16	32
Learning Rate	**0.012**	0.01	0.008	0.009	0.01
Scale	**1.0025**	0.9998	0.9995	0.9992	0.9997
Flip Probability	**0.55**	0.50	0.48	0.49	0.50

The computational complexity of the CHHO algorithm can be analyzed based on its four main components: population initialization, exploration phase, exploitation phase, and ranking mechanism. The initialization process, including the Tent Chaotic Mapping strategy, has a complexity of $O(n \times d)$, where n is the population size and d is the dimensionality of the search space. The exploration phase, responsible for global searches, follows the Harris Hawks Optimization (HHO) framework and has a complexity of $O(L \times n \times d)$, where L represents the maximum number of iterations. The exploitation phase integrates the Differential Evolution mechanism to refine the solution, contributing an additional complexity of $O(L \times n \times d)$. Finally, the ranking mechanism employs a fast sorting method, leading to a worst case complexity of $O(L \times n \log n)$. Combining these components, the overall complexity of CHHO can be expressed as $O(n \times d) + O(L \times (2n \times d + n \log n))$, which simplifies to $O(L \times n \log n)$, demonstrating that CHHO maintains a reasonable computational burden while significantly improving convergence efficiency through the combination of chaotic mapping and differential evolution mechanisms.

5.2. Comparative Results and Discussion of YOLOv7-tiny

YOLOv7-tiny Model Detection Results Analysis:

(1) Impact of Different Network Models on Weed Detection in Lanzhou Lily Fields.

In this study, we compared different network models [40–45] through experiments to identify the model with the highest accuracy for weed detection in Lanzhou lily fields. To address the issue of long inference time with the larger YOLOv7 model, we employed a dynamic pruning strategy to reduce the model's complexity and subsequently retrained the model. The results showed a notable improvement in accuracy across all models. The accuracy of the Lanzhou lily-weed detection model based on different network models is summarized in Table 8.

As shown in Table 8, selecting the appropriate model is crucial for object detection tasks. Due to differences in structure, parameters, and optimization methods, various models exhibit distinct performance during training. While the accuracy improvement varies significantly across different models, the YOLOv7 model consistently demonstrates superior overall metrics, with a substantial increase in accuracy. The average precision is 0.85 and the F1 score is 0.88. Therefore, in this study, YOLOv7 was selected for subsequent experiments.

(2) Impact of Different Parameter Counts on Weed Detection in Lanzhou Lily Fields.

To enhance the model's recognition capabilities without compromising accuracy, knowledge distillation was introduced to improve the model's learning speed. The experiment results indicate that knowledge distillation has effectively lightened the model to some extent while maintaining accuracy. Knowledge distillation allows knowledge to be transferred from a larger, more complex model (referred to as the "teacher model") to a smaller, simpler model (referred to as the "student model").

Table 8. Performance evaluation of different models for weed and lily classification.

Evaluation Metric	Model	Weed	Lily	Average Value
Precision	VGG-16	0.7008	0.6822	0.6915
	ResNet-50	0.7143	0.8195	0.7669
	DenseNet-121	0.7706	0.8738	0.8222
	EfficientNet-B5	0.8319	0.8472	0.83955
	MobileNet-V3	0.7130	0.8597	0.78635
	ResNeXt-50	0.8031	0.7838	0.79345
	YOLOv7	0.8712	0.8257	0.84845
TPR	VGG-16	0.6953	0.8036	0.74945
	ResNet-50	0.7188	0.8214	0.7701
	DenseNet-121	0.7500	0.8348	0.7924
	EfficientNet-B5	0.7344	0.8170	0.7757
	MobileNet-V3	0.7813	0.8482	0.81475
	ResNeXt-50	0.7969	0.8571	0.827
	YOLOv7	0.8769	0.8636	0.87025
F1_score	VGG-16	0.6980	0.7266	0.7123
	ResNet-50	0.7239	0.7907	0.7573
	DenseNet-121	0.7075	0.7778	0.74265
	EfficientNet-B5	0.8462	0.7965	0.82135
	MobileNet-V3	0.8131	0.8473	0.8302
	ResNeXt-50	0.8000	0.7553	0.77765
	YOLOv7	0.8615	0.8949	0.8782

By transferring the knowledge from the teacher model to the student model, the results show that this method contributes to model lightweighting without significantly compromising accuracy. Although accuracy may decline during the distillation process, careful selection of the teacher and student models, as well as optimization of the distillation process, allows this accuracy loss to be controlled within an acceptable range.

Comparing the parameter counts of different versions of the YOLOv7-based model in this study, the results are shown in Table 9. Among the YOLOv7 series models, YOLOv7-tiny' performed the best with an accuracy of 92.53%, an improvement of 6.7% over the previous model.

Table 9. Model performance comparison based on parameter quantity and accuracy.

Model	Parameter Quantity	Accuracy	GFLOPs	ms–FPS
YOLOv7	36.9 M	72.16%	105.7	8.9 ms (112 FPS)
YOLOv7-X	71.3 M	80.97%	189.9	15.8 ms (63 FPS)
YOLOv7-tiny	16.2 M	85.83%	4.5	2.1 ms (476 FPS)
YOLOv7-E6	97.2 M	83.00%	303.3	21.9 ms (46 FPS)
YOLOv7-D6	154.7 M	82.58%	453.2	31.2 ms (32 FPS)
YOLOv7-E6E	151.7 M	83.37%	375.6	28.7 ms (35 FPS)
YOLOv7-tiny'	10.7 M	92.53%	3.2	1.8 ms (555 FPS)

As shown in Table 9, when analyzing the YOLOv7 network models based on accuracy, the YOLOv7-tiny model achieved the highest accuracy of 92.53% with the fewest parameters. Despite the minimal decrease in accuracy compared to larger models, the YOLOv7-tiny model also demonstrated significant computational efficiency, with the lowest GFLOPs and the highest ms–FPS, making it well suited for real-time applications. Therefore, this study uses the YOLOv7-tiny model for the experiments, as it strikes an optimal balance between performance and efficiency.

(3) Detection Performance of Weeds in the Lily Field under Different Occlusion Conditions.

To investigate the impact of occlusion on the model's performance, three types of occlusion conditions were tested: no occlusion, light occlusion, and severe occlusion. As shown in Figure 10, when the images of Lanzhou lily and weeds are either unobstructed or lightly occluded, the model maintains a high recognition accuracy. In cases where the features are clear, the model does not miss any detections or make false positives. However,

when severe occlusion occurs, the irregular growth of weeds and lilies creates multiple gaps that expose limited features, providing insufficient information for the model to make accurate judgments. As a result, more missed detections are observed, though false detections are rare. Additionally, weak lighting caused by occlusion can further contribute to misclassification.

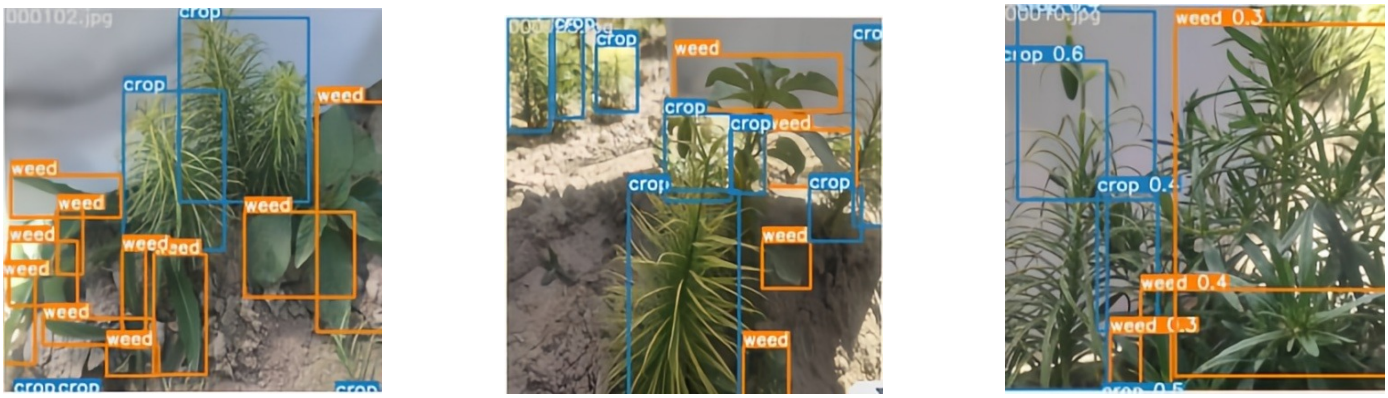

(**a**) (**b**) (**c**)

Figure 10. Results of weed detection in lily fields under different shielding conditions. (**a**) Cover of lily by weeds. (**b**) Slight occlusion. (**c**) Complete occlusion.

(4) The Impact of Different Dataset Sizes on Weed Detection in Lanzhou Lily Fields. Using YOLOv7-tiny as the base model, this study trains the Lanzhou lily-weed detection model, which incorporates pruning and distillation techniques, on datasets of various sizes. The aim is to explore how the proposed method performs under different dataset sizes. The comparison of the recognition accuracy of the lightweight YOLOv7-tiny model across datasets of varying sizes is shown in Figure 11.

In the comparison of different network models, as shown in Figure 11, YOLOv7-tiny exhibits the highest recognition accuracy, and the dataset size has the least impact on the model's performance. When the sample size is 500 images, YOLOv7-tiny achieves the highest recognition accuracy. However, when the number of samples per class increases to 1500 images, the recognition accuracy of each model is at its peak. As the sample size decreases, the recognition accuracy of all models gradually decreases. Yet, YOLOv7-tiny shows minimal accuracy loss, indicating that the proposed method maintains high classification accuracy even with fewer samples. This demonstrates that the method can handle situations with limited Lanzhou lily-weed samples.

However, when the dataset is extremely small, convolutional neural networks (CNNs) struggle to classify the data accurately. The experiment highlights the reduced dependence on large datasets by the proposed method.

The YOLOv7-tiny model, implemented for Lanzhou lily-weed detection, addresses issues related to low accuracy in CNN-based models for identifying common weeds in lily fields, as well as the high data requirements. By analyzing the impact of different network models, parameter sizes, dataset sizes, and occlusion conditions on model performance, the experiment validates the effectiveness of the proposed approach.

Figure 12 shows the detection results for the YOLOv7-tiny network model with dynamic pruning and knowledge distillation on the lily-weed dataset. Comparing image (b) with image (a), it is evident that the enhanced model accurately detects weeds and lilies with improved precision. This indicates that even after model compression, the network is capable of learning the similarities within the same category and distinguishing between different categories in a short time, leading to accurate identification of weeds and lilies.

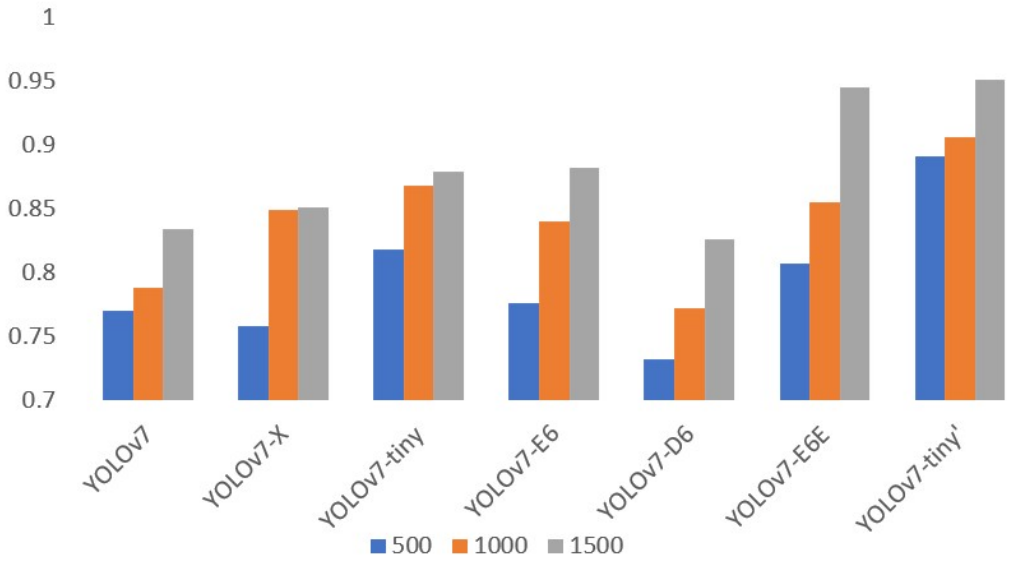

Figure 11. Comparison of recognition accuracy of lightweight YOLOv7-tiny network model under different dataset sizes.

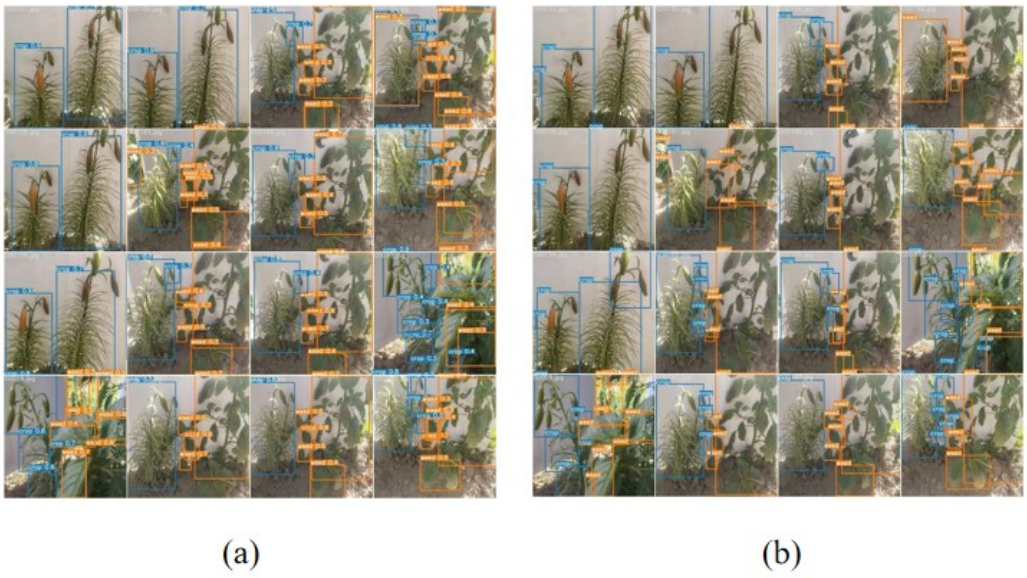

Figure 12. Comparison diagram between improved model and original model. (**a**) YOLOv7-tiny. (**b**) Our model.

As shown in Figure 13, the model's accuracy (P), recall rate (R), and P-R curve were recorded during the training process. From the plot in Figure 13a, it is evident that the accuracy increases rapidly during the initial training stages. Ultimately, the model achieves an accuracy of 89.2%, a recall rate of 81.5%, and a mAP (mean Average Precision) of 88.4% at an overlap threshold of 0.5. The variations in P, R, mAP, and loss values over iterations align with the experimental expectations. The series of network models proposed in this study, considering both parameter count and accuracy, offer significant advantages for practical applications.

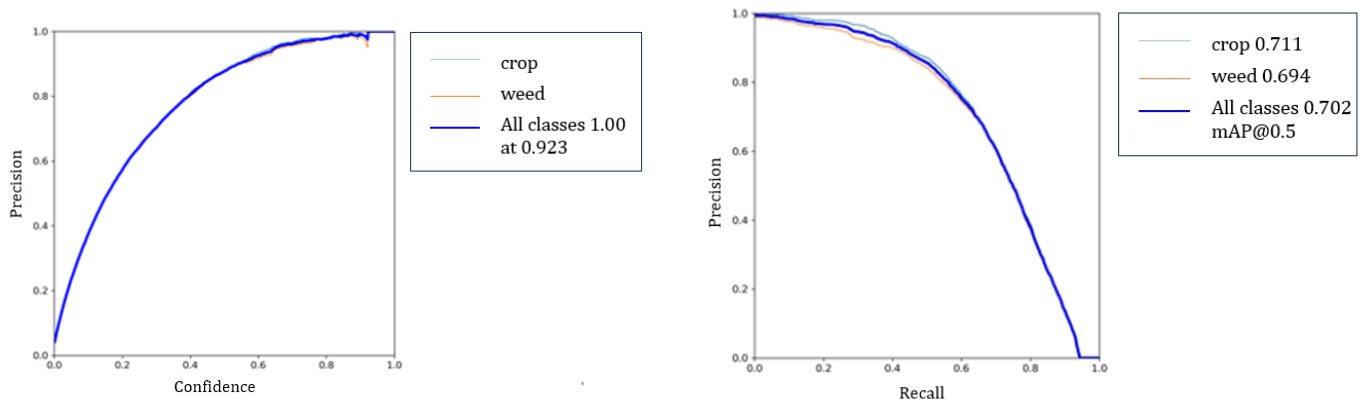

(**a**) (**b**)

Figure 13. (**a**) P and P-R change curves of the training process of the model are improved. (**b**) P and P-R change curves of the training process of the model are improved.

To address the issue of insufficient data, which can negatively impact the performance of the network model and even prevent it from learning effective feature representations, experiments were conducted using the YOLOv7-tiny model. The results demonstrated its outstanding overall performance. YOLOv7-tiny achieved the highest recognition accuracy and showed stability in performance across different datasets, reaching 93.53%. This result highlights the model's robustness and generalization capability when handling limited data. Additionally, the lightweight nature of YOLOv7-tiny enhances its flexibility and efficiency in practical applications. It can be deployed in resource-constrained environments, such as mobile devices or embedded systems, enabling real-time object detection and recognition. This makes it particularly valuable for precision weeding applications.

6. Discussion

Existing studies have applied deep learning to weed detection in agriculture. For example, Punithavathi et al. employed Faster-RCNN combined with an Extreme Learning Machine (ELM) to achieve high-accuracy classification; however, this method involves high computational complexity, making it unsuitable for real-time detection. Similarly, Jiang et al. used CNN-based feature extraction to distinguish crops from weeds but did not incorporate optimization techniques, leading to potential overfitting issues. Other studies, such as Peng Mingxia et al. [9], introduced residual networks and feature pyramids for weed detection in cotton fields, improving accuracy but with limited generalization across different crop environments. Additionally, Karaman et al. [15] optimized YOLOv5 using the Artificial Bee Colony (ABC) algorithm, enhancing detection performance. However, their optimization strategy suffered from premature convergence, and the network's complexity made it less suitable for lightweight applications.

In contrast, this study proposes a Chaotic-Based Harris Hawks Optimization (CHHO)-optimized YOLOv7-tiny model, addressing the limitations of previous research in multiple aspects. First, the knowledge distillation and dynamic pruning techniques applied to the YOLOv7-tiny model enable efficient and lightweight real-time detection, overcoming the high computational cost of Faster-RCNN-based methods. Second, by integrating Tent chaotic mapping and differential evolution strategies, the improved HHO algorithm enhances parameter optimization stability, avoiding the local optima issues observed in ABC-based methods. Furthermore, this study constructs a dedicated dataset for weed detection in Lanzhou lily fields, addressing the gap in existing research, which primarily

focuses on maize, soybean, and cotton fields. This dataset ensures that the proposed model is more robust and generalizable for practical applications in lily cultivation environments.

A key finding of the study is the correlation between dataset size and model performance. As expected, larger datasets generally lead to better accuracy, owing to the richer diversity of training samples. However, the marginal benefits diminish after reaching a certain threshold, highlighting the trade-off between data volume and computational cost. This suggests that while larger datasets are beneficial, an optimal size exists beyond which further data augmentation yields limited returns.

The analysis of different network architectures reveals a clear trade-off between accuracy and computational efficiency. Complex models with higher parameter counts, such as YOLOv7-D6 and YOLOv7-E6, achieve superior accuracy but require significantly more computational resources. On the other hand, simpler architectures, such as YOLOv7-tiny, demonstrate reasonable accuracy with much lower computational demands, making them suitable for resource-constrained environments.

Occlusion emerges as a critical factor affecting model performance. In real-world applications, weeds often overlap or are partially obscured by lily plants, which can lead to false positives or missed detections. This finding underscores the importance of robustness in model design, particularly for agricultural applications where such challenges are prevalent. Future work could explore techniques such as data augmentation with occlusion or advanced feature extraction methods to mitigate this issue.

The large-scale deployment of the CHHO-optimized YOLOv7-tiny model in agricultural applications presents both opportunities and challenges. In terms of cost, the model's lightweight architecture and optimized parameters reduce the need for expensive high-performance GPUs, making it a cost-effective solution for precision agriculture. Additionally, the use of knowledge distillation and pruning techniques significantly lowers computational resource requirements, enabling deployment on edge devices with limited hardware capabilities.

Regarding processing time and feasibility on mobile or embedded devices, the model's efficient structure allows for real-time weed detection with minimal latency. The CHHO optimization strategy accelerates convergence, ensuring rapid decision-making in dynamic field conditions. Moreover, its compatibility with low-power AI chips, such as NVIDIA Jetson and Raspberry Pi, makes it suitable for autonomous agricultural robots and drone-based monitoring systems, improving scalability in smart farming applications.

To address the balance between accuracy and efficiency, the YOLOv7 model is optimized to create YOLOv7-tiny. This lightweight variant reduces the number of parameters and computational complexity while maintaining a high level of accuracy. The model's performance is validated through visual analysis of training results, showing that YOLOv7-tiny effectively meets the demands of real-time weed detection in lily fields in Lanzhou.

The study demonstrates the potential of using lightweight, optimized models for precision agriculture. By integrating chaotic systems and optimization algorithms into neural network training, it is possible to enhance performance while addressing resource constraints. YOLOv7-tiny's balance of efficiency and accuracy makes it a strong candidate for deployment in agricultural monitoring systems, where real-time performance is crucial.

Despite its strong performance, the CHHO-optimized YOLOv7-tiny model has several limitations. One key constraint is its reliance on a specific dataset—Lanzhou lily fields—meaning its generalization to other crops or different weed species may be limited. Variations in soil conditions, lighting, and plant morphology across regions may require fine-tuning or retraining to maintain accuracy. Additionally, while knowledge distillation and pruning improve efficiency, further hardware-specific optimizations may be necessary for seamless deployment on ultra-low-power devices.

To enhance adaptability, future research could explore federated learning techniques, enabling collaborative model training across multiple agricultural regions while preserving data privacy. Expanding the dataset to include more diverse crop types and weed varieties would further improve generalization. Additionally, integrating self-supervised learning or adaptive fine-tuning mechanisms could help the model dynamically adjust to new environments, making it more robust for large-scale precision agriculture. In the future, we will increase lighting experiments to detect the effects of lighting changes on weed detection.

7. Conclusions

This study mainly introduced the Harris hawk algorithm using chaotic systems to optimize the lightweight YOLOv7 network model for detecting common weeds in lily fields. A series of experiments and comparative analyses were conducted. Seven different convolutional neural network models, including both classic and more recent architectures, were selected for training on the lily-weed dataset. The aim was to identify the best-performing model. During training, identical data preprocessing and training strategies were applied to ensure the comparability of the results. To assess the model's performance more comprehensively, datasets of varying sizes were used to analyze how dataset size affects model performance. The experimental results revealed that as the dataset size increased, the model's accuracy generally improved, but the gain gradually diminished after reaching a certain threshold.

In addition to dataset size, the effects of different network models, model parameters, and occlusion conditions on model performance were analyzed. The results indicated that more complex models generally achieved higher accuracy, but at the cost of increased computational load and memory usage. In contrast, simpler models, though slightly less accurate, were faster and more suitable for resource-constrained environments. The impact of occlusion on model performance is also significant, especially in real-world applications where weed occlusion can lead to false positives or missed detections.

To balance accuracy and efficiency, YOLOv7 was selected as the base model and further optimized to create the YOLOv7-tiny network. This model achieved a high level of accuracy while significantly reducing the number of parameters and computational complexity, making it more suitable for real-time weed detection in lily fields in Lanzhou. Finally, we compared the performance of different models using training result visuals. The results clearly showed that YOLOv7-tiny strikes a good balance between accuracy and efficiency. This validates the effectiveness of the experiment and demonstrates the potential of this approach for practical applications.

These findings offer valuable insights for practitioners aiming to implement efficient precision weeding solutions and provide researchers with a novel approach to optimizing deep learning models for agricultural applications.

Author Contributions: Methodology, J.T. and H.W.; Validation, M.Z. and P.S.; Resources, Y.H.; Writing—original draft, J.T.; Writing—review and editing, Z.Z.; Project administration, Z.Z. All authors have read and agreed to the published version of the manuscript.

Funding: This research was funded by the Open Foundation of the Qingdao Key Laboratory of Groundwater Resources Protection and Rehabilitation (No. DXSKF2022Y02), the Open Foundation of Key Laboratory of Geological Disaster Risk Prevention and Control of Shandong Provincial Emergency Management Department (No.801KF2024-DZ07), and the Open Foundation of the Key Laboratory of Coupling Process and Effect of Natural Resources Elements (No. 2024KFKT017). Open Research Fund Program of Anhui Provincial Institute of Modern Coal Processing Technology, Anhui University of Science and Technology (Grant No. MTY202307), and Hubei Key Laboratory of Transportation Internet of Things (Wuhan University of Technology).

Data Availability Statement: Data are contained within the article.

Conflicts of Interest: The authors declare no conflicts of interest.

References

1. Zhang, X.; Xue, L.; Wu, Z.; Zhang, W.; Zhang, H.; Zhao, C.; Liu, D. Insight into the Effects of Drying Methods on Lanzhou Lily Rehydration. *Foods* **2023**, *12*, 1817. [CrossRef] [PubMed]
2. Pouyanfar, S.; Sadiq, S.; Yan, Y.; Tian, H.; Tao, Y.; Reyes, M.P.; Shyu, M.-L.; Chen, S.H.; Iyengar, S.S. A Survey on Deep Learning: Algorithms, Techniques, and Applications. *ACM Comput. Surv.* **2018**, *51*, 92. [CrossRef]
3. Heidari, A.A.; Mirjalili, S.; Faris, H.; Aljarah, I.; Mafarja, M.; Chen, H. Harris hawks optimization: Algorithm and applications. *Future Gener. Comput. Syst.* **2019**, *97*, 849-872. [CrossRef]
4. Mirjalili, S.; Mirjalili, S. Genetic algorithm. In *Evolutionary Algorithms and Neural Networks: Theory and Applications*; Springer: Berlin/Heidelberg, Germany, 2019; pp. 43–55.
5. Marini, F.; Walczak, B. Particle swarm optimization (PSO). A tutorial. *Chemom. Intell. Lab. Syst.* **2015**, *149*, 153–165. [CrossRef]
6. Mirjalili, S.; Mirjalili, S.M.; Lewis, A. Grey wolf optimizer. *Adv. Eng. Softw.* **2014**, *69*, 46–61. [CrossRef]
7. Punithavathi, R.; Rani, A.D.C.; Sughashini, K.R.; Kurangi, C.; Nirmala, M.; Farhana, H.; Ahmed, T.; Balamurugan, S.P. Computer Vision and Deep Learning-enabled Weed Detection Model for Precision Agriculture. *Comput. Syst. Sci. Eng.* **2023**, *44*, 2759–2774. [CrossRef]
8. Jiang, H.; Zhang, C.; Qiao, Y.; Zhang, Z.; Zhang, W.; Song, C. CNN feature based graph convolutional network for weed and crop recognition in smart farming. *Comput. Electron. Agric.* **2020**, *174*, 105450. [CrossRef]
9. Mingxia, P.; Junfang, X.; Hui, P. Efficient recognition of cotton and weed in field based on Faster R-CNN by integrating FPN. *Trans. Chin. Soc. Agric. Eng. Trans. CSAE* **2019**, *35*, 202–209. [CrossRef]
10. Andrea, C.C.; Daniel, B.B.M.; Misael, J.B.J. Precise weed and maize classification through convolutional neuronal networks. In Proceedings of the 2017 IEEE Second Ecuador Technical Chapters Meeting (ETCM), Salinas, Ecuador, 16–20 October 2017; pp. 1–6.
11. Hu, K.; Coleman, G.; Zeng, S.; Wang, Z.; Walsh, M. Graph weeds net: A graph-based deep learning method for weed recognition. *Comput. Electron. Agric.* **2020**, *174*, 105520. [CrossRef]
12. Ahmad, A.; Saraswat, D.; Aggarwal, V.; Etienne, A.; Hancock, B. Performance of deep learning models for classifying and detecting common weeds in corn and soybean production systems. *Comput. Electron. Agric.* **2021**, *184*, 106081. [CrossRef]
13. Xu, W.; Liu, L. PCNN orchard heterologous image fusion with semantic segmentation of significance regions. *Comput. Electron. Agric.* **2024**, *216*, 108454. [CrossRef]
14. Mousavirad, S.J.; Ebrahimpour-Komleh, H. Human mental search: A new population-based metaheuristic optimization algorithm. *Appl. Intell.* **2017**, *47*, 850–887. [CrossRef]
15. Karaman, A.; Pacal, I.; Basturk, A.; Akay, B.; Nalbantoglu, U.; Coskun, S.; Sahin, O.; Karaboga, D. Robust real-time polyp detection system design based on YOLO algorithms by optimizing activation functions and hyper-parameters with artificial bee colony (ABC). *Expert Syst. Appl.* **2023**, *221*, 119741. [CrossRef]
16. Pacal, I.; Karaboga, D. A robust real-time deep learning based automatic polyp detection system. *Comput. Biol. Med.* **2021**, *134*, 104519. [CrossRef]
17. Zhou, S.; Cai, K.; Feng, Y.; Tang, X.; Pang, H.; He, J.; Shi, X. An accurate detection model of Takifugu rubripes using an improved YOLO-V7 network. *J. Mar. Sci. Eng.* **2023**, *11*, 1051. [CrossRef]
18. Wu, T.H.; Wang, T.W.; Liu, Y.Q. Real-time vehicle and distance detection based on improved YOLO v5 network. In Proceedings of the 2021 3rd World Symposium on Artificial Intelligence (WSAI), Guangzhou, China, 18–20 June 2021; pp. 24–28.
19. Ma, L.; Zhao, L.; Wang, Z.; Zhang, J.; Chen, G. Detection and counting of small target apples under complicated environments by using improved YOLOv7-tiny. *Agronomy* **2023**, *13*,1419. [CrossRef]
20. Tîrziu, E.; Vasilevschi, A.-M.; Alexandru, A.; Tudora, E. Enhanced Fall Detection Using YOLOv7-W6-Pose for Real-Time Elderly Monitoring. *Future Internet* **2024**, *16*, 472. [CrossRef]
21. Bochkovskiy, A.; Wang, C.Y.; Liao, H.Y.M. YOLOv4: Optimal speed and accuracy of object detection. *arXiv*, **2020**, arXiv:2004.10934.
22. Sarıkaya, M.S.; Hamida El Naser, Y.; Kaçar, S.; Yazıcı, İ.; Derdiyok, A. Chaotic-Based Improved Henry Gas Solubility Optimization Algorithm: Application to Electric Motor Control. *Symmetry* **2024**, *16*, 1435. [CrossRef]
23. Pant, M.; Zaheer, H.; Garcia-Hernandez, L.; Abraham, A. Differential Evolution: A review of more than two decades of research. *Eng. Appl. Artif. Intell.* **2020**, *90*, 103479.
24. Liu, Z.; Sun, M.; Zhou, T.; Huang, G. Rethinking the value of network pruning. *arXiv* **2018**, arXiv:1810.05270.
25. Gou, J.; Yu, B.; Maybank, S.J.; Tao, D. Knowledge distillation: A survey. *Int. J. Comput. Vis.*, **2021**, *129*, 1789–1819. [CrossRef]
26. Buciluǎ, C.; Caruana, R.; Niculescu-Mizil, A. Model compression. In Proceedings of the 12th ACM SIGKDD International Conference on Knowledge Discovery and Data Mining, Philadelphia, PA, USA, 20–23 August 2006; pp. 535–541.

27. Saxena, D.; Cao, J. Generative adversarial networks (GANs) challenges, solutions, and future directions. *ACM Comput. Surv. (CSUR)*, **2021**, *54*, 1–42. [CrossRef]
28. Wang, Y.; Bai, H.; Sun, L.; Tang, Y.; Huo, Y.; Min, R. The Rapid and Accurate Detection of Kidney Bean Seeds Based on a Compressed Yolov3 Model. *Agriculture* **2022**, *12*, 1202. [CrossRef]
29. Hasler, M.; Maistrenko, Y.L. An introduction to the synchronization of chaotic systems: Coupled skew tent maps. *IEEE Trans. Circuits Syst. Fundam. Theory Appl.* **1997**, *44*, 856–866. [CrossRef]
30. Tang, J.; Wang, L. A whale optimization algorithm based on atom-like structure differential evolution for solving engineering design problems. *Sci. Rep.* **2024**, *14*, 795. [CrossRef] [PubMed]
31. Tang, J.; Wang, L. Sine Cosine Algorithm for Elite Individual Collaborative Search and Its Application in Mechanical Optimization Designs. *Biomimetics* **2023**, *8*, 576. [CrossRef] [PubMed]
32. Rafikov, M.; Balthazar, J.M. On an optimal control design for Rössler system. *Phys. Lett. A* **2004**, *333*, 241–245. [CrossRef]
33. Wang, J.; Zhou, B.; Zhou, S. An improved cuckoo search optimization algorithm for the problem of chaotic systems parameter estimation. *Comput. Intell. Neurosci.* **2016**, *2016*, 2959370. [CrossRef] [PubMed]
34. Awrejcewicz, J.; Mrozowski, J. Bifurcations and chaos of a particular van der Pol-duffing oscillator. *J. Sound Vib.* **1989**, *132*, 89–100. [CrossRef]
35. Lazzús, J.A.; Rivera, M.; López-Caraballo, C.H. Parameter estimation of Lorenz chaotic system using a hybrid swarm intelligence algorithm. *Phys. Lett. A* **2016**, *380*, 1164–1171. [CrossRef]
36. Kocamaz, U.E.; Uyaroğlu, Y. Controlling Rucklidge chaotic system with a single controller using linear feedback and passive control methods. *Nonlinear Dyn.* **2014**, *75*, 63–72. [CrossRef]
37. Mirjalili, S. SCA: A Sine Cosine Algorithm for solving optimization problems. *Knowl. Based Syst.* **2016**, *96*, 120–133. [CrossRef]
38. Mirjalili, S.; Lewis, A. The Whale Optimization Algorithm. *Adv. Eng. Softw.* **2016**, *95*, 51–67. [CrossRef]
39. Kennedy, J.; Eberhart, R. Particle swarm optimization. In Proceedings of the ICNN'95—International Conference on Neural Networks, Perth, WA, Australia, 27 November–1 December 1995; Volume 4, pp. 1942–1948. [CrossRef]
40. Tammina, S. Transfer learning using vgg-16 with deep convolutional neural network for classifying images. *Int. J. Sci. Res. Publ. (IJSRP)* **2019**, *9*, 143–150. [CrossRef]
41. Koonce, B. ResNet 50. In *Convolutional Neural Networks with Swift for Tensorflow: Image Recognition and Dataset Categorization*; Springer: Cham, Switzerland, 2021; pp. 63–72.
42. Nandhini, S.; Ashokkumar, K. An automatic plant leaf disease identification using DenseNet-121 architecture with a mutation-based henry gas solubility optimization algorithm. *Neural Comput. Appl.* **2022**, *34*, 5513–5534. [CrossRef]
43. Dai, Q.; Guo, Y.; Li, Z.; Song, S.; Lyu, S.; Sun, D.; Wang, Y.; Chen, Z. Citrus disease image generation and classification based on improved FastGAN and EfficientNet-B5. *Agronomy* **2023**, *13*, 988. [CrossRef]
44. Kavyashree, P.S.P.; El-Sharkawy, M. Compressed mobilenet v3: A light weight variant for resource-constrained platforms. In Proceedings of the 2021 IEEE 11th Annual Computing and Communication Workshop and Conference (CCWC), Online, 27–30 January 2021.
45. Gu, Y.; Wang, Y.; Li, Z.; Zhang, T.; Li, Y.; Wang, G.; Cao, H. A fault diagnosis method of four-mass vibration MEMS gyroscope based on ResNeXt-50 with attention mechanism and improved EWT algorithm. *Micromachines* **2023**, *14*, 1287. [CrossRef] [PubMed]

Disclaimer/Publisher's Note: The statements, opinions and data contained in all publications are solely those of the individual author(s) and contributor(s) and not of MDPI and/or the editor(s). MDPI and/or the editor(s) disclaim responsibility for any injury to people or property resulting from any ideas, methods, instructions or products referred to in the content.

symmetry

MDPI

Article

On Superization of Nonlinear Integrable Dynamical Systems

Anatolij K. Prykarpatski [1,2,*], Radosław A. Kycia [1] and Volodymyr M. Dilnyi [2]

[1] Department of Computer Science and Telecommunication, Cracow University of Technology, 31-155 Kraków, Poland; radoslaw.kycia@pk.edu.pl
[2] Department of Advanced Mathematics, Lviv Polytechnic National University, 79013 Lviv, Ukraine; volodymyr.dilnyi@lpnu.ua
* Correspondence: pryk.anat@cybergal.com

Abstract: We study an interesting superization problem of integrable nonlinear dynamical systems on functional manifolds. As an example, we considered a quantum many-particle Schrödinger–Davydov model on the axis, whose quasi-classical reduction proved to be a completely integrable Hamiltonian system on a smooth functional manifold. We checked that the so-called "naive" approach, based on the superization of the related phase space variables via extending the corresponding Poisson brackets upon the related functional supermanifold, fails to retain the dynamical system super-integrability. Moreover, we demonstrated that there exists a wide class of classical Lax-type integrable nonlinear dynamical systems on axes in relation to which a superization scheme consists in a reasonable superization of the related Lax-type representation by means of passing from the basic algebra of pseudo-differential operators on the axis to the corresponding superalgebra of super-pseudodifferential operators on the superaxis.

Keywords: supersymmetry; super-differentiation; Lie superalgebra; algebra of pseudo-differential operators; coadjoint action; lax integrability; Lie-algebraic approach; gradient-holonomic scheme; casimir invariants; super-Poisson structure

MSC: 17B68; 17B80; 35Q53; 35G25; 35N10; 37K35; 58J70; 58J72; 34A34; 37K05; 37K10

1. Introduction

Main modern field theoretic string theories of fundamental interactions are essentially based [1–7] on supersymmetric generalizations both of the space–time variables and canonical field variables, making possible to construct governing evolution systems free of singularities and nonphysical peculiarities. As often from the very beginning field equations are considered on the usual classical phase spaces, an important problem of constructing their corresponding supersymmetric extensions [3,8–10] arises and which, during past decades, has been treated by means of various [11–21] mathematical tools and approaches. In particular, within the two-dimensional completely integrable field theories, like Sin–Gordon, Thirring, Nonlinear Schödinger, Born–Infeld, and others, their supersymmetric integrable extensions were constructed by means of natural supersymmetric generalizations either of physically motivated reasonings [1,12,13,22–33] about the system evolution regarding the energy interaction's Hamiltonian structure or the related hidden supersymmetry's Lie-algebraic structure [11,20,29,34–43], which are responsible for their complete integrability. Being interested in more detailed analysis of these superization

schemes, we considered a physically motivated [44–48] spatially one-dimensional quantum interacting many-particle model, described by the Hamiltonian operator

$$H_N = -\sum_{j=\overline{1,N}} \frac{\partial^2}{\partial x_j^2} + 2\sum_{j=\overline{1,N}} n(x_j), \tag{1}$$

of $N \in \mathbb{N}$ charged Bose-particles, specified by the position dependent intensities $n(x_j) \in \mathbb{R}$ at points $x_j \in \mathbb{R}$, $j = \overline{1,N}$, and acting on the Hilbert space $L_2(\mathbb{R}^N;\mathbb{C})$ of the corresponding quantum states. In case of a medium with an infinite number of particles, the Hamiltonian operator should be naturally considered [44,45,49] within the secondary quantized Fock space representation

$$\hat{H} = \int_{\mathbb{R}} dx[\psi_x^+(x)\psi_x(x) + 2n(x)\psi^+(x)\psi(x)], \tag{2}$$

acting already on the tensor product Fock space $\Phi \otimes \Theta$, generated by a vacuum state $|0) \in \Phi \otimes \Theta$ and, in part, creation–annihilation operators $\psi^+(x), \psi(x) : \Phi \to \Phi$, respectively, satisfying the following canonical operator commutation brackets:

$$\begin{aligned} [\psi(x), \psi^+(y)] &= \delta(x-y), \\ [\psi(x), \psi(y)] &= 0 = [\psi^+(x), \psi^+(y)] \end{aligned} \tag{3}$$

being supplemented with the operator commutation brackets

$$\begin{aligned} [\psi(x), n(y)] &= 0 = [n(x), \psi^+(y)], \\ [n(x), n(y)] &= \partial\delta(x-y)/\partial x \end{aligned} \tag{4}$$

at arbitrary points $x, y \in \mathbb{R}$ for the intensity operator $n(x) : \Theta \to \Theta$, describing the simplest self-interacting quantum medium, whose quantum states are modeled by the related Fock space Θ. The corresponding Heisenberg evolution in time $t \in \mathbb{R}$ equations [44,45,49] for the dynamical operator variables $\psi(x), \psi^+(s)$, and $n(x) : \Phi \otimes \Theta \to \Phi \otimes \Theta$ read as

$$\begin{aligned} \partial\psi/\partial t &= \frac{1}{i}[\hat{H}, \psi] = i\psi_{xx} - 2n\psi, \\ \partial n/\partial t &= \frac{1}{i}[\hat{H}, n] = -2n(\psi\ \psi^+)_x, \\ \partial\psi^+/\partial t &= \frac{1}{i}[\hat{H}, \psi^+] = -i\psi_{xx}^+ + 2n\psi^+, \end{aligned} \tag{5}$$

and were before intensively studied in [46,48] as a dynamical model for describing the mechanism of muscle contraction in living tissue. The obtained system of operator Schrödinger–Davydov-type Equation (5) allows the following quasi-classical Hamiltonian form

$$\begin{aligned} \partial\psi/\partial t &= \{H, \psi\}_P = i\psi_{xx} - 2n\psi, \\ \partial n/\partial t &= \{H, n\}_P = -2n(\psi\ \psi^*)_x, \\ \partial\psi^+/\partial t &= \{H, \psi^+\}_P = -i\psi_{xx}^* + 2n\psi^* \end{aligned} \tag{6}$$

endowed with the following quasi-classical Poisson brackets:

$$\begin{aligned} &\{\psi(x), \psi^*(y)\}_P = \delta(x-y), \{\psi(x), n(y)\}_P = 0 = \{n(x), \psi^*(y)\}_P, \\ &\{\psi(x), \psi(y)\}_P = 0 = \{\psi^*(x), \psi^*(y)\}_P, \{n(x), n(y)\}_P = \partial\delta(x-y)/\partial x \end{aligned} \tag{7}$$

at any points $x, y \in \mathbb{R}$ on a smooth functional manifold $M \subset \{(\psi, n, \psi^*) \in C^2(\mathbb{R}; \mathbb{C} \times \mathbb{R} \times \mathbb{C})\}$, easily following from (3) and (4) within the classical Dirac's correspondence [49] principle.

As was stated in [47,50,51], the derived hydrodynamic and Boltzmann–Vlasov-type kinetic equations there are related to System (7) and proved to be completely integrable Hamiltonian systems. Moreover, as will be demonstrated below, the above-derived nonlinear quasi-classical Schrödinger–Davydov system (6) proves to also be a completely integrable bi-Hamiltonian flow [52] on the functional manifold M and whose possible superization schemes are analyzed in detail in our work below.

2. Quasi-Classical Integrability and a Simple Superization Scheme

Let us begin with analyzing the integrability of the above-derived quasi-classical Schrödinger–Davydov-type nonlinear dynamical system

$$\left.\begin{array}{c} \partial\psi/\partial t = i\psi_{xx} - 2n\psi, \\ \partial n/\partial t = -2n(\psi\,\psi^*)_x \\ \partial\psi^*/\partial t = -i\psi^*_{xx} + 2n\psi^* \end{array}\right\} := K[\psi, n, \psi^*], \tag{8}$$

with respect to the evolution parameter $t \in \mathbb{R}$, considered as a smooth vector field $K : M \to T(M)$ on the functional manifold M, via making use of the gradient-holonomic scheme, devised in [51,53,54]. As a first step, we need to demonstrate the existence of an infinite hierarchy of conservation laws and to state their commuting to each other with respect the Poisson bracket (7), presented above. Namely, for any smooth functionals $\gamma, \mu \in \mathcal{D}(M)$, their Poisson bracket is calculated via the expression

$$\{\gamma, \mu\}_P = (\mathrm{grad}\gamma | P\mathrm{grad}\mu), \tag{9}$$

where $\mathrm{grad} : \mathcal{D}(M) \to T^*(M)$ denotes the Gateau derivative with respect to the usual bilinear form $(\cdot|\cdot) : T^*(M) \times T(M) \to \mathbb{C}$ and the Poisson operator $P : T^*(M) \to T(M)$ is skew-symmetric, satisfying the following weak functional relationship:

$$\{(\psi(x), n(x), \psi^*(x))^\intercal, (\psi(y), n(y), \psi^*(y))\}_P = P\delta(x - y) \tag{10}$$

for any $x, y \in \mathbb{R}$, $\delta(x - y)$—the classical generalized Dirac delta-function, acting on an arbitrary continuous function $f \in C(\mathbb{R}; \mathbb{C})$ via the symbolic integral operation $f(x) := \int_{\mathbb{R}} \delta(x - y) f(y) dy$, is satisfied for all $x \in \mathbb{R}$. To calculate the infinite hierarchy of conservation laws for the vector field (8), it is enough to study special solutions to the governing linear Noether–Lax equation:

$$\varphi_t + K'^{,*}\varphi = 0, \tag{11}$$

where $K'^{,*} : T^*(M) \to T^*(M)$ denotes the adjoint to the Frechet derivative operator $K' : T(M) \to T(M)$ of the vector field (8) and a covector $\varphi \in T^*(M)$ can be chosen as

$$\varphi = (1, a, b)^\intercal \exp(-i\lambda^2 t + \partial^{-1}\sigma(x; \lambda)), \ \ \partial/\partial x \cdot \partial^{-1} = 1, \tag{12}$$

and the expressions

$$\begin{aligned} &\sigma(x; \lambda) \sim \sum_{j \in \mathbb{Z}_+ \cup \{-2, -1\}} \sigma_j[\psi, n, \psi^*]\lambda^{-j}, a(x; \lambda) \sim \sum_{j \in \mathbb{Z}_+} a_j[\psi, n, \psi^*]\lambda^{-j}, \\ &b(x; \lambda) \sim \sum_{j \in \mathbb{Z}_+} b_j[\psi, n, \psi^*]\lambda^{-j}, \end{aligned} \tag{13}$$

are considered asymptotic with respect to an arbitrary complex parameter $\mathbb{C} \ni \lambda \to \infty$. Taking into account that

$$K'^{,*} = \begin{pmatrix} i\partial^2 - 2in & 2\psi^*\partial & 2in \\ -2i\psi & 0 & 2i\psi^* \\ 0 & 2\psi & 2in - i\partial^2 \end{pmatrix}, \tag{14}$$

one easily obtains a system of recurrent differential–algebraic relationships, giving rise to the following functional expressions:

$$\sigma_{-2} = -i, \sigma_{-1} = 1, \sigma_0 = \frac{1}{2}n, \sigma_1 = \psi^*\psi, \sigma_2 = \frac{1}{2}[n^2 - i(\psi^*\psi_x - \psi\psi_x^*)], \sigma_3 = \psi_x^*\psi_x + 2n\psi^*\psi, \tag{15}$$
$$\sigma_4 = \frac{1}{2}n^2 - 6(\psi^*\psi)^2 - \frac{1}{2}n_x^2 + 6in(\psi^*\psi_x - \psi\psi_x^*) - 2i(\psi^*\psi_{3x} - \psi\psi_{3x}^*), \ldots,$$

and so on. Since, owing to Representation (12), the quantity $\gamma(\lambda) := \int_{\mathbb{R}} dx\sigma(x;\lambda)$ is conservative with respect to the evolution parameter $t \in \mathbb{R}$ for all $\lambda \in \mathbb{C}$, we find that all functionals

$$H_0 = \frac{1}{2}\int_{\mathbb{R}} ndx, H_1 = \int_{\mathbb{R}} \psi^*\psi dx, H_2 = 1/2\int_{\mathbb{R}}[n^2 - i(\psi^*\psi_x - \psi\psi_x^*)]dx, H_3 = \int_{\mathbb{R}}(\psi_x^*\psi_x + 2n\psi^*\psi)dx, \tag{16}$$
$$H_4 = \frac{1}{2}\int_{\mathbb{R}}[n^2 - 12(\psi^*\psi)^2 - n_x^2 + 12in(\psi^*\psi_x - \psi\psi_x^*) - 4i(\psi^*\psi_{3x} - \psi\psi_{3x}^*)]dx, \ldots$$

are also conservative. To confirm now that the vector field (8) on the functional manifold M is Hamiltonian, it is enough within the gradient-holonomic scheme [53] to show that the respectively constructed conservation law

$$H_p = (\xi_p|(\psi_x, n_x, \psi_x^*)^\intercal) \tag{17}$$

for some suitably chosen $p \in \mathbb{N}$ generates the Poisson operator $P : T^*(M) \to T(M)$ for the flow (8) as

$$P = \left(\xi_p'^{,*} - \xi_p'\right)^{-1}. \tag{18}$$

For the case $p = 2$ one obtains that

$$\begin{array}{cc} H_2 = 1/2\int_{\mathbb{R}}[n^2 - i(\psi^*\psi_x - \psi\psi_x^*)]dx = & ((-i\psi^*, -\partial^{-1}n, i\psi)^\intercal|(\psi_x, n_x, \psi_x^*)^\intercal) = \\ = (\xi_2|(\psi_x, n_x, \psi_x^*)^\intercal), & \xi_2 := (-i\psi^*, -\partial^{-1}n, i\psi)^\intercal, \end{array} \tag{19}$$

giving rise to the following Poisson operator:

$$P = \left(\xi_2'^{,*} - \xi_2'\right)^{-1} = \begin{pmatrix} 0 & 0 & i \\ 0 & \partial & 0 \\ -i & 0 & 0 \end{pmatrix}. \tag{20}$$

In a similar way, as above, for the case $p = 4$, one derives the second Poisson operator:

$$Q = \left(\xi_4'^{,*} - \xi_4'\right)^{-1} = \begin{pmatrix} -12\psi\partial^{-1}\psi & 4\partial\psi + 2\psi\partial & 12\psi\partial^{-1}\psi^* - 4i\partial^2 + 8in \\ 4\psi\partial + 2\partial\psi & -\partial^3 + 4n\partial + 4\partial n & 4\psi^*\partial + 2\partial\psi^* \\ -i & 4\partial\psi^* + 2\psi^*\partial & -12\psi^*\partial\psi \end{pmatrix}, \tag{21}$$

where, by definition, $H_4 = (\xi_4|(\psi_x, n_x, \psi_x^*)^\intercal)$. Moreover, one can check that the recurrent relationships

$$Q\mathrm{grad}H_j = 2P\mathrm{grad}H_{j+2} \tag{22}$$

hold for all $j \in \mathbb{Z}_+$, meaning that the Poisson operators (20) and (21) are compatible—that is, the affine sum $\lambda P + Q : T^*(M) \to T(M)$ is also a Poisson operator for all $\lambda \in \mathbb{C}$. The latter makes it possible to state that the infinite hierarchy of conservation laws (16) is such that they are commuting to each other with respect to both Poisson brackets

$$\{H_j, H_k\}_P = 0 = \{H_j, H_k\}_Q \tag{23}$$

for all $j, k \in \mathbb{Z}_+$. Since our dynamical system (8) allows the Hamiltonian representation

$$(\psi_t, n_t, \psi_t^*)^\intercal = \{H_3, (\psi, n, \psi^*)^\intercal)\}_P = -P\text{grad } H_1[\psi, n, \psi^*], \tag{24}$$

coinciding with (6), we can formulate our first proposition.

Proposition 1. *The nonlinear Schrödinger–Davydov dynamical system (8) possesses an infinite hierarchy of conservation laws (16) commuting to each other and is an integrable bi-Hamiltonian flow on the functional manifold M.*

Remark 1. *Since the representation $(\psi_t, n_t, \psi_t^*)^\intercal = -Q\text{grad } H_1[\psi, n, \psi^*]$ holds, one states that the dynamical system (8) is bi-Hamiltonian with respect to both Poisson structures (20) and (21) on the functional manifold M.*

Recall now the Poisson brackets (7) on the functional manifold M

$$\begin{gathered}\{\psi(x), \psi^*(y)\}_P = i\delta(x-y), \{\psi(x), n(y)\}_P = 0 = \{n(x), \psi^*(y)\}_P, \\ \{\psi(x), \psi(y)\}_P = 0 = \{\psi^*(x), \psi^*(y)\}_P, \{n(x), n(y)\}_P = \partial\delta(x-y)/\partial x\end{gathered} \tag{25}$$

at all points $x, y \in \mathbb{R}$ and observe that they are canonically ultra-local [45,55] except the field variable $n \in M$, depending on the delta-function derivative.

The latter, in particular, means that this field variable cannot be secondly quantized on some suitably chosen Fock space Θ. Nonetheless, this quantization can be performed, if carried out to superize the functional manifold M by means of the following scheme: $(\psi, n, \psi^*) \ni M \to (\tilde{\psi}, \tilde{n}, \tilde{\psi}^*) \simeq (\tilde{\psi}, \tilde{u}, \tilde{\psi}^*) \in \tilde{M} \in C^2(\mathbb{R}^{1|1}; \Lambda_0 \times \Lambda_1 \times \Lambda_0^*)$, where $\mathbb{R}^{1|1} := (x, \theta) \in \mathbb{R} \times \Lambda_1, \Lambda_0 \oplus \Lambda_1 := \Lambda^{(1|1)}$ is the classical one-dimensional Grassmann algebra over the complex field $\mathbb{C}$. To specify in more detail the superanalysis concepts used further, as well as the related superization scheme, we proceed below with some brief superanalysis preliminaries on functional supermanifolds.

3. Superanalysis Preliminaries on Superaxis $\mathbb{R}^{1|1}$

Consider the usual one-dimensional axis $\mathbb{R}^1$ and its supermanifold [8,9] extension $\mathbb{R}^{1|1}$ by means of coordinate variables $(x, \theta) \in \mathbb{R}^{1|1} \simeq \mathbb{R}^1 \times \Lambda_1$, specified by the $\mathbb{Z}_2$-graded Grassmann algebra $\Lambda^{(1|1)} = \Lambda_0 \oplus \Lambda_1$ over the field $\mathbb{C}$ with parities $p|_{\Lambda_s^{(1)}} = s, s \in \{0, 1\}$, where $x \in \mathbb{R}^1$, $\theta \in \Lambda_1^{(1)}$ and $\theta^2 = 0$, respectively. An arbitrary smooth uniform function $f \in C^\infty(\mathbb{R}^{1|1}; \Lambda^{(1|1)}) \simeq C^\infty(\mathbb{R}^1; \Lambda^{(1|1)}) \times \Lambda^{(1)}, p(f) \in \{0, 1\}$ is at point $(x, \theta) \in \mathbb{R}^1 \times \Lambda_1$, representable as

$$f(x, \theta) = f_0(x) + \theta f_1(x), \tag{26}$$

where the coefficients $f_0, f_1 \in C^\infty(\mathbb{R}^1; \Lambda_{k\,\mathrm{mod}\,2}^{(1|1)})$ and their parities $p(f_k) = p(f) + k\mathrm{mod}2$. The linear space of functions (26) over the $\mathbb{Z}_2$-graded Grassmann algebra $\Lambda^{(1)}$ generates the $\mathbb{Z}_2$-graded algebra $C^\infty(\mathbb{R}^{1|1}; \Lambda^{(1|1)})$, and the linear subspace of functions (26) with component $f_0(x) = 0, x \in \mathbb{R}^1$, generates its nilpotent ideal $J(\mathbb{R}^{1|1}; \Lambda^{(1)}) \subset C^\infty(\mathbb{R}^{1|1}; \Lambda^{(1|1)})$.

We also remark that the factor space $C^\infty(\mathbb{R}^{1|1};\Lambda^{(1|1)})/J(\mathbb{R}^{1|1};\Lambda^{(1)}) \simeq C^\infty(\mathbb{R}^1;\Lambda^{(1|1)})$ is equivalent to the space of coefficients of the algebra $C^\infty(\mathbb{R}^{1|1};\Lambda^{(1)})$.

Consider now a diffeomorphism of the superaxis $\mathbb{R}^{1|1}$, which is, by definition, a parity preserving the algebra automorphism of $C^\infty(\mathbb{R}^{1|1};\Lambda^{(1|1)})$, inducing a related homomorphism of $C^\infty(\mathbb{R}^1;\Lambda^{(1)})$.

Definition 1. *The corresponding linear space $\mathcal{G}(1,1) := Vect(\mathbb{R}^{1|1};\Lambda^{(1)})$ of vector fields on the superaxis $\mathbb{R}^{1|1}$ is, by definition, the Lie superalgebra of all derivations of the superalgebra $C^\infty(\mathbb{R}^{1|1};\Lambda^{1,1})$: that is, for any uniform vector field $a \in \mathcal{G}(1|1)$ with parity $p(a) \in \{0,1\}$, the condition $a(fg) = a(f)g + (-1)^{p(a)p(f)}fa(g)$ holds for any uniform function $f \in C^\infty(\mathbb{R}^{1|1};\Lambda^{(1)})$, $p(f) \in \{0,1\}$, and $g \in C^\infty(\mathbb{R}^{1|1};\Lambda^{(1)})$.*

The Lie superalgebra $\mathcal{G}(1|1)$-graded commutators of any uniform elements $a, b \in \mathcal{G}(1|1)$ can be recalculated as

$$[a,b](f) = a(b(f)) - (-1)^{p(a)p(b)}b(a(f)), \tag{27}$$

where $f \in C^\infty(\mathbb{R}^{1|1};\Lambda^{(1)})$. The above-constructed Lie superalgebra $\mathcal{G}(1|1)$ satisfies the Leibnitz super-commutator relationships

$$[a,b] = -(-1)^{p(a)p(b)}[b,a],$$
$$[a,[b,c]] = [[a,b],c] + (-1)^{p(a)p(b)}[b,[a,c]]$$

for arbitrary a, b, and $c \in \mathcal{G}(1|1)$, and is generated by sections $\Gamma(\mathbb{R}^{1|1})$ of the tangent bundle $\left(T(\mathbb{R}^{1|1}),\pi,\mathbb{R}^{1|1}\right)$ over the superaxis $\mathbb{R}^{1|1}$, being equivalent to the free left $C^\infty(\mathbb{R}^{1|1};\Lambda^{(1)})$-module with basis $(\partial/\partial x;\partial/\partial\theta)$ and parities $p(\partial/\partial x) = 0, p(\partial/\partial\theta) = 1$, respectively.

Consider now an infinite-dimensional functional supermanifold $M^{n|1} \subset C^\infty(\mathbb{R}^{1|1};\Lambda^{(1)n})$, $n \in \mathbb{N}$, and a smooth vector field $K : M^{n|1} \to T(M^{n|1})$, where $T(M^{n|1})$ denotes the corresponding tangent space to $M^{n|1}$, and let $du/d\tau \in T(M^{n|1}), \tau \in \Lambda^{(1|1)}$, be the related one-parametric superflow on $M^{n|1}$, satisfying at each point $u \in M^{n|1}$ the relationship

$$du/d\tau = K[u], \tag{28}$$

called a dynamical supersystem on the supermanifold $M^{n|1}$.

Definition 2. *The above-introduced vector superfield $d/d\tau : M^{n|1} \to T(M^{n|1})$ with respect to the evolution superparameter $\tau \in \Lambda^{(1)}$ is called supersymmetric if it allows the following representation: $d/d\tau = \partial/\partial\theta + \theta\partial/\partial t$, where $t \in \mathbb{R}$ is a real evolution parameter.*

As we are interested in describing infinite-dimensional dynamical superflows (28), which are super-integrable Hamiltonian flows on the supermanifold $M^{n|1}, n \in \mathbb{N}$, that is possessing infinite hierarchies of commuting to each other conservation laws with respect to the corresponding Poisson structures on $M^{n|1}$, we need to provide at least sufficient conditions imposed on a superflow under regard allowing to state that it is superintegrable. The latter, in particular, means that this superflow is invariant with respect to some hidden supergroup symmetry, whose coadjoint orbits [53,55,56] prove to be equivalent to the superflow under regard. Within the gradient-holonomic approach, devised in [53,57], the existence of conservation laws to a given dynamical superflow (28) is ensured by solutions to the following Noether-Lax differential-functional equation

$$\partial\varphi/\partial\tau + K'^{,*}[u]\varphi = 0, \tag{29}$$

on the element $\varphi := \mathrm{grad}\,\gamma \in T^*(M^{n|1})$, where $K'^{,*}[u] : T^*(M^{n|1}) \to T^*(M^{n|1})$ denotes the usual adjoint Frechet derivative of the mapping $K : M^{n|1} \to T(M^{n|1})$ at a point $u \in M^{n|1}$ and $\gamma \in \mathcal{D}(M^{n|1})$ is a smooth functional on the supermanifold $M^{n|1}$ *a priori* invariant with respect to the superflow (28). To describe in more detail the supersymmetry properties of the superflow (28), we will consider the supersymmetric vector field $D_\theta := \partial/\partial\theta + \theta\partial/\partial x$ on the supermanifold $M^{n|1}$, which satisfies the following important for further properties:

$$D_\theta^2 = \partial/\partial x, \quad i_{D_\theta}\alpha^{(1)} = 0 \tag{30}$$

for all $(x,\theta) \in \mathbb{R}^{1|1}$, where $\alpha^{(1)} := dx + \theta d\theta \in T^*(\mathbb{R}^{1|1})$ denotes the canonical contact form [18,29,58,59] on the superaxis $\mathbb{R}^{1|1}$. In particular, the linear space $\mathcal{K}(1|1)$ over $\Lambda^{(1)}$ of all conformal vector fields $K_f : \mathbb{R}^{1|1} \to T(\mathbb{R}^{1|1})$ for $f \in C^\infty(\mathbb{R}^{1|1};\Lambda^{(1)}) \simeq M_c^{1|1}$, leaving the contact form invariant, compile a conformal Lie superalgebra, whose coadjoint action on the naturally related adjoint space $\mathcal{K}(1|1)^*$ regarding the canonical bilinear form

$$(l|K_f) := \int_{\mathbb{R}^1} dx \int d\theta f(x,\theta) l(x,\theta) \tag{31}$$

for $(l, K_f) \in \mathcal{K}(1|1)^* \times \mathcal{K}(1|1)$, generates [29,53,55,59] the corresponding dynamical supersystems on the supermanifold $M_c^{1|1}$. Here, the super-integration $\int dx \int d\theta(\cdot)$ "measure" is defined [8] on the superaxis $\mathbb{R}^{1|1}$ via the following rules:

$$\int \theta d\theta = 1, \int d\theta = 0. \tag{32}$$

Moreover, taking into account that the adjoint space $\mathcal{K}(1|1)^*$ is Poissonian, carrying the canonical Lie-Poisson structure [55], this algebraic scheme makes it possible to construct on the supermanifold $M_c^{1|1}$ a special subset of so called super-Hamiltonian vector fields, which prove to be completely integrable within the classical Liouville-Arnold integrability type definition.

Returning now to our Hamiltonian system (24) on the functional supermanifold $\tilde{M} \subset C^\infty(\mathbb{R}^{1|1}; \times\Lambda_1^{(1)} \times \Lambda_0^{(1)*})$, let us analyze the two most natural ways of its superization:

The first one consists in constructing on the supermanifold $\tilde{M}$ a superflow

$$\tilde{K} : \tilde{M} \to T(\tilde{M}), \tag{33}$$

related with a suitably chosen super-connection [11,14,15,41] on the two-dimensional spacetime $\mathbb{R}^2$ with the vanishing curvature, and whose structure supergroup leaves invariant the corresponding Casimir invariants and generates, respectively, an infinite hierarchy of conservation laws, reducing to *a priori* given quasi-classical conservation laws of the dynamical system (8) under regard. In particular, the supermanifold $\tilde{M}$ is equipped with the corresponding super-variables $(\tilde{\psi}, \tilde{u}, \tilde{\psi}^*) \in \tilde{M}$, which admit the following superalgebraic expansions:

$$\begin{aligned} &\tilde{\psi}(x,\theta) = \psi_0(x) + \theta\psi_1(x) \in \Lambda_0, \tilde{\psi}^*(x,\theta) = \psi_0^*(x) + \theta\psi_1^*(x) \in \Lambda_0^*, \\ &\tilde{u}(x,\theta) = u_1(x) + \theta u_0(x) \in \Lambda_0, \end{aligned} \tag{34}$$

entering in the corresponding Hamiltonian function

$$\tilde{H} = \int_{\mathbb{R}} dx \int d\theta [\tilde{\psi}_{\theta\theta}^*(x,\theta)\tilde{\psi}_{\theta\theta}(x,\theta) + 2\tilde{n}(x,\theta)\tilde{\psi}^*(x,\theta)\tilde{\psi}(x,\theta)], \tag{35}$$

This superization scheme is mainly based on the super-analysis techniques, first described in [7–9] and developed later, regarding integrable super-symmetric dynamical systems,

in [4,11,14–18,20,28,59]. In particular, in [11], as well as in [14], there were proposed superization schemes, generalizing the classical associated zero curvature condition for the components of the corresponding super connection on the two-dimensional space-time $\mathbb{R}^2$, rigged with the Lie supergroup $SL(2|1)$, that allowed them to construct integrable supersymmetric Korteweg-deVries and Nonlinear Schrödinger type dynamical systems on supermanifolds.

The second one consists in the natural superization of a given quasi-classical Poisson structure to that on the corresponding functional supermanifold $\tilde{M}$ and was originally proposed in [1,13,60], which regarding to our quasi-classical Poisson brackets (25), leads to introducing the superfield $\tilde{n} := \tilde{u}_\theta = D_\theta \tilde{u}$ and next transforming the quasi-classical Poisson brackets (25) into the following ultra-canonical super-Poisson brackets

$$\{\tilde{\psi}(x,\theta),\tilde{\psi}^*(y,\eta)\}_{\tilde{P}} = i\delta(x,\theta|y,\eta), \{\tilde{\psi}(x,\theta),\tilde{u}(y,\eta)\}_{\tilde{P}} = 0 = \{\tilde{u}(x,\theta),\tilde{\psi}^*(y,\eta)\}_{\tilde{P}}, \quad (36)$$
$$\{\tilde{\psi}(x,\theta),\tilde{\psi}(y,\eta)\}_{\tilde{P}} = 0 = \{\tilde{\psi}^*(x,\theta),\tilde{\psi}^*(y,\eta)\}_{\tilde{P}}, \{\tilde{u}(x,\theta),\tilde{u}(y,\eta)\}_{\tilde{P}} = \delta(x,\theta|y,\eta)$$

at all super-points $(x,\theta),(y,\eta) \in \mathbb{R}^{1|1}$, where

$$\delta(x,\theta|y,\eta) = \delta(x-y-\theta\eta)(\theta-\eta) \quad (37)$$

denotes the supersymmetric Dirac delta-function, satisfying for any continuous super-function $\tilde{f} \in C^0(\mathbb{R}^{1|1};\Lambda)$ the determining relationship

$$\tilde{f}(x,\theta) := \int_{\mathbb{R}} dy \int d\eta \delta(x,\theta|y,\eta)\tilde{f}(y,\eta) \quad (38)$$

for all $(x,\theta) \in \mathbb{R}^{1|1}$ jointly with the mentioned above (32) Berezin integrals [8–10], assumed to be fulfilled, and which is appropriately applied to the super-generalized quasi-classical Hamiltonian function (35). Since the super-Poisson operator $\tilde{P} : T^*(\tilde{M}) \to T^*(M)$, corresponding to the Poisson superbrackets (36), acts on the cotangent superspace $T^*(\tilde{M})$, adjoint to the supersymmetric tangent space $T(\tilde{M})$, the latter can be endowed with the following super-bilinear form $(\cdot|\cdot) : T^*(\tilde{M}) \times T(\tilde{M}) \to \Lambda_0$, where for any $\tilde{f} \in T^*(\tilde{M}), \tilde{g} \in T(\tilde{M})$:

$$(\tilde{f}|\tilde{g}) := \int_{\mathbb{R}} dx \int d\theta \langle \tilde{f}(x,\theta)|\tilde{g}(x,\theta)\rangle_{\mathbb{E}^3}. \quad (39)$$

Having now applied the super-Poisson operator $\tilde{P} : T^*(\tilde{M}) \to T(\tilde{M})$ brackets (36) to the superized Hamiltonian function $H \in \mathcal{D}(M)$ in the form

$$\tilde{H} = \int_{\mathbb{R}} dx \int d\theta [\tilde{\psi}^*_{\theta\theta}(x,\theta)\tilde{\psi}_{\theta\theta}(x,\theta) + 2\tilde{u}_\theta(x,\theta)\tilde{\psi}^*(x,\theta)\tilde{\psi}(x,\theta)], \quad (40)$$

one derives the super-Hamiltonian system

$$\tilde{\psi}_t = \{\tilde{H},\tilde{\psi}\}_{\tilde{P}} = i\tilde{\psi}_{4\theta} - 2\tilde{u}_\theta\tilde{\psi}, \tilde{u}_t = -2(\tilde{\psi}^*\tilde{\psi})_\theta, \quad (41)$$
$$\tilde{\psi}^*_t = \{\tilde{H},\tilde{\psi}^*\}_{\tilde{P}} = -i\tilde{\psi}^*_{4\theta} + 2\tilde{u}_\theta\tilde{\psi}^*,$$

with respect to the real temporal parameter $t \in \mathbb{R}$, in relation to which one poses the following natural question:

Problem 1. *Does it inherit the classical integrability property of the Schrödinger–Davydov dynamical system (8) as considered on the functional supermanifold $\tilde{M}$? This will be analyzed in the section to follow.*

The question posed above is deeply motivated by the fact that the obtained superized Schrödinger–Davydov dynamical system (41) both reduces to its classical version (8) on the functional supermanifold M and simultaneously describes the related evolution of two anticommuting fermionic fields, nontrivially interacting with basic bosonic fields, defined by means of the expansions (34). The latter can be in part interpreted as the existence of an additional yet hidden inter-particle vacuum-based interaction, not taken into account a priori within the quantum Hamiltonian operator (2).

Remark 2. *The superization scheme that we applied to the quasi-classical Schrödinger–Davydov dynamical system (8) is strictly based on the superization of the classical field supermanifold M via the superization of the related non-ultralocal Poisson structure (25). The corresponding Hamiltonian equations (41), determining the evolution on the constructed functional supermanifold $\tilde{M}$, are those which presumably can describe additional hidden interparticle vacuum-based interaction of the quasi-classical fields under consideration, which are interesting for applications both in solid-state physics and modeling the muscle contraction mechanism in living tissue, as mentioned before.*

4. Superintegrability Analysis

Since we are interested in studying the superintegrability of the infinite-dimensional dynamical superflow (41) as a Hamiltonian flow on the supermanifold $\tilde{M}$, which possesses an infinite hierarchy of conservation laws commuting to each other with respect to the corresponding Poisson structures on $\tilde{M}$, we need to provide at least sufficient conditions imposed on a given superflow allowing us to state that it really passes them. The latter, in particular, means that this superflow is invariant with respect to some hidden supergroup symmetry, whose structure can be revealed within the effective gradient-holonomic approach, devised before in [51,53,54,57] and applied to diverse nonlinear dynamical systems. Concerning the super-integrability problem regarding the super-Hamiltonian system (41), we will rewrite it as the vector superfield

$$\left.\begin{array}{c} \partial\tilde{\psi}/\partial t = i\tilde{\psi}_{4\theta} - 2\tilde{u}_\theta\tilde{\psi}, \\ \partial\tilde{u}/\partial t = -2(\tilde{\psi}^*\tilde{\psi})_\theta \\ \partial\tilde{\psi}^*/\partial t = -i\tilde{\psi}^*_{4\theta} + 2\tilde{u}_\theta\tilde{\psi}^* \end{array}\right\} := \tilde{K}[\tilde{\psi}, \tilde{u}, \tilde{\psi}^*], \tag{42}$$

on the superized functional supermanifold $\tilde{M}$, and look within the gradient-holonomic approach [53,57] for special solutions to the corresponding Noether–Lax equation

$$\tilde{\varphi}_t + \tilde{K}'^{,*}\tilde{\varphi} = 0 \tag{43}$$

in the following asymptotic ax $\mathbb{C} \ni \lambda \to \infty$ form:

$$\tilde{\varphi} = (1, \tilde{a}, \tilde{b})^\intercal \exp[-i\lambda^2 t + D_\theta^{-1}\tilde{\sigma}(x,\theta)], \tag{44}$$

where

$$\begin{aligned} &\tilde{\sigma}(x,\theta;\lambda) \sim \sum_{j\in\mathbb{Z}_+\cup\{-2,-1\}} \tilde{\sigma}_j[\tilde{\psi}, \tilde{u}, \tilde{\psi}^*]\lambda^{-j}, \tilde{a}(x,\theta;\lambda) \sim \sum_{j\in\mathbb{Z}_+} \tilde{a}_j[\tilde{\psi}, \tilde{u}, \tilde{\psi}^*]\lambda^{-j}, \\ &\tilde{b}(x,\theta;\lambda) \sim \sum_{j\in\mathbb{Z}_+} \tilde{b}_j[\tilde{\psi}, \tilde{u}, \tilde{\psi}^*]\lambda^{-j}, \end{aligned} \tag{45}$$

at arbitrary point $(x,\theta)\in\mathbb{R}^{1|1}$. Taking into account that the adjoint operator $\tilde{K}'^{,*}: T^*(\tilde{M})\to T^*(\tilde{M})$ is given by the expression

$$\tilde{K}'^{,*}=\begin{pmatrix} iD_\theta^4-2i\tilde{u}_\theta & -2\tilde{\psi}^*D_\theta & 0\\ 2iD_\theta\tilde{\psi} & 0 & -2iD_\theta\tilde{\psi}^*\\ 0 & -2\tilde{\psi}D_\theta- & 2i\tilde{u}_\theta-iD_\theta^4 \end{pmatrix}, \tag{46}$$

one obtains easily the following infinite recurrent system:

$$\begin{gathered} -i\delta_{j,-2}+\ D_\theta^{-1}\tilde{\sigma}_{j-k,\theta}\tilde{\sigma}_{k,\theta}+i\tilde{\sigma}_{j,x\theta}-2i\tilde{u}_\theta\delta_{j,0}-2\tilde{\psi}^*\tilde{a}_{j,\theta}+2\tilde{\psi}\tilde{a}_{j-k}\tilde{a}_k=0,\\ \tilde{a}_{j,\theta}-i\tilde{a}_{j+2}+\tilde{a}_{j-k,\theta}D_\theta^{-1}\tilde{\sigma}_{k,t}+2i\tilde{\psi}_\theta\delta_{j,0}+2i\tilde{\psi}\tilde{\sigma}_j-2i\tilde{\psi}_\theta^*\tilde{b}_j-2i\tilde{\psi}^*\tilde{b}_{j,\theta}-2i\tilde{\psi}^*\tilde{b}_{j-k}\ \tilde{\sigma}_k=0,\\ \tilde{b}_{j,\theta}-i\tilde{b}_{j+2}+\tilde{b}_{j-k,\theta}D_\theta^{-1}\tilde{\sigma}_{k,t}-2\tilde{\psi}\tilde{a}_{j,\theta}+2\tilde{\psi}\tilde{a}_{j-k,}\tilde{\sigma}_k+2i\tilde{u}_\theta\tilde{b}_j-\\ -i(\tilde{b}_{j,xx}+2\tilde{b}_{j-k}\tilde{\sigma}_{k,\theta}+\tilde{b}_{j-k}\tilde{\sigma}_{k,\theta x}+\tilde{b}_{j-k}\tilde{\sigma}_{k-s,\theta}\tilde{\sigma}_{s,\theta})=0 \end{gathered} \tag{47}$$

for all $j\in\mathbb{Z}_+\cup\{-2,-1\}$. Trying to dissolve recurrently the above system (47), we obtain that first its coefficients are equal to

$$\begin{gathered} \tilde{\sigma}_{-1}=\theta,\tilde{\sigma}_0=0,\tilde{\sigma}_1=\tilde{u},\tilde{a}_0=0,\tilde{a}_1=2\tilde{\psi}\theta,\\ \tilde{a}_2=2\tilde{\psi}_\theta,\tilde{b}_0=0,\tilde{b}_1=0,b_2=0, \end{gathered} \tag{48}$$

but the second coefficient $\tilde{\sigma}_2$ satisfies the locally unsolvable differential–algebraic relationship

$$\tilde{\sigma}_{2,\theta}=-\frac{1}{2}\tilde{u}_{x\theta}+3\tilde{\psi}^*\tilde{\psi}, \tag{49}$$

saying us that the recurrent system (47) fails to be infinitely continued. As an inference from this failure, we need to state that our naively constructed super-Hamiltonian system (41) does not possess an infinite hierarchy of conservation laws and is suitably not super-integrable on the superized functional supermanifold $\tilde{M}$. This negative result is also instructive, per se, informing us that a simple naive a priori superization of a classical integrable nonlinear dynamical system generally loses its integrability, or, in other words, "*Der Irrtum ist eine ebenso wichtige Lebensbedingung wie die Wahrheit*", i.e., "*Error is as important a condition for the progress of life as truth*" (by C.G. Jung: [61]).

In order to construct a more feasible and in some sense natural superization of the nonlinear dynamical Schrödinger-Davydov system (8), we first proceed to present its classical Lax-type operator representation, and then its suitably superized generalization, which will generate a priori integrable super-Hamiltonian flows, which we are interested in finding.

5. The Lax-Type Representation Scheme

We will start from the infinite hierarchy of gradient relationships (22) and observe that it can be rewritten as

$$Q\mathrm{grad}\ \gamma(\lambda)=2\lambda^2P\mathrm{grad}\ \gamma(\lambda), \tag{50}$$

where, by definition,

$$\gamma(\lambda):=\int_{\mathbb{R}}dx\sigma(x;\lambda)\sim\sum_{j\in\mathbb{Z}_+}\lambda^{-j}\int_{\mathbb{R}}H_j[\psi,n,\psi^*]dx \tag{51}$$

is a generating as $\mathbb{C} \ni \lambda \to \infty$ function of conservation laws for the dynamical system (8), which can be identified [51,53,55] with the trace-functional of the monodromy matrix $S(x;\lambda) \in \text{End}\, \mathbb{E}^m$, $x \in \mathbb{R}$, naturally assigned to a matrix Lax-type "spectral" problem:

$$\partial f/\partial x = l[\psi, n, \psi^*; \lambda] f, \tag{52}$$

where $l[\psi, n, \psi^*; \lambda] \in \text{End}\, \mathbb{E}^m$ for some finite $m \in \mathbb{N}$ is considered—for brevity, 2π-periodic in $x \in \mathbb{R}$ and $f \in L_\infty(\mathbb{R}; \mathbb{E}^m)$. Namely, given

$$\gamma(\lambda) := \text{tr}\, S(x;\lambda), \tag{53}$$

where by definition, $S(x;\lambda) := F(x + 2\pi\pi, x; \lambda)$ and $F(x, y; \lambda) \in \text{End}\, \mathbb{E}^m$, $F(x, x; \lambda) = I$, $x \in \mathbb{R}$, denotes the fundamental matrix for the linear problem (52), depending on a point $(\psi, n, \psi^*) \in M$. Taking into account that the gradient element $\varphi(x;\lambda) := \text{grad}\gamma(\lambda) \in T^*(M)$ for all $(x;\lambda) \in \mathbb{R} \times \mathbb{C}$ satisfies the gradient relationship (50) and can be simultaneously represented as

$$\varphi(x;\lambda) = \text{tr}(l[\psi, n, \psi^*; \lambda]'^* S(x;\lambda))), \tag{54}$$

where the monodromy matrix $S(x;\lambda) \in \text{End}\, \mathbb{E}^m$ solves [62] on the axis $\mathbb{R}$ the linear Novikov equation

$$\partial S/\partial x = [l, S], \tag{55}$$

one can suitably construct within the gradient-holonomic scheme [51,53] a finite set of differential algebraic matrix relationships on a searched mapping $l[\psi, n, \psi^*; \lambda] \in \text{End}\, \mathbb{E}^m$, tr $l[\psi, n, \psi^*; \lambda] = 0$, whose solution gives rise via simple enough but cumbersome calculations to the following result: $m = \dim l[\psi, n, \psi^*; \lambda] = 3$ and

$$l[\psi, n, \psi^*; \lambda] = \begin{pmatrix} 2i\lambda - \frac{in}{2\lambda} & \psi^* & -\frac{in}{2\lambda} \\ \frac{\psi}{2\lambda} & 0 & \frac{\psi}{2\lambda} \\ \frac{in}{2\lambda} & \psi^* & \frac{in}{2\lambda} - 2i\lambda \end{pmatrix}. \tag{56}$$

It is now easy to observe that the linear Lax-type spectral problem (52) reduces to the following pseudo-differential form:

$$-\partial^2 f/\partial x^2 + 2nf - 2i\psi^* \partial^{-1} \psi f = 4\lambda^2 f, \tag{57}$$

where $f \in W \subset L_\infty(\mathbb{R}; \mathbb{C})$ is a scalar function and $\lambda \in \mathbb{C}$ serves as a true spectral parameter.

Remark 3. *If one denotes the pseudo-differential expression from (57) as*

$$L := -\partial^2/\partial x^2 + 2n - 2i\psi^* \partial^{-1} \psi, \tag{58}$$

then one can construct [53,54,56,63] the same infinite hierarchy of conservation laws as (16) by means of the operator traces

$$H_j = \text{Tr}\left(L^{1/2} L^j\right), \tag{59}$$

where $L, L^{j/2} \in \Psi OP, j \in \mathbb{Z}_+$, *and* Tr $: \Psi OP \to \mathbb{C}$ *is the trace operation on the algebra* ΨOP *of pseudo-differential operators on the axis, coinciding with the integral over* $\mathbb{R}$ *of the functional coefficient at the inverse differentiation* ∂^{-1}.

The spectral problem (57) looks very interesting and represents [4,64,65] the Backlund-type operator transformation

$$DOP \ni L_0 \to L_0 + \alpha\psi^*\partial^{-1}\psi \in \Psi OP \tag{60}$$

from the algebra DOP of differential operators to that of pseudo-differential operators, ΨOP, where, by definition, ψ and $\psi^* \in W$ serve, respectively, as the eigenfunctions of the spectral problem

$$L_0\psi = \mu\psi \tag{61}$$

for some $\mu \in \mathbb{C}$ and its adjoint:

$$L_0^*\psi^* = \nu^*\ \psi^* \tag{62}$$

for some $\nu^* \in \mathbb{C}$.

Remark 4. *More details of this Backlund-type operator transformation (60) can be found in [64]. We should also mention here that the compatible pair of Poisson operators (20) (21) we found follows from the canonical Poisson bracket on the space $\Psi OP \times W \times W^*$ via the operator mapping (60).*

Since the above-obtained pseudo-differential operator (60) is a shifted classical Sturm–Liouville operator on the axis $\mathbb{R}$ of the second order, whose natural superization was first studied in [59], we can logically proceed to generalizing this result on the subject of the corresponding superization of the completely integrable Schrödinger–Davydov dynamical system under consideration.

6. Spectral Operator Problem and Related Superization Scheme

Let us consider the classical Sturm–Liouville operator expression

$$L_0 := -\partial^2/\partial x^2 + 2n(x) \tag{63}$$

on the real axis with a real potential $n(x) \in \mathbb{R}$ for all $x \in \mathbb{R}$ on the functional space W and its super-differential analog

$$\tilde{L}_0 := -D_\theta^3 + 2\tilde{n}(x,\theta) \tag{64}$$

on the super-axis, constructed in [59], where $\tilde{n}(x,\theta) \in \Lambda_1^{(1)}$ for all $(x,\theta) \in \mathbb{R}^{1|1}$. The super-differential spectral problem related to (64)

$$\tilde{L}_0\tilde{\psi} = (-D_\theta^3 + 2\tilde{n})\tilde{\psi} = \mu\tilde{\psi}, \tag{65}$$

where $\mu \in \Lambda_1$ and $\tilde{\psi} \in \tilde{W} \subset L_\infty(\mathbb{R}^{1|1}; \Lambda_0)$, and its adjoint problem

$$\tilde{L}_0^*\tilde{\psi}^* = (D_\theta^3 + 2\tilde{n})\tilde{\psi} = \nu^*\tilde{\psi}, \tag{66}$$

where $\nu^* \in \Lambda_1^*$ and $\tilde{\psi}^* \in \tilde{W}^* \subset L_\infty(\mathbb{R}^{1|1}; \Lambda_0^*)$ make it possible to superize the super-differential operator (64) as

$$\tilde{L}_0 \to \tilde{L} := -D_\theta^3 + 2\tilde{n} - \ 2i\tilde{\psi}^* D_\theta^{-1}\tilde{\psi} \tag{67}$$

by shifting on the Backlund transformed term $-2i\tilde{\psi}^* D_\theta^{-1}\tilde{\psi} \in s\Psi OP$ from the algebra $s\Psi OP$ of super-pseudo-differential operators. Based on the super pseudo-differential expression (67), one can calculate [20,26,27,31,32,36–39] the corresponding conserved super-laws as the following Casimir invariant functionals:

$$\tilde{H}_j = \mathrm{sTr}\left(\tilde{L}^{2j/3}\right), \tag{68}$$

for $j \in \mathbb{Z}_+$ regarding the related Lie superalgebra Lie$(s\Psi OP)$, where the super-trace operation sTr : $s\Psi OP \to \Lambda$ is defined as the super-integral over the super-axis $\mathbb{R}^{1|1}$ of the coefficient at the inverse super-differentiation D_θ^{-1}. In particular, taking into account that

$$\begin{aligned}\tilde{L}^{1/3} \sim -D_\theta + \tilde{w}_0^1 + (\tilde{w}_1^1 + \tilde{w}_1^0 D_\theta)\partial^{-1} + (\tilde{w}_2^1 + \tilde{w}_2^0 D_\theta)\partial^{-2} + \\ + (\tilde{w}_3^1 + \tilde{w}_3^0 D_\theta)\partial^{-3} + (\tilde{w}_4^1 + \tilde{w}_4^0 D_\theta)\partial^{-4}) + \ldots,\end{aligned} \tag{69}$$

with the coefficients

$$\begin{aligned}&\tilde{w}_1^1 = 2u, \tilde{w}_2^1 = 2/3(i\overline{\Psi}_\theta\Psi - 2i\overline{\Psi}\Psi_\theta - 2u_x), \tilde{w}_3^0 = 2/3(2i\overline{\Psi}\Psi_x + u_{x,\theta} - i\overline{\Psi}_\theta\Psi_\theta),\\ &\quad \tilde{w}_2^0 = -2/3(i\overline{\Psi}\Psi + u_\theta),\\ &\tilde{w}_3^1 = 2/3(-i\overline{\Psi}_{x,\theta}\Psi - 2i\overline{\Psi}_\theta\Psi_x + 3i\overline{\Psi}\Psi_{x,\theta} + i\overline{\Psi}_x\Psi_\theta + u_{xx} - 4iu\overline{\Psi}\Psi + 2uu_\theta), \ldots\end{aligned} \tag{70}$$

and so on, we can easily calculate the super-conservation laws:

$$\begin{aligned}&\tilde{H}_{1/2} = 0, \quad \tilde{H}_1 = 0, \quad \tilde{H}_{3/2} = -2i\int dx \int d\theta\overline{\Psi}\Psi,\\ &\tilde{H}_2 = 4/3\int dx \int d\theta[i(\overline{\Psi}\Psi)_\theta + u_x],\\ &\tilde{H}_{5/2} = 2/3i\int dx \int d\theta(2\overline{\Psi}\Psi_x - 2\overline{\Psi}_x\Psi - \overline{\Psi}_\theta\Psi_\theta),\\ &\tilde{H}_3 = 2i\int dx \int d\theta(\overline{\Psi}_{x,\theta}\Psi - \overline{\Psi}\Psi_{x,\theta}), \ldots,\\ &\tilde{H}_{9/2} = \int dx \int d\theta(6i\Psi_{xxx}\overline{\Psi} + 8i\Psi_{xx}\overline{\Psi}_x - 8\Psi_x\Psi\overline{\Psi}^2 + 8\Psi^2\overline{\Psi}_x\overline{\Psi} -\\ &\quad - 2i\Psi\overline{\Psi}_{xxx} - 4iu_\theta^{(1)}\Psi_x\overline{\Psi} + 4iu_\theta^{(1)}\Psi\overline{\Psi}_x - 2i\Psi_{\theta,xx}\overline{\Psi}_\theta -\\ &\quad - 2i\Psi_{\theta,x}\overline{\Psi}_{\theta,x} - 4\Psi_\theta\overline{\Psi}_\theta\Psi\overline{\Psi} - 4iu_x^{(1)}\overline{\Psi}_\theta\Psi + 4iu_x^{(1)}\Psi_\theta\overline{\Psi} +\\ &\quad + +4iu^{(1)}\overline{\Psi}_{\theta,x}\Psi - 4iu^{(1)}\Psi_{\theta,x}\overline{\Psi})\\ &\tilde{H}_5 = \int dx \int d\theta(\tilde{\psi}_\theta^*\tilde{\psi}_{\theta\theta} - \tilde{\psi}_{\theta\theta}^*\tilde{\psi}_\theta + 2\tilde{\psi}^*\tilde{\psi}\tilde{n} - \tilde{\psi}_\theta^*\tilde{\psi}^*\ \tilde{\psi}_\theta\tilde{\psi}), \ldots\end{aligned} \tag{71}$$

and so on, which are invariant with respect to the super-evolution flow on $\tilde{M}$, which is equivalently represented [53,55,56] via the Lax-type dynamical super-operator flow

$$\partial\tilde{L}/\partial\tau = [\tilde{L}, \left(\tilde{L}^{10/3}\right)_+] \tag{72}$$

with respect to a super-temporal odd evolution parameter $\tau \in \Lambda_1$, where the sign "+" denotes the strictly nonnegative super-differential part of an expression in the brackets.

Remark 5. *Here, one must mention that the flow (72) is naturally interpreted [53–56,63] from the Lie-algebraic point of view as the coadjoint action of the operator Lie susperalgebra element* $\left(\tilde{L}^{10/3}\right)_+ \in$ Lie$(s\Psi OP_+)$ *on the element* $\tilde{L} \in$ Lie$(s\Psi OP)^*$, *where* Lie$(s\Psi OP_+)$ *denotes the nonnegative part of the natural direct sum splitting* Lie$(s\Psi OP) =$ Lie$(s\Psi OP_+) \oplus$ Lie$(s\Psi OP_-)$.

Having recalculated the flow (72) regarding the superized variables $(\tilde{\psi}, \tilde{n}, \tilde{\psi}^*) \in \tilde{M}$, one obtains the following Schrödinger–Davydov evolution flow:

$$\left.\begin{aligned}\partial\tilde{\psi}/\partial\tau = i\tilde{\psi}_{\theta\theta\theta} - 2i\tilde{n}\tilde{\psi}^*\tilde{\psi} + i\tilde{\psi}^*\tilde{\psi}\tilde{\psi}_\theta\\ \partial\tilde{n}/\partial\tau = -2\tilde{\psi}^*\tilde{\psi}\tilde{w}_0^1 - 2(\tilde{\psi}_\theta^*\tilde{\psi} - \tilde{\psi}^*\tilde{\psi}_\theta)\tilde{n}_\theta\\ \partial\tilde{\psi}^*/\partial\tau = -i\tilde{\psi}_{\theta\theta\theta}^* + 2i\tilde{n}\tilde{\psi}^*\tilde{\psi} - i\tilde{\psi}^*\tilde{\psi}\tilde{\psi}_\theta\end{aligned}\right\} := \tilde{K}[\tilde{\psi}, \tilde{n}, \tilde{\psi}^*], \tag{73}$$

which is a super-Hamiltonian system with respect to the super-Poisson structure

$$\{\tilde{\psi}(x,\theta),\tilde{\psi}^*(y,\eta)\}_{\tilde{P}} = i\delta(x,\theta|y,\eta), \{\tilde{\psi}(x,\theta),\tilde{n}(y,\eta)\}_{\tilde{P}} = \tilde{\psi}^*(x,\theta)\delta(x,\theta|y,\eta), \quad (74)$$
$$\{\tilde{n}(x,\theta),\tilde{\psi}^*(y,\eta)\}_{\tilde{P}} = \tilde{\psi}(x,\theta)\delta(x,\theta|y,\eta), \{\tilde{n}(x,\theta),\tilde{n}(y,\eta)\}_{\tilde{P}} = D_\theta\delta(x,\theta|y,\eta),$$
$$\{\tilde{\psi}(x,\theta),\tilde{\psi}(y,\eta)\}_{\tilde{P}} = 0 = \{\tilde{\psi}^*(x,\theta),\tilde{\psi}^*(y,\eta)\}_{\tilde{P}}, \{\tilde{u}(x,\theta),\tilde{u}(y,\eta)\}_{\tilde{P}} = \delta(x,\theta|y,\eta)$$

on the functional supermanifold $\tilde{M}$—that is, $(\tilde{\psi}_\tau,\tilde{n}_\tau,\tilde{\psi}^*_\tau)^\intercal = \{\tilde{H}_{10},(\tilde{\psi},\tilde{n},\tilde{\psi}^*)^\intercal\}_{\tilde{P}}$—coinciding with that of (73), where the evolution parameter $\tau \in \Lambda_1$, as mentioned above, is considered odd. The derived superflow (73) presents a searched superization regarding the quasi-classical integrable Schrödinger–Davydov dynamical system defined on the functional field manifold M. It is worth noting here that in some cases, one can anticipate that the corresponding super-evolution vector field $\tilde{K} : \tilde{M} \to T(\tilde{M})$ on the functional superfield manifold $\tilde{M}$ is represented as the supersymmetric super-differentiation $d/d\tau = \partial/\partial\theta + \theta\partial/\partial t$ with respect to the super-variable $\theta \in \Lambda_1$ and the real evolution parameter $t \in \mathbb{R}$. The latter suitably makes it possible to construct real-time evolution equations with respect to this temporal parameter $t \in \mathbb{R}$, thus representing the corresponding quasi-classical Schrödinger–Davydov dynamical system on the functional superfield manifold $\tilde{M}$, possessing interesting physical properties from application point of view. This dynamical supersystem provides an extraordinary example of a nonlinear integrable dynamical superflow with respect to a real evolution parameter, subject to which the Hamiltonian representation of the reduced vector field $d/dt : \tilde{M} \to T(\tilde{M})$ on the functional superfield manifold $\tilde{M}$ is still not clear and can be investigated in the future.

7. Conclusions

We have studied two interesting examples of the superization scheme regarding the classical Schrödinger–Davydov integrable nonlinear dynamical system on a functional manifold. In particular, we checked that the so-called "naive" approach, based on the superization of the phase space variables and extending the corresponding Poisson brackets upon the related functional supermanifold, fails to retain the dynamical system's super-integrability. Nonetheless, for a wide class of classical Lax-type integrable nonlinear dynamical systems on functional manifolds, a possible superization scheme consists in a reasonable superization of the related Lax-type representation by means of a transition from the basic algebra of pseudo-differential operators on the real axis to the corresponding superalgebra of super-pseudo-differential operators on the superaxis.

Author Contributions: Conceptualization, A.K.P. and R.A.K.; methodology, A.K.P.; software, R.A.K.; validation, R.A.K. and V.M.D.; formal analysis, V.M.D.; investigation, A.K.P., R.A.K. and V.M.D.; resources, V.M.D.; data curation, V.M.D.; writing—original draft preparation, A.K.P.; writing—review and editing, R.A.K.; visualization, V.M.D.; supervision, A.K.P.; project administration, R.A.K.; funding acquisition, R.A.K. All authors have read and agreed to the published version of the manuscript.

Funding: This research received no external funding.

Data Availability Statement: The original contributions presented in this study are included in the article. Further inquiries can be directed to the corresponding author(s).

Acknowledgments: The authors are cordially indebted to Victor A. Bovdi and Dmitri Leites for fruitful discussions on super-integrable nonlinear dynamical systems on functional supermanifolds. A.K.P. and R.A.K. are very grateful to the Department of Computer Science and Telecommunication at the Cracov University of Technology for the local grant that fruitfully contributed to this research. Last but not least, the authors thank the Referees, whose remarks and instrumental comments were useful in preparing tye manuscript.

Conflicts of Interest: The authors declare no conflicts to interest.

References

1. Gervais, J.-L. Infinite family of polynomial functions of the Virassoro generators with vanishing Poisson brackets. *Phy. Lett. B* **1985**, *160*, 277–278. [CrossRef]
2. Green, M.; Schwarz, J.H.; Witten, E. Superstring Theory. Introduction. In *Cambridge Monographs on Mathematical Physics*; Cambridge University Press: Cambridge, UK, 1988; Volume 1, ISBN 978-0-521-35752-4.
3. Grozman, P.; Leites, D.; Shchepochkina, I. Lie superalgebras of string theories. *arXiv* **1997**, arXiv:hep-th/9702120.
4. Lie, A.; Shemyakova, E.; Voronov, T. Differential operators on the superline, Berezinians, and Darboux transformations. *Lett. Math. Phys.* **2017**, *107*, 1689–1714. [CrossRef]
5. Seiberg, N. The power of duality-exact results in 4D SUSY field theory. *Int. J. Mod. Phys.* **2001**, *16*, 4365–4376. [CrossRef]
6. Shifman, M. Lessons for QCD from supersymmetry. *Nuclear Phys. B* **2002**, *106–107*, 125–132. [CrossRef]
7. Witt De, B. *Supermanifolds*, 2nd ed.; MIT Press: Cambridge, MA, USA, 1992.
8. Berezin, F.A. The method of second quantization. In *Pure & Applied Physics 24*; Academic Press: New York, NY, USA; London, UK, 1966.
9. Leites, D. Introduction to supermanifolds. *Russ. Math. Surveys* **1980**, *35*, 1–64. [CrossRef]
10. Leites, D. Lie superalgebras. *J. Sov. Math.* **1985**, *30*, 2481–2512. [CrossRef]
11. Bellucci, S.; Ivanov, E.; Krivonos, S. On $N = 3$ super Korteweg–de Vries Equation. *J. Math. Phys.* **1993**, *34*, 3087–3097. [CrossRef]
12. Brunelli, J.C.; Das, A. Supersymmetric two boson equation, its reductions and the nonstandard supersymmetric KP hierarchy. *Int. J. Modern Phys. A*. **1995**, *10*, 4563–4599. [CrossRef]
13. Chaichian, M.; Kulish, P.P. Superconformal algebras and their relation to integrable nonlinear systems. *Phys. Lett. B* **1987**, *183*, 169–174. [CrossRef]
14. Gurses, M.; Oguz, O. A super AKNS scheme. *Phys Lett. A* **1985**, *108*, 437–440. [CrossRef]
15. Gurses, M.; Oguz, O. A supersoliton connection. *Lett. Math. Phys.* **1986**, *11*, 235–246. [CrossRef]
16. Hentosh, O. Compatibly bi-Hamiltonian superconformal analogs of the Lax-integrable nonlinear dynamical systems. *Ukr. Math.* **2006**, *58*, 1001–1015. [CrossRef]
17. Hentosh, O. Lax Integrable Supersymmetric Hierarchies on Extended Phase Spaces of Two Anticommuting Variables. *Oper. Theory Advances Appl.* **2009**, *191*, 365–379.
18. Hentosh, O.; Prykarpatsky, Y. The Lax-Sato integrable heavenly equations on functional supermanifolds and their Lie-algebraic structure. *Eur. Math.* **2020**, *6*, 232–247. [CrossRef]
19. Hentosh, O.; Prytula, M.; Prykarpatsky, A. *Differential-GeoMetRic and Li-Algebraic Foundations of Investigating Integrable Nonlinear Dynamical Systems on Functional Manifolds*; Lviv University: Lviv, Ukraine, 2006; 408p.
20. Popowicz, Z. The fully supersymmetric AKNS equations. *Phys. Lett. A Math. Gen.* **1990**, *23*, 1127–1136. [CrossRef]
21. Delduc, F.; Ivanov, E.; Krivonos, S. $N = 4$ super KdV hierarchy in $N = 4$ and $N = 2$ superspaces. *J. Math. Phys.* **1996**, *37*, 1356–1381. [CrossRef]
22. Gawędzki, K. Supersymmetric extension of the Korteweg-de Vries equation. *Ann. Inst. Henri Poincare* **1997**, *27*, 335–366.
23. Geng, X.; Wu, L. A new super-extension of the KdV hierarchy. *Appl. Math. Lett.* **2010**, *23*, 716–721. [CrossRef]
24. Helminck, G.; van de Leur, J. Constrained and rational reductions of the KP hierarchy. Supersymmetry and Integrable Models. *Lect. Notes. Phys.* **1998**, *502*, 167–181.
25. Kupershmidt, B.A. Integrable systems. *Proc. Nat. Acad. Sci. USA* **1984**, *81*, 6562–6563. [CrossRef] [PubMed]
26. Labelle, M.; Mathieu, P. A new $N = 2$ supersymmetric Kortteweg-de Vries equation. *J. Math. Phys.* **1991**, *32*, 923–927. [CrossRef]
27. Laberge, C.-A.; Mathieu, P. $N = 2$ superconformal algebra and integrable O(2) fermionic extensions of the Korteweg–de Vries equation. *Phys. Lett. B* **1988**, *215*, 718–722. [CrossRef]
28. Leites, D.; Xuan, P. Supersymmetry of the Schrodinger and Korteweg-de Vries operators. *arXiv* **1997**, arXiv:hep-th/9710045.
29. Lenells, J.; Lechtenfeld, O. On the $N = 2$ supersymmetric Camassa–Holm and Hunter–Saxton equations. *J. Math. Phys.* **2009**, *50*, 012704. https://doi.org10.1063/1.3060125. [CrossRef]
30. Marcel, P.; Ovsienko, V.; Roger, C. Extension of the Virasoro and Neveu-Schwarz algebras and generalized Sturm-Liouville operators. *Lett. Math. Phys.* **1997**, *40*, 31–39. [CrossRef]
31. Mathieu, P. Supersymmetric extension of the Korteweg-de Vries equation. *J. Math. Phys.* **1988**, *29*, 2499–2506. [CrossRef]
32. Mathieu, P. Hamiltonian Structure of Graded and Super Evolution Equations. *Lett. Math. Phys.* **1988**, *16*, 199–206. [CrossRef]
33. Yamanaka, I.; Sasaki, R. Super Virasoro Algebra and Solvable Supersymmetric Quantum Field Theories. *Prog. Theor. Phys.* **1988**, *79*, 1167–1184. [CrossRef]
34. Manin, Y.I.; Radul, A.O. A supersymmetric extension of the Kadomtsev-Petviashvili hierarchy. *Comm. Math. Phys.* **1985**, *98*, 65–77. [CrossRef]
35. Morosi, C.; Pizzocchero, L. The $osp(3;2)$ and $gl(3;3)$ supersymmetric KdV hierarchies. *Phys. Lett. A.* **1994**, *185*, 241–252. [CrossRef]
36. Nissimov, E.; Pacheva, S. Properties of supersymmetric integrable systems of KP type. *Eur. Phys. J. B* **2002**, *29*, 197–201. [CrossRef]

37. Oevel, W.; Popowicz, Z. The bi-Hamiltonian structure of fully supersymmetric Korteweg-de Vries systems. *Comm. Math. Phys.* **1991**, *139*, 441–460. [CrossRef]
38. Popowicz, Z.; Toppan, F. The $N = 2$ supersymmetric heavenly equation and super-hydrodynamical reduction. *J. Phys. A: Math. Gen.* **2003**, *36*, 9701–9709. [CrossRef]
39. Popowicz, Z. $N = 2$ Super-complexification of the Korteweg-de Vries, Sawada-Kotera and Kaup-Kupershmidt Equations. *J. Nonlinear Math. Phys.* **2019**, *26*, 294–312. [CrossRef]
40. Popowicz, Z. A 2-component or N = 2 supersymmetric Camassa-Holm equation. *Phys. Lett. A* **2006**, *354*, 110–114 [CrossRef]
41. Saveliev, M.V. Communic. *Math. Phys.* **1986**, *95*, 199–211. [CrossRef]
42. Stanciu, S. Additional Symmetries of Supersymmetric KP Hierarchies. *Commun. Math. Phys.* **1994**, *165*, 261–279. [CrossRef]
43. Zhou, H.; Tian, K.; Li, N. Four super integrable equations: Nonlocal symmetries and applications. *J. Phys. A Math. Theor.* **2022**, *55*, 225207. [CrossRef]
44. Bogolubov, N.N.; Bogolubov, N.N., Jr. *Introduction to Quantum Statistical Mechanics*; Gordon and Breach: New York, NY, USA; London, UK, 1994.
45. Bogolubov, N.N.; Shirkov, D.V. *Introduction to the Theory of Quantized Fields*, 3rd ed.; John Wiley and Sons: Hoboken, NJ, USA, 1980.
46. Davydov, A.S. Theoretical investigation of high tempereature superconductovity. *Phys. Rep. (Rev. Sect. Phys. Lett.)* **1990**, *190*, 191–306.
47. Prykarpatsky, A.K.; Blackmore, D.; Bogolubov, N.N., Jr. Hamiltonian structure of benney type and Boltzmann-Vlasov kinetic equations on axis and some applications to manufacturing science. *Open Syst. Inf. Dyn.* **1999**, *6*, 335–373. [CrossRef]
48. Scott, A. Davydov's solitons. *Phys. Rep. (Rev. Sect. Phys. Lett.)* **1992**, *217*, 1–67. [CrossRef]
49. Dirac, P.A.M. *The Principles of Quantum Mechanics*, 2nd ed.; Clarendon Press: Oxford, UK, 1935.
50. Bogoliubov, N.N., Jr.; Prykarpatsky, A.K.; Blackmore, D. *On Benney-Type Hydrodynamical Systerms and Their Boltzmann-Vlasov Type Equations Kinetic Models*; Preprint IC/2006/006; ICTP: Trieste, Italy, 2006.
51. Mitropolski, Y.A.; Bogoliubov, N.N., Jr.; Prykarpatsky, A.K.; Samoilenko, V.H. *Integrable Dynamical Systems*; Naukova Dumka' Public: Kiev, Ukraine, 1987.
52. Magri, F. A simple model of the integrable Hamiltonian equation. *J. Math. Phys.* **1978**, *19*, 1156–1162. [CrossRef]
53. Blackmore, D.; Prykarpatsky, A.K.; Samoylenko, V.H. *Nonlinear Dynamical Systems of Mathematical Physics*; World Scientific: Publisher, NJ, USA, 2011.
54. Prykarpatsky, A.; Mykytyuk, I. *Algebraic Integrability of Nonlinear Dynamical Systems on Manifolds*; Kluwer Acad. Publishers: Amsterdam, The Netherlands, 1998.
55. Takhtajan, L.A.; Faddeev, L.D. *Hamiltonian Approach in Soliton Theory*; Springer: Berlin/Heidelberg, Germany, 1987.
56. Blaszak, M. *Multi-Hamiltonian Theory of Dynamical Systems*; Springer: New York, NY, USA, 1998.
57. Prykarpats'ky, A.K.; Fil', B.M. Category of topological jet-manifolds and certain applications in the theory of nonlinear infinite dimensional dynamical systems. *Ukr. Math. J.* **1993**, *44*, 1136–1148. [CrossRef]
58. Godbillon, C. *Geometrie Differentielle et Mecanique Analytique*; Hermann: Paris, France, 1969.
59. Kulish, P.P. Analog of the Korteweg–de Vries equation for the superconformal algebra. *J. Soviet Math.* **1988**, *41*, 970–975. [CrossRef]
60. Nam S. The Kac formula for the $N = 1$ and the $N = 2$ super-conformal algebras. *Phys. Lett. B* **1986**, *172*, 323–327. [CrossRef]
61. Jung, C.G. *Versucheiner Darstellung der Psychoanalytischen Theorie*; Rascher: Zurich, Switzerland, 1955; p. 160.
62. Novikov, S.P. The periodic problem for the Korteweg—de vries equation. *Funct. Anal. Its Appl.* **1974**, *8*, 236–246. [CrossRef]
63. Newell, A.C. *Solitons in Mathematics and Physics*; CBMS-NSF, Regional Conference Series in Applied Mathematics; SIAM: New Delhi, India, 1985.
64. Golenia, J.; Hentosh, O.Y.; Prykarpatsky, A.K. Integrable three-dimensional coupled nonlinear dynamical systems related with centrally extended operator Lie algebra. *Opusc. Math.* **2007**, *27*, 231–244.
65. Prykarpatsky, Y.A. Structure of integrable Lax flows on nonlocal manifolds: Dynamical systems with sources. *Math. Methods Phys.-Mech. Fields* **1997**, *40*, 106–115. [CrossRef]

Disclaimer/Publisher's Note: The statements, opinions and data contained in all publications are solely those of the individual author(s) and contributor(s) and not of MDPI and/or the editor(s). MDPI and/or the editor(s) disclaim responsibility for any injury to people or property resulting from any ideas, methods, instructions or products referred to in the content.

symmetry

MDPI

Article

A New High-Order Fractional Parallel Iterative Scheme for Solving Nonlinear Equations

Mudassir Shams [1,2] and Bruno Carpentieri [1,*]

[1] Faculty of Engineering, Free University of Bozen-Bolzano (BZ), 39100 Bozen-Bolzano, Italy; mudassir4shams@gmail.com or mudassir.shams@unibz.it
[2] Department of Mathematics and Statistics, Riphah International University I-14, Islamabad 44000, Pakistan
* Correspondence: bruno.carpentieri@unibz.it

Abstract: Solving fractional-order nonlinear equations is crucial in engineering, where precision and accuracy are essential. This study introduces a novel fractional parallel technique for solving nonlinear equations. To enhance convergence, we incorporate a simple root-finding method of order $3\gamma + 1$ as a correction term in the parallel scheme. Theoretical analysis shows that the parallel scheme achieves a convergence order of $6\gamma + 3$. Using a dynamical system approach, we identify optimal parameter values, and the symmetry in the dynamical planes for different fractional parameters demonstrates the method's stability and consistency in handling nonlinear problems. These parameter values are applied to the parallel scheme, yielding highly consistent results. Several engineering problems are examined to assess the method's efficiency, stability, and consistency compared to existing methods.

Keywords: nonlinear functions; stability; local error; parametric planes; elapsed time

1. Introduction

In 1695, Leibniz and L'Hôpital introduced the concept of the semi-derivative [1–3], which laid the foundation for both classical and fractional calculus. Fractional calculus [4], an extension of classical calculus to non-integer orders, has gained attention for its effectiveness in modeling complex systems with non-local and memory-dependent behaviors. This makes it particularly valuable in engineering, where fractional-order nonlinear equations are used to simulate systems with memory effects and anomalous diffusion.

One form of the nonlinear problems we are particularly interested in is represented by the following equation:

$$\begin{cases} \left[{}_{\zeta}\eth^{\gamma}_{\gamma_1}\right] y(x) + \hbar(y(x)) = g(x), \\ y(x_0) = y_0, y'(x_0) = y_1, \theta_0^{[*]} < \gamma \leq \theta_1^{[*]}, \end{cases} \tag{1}$$

In Equation (1), x_0 is the initial point and fractional parameter γ lies within the interval $\left(\theta_0^{[*]}, \theta_1^{[*]}\right]$. While obtaining exact solutions to these equations would be computationally attractive due to their precision and lack of approximation, the inherent complexities of fractional-order systems often make such solutions unattainable. In these cases, analytical methods, such as series expansions and integral transformations, play a critical role. These methods provide closed-form or semi-closed-form solutions, which not only offer valuable insights into the system's behavior, but also serve as reference points for validating and guiding numerical solutions. By doing so, they help ensure that numerical approaches remain accurate and reliable when exact solutions are not feasible.

The Caputo derivative retains the benefits of classical calculus while enabling the development of more detailed models that can accurately capture the complex dynamics observed in various real-world applications, including finance [5], engineering [6,7],

physics [8], and many more. Due to their inherent complexity, nonlinear equations remain one of the most challenging problems in science and engineering. Unlike the Caputo derivative, most other fractional derivatives do not satisfy the condition $[\eth^{\gamma}](1) = 0$ when γ is not a natural number. Because of this, we will explore the fundamental concepts of fractional calculus and discuss the fractional iterative approach for solving nonlinear equations using Caputo-type derivatives.

Definition 1. *The Gamma function, also known as the generalized factorial function [9], is defined as:*

$$\lceil(x) = \int_0^{+\infty} u^{x-1}e^{-u}du, \tag{2}$$

where $x > 0$. The Gamma function satisfies the properties $\lceil(1) = 1$ and $\lceil(n+1) = n!$ for any positive integer n.

Definition 2. *Let $\hbar : \mathbb{R} \to \mathbb{R}$, where*

$$\hbar \in \mathbb{C}^{+\infty}([\gamma_1, x]), -\infty < \gamma_1 < x < +\infty, \gamma_1 \geq 0, m = [\gamma_1] + 1. \tag{3}$$

The Caputo fractional derivative [10] of order γ_1 is defined as:

$$\left[{}_{\check{c}}\eth^{\gamma}_{\gamma_1}\right]\hbar(x) = \begin{cases} \frac{1}{\lceil(m-\gamma)} \int_{\gamma_1}^{x} \left[\frac{d^m}{dt^m}\hbar(t)\frac{1}{(x-t)^{\gamma-m+1}}\right]dt, \gamma \notin N, \\ \frac{d^{m-1}}{dt^{m-1}}\hbar(x), \ \ \gamma = m-1 \in N \cup \{0\}, \end{cases} \tag{4}$$

where $\lceil(x)$ is a gamma function for $x > 0$.

Theorem 1. *Suppose that $\left[{}_{\check{c}}\eth^{m\gamma}_{\gamma_1}\right]\hbar(x) \in C[\gamma_1, \gamma_2]$ for $m = 1, \ldots, n+1$ where $\gamma \in (0, 1]$. Then, the Generalized Taylor Formula [11] is given by:*

$$\hbar(x) = \left[\sum_{i=0}^{n}\left[{}_{\check{c}}\eth^{i\gamma}_{\gamma_1}\right]\hbar(\gamma_1)\frac{(x-\gamma_1)^{i\gamma}}{\lceil(i\gamma+1)} + \left[{}_{\check{c}}\eth^{(n+1)\gamma}_{\gamma_1}\right]\hbar(\xi)\frac{(x-\gamma_1)^{(n+1)\gamma}}{\lceil((n+1)\gamma+1)}\right], \tag{5}$$

where

$$\gamma_1 \leq \xi \leq x, \forall x \in (\gamma_1, \gamma_2], \tag{6}$$

and

$$\left[{}_{\check{c}}\eth^{n\gamma}_{\gamma_1}\right] = \left[\left[{}_{\check{c}}\eth^{\gamma}_{\gamma_1}\right].\left[{}_{\check{c}}\eth^{\gamma}_{\gamma_1}\right]\ldots\left[{}_{\check{c}}\eth^{\gamma}_{\gamma_1}\right](n-times)\right]. \tag{7}$$

Consider the Caputo-type Taylor expansion of $\hbar(x)$ around $\gamma_1 = \xi$:

$$\hbar(x) = \left[\frac{\left[{}_{\check{c}}\eth^{1\gamma}_{\xi}\right]\hbar(\xi)}{\lceil(+1)}(x-\xi)^{\gamma} + \frac{\left[{}_{\check{c}}\eth^{2\gamma}_{\xi}\right]\hbar(\xi)}{\lceil(2\gamma+1)}(x-\xi)^{2\gamma} + O(x-\xi)^{3\gamma}\right]. \tag{8}$$

By factoring out $\frac{\left[{}_{\check{c}}\eth^{1\gamma}_{\xi}\right]\hbar(\xi)}{\lceil(\gamma+1)}$, we obtain:

$$\hbar(x) = \left[\frac{\left[{}_{\check{c}}\eth^{1\gamma}_{\xi}\right]\hbar(\xi)}{\lceil(\gamma+1)}\left[\begin{array}{c}(x-\xi)^{\gamma}+\\ \check{c}_2(x-\xi)^{2\gamma}\end{array}\right] + O(x-\xi)^{3\gamma},\right] \tag{9}$$

where

$$\check{c}_j = \frac{\lceil(\gamma+1)}{\lceil(m\gamma+1)}\frac{\left[{}_{\check{c}}\eth^{m\gamma}_{\xi}\right]\hbar(\xi)}{\left[{}_{\check{c}}\eth^{\gamma}_{\xi}\right]\hbar(\xi)}, m = 2, 3, \ldots \tag{10}$$

The corresponding Caputo-type derivative of $\hbar(x)$ around ξ is:

$$\left[{}_{\check{c}}\eth_{\xi}^{\gamma}\right]\hbar(x) = \left[\frac{\left[{}_{\check{c}}\eth_{\xi}^{1\gamma}\right]\hbar(\xi)}{\lceil(\gamma+1)}\left[\begin{array}{c}\lceil(\gamma+1)+\\ \frac{\lceil(2\gamma+1)}{\lceil(\gamma+1)}\check{c}_2(x-\xi)^{\gamma}\end{array}\right]+O(x-\xi)^{2\gamma}\right]. \tag{11}$$

These expansions are used in the convergence analysis of the proposed method.

The rest of the paper is structured as follows: Section 2 discusses the development, convergence, and complex dynamical analysis of fractional-order schemes for solving Equation (1). Section 3 evaluates the effectiveness and stability of the proposed method through numerical examples and comparisons with other techniques. Finally, the conclusions are presented in Section 5.

2. Construction and Dynamic Analysis of Fractional Iterative Scheme

The Newton method [12,13] refines an initial guess for solving a nonlinear problem by using a sequence of linear approximations. This technique, known for its rapid convergence—often quadratic—has been widely used since its development in the late 14th century to solve nonlinear equations. The fractional Newton method is an extension of the traditional Newton method, designed for nonlinear equations involving fractional derivatives. It incorporates fractional calculus operators, such as fractional integrals and derivatives, into the iterative process. This approach has demonstrated strong convergence properties and has been effective in solving complex nonlinear equations where other methods may fail. Several studies, including those by Torres-Hernandez et al. [14], Akgül et al. [15], Gajori et al. [16], Kumar et al. [17], and Candelario et al. [18] describe a fractional version of the Newton technique with various fractional derivatives.

Based on both stability and efficiency, the method presented in [19] is preferable to other well-known root-finding methods for nonlinear equations, such as those in [20–23] and the references cited therein. Nonlinear equations, particularly those involving fractional approaches, have gained significant attention due to their wide applications in addressing complex engineering problems. The numerical algorithm discussed exhibits local convergence in approximating simple solutions to fractional-order nonlinear problems. In addition to the basic iterative strategies for solving (1) with integer or fractional convergence orders, there are parallel schemes with global convergence that can find all solutions to a nonlinear equation simultaneously. These schemes are more stable, consistent, and are particularly useful in parallel computing (see, e.g., [24–26] and the references cited therein). However, a comprehensive literature review reveals that little work has focused on fractional-order numerical techniques for solving fractional nonlinear problems.

The primary goal of the current research is to enhance the convergence rate, stability, and accuracy of these parallel schemes. Challenges remain, particularly in ensuring efficient computation in higher dimensions. A comprehensive review of these trends, along with their limitations—such as handling fractional-order nonlinearities—provides context for the new numerical scheme. The proposed fractional family of parallel numerical schemes addresses several limitations of traditional iterative methods in the following ways:

- *Parallel computation*: Unlike simple root-finding methods, parallel approaches compute all solutions simultaneously.
- *Global convergence*: Parallel schemes exhibit global convergence, as all roots contribute to solving nonlinear problems.
- *Robustness*: Parallel schemes outperform other methods in terms of robustness and sensitivity to initial values for exact solutions.
- *Efficiency in parallel computing*: Fractional-order parallel methods are highly suitable for multicore and distributed systems, as updates for each solution can be computed independently. In contrast to simpler schemes, which often require shared access

to derivatives and global convergence checks, parallel updates can be handled with minimal communication overhead.

- *Accuracy and consistency*: Compared to simple iterative methods for solving (1), fractional parallel approaches—relying on differences between approximated roots—tend to be more accurate and consistent, requiring fewer modifications to maintain global convergence.
- *Memory efficiency*: Fractional-order parallel methods are more memory-efficient in practical implementations compared to basic schemes.

On the other hand, when applied to nonlinear fractional-order differential equations with movable conditions, the method may exhibit slower convergence rates and higher computational demands. These challenges can introduce complex dynamics that might affect the overall effectiveness of the approach. Therefore, while the method is generally reliable, a careful analysis of the problem's specific nature and conditions is essential to optimize its performance. In most cases, the method performs well, but in certain instances, additional strategies may be necessary to improve convergence and reduce computational costs.

Building on the method described in [19], we consider the following fractional iterative scheme:

$$v^{[l]} = x^{[l]} - \frac{\hbar(x^{[l]})}{\hbar'(x^{[l]})}\left(\left(\frac{\hbar(\varsigma^{[l]})}{\hbar(x^{[l]})}\right) + 2\left(\frac{\hbar(\varsigma^{[l]})}{\hbar(x^{[l]})}\right)^2 + \beta^{[*]}\left(\frac{\hbar(\varsigma^{[l]})}{\hbar(x^{[l]})}\right)^4\right), \tag{12}$$

where $\varsigma^{[l]} = x^{[l]} - \frac{\hbar(x^{[l]})}{\hbar'(x^{[l]})}$. This method has a convergence order of 4 (abbreviated as $\mathrm{M}^{[\gamma]}$), which satisfies the following error equation:

$$e_i^{[*]} = \left(\beta^{[*]}\check{c}_2^3 + 5\check{c}_2^3 - \check{c}_2\check{c}_3\right)\left(e^{[l]}\right)^4 + O\left(\left(e^{[l]}\right)^5\right), \tag{13}$$

where $e_i^{[*]} = x^{[1]} - \xi$, $e^{[l]} = x^{[l]} - \xi$, and $\check{c}_j = \frac{1}{m!}\frac{\left[\check{c}\eth_\xi^m\right]\hbar(\xi)}{\left[\check{c}\eth_\xi^\gamma\right]\hbar(\xi)}$, $m \geq 2, 3, \ldots$ The fractional version of this method is given by:

$$v^{[l]} = x^{[l]} - \left(\lceil(\gamma+1)\frac{\hbar(x^{[l]})}{\hbar'(x^{[l]})}\left(\begin{array}{c}\left(\frac{\hbar(\varsigma^{[l]})}{\hbar(x^{[l]})}\right) + 2\left(\frac{\hbar(\varsigma^{[l]})}{\hbar(x^{[l]})}\right)^2\\ +\beta^{[*]}\left(\frac{\hbar(\varsigma^{[l]})}{\hbar(x^{[l]})}\right)^4\end{array}\right)\right)^{1/\gamma}, \tag{14}$$

where $\varsigma^{[l]} = x^{[l]} - \left(\lceil(\gamma+1)\frac{\hbar(x^{[l]})}{\left[\check{c}\eth_{\gamma_1}^\gamma\right]\hbar(x^{[l]})}\right)^{1/\gamma}$. We abbreviate this method as $\mathrm{MM}^{[\gamma]}$.

2.1. Convergence Analysis

For the iterative scheme given by Equation (14), we establish the following theorem to determine its order of convergence.

Theorem 2. *Let*

$$\hbar : \eth \subseteq \mathbb{R} \to \mathbb{R} \tag{15}$$

be a continuous function, with $\left[{}_{\xi}\eth_{\gamma_1}^{m\gamma}\right]\hbar(x)$ *of order m for any* $\gamma \geq 0$ *and* $\gamma \in (0,1]$ *containing the exact root* ξ *of* $\hbar(x)$*. Furthermore, given a sufficiently close starting value* x_0*, the convergence order of the Caputo-type fractional iterative scheme*

$$v^{[l]} = x^{[l]} - \left(\lceil(\gamma+1)\frac{\hbar(x^{[l]})}{\hbar'(x^{[l]})} \begin{pmatrix} \left(\frac{\hbar(\varsigma^{[l]})}{\hbar(x^{[l]})}\right) \\ +2\left(\frac{\hbar(\varsigma^{[l]})}{\hbar(x^{[l]})}\right)^2 \\ +\beta^{[*]}\left(\frac{\hbar(\varsigma^{[l]})}{\hbar(x^{[l]})}\right)^4 \end{pmatrix} \right)^{1/\gamma}, \tag{16}$$

is least $2\gamma+1$*, with the error equation given by:*

$$e^{[*]} = e^{[*]} = \begin{pmatrix} \pounds_1^{[*]} + \pounds_2^{[*]} \\ +\pounds_3^{[*]} + \pounds_4^{[*]} \\ +\pounds_5^{[*]} + \pounds_6^{[*]} \end{pmatrix} \left[e^{[l]}\right]^{3\gamma+1} + O\left(\left[e^{[l]}\right]^{4\gamma+1}\right), \tag{17}$$

where the constants $\pounds_i^{[*]}$ *are defined as follows:*

$$\pounds_1^{[*]} = -9\frac{9{c_2}^3(2^\gamma)^4(\lceil(\gamma+1/2))^2}{(\lceil(\gamma))^2\gamma^2\pi}, \pounds_2^{[*]} = +\frac{4{c_2}^3(2^\gamma)^6(\lceil(\gamma+1/2))^3}{(\lceil(\gamma))^3\gamma^3\pi^{3/2}},$$

$$\pounds_3^{[*]} = -\frac{c_3(3^\gamma)^3\sqrt{3}\lceil(\gamma+1/3)\lceil(\gamma+2/3)c_2}{(\lceil(\gamma))^2\gamma^2\pi}, \pounds_4^{[*]} = \frac{3}{2}\frac{c_3(3^\gamma)^3\sqrt{3}\lceil(\gamma+1/3)\lceil(\gamma+2/3)c_2}{\lceil(\gamma)\gamma\sqrt{\pi}(2^\gamma)^2\lceil(\gamma+1/2)},$$

$$\pounds_5^{[*]} = -4\,c_2c_3 + {c_2}^3, \pounds_6^{[*]} = \frac{3(2^\gamma)^2\lceil(\gamma+1/2)c_2c_3}{\lceil(\gamma)\gamma\sqrt{\pi}} + \frac{4{c_2}^3(2^\gamma)^2\lceil(\gamma+1/2)}{\lceil(\gamma)\gamma\sqrt{\pi}}.$$

Here, $\check{c}_j = \frac{\lceil(\gamma+1)}{\lceil(m\gamma+1)}\frac{\left[{}_{\xi}\eth_{\xi}^{m\gamma}\right]\hbar(\xi)}{\left[{}_{\xi}\eth_{\xi}^{\gamma}\right]\hbar(\xi)}, m \geq 2,3,\ldots$ *and* $[\lceil(.)]^n = \lceil^n(.)$.

Proof. Let ξ be a root of $\hbar$ and assume $x^{[l]} = \xi + e^{[l]}$. Using a Taylor series expansion of $\hbar(x^{[l]})$ and $\left[{}_{\xi}\eth_{\gamma_1}^{\gamma}\right]\hbar(x^{[l]})$ around $x = \xi$, and considering that $\hbar(\xi) = 0$, we obtain:

$$\hbar(x^{[l]}) = \frac{\left[{}_{\xi}\eth_{\xi}^{1\gamma}\right]\hbar(\xi)}{\lceil(\gamma+1)}\left[\left[e^{[l]}\right]^{\gamma} + \check{c}_2\left[e^{[l]}\right]^{2\gamma} + \check{c}_3\left[e^{[l]}\right]^{3\gamma}\right] + O(\left[e^{[l]}\right]^{4\gamma}), \tag{18}$$

$$\left[{}_{\xi}\eth_{\gamma_1}^{\gamma}\right]\hbar(x^{[l]}) = \frac{\left[{}_{\xi}\eth_{\xi}^{1\gamma}\right]\hbar(\xi)}{\lceil(\gamma+1)}\begin{bmatrix} \lceil(\gamma+1) + \frac{\lceil(2\gamma+1)}{\lceil(\gamma+1)}\check{c}_2\left[e^{[l]}\right]^{\gamma} \\ +\frac{\lceil(3\gamma+1)}{\lceil(2\gamma+1)}\check{c}_3\left[e^{[l]}\right]^{2\gamma} \end{bmatrix} + O(\left[e^{[l]}\right]^{3\gamma}), \tag{19}$$

$$\frac{1}{\left[{}_{\xi}\eth_{\gamma_1}^{\gamma}\right]\hbar(x^{[l]})} = \frac{1}{\lceil(\gamma+1)} - \frac{\lceil(2\,\gamma+1)c_2\left[e^{[l]}\right]^{\gamma}}{(\lceil(\gamma+1))^3} + \Theta_1^{[*]} + \Theta_2^{[*]} + \Theta_3^{[*]} + \ldots \tag{20}$$

where $\Theta_1^{[*]} = \frac{\left[e^{[l]}\right]^{2\gamma}}{\lceil(\gamma+1)}\begin{pmatrix} -\frac{\lceil(3\,\gamma+1)c_3}{\lceil(\gamma+1)\lceil(2\,\gamma+1)} \\ +\frac{(\lceil(2\gamma+1))^2{c_2}^2}{(\lceil(\gamma+1))^4} \end{pmatrix}$,

$$\Theta_2^{[*]} = \frac{\left[e^{[l]}\right]^{3\gamma}}{\lceil(\gamma+1)}\left(\frac{c_2\lceil(3\,\gamma+1)c_3}{(\lceil(\gamma+1))^3} - \frac{\begin{pmatrix} (\lceil(2\,\gamma+1))^3{c_2}^2- \\ \lceil(3\,\gamma+1)c_3(\lceil(\gamma+1))^3 \end{pmatrix}c_2}{(\lceil(\gamma+1))^6}\right),$$

$$\Theta_3^{[*]} = \frac{\left[e^{[l]}\right]^{3\gamma}}{\lceil(\gamma+1)}\left(\frac{c_2\lceil(3\,\gamma+1)c_3}{(\lceil(\gamma+1))^3} - \frac{\begin{pmatrix} (\lceil(2\,\gamma+1))^3{c_2}^2- \\ \lceil(3\,\gamma+1)c_3(\lceil(\gamma+1))^3 \end{pmatrix}c_2}{(\lceil(\gamma+1))^6}\right).$$

Thus, by multiplying Equations (18) and (20), we obtain

$$\frac{\hbar(x^{[l]})}{\left[\check{c}\eth_{\gamma_1}^{\gamma}\right]\hbar\left(x^{[l]}\right)} = \begin{bmatrix} \frac{\left[e^{[l]}\right]^{\gamma}}{\lceil(\gamma)\gamma} + \left(\Theta_4^{[*]}\right)\left[e^{[l]}\right]^{2\gamma} \\ +\left(\Theta_5^{[*]}\right)\left[e^{[l]}\right]^{3\gamma} + \dots \end{bmatrix}, \tag{21}$$

where $\Theta_4^{[*]} = \frac{c_2}{\lceil(\gamma)\gamma} - \frac{(2^{\gamma})^2\lceil(\gamma+1/2)c_2}{\gamma^2\sqrt{\pi}(\lceil(\gamma))^2}$,

$$\Theta_5^{[*]} = \begin{pmatrix} \frac{c_3}{\lceil(\gamma)\gamma} - \frac{(2^{\gamma})^2\lceil(\gamma+1/2)c_2{}^2}{\gamma^2\sqrt{\pi}(\lceil(\gamma))^2} - \\ \frac{1}{2}\frac{c_3(3^{\gamma})^3\sqrt{3}\lceil(\gamma+1/3)\lceil(\gamma+2/3)}{\gamma^2\sqrt{\pi}(\lceil(\gamma))^2(2^{\gamma})^2\lceil(\gamma+1/2)} \\ +\frac{(2^{\gamma})^4(\lceil(\gamma+1/2))^2c_2{}^2}{(\lceil(\gamma))^3\gamma^3\pi} \end{pmatrix},$$

$$\varsigma^{[l]} = \left(-c_2 + \frac{(2^{\gamma})^2\lceil(\gamma+1/2)c_2}{\lceil(\gamma)\gamma\sqrt{\pi}}\right)\left[e^{[l]}\right]^{\gamma+1} + \Theta_6^{[*]}\left[e^{[l]}\right]^{2\gamma+1} + \dots \tag{22}$$

and $\Theta_6^{[*]} = \begin{pmatrix} -c_3 + \frac{(2^{\gamma})^2\lceil(\gamma+1/2)c_2{}^2}{\lceil(\gamma)\gamma\sqrt{\pi}} + \\ \frac{1}{2}\frac{c_3(3^{\gamma})^3\sqrt{3}\lceil(\gamma+1/3)\lceil(\gamma+2/3)}{\lceil(\gamma)\gamma\sqrt{\pi}(2^{\gamma})^2\lceil(\gamma+1/2)} \\ -\frac{(2^{\gamma})^4(\lceil(\gamma+1/2))^2c_2{}^2}{(\lceil(\gamma))^2\gamma^2\pi} \end{pmatrix}$. We have:

$$\hbar\left(\varsigma^{[l]}\right) = \begin{bmatrix} \Lambda^{\{2\}}\left[e^{[l]}\right]^{4\gamma+1} + \Lambda^{\{3\}}\left[e^{[l]}\right]^{3\gamma+1} + -1/2\Lambda^{\{6\}}\left[e^{[l]}\right]^{2\gamma+1} \\ +\Lambda^{\{7\}}\left[e^{[l]}\right]^{\gamma+1} + \dots \end{bmatrix}, \tag{23}$$

where $\Lambda^{\{1\}} = \begin{pmatrix} 2\,c_3(\lceil(\gamma))^2\gamma^2\pi^{3/2}(2^{\gamma})^2\lceil(\gamma+1/2) - \\ 2\,(2^{\gamma})^4(\lceil(\gamma+1/2))^2c_2{}^2\lceil(\gamma)\gamma\,\pi \\ -c_3(3^{\gamma})^3\sqrt{3}\lceil(\gamma+1/3) \\ \lceil(\gamma+2/3)\lceil(\gamma)\gamma\,\pi + \\ 2\,(2^{\gamma})^6(\lceil(\gamma+1/2))^3c_2{}^2\sqrt{\pi} \end{pmatrix}$,

$\Lambda^{\{2\}} = \frac{c_2{}^2\left(\lceil(\gamma)\gamma\sqrt{\pi} - (2^{\gamma})^2\lceil(\gamma+1/2)\right)\left(\Lambda^{\{1\}}\right)}{(\lceil(\gamma))^3\gamma^3\pi^2(2^{\gamma})^2\lceil(\gamma+1/2)}$,

$\Lambda^{\{3\}} = \frac{c_2{}^3\left(\lceil(\gamma)\gamma\sqrt{\pi} - (2^{\gamma})^2\lceil(\gamma+1/2)\right)^2}{(\lceil(\gamma))^2\gamma^2\pi}$,

$\Lambda^{\{4\}} = \begin{pmatrix} 2\,c_3(\lceil(\gamma))^2\gamma^2\pi^{3/2}(2^{\gamma})^2\lceil(\gamma+1/2) \\ -2\,(2^{\gamma})^4(\lceil(\gamma+1/2))^2c_2{}^2 \\ \lceil(\gamma)\gamma\,\pi - c_3(3^{\gamma})^3\sqrt{3}\lceil(\gamma+1/3) \\ \lceil(\gamma+2/3)\lceil(\gamma)\gamma\,\pi + \\ 2\,(2^{\gamma})^6(\lceil(\gamma+1/2))^3c_2{}^2\sqrt{\pi}, \end{pmatrix}$,

$\Lambda^{\{5\}} = (\lceil(\gamma))^2\gamma^2\pi^{3/2}(2^{\gamma})^2\lceil(\gamma+1/2)$,

$\Lambda^{\{6\}} = \frac{\Lambda^{\{4\}}}{\Lambda^{\{5\}}}$, and

$\Lambda^{\{7\}} = -\frac{c_2\left(\lceil(\gamma)\gamma\sqrt{\pi} - (2^{\gamma})^2\lceil(\gamma+1/2)\right)}{\lceil(\gamma)\gamma\sqrt{\pi}}$. Thus,

$$\frac{1}{\hbar\left(x^{[l]}\right)} = e_n{}^{-1} - c_2 + \left(c_2{}^2 - c_3\right)e_n + \begin{pmatrix} c_2c_3 \\ -c_4 + \\ \left(\begin{array}{c} -c_2{}^2 \\ +c_3 \end{array}\right)c_2 \end{pmatrix}e_n{}^2 + \dots \tag{24}$$

$$\frac{\hbar\left(\varsigma^{[l]}\right)}{\hbar\left(x^{[l]}\right)} = \begin{bmatrix} \Lambda^{\{8\}}\left[e^{[l]}\right]^{\gamma} + \Lambda^{\{9\}}\left[e^{[l]}\right]^{\gamma+1} + \Lambda^{\{10\}}\left[e^{[l]}\right]^{2\gamma+1} \\ +\Lambda^{\{11\}}\left[e^{[l]}\right]^{3\gamma+1} + \dots \end{bmatrix} \tag{25}$$

$$\text{where } \Lambda^{\{8\}} = \left(-c_2 + \frac{(2^\gamma)^2\lceil(\gamma+1/2)c_2}{\lceil(\gamma)\gamma\sqrt{\pi}}\right),$$

$$\Lambda^{\{9\}} = \begin{pmatrix} -\frac{(2^\gamma)^4(\lceil(\gamma+1/2))^2{c_2}^2}{(\lceil(\gamma))^2\gamma^2\pi} + \\ \frac{1}{2}\frac{c_3(3^\gamma)^3\sqrt{3}\lceil(\gamma+1/3)\lceil(\gamma+2/3)}{\lceil(\gamma)\gamma\sqrt{\pi}(2^\gamma)^2\lceil(\gamma+1/2)} \\ -{c_3} + {c_2}^2 \end{pmatrix},$$

$$\Lambda^{\{10\}} = \begin{pmatrix} -\frac{2{c_2}^3(2^\gamma)^2\lceil(\gamma+1/2)}{\lceil(\gamma)\gamma\sqrt{\pi}} + \\ \frac{2{c_2}^3(2^\gamma)^4(\lceil(\gamma+1/2))^2}{(\lceil(\gamma))^2\gamma^2\pi} - \\ \frac{1}{2}\frac{c_3(3^\gamma)^3\sqrt{3}\lceil(\gamma+1/3)\lceil(\gamma+2/3)c_2}{\lceil(\gamma)\gamma\sqrt{\pi}(2^\gamma)^2\lceil(\gamma+1/2)} \\ -\frac{(2^\gamma)^2\lceil(\gamma+1/2)c_2c_3}{\lceil(\gamma)\gamma\sqrt{\pi}} \\ +2\,c_2c_3 \end{pmatrix},$$

$$\Lambda^{\{11\}} = \begin{pmatrix} \frac{2\,{c_2}^4(2^\gamma)^4(\lceil(\gamma+1/2))^2}{(\lceil(\gamma))^2\gamma^2\pi} - {c_2}^2c_3 \\ -\frac{2{c_2}^4(2^\gamma)^6(\lceil(\gamma+1/2))^3}{(\lceil(\gamma))^3\gamma^3\pi^{3/2}} - \\ \frac{{c_3}^2(3^\gamma)^3\sqrt{3}\lceil(\gamma+1/3)\lceil(\gamma+2/3)}{\lceil(\gamma)\gamma\sqrt{\pi}(2^\gamma)^2\lceil(\gamma+1/2)} - \\ \frac{1}{2}\frac{{c_2}^2c_3(3^\gamma)^3\sqrt{3}\lceil(\gamma+1/3)\lceil(\gamma+2/3)}{\lceil(\gamma)\gamma\sqrt{\pi}(2^\gamma)^2\lceil(\gamma+1/2)} + \\ \frac{{c_2}^2c_3(3^\gamma)^3\sqrt{3}\lceil(\gamma+1/3)\lceil(\gamma+2/3)}{(\lceil(\gamma))^2\gamma^2\pi} \\ -\frac{(2^\gamma)^2\lceil(\gamma+1/2){c_2}^2c_3}{\lceil(\gamma)\gamma\sqrt{\pi}} + {c_3}^2 + \\ \frac{(2^\gamma)^4(\lceil(\gamma+1/2))^2{c_2}^2c_3}{(\lceil(\gamma))^2\gamma^2\pi} \\ -\frac{(2^\gamma)^2\lceil(\gamma+1/2)c_2c_4}{\lceil(\gamma)\gamma\sqrt{\pi}} + c_2c_4 \end{pmatrix},$$

$$\begin{pmatrix} \left(\frac{\hbar(\varsigma^{[l]})}{\hbar(x^{[l]})}\right) + \\ 2\left(\frac{\hbar(\varsigma^{[l]})}{\hbar(x^{[l]})}\right)^2 \\ +\beta^{[*]}\left(\frac{\hbar(\varsigma^{[l]})}{\hbar(x^{[l]})}\right)^4 \end{pmatrix} = \Lambda_1^{\{*\}}\left[e^{[l]}\right]^\gamma + \Lambda_2^{\{*\}}\left[e^{[l]}\right]^{\gamma+1} + \Lambda_3^{\{*\}}\left[e^{[l]}\right]^{2\gamma+1} + \ldots \tag{26}$$

$$\text{where } \Lambda_1^{\{*\}} = \left(-c_2 + \frac{(2^\gamma)^2\lceil(\gamma+1/2)c_2}{\lceil(\gamma)\gamma\sqrt{\pi}}\right)$$

$$\Lambda_2^{\{*\}} = \begin{pmatrix} \frac{(2^\gamma)^4(\lceil(\gamma+1/2))^2{c_2}^2}{(\lceil(\gamma))^2\gamma^2\pi} - 4\frac{4(2^\gamma)^2\lceil(\gamma+1/2){c_2}^2}{\lceil(\gamma)\gamma\sqrt{\pi}} \\ +\frac{1}{2}\frac{c_3(3^\gamma)^3\sqrt{3}\lceil(\gamma+1/3)\lceil(\gamma+2/3)}{\lceil(\gamma)\gamma\sqrt{\pi}(2^\gamma)^2\lceil(\gamma+1/2)} - {c_3} + 3\,{c_2}^2 \end{pmatrix}$$

$$\Lambda_3^{\{*\}} = \begin{pmatrix} \frac{2c_3(3^\gamma)^3\sqrt{3}\lceil(\gamma+1/3)\lceil(\gamma+2/3)c_2}{(\lceil(\gamma))^2\gamma^2\pi} - \\ 4\,{c_2}^3 - 5\,\frac{(2^\gamma)^2\lceil(\gamma+1/2)c_2c_3}{\lceil(\gamma)\gamma\sqrt{\pi}} \\ -\frac{5}{2}\frac{c_3(3^\gamma)^3\sqrt{3}\lceil(\gamma+1/3)\lceil(\gamma+2/3)c_2}{\lceil(\gamma)\gamma\sqrt{\pi}(2^\gamma)^2\lceil(\gamma+1/2)} - \\ \frac{4{c_2}^3(2^\gamma)^6(\lceil(\gamma+1/2))^3}{(\lceil(\gamma))^3\gamma^3\pi^{3/2}} \\ +2\,\frac{{c_2}^3(2^\gamma)^2\lceil(\gamma+1/2)}{\lceil(\gamma)\gamma\sqrt{\pi}} + 6\,c_2c_3 \\ +6\,\frac{{c_2}^3(2^\gamma)^4(\lceil(\gamma+1/2))^2}{(\lceil(\gamma))^2\gamma^2\pi} \end{pmatrix}. \text{ Therefore,}$$

$$h_1^{[*]} = \frac{\hbar(x^{[l]})}{\left[\check{c}\eth_{\gamma_1}^{\gamma}\right]\hbar\left(x^{[l]}\right)}\begin{pmatrix} \left(\frac{\hbar(\varsigma^{[l]})}{\hbar(x^{[l]})}\right) + 2\left(\frac{\hbar(\varsigma^{[l]})}{\hbar(x^{[l]})}\right)^2 \\ +\beta^{[*][*]}\left(\frac{\hbar(\varsigma^{[l]})}{\hbar(x^{[l]})}\right)^4 \end{pmatrix}, \tag{27}$$

$$h_1^{[*]} = \Lambda^{\{12\}}\left[e^{[l]}\right]^{\gamma+1} + \Lambda^{\{13\}}\left[e^{[l]}\right]^{2\gamma+1} + \Lambda^{\{14\}}\left[e^{[l]}\right]^{3\gamma+1} + \ldots \tag{28}$$

where $\Lambda^{\{12\}} = \left(\frac{(2^\gamma)^2 \lceil(\gamma+1/2) c_2}{\gamma^2 \sqrt{\pi} (\lceil(\gamma))^2} - \frac{c_2}{\lceil(\gamma)\gamma} \right)$,

$$\Lambda^{\{13\}} = \begin{pmatrix} -\frac{2(2^\gamma)^2 \lceil(\gamma+1/2) {c_2}^2}{\gamma^2 \sqrt{\pi} (\lceil(\gamma))^2} + \frac{1}{2} \frac{c_3 (3^\gamma)^3 \sqrt{3} \lceil(\gamma+1/3) \lceil(\gamma+2/3)}{\gamma^2 \sqrt{\pi} (\lceil(\gamma))^2 (2^\gamma)^2 \lceil(\gamma+1/2)} \\ -\frac{c_3}{\lceil(\gamma)\gamma} + \frac{2 {c_2}^2}{\lceil(\gamma)\gamma} \end{pmatrix},$$

$$\Lambda^{\{14\}} = \begin{pmatrix} \frac{9 {c_2}^3 (2^\gamma)^4 (\lceil(\gamma+1/2))^2}{(\lceil(\gamma))^3 \gamma^3 \pi} - \\ \frac{4 {c_2}^3 (2^\gamma)^6 (\lceil(\gamma+1/2))^3}{(\lceil(\gamma))^4 \gamma^4 \pi^{3/2}} + \\ \frac{c_3 (3^\gamma)^3 \sqrt{3} \lceil(\gamma+1/3) \lceil(\gamma+2/3) c_2}{(\lceil(\gamma))^3 \gamma^3 \pi} - \\ \frac{3}{2} \frac{c_3 (3^\gamma)^3 \sqrt{3} \lceil(\gamma+1/3) \lceil(\gamma+2/3) c_2}{\gamma^2 \sqrt{\pi} (\lceil(\gamma))^2 (2^\gamma)^2 \lceil(\gamma+1/2)} + \\ \frac{4 c_2 c_3}{\lceil(\gamma)\gamma} - \frac{{c_2}^3}{\lceil(\gamma)\gamma} - \\ \frac{3(2^\gamma)^2 \lceil(\gamma+1/2) c_2 c_3}{\gamma^2 \sqrt{\pi} (\lceil(\gamma))^2} - \frac{4 {c_2}^3 (2^\gamma)^2 \lceil(\gamma+1/2)}{\gamma^2 \sqrt{\pi} (\lceil(\gamma))^2} \end{pmatrix},$$

$$\left(\lceil(\gamma+1) h_1^{[*]} \right)^{\frac{1}{\gamma}} = \Lambda^{\{15\}} \left[e^{[l]} \right]^{2\gamma+1} + \Lambda^{\{16\}} \left[e^{[l]} \right]^{3\gamma+1} + \ldots \tag{29}$$

where $\Lambda^{\{15\}} = \left(\frac{3(2^\gamma)^2 \lceil(\gamma+1/2) {c_2}^2}{\lceil(\gamma)\gamma \sqrt{\pi}} - \frac{(2^\gamma)^4 (\lceil(\gamma+1/2))^2 {c_2}^2}{(\lceil(\gamma))^2 \gamma^2 \pi} - 2 {c_2}^2 \right)$,

$$\Lambda^{\{16\}} = \begin{pmatrix} -\frac{9 {c_2}^3 (2^\gamma)^4 (\lceil(\gamma+1/2))^2}{(\lceil(\gamma))^2 \gamma^2 \pi} + \\ 4 \frac{4 {c_2}^3 (2^\gamma)^6 (\lceil(\gamma+1/2))^3}{(\lceil(\gamma))^3 \gamma^3 \pi^{3/2}} \\ -\frac{c_3 (3^\gamma)^3 \sqrt{3} \lceil(\gamma+1/3) \lceil(\gamma+2/3) c_2}{(\lceil(\gamma))^2 \gamma^2 \pi} + \\ \frac{3}{2} \frac{c_3 (3^\gamma)^3 \sqrt{3} \lceil(\gamma+1/3) \lceil(\gamma+2/3) c_2}{\lceil(\gamma)\gamma \sqrt{\pi} (2^\gamma)^2 \lceil(\gamma+1/2)} \\ -4 c_2 c_3 + {c_2}^3 + \\ \frac{3(2^\gamma)^2 \lceil(\gamma+1/2) c_2 c_3}{\lceil(\gamma)\gamma \sqrt{\pi}} + 4 \frac{4 {c_2}^3 (2^\gamma)^2 \lceil(\gamma+1/2)}{\lceil(\gamma)\gamma \sqrt{\pi}} \end{pmatrix},$$

$$v^{[l]} = x^{[l]} - \left(\lceil(\gamma+1) \frac{\hbar(x^{[l]})}{\hbar'(x^{[l]})} \begin{pmatrix} \left(\frac{\hbar(\varsigma^{[l]})}{\hbar(x^{[l]})} \right) + 2 \left(\frac{\hbar(\varsigma^{[l]})}{\hbar(x^{[l]})} \right)^2 \\ + \beta^{[*][*]} \left(\frac{\hbar(\varsigma^{[l]})}{\hbar(x^{[l]})} \right)^4 \end{pmatrix} \right)^{1/\gamma}, \tag{30}$$

$$e^{[*]} = e^{[*]} = \begin{pmatrix} \pounds_1^{[*]} + \pounds_2^{[*]} \\ + \pounds_3^{[*]} \\ + \pounds_4^{[*]} \\ + \pounds_5^{[*]} \\ + \pounds_6^{[*]} \end{pmatrix} \left[e^{[l]} \right]^{3\gamma+1} + O\left(\left[e^{[l]} \right]^{4\gamma+1} \right), \tag{31}$$

where $\pounds_1^{[*]} = -9 \frac{9 {c_2}^3 (2^\gamma)^4 (\lceil(\gamma+1/2))^2}{(\lceil(\gamma))^2 \gamma^2 \pi}$, $\pounds_2^{[*]} = +\frac{4 {c_2}^3 (2^\gamma)^6 (\lceil(\gamma+1/2))^3}{(\lceil(\gamma))^3 \gamma^3 \pi^{3/2}}$, $\pounds_3^{[*]} = -\frac{c_3 (3^\gamma)^3 \sqrt{3} \lceil(\gamma+1/3) \lceil(\gamma+2/3) c_2}{(\lceil(\gamma))^2 \gamma^2 \pi}$, $\pounds_4^{[*]} = \frac{3}{2} \frac{c_3 (3^\gamma)^3 \sqrt{3} \lceil(\gamma+1/3) \lceil(\gamma+2/3) c_2}{\lceil(\gamma)\gamma \sqrt{\pi} (2^\gamma)^2 \lceil(\gamma+1/2)}$,

$\pounds_5^{[*]} = -4 c_2 c_3 + {c_2}^3$, $\pounds_6^{[*]} = \frac{3(2^\gamma)^2 \lceil(\gamma+1/2) c_2 c_3}{\lceil(\gamma)\gamma \sqrt{\pi}} + \frac{4 {c_2}^3 (2^\gamma)^2 \lceil(\gamma+1/2)}{\lceil(\gamma)\gamma \sqrt{\pi}}$.

Thus, the theorem is proven. □

2.2. Dynamical Analysis of the Fractional Scheme MM$^\gamma$

Ensuring the robustness and reliability of solving nonlinear equations requires a careful examination of the dynamical behavior of solution techniques [19]. Dynamical analysis in this context refers to a method's ability to converge on the true root from an initial guess, even when there are small perturbations or errors in the calculations. Single root-finding algorithms generally have local convergence around the root, making them effective when the initial guess is close enough. However, their stability depends on the characteristics of the function and the initial approximation. If the function is poorly

behaved or the initial guess is far from the root, these methods may diverge or converge to an incorrect solution.

The stability of a root-finding method can be analyzed using concepts from complex dynamical systems, which examine how sensitive the root is to variations in the input, as well as the convergence criterion, which evaluates how quickly the method approaches the root. The choice of parameters plays a crucial role in the method's performance, particularly within the convergence zone (the red region) on the parametric plane. Stability and faster convergence are achieved when optimal parameters are selected from this region. However, choosing parameters near the boundary of this zone, or from the divergence zone, may lead to reduced stability or slower convergence rates. Selecting parameters from the divergence region can result in failure or divergence, as the method may become unstable. To mitigate the effects of computational errors and ensure reliable performance, stability is typically maintained by carefully balancing the method's convergence properties with the appropriate selection of the initial guess, function parameters, and stopping criteria.

The following rational map $R(x) = (x-a)(x-b)$ is obtained as:

$$R(x) = y = \left[x - 2^{-\gamma^{-1}} \left(\frac{\lceil (\gamma+1)(x^2-1) \rceil}{x} \right)^{\gamma^{-1}} - 2^{-\gamma^{-1}} \wp^{[*]} \right], \tag{32}$$

where $\wp^{[*]} = \left(\frac{\lceil (\gamma+1) \rceil}{(x^2-1)^3 x} \right)^{\gamma^{-1}} \begin{pmatrix} \wp_{11}^{[i]} + \wp_{12}^{[i]} \\ +\wp_{13}^{[i]} \\ +\wp_{14}^{[i]} + \wp_{15}^{[i]} \\ \wp_{16}^{[i]} + \wp_{17}^{[i]} \\ +\wp_{18}^{[i]} \\ +\wp_{19}^{[i]} + \wp_{20}^{[i]} \\ \wp_{21}^{[i]} + \wp_{22}^{[i]} \\ +\wp_{23}^{[i]} \\ +\wp_{14}^{[i]} + \wp_{15}^{[i]} \end{pmatrix}$,

$$\wp_{11}^{[i]} = \begin{pmatrix} 3 + 16^{\frac{\gamma-1}{\gamma}} \left(\frac{\lceil (\gamma+1)(x^2-1) \rceil}{x} \right)^{4\gamma^{-1}} \beta^{[*][*]} x^4 - \\ 42^{\frac{\gamma-1}{\gamma}} \left(\frac{\lceil (\gamma+1)(x^2-1) \rceil}{x} \right)^{\gamma^{-1}} \beta^{[*][*]} x^7 + \\ 122^{\frac{\gamma-1}{\gamma}} \left(\frac{\lceil (\gamma+1)(x^2-1) \rceil}{x} \right)^{\gamma^{-1}} \beta^{[*][*]} x^5 - \\ 124^{-\gamma^{-1}} \left(\frac{\lceil (\gamma+1)(x^2-1) \rceil}{x} \right)^{2\gamma^{-1}} \beta^{[*][*]} x^4 \end{pmatrix},$$

$$\wp_{12}^{[i]} = \begin{pmatrix} -122^{\frac{\gamma-1}{\gamma}} \left(\frac{\lceil (\gamma+1)(x^2-1) \rceil}{x} \right)^{\gamma^{-1}} \beta^{[*][*]} x^3 + \\ 124^{-\gamma^{-1}} \left(\frac{\lceil (\gamma+1)(x^2-1) \rceil}{x} \right)^{2\gamma^{-1}} \beta^{[*]} x^2 \\ +42^{\frac{\gamma-1}{\gamma}} \left(\frac{\lceil (\gamma+1)(x^2-1) \rceil}{x} \right)^{\gamma^{-1}} \beta^{[*]} x - \\ 48^{\frac{\gamma-1}{\gamma}} \left(\frac{\lceil (\gamma+1)(x^2-1) \rceil}{x} \right)^{3\gamma^{-1}} \beta^{[*]} x^5 \end{pmatrix},$$

$$\begin{pmatrix} +74^{\frac{\gamma-1}{\gamma}}\left(\frac{\lceil(\gamma+1)\left(x^2-1\right)}{x}\right)^{2\gamma^{-1}}\beta^{[*][*]}x^6+ \\ 48^{\frac{\gamma-1}{\gamma}}\left(\frac{\lceil(\gamma+1)\left(x^2-1\right)}{x}\right)^{3\gamma^{-1}}\beta^{[*][*]}x^3+ \\ 464^{-\gamma^{-1}}\left(\frac{\lceil(\gamma+1)\left(x^2-1\right)}{x}\right)^{6\gamma^{-1}}\beta^{[*][*]}x^2 \end{pmatrix},$$

$$\wp_{13}^{[i]}=\begin{pmatrix} +616^{-\gamma^{-1}}\left(\frac{\lceil(\gamma+1)\left(x^2-1\right)}{x}\right)^{4\gamma^{-1}}\beta^{[*]}x^4- \\ 124^{\frac{\gamma-1}{\gamma}}\left(\frac{\lceil(\gamma+1)\left(x^2-1\right)}{x}\right)^{2\gamma^{-1}}\beta^{[*]}x^4 \\ -1216^{-\gamma^{-1}}\left(\frac{\lceil(\gamma+1)\left(x^2-1\right)}{x}\right)^{4\gamma^{-1}}\beta^{[*]}x^2 \\ +64^{\frac{\gamma-1}{\gamma}}\left(\frac{\lceil(\gamma+1)\left(x^2-1\right)}{x}\right)^{2\gamma^{-1}}\beta^{[*]}x^2 \end{pmatrix},$$

$$\wp_{14}^{[i]}=\begin{pmatrix} -4^{\frac{\gamma-1}{\gamma}}\left(\frac{\lceil(\gamma+1)\left(x^2-1\right)}{x}\right)^{2\gamma^{-1}}- \\ 4^{\frac{\gamma-1}{\gamma}}\left(\frac{\lceil(\gamma+1)\left(x^2-1\right)}{x}\right)^{3\gamma^{-1}}2^{\frac{\gamma-1}{\gamma}}x^5+ \\ 84^{-\gamma^{-1}}\left(\frac{\lceil(\gamma+1)\left(x^2-1\right)}{x}\right)^{3\gamma^{-1}}2^{\frac{\gamma-1}{\gamma}}x^3 \end{pmatrix},$$

$$\wp_{15}^{[i]}=\begin{pmatrix} -4^{\frac{\gamma-1}{\gamma}}\left(\frac{\lceil(\gamma+1)\left(x^2-1\right)}{x}\right)^{3\gamma^{-1}}2^{\frac{\gamma-1}{\gamma}}x- \\ 124^{\frac{-2+\gamma}{\gamma}}\left(\frac{\lceil(\gamma+1)\left(x^2-1\right)}{x}\right)^{4\gamma^{-1}}\beta^{[*]}x^2 \\ +124^{\frac{-2+\gamma}{\gamma}}\left(\frac{\lceil(\gamma+1)\left(x^2-1\right)}{x}\right)^{4\gamma^{-1}}\beta^{[*]}x^4 \\ -4^{\frac{\gamma-1}{\gamma}}\left(\frac{\lceil(\gamma+1)\left(x^2-1\right)}{x}\right)^{2\gamma^{-1}}\beta^{[*]} \end{pmatrix},$$

$$\wp_{16}^{[i]}=\begin{pmatrix} -416^{-\gamma^{-1}}\left(\frac{\lceil(\gamma+1)\left(x^2-1\right)}{x}\right)^{4\gamma^{-1}}x^2+ \\ 24^{\frac{\gamma-1}{\gamma}}\left(\frac{\lceil(\gamma+1)\left(x^2-1\right)}{x}\right)^{2\gamma^{-1}}x^2 \\ +616^{-\gamma^{-1}}\left(\frac{\lceil(\gamma+1)\left(x^2-1\right)}{x}\right)^{4\gamma^{-1}}\beta^{[*]}- \\ 4^{\frac{2\gamma-1}{\gamma}}\left(\frac{\lceil(\gamma+1)\left(x^2-1\right)}{x}\right)^{2\gamma^{-1}}x^4 \end{pmatrix},$$

$$\wp_{17}^{[i]}=\begin{pmatrix} -464^{-\gamma^{-1}}\left(\frac{\lceil(\gamma+1)\left(x^2-1\right)}{x}\right)^{6\gamma^{-1}}\beta^{[*]}+ \\ 216^{-\gamma^{-1}}\left(\frac{\lceil(\gamma+1)\left(x^2-1\right)}{x}\right)^{4\gamma^{-1}}x^4 \\ +34^{\frac{\gamma-1}{\gamma}}\left(\frac{\lceil(\gamma+1)\left(x^2-1\right)}{x}\right)^{2\gamma^{-1}}x^6+ \\ 256^{-\gamma^{-1}}\left(\frac{\lceil(\gamma+1)\left(x^2-1\right)}{x}\right)^{8\gamma^{-1}}\beta^{[*]} \end{pmatrix},$$

$$\wp_{18}^{[i]} = \begin{pmatrix} +216^{-\gamma^{-1}}\left(\frac{\lceil(\gamma+1)\left(x^2-1\right)}{x}\right)^{4\gamma^{-1}} + 3\,x^8 - \\ 52^{\frac{\gamma-1}{\gamma}}\left(\frac{\lceil(\gamma+1)\left(x^2-1\right)}{x}\right)^{\gamma^{-1}} x^7 \\ +4^{-\gamma^{-1}}\left(\frac{\lceil(\gamma+1)\left(x^2-1\right)}{x}\right)^{2\gamma^{-1}} x^6 + \\ 122^{\frac{\gamma-1}{\gamma}}\left(\frac{\lceil(\gamma+1)\left(x^2-1\right)}{x}\right)^{\gamma^{-1}} x^5 \end{pmatrix},$$

$$\wp_{19}^{[i]} = \begin{pmatrix} +62^{-\gamma^{-1}}\left(\frac{\lceil(\gamma+1)\left(x^2-1\right)}{x}\right)^{\gamma^{-1}} x^5 - \\ 154^{-\gamma^{-1}}\left(\frac{\lceil(\gamma+1)\left(x^2-1\right)}{x}\right)^{2\gamma^{-1}} x^4 \\ -122^{\frac{\gamma-1}{\gamma}}\left(\frac{\lceil(\gamma+1)\left(x^2-1\right)}{x}\right)^{\gamma^{-1}} x^3 - \\ 62^{-\gamma^{-1}}\left(\frac{\lceil(\gamma+1)\left(x^2-1\right)}{x}\right)^{\gamma^{-1}} x^3 \end{pmatrix},$$

$$\wp_{20}^{[i]} = \begin{pmatrix} +154^{-\gamma^{-1}}\left(\frac{\lceil(\gamma+1)\left(x^2-1\right)}{x}\right)^{2\gamma^{-1}} x^2 + \\ 52^{\frac{\gamma-1}{\gamma}}\left(\frac{\lceil(\gamma+1)\left(x^2-1\right)}{x}\right)^{\gamma^{-1}} x \\ +\beta^{[*]}\,x^8 - 4\,\beta^{[*]}\,x^6 + \\ 6\,\beta^{[*]}\,x^4 - 4\,\beta^{[*]}\,x^2 + 18\,x^4 \\ -12\,x^6 - 4^{-\gamma^{-1}}\left(\frac{\lceil(\gamma+1)\left(x^2-1\right)}{x}\right)^{2\gamma^{-1}} \end{pmatrix},$$

$$\wp_{21}^{[i]} = \begin{pmatrix} -1216^{-\gamma^{-1}}\left(\frac{\lceil(\gamma+1)\left(x^2-1\right)}{x}\right)^{5\gamma^{-1}} 2^{\frac{\gamma-1}{\gamma}}\beta^{[*]}\,x^3 - \\ 124^{-\gamma^{-1}}\left(\frac{\lceil(\gamma+1)\left(x^2-1\right)}{x}\right)^{3\gamma^{-1}} 2^{\frac{\gamma-1}{\gamma}}\beta^{[*]}\,x^5 \\ +1216^{-\gamma^{-1}}\left(\frac{\lceil(\gamma+1)\left(x^2-1\right)}{x}\right)^{5\gamma^{-1}} 2^{\frac{\gamma-1}{\gamma}}\beta^{[*]}\,x \\ +244^{-\gamma^{-1}}\left(\frac{\lceil(\gamma+1)\left(x^2-1\right)}{x}\right)^{3\gamma^{-1}} \end{pmatrix},$$

$$\wp_{22}^{[i]} = \begin{pmatrix} 2^{\frac{\gamma-1}{\gamma}}\beta^{[*]}\,x^3 - \\ 124^{-\gamma^{-1}}\left(\frac{\lceil(\gamma+1)\left(x^2-1\right)}{x}\right)^{3\gamma^{-1}} 2^{\frac{\gamma-1}{\gamma}}\beta^{[*]}\,x - \\ 4^{\frac{\gamma-1}{\gamma}}\left(\frac{\lceil(\gamma+1)\left(x^2-1\right)}{x}\right)^{5\gamma^{-1}} 8^{\frac{\gamma-1}{\gamma}}\beta^{[*]}\,x^3 \\ +616^{-\gamma^{-1}}\left(\frac{\lceil(\gamma+1)\left(x^2-1\right)}{x}\right)^{6\gamma^{-1}} 4^{\frac{\gamma-1}{\gamma}}\beta^{[*]}\,x^2 \end{pmatrix},$$

$$\begin{aligned} \wp_{23}^{[i]} \quad = \quad & -464^{-\gamma^{-1}}\left(\frac{\lceil(\gamma+1)\left(x^2-1\right)}{x}\right)^{7\gamma^{-1}} 2^{\frac{\gamma-1}{\gamma}}\beta^{[*]}\,x \\ & +\beta^{[*]} - 12\,x^2. \end{aligned}$$

For $\gamma \approx 1$, we have

$$R(x) = -\frac{\varphi_1^{[*]} x^{10} + \varphi_2^{[*]} x^8 + \varphi_3^{[*]} x^6 + \varphi_4^{[*]} x^4 + (5x^2 - 1)\beta^{[*]}}{512x^9}, \tag{33}$$

where $\varphi_1^{[*]} = \left(\beta^{[*]} - 160\right)$, $\varphi_1^{[*]} = \left(-5\beta^{[*]} - 480\right)$, $\varphi_1^{[*]} = \left(10\beta^{[*]} + 160\right)$, $\varphi_1^{[*]} = \left(-10\beta^{[*]} - 32\right)$ and a, b belong to $\mathbb{C}$. Thus, $R(x)$ depends on a, b, and x. Using the Möbius transformation $M(x) = \frac{x-a}{x-b}$, we see that $R(x)$ is conjugate with the operator, and for $\gamma \approx 1$, we have [19]

$$\mathrm{O}(x) = \frac{x^4\left(-x^6 - 8x^5 - 27x^4 - 48x^3 + \beta^{[*]}x - 47x^2 - 24x - 5\right)}{\left(\beta^{[*]}x^5 - 5x^6 - 24x^5 - 47x^{4\cdot} - 48x^3 - 27x^2 - 8x - 1\right)^3}, \tag{34}$$

which is independent of a and b, as shown using Maple with 0 or ∞. Thus, $R(x)$ fits precisely with:

$$R^{[*]}(x) = \frac{\sum_{i=0}^{n}\left(a_i x^i\right)}{\sum_{i=0}^{n}\left(a_{n-i}x^i\right)};\ \{a_i\}_{i=0}^{n} \in R, \tag{35}$$

which exhibits interesting properties [27].

Proposition 1. *The fixed points of* $\mathrm{O}(\tau)$ *are as follows:*

- $\tau_0 = 0; \tau_\infty = \infty$ *are super-attracting points.*
- $\tau_1 = 1$ *is a repelling point, and*
- *The critical points* 0 *and* 1 *are super-attracting and repelling points, respectively, for* $\gamma \approx 1$, *and are given by:*

$$\begin{aligned}
C_1^{[*]} &= \frac{-16.0 + \beta^{[*]}}{16.0} - \frac{\sqrt{\beta^{[*]}\left(5\beta^{[*]} - 288\right)}}{16\sqrt{5.0}} - \frac{\sqrt{\beta_1^{[*]}}}{8\sqrt{10.0}},\\
C_2^{[*]} &= \frac{-16.0 + \beta^{[*]}}{16.0} - \frac{\sqrt{\beta^{[*]}\left(5\beta^{[*]} - 288\right)}}{16\sqrt{5.0}} + \frac{\sqrt{\beta_1^{[*]}}}{8\sqrt{10.0}},\\
C_3^{[*]} &= \frac{-16.0 + \beta^{[*]}}{16.0} - \frac{\sqrt{\beta^{[*]}\left(5\beta^{[*]} - 288\right)}}{16\sqrt{5.0}} + \frac{\sqrt{\beta_2^{[*]}}}{2},\\
C_4^{[*]} &= \frac{-16.0 + \beta^{[*]}}{16.0} - \frac{\sqrt{\beta^{[*]}\left(5\beta^{[*]} - 288\right)}}{16\sqrt{5.0}} - \frac{\sqrt{\beta_2^{[*]}}}{2},
\end{aligned}$$

where $\beta_1^{[*]} = -224\beta^{[*]} + 5\left(\beta^{[*]}\right)^2 - \frac{4608\sqrt{5}\beta^{[*]}}{\sqrt{5\beta^{[*]}-288}} + \frac{268\sqrt{5}\left(\beta^{[*]}\right)^{2/3}}{\sqrt{5\beta^{[*]}-288}} - \frac{5\sqrt{5}\left(\beta^{[*]}\right)^{5/2}}{\sqrt{5\beta^{[*]}-288}}$,

$\beta_2^{[*]} = -2 + \left(\frac{16-\left(\beta^{[*]}\right)^2}{32}\right) - \frac{30+2\beta^{[*]}}{5} + \frac{\beta_3^{[*]}}{\sqrt{5\beta^{[*]}-288}}$, $\beta_3^{[*]} = 2\sqrt{5}\left(\left(\beta^{[*]} - 32\right) - \frac{\left(64-\beta^{[*]}\right)^2}{64} + \frac{2\left(16-\beta^{[*]}\right)\left(15+\beta^{[*]}\right)}{5}\right)$.

The stability function for $\gamma \approx 1$ in the single root-finding method is given by:

$$\left(1, \beta^{[*]}\right) = \frac{-81,920 + 512\beta^{[*]}}{\left(-160 + \beta^{[*]}\right)^2}. \tag{36}$$

For other values of the fractional parameter $\gamma \in [0, 1]$, the stability regions are examined, as shown in Figure 1a–c.

The stability region of the fractional iterative method MM^{γ} for finding the root of nonlinear equations illustrates the initial guesses or parameters for which the method converges to the correct root, as seen in Figure 1a–c. The behavior in which the fractions contribute to assessing the method's resilience and effectiveness in solving nonlinear equations under a range of γ values is seen in Figure 1a,c. The role of the fractional parameter γ in determining the method's stability and effectiveness is highlighted in these figures. The method is more stable when $\gamma = 1$, with stability decreasing as γ approaches zero.

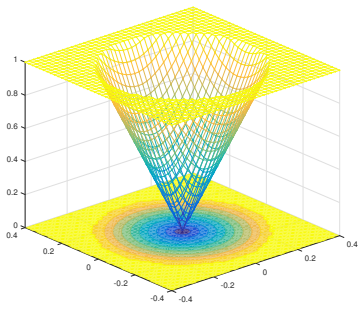

(**a**) Stability region for $\gamma \approx 1$.

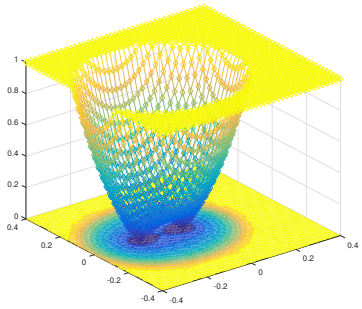

(**b**) Stability region for $\gamma \approx 0.7$.

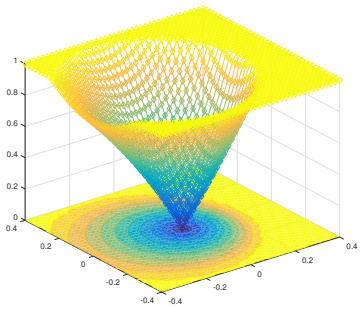

(**c**) Stability region for $\gamma \approx 0.5$.

Figure 1. (**a**–**c**): Stability regions of the scheme MM^{γ} for different values of γ.

By using critical points as starting values, parametric planes are generated (see Figure 2a–c), which depict the behavior of the method's iterations, including patterns such as convergence, divergence, and chaotic behavior (Figures 3a–h and 4a–c). These figures highlight stable and unstable behavior at various $\beta^{[*]}$ values and $\gamma = 1$. In Figures 2–4, small circles represent fixed points, squares with stars indicate super-attracting fixed points, and squares denote critical points.

Parametric planes are essential for understanding the convergence behavior of iterative methods used to solve nonlinear equations. They provide insights into the stability and efficiency of iterations, helping to identify optimal parameters for fast and accurate convergence. These planes also reveal divergence zones, allowing for the avoidance of parameters that may cause instability or failure. By analyzing parametric planes, the optimal parameters for minimizing the number of iterations and improving solution reliability can be determined.

The figures also illustrate the method's sensitivity to parameter changes, showing whether the approach is robust or requires careful tuning. Additionally, they display the nature of convergence—whether linear, super-linear, or quadratic—indicating how quickly the method reaches the solution. This information is crucial for selecting and optimizing parameters to ensure efficient and reliable problem-solving.

Understanding the dynamics of iterative methods is essential for solving nonlinear problems over time. Dynamic analysis helps evaluate how initial estimates affect outcomes, convergence rates, and overall stability. By analyzing these dynamics, one can ensure the reliability and efficiency of the approach, avoiding issues like slow convergence or divergence. In applied sciences and engineering, dynamic analysis plays a critical role in generating accurate solutions from iterative processes.

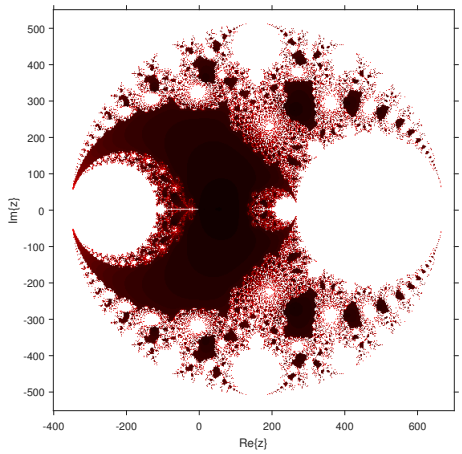

(**a**) Parametric plane for $\gamma \approx 0.99$.

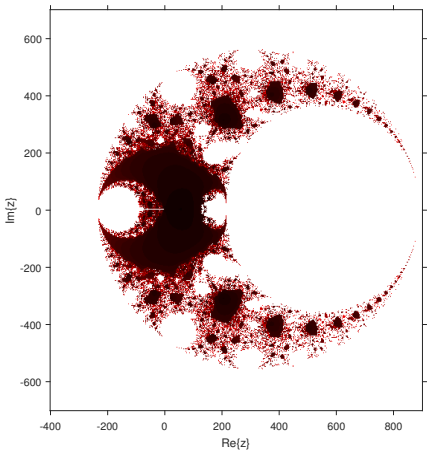

(**b**) Parametric plane for $\gamma \approx 0.8$.

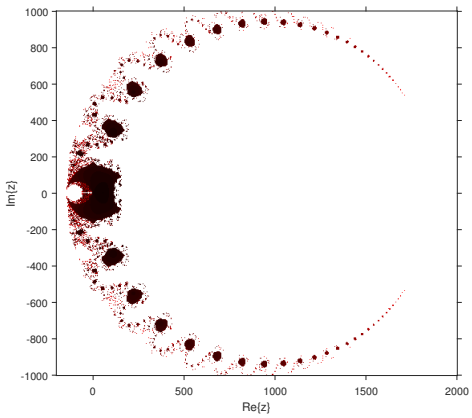

(**c**) Parametric plane for $\gamma \approx 0.5$.

Figure 2. (**a**–**c**): Dynamical planes for various parameter values of the rational map $O(\varepsilon)$.

Dynamic planes offer insights into solution stability, convergence patterns, and behavior throughout the iterations. These planes reveal zones of attraction, where iterations converge, and regions of repulsion, where they diverge. They also highlight fixed points, cycles, and chaotic behavior, providing a deeper understanding of the methods' sensitivity to initial conditions. This analysis is crucial for optimizing iterative methods and ensuring consistency in solving nonlinear equations. Similar to parametric planes, dynamic planes are generated to evaluate the stability of different schemes. Figure 3a–h shows the stable behavior of the schemes for various values of γ and $\beta^{[*]}$. Choosing $\beta^{[*]}$ values from the divergence zone of the parametric planes leads to unstable behavior, as illustrated in Figure 4a,c for different γ values.

Using the dynamical and parametric plane notation, we find the best parameter value that accelerates the rate of convergence of the simple root-finding method. Then, using the

newly developed stable fractional-order scheme MM^{γ} as a correction factor, we propose a novel parallel fractional scheme for analyzing (1) in the following section.

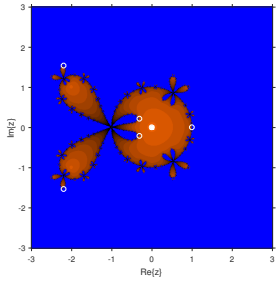

(**a**) Dynamical planes for $\gamma \approx 1$ and $\beta^{[*]} = 0.5$.

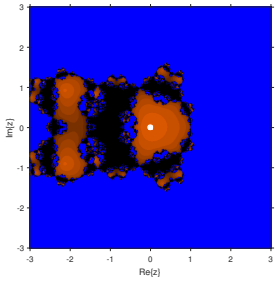

(**b**) Dynamical planes for $\gamma \approx 0.9$ and $\beta^{[*]} = 0.5$.

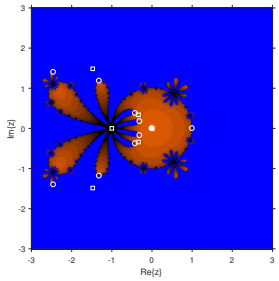

(**c**) Dynamical planes for $\gamma \approx 1$ and $\beta^{[*]} = 2.5$.

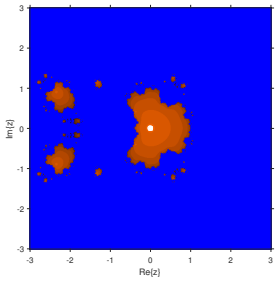

(**d**) Dynamical planes for $\gamma \approx 0.9$ and $\beta^{[*]} = 2.5$.

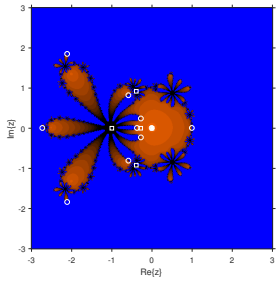

(**e**) Dynamical planes for $\gamma \approx 1$ and $\beta^{[*]} = 16$.

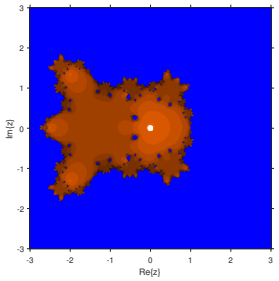

(**f**) Dynamical planes for $\gamma \approx 0.9$ and $\beta^{[*]} = 0.5$.

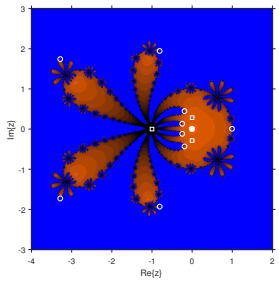

(**g**) Dynamical planes for $\gamma \approx 1$ and $\beta^{[*]} = -30$.

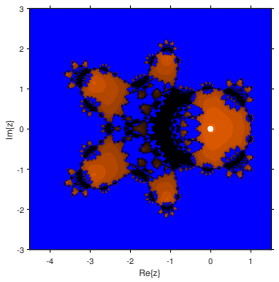

(**h**) Dynamical planes for $\gamma \approx 0.9$ and $\beta^{[*]} = -30$.

Figure 3. (**a**–**h**): Stable behavior for various dynamical planes of the rational map $O(\varepsilon)$.

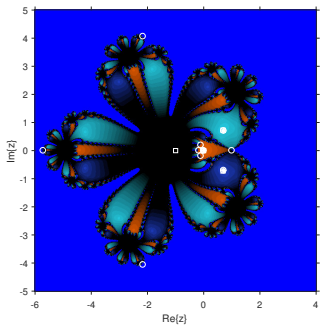

(**a**) Unstable behavior for $\gamma \approx 1$ and $\beta^{[*]} = 200$.

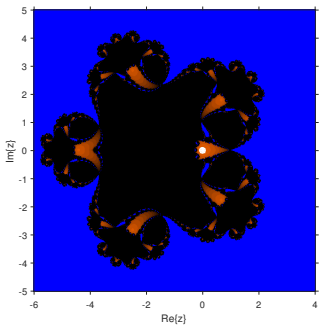

(**b**) Unstable behavior for $\gamma \approx 0.9$ and $\beta^{[*]} = -200$.

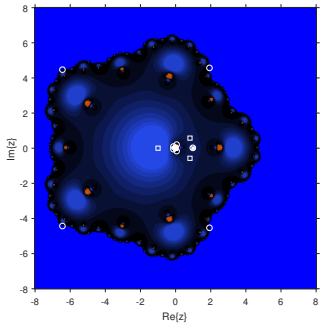

(**c**) Unstable behavior for $\gamma \approx 0.7$ and $\beta^{[*]} = 500$.

Figure 4. (**a**–**c**): Unstable dynamical behavior for various parameter values γ of the rational map $O(\varepsilon)$.

3. Development and Analysis of Fractional Parallel Scheme

Among derivative-free simultaneous methods, the Weierstrass–Durand–Kerner (also known as Weierstrass–Dochive) method [28] is one of the most effective approaches. It is defined as:

$$x_i^{[l+1]} = x_i^{[l]} - w(x_i^{[l]}), \tag{37}$$

where

$$w(x_i^{[l]}) = \frac{\hbar(x_i^{[l]})}{\prod\limits_{\substack{j=1 \\ j\neq i}}^{n} (x_i^{[l]} - x_j^{[l]})}, \quad (i, j = 1, \ldots, n), \tag{38}$$

is known as Weierstrass' correction. This method exhibits local quadratic convergence.

In 1977, Ehrlich [29] introduced the following third-order simultaneous method:

$$x_i^{[l+1]} = x_i^{[l]} - \frac{1}{\frac{1}{N_i(x_i^{[l]})} - \sum\limits_{\substack{j=1 \\ j\neq i}}^{n} \left(\frac{1}{\left(x_i^{[l]} - x_j^{[l]}\right)} \right)}, \tag{39}$$

where $x_j^{[l]} = u_j^{[l]}$ is used as a correction in (15). Petkovic et al. [30] improved the convergence order of this method from three to six:

$$x_i^{[l+1]} = x_i^{[l]} - \frac{1}{\frac{1}{N_i(x_i^{[l]})} - \sum\limits_{\substack{j=1 \\ j\neq i}}^{n} \left(\frac{1}{\left(x_i^{[l]} - x_j^{[l]}\right)} \right)}, \tag{40}$$

with the correction term: $u_j^{[l]} = x_i^{[l]} - \frac{\hbar(s_j^{[l]}) - \hbar(x_i^{[l]})}{2*\hbar(s_j^{[l]}) - \hbar(x_i^{[l]})} \frac{\hbar(x_i^{[l]})}{\hbar'(x_i^{[l]})}$, where $s_j^{[l]} = x_j^{[l]} - \frac{\hbar(x_j^{[l]})}{\hbar'(x_j^{[l]})}$.

Petkovic et al. [31] further accelerated the convergence order of this method from three to ten, giving the method (PM$^{[*]}$) as:

$$x_i^{[l+1]} = x_i^{[l]} - \frac{1}{\frac{1}{N_i(x_i^{[l]})} - \sum\limits_{\substack{j=1 \\ j\neq i}}^{n} \left(\frac{1}{\left(x_i^{[l]} - T_j^{[l]}\right)} \right)}, \tag{41}$$

where $T_j^{[l]} = \gamma_j^{[l]} - \frac{\left(\varsigma_j^{[l]} - \gamma_j^{[l]}\right)\hbar\left(\gamma_j^{[l]}\right)\left(\frac{\hbar\left(x_j^{[l]}\right)}{\hbar'\left(x_j^{[l]}\right)}\right)}{\left(\hbar\left(x_j^{[l]}\right) - \hbar\left(\gamma_j^{[l]}\right)\right)^2}\left[\hbar\left(\varsigma_j^{[l]}\right) - \frac{\hbar\left(x_j^{[l]}\right)}{\hbar\left(\varsigma_j^{[l]}\right) - \hbar\left(\gamma_j^{[l]}\right)}\right]$, $\gamma_j^{[l]} = \varsigma_j^{[l]} - \frac{\hbar\left(x_j^{[l]}\right)\hbar\left(\varsigma_j^{[l]}\right)\left(\frac{\hbar\left(x_j^{[l]}\right)}{\hbar'\left(x_j^{[l]}\right)}\right)}{\left(\hbar\left(x_j^{[l]}\right) - \hbar\left(\varsigma_j^{[l]}\right)\right)^2}$, $\varsigma_j^{[l]} = x_j^{[l]} - \frac{\hbar\left(x_j^{[l]}\right)}{\hbar'\left(x_j^{[l]}\right)}$.

Using the method (38) in (16), we developed a new parallel scheme MM$^{[*]}$ for simultaneously finding all solutions of Equation (1). The updated iterative scheme is:

$$s_i^{[l]} = \varsigma_i^{[l]} - \frac{\hbar(\varsigma_i^{[l]})}{\prod\limits_{\substack{j=1 \\ j\neq i}}^{n} (\varsigma_i^{[l]} - \varsigma_j^{[l]})} \left(\begin{array}{c} \left(\frac{\hbar(\varsigma_i^{[l]})}{\hbar(x_i^{[l]})}\right) + 2\left(\frac{\hbar(\varsigma_i^{[l]})}{\hbar(x_i^{[l]})}\right)^2 \\ +\beta^{[*]}\left(\frac{\hbar(\varsigma_i^{[l]})}{\hbar(x_i^{[l]})}\right)^4 \end{array} \right), \tag{42}$$

where $\varsigma_i^{[k]} = x_i^{[l]} - \frac{\hbar(x_i^{[l]})}{\prod\limits_{\substack{j=1 \\ j\neq i}}^{n} (x_i^{[l]} - v_j^{[l]})}$ and

$$v_j^{[l]} = x_j^{[l]} - \left(\lceil (\gamma+1) \frac{\hbar(x_j^{[l]})}{\hbar'(x_j^{[l]})} \left(\begin{array}{c} \left(\frac{\hbar(\varsigma_j^{[l]})}{\hbar(x_j^{[l]})}\right) \\ +2\left(\frac{\hbar(\varsigma_j^{[l]})}{\hbar(x_j^{[l]})}\right)^2 \\ +\beta^{[*]}\left(\frac{\hbar(\varsigma_j^{[l]})}{\hbar(x_j^{[l]})}\right)^4 \end{array} \right) \right)^{1/\gamma},$$

$$\varsigma_j^{[l]} = x_j^{[l]} - \left(\lceil (\gamma+1) \frac{\hbar(x_j^{[l]})}{\left[\mathfrak{D}_{\gamma_1}^{\gamma}\right]\hbar(x_j^{[l]})} \right)^{1/\gamma}; \beta^{[*]} \in R.$$

The following theorem defines the local order of convergence for the inverse fractional scheme.

Theorem 3. *Let $\zeta_1, \ldots, \zeta_\sigma$ be simple roots of a nonlinear equation, and assume that the initial distinct estimates $x_1^{[0]}, \ldots, x_n^{[0]}$ are sufficiently close to the true roots. Then, the MM$^{[*]}$ method achieves a convergence order of $6\gamma + 3$.*

Proof. Let $e_i = x_i^{[l]} - \zeta_i, e_\varsigma = \varsigma_i^{[l]} - \zeta_i$ and $e_i^{[*]} = s_i^{[l]} - \zeta_i$ represent the errors in $x_i^{[l]}$, $\varsigma_i^{[l]}$, and $s_i^{[l]}$, respectively. From the first-step of MM$^{[*]}$, we have:

$$\varsigma_i^{[l]} - \zeta_i = x_i^{[l]} - \zeta_i - \frac{\hbar(x_j^{[l]})}{\prod\limits_{\substack{j=1 \\ j\neq i}}^{n} (x_i^{[l]} - v_j^{[l]})}, \tag{43}$$

$$e_i' = e_i - e_i \prod_{\substack{j=1 \\ j\neq i}}^{n} \left[\frac{x_i^{[l]} - \zeta_j}{x_i^{[l]} - v_j^{[l]}} \right], \tag{44}$$

$$e_\varsigma = e_i \left(1 - \prod_{\substack{j=1 \\ j\neq i}}^{n} \left[\frac{x_i^{[l]} - \zeta_j}{x_i^{[l]} - v_j^{[l]}} \right] \right), \tag{45}$$

where $\prod_{\substack{j=1 \\ j\neq i}}^{n} \left[\frac{x_i^{[l]} - \zeta_j}{x_i^{[l]} - u_j^{[l]}} \right] = 1 + \frac{v_j^{[l]} - \zeta_j}{x_i^{[l]} - v_j^{[l]}} = \left(1 + O\left([e_i]^{3\gamma+1} \right) \right)^{l+1}$ and, from (31), $v_j^{[l]} - \zeta_j = O\left(\left| [e_i]^{3\gamma+1} \right| \right)$. Thus,

$$e_\varsigma = e_i \left(1 + (l-1) O\left(\left| [e_i]^{3\gamma+1} \right| \right) \right), \tag{46}$$

Assuming $\left| e_i^{2\gamma+1} \right| = \left| e_j^{2\gamma+1} \right|$, we have

$$e_\varsigma = O\left(\left| [e_i]^{3\gamma+2} \right| \right). \tag{47}$$

In the second step, we obtain:

$$s_i^{[l]} - \zeta_i = x_i^{[l]} - \zeta_i - \frac{\hbar(\varsigma_i^{[l]})}{\prod_{\substack{j=1 \\ j\neq i}}^{n} (\varsigma_i^{[l]} - \varsigma_j^{[l]})} \begin{pmatrix} \left(\frac{\hbar(\varsigma_i^{[l]})}{\hbar(x_i^{[l]})} \right) \\ +2 \left(\frac{\hbar(\varsigma_i^{[l]})}{\hbar(x_i^{[l]})} \right)^2 \\ +\beta^{[*]} \left(\frac{\hbar(\varsigma_i^{[l]})}{\hbar(x_i^{[l]})} \right)^4 \end{pmatrix}, \tag{48}$$

leading to:

$$e_i^{[*]} = e_\varsigma - \frac{\hbar(\varsigma_i^{[l]})}{\prod_{\substack{j=1 \\ j\neq i}}^{n} (\varsigma_i^{[l]} - \varsigma_j^{[l]})} \begin{pmatrix} \left(\frac{\hbar(\varsigma_i^{[l]})}{\hbar(x_i^{[l]})} \right) + 2 \left(\frac{\hbar(\varsigma_i^{[l]})}{\hbar(x_i^{[l]})} \right)^2 \\ +\beta^{[*]} \left(\frac{\hbar(\varsigma_i^{[l]})}{\hbar(x_i^{[l]})} \right)^4 \end{pmatrix}, \tag{49}$$

or

$$e_i^{[*]} = e_\varsigma - e_\varsigma \prod_{\substack{j=1 \\ j\neq i}}^{n} \left[\frac{x_i^{[l]} - \zeta_j}{x_i^{[l]} - u_j^{[l]}} \right] \begin{pmatrix} \left(\frac{e_\varsigma \vartheta^{[*]}}{e_i} \right) + \\ 2 \left(\frac{e_\varsigma \vartheta^{[*]}}{e_i} \right)^2 \\ +\beta^{[*]} \left(\frac{e_\varsigma \vartheta^{[*]}}{e_i} \right)^4 \end{pmatrix}, \tag{50}$$

where $\frac{\hbar(\varsigma_i^{[l]})}{\hbar(x_i^{[l]})} = \frac{e_\varsigma \vartheta^{[*]}}{e_i}$. Thus,

$$e_i^{[*]} = e_\varsigma \left(1 - \frac{e_i}{e_\varsigma} \prod_{\substack{j=1 \\ j\neq i}}^{n} \left[\frac{x_i^{[l]} - \zeta_j}{x_i^{[l]} - u_j^{[l]}} \right] \begin{pmatrix} \left(\frac{\vartheta^{[*]}}{e_i} \right) + \\ 2 e_\varsigma \left(\frac{\vartheta^{[*]}}{e_i} \right)^2 + \\ \beta^{[*](e_\varsigma)^3} \left(\frac{\vartheta^{[*]}}{e_i} \right)^4 \end{pmatrix} \right). \tag{51}$$

leading to:

$$e_i^{[*]} = e_\varsigma\left(1 - \vartheta^{[*]}\left(\begin{array}{c}\left(\frac{\vartheta^{[*]}}{e_i}\right) + 2e_\varsigma\left(\frac{\vartheta^{[*]}}{e_i}\right)^2 \\ +\beta^{[*](e_\varsigma)^3}\left(\frac{\left(\vartheta^{[*]}\right)^4}{(e_i)^3}\right)\end{array}\right)\right), \tag{52}$$

$$e_i^{[*]} = e_\varsigma\left(1 - O\left(\left|[e_i]^{3\gamma+1}\right|\right)\left(\frac{\Theta^{[**]}}{(e_i)^3}\right)\right), \tag{53}$$

where $\Theta^{[**]} = \left((e_i)^2\vartheta^{[*]} + 2e_ie_\varsigma\vartheta^{[*]} + \beta^{[*]}(e_\varsigma)^3\left(\vartheta^{[*]}\right)^4\right)$. We conclude that:

$$e_i^{[*]} = e_\varsigma\left(O\left(\left|[e_i]^{3\gamma+1}\right|\right)\right), \tag{54}$$

$$e_i^{[*]} = O\left(\left|[e_i]^{6\gamma+3}\right|\right). \tag{55}$$

This completes the proof. □

4. Numerical Results

In this section, we demonstrate the effectiveness and stability of the method by examining several engineering applications using the following termination criteria implemented in Maple 18:

$$(i) \qquad e_i = \left\|x_i^{[1+1]} - x_i^{[1]}\right\| < \in = 10^{-18} \tag{56}$$

where e_i represents the residual error norm-2. We compare our method with the PM$^{[*]}$ method and the approach presented in [32], referred to as ZM$^{[*]}$. Using Algorithm 1, we find all solutions to the nonlinear problem (1) simultaneously.

Algorithm 1 Parallel fractional numerical scheme MM$^{[*]}$ implementation on computer for solving nonlinear problems.

Algorithm 1 Parallel fractional numerical scheme MM$^{[*]}$.

Given initial values $x_i^{[0]}(j = 1, .., N)$, tolerance $\in > 0$ and set $l = 0$ for iterations qq

Compute:
$$\left\{\begin{array}{c}\varsigma_j^{[l]} = x_j^{[l]} - \left(\lceil(\gamma+1)\frac{\hbar(x_j^{[l]})}{\left[\varepsilon\supset_{\gamma_1}^{\gamma}\right]\hbar(x_j^{[l]})}\right)^{1/\gamma} \\ v_j^{[l]} = x_j^{[l]} - \left(\lceil(\gamma+1)\frac{\hbar(x_j^{[l]})}{\hbar'(x_j^{[l]})}\left(\begin{array}{c}\left(\frac{\hbar(\varsigma_j^{[l]})}{\hbar(x_j^{[l]})}\right) \\ +2\left(\frac{\hbar(\varsigma_j^{[l]})}{\hbar(x_j^{[l]})}\right)^2 \\ +\beta^{[*]}\left(\frac{\hbar(\varsigma_j^{[l]})}{\hbar(x_j^{[l]})}\right)^4\end{array}\right)\right)^{1/\gamma},\end{array}\right.$$

Update
$$\left\{\begin{array}{c}\varsigma_i^{[k]} = x_i^{[l]} - \frac{\hbar(x_i^{[l]})}{\prod_{\substack{j=1\\ j\neq i}}^{n}(x_i^{[l]} - v_j^{[l]})} \\ s_i^{[l]} = \varsigma_i^{[l]} - \frac{\hbar(\varsigma_i^{[l]})}{\prod_{\substack{j=1\\ j\neq i}}^{n}(\varsigma_i^{[l]} - \varsigma_j^{[l]})}\left(\begin{array}{c}\left(\frac{\hbar(\varsigma_i^{[l]})}{\hbar(x_i^{[l]})}\right) + 2\left(\frac{\hbar(\varsigma_i^{[l]})}{\hbar(x_i^{[l]})}\right)^2 \\ +\beta^{[*]}\left(\frac{\hbar(\varsigma_i^{[l]})}{\hbar(x_i^{[l]})}\right)^4\end{array}\right),\end{array}\right.$$

$s_i^{[1]} = x_i^{[l]}(i = 1, \ldots, n)$.

if $e_i^{[l]} = \left\|x_i^{[1+1]} - x_i^{[1]}\right\| < \in = 10^{-18}$ or $\sigma > qq$, then stop.

Set $l = l + 1$and go to step 2.

End do.

4.1. Example 1

Fractional differential equations are particularly useful in modeling complex engineering systems, such as the quarter car suspension model, where memory effects and damping properties play a critical role. Unlike traditional integer-order equations, fractional equations provide more accurate representations of systems with hereditary behaviors, such as viscoelasticity and energy dissipation in suspension systems. In this context, fractional differential equations are employed to design suspension models with improved performance and stability, making them powerful tools for addressing the challenges in automotive engineering and control system design. This leads to the following fractional differential equation:

$$\begin{cases} \left[{}_{\check{c}}\eth^{\gamma}_{\gamma_1}\right] y(x) + \alpha\Big(U^{[*]} - y(x)\Big)^4 = 0, \\ y(0) = 0, 0 < \gamma \leq 1, x \geq 0 \end{cases} \tag{57}$$

Using the method from [32], we simulate Equation (57) using the following nonlinear approximation:

$$y(x) \approx \begin{bmatrix} \frac{\alpha\left(U^{[*]}\right)^4}{\lceil(\gamma+1)} x^{\gamma} - \frac{4\alpha^2\left(U^{[*]}\right)^7}{\lceil(3\gamma+1)} x^{2\gamma} \\ + \left(\frac{16\alpha^3\left(U^{[*]}\right)^{10}\lceil(2\gamma+1)}{\lceil^2(\gamma+1)\lceil(3\gamma+1)}\right) x^{3\gamma} + \ldots \end{bmatrix}. \tag{58}$$

If we set $U^{[*]} = 1$, $\alpha = 1$, and $\gamma = 1$, Equation (58) becomes:

$$y_5(x) \approx x - 2x^2 + \frac{14x^3}{3} - \frac{35x^4}{3} + \frac{91}{3}x^5. \tag{59}$$

Equation (59) has five solutions:

$$\begin{aligned} \zeta_1 &= 0.0, \\ \zeta_{2,3} &= -0.152018637 \pm 03931364228i, \\ \zeta_{4,5} &= 0.314432633 \pm 0.25883527180i. \end{aligned}$$

The Caputo-type derivative of Equation (59) is:

$$\left[{}_{\check{c}}\eth^{\gamma}_{\gamma_1}\right] y_5(x) = \begin{bmatrix} \frac{91}{3}\frac{\lceil(6)}{\lceil(6-\gamma)}x^{5-\gamma} - \frac{35}{3}\frac{\lceil(5)}{\lceil(5-\gamma)}x^{4-\gamma} \\ + \frac{14}{3}\frac{\lceil(4)}{\lceil(4-\gamma)}x^{3-\gamma} \\ -2\frac{\lceil(3)}{\lceil(3-\gamma)}x^{2-\gamma} + \frac{\lceil(2)}{\lceil(2-\gamma)}x^{1-\gamma} \end{bmatrix}. \tag{60}$$

For the dynamical analysis, we set $\gamma = \frac{1}{2}$ in Equation (58) and obtain the following nonlinear equation:

$$y_5(x) \approx \frac{2\sqrt{x}}{\sqrt{\pi}} - 4x + \frac{32(3+2\pi)x^{\frac{3}{2}}}{3\pi^{\frac{3}{2}}} + \left(68 - \frac{60}{\pi}\right)x^2, \tag{61}$$

The exact root of Equation (61) is zero. The dynamical analysis of the simple root-finding method for this equation includes measurements of elapsed time, percentage convergence, total points, and the number of iterations for different $\beta^{[*]}$ values, as shown in Table 1 and Figure 5a–c.

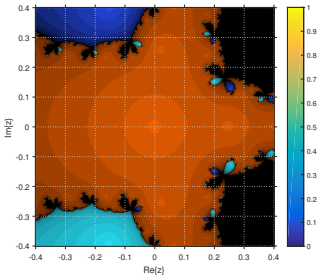

(**a**) Dynamical planes for $\gamma \approx 0.9$ and $\beta^{[*]} = 0.5$.

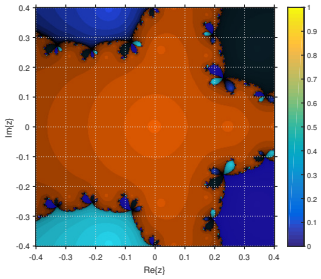

(**b**) Dynamical planes for $\gamma \approx 0.9$ and $\beta^{[*]} = 1.5$.

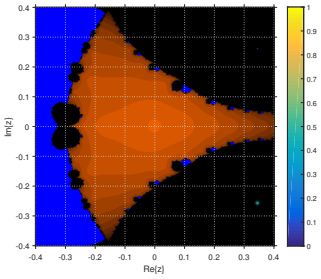

(**c**) Dynamical planes for $\gamma \approx 0.9$ and $\beta^{[*]} = 16$.

Figure 5. (**a**–**c**) Dynamical planes of the iterative technique for different values of $\beta^{[*]}$ while keeping fractional parameter $\gamma \approx 0.9$ for solving (61).

Using the information from Table 1 and the optimal parameter values from the dynamical analysis, these values are applied in parallel schemes to find all solutions to the nonlinear problems. Using initial guesses close to the exact solution $\in = 10^{-2}$, the convergence rate of the simultaneous methods increases, leading to faster convergence to the exact roots with fewer iterations.

Table 1. Dynamical outcomes of $\mathrm{MM}^{[\gamma]}$ for solving (61).

$\beta^{[*]}$	**Iterations**	**Total Points**	**Converging Points**	**Elapsed Time**
0.9	21	640,000	54%	2.14584165
0.7	22	640,000	59%	3.65483535
0.5	27	640,000	58%	5.36528456

In Table 2, $\sigma_i^{[4]}$ represents the local computational order of convergence [33]. The table clearly demonstrates that when $\gamma \approx 1$, the residual error for each root, along with the order and rate of convergence, is significantly improved compared to existing methods. This indicates higher efficiency and stability of the approach.

Tables 2 and 3 clearly show that across a range of γ, $\mathrm{MM}^{[*]}$ outperforms $\mathrm{ZM}^{[*]}$ and $\mathrm{PM}^{[*]}$ in terms of efficiency, computation time (CPU time), number of iterations (n), and residual error $\left(\left\|x_i^{[1+1]} - x_i^{[1]}\right\|\right)$. The convergence order of a fractional parallel iterative scheme is influenced by the fractional parameter, which captures memory effects. The convergence order of parallel systems is determined by the order of the fractional derivative, with faster convergence observed as γ increases. Our method, $\mathrm{MM}^{[*]}$, outperforms the

existing methods ZM$^{[*]}$ and PM$^{[*]}$ in the literature, achieving a convergence order of 9.002313 when $\gamma \approx 0.99$.

Table 2. Numerical results for Example 1.

Err	**PM**$^{[*]}$	**ZM**$^{[*]}$	**MM**$^{[*]}$
$e_1^{[5]}$	9.31×10^{-45}	1.11×10^{-99}	1.1×10^{-104}
$e_2^{[5]}$	2.09×10^{-55}	3.02×10^{-76}	0.0
$e_3^{[5]}$	0.17×10^{-76}	0.12×10^{-85}	0.0
$e_4^{[5]}$	0.07×10^{-39}	6.27×10^{-101}	4.9×10^{-165}
$e_4^{[5]}$	1.07×10^{-39}	6.27×10^{-101}	4.9×10^{-165}
$\sigma_i^{[4]}$	8.127654	9.001923	9.125432

Table 3. Outcomes of the fractional scheme MM$^{[*]}$ for different γ values for solving engineering application 1.

γ	**Iteration**	$\left\|x_i^{[1+1]} - x_i^{[1]}\right\|$	$\sigma_i^{[n-1]}$	**CPU Time**
0.1	36	0.2×10^{-5}	3.2132	0.097
0.2	24	1.4×10^{-6}	4.2654	0.096
0.3	22	0.7×10^{-6}	4.8236	0.076
0.4	12	0.5×10^{-4}	5.4455	0.066
0.5	10	5.4×10^{-6}	6.0432	0.035
0.6	08	1.3×10^{-7}	6.6653	0.038
0.7	08	0.6×10^{-9}	7.2124	0.015
0.8	07	0.3×10^{-11}	7.5434	0.004
0.9	06	2.6×10^{-16}	8.1325	0.001

4.2. Example 2

In order to extend classical differential equations and enable more accurate descriptions of physical systems, such as electrical circuits, fluid flow, and viscoelastic materials, fractional calculus is added. This method also enables a more flexible representation of anomalous diffusion and wave propagation, which improves predictions in fields such as biology and materials science and leads to the following fractional initial value problem [34]:

$$\begin{cases} \left[{}_{\mathcal{L}}\eth_{\gamma_1}^{\gamma}\right] y(x) + e^{y(x)} = 0, \\ y(0) = 0, y'(0) = 0, 1 < \gamma \leq 2, x \geq 0 \end{cases} \tag{62}$$

Using the method from [32], we simulate Equation (62) with the following nonlinear approximation:

$$y_n(x) \approx \left[\begin{array}{c} -\frac{1}{\lceil(\gamma+1)} x^{\gamma} + \frac{1}{\lceil(3\gamma+1)} x^{2\gamma} \\ + \left(\frac{2(\lceil(\gamma+1))^2 \lceil(2\gamma+1)}{2\lceil^2(\gamma+1)\lceil(3\gamma+1)} \right) x^{3\gamma} + \ldots \end{array} \right]. \tag{63}$$

For $\gamma = 1$, Equation (63) simplifies to:

$$y_3(x) \approx -x + \frac{1}{2}x^2 - 2x^3, \tag{64}$$

Equation (64) has the following solutions:

$$\begin{aligned} \zeta_1 &= 0.0, \\ \zeta_{2,3} &= 0.1250000 \pm 0.695970545i. \end{aligned}$$

The Caputo-type derivative of Equation (63) is:

$$\left[{}_{\breve{c}}\eth_{\gamma_1}^{\gamma}\right] y_5(x) = \begin{bmatrix} -\frac{2\lceil(4)}{\lceil(4-\gamma)}x^{3-\gamma} + \frac{1}{2}\frac{\lceil(3)}{\lceil(3-\gamma)}x^{2-\gamma} \\ -\frac{\lceil(2)}{\lceil(2-\gamma)}x^{1-\gamma} \end{bmatrix}. \tag{65}$$

For the dynamical analysis, we set $\gamma = \frac{1}{2}$ in Equation (63) and obtain the following nonlinear equation:

$$y_5(x) \approx x - \frac{2\sqrt{x}}{\sqrt{\pi}} - \frac{2\left(\frac{1}{2}\pi + 1\right)x^{\frac{3}{2}}}{\pi\left(\frac{3}{4}\sqrt{\pi}\right)}, \tag{66}$$

The exact root of Equation (66) is zero. The dynamical analysis of the simple root-finding method for this equation includes elapsed time, percentage convergence, total points, and the number of iterations for different $\beta^{[*]}$ values, as shown in Table 4.

Table 4. Dynamical outcomes of $\mathrm{MM}^{[\gamma]}$ for solving (66).

$\beta^{[*]}$	**Iterations**	**Total Points**	**Converging Points**	**Elapsed Time**
0.9	21	640,000	54%	1.33464564
0.7	18	640,000	59%	2.67454366
0.5	20	640,000	58%	5.233554675

Using initial guesses close to the exact solution (up to $\in = 10^{-2}$), the convergence rate of the simultaneous methods improves, reaching the exact roots with fewer iterations. Table 4 clearly shows that when $\gamma \approx 1$, the residual error for each root, as well as the convergence order and rate of convergence, are superior to existing methods, indicating better efficiency and stability. The numerical outcomes for random initial guesses are presented in Table 5 and Figure 6a–c.

Table 5. Numerical results for Example 2.

Err	$\mathbf{PM}^{[*]}$	$\mathbf{ZM}^{[*]}$	$\mathbf{MM}^{[*]}$
$e_1^{[3]}$	0.2×10^{-53}	1.1×10^{-51}	0.0
$e_2^{[3]}$	1.4×10^{-44}	0.0	0.0
$e_3^{[3]}$	0.6×10^{-45}	5.0×10^{-57}	5.0×10^{-65}
$e_4^{[3]}$	0.6×10^{-45}	5.0×10^{-57}	5.0×10^{-65}
$e_5^{[3]}$	0.6×10^{-45}	5.0×10^{-57}	5.0×10^{-65}
$\sigma_i^{[2]}$	7.993434	8.991923	9.001232

In Table 5, $\sigma_i^{[n-1]}$ represents the local computational order of convergence. The table clearly demonstrates that when $\gamma \approx 1$, the residual error for each root, as well as the convergence order and rate of convergence, are significantly improved compared to existing methods. This highlights the method's enhanced efficiency and stability.

The numerical results in Table 6 show that across a range of γ values, $\mathrm{MM}^{[*]}$ outperforms both $\mathrm{ZM}^{[**]}$ and $\mathrm{PM}^{[*]}$ in terms of efficiency, CPU time (in seconds), number of iterations, and residual error. The convergence order of a fractional parallel iterative scheme is influenced by the fractional parameter, which captures memory effects. The convergence order of parallel systems is determined by the order of the fractional derivative, with faster convergence observed as γ increases. Our method, $\mathrm{MM}^{[*]}$, outperforms the existing methods $\mathrm{ZM}^{[*]}$ and $\mathrm{PM}^{[*]}$ from the literature, achieving a convergence order of 9.002313 when $\gamma \approx 0.99$.

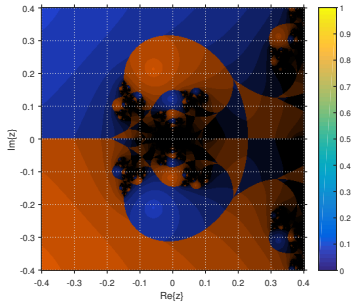

(**a**) Dynamical planes for $\gamma \approx 0.9$ and $\beta^{[*]} = 0.5$.

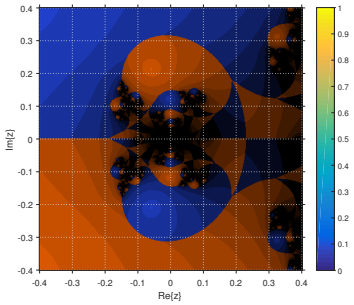

(**b**) Dynamical planes for $\gamma \approx 0.9$ and $\beta^{[*]} = 1.5$.

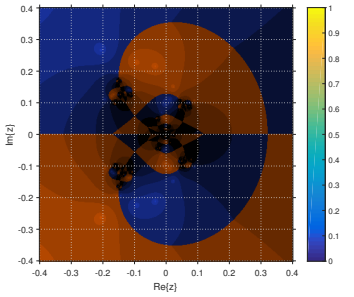

(**c**) Dynamical planes for $\gamma \approx 0.9$ and $\beta^{[*]} = 16$.

Figure 6. (**a**–**c**) Dynamical planes of the iterative technique for different values of $\beta^{[*]}$ while keeping fractional parameter $\gamma \approx 0.9$ for solving (66).

Table 6. Outcomes of the fractional scheme $\mathrm{MM}^{[*]}$ for different γ values for solving engineering application 2.

γ	n	$\left\|x_i^{[1+1]} - x_i^{[1]}\right\|$	$\sigma_i^{[n-1]}$	CPU Time
0.1	05	0.3×10^{-4}	3.0976	0.097
0.2	05	1.5×10^{-8}	4.2004	0.086
0.3	06	0.7×10^{-8}	4.8546	0.088
0.4	06	7.4×10^{-9}	5.4132	0.076
0.5	05	0.5×10^{-11}	5.9962	0.063
0.6	06	0.4×10^{-15}	6.2353	0.058
0.7	06	0.1×10^{-19}	6.9864	0.045
0.8	05	0.4×10^{-20}	7.1243	0.038
0.9	05	3.7×10^{-27}	7.9876	0.001

5. Conclusions

We developed a new Caputo-type fractional scheme with a convergence order of $3\gamma + 1$ to find simple solutions to Equation (1) and extended it into a fractional parallel numerical scheme for solving all nonlinear fractional problems. The parallel schemes were shown to have a convergence order of $6\gamma + 3$ based on our convergence analysis. To improve the convergence rate of these fractional schemes, dynamical planes were used to select optimal initial guesses, ensuring convergence to exact solutions. Several nonlinear problems were tested to assess the stability and consistency of $\mathrm{MM}^{[*]}$ in comparison to

$ZM^{[**]}$, $PM^{[*]}$. The numerical results demonstrate that the $MM^{[*]}$ method is more stable and consistent in terms of residual error, CPU time, and error graphs for different γ values, outperforming both $ZM^{[**]}$ and $PM^{[*]}$. Future research will focus on applying our fractional-order parallel technique to advanced control systems, biological processes, financial models, complex networks, and chaotic dynamics. Additionally, integrating fractional-order parallel schemes with machine learning [35,36] and enhancing computational efficiency could further expand its applicability and impact.

Author Contributions: Conceptualization, M.S. and B.C.; methodology, M.S.; software, M.S.; validation, M.S.; formal analysis, B.C.; investigation, M.S.; resources, B.C.; writing—original draft preparation, M.S. and B.C.; writing—review and editing, B.C.; visualization, M.S. and B.C.; supervision, B.C.; project administration, B.C.; funding acquisition, B.C.; All authors have read and agreed to the published version of the manuscript.

Funding: The work is supported by the Free University of Bozen-Bolzano (IN200Z SmartPrint) and by Provincia Autonoma di Bolzano/Alto Adige—Ripartizione Innovazione, Ricerca, Università e Musei (CUP codex I53C22002100003 PREDICT). Bruno Carpentieri is a member of the *Gruppo Nazionale per il Calcolo Scientifico* (GNCS) of the Istituto Nazionale di Alta Matematica (INdAM), and this work was partially supported by INdAM-GNCS under Progetti di Ricerca 2024.

Data Availability Statement: Data are contained within the article.

Acknowledgments: The work is supported by the Free University of Bozen-Bolzano (IN200Z SmartPrint) and by Provincia Autonoma di Bolzano/Alto Adige—Ripartizione Innovazione, Ricerca, Università e Musei (CUP codex I53C22002100003 PREDICT). Bruno Carpentieri is a member of the *Gruppo Nazionale per il Calcolo Scientifico* (GNCS) of the Istituto Nazionale di Alta Matematica (INdAM) and this work was partially supported by INdAM-GNCS under Progetti di Ricerca 2024.

Conflicts of Interest: The authors declare that there are no conflicts of interest regarding the publication of this article.

Abbreviations

The following abbreviations are used in this manuscript:

$MM^{[*]}$	Newly developed Schemes
n	Iterations
CPU time	Computational Time in Seconds
e-	$10^{-()}$
$\rho_{\zeta}^{[k-1]}$	Computational local convergence order

References

1. Shafiq, F.; Malik, M. Fractional Derivatives with Applications: A Review. *Math. Sci. Appl.* **2023**, *2*, 33–50.
2. Mainardi, F. Fractional calculus: Theory and applications. *Mathematics* **2018**, *6*, 145. [CrossRef]
3. Liu, P.; Zhang, Y.; Mohammed, K.J.; Lopes, A.M.; Saberi-Nik, H. The global dynamics of a new fractional-order chaotic system. *Chaos Solitons Fractals* **2023**, *175*, 114006. [CrossRef]
4. Machado, J.T.; Kiryakova, V.; Mainardi, F. Recent history of fractional calculus. *Commun. Nonlinear Sci. Numer. Simul.* **2011**, *16*, 1140–1153. [CrossRef]
5. Venkateshan, S.P.; Swaminathan, P. *Computational Methods in Engineering*; Academic Press: Cambridge, MA, USA, 2014; pp. 317–373.
6. Hiptmair, R. Finite elements in computational electromagnetism. *Acta Numer.* **2002**, *11*, 237–339. [CrossRef]
7. Lomax, H.; Pulliam, T.H.; Zingg, D.W.; Kowalewski, T.A. Fundamentals of computational fluid dynamics. *Appl. Mech. Rev.* **2002**, *55*, B61. [CrossRef]
8. Cantwell, B.J. Organized motion in turbulent flow. *Annu. Rev. Fluid Mech.* **1981**, *13*, 457–515. [CrossRef]
9. Sebah, P.; Gourdon, X. Introduction to the gamma function. *Am. J. Sci. Res.* **2002**, *1*, 2–18.
10. Gao, G.H.; Sun, Z.Z.; Zhang, H.W. A new fractional numerical differentiation formula to approximate the Caputo fractional derivative and its applications. *J. Comput. Phys.* **2014**, *259*, 33–50. [CrossRef]
11. El-Ajou, A.; Arqub, O.A.; Al-Smadi, M. A general form of the generalized Taylor's formula with some applications. *Appl. Math. Comput.* **2015**, *256*, 851–859. [CrossRef]

12. Neta, B. New third order nonlinear solvers for multiple roots. *Appl. Math. Comput.* **2008**, *202*, 162–170. [CrossRef]
13. Liu, C.S.; Chang, C.W. New memory-updating methods in two-step Newton's variants for solving nonlinear equations with high efficiency index. *Mathematics* **2024**, *12*, 581. [CrossRef]
14. Torres-Hernandez, A.; Brambila-Paz, F. Sets of fractional operators and numerical estimation of the order of convergence of a family of fractional fixed-point methods. *Fractal Fract.* **2021**, *4*, 240. [CrossRef]
15. Akgül, A.; Cordero, A.; Torregrosa, J.R. A fractional Newton method with 2th-order of convergence and its stability. *Appl. Math. Lett.* **2019**, *98*, 344–351. [CrossRef]
16. Cajori, F. Historical note on the Newton-Raphson method of approximation. *Am. Math. Mon.* **1911**, *18*, 29–32. [CrossRef]
17. Kumar, P.; Agrawal, O.P. An approximate method for numerical solution of fractional differential equations. *Signal Process.* **2006**, *86*, 2602–2610 [CrossRef]
18. Candelario, G.; Cordero, A.; Torregrosa, J.R. Multipoint fractional iterative methods with $(2\alpha + 1)$ th-order of convergence for solving nonlinear problems. *Mathematics* **2020**, *8*, 452. [CrossRef]
19. Rafiq, N.; Akram, S.; Mir, N.A.; Shams, M. Study of dynamical behavior and stability of iterative methods for nonlinear equation with applications in engineering. *Math. Probl. Eng.* **2020**, *2020*, 3524324. [CrossRef]
20. Cordero, A.; Hueso, J.L.; MartÃ-nez, E.; Torregrosa, J.R. New modifications of Potra-Patk method with optimal fourth and eighth orders of convergence. *J. Comput. Appl. Math.* **2010**, *234*, 2969–2976. [CrossRef]
21. Sivalingam, S.M.; Govindaraj, V. Physics informed neural network based scheme and its error analysis for ψ-Caputo type fractional differential equations. *Phys. Scr.* **2024**, *99*, 096002. [CrossRef]
22. Chun, C. Some variants of King's fourth-order family of methods for nonlinear equations. *Appl. Math. Comput.* **2007**, *190*, 57–62. [CrossRef]
23. Chun, C. Some fourth-order iterative methods for solving nonlinear equations. *Appl. Math. Comput.* **2008**, *195*, 454–459. [CrossRef]
24. Kyncheva, V.K.; Yotov, V.V.; Ivanov, S.I. Convergence of Newton, Halley and Chebyshev iterative methods as methods for simultaneous determination of multiple polynomial zeros. *Appl. Numer. Math.* **2017**, *112*, 146–154. [CrossRef]
25. Marcheva, P.I.; Ivanov, S.I. Convergence analysis of a modified Weierstrass method for the simultaneous determination of polynomial zeros. *Symmetry* **2020**, *12*, 1408. [CrossRef]
26. Sivalingam, S.M.; Kumar, P.; Govindaraj, V. A Chebyshev neural network-based numerical scheme to solve distributed-order fractional differential equations. *Comp. Math. Appl.* **2024**, *164*, 150–165. [CrossRef]
27. Chicharro, F.I.; Cordero, A.; Garrido, N.; Torregrosa, J.R. Stability and applicability of iterative methods with memory. *J. Math. Chem.* **2019**, *57*, 1282–1300. [CrossRef]
28. Herceg, D.; Tričković, S.; Petković, M. On the fourth order methods of Weierstrass' type. *Nonlinear Anal. Theory, Methods Appl.* **1997**, *30*, 83–88. [CrossRef]
29. Ehrlich, L.W. A modified Newton method for polynomials. *Commun. ACM* **1967**, *10*, 107–108. [CrossRef]
30. Petkovic, M.S.; Petkovic, L.D.; Dzunic, J. On an efficient method for the simultaneous approximation of polynomial multiple roots. *Appl. Anal. Discrete Math.* **2014**, *1*, 73–94. [CrossRef]
31. Petkovic, M.S.; Petkovic, L.D.; Dzunic, J. On an efficient simultaneous method for finding polynomial zeros. *Appl. Math. Lett.* **2014**, *28*, 60–65. [CrossRef]
32. Shams, M.; Carpentieri, B. On highly efficient fractional numerical method for solving nonlinear engineering models. *Mathematics* **2023**, *11*, 4914. [CrossRef]
33. Jay, L.O. A note on Q-order of convergence. *BIT Numer. Math.* **2001**, *41*, 422–429. [CrossRef]
34. Duan, J.S.; Chaolu, T.; Rach, R.; Lu, L. The Adomian decomposition method with convergence acceleration techniques for nonlinear fractional differential equations. *Comput. Math. Appl.* **2013**, *66*, 728–736. [CrossRef]
35. King, R.F. A family of fourth order methods for nonlinear equations. *SIAM J. Numer. Anal.* **1973**, *10*, 876–879. [CrossRef]
36. Monsi, M.; Hassan, N.; Rusli, S.F. The Point Zero Symmetric Single-Step Procedure for Simultaneous Estimation of Polynomial Zeros. *J. Appl. Math.* **2012**, *2012*, 709832. [CrossRef]

Disclaimer/Publisher's Note: The statements, opinions and data contained in all publications are solely those of the individual author(s) and contributor(s) and not of MDPI and/or the editor(s). MDPI and/or the editor(s) disclaim responsibility for any injury to people or property resulting from any ideas, methods, instructions or products referred to in the content.

symmetry

MDPI

Article

Chaotic-Based Improved Henry Gas Solubility Optimization Algorithm: Application to Electric Motor Control

Muhammed Salih Sarıkaya [1,*], Yusuf Hamida El Naser [1], Sezgin Kaçar [2], İrfan Yazıcı [3] and Adnan Derdiyok [1]

[1] Mechatronics Engineering, Faculty of Technology, Sakarya University of Applied Sciences, Sakarya 54050, Turkey; yusufelnaser@subu.edu.tr (Y.H.E.N.); derdiyok@subu.edu.tr (A.D.)
[2] Electrical and Electronics Engineering, Faculty of Technology, Sakarya University of Applied Sciences, Sakarya 54050, Turkey; skacar@subu.edu.tr
[3] Electrical and Electronics Engineering, Faculty of Engineering, Sakarya University, Sakarya 54050, Turkey; iyazici@sakarya.edu.tr
* Correspondence: salihsarikaya@subu.edu.tr

Abstract: This study presents a novel meta-heuristic optimization method that combines the Henry Gas Solubility Optimization (HGSO) technique with symmetric chaotic systems. By leveraging the randomness of chaotic systems, the parameters of the HGSO algorithm that require random generation are produced through chaotic processes, allowing the algorithm to exhibit chaotic behavior in its pursuit of optimal values. This innovative approach is termed Chaotic Henry Gas Solubility Optimization (CHGSO), with the primary objective of enhancing the performance of the HGSO method. The randomness of the data obtained from chaotic systems was validated using NIST-800-22 tests. The CHGSO method was applied to both 47 benchmark functions and the optimization of parameters for a PID controller utilized in the speed control of a DC motor. To evaluate the effectiveness of the proposed method, it was compared with several widely recognized algorithms in the literature, including PSO, WOA, GWO, EA, SA, and the original HGSO algorithm. The results demonstrate that the proposed method achieved the best performance in 43 of the benchmark functions, outperforming the other algorithms. In the context of controller design, the PID parameters were optimized using the error-based ITSE objective function. According to the controller responses, the proposed method has achieved the best results in the simulation studies, with a settling time of 0.035 and a rise time of 0.014 without overshooting, and in the experimental studies, with a settling time of 0.15 and a settling time of 1.4%. When the results are examined, it is observed that it has achieved successful results in the controller design problem.

Keywords: Henry gas solubility optimization; hybrid metaheuristic optimization; PID controller; DC motor

1. Introduction

Optimization has an important place in every field in the world. Recently, meta-heuristic optimization methods have been frequently preferred. In the current literature, various optimization methods are being applied across different fields. For instance, the Bonobo Optimization Algorithm has been utilized to optimize Support Vector Machine for establishing a relationship between entropy-based features and fault types in bearing fault diagnosis [1]. Horse Herd Optimization has been employed for the optimal sizing of photovoltaic/hydropower/fuel cell systems to minimize energy costs [2]. Ant Colony Optimization has been applied to a distributed flexible job shop problem developed for maintenance and transportation operations [3]. Multi-Objective Hybrid Teaching–Learning-Based Optimization–Grey Wolf Optimizer (MOHTLBOGWO) has been used to solve the optimal placement problem of energy resources, aiming to reduce losses and improve reliability in radial distribution systems [4]. A sinusoidal-cosine algorithm has been developed for the optimal design and energy management of hybrid photovoltaic/wind/fuel cell

systems [5]. Brain Storm Optimization and the Learning-Driven Brain Storm Optimization Algorithm have been proposed for open shop, vehicle routing, and energy efficiency problems [6,7]. Additionally, a multi-objective evolutionary algorithm has been implemented for scheduling in distributed flexible job shops with random processing times [8]. As these examples illustrate, a wide variety of current optimization methods are employed in various domains. One of the optimization methods that maintains its relevance in the literature, demonstrate advantages in computational cost, and has shown convergence to optimal values is the Henry Gas Solubility Optimization method, which is discussed in this study. The Henry Gas Solubility Optimization (HGSO) method is based on Henry's Law, formulated by William Henry in the 19th century. Henry's Law states that the solubility of gases in liquids at a constant temperature is directly proportional to the partial pressure of the gas. HGSO mimics this law and thus belongs to the class of physics-based metaheuristic optimization methods. Integration with various test functions and engineering problems has shown that HGSO yields more successful results than other algorithms, such as particle swarm optimization, the gravitational search algorithm, the cuckoo search algorithm, the grey wolf optimization algorithm, the whale optimization algorithm, the elephant herding algorithm, and the simulated annealing algorithm [9]. HGSO is also used in fields, such as optimizing maximum power point tracking (MPPT) [10], feature selection for data mining and the classification of big data [11], and optimizing power system stabilizer (PSS) [12] and PID [13] parameters.

Chaotic systems are a subgroup of nonlinear systems. They were first introduced to the scientific world through the work of Lorenz. This field has gained recognition over time and continues to be the focus of numerous academic studies. The most notable characteristic of chaotic systems is their high sensitivity to initial conditions. Different initial conditions lead to entirely distinct trajectories for chaotic systems. Hence, when dealing with chaotic systems, having knowledge about not only the mathematical model of the system but also the specific initial conditions used in the system is essential.

In the studies found in the literature, the chaos-based Henry Gas Solubility Optimization method has been proposed for optimizing various engineering problems [14], classifying soil images in smart agriculture systems [15], feature selection for an LSTM (Long Short-Term Memory) model [16], and for optimizing the same 47 benchmark functions and 3 engineering problems compared to the original HGSO method [17].

In this conducted research, the pseudorandomness of chaotic systems is integrated with the HGSO method, proposing a new optimization approach named Chaotic Henry Gas Solubility Optimization (CHGSO). This proposal has been rigorously evaluated through international standards, such as NIST tests, supporting the randomness aspect.

In this study, an application for the speed control of a dc motor has been realized by tuning PID parameters with CHGSO. There are many studies in the literature that focus on setting the parameters of PID controllers. Recently, metaheuristic optimization methods have become frequently used to tune these parameters. The HGSO [5], Particle Swarm Optimization (PSO) [18,19], Evolutionary Algorithm (EA) [20], Simulated Annealing (SA) [21], Artificial Bee Colony (ABC) [22–24], Jaya Optimization Algorithm (JOA) [25], Invasive Weed Optimization (IWO) [26], Gravitational Search Algorithm (GSA) [27], Harris Hawks Optimization (HHO) [28], Genetic Algorithm (GA) [29,30], and Whale Optimization Algorithm (WOA) [31] are some of the meta-heuristic optimization methods that are used for this purpose.

A literature review shows that the HGSO algorithm is a modern approach to optimization. Studies demonstrate that it consistently converges closer to the optimal value while incurring lower computational costs compared to other methods. Therefore, the HGSO algorithm was chosen for this study.

The effectiveness of the proposed algorithm is tested by optimizing the PID parameters for the speed control of a DC motor. The optimization process has been assessed through comprehensive tests, such as the unit step response, unit parabolic response, error-based

performance criterion analysis, and disturbance load analyses. The obtained results detail the control performance of CHGSO.

The research is supported not only by simulations but also by experimental studies. Both simulation and experimental work demonstrate a significant improvement in CHGSO over other algorithms, such as WOA, GWO, EA, SA, PSO, and HGSO, in terms of optimization time and PID controller performance, as commonly used in the literature.

This study offers a new perspective on optimization methods utilizing chaotic systems, highlighting the potential of obtaining more effective and faster solutions in control systems through the CHGSO method. The findings obtained from this research may have a broad impact not only on industrial applications but also on scientific research, serving as inspiration for future studies.

The paper is structured into several chapters. The first chapter includes a brief introduction, along with evaluations of recent studies and the current study. Chapter 2 provides information about the HGSO method, the chaotic systems used, and NIST randomness test results. The third chapter presents the proposed method, CHGSO, along with its performance analysis based on 47 different benchmark functions. Chapter 4 describes the optimization of PID parameters for DC motor speed control using the CHGSO method. The designed controller's speed responses and performance analyses are compared to commonly used optimization methods in the literature, both in simulation and real-time environments. Chapter 5 concludes the study with assessments of the findings.

2. Technical Background

2.1. Henry Gas Solubility Optimization

2.1.1. Henry's Law

Henry's law states that the solubility of gases in a liquid at a constant temperature is directly proportional to the partial pressure [9].

Henry's Law is given below (1).

$$S_g = H * \ P_g \tag{1}$$

In Equation (1), S_g is the gas solubility, H is Henry's constant, and P_g is the partial pressure of the gas. Note that Henry's constant is temperature-dependent and changes with the change in temperature.

$$\frac{d\ lnH}{d\ (\frac{1}{T})} = \frac{-\nabla E}{R} \tag{2}$$

In Equation (2), ∇E is the enthalpy of dissolution, R is the gas constant, and T is the temperature parameters [9].

$$H(T) = \exp\left(\frac{B}{T}\right) * \ A \tag{3}$$

In Equation (3), A and B are two parameters dependent on T. The reference temperature is [9].

$$T = 298.15\ K$$

When the equations are solved together and the dissolution enthalpy is assumed to be constant, Equation (4) is obtained.

$$H(T) = \exp\left(-C * \ (\frac{1}{T} - \frac{1}{T^0})\right) * \ H^0 \tag{4}$$

2.1.2. HGSO Algorithm

The HGSO algorithm takes place in 8 steps.

Step 1: Initialization process. In this step, the gas particle number (N) is determined. The initial positions of these gas particles are established. Initial values of Henry's constant, partial gas pressure, and the *C* constant (enthalpy) are assigned.

$$X_i(t+1) = X_{min} + r * (X_{max} - X_{min}) \tag{5}$$

The initial positions of the gas particles are determined by Equation (5). X_{min} and X_{max} define the limits of the problem, r is random number between 0 and 1, and X_i represents the position of the ith gas particle in the gas particle population.

$$\begin{array}{l} H_j(t) = l_1 * \ r \\ P_{ij}(t) = l_2 * \ r \\ C_j(t) = l_3 * \ r \end{array} \tag{6}$$

Based on Equation (6), values of Henry's constant, the partial gas pressure, and C constant are assigned. H_j is the Henry constant of the cluster j, P_{ij} represents the partial gas pressure of the ith gas particle of the cluster j, C_j is the enthalpy constant of the cluster j, and t is the number of iterations. Note that l_1, l_2, and l_3 are constant values. ($l_1 = 0.05$, $l_2 = 100$, $l_3 = 0.01$) [9].

Step 2: Clustering. The gas particle population is divided into clusters consisting of an equal number of gas particles. Since similar gases are present in the clusters, the Henry and enthalpy constants of the cluster are the same.

Step 3: Evaluation. All gas particles in the clusters are evaluated according to the objective function. Based on this evaluation, the gas particles are sorted from good to bad results.

Step 4: Updating the Henry constant. The Henry constant is updated according to Equation (7).

$$\begin{array}{l} H_j(t+1) = H_j(t) * \ \exp\Big(-C * (\frac{1}{T(t)} - \frac{1}{T^0})\Big) \\ T(t) = \exp\big(-\frac{t}{iter}\big) \end{array} \tag{7}$$

In Equation (7), H_j is Henry's constant of cluster j, T is temperature, $T^0 = 298.15$ is the reference temperature, t is the iteration, and $iter$ is the total number of iterations.

Step 5: Updating the solubility. Gas solubility is updated according to Equation (8).

$$S_{ij}(t) = K * \ H_j(t+1) * \ P_{ij}(t) \tag{8}$$

In Equation (8), S_{ij} is the solubility of the ith gas particle of cluster j, P_{ij} is the partial gas pressure of ith gas particle of cluster j, and K is a constant value.

Step 6: Updating the positions. The positions of gas particles are updated according to Equation (9).

$$\begin{array}{c} X_{ij}(t+1) = X_{ij}(t) + F * \ r * \ \gamma * \big(X_{ibest}(t) - X_{ij}(t)\big) \\ +F * \ r * \ a * \big(S_{ij}(t) \ \times \ X_{best}(t) - X_{ij}(t)\big) \\ \gamma = \beta * \exp\Big(-\frac{F_{best}(t)+\varepsilon}{F_{ij}(t)+\varepsilon}\Big) \\ \varepsilon = 0.05 \end{array} \tag{9}$$

In Equation (9), X_{ij} represents the position of the ith gas particle in cluster j, and r is a random number between 0 and 1. X_{ibest} refers to the position of optimal gas particle, while X_{best} represents the position of optimal gas particle in the entire population. γ represents the ability of the ith gas particle in cluster j to interact with other gases in its cluster. Parameter a determines the effect of gas particles on the ith gas particle in cluster j ($a = 1$), while β is a constant value. F_{ij} denotes the value of the objective function for the ith gas particle in cluster j, while F_{best} refers to the value of the objective function for the optimal gas particle in the entire population. ε is a constant value with a small value to avoid the error of dividing by zero. Additionally, F is a flag ($F = \pm 1$) that changes the direction of advancement at the gas particle's position.

Step 7: Escape from local optima. To escape the local optimum, the gas particles are aligned and the worst gas particles are identified. The selection process is performed by Equation (10).

$$\begin{aligned} N_w(t) &= N * (r * \ (c_2 - c_1) + c_1) \\ c_1 &= 0.1 \\ c_2 &= 0.2 \end{aligned} \tag{10}$$

Here, N is the gas particle number, and N_w is the worst gas particle number to be selected.

Step 8: Updating the positions of the worst agents. The positions of the gas particles selected in step 7 are randomly updated within the global boundaries of the problem.

$$G_{ij}(t+1) = G_{\min} + r * (G_{max} - G_{min}) \tag{11}$$

In Equation (11), G_{ij} is the position of the ith gas particle in cluster j, and $G_{\min}$ and G_{max} are the global limits of the problem. To facilitate better comprehension of the equations given above, a flowchart depicting the optimization method for Henry gas solubility is presented as Figure 1.

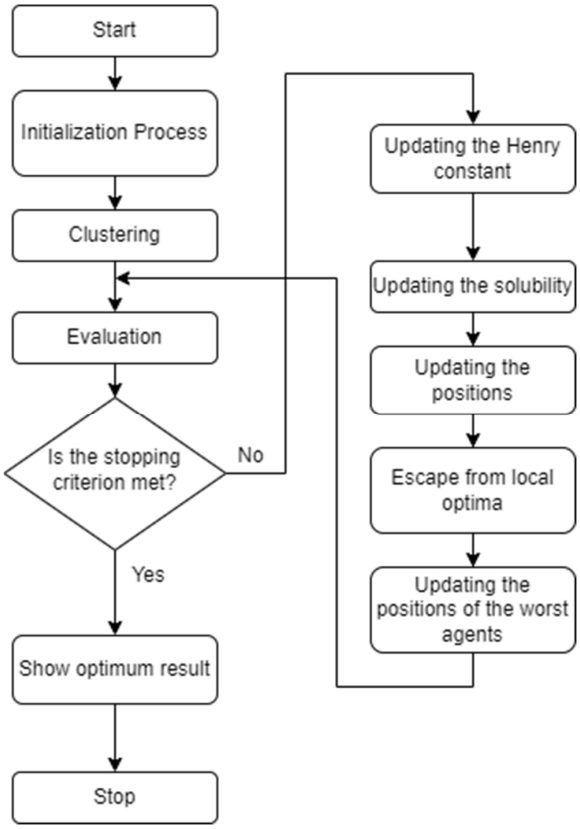

Figure 1. HGSO flowchart diagram.

2.2. Chaotic Systems

Chaotic systems exhibit high sensitivity to initial conditions and parameters. Small perturbations in the initial conditions of a chaotic system can cause significant changes in its long-term behavior. However, despite the seemingly random and unpredictable nature of chaotic systems, they exhibit some level of self-organization and coherence. This study aims to harness the random characteristics of chaotic systems to create the necessary stochastic behavior required in metaheuristic optimization methods. To achieve this, various widely-used chaotic systems from the existing literature are considered and analyzed.

2.2.1. Duffing-Van Der Pol Chaotic System

$$\begin{aligned} \dot{x} &= y \\ \dot{y} &= \mathrm{a} * \left(1 - x^2\right) * \mathrm{y} - \mathrm{x}^3 + \mathrm{b} * \cos(\mathrm{c} * \mathrm{z}) \\ \dot{z} &= 1 \end{aligned} \tag{12}$$

The parameters a, b, and c are taken as 0.2, 5.8, and 3, respectively [32]. The initial conditions of the system are chosen as $x(0) = 0$, $y(0) = 0$, and $z(0) = 0$. It should be noted that this non-autonomous system has been made autonomous by transforming $z = t$.

2.2.2. Lorenz Chaotic System

$$\begin{aligned} \dot{x} &= \sigma * (\mathrm{y} - \mathrm{x}) \\ \dot{y} &= -\mathrm{x} * \mathrm{z} + \rho * \mathrm{x} - \mathrm{y} \\ \dot{z} &= \mathrm{x} * \mathrm{y} - \beta * \mathrm{z} \end{aligned} \tag{13}$$

The parameters are σ = 10, ρ = 28, and β = 8/3 [33].
The initial conditions are $x(0) = 0, y(0) = -0.01,$ and $z(0) = 9$.

2.2.3. Rucklidge Chaotic System

$$\begin{aligned} \dot{x} &= -\mathrm{k} * \mathrm{x} + \mathrm{l} * \mathrm{y} - \mathrm{y} * \mathrm{z} \\ \dot{y} &= x \\ \dot{z} &= -\mathrm{z} + y^2 \end{aligned} \tag{14}$$

The parameters are k = 2 and l = 6.7 [34].
The initial conditions are $x(0) = 0, y(0) = 0,$ and $z(0) = 4.5$.

2.2.4. Rössler Chaotic System

$$\begin{aligned} \dot{x} &= -\mathrm{y} - \mathrm{z} \\ \dot{y} &= \mathrm{x} + \mathrm{a} * \mathrm{y} \\ \dot{z} &= \mathrm{b} + \mathrm{z} * (\mathrm{x} - \mathrm{c}) \end{aligned} \tag{15}$$

The parameters are a = 0.2, b = 0.2, and c = 5.7 [35].
The initial conditions are $x(0) = -9,\ y(0) = 0,$ and $z(0) = 0$.

2.2.5. Rikitake Chaotic System

$$\begin{aligned} \dot{x} &= -\mathrm{m} * \mathrm{x} + \mathrm{z} * \mathrm{y} \\ \dot{y} &= \mathrm{m} * \mathrm{x} + (\mathrm{z} - \mathrm{a}) * \mathrm{x} \\ \dot{z} &= 1 - \mathrm{x} * \mathrm{y} \end{aligned} \tag{16}$$

The parameters are m = 2 and a = 5 [36].
The initial conditions are $x(0) = 0, y(0) = 0.1,$ and $z(0) = 0$.

2.2.6. Duffing Chaotic System

$$\begin{aligned} \dot{x} &= y \\ \dot{y} &= -\mathrm{k} * \mathrm{y} - \mathrm{x}^3 + \mathrm{b} * \cos(\mathrm{z}) \\ \dot{z} &= 1 \end{aligned} \tag{17}$$

The parameters are k = 0.1 and b = 11 [37].
The initial conditions are $x(0) = 0,\ y(0) = 0,$ and $z(0) = 2$.
Note: This non-autonomous system has been made autonomous by transforming $z = t$.

2.2.7. Chen Chaotic System

$$\begin{aligned} \dot{x} &= a * (y - x) \\ \dot{y} &= -x * z + (c - a) * x + c * y \\ \dot{z} &= x * y - b * z \end{aligned} \tag{18}$$

The parameters are a = 35, b = 3, and c = 28 [38].

The initial conditions are $x(0) = -10, y(0) = 0,$ and $z(0) = 37$.

Chaotic systems often lack traditional symmetry due to their complex and nonlinear nature. However, their state spaces frequently exhibit fractal patterns that imply a form of pseudo-symmetry. For example, the renowned Lorenz attractor displays this pseudo-symmetry through its fractal-like geometry, which arises from its chaotic trajectories. Thus, although chaotic systems do not adhere to conventional symmetry, their fractal structures reveal a kind of pseudo-symmetry. The phase portraits of the chaotic systems used in this study are presented in Figure 2.

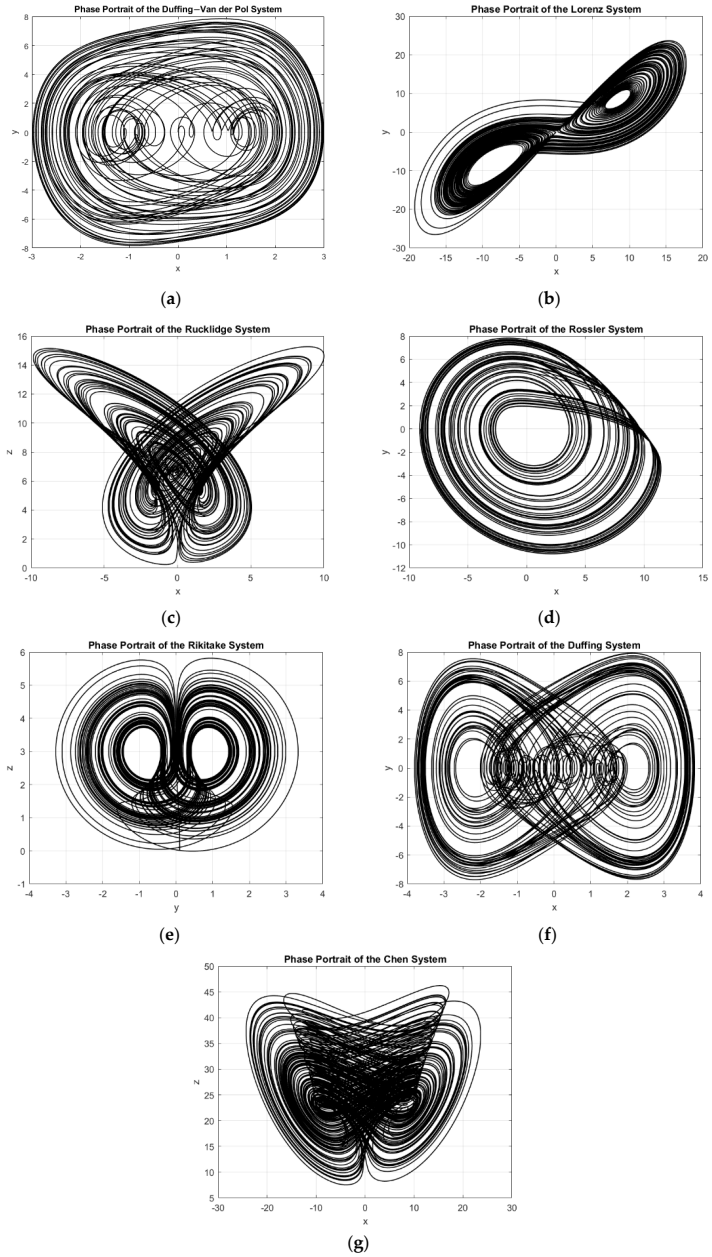

Figure 2. Phase portraits of the chaotic systems.

2.3. NIST Tests

Random numbers obtained from chaotic systems are converted into random bit sequences and subjected to NIST randomness tests. NIST tests are considered the highest international standard for randomness. NIST-800-22 consists of 15 statistical tests [39]. Float numbers obtained from chaotic systems are converted into 32-bit number arrays. A 1 million-bit random bit sequence is created using these arrays and precise digits. The randomness of the generated 1 million-bit sequence is evaluated by running NIST-800-22 tests. Table 1 shows the pass/fail results of chaotic systems in NIST-800-22 randomness tests.

Table 1. Test results of chaotic systems (NIST-800-22).

	Duffing-Van Der Pol	**Lorenz**	**Rössler**	**Rikitake**	**Duffing**	**Chen**	**Rucklidge**
Frequency (monobit) test	Passed	Passed	Passed	Passed	Passed	Passed	Passed
Block frequency test	Passed	Passed	Passed	Passed	Passed	Passed	Passed
Cumulative sum test	Passed	Passed	Passed	Passed	Passed	Passed	Passed
Runs test	Passed	Passed	Passed	Passed	Passed	Passed	Passed
Longest run test	Passed	Passed	Passed	Passed	Passed	Passed	Passed
Binary matrix rank test	Passed	Passed	Passed	Passed	Passed	Passed	Passed
Discrete Fourier transform test	Passed	Passed	Passed	Passed	Passed	Passed	Passed
Non overlapping templates test	Passed	Passed	Passed	Passed	Passed	Failed	Failed
Overlapping templates test	Passed	Passed	Passed	Passed	Passed	Passed	Passed
Maurer's universal statistical test	Passed	Passed	Passed	Passed	Passed	Passed	Passed
Approximate entropy test	Passed	Passed	Passed	Passed	Passed	Passed	Passed
Random excursions test	Passed	Passed	Passed	Passed	Passed	Passed	Passed
Random excursions variant test	Passed	Passed	Passed	Passed	Passed	Passed	Passed
Serial test	Passed	Passed	Passed	Passed	Passed	Passed	Passed
Linear complexity test	Passed	Passed	Passed	Passed	Passed	Passed	Passed

The findings of the test results presented in Table 1 categorize the randomness of chaotic systems based on relevant tests. It is evident from these results that the use of chaotic equation systems does not necessarily guarantee the required level of randomness. This observation underscores the importance of employing randomness tests. The requirement for a chaotic system to pass all randomness tests has been a crucial criterion in the selection of the system to be hybridized.

3. A Novel Optimization Algorithm (CHGSO)

The aim of this study is to investigate the integration of chaotic systems to enhance the performance of the HGSO algorithm. HGSO is an algorithm that models the physical processes of gas solutions and has the potential to yield effective results in solving complex optimization problems. However, a fundamental challenge with such optimization algorithms is ensuring that the algorithm effectively explores a vast search space. In this context, while the use of stochastic processes is common, these processes can be prone to getting trapped in local minima under certain conditions. Chaotic systems can be employed to address this issue. Despite their deterministic structure, chaotic systems exhibit a high degree of complexity and randomness due to their dynamic characteristics. These features make chaotic systems effective tools for exploration in optimization algorithms. One key attribute of chaotic systems is their sensitivity to initial conditions, where small changes can lead to significant differences in outcomes. These systems can exhibit unpredictable behaviors over the long term, thereby reducing the risk of getting trapped in local minima and allowing the algorithm to explore a broader search space. The conducted study aims to integrate the random-number-generation capabilities of chaotic systems into the HGSO algorithm, enhancing both exploration and exploitation capabilities. Stochastic search

methods are often limited by their inability to reach a global optimum or effectively explore the solution space. To overcome these issues, the complex, ergodic [40], and random characteristics offered by chaotic systems will be utilized to improve the performance of the HGSO algorithm. The ergodic property of chaotic systems ensures that all possible states in the solution space emerge over time. This allows chaotic systems to create a comprehensive search strategy. In ergodic systems, the likelihood of visiting each point over time is higher, thus increasing the chances of reaching a global optimum. With this characteristic of chaotic systems, it is anticipated that the HGSO algorithm may develop a more balanced and effective exploration strategy. Consequently, the performance of the algorithm can be enhanced during both exploration and exploitation phases. The proposed Chaotic HGSO (CHGSO) algorithm integrates these chaotic characteristics into the search processes of HGSO. This integration occurs through the influence of chaotic systems, from the initial positions of gas particles to the position updates during the search process. The CHGSO algorithm involves the use of random numbers obtained from chaotic systems in both the initial and subsequent stages. This process is visualized as a flowchart in Figure 3.

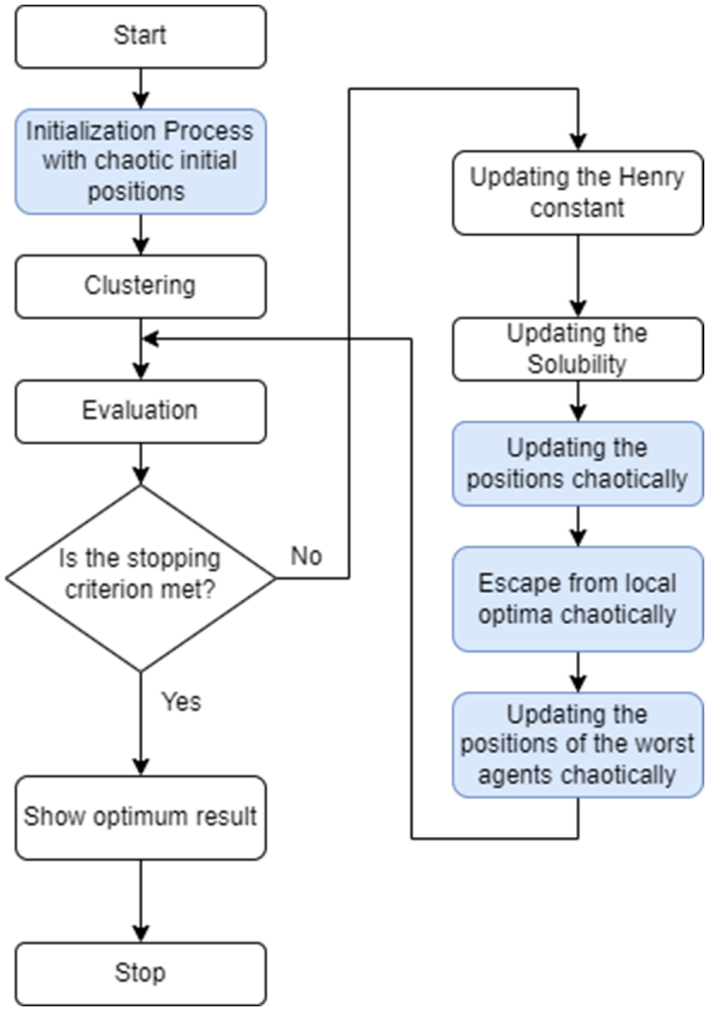

Figure 3. CHGSO flowchart diagram.

The algorithm of the HGSO method proposed by Hashim et al. (2019) [9] is provided as pseudocode in Algorithm 1, with updates clearly defined to facilitate an understanding of the chaotic hybridization.

Algorithm 1 Pseudo-code of CHGSO algorithm [9]

1: ***Chaotically*** initialization X_i (i = 1, 2,... N), number of gas types i, H_j, P_{ij}, C_j, l_1, l_2 and l_3. Equations (19) and (20)
2: Divide the population agents into number of gas types (cluster) with the same Henry's constant value (H_j).
3: Evaluate each cluster j.
4: Get the best gas X_{ibest} in each cluster, and the best search agent X_{best}.
5: **while** t < maximum number of iterations **do**
6: **for** each search agent **do**
7: ***Chaotically*** update the positions of all search agents using Equation (21)
8: **end for**
9: Update Henry's constant of each gas type using Equation (7)
10: Update solubility of each gas using Equation (8)
11: Rank and ***chaotically*** select number of worst agents using Equation (22).
12: ***Chaotically*** update the position of the worst agents using Equation (23).
13: Update the best gas X_{ibest}, and the best search agent X_{best}.
14: **end while**
15: $t = t + 1$
16: **return** X_{best}

Chaotic initialization process: One of the most fundamental characteristics of chaotic systems is their extreme sensitivity to initial conditions. When this property is applied to the determination of initial states in optimization algorithms, it may significantly enhance their performance. In the traditional HGSO algorithm, the initial positions of gas particles are determined by random numbers. However, in the proposed CHGSO algorithm, these initial positions are determined using random numbers generated by chaotic systems. This makes the initialization phase both dynamic and unpredictable. Through chaotic systems, the positions of the gas particles are not merely random but are set according to a complex, chaotic structure. This approach reconfigures the Equations (5) and (6) of the HGSO algorithm to fit a chaotic framework. The equations have been adapted to the chaotic initialization process, and the formulation for determining the initial positions of the gas particles is as follows:

$$X_i(t+1) = X_{min} + r_c * (X_{max} - X_{min}) \tag{19}$$

In this context, r_c represents a random number derived from a chaotic system, while X_{min} and X_{max} denote the lower and upper bounds of the solution space, respectively. In the traditional HGSO algorithm, this value is randomly chosen between 0 and 1, whereas in the proposed CHGSO algorithm, it is derived from a chaotic system within the same range. This modification ensures that the initial positions are distributed across a more diverse and expansive solution space. Consequently, it reduces the risk of getting trapped in local minima early in the process, allowing for a more comprehensive exploration of the solution space.

Additionally, other critical parameters in the HGSO algorithm, such as the Henry constant, partial gas pressure, and constant C, are also determined by random numbers generated from chaotic systems. These parameters play a crucial role in enhancing the algorithm's performance. The use of chaotic systems to determine these values increases randomness in the initialization phase, enabling the implementation of a more complex and effective exploration strategy. In this regard, Equation (20) has been reformulated as follows:

$$\begin{aligned} H_j(t) &= l_1 * r_c \\ P_{ij}(t) &= l_2 * r_c \\ C_j(t) &= l_3 * r_c \end{aligned} \tag{20}$$

These equations illustrate how key parameters, such as the Henry constant (H_j), partial gas pressure (P_{ij}), and constant (C_j), are determined using random numbers derived from chaotic systems. By integrating chaotic dynamics into the initialization phase, the algorithm's inherent randomness is significantly enhanced, allowing for a broader and more

thorough exploration of the solution space. This chaotic structure reduces the likelihood of early convergence to local minima and promotes a more effective search for global optima.

Updating the positions chaotically: The update of gas particle positions is a critical step in optimization processes. These position updates form the foundation of the algorithm's search strategy and play a vital role in reaching local or global optima. In the traditional HGSO algorithm, these updates are determined by stochastic processes. However, in the CHGSO algorithm, this process is transformed into a chaotic structure. Random numbers generated by chaotic systems are used for updating the positions of gas particles, enabling them to follow a more complex and dynamic search strategy.

The chaotic position update process is performed through the modification of Equation (9) as follows:

$$\begin{gathered} X_{ij}(t+1) = X_{ij}(t) + F * \ r_c * \ \gamma * \left(X_{ibest}(t) - X_{ij}(t)\right) \\ +F * \ r_c * \ a * \left(S_{ij}(t) \ \times \ X_{best}(t) - X_{ij}(t)\right) \\ \gamma = \beta * \exp\left(-\frac{F_{best}(t)+\varepsilon}{F_{ij}(t)+\varepsilon}\right) \varepsilon = 0.05 \end{gathered} \tag{21}$$

In this equation, the new positions of the gas particles are updated based on a chaotic progression derived from their previous positions. Here, r_c represents a random number generated from a chaotic system. This randomness prevents the gas particles from focusing solely on local optima during position updates, thereby facilitating a faster convergence toward the global optimum. Additionally, the parameter γ is adjusted according to the best and worst fitness values of the gas particles, and it is further influenced by chaotic dynamics. ε is a constant value with a small value to avoid the error of dividing by zero.

Chaotically select number of worst agents: In the HGSO algorithm, selecting the agents with the worst performance and updating their positions is a critical step in enhancing the algorithm's efficiency. During this phase, rather than selecting the worst-performing agents randomly, the chaotic systems guide the selection. In this context, the original Equation (10) of the algorithm has been modified as follows:

$$\begin{gathered} N_w(t) = N * (r_c \ x \ (c_2 - c_1) + c_1) \\ c_1 = 0.1 \\ c_2 = 0.2 \end{gathered} \tag{22}$$

This equation ensures that the agents with the worst performance are selected in a chaotic manner.

Chaotically updating the position of the worst agents: The positions of these selected agents are updated within the global boundaries of the problem space using chaotic dynamics. This process involves adjusting the positions of the agents based on values generated by chaotic systems. The update operation is expressed by the following equation:

$$G_{ij}(t+1) = G_{\min} + r_c * (G_{max} - G_{min}) \tag{23}$$

This equation illustrates how the positions of the worst-performing agents are updated chaotically. By utilizing chaotic behavior in the position updates, the exploration capability of the algorithm is significantly enhanced, enabling a more efficient search process.

The proposed method was evaluated with 47 benchmark functions, listed in Appendix A [1]. The benchmark function results are compared with two different HGSO studies based on Mohammadi et al.'s (2022) proposed QHGSO algorithm with chaos [17], the original HGSO study with the same parameters as CHGSO, and the optimization methods commonly used in literature, PSO, WOA, GWO, EA, and SA. The optimization parameters used in these studies are given in Table 2.

Table 2. Parameter value of compered algorithms.

CHGSO (proposed method)	Number of iterations: 200 Number of gas particles: 30 Number of clusters: 5 M1 = 0.1, M2 = 0.2, L1 = 0.005, l2 = 100, l3 = 0.01, a, b, k = 1, e = 0.05
HGSO	Number of iterations: 200 Number of gas particles: 30 Number of clusters: 5 M1 = 0.1, M2 = 0.2, L1 = 0.005, l2 = 100, l3 = 0.01, a, b, k = 1, e = 0.05
QHGSO	Number of iterations: 200 Number of gas particles: 30 Number of clusters: N/A M1 = 0.1, M2 = 0.2, L1 = 0.005, l2 = 100, l3 = 0.01, a, b, k = 1, e = 0.05
PSO	Number of iterations: 200 Number of swarm: 30 C1 = 2.1, C2 = 2.1
EA	Number of iterations: 200 Number of parents: 20 Number of children: 4
GWO	Number of iterations: 200 Number of wolves: 30
SA	Number of iterations: 200 Number of materials: 30 Cooling rate: 0.98
WOA	Number of iterations: 200 Number of whales: 30

Benchmark functions are commonly employed to evaluate the performance of optimization methods. The effectiveness of optimization algorithms is assessed based on these benchmark functions. Therefore, the benchmark functions presented in the Appendix A are utilized to compare the performance of the proposed algorithm.

Utilizing the parameters specified in Table 2, CHGSO, HGSO, PSO, GWO, WOA, EA, and SA algorithms are used to optimize the benchmark functions provided in Appendix A. The results are compared with QHGSO [17], obtained using the same benchmark functions, with other optimization algorithms. The comparisons are presented in Table 3.

Table 3. Optimization results of the benchmark functions.

	Fmin		CHGSO	HGSO	QHGSO	PSO	EA	GWO	SA	WOA
F1	0.00×10^{0}	MEAN	0.00×10^{0}	4.13×10^{-158}	0.00×10^{0}	7.62×10^{1}	4.35×10^{9}	1.26×10^{-16}	2.00×10^{9}	9.28×10^{-43}
		STD	0.00×10^{0}	8.13×10^{-159}	0.00×10^{0}	1.31×10^{2}	9.81×10^{8}	3.87×10^{-16}	3.79×10^{8}	3.39×10^{-42}
F2	0.00×10^{0}	MEAN	0.00×10^{0}	1.60×10^{-81}	0.00×10^{0}	8.18×10^{0}	1.51×10^{-3}	2.64×10^{-11}	1.22×10^{2}	1.51×10^{-24}
		STD	0.00×10^{0}	1.12×10^{-80}	0.00×10^{0}	5.71×10^{0}	9.07×10^{-4}	3.62×10^{-11}	1.07×10^{1}	7.03×10^{-24}
F3	0.00×10^{0}	MEAN	0.00×10^{0}	7.72×10^{-80}	0.00×10^{0}	5.74×10^{4}	1.10×10^{2}	2.06×10^{-2}	5.96×10^{4}	1.92×10^{-24}
		STD	0.00×10^{0}	5.37×10^{-79}	0.00×10^{0}	6.40×10^{4}	6.17×10^{1}	3.4×10^{-2}	3.72×10^{4}	1.21×10^{-23}
F4	0.00×10^{0}	MEAN	0.00×10^{0}	1.03×10^{-79}	0.00×10^{0}	7.61×10^{4}	8.21×10^{-1}	2.01×10^{-7}	1.50×10^{-1}	4.39×10^{-24}
		STD	0.00×10^{0}	4.35×10^{-79}	0.00×10^{0}	1.04×10^{5}	5.96×10^{-1}	2.76×10^{-7}	6.10×10^{-2}	2.93×10^{-23}
F5	0.00×10^{0}	MEAN	0.00×10^{0}	1.87×10^{-125}	0.00×10^{0}	5.00×10^{15}	3.45×10^{-6}	4.02×10^{-37}	9.05×10^{3}	2.16×10^{-36}
		STD	0.00×10^{0}	1.09×10^{-124}	0.00×10^{0}	3.11×10^{16}	1.48×10^{-6}	1.69×10^{-37}	1.34×10^{3}	1.03×10^{-35}
F6	0.00×10^{0}	MEAN	0.00×10^{0}	6.82×10^{-41}	0.00×10^{0}	5.38×10^{0}	9.28×10^{0}	5.52×10^{-5}	9.25×10^{2}	1.94×10^{-16}
		STD	0.00×10^{0}	3.40×10^{-40}	0.00×10^{0}	2.14×10^{0}	5.21×10^{0}	2.98×10^{-5}	5.36×10^{1}	4.61×10^{-16}
F7	0.00×10^{0}	MEAN	0.00×10^{0}	5.43×10^{-40}	0.00×10^{0}	8.47×10^{0}	2.17×10^{1}	3.08×10^{-2}	7.48×10^{1}	6.07×10^{1}
		STD	0.00×10^{0}	2.75×10^{-39}	0.00×10^{0}	1.49×10^{0}	8.44×10^{0}	2.01×10^{-2}	2.48×10^{0}	2.78×10^{1}
F8	0.00×10^{0}	MEAN	0.00×10^{0}	8.82×10^{-41}	0.00×10^{0}	1.29×10^{2}	6.09×10^{28}	8.71×10^{-5}	1.50×10^{37}	1.35×10^{-16}
		STD	0.00×10^{0}	3.91×10^{-40}	0.00×10^{0}	1.87×10^{2}	3.37×10^{29}	4.77×10^{-5}	3.47×10^{37}	4.05×10^{-16}
F9	0.00×10^{0}	MEAN	0.00×10^{0}	0.00×10^{0}	0.00×10^{0}	6.95×10^{7}	1.19×10^{9}	4.61×10^{-30}	1.66×10^{9}	3.70×10^{-43}
		STD	0.00×10^{0}	0.00×10^{0}	0.00×10^{0}	1.28×10^{8}	8.54×10^{8}	1.92×10^{-29}	6.23×10^{8}	2.60×10^{-42}
F10	0.00×10^{0}	MEAN	0.00×10^{0}	-1.79×10^{3}	0.00×10^{0}	-3.00×10^{3}	-2.96×10^{3}	-2.77×10^{3}	-2.09×10^{3}	-3.00×10^{3}
		STD	0.00×10^{0}	2.21×10^{2}	0.00×10^{0}	4.80×10^{-1}	3.55×10^{1}	1.48×10^{2}	5.02×10^{1}	0.00×10^{0}
F11	0.00×10^{0}	MEAN	0.00×10^{0}	1.89×10^{-77}	0.00×10^{0}	8.48×10^{1}	2.94×10^{0}	9.47×10^{-10}	6.04×10^{3}	2.65×10^{-23}
		STD	0.00×10^{0}	1.28×10^{-76}	0.00×10^{0}	7.17×10^{1}	2.56×10^{0}	1.24×10^{-9}	6.11×10^{2}	8.28×10^{-23}

Table 3. *Cont.*

	Fmin		CHGSO	HGSO	QHGSO	PSO	EA	GWO	SA	WOA
F12	0.00×10^{0}	MEAN	8.88×10^{-16}	8.88×10^{-16}	8.70×10^{0}	2.03×10^{1}	1.41×10^{1}	1.98×10^{-5}	2.03×10^{1}	8.61×10^{-13}
		STD	2.06×10^{-31}	8.96×10^{-31}	6.12×10^{0}	3.31×10^{0}	8.19×10^{0}	7.83×10^{-6}	1.73×10^{-1}	1.93×10^{-12}
F13	0.00×10^{0}	MEAN	0.00×10^{0}	9.43×10^{-43}	8.65×10^{-1}	4.80×10^{1}	4.11×10^{0}	4.17×10^{-3}	4.61×10^{1}	5.10×10^{-1}
		STD	4.13×10^{-139}	4.44×10^{-42}	2.31×10^{0}	3.10×10^{1}	2.02×10^{0}	1.76×10^{-3}	2.97×10^{0}	3.61×10^{0}
F14	0.00×10^{0}	MEAN	0.00×10^{0}	1.51×10^{-81}	7.17×10^{2}	1.56×10^{-9}	1.94×10^{-3}	1.97×10^{-11}	6.81×10^{1}	6.56×10^{-26}
		STD	0.00×10^{0}	9.48×10^{-81}	1.90×10^{3}	1.07×10^{-9}	1.90×10^{-3}	2.97×10^{-11}	1.44×10^{1}	2.06×10^{-25}
F15	0.00×10^{0}	MEAN	0.00×10^{0}	2.62×10^{-73}	9.98×10^{-1}	4.49×10^{6}	6.58×10^{10}	5.26×10^{-3}	4.29×10^{10}	5.28×10^{-15}
		STD	0.00×10^{0}	1.56×10^{-72}	-9.98×10^{-1}	2.61×10^{6}	6.74×10^{9}	4.84×10^{-3}	3.76×10^{9}	3.53×10^{-14}
F16	-1.00×10^{0}	MEAN	-1.00×10^{0}	-1.00×10^{0}	1.48×10^{0}	-1.00×10^{0}	-1.00×10^{0}	-1.00×10^{0}	-1.03×10^{-1}	-1.00×10^{0}
		STD	0.00×10^{0}	0.00×10^{0}	1.49×10^{0}	0.00×10^{0}	2.25×10^{-5}	0.00×10^{0}	1.26×10^{-2}	0.00×10^{0}
F17	0.00×10^{0}	MEAN	0.00×10^{0}	0.00×10^{0}	1.61×10^{1}	3.66×10^{-1}	9.15×10^{-1}	1.18×10^{-2}	3.99×10^{2}	7.20×10^{-3}
		STD	0.00×10^{0}	0.00×10^{0}	1.36×10^{1}	2.29×10^{-1}	1.28×10^{-1}	1.50×10^{-2}	3.75×10^{1}	5.09×10^{-2}
F18	2.00×10^{0}	MEAN	2.00×10^{0}	1.89×10^{1}	4.35×10^{0}	-1.54×10^{6}	1.11×10^{7}	8.10×10^{0}	3.80×10^{10}	2.00×10^{0}
		STD	0.00×10^{0}	8.87×10^{1}	1.78×10^{1}	8.96×10^{6}	6.72×10^{7}	1.39×10^{1}	5.58×10^{10}	0.00×10^{0}
F19	2.00×10^{0}	MEAN	2.00×10^{0}	4.84×10^{1}	7.35×10^{-19}	-6.49×10^{6}	3.89×10^{6}	2.30×10^{1}	7.79×10^{10}	2.00×10^{0}
		STD	0.00×10^{0}	3.03×10^{2}	4.08×10^{-17}	4.58×10^{7}	2.56×10^{7}	3.85×10^{1}	1.54×10^{11}	0.00×10^{0}
F20	0.00×10^{0}	MEAN	0.00×10^{0}	0.00×10^{0}	4.16×10^{-1}	2.89×10^{-5}	9.01×10^{-12}	5.38×10^{-8}	1.37×10^{-1}	0.00×10^{0}
		STD	0.00×10^{0}	0.00×10^{0}	2.56×10^{-1}	9.79×10^{-5}	9.31×10^{-12}	4.00×10^{-8}	2.80×10^{-2}	0.00×10^{0}
F21	0.00×10^{0}	MEAN	6.57×10^{-6}	3.01×10^{-4}	6.56×10^{1}	1.71×10^{3}	3.03×10^{-1}	7.10×10^{-3}	5.53×10^{1}	1.18×10^{-2}
		STD	1.63×10^{-5}	2.79×10^{-4}	4.64×10^{1}	1.42×10^{3}	1.16×10^{-1}	3.61×10^{-3}	7.56×10^{0}	1.28×10^{-2}
F22	0.00×10^{0}	MEAN	0.00×10^{0}	0.00×10^{0}	2.69×10^{2}	2.20×10^{2}	1.08×10^{2}	1.36×10^{1}	3.58×10^{2}	2.55×10^{0}
		STD	0.00×10^{0}	0.00×10^{0}	1.95×10^{2}	4.79×10^{1}	2.35×10^{1}	1.08×10^{1}	1.65×10^{1}	1.78×10^{1}
F23	0.00×10^{0}	MEAN	5.14×10^{-1}	1.61×10^{1}	3.27×10^{-9}	2.20×10^{2}	8.74×10^{-2}	5.15×10^{0}	1.06×10^{4}	1.61×10^{1}
		STD	4.17×10^{0}	2.32×10^{0}	1.03×10^{-9}	4.79×10^{1}	5.83×10^{-2}	1.93×10^{0}	1.96×10^{3}	6.44×10^{0}
F24	0.00×10^{0}	MEAN	4.17×10^{-12}	3.15×10^{-11}	1.94×10^{-8}	2.91×10^{-4}	1.91×10^{-11}	1.61×10^{-7}	1.48×10^{-5}	5.72×10^{-12}
		STD	1.07×10^{-11}	6.19×10^{-13}	1.94×10^{-8}	3.78×10^{-4}	1.22×10^{-11}	5.58×10^{-7}	1.34×10^{-5}	3.25×10^{-12}
F25	0.00×10^{0}	MEAN	4.34×10^{-236}	4.34×10^{-232}	2.43×10^{2}	0.00×10^{0}	1.07×10^{-97}	1.27×10^{-103}	1.72×10^{-53}	-1.40×10^{-1}
		STD	3.89×10^{-1}	0.00×10^{0}	9.38×10^{1}	0.00×10^{0}	7.60×10^{-97}	8.97×10^{-103}	8.26×10^{-53}	3.51×10^{-1}
F26	0.00×10^{0}	MEAN	0.00×10^{0}	1.49×10^{-75}	9.38×10^{1}	1.15×10^{9}	2.94×10^{10}	2.90×10^{-9}	3.86×10^{8}	1.02×10^{-21}
		STD	0.00×10^{0}	1.06×10^{-74}	-2.00×10^{2}	2.10×10^{9}	3.49×10^{10}	4.12×10^{-9}	1.39×10^{8}	4.66×10^{-21}
F27	-200×10^{2}	MEAN	-2.00×10^{2}	-2.00×10^{2}	-2.00×10^{2}	-2.00×10^{2}	-2.00×10^{2}	-2.00×10^{2}	-1.98×10^{2}	-2.00×10^{2}
		STD	0.00×10^{0}	0.00×10^{0}	0.00×10^{0}	0.00×10^{0}	0.00×10^{0}	0.00×10^{0}	9.13×10^{-1}	0.00×10^{0}
F28	1.00×10^{0}	MEAN	1.00×10^{0}	1.00×10^{0}	1.00×10^{0}	1.00×10^{0}	1.00×10^{0}	1.00×10^{0}	8.40×10^{1}	1.00×10^{0}
		STD	0.00×10^{0}	0.00×10^{0}	0.00×10^{0}	0.00×10^{0}	7.99×10^{-6}	0.00×10^{0}	6.57×10^{1}	0.00×10^{0}
F29	0.00×10^{0}	MEAN	0.00×10^{0}	0.00×10^{0}	0.00×10^{0}	0.00×10^{0}	8.88×10^{-18}	0.00×10^{0}	4.25×10^{0}	4.44×10^{-18}
		STD	0.00×10^{0}	0.00×10^{0}	0.00×10^{0}	0.00×10^{0}	6.28×10^{-17}	0.00×10^{0}	3.43×10^{0}	3.14×10^{-17}
F30	0.00×10^{0}	MEAN	1.80×10^{-1}	1.80×10^{-1}	1.80×10^{-1}	1.80×10^{-1}	1.80×10^{-1}	1.80×10^{-1}	4.93×10^{0}	1.92×10^{-1}
		STD	2.90×10^{-17}	1.12×10^{-16}	0.00×10^{0}	1.12×10^{-16}	1.12×10^{-16}	1.12×10^{-16}	3.72×10^{0}	4.61×10^{-2}
F31	0.00×10^{0}	MEAN	0.00×10^{0}	0.00×10^{0}	0.00×10^{0}	7.77×10^{-18}	0.00×10^{0}	0.00×10^{0}	2.93×10^{0}	2.05×10^{-4}
		STD	0.00×10^{0}	0.00×10^{0}	0.00×10^{0}	2.25×10^{-17}	0.00×10^{0}	0.00×10^{0}	2.67×10^{0}	5.25×10^{-4}
F32	0.00×10^{0}	MEAN	0.00×10^{0}	3.79×10^{-110}	0.00×10^{0}	9.42×10^{-32}	4.01×10^{-21}	2.53×10^{-74}	1.25×10^{-2}	3.09×10^{-28}
		STD	0.00×10^{0}	2.68×10^{-109}	0.00×10^{0}	5.05×10^{-31}	6.57×10^{-21}	1.66×10^{-73}	1.13×10^{-2}	1.93×10^{-27}
F33	-4.33×10^{1}	MEAN	-4.35×10^{1}	-4.29×10^{1}	-4.26×10^{1}	-4.27×10^{1}	-4.27×10^{1}	-4.27×10^{1}	-4.26×10^{1}	-4.25×10^{1}
		STD	5.02×10^{-2}	3.38×10^{-2}	1.54×10^{-1}	2.26×10^{-1}	2.17×10^{-1}	2.10×10^{-1}	1.17×10^{-1}	1.18×10^{-1}
F34	-2.06×10^{0}	MEAN	-2.10×10^{0}	-2.11×10^{0}	-2.06×10^{0}	-2.11×10^{0}	-2.11×10^{0}	-2.11×10^{0}	-2.10×10^{0}	-2.11×10^{0}
		STD	4.00×10^{-4}	3.14×10^{-7}	$1.17 \times 10-7$	8.97×10^{-16}	8.97×10^{-16}	8.97×10^{-16}	1.06×10^{-3}	2.81×10^{-6}
F35	-1.00×10^{0}	MEAN	-1.00×10^{0}	-7.40×10^{-2}	6.55×10^{4}	-3.29×10^{-1}	-1.92×10^{-2}	-2.17×10^{-4}	-1.75×10^{-4}	-6.84×10^{-3}
		STD	4.52×10^{-1}	2.38×10^{-1}	0.00×10^{0}	3.14×10^{-1}	3.63×10^{-3}	5.12×10^{-5}	2.16×10^{-5}	4.46×10^{-2}
F36	0.00×10^{0}	MEAN	0.00×10^{0}	4.45×10^{-111}	0.00×10^{0}	1.24×10^{-30}	1.90×10^{-1}	6.00×10^{-78}	1.86×10^{-1}	5.50×10^{-37}
		STD	0.00×10^{0}	2.40×10^{-110}	0.00×10^{0}	8.44×10^{-30}	1.34×10^{0}	4.24×10^{-77}	1.88×10^{-1}	3.59×10^{-36}
F37	-3.32×10^{0}	MEAN	-2.81×10^{0}	-3.01×10^{0}	-2.33×10^{0}	-1.33×10^{-2}	-3.26×10^{0}	-3.25×10^{0}	-2.97×10^{0}	-3.11×10^{0}
		STD	2.67×10^{-1}	8.62×10^{-2}	3.79×10^{-1}	6.56×10^{-2}	6.03×10^{-2}	8.72×10^{-2}	1.16×10^{-1}	2.45×10^{-1}
F38	0.00×10^{0}	MEAN	0.00×10^{0}	3.88×10^{-111}	0.00×10^{0}	5.39×10^{-33}	2.44×10^{-21}	6.65×10^{-82}	5.40×10^{-3}	2.67×10^{-42}
		STD	0.00×10^{0}	2.33×10^{-110}	0.00×10^{0}	2.54×10^{-32}	3.98×10^{-21}	4.51×10^{-81}	4.56×10^{-3}	1.70×10^{-41}
F39	9.00×10^{-1}	MEAN	9.00×10^{-1}	9.00×10^{-1}	9.00×10^{-1}	9.90×10^{-1}	9.80×10^{-1}	9.32×10^{-1}	9.29×10^{-1}	9.28×10^{-1}
		STD	2.32×10^{-16}	8.97×10^{-16}	4.52×10^{-16}	3.03×10^{-2}	4.04×10^{-2}	4.72×10^{-2}	2.75×10^{-2}	4.54×10^{-2}
F40	0.00×10^{0}	MEAN	0.00×10^{0}	-1.90×10^{34}	0.00×10^{0}	-1.93×10^{21}	-1.85×10^{17}	-1.25×10^{69}	1.93×10^{6}	-8.10×10^{69}
		STD	0.00×10^{0}	1.08×10^{35}	0.00×10^{0}	7.16×10^{21}	5.46×10^{17}	5.45×10^{69}	9.58×10^{6}	5.43×10^{70}
F41	0.00×10^{0}	MEAN	0.00×10^{0}	1.84×10^{-107}	0.00×10^{0}	1.31×10^{-30}	6.73×10^{-17}	2.99×10^{-65}	4.29×10^{1}	6.05×10^{-52}
		STD	0.00×10^{0}	1.18×10^{-106}	0.00×10^{0}	6.25×10^{-30}	2.03×10^{-16}	2.05×10^{-64}	4.98×10^{1}	4.28×10^{-51}
F42	0.00×10^{0}	MEAN	0.00×10^{0}	733×10^{-110}	0.00×10^{0}	4.59×10^{-31}	5.33×10^{-20}	7.34×10^{-74}	1.59×10^{-1}	4.98×10^{-25}
		STD	0.00×10^{0}	3.62×10^{-109}	0.00×10^{0}	3.21×10^{-30}	1.10×10^{-19}	5.04×10^{-73}	1.48×10^{-1}	3.45×10^{-24}
F43	0.00×10^{0}	MEAN	0.00×10^{0}	0.00×10^{0}	0.00×10^{0}	0.00×10^{0}	3.39×10^{-1}	0.00×10^{0}	7.61×10^{-2}	1.57×10^{-4}
		STD	0.00×10^{0}	0.00×10^{0}	0.00×10^{0}	0.00×10^{0}	2.17×10^{-1}	0.00×10^{0}	7.75×10^{-2}	4.75×10^{-4}
F44	0.00×10^{0}	MEAN	0.00×10^{0}	0.00×10^{0}	0.00×10^{0}	5.24×10^{-3}	4.42×10^{-1}	1.93×10^{-2}	9.03×10^{-2}	2.18×10^{-2}
		STD	0.00×10^{0}	0.00×10^{0}	0.00×10^{0}	1.43×10^{-2}	1.21×10^{-1}	2.18×10^{-2}	7.74×10^{-2}	2.21×10^{-2}

Table 3. *Cont.*

Fmin			CHGSO	HGSO	QHGSO	PSO	EA	GWO	SA	WOA
F45	0.00×10^{0}	MEAN	0.00×10^{0}	2.49×10^{-13}	0.00×10^{0}	2.80×10^{-7}	1.10×10^{-8}	6.44×10^{-9}	3.11×10^{-4}	4.95×10^{-12}
		STD	0.00×10^{0}	1.44×10^{-12}	0.00×10^{0}	6.68×10^{-7}	4.21×10^{-8}	9.10×10^{-9}	4.16×10^{-4}	1.65×10^{-11}
F46	0.00×10^{0}	MEAN	0.00×10^{0}	3.60×10^{-109}	0.00×10^{0}	-1.88×10^{-15}	-1.78×10^{-15}	2.00×10^{-6}	3.73×10^{-3}	1.32×10^{-5}
		STD	0.00×10^{0}	1.80×10^{-108}	0.00×10^{0}	1.77×10^{-15}	1.79×10^{-15}	5.65×10^{-6}	3.27×10^{-3}	4.04×10^{-5}
F47	-4.00×10^{2}	MEAN	-4.00×10^{2}	-4.00×10^{2}	-4.00×10^{2}	-4.00×10^{2}	-3.78×10^{2}	-4.00×10^{2}	-3.86×10^{2}	-4.00×10^{2}
		STD	0.00×10^{0}	0.00×10^{0}	0.00×10^{0}	0.00×10^{0}	6.05×10^{1}	0.00×10^{0}	1.45×10^{1}	0.00×10^{0}

In Table 3, the green background indicates the results that converge most closely with the minimum value of the function, while the blue background indicates the results that converge second most effectively. The proposed method achieved the best result for a total of 43 functions and the second-best result for 2 functions. The chaotic version of the HGSO (QHGSO) attained the best results in 31 instances and the second-best results in 2 instances. In contrast, the original HGSO algorithm produced the best results in 15 cases and the second-best results in 23 cases. The PSO algorithm achieved the best results in 9 cases and the second-best results in 3 cases. The EA algorithm yielded the best results in 6 cases and the second-best results in 2 cases. The GWO algorithm produced the best results in 8 cases, while the SA algorithm achieved the second-best results in 6 cases. The WOA algorithm attained the best results in 7 cases and the second-best results in 9 cases. Notably, when the CHGSO algorithm was run with the same parameters, a significant improvement in the results was observed.

A key characteristic of metaheuristic algorithms is their sensitivity to parameters that significantly influence the algorithm's performance. The efficiency and effectiveness of these algorithms are directly tied to the parameters that guide the search processes. These parameters determine how the solution space is explored, which solutions are emphasized, and which strategies are followed in the search for an optimal solution. Even small changes in these parameters can lead to notable differences in the algorithm's performance, greatly affecting the quality of the results obtained. Therefore, to observe the sensitivity of the model to parameter variations, the proposed method was executed with different sets of parameters. The selected parameters are provided in Table 4, and the results produced by the algorithm corresponding to these parameters are presented in Table 5.

Table 4. Different parameter values of the proposed method.

CHGSO_1	Number of iterations: 100 Number of gas particles: 50 Number of clusters: 5 M1 = 0.1, M2 = 0.2, L1 = 0.005, l2 = 100, l3 = 0.01, a, b, k = 1, e = 0.05
CHGSO_2	Number of iterations: 50 Number of gas particles: 50 Number of clusters: 5 M1 = 0.1, M2 = 0.2, L1 = 0.005, l2 = 100, l3 = 0.01, a, b, k = 1, e = 0.05
CHGSO_3	Number of iterations: 100 Number of gas particles: 30 Number of clusters: 5 M1 = 0.1, M2 = 0.2, L1 = 0.005, l2 = 100, l3 = 0.01, a, b, k = 1, e = 0.05
CHGSO_4	Number of iterations: 50 Number of gas particles: 30 Number of clusters: 5 M1 = 0.1, M2 = 0.2, L1 = 0.005, l2 = 100, l3 = 0.01, a, b, k = 1, e = 0.05
CHGSO_5	Number of iterations: 100 Number of gas particles: 50 Number of clusters: 10 M1 = 0.1, M2 = 0.2, L1 = 0.005, l2 = 100, l3 = 0.01, a, b, k = 1, e = 0.05

Table 4. *Cont.*

CHGSO_6	Number of iterations: 50 Number of gas particles: 50 Number of clusters: 10 M1 = 0.1, M2 = 0.2, L1 = 0.005, l2 = 100, l3 = 0.01, a, b, k = 1, e = 0.05
CHGSO_7	Number of iterations: 100 Number of gas particles: 30 Number of clusters: 10 M1 = 0.1, M2 = 0.2, L1 = 0.005, l2 = 100, l3 = 0.01, a, b, k = 1, e = 0.05
CHGSO_8	Number of iterations: 50 Number of gas particles: 30 Number of clusters: 10 M1 = 0.1, M2 = 0.2, L1 = 0.005, l2 = 100, l3 = 0.01, a, b, k = 1, e = 0.05

Table 5. Benchmark function results for different parameter values of the proposed method.

	Fmin		**CHGSO_1**	**CHGSO_2**	**CHGSO_3**	**CHGSO_4**	**CHGSO_5**	**CHGSO_6**	**CHGSO_7**	**CHGSO_8**
F1	0.00×10^{0}	MEAN	1.68×10^{-118}	3.50×10^{-58}	6.31×10^{-108}	2.47×10^{-53}	1.18×10^{-114}	1.27×10^{-53}	2.18×10^{-103}	9.94×10^{-51}
		STD	8.18×10^{-31}	8.29×10^{-17}	2.33×10^{-27}	8.85×10^{-14}	1.11×10^{-27}	6.83×10^{-14}	4.74×10^{-24}	9.85×10^{-12}
F2	0.00×10^{0}	MEAN	1.14×10^{-60}	8.66×10^{-31}	6.82×10^{-60}	6.51×10^{-29}	4.51×10^{-59}	5.34×10^{-30}	1.83×10^{-56}	3.33×10^{-29}
		STD	5.76×10^{-17}	1.58×10^{-9}	6.62×10^{-15}	3.70×10^{-9}	3.81×10^{-14}	1.41×10^{-8}	1.15×10^{-13}	3.91×10^{-8}
F3	0.00×10^{0}	MEAN	2.94×10^{-62}	5.40×10^{-30}	1.99×10^{-59}	2.29×10^{-30}	1.51×10^{-59}	2.95×10^{-29}	1.69×10^{-56}	3.25×10^{-28}
		STD	5.87×10^{-17}	3.21×10^{-11}	9.86×10^{-18}	4.65×10^{-10}	4.65×10^{-15}	1.84×10^{-10}	4.54×10^{-14}	1.26×10^{-8}
F4	0.00×10^{0}	MEAN	5.22×10^{-60}	2.92×10^{-29}	2.08×10^{-56}	1.54×10^{-47}	1.80×10^{-58}	1.14×10^{-28}	5.95×10^{-54}	1.23×10^{-26}
		STD	4.25×10^{-15}	3.63×10^{-9}	5.72×10^{-15}	6.28×10^{-9}	1.57×10^{-14}	3.48×10^{-10}	1.62×10^{-13}	1.07×10^{-7}
F5	0.00×10^{0}	MEAN	5.50×10^{-136}	1.51×10^{-71}	5.42×10^{-141}	4.77×10^{-65}	3.28×10^{-126}	1.29×10^{-65}	1.43×10^{-142}	2.01×10^{-64}
		STD	7.85×10^{-31}	4.38×10^{-22}	4.38×10^{-30}	1.72×10^{-8}	6.86×10^{-28}	2.27×10^{-20}	4.46×10^{-29}	7.54×10^{-16}
F6	0.00×10^{0}	MEAN	5.78×10^{-30}	2.11×10^{-14}	1.40×10^{-27}	9.41×10^{-14}	8.35×10^{-28}	2.30×10^{-13}	2.76×10^{-26}	4.92×10^{-13}
		STD	9.44×10^{-9}	1.49×10^{-4}	1.66×10^{-08}	1.49×10^{-4}	1.86×10^{-8}	1.64×10^{-4}	1.10×10^{-6}	1.48×10^{-3}
F7	0.00×10^{0}	MEAN	1.60×10^{-29}	1.03×10^{-14}	3.17×10^{-27}	2.62×10^{-14}	2.69×10^{-29}	4.72×10^{-14}	1.12×10^{-26}	2.22×10^{-13}
		STD	2.92×10^{-9}	7.53×10^{-6}	7.68×10^{-8}	2.75×10^{-4}	2.91×10^{-8}	1.05×10^{-4}	3.23×10^{-7}	9.12×10^{-4}
F8	0.00×10^{0}	MEAN	5.12×10^{-30}	1.46×10^{-14}	3.63×10^{-28}	4.98×10^{-85}	1.82×10^{-27}	1.09×10^{-13}	2.92×10^{-26}	7.06×10^{-13}
		STD	6.77×10^{-8}	5.79×10^{-5}	8.36×10^{-8}	6.73×10^{-4}	1.79×10^{-6}	1.36×10^{-3}	2.04×10^{-6}	2.15×10^{-3}
F9	0.00×10^{0}	MEAN	1.21×10^{-298}	2.10×10^{-153}	4.02×10^{-295}	-3.00×10^{3}	1.67×10^{-297}	1.48×10^{-142}	1.46×10^{-262}	3.65×10^{-138}
		STD	1.55×10^{-75}	5.67×10^{-43}	1.76×10^{-70}	8.66×10^{2}	2.32×10^{-64}	2.64×10^{-38}	6.98×10^{-63}	8.81×10^{-35}
F10	0.00×10^{0}	MEAN	-3.00×10^{3}	-3.00×10^{3}	-3.00×10^{3}	-3.00×10^{3}	-3.00×10^{-3}	-3.00×10^{3}	-3.00×10^{3}	-3.00×10^{-3}
		STD	1.58×10^{2}	2.85×10^{2}	2.96×10^{2}	8.74×10^{2}	6.22×10^{1}	3.28×10^{2}	3.83×10^{2}	3.86×10^{2}
F11	0.00×10^{0}	MEAN	2.83×10^{-60}	6.91×10^{-30}	3.36×10^{-57}	1.10×10^{-26}	5.92×10^{-59}	2.15×10^{-27}	8.95×10^{-56}	4.27×10^{-26}
		STD	4.32×10^{-17}	2.89×10^{-9}	7.13×10^{-14}	5.16×10^{-8}	4.93×10^{-14}	9.64×10^{-8}	4.55×10^{-14}	5.53×10^{-7}
F12	0.00×10^{0}	MEAN	8.88×10^{-16}	4.44×10^{-15}	8.88×10^{-16}	7.99×10^{-15}	8.88×10^{-16}	7.99×10^{-15}	8.88×10^{-16}	4.44×10^{-15}
		STD	1.08×10^{-8}	9.70×10^{-6}	2.65×10^{-9}	9.58×10^{-6}	8.07×10^{-8}	2.19×10^{-5}	4.10×10^{-8}	2.99×10^{-5}
F13	0.00×10^{0}	MEAN	3.83×10^{-31}	6.79×10^{-16}	6.69×10^{-33}	2.17×10^{-15}	7.72×10^{-31}	2.85×10^{-15}	1.27×10^{-28}	2.10×10^{-15}
		STD	1.25×10^{-09}	4.64×10^{-06}	4.80×10^{-8}	5.11×10^{-5}	6.25×10^{-9}	1.36×10^{-5}	1.28×10^{-7}	3.36×10^{-5}
F14	0.00×10^{0}	MEAN	1.71×10^{-61}	5.47×10^{-32}	8.58×10^{-63}	8.16×10^{-29}	1.56×10^{-61}	1.04×10^{-30}	2.66×10^{-56}	2.67×10^{-27}
		STD	1.07×10^{-15}	9.19×10^{-10}	9.57×10^{-17}	9.97×10^{-10}	2.29×10^{-15}	2.49×10^{-8}	6.64×10^{-14}	6.49×10^{-9}
F15	0.00×10^{0}	MEAN	7.52×10^{-55}	6.71×10^{-25}	1.47×10^{-49}	7.43×10^{-21}	5.18×10^{-51}	6.56×10^{-22}	4.41×10^{-47}	5.63×10^{-21}
		STD	3.54×10^{-13}	4.54×10^{-5}	1.70×10^{-10}	2.90×10^{-18}	6.45×10^{-9}	1.43×10^{-2}	1.82×10^{-9}	7.95×10^{-2}
F16	-1.00×10^{0}	MEAN	-1.00×10^{0}	-1.00×10^{0}	-1.00×10^{0}	-1.00×10^{0}	-1.00×10^{0}	-1.00×10^{0}	-1.00×10^{0}	-1.00×10^{0}
		STD	0.00×10^{0}	0.00×10^{0}	0.00×10^{0}	2.89×10^{-1}	0.00×10^{0}	0.00×10^{0}	0.00×10^{0}	0.00×10^{0}
F17	0.00×10^{0}	MEAN	0.00×10^{0}	0.00×10^{0}	0.00×10^{0}	0.00×10^{0}	0.00×10^{0}	0.00×10^{0}	0.00×10^{0}	0.00×10^{0}
		STD	1.02×10^{-14}	2.21×10^{-8}	4.96×10^{-13}	5.77×10^{-1}	2.64×10^{-13}	2.79×10^{-7}	5.47×10^{-14}	1.72×10^{-6}
F18	2.00×10^{0}	MEAN	2.00×10^{0}	2.00×10^{0}	2.00×10^{0}	2.00×10^{0}	2.00×10^{0}	2.00×10^{0}	2.00×10^{0}	2.00×10^{0}
		STD	0.00×10^{0}	0.00×10^{0}	0.00×10^{0}	0.00×10^{0}	0.00×10^{0}	0.00×10^{0}	0.00×10^{0}	0.00×10^{0}
F19	2.00×10^{0}	MEAN	2.00×10^{0}	2.00×10^{0}	2.00×10^{0}	0.00×10^{0}	2.00×10^{0}	2.00×10^{0}	2.00×10^{0}	2.00×10^{0}
		STD	0.00×10^{0}	0.00×10^{0}	0.00×10^{0}	5.77×10^{-1}	0.00×10^{0}	0.00×10^{0}	0.00×10^{0}	0.00×10^{0}
F20	0.00×10^{0}	MEAN	0.00×10^{0}	0.00×10^{0}	0.00×10^{0}	0.00×10^{0}	0.00×10^{0}	0.00×10^{0}	0.00×10^{0}	0.00×10^{0}
		STD	0.00×10^{0}	0.00×10^{0}	0.00×10^{0}	1.10×10^{-4}	0.00×10^{0}	0.00×10^{0}	0.00×10^{0}	0.00×10^{0}
F21	0.00×10^{0}	MEAN	3.81×10^{-5}	4.87×10^{-5}	5.12×10^{-5}	0.00×10^{0}	7.12×10^{-5}	7.11×10^{-5}	5.20×10^{-5}	2.19×10^{-4}
		STD	2.08×10^{-4}	1.48×10^{-3}	6.81×10^{-4}	6.57×10^{-4}	3.28×10^{-4}	7.67×10^{-4}	4.95×10^{-4}	1.41×10^{-3}

Table 5. *Cont.*

Fmin		CHGSO_1	CHGSO_2	CHGSO_3	CHGSO_4	CHGSO_5	CHGSO_6	CHGSO_7	CHGSO_8
F22 0.00×10^{0}	MEAN	0.00×10^{0}	0.00×10^{0}	0.00×10^{0}	0.00×10^{0}	0.00×10^{0}	0.00×10^{0}	0.00×10^{0}	0.00×10^{0}
	STD	0.00×10^{0}	6.12×10^{-9}	1.15×10^{-13}	3.63×10^{0}	2.13×10^{-13}	4.61×10^{-7}	1.90×10^{-11}	3.05×10^{-6}
F23 0.00×10^{0}	MEAN	6.62×10^{-1}	8.53×10^{-1}	3.88×10^{-1}	2.45×10^{-11}	6.04×10^{-1}	6.05×10^{-1}	1.34×10^{0}	1.34×10^{0}
	STD	4.90×10^{0}	5.03×10^{0}	5.10×10^{0}	5.64×10^{0}	4.14×10^{0}	4.26×10^{0}	4.42×10^{0}	4.45×10^{0}
F24 0.00×10^{0}	MEAN	4.17×10^{-12}	4.17×10^{-12}	5.92×10^{-12}	4.34×10^{-232}	4.22×10^{-12}	4.22×10^{-12}	4.35×10^{-12}	4.35×10^{-12}
	STD	1.32×10^{-11}	5.53×10^{-11}	1.16×10^{-11}	1.21×10^{-11}	1.53×10^{-11}	1.22×10^{-8}	3.86×10^{-8}	3.93×10^{-8}
F25 0.00×10^{0}	MEAN	4.34×10^{-232}	4.34×10^{-232}	4.34×10^{-232}	4.34×10^{-232}	4.34×10^{-232}	4.34×10^{-232}	4.34×10^{-232}	4.34×10^{-232}
	STD	0.00×10^{0}	0.00×10^{0}	0.00×10^{0}	2.60×10^{-15}	0.00×10^{0}	0.00×10^{0}	0.00×10^{0}	0.00×10^{0}
F26 0.00×10^{0}	MEAN	1.89×10^{-62}	2.70×10^{-30}	9.20×10^{-60}	-2.00×10^{2}	6.15×10^{-60}	6.83×10^{-29}	5.17×10^{-54}	8.69×10^{-27}
	STD	5.30×10^{-16}	1.85×10^{-10}	7.45×10^{-15}	5.77×10^{1}	4.03×10^{-16}	4.14×10^{-10}	5.04×10^{-14}	6.72×10^{-9}
F27 -2.00×10^{2}	MEAN	-2.00×10^{2}	-2.00×10^{-2}	-2.00×10^{2}	-2.0×10^{2}	-2.00×10^{2}	-2.00×10^{2}	-2.00×10^{2}	-2.00×10^{2}
	STD	0.00×10^{0}	0.00×10^{0}	0.00×10^{0}	5.80×10^{1}	0.00×10^{0}	2.89×10^{-5}	0.00×10^{0}	2.89×10^{-5}
F28 1.00×10^{0}	MEAN	1.00×10^{0}	1.00×10^{0}	1.00×10^{0}	0.00×10^{0}	1.00×10^{0}	1.00×10^{0}	1.00×10^{0}	1.00×10^{0}
	STD	0.00×10^{0}	0.00×10^{0}	0.00×10^{0}	2.89×10^{-1}	0.00×10^{0}	8.66×10^{-7}	0.00×10^{0}	2.89×10^{-7}
F29 0.00×10^{0}	MEAN	0.00×10^{0}	0.00×10^{0}	0.00×10^{0}	0.00×10^{0}	0.00×10^{0}	0.00×10^{0}	0.00×10^{0}	0.00×10^{0}
	STD	0.00×10^{0}	2.93×10^{-12}	3.20×10^{-17}	5.20×10^{-2}	0.00×10^{0}	2.30×10^{-11}	1.67×10^{-15}	1.80×10^{-10}
F30 0.00×10^{0}	MEAN	1.80×10^{-1}	1.80×10^{-1}	1.80×10^{-1}	0.00×10^{0}	1.80×10^{-1}	1.80×10^{-1}	1.80×10^{-1}	1.80×10^{-1}
	STD	2.90×10^{-17}	2.90×10^{-17}	2.90×10^{-17}	5.20×10^{-2}	2.90×10^{-17}	2.90×10^{-17}	2.90×10^{-17}	2.90×10^{-17}
F31 0.00×10^{0}	MEAN	0.00×10^{0}	0.00×10^{0}	0.00×10^{0}	0.00×10^{0}	0.00×10^{0}	0.00×10^{0}	0.00×10^{0}	0.00×10^{0}
	STD	0.00×10^{0}	3.30×10^{-12}	1.60×10^{-17}	3.07×10^{-10}	0.00×10^{0}	5.89×10^{-10}	2.68×10^{-15}	6.02×10^{-10}
F32 0.00×10^{0}	MEAN	9.57×10^{-154}	1.09×10^{-78}	7.22×10^{-131}	-4.20×10^{1}	8.85×10^{-110}	8.87×10^{-57}	1.51×10^{-105}	4.71×10^{-52}
	STD	7.36×10^{-27}	1.54×10^{-14}	1.18×10^{-21}	1.21×10^{1}	3.61×10^{-22}	5.25×10^{-12}	3.98×10^{-18}	2.64×10^{-12}
F33 -4.33×10^{1}	MEAN	-4.25×10^{1}	-4.25×10^{1}	-4.25×10^{1}	-4.25×10^{1}	-4.25×10^{1}	-4.25×10^{1}	-4.25×10^{1}	-4.25×10^{1}
	STD	2.02×10^{-1}	1.65×10^{-1}	8.95×10^{-1}	1.15×10^{1}	2.98×10^{-1}	5.53×10^{-1}	1.83×10^{0}	1.82×10^{0}
F34 -2.06×10^{0}	MEAN	-2.11×10^{0}	-2.11×10^{0}	-2.11×10^{0}	-2.11×10^{0}	-2.11×10^{0}	-2.11×10^{0}	-2.11×10^{0}	-2.11×10^{0}
	STD	6.91×10^{-4}	1.03×10^{-3}	1.38×10^{-2}	6.04×10^{-1}	6.99×10^{-4}	1.55×10^{-3}	3.48×10^{-3}	4.20×10^{-3}
F35 -1.00×10^{0}	MEAN	-1.15×10^{-2}	-9.01×10^{-3}	-9.94×10^{-1}	-1.30×10^{-2}	-2.54×10^{-4}	-1.65×10^{-4}	-1.00×10^{0}	-2.48×10^{-2}
	STD	3.90×10^{-3}	2.55×10^{-3}	3.87×10^{-1}	5.00×10^{-3}	3.62×10^{-5}	1.63×10^{-5}	3.86×10^{-1}	9.54×10^{-3}
F36 0.00×10^{0}	MEAN	1.60×10^{-138}	3.77×10^{-68}	1.05×10^{-104}	-2.35×10^{0}	9.41×10^{-107}	6.89×10^{-54}	9.50×10^{-109}	3.73×10^{-51}
	STD	5.77×10^{-27}	3.09×10^{-14}	6.43×10^{-19}	6.79×10^{-1}	1.38×10^{-21}	7.88×10^{-12}	2.64×10^{-18}	7.33×10^{-13}
F37 -3.32×10^{0}	MEAN	-2.66×10^{0}	-2.52×10^{0}	-2.63×10^{0}	-2.58×10^{0}	-2.59×10^{0}	-2.59×10^{0}	-2.49×10^{0}	-2.33×10^{0}
	STD	3.00×10^{-1}	2.73×10^{-1}	2.90×10^{-1}	6.71×10^{-1}	2.88×10^{-1}	3.05×10^{-1}	2.37×10^{-1}	2.06×10^{-1}
F38 0.00×10^{0}	MEAN	2.24×10^{-139}	3.06×10^{-70}	9.83×10^{-112}	1.84×10^{-56}	3.23×10^{-110}	9.51×10^{-57}	6.56×10^{-111}	3.14×10^{-52}
	STD	5.50×10^{-26}	2.54×10^{-13}	6.57×10^{-21}	2.60×10^{-1}	2.61×10^{-24}	1.28×10^{-12}	1.46×10^{-18}	2.65×10^{-13}
F39 9.00×10^{-1}	MEAN	9.00×10^{-1}	9.00×10^{-1}	9.00×10^{-1}	-3.37×10^{3}	9.00×10^{-1}	9.00×10^{-1}	9.00×10^{-1}	9.00×10^{-1}
	STD	2.32×10^{-16}	2.32×10^{-16}	2.32×10^{-16}	9.74×10^{2}	2.32×10^{-16}	2.32×10^{-16}	2.32×10^{-16}	2.32×10^{-16}
F40 0.00×10^{0}	MEAN	-1.39×10^{7}	-1.94×10^{5}	-4.41×10^{6}	-1.87×10^{5}	-1.92×10^{5}	-2.42×10^{4}	-2.23×10^{5}	-6.54×10^{4}
	STD	4.00×10^{6}	5.52×10^{4}	1.27×10^{6}	6.08×10^{4}	7.12×10^{4}	8.24×10^{3}	7.91×10^{4}	1.87×10^{4}
F41 0.00×10^{0}	MEAN	1.94×10^{-131}	5.56×10^{-68}	3.53×10^{-104}	3.82×10^{-47}	1.13×10^{-106}	2.52×10^{-50}	3.95×10^{-107}	3.32×10^{-45}
	STD	5.02×10^{-24}	1.24×10^{-12}	1.07×10^{-18}	3.12×10^{-11}	7.49×10^{-20}	1.78×10^{-11}	1.08×10^{-15}	5.46×10^{-10}
F42 0.00×10^{0}	MEAN	2.60×10^{-139}	5.67×10^{-68}	1.93×10^{-108}	0.00×10^{0}	9.50×10^{110}	1.87×10^{-53}	8.12×10^{-113}	5.64×10^{-52}
	STD	5.65×10^{-25}	2.86×10^{-13}	4.54×10^{-21}	7.86×10^{-14}	9.55×10^{-22}	7.16×10^{-13}	1.15×10^{-17}	4.75×10^{-12}
F43 0.00×10^{0}	MEAN	0.00×10^{0}	0.00×10^{0}	0.00×10^{0}	0.00×10^{0}	0.00×10^{0}	0.00×10^{0}	0.00×10^{0}	0.00×10^{0}
	STD	0.00×10^{0}	0.00×10^{0}	0.00×10^{0}	0.00×10^{0}	0.00×10^{0}	0.00×10^{0}	0.00×10^{0}	0.00×10^{0}
F44 0.00×10^{0}	MEAN	0.00×10^{0}	0.00×10^{0}	0.00×10^{0}	0.00×10^{0}	0.00×10^{0}	0.00×10^{0}	0.00×10^{0}	0.00×10^{0}
	STD	0.00×10^{0}	8.23×10^{-8}	1.26×10^{-2}	6.98×10^{-5}	6.41×10^{-17}	1.39×10^{-8}	3.77×10^{-11}	1.30×10^{-7}
F45 0.00×10^{0}	MEAN	1.13×10^{-102}	1.75×10^{-47}	3.39×10^{-43}	4.85×10^{-41}	8.97×10^{-38}	9.94×10^{-31}	8.84×10^{-34}	1.70×10^{-26}
	STD	2.72×10^{-16}	1.43×10^{-13}	3.49×10^{-14}	2.12×10^{-14}	1.45×10^{-18}	9.71×10^{-15}	1.98×10^{-14}	9.87×10^{-13}
F46 0.00×10^{0}	MEAN	2.01×10^{-147}	1.17×10^{-79}	3.29×10^{-109}	5.83×10^{-54}	2.67×10^{-110}	1.42×10^{-56}	3.44×10^{-115}	1.12×10^{-54}
	STD	1.21×10^{-25}	2.74×10^{-13}	6.83×10^{-22}	3.12×10^{-14}	1.36×10^{-21}	3.52×10^{-13}	5.24×10^{-18}	3.19×10^{-12}
F47 -4.00×10^{2}	MEAN	-4.00×10^{2}	-4.00×10^{2}	-4.00×10^{2}	-4.00×10^{2}	-4.00×10^{2}	-4.00×10^{2}	-4.00×10^{2}	-4.00×10^{2}
	STD	0.00×10^{0}	0.00×10^{0}	0.00×10^{0}	0.00×10^{0}	0.00×10^{0}	0.00×10^{0}	0.00×10^{0}	0.00×10^{0}

4. Optimization of PID Parameters for Speed Control of DC Motor with Proposed CHGSO Method

The performance of the proposed algorithm was tested on a real engineering problem: the DC motor speed control application. For the purpose of comparison, other recent and

commonly used optimization methods, such as HGSO, PSO, WOA, EA, and SA, were also applied to the same problem.

The mathematical model of the DC motor is given in Equation (24). In Equation (24), V_a is the applied voltage to the motor, R_a is the resistance of the motor windings, L_a is the inductance of the motor windings, e_b is the back electromotive force, K_e is the electrical constant, T is the generated torque, J is the moment of inertia, B is the damping constant, T_l is the load torque, K_m is the mechanical constant, i is the current, and w is the angular velocity of the motor.

$$\begin{aligned} V_a(t) &= i_a R_a + L_a \tfrac{di_a}{dt} + e_b \\ e_b(t) &= K_e w(t) \\ T(t) &= J\tfrac{dw}{dt} + Bw + T_l \\ T(t) &= K_m i(t) \end{aligned} \tag{24}$$

By applying the Laplace transform to the equations given in Equation (24), the block diagram of the motor is shown in Figure 4.

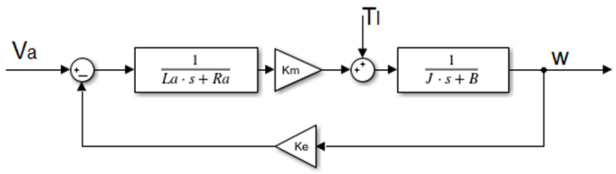

Figure 4. Block diagram of the DC motor.

Based on the block diagram given above, it can be seen that the input of the motor system is voltage and the output is angular velocity. No load is applied to the DC motor. The transfer function of the DC motor is given in Equation (25).

$$G_m(s) = \frac{K_m}{(L_a s + R_a)(Js + B) + K_e K_m} \tag{25}$$

The speed of the DC motor is controlled by the applied voltage. The PID controller determines the applied voltage depending on the desired speed by adjusting the coefficients of K_p, K_i, and K_d. The mathematical model of the PID controller is given in Equation (26).

$$G_{PID}(s) = K_p + \frac{K_i}{s} + K_d s \tag{26}$$

The closed−loop block diagram of the system designed with the PID controller for which the parameters are set by CHGSO for the speed control of the DC motor is given in Figure 5.

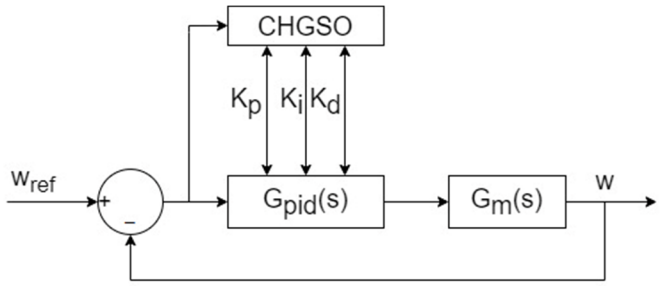

Figure 5. Block diagram of DC motor control system.

The parameters of the motor are Ra = 0.517 ohm, La = 0.057 mH, J = 14.4 gcm^2, B = 0.00024 Nms/rad, Km = 0.0115, and Ke = 0.0115. The motor reduction gear ratio is 1/53.

The ITSE (integrated of time−weighted−squared−error) performance criterion is used as the objective function for tuning PID parameters. The objective function is given in Equation (27).

$$ITSE = \int te^2(t)dt \tag{27}$$

4.1. Results

The main objective of this study is to minimize the error by optimizing the Kp, Ki, and Kd coefficients of the PID controller used to control the speed of the DC motor with optimization algorithms. The HGSO algorithm is combined with the chaotic systems described in Section 2.2. The HGSO algorithm was run with each system. Table 6 shows the optimization times, results of the objective function, and Kp, Ki, and Kd values.

Table 6. Results of the CHGSO for different chaotic systems.

	Kp	Ki	Kd	Fitness	Optimization Time(s)
Duffing−VanDerPol	**11.88994**	**196.9933**	**0.078988**	**0.000040**	**90.17311**
Rucklidge	12.35782	196.81	0.106938	0.000056	88.16251
Chen	11.74649	192.8399	0.101465	0.000060	85.78418
Duffing	10.81011	173.7897	0.094326	0.000069	86.83223
Rössler	12.52376	191.5878	0.117096	0.000075	86.21741
Rikitake	12.52376	191.5878	0.117096	0.000075	86.9942
Lorenz	10.96456	179.5598	0.103868	0.000079	89.74064

Optimization time refers to the operations an algorithm performs to determine the most appropriate Kp, Ki, and Kd values for the control system. This time is the completion time of 50 iterations required for the algorithm to reach the best performance in these parameters. That is, it is a measure of how effective and fast the algorithm is in the process of optimizing these critical parameters. As shown in Table 6, the best result in terms of the objective function was obtained with the Duffing–Van Der Pol chaotic system.

For the practical implementation of the addressed problem, a Maxon DC motor was utilized. The motor parameters were modeled in a computer environment, and simulation studies were conducted. Experimental investigations were carried out by transferring data between the motor and the computer using a data acquisition card. All simulation and experimental studies were implemented using MATLAB R2022a installed on a Windows 10 64−bit system with a 2.60 GHz processor and 12 GB RAM.

4.1.1. Simulation Results

The CHGSO algorithm is obtained by hybridizing HGSO with the chaotic systems described in the study. The HGSO algorithms hybridized with each chaotic system and were utilized to optimize the PID controller parameters. The simulation results for the unit step response of the DC motor controlled by these controllers are presented in Figure 6.

According to Figure 6, all seven controllers reach the reference value without exceeding the system responses. Among them, the CHGSO−PID system achieved the 1% settling band in the shortest time of 0.035 s. The performance of the other controllers is as follows: the Chen CHGSO−PID reached this settling time in 0.045 s, the Rucklidge CHGSO−PID in 0.047 s, the Duffing CHGSO−PID in 0.049 s, the Lorenz CHGSO−PID in 0.050 s, the Rössler CHGSO−PID in 0.052 s, and the Rikitake CHGSO−PID in 0.053 s.

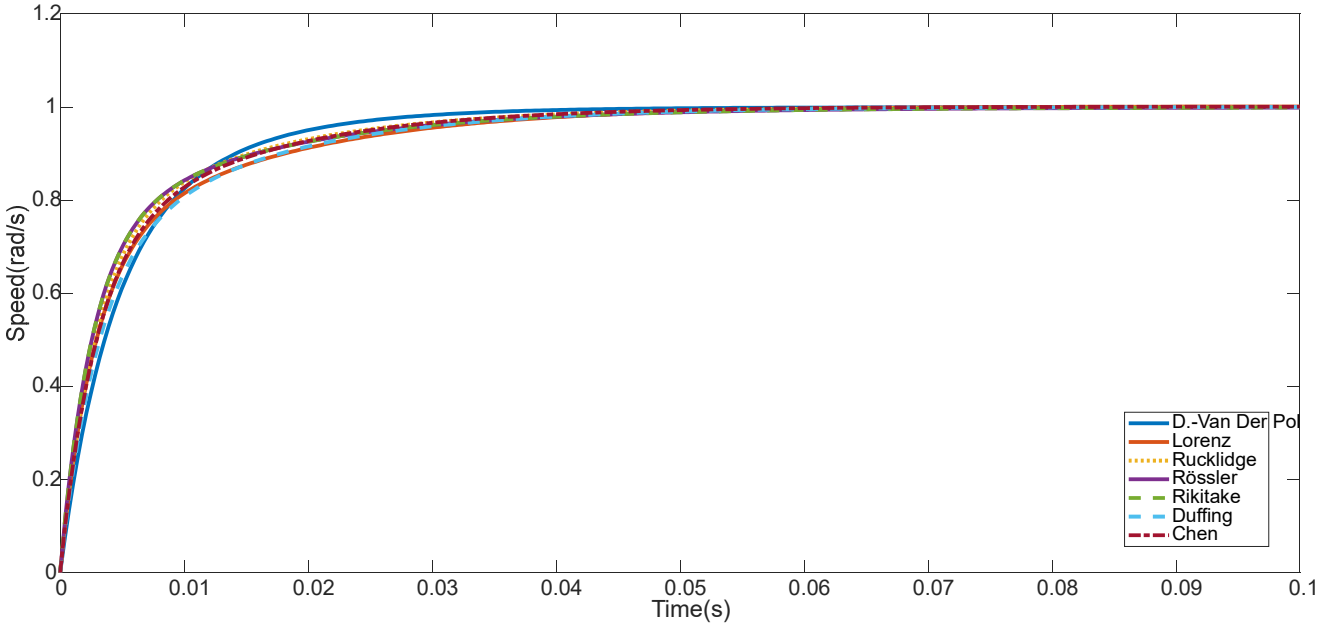

Figure 6. Response of the best three CHGSO−PIDs.

The Duffing–Van Der Pol chaotic system provides the fastest response and converges to a value close to the minimum in the objective function, successfully passing the NIST tests. Therefore, the Duffing–Van Der Pol chaotic system has been hybridized with the HGSO algorithm.

The proposed CHGSO algorithm is compared with that widely used in the literature, PSO [41], WOA [42], SA [43], EA [44], GWO [45], and HGSO [9] optimization methods in the literature. The parameters used in the comparison of optimization algorithms were selected through experimental methods, ensuring alignment with commonly used approaches in the literature. In this process, the effects of the parameters on optimization results were considered, and parameters, such as the number of search agents and the number of iterations, were kept constant, aiming to compare the algorithms solely based on solution quality. To ensure a fair and objective comparison of the optimization methods, all computational parameters are presented in detail in Table 7.

Table 7. Parameters of the algorithms.

CHGSO	Number of iterations: 50 Number of gas particles: 50 Number of clusters: 5 M1 = 0.1, M2 = 0.2 L1 = 0.005, l2 = 100, l3 = 0.01 a, b, k = 1, e = 0.05 Global boundaries = [0–200]
HGSO	Number of iterations: 50 Number of gas particles: 50 Number of clusters: 5 M1 = 0.1, M2 = 0.2 L1 = 0.005, l2 = 100, l3 = 0.01 a, b, k = 1, e = 0.05 Global boundaries = [0–200]
PSO	Number of iterations: 50 Number of swarm: 50 C1 = 2.1 C2 = 2.1 Global boundaries = [0–200]

Table 7. *Cont.*

WOA	Number of iterations: 50 Number of whales: 50 Global boundaries = [0–200]
EA	Number of iterations: 50 Number of parents: 20 Number of children: 4 Global boundaries = [0–200]
SA	Number of iterations: 50 Number of materials: 50 Cooling rate: 0.98 Global boundaries = [0–200]
GWO	Number of iterations: 50 Number of wolves: 50 Global boundaries = [0–200]

The HGSO, PSO, GWO, WOA, EA, and SA algorithms were executed 30 times each. The minimum, maximum, and mean values of the objective function obtained from these 30 runs and the corresponding optimization times are presented in Table 8. These results are compared with those obtained from the CHGSO (Duffing–Van Der Pol chaotic HGSO) system.

Table 8. Results of the optimization algorithms.

	MIN_Fitness	MAX_Fitness	Mean_Fitness	Optimization Time (s)
CHGSO	**0.000040**	**0.000043**	**0.000041**	**90.17311**
HGSO	0.000039	0.000059	0.000049	103.72647
GWO	0.000052	0.000097	0.000075	944.2524
PSO	0.000028	0.000273	0.000093	286.7835
WOA	0.000026	0.000109	0.000101	357.4827
EA	0.000105	0.000589	0.000198	1369.41
SA	0.000116	0.000545	0.000310	911.7728

Table 6 indicates that the CHGSO algorithm is more effective in converging with the minimum value of the objective function. In terms of the optimization time, it is observed that CHGSO is the most efficient method, followed by the original HGSO. HGSO reduces the optimization time by approximately 64% compared to the PSO method, while CHGSO reduces the optimization time by approximately 13% compared to HGSO. The simulation responses of the PID controllers optimized with these methods are listed in Table 7 and illustrated in Figure 7 for a unit step input.

According to Figure 7, the PSO−PID controller has an overshoot of 15% and the WOA−PID controller has an overshoot of 10.2% and the GWO_PID controller has a overshoot of 3.3% relative to the reference value. It is observed that the CHGSO−PID controller is the fastest system, settled within the 1% settling band in 0.035 s. The second fastest is the HGSO−PID controller, which settled within the 1% band in 0.040 s. The settling time, rise time, and overshoot values for all systems are given below in Table 9.

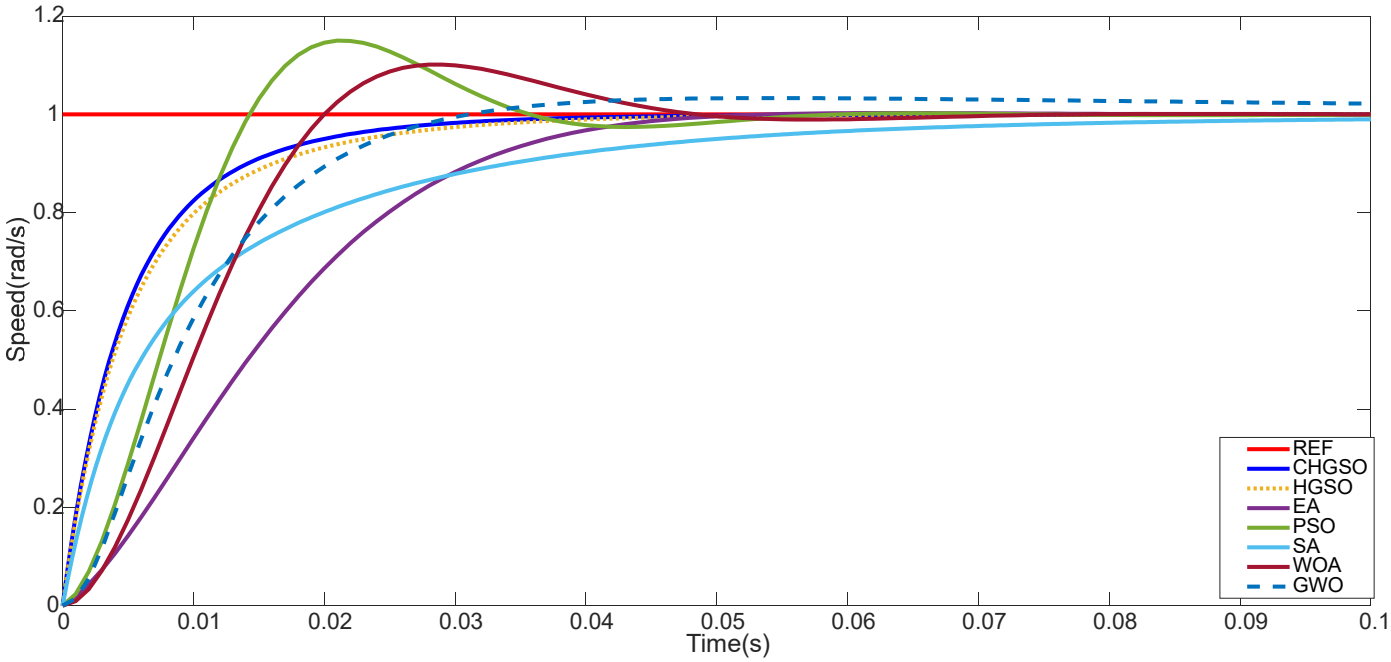

Figure 7. Responses of the PID controllers that are optimized with CHGSO, HGSO, EA, PSO, SA, and WOA.

Table 9. Comparison of controller responses.

	Overshoot (%)	Settling Time (s)	Rise Time (s)
CHGSO−PID	**0**	**0.035**	0.014
HGSO−PID	0	0.040	0.016
EA−PID	0.3	0.047	0.028
PSO−PID	15	0.053	**0.012**
SA−PID	0	0.099	0.033
WOA−PID	10.2	0.046	0.014
GWO−PID	3.3	0.17	0.020

As can be seen from Table 7, the controller with the best results is CHGSO−PID, followed by the original HGSO−PID. In the simulation environment, a disturbance effect of 0.01 Nm in 0.05 s was applied to the DC motor controlled by all PID controllers. The results are shown in Figure 8.

The performance of the controllers is demonstrated in Figure 8. The CHGSO−PID controller exceeds the reference value by 2.8%, and the HGSO−PID controller exceeds it by 4.4%. The settling times within the 1% band for the CHGSO−PID and HGSO−PID controllers are 0.021 s and 0.022 s, respectively. After the disturbance, both controllers' system responses are reduced by 25% compared to the reference value. During the disturbance, the HGSO−PID controller overshoots 1.4% and settles within the 1% band at 0.67 s, whereas the CHGSO−PID controller overshoots 0.6% and settles within the 1% band at 0.63 s.

A quarter−period sinusoidal reference signal was applied to all PID controllers. The responses of controllers to the reference signal are presented in Figure 9.

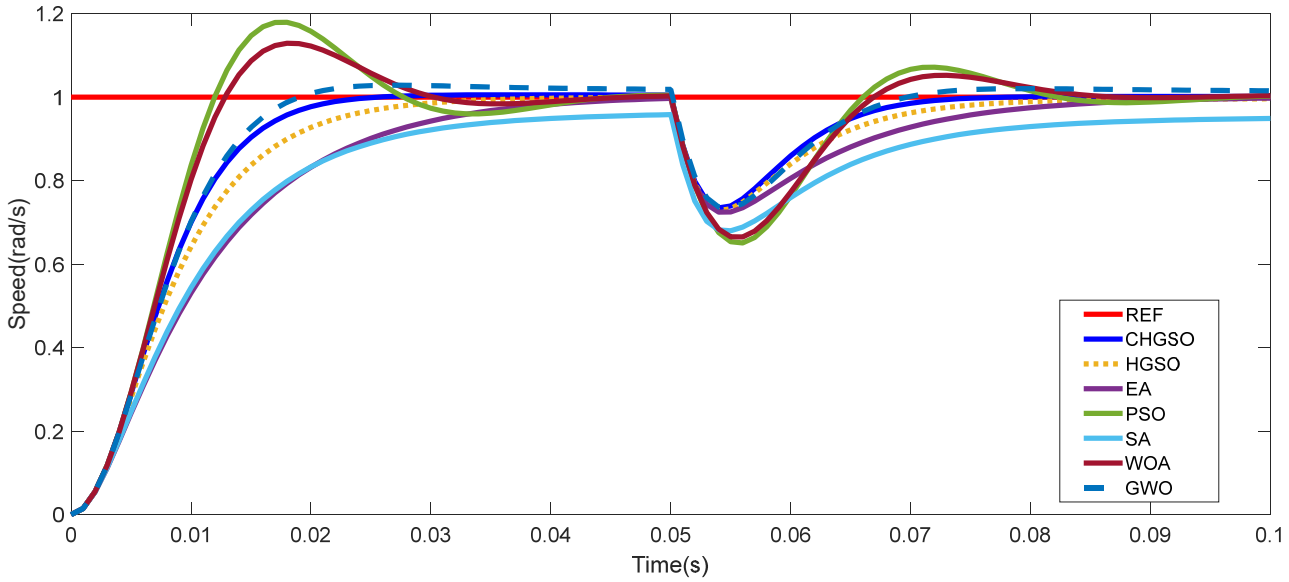

Figure 8. Responses of controllers under load.

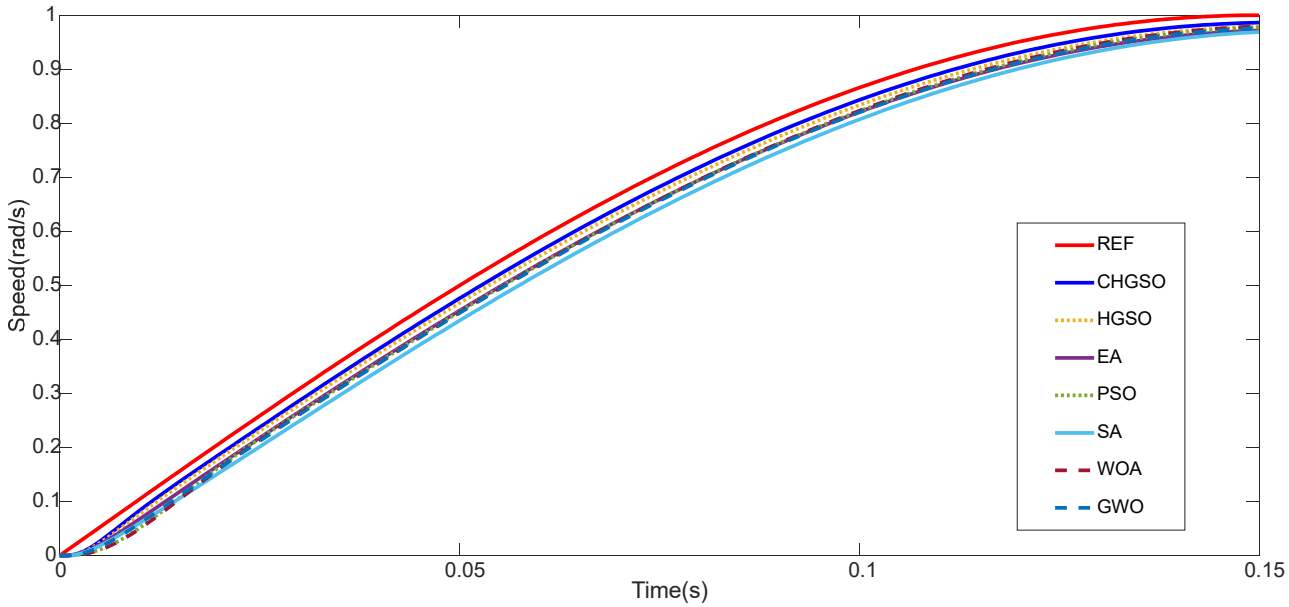

Figure 9. Responses of controllers for quarter−period sinusoidal reference.

Figure 9 shows that the CHGSO−PID controller tracks the reference signal with less error than the other controller. The type 1 norms of the errors produced by all controllers are shown in Figure 10. The type 1 norm of the error produced by the CHGSO−PID is 2.3685, and the type 1 norm of the error produced by the HGSO−PID controller is 3.6477. The norm values of the errors produced by the other controllers, in order, are as follows: EA−PID = 5.142, PSO−PID = 5.249, SA−PID = 6.812, WOA−PID = 5.288, and GWO−PID = 5.428.

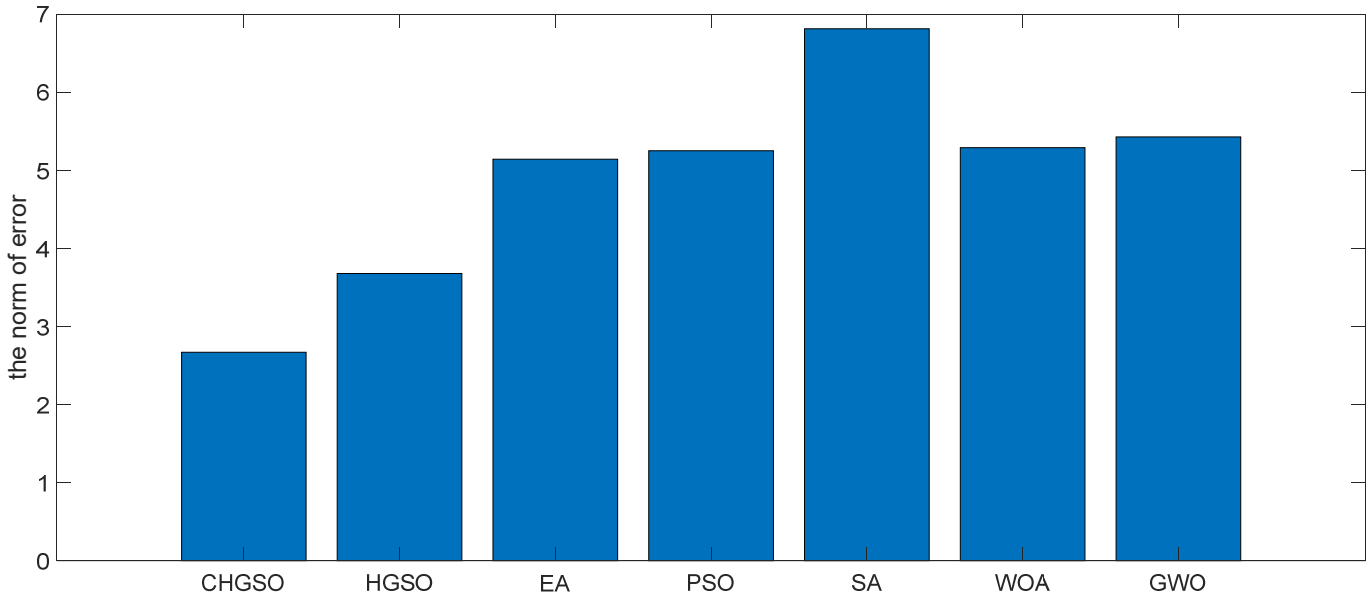

Figure 10. Norms of errors.

4.1.2. Experimental Results

An experimental setup has been established for the studies, as shown in Figure 11. The experimental setup includes the following: (1) a computer in which the software is installed and control is executed, (2) a DAQ card that facilitates data transfer between the controlled system and the computer, (3) the driver circuit board for the controlled system (DC motor), (4) a line driver circuit board, (5) a power supply, (6) an oscilloscope, and (7) the DC motor.

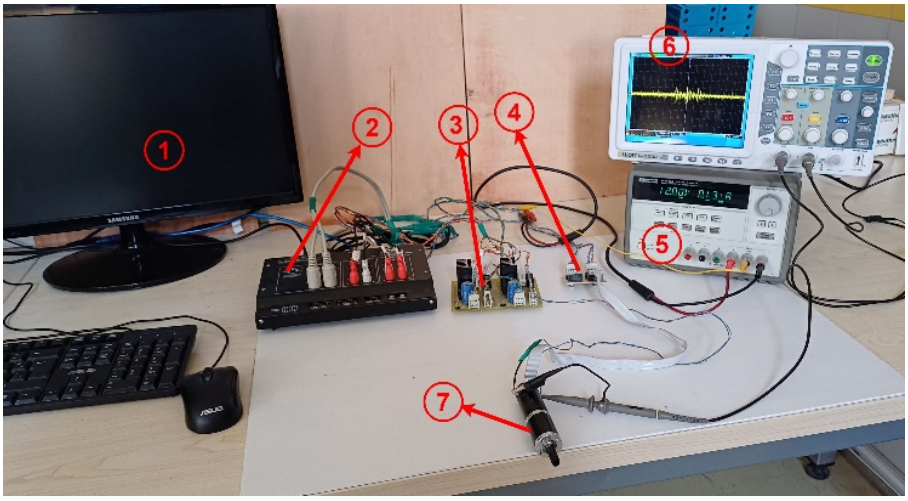

Figure 11. Experimental setup.

Unit Step Response of Unloaded DC Motor

In the studies carried out in the simulation environment, HGSO−PID and CHGSO−PID controllers provided very accurate results. In the experimental study, the controllers were tested by applying it to a DC motor for real−time speed control. The unit step reference input responses of the controllers are given in Figure 12.

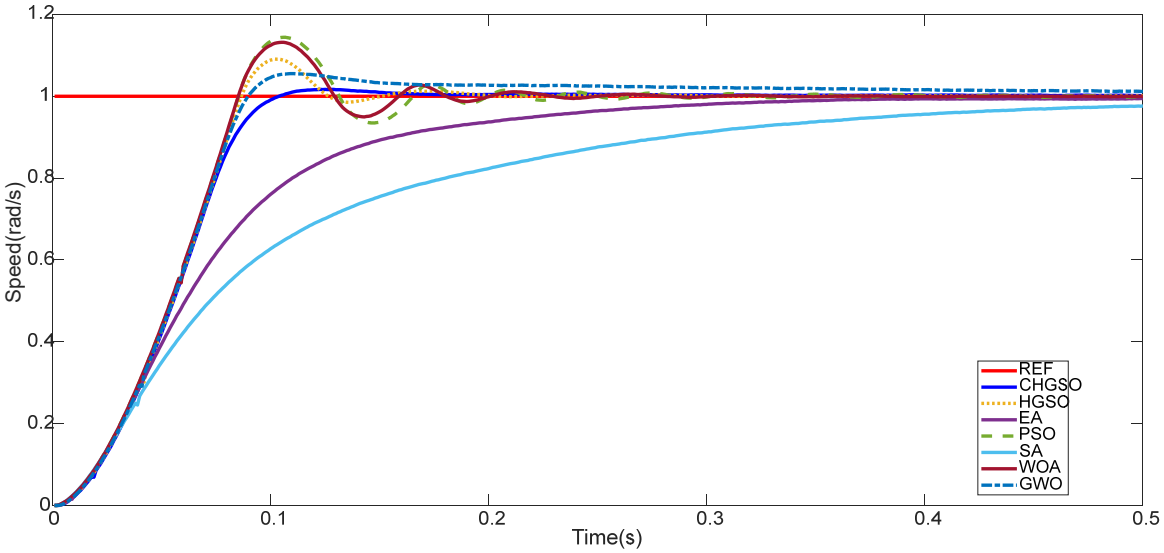

Figure 12. Real−time responses of the controllers.

In Figure 12, performances of the all controllers are observed. The overshoots of the controllers are as follows: PSO−PID exhibited 14.5%, WOA−PID 13.2%, HGSO−PID 8.9%, GWO−PID 5.4%, and CHGSO−PID 1.4%. The controllers reached the 1% settling band in the following times: CHGSO−PID in 0.15 s, HGSO−PID in 0.18 s, WOA−PID in 0.21 s, PSO−PID in 0.22 s, EA−PID in 0.36 s, GWO−PID in 0.55 s, and SA−PID in 0.65 s.

Unit Step Response of Under Load DC Motor

The motor under a load of 10 kg, CHGSO−PID, and other controllers were applied. The responses of the controllers for a unit step input are given in Figure 13.

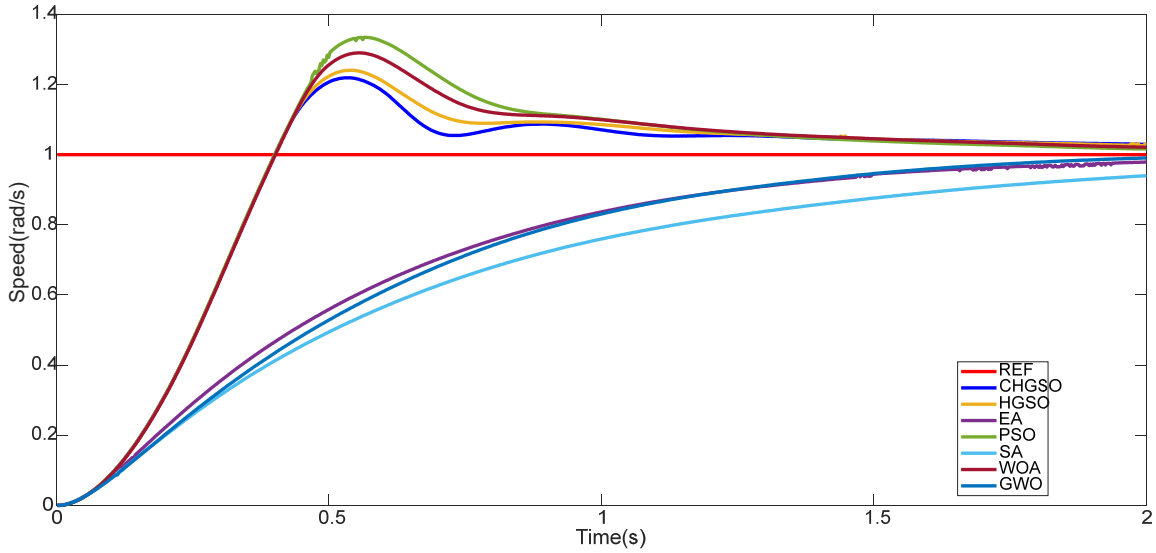

Figure 13. Real−time responses of motor under load.

As seen in Figure 13, CHGSO−PID produces a better response. The overshoot percentages of the controllers are as follows: PSO−PID exhibited 33.5%, WOA−PID 28.9%, HGSO−PID 24.1%, and CHGSO−PID 21%. The controllers reached the 1% settling band in the following times: CHGSO−PID and HGSO−PID both in 1.95 s, WOA−PID in 1.98 s, and GWO−PID in 1.99 s. The other controllers were unable to reach the settling band within 2 s.

Parabolic Input Response of Unloaded DC Motor

Real−time control of the DC motor using controllers was carried out by applying a quarter−period sinusoidal speed reference signal. The speed responses of the motor running without load for the all controllers are given in Figure 14.

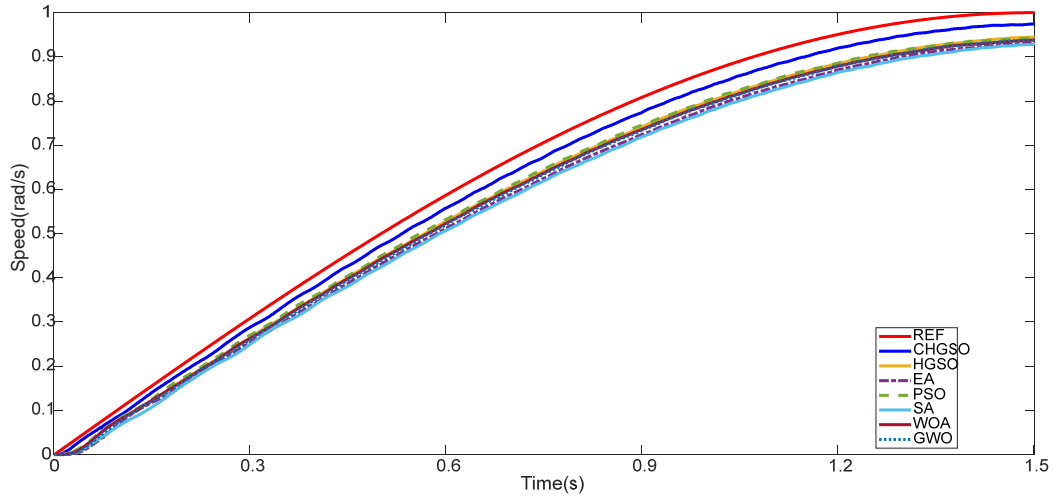

Figure 14. Real−time responses of motor for quarter−period sinusoidal reference.

As seen from Figure 14, the unloaded DC motor controlled by CHGSO−PID follows the speed reference signal with a lower error compared to the other controller. The type 1 norms of the errors generated with these controllers are given in Figure 15.

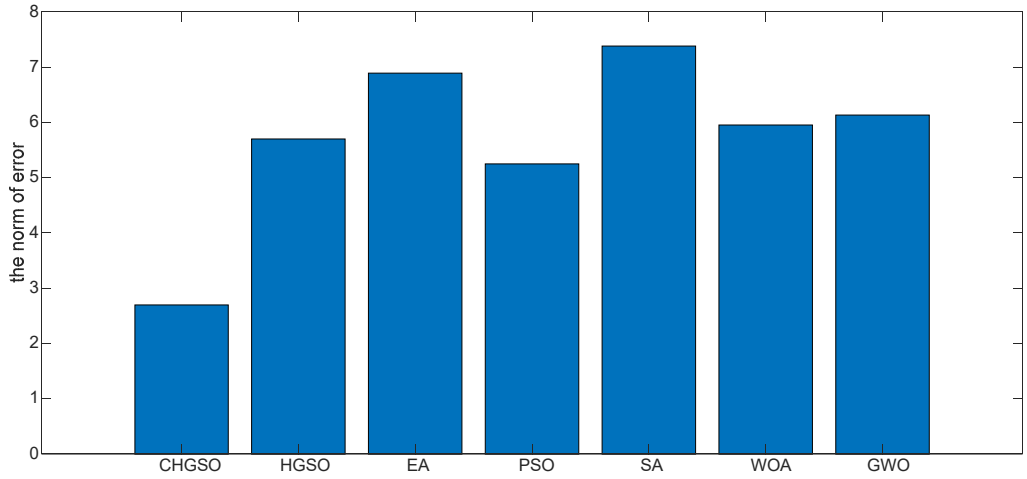

Figure 15. Norm of the error for unloaded motor.

The Type 1 norm values of the errors generated by the controllers for the motor running without load are as follows: CHGSO−PID = 2.6981, HGSO−PID = 5.7012, EA−PID = 6.89, PSO−PID = 5.25, SA−PID = 7.382, WOA−PID = 5.953, and GWO−PID = 6.133.

Parabolic Input Response of Under Load DC Motor

A load of 10 kg was applied to the DC motor, which was controlled without load in Section 4.1.2. A quarter period sinusoidal signal is applied as input, and the speed response of the motor is presented in Figure 16.

As seen in Figure 16, the DC motor controlled by the CHGSO−PID tracks the speed reference signal with a lower error compared to those controlled by the other controllers. The Type 1 norms of the errors produced by these controllers are presented in Figure 17.

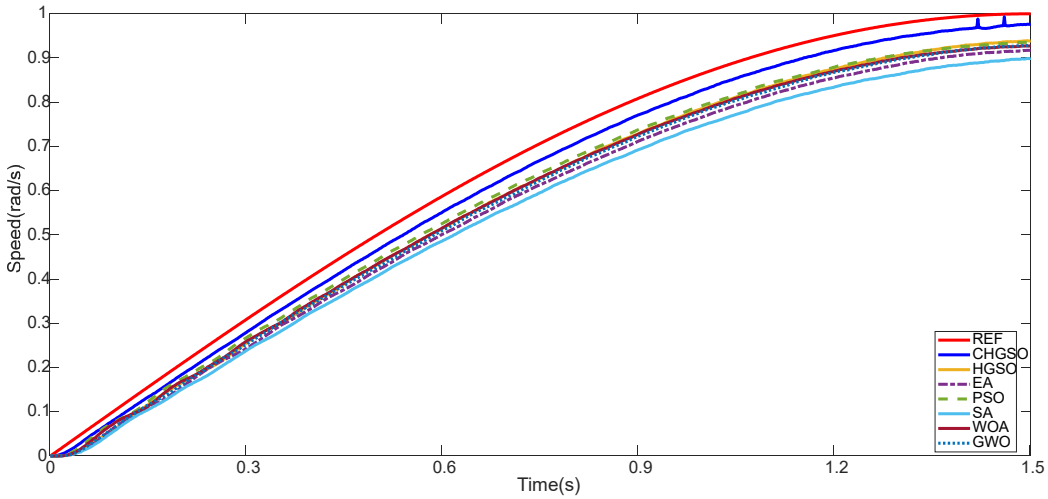

Figure 16. Real−time responses of loaded motor for quarter−period sinusoidal reference.

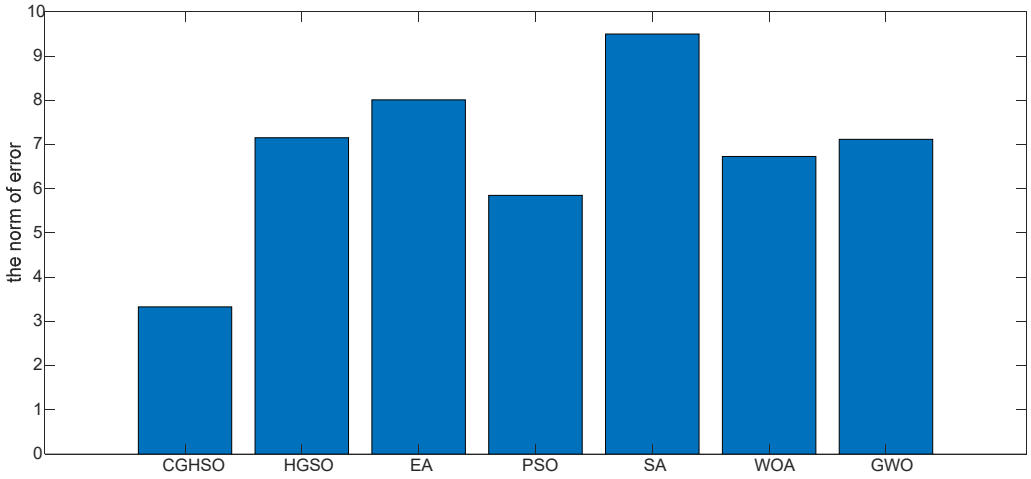

Figure 17. Norm of the error for under−loaded motor.

The Type 1 norm values of the errors generated by the controllers for the motor operating under load are as follows: CHGSO−PID = 3.3278, HGSO−PID = 7.1539, EA−PID = 8.012, PSO−PID = 5.849, SA−PID = 9.5, WOA−PID = 6.73, and GWO−PID = 7.118.

5. Conclusions

In this study, the CHGSO method is proposed and applied to both benchmark functions and tuning PID parameters. Benchmark functions are utilized to evaluate the performance of optimization algorithms. The results from these benchmark functions demonstrate that the proposed method converges most closely with the global minimum values compared to the other algorithms analyzed. The main objective of this research is to enhance the HGSO algorithm. When both the HGSO and CHGSO algorithms are tested with the same parameters, the HGSO algorithm achieves the best results in 15 functions, while the CHGSO algorithm excels in 43 functions. The experimental findings reveal that the proposed optimization algorithm demonstrates superior convergence performance compared to other optimization methods evaluated under the same conditions. Notably, the algorithm successfully reaches the global minimum within the search boundaries of the function in 39 different test functions. This demonstrates that the CHGSO algorithm effectively converges with global minimum values, outperforming both commonly used algorithms in the literature and the original HGSO algorithm.

The PID control with tuned parameters is applied to DC motor application in both simulation and experimental environments. To demonstrate the capabilities of the proposed

CHGSO−PID, comparative performance analyses of PID controllers optimized with the original HGSO, PSO, GWO, WOA, EA, and SA algorithms commonly used in the literature are carried out. It has been shown that the proposed method provides superiority compared to other methods in the simulation time, performance analysis, operation under load, and sudden changes due to disturbing the load moment. In practice, when the motor starts with zero initial velocity, it must overcome mechanical limitations and the motor's inertia to reach the reference signal. This situation leads to an initial error, but the optimization process aims to minimize this error. Theoretically, the global minimum value of the objective function is zero, but experimental results have shown that the proposed method reaches an average value very close to this, specifically 0.000041. During the experiments, the objective function values ranged between 0.000040 and 0.000043, indicating results that are quite close to the global minimum. When compared to other optimization algorithms, the results demonstrate that the original HGSO algorithm reached a value of 0.000049, the GWO algorithm reached 0.000075, the PSO algorithm 0.00093, the WOA algorithm 0.00101, the EA algorithm 0.000198, and the SA algorithm 0.000310. These results indicate that the proposed method converges with the global minimum more effectively than both the HGSO and other algorithms. This demonstrates that the proposed optimization algorithm is more capable of approaching the global minimum, even in complex problems.

Computational complexity expresses the extent to which an optimization method utilizes resources. In this study, the computational complexity of various optimization methods was compared while evaluating their effectiveness. This comparison focused on the time taken by the optimization methods to reach the optimal solution. When examining the computational complexity, the CHGSO algorithm was found to require the least amount of time to achieve the optimal result. Compared to other widely used algorithms in the literature, the speed of the HGSO algorithm is a key reason for its selection in this study. Additionally, the proposed method for improving the HGSO algorithm resulted in a 13% reduction in running time.

In future studies, the utilization of various algorithms for optimizing controller parameters holds significant potential across a broad spectrum of engineering applications. For instance, methods, such as the Artificial Bee Colony Algorithm, the Harris Hawks Optimization Algorithm, the Grey Wolf Optimization Algorithm, the cuckoo search algorithm, and the grasshopper optimization algorithm can be concurrently tested in both computer simulations and real−time applications. This approach will allow for the identification of optimal values for controller parameters, and the performances of these algorithms can be compared to determine the most effective approach. Furthermore, successful results obtained from these studies can be utilized to create a more robust and flexible optimization strategy by hybridizing different algorithms with chaotic systems. This hybridization has the potential to enhance the process of optimizing control parameters. In future studies, this integration can be extended to address specific topics, such as structural, thermal, and hydraulic–pneumatic engineering problems. For instance, structural design problems, like the material selection, shape, and topology optimization of a beam, can be used to assess the effectiveness of these algorithms. Such investigations could represent a crucial step in the development of effective optimization strategies for a variety of engineering applications.

Author Contributions: Methodology, M.S.S. and Y.H.E.N.; Validation, S.K.; Resources, M.S.S. and Y.H.E.N.; Writing—original draft, M.S.S.; Writing—review & editing, S.K., İ.Y. and A.D.; Project administration, A.D. All authors have read and agreed to the published version of the manuscript.

Funding: No funding support was received while preparing this article.

Data Availability Statement: Data is contained within the article.

Conflicts of Interest: The authors declare no conflict of interest.

Appendix A

Table A1. Benchmark functions [21].

No	Function	Name	Dim	R	Fmin
F1	$f(x) = \left(\sum_{i=1}^{n} x_i^2\right)^2$	Chung Reynolds	30	[−100,100]	0
F2	$f(x) = \sum_{i=1}^{n} x_i^2$	Sphere	30	[−5.12,5.12]	0
F3	$f(x) = \sum_{i=1}^{D/4} (x_{4i-3} - 10x_{4i-2})^2 + 5(x_{4i-1} - x_{4i})^2 + (x_{4i-2} - x_{4i-1})^4 + 10(x_{4i-3} - x_{4i})^4$	Powell singular 1	30	[−4,5]	0
F4	$f(x) = \sum_{i=2}^{D-2} (x_{i-1} - 10x_i)^2 + 5(x_{i+1} - x_{i+2})^2 + (x_i - 2x_{i+1})^4 + 10(x_{i-1} - x_{i+2})^4$	Powell singular 2	30	[−4,5]	0
F5	$f(x) = \sum_{i=1}^{n} \lvert x_i \rvert^{i+1}$	Powell Sum	30	[−1,1]	0
F6	$f(x) = -\sum_{i=1}^{n} \lvert x_i \rvert$	Schwefel 2.20	30	[−100,100]	0
F7	$f(x) = max_{1 \le n \le n} \lvert x_i \rvert$	Schwefel 2.21	30	[−100,100]	0
F8	$f(x) = \sum_{i=1}^{n} \lvert x_i \rvert + \prod_{i=1}^{n} \lvert x_i \rvert$	Schwefel 2.22	30	[−100,100]	0
F9	$f(x) = \sum_{i=1}^{n} x_i^{10}$	Schwefel 2.23	30	[−10,10]	0
F10	$f(x) = \sum_{i=1}^{n} [\![x_i]\!]$	Step 1	30	[−100,100]	0
F11	$f(x) = \sum_{i=1}^{n} i * x_i^2$	Sum Squares	30	[−10,10]	0
F12	$f(x) = -20\exp\left(-0.02\sqrt{\frac{1}{d}\sum_{i=1}^{n} x_i^2}\right) - \exp\left(\frac{1}{d}\sum_{i=1}^{n} cos(2\pi x_i)\right) + 20 + \exp(1)$	Ackley	30	[−35,35]	0
F13	$f(x) = \sum_{i=1}^{n} \lvert x_i sin(x_i) + 0.1x_i \rvert$	Alpine	30	[−10,10]	0

Table 1. *Cont.*

No	Function	Name	Dim	R	Fmin
F14	$f(x) = \sum_{i=1}^{n} \left(\left(x_i^2\right)^{\left(x_{i+1}^2+1\right)} + \left(x_{i+1}^2\right)^{\left(x_i^2+1\right)} \right)$	Brown	30	[−1,4]	0
F15	$f(x) = x_1^2 + 10^6 \sum_{i=2}^{n} x_i^2$	Cigar	30	[−100,100]	0
F16	$f(x) = -\exp\left(-0.5 \sum_{i=1}^{n} x_i^2\right)$	Exponential	30	[−1,1]	−1
F17	$f(x) = \sum_{i=1}^{n} \frac{x_i^2}{4000} - \prod_{i=1}^{n} \cos\left(\frac{x_i}{\sqrt{i}}\right) + 1$	Griewank	30	[−600,600]	0
F18	$f(x) = \left(1 - n - \sum_{i=1}^{n-1} x_i\right)^{n - \sum_{i=1}^{n-1} x_i}$	Mishra 1	30	[0,1]	2
F19	$f(x) = \left(1 - n - \sum_{i=1}^{n-1} 0.5(x_i + x_{i+1})\right)^{n - \sum_{i=1}^{n-1} 0.5(x_i + x_{i+1})}$	Mishra 1	30	[0,1]	2
F20	$f(x) = \left[\frac{1}{n} \sum_{i=1}^{n} \lvert x_i \rvert - \left(\prod_{i=1}^{n} \lvert x_i \rvert\right)^{\frac{1}{n}}\right]^2$	Mishra 11	30	[0,10]	0
F21	$f(x) = \sum_{i=1}^{n} i x_i^4 + random[0,1]$	Quartic	30	[−1.28,1.28]	0
F22	$f(x) = 10n + \sum_{i=1}^{n} \left[x_i^2 - 10\cos(2\pi x_i)\right]$	Rastring	30	[−5.12,5.12]	0
F23	$f(x) = \sum_{i=1}^{n} \left[(x_i - 1)^2 + \left(x_1 - x_i^2\right)^2\right]$	Schwefel 2.25	30	[0,10]	0
F24	$f(x) = \left[\left(-\sum_{i=1}^{n} \lvert x_i \rvert\right) * \exp\left(-\sum_{i=1}^{n} \sin(x_i)^2\right)\right]$	Xin−She Yang 2	30	[−2π, 2π]	0
F25	$f(x) = \left[\exp\left(-\sum_{i=1}^{n} \left(\frac{x_i}{15}\right)^{10}\right) - 2\exp\left(-\sum_{i=1}^{n} (x_i)^2\right) * \prod_{i=1}^{n} \cos^2(x_i)\right]$	Xin−She Yang 3	30	[−20, 20]	0
F26	$f(x) = \sum_{i=1}^{n} x_i^2 + \left(\frac{1}{2} \sum_{i=1}^{n} i x_i^2\right)^2 + \left(\frac{1}{2} \sum_{i=1}^{n} i x_i^2\right)^4$	Zakharov	30	[−5,10]	0

Table 1. *Cont.*

No	Function	Name	Dim	R	Fmin
F27	$f(x) = 200 * \exp\left(-0.02 * \left(\sqrt{x_1^2 + x_2^2}\right)\right)$	Ackley 2	2	[−32,32]	−200
F28	$f(x) = \left\|x_1^2 + x_2^2 + x_1 * x_2\right\| + \left\|\sin(x_1)\right\| + \left\|\cos(x_2)\right\|$	Bartels Conn	2	[−500,500]	1
F29	$f(x) = x_1^2 + 2x_2^2 - 0.3\cos(3\pi\, x_1) - 0.4\cos(4\pi\, x_2) + 0.7$	Bohachevsky 1	2	[−100,100]	0
F30	$f(x) = x_1^2 + 2x_2^2 - 0.3\cos(3\pi\, x_1) * 0.4\cos(4\pi\, x_2) + 0.3$	Bohachevsky 2	2	[−100,100]	0
F31	$f(x) = x_1^2 + 2x_2^2 - 0.3\cos(3\pi\, x_1 + 4\pi\, x_2) + 0.3$	Bohachevsky 3	2	[−100,100]	0
F32	$f(x) = 2x_1^2 + 1.05x_1^4 + \frac{x_1^6}{6} + x_1x_2 + x_2^2$	Camel−Three Hump	2	[−5,5]	0
F33	$f(x) = x_1^2 + 12x_1 + 11 + 10\cos\left(\frac{\pi x_1}{2}\right) + 8\sin\left(\frac{5\pi x_1}{2}\right) - \left(\frac{1}{5}\right)^{0.5}\exp\left(-0.5(x_2 - 0.5)^2\right)$	Chichinadze	2	[−30,30]	−43.3159
F34	$f(x) = -10^{-4}\left[\left\|\sin(x_1)\sin(x_2)\exp\left\|100 - \frac{\left[\left(x_1^2 + x_2^2\right)\right]^{0.5}}{\pi}\right\|\right\| + 1\right]^{0.1}$	Cross−in−Tray	2	[−10,10]	−2.06261218
F35	$f(x) = -\left(\left(\left(\frac{1}{\left\|e^{\left\|100 - \frac{\sqrt{x_1^2 + x_2^2}}{\pi}\right\|}\sin(x_1)\sin(x_2)\right\| + 1}\right)\right)^{0.1}\right)$	ScCrossLegTable	2	[−10,10]	−1
F36	$f(x) = x_1^2 + x_2^2 + 25\left(\sin^2(x_1) + \sin^2(x_2)\right)$	Egg Crate	2	[−5,5]	0
F37	$f(x) = -\sum_{i=1}^{4} c_i \exp\left[-\sum_{j=1}^{6} a_{ij}\left(x_j - p_{ij}\right)^2\right]$	Hartman	6	[0,1]	−3.32236
F38	$f(x) = 0.26\left(x_1^2 + x_2^2\right) - 0.04x_1x_2$	Matyas	2	[−10,10]	0
F39	$f(x) = 1 + \sin^2 x_1 + \sin^2 x_2 - 0.1e^{-x_1^2 - x_2^2}$	Periodic	2	[−10,10]	0.9
F40	$f(x) = \left(333.75 - x_1^2\right)x_2^6 + x_1^2\left(11x_1^2x_2^4 - 2\right) + 5.5x_2^8 + \frac{x_1}{2x_2}$	Rump	2	[−500,500]	0

Table 1. *Cont.*

No	Function	Name	Dim	R	Fmin
F41	$f(x) = x_1^2 - x_1x_2 + x_2^2$	Rotated Ellipse	2	[−500,500]	0
F42	$f(x) = g(r), h(t),\ where,$ $g(r) = \left[\sin(r) - \frac{\sin(2r)}{2} + \frac{\sin(3r)}{3} + \frac{\sin(4r)}{4} + 4\right]\left(\frac{r^2}{r+1}\right),$ $h(t) = 0.5\cos(2t - 0.5) + \cos(t) + 2,$ $r = \sqrt{x_1^2 + x_2^2},$ $t = atan2(x1, x2)$	Sawtoothxy	2	[−20,20]	0
F43	$f(x) = 0.5 + \frac{\sin^2\left(x_1^2+x_2^2\right)^2 - 0.5}{1+0.001\left(x_1^2+x_2^2\right)^2}$	Scahffer1	2	[−100,100]	0
F44	$f(x) = 0.5 + \frac{\sin^2\sqrt{x_1^2+x_2^2} - 0.5}{1+0.001\left(x_1^2+x_2^2\right)^2}$	Scahffer6	2	[−100,100]	0
F45	$f(x) = \left(x_1^2 - 4x_2\right)^2 + \left(x_2^2 - 2x_1 + 4x_2\right)^2$	Stenger	2	[−1,4]	0
F46	$f(x) = 4 - 4x_1^3 + 4x_1 + x_2^2$	Trecanni	2	[−5,5]	0
F47	$f(x) = x_1^2 - 100\cos\left(\frac{x_1^2}{30}\right) + x_2^2 - 100\cos^2(x_2) - 100\cos\left(\frac{x_2^2}{30}\right)$	Venter	2	[−50,50]	−400

References

1. Wang, Z.; Luo, Q.; Chen, H.; Zhao, J.; Yao, L.; Zhang, J.; Chu, F. A high−accuracy intelligent fault diagnosis method for aero−engine bearings with limited samples. *Comput. Ind.* **2024**, *159*, 104099. [CrossRef]
2. Alanazi, A.; Alanazi, M.; Nowdeh, S.A.; Abdelaziz, A.Y.; El−Shahat, A. An optimal sizing framework for autonomous photovoltaic/hydrokinetic/hydrogen energy system considering cost, reliability and forced outage rate using horse herd optimization. *Energy Rep.* **2022**, *8*, 7154–7175. [CrossRef]
3. Zhang, Z.; Fu, Y.; Gao, K.; Pan, Q.; Huang, M. A learning−driven multi−objective cooperative artificial bee colony algorithm for distributed flexible job shop scheduling problems with preventive maintenance and transportation operations. *Comput. Ind. Eng.* **2024**, *196*, 110484. [CrossRef]
4. Nowdeh, S.A.; Davoudkhani, I.F.; Moghaddam, M.H.; Najmi, E.S.; Abdelaziz, A.Y.; Ahmadi, A.; Gandoman, F.H. Fuzzy multi−objective placement of renewable energy sources in distribution system with objective of loss reduction and reliability improvement using a novel hybrid method. *Appl. Soft Comput.* **2019**, *77*, 761–779. [CrossRef]
5. Jahannoush, M.; Nowdeh, S.A. Optimal designing and management of a stand−alone hybrid energy system using meta−heuristic improved sine–cosine algorithm for Recreational Center, case study for Iran country. *Appl. Soft Comput.* **2020**, *96*, 106611. [CrossRef]
6. Fu, Y.; Wang, Y.; Gao, K.; Suganthan, P.N.; Huang, M. Integrated scheduling of multi−constraint open shop and vehicle routing: Mathematical model and learning−driven brain storm optimization algorithm. *Appl. Soft Comput.* **2024**, *163*, 111943. [CrossRef]
7. Fu, Y.; Zhou, M.; Guo, X.; Qi, L.; Gao, K.; Albeshri, A. Multiobjective Scheduling of Energy−Efficient Stochastic Hybrid Open Shop With Brain Storm Optimization and Simulation Evaluation. *IEEE Trans. Syst. Man Cybern. Syst.* **2024**, *54*, 4260–4272. [CrossRef]
8. Fu, Y.; Gao, K.; Wang, L.; Huang, M.; Liang, Y.C.; Dong, H. Scheduling stochastic distributed flexible job shops using an multi−objective evolutionary algorithm with simulation evaluation. *Int. J. Prod. Res.* **2024**, *62*, 1–18. [CrossRef]
9. Hashim, F.A.; Houssein, E.H.; Mabrouk, M.S.; Al−Atabany, W.; Mirjalili, S. Henry gas solubility optimization: A novel physics−based algorithm. *Future Gener. Comput. Syst.* **2019**, *101*, 646–667. [CrossRef]
10. Mirza, A.F.; Mansoor, M.; Ling, Q. A novel MPPT technique based on Henry gas solubility optimization. *Energy Convers. Manag.* **2020**, *225*, 113409. [CrossRef]
11. Neggaz, N.; Houssein, E.H.; Hussain, K. An efficient henry gas solubility optimization for feature selection. *Expert Syst. Appl.* **2020**, *152*, 113364. [CrossRef]
12. Ekinci, S.; İzci, D.; Hekimoğlu, B. Implementing the Henry gas solubility optimization algorithm for optimal power system stabilizer design. *Electrica* **2021**, *21*, 250–258. [CrossRef]
13. Mousakazemi, S.M.H. Henry gas solubility optimization for control of a nuclear reactor: A case study. *Nucl. Eng. Technol.* **2022**, *54*, 940–947. [CrossRef]
14. Yıldız, B.S.; Pholdee, N.; Panagant, N.; Bureerat, S.; Yildiz, A.R.; Sait, S.M. A novel chaotic Henry gas solubility optimization algorithm for solving real−world engineering problems. *Eng. Comput.* **2022**, *38*, 871–883. [CrossRef]
15. Agarwal, R.; Shekhawat, N.S.; Luhach, A.K. Automated classification of soil images using chaotic Henry's gas solubility optimization: Smart agricultural system. *Microprocess. Microsyst.* **2021**, *in press*. [CrossRef]
16. Karasu, S.; Altan, A. Crude oil time series prediction model based on LSTM network with chaotic Henry gas solubility optimization. *Energy* **2022**, *242*, 122964. [CrossRef]
17. Mohammadi, D.; Abd Elaziz, M.; Moghdani, R.; Demir, E.; Mirjalili, S. Quantum Henry gas solubility optimization algorithm for global optimization. *Eng. Comput.* **2022**, *38*, 2329–2348. [CrossRef]
18. Chang, W.D. PID control for chaotic synchronization using particle swarm optimization. *Chaos* **2009**, *39*, 910–917. [CrossRef]
19. Rastogi, A.; Tiwari, P. Optimal tuning of fractional order PID controller for DC motor speed control using particle swarm optimization. *Int. J. Soft Comput. Eng.* **2013**, *3*, 150–157.
20. Iruthayarajan, M.W.; Baskar, S. Evolutionary algorithms based design of multivariable PID controller. *Expert Syst. Appl.* **2009**, *36*, 9159–9167. [CrossRef]
21. Hung, M.H.; Shu, L.S.; Ho, S.J.; Hwang, S.F.; Ho, S.Y. A novel intelligent multiobjective simulated annealing algorithm for designing robust PID controllers. *Syst. Man Cybern. Part A Syst. Humans* **2008**, *38*, 319–330. [CrossRef]
22. Pareek, S.; Kishnani, M.; Gupta, R. Application of artificial bee colony optimization for optimal PID tuning. In Proceedings of the 2014 International Conference on Advances in Engineering & Technology Research (ICAETR−2014), Unnao, India, 1–2 August 2014; pp. 1–5. [CrossRef]
23. El−Telbany, M.E. Tuning PID controller for DC motor: An artificial bees optimization approach. *Int. J. Comput. Appl.* **2013**, *77*, 18–21. [CrossRef]
24. Liao, W.; Hu, Y.; Wang, H. Optimization of PID control for DC motor based on artificial bee colony algorithm. In Proceedings of the 2014 International Conference on Advanced Mechatronic Systems, Kumamoto, Japan, 10–12 August 2014; pp. 23–27. [CrossRef]
25. Achanta, R.K.; Pamula, V.K. DC motor speed control using PID controller tuned by jaya optimization algorithm. In Proceedings of the 2017 IEEE International Conference on Power, Control, Signals and Instrumentation Engineering (ICPCSI), Chennai, India, 21–22 September 2017; pp. 983–987. [CrossRef]

26. Khalilpour, M.; Razmjooy, N.; Hosseini, H.; Moallem, P. Optimal control of DC motor using invasive weed optimization (IWO) algorithm. In Proceedings of the Majlesi Conference on Electrical Engineering, Majlesi New Town, Isfahan, Iran, 25 August 2011.
27. Aziz, M.S.I.; Nawawi, S.W.; Sudin, S.; Wahab, N.A.; Faramarzi, M.; Yusof, M.A.M. Gravitational search algorithm optimization for PID controller tuning in waste−water treatment process. *J. Teknol.* **2015**, *73*, 103–109. [CrossRef]
28. Izci, D.; Ekinci, S.; Demirören, A.; Hedley, J. HHO algorithm based PID controller design for aircraft pitch angle control system. In Proceedings of the 2020 International Congress on Human−Computer Interaction, Optimization and Robotic Applications (HORA), Ankara, Turkey, 26–28 June 2020; pp. 1–6. [CrossRef]
29. Elbayomy, K.M.; Zongxia, J.; Huaqing, Z. PID controller optimization by GA and its performances on the electro−hydraulic servo control system. *Chin. J. Aeronaut.* **2008**, *21*, 378–384. [CrossRef]
30. Zahir, A.M.; Alhady, S.S.N.; Wahab, A.A.A.; Ahmad, M.F. Objective functions modification of GA optimized PID controller for brushed DC motor. *Int. J. Electr. Comput. Eng.* **2020**, *10*, 2426. [CrossRef]
31. Loucif, F.; Kechida, S.; Sebbagh, A. Whale optimizer algorithm to tune PID controller for the trajectory tracking control of robot manipulator. *J. Braz. Soc. Mech. Sci. Eng.* **2020**, *42*, 1. [CrossRef]
32. Awrejcewicz, J.; Mrozowski, J. Bifurcations and chaos of a particular van der Pol−duffing oscillator. *J. Sound Vib.* **1989**, *132*, 89–100. [CrossRef]
33. Lazzús, J.A.; Rivera, M.; López−Caraballo, C.H. Parameter estimation of Lorenz chaotic system using a hybrid swarm intelligence algorithm. *Phys. Lett. A* **2016**, *380*, 1164–1171. [CrossRef]
34. Kocamaz, U.E.; Uyaroğlu, Y. Controlling Rucklidge chaotic system with a single controller using linear feedback and passive control methods. *Nonlinear Dyn.* **2014**, *75*, 63–72. [CrossRef]
35. Rafikov, M.; Balthazar, J.M. On an optimal control design for Rössler system. *Phys. Lett. A* **2004**, *333*, 241–245. [CrossRef]
36. Khan, A.; Trikha, P. Compound difference anti−synchronization between chaotic systems of integer and fractional order. *SN Appl. Sci.* **2019**, *1*, 1–13. [CrossRef]
37. Ueda, Y. Randomly transitional phenomena in the system governed by Duffing's equation. *J. Stat. Phys.* **1979**, *20*, 181–196. [CrossRef]
38. Wang, J.; Zhou, B.; Zhou, S. An improved cuckoo search optimization algorithm for the problem of chaotic systems parameter estimation. *Comput. Intell. Neurosci.* **2016**, *2016*, 1–8. [CrossRef]
39. Bassham, L.E., III; Rukhin, A.L.; Soto, J.; Nechvatal, J.R.; Smid, M.E.; Barker, E.B.; Vo, S. *A Statistical Test Suite for Random and Pseudorandom Number Generators for Cryptographic Applications*; National Institute of Standards & Technology: Gaithersburg, MD, USA, 2010.
40. Jenkinson, O. Ergodic optimization in dynamical systems. *Ergod. Theory Dyn. Syst.* **2019**, *39*, 2593–2618. [CrossRef]
41. Shi, Y.; Eberhart, R.C. A modified particle swarm optimizer. In Proceedings of the IEEE International Conference on Evolutionary Computation, Anchorage, AK, USA, 4–9 May 1998; pp. 69–73.
42. Mirjalili, S.; Lewis, A. The whale optimization algorithm. *Adv. Eng. Softw.* **2016**, *95*, 51–67. [CrossRef]
43. Van Laarhoven, P.J.; Aarts, E.H.; van Laarhoven, P.J.; Aarts, E.H. *Simulated Annealing*; Springer: Berlin/Heidelberg, Germany, 1987; pp. 7–15.
44. Beyer, H.G.; Schwefel, H.P. Evolution strategies–a comprehensive introduction. *Nat. Comput.* **2002**, *1*, 3–52. [CrossRef]
45. Mirjalili, S.; Mirjalili, S.M.; Lewis, A. Grey wolf optimizer. *Adv. Eng. Softw.* **2014**, *69*, 46–61. [CrossRef]

Disclaimer/Publisher's Note: The statements, opinions and data contained in all publications are solely those of the individual author(s) and contributor(s) and not of MDPI and/or the editor(s). MDPI and/or the editor(s) disclaim responsibility for any injury to people or property resulting from any ideas, methods, instructions or products referred to in the content.

symmetry

MDPI

Article

The Linear Quadratic Optimal Control Problem for Stochastic Systems Controlled by Impulses

Vasile Dragan [1,2,†] and Ioan-Lucian Popa [3,4,*,†]

[1] Institute of Mathematics "Simion Stoilow" of the Romanian Academy, P.O. Box 1-764, 014700 Bucharest, Romania; vasile.dragan@imar.ro
[2] Academy of the Romanian Scientists, 3 Ilfov, 050044 Bucharest, Romania
[3] Department of Computing, Mathematics and Electronics, "1 Decembrie 1918" University of Alba Iulia, 510009 Alba Iulia, Romania
[4] Faculty of Mathematics and Computer Science, Transilvania University of Braşov, Iuliu Maniu Street 50, 500091 Braşov, Romania
* Correspondence: lucian.popa@uab.ro
† These authors contributed equally to this work.

Abstract: This paper focuses on addressing the linear quadratic (LQ) optimal control problem on an infinite time horizon for stochastic systems controlled by impulses. No constraint regarding the sign of the quadratic functional is applied. That is why our first concern is to find conditions which guarantee that the considered optimal control problem is well posed. Then, when the optimal control problem is well posed, it is natural to look for conditions which guarantee the attainability of the optimal control problem that is being evaluated. The main tool involved in the solution of the problems stated before is a backward jump matrix linear differential equation (BJMLDE) with a Riccati-type jumping operator. This is formulated using the matrix coefficients of the controlled system and the weight matrices of the performance criterion. We show that the well posedness of the optimal control problem under investigation is guaranteed by the existence of the maximal and bounded solution of the associated BJMLDE with a Riccati-type jumping operator. Further, we show that when the associated BJMLDE with a Riccati-type jumping operator has a maximal solution which satisfies a suitable sign condition, then the optimal control problem is attainable if and only if it has an optimal control in a state feedback form, or if and only if the maximal solution of the BJMLDE with a Riccati-type jumping operator is a stabilizing solution. In order to make the paper more self-contained, we present a set of conditions that correspond to the existence of the maximal solution of the BJMLDE satisfying the desired sign condition.

Keywords: LQ optimal control problem; stabilizing solution; stochastic systems controlled by impulses; well posedness; attainability

MSC: 93E20; 93E03; 93E15

1. Introduction

Studying impulsive systems holds significant theoretical and practical significance. In more formal terms, impulsive systems belong to a category of dynamic systems, where state evolution follows continuous time dynamics, except for a number of instances where the state undergoes instantaneous changes. Numerous examples of such systems exist as referenced in [1–3]. These systems serve as valuable models for diverse real-world applications across engineering [4–6], environmental science [7], and mathematical finance [8]. For the latest insights into the subject matter, readers can consult the review article [9].

LQ control theory and its utilization of Riccati equations has grown substantially. This initial expansion includes investigations into both deterministic systems [10,11] and stochastic systems [12,13], marking it as a significant area within control theory. In 2000,

Rami, Zhou, and Moore [14] examined the attainability of the LQ problem; specifically, the existence of an optimal control is established using the generalized algebraic Riccati equation. Numerous developments have been made in this area, and we will highlight only a few that are particularly relevant: in [15], the examination revolves around studying LQ optimal control problems in an infinite horizon characterized by stochastic coefficients. In [16], the investigation centers on exploring optimal quadratic control for an affine equation in the infinite horizon driven by Levy processes. In [17], the authors examine an LQ optimal control problem in the infinite horizon case pertaining to mean-field stochastic differential equations. Also worth considering are references [18–21].

In [22,23], several criteria for exponential stability in the mean square and mean square stabilizability of linear stochastic systems controlled by impulses are provided.

In the present work, we consider a linear quadratic (LQ) optimal control problem for a dynamical system described by the Ito differential equation controlled by impulses. Often, such an optimal control problem by impulses is obtained as an equivalent version of an optimal control problem requiring the minimization of a quadratic criterion along the trajectories of a stochastic dynamical system controlled by piece-wise constant controls; see [24]. No constraint regarding the sign of the quadratic functional is applied. That is why our first concern is to find conditions which guarantee that the considered optimal control problem is well posed. Then, when the optimal control problem is well posed, it is natural to look for conditions which guarantee the attainability of the optimal control problem that is being evaluated. The main tool involved in the solution of the problems stated before is a backward jump matrix linear differential equation (BJMLDE) with a Riccati-type jumping operator. This is formulated using the matrix coefficients of the controlled system and the weight matrices of the performance criterion.

It is worth mentioning that in the case of an LQ control problem for a stochastic system controlled by impulses, the BJMLDE with a Riccati-type jumping operator plays the role which the Riccati differential equation or the Riccati algebraic equation, respectively, has in the case of an LQ control problem, where the control laws do not act by impulses. That is why it is natural to introduce the concepts of maximal solution and stabilizing solution of a BJMLDE with a Riccati-type jumping operator.

The principal contributions of the present paper encompass the following:

- We introduce the concepts of maximal solution and stabilizing solution of the BJMLDE with a Riccati-type jumping operator and provide necessary and sufficient conditions which guarantee the existence of these solutions.
- We show that the existence of the maximal solution of the BJMLDE with a Riccati-type jumping operator satisfying a suitable sign condition guarantees the well posedness of the optimal control problem under consideration. We introduce the value function $\mathbf{v}(t_0, x_0)$ associated to the optimal control problem and compute its value for all initial pairs $(t_0, x_0) \in [0, \infty) \times \mathbb{R}^n$.
- Under the assumption that the corresponding BJMLDE with a Riccati-type jumping operator has a maximal solution which satisfies a suitable sign condition, the optimal control problem under consideration is attainable if and only if it admits a unique optimal control which is in a state feedback form, or equivalently, if and only if the maximal solution of the BJMLDE with a Riccati-type jumping operator is a stabilizing solution too.

The derivations use the equivalence of the exponential stability in the mean square of a continuous time jump linear stochastic system with the exponential stability of the companion discrete-type linear equation. That is why we do not need to refer to the criteria for the exponential stability in the mean square or to the criteria for stabilizability in the mean square of the linear stochastic systems controlled by impulses existing in the literature, such as those from [22,23].

The rest of the paper is structured as follows: In Section 2, we introduce the problem and provide necessary preliminary concepts. In Section 3, we introduce the backward jump matrix linear differential equation (BJMLDE) with a Riccati-type jumping operator and

provide a necessary and sufficient condition for the existence of the maximal and bounded solution for this (see Theorems 1 and 2). Section 4 is centered on the the well posedness (see Theorem 3) and attainability (see Theorem 4) of the optimal control problem. Finally, Section 5 offers the concluding remarks for the paper.

2. The Problem

Consider the impulsive controlled linear stochastic system (ICLSS) described by

$$dx(t) = A_0x(t)dt + A_1x(t)dw(t), \quad kh < t \leq (k+1)h, \tag{1a}$$

$$x(kh^+) = \mathcal{A}_0x(kh) + \mathcal{B}_0u(k) + w_d(k)(\mathcal{A}_1x(kh) + \mathcal{B}_1u(k)),$$
$$h > 0 \text{ is given }, \quad k \in \mathbb{Z}_+ = \{0, 1, \ldots\}, \tag{1b}$$

$$x(0) = x_0, \tag{1c}$$

where we denote by $x(t) \in \mathbb{R}^n$ the state vector of the system and by $u(k) \in \mathbb{R}^m$ the control parameters. In (1a), $\{w(t)\}_{t\geq 0}$ is a one-dimensional standard Wiener process (or process of the Brownian motion). This is defined on a given probability space $(\Omega, \mathfrak{F}, \mathcal{P})$, and in (1b), $\{w_d(k)\}_{k\in\mathbb{Z}_+}$ is a sequence of independent random variables with zero mean and variance one. For further information on the definition and characteristics of the Wiener process, we can refer to [25,26].

Throughout the work, we assume that $\{w(t)\}_{t\geq 0}$ and $\{w_d(k)\}_{k\in\mathbb{Z}_+}$ are independent stochastic processes. For each $t \geq 0$, $\mathcal{F}_t \subset \mathfrak{F}$ represents the $\sigma-$algebra generated by the random variables $w(s)$, $w_d(k)$, $t \geq s \geq 0$, and $\frac{t}{h} > k \geq 0$, augmented with all subsets $\mathfrak{A} \in \mathfrak{F}$ with $\mathcal{P}(\mathfrak{A}) = 0$.

In (1) the controls $u(k)$ act at impulsive time instances $\tau_k = kh$, $k = 0, 1, \ldots$. That is why this kind of system is called **impulsive controlled systems**.

Based on Theorem 5.2.1 from [27] used on each interval $[kh, (k+1)h]$, we can demonstrate the following.

Proposition 1. *For each initial pair $(t_0, x_0) \in \mathbb{R}_+ \times \mathbb{R}^n$ and for any random vectors $u(k) : \Omega \to \mathbb{R}^m$ which are $\mathcal{F}_{kh}-$measurable with*

$$\mathbb{E}[|u(k)|^2] < \infty,$$

the ICLSS (1) has a unique solution $x(t) = x(t; t_0, x_0, \mathbf{u})$, $t \geq 0$, with the following properties:

(a) $x(\cdot; t_0, x_0, \mathbf{u})$ *is continuous (with probability 1) in any $t \neq kh$, left continuous in kh, for $kh > t_0$;*

(b) $x(\cdot; t_0, x_0, \mathbf{u}) \in \mathcal{L}^2_{\mathcal{F}}\{[t_0, T], \mathbb{R}^n\}$ *for all $T > t_0$;*

(c) $x(t_0; t_0, x_0, \mathbf{u}) = x_0$ *and* $\lim\limits_{\substack{t\to kh \\ t>kh}} x(t; t_0, x_0, \mathbf{u}) = x(kh^+)$, *where $x(kh^+)$ is provided by (1b).*

We recall that $\mathbb{R}_+ = [0, \infty)$, and $\mathbb{E}[\cdot]$ is used for the mathematical expectation. If $\mathcal{I} \subset \mathbb{R}_+$ is an interval, then $\mathcal{L}^2_{\mathcal{F}}\{\mathcal{I}, \mathbb{R}^p\}$ denotes the Hilbert space of the stochastic processes $\mathbf{Y} = \{y(t)\}_{t\in\mathcal{I}}$, which are non-anticipative with respect to the filtration $\mathcal{F} = \{\mathcal{F}_t\}_{t\in\mathcal{I}}$ and satisfies

$$\mathbb{E}\left[\int_{\mathcal{I}} |y(t)|^2 dt\right] < \infty.$$

For each initial pair $(t_0, x_0) \in \mathbb{R}_+ \times \mathbb{R}^n$, we denote $\mathcal{U}_{ad}(t_0, x_0)$ the set of controls $\mathbf{u} = \{u(k)\}_{k\geq\kappa(t_0)}$ satisfying the following properties:

(a) $u(k) : \Omega \to \mathbb{R}^m$ are $\mathcal{F}_{kh}-$measurable and

$$\sum_{k=\kappa(t_0)}^{\infty} \mathbb{E}[|u(k)|^2] < \infty;$$

(b)

$$\mathbb{E}\left[\int_{t_0}^{\infty} |x(t;t_0,x_0,\mathbf{u})|^2 dt\right] + \sum_{k=\kappa(t_0)}^{\infty} \mathbb{E}[|x(kh;t_0,x_0,\mathbf{u})|^2] < \infty, \tag{2a}$$

$$\lim_{t\to\infty} \mathbb{E}[|x(t;t_0,x_0,\mathbf{u})|^2] = 0. \tag{2b}$$

Here and in the sequel, $\kappa(t_0)$ is the integer with the property that

$$(\kappa(t_0)-1)h < t_0 \leq \kappa(t_0)h. \tag{3}$$

In (2), $x(\cdot;t_0,x_0,\mathbf{u})$, $t \geq t_0$ is the trajectory of ICLSS (1) starting from x_0 at the initial time t_0, and it is determined by the input $\mathbf{u} = \{u(k)\}_{k\geq\kappa(t_0)}$.

It is worth noticing that if the ICLSS (1) is mean square stabilizable by the linear state feedback in the sense of Definition 2 from [28], then the sets $\mathcal{U}_{ad}(t_0,x_0)$ are not empty for any initial pair $(t_0,x_0) \in \mathbb{R}_+ \times \mathbb{R}^n$. In the sequel, $\mathcal{U}_{ad}(t_0,x_0)$ will be called the set of **admissible controls** associated to the initial pair (t_0,x_0).

To the pair formed by the ICLSS (1) and the admissible controls $\mathcal{U}_{ad}(t_0,x_0)$, we associate the following quadratic functional:

$$J(t_0,\infty,x_0;\mathbf{u}) = \int_{t_0}^{\infty} \mathbb{E}[x_{\mathbf{u}}^{\top}(t)Mx_{\mathbf{u}}(t)]dt \tag{4}$$

$$+ \sum_{k=\kappa(t_0)}^{\infty} \mathbb{E}[x_{\mathbf{u}}^{\top}(kh)M_d x_{\mathbf{u}}(kh) + 2x_{\mathbf{u}}^{\top}(kh)L_d u(k) + u^{\top}(k)R_d u(k)],$$

where $x_{\mathbf{u}}(\cdot) = x(\cdot;t_0,x_0,\mathbf{u})$.

Regarding the matrix coefficients of (1) and the weight matrices from (4), we assume that A_j, $\mathcal{A}_j \in \mathbb{R}^{n\times n}$, $\mathcal{B}_j \in \mathbb{R}^{n\times m}$, $j = 0,1$, $M, M_d \in \mathcal{S}_n$, $R_d \in \mathcal{S}_m$, $L_d \in \mathbb{R}^{n\times m}$ are known matrices. Here and in the sequel, $\mathcal{S}_q$ represents the linear space of real symmetric matrices of size $q \times q$.

The optimal control problem we aim to solve in this work involves finding conditions that ensure the existence of an admissible control $\widetilde{\mathbf{u}} = \{\widetilde{u}\}_{k\geq\kappa(t_0)}$ which is satisfying the optimality condition

$$-\infty < J(t_0,\infty,x_0;\widetilde{\mathbf{u}}) \leq J(t_0,\infty,x_0;\mathbf{u}), \tag{5}$$

for any $\mathbf{u} \in \mathcal{U}_{ad}(t_0,x_0)$.

Since we do not impose any condition regarding the sign of the considered weighting matrices from (4), it is necessary to find first conditions which guarantee that the functional (4) is bounded below across the set of the admissible controls $\mathcal{U}_{ad}(t_0,x_0)$.

To this end, we introduce the so-called value function $\mathbf{v}(\cdot,\cdot)$ associated to the optimal control problem under consideration. We set

$$\mathbf{v}(t_0,x_0) \stackrel{\Delta}{=} \inf_{\mathbf{u}\in\mathcal{U}_{ad}(t_0,x_0)} J(t_0,\infty,x_0;\mathbf{u}). \tag{6}$$

Definition 1. *We say that the optimal control problem described by the performance criterion (4), the controlled system (1), and the set of the admissible controls $\mathcal{U}_{ad}(t_0,x_0)$ is as follows:*

(a) Well posed if

$$\mathbf{v}(t_0,x_0) > -\infty,$$

for any initial pair $(t_0,x_0) \in \mathbb{R}_+ \times \mathbb{R}^n$;

(b) Attainable, if for each $(t_0,x_0) \in \mathbb{R}_+ \times \mathbb{R}^n$, there exists the control $\widetilde{\mathbf{u}} \in \mathcal{U}_{ad}(t_0,x_0)$ with

$$J(t_0,\infty,x_0;\widetilde{\mathbf{u}}) = \mathbf{v}(t_0,x_0) > -\infty. \tag{7}$$

In Section 3, we examine the issue of whether a maximal solution and a stabilizing solution exist for this type of backward jump matrix linear differential equation.

In Section 4, we shall develop conditions which guarantee that the optimal control problem under consideration is well posed and attainable. The primary instrument is a BJMLDE with a Riccati-type jumping operator.

3. BJMLDE with Riccati-Type Jumping Operators

Based on the matrix coefficients of the ICLSS (1) and the weighting matrices provided by the performance criterion (4), we introduce the following BJMLDE with a Riccati-type jumping operator:

$$\dot{X}(t) + A_0^\top X(t) + X(t)A_0 + A_1^\top X(t)A_1 + M = 0, \;\; kh \le t < (k+1)h, \tag{8a}$$

$$\begin{aligned} X(kh^-) = {} & \sum_{j=0}^{1} \mathcal{A}_j^\top X(kh)\mathcal{A}_j - \left(\sum_{j=0}^{1} \mathcal{A}_j^\top X(kh)\mathcal{B}_j + L_d\right) \\ & \cdot \left(\sum_{j=0}^{1} \mathcal{B}_j^\top X(kh)\mathcal{B}_j + R_d\right)^{-1} \left(\sum_{j=0}^{1} \mathcal{B}_j^\top X(kh)\mathcal{A}_j + L_d^\top\right) \\ & + M_d, \;\; k \in \mathbb{Z}_+. \end{aligned} \tag{8b}$$

Γ^Σ is the set of all bounded functions $Z : \mathbb{R}_+ \to \mathcal{S}_n$ satisfying the following:

(a) $Z(\cdot)$ is a differentiable function on each interval $(kh, (k+1)h)$, right continuous in $t_k = kh$, $k \in \mathbb{Z}_+$;

(b) $Z(\cdot)$ verify the following jump matrix linear differential inequalities:

$$\dot{Z}(t) + A_0^\top Z(t) + Z(t)A_0 + A_1^\top Z(t)A_1 + M \ge 0, \;\; kh \le t < (k+1)h, \tag{9a}$$

$$\begin{pmatrix} -Z(kh^-) + M_d & L_d \\ L_d^\top & R_d \end{pmatrix} + \sum_{j=0}^{1} \begin{pmatrix} \mathcal{A}_j & \mathcal{B}_j \end{pmatrix}^\top Z(kh) \begin{pmatrix} \mathcal{A}_j & \mathcal{B}_j \end{pmatrix} \ge 0, \tag{9b}$$

$$\sum_{j=0}^{1} \mathcal{B}_j^\top Z(kh)\mathcal{B}_j + R_d \ge \gamma I_m > 0, \tag{9c}$$

for all $k \in \mathbb{Z}_+$, $\gamma > 0$.

Remark 1. *Employing the Schur complement technique (Theorem 1 from [29]), one may show that the set Γ^Σ contains all the bounded solutions $t \to X(t) : \mathbb{R}_+ \to \mathcal{S}_n$ of the BJMLDE (8) which are satisfying the sign conditions*

$$\sum_{j=0}^{1} \mathcal{B}_j^\top X(kh)\mathcal{B}_j + R_d \ge \gamma I_m > 0,$$

for all $k \in \mathbb{Z}_+$.

A significant role will be performed by the subset $\widetilde{\Gamma}^\Sigma$ which contains all bounded functions $Z(\cdot) \in \Gamma^\Sigma$ satisfying the stronger condition:

$$\begin{pmatrix} -Z(kh^-) + M_d & L_d \\ L_d^\top & R_d \end{pmatrix} + \sum_{j=0}^{1} \begin{pmatrix} \mathcal{A}_j & \mathcal{B}_j \end{pmatrix}^\top Z(kh) \begin{pmatrix} \mathcal{A}_j & \mathcal{B}_j \end{pmatrix} \ge \widehat{\gamma} I_{n+m} > 0, \tag{10}$$

for all $k \in \mathbb{Z}_+$.

Definition 2. *A globally defined solution $t \to X_{max}(t) : \mathbb{R}_+ \to \mathcal{S}_n$ of the BJMLDE (8) is named a maximal solution if*

$$X_{max}(t) \ge Z(t),$$

for all $t \in \mathbb{R}_+$ *for any* $Z(\cdot) \in \Gamma^{\Sigma}$.

Definition 3. *A globally defined solution* $t \to X_s(t) : \mathbb{R}_+ \to \mathcal{S}_n$ *of the BJMLDE (8) is called the* ***stabilizing solution*** *if the closed-loop jump stochastic linear differential equation, JSLDE,*

$$dx(t) = A_0 x(t)dt + A_1 x(t)dw(t), \;\; kh < t \leq (k+1)h, \tag{11a}$$
$$x(kh^+) = (\mathcal{A}_0 + \mathcal{B}_0 F_s(kh))x(kh) + w_d(k)(\mathcal{A}_1 + \mathcal{B}_1 F_s(kh))x(kh), \tag{11b}$$

$k \in \mathbb{Z}_+$ *is exponentially stable in mean square (ESMS), where*

$$F_s(kh) = -\left(\sum_{j=0}^{1} \mathcal{B}_j^\top X_s(kh)\mathcal{B}_j + R_d\right)^{-1}\left(\sum_{j=0}^{1} \mathcal{B}_j^\top X_s(kh)\mathcal{A}_j + L_d^\top\right). \tag{12}$$

Definition 4. *The ICLSS is mean square stabilizable by the linear state feedback if there exists a matrix* $F \in \mathbb{R}^{m\times n}$ *such that the following closed-loop JSLDE*

$$dx(t) = A_0 x(t)dt + A_1 x(t)dw(t), \;\; kh < t \leq (k+1)h, \tag{13a}$$
$$x(kh^+) = (\mathcal{A}_0 + \mathcal{B}_0 F)x(kh) + w_d(k)(\mathcal{A}_1 + \mathcal{B}_1 F)x(kh), \tag{13b}$$

$k \in \mathbb{Z}_+$, *is ESMS.*

A set of necessary and sufficient criteria for the mean square stabilizability by the linear state feedback of an ICLSS of type (1) is provided by Theorem 6 in [28].

In this section, we shall highlight the necessary and sufficient conditions for the existence of the maximal solution and the stabilizing solution of a BJMLDE of type (8). To this end, we will appeal to the properties of the linear and positive operators and of the linear operators which are defining a positive evolution on an ordered Hilbert space.

We recall that $\mathcal{S}_n$ is a finite dimensional real Hilbert space with the inner product:

$$\langle X, Y\rangle := \mathrm{Tr}[XY], \tag{14}$$

for all $X, Y \in \mathcal{S}_n$, here, $\mathrm{Tr}[\cdot]$ stands for the trace operator. Furthermore, $\mathcal{S}_n$ becomes an ordered Hilbert space with the order relation $\succeq$ provided by the convex cone

$$\mathcal{S}_n^+ := \{X \in \mathcal{S}_n \mid X \text{ is a positive semidefinite matrix }\}.$$

Consider $X \to \mathcal{L}[X] : \mathcal{S}_n \to \mathcal{S}_n$ the linear operator defined as

$$\mathcal{L}[X] = A_0 X + X A_0^\top + A_1 X A_1^\top, \tag{15}$$

for all $X \in \mathcal{S}_n$. Based on the inner product (14), we consider the adjoint operator $\mathcal{L}^*[\cdot]$ which is described by

$$\mathcal{L}^*[X] = A_0^\top X + X A_0 + A_1^\top X A_1, \tag{16}$$

for all $X \in \mathcal{S}_n$. With these notations, the differential Equation (8a) can be expressed in a compact form as

$$\dot{X}(t) + \mathcal{L}^*[X(t)] + M = 0, \;\; kh < t \leq (k+1)h. \tag{17}$$

Let $t \to X(t) : \mathbb{R}_+ \to \mathcal{S}_n$ be a globally defined solution of (8). From (17), we obtain that

$$X(t) = e^{\mathcal{L}^*((k+1)h-t)}[X((k+1)h^-)] + \int_t^{(k+1)h} e^{\mathcal{L}^*(s-t)}[M]ds,$$
$$t \in (kh, (k+1)h), \;\; k \in \mathbb{Z}_+. \tag{18}$$

Letting $t \to kh$, $t > kh$ in (18) and substituting the result in (8b), one obtains that the sequence $\{X(kh^-)\}_{k\in\mathbb{Z}_+}$ solves the next generalized discrete-time Riccati-type equation (GDTRE):

$$\begin{aligned} Y(k) =& \Pi_1[Y(k+1)] + \widetilde{M} - (\Pi_2[Y(k+1)] + \widetilde{L}) \\ & \cdot (\Pi_3[Y(k+1)] + \widetilde{R})^{-1}(\Pi_2[Y(k+1)] + \widetilde{L})^\top, \end{aligned} \tag{19}$$

where

$$\Pi_1[Y] := \sum_{j=0}^{1} \mathcal{A}_j^\top e^{\mathcal{L}^* h}[Y]\mathcal{A}_j, \tag{20a}$$

$$\Pi_2[Y] := \sum_{j=0}^{1} \mathcal{A}_j^\top e^{\mathcal{L}^* h}[Y]\mathcal{B}_j, \tag{20b}$$

$$\Pi_3[Y] := \sum_{j=0}^{1} \mathcal{B}_j^\top e^{\mathcal{L}^* h}[Y]\mathcal{B}_j, \tag{20c}$$

$$\widetilde{M} := M_d + \sum_{j=0}^{1} \mathcal{A}_j^\top \int_0^h e^{\mathcal{L}^* s}[M]ds\ \mathcal{A}_j, \tag{21a}$$

$$\widetilde{L} := L_d + \sum_{j=0}^{1} \mathcal{A}_j^\top \int_0^h e^{\mathcal{L}^* s}[M]ds\ \mathcal{B}_j, \tag{21b}$$

$$\widetilde{R} := R_d + \sum_{j=0}^{1} \mathcal{B}_j^\top \int_0^h e^{\mathcal{L}^* s}[M]ds\ \mathcal{B}_j. \tag{21c}$$

Employing Theorem 2.6.1 from [30], we obtain the following.

Corollary 1. *If $\mathcal{L}$ and $\mathcal{L}^*$ are the linear operators, defined by (15) and (16), then both $e^{\mathcal{L}t}$ as well as $e^{\mathcal{L}^* t}$, $t \geq 0$, are positive operators defined on the ordered Hilbert space $(\mathcal{S}_n, \mathcal{S}_n^+)$, that is*

$$e^{\mathcal{L}t}[Y] \succeq 0,$$

and

$$e^{\mathcal{L}^* t}[Y] \succeq 0,$$

for all $t \geq 0$ if $Y \succeq 0$.

Based on (20), we introduce the following linear operator $Y \to \Pi[Y] : \mathcal{S}_n \to \mathcal{S}_{n+m}$ defined by

$$\Pi[Y] := \begin{pmatrix} \Pi_1[Y] & \Pi_2[Y] \\ \Pi_2^\top[Y] & \Pi_3[Y] \end{pmatrix}, \tag{22}$$

for all $Y \in \mathcal{S}_n$. From (20) and (22), one obtains via Corollary 1 that

$$\Pi[Y] \succeq 0 \ \text{ if } \ Y \succeq 0.$$

This allows us to conclude that the GDTRE (19) is a special case of the relation 5.8 from [31].

The GDTRE (19) is determined by the pair $\Sigma_d = (\Pi, \mathcal{Q})$, where $\Pi : \mathcal{S}_n \to \mathcal{S}_{n+m}$ is the linear operator defined in (22), while

$$\mathcal{Q} = \begin{pmatrix} \widetilde{M} & \widetilde{L} \\ \widetilde{L}^\top & \widetilde{R} \end{pmatrix},$$

with $\widetilde{M}$, $\widetilde{L}$, and $\widetilde{R}$ being described in (21). To the pair Σ_d, we associate the following sets of sequences of symmetric matrices:

$$\Gamma^{\Sigma_d} := \{\mathbf{Z} = \{Z(k)\}_{k\geq 0} \mid \mathcal{D}[\mathbf{Z}](k) \succeq 0,\ \ \Pi_3[Z(k+1)] + \widetilde{R} \succeq \gamma_d I_m > 0,\ \ k \geq 0\}, \tag{23}$$

$$\widetilde{\Gamma}^{\Sigma_d} := \{\mathbf{Z} = \{Z(k)\}_{k\geq 0} \mid \mathcal{D}[\mathbf{Z}](k) \succeq \widehat{\gamma}_d I_{n+m} > 0,\ \ \text{for all}\ \ k \geq 0\}, \tag{24}$$

where

$$\mathcal{D}[\mathbf{Z}](k) := \begin{pmatrix} -Z(k) & 0 \\ 0 & 0 \end{pmatrix} + \Pi[Z(k+1)] + \mathcal{Q}. \tag{25}$$

Lemma 1.

(a) *There exists a one-to-one correspondence between the set Γ^{Σ} of the matrix valued functions $Z(\cdot)$ which are satisfying the linear matrix differential inequalities with jumps (9) and the set Γ^{Σ_d} of the sequences of symmetric matrices $\mathbf{Z} = \{Z(k)\}_{k\geq 0}$ which are satisfying the linear matrix inequalities (23);*

(b) *There exists a one-to-one correspondence between the set $\widetilde{\Gamma}^{\Sigma}$ of the matrix valued functions which satisfy the linear matrix inequalities (9a) with jumps described by (10) and the set $\widetilde{\Gamma}^{\Sigma_d}$ of the matrix valued sequences $\mathbf{Z} = \{Z(k)\}_{k\geq 0}$ which satisfy the linear matrix inequalities (24).*

Proof. (a) If $Z(\cdot)$ is satisfying (9a), we define

$$\Delta(t) := \dot{Z}(t) + \mathcal{L}^*[Z(t)] + M.$$

So (9a) can be expressed as

$$-\dot{Z}(t) = \mathcal{L}^*[Z(t)] + M - \Delta(t),\ \ kh \leq t < (k+1)h,\ \ k \in \mathbb{Z}_+,$$

where

$$\Delta(t) \geq 0,\ \ \text{for all}\ \ t \in \mathbb{R}_+.$$

Hence, if $Z(\cdot)$ is satisfying (9a), it also satisfies

$$\begin{aligned} Z(t) =& e^{\mathcal{L}^*((k+1)h-t)}[Z((k+1)h^-)] + \int_t^{(k+1)h} e^{\mathcal{L}^*(s-t)}[M]ds \\ &- \int_t^{(k+1)h} e^{\mathcal{L}^*(s-t)}[\Delta(s)]ds,\ \ kh \leq t < (k+1)h,\ \ k \in \mathbb{Z}_+. \end{aligned} \tag{26}$$

Letting $t \to kh$, $t > kh$ in (26) and substituting the result in (9b) and in (9c), we obtain via (20) and (21) that the sequence $\{Z(kh^-)\}_{k\in\mathbb{Z}_+}$ lies in Γ^{Σ_d} because

$$\int_t^{(k+1)h} e^{\mathcal{L}^*(s-t)}[\Delta(s)]ds \geq 0,\ \ \text{for all}\ \ k \in \mathbb{Z}_+.$$

Conversely, if $\mathbf{Y} = \{Y(k)\}_{k\geq 0}$ lies in Γ^{Σ_d}, we define

$$Z(t) := e^{\mathcal{L}^*((k+1)h-t)}[Y(k+1)] + \int_t^{(k+1)h} e^{\mathcal{L}^*(s-t)}[M]ds, \tag{27}$$

for all $kh \leq t < (k+1)h$, for any $k \in \mathbb{Z}_+$. Letting $t \to (k+1)h$, $t < (k+1)h$ in (27), we obtain that

$$Z((k+1)h^-) = Y(k+1), \text{ for all } k \in \mathbb{Z}_+. \tag{28}$$

Differentiating (27) with respect to the parameter t, we obtain

$$\dot{Z}(t) + \mathcal{L}^*[Z(t)] + M = 0, \quad kh \leq t < (k+1)h.$$

Employing (20), (23), (25), and (27) written for $t = kh$ with (28) written for k replaced by $k-1$, we obtain that $Z(\cdot)$ satisfies (9b) and (9c). Hence, $Z(\cdot)$ defined in (27) lies in Γ^{Σ}. Thus, the proof of (a) is complete.

Part (b) may be proved in a similar manner. □

Particularizing the Definition 4.7 from [31] for the stabilizability of a sequence of linear operators to the case of the linear operator Π defined by (20) and (22), we obtain the following.

Definition 5. *The linear operator $\Pi : \mathcal{S}_n \to \mathcal{S}_{n+m}$ is stabilizable if there exists a matrix $F \in \mathbb{R}^{m \times n}$ with the property that the discrete time linear equation on the Hilbert space $\mathcal{S}_n$*

$$S(k+1) = \Pi_F^*[S(k)], \tag{29}$$

is exponentially stable. $\Pi_F^*[\cdot]$ is the adjoint of the linear operator $X \to \Pi_F[X] : \mathcal{S}_n \to \mathcal{S}_n$ with respect to the inner product (14), where

$$\Pi_F[X] := \begin{pmatrix} I_n & F^\top \end{pmatrix} \Pi[X] \begin{pmatrix} I_n & F^\top \end{pmatrix}^\top. \tag{30}$$

By direct calculation, involving (20), (22), (29), and (30), we obtain the following.

Corollary 2. *On the linear operator specified by (20) and (22), we have the following equivalences:*

(i) *The operator Π is stabilizable (in the framework of Definition 5);*

(ii) *There exists a matrix $F \in \mathbb{R}^{m \times n}$ with the property that the discrete-time linear equation on the Hilbert space $\mathcal{S}_n$*

$$S(k+1) = \sum_{j=0}^{1} e^{\mathcal{L}h}[(\mathcal{A}_j + \mathcal{B}_j F) S(k) (\mathcal{A}_j + \mathcal{B}_j F)^\top], \tag{31}$$

is exponentially stable.

Invoking Proposition 3.1 and Proposition 3.3 from [28] in the case of the JSLDE (13), we obtain via Corollary 2 Definitions 4 and 5.

Corollary 3. *The ICLSS (1) is mean square stabilizable by the linear state feedback if and only if the accompanying linear operator Π associated via (20) and (22) is stabilizable.*

The following result establishes the conditions that are both necessary and sufficient conditions for the existence of the maximal and bounded solution of the BJMLDE (8).

Theorem 1. *If the ICLSS (1) is mean square stabilizable by the linear state feedback, then we have the following equivalences:*

(i) *The set Γ^{Σ} is not empty;*

(ii) *The BJMLDE (8) with a Riccati-type jumping operator has a unique maximal and bounded solution $X_{max} : \mathbb{R}_+ \to \mathcal{S}_n$ which satisfies the sign condition*

$$R_d + \sum_{j=0}^{1} \mathcal{B}_j^\top X_{max}(kj)\mathcal{B}_j \geq \nu I_m > 0, \tag{32}$$

for all $k \in \mathbb{Z}_+$. Furthermore, $X_{max}(\cdot)$ is a periodic function of period h.

Proof. The implication $(ii) \Rightarrow (i)$ follows immediately because, according to Remark 1, the maximal solution, if any, lies in Γ^{Σ}.

In order to prove the implication $(i) \Rightarrow (ii)$, let us remark that Lemma 1 (a) together with Corollary 3 guarantees that in the case of GDTRE (19), the assumptions from Theorem 5.3 in [31] are fulfilled. Hence, under the considered assumptions, the GDTRE (19) has a unique maximal solution $Y_{max} \in \mathcal{S}_n$ which satisfies the following sign condition:

$$\Pi_3[Y_{max}] + \widetilde{R} > 0. \tag{33}$$

For each $k \geq 0$ and $t \in [kh, (k+1)h)$, we define

$$X_{max}(t) := e^{\mathcal{L}^*((k+1)h-t)}[Y_{max}] + \int_t^{(k+1)h} e^{\mathcal{L}^*(s-t)}[M]ds. \tag{34}$$

So,

$$X_{max}((k+1)h^-) = \lim_{\substack{t\to(k+1)h \\ t<(k+1)h}} X_{max}(t) = Y_{max}, \text{ for all } k = 0, 1, \dots .$$

One shows that (34) defines a periodic function of period h, and (33) becomes (32).

Finally, employing (20), (21), and (34), one see that $X_{max}(\cdot)$ is a solution of the BJMLDE (8). Employing again Lemma 1 (a), one obtains that $X_{max}(\cdot)$ defined in (34) is just the unique bounded and maximal solution of the BJMLDE (8). Thus, the proof ends. □

Theorem 2. *The following are equivalent:*

(i) *The ICLSS (1) is mean square stabilizable by the linear state feedback, and the set $\widetilde{\Gamma}^{\Sigma}$ is not empty;*

(ii) *The BJMLDE with a Riccati-type jumping operator (8) has a unique bounded and stabilizing solution $X_s(\cdot) : \mathbb{R}_+ \to \mathcal{S}_n$ which satisfies the following sign condition:*

$$R_d + \sum_{j=0}^{1} \mathcal{B}_j^\top X_s(kh)\mathcal{B}_j \geq \widetilde{\nu} I_m > 0, \tag{35}$$

for all $k \in \mathbb{Z}_+$. Further, $X_s(\cdot)$ is a periodic function of period h, and it coincides with the maximal bounded solution $X_{max}(\cdot)$ of (8).

Proof. Invoking Lemma 1 (b) together with Corollary 3, we see that we can apply the implication $(i) \Rightarrow (ii)$ of Theorem 5.5 and Theorem 5.6 from [31] to deduce that the GDTRE (19) has a stabilizing solution Y_s which satisfies the following sign condition:

$$\widetilde{R} + \Pi_3[Y_s] > 0. \tag{36}$$

We define

$$X_s(t) := e^{\mathcal{L}^*((k+1)h-t)}[Y_s] + \int_t^{(k+1)h} e^{\mathcal{L}^*(s-t)}[M]ds, \tag{37}$$

for any $k = 0, 1, \ldots$, and for all $t \in [kh, (k+1)h)$

One shows that $X_s(\cdot)$ defined as before is just the stabilizing solution of (8). Thus, the proof of the implication $(i) \Rightarrow (ii)$ ends.

To prove $(ii) \Rightarrow (i)$, one takes into account that if $X_s(\cdot)$ is the stabilizing and bounded solution of (8), then the sequence $\{X_s(kh)\}_{k\geq 0}$ is the stabilizing solution of the GDTRE (19). Reasoning from $(ii) \Rightarrow (i)$ from Theorem 5.6 of [31], we obtain that the operator Π is stabilizable (in the framework of Definition 5), and the set $\widetilde{\Gamma}^{\Sigma}$ is not empty.

Invoking again Lemma 1 (b) together with Corollary 3, we may conclude that the set $\widetilde{\Gamma}^{\Sigma}$ is not empty, and the ICLSS (1) is mean square stabilizable by the linear state feedback. □

Remark 2. *According to the equivalence $(i) \Leftrightarrow (iii)$ from Proposition 5.2 from [31] applied in the particular case of the GDTRE (19), if the set $\widetilde{\Gamma}^{\Sigma}$ is not empty, it necessarily contains constant sequences. That is why in view of Lemma 1 (b), in order to test if the set $\widetilde{\Gamma}^{\Sigma}$ is not empty, it is sufficient to check if the linear matrix inequality (LMI) (24)–(25) has a solution which is not dependent upon $k \in \mathbb{Z}_+$.*

4. Well Posedness and Attainability of the Optimal Control Problem

First, we present an auxiliary result.

Lemma 2. *Let $X(\cdot) : \mathcal{I}^X \subset \mathbb{R}_+ \to \mathcal{S}_n$ be a solution of the BJMLDE (8). For each $[t_0, T] \subset \mathcal{I}^X$, we have*

$$\begin{aligned}
&\int_{t_0}^{T} \mathbb{E}[x_{\mathbf{u}}^{\top}(t) M x_{\mathbf{u}}(t)] + \sum_{k=\kappa(t_0)}^{\kappa(T)-1} \mathbb{E}[x_{\mathbf{u}}^{\top}(kh) M_d x_{\mathbf{u}}(kh) + 2x_{\mathbf{u}}^{\top}(kh) L_d u(k) \\
&+ u^{\top}(k) R_d u(k)] = x_0^{\top} X(t_0^-) x_0 - \mathbf{E}[x_{\mathbf{u}}^{\top}(T) X(T^-) x_{\mathbf{u}}(T)] \\
&+ \sum_{k=\kappa(t_0)}^{\kappa T-1} \mathbb{E}[(u(k) - F^X(kh) x_{\mathbf{u}}(kh))^{\top} \mathbb{R}(X(kh))(u(k) - F^X(kh) x_{\mathbf{u}}(kh))],
\end{aligned} \tag{38}$$

where $\kappa(T)$ follows the definition provided in (3) but with t_0 replaced by T and

$$\mathbb{R}(X(kh)) := R_d + \sum_{j=0}^{1} \mathcal{B}_j^{\top} X(kh) \mathcal{B}_j, \tag{39}$$

and

$$F^X(kh) := -(\mathbb{R}(X(kh)))^{-1} \left(\sum_{j=0}^{1} \mathcal{B}_j^{\top} X(kh) \mathcal{A}_j + L_d^{\top} \right). \tag{40}$$

In (38), $x_0^{\top} X(t_0^-) x_0$ is replaced by $x_0^{\top} X(t_0) x_0$ whenever $t_0 < \kappa(t_0)h$.

Proof. Employing the Itô formula (see [27]) to $V(t, x) = x^{\top} X(t) x$ and to the stochastic process $x_{\mathbf{u}}(t)$ which is satisfying (1a) on the interval of the form $[a_p, b_p] \subset [kh, (k+1)h]$ if $\kappa(t_0) \leq k \leq \kappa(T) - 2$ or $[a_p, b_p] \subset [(\kappa(T) - 1)h, T]$ and letting $a + p \to kh$, $b_p \to (k+1)h$, or $a_p \to (\kappa(T) - 1)h$ and $b_p \to T$, we obtain via (8a) that

$$\begin{aligned}
\int_{kh}^{(k+1)h} \mathbb{E}[x_{\mathbf{u}}^{\top}(t) M x_{\mathbf{u}}(t)] dt &= \mathbb{E}[x_{\mathbf{u}}^{\top}(kh^+) X(kh) x_{\mathbf{u}}(kh^+)] \\
&\quad - \mathbb{E}[x_{\mathbf{u}}^{\top}((k+1)h) X((k+1)h^-) x_{\mathbf{u}}((k+1)h)],
\end{aligned} \tag{41}$$

for $\kappa(t_0) \leq k \leq \kappa(T) - 2$ and

$$\int_{(\kappa(T)-1)h}^{T} \mathbb{E}[x_{\mathbf{u}}^{\top}(t) M x_{\mathbf{u}}(t)]dt = \mathbb{E}[x_{\mathbf{u}}^{\top}((\kappa(T)-1)h^{+}) X((\kappa(T)-1)h) \cdot x_{\mathbf{u}}((\kappa(T)-1)h^{+})] - \mathbb{E}[x_{\mathbf{u}}^{\top}((T) X(T^{-}) x_{\mathbf{u}}((T)]. \tag{42}$$

From (1b), we obtain that

$$\begin{aligned} &\mathbb{E}[x_{\mathbf{u}}^{\top}(kh^{+}) X(kh) x_{\mathbf{u}}(kh^{+})] \\ &= \sum_{j=0}^{1} \mathbb{E}[(\mathcal{A}_j X(kh) \mathcal{B}_j u(k))^{\top} X(kh) (\mathcal{A}_j X(kh) + \mathcal{B}_j u(k))]. \end{aligned}$$

After some computations involving (8b) and the technique of square computations, we obtain

$$\begin{aligned} &\mathbb{E}[x_{\mathbf{u}}^{\top}(kh^{+}) X(kh) x_{\mathbf{u}}(kh^{+})] = \mathbb{E}[x_{\mathbf{u}}^{\top}(kh) X(kh^{-}) x_{\mathbf{u}}(kh)] \\ &+ \mathbb{E}[(u(k) - F^{X}(kh) x_{\mathbf{u}}(kh))^{\top} \mathbb{R}(X(kh))(u(k) - F^{X}(kh) x_{\mathbf{u}}(kh))] \\ &- \mathbb{E}[x_{\mathbf{u}}^{\top}(kh) M_d x_{\mathbf{u}}(kh) + 2 x_{\mathbf{u}}^{\top}(kh) L_d u(k) + u^{\top}(k) R_d u(k)], \end{aligned} \tag{43}$$

$\kappa(t_0) \leq k \leq \kappa(T) - 1$. Substituting (43) in (41) and (42) and summing from $k = \kappa(t_0)$ to $k = \kappa(T) - 1$, we obtain

$$\begin{aligned} &\int_{\kappa(t_0)}^{T} \mathbb{E}[x_{\mathbf{u}}^{\top}(t) M x_{\mathbf{u}}(t)]dt \\ &+ \sum_{k=\kappa(t_0)}^{\kappa(T)-1} \mathbb{E}[x_{\mathbf{u}}^{\top}(kh) M_d x_{\mathbf{u}}(kh) + 2 x_{\mathbf{u}}(kh) L_d u(k) u^{\top}(k) R_d u(k)] \\ &= \mathbb{E}[x_{\mathbf{u}}^{\top}(\kappa(t_0)h) X(\kappa(t_0)h^{-}) x_{\mathbf{u}}(\kappa(t_0)h)] - \mathbb{E}[x_{\mathbf{u}}^{\top}(T) X(T^{-}) x_{\mathbf{u}}(T)] \\ &+ \sum_{k=\kappa(t_0)}^{\kappa(T)-1} \mathbb{E}[(u(k) - F^{X}(kh) x_{\mathbf{u}}(kh))^{\top} \mathbb{R}(X(kh))(u(k) - F^{X}(kh) x_{\mathbf{u}}(kh)]. \end{aligned} \tag{44}$$

If $t_0 = \kappa(t_0)h$, then (44) is just (38). In this case, the proof would be complete.

If $(\kappa(t_0) - 1)h < t_0 < \kappa(t_0)h$, we use Itô's formula to $V(t, x) = x^{\top} X(t) x$ and to the stochastic process $x_{\mathbf{u}}(t)$, $t \in [t_0, \kappa(t_0)h]$, and we obtain via (8a) that

$$\int_{t_0}^{\kappa(t_0)h} \mathbb{E}[x_{\mathbf{u}}^{\top}(t) M x_{\mathbf{u}}(t)]dt = x_0^{\top} X(t_0) x_0 - \mathbb{E}[x_{\mathbf{u}}^{\top}(\kappa(t_0)h) X(\kappa(t_0)h^{-}) x_{\mathbf{u}}(\kappa(t_0)h)].$$

Adding this equality to (44), we obtain (38). Thus, the proof ends. □

The next result provides a sufficient condition for the attainability of the optimal control problem under consideration.

Proposition 2. *Assume that the BJMLDE with a Riccati-type jumping operator (8) has a bounded and stabilizing solution $X_s(\cdot) : \mathbb{R}_+ \to \mathcal{S}_n$ satisfying the sign condition (35).*

Let us explore the control law $\widetilde{\mathbf{u}} = \{\widetilde{u}(k)\}_{k \geq \kappa(t_0)}$ defined by

$$\widetilde{u}(k) := F_s(kh) \widetilde{u}(kh), \quad k \geq \kappa(t_0), \tag{45}$$

where $F_s(kh)$ are the gain matrices associated to the stabilizing solution $X_s(\cdot)$ via (12), and $\widetilde{x}(kh)$, $kh \geq t_0$ are the value of the solution of the IVP (11).

Under these conditions, the control defined by (45) lies in $\mathcal{U}_{ad}(t_0, x_0)$ and satisfies the optimality condition (5). The minimal value of the cost function (4) is:

$$J(t_0, \infty, x_0; \widetilde{\mathbf{u}}) = x_0^\top X_s(t_0^-) x_0,$$

with the remark that $X_s(t_0^-) = X_s(t_0)$ whenever $t_0 < \kappa(t_0)h$.

Proof. The fact that the control (45) satisfies the constraints (2) follows immediately from Definition 3 of the stabilizing solution. Since $X_s(\cdot)$ is a bounded function, then there exists $\widetilde{c} > 0$ with the property that

$$|X_s(T)| \leq \widetilde{c},$$

and

$$|X_s(T^-)| \leq \widetilde{c},$$

for all $T \geq 0$. Employing (2b), we may infer that

$$\lim_{T \to \infty} \mathbb{E}[x_{\mathbf{u}}^\top(T) X_s(T^-) x_{\mathbf{u}}(T)] = 0, \tag{46}$$

for all $\mathbf{u} \in \mathcal{U}_{ad}(t_0, x_0)$ for any $(t_0, x_0) \in \mathbb{R}_+ \times \mathbb{R}^n$.

Writing (38) for $X(\cdot)$ replaced by $X_s(\cdot)$, we obtain via (2a) and (46) that

$$\begin{aligned} J(t_0, \infty, x_0; \mathbf{u}) &= x_0^\top X_s(t_0^-) x_0 \\ &+ \sum_{k=\kappa(t_0)}^{\infty} \mathbb{E}[(u(k) - F_s(kh) x_{\mathbf{u}}(kh))^\top \mathbb{R}(X_s(kh))(u(k) - F_s(kh) x_{\mathbf{u}}(kh))], \end{aligned} \tag{47}$$

for all $\mathbf{u} \in \mathcal{U}_{ad}(t_0, x_0)$, $(t_0, x_0) \in \mathbb{R}_+ \times \mathbb{R}^n$. For the unicity of the solution of the IVP (1) directed by a control $\mathbf{u} \in \mathcal{U}_{ad}(t_0, x_0)$, we deduce that in the case of the control (45), we have

$$x_{\widetilde{\mathbf{u}}}(t) = \widetilde{x}(t),$$

for all $t \geq t_0$, $\widetilde{x}(\cdot)$ being the solution of (11) which satisfies

$$\widetilde{x}(t_0) = x_0.$$

This allows us to conclude that, in the case of the control (45), the equality (47) gives

$$J(t_0, \infty, x_0; \widetilde{\mathbf{u}}) = x_0^\top X_s(t_0^-) x_0. \tag{48}$$

From (35), (47) and (48), we conclude that the control (45) satisfies the optimality condition (5), and (48) provides the maximal value of the cost function (4) over the set of the admissible controls. Thus, the proof ends. □

The next theorem provides a sufficient condition for the well posedness of the optimal control problem under consideration.

Theorem 3. *Assume the following:*

(a) The ICLSS (1) is mean square stabilizable by the linear state feedback;

(b) The set Γ^{Σ} of the functions $Z(\cdot)$ which satisfy the constraints (9) is not empty.

Under these conditions, the optimal control problem described by the performance criterion (4), the controlled system (1), and the set of the admissible controls $\mathcal{U}_{ad}(t_0, x_0)$ is well posed. Furthermore,

$$\mathbf{v}(t_0, x_0) = x_0^\top X_{max}(t_0^-) x_0, \tag{49}$$

for all $(t_0, x_0) \in \mathbb{R}_+ \times \mathbb{R}^n$. $X_{max}(\cdot)$ *is the unique maximal and bounded solution of the BJMLDE (8) which satisfies the sign condition (32). In (49),* $X_{max}(t_0^-)$ *coincides to* $X_{max}(t_0)$ *whenever* $(\kappa(t_0) - 1)h < t_0 < \kappa(t_0)h$.

Proof. If the assumption (a) holds, then the set $\mathcal{U}_{ad}(t_0, x_0)$ is not empty for any initial pair (t_0, x_0). Further, Theorem 1 guarantees the existence of the maximal and bounded solution $X_{max}(\cdot)$ which satisfies the sign condition (32), and it is a periodic function with period h. Applying Lemma 2, taking $X_{max}(\cdot)$ instead of $X(\cdot)$, we obtain

$$\begin{aligned}
&\int_{t_0}^{T} \mathbb{E}[x_{\mathbf{u}}^\top(t) M x_{\mathbf{u}}(t)]dt \\
&+ \sum_{k=\kappa(t_0)}^{\kappa(T)-1} \mathbb{E}[x_{\mathbf{u}}^\top(kh) M_d x_{\mathbf{u}}(kh) + 2x_{\mathbf{u}}^\top(kh) L_d u(k) + u^\top(k) R_d u(k)] \\
&= x_0^\top X_{max}(t_0^-) x_0 - \mathbb{E}[x_{\mathbf{u}}^\top(T) X_{max}(T^-) x_{\mathbf{u}}(T)] \\
&+ \sum_{k=\kappa(t_0)}^{\kappa(T)-1} \mathbb{E}[(u(k) - F_{max}(kh) x_{\mathbf{u}}(kh))^\top \mathbb{R}(X_{max}(kh))(u(k) - F_{max}(kh) x_{\mathbf{u}}(kh)],
\end{aligned} \tag{50}$$

for all $T > \kappa(t_0)h$ and any $\mathbf{u} \in \mathcal{U}_{ad}(t_0, x_0)$ for any $(t_0, x_0) \in \mathbb{R}_+ \times \mathbb{R}^n$. Here, $F_{max}(kh)$ is computed as in (40) with $X_{max}(\cdot)$ instead of $X(\cdot)$. Since $X_{max}(\cdot)$ is a bounded function, then there exists $\widehat{c} > 0$ such that

$$|X_{max}(T)| \leq \widehat{c},$$

and

$$|X_{max}(T^-)| \leq \widehat{c},$$

for all $T \geq 0$. Based on (2b), we may infer that

$$\lim_{T \to \infty} \mathbb{E}[x_{\mathbf{u}}^\top(T) X_{max}(T^-) x_{\mathbf{u}}(T)] = 0, \tag{51}$$

for all $\mathbf{u} \in \mathcal{U}_{ad}(t_0, x_0)$ for an arbitrary initial pair $(t_0, x_0) \in \mathbb{R}_+ \times \mathbb{R}^n$. Further, taking the limit for $T \to \infty$ in (50), we obtain via (2a) and (51) that

$$\begin{aligned}
J(t_0, \infty, x_0; \mathbf{u}) &= x_0^\top X_{max}(t_0^-) x_0 \\
&+ \sum_{k=\kappa(t_0)}^{\infty} \mathbb{E}[(u(k) - F_{max}(kh) x_{\mathbf{u}}(kh))^\top \mathbb{R}(X_{max}(kh))(u(k) - F_{max}(kh) x_{\mathbf{u}}(kh))],
\end{aligned} \tag{52}$$

for all $u = \{u(k)\}_{k \geq \kappa(t_0)} \in \mathcal{U}_{ad}(t_0, x_0)$ for arbitrary $(t_0, x_0) \in \mathbb{R}_+ \times \mathbb{R}^n$. Bearing in mind (32), we may deduce from (52) that

$$J(t_0, \infty, x_0; \mathbf{u}) \geq x_0^\top X_{max}(t_0^-) x_0, \tag{53}$$

for all $\mathbf{u} \in \mathcal{U}_{ad}(t_0, x_0)$. From (53) and (6), we may conclude that

$$\mathbf{v}(t_0, x_0) \geq x_0^\top X_{max}(t_0^-) x_0, \tag{54}$$

for all $(t_0, x_0) \in \mathbb{R}_+ \times \mathbb{R}^n$. Thus, from Definition 1 (a), it follows that the optimal control problem under consideration is well posed.

To end the proof, it remains to show that in (54), we have equality. To accomplish this, we consider a sequence $\{\delta_q\}_{g \geq 1}$ with the following properties:

$$\delta_q \geq \delta_{q+1} > 0,$$

and

$$\lim_{q\to\infty}\delta_q=0.$$

We consider the following perturbation of (4):

$$J_{\delta_q}(t_0,\infty,x_0;\mathbf{u})=J(t_0,\infty,x_0;\mathbf{u})+\delta_q\sum_{k=\kappa(t_0)}^{\infty}\mathbb{E}[|x_{\mathbf{u}}(kh)|^2],\tag{55}$$

for all $\mathbf{u}=\{u(k)\}_{k\geq\kappa(t_0)}\in\mathcal{U}_{ad}(t_0,x_0)$.

The BJMLDE of type (8) associated to the pair formed by the ICLSS (1) and the quadratic functional (55) is

$$\dot{X}(t)+\mathcal{L}^*[X(t)]+M=0,\ \ kh\leq t<(k+1)h,\tag{56a}$$

$$X(kh^-)=\mathcal{R}_d(X(kh))+\delta_q I_n,\ \ k\in\mathbb{Z}_+,\tag{56b}$$

where $\mathcal{L}^*(\cdot)$ is introduced by (16), while $\mathcal{R}_d(X(kh))$ is described by the right-hand side of (8b).

The accompanying GDTRE of the form (19) associated to (56) is

$$\begin{aligned}Y(k)=&\Pi_1[Y(k+1)]+\widetilde{M}+\delta_q I_n-(\Pi_2[Y(k+1)]+\widetilde{L})\\&\cdot(\Pi_3[Y(k+1)]+\widetilde{R})^{-1}(\Pi_2[Y(k+1)]+\widetilde{L})^{\top},\end{aligned}\tag{57}$$

where $\Pi_k[\cdot]$, $j=1,2,3$ are defined as in (20) and $\widetilde{M}$, $\widetilde{L}$, $\widetilde{R}$ are those computed in (21). Hence, the GDTRE (57) is described by the pair

$$\sigma_d^{\delta_q}=(\Pi,\mathcal{Q}_{\delta_q}),$$

where $\Pi:\mathcal{S}_n\to\mathcal{S}_{n+m}$ is the operator defined in (22) and

$$\mathcal{Q}_{\delta_q}=\begin{pmatrix}\widetilde{M}+\delta_q I_n & \widetilde{L}\\ \widetilde{L}^{\top} & \widetilde{R}\end{pmatrix},\ \ q\geq 1.\tag{58}$$

Let $\widetilde{\Gamma}^{\Sigma_d^{\delta_q}}$ be the set of the sequences of symmetric matrices $\mathbf{Z}=\{Z(k)\}_{k\geq 0}$ which satisfy

$$\mathcal{D}^{\delta_q}(\mathbf{Z})(k)\geq\gamma I_{n+m}>0,\tag{59}$$

for all $k\geq 0$, where

$$\mathcal{D}^{\delta_q}(\mathbf{Z})(k):=\begin{pmatrix}-Z(k) & 0\\ 0 & 0\end{pmatrix}+\Pi[Z(k+1)]+\mathcal{Q}^{\delta_q}.\tag{60}$$

From Lemma 1 (a) together with (23), (59) and (60) we may infer that if the set Γ^{Σ} is not empty, then the set $\widetilde{\Gamma}^{\Sigma_d^{\delta_q}}$ associated to the BJMLDE (56) is not empty. Invoking the implication $(i)\Rightarrow(ii)$ from Theorem 2, we may conclude that the BJMLDE (56) has a stabilizing solution $X_s^{\delta_q}(\cdot)$ which satisfies the sign conditions

$$R_d+\sum_{j=0}^{1}\mathcal{B}_j^{\top}X_s^{\delta_q}(kh)\mathcal{B}_j\geq\gamma_1 I_m>0,$$

for all $k\in\mathbb{Z}_+$. One proves via Theorem 5.4 from [31] that

$$X_s^{\delta_q}(t)\geq X_s^{\delta_{q+1}}(t)\geq X_{max}(t),$$

for all $q \geq 1$ and

$$\lim_{q\to\infty} X_s^{\delta_q}(t) = X_{max}(t), \quad t \in \mathbb{R}_+. \tag{61}$$

Let $F_s^{\delta_q}(t)$ be the stabilizing gain matrix associated to the solution $X_s^{\delta_q}(\cdot)$ as in (12). We consider the control law

$$\widetilde{u}_{\delta_q}(k) := F_s^{\delta_q}(kh)\widetilde{x}_{\delta_q}(kh), \tag{62}$$

$\widetilde{x}_{\delta_q}(\cdot)$ being the solution of the IVP obtained when the control (62) is plugged in (1). Applying Proposition 2 in the case of the optimal control problem described by the cost function (55), we obtain via (52) and (55) that

$$\begin{aligned} x_0^\top X_{max}(t_0^-)x_0 \leq \mathbf{v}(t_0, x_0) \leq J(t_0, \infty, x_0; \widetilde{\mathbf{u}}_{\delta_q}) \\ \leq J_{\delta_q}(t_0, \infty, x_0; \widetilde{\mathbf{u}}_{\delta_q}) = x_0^\top X_s^{\delta_q}(t_0^-)x_0, \end{aligned} \tag{63}$$

for all $q \geq 1$. Taking the limit for $q \geq \infty$ in (63), we obtain via (61) that

$$\mathbf{v}(t_0, x_0) = x_0^\top X_{max}(t_0^-)x_0,$$

which complete the proof. □

The next result provides a necessary and sufficient condition for the attainability of the optimal control problem under consideration.

Theorem 4. *Under the assumptions of Theorem 3, the following are equivalent:*

(i) *The optimal control problem described by the cost functional (4), the controlled system (1), and the set of the admissible controls $\mathcal{U}_{ad}(t_0, x_0)$ is attainable.*

(ii) *The unique bounded and maximal solution of the BJMLDE (8) is also a stabilizing solution of the BJMLDE (8).*

Proof. The implication $(ii) \Rightarrow (i)$ follows directly from Proposition 2. It remains to prove the implication $(i) \Rightarrow (ii)$. If the assumptions from Theorem 3 hold, then the BJMLDE (8) has a maximal and bounded solution $X_s(\cdot)$ which satisfies the sign condition (32).

Let $\widetilde{\mathbf{u}} \in \mathcal{U}_{ad}(t_0, x_0)$ satisfy (7). Then, from (7), (49), and (52), we deduce that

$$\sum_{k=\kappa(t_0)}^{\infty} \mathbb{E}[(\widetilde{u}(k) - F_{max}(kh)x_{\widetilde{\mathbf{u}}}(kh))^\top \mathbb{R}(X_{max}(kh))(\widetilde{u}(k) - F_{max}(kh)x_{\widetilde{\mathbf{u}}}(kh))] = 0. \tag{64}$$

Bearing in mind (32), we may infer that (64) holds if and only if

$$\widetilde{u}(k) = F_{max}(kh)x_{\widetilde{\mathbf{u}}}(kh) \ \ a.s.\,, \tag{65}$$

for all $k \geq \kappa(t_0)$. Moreover,

$$\lim_{t\to\infty} \mathbb{E}[|x_{\widetilde{\mathbf{u}}}(t)|^2] = 0, \tag{66}$$

because $\widetilde{\mathbf{u}} \in \mathcal{U}_{ad}(t_0, x_0)$. Taking into account that $X_{max}(\cdot)$ is a periodic function of period h, it follows that

$$F_{max}(kh) = F_{max}(0),$$

for all $k \in \mathbb{Z}_+$. Hence, (65) becomes

$$\widetilde{u}(k) = F_{max}(0)x_{\widetilde{\mathbf{u}}}(kh) \ \ a.s.\,, \tag{67}$$

for all $k \in \mathbb{Z}_+$. Because of the unicity of the solution of an IVP, we deduce that $x_{\widetilde{\mathbf{u}}}(\cdot)$ coincides to $x(\cdot; t_0, x_0)$, where $x(\cdot; t_0, x_0)$ is the solution of the jump linear stochastic system (JLSS):

$$dx(t) = A_0 x(t)dt + A_1 x(t)dw(t), \quad kh < t \leq (k+1)h, \tag{68a}$$

$$x(kh^+) = (\mathcal{A}_0 + \mathcal{B}_0 F_{max}(0))x(kh) + w_d(k)(\mathcal{A}_1 + \mathcal{B}_1 F_{max}(0))x(kh), \tag{68b}$$

$$x(t_0) = x_0, \tag{68c}$$

obtained when (67) is substituted in (1). Thus, (66) yields

$$\lim_{t\to\infty} \mathbb{E}[x(t; t_0, x_0)|^2] = 0,$$

for all $(t_0, x_0) \in \mathbb{R}_+ \times \mathbb{R}^n$. This means that the JLSS (68) is asymptotic stable in mean square (ASMS).

Reasoning as in the proofs of Propositions 2 and Proposition 3 from [28], one may prove that the JLSS (68) is ASMS if and only if the companion DTLE

$$Z(k+1) = \mathcal{L}_d[Z(k)], \tag{69}$$

is asymptotic stable, where

$$\mathcal{L}_d[Z] := \sum_{j=0}^{1} e^{\mathcal{L}h}[(\mathcal{A}_j + \mathcal{B}_j F_{max}(0))Z(\mathcal{A}_j + \mathcal{B}_j F_{max}(0))^\top].$$

Since the DTLE (69) is a linear time-invariant equation, it follows that it is asymptotic stable if and only if it is exponentially stable. According to the Remark 3 from [28], we deduce that (69) is exponentially stable if and only if the JLSS (68) is ESMS. Thus, the proof ends. □

5. Conclusions

This paper has contributed to the further development of the LQ control problem for stochastic systems controlled by impulses. A sufficient condition for the well posedness of the LQ control problem under consideration is expressed in terms of the existence of a maximal solution satisfying a suitable sign condition of the BJMLDE with a Riccati-type jumping operator constructed based on the matrix coefficients of the controlled system and the weight matrices of the performance criterion. When the condition for the well posedness is fulfilled, the LQ control problem is attainable if and only if the maximal solution of the BJMLDE with a Riccati-type jumping operator is also a stabilizing solution.

According to the terminology introduced in [32] for the deterministic framework, the problem analyzed in the present work is a generalization to the stochastic case of a fixed-endpoint LQ control problem. A remaining challenge for future research is the analysis of the well-posedness and attainability of a free-endpoint LQ control problem for a stochastic system controlled by impulses.

Another challenge for future research could be the investigation of the well-posedness and attainability of an LQ optimal control problem for a stochastic system controlled by impulses in which the length of the intervals between two impulse instances is not constant, it being time varying or just driven by a stochastic process.

The derivation of some efficient numerical procedures for the computation of the maximal solution and the stabilizing solution (if any) of the BJMLDE with a Riccati-type jumping operator associated to the control problems under consideration is necessary in order to be able to illustrate the applicability of the theoretical developments both in the constant dwell time case as well as in the time-varying dwell time case.

Author Contributions: Conceptualization, V.D. and I.-L.P.; methodology, V.D. and I.-L.P.; investigation, V.D. and I.-L.P.; writing—original draft preparation, V.D. and I.-L.P. All authors have read and agreed to the published version of the manuscript.

Funding: This research received no external funding.

Data Availability Statement: The original contributions presented in the study are included in the article, further inquiries can be directed to the corresponding author.

Conflicts of Interest: The authors declare no conflicts of interest.

References

1. Yang, T. *Impulsive Control Theory*; Springer: Berlin/Heidelberg, Germany, 2001.
2. Yang, T. *Impulsive Systems and Control: Theory and Applications*; Nova Science Publishers: Hauppauge, NY, USA, 2001.
3. Chen, X.; Luo, S.; Chen, W.H. Moment observability and output feedback stabilisation for linear stochastic impulsive systems. *Int. J. Syst. Sci.* **2023**, *54*, 1015–1032. [CrossRef]
4. Stamova, I.; Stamov, T.; Li, X. Global exponential stability of a class of impulsive cellular neural networks with supremums. *Internat. J. Adapt. Control Signal Process* **2015**, *28*, 1227–1239. [CrossRef]
5. Morris, K. Linear-Quadratic Optimal Actuator Location. *IEEE Trans. Automat. Contr.* **2011**, *56*, 113–124. [CrossRef]
6. Ji, X.; Lu, J.; Li, X. Pinning Impulsive Synchronization of Complex Dynamical Networks: A Stabilizing Delay Perspective. *IEEE Trans. Circuits Syst. II Express Briefs* **2024**, *71*, 3091–3095. [CrossRef]
7. Newman, C.; Costanza, V. Deterministic impulse control in native forest ecosystems management. *J. Optim. Theory Appl.* **1990**, *66*, 173–196. [CrossRef]
8. Korn, R. Some applications of impulse control in mathematical finance. *Math. Methods Oper. Res.* **1999**, *50*, 493–518. [CrossRef]
9. Yang, X.; Peng, D.; Lv, X.; Li, X. Recent progress in impulsive control systems. *Math. Comput. Simul.* **2019**, *155*, 244–268. [CrossRef]
10. Kalman, R. Contribution to the theory of optimal control. *Bol. Soc. Mat. Mex.* **1960**, *5*, 102–119.
11. Anderson, B.; Moore, J.B. *Optimal Control: Linear Quadratic Methods*; Prentice Hall: Hoboken, NJ, USA, 1990.
12. Wonham, W. On a matrix Riccati equation of stochastic control. *SIAM J. Control* **1968**, *6*, 312–325. [CrossRef]
13. Davis, M. *Linear Estimation and Stochastic Control*; Chapman & Hall: London, UK, 1977.
14. Rami, M.A.; Zhoua, X.Y.; Moore, J. Well-posedness and attainability of inde nite stochastic linear quadratic control in infinite time horizon. *Syst. Control Lett.* **2000**, *41*, 123–133. [CrossRef]
15. Guatteri, G.; Tessitore, G. Backward stochastic Riccati equations and infinite horizon L-Q optimal control problems with stochastic coefficients. *Appl. Math. Optim.* **2008**, *57*, 159–194. [CrossRef]
16. Hu, S. Infinite horizontal optimal quadratic control for an affine equation driven by Levy processes. *Chin. Ann. Math.* **2013**, *34A*, 179–204.
17. Huang, J.; Li, X.; Yong, J. A linear-quadratic optimal control problem for mean-field stochastic differential equations in infinite horizon. *Math. Optim. Control.* **2015**, *5*, 179–204. [CrossRef]
18. Rami, M.A.; Moore, J.; Zhoua, X.Y. Indefinite Stochastic Linear Quadratic Control and Generalized Differential Riccati Equation. *Siam. J. Control. Optim.* **2001**, *40*, 1296–1311. [CrossRef]
19. Wu, H.; Zhou, X.Y. Characterizing all optimal controls for an indefinite stochastic linear quadratic control problem. *IEEE Trans. Autom. Control.* **2002**, *47*, 4042–4078.
20. Chen, X.; Zhou, X.Y. Stochastic linear-quadratic control with conic control constraints on an infinite time horizon. *SIAM J. Control. Optim.* **2004**, *43*, 1120–1150. [CrossRef]
21. Sun, J.; Yong, J. Stochastic Linear Quadratic Optimal Control Problems in Infinite Horizon. *Appl. Math. Optim.* **2018**, *78*, 145–183. [CrossRef]
22. Briat, C. Stability analysis and stabilization of stochastic linear impulsive, switched and sampled-data systems under dwell-time constraints. *Automatica* **2016**, *74*, 279–287. [CrossRef]
23. Briat, C. Stability analysis and stabilization of linear symmetric matrix-valued continuous, discrete, and impulsive dynamical systems—A unified approach for the stability analysis and the stabilization of linear systems. *Nonlinear Anal. Hybrid Syst.* **2022**, *46*, 101242. [CrossRef]
24. Drăgan, V.; Popa, I.L.; Aberkane, S. On the stochastic linear quadratic optimal control problem by piecewise constant controls: The infinite horizon time case. *Math. Methods Appl. Sci.* **2024**, *45*, 3734–3762. [CrossRef]
25. Lipser, A.; Shiryaev, A. *Statistics of Random Processes*; Springer: Berlin, Germany, 1977 .
26. Friedman, A. *Stochastic Differential Equations and Applications*; Academic Press: Cambridge, MA, USA, 1975; Volume 1.
27. Øksendal, B. *Stochastic Differential Equations*; Springer: Berlin/Heidelberg, Germany, 2003.
28. Drăgan, V.; Aberkane, S.; Popa, I.L.; Morozan, T. On the stability and mean square stabilization of a class of linear stochastic systems controlled by impulses. *Ann. Acad. Rom. Sci. Ser. Math. Appl.* **2023**, *15*, 45–72. [CrossRef]
29. Albert, A. Conditions for positive and nonnegative definiteness in terms of pseudoinverses. *SIAM J. Appl. Math.* **1969**, *17*, 434–440. [CrossRef]

30. Drăgan, V.; Morozan, T.; Stoica, A.M. *Mathematical Methods in Robust Control of Linear Stochastic Systems*; Springer: New York, NY, USA, 2013.
31. Drăgan, V.; Morozan, T.; Stoica, A.M. *Mathematical Methods in Robust Control of Discrete-Time Linear Stochastic Systems*; Springer: New York, NY, USA, 2010.
32. Vukosavljev, M.; Schoellig, A.P.; Broucke, M.E. The regular indefinite linear quadratic optimal control problem: stabilizable case. *Siam J. Control Optim.* **2018**, *56*, 496–516. [CrossRef]

Disclaimer/Publisher's Note: The statements, opinions and data contained in all publications are solely those of the individual author(s) and contributor(s) and not of MDPI and/or the editor(s). MDPI and/or the editor(s) disclaim responsibility for any injury to people or property resulting from any ideas, methods, instructions or products referred to in the content.

symmetry

MDPI

Article

Multistability, Chaos, and Synchronization in Novel Symmetric Difference Equation

Othman Abdullah Almatroud [1], Ma'mon Abu Hammad [2], Amer Dababneh [2], Louiza Diabi [3,*], Adel Ouannas [4], Amina Aicha Khennaoui [5] and Saleh Alshammari [1]

[1] Department of Mathematics, Faculty of Science, University of Ha'il, Ha'il 2440, Saudi Arabia; o.almatroud@uoh.edu.sa (O.A.A.); saleh.alshammari@uoh.edu.sa (S.A.)
[2] Department of Mathematics, Al-Zaytoonah University of Jordan, Amman 11733, Jordan; m.abuhammad@zuj.edu.jo (M.A.H.); dababneh.amer@zuj.edu.jo (A.D.)
[3] Laboratory of Dynamical Systems and Control, University of Larbi Ben M'hidi, Oum El Bouaghi 04000, Algeria
[4] Department of Mathematics and Computer Sciences, University of Larbi Ben M'hidi, Oum El Bouaghi 04000, Algeria; ouannas.adel@univ-oeb.dz
[5] NTIC Faculty, University of Constantine 2, Constantine 25000, Algeria; amina.khennaoui@univ-constantine2.dz
* Correspondence: louiza.diabi@univ-oeb.dz

Abstract: This paper presents a new third-order symmetric difference equation transformed into a 3D discrete symmetric map. The nonlinear dynamics and symmetry of the proposed map are analyzed with two initial conditions for exploring the sensitivity of the map and highlighting the influence of the map parameters on its behaviors, thus comparing the findings. Moreover, the stability of the zero fixed point and symmetry are examined by theoretical analysis, and it is proved that the map generates diverse nonlinear traits comprising multistability, chaos, and hyperchaos, which is confirmed by phase attractors in 2D and 3D space, Lyapunov exponents (LE_s) analysis and bifurcation diagrams; also, 0-1 test and sample entropy (SampEn) are used to confirm the existence and measure the complexity of chaos. In addition, a nonlinear controller is introduced to stabilize the symmetry map and synchronize a duo of unified symmetry maps. Finally, numerical results are provided to illustrate the findings.

Keywords: symmetric map; difference equation; multistability; fixed point; chaos; control

1. Introduction

Multistability, chaos, and symmetry maps have garnered significant interest from researchers [1,2]. Discrete models mean that a model's behaviors change swiftly over time and are subject to discrete events; it is used to describe the behavior of systems that evolve in discrete steps. Therefore, discrete maps exhibit rich dynamics and have been studied extensively in various fields, including mathematics, engineering, and physics [3,4]. In physics, discrete-time models have been used to study phenomena dynamics. These models can capture the discrete nature of physics events. Overall, the study of maps has led to significant advancements in many fields and is an essential area of research in its own right [5,6].

Difference equations have an essential role in the analysis of discrete maps. These equations are also used to model and study changes that occur in systems measured over discrete time intervals [7]. They are not just mathematical tools but powerful analytical tools used to understand and develop solutions to a wide range of practical problems, making them an essential part of many scientific and engineering domains. Moreover, studying difference equations contributes to understanding dynamic chaos, where nonlinear interactions within these systems can lead to complex and unpredictable behaviors.

This understanding enhances the ability to design more stable and controlled systems and enables innovative applications in multiple fields such as neural networks [8,9] and encryption [10]. A 2D discrete polynomial hyper-chaotic map and 3D Lorenz chaotic system for high-performance multi-image encryption have been developed in [11], while in [12], the authors revealed the hyperchaotic 2D discrete Rosenbrock system with the Rosenbrock function.

Chaotic maps are distinguished primarily by how sensitive they are to initial conditions, resulting in unpredictable and random behavior [13,14]. Although chaotic systems were initially discovered and studied in continuous models, discrete models have also been the focus of research on chaos and its properties. Moreover, sine maps exhibit multiple significance in exploring and analyzing the dynamics and can provide insights into the stability, chaos, and specific periods of interactions within a map. For example, in [15], Bao et al. presented a novel 2D sine map by introducing the sine functions. In [16], Rajagopal et al. developed 3D sine maps by proposing the self-feedback parameter. Moreover, symmetry plays a significant role in the behavior of discrete maps [17,18].

Recently, researchers have been giving attention to studying the chaotic symmetry systems [19,20]. The advantages of symmetry maps are a valuable tool in chaos and multistability [21]. In general, multistability signifies the presence of many shapes of attractors in answer to a range of initial conditions and system values. However, it is an active topic of research to discover new applications and understanding in dynamic systems. Leutcho et al. [22] discovered the rich chaos of the snap system both in symmetric and nonsymmetric cases. Pang et al. proposed different memristive sine maps [23], whereas in [24], the authors studied the multistability of a new sinusoidal map using the sampling method. In [25], the authors presented a new image encryption scheme with a convex sinusoidal map. In contrast, some manuscripts have been published to the asymmetric. For example, Xu et al. [26] analyzed the multistability and coexisting bifurcation of an asymmetric memristive jerk circuit, while in [27], Lin et al. proposed asymmetric chaotic memristor-coupled neural networks and encryption implementation. In addition, the prospects of using chaos in various applications motivated researchers to study the possibility of controlling and synchronizing chaos. Moreover, the different linear and nonlinear stabilization controllers have been published in [28–30]. Various approaches and methods have been applied to synchronize chaos and hyperchaos. Chaos synchronization in discrete-time maps is notable due to its applications in several fields [31–34]. The study and exploration of the behaviors of the new symmetric map is an interesting subject. This paper aims to contribute the discoveries of the findings by the following points:

1. The construction of a new third-order symmetric difference equation transformed into a 3D discrete symmetry map and its proprieties are explored.
2. The diverse nonlinear traits generate the symmetry map, such as multistability, chaos, and hyperchaos, illustrated with bifurcation diagrams, Lyapunov exponents, and phase attractors.
3. We use the 0-1 test and the sample entropy (SampEn) to measure and evaluate the complexity of chaos in the chaotic symmetric map.
4. The stabilization and synchronization scheme of the chaotic symmetric map is realized based on the stability conditions of the discrete-time system.

The manuscript is detailed as follows: The integer-order structure of the map is introduced, and stability analysis of the fixed points is given in Section 2. Varied parameters that influence the behavior of a symmetric map are analyzed and verified through numerical simulations as seen in Section 3. We compute the 0-1 test and use the sample entropy approach to comprehend the various types of behavior and the effect of the parameters on the chaotic symmetry map in Section 4. We discuss the nonlinear stability controller that forces the orientations asymptotically towards zero points in Section 5. Additionally, Section 6 assures that the master (drive) and the slave (response) discrete maps achieve synchronization. In Section 7, our paper concludes with a discussion and perspectives for future work.

2. The New Symmetric Map and Its Proprieties

Symmetric maps are commonly observed by the elements arranged in equilibrium and equivalent manner relative to a line, center, or plane [35,36]. In this work, a new symmetric map possessing rich dynamics is proposed. Firstly, the third-order difference equation of the map is defined as follows:

$$y_{\kappa+1} = \beta_1 y_{\kappa-2} + \beta_2 y_{\kappa-1} - \gamma \sin(y_\kappa). \tag{1}$$

The difference Equation (1) can be transformed into a 3D symmetric map:

$$\begin{cases} y_1(\nu+1) = y_2(\nu), \\ y_2(\nu+1) = \sin(y_3(\nu)), \\ y_3(\nu+1) = \beta_1 y_1(\nu) + \beta_2 y_2(\nu) - \gamma \sin(y_3(\nu)). \end{cases} \tag{2}$$

The map (2) is symmetric due to the transformation with the following standard method $H : (Y_1, Y_2, Y_3) \to (-Y_1, -Y_2, -Y_3)$. Here, β_1, β_2, γ is the bifurcation parameter. y_1, y_2 and y_3 are the state variables. Therefore, every attractor of (2) will show in mutually similar pairs with sensitivity to the initial conditions. Symmetry and asymmetry are advantages of dynamic analysis. For this purpose, two initial states are chosen as $IN1 = (-0.8, -2, 0)$, $IN2 = (0.8, 2, 0)$.

Now, the stability of the fixed points of the map (2) is analyzed, so the fixed points will be discovered by $y_1(\nu+1) = y_1(\nu)$, $y_2(\nu+1) = y_2(\nu)$, $y_3(\nu+1) = y_3(\nu)$ as follows:

$$\begin{cases} y_2(\nu) = y_1(\nu), \\ \sin(y_3(\nu)) = y_2(\nu), \\ \beta_1 y_1(\nu) + \beta_2 y_2(\nu) - \gamma \sin(y_3(\nu)) = y_3(\nu). \end{cases} \tag{3}$$

We obtain $y_3(\nu) - (\beta_1 + \beta_2 - \gamma)\sin(y_3(\nu)) = 0$, and thus, the map (2) has an $(0, 0, 0)$ fixed point for all $(\beta_1, \beta_2, \gamma) \in \mathbb{R}^3$. Clearly, the stability analysis also depends on the parameters of the systems.

Proposition 1. *The symmetric map* (2) *is asymptotically stable if* $-1 < \beta_1 < 1$ *and* $\gamma\beta_1 > \beta_2$.

Proof. The Jacobian matrix J_S of the map evaluated at $(0, 0, 0)$ is as follows:

$$J_S = \begin{pmatrix} 0 & 1 & 0 \\ 0 & 0 & 1 \\ \beta_1 & \beta_2 & -\gamma \end{pmatrix}. \tag{4}$$

The associated characteristic equation is defined by:

$$Q(\lambda) = \lambda^3 + \gamma\lambda^2 - \beta_2\lambda - \beta_1 = 0, \tag{5}$$

and based on the Jury criterion [37], we verify that the following conditions hold: (1) $|\beta_1| < 1$, (2) $1 - \beta_2 - \beta_1 + \gamma > 0$, (3) $-1 + \beta_2 + \gamma - \beta_1 > 0$, (4) $1 - \beta_1^2 > 2\beta_1 - \beta_2$. So, $-1 < \beta_1 < 1$ is verified by (1), and $\gamma\beta_1 > \beta_2$ is proven by (2), (3), (4). Then, the conditions of the asymptotic stability are validated. □

Next, the two cases below are given as examples.

Case 1. Consider $\beta_1 = 0.7$, $\beta_2 = 0.1$, $\gamma = 0.5$. The associated characteristic equation is defined by:

$$-\lambda^3 - 0.5\lambda^2 + 0.1\lambda + 0.7 = 0, \tag{6}$$

and there are three eigenvalues $\lambda_{1,2} = -0.63985 \pm 0.698837i$, and $\lambda_3 = 0.7797$. Thus, $|\lambda_j| < 1, \forall j = 1, 2, 3$. So, the fixed point of the symmetric map (2) is asymptotically stable in this case.

Case 2. Let us assume that $\beta_1 = 1.7$, $\beta_2 = 1.9$, $\gamma = 0.5$. The characteristic equation is given by:

$$-\lambda^3 - 0.5\lambda^2 + 1.9\lambda + 1.7 = 0, \tag{7}$$

and there exist three eigenvalues $\lambda_{1,2} = -1.00391 \pm 0.345847i$, and $\lambda_3 = 1.50783$. It is verified that $|\lambda_j| > 1, j = 1, 2, 3$. Then, the fixed point of map (2) is unstable, so here, the symmetric map satisfies the necessary condition to present a chaotic behavior.

3. Chaotic Analysis

In this section, the dynamical behaviors of the symmetric map (2) are investigated numerically under various levels of parameters β_1, β_2, γ.

Case 1. In Figure 1a,b, the bifurcation diagram and the associated LE_s of the map (2) are plotted using MATLAB R2024a code. Considering β_1 to be the bifurcation parameter versus $[-10, 10]$ with $\beta_2 = 1.9$, $\gamma = 0.5$ maps the parameters and IN1 and IN2. Subsequently, a small portion of the zone proximal to the bifurcation and the associated LE_s are plotted at $\beta_1 \in [-5, 5]$, presented in detailed view as shown in Figure 1c,d. When $\beta_1 \in [-10, -6.899] \cup [-5.294, -4.587] \cup [-3.912, -0.999]$, and $\beta_1 \in [4.988, 7.199] \cup [7.9, 10]$, the map is chaotic with only three LE_s values being positive. Additionally, when $\beta_1 \in [-6.7, -5.295] \cup [1.1, 3.899]$, $\beta_1 \in [3.9, 4.499]$ is hyperchaotic, where LE_s shows two positive and one displaying negative values. Moreover, the symmetric map is periodic at $\beta_1 \in [-1, 1] \cup [4.5, 4.987]$, and $\beta_1 \in [7.2, 7.899]$, where all LE_s values are negative. The map is quasi-periodic in $\beta_1 \in [-4.588, -4.111]$, where one LE has zero values.

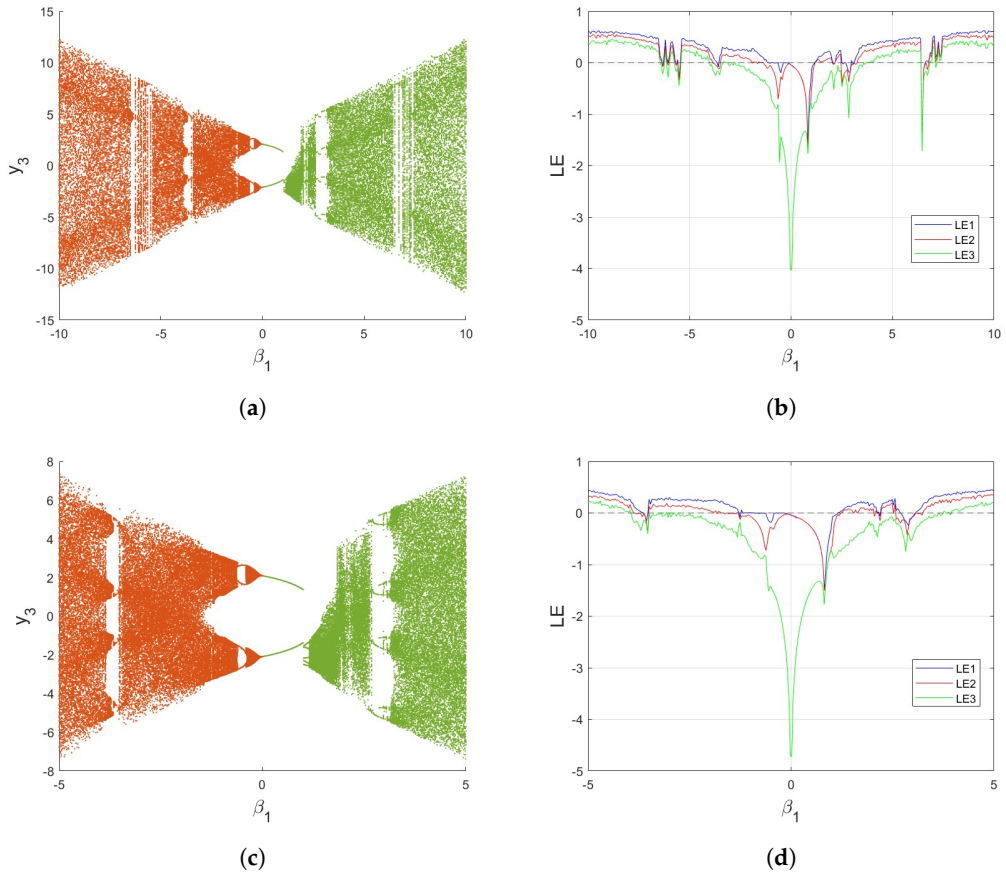

Figure 1. (**a**) Bifurcation of symmetric map (2) versus $\beta_1 \in [-10, 10]$ and $\beta_2 = 1.9$, $\gamma = 0.5$ with IN1 (orange colour) and IN2 (green colour). (**b**) The associated LE_s, (**c**,**d**) a detailed view with $\beta_1 \in [-5, 5]$.

Case 2. For β_2 versus in $[-15, 15]$ with $\beta_1 = 1.7$, $\gamma = 0.5$ and IN1 and IN2. The symmetric map changes the dynamics between the hyperchoas, periodic, and quasi-periodic behaviors as illustrated in Figure 2a,b. For more details on $\beta_2 \in [-5, 5]$, view Figure 2c,d. When

$\beta_2 \in [-15, -12.699] \cup [-12.298, -6.3]$, $\beta_2 \in [-5.999, -1] \cup [1.1, 3.498]$ and $\beta_2 \in [3.811, 15]$, the map become hyperchaotic with two positive LE_s, and one negative value. It shows the periodic behavior when $\beta_2 \in [-12.5, -12.299] \cup [-6.399, -6] \cup [-1, 0]$, and $\beta_2 \in [3.499, 3.8]$, where all three LE_s values are negative. The presence of one zero LE and the others is negatively expressed in the progression to quasi-periodic in the interval $\beta_2 \in [0.5, 1]$.

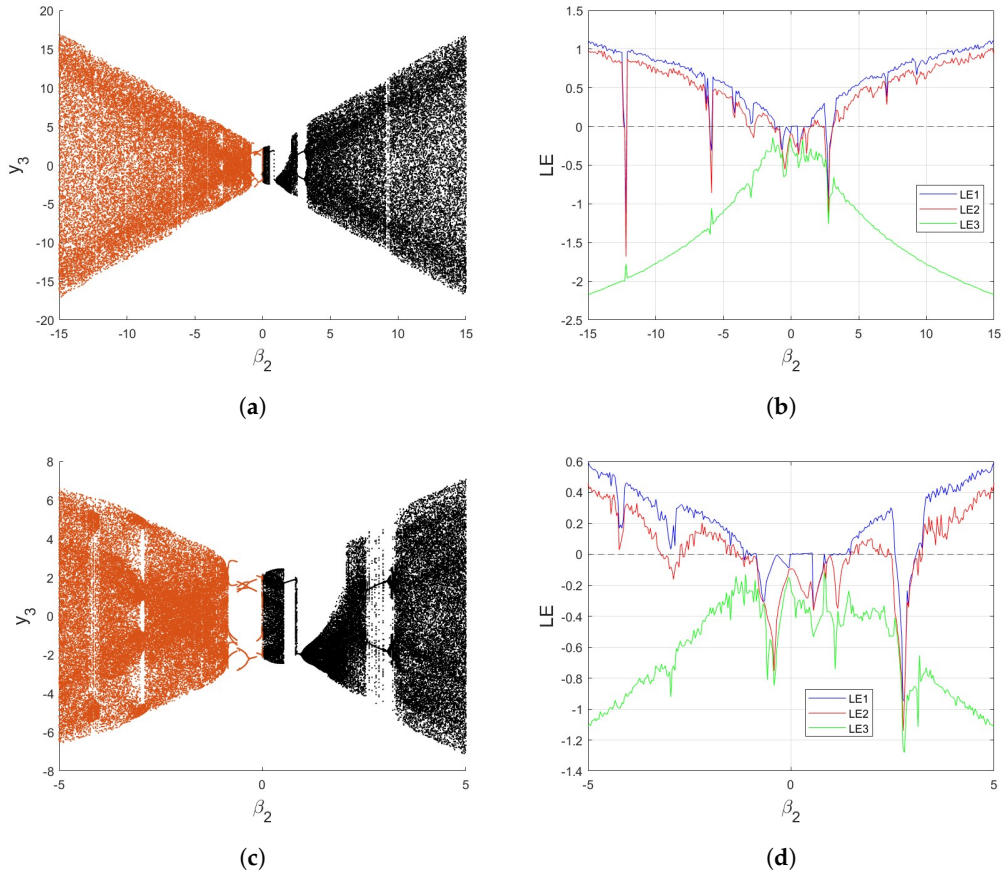

Figure 2. (**a**) Bifurcation of symmetric map (2) versus $\beta_2 \in [-15, 15]$ and $\beta_1 = 1.7$, $\gamma = 0.5$ with IN1 (orange colour) and IN2 (black colour). (**b**) The associated LE_s. (**c**,**d**) Detailed view of $\beta_2 \in [-5, 5]$.

Case 3. Similarly, take $\beta_1 = 1.7$ and $\beta_2 = 1.9$ versus γ in $[-20, 20]$ as shown in Figure 3a, Figure 3b as well as the detailed view in Figure 3c,d with $\gamma \in [-5, 5]$. The chaotic behavior appears when $\gamma \in [-20, -4.899] \cup [-4.5, -1.989] \cup [0, 0.999]$, $\gamma \in [1.558, 1.7] \cup [2.599, 4.7] \cup [4.8, 5.099]$, where one of the LE is positive. Conversely, the periodic region exists when all the LE_s are negative at $\gamma \in [-4.7, -4.559] \cup [-1.990, -1] \cup [1, 1.557]$, and $\gamma \in [7.6, 7.79] \cup [14.5, 14.999]$. When $\gamma \in [-1, 0]$, the map has a quasi-periodic attractor characterized by one LE equal to zero. Thus, $\gamma \in [5.1, 7.5] \cup [7.8, 14.499] \cup [15, 20]$ becomes chaotic again. According to these results, the characteristic of symmetry in the behaviors' evolution becomes observable, reappearing over a wide field of the parameters' systems. In contrast, symmetry breaking also occurs within a small scope.

Importantly, for us to have a higher-quality description of these dynamics, the symmetric attractor is plotted in 3D and 2D space, as well as the sensitivity states of the symmetry map (2), choosing $\beta_1 = 1.7$, $\beta_2 = 1.9$ and $\gamma = 0.5$ with IN1, IN2 as shown in Figures 4 and 5, which proves the results obtained above in the paper. Furthermore, one can see that the variation of IN1 and IN2, and the changing of the parameters systems $(\beta_1, \beta_2, \gamma)$ induces multistability attractors of the symmetric map (2) as shown in Figure 6.

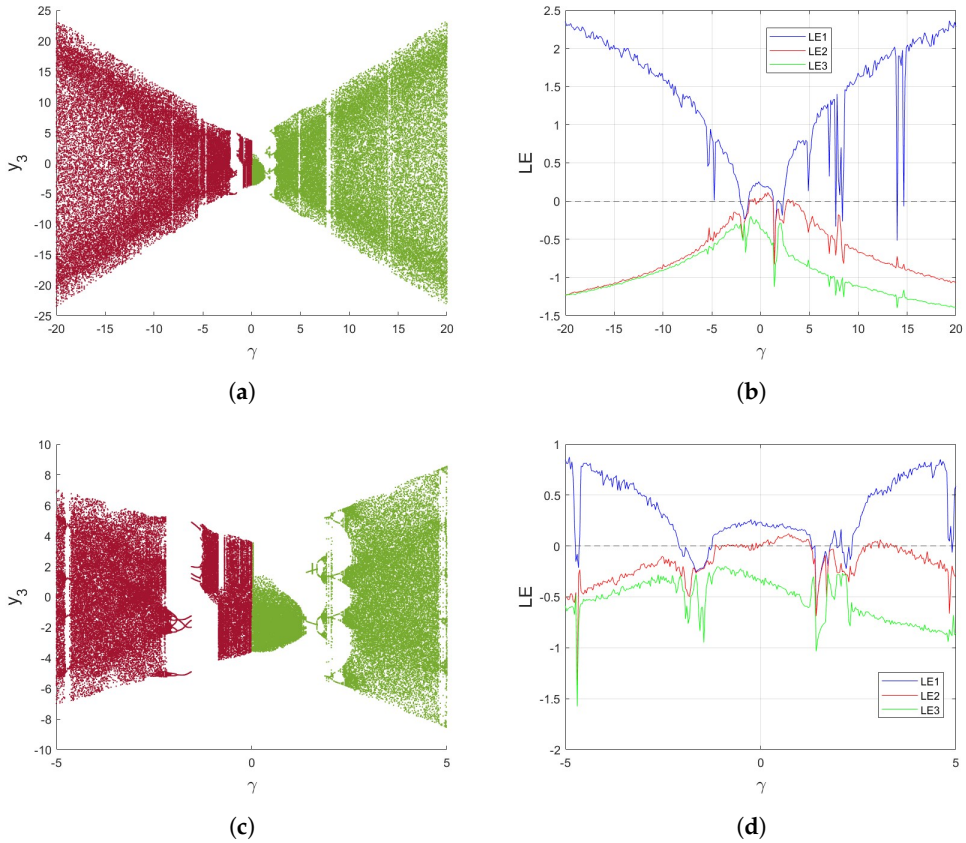

Figure 3. (**a**) Bifurcation of symmetric map (2) versus $\gamma \in [-20, 20]$ and $\beta_1 = 1.7$, $\beta_2 = 1.9$ with IN1 (maroon colour) and IN2 (green colour). (**b**) The associated LE_s, and (**c**,**d**) a detailed view of $\gamma \in [-5, 5]$.

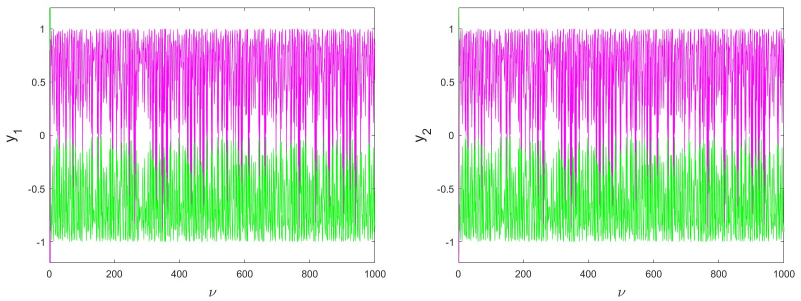

(**a**) Numerical simulation of y_1 (**b**) Numerical simulation of y_2

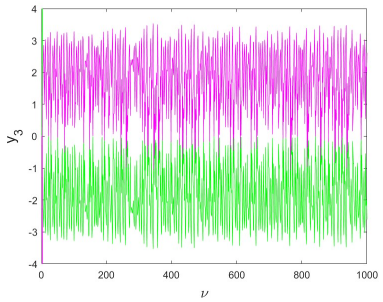

(**c**) Numerical simulation of y_3

Figure 4. Sensitivity of symmetric map (2) with $\beta_1 = 1.7$, $\beta_2 = 1.9$, $\gamma = 0.5$ and IN1 (pink colour) and IN2 (green colour).

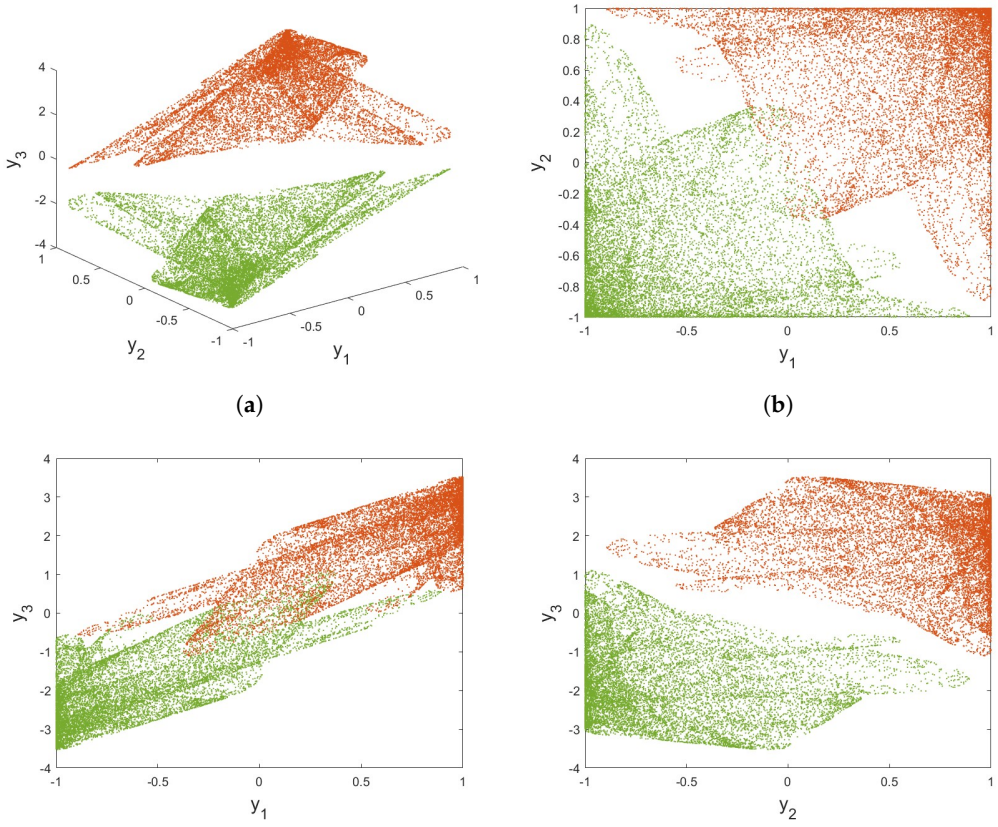

Figure 5. (**a**–**d**) Chaotic attractor of symmetric map (2) for $(\beta_1, \beta_2, \gamma) = (1.7, 1.9, 0.5)$ with IN1 (orange colour) and IN2 (green colour).

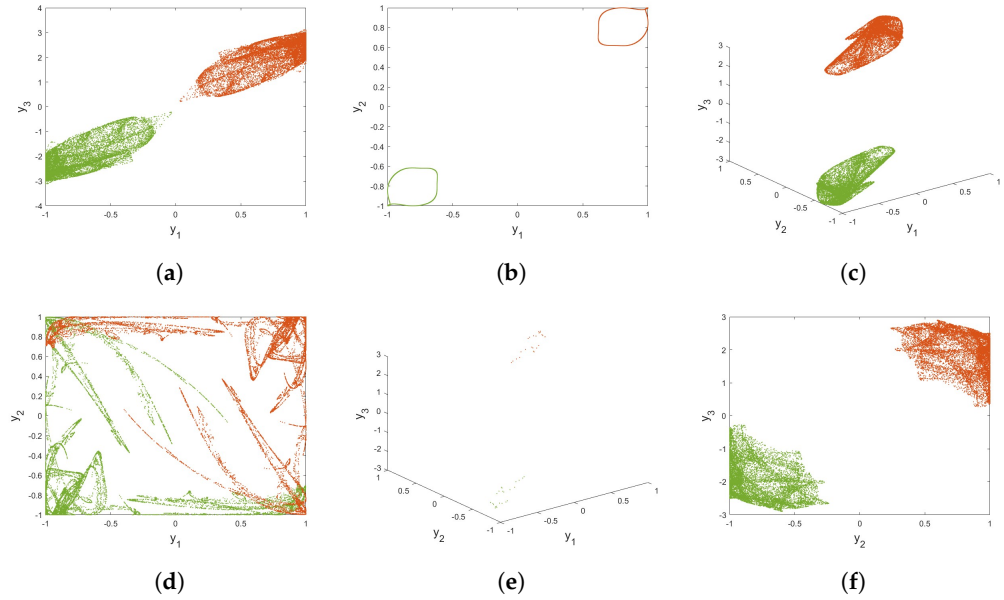

Figure 6. Multistability attractors of symmetric map (2) with IN1 (orange colour), IN2 (green colour) and for (**a**) $(\beta_1 = 1.7, \beta_2 = 1.6, \gamma = 0.5)$, (**b**) $(\beta_1 = 1.7, \beta_2 = 1.2, \gamma = 0.5)$, (**c**) $(\beta_1 = 1.4, \beta_2 = 1.9, \gamma = 0.5)$, (**d**) $(\beta_1 = 1.7, \beta_2 = 1.9, \gamma = 1.2)$, (**e**) $(\beta_1 = 1.6, \beta_2 = 2, \gamma = 1.3)$, (**f**) $(\beta_1 = 2, \beta_2 = 1.5, \gamma = 1)$.

4. Chaos Complexity

4.1. 0-1 Test

The 0-1 technique [38] is another way to confirm that chaos exists in the symmetry map also employed for the confirmation of chaotic regions and the regular behavior of the chaotic symmetry map (2). Then, this technique is described as follows:

$$p_\zeta(a) = \sum_{\bar{\ell}=1}^{a} x(\bar{\ell}) \cos(\bar{\ell}\zeta), \quad q_\zeta(a) = \sum_{\bar{\ell}=1}^{a} x(\bar{\ell}) \sin(\bar{\ell}\zeta), \tag{8}$$

where $x(\bar{\ell}), \bar{\ell} = \overline{1, N}$ is the time series employed for the translation variables, and ζ is randomly chosen to be constant in $(0, \pi)$. The plotting of p_ζ and q_ζ in the $(p_\zeta - q_\zeta)$ plane is utilized to determine the existence or absence of chaos.

Given the definition of mean square displacement:

$$M_\zeta(a) = \lim_{N\to\infty} \frac{1}{N} \sum_{\bar{\ell}=1}^{N} \left[\left(p_\zeta(\bar{\ell}+a) - p_\zeta(\bar{\ell})\right)^2 + \left(q_\zeta(\bar{\ell}+a) - q_\zeta(\bar{\ell})\right)^2 \right], \quad a \leq \frac{N}{10}. \tag{9}$$

Moreover, the asymptotic growth rate K_ζ is represented by

$$K_\zeta = \lim_{\ell\to\infty} \frac{\log M_\zeta(\ell)}{\log \ell}. \tag{10}$$

Hence, if $K = median(K_\zeta)$ closes to 1, the plot of p_τ and q_τ in the $p_\zeta - q_\zeta$ plane will exhibit Brownian-like behavior, and if K is close to 0, the symmetry map dynamics will become regular and exhibit bounded-like behavior.

In Figure 7, the $p - q$ plots for chaotic and balanced dynamics of the chaotic symmetry map are explained for various values of the system parameters. When $(\beta_1, \beta_2, \gamma) = (1.7, 1.9, 0.5)$, Figure 7a illustrates the Brownian-like trajectories, which imply that the symmetry map is chaotic. As another example, Figure 7b shows bounded-like trajectories when $(\beta_1, \beta_2, \gamma) = (0.8, 0.01, 0.5)$, which confirms that the symmetry map is periodic. As a result, the 0-1 test findings are clearly in agreement with (LE_s) and bifurcation.

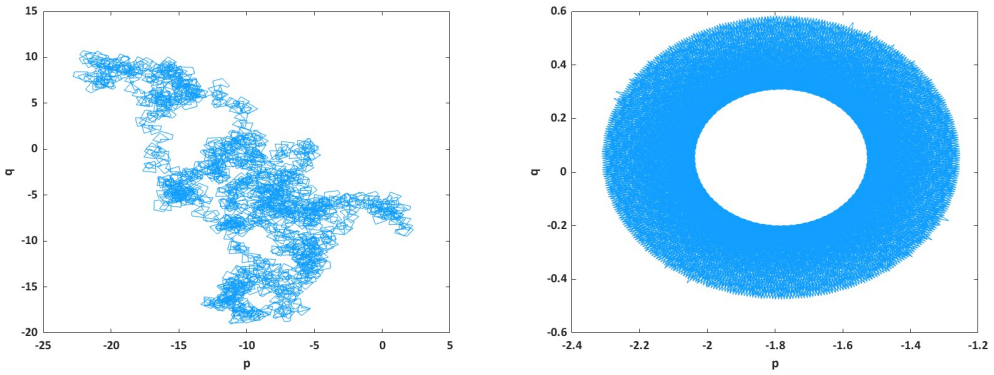

(**a**) (**b**)

Figure 7. The 0-1 test of the symmetric map (2) for (**a**) $(\beta_1, \beta_2, \gamma) = (1.7, 1.9, 0.5)$, (**b**) $(\beta_1, \beta_2, \gamma) = (0.8, 0.01, 0.5)$.

4.2. Sample Entropy

Here, we use the sample entropy (SampEn) approach [39] to determine the complexity of the symmetry map (2). This approach allows for deeper insights into the nature of the behaviors and more accurate and reliable analysis than traditional methods. Compared to

ApEn [40], the SampEn is a more consistent and conservative measure. So, the SampEn algorithm is run in the manner specified:

$$SampEn = -\log \frac{\Omega^{J+1}(k)}{\Omega^{J}(k)}, \tag{11}$$

where $\Omega^{J}(k)$ is given by

$$\Omega^{J}(k) = \frac{1}{\rho - J + 1} \sum_{\iota=1}^{\rho-J+1} \log C_{\iota}^{J}(k), \tag{12}$$

we put $k = 0.2std(Y)$, is the tolerance defined.

Figure 8 illustrates the sample entropy approximation of symmetry map (2), with $(\beta_1, \beta_2, \gamma) = (1.7, 1.9, 0.5)$ and the initial states IN2. The findings of SampEn prove that the symmetry map display higher complexity as shown by their larger sample entropy values. These results agree with the previous LE_s analysis.

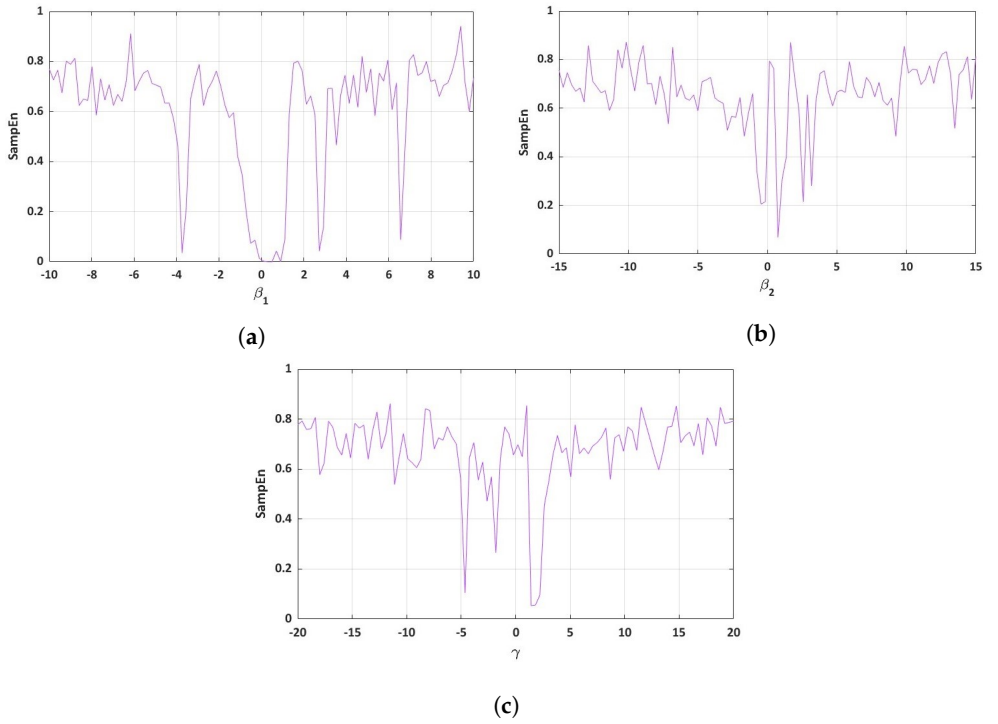

Figure 8. SampEn of symmetric map (2) for, (**a**) versus β_1 in $[-10, 10]$, (**b**) versus β_2 in $[-15, 15]$, (**c**) versus γ in $[-20, 20]$.

5. Chaos Control

Here, the interest is our ability to control the symmetric map (2) by introducing a simple nonlinear control law with the aim to ensure that all states of the map converge to the origin. The controlled symmetric map is defined by

$$\begin{cases} y_1(\nu+1) = y_2(\nu) + L_1(\nu), \\ y_2(\nu+1) = \sin(y_3(\nu)) + L_2(\nu), \\ y_3(\nu+1) = \beta_1 y_1(\nu) + \beta_2 y_2(\nu) - \gamma \sin(y_3(\nu)) + L_3(\nu), \end{cases} \tag{13}$$

where $L = (L_1, L_2, L_3)^T$ represent the adaptive controller. The following proposition introduces control laws for the symmetric map based on the stability conditions of the discrete system in [41].

Proposition 2. *The new symmetric map is stable under the 3D control law*

$$\begin{cases} L_1(\nu) = -\xi_1 y_1(\nu) \\ L_2(\nu) = -\sin(y_3(\nu)) - \xi_2 y_2(\nu) \\ L_3(\nu) = \gamma \sin(y_3(\nu)) - \xi_3 y_3(\nu), \end{cases} \tag{14}$$

where $|\xi_1| < 1$, $|\xi_2| < 1$ *and* $|\xi_3| < 1$. *Then, the symmetric map can be stabilized at* $(0,0,0)$ *point.*

Proof. Substituting (14) into (13) yields the system dynamics

$$\begin{pmatrix} y_1(\nu+1) \\ y_2(\nu+1) \\ y_3(\nu+1) \end{pmatrix} = \begin{pmatrix} -\xi_1 & 1 & 0 \\ 0 & -\xi_2 & 0 \\ \beta_1 & \beta_2 & -\xi_3 \end{pmatrix} \begin{pmatrix} y_1(\nu) \\ y_2(\nu) \\ y_3(\nu) \end{pmatrix}, \tag{15}$$

observably, the eigenvalues $\lambda_1 = \xi_1$, $\lambda_2 = \xi_2$, and $\lambda_3 = \xi_3$ satisfy $|\lambda_j| < 1$ for $j = 1,2,3$. Consequently, the controlled map (14) is asymptotically stable. □

To validate the results of Proposition 2, Figure 9 indicate the states evolution and phase space of (13), where $(\xi_1, \xi_2, \xi_3) = (-0.6, -0.8, -0.3)$ and the initial values IN2. Clearly, from the figure, the states of the controlled symmetric map (13) converge toward zero asymptotically.

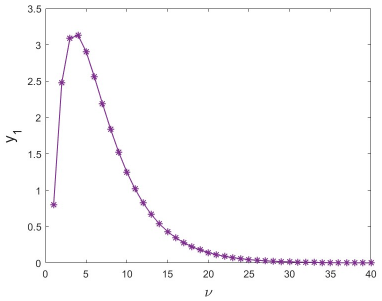

(**a**) Stabilization of y_1

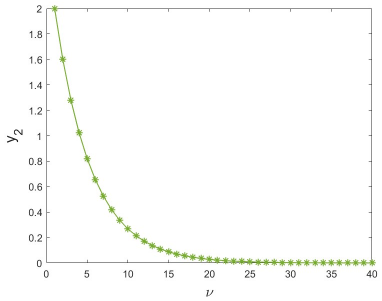

(**b**) Stabilization of y_2

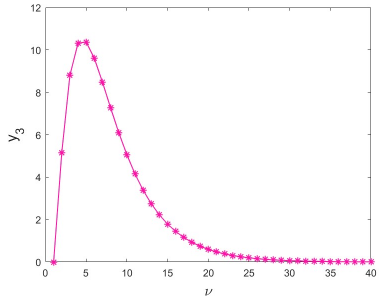

(**c**) Stabilization of y_3

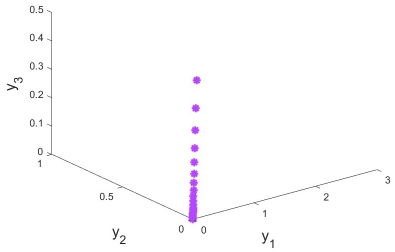

(**d**) Phase space

Figure 9. Stabilization states and phase space of the controlled map (13).

6. Synchronization Scheme

The complete synchronization criteria are applicable for a wide range of chaotic maps. Therefore, the chaotic symmetric map can be synchronized, considering the symmetric map (2) as the master map and defining the slave symmetric map as follow:

$$\begin{cases} y_{1c}(\nu+1) = y_{2c}(\nu), \\ y_{2c}(\nu+1) = \sin(y_{3c}(\nu)) + N_1(\nu), \\ y_{3c}(\nu+1) = \beta_1 y_{1c}(\nu) + \beta_2 y_{2c}(\nu) - \gamma \sin(y_{3c}(\nu)) + N_2(\nu). \end{cases} \tag{16}$$

N_1 and N_2 represent the synchronization controllers, given by

$$\begin{cases} N_1(\nu) = -(\sin(y_{3c}(\nu)) - \sin(y_3(\nu) \\ N_2(\nu) = -(\sin(y_{3c}(\nu)) - \sin(y_3(\nu). \end{cases} \tag{17}$$

Let the error according to the synchronization conditions [42] be as follows

$$\begin{cases} e_1(\nu) = y_{1c}(\nu) - y_1(\nu), \\ e_2(\nu) = y_{2c}(\nu) - y_2(\nu), \\ e_3(\nu) = y_{3c}(\nu) - y_3(\nu), \end{cases} \tag{18}$$

when $\lim_{\nu\to\infty} \parallel e_j(\nu) \parallel = \lim_{\nu\to\infty} \parallel y_{jc}(\nu) - y_j(\nu) \parallel = 0, \forall j = 1, 2, 3.$

The synchronization error (18) is asymptotically stable. Then, the master symmetric map (2) and slave map (16) are synchronized.

Figure 10 describes the phase space and the evolution states of the error map (18) for $(e_1(0), e_2(0), e_3(0)) = (0.05, 0.2, 0.01)$ initial values. Obviously, the errors converge to zero asymptotically. Hence, the results of the synchronization mechanism are validated.

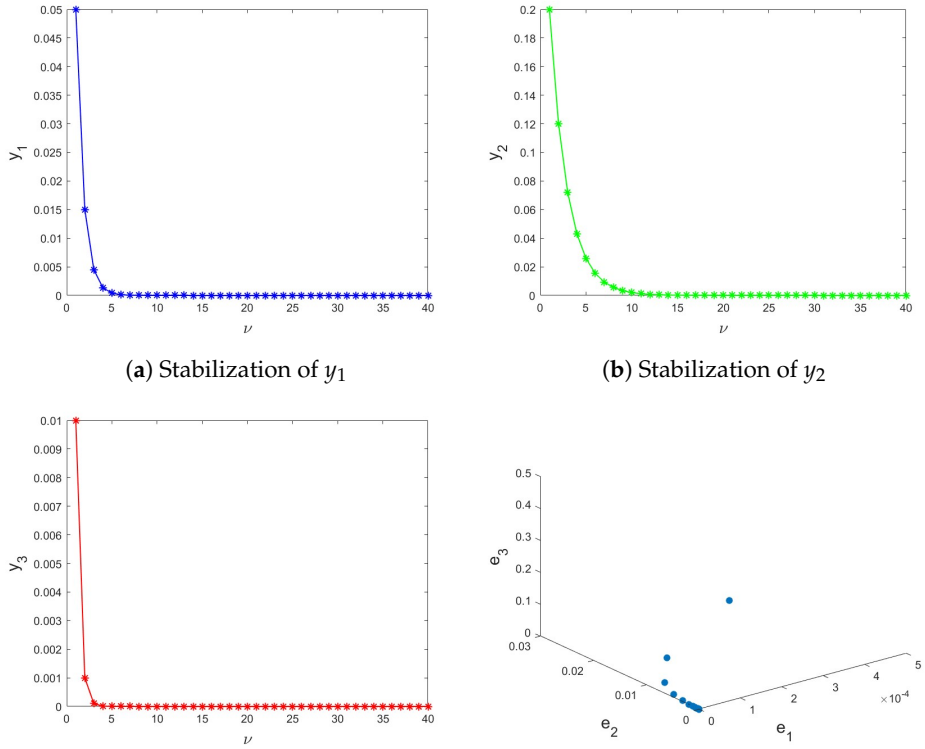

(**a**) Stabilization of y_1 (**b**) Stabilization of y_2

(**c**) Stabilization of y_3 (**d**) Phase space

Figure 10. Synchronization of the error map (18).

7. Discussion and Perspectives

This work explored a new third-order symmetric difference equation transformed into a three-dimensional discrete symmetry map containing specific sine terms, where changes in the map parameters and the two initial states IN1 and IN2 are taken into account. Therefore, the discrete map has standard dynamics characteristics that give rise to symmetric attractors.

The stability of the zero fixed point is examined, and the necessary conditions for its instability are met as evidence of the presence of chaos. Numerical simulations demonstrate the rich dynamics such as symmetry, chaos, hyperchaos, and multistability using 2D and 3D phase attractors, bifurcation diagrams, and the associated LE_s. Furthermore, the 0-1 test and

sample entropy (SampEn) are used to confirm the existence and measure the complexity of chaos. The dynamics are illustrated while varying the three map parameters β_1, β_2, and γ. In the context of the findings, the characteristic of symmetry in the evolution of the behaviors becomes observable, reappearing over a broad field of system parameters, with the occurrence of symmetry breaking within a small scope. The asymptotic convergence to zero of the trajectories is ensured using a new control law proposed to synchronize two paired maps perfectly with errors converging towards zero.

Ultimately, our future work will explore the rich dynamics of other symmetric maps to discover novel symmetry characteristics and their importance in dynamics, particularly to explore how symmetry maps can be used in more fields, such as economics, finance, and encryption.

Author Contributions: Conceptualization, O.A.A., M.A.H. and A.O.; Data curation, A.D., S.A.; Formal analysis, A.O. and L.D.; Funding acquisition, A.D. and A.A.K.; Investigation, S.A.; Methodology, O.A.A.; Project administration, M.A.H. and A.O.; Resources, O.A.A., M.A.H., A.D., L.D., A.A.K. and S.A.; Software, M.A.H. and A.A.K.; Supervision, M.A.H. and A.O.; Validation, A.D. and A.O.; Visualization, O.A.A. and A.A.K.; Writing—original draft, L.D. and S.A.; Writing—review and editing, L.D. All authors have read and agreed to the published version of the manuscript.

Funding: This research has been funded by Scientific Research Deanship at University of Ha'il-Saudi Arabia through project number RG-23 150.

Data Availability Statement: All data that support the findings of this study are included within the article.

Acknowledgments: Scientific Research Deanship at University of Ha'il-Saudi Arabia through project number RG-23 150.

Conflicts of Interest: The authors declare no conflicts of interest.

References

1. Zhou, X.; Sun, K.; Wang, H.; Yao, Z. Coexisting hyperchaos and multistability in a discrete memristor-coupled bi-neuron model. *Nonlinear Dyn.* **2024**, *112*, 9547–9561. [CrossRef]
2. Ahmadi, A.; Parthasarathy, S.; Pal, N.; Rajagopal, K.; Jafari, S.; Tlelo-Cuautle, E. Extreme multistability and extreme events in a novel chaotic circuit with hidden attractors. *Int. J. Bifurc. Chaos* **2022**, *33*, 2330016. [CrossRef]
3. Strogatz, S.H. *Nonlinear Dynamics and Chaos: With Applications to Physics, Biology, Chemistry, and Engineering*; CRC Press: Boca Raton, FL, USA, 2018.
4. Elaydi, S.N. *Discrete Chaos: With Applications in Science and Engineering*; Chapman and Hall/CRC: Boca Raton, FL, USA, 2007.
5. Karimov, T.; Rybin, V.; Kolev, G.; Rodionova, E.; Butusov, D. Chaotic communication system with symmetry-based modulation. *Appl. Sci.* **2021**, *11*, 3698. [CrossRef]
6. Hamadneh, T.; Abbes, A.; Falahah, I.A.; AL-Khassawneh, Y.A.; Heilat, A.S.; Al-Husban, A.; Ouannas, A. Complexity and Chaos Analysis for Two-Dimensional Discrete-Time Predator–Prey Leslie–Gower Model with Fractional Orders. *Axioms* **2023**, *12*, 561. [CrossRef]
7. Hamadneh, T.; Hioual, A.; Alsayyed, O.; Al-Khassawneh, Y.A.; Al-Husban, A.; Ouannas, A. The FitzHugh–Nagumo Model Described by Fractional Difference Equations: Stability and Numerical Simulation. *Axioms* **2023**, *12*, 806. [CrossRef]
8. Li, H.L.; Cao, J.; Hu, C.; Jiang, H.; Alsaadi, F.E. Synchronization analysis of discrete-time fractional-order quaternion-valued uncertain neural networks. *IEEE Trans. Neural Netw. Learn. Syst.* **2023**. [CrossRef]
9. Hioual, A.; Alomari, S.; Al-Tarawneh, H.; Ouannas, A.; Grassi, G. Fractional discrete neural networks with variable order: Solvability, finite time stability and synchronization. *Eur. Phys. J. Spec. Top.* **2024**, 1–14. [CrossRef]
10. Feng, W.; Zhao, X.; Zhang, J.; Qin, Z.; Zhang, J.; He, Y. Image encryption algorithm based on plane-level image filtering and discrete logarithmic transform. *Mathematics* **2022**, *10*, 2751. [CrossRef]
11. Feng, W.; Wang, Q.; Liu, H.; Ren, Y.; Zhang, J.; Zhang, S.; Qian, K.; Wen, H. Exploiting newly designed fractional-order 3D Lorenz chaotic system and 2D discrete polynomial hyper-chaotic map for high-performance multi-image encryption. *Fractal Fract.* **2023**, *7*, 887. [CrossRef]
12. Erkan, U.; Toktas, A.; Lai, Q. Design of two dimensional hyperchaotic system through optimization benchmark function. *Chaos Solitons Fractals* **2023**, *167*, 113032. [CrossRef]
13. Wang, R.; Li, C.; Kong, S.; Jiang, Y.; Lei, T. A 3D memristive chaotic system with conditional symmetry. *Chaos Solitons Fractals* **2022**, *158*, 111992. [CrossRef]
14. Huang, L.; Zhang, X.; Zang, H.; Lei, T.; Fu, H. An Offset-Boostable Chaotic Oscillator with Broken Symmetry. *Symmetry* **2022**, *14*, 1903. [CrossRef]

15. Bao, H.; Hua, Z.; Wang, N.; Zhu, L.; Chen, M.; Bao, B. Initials-boosted coexisting chaos in a 2-D sine map and its hardware implementation. *IEEE Trans. Ind. Inform.* **2020**, *17*, 1132–1140. [CrossRef]
16. Rajagopal, K.; Kanagaraj, S.; Volos, C.; Karthikeyan, A. Influence of parametric symmetry on the dynamics of 3D sinusoidal discrete systems. *Symmetry* **2023**, *15*, 780. [CrossRef]
17. Zhang, J. Control Analysis of Stochastic Lagging Discrete Ecosystems. *Symmetry* **2022**, *14.5*, 1039. [CrossRef]
18. Ramadoss, J.; Almatroud, O.A.; Momani, S.; Pham, V.T.; Thoai, V.P. Discrete memristance and nonlinear term for designing memristive maps. *Symmetry* **2022**, *14*, 2110. [CrossRef]
19. Montoya, F.G.; Baños, R.; Alcayde, A. Symmetry in engineering sciences. *Symmetry* **2021**, *11*, 3698.
20. Andrianov, I.; Koblik, S.; Starushenko, G. Transition from discrete to continuous media: The impact of symmetry changes on asymptotic behavior of waves. *Symmetry* **2021**, *13*, 1008. [CrossRef]
21. Li, C.; Sprott, J.C.; Zhang, X.; Chai, L.; Liu, Z. Constructing conditional symmetry in symmetric chaotic systems. *Chaos Solitons Fractals* **2022**, *155*, 111723. [CrossRef]
22. Leutcho, G.D.; Wang, H.; Kengne, R.; Kengne, L.K.; Njitacke, Z.T.; Fozin, T.F. Symmetry-breaking, amplitude control and constant Lyapunov exponent based on single parameter snap flows. *Eur. Phys. J. Spec. Top.* **2022**, *230*, 1887–1903. [CrossRef]
23. Peng, Y.; Lan, Z.; Li, W.; Li, Y.; Peng, J. Modeling different discrete memristive sine maps and its parameter identification. *Eur. Phys. J. Spec. Top.* **2022**, *231*, 3187–3196. [CrossRef]
24. Ali, A.M.A.; Sriram, S.; Natiq, H.; Ahmadi, A.; Rajagopal, K.; Jafari, S. A novel multi-stable sinusoidal chaotic map with spectacular behaviors. *Commun. Theor. Phys.* **2022**, *75*, 115001. [CrossRef]
25. Abu-Amara, F.; Abdel-Qader, I. Chaotic image encryption via convex sinusoidal map. *Wseas Trans. Signal Process.* **2013**, *9*, 177–184.
26. Xu, Q.; Cheng, S.; Ju, Z.; Chen, M.; Wu, H. Asymmetric coexisting bifurcations and multi-stability in an asymmetric memristive diode-bridge-based jerk circuit. *Chin. J. Phys.* **2021**, *70*, 69–81. [CrossRef]
27. Lin, H.; Wang, C.; Sun, J.; Zhang, X.; Sun, Y.; Iu, H.H. Memristor-coupled asymmetric neural networks: Bionic modeling, chaotic dynamics analysis and encryption application. *Chaos Solitons Fractals* **2023**, *166*, 112905. [CrossRef]
28. Xia, Y.; Xie, B.; Yu, Y. A novel chaos control method based on conjugate direction and adaptive step size. *Structures* **2024**, *63*, 106458. [CrossRef]
29. Almatrafi, M.B.; Berkal, M. Bifurcation analysis and chaos control for prey-predator model with Allee effect. *Int. J. Anal. Appl.* **2023**, *21*, 131. [CrossRef]
30. Ramasamy, S.; Banjerdpongchai, D.; Park, P. Chaos control of a delayed tri-trophic food chain model with fear and its carry over effects. *Symmetry* **2023**, *15*, 484. [CrossRef]
31. Ouannas, A.; Al-sawalha, M.M. On inverse full state hybrid projective synchronization of chaotic dynamical systems in discrete-time. *Int. J. Dyn. Control* **2017**, *5*, 252–258. [CrossRef]
32. Ouannas, A.; Odibat, Z. On inverse generalized synchronization of continuous chaotic dynamical systems. *Int. J. Appl. Comput. Math.* **2016**, *2*, 1–11. [CrossRef]
33. Ouannas, A. A new synchronization scheme for general 3D quadratic chaotic systems in discrete-time. *Nonlinear Dyn. Syst. Theory* **2015**, *15*, 163–170.
34. Ouannas, A. A new chaos synchronization criterion for discrete dynamical systems. *Appl. Math. Sci.* **2014**, *8*, 2025–2034. [CrossRef]
35. Kong, S.; Li, C.; Jiang, H.; Lai, Q.; Jiang, X. Symmetric image encryption algorithm based on a new product trigonometric chaotic map. *Symmetry* **2022**, *14*, 373. [CrossRef]
36. Toktas, F.; Erkan, U.; Yetgin, Z. Cross-channel color image encryption through 2D hyperchaotic hybrid map of optimization test functions. *Expert Syst. Appl.* **2024**, *249*, 123583. [CrossRef]
37. Ogata, K. *Discrete-Time Control Systems*; Prentice-Hall, Inc.: Hoboken, NJ, USA, 1995.
38. Gottwald, G.A.; Melbourne, I. The 0-1 test for chaos: A review. In *Chaos Detection and Predictability*; Springer: Berlin/Heidelberg, Germany, 2016; pp. 221–247.
39. Li, Y.; Wang, X.; Liu, Z.; Liang, X.; Si, S. The entropy algorithm and its variants in the fault diagnosis of rotating machinery: A review. *IEEE Access* **2018**, *6*, 66723–66741. [CrossRef]
40. Richman, J.S.; Moorman, J.R. Physiological time-series analysis using approximate entropy and sample entropy. *Am. J. Physiol.-Heart Circ. Physiol.* **2000**, *278*, H2039–H2049. [CrossRef]
41. Elaydi, S. *An Antroduction to Difference Equations*, 3rd ed.; Springer: New York, NY, USA, 2005.
42. Li, H.L.; Wang, Z.; Jiang, Y.L.; Zhang, L.; Teng, Z. Anti-synchronization and intermittent anti-synchronization of two identical delay hyperchaotic Chua systems via linear control. *Asian J. Control* **2017**, *19*, 202–214. [CrossRef]

Disclaimer/Publisher's Note: The statements, opinions and data contained in all publications are solely those of the individual author(s) and contributor(s) and not of MDPI and/or the editor(s). MDPI and/or the editor(s) disclaim responsibility for any injury to people or property resulting from any ideas, methods, instructions or products referred to in the content.

symmetry

MDPI

Article

Dynamical Analysis and Synchronization of Complex Network Dynamic Systems under Continuous-Time

Rui Yang [1], Huaigu Tian [1,2], Zhen Wang [3,*], Wei Wang [1] and Yang Zhang [1]

[1] Xi'an Key Laboratory of Human-Machine Integration and Control Technology for Intelligent Rehabilitation, Xijing University, Xi'an 710123, China; 20240008@xijing.edu.cn (R.Y.); 20210002@xijing.edu.cn (H.T.); 2208540402015@stu.xijing.edu.cn (W.W.); 220809011220@stu.xijing.edu.cn (Y.Z.)

[2] Shaanxi International Joint Research Center for Applied Technology of Controllable Neutron Source, Xijing University, Xi'an 710123, China

[3] School of Mathematics and Computer Science, Yan'an University, Yan'an 716000, China

* Correspondence: williamchristian@163.com

Abstract: In multilayer complex networks, the uncertainty in node states leads to intricate behaviors. It is, therefore, of great importance to be able to estimate the states of target nodes in these systems, both for theoretical advancements and practical applications. This paper introduces a state observer-based approach for the state estimation of such networks, focusing specifically on a class of complex dynamic networks with nodes that correspond one-to-one. Initially, a chaotic system is employed to model the dynamics of each node and highlight the essential state components for analysis and derivation. A network state observer is then constructed using a unique diagonal matrix, which underpins the driver and response-layer networks. By integrating control theory and stability function analysis, the effectiveness of the observer in achieving synchronization between complex dynamic networks and target systems is confirmed. Additionally, the efficacy and precision of the proposed method are validated through simulation.

Keywords: complex network system; topological structure; synchronization; state observer

1. Introduction

In the real world, complex dynamic networks are omnipresent and ubiquitous. Complex networks can be considered as dynamical systems in which connections between nodes represent interactions between nodes. The study of complex network dynamics helps to explain various real-world problems and increase the understanding of dynamical properties such as network stability, consistency, optimization and synchronization. Many natural or man-made systems can be modeled and described by complex dynamic networks, such as the World Wide Web, genetic networks [1,2], power networks [3–5], social communication networks [6–8], transportation networks [9–12], and so on. In addition, complex network topologies can be studied to solve problems in real networks, such as large-scale power outages in power networks and virus propagation in networks.

Euler adeptly resolved the "Königsberg Seven Bridges Problem" using foundational graph theory [13]. Erdős and Rényi collaboratively developed random graph theory, laying the groundwork for systematic studies in complex network theory [14]. Watts and Strogatz discovered the small world of networks [15], and Barabási and Albert revealed the scale-free characteristics and small-world properties of complex dynamic networks through the scale-free nature of networks [16]. These mathematical models provided a robust theoretical foundation that inspired increasing scholarly interest in complex dynamic networks. Targui et al. proposed an observer based on the hydrodynamic model to estimate the state of each node in the communication network [17]. Fan studies the topology identification of complex dynamic networks through systems with chaotic nodes [18]. Wu studies the state estimation problem of discrete-time general complex dynamic networks with packet loss in

the transmission channel between the original network and the observation network [19]. Alsaadi et al. also discussed the problem of network state estimation on single-layer complex networks [20–23]. Lü summarizes the link prediction in complex networks [24]. Yu analyzed the complex network of China's innovation and development [25]. Laumann discusses the complex network of climate sustainable development [26]. These studies highlight the ubiquity and importance of complex networks in nature and human society, not only advancing theoretical progress in mathematics and physics, but also having a profound impact on practical applications in fields such as engineering, economics, social sciences, and environmental science.

In complex dynamic networks, the phenomenon of synchronization is a striking collective behavior. However, since most networks cannot achieve synchronization spontaneously, control is often considered an effective method to realize network synchronization. Consequently, this topic has attracted considerable attention from scholars, encompassing various types such as complete synchronization [27], cluster synchronization [28], exponential synchronization [29,30], finite-time synchronization [31–33], and other synchronization schemes [34,35]. Soudbakhsh studies the problem of wide-area power system control using synchronization measurement in the presence of network delay [36]. Yu studies the long-term prediction of continuous-time dynamic graph networks [37]. Wu gives new criteria for the boundedness and asymptotic stability of neural networks under impulsive control on time scales [38]. Li studies the model following adaptive control problem for a class of time-varying complex dynamic networks [39]. Chen focuses on a new observer-based synchronization problem of discrete-time complex networks with Markov switching topology, and develops a non-homogeneous observer with asynchronous topology and gain to estimate the state of nodes [40]. However, these studies typically assume that complex networks are single-layer, neglecting the interactions between multiple networks that occur in real-world scenarios. For example, in social networks, daily communications among individuals occur through various channels, including telephone and email. Transportation networks consist of trains, cars, and airplanes. Given the limitations of single-layer network models, which fail to adequately describe many practical situations, it is essential to explore multilayer complex networks.

The existing synchronization research literature primarily focuses on achieving uniformity across all state components of network nodes [41,42]. However, practical network applications often require synchronization of only certain state components. In networks composed of high-dimensional nodes, attention may only be necessary for the dynamics of specific state components in certain applications. Therefore, studying the synchronization of partial state components is not only more cost effective but also economically feasible, especially in networks with varying dynamics, such as different parameters or structures. For instance, Motter explored the dynamics of nonlinear networks [43], Li studied state estimation in multilayer complex dynamic networks under time-varying delay conditions [44], and Wu et al. used observable state information from certain nodes in multilayer networks to estimate the states of target nodes in other layers [45]. Berner discussed the spectra of multilayer complex dynamic networks and the correlations between the eigenvalues of different layers [46]. Liu examined state changes in each layer of a dual-layer complex network [47]. Currently, theoretical research on the synchronization of partial state components primarily focuses on achieving synchronization over an infinite duration. However, in practical applications, there is a preference for achieving synchronization within a finite time to save time and reduce costs; yet, studies on finite-time partial state component synchronization in complex dynamic networks are still lacking.

This paper primarily examines the continuous-time state component synchronization issue of a specific type of complex dynamic network with one-to-one corresponding nodes. The key contributions of this paper are outlined as follows: In order to resolve the issue of target-layer state estimation in multilayer complex dynamic networks, an adaptive observer is designed, and the observability is studied by utilizing functional analysis. The structure of this paper is as follows: In Section 2, a mathematical model of a complex

network dynamic system is established, and the stability of complete synchronization is analyzed. In Section 3, the state estimation problem of a two-layer complex dynamic network with one-to-one corresponding nodes is studied. The original network is regarded as the driving layer to construct the response-layer network. The topology identification of the network is realized by combining the Lyapunov stability principle. In Section 4, the efficacy of the method is validated through numerical simulations. Finally, the conclusions are presented in Section 5.

2. Construction of Mathematical Model of Complex Network Dynamic System

2.1. Problem Description

A network is considered, comprising N chaotic oscillator rings with an M-layer topology and N identical nonlinear systems, which are considered nodes. The state equation of the first node can be expressed as

$$\dot{X}_i(t) = f(X_i(t)) + c\sum_{j=1}^{N} a_{ij}\Gamma(X_j(t) - X_i(t)) \tag{1}$$

where $X_i(t) = (x_i^1, x_i^2, \cdots, x_i^n)^T \in R^n$ is the state variable of the i-th node; $f(X_i(t)) : R^n \to R^n$ is a mapping of nonlinear functions, representing the dynamic behavior of each node; the constant c is the coupling strength of the state variable of the i-th node of the network, that is, the coupling strength $c > 0$ of the network, and $A = (a_{ij})_{N\times N}$ represents the topological structure of the network. The topological structure of the network is shown by A, which meets the dissipative coupling condition $\sum_{j=1}^{N} a_{ij} = 0, i = 1, \cdots, N$, and is called the external coupling matrix a_{ij}. It meets the following conditions:

A satisfies the dissipative coupling condition $\sum_{j=1}^{N} a_{ij} = 0, i = 1, \cdots, N$, A is called external coupling a_{ij}, which satisfies the following conditions:

when the external coupling A is a simple topological structure with no right and no direction, if there is a connected edge between node i and node j, then $a_{ij} = a_{ji} = 1$, otherwise $a_{ij} = a_{ji} = 1$, the diagonal element is $a_{ii} = -\sum_{j=1,j\neq i}^{N} a_{ij} = -\sum_{j=1,j\neq i}^{N} a_{ji} = -k_i, i = 1, 2, \cdots, N$, where k_i is the degree of node i; Γ, the coupling matrix, links the internal state variables of each node and is known as the output function of each node.

2.2. Stability Analysis of Complete Synchronization of Complex Dynamic Networks

For the network Equation (1), can express the dynamic equation of the network's synchronous target trajectory as follows:

$$\dot{S}(t) = f(S(t)) \tag{2}$$

In the dynamic network Equation (1), the coupling A has a single zero eigenvalue with multiplicity one. The corresponding eigenvector represents the invariant manifold of the system, which is given by the vector $(1, 1, 1, \cdots, 1)^T$. When $t \to \infty$, $X_1(t) \to X_2(t) \to \cdots \to X_N(t) \to S(t)$, that is,

$$\lim_{t\to\infty} X_i(t) = S(t) \tag{3}$$

Due to the dissipative coupling condition, the synchronized state vector $S(t) \in R^m$ must be the outcome of a solitary node, satisfying $\dot{S}(t) = f(S(t))$. $S(t)$ may signify the equilibrium point of a single node, periodic orbits, or chaotic orbits.

For discrete cases, the discrete-time dissipative coupled dynamic network corresponding to Equation (1) is as follows:

$$\dot{X}_i^{(n+1)}(t) = f(X_i^{(n)}(t)) + c\sum_{j=1}^{N} a_{ij}\Gamma X_j^n(t) \tag{4}$$

where $X_j^n(t)$ represents the state of the j-th node at the n-th time.

Similarly, if in the dynamic network model (4) there exists a condition where $n \to \infty$ implies $\lim_{n\to\infty} X_i^n(t) = S(t)(i = 1, 2, \cdots, N)$, then the dynamic network is said to have achieved complete synchronization.

By analyzing the linear stability of Equation (1) of a continuous-time dynamic network with respect to the synchronous state $S(t)$, and linearizing the state Equation (1) with respect to the synchronous state $S(t)$, where ξ_i is the state component of the i-th node, we can obtain

$$\dot{\xi}_i = Df(S)\xi_i + c\sum_{j=1}^{N} a_{ij}D\Gamma(S)\xi_j \tag{5}$$

where $Df(S)$ and $D\Gamma(S)$ are the Jacobi matrices of $f(S)$ and $\Gamma(S)$ with respect to S, respectively, and then, $\xi = [\xi_1, \xi_2, \cdots, \xi_N]$ is given; then, the above Equation (1) can be written in matrix form:

$$\dot{\xi} = Df(S)\xi + cD\Gamma(S)\xi \mathrm{A}^T \tag{6}$$

Let $\mathrm{A}^T = P\Lambda P^{-1}$, perform the Jacobi–Jordan factorization of A, assuming that Λ is a diagonal matrix, then $\Lambda = \mathrm{diag}(\lambda_1, \lambda_2, \cdots, \lambda_N)$, where $\lambda_i(i = 1, 2, \cdots, N)$ is the eigenvalue of A and $\lambda_1 = 0$. Then, making $\eta = [\eta_1, \eta_2, \cdots, \eta_N] = \xi P$, gives

$$\dot{\eta} = Df(S)\eta + cD\Gamma(S)\eta\Lambda \tag{7}$$

In other words, the above formula can be equivalent to

$$\dot{\eta}_k = [Df(S) + c\lambda_i D\Gamma(S)]\eta_i \tag{8}$$

where $i = 2, 3, \cdots, N$.

Secondly, the Lyapunov exponent method judges the stability of a synchronous manifold. In Equation (8), only λ_i is connected to η_i and i. If the external coupling matrix A is not symmetric, its eigenvalue might be complex, which leads to the main stability equation:

$$\dot{Y} = [Df(S) + c(\alpha + i\beta)D\Gamma(S)]Y \tag{9}$$

The principal stability function of a dynamic network is the maximum Lyapunov exponent $\gamma_{\max}$, which is a function of the real variables α and β. By identifying the fixed point $c\lambda_i$ on the complex plane where (α, β) is located, we can determine the stability of the network, represented by the positive and negative values of the maximum Lyapunov exponent at this point. The coupling strength c plays a crucial role in this regard.

By identifying the fixed point $c\lambda_i$ on the complex plane where (α, β) is located, we can determine the stability of the network, represented by the positive and negative values of the maximum Lyapunov exponent at this point.

When the maximum Lyapunov exponent corresponding to this point is positive, $\gamma_{\max} > 0$, the characteristic state is deemed unstable.

When the maximum Lyapunov exponent corresponding to this point is positive, $\gamma_{\max} > 0$, the characteristic state is deemed unstable.

Conversely, when the maximum Lyapunov exponent corresponding to this point is negative, $\gamma_{\max} < 0$, the characteristic state is considered stable. If all the Lyapunov exponents corresponding to the eigenvalues $\lambda_i(i = 1, 2, \cdots, N)$ are negative, the entire network's synchronization manifold becomes asymptotically stable under the coupling strength c.

When the network has no power and no connection, the eigenvalues of the external coupling matrix A are all real numbers, i.e., $0 = \lambda_1 > \lambda_2 \geq \cdots \geq \lambda_N$, and the main stability equation is

$$\dot{Y} = [Df(S) + c\alpha D\Gamma(S)]Y \tag{10}$$

So, the negative value range G of the main stability function is set by the dynamic function f, the coupling strength c, the outer coupling matrix A, and the inner coupling function Γ on the isolated node. This range is also known as the dynamic network's synchronization region. If the product of the coupling strength c and each negative eigenvalue of the outer coupling matrix A is within the synchronization region, that is,

$$c\lambda_i \in G \tag{11}$$

then, the synchronous manifold of the network is asymptotically stable.

3. State Estimation of Dynamic Systems with Multilayer Complex Networks

According to Equation (1), we can obtain the following dynamic equation for a multilayer complex network dynamic model with the same number of nodes in each layer and one-to-one correspondence between layers:

$$\begin{aligned} \dot{x}_i^K &= f(x_i^K) + c_K \sum_{j=1}^{N} d_{ij}^K \Gamma x_j^K + \sum_{R=1}^{M} d_i^{KR} \Gamma x_i^R \\ y_i^K &= H x_i^K \end{aligned} \tag{12}$$

where $1 \leq i \leq R$; $x_i^K = [x_{i1}^K, x_{i2}^K, \cdots, x_{in}^K] \in R^N$ represents the state variable of the i-th node in the $K(1 \leq K \leq M)$-th layer in the M-layer network, $y_i^K \in R$ represents the state variable of the i-th node in the K-th layer, and $f : R^n \to R^n$ is the dynamic equation of the node; c_K is the intra-layer coupling strength of the K-layer network; $D^K = (d_{ij}^K) \in R^{N \times N}$ is the intra-layer coupling matrix of the K-layer network. If there is a connecting edge from node i to node j, then $d_{ij}^K = 1$, otherwise $d_{ij}^K = 0$, and $d_{ij}^K = -\sum_{j=1, j \neq i}^{N} d_{ij}^K$; the coupling strength between the i-th node of the K-th layer network and the i-th node of the R $(1 \leq R \leq M)$-layer network is denoted by d_i^{KR}, and $d_i^{KK} = -\sum_{R=1, R \neq K}^{N} d_i^{KR}$; Γ is the inline matrix within and between layers of network nodes, which is a unit matrix; $H = [h_1, h_2, \cdots, h_n]$ is the output matrix of nodes.

When the network layer's topology is unknown or uncertain, we can identify it by constructing the driving response. In this paper, we use the original network's output variables as state observers at the driving end, and construct state observers at the response end to approximate the multilayer complex dynamic network. The state observers at the response end are constructed as follows:

$$\begin{aligned} \hat{x}_i^K &= f(\hat{x}_i^K) + c_K \sum_{j=1}^{N} d_{ij}^K \Gamma \hat{x}_j^K + \sum_{R=1}^{M} d_i^{KR} \Gamma \hat{x}_i^R + \sigma_{Ki}(y_i^K - \hat{y}_i^K) \\ \hat{y}_i^K &= H \hat{x}_i^K \end{aligned} \tag{13}$$

In the formula, $1 \leq i \leq R$; $\hat{x}_i^K = [\hat{x}_{i1}^K, \hat{x}_{i2}^K, \cdots, \hat{x}_{in}^K] \in R^N$ represents the state observation value of the i-th node of the K-th layer; $\hat{y}_i^K \in R$ represents the output observation value of the i-th node of the K-th layer network; and σ_{Ki} is the adaptive parameter.

Making the state observation error $e_i^K = \hat{x}_i^K - x_i^K$, the state error of the system can be obtained from the driving-layer network (Equation (12)) and the response-layer network (Equation (13)) as follows:

$$\begin{aligned}\dot{e}_i^K &= \hat{x}_i^K - \dot{x}_i^K \\ &= f(\hat{x}_i^K) - f(\dot{x}_i^K) + c_K \sum_{j=1}^{N} d_{ij}^K \Gamma \hat{x}_j^K - c_K \sum_{j=1}^{N} d_{ij}^K \Gamma x_j^K + \sum_{R=1}^{M} d_i^{KR} \Gamma \hat{x}_i^R - \sum_{R=1}^{M} d_i^{KR} \Gamma x_i^R + \sigma_{Ki}(y_i^K - \hat{y}_i^K) \\ &= f(\hat{x}_i^K) - f(\dot{x}_i^K) + c_K \sum_{j=1}^{N} d_{ij}^K \Gamma e_j^K + \sum_{R=1}^{M} d_i^{KR} \Gamma e_i^R + \sigma_{Ki} H e_i^K\end{aligned} \tag{14}$$

It can be observed that the state observer requires information solely about nodes and network trajectories, and not about other nodes in the network. Consequently, the continuous-time state component synchronous controller proposed in this paper exhibits the advantages of low dimensionality, low cost, and easy implementation. It is worth noting that the finite-time synchronization controller proposed in the literature [10,22–26] not only requires information about its own node and reference trajectory, but also requires information about other nodes in the network. This differs from the state observation designed in this paper, which does not require information about other nodes.

This paper presents an effective state observer designed to determine the adaptive parameter σ_{Ki}. Upon synchronizing the complex networks of the driving and response layers, the state error of the network converges to 0, allowing the corresponding layer to identify the driving-layer network. The following assumptions and lemmas are provided for the subsequent derivation and proof.

Suppose 1. *$f(x)$ is Lipschitz continuous, that is, there is a positive constant α so that for any vector $x \in R^N$, $y \in R^N$, $\|f(x) - f(y)\| \leq \alpha\|x - y\|$ holds. Where $\|\bullet\|$ is the European norm.*

Lemma 1. *For any vector $x \in R^N$, $y \in R^N$, the following inequalities hold:*

$$2x^T y \leq x^T x + y^T y \tag{15}$$

Lemma 2. *Schur's theorem: For a given symmetric $S = \begin{pmatrix} S_{11} & S_{12} \\ S_{21} & S_{22} \end{pmatrix}$, where $S_{11} = S_{11}^T$, $S_{12} = S_{21}^T$, $S_{22} = S_{22}^T$, then $S < 0$ is equivalent to*

$$S_{11} < 0, S_{22} - S_{21} S_{11}^{-1} S_{12} < 0$$

$$S_{22} < 0, S_{11} - S_{12} S_{22}^{-1} S_{21} < 0$$

Theorem 1. *If hypothesis 1 holds, given an arbitrary constant $k_i (k_i > 0)$, the following equation holds:*

$$\begin{aligned} d_{ij}^K &= -c_K (e_i^K)^T \Gamma \hat{x}_j^K \\ d_i^{KR} &= (e_i^K)^T \Gamma \hat{x}_i^R \\ \sigma_{Ki} &= k_i (e_i^K)^T H e_i^K \end{aligned} \tag{16}$$

When time tends to infinity, the error dynamic network (Equation (14)) will converge to the origin. This is demonstrated by the fact that when x_j^K is approximately equal to $\hat{x}_j^K$, the designed state observer network (Equation (13)) can estimate the state between the practical nodes of the complex network in the response layer.

Theorem 2. *For a network as Equation (12) composed of chaotic nodes, let the maximum Lyapunov exponent of isolated nodes be $h_{\max}$. If $H = I_n$ and satisfies*

$$|c\lambda_2| > h_{\max} \tag{17}$$

then, the synchronous flow form is exponentially stable.

Proof. Build the Lyapunov function:

$$V = \frac{1}{2}\sum_{i=1}^{N}\left(e_i^K\right)^T e_i^K \tag{18}$$

Deriving it leads to

$$\dot{V} = \frac{1}{2}\sum_{i=1}^{N}\left(\left(\dot{e}_i^K(t)\right)^T e_i^K(t) + \left(e_i^K(t)\right)^T \dot{e}_i^K(t)\right) = \sum_{i=1}^{N}\left(e_i^K(t)\right)^T \dot{e}_i^K(t) \tag{19}$$

$\dot{V} > 0$, $V \geq 0$, by bringing in Equation (14):

$$\begin{aligned}
\dot{V} &= \tfrac{1}{2}\sum_{i=1}^{N}\left(\left(\dot{e}_i^K(t)\right)^T e_i^K(t) + \left(e_i^K(t)\right)^T \dot{e}_i^K(t)\right) \\
&= \tfrac{1}{2}\sum_{i=1}^{N}\left(\begin{array}{l}
\left(f(\hat{x}_i^K) - f(\dot{x}_i^K)\right)^T e_i^K(t) + \left(c_K\sum_{j=1}^{N} d_{ij}^K \Gamma e_j^K\right)^T e_i^K(t) \\
+\left(\sum_{R=1}^{M} d_i^{KR}\Gamma e_i^R\right)^T e_i^K(t) + \left(\sigma_{Ki} H e_i^K\right)^T e_i^K(t) + \left(f(\hat{x}_i^K) - f(\dot{x}_i^K)\right)\left(e_i^K(t)\right)^T \\
+\left(c_K\sum_{j=1}^{N} d_{ij}^K \Gamma e_j^K\right)^T \left(e_i^K(t)\right)^T + \left(\sum_{R=1}^{M} d_i^{KR}\Gamma e_i^R\right)^T \left(e_i^K(t)\right)^T + \sigma_{Ki} H e_i^K \left(e_i^K(t)\right)^T
\end{array}\right)
\end{aligned} \tag{20}$$

According to Hypothesis 1 and Lemma 1, we can simplify Equation (20) and obtain

$$\begin{aligned}
\dot{V} &= \tfrac{1}{2}\sum_{i=1}^{N}\left(\begin{array}{l}
\left(f(\hat{x}_i^K) - f(\dot{x}_i^K)\right)^T e_i^K(t) + \left(c_K\sum_{j=1}^{N} d_{ij}^K \Gamma e_j^K\right)^T e_i^K(t) \\
+\left(\sum_{R=1}^{M} d_i^{KR}\Gamma e_i^R\right)^T e_i^K(t) + \left(\sigma_{Ki} H e_i^K\right)^T e_i^K(t) + \left(f(\hat{x}_i^K) - f(\dot{x}_i^K)\right)\left(e_i^K(t)\right)^T \\
+\left(c_K\sum_{j=1}^{N} d_{ij}^K \Gamma e_j^K\right)^T \left(e_i^K(t)\right)^T + \left(\sum_{R=1}^{M} d_i^{KR}\Gamma e_i^R\right)^T \left(e_i^K(t)\right)^T + \sigma_{Ki} H e_i^K \left(e_i^K(t)\right)^T
\end{array}\right) \\
&= \tfrac{1}{2}\sum_{i=1}^{N}\left(\begin{array}{l}
\left(f(\hat{x}_i^K) - f(\dot{x}_i^K)\right)^T e_i^K(t) + \left(f(\hat{x}_i^K) - f(\dot{x}_i^K)\right)\left(e_i^K(t)\right)^T \\
+\left(c_K\sum_{j=1}^{N} d_{ij}^K \Gamma e_j^K\right)^T e_i^K(t) + \left(c_K\sum_{j=1}^{N} d_{ij}^K \Gamma e_j^K\right)^T \left(e_i^K(t)\right)^T \\
+\left(\sum_{R=1}^{M} d_i^{KR}\Gamma e_i^R\right)^T e_i^K(t) + \left(\sum_{R=1}^{M} d_i^{KR}\Gamma e_i^R\right)^T \left(e_i^K(t)\right)^T \\
+\left(\sigma_{Ki} H e_i^K\right)^T e_i^K(t) + \sigma_{Ki} H e_i^K \left(e_i^K(t)\right)^T
\end{array}\right) \\
&= \tfrac{1}{2}\sum_{i=1}^{N}\left(\begin{array}{l}
\left(e_i^K(t)\right)^T 2\alpha e_i^K(t) + \left(c_K\sum_{j=1}^{N} d_{ij}^K \Gamma e_j^K\right)^T e_i^K(t) + \left(c_K\sum_{j=1}^{N} d_{ij}^K \Gamma e_j^K\right)^T \left(e_i^K(t)\right)^T \\
+\left(\sum_{R=1}^{M} d_i^{KR}\Gamma e_i^R\right)^T e_i^K(t) + \left(\sum_{R=1}^{M} d_i^{KR}\Gamma e_i^R\right)^T \left(e_i^K(t)\right)^T \\
+\left(\sigma_{Ki} H e_i^K\right)^T e_i^K(t) + \sigma_{Ki} H e_i^K \left(e_i^K(t)\right)^T
\end{array}\right)
\end{aligned} \tag{21}$$

$$
\begin{aligned}
\dot{V} &\le \tfrac{1}{2}\sum_{i=1}^{N}\left(\begin{array}{l}\left(e_i^K(t)\right)^T 2\alpha e_i^K(t)+e_i^K(t)\left(\sigma_{Ki}He_i^K\right)^T+\left(e_i^K(t)\right)^T\sigma_{Ki}He_i^K\\ +\left(e_i^K(t)\right)^T c_K\sum_{j=1}^{N}d_{ij}^K\Gamma e_j^K+e_i^K(t)\left(\sum_{R=1}^{M}d_i^{KR}\Gamma e_i^R\right)^T+2\left(e_i^K(t)\right)^T\sum_{R=1}^{M}d_i^{KR}\Gamma e_i^R\end{array}\right)\\
&\le \tfrac{1}{2}\sum_{i=1}^{N}\left(\begin{array}{l}\alpha\left(e_i^K(t)\right)^T e_i^K(t)+\sigma_{Ki}{}^T H^T\left(e_i^K(t)\right)^T e_i^K(t)+\left(e_i^K(t)\right)^T\sigma_{Ki}He_i^K\\ +\left(e_i^K(t)\right)^T c_K\sum_{j=1}^{N}d_{ij}^K\Gamma e_j^K+e_i^K(t)\left(\sum_{R=1}^{M}d_i^{KR}\Gamma e_i^R\right)^T+2\left(e_i^K(t)\right)^T\sum_{R=1}^{M}d_i^{KR}\Gamma e_i^R\end{array}\right)\\
&\le \tfrac{1}{2}\left(\left(E^K\right)^T\alpha E^K+c_K\left(E^K\right)^T Q_1E^K+\sum_{R=1}^{M}\left(E^K\right)^T Q_2E^R\right)\\
&\le \tfrac{1}{2}\left(\left(E^K\right)^T\alpha E^K+c_K\left(E^K\right)^T Q_1E^K+\tfrac{1}{2}\sum_{R=1}^{M}\left(E^K\right)^T E^K+\tfrac{1}{2}\sum_{R=1}^{M}\left(Q_2E^R\right)^T Q_2E^R\right)\\
&\le \tfrac{1}{2}\left(\left(E^K\right)^T(\alpha+c_KQ_1+\tfrac{M}{2})E^K+\tfrac{M}{2}\left(E^R\right)^T Q_2{}^T Q_2E^R\right)
\end{aligned}
\tag{22}
$$

Among them, $E^K=\left(\left(e_1^K\right)^T,\left(e_2^K\right)^T,\cdots,\left(e_N^K\right)^T\right)$; $E^R=\left(\left(e_1^R\right)^T,\left(e_2^R\right)^T,\cdots,\left(e_N^R\right)^T\right)$; $Q_1=\left(d_{ij}^K\otimes\Gamma\right)$; and $Q_2=\left(d_i^{KR}\otimes\Gamma\right)$. Q_1 and Q_2 depend on the parameters in the network layer. When $(\alpha+c_KQ_1+\frac{M}{2})$ is small enough, the latter term of the above Equation (22) can be obtained. According to the Lasalle invariance principle, the dynamics of the error system is asymptotically stable, and the error Equation (14) will gradually converge to the origin and remain unchanged. That is, the driving-layer network Equation (12) and the response-layer network Equation (13) reach a synchronous state, and the topology of the driving-layer network Equation (12) can be successfully identified. □

4. Simulation and Result Analysis

A two-layer dynamic network represents a specific instance of a multilayer complex dynamic network. This section employs a two-layer complex dynamic network as a case study to assess the viability of the adaptive synchronization scheme. The selection of a chaotic system as the node dynamic characteristic of a complex dynamic network is motivated by its well-documented sensitivity to changes in its initial value. This paper examines a two-layer complex dynamic network with a topological structure of chaotic oscillators and nonlocal interactions. The network's nodes are Lorenz oscillators. The single Lorenz oscillator's dynamic equation is as follows:

$$
\begin{cases}\dot{x}=-ax+ay\\ \dot{y}=bx-y-xz\\ \dot{z}=xy-cz\end{cases}
\tag{23}
$$

where x, y, and z are the dynamic variables and a, b, and c are the control parameters of the oscillator. Parameters a, b, and c determine the characteristics of the dynamic state, and their change factors affect the attractor of the phase space of the system. According to Equation (22), three fixed solutions are obtained, $x=y=z=0$, $x=y=\pm[c(b-1)]^{\frac{1}{2}}$, and $z=b-1$, where the last two solutions exist at $b\ge 1$. When $a=10, b=28$, and $c=1$, the system will appear as a chaotic phenomenon and produce strange attractors. The phase diagram corresponding to the system Equation (23) is as follows:

The chaotic attractor in Figure 1 can be made using numerical simulation, and it can be shown that the Lorenz oscillator has rich chaotic behavior. Figure 2 displays the complexity diagram of the Lorenz oscillator. The parameter settings are consistent with the dynamic phenomena studied above. The different colors in the diagram represent the chaotic, periodic, and divergent states of the Lorenz oscillator. The diagram reveals that chaotic areas dominate, and complex chaotic behaviors emerge. The boundary between high and low complexity is obvious. The evolution diagram of the x-, y-, and z-direction values in the Lorenz oscillator with time is shown in Figure 3 below. We find that while their trajectories remain within the Lorenz oscillator's attractors' range, they lack synchronization.

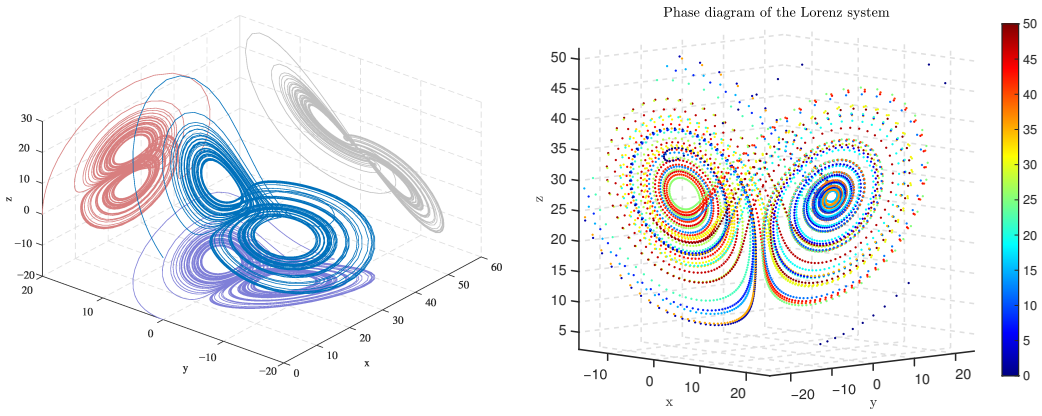

(**a**) (**b**)

Figure 1. Phase diagram of Lorenz oscillator. (**a**) Lorentz system 3D projection. (**b**) Phase diagram of Lorenz system.

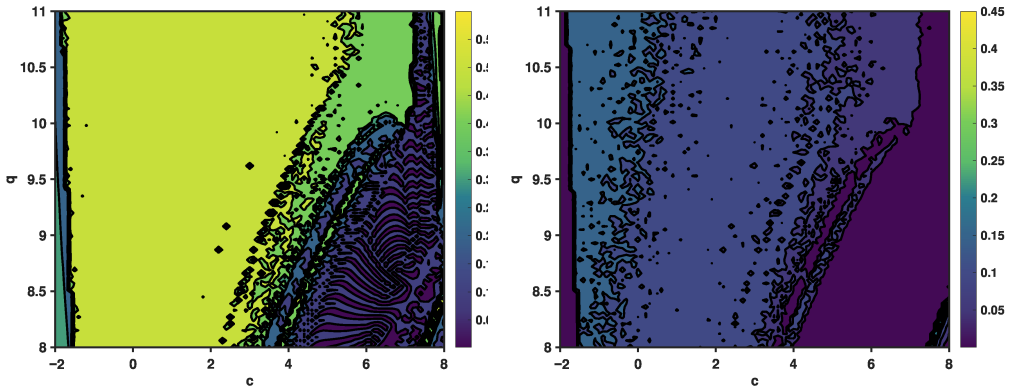

(**a**) (**b**)

Figure 2. Complexity of Lorenz oscillator. (**a**) Lorenz system chaos map 1. (**b**) Lorenz system chaos map 2.

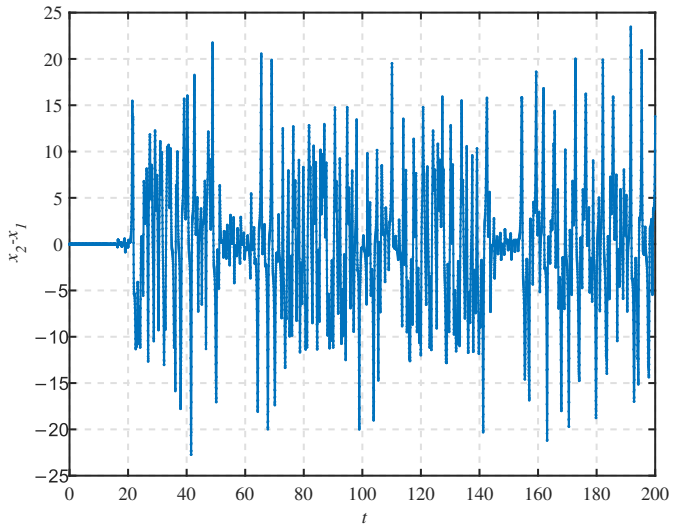

Figure 3. Evolution curve of Lorenz oscillator with initial value.

Through numerical simulation, the chaotic attractor shown in Figure 1 can be generated, and it can be determined that the Lorenz oscillator has rich chaotic behavior; Figure 2 shows the Lorenz oscillator's complexity diagram. The parameter settings are consistent

with the dynamic phenomena studied above. The diagram depicts the chaotic, periodic, and divergent states of the Lorenz oscillator, with different colors representing these states. It can be observed that the majority of the diagram is occupied by chaotic areas, which exhibit complex chaotic behaviors. The boundary between high and low complexity is clearly delineated. Figure 3 below illustrates the evolution diagram of the x-, y-, and z-direction values in the Lorenz oscillator over time. It is observed that although the trajectories of the two systems were not outside the range of the attractors of the Lorenz oscillator, they are not synchronized with each other.

Through computer simulation, the Lyapunov exponents of isolated nodes of Lorenz oscillator can be obtained as $h_1 \approx -0.5839$, $h_2 \approx 0.0569$, and $h_3 \approx -11.4730$, namely, $h_{\max} \approx 0.06$. According to Theorem 2, the synchronization condition of isolated nodes of the Lorenz oscillator can be obtained as $c > 0.06/3 = 0.02$. Figure 4 shows the Lyapunov exponent diagram of the Lorenz oscillator. To sum up, by analyzing the dynamics of the Lorenz oscillator, we can find that the Lorenz oscillator has abundant chaotic characteristics.

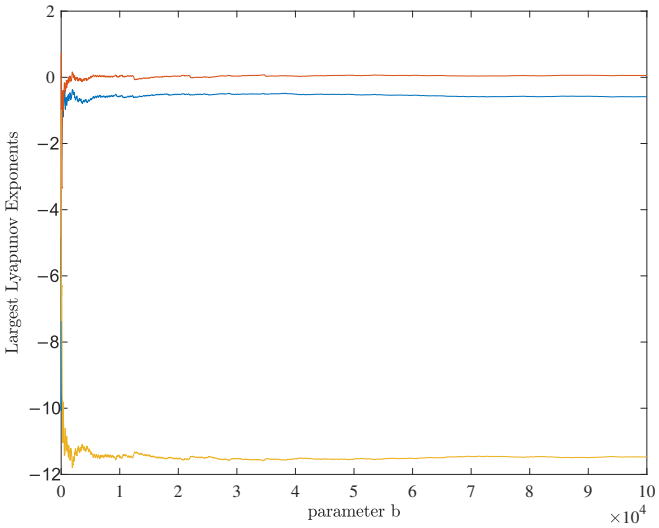

Figure 4. LLE and parameter b of Lorenz oscillator.

For any two state variables x_i and x_j of a Lorenz oscillator, because the chaotic attractor is bounded, there exists a constant β such that $\|x_{ik}\| \leq \beta$, $\left\|x_{jk}\right\| \leq \beta$ $(k = 1, 2, 3)$ and

$$\begin{aligned} &\left\|f(x_i) - f(x_j)\right\| \\ &= \sqrt{\left(-x_{i3}(x_{i1} - x_{j1}) - x_{j1}(x_{i3} - x_{j3})\right)^2 + \left(x_{i2}(x_{i1} - x_{j1}) - x_{j1}(x_{i2} - x_{j2})\right)^2} \\ &= \sqrt{\left(x_{j1}x_{j3} - x_{j1}x_{i3}\right)^2 + \left(x_{i1}x_{i2} - x_{j1}x_{j2}\right)^2} \\ &\leq 2\beta\left\|x_i - x_j\right\| \\ &= \alpha\left\|x_i - x_j\right\| \end{aligned} \tag{24}$$

Therefore, the Lorenz oscillator satisfies Hypothesis 1. The dynamic model of a two-layer complex network with the same number of nodes in each layer and one-to-one correspondence is selected, and the state equation of the driving layer of the two-layer network is as follows:

$$\begin{aligned} \dot{x}_i^1 &= f(x_i^1) + c_1 \sum_{j=1}^{N} d_{ij}^1 \Gamma x_j^1 + d_i^{11} \Gamma x_i^1 + d_i^{12} \Gamma x_i^2 \\ \dot{x}_i^2 &= f(x_i^2) + c_2 \sum_{j=1}^{N} d_{ij}^2 \Gamma x_j^2 + d_i^{21} \Gamma x_i^1 + d_i^{22} \Gamma x_i^2 \end{aligned} \tag{25}$$

The topological structure of the two-layer complex network consists of a ring network with 10 nodes, where the nodes of the two-layer network have a one-to-one correspondence.

The couplings of the first-layer network (D^1), the second layer (D^2), and the inter-layer ($D^{11}, D^{12}, D^{21}, D^{22}$) are as follows:

$$D^1 = D^2 = \begin{bmatrix} -2 & 1 & 0 & 0 & 0 & 0 & 0 & 0 & 0 & 1 \\ 1 & -2 & 1 & 0 & 0 & 0 & 0 & 0 & 0 & 0 \\ 0 & 1 & -2 & 1 & 0 & 0 & 0 & 0 & 0 & 0 \\ 0 & 0 & 1 & -2 & 1 & 0 & 0 & 0 & 0 & 0 \\ 0 & 0 & 0 & 1 & -2 & 1 & 0 & 0 & 0 & 0 \\ 0 & 0 & 0 & 0 & 1 & -2 & 1 & 0 & 0 & 0 \\ 0 & 0 & 0 & 0 & 0 & 1 & -2 & 1 & 0 & 0 \\ 0 & 0 & 0 & 0 & 0 & 0 & 1 & -2 & 1 & 0 \\ 0 & 0 & 0 & 0 & 0 & 0 & 0 & 1 & -2 & 1 \\ 1 & 0 & 0 & 0 & 0 & 0 & 0 & 0 & 1 & -2 \end{bmatrix} \tag{26}$$

$$D^{11} = D^{22} = \begin{bmatrix} -1 & 1 & 0 & 0 & 0 & 0 & 0 & 0 & 0 & 0 \\ 0 & -1 & 1 & 0 & 0 & 0 & 0 & 0 & 0 & 0 \\ 0 & 0 & -1 & 1 & 0 & 0 & 0 & 0 & 0 & 0 \\ 0 & 0 & 0 & -1 & 1 & 0 & 0 & 0 & 0 & 0 \\ 0 & 0 & 0 & 0 & -1 & 1 & 0 & 0 & 0 & 0 \\ 0 & 0 & 0 & 0 & 0 & -1 & 1 & 0 & 0 & 0 \\ 0 & 0 & 0 & 0 & 0 & 0 & -1 & 1 & 0 & 0 \\ 0 & 0 & 0 & 0 & 0 & 0 & 0 & -1 & 1 & 0 \\ 0 & 0 & 0 & 0 & 0 & 0 & 0 & 0 & -1 & 1 \\ 0 & 0 & 0 & 0 & 0 & 0 & 0 & 0 & 1 & -1 \end{bmatrix} \tag{27}$$

$$D^{12} = D^{21} = \begin{bmatrix} 1 & 0 & 0 & 0 & 0 & 0 & 0 & 0 & 0 & 0 \\ 0 & 1 & 0 & 0 & 0 & 0 & 0 & 0 & 0 & 0 \\ 0 & 0 & 1 & 0 & 0 & 0 & 0 & 0 & 0 & 0 \\ 0 & 0 & 0 & 1 & 0 & 0 & 0 & 0 & 0 & 0 \\ 0 & 0 & 0 & 0 & 1 & 0 & 0 & 0 & 0 & 0 \\ 0 & 0 & 0 & 0 & 0 & 1 & 0 & 0 & 0 & 0 \\ 0 & 0 & 0 & 0 & 0 & 0 & 1 & 0 & 0 & 0 \\ 0 & 0 & 0 & 0 & 0 & 0 & 0 & 1 & 0 & 0 \\ 0 & 0 & 0 & 0 & 0 & 0 & 0 & 0 & 1 & 0 \\ 0 & 0 & 0 & 0 & 0 & 0 & 0 & 0 & 0 & 1 \end{bmatrix} \tag{28}$$

The parameters in the network are set as follows: the coupling strength of each layer of network is $c_1 = c_2 = 1$; inline $\Gamma = diag(1, 1, 1)$ within and between layers of network nodes; output $H = [1, 0, 0]$ of nodes. The complex network for building the response side is

$$\begin{aligned} \dot{x}_i^1 &= f(x_i^1) + c_1 \sum_{j=1}^{N} d_{ij}^1 \Gamma x_j^1 + d_i^{11} \Gamma x_i^1 + d_i^{12} \Gamma x_i^2 + \sigma_{Ki}(x_i^1 - \hat{x}_i^1) \\ \dot{x}_i^2 &= f(x_i^2) + c_2 \sum_{j=1}^{N} d_{ij}^2 \Gamma x_j^2 + d_i^{21} \Gamma x_i^1 + d_i^{22} \Gamma x_i^2 + \sigma_{Ki}(x_i^2 - \hat{x}_i^2) \end{aligned} \tag{29}$$

The dynamic network equation of its error system is $\dot{e}_i^1 = \dot{\hat{x}}_i^1 - \dot{x}_i^1$, $\dot{e}_i^2 = \dot{\hat{x}}_i^2 - \dot{x}_i^2$.

Coupling the x, y, and z variables, the network equation of the Lorenz oscillator can be written as

$$\begin{cases} \dot{x}_{i1} = -a x_{i1} + a x_{i2} + c \sum_{j=1}^{10} d_{ij}^1 \Gamma x_j^1 \\ \dot{x}_{i2} = b x_{i1} - x_{i2} - x_{i1} x_{i3} + c \sum_{j=1}^{10} d_{ij}^1 \Gamma x_{j2}^1 \\ \dot{x}_{i3} = x_{i1} x_{i2} - c x_{i3} + c \sum_{j=1}^{10} d_{ij}^1 \Gamma x_{j3}^1 \end{cases} \tag{30}$$

The evolution of the x, y, and z components of 10 nodes in a complex network dynamic system with a Lorenz oscillator can be obtained by estimating the states of the 10 nodes over time.

Figures 5–7 illustrate the temporal evolution of errors between each node of the two-layer complex dynamic network and the target system. From the figure, it can be observed that when the initial values are disparate, the network error of the system is conspicuous in the initial period of time. However, with the implementation of the state observer, the system attains a synchronous state and the error value tends to 0 asymptotically, thereby realizing synchronous tracking between the driving-layer network and the response-layer network and achieving the desired synchronous state.

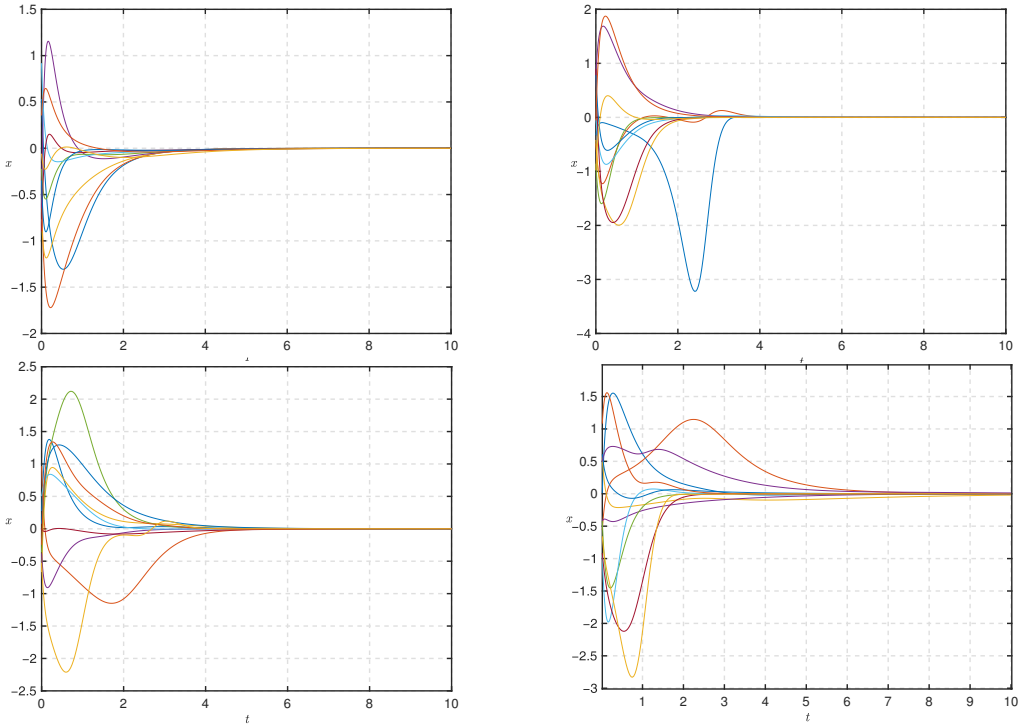

Figure 5. Variation curves of x_1^1 node.

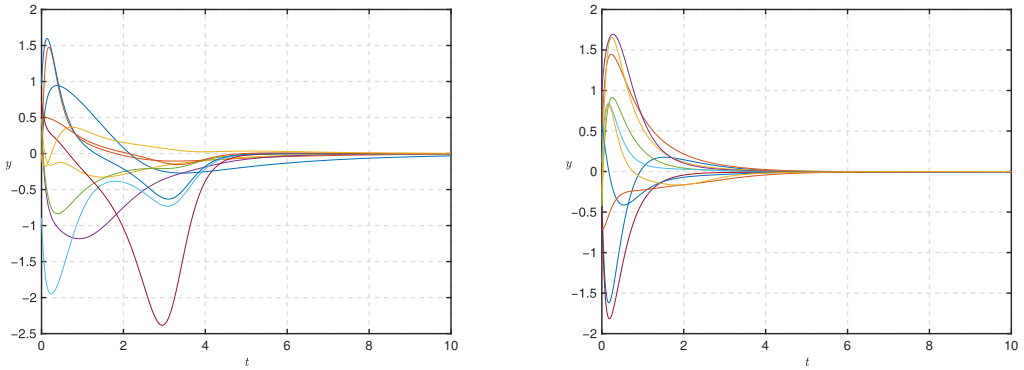

Figure 6. *Cont.*

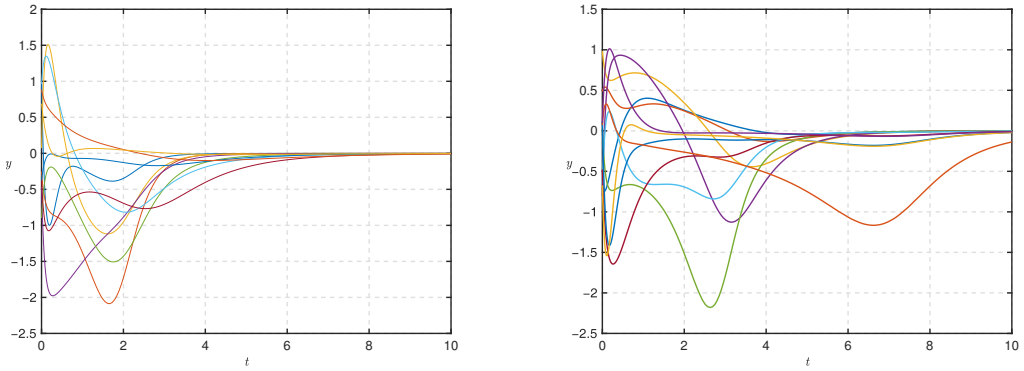

Figure 6. Variation curves of x_2^1 node.

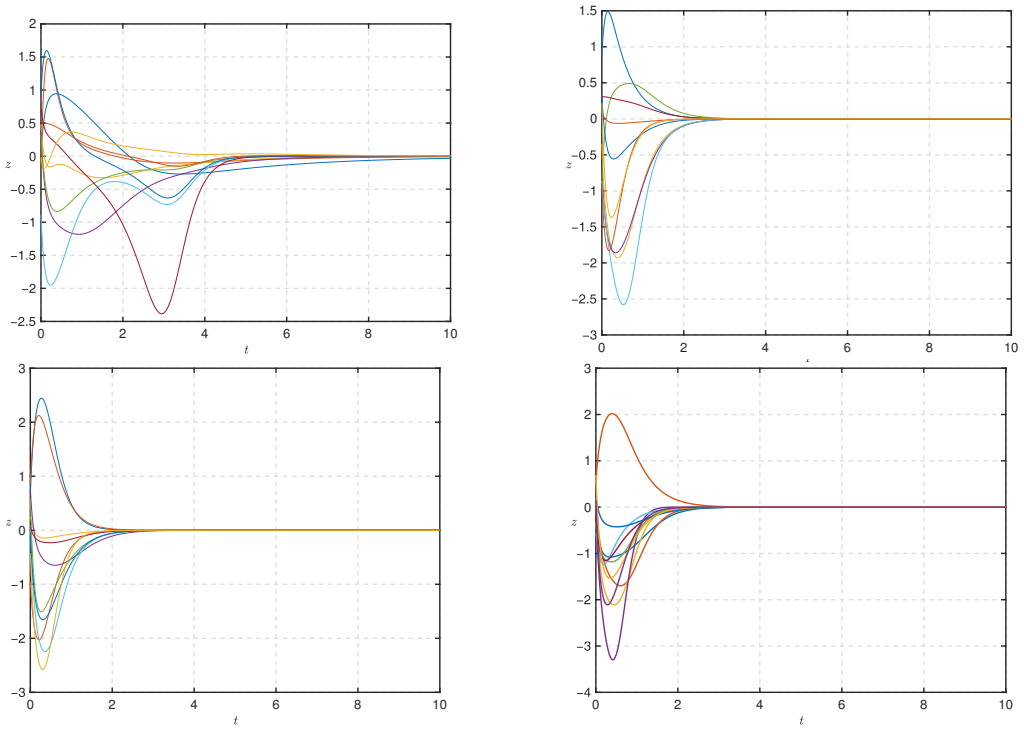

Figure 7. Variation curves of x_3^1 node.

Due to the initial values and network topology, the driving and response layers initially exhibit significant errors. However, over time, the state observer begins to function, and after a certain period, the network's total error tends towards zero. As the state error approaches zero, the rate of parameter change in the adaptive synchronization scheme also approaches zero, ultimately leading to a stable state. The above simulation results demonstrate that the discrepancy between the driving-layer network and the response-layer network rapidly diminishes and remains at a negligible level from approximately $t = 0.4$, as illustrated in Figures 8 and 9. Furthermore, the node state information within the driving-layer network gradually aligns with that of the response-layer network and persists in maintaining alignment with the node state information of the original network over time. The structure of the multilayered, complex dynamic network can be identified through the adaptive synchronization approach. It has been demonstrated that the adaptive synchronization scheme can precisely assess the state of unfamiliar nodes in multilayered, complex dynamic networks with a one-to-one correlation.

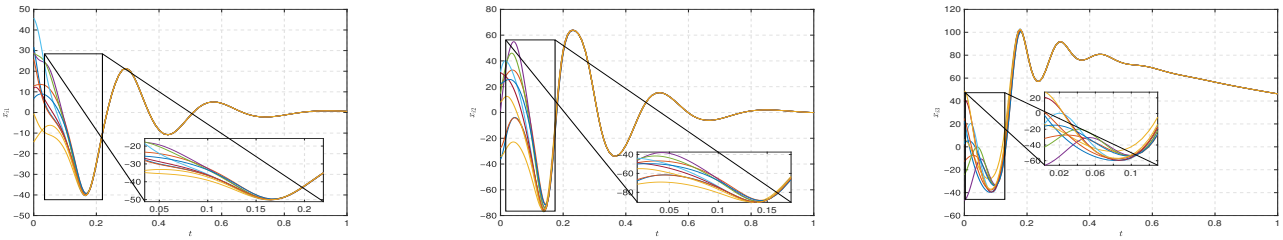

Figure 8. All-dimensional trajectory diagram. (**a**) x_{i1}-dimensional trajectory diagram; (**b**) x_{i2}-dimensional trajectory diagram; (**c**) x_{i3}-dimensional trajectory diagram.

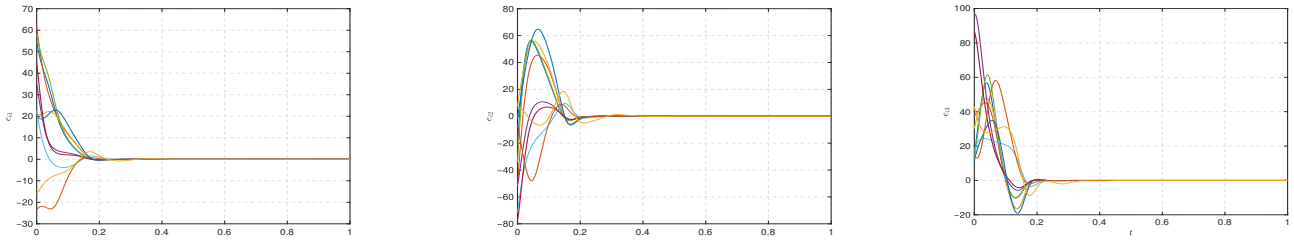

Figure 9. Error graph of each dimension of each node and isolated node. (**a**) Error plot of x dimension and isolated node; (**b**) error plot of y dimension and isolated node; (**c**) error plot of z dimension and isolated node.

5. Conclusions

This paper investigates the synchronization issue between complex dynamic networks and chaotic systems. It proposes a state estimation scheme for multilayer complex networks, based on a state observer. The proposed scheme targets a multilayer complex network dynamic model, which exhibits the same number of nodes in each layer, and follows one-to-one correspondence. Firstly, the study focuses on estimating the state of a general multilayer complex dynamic network. We construct a corresponding network state observer based on the information of the node dynamics and topology of the original network, and establish the driving- and response-layer networks. Secondly, we analyze the stability of the system through the primary stability function analysis method, resulting in proof of the network state observer's ability to achieve synchronization between the complex dynamic network and the target system. Finally, we present numerical simulations of a network consisting of 10 Lorenz oscillators and demonstrate the effectiveness of the proposed method through the results obtained. In the future, we will further study the synchronization problem of continuous-time partial state components in directed time-varying time-delay complex networks, and will consider using different control methods such as sliding mode control, pulse control, and intermittent control to achieve synchronization of the network.

6. Use of AI Tools Declaration

The authors declare they have not used artificial intelligence (AI) tools in the creation of this article.

Author Contributions: Software, H.T.; Validation, R.Y. and Z.W.; Formal analysis, W.W.; Investigation, Y.Z.; Resources, W.W.; Writing—original draft preparation, R.Y.; Writing—review and editing, Z.W.; Visualization, Z.W.; Supervision, Z.W. All authors have read and agreed to the published version of the manuscript.

Funding: This paper is supported by the Scientific Research Program Funded by Education Department of Shaanxi Provincial Government (23JK0706), the Scientific Research Foundation of Xijing University (XJ230108, XJ21B01), the Horizontal Project (2024610002002867), the National Natural Science Foundation of China (22278338, 12172281), the Fund of the Science and Technology Innovation

Team of Shaanxi (2022TD-61),the Natural Science Basic Research Program of Shaanxi (2024JC-YBMS-064, 2024JC-YBMS-068), the Support Plan for Sanqin Scholars Innovation Team in Shaanxi Province of China, and the Fund of the Youth Innovation Team of Shaanxi Universities.

Data Availability Statement: The raw data supporting the conclusions of this article will be made available by the authors on request.

Acknowledgments: The authors acknowledge the referees and the editor for carefully reading this paper and giving many helpful comments. The authors also express their gratitude to the reviewers for their insightful comments.

Conflicts of Interest: The authors declare no conflicts of interest.

References

1. Yang, L.; Li, Z.; Giua, A. Containment of rumor spread in complex social networks. *Inf. Sci.* **2020**, *506*, 113–130. [CrossRef]
2. Ullah, A.; Shao, J.; Yang, Q.; Khan, N.; Bernard, C.M.; Kumar, R. LSS: A locality-based structure system to evaluate the spreader's importance in social complex networks. *Expert Syst. Appl.* **2023**, *228*, 120326. [CrossRef]
3. Alexandridis, A.T.; Papageorgiou, P.C. A complex network deployment suitable for modern power distribution analysis at the primary control level. *IFAC-PapersOnLine* **2017**, *50*, 9186–9191. [CrossRef]
4. Xia, Y.; Kanna, S.; Mandic, D.P. Diffusion Augmented Complex Extended Kalman Filtering for Adaptive Frequency Estimation in Distributed Power Networks. In *Cooperative and Graph Signal Processing*; Elsevier: Amsterdam, The Netherlands, 2018; pp. 735–755.
5. Dehdarian, A.; Tucci, C.L. A complex network approach for analyzing early evolution of smart grid innovations in Europe. *Appl. Energy* **2021**, *298*, 117143. [CrossRef]
6. Schimit, P.H.; Pereira, F.H. Disease spreading in complex networks: A numerical study with Principal Component Analysis. *Expert Syst. Appl.* **2018**, *97*, 41–50. [CrossRef]
7. Sun, Y.F.; Sun, Z.Y. Target observation of complex networks. *Phys. A Stat. Mech. Its Appl.* **2019**, *517*, 233–245. [CrossRef]
8. Medina, P.; Carrasco, S.; Correa-Burrows, P.; Rogan, J.; Valdivia, J.A. Nontrivial and anomalous transport on weighted complex networks. *Commun. Nonlinear Sci. Numer. Simul.* **2022**, *114*, 106684. [CrossRef]
9. Ji, P.; Ye, J.; Mu, Y.; Lin, W.; Tian, Y.; Hens, C.; Perc, M.; Tang, Y.; Sun, J.; Kurths, J. Signal propagation in complex networks. *Phys. Rep.* **2023**, *1017*, 1–96.
10. Dramsch, J.S.; Lüthje, M.; Christensen, A.N. Complex-valued neural networks for machine learning on non-stationary physical data. *Comput. Geosci.* **2021**, *146*, 104643. [CrossRef]
11. Qiao, H.H.; Deng, Z.H.; Li, H.J.; Hu, J.; Song, Q.; Gao, L. Research on historical phase division of terrorism: An analysis method by time series complex network. *Neurocomputing* **2021**, *420*, 246–265. [CrossRef]
12. Rocha, R.V.; de Souza Filho, F.D.A. Stream gauge clustering and analysis for non-stationary time series through complex networks. *J. Hydrol.* **2023**, *616*, 128773. [CrossRef]
13. Räz, T. Euler's Königsberg: The explanatory power of mathematics. *Eur. J. Philos. Sci.* **2018**, *8*, 331–346. [CrossRef]
14. Cohen, R.; Havlin, S. Scale-free networks are ultrasmall. *Phys. Rev. Lett.* **2003**, *90*, 058701. [CrossRef]
15. Strogatz, S.H. Exploring complex networks. *Nature* **2001**, *410*, 268–276. [CrossRef]
16. Saleh, M.; Esa, Y.; Mohamed, A. Applications of complex network analysis in electric power systems. *Energies* **2018**, *11*, 1381. [CrossRef]
17. Targui, B.; Frikel, M.; M'saad, M.; Safi, S. Observer design for the state estimation of a class of communication networks. In Proceedings of the 18th Mediterranean Conference on Control and Automation, MED'10, Marrakech, Morocco, 23–25 June 2010; IEEE: New York, NY, USA, 2010; pp. 495–499.
18. Fan, C.X.; Wan, Y.H.; Jiang, G.P. Topology identification for a class of complex dynamical networks using output variables. *Chin. Phys. B* **2012**, *21*, 020510. [CrossRef]
19. Wu, X.; Jiang, G.P.; Wang, X. State estimation for general complex dynamical networks with packet loss. *IEEE Trans. Circuits Syst. II Express Briefs* **2017**, *65*, 1753–1757. [CrossRef]
20. Zhang, H.; Hu, J.; Liu, H.; Yu, X.; Liu, F. Recursive state estimation for time-varying complex networks subject to missing measurements and stochastic inner coupling under random access protocol. *Neurocomputing* **2019**, *346*, 48–57. [CrossRef]
21. Hu, B.; Song, Q.; Zhao, Z. Robust state estimation for fractional-order complex-valued delayed neural networks with interval parameter uncertainties: LMI approach. *Appl. Math. Comput.* **2020**, *373*, 125033. [CrossRef]
22. Alsaadi, F.E.; Wang, Z.; Wang, D.; Alsaadi, F.E.; Alsaade, F.W. Recursive fusion estimation for stochastic discrete time-varying complex networks under stochastic communication protocol: The state-saturated case. *Inf. Fusion* **2020**, *60*, 11–19. [CrossRef]
23. Hu, W.X.; Ruan, Z.H.; Xiao, X.Y.; Xiong, X.Y.; Wang, J.Q. A novel voltage sag state estimation method based on complex network analysis. *Int. J. Electr. Power Energy Syst.* **2022**, *140*, 108119. [CrossRef]
24. Lü, L.; Zhou, T. Link prediction in complex networks: A survey. *Phys. A Stat. Mech. Its Appl.* **2011**, *390*, 1150–1170. [CrossRef]
25. Yu, G.; Wan, Y.; Jiang, C. Complex network analysis on provincial innovation development in China. *Appl. Math. Comput.* **2023**, *455*, 128103. [CrossRef]

26. Laumann, F.; von Kügelgen, J.; Uehara, T.H.K.; Barahona, M. Complex interlinkages, key objectives, and nexuses among the Sustainable Development Goals and climate change: A network analysis. *Lancet Planet. Health* **2022**, *6*, e422–e430. [CrossRef] [PubMed]
27. Lü, L.; Li, C.; Bai, S.; Li, G.; Rong, T.; Gao, Y.; Yan, Z. Synchronization of uncertain time-varying network based on sliding mode control technique. *Phys. A Stat. Mech. Its Appl.* **2017**, *482*, 808–817. [CrossRef]
28. Tong, L.; Liang, J.; Liu, Y. Generalized cluster synchronization of Boolean control networks with delays in both the states and the inputs. *J. Frankl. Inst.* **2022**, *359*, 206–223. [CrossRef]
29. Aadhithiyan, S.; Raja, R.; Zhu, Q.; Alzabut, J.; Niezabitowski, M.; Lim, C.P. Exponential synchronization of nonlinear multi-weighted complex dynamic networks with hybrid time varying delays. *Neural Process. Lett.* **2021**, *53*, 1035–1063. [CrossRef]
30. He, X.; Zhang, H. Exponential synchronization of complex networks via feedback control and periodically intermittent noise. *J. Frankl. Inst.* **2022**, *359*, 3614–3630. [CrossRef]
31. Tian, H.; Wang, Z.; Zhang, P.; Chen, M.; Wang, Y. Dynamic analysis and robust control of a chaotic system with hidden attractor. *Complexity* **2021**, *2021*, 8865522 . [CrossRef]
32. Li, X.; Wu, H.; Cao, J. Synchronization in finite time for variable-order fractional complex dynamic networks with multi-weights and discontinuous nodes based on sliding mode control strategy. *Neural Netw.* **2021**, *139*, 335–347. [CrossRef]
33. Tian, H.; Wang, Z.; Zhang, H.; Cao, Z.; Zhang, P. Dynamical analysis and fixed-time synchronization of a chaotic system with hidden attractor and a line equilibrium. *Eur. Phys. J. Spec. Top.* **2022**, *231*, 2455–2466. [CrossRef]
34. Wang, Z.; Veeman, D.; Zhang, M.; Natiq, H.; Yang, R.; Hussain, I. A symmetric oscillator with multi-stability and chaotic dynamics: bifurcations, circuit implementation, and impulsive control. *Eur. Phys. J. Spec. Top.* **2022**, *231*, 2153–2161. [CrossRef]
35. Tian, H.; Liu, J.; Wang, Z.; Xie, F.; Cao, Z. Characteristic Analysis and Circuit Implementation of a Novel Fractional-Order Memristor-Based Clamping Voltage Drift. *Fractal Fract.* **2022**, *7*, 2. [CrossRef]
36. Soudbakhsh, D.; Chakrabortty, A.; Annaswamy, A.M. A delay-aware cyber-physical architecture for wide-area control of power systems. *Control Eng. Pract.* **2017**, *60*, 171–182. [CrossRef]
37. Li, Z.; Yu, J.; Zhang, G.; Xu, L. Dynamic spatio-temporal graph network with adaptive propagation mechanism for multivariate time series forecasting. *Expert Syst. Appl.* **2023**, *216*, 119374. [CrossRef]
38. Wu, Y.; Huang, Z.; Bohner, M.; Cao, J. Impulsive boundedness for nonautonomous dynamic complex networks with constraint nonlinearity. *Appl. Math. Model.* **2023**, *115*, 853–867. [CrossRef]
39. Li, X.; Wang, Y.; Liu, L. Model Following Adaptive Control for a Class of Complex Dynamic Networks Based on the Dynamics of Links. *Int. J. Control Autom. Syst.* **2022**, *20*, 2202–2210. [CrossRef]
40. Wu, Z.; Chen, J.; Zhang, X.; Xiao, Z.; Tao, J.; Wang, X. Dynamic event-triggered synchronization of complex networks with switching topologies: Asynchronous observer-based case. *Appl. Math. Comput.* **2022**, *435*, 127413. [CrossRef]
41. Wan, X.; Li, Y.; Li, Y.; Wu, M. Finite-time H state estimation for two-time-scale complex networks under stochastic communication protocol. *IEEE Trans. Neural Netw. Learn. Syst.* **2020**, *33*, 25–36. [CrossRef]
42. Hongsri, A.; Botmart, T.; Weera, W.; Junsawang, P. New delay-dependent synchronization criteria of complex dynamical networks with time-varying coupling delay based on sampled-data control via new integral inequality. *IEEE Access* **2021**, *9*, 64958–64971. [CrossRef]
43. Motter, A.E. Networkcontrology. *Chaos Interdiscip. J. Nonlinear Sci.* **2015**, *25*, 097621. [CrossRef] [PubMed]
44. Li, K.; Wang, X.; Jiang, G.P. State estimation for multi-layer complex dynamical networks with time-varying delay. In Proceedings of the 2021 40th Chinese Control Conference (CCC), Shanghai, China, 26–28 July 2021; IEEE: New York, NY, USA, 2021; pp. 717–723.
45. Wu, Y.; Wang, X.; Jiang, G.P.; Gu, M. Target layer state estimation in multilayer complex dynamical networks using functional observability. *J. Frankl. Inst.* **2023**, *360*, 8178–8199. [CrossRef]
46. Berner, R.; Mehrmann, V.; Scholl, E.; Yanchuk, S. The multiplex decomposition: An analytic framework for multilayer dynamical networks. *SIAM J. Appl. Dyn. Syst.* **2021**, *20*, 1752–1772. [CrossRef]
47. Liu, L.; Feng, M.; Xia, C.; Zhao, D.; Perc, M. Epidemic trajectories and awareness diffusion among unequals in simplicial complexes. *Chaos Solitons Fractals* **2023**, *173*, 113657. [CrossRef]

Disclaimer/Publisher's Note: The statements, opinions and data contained in all publications are solely those of the individual author(s) and contributor(s) and not of MDPI and/or the editor(s). MDPI and/or the editor(s) disclaim responsibility for any injury to people or property resulting from any ideas, methods, instructions or products referred to in the content.

symmetry

MDPI

Article

Fixed Point Dynamics in a New Type of Contraction in b-Metric Spaces

María A. Navascués [1,*] and Ram N. Mohapatra [2]

[1] Department of Applied Mathematics, Universidad de Zaragoza, 50018 Zaragoza, Spain
[2] Department of Mathematics, University of Central Florida, Orlando, FL 32816, USA; ram.mohapatra@ucf.edu
* Correspondence: manavas@unizar.es

Abstract: Since the topological properties of a b-metric space (which generalizes the concept of a metric space) seem sometimes counterintuitive due to the fact that the "open" balls may not be open sets, we review some aspects of these spaces concerning compactness, metrizability, continuity and fixed points. After doing so, we introduce new types of contractivities that extend the concept of Banach contraction. We study some of their properties, giving sufficient conditions for the existence of fixed points and common fixed points. Afterwards, we consider some iterative schemes in quasi-normed spaces for the approximation of these critical points, analyzing their convergence and stability. We apply these concepts to the resolution of a model of integral equation of Urysohn type. In the last part of the paper, we refine some results about partial contractivities in the case where the underlying set is a strong b-metric space, and we establish some relations between mutual weak contractions and quasi-contractions and the new type of contractivity.

Keywords: iteration; fixed-point theorems; contractions; b-metric spaces; quasi-normed spaces; Urysohn integral equations

1. Introduction

Since the existence and approximation of fixed points plays a central role in the implementation of numerical methods for the resolution of all kinds of equations, a great number of authors are focusing on the generalizations of previous theories related to this topic in order to extend them to wider contexts. In particular, many different distance spaces are being considered. There are extensive works dealing with the structure of b-metric space. This kind of framework was formerly called quasi-metric (see, for instance, references [1,2]). However, there are a lot of different generalizations of the concept of metric space with this terminology (see articles [2–4]). Lately, the name b-metric space is predominantly used to describe a set X endowed with a kind of distance, where the triangular inequality is substituted by the general expression

$$d(x,y) \leq s(d(x,z) + d(z,y)),$$

for $x, y, z \in X$ and some fixed real number $s \geq 1$.

In this paper, we review first the topological background of b-metric spaces, regarding compactness, metrizability, continuity and existence of fixed points of self-maps (Section 2).

In Section 3, we define new types of contractions and mutual contractions on b-metric spaces. We prove that the novel mappings include many others present in the literature when the associated constants satisfy certain restrictions. That is true for the quasi-contractions defined by Ćirić, which include, in turn, the Kannan [5–7], Chatterjea [8], and other self-maps. We also give sufficient conditions for the existence of common fixed points for mappings related by an inequality of partial contractivity type.

Section 4 is devoted to the analysis of the Noor algorithm and the so-called SP iterative procedure for the approximation of fixed points, in the context of quasi-normed spaces

(the distance associated with a quasi-norm is a particular case of b-metric space). We study the convergence and stability of these iterative methods, regarding the values of their parameters.

Section 5 presents an application to obtain the solution of an integral equation of Urysohn type, when the integrand satisfies certain conditions. Urysohn's equation [9] is a prototypical example of a nonlinear integral equation. Depending on the integrand, the equation may not have an explicit exact solution. In this section, we tackle the problem of finding solutions of this type of equation by means of iterative methods of fixed-point approximation in the context of functional b-metric spaces.

Section 6 is devoted to refining some results about partial contractivities in the case where the underlying set is a strong b-metric space.

In the paper's last part, some relations between mutual weak, partial and quasi-contractions are established, and a collage theorem for weak contractions is proved. The article finishes with a section of Conclusions.

2. Topology of b-Metric Spaces and Continuous Maps

The metric, normed and quasi-normed spaces are particular cases of b-metric structures. According to the exhaustive historical review on the introduction of these spaces carried out in reference [10], the first authors to define and use the concept of a b-metric were Coifman and Guzmán in an article of 1970 [11]. This fact is quoted in references [12,13], for instance. In general, it is considered that the papers by Bakhtin [14] and Czerwik [15,16] are foundational for this topic as well. The readers are encouraged to consult the quoted article by Berinde and Pacurar [10] for historical details and clarifications.

Since the topological properties of a b-metric space seem sometimes counterintuitive due to the fact that the "open" balls may not be open sets, we mention in this section a review of some aspects of a space of this type, concerning compactness, metrizability and fixed points of mappings. These results have been collected from references [1,2,13,17–21] and the authors. For new insights on the topic, see, for instance, [22–24].

Definition 1. *A b-metric space X is a set endowed with a mapping $d : X \times X \to \mathbb{R}^+$ with the following properties:*

1. $d(x,y) \geq 0$, $d(x,y) = 0$ *if and only if* $x = y$.
2. $d(x,y) = d(y,x)$ *for any* $x, y \in X$.
3. *There exists* $s \geq 1$ *such that* $d(x,y) \leq s(d(x,z) + d(z,y))$ *for any* $x, y, z \in X$.

The constant s is the index of the b-metric space, and d is called a b-metric.

Remark 1. *For $s = 1$, this structure agrees with the usual metric space.*

The definition of ball $B(x,r)$, for $x \in X$ and $r > 0$, is similar to the metric case.

Definition 2. *A subset A of a b-metric space X is open if $\forall x \in X$, there exists $r > 0$ such that $B(x,r) \subseteq A$. A subset $F \subset X$ is closed if its complementary subset is open.*

The previous definition of open sets endows X with a topology τ. The definition of compact set agrees with the given by this topology.

Proposition 1. *A subset F of a b-metric space X is closed if and only if for any sequence $(x_n) \subset X$ with $\lim_{n\to\infty} x_n = x$, the limit $x \in F$.*

Let $\bar{A}$ be the intersection of all closed subsets of X that contain a subset A, then $x \in \bar{A}$ if for any $\epsilon > 0$, $B(x,\epsilon) \cap A \neq \emptyset$.

Proof. See Prop 2 of [20]. □

$\bar{A}$ is the (topological) closure of A.

Proposition 2. *$\bar{A}$ is a closed set.*

Proof. See Proposition 3.2 of reference [2]. □

The convergence of sequences in this type of spaces can be easily characterized. We mention the following result.

Proposition 3. *A sequence $(x_n) \subset X$ is convergent to a limit $x \in X$ if and only if $\lim_{n\to\infty} d(x_n, x) = 0$.*

Proof. See Corollary 2.3 of the reference [13]. □

For sequences $(x_n), (y_n) \subseteq X$ such that $\lim_{n\to\infty} x_n = x$ and $\lim_{n\to\infty} y_n = y$, one has

$$\frac{1}{s^2} d(x, y) \leq \liminf_{n\to\infty} d(x_n, y_n) \leq \limsup_{n\to\infty} d(x_n, y_n) \leq s^2 d(x, y) \tag{1}$$

(see Lemma 3.1 of [2]).

Thus, in general, $\lim_{n\to\infty} d(x_n, y_n)$ does not agree with $d(x, y)$, and d is not continuous. For a metric space ($s = 1$), the former chain of inequalities gives the equality $\lim_{n\to\infty} d(x_n, y_n) = d(x, y)$, and consequently, d is continuous.

Proposition 4. *If a sequence (x_n) of a b-metric space is convergent, its limit is unique.*

Proof. It is a consequence of (1) taking $x_n = y_n$. □

The definition of a Cauchy sequence is similar to the metric case.

Definition 3. *X is a complete b-metric space if every Cauchy sequence is convergent.*

The next result is similar to the metric case.

Proposition 5. *Let X be a complete b-metric space. A subset $Y \subseteq X$ is complete if and only if Y is closed.*

Definition 4. *Let (X, d) be a b-metric space, then $A \subseteq X$ is totally bounded if for any $\epsilon > 0$ there exist $x_1, x_2, \ldots x_n \in A$ such that*

$$A \subseteq (\cup_{i=1}^{n} B(x_i, \epsilon)).$$

Definition 5. *Let (X, d) be a b-metric space, then $A \subseteq X$ is sequentially compact if any sequence contained in A has a convergent subsequence whose limit belongs to A.*

Definition 6. *A subset A is bounded if $\sup_{x,y\in A} d(x, y) < \infty$. In this case the diameter of A is defined as $diam(A) := \sup_{x,y\in A} d(x, y)$.*

Proposition 6. *A is bounded if and only if there exist $x \in X$ and a real number $R > 0$ such that $A \subseteq B(x, R)$.*

Proof. Let $\epsilon > 0$; if A is bounded, let us consider any $x \in A$; then, for any $y \in A$, $d(y, x) \leq diam(A) < diam(A) + \epsilon$ and consequently, $y \in B(x, diam(A) + \epsilon)$. Then, we can take $R = diam(A) + \epsilon$ and $A \subseteq B(x, R)$.

For the reverse implication, if $A \subseteq B(x, R)$ then for any $y, z \in A$,

$$d(y, z) \leq sd(x, y) + sd(x, z) \leq 2sR < \infty.$$

□

Proposition 7. *Let A be a nonempty subset of a b-metric space X; then,*

- *A is compact if and only if A is sequentially compact.*
- *If A is compact then A is totally bounded.*

Proof. See Theorem 3.1 of the reference [20]. □

Proposition 8. *If A is compact, then A is bounded.*

Proof. Since A is totally bounded by Proposition 7, for a fixed $\epsilon > 0$, there exist $x_1, x_2, \ldots$ $x_n \in A$ such that

$$A \subseteq (\cup_{i=1}^{n} B(x_i, \epsilon)).$$

Let us define $K = \sup_{i,j} d(x_i, x_j)$. For any $x \in A$, $x \in B(x_i, \epsilon)$, for some $i = 1, 2, \ldots$ n and

$$d(x, x_1) \leq sd(x, x_i) + sd(x_i, x_1) < s\epsilon + sK = K'.$$

Consequently $A \subseteq B(x_1, K')$, and A is bounded. □

Proposition 9. *If A is compact, then A is closed.*

Proof. Let $(x_n) \subseteq A$ be a sequence such that $\lim_{n\to\infty} x_n = x$. Then, A is sequentially compact according to Proposition 7, and consequently, there exists a subsequence $(x_{n_j}) \subseteq A$ such that $\lim_{n\to\infty} x_{n_j} = x' \in A$. Since the limit is unique, $x = x' \in A$, and A is closed. □

2.1. Continuous Functions and Compactness

In this subsection, we review some properties of the continuous maps defined on compact sets of a b-metric space.

We will consider the definition of a continuous function $T : X \to Y$, where X, Y are b-metric spaces, corresponding to the topologies defined in both spaces. An important fact is the following.

Proposition 10. *A map $T : X \to Y$, where X, Y are b-metric spaces, is continuous at $x \in X$ if and only if T is sequentially continuous at x, that is to say, if $\lim_{n\to\infty} x_n = x$ then $\lim_{n\to\infty} Tx_n = Tx$.*

Proof. It is similar to the metric case. □

The image of a compact by a continuous function is compact. As a consequence:

Proposition 11. *If the map $T : X \to Y$, where X, Y are b-metric spaces, is continuous, and K is a compact subset of X, then $T(K)$ is bounded.*

Proof. It is a consequence of Proposition 8. □

Proposition 12. *If the map $T : X \to \mathbb{R}$, where X is a b-metric space, is continuous, then T attains its extreme values, that it is to say, T has a maximum and a minimum.*

Proof. By Propositions 8 and 9, $T(X) \subseteq \mathbb{R}$ is closed and bounded' consequently, $\inf T(X)$, $\sup T(X) \in T(X)$. □

It is well known that a b-metric need not be continuous. The following important result can be read from reference [13].

Proposition 13. *Let X be a b-metric space; then, a ball $B(x, r)$, and $r > 0$ is open for any $x \in X$ if and only if $d(x, \cdot)$ is upper semi-continuous.*

Proof. See Remark 2.5 of reference [13]. □

Remark 2. *In particular, if d is continuous, all the "open" balls are open sets.*

2.2. Metrizability of a b-Metric Space

In this section, we consider some results concerning the existence of a metric equivalent to a b-metric.

Let X be a b-metric space and $p \in \mathbb{R}$ such that $0 < p \leq 1$. Let us define

$$d_p(x,y) := \inf\{\sum_{i=1}^{n} d^p(x_{i-1}, x_i)\}, \tag{2}$$

where $x_i \in X$, for $i = 0, 1, \ldots, n$, are arbitrary such that $x = x_0$ and $y = x_n$. The function d_p is a pseudo-metric and the following inequality holds:

$$d_p(x,y) \leq d^p(x,y) \tag{3}$$

for any $x, y \in X$.

If p is suitably chosen, d_p is a metric, and we have a kind of equivalence between d_p and d. Paluszyinski and Stempak [1] proved that if the relation between the index s of the b-metric d and p is given by the equation

$$(2s)^p = 2$$

then d_p is a metric on X and

$$d_p(x,y) \leq d^p(x,y) \leq 2d_p(x,y), \tag{4}$$

for any $x, y \in X$. This implies that the topology τ of X is such that $\tau = \tau_{d_p}$, that is to say, τ is metrizable. As a consequence, the convergence of a sequence (x_n) to $x \in X$ is given if and only if $d(x_n, x) \to 0$ as stated in Proposition 3.

Remark 3. *Paluszyinski and Stempak use in reference [1] the term quasi-metric space instead of b-metric space, as noted in the Introduction.*

2.3. Fixed Points of Self-Maps in b-Metric Spaces

Let X be a b-metric space with index s. We consider functions $\phi : \mathbb{R}^+ \to \mathbb{R}^+$ satisfying the following conditions:

1. ϕ is non-decreasing.
2. $\lim_{n\to\infty} \phi^n(t) = 0$.
3. $\phi(t) < ts^{-1}$, for any $t > 0$.

The first and second conditions imply that $\phi(t) < t$ for any $t > 0$. The next theorem is proved in [13] (Theorem 4.2).

Theorem 1. *Let X be a complete b-metric space and let $\phi : \mathbb{R}^+ \to \mathbb{R}^+$ satisfy the conditions (1)–(3). If a self-map $T : X \to X$ is such that*

$$d(Tx, Ty) \leq \phi(d(x,y))$$

for any $x, y \in X$, then T has a unique fixed point $x^* \in X$ and $\lim_{n\to\infty} T^n x = x^*$ for any $x \in X$ (T is called a Picard operator).

Corollary 1. *If X is a complete b-metric space and $T : X \to X$ is a Banach contraction, that is to say, there exists $k \in \mathbb{R}$, $0 < k < s^{-1}$, and*

$$d(Tx, Ty) \leq kd(x,y)$$

for any $x, y \in X$, then T has a unique fixed point $x^* \in X$ and $\lim_{n\to\infty} T^n x = x^*$ for any $x \in X$ (T is a Picard operator).

However, in reference [18] (Theorem 3.1), for instance, it is proved that the condition $k < s^{-1}$ is not necessary, and $k < 1$ is sufficient to have the same result about the existence of fixed point and convergence.

2.4. Strong b-Metric Spaces and Metrizability

In this subsection, we consider a particular case of a b-metric, the so-called strong b-metric.

Definition 7. *A strong b-metric space X is a set endowed with a mapping $d : X \times X \to \mathbb{R}^+$ with the following properties:*

1. *$d(x, y) \geq 0$, $d(x, y) = 0$ if and only if $x = y$.*
2. *$d(x, y) = d(y, x)$ for any $x, y \in X$.*
3. *There exists $s \geq 1$ such that, for any $x, y, z \in X$,*

$$d(x, y) \leq d(x, z) + sd(z, y). \tag{5}$$

The constant s is the index of the strong b-metric space, and d is called a strong b-metric.

References [22,24,25], for instance, contain several interesting examples of strong b-metric spaces.

The third property implies the "s-relaxed polygonal inequality" or "s-polygonal inequality":

$$d(x_0, x_n) \leq s(\sum_{j=1}^{n} d(x_{j-1}, x_j)),$$

for any $n \geq 1$ and $x_0, x_1, \ldots x_n \in X$.

Remark 4. *A strong b-metric space is a b-metric space, but the converse may not be true [21].*

The main topological difference between a b-metric and a strong b-metric concerns the openness of the balls. In a strong b-metric space, the "open" balls are open sets [21]. The second difference is the continuity of d. A strong b-metric is always continuous (see, for instance, Lemma 2 of [26]).

There is also an important difference regarding the metrizability. According to Theorem 4.4 of reference [19], a strong b-metric d is Lipschitz equivalent to a metric ρ in X, that is to say, there exist constants $c, C \geq 0$ such that

$$c\rho(x, y) \leq d(x, y) \leq C\rho(x, y), \tag{6}$$

for any $x, y \in X$. The Lipschitz equivalence implies the topological equivalence.

The property (6) implies the preservation of the completeness as well. Thus, (X, d) is complete if and only if (X, ρ) is complete. Another important feature of the strong b-metric spaces is the existence of completion [17]. That is to say, for any strong b-metric space (X, d), there exists a complete strong b-metric space $(\bar{X}, \bar{d})$ and a mapping $h : X \to \bar{X}$ such that $\bar{d}(j(x), j(y)) = d(x, y)$ for all $x, y \in X$. The completion is unique up to an isometry.

3. Some Properties of a Partial Contractivity

In this section, we propose a new type of contraction on a b-metric space, and prove some of its properties.

Definition 8. *Given a b-metric space (X, d), a self-map $T : X \to X$ is a partial contractivity if there exist real constants a, b such that $0 < a < 1$ and $B \geq 0$ such that for all $x, y \in X$*

$$d(Tx, Ty) \leq ad(x, y) + Bd(x, Tx). \tag{7}$$

Due to the symmetry of the b-metric, inequality (7) is equivalent to

$$d(Tx, Ty) \leq ad(x, y) + Bd(y, Ty), \tag{8}$$

for any $x, y \in X$.

A Banach contraction is a particular case of partial contractivity (for $B = 0$).

Next, we provide examples and counterexamples of partial contractivities.

Example 1. *Let us consider the set $X = [0, 1] \cup [9/4, 11/4]$ with the b-metric of index $s = 2$ defined as $d_2(x, y) = (x - y)^2$ for any $x, y \in X$ (see, for instance, reference [2]). Let $T : X \to X$ be defined as $Tx = 0$ for all $x \in [0, 1]$ and $Tx = 1$ for all $x \in [9/4, 11/4]$. Let us check that T is a partial contractivity:*

1. *If $x, y \in [0, 1]$ or $x, y \in [9/4, 11/4]$ then $d_2(Tx, Ty) = 0$ and inequality (7) is satisfied.*
2. *If $x \in [0, 1]$ and $y \in [9/4, 11/4]$ then $d_2(Tx, Ty) = 1$ and*

$$d_2(x, y) = (y - x)^2,$$

$$d_2(x, Tx) = d_2(x, 0) = x^2,$$

$$d_2(y, Ty) = d_2(y, 1) = (y - 1)^2.$$

Taking $a = B = 4/5$ we have

$$d_2(Tx, Ty) = 1 \leq \frac{4}{5}(y - x)^2 + \frac{4}{5}x^2 = \frac{4}{5}d_2(x, y) + \frac{4}{5}d_2(x, Tx),$$

$$d_2(Tx, Ty) = 1 \leq \frac{4}{5}(y - x)^2 + \frac{4}{5}(y - 1)^2 = \frac{4}{5}d_2(x, y) + \frac{4}{5}d_2(y, Ty).$$

Consequently T is a partial contractivity.

Example 2. *Let us consider the set $X = [0, 1] \cup [9/4, 11/4]$ with the usual metric and $T : X \to X$ defined as in Example 1. It is easy to check that T is also a partial contractivity with the same constants.*

Example 3. *The identity map is not a partial contractivity (condition (7) is incompatible with this type of mappings).*

The next example proves that a partial contractivity need not be continuous. It also shows that there exist partial contractivities that are not Banach contractions.

Example 4. *Let X be the interval $[0, 1]$ with the b-metric d_2 defined in Example 1, and $T : X \to X$ be defined as $Tx = x/2$ if $x \in [0, 1)$ and $T(1) = 0$. Let us see that T is a partial contractivity.*

1. *If $x, y \in [0, 1)$ then $d_2(Tx, Ty) = (x - y)^2/4$.*
2. *If $x \in [0, 1)$ and $y = 1$ then $d_2(Tx, Ty) = d_2(x/2, 0) = x^2/4$, $d_2(x, Tx) = d_2(x, x/2)^2 = x^2/4$, then*

$$d_2(Tx, Ty) = \frac{x^2}{4} \leq ad_2(x, y) + Bd_2(x, Tx) = a(x - y)^2 + B\frac{x^2}{4},$$

for $B = 1$.

Inequality (7) holds for any $x, y \in X$ taking $a = 1/4$ and $B = 1$. Consequently, T is a partial contractivity and T is discontinuous. T is not a Banach contraction since these types of maps are continuous.

In the reference [27], L. Ćirić proposed the concept of a quasi-contraction in a metric space. Next, we generalize it to a b-metric space.

Definition 9. *For a b-metric space (X, d), a self-map $T : X \to X$ is a quasi-contraction if there exists a real constant λ such that $0 < \lambda < 1$ such that for all $x, y \in X$*

$$d(Tx, Ty) \leq \lambda \max\{d(x, y), d(x, Tx), d(y, Ty), d(x, Ty), d(y, Tx)\}. \tag{9}$$

The quasi-contraction contains some other types of contractivities as particular cases, like Kannan, Chatterjea, and Reich self-maps. The next results states that a quasi-contraction is a partial contractivity if there is some relation between the ratio λ and the index s of the b-metric.

Proposition 14. *If (X, d) is a b-metric space and $T : X \to X$ is a quasi-contraction with ratio $\lambda > 0$ such that $\lambda < 1/(s(s + 1))$, then T is a partial contractivity with*

$$a = \frac{\lambda s}{1 - \lambda s^2}$$

and

$$B = \frac{\lambda s^2}{1 - \lambda s^2}.$$

Proof. For $x, y \in X$ let us denote

$$K = \max\{d(x, y), d(x, Tx), d(y, Ty), d(x, Ty), d(y, Tx)\}.$$

If $K = d(x, y)$, the expression (9) takes the form of (7) with $a = \lambda$ and $B = 0$.
If $K = d(x, Tx)$, we have the same result with $a = 0$ and $B = \lambda$.
In the case $K = d(y, Ty)$, we have

$$d(Tx, Ty) \leq \lambda s d(x, y) + \lambda s^2 d(x, Tx) + \lambda s^2 d(Tx, Ty),$$

and thus

$$d(Tx, Ty) \leq \frac{\lambda s}{1 - \lambda s^2} d(x, y) + \frac{\lambda s^2}{1 - \lambda s^2} d(x, Tx),$$

For $K = d(x, Ty)$, then

$$d(Tx, Ty) \leq \lambda s d(x, Tx) + \lambda s d(Tx, Ty),$$

and

$$d(Tx, Ty) \leq \frac{\lambda s}{1 - \lambda s} d(x, Tx).$$

For $K = d(y, Tx)$ then

$$d(Tx, Ty) \leq \lambda s d(x, y) + \lambda s d(x, Tx).$$

Since $\lambda \leq \lambda s \leq \frac{\lambda s}{1-\lambda s} \leq \frac{\lambda s}{1-\lambda s^2} \leq \frac{\lambda s^2}{1-\lambda s^2}$, in all the cases we have the expression (7) with the constants a, B given in the statement. □

Corollary 2. *If X is a metric space, any quasi-contraction with $0 < \lambda < 1/2$ is a partial contractivity.*

In the following example, we prove that the condition given for λ in Proposition 14 is sufficient, but it is not necessary.

Example 5. *Let Q_1, Q_2 be two subsets of natural numbers defined as*

$$Q_1 = \{\frac{p}{q} : p = \dot{3}, q = \dot{3} + 1\}$$

$$Q_2 = \{\frac{p}{q} : p = \dot{3}, q = \dot{3} + 2\},$$

and let us consider $X = Q_1 \cup Q_2$ with the metric d_2 defined in Example 1. Let $T : X \to X$ be defined as $Tx = 3x/5$ if $x \in Q_1$ and $Tx = x/8$ if $x \in Q_2$. Then,

1. *If $x, y \in Q_1$ or $x, y \in Q_2$, then $d_2(Tx, Ty) \leq \frac{9}{25} d_2(x, y)$.*
2. *If $x \in Q_1$ and $y \in Q_2$, then*
   If $x < \frac{5}{24} y$,

$$d_2(Tx, Ty) \leq \frac{9}{25}(\frac{5}{24}y - x)^2 \leq \frac{9}{25}(y - x)^2 = \frac{9}{25} d_2(x, y). \tag{10}$$

If $x > \frac{5}{24} y$,

$$d_2(Tx, Ty) \leq \frac{9}{25}(x - \frac{5}{24}y)^2 \leq \frac{9}{25}(x - \frac{y}{8})^2 = \frac{9}{25} d_2(x, Ty). \tag{11}$$

Then,

$$d_2(Tx, Ty) \leq \frac{18}{25} d_2(x, Tx) + \frac{18}{25} d_2(Tx, Ty),$$

and

$$d_2(Tx, Ty) \leq \frac{18}{7} d_2(x, Tx).$$

As a consequence, T is a partial contractivity with constants $a = \frac{9}{25}$ and $B = \frac{18}{7}$. The inequalities (10) and (11) prove that T is also a quasi-contraction for $\lambda = \frac{9}{25}$. However, the ratio λ does not satisfy the condition $\lambda < 1/(s(s+1))$ given in Proposition 14.

In the following, we give a theorem of collage type for partial contractivities.

Theorem 2. *If X is a b-metric space and $T : X \to X$ is a partial contractivity with a fixed point x^* and such that as <1, then, for any $x \in X$,*

$$\frac{1}{s(1+a)} d(x, Tx) \leq d(x, x^*) \leq \frac{s}{1 - sa} d(x, Tx).$$

Proof. For any $x \in X$, using (7),

$$d(x, Tx) \leq sd(x, x^*) + sd(x^*, Tx) \leq sd(x, x^*) + sad(x, x^*),$$

obtaining the left inequality. Now,

$$d(x, x^*) \leq sd(x, Tx) + sd(Tx, Tx^*) \leq sd(x, Tx) + sad(x, x^*).$$

Consequently,

$$d(x, x^*) \leq \frac{s}{1 - sa} d(x, Tx).$$

□

Corollary 3. *If X is a metric space and $T : X \to X$ is a partial contractivity with a fixed point x^*, then for any $x \in X$,*

$$\frac{1}{(1+a)} d(x, Tx) \leq d(x, x^*) \leq \frac{1}{(1-a)} d(x, Tx).$$

Remark 5. *Note that the collage theorem for a partial contractivity is identical to the corresponding result with a Banach contraction.*

Two Extensions of the Concept of Partial Contractivity

In this subsection, we propose two different ways of generalizing a partial contractivity. As a collateral result, we obtain sufficient conditions for the existence and uniqueness of fixed points for these type of mapping.

Definition 10. *Let us consider a map $\phi : \mathbb{R}^+ \to \mathbb{R}^+$ (called comparison function) such that $\phi^n(t)$ tends to zero for any t when n tends to infinity, and ϕ is increasing. Let $\psi : \mathbb{R}^+ \to \mathbb{R}^+$ be such that $\psi(t) \geq 0$ for any t and $\psi(0) = 0$.*

Let X be a b-metric space and $T : X \to X$ such that

$$d(Tx, Ty) \leq \phi(d(x, y)) + \psi(d(x, Tx)), \tag{12}$$

for any $x, y \in X$. Then, T is a (ϕ, ψ)-partial contractivity.

Remark 6. *For $\phi(t) = at$ with $0 < a < 1$ and $\psi(t) = Bt$ with $B \geq 0$ a (ϕ, ψ)-partial contractivity fits Definition 8.*

Remark 7. *The hypotheses given for the comparison function ϕ imply that $\phi(0) = 0$ and $\phi(t) < t$ (see, for instance, [28]).*

We have the following result.

Proposition 15. *If T is a (ϕ, ψ)-partial contractivity and it has a fixed point $x^* \in X$, then it is unique and the Picard iterations of any point converge to $x^* \in X$.*

Proof. Let x^* be a fixed point of T, and define $x_n := T^n x$ for $x \in X$. Applying the contractivity condition, we obtain:

$$d(x_n, x^*) \leq \phi(d(x_{n-1}, x^*)) \leq \ldots \leq \phi^n(d(x_0, x^*)).$$

The limit condition on the mapping ϕ implies that $x_n \to x^*$. This fact ensures that the fixed point is unique and the Picard iterations of any point converge to it. □

Corollary 4. *If T is a partial contractivity on a b-metric space X and it has a fixed point $x^* \in X$, then it is unique.*

The next concept involves a relation of partial type between two operators, which may have a common fixed point.

Definition 11. *The operators $T_1, T_2 : X \to X$, where X is a b-metric space, are mutual partial contractivities if there exists a positive constant a with $0 < a < 1$ and $B \geq 0$ such that for all $x, y \in X$*

$$d(T_1 x, T_2 y) \leq a d(x, y) + B \min\{d(x, T_1 x), d(y, T_2 y)\}. \tag{13}$$

Example 6. *Let us consider the space $X = [0, 1] \cup [9/4, 11/4]$ with the b-metric d_2 defined in Example 1, and the maps $T_1 : X \to X$ defined as $T_1 x = 0$ for all $x \in [0, 1]$ and $T_1 x = 1$ for*

all $x \in [9/4, 11/4]$, $T_2 : X \to X$, *defined as* $T_2 x = 0$ *for all* $x \in [0,1]$ *and* $T_2 x = 1/2$ *for all* $x \in [9/4, 11/4]$. *Let us check that* T_1 *and* T_2 *are mutual partial contractivities:*

For $x, y \in X$, *we have the following:*

1. *If* $x, y \in [0,1]$, *then* $d_2(T_1 x, T_2 y) = 0$, *and the inequality (13) holds.*
2. *If* $x, y \in [\frac{9}{4}, \frac{11}{4}]$, *then* $d_2(T_1 x, T_2 y) = 1/4$. *Then,* $d_2(x, T_1 x) = (x-1)^2$, $d_2(y, T_2 y) = (y - 1/2)^2$. *Taking* $a = B = 2/5$,

$$d_2(T_1 x, T_2 y) = \frac{1}{4} \leq \frac{2}{5}|x-y|^2 + \frac{2}{5}(x-1)^2 = \frac{2}{5}d_2(x,y) + \frac{2}{5}d_2(x, T_1 x)$$

and

$$d_2(T_1 x, T_2 y) = \frac{1}{4} \leq \frac{2}{5}|x-y|^2 + \frac{2}{5}(y-\frac{1}{2})^2 = \frac{2}{5}d_2(x,y) + \frac{2}{5}d_2(y, T_2 y)$$

3. $x \in [0,1]$ *and* $y \in [\frac{9}{4}, \frac{11}{4}]$ *then* $d_2(T_1 x, T_2 y) = 1/4$, $d_2(x, T_1 x) = x^2$, $d_2(y, T_2 y) = (y - 1/2)^2$. *Taking* $a = B = 2/5$,

$$d_2(T_1 x, T_2 y) = \frac{1}{4} \leq \frac{2}{5}|x-y|^2 + \frac{2}{5}x^2 = \frac{2}{5}d_2(x,y) + \frac{2}{5}d_2(x, T_1 x),$$

$$d_2(T_1 x, T_2 y) = \frac{1}{4} \leq \frac{2}{5}|x-y|^2 + \frac{2}{5}(y-\frac{1}{2})^2 = \frac{2}{5}d_2(x,y) + \frac{2}{5}d_2(y, T_2 y).$$

Consequently T_1, T_2 *are mutual partial contractivities with constants* $a = B = 2/5$.

Example 7. *Let us consider the space* $X = [0,1] \cup [9/4, 11/4]$ *with the usual metric and the maps* T_1, T_2 *defined as the previous example. It is easy to check that* T_1 *and* T_2 *are mutual partial contractivities as well, with the same constants.*

Let us obtain sufficient conditions for the existence of a common fixed point for mutual partial contractivities. For it, we will use a result given in [29].

Proposition 16. *Let* (X, d) *be a b-metric space. Any sequence* $(x_n) \subseteq X$ *such that there exists* $\alpha \in [0,1)$ *satisfying the inequality*

$$d(x_{n+1}, x_n) \leq \alpha d(x_n, x_{n-1})$$

for all $n \geq 1$ *is a Cauchy sequence.*

Theorem 3. *Let* (X, d) *be a complete b-metric space and* T_1, T_2 *be two mutual partial contractivities with constants a and B. Then, if* $a + B < 1$, T_1, T_2 *have a unique common fixed point.*

Proof. Let us consider any element $x \in X$ and construct the sequence: $x_0 := x$, $x_1 := T_1 x_0$, $x_2 := T_2 x_1$, $x_3 := T_1 x_2$, and so on. Using the contractivity condition, we have

$$d(x_1, x_2) = d(T_1(x_0), T_2(x_1)) \leq a d(x_0, x_1) + B d(x_0, x_1) = (a + B) d(x_0, x_1).$$

In general, we find that

$$d(x_n, x_{n+1}) \leq (a + B) d(x_{n-1}, x_n).$$

This condition implies that the sequence is Cauchy (Proposition 16). Consequently, the sequence (x_n) is convergent and $x^* = \lim_{n \to \infty} x_n$. Let us see that the limit x^* is the common fixed point of T_1 and T_2. Considering an even $n \in \mathbb{N}$,

$$d(x^*, T_1(x^*)) \leq s d(x^*, x_n) + s d(x_n, T_1(x^*)) = s d(x^*, x_n) + s d(T_2(x_{n-1}), T_1(x^*)).$$

Applying the condition of mutual partial contractivity in the last term,

$$d(x^*, T_1(x^*)) \leq sd(x^*, x_n) + s(ad(x_{n-1}, x^*) + Bd(x_{n-1}, x_n)).$$

Since the right terms tend to zero, we obtain that $T_1(x^*) = x^*$. The equality $x^* = T_2(x^*)$ is proved in a similar way.

Let us assume that there exist two common fixed points x^*, x^+:

$$d(x^*, x^+) = d(T_1 x^*, T_2 x^+) \leq ad(x^*, x^+).$$

This implies that $x^* = x^+$. □

Corollary 5. *Let (X, d) be a complete b-metric space and T be a partial contractivity such that $a + B < 1$; then, T has a unique fixed point. In particular, if T is a Banach contraction and the ratio is such that $a < 1$, then it has a unique fixed point.*

Remark 8. *Note that the relation $a + B < 1$ is a sufficient condition for the existence of fixed point, but it is not necessary. For instance, the contractivity of Example 1 has a fixed point $x^* = 0$, but $a + B = 8/5$.*

Corollary 6. *Let (X, d) be a complete b-metric space and T be such that there exists $B < 1$ satisfying*

$$d(Tx, Ty) \leq Bd(x, Tx),$$

for all $x, y \in X$. Then, T has a unique fixed point.

4. Iterative Procedures for the Approximation of Fixed Points of a Partial Contractivity

In this section, we study the convergence and stability of some types of iterations for the approximation of fixed points of partial contractivities.

We have seen in Proposition 15 that if X is a b-metric space, and $T : X \to X$ is a partial contractivity with a fixed point $x^* \in X$, then the Picard iterations $T^n(x)$ converge to it for any $x \in X$.

Moreover, let $x^* \in X$ be the fixed point of T. Applying the contractivity condition for any $x \in X$:

$$d(T^n(x), x*) \leq ad(T^{n-1}x, x^*) \leq \ldots \leq a^n d(x, x^*),$$

and consequently, $d(T^n x, x^*) \to 0$ with a rate of convergence of $O(a^n)$.

In the following, we study two different iterative methods to approach a fixed point of a partial contractivity in the framework of a quasi-normed space (see, for instance, [30]).

Definition 12. *If X is a real linear space, the mapping $|\cdot|_s : X \times X \to \mathbb{R}^+$ is a quasi-norm of index s if*

1. $|x|_s \geq 0$; $x = 0$ *if and only if* $|x|_s = 0$.
2. $|\lambda x|_s = |\lambda||x|_s$.
3. *There exists $s \geq 1$ such that $|x + y|_s \leq s(|x|_s + |y|_s)$ for any $x, y \in X$.*

Then, the space $(X, |\cdot|_s)$ is a quasi-normed space.

Remark 9. *A quasi-normed space is a particular case of b-metric space, concerning the distance induced by the quasi-norm. If X is complete for this b-metric, then X is a quasi-Banach space.*

The Noor algorithm (see, for instance, [31]) is a method for the approximation of fixed points for self-maps defined on normed spaces. This is based on the three-step iterative procedure given for $n \geq 0$ by

$$x_{n+1} = (1 - a_n)x_n + a_n T y_n, \tag{14}$$

$$y_n = (1 - b_n)x_n + b_n T z_n, \tag{15}$$

$$z_n = (1 - c_n)x_n + c_n T x_n, \tag{16}$$

for $0 \leq a_n \leq 1$, $0 \leq b_n \leq 1$, $0 \leq c_n \leq 1$.

As particular cases of this method, we have:

- For $c_n = 0$ for all n, the procedure agrees with the Ishikawa iteration [32].
- In the case $b_n = c_n = 0$ for all n, the algorithm is a Mann iteration [33]. If, additionally, a_n is constant, we have the Krasnoselskii iteration [34].

Let us consider a partial contractivity $T : X \to X$ with a fixed point $x^* \in X$, where X is a quasi-normed space, and let us study the convergence of the Noor iterations under the hypothesis $as^2 < 1$. Let us note that for a metric space, this condition is satisfied by any partial contractivity.

For the sake of simplicity, we will denote as $|\cdot|$ the quasi-norm written before as $|\cdot|_s$.

Applying (14) and the contractivity condition,

$$|x_{n+1} - x^*| = |(1 - a_n)(x_n - x^*) + a_n(Ty_n - x^*)| \leq s(1 - a_n)|x_n - x^*| + sa_n|Ty_n - x^*|. \tag{17}$$

and

$$|x_{n+1} - x^*| \leq s(1 - a_n)|x_n - x^*| + saa_n|y_n - x^*|. \tag{18}$$

By (15),

$$|y_n - x^*| = |(1 - b_n)(x_n - x^*) + b_n(Tz_n - x^*)| \leq s(1 - b_n)|x_n - x^*| + sb_n|Tz_n - x^*|. \tag{19}$$

Using step (16),

$$|Tz_n - x^*| \leq a|z_n - x^*| \leq a|(1 - c_n)(x_n - x^*) + c_n(Tx_n - x^*)|, \tag{20}$$

$$|Tz_n - x^*| \leq as(1 - c_n)|x_n - x^*| + a^2sc_n|x_n - x^*| \tag{21}$$

and consequently,

$$|Tz_n - x^*| \leq as|x_n - x^*|. \tag{22}$$

Applying (22) in (19),

$$|y_n - x^*| \leq (s(1 - b_n) + as^2b_n)|x_n - x^*|. \tag{23}$$

As a consequence, by (18),

$$|x_{n+1} - x^*| \leq (s(1 - a_n) + asa_n(s - sb_n(1 - as)))|x_n - x^*|. \tag{24}$$

Since $s - sb_n(1 - as) \leq s$, we have

$$|x_{n+1} - x^*| \leq (s(1 - a_n(1 - sa))|x_n - x^*|. \tag{25}$$

Let us consider a constant k such that $s(1 - a_n(1 - sa)) < k < 1$. Then,

$$|x_{n+1} - x^*| \leq k|x_n - x^*| \tag{26}$$

for

$$\frac{1 - s^{-1}k}{1 - as} < a_n \leq 1 \tag{27}$$

and $as^2 < k < 1$.

In this case, the convergence of x_n to x^* is ensured due to the bounding

$$|x_n - x^*| \leq k^n |x_0 - x^*|,$$

and the stability is asymptotic. This is limited to the values of a_n satisfying inequalities (27).

Now, we consider the so-called SP-algorithm (see, for instance, [35]) for the approximation of fixed points. We are going to apply this procedure for the case of a partial contractivity with a fixed point in a quasi-normed space. This is based on a different three-step iterative procedure given for $n \geq 0$ by:

$$x_{n+1} = (1 - a_n)y_n + a_n T y_n, \tag{28}$$

$$y_n = (1 - b_n)z_n + b_n T z_n, \tag{29}$$

$$z_n = (1 - c_n)x_n + c_n T x_n, \tag{30}$$

for $0 \leq a_n \leq 1$, $0 \leq b_n \leq 1$, $0 \leq c_n \leq 1$.

For $a_n = c_n = 1$ for all n, one obtains the Karakaya method as a particular case of the SP-algorithm (see, for instance, [36,37]).

Let us consider $x^* \in Fix(T)$, where $Fix(T)$ represents the set of fixed points of a partial contractivity $T : X \to X$, where X is a quasi-normed space, and let us study the convergence of these iterations under the hypothesis $as < 1$.

Applying (30) and the contractivity condition,

$$|z_n - x^*| \leq s(1 - c_n)|x_n - x^*| + sc_n a|x_n - x^*| \leq s(1 - c_n(1 - a))|x_n - x^*|. \tag{31}$$

Using (29) and (31),

$$|y_n - x^*| \leq s(1 - b_n)|z_n - x^*| + sb_n a|z_n - x^*| \leq s^2(1 - b_n(1 - a))(1 - c_n(1 - a))|x_n - x^*|. \tag{32}$$

By (28),

$$|x_{n+1} - x^*| \leq s^3(1 - a_n(1 - a))(1 - b_n(1 - a))(1 - c_n(1 - a))|x_n - x^*|. \tag{33}$$

Let us consider a constant k such that

$$(1 - a_n(1 - a)) < k < s^{-1},$$

$$(1 - b_n(1 - a)) < k < s^{-1},$$

$$(1 - c_n(1 - a)) < k < s^{-1}.$$

Then, by (33),

$$|x_{n+1} - x^*| \leq (ks)^3 |x_n - x^*|. \tag{34}$$

The values of a_n, b_n, c_n must be

$$\frac{1 - s^{-1}}{1 - a} < \frac{1 - k}{1 - a} < a_n, b_n, c_n \leq 1. \tag{35}$$

Then, we must take $a < k < s^{-1}$.

In this case, the convergence of x_n to x^* is ensured and the stability is asymptotic. The rate of convergence is $O((ks)^{3n})$.

Remark 10. *Note that the condition on the ratio of the SP-algorithm ($as < 1$) is better than the one of Noor's method ($as^2 < 1$). If X is a normed space, both are reduced to the basic hypothesis $a < 1$. The condition on k ($k > a$) is also better in the SP-algorithm than that of the Noor procedure ($k > as^2$).*

For a normed space, the order of convergence is k^n for Noor and k^{3n} for SP. We can conclude that generally speaking, for convergence with asymptotic stability, the SP-algorithm is better for coefficients a_n, b_n, c_n satisfying the conditions prescribed.

5. An Application to the Solution of an Integral Equation

In this section, we consider an application to finding the solution of an integral equation of Urysohn type. This is expressed as

$$u(x) = f(x) + \int_0^1 F(x, y, u(y))dy, \tag{36}$$

where $x \in [0, 1]$, and $f : [0, 1] \to \mathbb{R}$, $F : [0, 1]^2 \times \mathbb{R} \to \mathbb{R}$ are given continuous maps. If $F(x, y, u(y)) = K(x, y)G(y, u(y))$, we obtain Hammerstein's integral equation ([38,39]), but we will study here the general case.

We consider the space of continuous functions $C[0, 1]$ endowed with the b-metric:

$$d(u, v) := |u - v|_2 := \sup\{(u(x) - v(x))^2 : x \in [0, 1]\}.$$

for all $u, v \in C[0, 1]$. Let us consider the operator

$$Tu(x) = f(x) + \int_0^1 F(x, y, u(y))dy. \tag{37}$$

It is obvious that finding the solution of Equation (36) is equivalent to the search for a fixed point of the operator T on $C[0, 1]$. In the following, we define some sufficient conditions for the existence of such fixed point.

Let us assume that the map F is such that

$$|F(x, y, u(y)) - F(x, y, v(y))| \leq G(x, y, u(y), v(y))g(x, u), \tag{38}$$

where $G : [0, 1]^2 \times \mathbb{R}^2 \to [0, \nu)$, $\nu < 1$, and $g(x, u) = |(u - f)(x) - \int_0^1 F(x, y, u(y))dy|$ for $x, y \in I$ and $u \in C[0, 1]$. Then,

$$|Tu - Tv|_2 \leq \sup_{x \in I}(\int_0^1 |F(x, y, u(y) - F(x, y, v(y)|dy)^2.$$

Thus, applying condition (38),

$$|Tu - Tv|_2 \leq \nu^2 \sup_{x \in I} \int_0^1 (u(x) - Tu(x))^2 dy \leq \nu^2 |u - Tu|_2.$$

The operator T is a partial contractivity with $a = 0$ and $B = \nu^2$. Since the considered space is complete and $a + B < 1$, according to Corollary 5, there is a single fixed point, and Equation (36) has a unique solution. To obtain this solution, we can use the Picard iterative scheme, defining, for $v \in C[0, 1]$, $v_0 := v$; and for $k \geq 0$

$$v_{k+1}(x) := f(x) + \int_0^1 F(x, y, v_k(y))dy.$$

SP and Noor algorithms may also be used, with the convergence values of a_n, b_n, c_n obtained in the previous section.

We consider now a different case. Let $C_w[0, 1]$ denote the set of continuous real functions defined on the interval $I = [0, 1]$ endowed with the general norm

$$||g||_w = \sup_{x \in I} w(x)|g(x)|,$$

for all $g \in C_w[0,1]$, and a fixed continuous function $w : I \to \mathbb{R}$ such that $w(x) > 0$ for any $x \in I$. Let us assume that $F(x,y,z) = j(x,y)(h(x) + M|z|)$, for $j \in C([0,1]^2)$, $h \in C[0,1]$ and $M \in \mathbb{R}$. Let us see that in this case, the Urysohn equation has also a solution for some conditions on M and j.

$$|F(x,y,u(y)) - F(x,y,v(y))| \leq |M||j(x,y)||u(y) - v(y)| \leq |M|||j||_\infty |u(y) - v(y)|.$$

Then

$$||Tu - Tv||_w \leq \sup_{x \in I} w(x) \int_0^1 |F(x,y,u(y) - F(x,y,v(y)|dy \leq |M|||j||_\infty ||u - v||_w.$$

If $|M|||j||_\infty < 1$, then T is a partial contractivity with $a = |M|||j||_\infty$ and $B = 0$. Hence, T has a fixed point and Equation (36) has a solution. The way to find it iteratively is similar to the previous case.

6. Partial Contractivities in Strong b-Metric Spaces

We refine here some results given in previous sections in the case where X is a strong b-metric space.

Proposition 17. *Let (X,d) be a strong b-metric space. If $T : X \to X$ is a quasi-contraction with $\mu < (1+s)^{-1}$, then T is a partial contractivity with constants $a = \frac{\mu}{1-\mu s} < 1$ and $B = \frac{\mu s^2}{1-\mu s}$.*

Proof. The definition of a quasi-contraction implies, for any $x, y \in X$,

$$d(Tx,Ty) \leq \mu M(x,y),$$

where $M(x,y) = \max\{d(x,y), d(x,Tx), d(y,Ty), d(x,Ty), d(y,Tx)\}$.

If $M(x,y) = d(x,Ty)$ then

$$d(Tx,Ty) \leq \mu d(x,Ty) \leq \mu d(x,Tx) + \mu s d(Tx,Ty).$$

Consequently,

$$d(Tx,Ty) \leq \frac{\mu}{1-\mu s} d(x,Tx).$$

If $M(x,y) = d(y,Ty)$ then

$$d(Tx,Ty) \leq \mu d(y,Ty) \leq \mu d(x,y) + \mu s d(x,Ty),$$

and

$$d(Tx,Ty) \leq \mu d(x,y) + \mu s(s d(x,Tx) + d(Tx,Ty)).$$

Then,

$$d(Tx,Ty) \leq \frac{\mu}{1-\mu s} d(x,y) + \frac{\mu s^2}{1-\mu s} d(x,Tx).$$

If $M(x,y) = d(y,Tx)$ then

$$d(Tx,Ty) \leq \mu d(y,Tx) \leq \mu d(x,y) + \mu s d(x,Tx).$$

For all the cases, we have

$$d(Tx,Ty) \leq \frac{\mu}{1-\mu s} d(x,y) + \frac{\mu s^2}{1-\mu s} d(x,Tx).$$

Thus, taking $a = \frac{\mu}{1-\mu s} < 1$ for the hypothesis given, and $B = \frac{\mu s^2}{1-\mu s}$, we obtain the inequality corresponding to a partial contractivity. □

In the following, we refine the collage theorem for partial contractivities in the case of strong b-metric spaces.

Theorem 4. *If X is a strong b-metric space and $T : X \to X$ is a partial contractivity with a fixed point x^*, then for any $x \in X$,*

$$\frac{1}{(s+a)} d(x, Tx) \leq d(x, x^*) \leq \frac{s}{1-a} d(x, Tx).$$

Proof. For any $x \in X$, using (5),

$$d(x, Tx) \leq sd(x, x^*) + d(x^*, Tx) \leq sd(x, x^*) + ad(x, x^*),$$

obtaining the left inequality. Now,

$$d(x, x^*) \leq sd(x, Tx) + d(Tx, Tx^*) \leq sd(x, Tx) + ad(x, x^*).$$

Consequently,

$$d(x, x^*) \leq \frac{s}{1-a} d(x, Tx).$$

□

7. Mutual Contractions

The concepts of weak contraction [28,40] and quasi-contraction [27] include in the metric case some other contractivities present in the current literature of fixed point theory. In this section, we prove some relations between mutual partial contractivities (Definition 11), mutual quasi-contractions (Definition 13) and mutual weak contractions (Definition 14).

As said previously, a quasi-contraction was defined by L. Ćirić [27] as a self-map $T : X \to X$ satisfying the inequality

$$d(Tx, Ty) \leq \mu \max\{d(x, y), d(x, Tx), d(y, Ty), d(x, Ty), d(y, Tx)\}. \tag{39}$$

for any $x, y \in X$, with μ being a fixed real constant such that $0 < \mu < 1$. Let us consider now a b-metric space, and let us extend the concept of a quasi-contraction and weak contraction to two operators with a common condition.

Definition 13. *The operators $T_1, T_2 : X \to X$, where X is a b-metric space, are mutual quasi-contractions of if there exists a positive constant μ such that $\mu < 1$ and for all $x, y \in X$*

$$d(T_1x, T_2y) \leq \mu \max\{d(x, y), d(x, T_1x), d(y, T_2y), d(x, T_2y), d(y, T_1x)\}. \tag{40}$$

Definition 14. *The operators $T_1, T_2 : X \to X$, where X is a b-metric space, are mutually weak contractive (or mutual weak contractions) if there exist a constant c, such that $0 < c < 1$, and $L \geq 0$ satisfying for all $x, y \in X$*

$$d(T_1x, T_2y) \leq cd(x, y) + Ld(y, T_1x). \tag{41}$$

Remark 11. *Taking $T_1 = T_2$ in Definition 13 we obtain a quasi-contraction. Definition 14 for $T_1 = T_2$ provides a weak contraction. In this way, these definitions extend the concept of the corresponding contractivities given in the previous literature.*

Proposition 18. *Let X be a b-metric space and T_1, T_2 be mutual quasi-contractions with constant μ such that $\mu < s^{-1}(s+1)^{-1}$; then, T_1, T_2 are mutual weak contractions.*

Proof. For any $x, y \in X$, let us define

$$M(x, y) := \{d(x, y), d(x, T_1x), d(y, T_2y), d(x, T_2y), d(y, T_1x)\}.$$

If $\max M(x,y) = d(x,y)$, then obviously, inequality (40) takes the form (41) with $L = 0$.
If $\max M(x,y) = d(x,T_1x)$, then

$$d(T_1x, T_2y) \leq \mu d(x,T_1x) \leq \mu s d(x,y) + \mu s d(y,T_1x).$$

In the case where $\max M(x,y) = d(y,T_2y)$, we have

$$d(T_1x, T_2y) \leq \mu d(y,T_2y) \leq \mu s d(y,T_1x) + \mu s d(T_1x,T_2y)$$

and thus,

$$d(T_1x, T_2x) \leq \frac{\mu s}{1-\mu s} d(y,T_1x),$$

since $\mu s < (s+1)^{-1} < 1$.
If $\max M(x,y) = d(x,T_2y)$ then

$$d(T_1x, T_2y) \leq \mu d(x,T_2y) \leq \mu s d(x,y) + \mu s d(y,T_2y)$$

and

$$d(T_1x, T_2y) \leq \mu s d(x,y) + \mu s(s d(y,T_1x) + s d(T_1x,T_2y)).$$

Thus, since $\mu < s^{-1}(s+1)^{-1} < s^{-2}$,

$$d(T_1x, T_2y) \leq \frac{\mu s}{1-\mu s^2} d(x,y) + \frac{\mu s^2}{1-\mu s^2} d(y,T_1x).$$

If $\max M(x,y) = d(y,T_1x)$ then obviously,

$$d(T_1x, T_2y) \leq \mu d(y,T_1x).$$

As

$$\mu \leq \mu s < \frac{\mu s}{1-\mu s^2}$$

and

$$\mu s < \frac{\mu s}{1-\mu s} \leq \frac{\mu s^2}{1-\mu s^2}$$

we obtain inequality (41) in all the cases for $c = \frac{\mu s}{1-\mu s^2}$ and $L = \frac{\mu s^2}{1-\mu s^2}$. The condition given for μ in the statement implies that $c < 1$. Consequently, T_1, T_2 are mutual weak contractions. □

Corollary 7. *If T is a quasi-contraction on a b-metric space and $\mu < s^{-1}(s+1)^{-1}$, then T is a weak contraction.*

The condition given in this corollary is sufficient, but it is not necessary. In reference [41], the author presents the following example: Let $X = [0,1]$ be endowed with the usual metric, and $T : X \to X$ be defined as $Tx = 2/3$ for $x \in [0,1)$ and $T(1) = 0$. Then, T is a quasi-contraction with $\mu \in [2/3, 1)$ and a weak contraction for $c \geq 2/3$ and $L \geq c$. However, μ does not satisfy the condition $\mu < s^{-1}(s+1)^{-1}$. The map T is not a partial contractivity (see Example 2 of Reference [41]). Consequently, a weak contraction need not be a partial contractivity.

The next result proves that two mutually weak contractive maps have always a common fixed point.

Theorem 5. *Let (X,d) be a complete b-metric space and T_1, T_2 two mutual weak contractions. Then, T_1, T_2 have a common fixed point. If $c + L < 1$, the fixed point is unique.*

Proof. Let us consider any element $x \in X$ and construct the sequence $x_0 := x$, $x_1 := T_1 x_0$, $x_2 := T_2 x_1$, $x_3 := T_1 x_2$, and so on. Using inequality (41), we have

$$d(x_1, x_2) = d(T_1(x_0), T_2(x_1)) \leq cd(x_0, x_1)$$

$$d(x_2, x_3) = d(T_2(x_1), T_1(x_2)) \leq cd(x_1, x_2) \leq c^2 d(x_0, x_1).$$

Thus, we obtain

$$d(x_n, x_{n+1}) \leq cd(x_{n-1}, x_n).$$

This condition implies that the sequence is Cauchy (see Proposition 16). Consequently, the sequence (x_n) is convergent to $x^* = \lim_{n\to\infty} x_n$. Let us see that the limit x^* is the common fixed point of T_1 and T_2. Considering an even $n \in \mathbb{N}$,

$$d(x^*, T_1(x^*)) \leq sd(x^*, x_n) + sd(x_n, T_1(x^*)) = sd(x^*, x_n) + sd(T_2(x_{n-1}), T_1(x^*)).$$

Applying the condition of weak contractivity in the last term,

$$d(x^*, T_1(x^*)) \leq sd(x^*, x_n) + s(cd(x_{n-1}, x^*) + Ld(x^*, x_n)).$$

Thus,

$$d(x^*, T_1(x^*)) \leq (Ls + s)d(x^*, x_n) + csd(x_{n-1}, x^*).$$

Since the right terms tend to zero, we obtain that $T_1(x^*) = x^*$. The equality $x^* = T_2(x^*)$ is proved in a similar way.

If $c + L < 1$, let us assume that there exist two common fixed points x^*, x^+:

$$d(x^*, x^+) = d(T_1 x^*, T_2 x^+) \leq cd(x^*, x^+) + Ld(x^*, T_2 x^+) = (c + L)d(x^*, x^+).$$

This implies that $x^* = x^+$. □

Corollary 8. *Let (X, d) be a complete b-metric space and T a weak contraction. Then T has a fixed point. If $c + L < 1$ then it is unique.*

Theorem 6. *Let (X, d) be a complete b-metric space and T_1, T_2 two mutual weak contractions and mutual quasi-contractions. Then, T_1, T_2 have a unique common fixed point.*

Proof. The existence of common fixed points has been proved in Theorem 5. For the uniqueness, let us assume that there are two common fixed points: x^*, x^+, and let us apply the condition of mutual quasi-contraction (40):

$$d(x^*, x^+) \leq \mu d(x^*, x^+).$$

Since $\mu < 1$, we have the equality $x^* = x^+$. □

Theorem 7. *Let (X, d) be a complete b-metric space and T_1, T_2 two mutual quasi-contractions with $\mu < s^{-1}(1 + s)^{-1}$; then, T_1, T_2 have a unique common fixed point.*

Proof. According to the Proposition 18, T_1, T_2 are also weak contractions, and we are in the conditions of the Theorem 6. □

Theorem 8. *Let (X, d) be a complete b-metric space, T_1, T_2 be mutual weak contractions and there exist $c, L' \in \mathbb{R}$ with $0 < c < 1$, $L \geq 0$ such that for any $x, y \in X$*

$$d(T_1 x, T_2 y) \leq cd(x, y) + Ld(x, T_1 x), \tag{42}$$

(that is to say, T_1 and T_2 are mutual partial contractivities); then, the common fixed point of T_1 and T_2 is unique.

Proof. According to Theorem 5, T_1, T_2 have a common fixed point. Let us assume that x^*, x^+ are two common fixed points, applying the inequality (42),

$$d(x^*, x^+) = d(T_1 x^*, T_2 x^+) \leq c d(x^*, x^+),$$

and consequently, $x^* = x^+$. □

Let us consider now a collage theorem for weak contractions, with some conditions on the constants. In this case, we obtain upper and lower bounds for the distance between an element and the fixed point of a weak contraction T.

Theorem 9. *Let X be a b-metric space and $T : X \to X$ be a weak contraction with a fixed point x^*. Then, for any $x \in X$,*

$$\frac{1}{(s + cs + Ls)} d(x, Tx) \leq d(x, x^*).$$

If the constants are such that $(c + L) < s^{-1}$ then, for any $x \in X$,

$$d(x, x^*) \leq \frac{s}{(1 - cs - Ls)} d(x, Tx).$$

Proof. We assume that T owns a fixed point x^*. For the lower bound of $d(x, x^*)$, let us consider that

$$d(x, Tx) \leq s d(x, x^*) + s d(Tx^*, Tx)$$

and thus,

$$d(x, Tx) \leq s d(x, x^*) + scd(x, x^*) + sLd(x, x^*).$$

$$\frac{1}{(s + cs + Ls)} d(x, Tx) \leq d(x, x^*).$$

For the second inequality, applying the third property of a b-metric and the contractivity condition (41), for any $x \in X$,

$$d(x, x^*) \leq s d(x, Tx) + s d(Tx, Tx^*) \leq s d(x, Tx) + scd(x, x^*) + sLd(x, x^*),$$

obtaining that

$$(1 - cs - Ls) d(x, x^*) \leq s d(x, Tx),$$

and the result is completed. □

Remark 12. *If X is complete and $c + L < s^{-1}$, then the fixed point x^* exists according to Corollary 8, and the inequalities of Theorem 9 hold.*

Corollary 9. *In particular, for a metric space X, we obtain that for for any $x \in X$, a fixed point x^* and a weak contraction T, one has*

$$\frac{1}{(1 + c + L)} d(x, Tx) \leq d(x, x^*) \leq \frac{1}{(1 - c - L)} d(x, Tx),$$

if $c + L < 1$. For a Banach contraction, we obtain the chain of inequalities

$$\frac{1}{(1 + c)} d(x, Tx) \leq d(x, x^*) \leq \frac{1}{(1 - c)} d(x, Tx).$$

8. Conclusions

In the first place, we have reviewed some topological aspects of b-metric spaces, in order to give a brief background for this type of structure. The results given establish, for instance, that a compact set is totally bounded in this framework. We have summarized

important results related to continuous functions, the existence of extreme values and metrizability.

In subsequent sections, we have described some properties of a partial contractivity (introduced by the first author in reference [37]. This concept has some similarities with a weak contraction as, for instance, the fact of containing several well-known contractions as particular cases. A difference lies in the existence of fixed points: a weak contraction defined on a complete metric space has always some fixed point; however, a partial contractivity may not have it. This lack does not prevent the self-map of having periodic points and a rich dynamics.

We have proved that a quasi-contraction is a partial contractivity if the constant associated is related to the index of the b-metric through a specific inequality. We have also extended the definition to a more general setting, and considered mutual partial contractivities, which relate two self-maps satisfying a joint inequality. In the latter case, we established sufficient conditions for the existence of a common fixed point.

In the case of quasi-normed spaces (particular cases of b-metric sets), we have studied the convergence and stability of two different iterative algorithms: the three-step Noor's procedure and the so-called SP-algorithm. We have obtained values on the parameters of these methods that assure convergence to a fixed point and stability of the computations. We have applied the concepts described to the resolution of an integral equation of Urysohn type, in the framework of b-metric spaces. We have given sufficient conditions on the integrand to ensure the existence and uniqueness of the solution, and some iterative methods for approximating it.

In subsequent sections, we have refined some results obtained for partial contractivities in the case of a strong b-metric space. We have established also some relations between weak and quasi-contractions and the new types of contractivity.

Through the results obtained, we generalize to some extent the modern theory of fixed points and common fixed points of self-maps defined on b-metric and quasi-normed spaces, and their approximation methods.

Author Contributions: Conceptualization, M.A.N. and R.N.M.; methodology, M.A.N.; validation, M.A.N. and R.N.M.; formal analysis, M.A.N. and R.N.M.; writing—original draft preparation, M.A.N.; writing—review and editing, M.A.N.; supervision, R.N.M. All authors have read and agreed to the published version of the manuscript.

Funding: The first author was partially funded by the Mohapatra Family Foundation.

Data Availability Statement: Data are contained within the article.

Acknowledgments: The first author acknowledges the invitation of University of Central Florida for several research stays, and the second author is grateful to the Mohapatra Family Foundation for supporting the visit of María A. Navascués, which made this work possible.

Conflicts of Interest: The authors declare that the publication of this paper has no conflicts of interest.

References

1. Paluszyinski, M.; Stempak, K. On quasi-metric and metric spaces. *Proc. AMS* **2009**, *137*, 4307–4312. [CrossRef]
2. Rano, G.; Bag, T. Quasi-metric space and fixed point theorems. *Int. J. Math. Sci. Comp.* **2013**, *3*, 27–31.
3. Hitzler, P. Generalized Metrics and Topology in Logic Programming Semantics. Ph.D. Thesis, Department of Mathematics, National University of Ireland, University College Cork, Cork, Ireland, 2001.
4. Wilson, W.A. On quasi-metric spaces. *Am. J. Math.* **1931**, *53*, 675–684. [CrossRef]
5. Kannan, R. Some results on fixed points. *Bull. Calcutta Math. Soc.* **1968**, *60*, 71–76.
6. Kannan, R. Some results on fixed points. II. *Am. Math. Mon.* **1969**, *76*, 405–408.
7. Mohapatra, R.N.; Navascués, M.A.; Sebastián, M.V.; Verma, S. Iteration of operators with contractive mutual relations of Kannan type. *Mathematics* **2022**, *10*, 2632. [CrossRef]
8. Chatterjea, S.K. Fixed-point theorems. *CR Acad. Bulg. Sci.* **1972**, *25*, 727–730. [CrossRef]
9. Urysohn, P.S. Sur une classe d'equations integrales non lineaires. *Mat. Sb.* **1923**, *31*, 236–255.
10. Berinde, V.; Pacurar, M. The early developments in fixed point theory on b-metric spaces: A brief survey and some important related aspects. *Carpathian J. Math.* **2022**, *38*, 523–538. [CrossRef]

11. Coifman, R.R.; de Guzmán, M. Singular integrals and multipliers on homogeneous spaces. *Rev. Un. Mat. Argent.* **1970**, *25*, 137–143.
12. Aimar, H.; Iaffei, B.; Nitti, L. On the Macías-Segovia metrization of quasi-metric spaces. *Rev. Un. Mat. Argent.* **1998**, *41*, 67–75.
13. Cobzas, S.; Czerwik, S. The completion of generalized b-metric spaces and fixed points. *Fixed Point Theory* **2020**, *21*, 133–150. [CrossRef]
14. Bakhtin, I.A. Contraction mapping principle in an almost metric space. *Funkts. Anal.* **1989**, *30*, 26–37. (In Russian)
15. Czerwick, S. Contraction mappings in b-metric spaces. *Acta Math. Inform. Univ. Ostrav.* **1993**, *I* , 5–11.
16. Czerwick, S. Non-linear set-valued contraction mappings in b-metric spaces. *Atti. Sem. Math. Fiz. Univ. Modena* **1998**, *46*, 263–276.
17. An T.V.; Tuyen, L.Q.; Dung, N.V. Answers to Kirk-Shahzad's questions on strong b-metric spaces. *Taiwan. J. Math.* **2016**, *20*, 1175–1180. [CrossRef]
18. Dung, N.V.; An, T.V.; Le Hang, V.T. Remarks on Frinck's metrization technique and applications. *Fixed Point Theory Appl.* **2019**, *20*, 157–176. [CrossRef]
19. Fagin, R.; Kumar, R.; Sivakumar, D. Comparing top k lists. *SIAM J. Discret. Math.* **2003**, *17*, 134–160. [CrossRef]
20. Khamsi, M.A.; Hussain, N. KKM mappings in metric type spaces. *Nonlinear Anal.* **2010**, *73*, 3123–3129. [CrossRef]
21. Kirk, W.; Shahz, N. *Fixed Point Theory in Distance Spaces*; Springer: Cham, Switzerland, 2014.
22. Oner, T.; Sostak, A. On metric-type spaces based on extended t-conorms. *Mathematics* **2020**, *8*, 1097. [CrossRef]
23. Sostak, A. Some remarks on fuzzy k-pseudometric spaces. *Filomat* **2018**, *32*, 3567–3580. [CrossRef]
24. Sostak, A.; Oner, T.; Duman, I.C. On topological and metric properties of $\oplus$-sb-Metric Spaces. *Mathematics* **2023**, *11*, 4090. [CrossRef]
25. Doan, H. A new type of Kannan's fixed point theorem in strong b-metric spaces. *AIMS Math.* **2021**, *6*, 7895–7908. [CrossRef]
26. Navascués, M.A.; Jha, S.; Ch, A.K.B.; Mohapatra, R.N. Iterative schemes involving several mutual contractions. *Mathematics* **2023**, *11*, 2019. [CrossRef]
27. Ćirić, L.B. A generalization of Banach's contraction principle. *Proc. Am. Math. Soc.* **1974**, *45*, 267–273. [CrossRef]
28. Berinde, V. Iterative Approximation of Fixed Points. In *Lecture Notes in Mathematics*; Springer: Berlin-Heidelberg, Germany, 2007.
29. Miculescu, R.; Mihail, A. New fixed point theorems for set-valued contractions in b-metric spaces. *J. Fixed Point Theory Appl.* **2017**, *19*, 2153–2163. [CrossRef]
30. Köthe, G. *Topological Vector Spaces*; Springer: Berlin/Heidelberg, Germany, 1969.
31. Noor, M.A. New approximation schemes for general variational inequalities. *J. Math. Analysis Appl.* **2000**, *251*, 217–229. [CrossRef]
32. Ishikawa, S. Fixed points by a new iteration method. *Proc. Am. Math. Soc.* **1974**, *44*, 147–150. [CrossRef]
33. Mann, W.R. Mean value methods in iteration. *Proc. Am. Math. Soc.* **1953**, *44*, 506–510. [CrossRef]
34. Krasnoselskij, M.A. Two remarks on the method of successive approximations. *Usp. Mat. Nauk.* **1955**, *10*, 123–127. (In Russian)
35. Pheungrattana, W.; Suantai, S. On the rate of convergence of Mann, Ishikawa, Noor and SP iterations for continuous functions on an arbitrary interval. *J. Comput. Appl. Math.* **2011**, *235*, 3006–3014. [CrossRef]
36. Karakaya, V.; Atalan, Y.; Dogan, K.; Bouzara, N.E.H. Some fixed point results for a new three steps iteration process in Banach spaces. *Fixed Point Theory Appl.* **2017**, *18*, 625–640. [CrossRef]
37. Navascués, M.A. Approximation of fixed points and fractal functions by means of different iterative algorithms. *Chaos Solitons Fractals* **2024**, *180*, 114535. [CrossRef]
38. Hammerstein, A. Nichtlineare integralgleichungen nebst anwendungen. *Acta Math.* **1930**, *54*, 117–176. [CrossRef]
39. Banas, J. Integrable solutions of Hammerstein and Urysohn integral equations. *J. Austral. Math. Soc.* **1989**, *46*, 61–68. [CrossRef]
40. Berinde, V. On the approximation of fixed points of weak contractive mappings. *Carpathian J. Math.* **2003**, *19*, 7–22.
41. Berinde, V. Approximation of fixed points of weak contractions using the Picard iteration. *Nonlinear Anal. Forum* **2004**, *9*, 43–53.

Disclaimer/Publisher's Note: The statements, opinions and data contained in all publications are solely those of the individual author(s) and contributor(s) and not of MDPI and/or the editor(s). MDPI and/or the editor(s) disclaim responsibility for any injury to people or property resulting from any ideas, methods, instructions or products referred to in the content.

symmetry

MDPI

Article

Influence of the Plan Structural Symmetry on the Non-Linear Seismic Response of Framed Reinforced Concrete Buildings

Juan Carlos Vielma-Quintero, Edgar Giovanny Diaz-Segura nd Juan Carlos Vielma *

Civil Engineering School, Pontificia Universidad Católica de Valparaíso, Valparaíso 2340000, Chile; juan.vielma.q@mail.pucv.cl (J.C.V.-Q.); edgar.diaz@pucv.cl (E.G.D.-S.)
* Correspondence: juan.vielma@pucv.cl

Abstract: Seismic-resistant design incorporates measures to ensure that structures perform adequately under specific limit states, focusing on seismic forces derived from both the equivalent static and spectral modal methods. This study examined buildings on slopes in densely built urban areas, a common scenario in Latin American cities with high seismic risks. The adjustment of high-rise buildings to sloping terrains induces structural asymmetry, leading to plan and elevation irregularities that significantly impact their seismic response. This paper explores the asymmetry in medium-height reinforced concrete frame buildings on variable inclines (0°, 15°, 30°, and 45°) and its effect on their nonlinear response, assessed via displacements, rotations, and damage. Synthetic accelerograms matched with Chile's high seismic hazard design spectrum, scaled for different performance states and seismic records from the Chilean subduction zone, were applied. The findings highlight structural asymmetry's role in influencing nonlinear response parameters such as ductility, transient interstory drifts, and roof rotations, and uncover element demand distributions surpassing conventional analysis and in earthquake-resistant design expectations.

Keywords: hillside buildings; slope adaptation; structural asymmetry; nonlinear response; earthquake-resistant design; synthetic accelerograms; seismic records

1. Introduction

A detailed understanding of the seismic response of reinforced concrete (RC) structures on hillside terrains is crucial for advancing seismic engineering, particularly in light of the interaction between topography, structure, and soil. Recent studies highlight the essential role of considering complex effects such as seismic amplification induced by topography and the interaction between soil and structure for an accurate assessment of these structures' seismic vulnerability [1–3]. This understanding is particularly relevant in Chile, which is situated along the Pacific subduction zone, where frequent large-magnitude earthquakes, such as the 1960 Valdivia earthquake (Mw 9.5), the 1985 Algarrobo earthquake (Mw 8.0), and the 2010 Maule earthquake (Mw 8.8), underscore the country's high seismic risk. The research underscores the necessity of an integrated approach that includes both topographic and geological considerations due to their significant impact on the seismic response magnitude [4,5]. Such studies are often situated in developing countries, including those in Latin America, which have witnessed the devastating effects of earthquakes on slope constructions, thereby underscoring the relevance of incorporating these considerations into seismic design and analysis practices.

Recurrent earthquakes have historically led to significant human and material losses, particularly associated with the vulnerability of structures. The implementation of modern building codes, underpinned by research into material behaviors and their interactions with the dynamic loads imposed by earthquakes, has significantly reduced the number of losses during major seismic events. However, certain structural typologies, when adapted to specific topographical conditions, produce alterations in how structures respond to

earthquake actions. Thus, the response of a building classified as regular by seismic codes can be significantly altered if the building's structure is modified to adapt to hillside locations. Additionally, research has been conducted on the dynamic amplification that topographic irregularities can introduce to foundations [6–9]. This aspect, however, remains beyond the scope of this research.

The assessment of the vulnerability of RC buildings on precarious hillsides to the combined action of ground shaking and seismic-induced landslides has led to the development of specific methodologies that incorporate the analysis of permanent ground displacements and topographic amplification. Such methodologies aim to generate fragility curves that effectively consider these combined effects, thus offering a more realistic evaluation of seismic hazards [7,10]. Conducting parametric studies examining the influence of structural configuration and geological and topographic conditions is underlined by the necessity to optimize design practices to enhance the resilience of structures against seismic events [4,11–13]. However, it is necessary to indicate that the findings of these recent studies have not yet been incorporated into global seismic codes and, therefore, into common design practice for structures located on hillsides [14–17].

Soil–structure interactions have proven to be a determining factor in modifying the seismic response, emphasizing the importance of considering this effect in seismic design to ensure structural safety [18–21]. Studies that include this interaction suggest a more holistic and detailed design approach, which is crucial for structures situated on hillsides [6,22,23]. On the other hand, seismic microzonation emerges as an essential tool for identifying risk areas and formulating mitigation strategies based on specific site characteristics [24–26], which can encompass areas with similar geological and topographic conditions that require the consideration of specific design conditions.

Research on the seismic response and vulnerability of structures on inclined terrains has significantly advanced in recent times, incorporating complex analyses that consider the variability in slope inclination, soil–structure interactions, and structural configurations [27–29]. These recent studies have broadened the understanding of the problem, addressing the location-specific seismic microzonation relative to the slope and detailed analyses of the nonlinear structural response under specific seismic loads [27,30–32].

The interaction between topography and structure is crucial for evaluating the seismic response of buildings located on hillsides, where topography can significantly alter the ground motion amplification pattern. Research has shown that the proximity to crests or valleys can influence the magnitude of the seismic response, requiring an informed and adapted structural design for these specific conditions [24,32,33]. The influence of topography on seismic amplification, combined with soil–structure interactions, highlights the need for more sophisticated design approaches that integrate these effects in a comprehensive manner [33–35].

Furthermore, the analysis of the seismic vulnerability of structures on inclined terrains has evolved towards more complex models that consider not only the structure itself but also the geological and topographic environment in which it is located. These models seek to more accurately predict the behavior of structures during seismic events, considering effects such as the induction of ground displacements and the dynamic interaction between the soil and structure [36,37]. Three-dimensional simulations and nonlinear analysis have provided valuable insights into how these interactions affect the safety and performance of structures during and after seismic events [28,29,38–41].

The seismic design of structures is conducted through regulatory precepts aimed at ensuring safety for the occupants, the building, and its contents. The continuous improvement of construction standards has allowed for the incorporation of principles intended to rectify the failures observed during previous catastrophic seismic events, preventing such failures from affecting buildings throughout their lifespan. Currently, the design is based on results from linear dynamic analyses, where seismic demands are introduced through design spectra corresponding to a specific demand level for the building's location [16,42–44]. These demands must be met by the structure's overall capacity and

that of its individual components, necessitating the structural engineer to conduct careful design and detailing, taking into account the characteristics of the materials constituting the structure. Regarding existing buildings, it is necessary under certain circumstances to carry out capacity upgrade processes, in which case, a seismic capacity assessment is required, for which, analyses in both linear and nonlinear ranges are often applied [45,46].

Among the limitations of this study, the following can be mentioned. The structural typology corresponds to medium-height buildings with reinforced concrete frames, designed for areas of high seismic threat (0.4 g), situated on terrains with variable inclinations (between 0° and 45°), representing a wide range of slopes. The challenges of the research are to capture the nonlinear response of buildings that are assumed to be regular, but due to the necessity of adapting to the local topography, acquire certain characteristics of asymmetry that are not covered by current standards, and are therefore, lacking specific prescriptions for their analysis and design. This could lead to nonlinear structural performances that cause unexpected damage during the occurrence of strong earthquakes, putting the safety of people and property at risk.

In this context, the present study focused on the application of detailed numerical analyses to evaluate the seismic response of RC frame building archetypes located on hillsides, using a methodological approach that incorporates both nonlinear dynamic analyses and static analyses to assess the nonlinear structural response under combined loading conditions. This approach allows for a comprehensive evaluation of the effects of the structural irregularity caused by the geometric asymmetry found in buildings on slopes, specifically considering the combined effects of gravitational actions with ground movements during strong earthquakes. By employing such analyses, this study aspires to significantly contribute to the body of knowledge in seismic engineering, offering valuable insights for the design and evaluation of RC structures on inclined terrains, and aimed at mitigating seismic hazards and protecting lives and properties.

2. Methodology

To analyze the influence of structural asymmetry on the nonlinear response of buildings, the study began with the conception and design of a series of representative archetypes of typical structures located on terrains with different slopes. To make the responses obtained comparable, the general geometry was kept constant, with variations only in the slope of the terrain. The archetypes were sized and structurally designed to be competent against the combined impacts of gravitational and seismic effects, according to conventional normative procedures. For this purpose, spectral modal analysis was initially carried out, considering the demand that was defined according to the seismic hazard level of the location.

The buildings' responses were evaluated using analysis methods based on nonlinear responses, starting with an incremental pushover analysis, which preliminarily allows us to capture the effects of nonlinearity under a pattern of statically applied loads. Subsequently, a dynamic analysis was carried out, for which, two sets of accelerograms (artificial and from seismic records) were used.

The parameters chosen to evaluate the nonlinear response, which are typically used to determine the displacements that evidence damage [30,44,47], are given in the following list:

- Interstory drifts;
- Roof rotations;
- Demand–capacity ratios of structural elements.

With the selected parameters, an assessment of the influence of structural irregularity caused by the modification of the archetypes' geometry on the seismic responses of these archetypes was carried out.

At this point, it is crucial to note that the archetypes were conventionally designed, considering the implications that irregularities in both plan and elevation, which were generated by adapting the structure to the slope of the terrain. Regarding regulatory considerations related to slopes, only Eurocode 8 [43] provides recommendations that consider the presence of slopes, but these are limited to the foundation design process. As for the main international

standards, there are no specific recommendations for the design of structures situated on slopes [14,16,44].

2.1. Description of the Archetypes

The archetypes studied consisted of regular reinforced concrete buildings, designed for a high seismic hazard zone, located on terrains with different inclinations, the latter of which were defined by the slope of the terrain. The study began with a basic archetype consisting of a frame building located on non-inclined terrain; its response was used as a point of comparison.

Geometry of the Archetypes

The archetypes, regardless of the terrain inclination, had nine levels with a height of 3.00 m each. The structuring of the buildings was carried out using moment-resisting frames, defined according to an orthogonal arrangement with five axes in the X direction, spaced equidistantly every 6.00 m, and four axes in the Y direction, spaced every 5.00 m, see Figure 1.

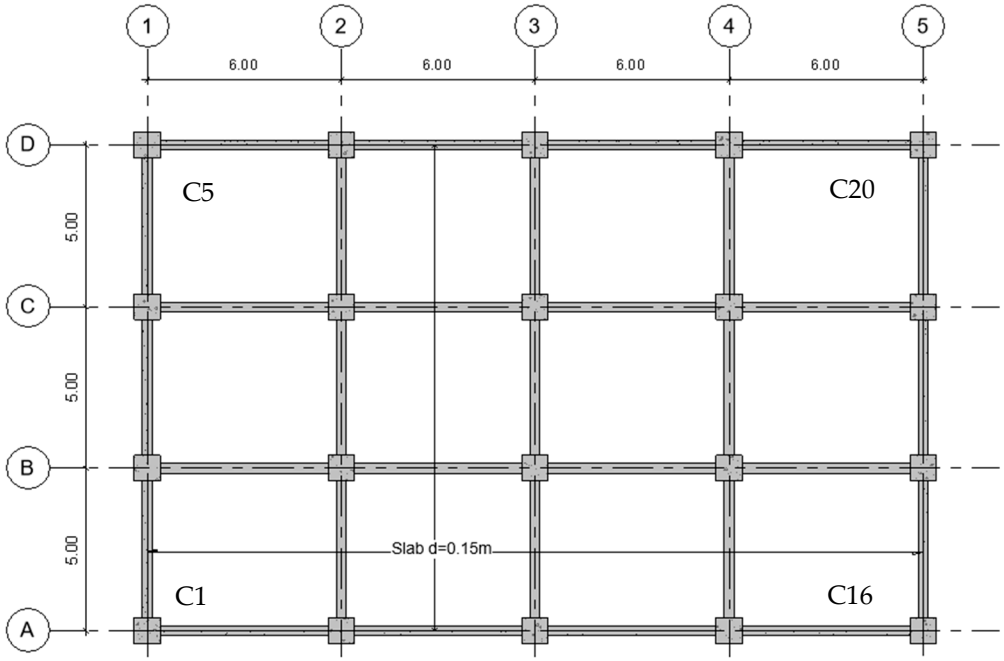

Figure 1. View of the typical floor plan of the archetypes.

The slope of the terrain influences the structuring. It is assumed that the buildings will have a general access from the lower part of the building, not from some intermediate level. Accordingly, the structure adapts to the slope of the terrain by reducing the height of the columns from the access facade towards the rear facade. This even leads to, for buildings on steeper slopes, the slabs of the first levels, in some cases, having to be reduced in their extension or simply eliminated for not being able to include them within the support structure, see Figure 2a–d.

The removal of floors as a result of adapting the structure to the slope is not directly limited or regulated by standards. However, it should be noted that when a floor is partially or completely removed, structural regularity is altered in two ways. The first involves the alteration of regularity in elevation; when an entire floor is removed, it results in floors with heights that can double those of existing floors, altering the building's dynamic response. Additionally, double-height floors produce the undesired effect of a weak story due to their reduced stiffness, thus creating a weak link within the structural chain. The second alteration concerns irregularity in the plan. If a floor is partially removed, its center of gravity shifts

relative to the centers of gravity of the unaltered floors, leading to uncoupled vibration that creates torsional effects on the columns connecting those floors. These torsional effects tend to concentrate in the columns located at the periphery of the floors, making it especially important to study the displacement demands on such columns.

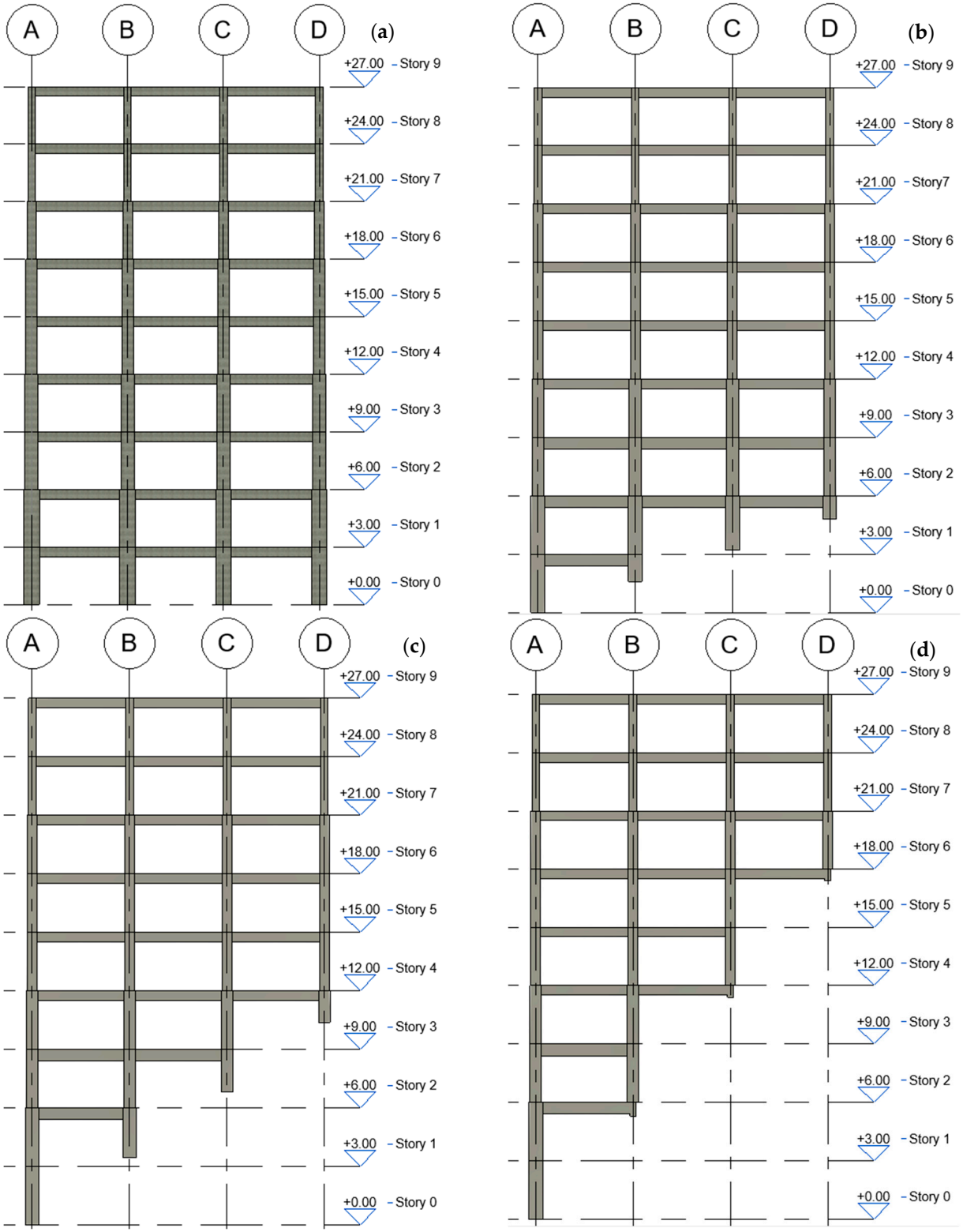

Figure 2. Elevation views of the archetypes: (**a**) 0° archetype, (**b**) 15° archetype, (**c**) 30° archetype, and (**d**) 45° archetype. In this figure, A, B, C and D are structural axis.

The structural elements of the archetypes were modeled using nonlinear constitutive parameters corresponding to the materials that represent the reinforced concrete in the analysis and design. Firstly, there is concrete, designated as G30, whose mechanical characteristics are provided in Table 1. To model the nonlinear behavior of concrete, the constitutive parameters by Mander et al. [48] has been employed. On the other hand, the reinforcing steel corresponds to the designation A630-420H, whose mechanical characteristics can be observed in Table 2. The constitutive parameters of this material are from Menegotto and Pinto [49].

Table 1. Constitutive model parameters by Mander et al. for concrete grades G25, G30, and G35.

Parameter	Concrete G30
Compression strength (MPa)	38.00
Strength lower bound (MPa)	30.00
Tension strength (MPa)	2.90
Modulus of elasticity (MPa)	28,973.00
Specific weight (kN/m^3)	24.00

Table 2. Constitutive model parameters by Menegotto and Pinto for A630-420H-grade steel.

Parameter	Value
Modulus of elasticity E (MPa)	200,000.00
Yield strength F_y (MPa)	490.00
Strain hardening parameter (dimensionless)	0.0050
Transition curve initial shape parameter (dimensionless)	20.00
Transition curve shape calibrating coefficient A1 (dimensionless)	18.50
Transition curve shape calibrating coefficient A2 (dimensionless)	0.15
Transition curve shape calibrating coefficient A3 (dimensionless)	0.00
Transition curve shape calibrating coefficient A4 (dimensionless)	1.00
Fracture/buckling strain (dimensionless)	1.00
Specific weight (kN/m^3)	78.00

Table 3 shows the resulting sections of the structural elements. It is noted that, for design reasons, the column sections were kept as squares and with the same dimensions on each floor. The dimensions progressively decreased with height. For the beams, the same cross-sectional shapes were adopted for both the X and Y directions, adopting rectangular shapes. It is also noted that these too decreased with height.

Table 3. Sections resulting from the design of the archetypes. All the dimensions are in cm.

	Columns				**Beams X and Y**		
Archetype	**1-2**	**3-4**	**5-6-7**	**8-9**	**1-2-3**	**4-5-6**	**7-8-9**
Basic	70 × 70	60 × 60	50 × 50	40 × 40	30 × 70	30 × 60	30 × 50
15°	70 × 70	60 × 60	50 × 50	40 × 40	30 × 70	30 × 60	30 × 50
30°	70 × 70	60 × 60	50 × 50	40 × 40	30 × 70	30 × 60	30 × 50
45°	70 × 70	60 × 60	50 × 50	40 × 40	30 × 70	30 × 60	30 × 50

2.2. Analysis Type

To study the response of the archetypes, various types of analyses have been applied to assess their response to earthquake action. The first of these, defined according to the Chilean seismic code NCh433 [42], is the spectral modal analysis, which was required for the design of the archetypes. In this work, there were different types of definitions for the representative elements of the concrete slabs of the levels. These slabs were defined using rigid diaphragms and shell-type elements, so that the use of different elements in the modal response of the archetypes can be evaluated.

On the other hand, to assess the adequacy of the seismic response of the archetypes, it was necessary to carry out analyses considering the nonlinear behavior, for both the geometric and constitutive parameters of the elements and materials, respectively. The nonlinear analyses applied in this study are as follows:

- Nonlinear static analysis with incremental pushover;
- Nonlinear dynamic time-history analysis using artificial accelerograms;
- Nonlinear dynamic time-history analysis using recorded events.

2.2.1. Static Non-Linear Analysis

The nonlinear static analysis was conducted as a preliminary approach to determine the response of structures to lateral loads induced by ground motion from earthquakes [28,39,40]. In this study, this analysis was carried out considering two advanced aspects. The first pertains to the fact that the pattern of incremental lateral forces assumes a shape that corresponds to the modal displacements of the fundamental mode of vibration of the building in each of the analysis directions [50]. The second aspect considers the accidental eccentricity of the floors, for which, the following cases were considered:

+Modal Distribution in X + Eccentricity in Y;
+Modal Distribution in X − Eccentricity in Y;
−Modal Distribution in X + Eccentricity in Y;
−Modal Distribution in X − Eccentricity in Y;
+Modal Distribution in Y + Eccentricity in X;
+Modal Distribution in Y − Eccentricity in X;
−Modal Distribution in Y + Eccentricity in X;
−Modal Distribution in Y − Eccentricity in X.

For the capacity curves obtained through the static nonlinear analysis, a set of performance points was determined by applying the ASCE 41-17 [30] procedure, which allows us to obtain these points based on the seismic hazards defined through the elastic design spectrum for various return periods. In this study, the elastic design spectrum defined in the NCh433 for very stiff soil was considered, scaling the spectral ordinates according to the following return periods:

$$\delta_t = C_0 C_1 C_2 S_\alpha \left(\frac{T_e^2}{4\pi^2} \right) \mathrm{g} \quad (1)$$

where $S\alpha$ is the response spectrum acceleration at the effective fundamental period and damping ratio of the building in the direction under consideration, as calculated by the methods in Sections 2.4.1 or 2.4.2 of ASCE 41-17.

$C0$: Modification factor that relates the spectral displacement of the equivalent single degree of freedom (SDOF) system with the roof displacement of the building's multiple degree of freedom (MDOF) system.

$C1$: Modification factor to relate expected maximum inelastic displacements to displacements calculated for linear elastic response.

$C2$: Modification factor to represent the effect of pinched hysteresis shape, cyclic stiffness degradation, and strength deterioration on the maximum displacement response.

2.2.2. Time-History Non-Linear Dynamic Analysis Using Artificial Accelerograms

A set of short-duration synthetic accelerograms (10 s) was used, generated using the elastic design spectrum defined in the Chilean seismic code NCh433 for various hazard levels corresponding to different performance levels. The performance levels are shown in Table 4 along with the associated exceedance probability, with the acceptable performance levels located in the cells highlighted in green [30,44,45].

Table 4. Definition of performance limit states with their corresponding associated exceedance probabilities.

	Exceedance Probability	Target Building Performance Level			
		1-A	1-B	3-C	5-D
Earthquake Hazard Level	50% in 50 years	a	b	c	d
	20% in 50 years	e	f	g	h
	5% in 50 years	i	j	k	l
	2% in 50 years	m	n	o	p

In this table, the letters a through p represent the different levels of performance with respect to the probabilities of exceedance.

2.2.3. Time-History Non-Linear Dynamic Analysis Using Seismic Records

Finally, a nonlinear time-history analysis was conducted using a set of accelerograms from seismic records of earthquakes that occurred in the subduction zone in Chile, matched with the elastic design spectrum for the building sites.

The records chosen to carry out the nonlinear time-history analyses mentioned in the previous section correspond to strong earthquakes that occurred during the last two decades in the subduction zone that have affected Chile. The records were applied using their two horizontal components, leaving the inclusion of the vertical component for a subsequent study to avoid introducing an additional variable [32,46,51]. Table 5 displays the characteristics of the seismic records.

Table 5. Descriptive summary of Chilean records used.

Earthquake	Date	Magnitude (M_w)	Station	Epicentral Distance (km)	Component	PGA (cm/sec^2)
Maule	27-02-2010	8.8	Angol	209	E–W	684
					N–S	916
Maule	27-02-2010	8.8	Concepción San Pedro	109	97	598
					7	667
Maule	27-02-2010	8.8	Constitución	70	E–W	530
					N–S	618
Maule	27-02-2010	8.8	Llolleo	274	E–W	324
					N–S	549
Maule	27-02-2010	8.8	Santiago Maipú	69	E–W	481
					N–S	549
Coquimbo	16-09-2015	8.3	El pedregal	92	90	677
					360	561
Coquimbo	16-09-2015	8.3	Tololo	175	90	234
					360	338
Coquimbo	16-09-2015	8.3	San Esteban	168	90	268
					360	182
Puerto Quellón	25-12-2016	7.6	Loncomilla	136	90	136
					360	148
Puerto Quellón	25-12-2016	7.6	Hotel Espejo de Luna	75	90	371
					360	350
Valparaíso	24-07-2015	6.9	Torpederas	39	90	889
					360	731

Figure 3 summarizes the response spectra calculated from the records used in the analyses (set of gray lines). These spectra are shown along with the average calculated spectrum plus and minus one standard deviation. Also, for comparison purposes, the elastic design spectrum for stiff soil (soil type B), which is the type of soil idealized for the placement of the archetypes, was added. Eleven pairs of records were chosen to meet the requirements of ASCE 7, which requires at least this number of records to perform analyses in the nonlinear range, thereby allowing for the comparison of the design limit values against the averages of the characteristics calculated with these records [39,40]. Note that the pairs of records were applied simultaneously in the two main structural directions of each archetype. The records were downloaded from the CESMD database [52] and were corrected using the SeismoSpect [53] and SeismoMatch [54] programs to match these records with the elastic design spectrum.

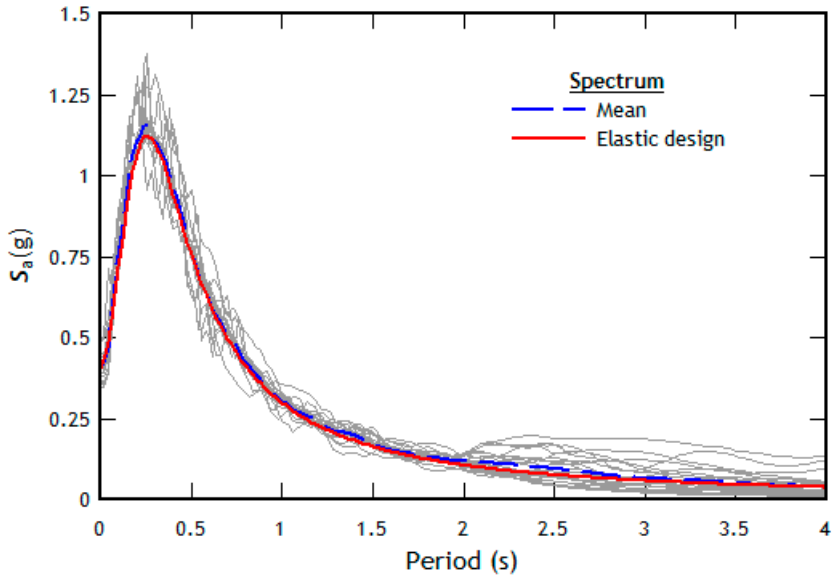

Figure 3. Response spectra of the matched records, with the SB soil elastic design spectrum and the mean spectrum.

As a result of the process of matching seismic records with the elastic design spectrum, the modified accelerograms were obtained (see Figure 3). Response spectra (continuous gray lines) were determined for these accelerograms, and with these, the average spectrum (blue long-dash line) was calculated; it can be seen that they are quite closely aligned with the elastic design spectrum. This good alignment has allowed for the validation of the record matching process through the requirements of ASCE 7, which, in the case of using a minimum of 11 pairs of records, enables the comparison with the average of the response spectra.

3. Results and Discussion

The results of the analyses are presented below, grouped according to the type of response. Firstly, the results of the linear analyses are shown, followed by the results of the nonlinear analyses. The analyses have been conducted using the SeismoStruct [55] and SeismoBuild [56] programs.

3.1. Results of Linear Analysis

The results obtained from the linear analysis of the structure showed the effect of asymmetry on the dynamic response of the buildings. This became evident when establishing the minimum number of vibration modes that ensured that the participative modal mass was at least equal to 95%.

It can be observed in Figure 4 that considering slabs modeled as rigid diaphragms implies a relatively low number of vibration modes necessary to obtain a participative mass of at least 95%, compared to the consideration of semi-rigid or shell-type diaphragms. Additionally, it can be noted that as the slope of the terrain increased, and hence the buildings lost their regularity both in plan and elevation, the number of modes required to meet the participative mass criterion increased dramatically [57].

3.2. Results from Non-Linear Analysis

The results corresponding to the nonlinear analysis with incremental pushover verified that, in both the X and Y directions, the archetypes exhibited adequate ductility. Figure 5 shows the capacity curves obtained through the pushover analysis with the combinations + Modal Distribution in X + Eccentricity in Y and + Modal Distribution in Y + Eccentricity in X (light blue and pink lines, respectively). Idealized capacity curves (blue and red lines) were determined for these capacity curves, and the locations of the performance points, defined using Equation (1) for the different limit states defined in Table 4, were also found [46,58]. To

make the results of the different buildings comparable, the capacity curves were normalized with respect to the total height and seismic weight of the buildings [59–61].

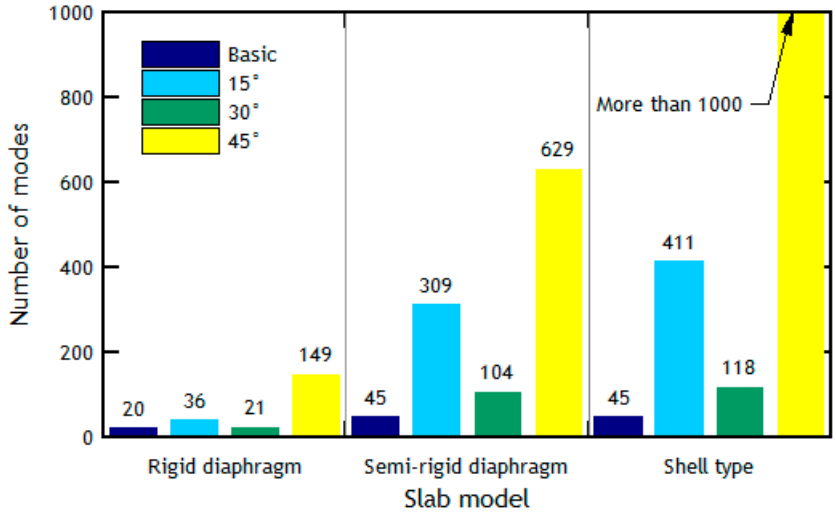

Figure 4. Minimum number of modes to achieve a minimum participative mass of 95%.

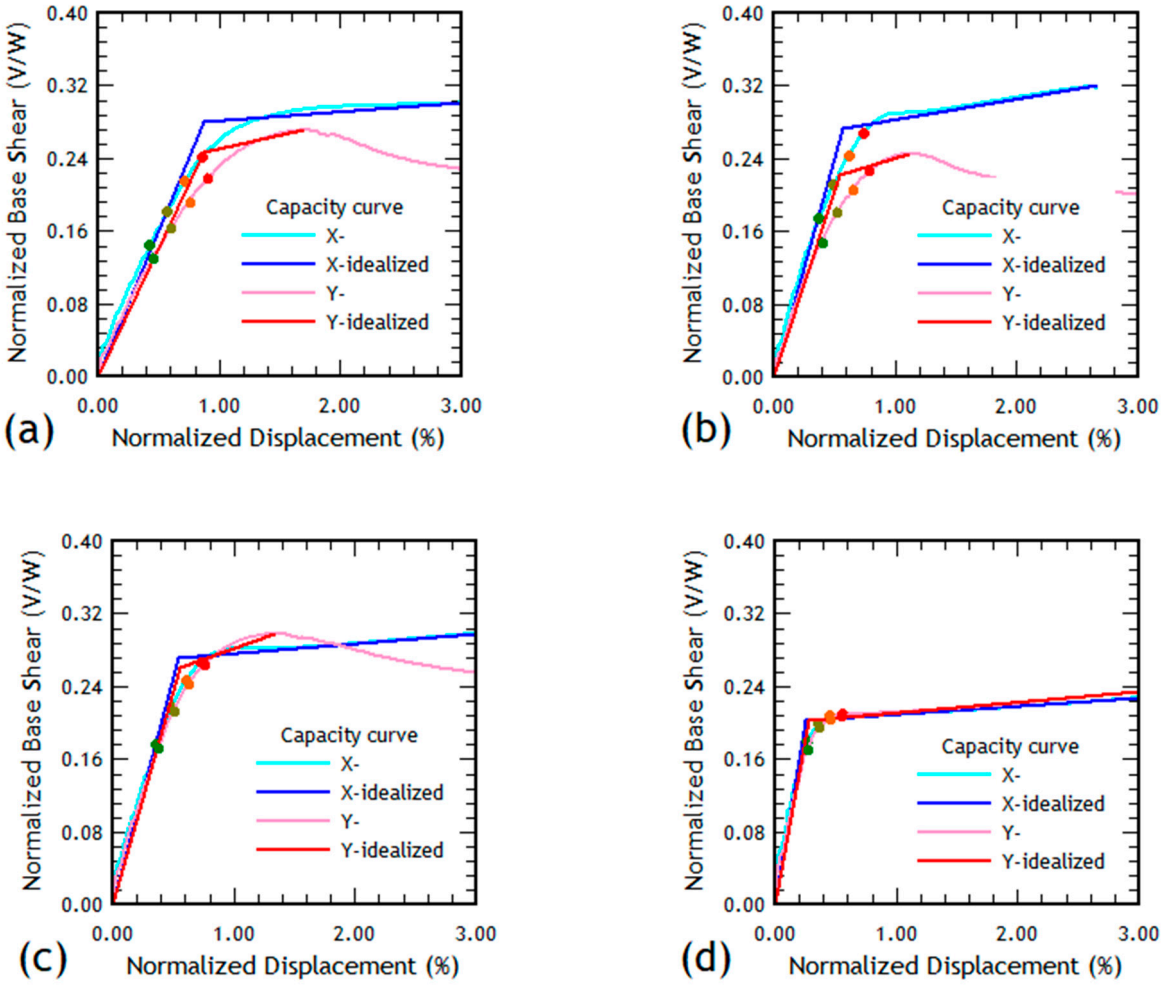

Figure 5. Capacity curves of the analyzed archetypes: (**a**) 0° Archetype, (**b**) 15° Archetype, (**c**) 30° Archetype, (**d**) 45° Archetype. In this figure, the light green dot represents the performance point for the limit state of the operational level (1-A), while the dark green, orange, and red dots represent the limit states of immediate occupancy (1-B), life safety (3-C), and collapse prevention (5-D), respectively.

The displacements (normalized with respect to the height of the archetypes) of the performance points corresponding to the limit states evaluated in this study are summarized in Table 6. Note that these displacements for each direction of the static nonlinear analysis represents those shown in Figure 5.

Table 6. Normalized displacements of the performance points calculated for the different archetypes and limit states.

Limit State	Basic		15°		30°		45°	
	X (%)	Y (%)	X (%)	Y (%)	X (%)	Y (%)	X (%)	Y (%)
Operational Level (1-A)	0.428	0.449	0.370	0.391	0.362	0.375	0.261	0.265
Immediate Occupancy (1-B)	0.571	0.599	0.493	0.522	0.483	0.499	0.354	0.356
Life Safety (3-C)	0.713	0.749	0.617	0.652	0.603	0.624	0.451	0.450
Collapse Prevention (5-D)	0.856	0.899	0.740	0.783	0.724	0.749	0.553	0.546

From the capacity curves and their idealized forms, it is possible to determine the displacement ductility and the reserve of strength [50,59,60]. It was noted that the ductility developed for the building located on a terrain inclined at 45° showed values much higher than those achieved by buildings located on less inclined soils (see Figure 6). As for the reserve of strength reached, the results did not show a great variation. This allows us to deduce that the asymmetry generated by the irregularity both in plan and elevation of the studied buildings affects the nonlinear displacement response more than the nonlinear strength response [62,63].

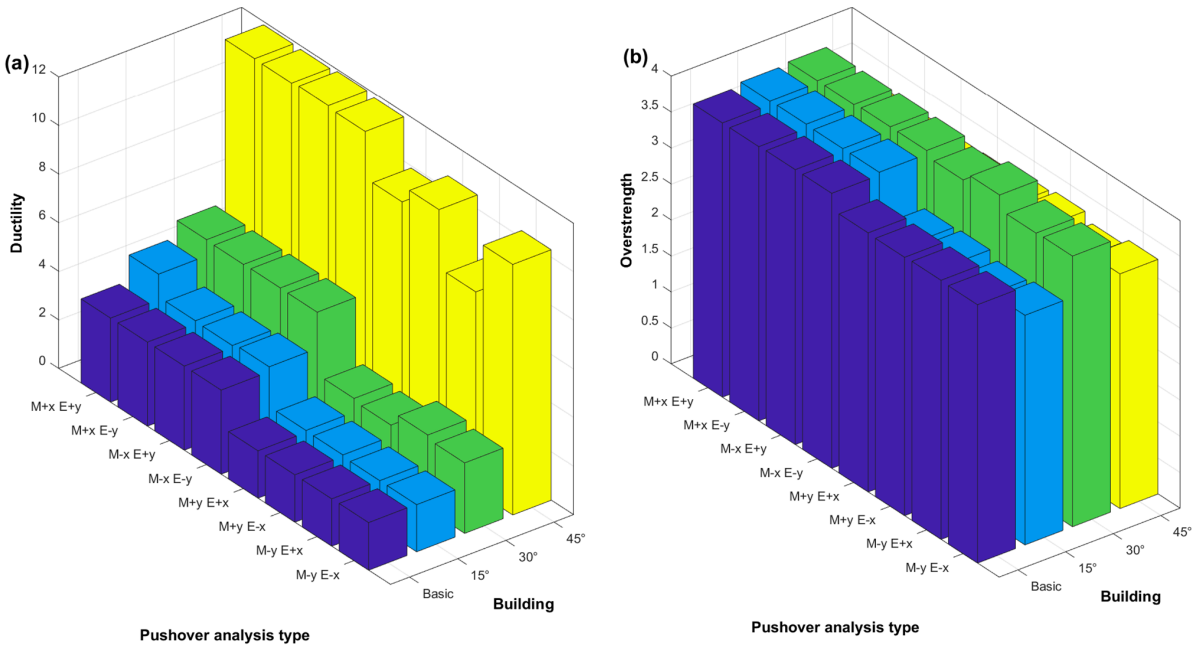

Figure 6. Results of the pushover analyses: (**a**) ductility and (**b**) overstrength. In this figure, the blue bars represent the drifts of the Basic Archetype, the light blue bars represent the drifts of the 15° Archetype, the green bars represent the drifts of the 30° Archetype, and the yellow bars represent the drifts of the 45° Archetype.

3.2.1. Interstory Drift Control

Seismic design standards employ dynamic nonlinear analyses to achieve a closer approximation of the seismic response of buildings. To counteract the high variability present in the seismic records used for these analyses, ASCE 7 requires the use of at least 11 records, with criteria that allow for the rejection of results, especially in cases where numerical convergence of the analyses is not achieved.

From the results of the dynamic nonlinear analysis, it was possible to calculate the transient interstory drifts, which were compared against thresholds to determine the damage to structural elements located at different stories of the building. The greater the transient interstory drift, the greater the damage achieved and the more the elements engaged in nonlinear behaviors.

The results must be analyzed in the two main structural directions, corresponding to the X and Y axes. Figure 7 shows the results of the maximum transient interstory drifts reached at the nine stories of the basic archetype in the X direction for each pair of records used in this research. The results were plotted for the four columns at the corners of the archetype, identifying them according to the intersection of the axes in Figure 1. Thus, in Figure 7, the drifts corresponding to columns C1 (A-1), C5 (D-1), C16 (A-5), and C20 (D-5) are shown. The review of the interstory drifts of these columns aimed to capture the effect of asymmetry and structural irregularity on the dynamic response, which tended to be magnified in the columns located at the corners of the buildings, where torsional effects increasingly manifested.

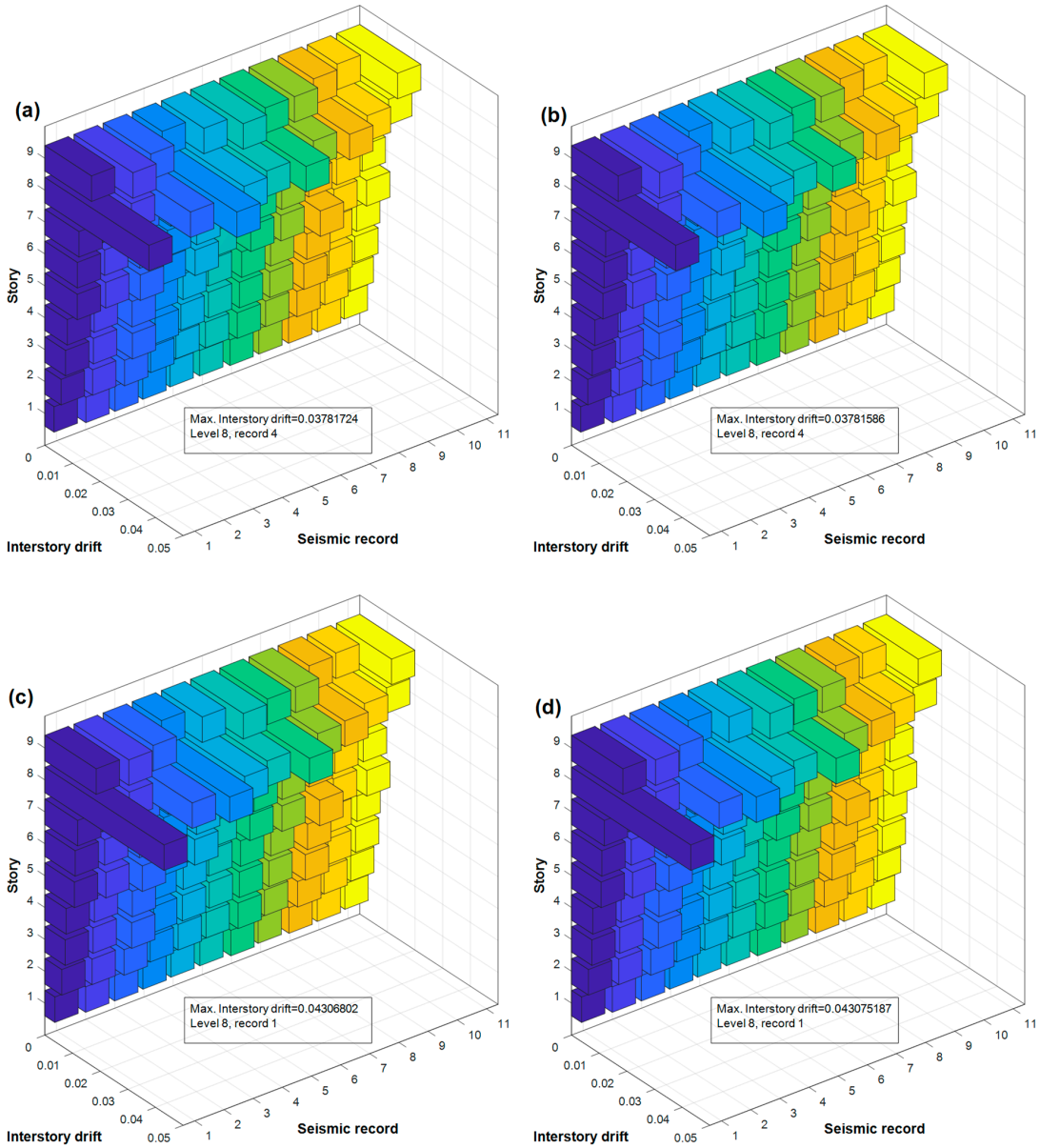

Figure 7. Maximum interstory drift in X direction of columns (**a**) C1, (**b**) C5, (**c**) C16, and (**d**) C20. In this figure, each color represents the interstory drifts calculated using each pair of seismic records.

In this figure, on the x-axis (horizontal and to the right), the 11 pairs of records used in this research are shown; on the y-axis (horizontal and to the left), the values of the maximum transient drifts achieved at the different levels of the studied archetype are displayed. Lastly, on the z-axis (vertical), the levels of the archetype are presented.

It was noted that the greatest interstory drifts occur, regardless of the records and the location of the columns, on the eighth story of the basic archetype. This is due to the reduction in the cross-sectional area of the columns at this level, with the maximum drift value being slightly above 0.04 for record 1 (see Table 5) for column C20. It can also be noted that the drifts of the lower stories maintained small values, indicating that significant damage did not occur at these levels. A similar behavior was observed in the results of the interstory drifts calculated in the Y direction, where the maximum value was also slightly above 0.04 for record 1 from Table 5, this time for column C1 (see Figure 8). Due to space limitations, it was not possible to show the results for all the archetypes, but can be made available for interested readers by correspondence.

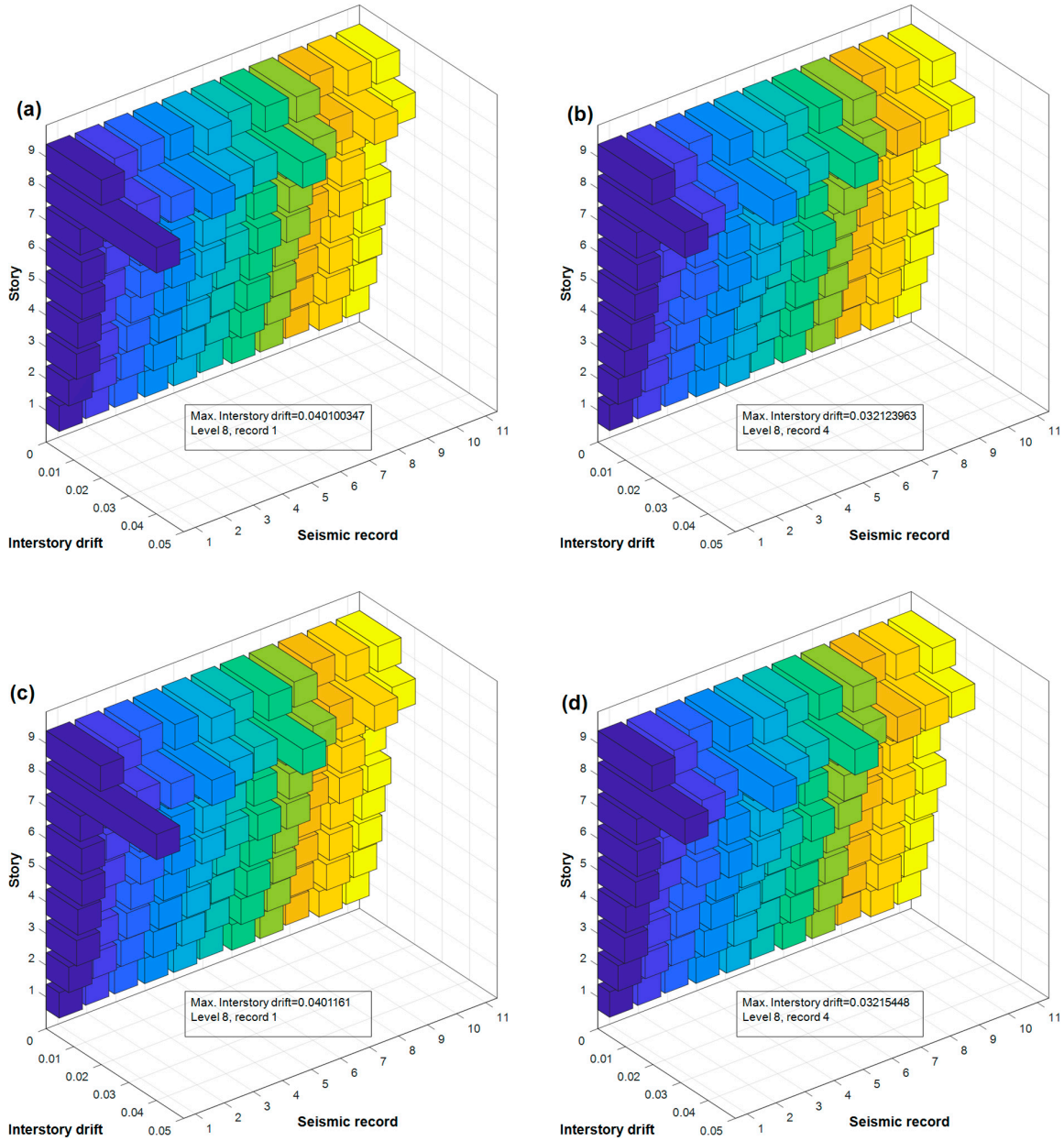

Figure 8. Maximum interstory drift in Y direction of columns (**a**) C1, (**b**) C5, (**c**) C16, and (**d**) C20. In this figure, each color represents the interstory drifts calculated using each pair of seismic records.

The consideration of the suitability of the structural design was carried out through the evaluation of the average interstory drifts, thanks to the use of 11 pairs of records (ASCE 7). Thus, the average results of the basic archetype in the X and Y directions for columns C1, C5, C16, and C20 discussed earlier can be appreciated. As expected, the maximum drifts were reached on the eighth story, in the analyses for both directions (see Figure 9). Similarly, Figures 10–12 show the average interstory drifts of the 15°, 30°, and 45° archetypes. Note that in these cases, the maximum average drifts occurred on the eighth story, but unlike the basic archetype, there were null drifts at the first level of these archetypes, due to the presence of supports placed on the slope, which nullifies the displacements of these initial levels. Despite this characteristic, it can be noted that the average interstory drifts reached in both directions were comparable in all the case studies.

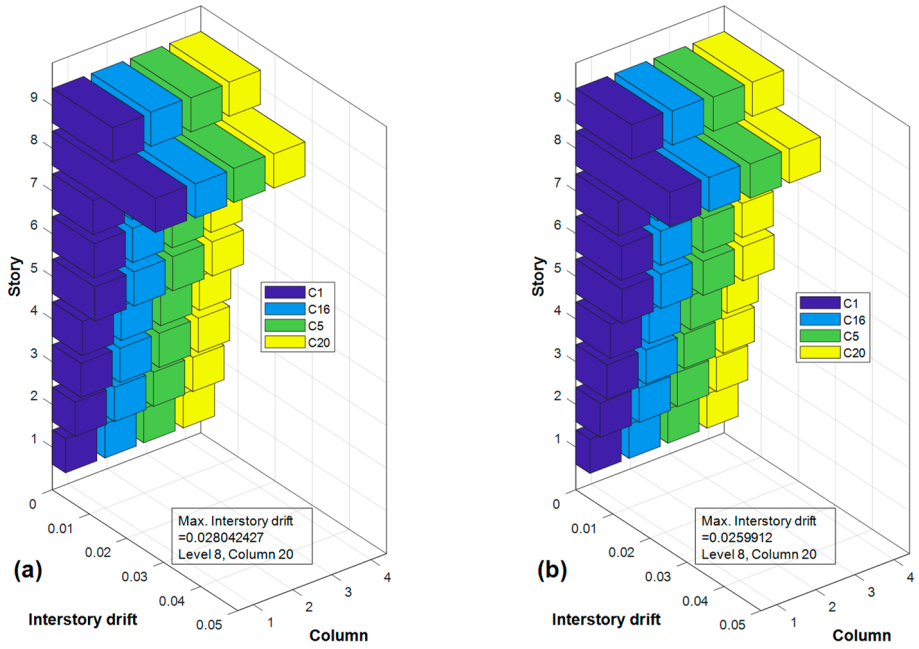

Figure 9. Mean interstory drift in (**a**) X and (**b**) Y directions of the basic archetype.

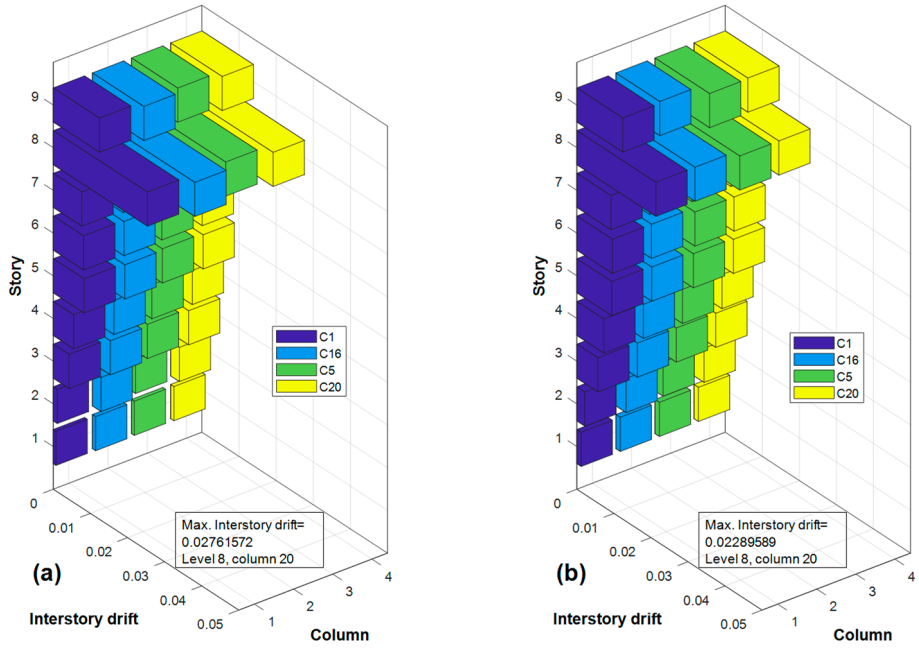

Figure 10. Mean interstory drift in (**a**) X and (**b**) Y directions of the 15° archetype.

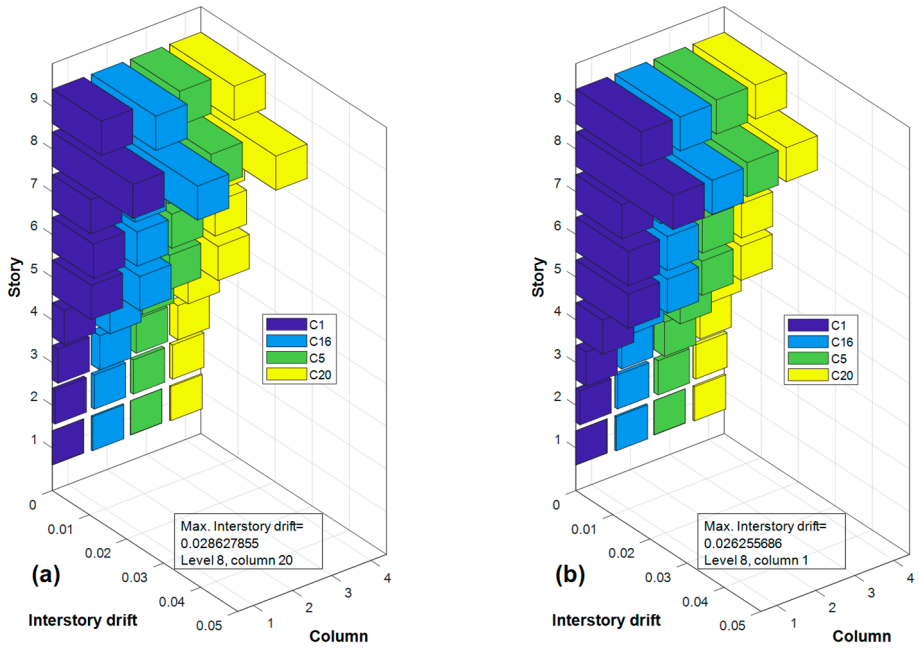

Figure 11. Mean interstory drift in (**a**) X and (**b**) Y directions of the 30° archetype.

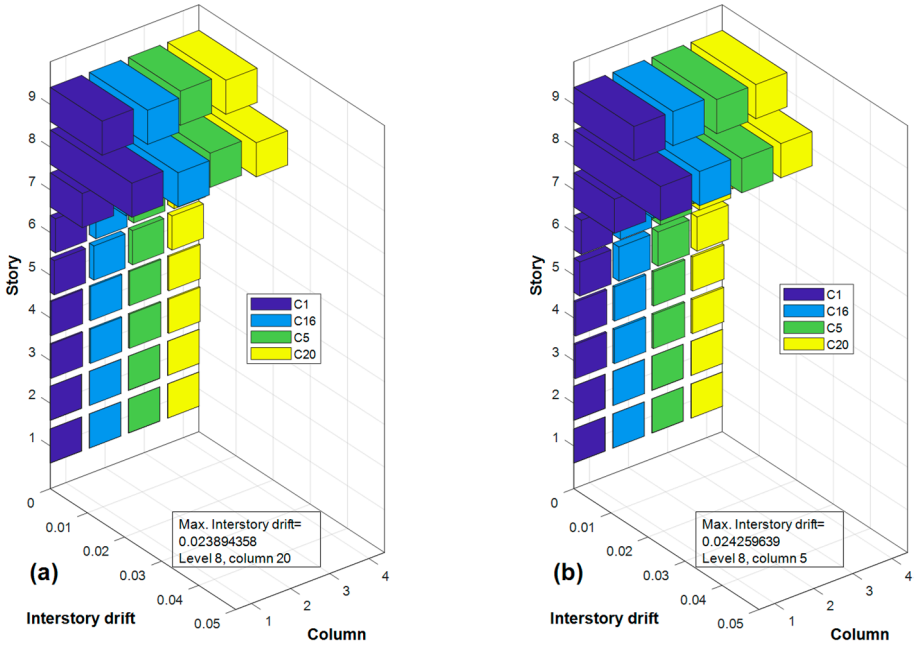

Figure 12. Mean interstory drift in (**a**) X and (**b**) Y directions of the 45° archetype.

In Figures 9–12, on the x-axis (horizontal to the right), the four columns located at the corners of the archetypes' floors, whose locations have already been indicated, are shown. On the y-axis (horizontal to the left), the average values of the maximum transient drifts achieved at the different levels of the studied archetype, using the eleven pairs of records, are displayed. Finally, on the z-axis (vertical), the levels of the archetype are presented.

3.2.2. Acceptance Criteria Based on the Transient Interstory Drift

The limits imposed by ASCE 7 for transient floor drifts are provided in the table in Section 12.12 [44]. For reinforced concrete buildings structured with frames, a limit value of $0.02h_{sx}$ has been established. The average transient floor drift should not exceed twice the value of the floor drift expressed in Table 12.12-1 of ASCE 7. Similarly, for buildings

exceeding 30 m in height, the average transient drift should not surpass the value calculated using the following expression:

$$\overline{\Delta} \leq h_{sx}\left(4.71{\cdot}10^{-2} - 2.34{\cdot}10^{-4}\cdot h_n\right) \tag{2}$$

where h_{sx} is the interstory height and h_n is the total height of the structure, both measured in meters. Although the application of this equation is valid only for buildings that exceed 30 m in height and the study cases only reached 27 m, it has been decided to apply it to have a referential comparison value as an acceptance criterion. The result of the above equation should not be less than:

$$h_{sx}\left(4.71{\cdot}10^{-2} - 2.34{\cdot}10^{-4}\cdot h_n\right) > 0.03{\cdot}h_{sx} \tag{3}$$

Using the data from the studied archetypes, a limit value for the average transient floor drift of $\overline{\Delta} = 0.122$ m was obtained, which is greater than the value obtained from the right term of the previous equation (0.09 m). This value, which is applicable to the drifts of all floors, implies that the maximum interstory drift for an interstory height of 3 m is 0.04. As can be observed in Figures 8–11, none of the average floor values reached this limit value.

Regarding the acceptance criterion for analyses based on transient interstory drifts, if an analysis yields a maximum transient interstory drift value greater than 150% of the value calculated using the equation, it will be necessary to discard the results of that analysis in the calculation of the building's performance. The maximum limit of the transient floor drift was then calculated, yielding a value of 0.184 m, which, when converted to interstory drift, gave a value of 0.06. Comparing this maximum value with the results reported in Figures 7 and 8, it can be noted that none of the floors exceeded this value, allowing for the consideration of all the results of the dynamic time-history analyses.

The other acceptance criterion was for residual floor drift. ASCE 7 sets an acceptance value of $0.03{\cdot}h_{sx}$ for drifts remaining in the structure when it reaches rest. In the interest of brevity, the results of these calculations are not shown, but it can be mentioned that the values of the residual floor drift in the different archetypes did not exceed the indicated limit value.

3.2.3. Rotation Control

Design standards do not use floor rotations as acceptance criteria [4,19,64,65]. The authors believe that such rotations can provide an interesting approximation for the response associated with torsion induced by the asymmetry of the archetypes. For this purpose, the maximum relative rotations between the roof level and the foundation level of each archetype for each pair of records used in the dynamic analysis were calculated, see Figure 13. It is noted that, contrary to expectations, the most irregular archetype (45°) did not exhibit the highest rotations, but rather it was the 30° archetype. To prevent the elevated values of the latter from overshadowing those of the 45° archetype, it was necessary to modify the order of result presentation in Figure 13.

3.2.4. Damage Control

Damage control was studied based on the outcomes of all the analyses utilized in this study. The demand versus capacity ratio was determined for each of the structural elements under the various types of applied loads, whether these were incremental lateral loads (from the pushover analysis) or loads induced by accelerations imposed on the archetypes, either defined by artificial accelerograms or by seismic records.

The results of the damage control were extensive, and in the interest of brevity, only some are shown, which illustrate two of the main issues detected in the analyses: the stiffness reduction of the eighth floor and the short columns that originate in the archetypes inclined at 30° and 45°. In Figure 14, the elements of the archetypes that have exceeded a value of one in the demand versus capacity ratio for the analyses using artificial accelerograms can

be observed. These results correspond to the limit states of the operational level (1-A) and immediate occupancy (1-B). In the case of the limit states for life safety (3-C) and collapse prevention (5-D), exceeding the value of one for the demand versus capacity ratios was not observed, indicating that these limit states were adequately protected in the conventional design applied [1,18,66]. The reader may notice that the 30° archetype presented deeper degrees of damage than the rest of the archetypes. Although, as previously mentioned, the 45° archetype exhibited greater irregularity due to the asymmetry created by the steeper slope, the presence of supports that restrict displacements prevented the occurrence of relative displacements that are responsible for producing the most severe damage.

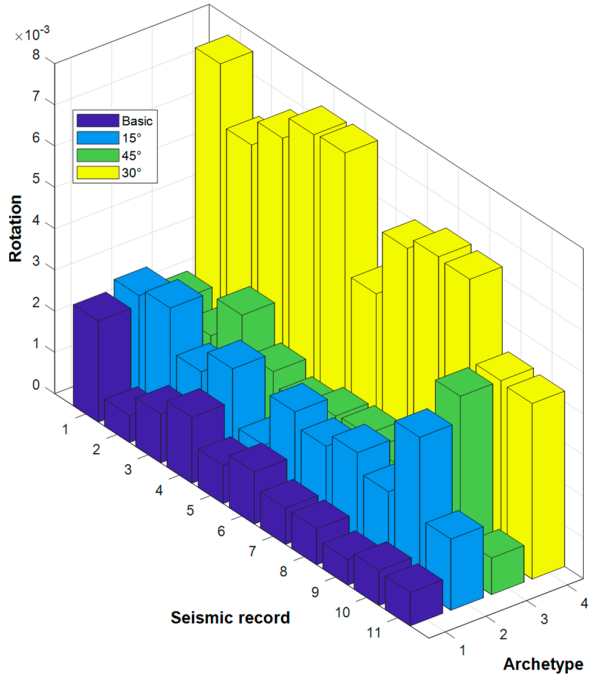

Figure 13. Maximum rotations reached in the gravity center of the roof in each archetype.

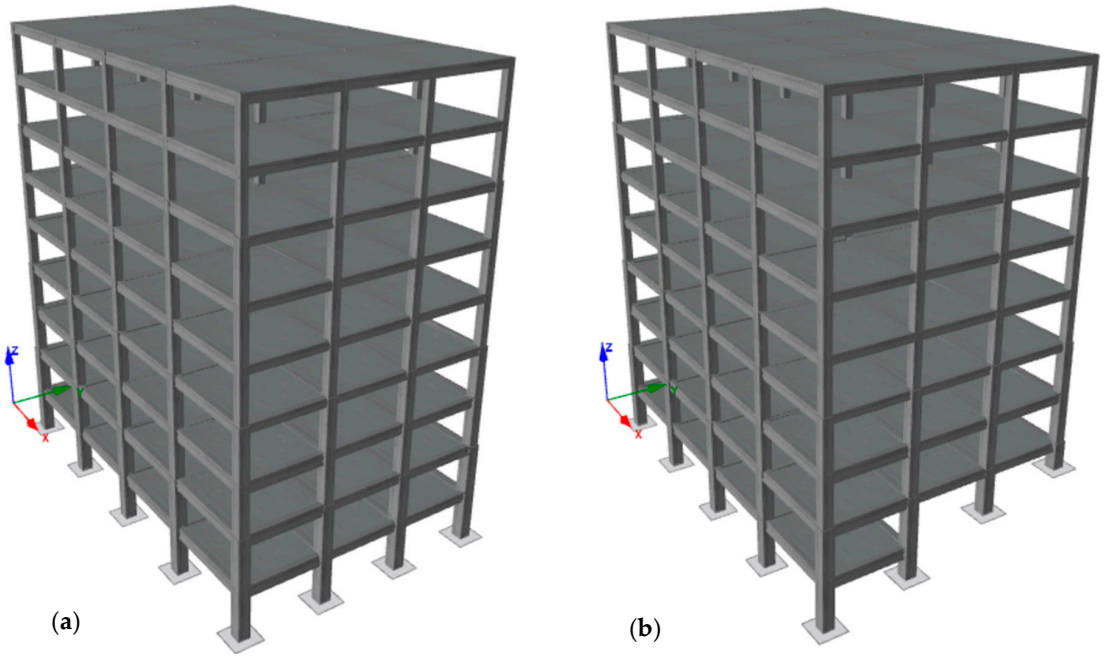

Figure 14. *Cont.*

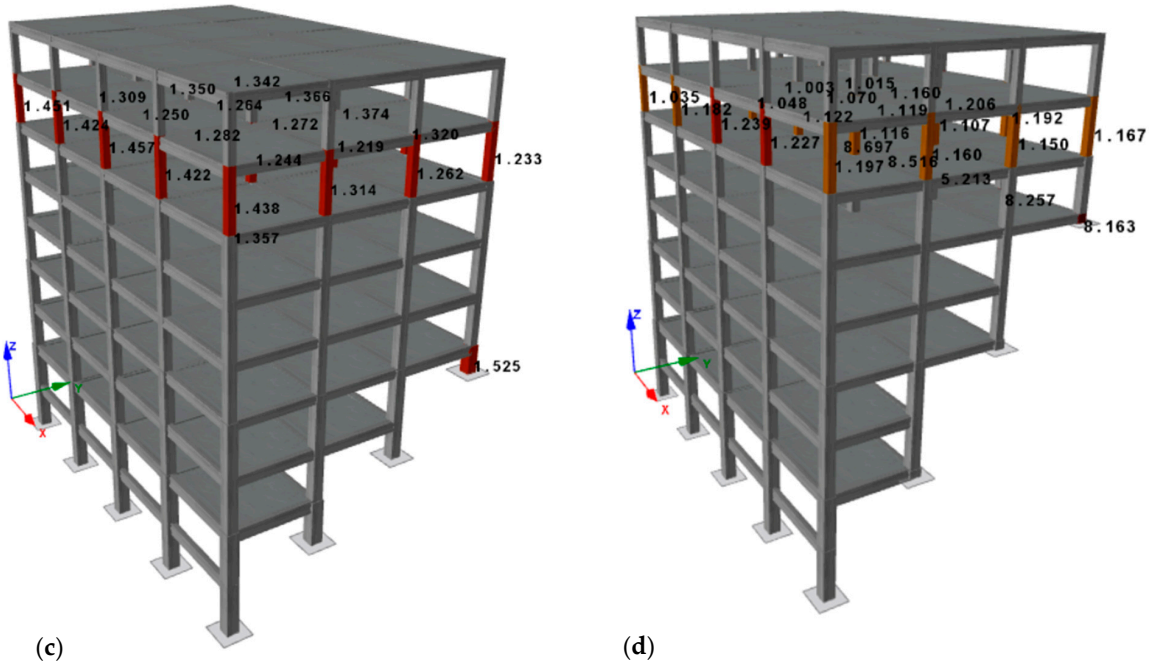

(**c**) (**d**)

Figure 14. Elements that exceed the limit for the demand-capacity relationship in the archetypes (**a**) 0°, (**b**) 15°, (**c**) 30°, and (**d**) 45° subjected to the action of synthetic accelerograms for the Immediate Occupancy limit state (1-B).

4. Conclusions

The study further confirms the complexity of the nonlinear response of buildings to seismic loads, which has a significant dependence on structural symmetry. The adaptation of buildings to sloped terrains introduces inherent asymmetries, even when attempts are made to maintain the regularity of the building's geometry. The identified irregularities, such as misaligned centers of gravity across successive stories, increased mass with height, double-story heights due to the impossibility of placing slabs on certain floors, and the formation of short columns due to vertical support shortening on slopes, underscore the challenges posed by slope-induced asymmetry.

Based on the comprehensive results and discussions presented in this study, the following conclusions can be drawn:

1. Influence of Asymmetry on Dynamic Response: The linear analysis indicated a significant impact of asymmetry on the dynamic response of the buildings, a factor that becomes increasingly critical as the slope of the terrain, and hence the irregularity of the buildings in both plan and elevation, increases. This underscores the need for considering a higher number of vibration modes to accurately capture the seismic behavior of structures located on sloped terrains.
2. Nonlinear Ductility and Capacity: The nonlinear analyses, particularly with incremental pushover, demonstrated that the archetypes exhibited adequate ductility in both the X and Y directions. This finding is pivotal, as it suggests that despite the geometric complexities introduced by slope-induced asymmetry, the designed archetypes can still achieve the desirable level of seismic performance.
3. Transient Interstory Drift and Damage Control: The dynamic nonlinear analysis, essential for closely approximating the seismic response of buildings, highlights the significance of transient interstory drift as a critical measure of seismic damage. This study confirmed that the maximum allowable drift values, as dictated by ASCE 7, were not exceeded, ensuring that all the dynamic time-history analyses results can be considered reliable for performance evaluation.
4. Acceptance Criteria and Structural Design Suitability: The application of ASCE 7 acceptance criteria based on transient interstory drift offers a robust framework for

evaluating the seismic suitability of structural designs. Our findings reveal that despite the potential increases in drift due to architectural asymmetry, the structural integrity remains within safe limits, affirming the effectiveness of conventional design practices in mitigating seismic risks.

5. Rotations Control and Irregularity Effects: Contrary to expectations, archetypes with higher degrees of irregularity (45°) did not exhibit the highest rotations, challenging the preconceived notions about the relationship between structural asymmetry and torsional responses. This suggests that the presence of structural supports and the method of displacement restriction play a significant role in mitigating potential damage, especially in highly irregular structures.
6. Comprehensive Damage Analysis: The extensive damage control analysis, considering both demand versus capacity ratios and specific architectural features like short columns and reduced stiffness on upper stories, provides a nuanced understanding of seismic vulnerability. This approach allows for a detailed examination of how structural and non-structural elements contribute to the overall seismic resilience of buildings on sloped terrains.
7. Incorporation into Current Standards: There is a pressing need for current seismic design standards to include provisions that directly address the design of buildings located on slopes, ensuring that their dynamic response and the irregularity caused by asymmetry are considered in conventional design procedures. This inclusion would enhance the seismic safety and performance of such structures, acknowledging the unique challenges posed by sloped terrains.

In conclusion, this study contributes valuable insights into the seismic performance of reinforced concrete buildings on sloped terrains, emphasizing the critical role of asymmetry, structural ductility, and the application of dynamic nonlinear analyses in enhancing seismic design codes. The findings underscore the importance of integrating comprehensive dynamic analyses and conventional design practices with specific guidelines for sloped terrain construction to ensure the safety, durability, and resilience of structures in seismically active regions. In line with this, further studies are required on the response of buildings situated on slopes, including other structural typologies, materials, and configurations.

Author Contributions: Conceptualization, E.G.D.-S. and J.C.V.; Methodology, J.C.V.-Q., E.G.D.-S. and J.C.V.; Software, J.C.V.-Q.; Validation, E.G.D.-S. and J.C.V.; Formal analysis, J.C.V.-Q. and J.C.V.; Investigation, E.G.D.-S. and J.C.V.; Resources, J.C.V.-Q., E.G.D.-S. and J.C.V.; Data curation, J.C.V.-Q.; Writing—original draft, J.C.V.-Q., E.G.D.-S. and J.C.V.; Writing—review & editing, J.C.V.-Q., E.G.D.-S. and J.C.V.; Visualization, E.G.D.-S. and J.C.V.; Supervision, E.G.D.-S. and J.C.V.; Project administration, E.G.D.-S. and J.C.V.; Funding acquisition, E.G.D.-S. and J.C.V. All authors have read and agreed to the published version of the manuscript.

Funding: This research was funded by the Agencia Nacional de Investigación y Desarrollo (ANID Chile), grant number FOVI 210063. Council of the International Geoscience Program (UNESCO): Grant number 701: 2020-2022.

Data Availability Statement: The data from this research are available to interested parties upon request to the corresponding author.

Acknowledgments: The authors thank the Pontificia Universidad Católica de Valparaíso for the support provided in the development of the research, as well as the support in the publication of the article. The authors also acknowledge the support of the PUCV School of Civil Engineering in whose facilities the research activities that gave rise to this article have been carried out. The authors acknowledge accessing strong-motion data through the Center for Engineering Strong Motion Data (CESMD), last visited on 5 May 2023. The networks or agencies providing the data used in this report are the California Strong Motion Instrumentation Program (CSMIP) and the USGS National Strong Motion Project (NSMP).

Conflicts of Interest: The authors declare no conflicts of interest.

References

1. Fotopoulou, S.D.; Pitilakis, K.D. Vulnerability Assessment of Reinforced Concrete Buildings at Precarious Slopes Subjected to Combined Ground Shaking and Earthquake Induced Landslide. *Soil Dyn. Earthq. Eng.* **2017**, *93*, 84–98. [CrossRef]
2. Tripe, R.; Kontoe, S.; Wong, T.K.C. Slope Topography Effects on Ground Motion in the Presence of Deep Soil Layers. *Soil Dyn. Earthq. Eng.* **2013**, *50*, 72–84. [CrossRef]
3. Bourdeau, C.; Havenith, H.-B. Site Effects Modelling Applied to the Slope Affected by the Suusamyr Earthquake (Kyrgyzstan, 1992). *Eng. Geol.* **2008**, *97*, 126–145. [CrossRef]
4. Mohammad, Z.; Baqi, A.; Arif, M. Seismic Response of RC Framed Buildings Resting on Hill Slopes. *Procedia Eng.* **2017**, *173*, 1792–1799. [CrossRef]
5. Zaidi, S.A.; Naqvi, T.; Ibrahim, S.M. Study on the Effects of Seismic Soil-Structure Interaction of Concrete Buildings Resting on Hill Slopes. *Mater. Today Proc.* **2021**, *43*, 2250–2254. [CrossRef]
6. Fatahi, B.; Huang, B.; Yeganeh, N.; Terzaghi, S.; Banerjee, S. Three-Dimensional Simulation of Seismic Slope-Foundation-Structure Interaction for Buildings near Shallow Slopes. *Int. J. Geomech.* **2020**, *20*, 04019140. [CrossRef]
7. Shabani, M.J.; Shamsi, M.; Ghanbari, A. Slope Topography Effect on the Seismic Response of Mid-Rise Buildings Considering Topography-Soil-Structure Interaction. *Earthq. Struct.* **2021**, *20*, 187–200. [CrossRef]
8. Assimaki, D.; Kausel, E. Modified Topographic Amplification Factors for a Single-Faced Slope Due to Kinematic Soil-Structure Interaction. *J. Geotech. Geoenviron. Eng.* **2007**, *133*, 1414–1431. [CrossRef]
9. Paolucci, R. Amplification of Earthquake Ground Motion by Steep Topographic Irregularities. *Earthq. Engng. Struct. Dyn.* **2002**, *31*, 1831–1853. [CrossRef]
10. Schmitz, M.; Hernández, J.J.; Rocabado, V.; Domínguez, J.; Morales, C.; Valleé, M.; García, K.; Sánchez-Rojas, J.; Singer, A.; Oropeza, J.; et al. The Caracas, Venezuela, Seismic Microzoning Project: Methodology, Results, and Implementation for Seismic Risk Reduction. *Prog. Disaster Sci.* **2020**, *5*, 100060. [CrossRef]
11. Patel, M.U.F. A Performance Study and Seismic Evaluation of RC Frame Buildings on Sloping Ground. *IOSR J. Mech. Civ. Eng. (IOSR-JMCE)* **2018**, *2014*, 51–58. [CrossRef]
12. Vijayanarayanan, A.R.; Goswami, R. Floor Acceleration Spectrum for RC Moment Frame Buildings on Slopes. In Proceedings of the 17th World Conference on Earthquake Engineering, 17WCEE, Sendai, Japan, 13–18 September 2020.
13. Lang, D.; Singh, Y.; Molina, S.; Surana, M. Peculiarities of Seismic Risk in Hilly Regions: Topographic Effects on Hazard and Vulnerability. In *Progresses in European Earthquake Engineering and Seismology*; Vacareanu, R., Ionescu, C., Eds.; Springer Proceedings in Earth and Environmental Sciences; Springer International Publishing: Cham, Switzerland, 2022; pp. 295–307. ISBN 978-3-031-15103-3.
14. Standards New Zealand. *Structural Design Actions. Part 5, Earthquake Actions: New Zealand: Commentary*; Standards New Zealand: Wellington, New Zealand, 2004; ISBN 978-1-86975-019-0.
15. Athanasopoulou, A.; Fardis, M.; Pinto, P.; Aucun, B.; Tsionis, G.; Somja, H.; Plumier, A.; Pecker, A.; Franchin, P.; Carvalho, E.; et al. *Eurocode 8: Seismic Design of Buildings—Worked Examples*; Publications Office: Luxembourg, 2012; ISBN 978-92-79-23068-4.
16. International Code Council. *2018 IBC: International Building Code*; International Code Council, Inc.: Country Club Hills, IL, USA, 2017; ISBN 978-1-60983-735-8.
17. Shabani, M.J.; Ghanbari, A. Comparison of Seismic Behavior of Steel Building Adjacent to Slope Topography by Considering Fixed-Base, SSI and TSSI. *Asian J. Civ. Eng.* **2020**, *21*, 1151–1169. [CrossRef]
18. Aggarwal, Y.; Saha, S.K. Seismic Performance Assessment of Reinforced Concrete Hilly Buildings with Open Story. *Structures* **2021**, *34*, 224–238. [CrossRef]
19. Bhasker, R.; Menon, A. Torsional Irregularity Indices for the Seismic Demand Assessment of RC Moment Resisting Frame Buildings. *Structures* **2020**, *26*, 888–900. [CrossRef]
20. Raychowdhury, P.; Ray-Chaudhuri, S. Seismic Response of Nonstructural Components Supported by a 4-Story SMRF: Effect of Nonlinear Soil-Structure Interaction. *Structures* **2015**, *3*, 200–210. [CrossRef]
21. Foti, D. Local Ground Effects in Near-Field and Far-Field Areas on Seismically Protected Buildings. *Soil Dyn. Earthq. Eng.* **2015**, *74*, 14–24. [CrossRef]
22. Hasan, M.; Serker, N.H.M.K. Seismic Analysis of RC Buildings Resting on Sloping Ground with Varying Hill Slopes. In Proceedings of the International Conference on Planning, Architecture and Civil Engineering, Rajshahi, Bangladesh, 7–9 February 2019.
23. Chhetri, S.; Adhikari, S. Seismic Performance of Step Back, Step Back Set Back and Set Back Buildings in Sloping Ground Base. *Struct. Mech. Eng. Constr. Build.* **2021**, *17*, 538–547. [CrossRef]
24. Alitalesh, M.; Shahnazari, H.; Baziar, M.H. Parametric Study on Seismic Topography–Soil–Structure Interaction; Topographic Effect. *Geotech. Geol. Eng.* **2018**, *36*, 2649–2666. [CrossRef]
25. Amendola, C.; Pitilakis, D. Urban Scale Risk Assessment Including SSI and Site Amplification. *Bull. Earthq. Eng.* **2022**, *50*, 133–141. [CrossRef]
26. Daniel, J.; Sivakamasundari, S. Seismic Behaviour of Stiffness Irregular Building on Hill Slope. *Int. J. Aerosp. Lightweight Struct.* **2014**, *4*, 281–300.
27. Jamle, S. Response of Multistory Building Located on 20 Degree and 30 Degree Sloping Ground under Seismic Loading. *Int. Res. J. Eng. Technol.* **2020**, *6*, 1178252. [CrossRef]
28. Song, P.; Guo, S.; Zhao, W.; Xin, Q. Seismic Response Analysis of Reinforced Concrete Frame Structures Considering Slope Effects. *Appl. Sci.* **2023**, *13*, 5149. [CrossRef]

29. Priyanshu, K.; Kumar, V. Seismic Response of Special Moment Resisting Frames Constructed on Plain and Sloping Ground. *IOP Conf. Ser. Earth Environ. Sci.* **2023**, *1110*, 012068. [CrossRef]
30. American Society of Civil Engineers. *Seismic Evaluation and Retrofit of Existing Buildings*, 41st ed.; American Society of Civil Engineers: Reston, VA, USA, 2017; ISBN 978-0-7844-1485-9.
31. Razi, M.A.; Mohammad, Z.; Ali, S.A. Seismic Analysis of Hill Buildings. In Proceedings of the International Conference on Advances in Construction Materials and Structures (ACMS-2018), Uttarakhand, India, 7–8 March 2018.
32. Fan, Z.; Liu, T.; Yang, S. Analysis on Performances of Frame Structures on Sloping Ground. *Build. Struct.* **2016**, *46*, 1–9.
33. Ghosh, R.; Debbarma, R. Effect of Slope Angle Variation on the Structures Resting on Hilly Region Considering Soil–Structure Interaction. *Int. J. Adv. Struct. Eng.* **2019**, *11*, 67–77. [CrossRef]
34. Jarapala, R.; Menon, A. Seismic Performance of Reinforced Concrete Buildings on Hill Slopes: A Review. *J. Inst. Eng. India Ser. A* **2023**, *104*, 721–745. [CrossRef]
35. Farghaly, A.A. Evaluation of Seismic Performance of Buildings Constructed on Hillside Slope of Doronka Village-Egypt. *ISRN Civ. Eng.* **2014**, *2014*, 940923. [CrossRef]
36. Ganie, M.A.; Gupta, S. Seismic Behavior of Short Columns of an RC-Frame on Plane and Sloping Ground: Review. In Proceedings of the 2018 5th International Conference on "Computing for Sustainable Global Development", New Delhi, India, 14–16 March 2018.
37. Singh, A.; Tolani, S.; Bharti, S.D.; Datta, T.K. Seismic Analysis of Flat Slab Buildings on Hilly Ground. *ASPS Conf. Proc.* **2022**, *1*, 775–779. [CrossRef]
38. Aggarwal, Y.; Saha, S.K. An Improved Rapid Visual Screening Method for Seismic Vulnerability Assessment of Reinforced Concrete Buildings in Indian Himalayan Region. *Bull. Earthq. Eng.* **2023**, *21*, 319–347. [CrossRef]
39. Gómez, M.A.; Díaz-Segura, E.G.; Vielma, J.C. Nonlinear Numerical Assessment of the Seismic Response of Hillside RC Buildings. *Earthq. Eng. Eng. Vib.* **2021**, *20*, 423–440. [CrossRef]
40. Gómez, M.A.; Vielma, J.C.; Díaz-Segura, E.G. Evaluación numérica de la respuesta sísmica de estructuras fundadas en laderas. *Obras Y Proy.* **2022**, *31*, 68–76. [CrossRef]
41. Patil, R.T.; Raghunandan, M. Seismic Collapse Risk of Reinforced Concrete Hillside Buildings in Indian Himalayan Belt. *Bull Earthq. Eng* **2021**, *19*, 5665–5689. [CrossRef]
42. National Institute of Standardization. *Diseño Sísmico de Edificios Nch 433*; National Institute of Standardization: Santiago, Chile, 2009. (In Spanish)
43. CEN. *Eurocode 8: Design of Structures for Earthquake Resistance*; European Committee for Standardization: Brussels, Belgium, 2005.
44. ASCE. *Minimum Design Loads and Associated Criteria for Buildings and Other Structures: ASCE/SEI 7-22*; ASCE, American Society of Civil Engineer (Reston, Virginia), Ed.; American Society of Civil Engineers: Reston, VA, USA, 2022; ISBN 978-0-7844-1578-8.
45. Cook, D.; Sen, A.; Liel, A.; Basnet, T.; Creagh, A.; Koodiani, H.K.; Berkowitz, R.; Ghannoum, W.; Hortacsu, A.; Kim, I.; et al. ASCE/SEI 41 Assessment of Reinforced Concrete Buildings: Benchmarking Nonlinear Dynamic Procedures with Empirical Damage Observations. *Earthq. Spectra* **2023**, *39*, 1721–1754. [CrossRef]
46. Vielma-Quintero, J.C.; Carvallo, J.; Vielma, J.C. Comparative Assessment of Performance-Based Design Methodologies Applied to a R.C. Shear-Wall Building. *Buildings* **2023**, *13*, 1492. [CrossRef]
47. Bhasker, R.; Menon, A. Characterization of Ground Motion Intensity for the Seismic Fragility Assessment of Plan-Irregular RC Buildings. *Structures* **2020**, *27*, 1763. [CrossRef]
48. Mander, J.B.; Priestley, M.J.N.; Park, R. Theoretical Stress-Strain Model for Confined Concrete. *J. Struct. Eng.* **1998**, *114*, 1804–1826. [CrossRef]
49. Menegotto, M.; Pinto, M. *Method of Analysis for Cyclically Loaded, R.C. Plane Frames Including Changes in Geometry and Nonelastic Behavior of Elements under Combined Normal Force and Bending*; ETH Zürich: Zurich, Switzerland, 1973; pp. 15–22.
50. Vielma-Perez, J.; Mulder, M. Improved Procedure for Determining the Ductility of Buildings under Seismic Loads. *RIMNI* **2018**, *34*, 1–27. [CrossRef]
51. Hosseinpour, F.; Abdelnaby, A.E. Effect of Different Aspects of Multiple Earthquakes on the Nonlinear Behavior of RC Structures. *Soil Dyn. Earthq. Eng.* **2017**, *92*, 706–725. [CrossRef]
52. Center for Engineering Strong Motion Data (CESMD). 2023. Available online: https://www.strongmotioncenter.org/index.html (accessed on 5 May 2023).
53. Seismosoft Ltd. SeismoSpect. A Computer Program for Post-Processing of Groups of Earthquake Records. Pavia, Italy. 2021. Available online: https://seismosoft.com/ (accessed on 1 February 2021).
54. Seismosoft Ltd. SeismoMatch. A Computer Program for Spectrum Matching of Earthquake Records. Pavia, Italy. 2021. Available online: https://seismosoft.com/ (accessed on 1 February 2021).
55. Seismosoft Ltd. SeismoStruct 2021 User Manual—A Computer Program for Static and Dynamic Nonlinear Analysis of Framed Structures. Pavia, Italy. 2021. Available online: https://seismosoft.com/ (accessed on 1 February 2021).
56. Seismosoft Ltd. SeismoBuild. A Computer Program for Seismic Assessment of Reinforced Concrete Framed Structures. Pavia, Italy. 2021. Available online: https://seismosoft.com/ (accessed on 1 February 2021).
57. Khanal, B.; Chaulagain, H. Seismic Elastic Performance of L-Shaped Building Frames through Plan Irregularities. *Structures* **2020**, *27*, 22–36. [CrossRef]
58. Vielma, J.C.; Porcu, M.C.; López, N. Intensity Measure Based on a Smooth Inelastic Peak Period for a More Effective Incremental Dynamic Analysis. *Appl. Sci.* **2020**, *10*, 8632. [CrossRef]

59. Vielma, J.; Barbat, A.H.; Oller, S. Seismic Performance of Waffled-Slab Floor Buildings. *Proc. Inst. Civ. Eng.—Struct. Build.* **2009**, *162*, 169–182. [CrossRef]
60. Vielma, J.C.; Barbat, A.H.; Oller, S. Seismic Safety of Low Ductility Structures Used in Spain. *Bull Earthq. Eng* **2010**, *8*, 135–155. [CrossRef]
61. Uva, G.; Porco, F.; Fiore, A.; Ruggieri, S. Effects in Conventional Nonlinear Static Analysis: Evaluation of Control Node Position. *Structures* **2018**, *13*, 178–192. [CrossRef]
62. De Stefano, M.; Mariani, V. Pushover Analysis for Plan Irregular Building Structures. *Geotech. Geol. Earthq. Eng.* **2014**, *34*, 429–448. [CrossRef]
63. La Brusco, A.; Mariani, V.; Tanganelli, M.; Viti, S.; De Stefano, M. Seismic Assessment of a Real RC Asymmetric Hospital Building According to NTC 2008 Analysis Methods. *Bull. Earthq. Eng.* **2015**, *13*, 2973–2994. [CrossRef]
64. Rezazadeh, H.; Amini, F.; Afshar, M.A. Effect of Inertia Nonlinearity on Dynamic Response of an Asymmetric Building Equipped with Tuned Mass Dampers. *Earthq. Eng. Eng. Vib.* **2020**, *19*, 499–513. [CrossRef]
65. Kewalramani, M.A.; Syed, Z.I. Seismic Analysis of Torsional Irregularity in Multi-Storey Symmetric and Asymmetric Buildings. *Eurasian J. Anal. Chem.* **2018**, *13*, 286–292.
66. Zavala, D.J.; Torres, C.J.; Moreno, J.D. Influence of the P-Delta Effect and Stiffness Irregularity on the Structural Behavior of Reinforced Concrete Buildings. *J. Phys. Conf. Ser.* **2022**, *2287*, 012047. [CrossRef]

Disclaimer/Publisher's Note: The statements, opinions and data contained in all publications are solely those of the individual author(s) and contributor(s) and not of MDPI and/or the editor(s). MDPI and/or the editor(s) disclaim responsibility for any injury to people or property resulting from any ideas, methods, instructions or products referred to in the content.

symmetry

MDPI

Article

Symmetry Properties of Models for Reversible and Irreversible Thermodynamic Processes

S. A. Lurie [1,*], P. A. Belov [1] and H. A. Matevossian [2]

[1] Institute of Applied Mechanics of RAS, Moscow 125040, Russia; belovpa@yandex.ru
[2] Federal Research Center "Computer Science and Control", Russian Academy of Sciences, Moscow 119333, Russia; hmatevossian@graduate.org
* Correspondence: salurie@mail.ru

Abstract: The problem of formulating variational models for irreversible processes of media deformation is considered in this paper. For reversible processes, the introduction of variational models actually comes down to defining functionals with a given list of arguments of various tensor dimensions. For irreversible processes, an algorithm based on the principle of stationarity of the functional is incorrect. In this paper, to formulate a variational model of irreversible deformation processes with an expanded range of coupled effects, an approach is developed based on the idea of the introduction of the non-integrable variational forms that clearly separate dissipative processes from reversible deformation processes. The fundamental nature of the properties of symmetry and anti-symmetry of tensors of physical properties in relation to multi-indices characterizing independent arguments of bilinear forms in the variational formulation of models of thermomechanical processes has been established. For reversible processes, physical property tensors must necessarily be symmetric with respect to multi-indices. On the contrary, for irreversible thermomechanical processes, the tensors of physical properties that determine non-integrable variational forms must be antisymmetric with respect to the permutation of multi-indices. As a result, an algorithm for obtaining variational models of dissipative irreversible processes is proposed. This algorithm is based on determining the required number of dissipative channels and adding them to the known model of a reversible process. Dissipation channels are introduced as non-integrable variational forms that are linear in the variations of the arguments. The hydrodynamic models of Darcy, Navier–Stokes, and Brinkman are considered, each of which is determined by a different set of dissipation channels. As another example, a variational model of heat transfer processes is presented. The equations of heat conduction laws are obtained as compatibility equations by excluding the introduced thermal potential from the constitutive equations for temperature and heat flux. The Fourier and Maxwell–Cattaneo equations and the generalized heat conduction laws of Gaer–Krumhansl and Jeffrey are formulated.

Keywords: variational principle; dissipative processes; symmetry properties; dissipation channels; hydrodynamics; heat conduction laws; heat transfer equations

1. Introduction

Due to their relevance, coupled processes of deformation of media, taking into account heat and mass transfer and various physical fields, are subjects of tremendous interest in the scientific world in recent years. We note several recent monographs that provide an overview, analysis and comparison of such models [1–3].

Research and modeling of reversible and irreversible processes of deformation thermodynamics, taking into account the coupled interactions effects of various physical fields and deformation fields, are extremely in demand in applications [4–11]. The associated coupled thermodynamic effects are usually significant in highly heterogeneous systems with microstructures and nanostructures, where concentration and temperature gradients can be significant. In [4], the authors discussed thermal diffusion and diffusion-thermal

effects in an axisymmetric fluid flow along a stretching wall. It was shown in [5,6] that in the processes of heat and mass transfer, it is necessary to take into account the features of the structure, which manifest themselves through various cross-effects. Interesting studies of heat and mass transfer processes in deformable bodies and inhomogeneous structures are provided in [7–11]. Variational models were considered in [12] to describe the relationship between the processes of deformation and heating for periodic structures.

Although, in general, these effects are of a lower order in comparison with the effects due, for example, to the Fourier and Fick laws (which are associated with the basic variables), but coupled effects can manifest themselves in systems where concentration and temperature gradients can be significant, in particular, in highly inhomogeneous systems with micro- and nanostructures [11–15]. Undoubtedly, coupled effects can make a significant contribution to the modeling of reversible and irreversible processes of structures' deformation. An example of the importance of coupled effects can be the damping theory of oscillations, originally proposed in papers [16–18] and later improved in the research [19], which received remarkable experimental confirmation. Variational methods of modeling the processes of thermodynamics in complex environments are preferable because they allow you to propose the most complete and fully thermodynamically consistent models that are invariant with respect to coordinate transformations. In this regard, we also note papers [20–22], where variational models were used to describe irreversible processes and where the fundamental nature of the principle of possible displacements, which is valid for reversible and irreversible processes, was emphasized.

Determination of a list of generalized variables of functionals when modeling reversible and irreversible processes using variational methods is one of the main problems. This problem was initially considered in [23–26], related to coupled thermos-elasticity and heat transfer, and then was developed in relatively recent pioneering articles [13–15].

For modeling reversible thermodynamic deformation processes, variational methods are very effective [11,20–22,27,28], etc. They involve the introduction of thermodynamic potentials for models of media of varying complexity and the use of variational principles. The use of variational approaches makes it possible to formulate both the constitutive and balance equations and the boundary value problem as a whole.

For irreversible processes, this approach is not correct. Typically, to formulate models of irreversible processes, thermodynamic potentials and thermodynamic inequalities are used, reflecting the second law of thermodynamics [25,29,30]. This approach does not allow formulating a closed mathematical model in a variational way. A constructive alternative to this approach is to use the dissipative function [31,32]. In this case, the force factors are defined as the gradients of this dissipative function, which contradicts the definition of dissipative processes and, therefore, seems incorrect. Here, it is necessary to note the paper [32], where, although authors are talking about the introduction of a dissipative functional, nevertheless, the possibility of using the principle of possible displacements written in variations is briefly postulated, which formally allows us to correct the variational formulation (the structure of the dissipative linear form is not discussed).

In the present paper, to describe dissipative processes, we, for the first time, propose to introduce a universal variational model that can be written in the variations using a linear variational form of independent arguments (see also [33–35]). The variational equation is determined by adding the required number of dissipation channels to the known model of a reversible process (the known Lagrangian). Dissipation channels are introduced as non-integrable variational forms that characterize dissipative models of media of varying complexity depending on the tensor dimension of the arguments. We proposed an algorithm according to which the structure of the energy variational equality is established using the fundamental symmetry properties of tensors of physical characteristics for the functional of the reversible processes and, respectively, using the anti-symmetry properties for tensors of physical moduli in the non-integrable variational forms for the dissipative process. Complete mathematical models of reversible and irreversible processes are ob-

tained using stationarity principles. Hydrodynamic irreversible processes and heat transfer processes are considered as examples.

2. Variational Form in Thermodynamic Processes of Deformations: Dissipation Channels

It is known that for solid deformation problems, the Lagrange variational principle for reversible processes is written in the form:

$$\delta L = \delta(A - U) = 0$$

where, $L = A - U$ is the Lagrangian, A is the work of the external forces given in the volume V and on the surface of the body, $U = \int\limits_V U_V(\varepsilon_{ij}; \ldots)dV$ is the potential energy, and $U_V(\varepsilon_{ij}; \ldots)$ is the potential energy density. The following are dependent on a list of kinematic arguments: deformations tensor ε_{ij}, derivatives of the deformation tensor $\varepsilon_{ij,k}$, etc.

Necessary conditions for reversible processes are Green's formulas, which provide the possibility of generating energetically consistent constitutive relations.

Along with reversible processes, we also consider irreversible ones. In this case, the variational form $\delta\overline{U}$, which is the possible work of internal forces, is not integrable. Consequently, the tensor static factors corresponding to tensor kinematical arguments and performing possible work on these variables are not expressed in terms of derivatives of certain potential. We assume, in this case, that the static factors are continuous functions of the kinematic parameters.

For irreversible processes, the variational principle was proposed by L.I. Sedov [33–35]. The corresponding variational equation for dynamic processes is written as:

$$\delta I - \delta W^* = 0 \tag{1}$$

where $I = A - (U - K)$, K is the kinetic energy, $(U - K)$ is the reversible part of dynamic energy for the deformation process, and δW^* is the linear form with respect to variations in the kinematic parameters, which takes into account irreversible processes (i.e., a change in entropy and heat gain).

We further assume that the list of kinematical parameters (generalized arguments) for the dissipative part of the linear variational form δW^* coincides with the list of kinematical parameters of the variational form for the reversible part of the energy (potential energy and kinetic energy $U - K$).

Also, we propose that Equation (1) is obtained by integrating the corresponding densities over the volume of the body V and over the time interval from the moment t_0, corresponding to the initial configuration, to the time t_1, corresponding to the final configuration. The linear form δW^* can contain both integrals over the volume and over the hypersurface of the event space occupied by the body. In the general case, by volume integral of the event space, we mean the integral:

$$\int [\ldots] d\overline{V} = \int\limits_{t_0}^{t_1} \int\limits_V [\ldots] dV dt$$

Analyzing the general structure of the variational form δW^*, we use the symbolic form of notation, which permits simplification of the notation of the expressions under study. To perform the above, we introduce multi-indices for volume and surface parts of the linear form. Let us assume that the multi-indices a and b range from 1 to N (according to the number of tensor kinematic parameters). Along with δU, defined as a sum of all integrable forms for the process under consideration, let us consider the variational form $\overline{\delta U}$, which represents a particular non-integrable form. Then, the variational form will be written in the following form:

$$\overline{\delta U} = \int\limits_V P_a(Q_b)\delta Q_a dV \tag{2}$$

where the upper bar indicates that the corresponding variational form (2) is a non-integrable, Q_a indicates tensor objects of any tensor order (generalized kinematic variables), and P_a are internal force factors that perform possible work on the introduced generalized kinematic variables Q_a, respectively, in the volume.

For example, the value Q_a can be understood as a tensor of the second rank ε_{ij}, and/or a tensor of the third rank $\varepsilon_{ij,k}$. The value $P_a(Q_b)\delta Q_a$ is understood not as a convolution of vectors, but as a convolution of tensor objects P_a and δQ_a of the same rank.

Equation (1) can be generalized when the non-integrated variational form is defined not only in the volume but also on the surface of the body:

$$\overline{\delta U} = \int\limits_V P_a^V(Q_b^V)\delta Q_a^V d\overline{V} + \iint\limits_F P_a^F(Q_b^F)\delta Q_a^F d\overline{F} \tag{3}$$

where Q_a^V, Q_a^F and P_a^V, P_a^F are generalized kinematic variables (tensor objects) and internal force factors that perform possible work on the introduced generalized kinematic variables.

Both parts of Equation (3) are obtained by integrating the corresponding densities in the volume of the body and of its surface and over the time interval from the moment t_0, corresponding to the initial configuration, to the time t_1, corresponding to the final configuration.

It should be borne in mind that time is considered as a parameter. Therefore, the list of kinematic parameters (arguments) should also include time derivatives of kinematic parameters of various tensor dimensions − generalized velocities. For example, the deformation tensor ε_{ij} and the strain rate tensor $\dot{\varepsilon}_{ij}$ are the various generalized variables Q_a and Q_b, $Q_a \neq Q_b$, $a \neq b$.

We will model dissipative processes using the variational approach. Let us introduce the sufficient non-integrability conditions, which are constructed explicitly for the corresponding bilinear terms. Sufficient conditions of non-integrability of form (2) will have the form:

$$\begin{aligned} &\tfrac{\partial P_a}{\partial Q_b} - \tfrac{\partial P_b}{\partial Q_a} = 2\overline{C}_{ab}(Q_c), \\ &\overline{C}_{ba} = -\overline{C}_{ab}, \end{aligned} \tag{4}$$

Thus, for irreversible processes, the quantities of $\overline{C}_{ab}$ in the constitutive relations are not symmetrical with respect to multi-indices, while for reversible processes, similar parameters $C_{ab}(Q_c)$ (tensors of elastic moduli) are obviously symmetrical when permuting multi-indices, $C_{ab} = C_{ba}$. As an example, let us consider the form $\delta U = \sigma_{ij}\delta\varepsilon_{ij} + \sigma_{mn}\delta\varepsilon_{mn}$. Assume that this form is integrated. Then, $\sigma_{ij} = \frac{\partial U}{\partial \varepsilon_{ij}}$, $\sigma_{mn} = \frac{\partial U}{\partial \varepsilon_{mn}}$, $\sigma_{ij} = C_{ijmn}\varepsilon_{mn}$, and $C_{ijmn} = C_{mnij}$, where the last equation follows from the equality $\frac{\partial}{\partial \varepsilon_{ij}}\frac{\partial U}{\partial \varepsilon_{mn}} - \frac{\partial}{\partial \varepsilon_{mn}}\frac{\partial U}{\partial \varepsilon_{ij}} = 0$.

In this case, $\delta U = \sigma_{ij}\delta\varepsilon_{ij} + \sigma_{mn}\delta\varepsilon_{mn} = C_{ijmn}(\varepsilon_{mn}\delta\varepsilon_{ij} + \varepsilon_{ij}\delta\varepsilon_{mn}) = C_{ijmn}\delta(\varepsilon_{ij}\varepsilon_{mn})$.

On the other hand, if we can form $(\varepsilon_{mn}\delta\varepsilon_{ij} - \varepsilon_{ij}\delta\varepsilon_{mn})$, then it is impossible to construct a potential for it, and, consequently, such a form is non-integrable.

Generally, we can propose that $\frac{\partial P_a}{\partial Q_b}$ defines in (4) the tensor of effective modulus and includes the integrable and non-integrable constituent parts:

$$\frac{\partial P_a}{\partial Q_b} = C_{ab}(Q_c) + \overline{C}_{ab}(Q_c) \tag{5}$$

For reversible processes, it should be assumed that $\overline{C}_{ba} = 0$. Then, equalities (2) pass into the conditions of integrability of the linear form $\overline{\delta U}$, and $\overline{\delta U} = \delta U$. On the contrary, the presence of a value $\overline{C}_{ba}$ in expression (5) is a sign of the non-integrability of form (2).

Note that the sufficient conditions in non-integrable (4) can be used as links introduced on the Lagrange multipliers in the formulation of the extended linear form, which is the basis for the variational formulation of processes, including both reversible and irreversible processes.

However, for physically linear models, Equation (2) can be explicitly integrated and used to formulate the linear form $\delta\overline{U}$ for nonholonomic media directly.

Indeed, for physically linear models, the tensors of thermomechanical properties, C_{ab} and $\overline{C}_{ab}$, do not depend on the kinematic parameters (generalized deformation factors). Therefore, by direct integration (5), we can obtain:

$$P_a = (C_{ab} + \overline{C}_{ab})Q_b \tag{6}$$

Taking into account the constitutive Equation (6), we rewrite (2) in the form:

$$\begin{aligned}
&\overline{\delta U} = \int P_a \delta Q_a d\overline{V} = \\
&= \int (C_{ab} + \overline{C}_{ab}) Q_b \delta Q_a d\overline{V} = \\
&= \delta \int \tfrac{1}{2} C_{ab} Q_a Q_b d\overline{V} + \tfrac{1}{2} \int [\overline{C}_{ab}(Q_b \delta Q_a - Q_a \delta Q_b)] d\overline{V}
\end{aligned}$$

Comparing the last equality with the variational Equation (1), for physically linear nonholonomic media, we obtain the following general form of the terms of main variational Equation (1):

$$I = \int [P_i^V R_i - \frac{1}{2} C_{ab} Q_a Q_b] d\overline{V} \quad \delta W^* = \frac{1}{2} \int [\overline{C}_{ab}(Q_b \delta Q_a - Q_a \delta Q_b)] d\overline{V} \tag{7}$$

Following (7), we can state that obtaining the work of dissipative forces in general form required at least two objects of the same tensor dimension. So, for example, we can use two tensors, ε_{ij} and $\overset{\bullet}{\varepsilon}_{ij}$, to define the variant of dissipation work: $\varepsilon_{ij}\delta\overset{\bullet}{\varepsilon}_{mn} - \overset{\bullet}{\varepsilon}_{mn}\delta\varepsilon_{ij}$.

Thus, Equations (6) and (7) provide a generalized variational description of linear models of media with dissipation and, generally, determine the general algorithm for elaboration of the dissipative media models.

As a result, an algorithm for constructing a variational model of dissipative processes, which is reduced to the following sequence of steps, is proposed:

- Postulation of a kinematic model (assignment of a list of arguments);
- Formulation of the work of internal forces (definition of the force model);
- Formulation of conditions for integrability/non-integrability of the work of internal forces;
- Integration of the reversible part and formulation of the functional for the reversible part of the process under consideration;
- Formulation of dissipation channels.

3. Variational Equations

Let us consider linear isotropic media and present a general procedure for constructing a variational model of irreversible processes. The developed algorithm can be used for models of virtually any complexity. First of all, consider the stationary problem for a generalized gradient isotropic body and assume that the list of kinematic arguments is determined as distortion tensor and first derivatives of the distortion tensor in the stationary case. Let us use the most general principle of possible displacements, which can be used to formulate dissipative models of physically linear and nonlinear processes and can be extended to dynamic processes in the sense indicated above. Consider the possible work of internal forces:

$$\overline{\delta U} = \int\limits_V (\sigma_{ij}\delta R_{i,j} + \sigma_{ijk}\delta R_{i,jk}) d\overline{V} \tag{8}$$

where $(\sigma_{ij}\delta R_{i,j} + \sigma_{ijk}\delta R_{i,jk})$ is the possible work of internal forces density, $R_{i,j}$ and $R_{i,jk}$ are distortion and curvature of displacement (generalized kinematic arguments) and the tensors of stresses σ_{ij} and double stresses σ_{ijk}, which perform possible work on variations of the corresponding generalized kinematic arguments.

Taking into account (8), we determine the effective physical characteristics, generally, of a physically nonlinear medium—the tensors of the elastic moduli of the fourth and sixth ranks:

$$\frac{\partial \sigma_{ij}}{\partial R_{m,n}} = C_{ijkm}, \quad \frac{\partial \sigma_{ijk}}{\partial R_{m,nl}} = C_{ijkmnl} \tag{9}$$

We consider isotropic media and assume that stresses σ_{ij} do not depend on curvatures of displacement vector and that the double stresses do not depend on distortions, i.e., tensors of moduli of odd rank are equal to zero. The following necessary conditions for the reversibility of the deformation process under consideration must be in place:

$$\begin{cases} \frac{\partial \sigma_{ij}}{\partial R_{m,n}} - \frac{\partial \sigma_{mn}}{\partial R_{i,j}} = 0 \\ \frac{\partial \sigma_{ijk}}{\partial R_{m,nl}} - \frac{\partial \sigma_{mnl}}{\partial R_{i,jk}} = 0 \end{cases} \tag{10}$$

Equation (10) helps to formulate the definition for the tensors of elasticity moduli of the fourth and sixth ranks for reversible processes of deformation:

$$\begin{cases} \frac{\partial \sigma_{ij}}{\partial R_{m,n}} = \frac{\partial \sigma_{mn}}{\partial R_{i,j}} = C_{ijmn} \\ \frac{\partial \sigma_{ijk}}{\partial R_{m,nl}} = \frac{\partial \sigma_{mnl}}{\partial R_{i,jk}} = C_{ijkmnl} \end{cases} \tag{11}$$

Substitution of (11) into Equation (10) leads to the formulation of the symmetry properties of the tensors of the moduli of reversible deformation processes ($C_{ijmn} = C_{mnij}$, $C_{ijkmnl} = C_{mnlijk}$):

$$\begin{cases} C_{ijmn} - C_{mnij} = 0 \\ C_{ijkmnl} - C_{mnlijk} = 0 \end{cases} \tag{12}$$

In other words, symmetry conditions (12) are necessary conditions of integrability for the linear form $(\sigma_{ij}\delta R_{i,j} + \sigma_{ijk}\delta R_{i,jk})$. In symbolic form, the variation of the possible work of internal forces is written in unified form not only for a static problem, but also for the corresponding dynamic process. For linear processes, the variation of the possible work for internal forces and the conditions for its potentiality have the following simple form:

$$\begin{aligned} &\overline{\delta U} = \int P_a \delta Q_a d\overline{V} = \\ &= \int C_{ab} Q_b \delta Q_a d\overline{V} = \int C_{ba} Q_a \delta Q_b d\overline{V} = \delta \int C_{ab} Q_b Q_a d\overline{V} = \delta \int_{t_0}^{t_1} \int U_V dV dt, \; C_{ab} = C_{ba} \end{aligned} \tag{13}$$

Let us consider processes that, generally, can be irreversible. The following statement holds true for physically linear and nonlinear deformation models for isotropic media (the validity of the statement of the lemma for linear processes follows from (4), (6), and (12)).

Lemma: *Let us consider an irreversible process of deformation of a physically nonlinear gradient medium (a common case) for which the possible work of internal forces has the form (8). Then, the following assertions hold:*

1. *The necessary conditions for the existence of a potential energy density U_V are the symmetry properties of the tensors of the elastic moduli C_{ijmn}, C_{ijkmnl}:*

$$C_{ijmn} = C_{mnij}, \; C_{ijkmnl} = C_{mnlijk} \tag{14}$$

2. *Sufficient conditions for dissipative deformation processes are the antisymmetric properties of the tensors of dissipative moduli* $\overline{C}_{ijmn}$, $\overline{C}_{ijkmnl}$

$$\overline{C}_{ijmn} = -\overline{C}_{mnij},\ \overline{C}_{ijkmnl} = -\overline{C}_{mnlijk} \tag{15}$$

3. *The effective elastic moduli of media in which the deformation process occurs with energy dissipation are determined by tensor functions:*

$$\frac{\partial \sigma_{ij}}{\partial R_{m,n}} = C_{ijmn} + \overline{C}_{ijmn},\ \overline{C}_{ijkmnl} \neq 0,\ \overline{C}_{ijmn} \neq 0 \tag{16}$$

Proof: Let us write down the necessary conditions for the reversibility of the deformation process (conditions for the existence of a potential energy density):

$$\frac{\partial \sigma_{ij}}{\partial R_{m,n}} - \frac{\partial \sigma_{mn}}{\partial R_{i,j}} = 0,\ \frac{\partial \sigma_{ijk}}{\partial R_{m,nl}} - \frac{\partial \sigma_{mnl}}{\partial R_{i,jk}} = 0 \tag{17}$$

Obviously, Equation (17) can be rewritten in the form: $\frac{\partial \sigma_{ij}}{\partial R_{m,n}} = \frac{\partial \sigma_{mn}}{\partial R_{i,j}}$, $\frac{\partial \sigma_{ijk}}{\partial R_{m,nl}} = \frac{\partial \sigma_{mnl}}{\partial R_{i,jk}}$.

In the left and right parts of the last equations, there are tensors of the fourth and sixth rank, respectively.

We denote these as: C_{ijmn}, C_{ijkmnl}

$$\frac{\partial \sigma_{ij}}{\partial R_{m,n}} = \frac{\partial \sigma_{mn}}{\partial R_{i,j}} = C_{ijmn},\ \frac{\partial \sigma_{ijk}}{\partial R_{m,nl}} = \frac{\partial \sigma_{mnl}}{\partial R_{i,jk}} = C_{ijkmnl} \tag{18}$$

The tensors in (18) will be referred to as the effective moduli of elasticity. Formally excluding derivatives of stresses in (17) and, accordingly, double stresses with the help of (18), we obtain (14), which proves the first part of the lemma.

Next, we write the sufficient conditions for the dissipative (irreversibility) of the deformation process:

$$\frac{\partial \sigma_{ij}}{\partial R_{m,n}} - \frac{\partial \sigma_{mn}}{\partial R_{i,j}} = 2\overline{C}_{ijmn} \neq 0 \quad \frac{\partial \sigma_{ijk}}{\partial R_{m,nl}} - \frac{\partial \sigma_{mnl}}{\partial R_{i,jk}} = 2\overline{C}_{ijkmnl} \neq 0, \tag{19}$$

From (19), it follows that:

$$2\overline{C}_{mnij} = \frac{\partial \sigma_{mn}}{\partial R_{i,j}} - \frac{\partial \sigma_{ij}}{\partial R_{m,n}} = -(\frac{\partial \sigma_{ij}}{\partial R_{m,n}} - \frac{\partial \sigma_{mn}}{\partial R_{i,j}}) = -2\overline{C}_{ijmn}$$

$$2\overline{C}_{mnlijk} = \frac{\partial \sigma_{mnl}}{\partial R_{i,jk}} - \frac{\partial \sigma_{ijk}}{\partial R_{m,nl}} = -(\frac{\partial \sigma_{ijk}}{\partial R_{m,nl}} - \frac{\partial \sigma_{mnl}}{\partial R_{i,jk}}) = -2\overline{C}_{ijkmnl}$$

Hence, item 2 of the lemma is also proved.

If $\overline{C}_{ijkmnl} = 0$, $\overline{C}_{ijmn} = 0$, then expression (19) degenerates into the necessary conditions for the reversibility of deformation processes (see (17)). Therefore, for dissipative processes one, should consider nonhomogeneous Equation (19), $\overline{C}_{ijkmnl} \neq 0$, $\overline{C}_{ijmn} \neq 0$. The sufficient non-integrability conditions of (19), written with respect to effective moduli $\frac{\partial \sigma_{ij}}{\partial R_{m,n}}$, $\frac{\partial \sigma_{ijk}}{\partial R_{m,nl}}$ (see Equation (17)), are a system of inhomogeneous algebraic equations. The solution of these equations can be represented as:

$$\frac{\partial \sigma_{ijk}}{\partial R_{m,nl}} = C_{ijkmnl} + \overline{C}_{ijkmnl}\ \frac{\partial \sigma_{ij}}{\partial R_{m,n}} = C_{ijmn} + \overline{C}_{ijmn}. \tag{20}$$

Hence, item 3 of the lemma is also proved.

Constitutive Equation (20) can be integrated in the quadrature, and physically linear equations of Hooke's law can be obtained, if the modulus tensors do not depend on kinematic variables:

$$\begin{aligned} \sigma_{ij} &= (C_{ijmn} + \overline{C}_{ijmn})R_{i,j} \\ \sigma_{ijk} &= (C_{ijklmn} + \overline{C}_{ijklmn})R_{l,mn} \end{aligned} \tag{21}$$

□

Theorem 1. *Let the deformation processes of physically linear processes with kinematic variables $R_{i,j}$, $R_{i,jk}$ be considered. Then, the possible work (8) of internal forces is represented as the sum of variation of the functional corresponding to the reversible part of the deformation process (variation of the potential energy of deformation) and of the non-integrable linear variational form that models irreversible deformation processes associated with dissipation:*

$$\begin{aligned} &\overline{\delta U} = \delta U + \tfrac{1}{2}\int\limits_V [\overline{C}_{ijmn}(R_{m,n}\delta R_{i,j} - R_{i,j}\delta R_{m,n}) + \overline{C}_{ijkmnl}(R_{l,mn}\delta R_{i,jk} - R_{i,jk}\delta R_{l,mn})]dV \\ &U = \tfrac{1}{2}\int\limits_V [C_{ijmn}R_{m,n}R_{i,j} + C_{ijkmnl}R_{i,jk}R_{l,mn}]dV \end{aligned}$$

Proof: Let us use the results of the lemma and take into account Equation (21). Substituting (21) into (8), we obtain the following sequence of equalities:

$$\begin{aligned} &\overline{\delta U} = \int\limits_V (\sigma_{ijk}\delta R_{i,jk} + \sigma_{ij}\delta R_{i,j})dV = \\ &= \int\limits_V [(C_{ijmn} + \overline{C}_{ijmn})R_{m,n}\delta R_{i,j} + (C_{ijklmn} + \overline{C}_{ijklmn})R_{l,mn}\delta R_{i,jk}]dV = \\ &= \int\limits_V [C_{ijmn}(R_{m,n}\delta R_{i,j} + R_{i,j}\delta R_{m,n})/2 + C_{ijklmn}(R_{l,mn}\delta R_{i,jk} + R_{i,jk}\delta R_{l,mn})/2]dV + \\ &+ \int\limits_V [\overline{C}_{ijmn}(R_{m,n}\delta R_{i,j} - R_{i,j}\delta R_{m,n})/2 + \overline{C}_{ijklmn}(R_{l,mn}\delta R_{i,jk} - R_{i,jk}\delta R_{l,mn})/2]dV = \\ &= \delta\tfrac{1}{2}\int\limits_V [C_{ijklmn}R_{l,mn}R_{i,jk} + C_{ijmn}R_{m,n}R_{i,j}]dV + \\ &+ \tfrac{1}{2}\int\limits_V [\overline{C}_{ijmn}(R_{m,n}\delta R_{i,j} - R_{i,j}\delta R_{m,n}) + \overline{C}_{ijklmn}(R_{l,mn}\delta R_{i,jk} - R_{i,jk}\delta R_{l,mn})]dV \end{aligned} \tag{22}$$

The proof of the theorem follows from the expressions obtained on the right side in (22).

Then, a variational model of the considered processes is produced by the following equation:

$$\begin{aligned} &\delta I - \delta W^* = 0, \qquad I = A - U, \\ &U = \delta\tfrac{1}{2}\int\limits_V [C_{ijklmn}R_{l,mn}R_{i,jk} + C_{ijmn}R_{m,n}R_{i,j}]dV, \\ &\delta W^* = \tfrac{1}{2}\int\limits_V [\overline{C}_{ijmn}(R_{m,n}\delta R_{i,j} - R_{i,j}\delta R_{m,n}) + \overline{C}_{ijklmn}(R_{l,mn}\delta R_{i,jk} - R_{i,jk}\delta R_{l,mn})]dV \end{aligned} \tag{23}$$

Obviously, the statements of the lemma and Theorem 1 can also be generalized to dynamic processes for media with generalized properties, in which the generalized kinematic variables are tensor objects of various ranks and time derivatives of these variables. In this case, symbolic notation allows us to write the statement of the theorem in the following simple form:

$$\delta\overline{U} = \delta\frac{1}{2}\int\limits_{t_1}^{t_2}\int\limits_V C_{ab}Q_aQ_bdVdt + \frac{1}{2}\int\limits_{t_1}^{t_2}\int\limits_V [\overline{C}_{ab}(Q_b\delta Q_a - Q_a\delta Q_b)]dVdt$$

Then, the Hamilton–Ostrogradsky principle for describing irreversible dissipative processes in the mechanics of deformable media (the modified variational principle, the L.I. Sedov principle) has the form:

$$\delta I - \delta W^* = 0,\ I = A - U \tag{24}$$

$$\delta W^* = \frac{1}{2}\int_{t_1}^{t_2}\int_V [\overline{C}_{ab}(Q_b\delta Q_a - Q_a\delta Q_b)]dVdt,\ U = \delta\frac{1}{2}\int_{t_1}^{t_2}\int_V C_{ab}Q_aQ_bdVdt$$

It is clear that generalizations, in the case of dissipative processes, are defined not only in the volume but also on the surface of the body (see (3)). The variational linear non-integrable forms in (22) and (23) will be referred to as dissipation channels. On the other hand, this value can be associated terminologically with the dissipation function [31]. □

Theorem 2 (on the correspondence of the dissipation channels approach to the second law of thermodynamics). *Assume that the deformation process is completely modeled on the basis of variational equality (22). Then, the deformation process always occurs with positive dissipation; i.e., the dissipation function is always greater than zero $\delta W^* > 0$ for irreversible processes. The expression for the variational form for dissipation channels (23) is invariant with respect to the order of terms in them.*

Proof: Using Equation (23), we find:

$$\delta W^* = \delta(A - U) \tag{25}$$

For the gradient model of the media, the Clapeyron theorem takes place $A = 2U$. Then, we receive the following equation from (25):

$$\delta W^* = \delta\left(A - \frac{1}{2}\int_V [C_{ijklmn}R_{l,mn}R_{i,jk} + C_{ijmn}R_{m,n}R_{i,j}]dV\right) = \delta(A - U) = \frac{1}{2}\delta(A) = \delta U > 0$$

Any possible dissipation channel for linear media should also be considered. This dissipation channel is presented up to a constant amplitude, i.e., in the form of a product of a dissipative module and the corresponding non-integrable form of generalized arguments Q_a and Q_b. A factor in this form is a dissipative modulus. The correct sign of the dissipative module is determined by any particular problem in such a way that the simulated process corresponds to the physical meaning. For example, we can consider a closed cycle in the phase space defined by the generalized coordinates Q_a and Q_b. Then, the dissipative modulus must be chosen so that the integral corresponding to the dissipation channel, proportional to the area of the hysteresis loop for the considered cycle, will be greater than zero. Let us now consider two variational forms with different orders of the generalized variables Q_a and Q_b. Assume that the disssipative modulus in the variational form $\int[\overline{C}_{ab}(Q_b\delta Q_a - Q_a\delta Q_b)]d\overline{V}$ is chosen so that this form is positive $\int[\overline{C}_{ab}(Q_b\delta Q_a - Q_a\delta Q_b)]d\overline{V} > 0$, which corresponds to the correct description of the thermodynamic process for any particular problem. Along with this form, we consider another, formally possible, writing of the variational form as $\int[\overline{C}_{ab}(Q_a\delta Q_b - Q_d\delta Q_a)]d\overline{V}$. However, if we take into account that the dissipative moduli tensor is antisymmetric $\overline{C}_{ab} = -\overline{C}_{ba}, |\overline{C}_{ab}| = |\overline{C}_{ba}|$, then we obtain:

$$\begin{aligned}&\int[|\overline{C}_{ab}|(Q_a\delta Q_b - Q_d\delta Q_a)]d\overline{V} = -\int[\overline{C}_{ab}(Q_b\delta Q_a - Q_a\delta Q_b)]d\overline{V} = \\ &= \int[|\overline{C}_{ba}|(Q_b\delta Q_a - Q_a\delta Q_b)]d\overline{V} > 0\end{aligned}$$

The theorem is proved. □

To summarize, we note that we use the principle of possible displacements as the only variational principle that allows us to model dissipative processes, and we write it in the form of separate parts: relatively reversible processes and dissipative processes. Reversible processes are determined by the variation of the functional (integrable variational form), and irreversible processes are determined by dissipation channels, which are the non-integrable variational forms.

4. On Modeling Viscoelastic Processes

Consider an example of modeling viscous effects [31] in the mechanics of solids. The traditional approach is associated with the introduction of a dissipative function [31] as a certain potential with respect to deformation velocities in irreversible processes.

Let us show that the algorithm based on the introduction of dissipation channels is devoid of the fundamental contradictions of the traditional approach associated with the existence of the possibility of irreversible processes. Following the traditional approach [31], for the account of viscosity, a dissipative stress tensor $\sigma_{ij}{}'$ is introduced, which is determined in terms of the dissipative function R. The dissipative function $R = \eta\beta_{ij}\beta_{ij} + (\xi/3)v_{ii}v_{jj}$ for an isotropic body has a form similar to the strain energy density, where v_{ij} is the strain rate tensor, β_{ij} is the strain rate deviator tensor, v_{kk} is the spherical strain rate tensor, and the values η, ξ are viscosity coefficients. It is assumed [31] that for dissipative stress tensor $\sigma_{ij}{}'$, there are relations similar to Green's formulas $\sigma_{ij}{}' = \frac{\partial R}{\partial v_{ij}}$. Note that in our opinion, the traditional approach is contradictory since it actually asserts the existence of a potential in irreversible processes. It is believed, in the traditional approach, that viscosity can be taken into account in the equations of motion by replacing the elastic stress tensor σ_{ij} in these equations with the sum $\sigma_{ij} + \sigma_{ij}{}'$ where $\sigma_{ij}{}'$ is the dissipative stress tensor.

Regarding a viscoelastic medium, it can be shown that the method of introducing dissipation channels in a generalized Sedov's variational method, being correct, produces a result that is consistent with the traditional approach [31]. Let us assume that for viscoelastic processes, the lists of arguments of strain energy for reversible processes and of dissipation channels for irreversible processes depend on the distortion tensor $R_{i,j}$ and on the distortion rate tensor $\dot{R}_{i,j}$.

Since the process under consideration is dynamic by default, the dynamic Lagrangian depends on the displacement rates $\dot{R}_i$. If we let the reversible part of the dynamical Lagrangian coincide exactly with the corresponding energy density in the classical theory of elasticity, the variation of the dissipative energy, in accordance with the chosen kinematics, will have the form:

$$\delta W^* = \frac{1}{2}\int D_{ijmn}(\dot{R}_{m,n}\delta R_{i,j} - R_{m,n}\delta\dot{R}_{i,j})d\overline{V}$$

Let us take into account the dissipative part of the deformation energy and write down the generalized variational equality (24). We can obtain:

$$\begin{aligned}
&\delta A - \delta(U-K) - \delta W^* = \\
&= \delta A + \int \rho\dot{R}_i\delta\dot{R}_i d\overline{V} - \int \sigma_{ij}\delta R_{i,j}d\overline{V} - \tfrac{1}{2}\int\limits_V \overline{D}_{ijmn}(\dot{R}_{m,n}\delta R_{i,j} - R_{m,n}\delta\dot{R}_{i,j})dV = \\
&= \delta A + \int \rho\dot{R}_i\delta\dot{R}_i d\overline{V} - \int \sigma_{ij}\delta R_{i,j}d\overline{V} - \\
&- \int\limits_V \overline{D}_{ijmn}\dot{R}_{m,n}\delta R_{i,j}d\overline{V} + \tfrac{1}{2}\int\limits_V \overline{D}_{ijmn}R_{m,n}\delta R_{i,j}dV\Big|_{t_1}^{t_2} = \\
&= \delta A + \int \rho\dot{R}_i\delta\dot{R}_i d\overline{V} - \int (\sigma_{ij} + \sigma_{ij}{}')\delta R_{i,j}d\overline{V} + \tfrac{1}{2}\int\limits_V \overline{D}_{ijmn}R_{m,n}\delta R_{i,j}dV\Big|_{t_1}^{t_2}
\end{aligned} \tag{26}$$

where $\sigma_{ij}{}' = \overline{D}_{ijmn}\dot{R}_{m,n}$.

Equation (26) completely proves the assumption made above. Indeed, the first two terms in the last line of (26) determine the static and dynamic loading of the body under

consideration, and the third term allows us to state that the equation of motion and the static boundary condition are written with respect to $\sigma_{ij} + \sigma_{ij}{}'$.

This proves the statement that the equation of motion, in the case of viscosity, is written with respect to the sum of elastic and dissipative stresses $\sigma_{ij} + \sigma_{ij}{}'$, as follows from the traditional approach based on the introduction of a potential of dissipative function. The last term determines the initial "boundary" condition, which, as follows from (26), depends on the dissipative modulus of elasticity $\overline{D}_{ijmn}$ and $\overline{D}_{ijmn} = -\overline{D}_{mnij}$.

5. Examples of Modeling Dissipative Processes in Hydrodynamics

As examples of modeling dissipative processes, let us consider, in succession, the hydrodynamic models of Darcy, Navier–Stokes, and Brinkman. Further, in all examples, we will assume that the Lagrangian L is the same for the reversible part of the processes. The Lagrangian provides an introduction to the equations of motion of the term with the hydrodynamic pressure gradient $p_{,i}$ and the term with the inertial force $\rho\ddot{r}_i$:

$$L = A + K - U = A - \frac{1}{2}\int_0^t \int_V [(2\mu/3 + \lambda) r_{i,i} r_{j,j} - \rho \dot{r}_i \dot{r}_i] dV dt \tag{27}$$

We can see that the first term in Equation (27) leads to the appearance of a pressure gradient in the equations of equilibrium. The second term in (27) determines the inertial forces and is the classical kinetic energy.

5.1. Darcy Hydrodynamics

Let us show that the following dissipation channel, which determines Darcy hydrodynamics with laminar flow, has the structure:

$$\overline{\delta U_1} = \frac{1}{2}\int_0^t \int_V \frac{\eta}{K^D} (\dot{r}_i \delta r_i - r_i \delta \dot{r}_i) dV dt \tag{28}$$

where η is the fluid dynamic viscosity, and K^D is the Darcy permeability.

Then, taking into account (27) and (28) and following the generalized variational principle of Sedov (24), $\delta L - \overline{\delta U_1} = 0$, we obtain the following variational equation for the Darcy hydrodynamic model:

$$\begin{aligned} &\int_0^t \int_V [-\tfrac{\eta}{K^D}\dot{r}_i - \rho\ddot{r}_i + p_{,i} + p_i^V] \delta r_i dV dt + \int_0^t \int_F \left(p_i^F - p n_i\right) \delta r_i dF dt + \\ &\quad + \int_V [\rho \dot{r}_i + \tfrac{1}{2}\tfrac{\eta}{K^D} r_i] \, \delta r_i dV \Big|_0^t = 0 \end{aligned} \tag{29}$$

Here, the term $\int_0^t \int_V p_i^V \delta r_i dV dt + \int_0^t \int_F p_i^F \delta r_i dF dt \;\; = \delta A$ defines the external work of given pressure p_i^V, p_i^F in the volume V and, consequently, on the surface F.

The first term in Equation (29) provides the equation of motion, the second term defines the boundary conditions, and the third term allows one to obtain the boundary's "initial" conditions. Therefore, the motion equation of a non-stationary Darcy flow has the form:

$$\eta \dot{r}_i = K^D (p_{,i} + p_i^V - \rho\ddot{r}_i) \tag{30}$$

Let us transform these equations of motion to the form:

$$\dot{r}_i + \tau_D \ddot{r}_i = \frac{K^D}{\eta} (p_{,i} + p_i^V)$$

Here, the definition of the relaxation time of fluid flow velocity is introduced naturally:

$$\tau_D = K^D \rho / \eta$$

We can see that Darcy's hydrodynamic equation is similar to the Maxwell–Cattaneo heat equation written in terms of temperature. Fluid flow in a channel and heat propagation are governed by the same equation. This finding provides a basis for modeling heat propagation through hydrodynamic experiments and vice versa. Thus, a temperature–hydrodynamic analogy is established.

Let us consider the case of a steady flow of an incompressible weightless fluid in a flat capillary under the influence of a pressure difference at the ends of the capillary. In this case, $\ddot{r}_i = 0$, $r_{i,i} = 0$, $p_i^V = 0$, and the solution of Equation (30) has the form:

$$\dot{r}_x = \frac{K^D}{\eta} p_{,x}, \qquad p_{,x} = Const. \tag{31}$$

This solution (31) corresponds to ideal fluid sliding along the channel wall. Within the framework of Darcy hydrodynamics, the fluid flow is laminar, without any interaction of the fluid with the walls of the capillary.

5.2. Hydrodynamics Model of Navier–Stokes

Let us show that the linear hydrodynamic model of Navier–Stokes is determined using the following dissipation channel:

$$\overline{\delta U_2} = \frac{1}{2} \int_0^t \int_V \eta (\dot{r}_{i,j} \delta r_{i,j} - r_{i,j} \delta \dot{r}_{i,j}) dV dt. \tag{32}$$

In this case, variational Equation (30) leads to the variational model of Navier–Stokes hydrodynamics:

$$\begin{aligned} &\int_0^t \int_V \left(\eta \Delta \dot{r}_i - \rho \ddot{r}_i + p_{,i} + p_i^V\right) \delta r_i dV dt + \int_0^t \int_F \left(p_i^F - p n_i - \eta \dot{r}_{i,j} n_j\right) \delta r_i \} dF dt + \\ &\quad + \left[\int_V (\rho \dot{r}_i - \tfrac{1}{2} \eta \Delta r_i) \delta r_i dV + \int_F \tfrac{1}{2} \eta r_{i,j} n_j \delta r_i dF \right] \Bigg|_0^t = 0 \end{aligned} \tag{33}$$

The Navier–Stokes fluid dynamics equations of motion follow from (31) as the Euler equation:

$$\eta \Delta \dot{r}_i - \rho \ddot{r}_i + p_{,i} + p_i^V = 0 \tag{34}$$

For the steady flow of an incompressible, weightless fluid with conditions of complete adhesion (no velocities at the boundary of contact of fluid with the walls of a flat capillary at $y = \pm h$), Equation (34) has the following solution:

$$\dot{r}_x = \frac{K_D}{\eta} p_{,x} (1 - (y/h)^2) \frac{h^2}{K_D}, \qquad p_{,x} = Const \tag{35}$$

The solution presented above, (35), satisfies the condition of complete adhesion on the capillary wall ($\dot{r}_x(y = \pm h) = 0$) and corresponds to Poiseuille's law.

5.3. Model of Brinkman-Type Hydrodynamics

Let us consider one more hydrodynamic process whose dissipation is defined as the sum of dissipation channels (28) and (30):

$$\delta L - \overline{\delta U_1} - \overline{\delta U_2} = 0 \tag{36}$$

Therefore, taking into account the Equations (27), (28), (32), and (36), we obtain the following variational equation that completely determines the mathematical model of Brinkman hydrodynamics:

$$\int_0^t [\int_V (\eta \Delta \dot{r}_i - \rho \ddot{r}_i - \frac{\eta}{K_D}\dot{r}_i + p_{,i} + p_i^V)\delta r_i dV + \int_F (p_i^F - pn_i - \eta \dot{r}_{i,j} n_j)\delta r_i dF]dt + \\ + \left\{ \int_V [\rho \dot{r}_i + \tfrac{1}{2}\eta(-\Delta r_i + \tfrac{1}{K_D} r_i)]\delta r_i dV + \int_F (\tfrac{1}{2}\eta r_{i,j} n_j \delta r_i) dF \right\} |_0^t = 0. \tag{37}$$

From the variational Equation (37), we find the governing equations which are the equations of motion in Brinkman's hydrodynamics:

$$\eta \Delta \dot{r}_i - \frac{\eta}{h_m^2}\dot{r}_i + p_{,i} + p_i^V - \rho \ddot{r}_i = 0. \tag{38}$$

In the case of the steady flow of an incompressible, weightless fluid in a flat capillary of width $2h$, the solution of the Equation (38) with boundary conditions for complete adhesion on the capillary wall has the form:

$$\dot{r}_x = \frac{K_D}{\eta} p_{,x}\left(1 - \frac{ch(y/h_m)}{ch(h/h_m)}\right), \qquad p_{,x} = Const \tag{39}$$

Comparing the solutions corresponding to the Darcy (31), Navier–Stokes (35), and Brinkman models (39) of hydrodynamics, it can be noted that the Darcy model is characterized by a dissipative parameter K_D (Darcy permeability), the Navier–Stokes model is determined by a dissipative parameter η (dynamic viscosity), and the Brinkman model is characterized, accordingly, by a combination of two dissipative parameters, K_D and η.

The velocity profiles shown in Figure 1 are normalized to the value $p_{,x}K_D/\eta$, and the transverse coordinate is normalized to the half-width of the capillary h.

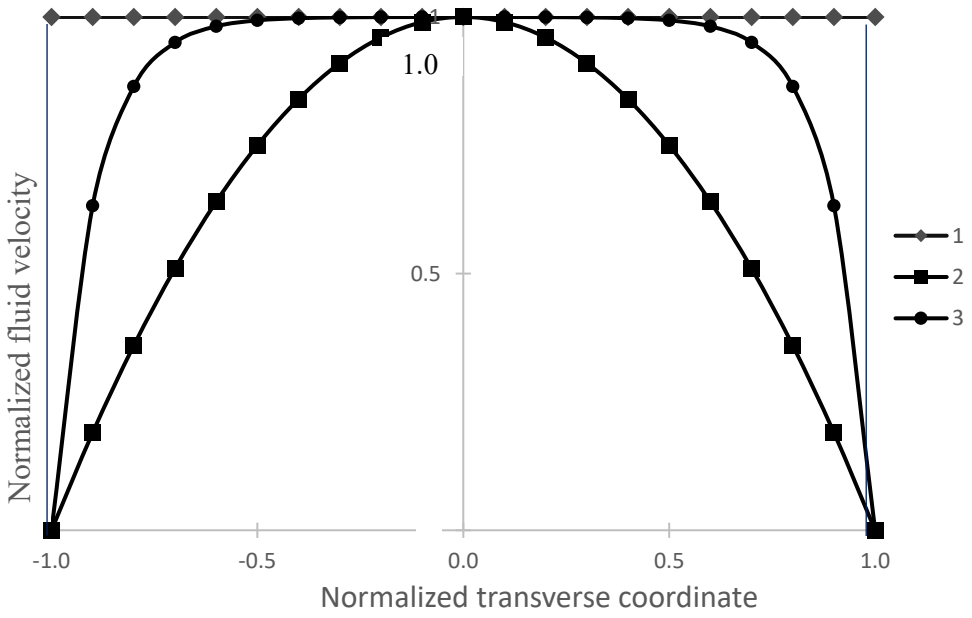

Figure 1. Normalized velocity profiles.

Darcy model-1, Navier–Stokes model-2 for $(h/h_m)^2 = h^2/K_D = 1$, and Brinkman model-3 for $(h/h_m)^2 = h^2/K_D = 1$.

Let us provide a comparative analysis of the velocity profiles for three models: the Darcy, Navier–Stokes, and Brinkman models. Darcy's hydrodynamic Equation (30) determines the velocity profile in the capillary that is constant in transverse coordinates, and the

Navier–Stokes Equation (34) defines a parabolic velocity profile known as Poiseuille's law (35). Neither of these two models of hydrodynamics can explain the presence of boundary layers in a liquid, and these two models do not allow one to determine the thickness of these boundary layers that arise near the walls of the capillary. The Brinkman model (38), in contrast to the Darcy and Navier–Stokes models, makes it possible to describe the boundary layer and scale effect associated with the characteristic thickness of the liquid boundary layer $h_m = \sqrt{K_D}$.

Finally, let us analyze the scale effects for the Brinkman model (see Figure 2). It is possible to detect the existence and determine the thickness of the boundary layer only within the framework of Brinkman hydrodynamics (38), when both the first and second dissipation forms (28) and (32) are taken into account in the hydrodynamic equations (see Equation (36)). In the Brinkman model, the motion equations have the form of inhomogeneous Helmholtz equations describing the boundary layer with a characteristic thickness equal to h_m. The boundary layer near the walls of the capillary and the corresponding scale effect are taken into account within the framework of the solution obtained above for the Brinkman hydrodynamics model. This is reflected in the structure of the solution (39) and is illustrated by the curves presented in Figure 2, which show the normalized velocity profiles for various values of the dimensionless parameter h/h_m.

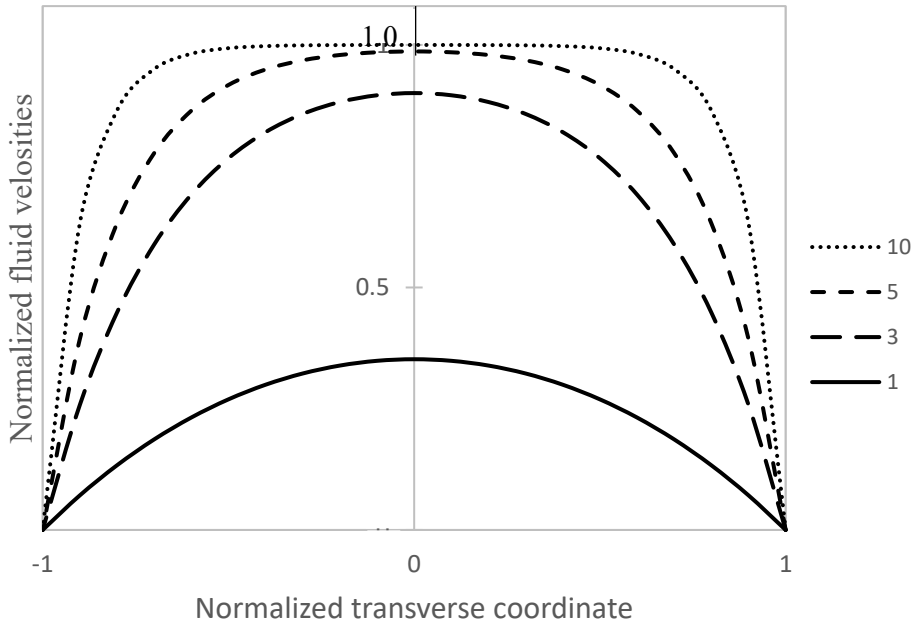

Figure 2. Normalized velocity profiles in the Brinkman model (dimensionless scale effect parameter h/h_m: 10; 5; 3; 1).

As a result, in addition to the traditional interpretation of the Darcy parameter K^D as a characteristic of the permeability of the filter medium, another physical interpretation of the permeability coefficient can be proposed as the square of the thickness of the "long" boundary layer characteristic of a given liquid, $K^D = h_m^2$.

6. On Variational Models of Dissipative Heat Transfer Processes

Let us consider irreversible heat transfer processes, the great interest in which is explained by their great applied value. The urgency of the problem of heat transfer and the interest in it are associated with well-known attempts to modify the classical equations of heat conduction to eliminate the contradictions of classical parabolic heat conduction [36–39] as well as with the desire to modify the theory of heat transfer for modeling size-dependent effects [27,28,40–42].

Heat transfer processes are modeled quite well, thanks to the use of first-principles approaches and molecular dynamics methods. On the other hand, methods for experi-

mental evaluation of heat transfer processes are well developed for them. Therefore, it is quite understandable that, recently, there has been a great interest in the study of coupled thermomechanical effects, transients, and scale effects in the problem of heat transfer in homogeneous and inhomogeneous media, including media with a microstructure [27,28,43]. To describe such effects, various modifications of the physical constitutive relations and, accordingly, the heat balance equations are proposed. These modifications are usually introduced phenomenologically to describe specific observed effects. The great importance of variational approaches in relation to such irreversible processes cannot be underestimated; they allow one to obtain energetically consistent mathematical models, regardless of their complexity, which is very important for modeling coupled physical and mechanical effects. In this work, the dissipative component of such processes is proposed to be modeled using the idea of introducing dissipation channels. In the present section we show that the known modifications of the heat conduction laws and the heat balance equations can be constructed by introducing various dissipation channels.

Since heat flux is usually introduced as a temperature gradient, we will proceed to show that it is sufficient to postulate the existence of a scalar potential whose gradient is proportional to temperature to construct a variational model. Indeed, let us postulate the existence of the potential R and introduce the following Lagrangian for the variational problem of a reversible heat transfer process:

$$\begin{aligned} &L = A + K - U, \\ &A = \int\limits_V P^V R dV + \int\limits_F P^F R dF,\ K = \tfrac{1}{2}\int\limits_V \tau \dot{R}\dot{R} dV, \quad U = \tfrac{1}{2}\int\limits_V k_V R_{,k} R_{,k} dV \end{aligned} \tag{40}$$

Here, L is the dynamic Lagrangian, A is the work of the external forces on the introduced arguments in the volume and on the surface, and K, U are the kinetic and potential energy for the reversible part of the considered processes.

We note that, for brevity—which does not reduce the generality of the proposed approach—we can omit terms appearing outside the volume integral as a result of integration by parts which form the boundary and initial conditions. These terms obviously arise during integration by parts of the variations from the derivatives of arguments. Let us focus exclusively on the equations of constitutive relations and heat transfer equations. We additionally assume, in Equation (40), that $A = 0$ and write the following variational equation for considered reversible process:

$$\delta L = \int\limits_0^t \int\limits_V (\tau \dot{R}\delta\dot{R} - k_V R_{,i}\delta R_{,i}) dV dt = \int\limits_0^t \int\limits_V (k_V \Delta R - \tau \ddot{R})\delta R dV dt + \ldots = 0 \tag{41}$$

Green's formulas make it possible to establish constitutive relations for a single scalar force factor and a single vector force factor. These relations can be interpreted as a heat flux and temperature, respectively:

$$T = \partial(K^V - U^V)/\partial\dot{R} = \tau\dot{R}\ q_i = \partial(K^V - U^V)/\partial R_{,i} = -k_V R_{,i} \tag{42}$$

where K^V and U^V are the kinetic and potential energy densities, respectively, $2K_V = \tau\dot{R}\dot{R}$, $2U_V = k_V R_{,k} R_{,k}$, and coefficients k_V and τ allow a physical interpretation as the coefficient of thermal conductivity and the relaxation time for the thermal conductivity flux, respectively, to be applied to them.

Indeed, excluding the scalar potential R in the Euler equation of the variational equality (41) using the constitutive relations (42), we obtain (see also [28,44]):

$$k_V \Delta T - \tau \ddot{T} = 0$$

Therefore, the proposed variational model produces, for reversible processes, a heat balance equation of a hyperbolic type (the coefficient k_V is treated as a thermal conductivity coefficient).

To obtain a more complete model of the heat balance equation with the diffusion mechanism of dissipation, we introduce the following dissipation channel, which we will refer to as the Fourier dissipation channel:

$$\overline{\delta U_{1T}} = \frac{1}{2}\int\limits_0^t \int\limits_V c_V(\dot{R}\delta R - R\delta\dot{R})dVdt \tag{43}$$

We have introduced a coefficient c_V to determine the last dissipation channel (43). In what follows, it will be shown that the coefficient c_V is a physical interpretation of the heat capacity coefficient at constant volume.

Remark 1. *Note that, in general, we assume that the list of arguments of the dissipative part coincides with the list of arguments of the Lagrange functional for the invertible part. Bilinear terms are sources for formulating dissipative channels. Therefore, for example, the dissipation channel (43) must correspond to a bilinear term* $2B\ R\dot{R}$ *in the potential energy density for the reversible part of the functional. Therefore, the full quadratic form in potential energy density must have the form* $-A\dot{R}\dot{R} + 2B\ R\dot{R}\ + CRR$*. At the same time, for a specific model, the potential energy density may not contain terms with modules B and/or C, because in the reversible part, these modules can be assumed as zero, leaving non-zero corresponding dissipative modules. Hereinafter, we will omit the discussion of the structure for the potential energy and kinetic energy densities, assuming that this question, clearly, can always be solved, whether the variational principle of the problem in the complete formulation is required, including both boundary conditions and "initial" conditions, or not. For example, for dissipation channels containing higher derivatives of generalized variables, reversible processes will correspond to the gradient models, which are easily formulated.*

The variational formulation of an irreversible process with a dissipation channel (43) is provided by the following version of Sedov's variational equality:

$$\begin{aligned}
&\delta L - \overline{\delta U_{1T}} = \int\limits_0^t \int\limits_V (\tau\dot{R}\delta\dot{R} - k_V R_{,i}\delta R_{,i})dVdt - \tfrac{1}{2}\int\limits_0^t \int\limits_V c_V(\dot{R}\delta R - R\delta\dot{R})dVdt = \\
&= \int\limits_0^t \int\limits_V [-k_V R_{,i}\delta R_{,i} + (c_V R + \tau\dot{R})\delta\dot{R}]dVdt + \ldots = \\
&= \int\limits_0^t \int\limits_V (k_V\Delta R - \tau\ddot{R} - c_V\dot{R})\delta R dVdt + \ldots = 0
\end{aligned} \tag{44}$$

The second line of the equalities (44) provides the structure of constitutive equations

$$\begin{cases} q_i = -k_V R_{,i} \\ T = c_V R + \tau\dot{R} \end{cases} \tag{45}$$

and the last line in (44) is the Euler equation of heat balance, written in terms of the potential R:

$$k_V\Delta R - \tau\ddot{R} - c_V\dot{R} = 0.$$

Taking into account the second Equation (45), we introduce the temperature operator $T = t(R)$:

$$t(\ldots) = c_V(\ldots) + \tau(\ldots)_{,t} \tag{46}$$

and will use it to eliminate the potential R in physical equations (45) and in the Euler equation.

Indeed, using a temperature operator $t(\ldots)$ (46) on the equation of Hooke's law for the heat flux q_i in (45), we obtain the Maxwell–Cattaneo heat law [27,28,36–39,45–47]:

$$c_V q_i + \tau \dot{q}_i = -k_V T_{,i} \tag{47}$$

Assume $\tau = 0$. Then, we can see that the heat conduction law (47) reduces into the Fourier heat law:

$$c_V q_i = -k_V T_{,i}$$

Eliminating the potential R with the help of the operator (46) in the Euler Equation (44), we obtain the heat balance equation for the Maxwell-Cattaneo thermal conductivity model, written with respect to temperature [46,47], etc.:

$$k_V \Delta T - \tau \ddot{T} - c_V \dot{T} = 0$$

Let us introduce a dissipation channel containing higher order derivatives of generalized variables (see remarks above):

$$\overline{\delta U_{2T}} = \frac{1}{2} \int\limits_0^t \int\limits_V a_2 (\Delta R \delta \dot{R} - \dot{R} \delta \Delta R) dV dt \tag{48}$$

We can assume that the heat conduction equation for the more general process that is being considered is determined as the sum of two dissipation channels, (43) and (48), and the energy density of (40) and (41). Using integration by parts, we write the part of the variational equation that provides the constitutive relations and the Euler equations (heat transfer equation):

$$\begin{aligned}
&\delta L - \overline{\delta U_{1T}} - \overline{\delta U_{2T}} = \\
&= \int\limits_0^t \int\limits_V (\tau \dot{R} \delta \dot{R} - k_V R_{,i} \delta R_{,i}) dV dt - \\
&- \tfrac{1}{2} \int\limits_0^t \int\limits_V c_V (\dot{R} \delta R - R \delta \dot{R}) dV dt - \tfrac{1}{2} \int\limits_0^t \int\limits_V a_2 (\Delta R \delta \dot{R} - \dot{R} \delta \Delta R) dV dt + \ldots = \\
&= \int\limits_0^t \int\limits_V [(\tau \dot{R} + c_V R - a_2 \Delta R) \delta \dot{R} - k_V R_{,i} \delta R_{,i}] dV dt + \ldots = \\
&= \int\limits_0^t \int\limits_V (a_2 \Delta \dot{R} + k_V \Delta R - \tau \ddot{R} - c_V \dot{R}) \delta R dV dt + \ldots = 0
\end{aligned} \tag{49}$$

Constitutive equations of the considered model are provided as follows:

$$\begin{cases} q_i = -k_V R_{,i} \\ T = t(R) = c_V R + \tau \dot{R} - a_2 \Delta R \;\rightarrow\; t(\ldots) = c_V (\ldots) + \tau (\ldots)_{,t} - a_2 \Delta (\ldots) \end{cases} \tag{50}$$

and the Euler equation has the following view:

$$(a_2 \Delta \dot{R} + k_V \Delta R - \tau \ddot{R} - c_V \dot{R}) = 0 \tag{51}$$

Using the temperature operator $t(\ldots) = c_V (\ldots) + \tau (\ldots)_{,t} - a_2 \Delta (\ldots)$ on the constitutive relation for the heat flux, (50) we obtain the Guyer–Krumhansl heat conduction law [47]:

$$c_V q_i + \tau \dot{q}_i - a_2 q_{j,ji} = -k_V T_{,i} \tag{52}$$

Using the temperature operator $t(\ldots)$, (50) for the equation, and (51), we find the heat balance equation corresponding to the Guyer–Krumhansl heat law:

$$a_2 \Delta \dot{T} + k_V \Delta T - \tau \ddot{T} - c_V \dot{T} = 0 \tag{53}$$

We considered a more complex model whose dissipative properties are determined by a combination of dissipation channels (43), (48), and the following channel:

$$\overline{\delta U_{3T}} = \frac{1}{2}\int\limits_V b\,(\dot{R}_{,j}\delta R_{,j} - R_{,j}\delta\dot{R}_{,j})dV \tag{54}$$

The variational model, in this case, is determined by the variational equality:

$$\delta L - \overline{\delta U_{1T}} - \overline{\delta U_{2T}} - \overline{\delta U_{3T}} = 0 \tag{55}$$

It is easy to verify that the substitution of the relations (43), (48), (54) in (55), and integration by parts leads, in this case, to the following variational equation:

$$\begin{array}{l}
\delta L - \overline{\delta U_{1T}} - \overline{\delta U_{2T}} - \overline{\delta U_{3T}} = \\
= \int\limits_V (\tau\dot{R}\delta\dot{R} - k_V R_{,i}\delta R_{,i})dV - \frac{1}{2}\int\limits_V c_V(\dot{R}\delta R - R\delta\dot{R})dV - \\
-\frac{1}{2}\int\limits_V a\,(\Delta R\delta\dot{R} - \dot{R}\delta\Delta R)dV - \frac{1}{2}\int\limits_V b\,(\dot{R}_{,j}\delta R_{,j} - R_{,j}\delta\dot{R}_{,j})dV + \ldots = \\
= \int\limits_V [(c_V R + \tau\dot{R} - a\,\Delta R)\delta\dot{R} - (k_V R_{,i} + b\,\dot{R}_{,i})\delta R_{,i}]dV = \\
= \int\limits_0^t \int\limits_V [(a+b)\Delta\dot{R} + k_V\Delta R - \tau\ddot{R} - c_V\dot{R}]\delta R dV dt + \ldots = 0
\end{array} \tag{56}$$

It follows from constitutive Equation (56) that the considered model can be interpreted as:

$$\begin{cases} q_i = -k_V R_{,i} - b\,\dot{R}_{,i} \\ T = t(R) = c_V R + \tau\dot{R} - a\Delta R \end{cases} \tag{57}$$

The heat transfer equation in terms of the potential R is written as follows (Euler's equation in (56)):

$$(a+b)\Delta\dot{R} + k_V\Delta R - \tau\ddot{R} - c_V\dot{R} = 0 \tag{58}$$

Using the temperature operator $t(R) = c_V R + \tau\dot{R} - a\,\Delta R$ on the first Equation (57), we can exclude the potential R and obtain the Jeffrey-type heat conduction law [43,47]:

$$c_V q_i + \tau\dot{q}_i - a\Delta q_i = -k_V T_{,i} - b\,\dot{T}_{,i} \tag{59}$$

The last equation for the steady state case has the form:

$$c_V q_i - a\Delta q_i = -k_V T_{,i}$$

It does not reduce to Fourier's law for steady state. Notably, the same result was established in [28].

Eliminating the potential R with the help of the constitutive equation for the temperature, i.e., using the temperature operator $t(\ldots)$ on (58), we obtain a heat transfer equation with the Jeffrey heat law [48]:

$$(a+b)\Delta\dot{T} + k_V\Delta T - \tau\ddot{T} - c_V\dot{T} = 0 \tag{60}$$

Notably, in models (49) and (56), Euler's equations (the heat transfer Equations (53) and (60)) actually coincide in the terms of the scalar potential R; however, the laws of heat conduction and, in general, mathematical formulations are different (compare (52) and (59)).

Obviously, using the technique of introducing dissipation channels, it is possible to establish the variants of high-order theories of heat conduction, not only in relation to

material coordinates but also in relation to time. Indeed, we can assume that the dissipative model is constructed as a linear combination of dissipation channels:

$$\overline{\delta U_{1T}} + \overline{\delta U_{2T}} + \overline{\delta U_{3T}} + \overline{\delta U_4}$$

where $\overline{\delta U_4} = \frac{1}{2}\int\limits_V c\ (\ddot{R}\delta\dot{R} - \dot{R}\delta\ddot{R})dV$.

For this case, the generalized thermal conductivity law and heat balance equation can be found as follows:

$$c_V q_i + \tau\dot{q}_i + c\ \ddot{q}_i - a\ \Delta q_i = -k_V T_{,i} - b\ \dot{T}_{,i}$$

and

$$(a+b)\Delta\dot{T} + k_V\Delta T - c\ \dddot{T} - \tau\ddot{T} - c_V\dot{T} = 0$$

Note that if, in particular, $a + b = 0$ in the last equation, then we arrive at an equation of the form:

$$k_V\Delta T - c\ \dddot{T} - \tau\ddot{T} - c_V\dot{T} = 0 \tag{61}$$

In [49], it was shown that heat transfer Equation (61) provides the possibility of predicting, with high precision, that the wave mechanism of heat transfer emerges at low temperatures (ballistic propagation of heat through solids) and of predicting size-dependent effects in thermal conductivity processes.

Remark 2. *Note that the heat conduction equations require a certain revision concern to the heat flux multiplier: this multiplier must be the specific heat coefficient at a constant volume in order to obtain the correct heat balance equations*.

7. Conclusions

We developed a variational principle which makes it possible for the considered model of a reversible process (using a Lagrangian) to add dissipative models by introducing the necessary number of dissipation channels. In particular, examples of formulations of the Darcy, Navier–Stokes, and Brinkman hydrodynamic models were considered. Each of these models is determined by same Lagrangian for the reversible part of process, but with a different set of dissipation channels. In the Brinkman hydrodynamic model, a synergistic effect was discovered which is associated with the simultaneous consideration of the Darcy and Navier–Stokes dissipation channels. This effect explains the existence of a boundary layer in a liquid and the scale effect associated with the thickness of the boundary layer.

Another example of modeling dissipative processes, which may be attractive for applied purposes, is a sequence of variational models of heat transfer processes. All heat conduction laws are obtained as compatibility equations which were received, with the exception of thermal potential, from the equations of Hooke's law for temperature and heat flow. The laws of thermal conductivity of Fourier, Maxwell–Cattaneo, Guyer–Krumhansl, and Jeffrey are obtained using a proposed universal approach. For different models, different dissipation channels are established, each of which determines the original model of thermal conductivity.

Author Contributions: Conceptualization, S.A.L.; Methodology, P.A.B.; Formal analysis, P.A.B.; Writing—original draft, S.A.L. and P.A.B.; Supervision, H.A.M. All authors have read and agreed to the published version of the manuscript.

Funding: This work was supported by the Russian Science Foundation grants 23-11-00275 issued to IAM RAS.

Data Availability Statement: Data are contained within the article.

Conflicts of Interest: The authors declare no conflict of interest.

References

1. Demirel, Y.; Gerbaud, V. Fundamentals of Nonequilibrium Thermodynamics. In *Nonequilibrium Thermodynamics*; Elsevier: Amsterdam, The Netherlands, 2019; pp. 135–186. [CrossRef]
2. Demirel, Y. Nonequilibrium Thermodynamics Approaches. In *Nonequilibrium Thermodynamics*; Elsevier: Amsterdam, The Netherlands, 2007; pp. 671–686. [CrossRef]
3. Hütter, M.; Theo, A.; Tervoort, T.A. Coarse Graining in Elasto-viscoplasticity: Bridging the Gap from Microscopic Fluctuations to Dissipation. *Adv. Appl. Mech.* **2009**, *42*, 253–317. [CrossRef]
4. Awais, M.; Hayat, T.; Nawaz, M.; Alsaedi, A. Newtonian Heating, Thermal-Diffusion and Diffusion-Thermo Effects in an Axisymmetric Flow of a Jeffery Fluid over a Stretching Surface. *Braz. J. Chem. Eng.* **2015**, *32*, 555–561. [CrossRef]
5. Knyazeva, A.G. Cross Effects in Solid Media with Diffusion. *J. Appl. Mech. Tech. Phys.* **2003**, *44*, 373–384. [CrossRef]
6. Parfenova, E.S.; Knyazeva, A.G. The Influence of Some Model Parameters on The Impurity Distribution Implanted into Substrate Surface. *IOP Conf. Ser. Mater. Sci. Eng.* **2016**, *124*, 012085. [CrossRef]
7. Aifantis, E.C. On the Problem of Diffusion in Solids. *Acta Mech.* **1980**, *37*, 265–296. [CrossRef]
8. Sherif, H.H.; Saleh, H.A. Half-Space Problem in the Theory of Generalized Thermoelastic Diffusion. *Int. J. Solids Struct.* **2005**, *42*, 4484–4493. [CrossRef]
9. Sherief, H.H.; Hamza, F.; Saleh, H. The Theory of Generalized Thermoelastic Diffusion. *Int. J. Eng. Sci.* **2004**, *42*, 591–608. [CrossRef]
10. Aouadi, M. Generalized Theory of Thermoelastic Diffusion for Anisotropic Media. *J. Therm. Stress.* **2008**, *31*, 270–285. [CrossRef]
11. Aouadi, M. On the Coupled Theory of Thermo-Magnetoelectroelacticity. *J. Mech. Appl. Math.* **2007**, *60*, 443–456. [CrossRef]
12. Lurie, S.; Volkov-Bogorodskii, D.; Altenbach, H.; Belov, P.; Nazarenko, L. Coupled Problems of Gradient Thermoelasticity for Periodic Structures. *Arch. Appl. Mech.* **2023**, *93*, 23–39. [CrossRef]
13. Forest, S.; Amestoy, M. Hypertemperature in Thermoelastic Solids. *Comptes Rendus Mec.* **2008**, *336*, 347–353. [CrossRef]
14. Khakalo, S.; Niiranen, J. Lattice Structures as Thermoelastic Strain Gradient Metamaterials: Evidence from Full-Field Simulations and Applications to Functionally Step-Wise-Graded Beams. *Compos. B Eng.* **2019**, *177*, 107224. [CrossRef]
15. Khakalo, S.; Niiranen, J. Anisotropic Strain Gradient Thermoelasticity for Cellular Structures: Plate Models, Homogenization and Isogeometric Analysis. *J. Mech. Phys. Solids.* **2020**, *134*, 103728. [CrossRef]
16. Zener, C. Internal Friction in Solids. I. Theory of Internal Friction in Reeds. *Phys. Rev.* **1937**, *52*, 230–235. [CrossRef]
17. Zener, C. Internal Friction in Solids. II. General Theory of Thermoelastic Internal Friction. *Phys. Rev.* **1937**, *53*, 90–99. [CrossRef]
18. Zener, C. The Intrinsic Inelasticity of Large Plates. *Phys. Rev.* **1941**, *59*, 669–673. [CrossRef]
19. Lifshitz, R.; Roukes, M.L. Thermoelastic Damping in Micro- and Nanomechanical Systems. *Phys. Rev.* **2000**, *61*, 5600–5609. [CrossRef]
20. dell'Isola, F.; Misra, A. Principle of Virtual Work as Foundational Framework for Metamaterial Discovery and Rational Design. *Comptes Rendus Mec.* **2023**, *351*, 1–25. [CrossRef]
21. Placidi, P.; Barchiesi, E.; Misra, A. A Strain Gradient Variational Approach to Damage: A Comparison with Damage Gradient Models and Numerical Results. *Math. Mech. Complex Syst.* **2018**, *6*, 77–100. [CrossRef]
22. Barchiesi, E.; Ciallella, A.; Scerrato, D. A Partial Report on the Controversies About the Principle of Virtual Work: From Archytas of Tarentum to Lagrange, Piola, Mindlin and Toupin. *Adv. Struct. Mater.* **2022**, *152*, 341–377. [CrossRef]
23. Forest, S.; Cardona, J.M.; Sievert, R. Thermoelasticity of Second-Grade Media. *Contin. Thermomech. Art Sci. Model. Mater. Behav.* **2000**, *76*, 163–176. [CrossRef]
24. Coleman, B.D.; Noll, W. The Thermodynamics of Elastic Materials with Heat Conduction and Viscosity. *Arch. Ration. Mech. Anal.* **1963**, *13*, 167–178. [CrossRef]
25. Maugin, G.A. Internal Variables and Dissipative Structures. *J. Non-Equilib. Thermodyn.* **1990**, *15*, 173–192. [CrossRef]
26. Müller, I.; Ruggeri, T. Extended Thermodynamics. In *Springer Tracts in Natural Philosophy*; Springer: Berlin/Heidelberg, Germany, 1993; Volume 37, pp. 118–141.
27. Lurie, S.A.; Belov, P.A.; Volkov-Bogorodskii, D.B. Variational Models of Coupled Gradient Thermoelasticity and Thermal Conductivity. *Mater. Phys. Mech.* **2019**, *42*, 564–581. [CrossRef]
28. Lurie, S.A.; Belov, P.A. On the Nature of the Relaxation Time, the Maxwell–Cattaneo and Fourier Law in the Thermodynamics of a Continuous Medium, and the Scale Effects in Thermal Conductivity. *Contin. Mech. Thermodyn.* **2020**, *32*, 709–728. [CrossRef]
29. Berezovski, A.; Engelbrecht, J.; Maugin, G.A. Internal Variables and Scale Separation in Dynamics of Microstructured Solids. *Solid Mech. Appl.* **2008**, *10*, 69–80. [CrossRef]
30. Ván, P.; Kovács, R. Variational Principles and Nonequilibrium Thermodynamics. *Philos. Trans. R. Soc. A Math. Phys. Eng. Sci.* **2020**, *378*, 20190178. [CrossRef] [PubMed]
31. Landau, L.D.; Lifshitz, E.M. *Theory of Elasticity*; Pergamon Press: New York, NY, USA, 1970.
32. dell'Isola, F.; Placidi, L. Variational principles are a powerful tool also for formulating field theories. In *Variational Models and Methods in Solid and Fluid Mechanics*; CISM Courses and Lectures; dell'Isola, F., Gavrilyuk, S., Eds.; Springer: Vienna, Austria, 2011; p. 535. [CrossRef]
33. Sedov, L.I. *On Fundamental Principles of Continuum Mechanics*; Izd-vo MGU: Moscow, Russia, 1961; p. 26. (In Russian)
34. Sedov, L.I. *On Fundamental Concepts of Continuum Mechanics*; SO AN SSSR: Novosibirsk, Russia, 1961; pp. 227–235. (In Russian)

35. Sedov, L.I.; Eglit, M.E. Construction of Nonholonomic Models of Continuum Mechanics with the Finiteness of Strains and Several Physical and Mathematical Effects Taken into Account. *Doklady AN SSSR* **1962**, *142*, 54–59.
36. Maxwell, J.C. On the Dynamical Theory of Gases. *Philos. Trans. R. Soc. Lond.* **1867**, *157*, 49–88. [CrossRef]
37. Cattaneo, C. Sulla Condizione, Del Calore. *Atti Sem. Mat. Fis. Univ. Modena* **1948**, *3*, 83–101.
38. Vernotte, M.P. La Véritable équation de Chaleur. *Comptes Rendus Hebd. Séances l'académie Sci.* **1958**, *247*, 2103–2105.
39. Vernotte, M.P. Les Paradoxes de la Théorie Continue de Léquation de la Chaleur. *Comptes Rendus Hebd. Séances l'académie Sci.* **1958**, *246*, 3154–3155.
40. Sellitto, A.; Cimmelli, V.A.; Jou, D. Mesoscopic Theories of Heat Transport in Nanosystems. In *SEMA SIMAI Springer Series*; Springer: Berlin/Heidelberg, Germany, 2016; Volume 6. [CrossRef]
41. Zhukovsky, K.V.; Srivastava, H.M. Analytical Solutions for Heat Diffusion beyond Fourier Law. *Appl. Math. Comput.* **2017**, *293*, 423. [CrossRef]
42. Sobolev, S.L. Nonlocal Two-Temperature Model: Application to Heat Transport in Metals Irradiated by Ultrashort Laser Pulses. *Int. J. Heat Mass Tran.* **2016**, *94*, 138. [CrossRef]
43. Joseph, D.D.; Preziosi, L. Heat Waves. *Rev. Mod. Phys.* **1989**, *61*, 375. [CrossRef]
44. Kamiński, W. Hyperbolic Heat Conduction Equation for Materials of Non-Homogeneous Inner Structure. *J. Heat Transf.* **1990**, *112*, 555–560. [CrossRef]
45. Belov, P.A.; Lurie, S.A.; Dobryanskiy, V.N. Variational Formulation of Linear Equations of Coupled Thermohydrodynamics and Heat Conductivity. *Lobachevskii J. Math.* **2020**, *41*, 1949–1963. [CrossRef]
46. Sobolev, S.L. Hyperbolic Heat Conduction, Effective Temperature, and Third Law for Nonequilibrium Systems with Heat Flux. *Phys. Rev. E* **2018**, *97*, 022122. [CrossRef] [PubMed]
47. Kovács, R.; Fehér, A.; Sobolev, S. On the Two-Temperature Description of Heterogeneous Materials. *Int. J. Heat Mass Transf.* **2022**, *194*, 123021. [CrossRef]
48. Ván, P. Weakly Nonlocal Irreversible Thermodynamics—The Guyer—Krumhansl and the Cahn—Hilliard Equations. *Phys. Lett. A.* **2001**, *290*, 88–92. [CrossRef]
49. Gusev, A.A.; Lurie, S.A. Wave-Relaxation Duality of Heat Propagation in Fermi—Pasta—Ulam Chains. *Mod. Phys. Lett. B* **2012**, *26*, 1250145. [CrossRef]

Disclaimer/Publisher's Note: The statements, opinions and data contained in all publications are solely those of the individual author(s) and contributor(s) and not of MDPI and/or the editor(s). MDPI and/or the editor(s) disclaim responsibility for any injury to people or property resulting from any ideas, methods, instructions or products referred to in the content.

symmetry

MDPI

Article

Chaotic Maps with Tunable Mean Value—Application to a UAV Surveillance Mission †

Lazaros Moysis [1,2,*], Marcin Lawnik [3], Christos Volos [1], Murilo S. Baptista [4] and Sotirios K. Goudos [5]

[1] Laboratory of Nonlinear Systems-Circuits & Complexity, Physics Department, Aristotle University of Thessaloniki, 54124 Thessaloniki, Greece; volos@physics.auth.gr
[2] Department of Mechanical Engineering, University of Western Macedonia, 50100 Kozani, Greece
[3] Department of Mathematics Applications and Methods for Artificial Intelligence, Faculty of Applied Mathematics, Silesian University of Technology, Kaszubska 23, 44-100 Gliwice, Poland; marcin.lawnik@polsl.pl
[4] Department of Physics, Institute for Complex Systems and Mathematical Biology, SUPA, University of Aberdeen, Aberdeen AB24 3UX, UK; murilo.baptista@abdn.ac.uk
[5] ELEDIA@AUTH, Physics Department, Aristotle University of Thessaloniki, 54124 Thessaloniki, Greece; sgoudo@physics.auth.gr
* Correspondence: lmousis@physics.auth.gr
† This paper is an extended version of our paper published in International Conference on Modern Circuits and Systems Technologies (MOCAST) on Electronics and Communications, Athens, Greece, 28–30 June 2023.

Abstract: Chaos-related applications are abundant in the literature, and span the fields of secure communications, encryption, optimization, and surveillance. Such applications take advantage of the unpredictability of chaotic systems as an alternative to using true random processes. The chaotic systems used, though, must showcase the statistical characteristics suitable for each application. This may often be hard to achieve, as the design of maps with tunable statistical properties is not a trivial task. Motivated by this, the present study explores the task of constructing maps, where the statistical measures like the mean value can be appropriately controlled by tuning the map's parameters. For this, a family of piecewise maps is considered, with three control parameters that affect the endpoint interpolations. Numerous examples are given, and the maps are studied through a collection of numerical simulations. The maps can indeed achieve a range of values for their statistical mean. Such maps may find extensive use in relevant chaos-based applications. To showcase this, the problem of chaotic path surveillance is considered as a potential application of the designed maps. Here, an autonomous agent follows a predefined trajectory but maneuvers around it in order to imbue unpredictability to potential hostile observers. The trajectory inherits the randomness of the chaotic map used as a seed, which results in chaotic motion patterns. Simulations are performed for the designed strategy.

Keywords: chaos; piecewise map; mean value; distribution; randomness; surveillance; path planning; UAV

1. Introduction

1.1. Chaos and Its Applications

Chaotic systems have become standardized tools in applications where a low-cost source of high entropy is required. Examples include secure communications [1], pseudo random bit and number generators [2–6], data encryption [7,8], exploration and surveillance [9–11], optimization [12–16], and many more [17]. The reasoning behind their use is that they can generate random-like trajectories, which can be fed into a design to improve its performance. For performance, different indexes can be measured, relevant to the application at hand.

For example, in applications related to data security, like encryption and secure communications [1–8], a chaotic signal is used to hide an information signal. The operations

used for hiding include addition between the chaotic series and information, permutation of the information data, and substitution of the data. The resulting encrypted data have a random-like structure, and reveal no information about the original signal. For this, the chaotic signal used should have statistical properties similar to a random process so as to, at least, resist any statistical attacks. So here, uniformity of the chaotic time series chosen is an important and desired feature in assuring the security of the final encrypted data. For an overview of recent developments of chaos-based encryption, see [7,8].

In chaos-based optimization [12–16], and especially in evolutionary algorithms, chaotic time series are used to replace random variables, for actions like selection, emigration, and mutation. The motivation behind this is to replace the uniformity of a random process with a chaotic time series, which is still unpredictable, but may showcase different value distributions on the state space, for different parameter values. So here, the different statistical characteristics of the maps used may improve or hinder the performance of the algorithm, which can then be evaluated by further testing.

In chaotic exploration [9–11], an autonomous agent is tasked with either exploring or surveilling a given area of interest. For this, an additional goal is to impart unpredictability in the agent's path, which can improve the security against intruders and adversaries. For example, the task of trajectory prediction will become hard, making it difficult for an intruder to trespass a secure space. So here, maps with different statistical properties can generate diverse trajectories for the agent to follow.

1.2. Design of New Chaotic Maps

Judging from the collection of diverse examples of chaos-based applications, it is clear that not all of the existing chaotic systems from the vast literature can be utilized in all of the existing applications. Before considering a possible system to use, it is important to not only analyze its dynamical behavior for all control parameters of interest but also consider its statistical behavior. This will facilitate the choosing of the control parameter ranges that will improve the overall performance of the given design.

Motivated by this, the goal of this work is to investigate the changes in the statistical measures of chaotic maps, as their control parameters vary. For this, a simple family of piecewise chaotic maps with three control parameters is proposed. For this family, simple rules can be followed for appropriately tuning the control parameters in order to affect the statistical mean of the resulting time series. Piecewise maps are chosen here, as they are very prominent in applications [3–5,18–23], and their shape is easy to control. They can also yield chaotic behavior for a wide range of parameter values. Five maps are proposed and studied based on this general model. One map is a generalization of the skewed tent map [20], two are modifications of the maps proposed in [18], and the last two are combinations of the previous ones.

The five chosen maps are analyzed numerically through a collection of tools of nonlinear analysis. First, the bifurcation diagrams and Lyapunov exponents are computed, which are used to identify parameter ranges that yield chaotic behavior. Then, for the parameter ranges that generate chaos, graphs that depict the mean value are generated. These graphs help identify the statistical behavior of the chaotic time series, as the control parameters vary, and follow works that explore the statistical properties of chaotic systems [24–27].

From all the above studies, the main conclusion is that it is possible to tune the mean value of the proposed maps by appropriately changing the control parameters. This can result in chaotic time series that are left/right-skewed, or closer to a uniform process, all while maintaining unpredictability. Due to the structure of the maps being fairly simple, the tuning guidelines of the control parameters for achieving the desired behavior can be fairly straightforward. Thus, the proposed family of maps can be a starting point for designing maps with controllable statistical measures, all while maintaining wide ranges of chaotic behavior so that the resulting maps can be considered in chaos-based applications.

Another approach to the research problem may be to designate the so-called invariant density. Invariant density shows the distribution of the iterated variable and thus

determines basic descriptive statistics, such as the arithmetic mean. This measure can be determined by solving the Frobenius–Perron equation [28]. However, it should be emphasized that in only certain cases (usually mappings composed of linear functions), it is possible to determine this measure analytically. In other cases, this density is approximated by determining histograms.

The problem of finding a mapping with a given density function is thus called the inverse Frobenius–Perron problem (IFPP) [28]. An overview of solutions to this problem can be found in [29]. Such a problem is analyzed, among others, in [30], where the tent map and the cumulative distribution function are used for this purpose. A similar solution using the inverting of the cumulative distribution function is presented in [31]. In turn in [32], a method using stationary densities of dynamical systems with input perturbations is presented. Still, other solutions to this problem can be found in [33,34]. However, it is worth emphasizing that the mentioned solutions of the inverse Frobenius–Perron problem may be ineffective in practical applications.

Motivated by this, the goal of this work is to investigate the changes in the statistical measures of chaotic maps, as their control parameters vary. For this, a simple family of piecewise maps is proposed and analyzed.

To further showcase their applicability, the proposed chaotic maps are applied to the problem of surveillance mentioned above. For this, a scenario is developed where an Unmanned Aerial Vehicle (UAV) follows a predefined trajectory. To introduce chaotic maneuvering into its motion, the chaotic map's values are utilized to rotate the UAV in a circular region around the predefined trajectory. By performing so, the UAVs trajectory varies as it surveils the area and never repeats itself.

Summarizing, the contributions of this work are outlined as follows:

- A family of piecewise maps with three parameters is proposed. The three parameters are tuned to control the endpoint interpolations.
- By appropriately tuning the control parameters, the statistical mean value of the resulting chaotic time series can be changed.
- The studied maps showcase a collection of dynamical phenomena, including wide uninterrupted parameteric ranges, where chaotic behavior is observed, or self-similar, fractal-like behavior in transitioning in and out of chaos.
- The maps are successfully applied to the problem of the trajectory of a UAV that surveils a given area being imbued with unpredictability.

Finally, it must be noted that this work extends the results of the conference work [35] by studying a wider collection of maps, providing a more in-depth analysis, and the additional application to surveillance. The remainder of the paper is outlined as follows. In Section 2, the family of maps considered here is presented. In Section 3, examples of different maps are presented, and their dynamical behavior is studied. Section 4 presents the chaotic surveillance application. Finally, Section 5 summarizes the paper, with a list of future topics of interest.

2. Proposed Family of Maps

Consider the general family of piecewise maps with two subfunctions of the form

$$x_i = g(x_{i-1}) = \begin{cases} g_1(x_{i-1}, a, b) & 0 \leq x_{i-1} \leq b \\ g_2(x_{i-1}, b, c) & b < x_{i-1} \leq 1 \end{cases}, \tag{1}$$

with $g(x) \in [0,1]$, so the mapping interval is $x_i \in [0,1]$. The function g_1 is increasing, and g_2 is decreasing. The maps (1) have three control parameters $a, b, c \in [0,1]$. These

parameters are used to control the shape of the functions g_1, g_2 so that they interpolate to the following three points:

$$g_1(0, a, b) = a, \tag{2a}$$
$$g_1(b, a, b) = 1, \tag{2b}$$
$$g_2(1, b, c) = c. \tag{2c}$$

Each subfunction can either be linear or nonlinear, as long as the above conditions hold. These conditions are imposed in order to affect the mapping on the interval $[0, 1]$ and change the map's distribution in the state space. The general rules for tuning each parameter are the following:

1. Parameter $a \in [0, 1]$. Increasing a affects the mapping interval of the first subfunction to $g_1(x_{i-1}, a, b) \in [a, 1]$. Thus, the first subfunction will only map to a subset of $[0, 1]$, which will result in a skewed distribution of the resulting time series.
2. Parameter $b \in [0, 1]$. Changing the parameter b will bend the piecewise function g to the left or right, with $b = 0.5$ being the symmetric instance. This again can affect the skewness of the resulting time series. For example, increasing the value of $b \in [0.5, 1]$, will result in the subfunction $g_1 : [0, b] \to [a, 1]$ having a wider input domain $[0, b] \supseteq [0, 0.5]$, while also mapping to a smaller interval $[a, 1] \subseteq [0, 1]$, which can result in a right-skewed distribution.
3. Parameter $c \in [0, 1]$. Increasing c changes the second subfunction to $g_2(x_{i-1}, b, c) \in [c, 1]$. Similar to g_1, this change can affect the distribution of the map, but it can also change the mapping interval of the whole mapping to a subset of $[0, 1]$ as will be shown through an example in the next section. Thus, in our upcoming analysis, the parameter c will be set to its default value $c = 0$.

The above general rules can be used to design numerous maps, as almost any function can be appropriately mapped to satisfy the conditions (2). Of course, the additional desired property would be to obtain maps that will showcase chaotic behavior for a wide range of parameter values. Such examples are studied next.

3. Considered Maps

In this section, several maps are considered and studied, with respect to the parameters a, b. In all cases, the initial condition is fixed to $x_0 = 0.111$.

3.1. Skewed Tent Map

Based on the well-known skewed tent map [20], the following generalization is proposed:

$$x_i = g(x_{i-1}) = \begin{cases} \frac{1-a}{b} x_{i-1} + a & 0 \le x_{i-1} \le b \\ \frac{1-c}{b-1} x_{i-1} + \frac{bc-1}{b-1} & b < x_{i-1} \le 1 \end{cases}, \tag{3}$$

where a, b, c are the map's parameters. The parameters a, c control the two endpoint interpolations $g(0) = a$, $g(1) = c$, and parameter b controls the skew between the two subfunctions.

In Figure 1 (top), the function $g(x)$ is shown for different parameter values. The effect of changing the values of a, b, c on the shape of the curve is clear. As discussed in the previous section, changing the parameters a, b can result in the right-skewness of the resulting time series, while changing c can affect the overall mapping interval. Such examples are shown in Figure 1 (bottom), where the corresponding histograms for 10^5 values of x_i are plotted. This is why in subsequent simulations for all maps, the choice is $c = 0$. In the symmetric case $a = 0$, $b = 0.5001$, the histogram is uniform. When increasing the values of a, b, the histogram becomes right-skewed as a result of the first subfunction having a wider domain, and mapping in a smaller interval. So, tuning a, b will have a direct effect on the statistical properties of the time series $\{x_i\}$. The value of parameter c will be kept to $c = 0$, as we want the mapping interval to be $[0, 1]$. Note that in the symmetric case,

the parameter is set to $b = 0.5001$ instead of $b = 0.5$ since with complete symmetry, the generalized tent map (3) is identical to the tent map, which falls into periodic behavior due to round-off errors.

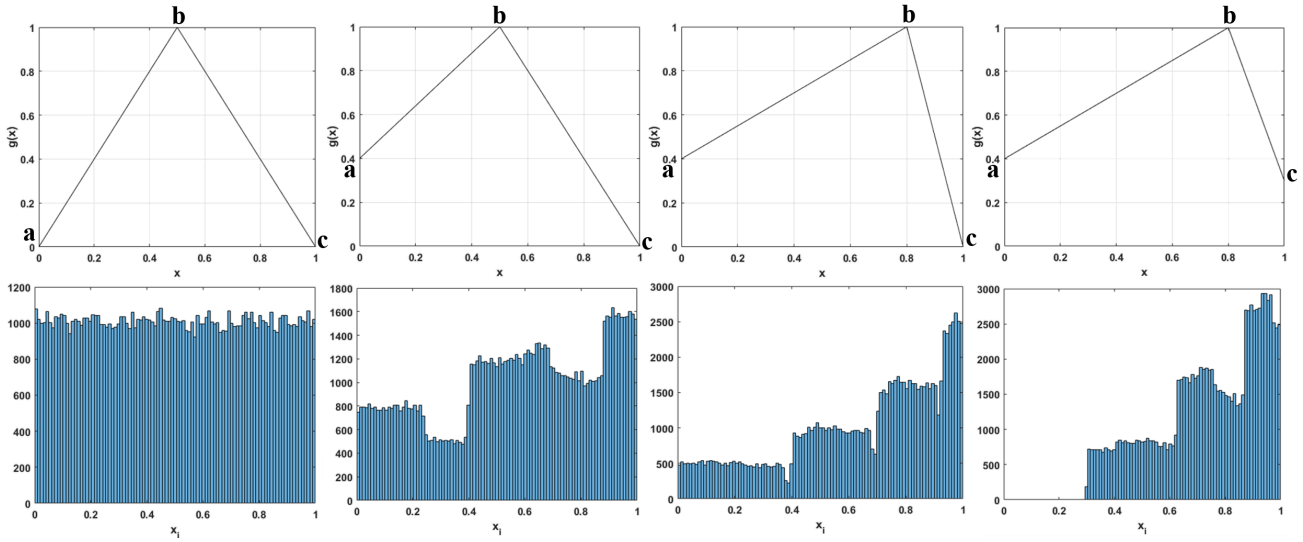

Figure 1. (**Top**) The graph of $g(x)$ in (3) under different parameters. (**Bottom**) Corresponding histograms for a time series x_i of the skewed tent map (3) of length 10^5. The parameter values (a, b, c) from left to right are $(0, 0.5001, 0)$, $(0.4, 0.5, 0)$, $(0.4, 0.8, 0)$, $(0.4, 0.8, 0.3)$.

To gain a first impression of the map's (3) behavior, its bifurcation diagram is computed. This is shown in Figure 2, with respect to parameter b, and $a = 0.5$, $c = 0$. The map behaves chaotically in this interval. This diagram gives some insight into the behavior of the map for a fixed a. But since the map has two parameters of interest (the third being fixed $c = 0$), a more practical approach is to study its behavior under all possible parameter pairs (a, b), see when the map behaves chaotically, and what is its mean value in each case.

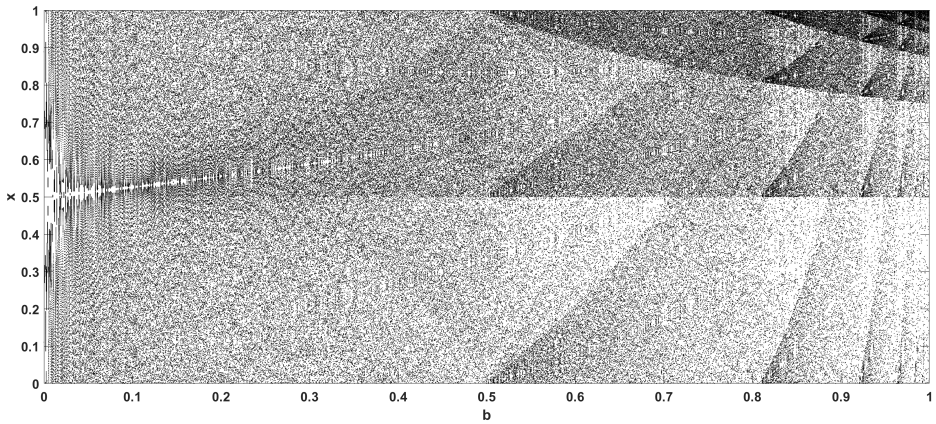

Figure 2. Bifurcation diagram of the skewed tent map (3) with respect to parameter b, for $a = 0.5$, and $c = 0$. The parameter iteration step is 0.0005.

Thus, to investigate the impact of the parameters a, b on the mean value, the parameter ranges of (3) that generate chaotic behavior are computed. For this, the Lyapunov exponent (LE) of the map is computed for all parameter pairs $(a, b) \in [0, 1] \times [0, 1]$. The result is shown in Figure 3a, where the colormap corresponds to the LE value achieved, with zero or negative values, that is, the non-chaotic cases, noted in black. The map exhibits chaos for a wide and uninterrupted range of parameter pairs, which is a desirable property, as it can facilitate easier parameter choice.

For the parameter pairs that yield chaotic behavior, the diagram in Figure 3b depicts the mean value obtained for a time series of length 10^5. From this diagram, it can be deduced that for lower parameter values, the mean is around 0.5, indicating a uniform histogram. As the parameters take higher values, the mean value also increases, indicating that the histogram of the time series becomes right-skewed. So with this diagram, changes in the statistical behavior of the map can be identified, which are not depicted in either the bifurcation diagram, or the LE diagram.

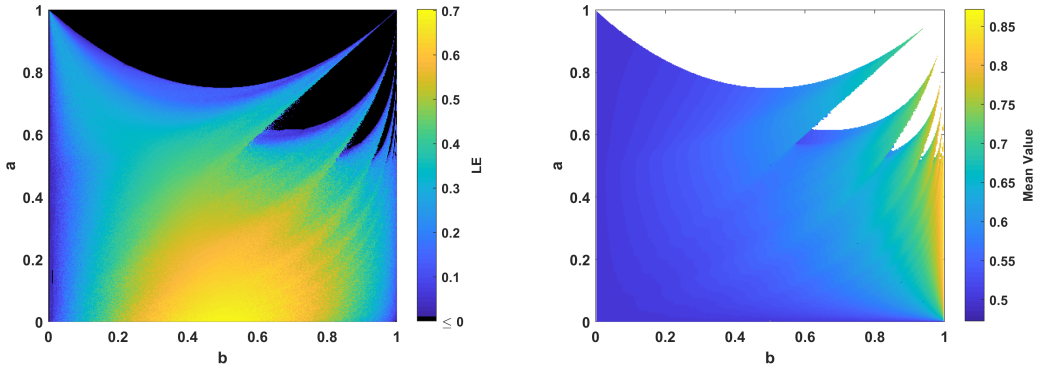

(**a**) (**b**)

Figure 3. Diagram depicting the LE values (**a**) and the mean values (**b**) of the skewed tent map (3) for different values of parameters a, b, and $c = 0$. The parameter iteration step is 0.0025.

3.2. Cosine Skewed Piecewise Map

In [18], various piecewise chaotic maps are proposed. Here, one such map is chosen, and a generalized version is proposed as:

$$x_i = g(x_{i-1}) = \begin{cases} \frac{f\left(\frac{x_{i-1}}{b}\right)-f(0)}{f(1)-f(0)} + \frac{-a}{b}x_{i-1} + a & 0 \le x_{i-1} \le b \\ \frac{f\left(\frac{x_{i-1}-1}{b-1}\right)-f(0)}{f(1)-f(0)} + \frac{-c}{b-1}x_{i-1} + \frac{bc}{b-1} & b < x_{i-1} \le 1 \end{cases}, \quad (4)$$

where $f(x) = \cos(e^{x-1})$. In the original map, the boundaries of the function g were mapped on $g(0) = 0$ and $g(1) = 1$. In the proposed map, $g(0) = a$ and $g(1) = c$, so the original map is modified to satisfy conditions (2). A graph of the function g, for $a = 0.1$, $b = 0.8$, $c = 0.2$, is shown in Figure 4. In contrast to the tent map (3), each subfunction is now nonlinear. The functions are also convex.

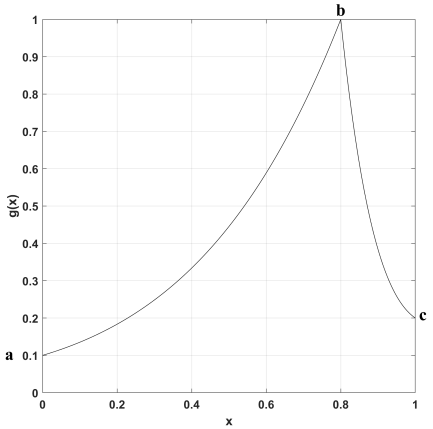

Figure 4. The function $g(x)$ of the map of (4), with $f(x) = \cos(e^{x-1})$, for $a = 0.1$, $b = 0.8$, and $c = 0.2$.

Figure 5 shows the bifurcation diagram of the map with respect to parameter b, and $a = 0.5$, $c = 0$. The map shows a very intricate behavior, as it traverses in and out of chaos,

following a period-doubling cascade, or a period-halving behavior. More impressively, we can observe multiple patterns of period-halving transition from chaos for lower values of b, and period-doubling transitions to chaos for higher values of b. A detailed view of this is shown in Figure 6 as well. This complex self-similar, fractal-like behavior will also be visible in the LE graphs shown next.

Figure 7a shows the LE value achieved for each parameter pair. Most parameter pairs generate chaos, but now there are non-chaotic regions appearing, which have a fractal-like structure, the so-called "shrimps". Figure 7b depicts the mean value of the time series for the parameter pairs that generate chaos. Lower and higher values are both achieved, so the histogram shifts from left- to right-skewed.

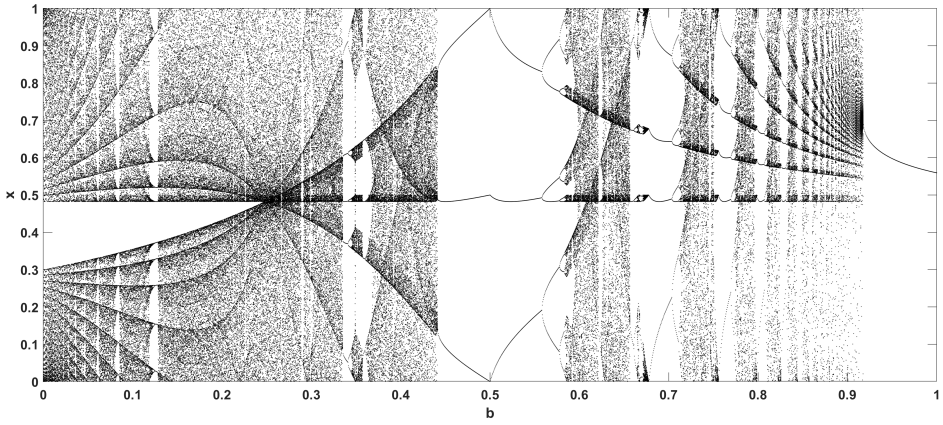

Figure 5. Bifurcation diagram of the map (4), with $f(x) = \cos(e^{x-1})$, with respect to parameter b, for $a = 0.5$ and $c = 0$. The parameter iteration step is 0.0005.

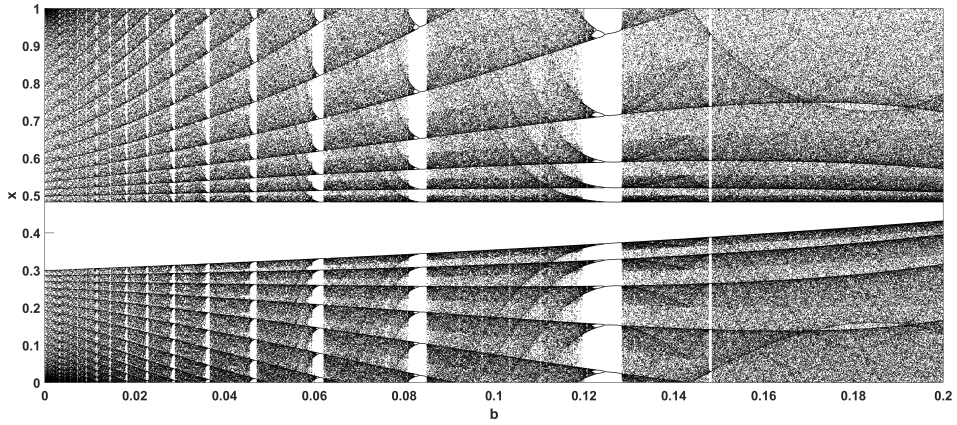

Figure 6. Detailed view of the bifurcation diagram of the map (4) showin in Figure 5, with $f(x) = \cos(e^{x-1})$, with respect to parameter $b \in [0, 0.2]$, for $a = 0.5$ and $c = 0$.

3.3. Secant Skewed Piecewise Map

An additional variation of Equation (4) is also studied, with the nonlinear function chosen as $f(x) = \sec(e^{x-1})$. Figure 8 shows the graph of $g(x)$ for $a = 0.1$, $b = 0.8$, and $c = 0.2$. The functions are again convex in shape.

Figure 9 shows the bifurcation diagram of the map with respect to parameter b, and $a = 0.5$ and $c = 0$. As with the previous map, this map also showcases intricate self-similar, fractal-like behavior in its transitions to and from chaos. As parameter b increases, the map falls into a period-1 behavior.

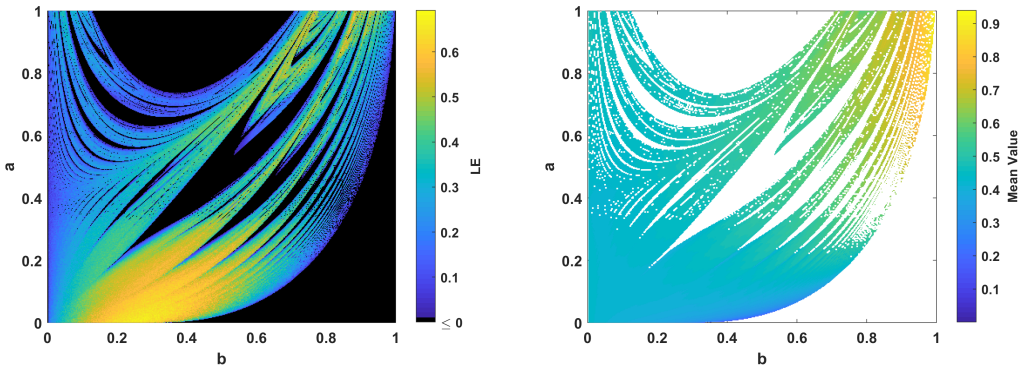

(**a**) (**b**)

Figure 7. Diagram depicting the LE values (**a**) and mean values (**b**) of the map (4), with $f(x) = \cos(e^{x-1})$, for different values of parameters a, b, and $c = 0$. The parameter iteration step is 0.0025.

As with previous maps, Figure 10a depicts the LE values for all parameter pairs (a, b). The chaotic regions follow a pattern similar to the Cosine Skewed Piecewise Map, with non-chaotic, self-similar fractal-like patterns appearing. For the chaotic regions, in Figure 10b, it can be observed that similar to the previous map, the mean value ranges from around 0.2 up to 0.8.

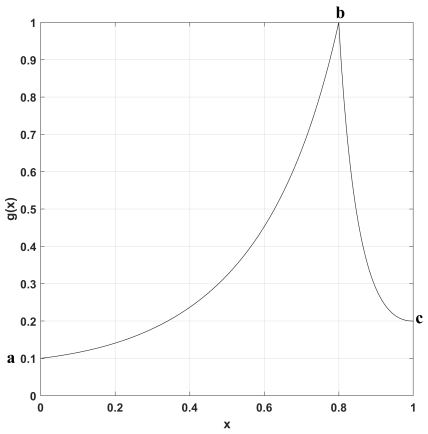

Figure 8. The function $g(x)$ of the map (4), with $f(x) = \sec(e^{x-1})$, for $a = 0.1$, $b = 0.8$, $c = 0.2$.

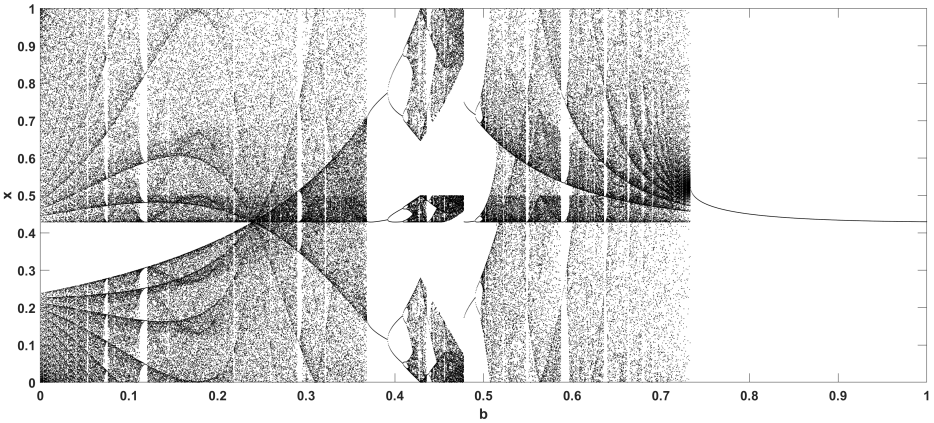

Figure 9. Bifurcation diagram of the map (4), with $f(x) = \sec(e^{x-1})$, with respect to parameter b, for $a = 0.5$ and $c = 0$. The parameter iteration step is 0.0005.

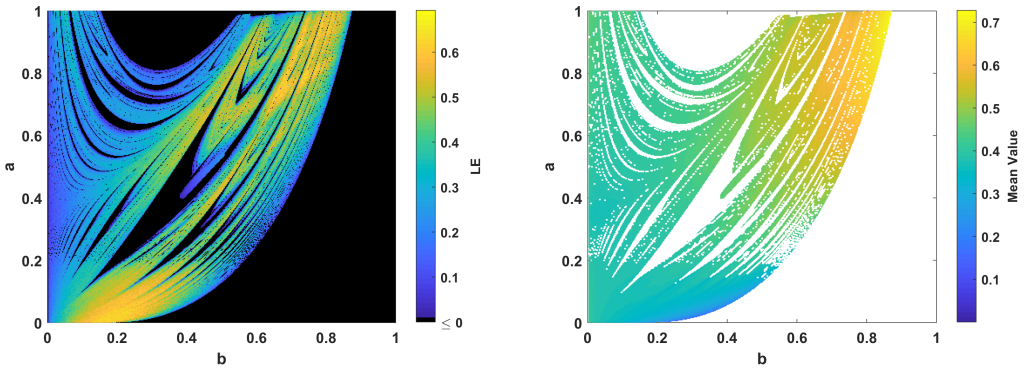

(**a**) (**b**)

Figure 10. Diagram depicting the LE values (**a**) and mean values (**b**) of the map (4), with $f(x) = \sec(e^{x-1})$, for different values of parameters a, b, and $c = 0$. The parameter iteration step is 0.0025.

3.4. Tent-Cosine Skewed Piecewise Map

Combining the previous maps, two combinations can be derived. The first map is the Tent-Cosine Skewed Piecewise Map, described by

$$x_i = g(x_{i-1}) = \begin{cases} \frac{1-a}{b} x_{i-1} + a & 0 \le x_{i-1} \le b \\ \frac{f\left(\frac{x_{i-1}-1}{b-1}\right) - f(0)}{f(1)-f(0)} + \frac{-c}{b-1} x_{i-1} + \frac{bc}{b-1} & b < x_{i-1} \le 1 \end{cases}, \quad (5)$$

where $f(x) = \cos(e^{x-1})$. So the first subfunction is taken from the tent map (3), while the second subfunction is taken from (4). The plot of this function in Figure 11 makes this clear.

Figure 12 shows the bifurcation diagram of the map with respect to parameter b, and $a = 0.5$, $c = 0$. The map shows wide regions of chaotic behavior, similar to the tent map (3). As parameter b increases, patterns of transition between chaos and periodic behavior start to emerge, as will be more evident from the next Figure 13a.

The diagram of LE values for the map (5) is shown in Figure 13a. Here, it can be observed that the behavior of this hybrid map is similar to that of the tent map (3) shown in Figure 3a, as the map exhibits wide parameter ranges of uninterrupted chaotic behavior, in contrast to the rest of the maps that exhibited self-similar, fractal-like, non-chaotic regions.

The same similarity between the tent map (5) also holds for the mean value. In Figure 13b, it can be seen that the map's behavior ranges from a mean of around 0.5, to higher values of around 0.85, which is similar to the behavior shown in Figure 3b.

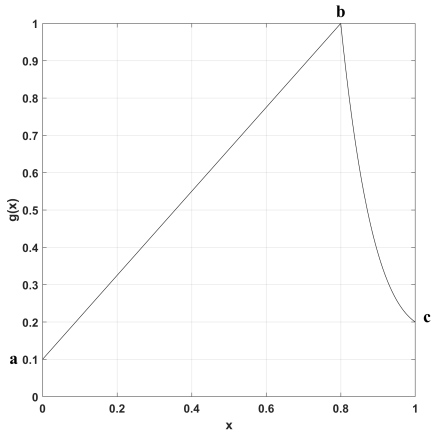

Figure 11. The function $g(x)$ of the map (5), with $f(x) = \cos(e^{x-1})$, for $a = 0.1$, $b = 0.8$, and $c = 0.2$.

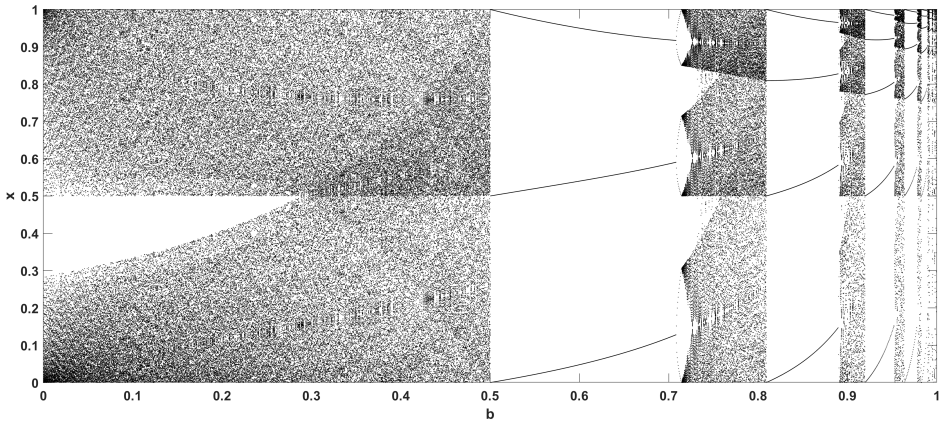

Figure 12. Bifurcation diagram of the map (5), with $f(x) = \cos(e^{x-1})$, with respect to parameter b, for $a = 0.5$, $c = 0$. The parameter iteration step is 0.0005.

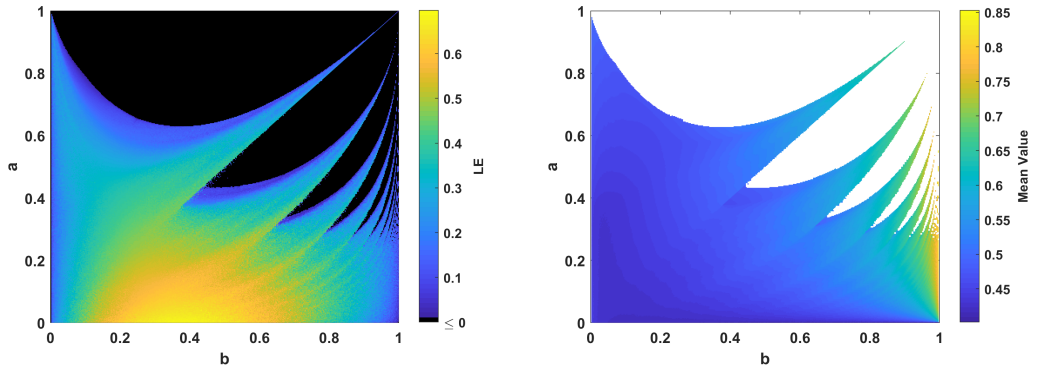

(**a**) LE values diagram. (**b**) Mean values diagram.

Figure 13. Diagram depicting the LE values (**a**) and mean values (**b**) of the map (5), with $f(x) = \cos(e^{x-1})$, for different values of parameters a, b, and $c = 0$. The parameter iteration step is 0.0025.

3.5. Cosine-Tent Skewed Piecewise Map

The second combination considered is the Cosine-Tent Skewed Piecewise Map, described by

$$x_i = g(x_{i-1}) = \begin{cases} \frac{f\left(\frac{x_{i-1}}{b}\right) - f(0)}{f(1) - f(0)} + \frac{-a}{b} x_{i-1} + a & 0 \leq x_{i-1} \leq b \\ \frac{1-c}{b-1} x_{i-1} + \frac{bc-1}{b-1} & b < x_{i-1} \leq 1 \end{cases}, \tag{6}$$

where $f(x) = \cos(e^{x-1})$. So the first subfunction is taken from (4), while the second subfunction is taken from the tent map (3). The graph of the function shown in Figure 14 illustrates this.

Figure 15 shows the bifurcation diagram of the map with respect to parameter b, and $a = 0.5$ and $c = 0$. This map is more similar to the modified map (4), as it shows self-similar, fractal-like patterns in its transitions to and from chaos, with a period-1 behavior emerging for higher values of b.

The chaotic behavior and statistical behavior of this map are more similar to the modified map (4). Its chaotic regions shown in Figure 16a showcase periodic interruptions of the fractal-like shape, and the mean value shown in Figure 16b ranges from low to high values. Comparing these two hybrid maps (5) and (6), it seems that the first subfunction is more influential to the behavior of the map.

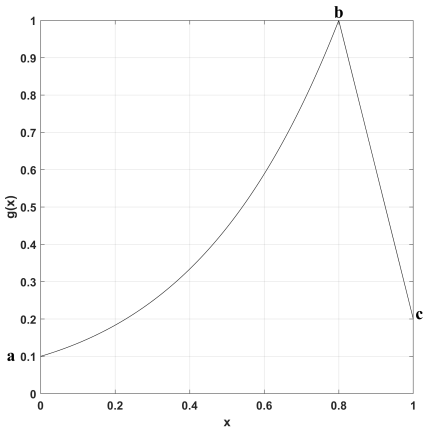

Figure 14. The function $g(x)$ of the map (6), with $f(x) = \cos(e^{x-1})$, for $a = 0.1$, $b = 0.8$, $c = 0.2$.

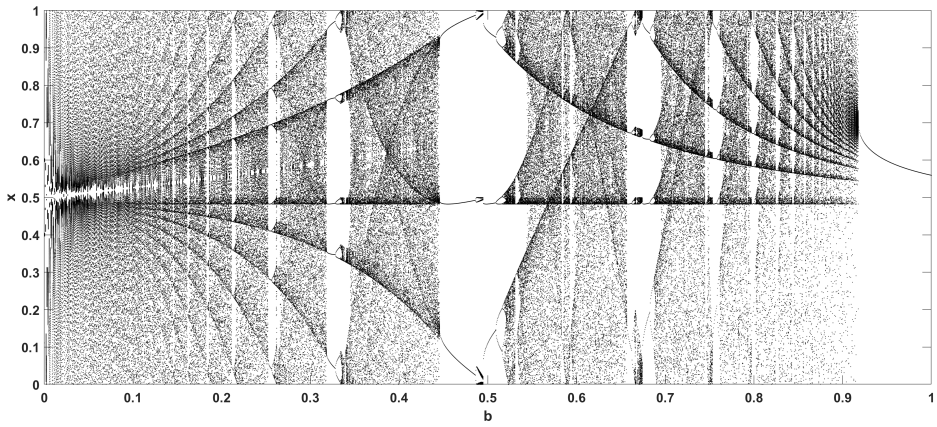

Figure 15. Bifurcation diagram of the map (6), with $f(x) = \cos(e^{x-1})$, with respect to parameter b, for $a = 0.5$, $c = 0$. The parameter iteration step is 0.0005.

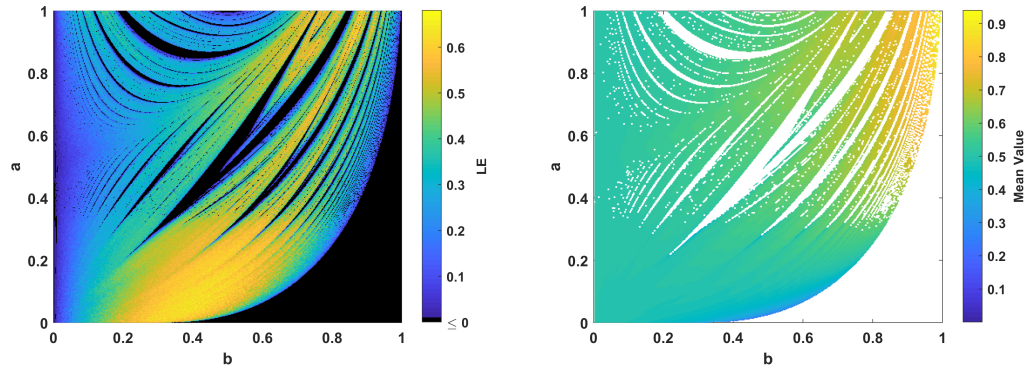

(**a**) (**b**)

Figure 16. Diagram depicting the LE values (**a**) and mean values (**b**) of the map (6), with $f(x) = \cos(e^{x-1})$, for different values of parameters a, b, and $c = 0$. The parameter iteration step is 0.0025.

3.6. Discussion

From the five different maps considered, rich dynamics were observed overall. The Skewed Tent map (3) and Tent-Cosine map (5) exhibited wider regions of uninterrupted chaotic behavior in contrast to the other three maps. They can thus be considered more suitable for applications, as their acceptable parameter range is easier to define. The Cosine

and Secant Skewed maps (4), and Cosine-Tent map (6) on the other hand exhibited rich dynamics, especially with respect to transitioning in and out of chaotic behavior.

What can also be observed from the bifurcation diagrams in Figures 5, 6, 9, 12 and 15 is that for some parameter pairs, the mapping interval consists of subregions of $[0, 1]$. Still, for all parameter pairs, as parameters are increased, the general trend of an increased mean value is observed from the mean value diagrams.

4. Application to UAV Surveillance Mission

4.1. Motivation

In this section, the application of chaotic surveillance will be considered for a patrolling agent. As mentioned in the introduction, the goal in chaotic surveillance is to impart an unpredictable element to an agent that patrols a given area and follows a predefined path, either for ground vehicles [9,36–38], or UAVs [10,11,37,39–41]. With the trajectory being non-repeating, the space can be more secure against intruders. Of course, such techniques can also be of use in more offensive scenarios, with an agent performing maneuvers to avoid adversary observers who want to predict its future location.

As examples of recent developments, in [42], two continuous chaotic systems were used to generate trajectories for monitoring around a predefined set of arbitrary many locations. In [37], a 2D Hénon map is used to maneuver chaotically in a closed curve in the 2D space. In [11], a chaotic and bioinspired method is used for 2D space as well. In [10], the problem is considered in the 3D space by mapping the Hénon map to the frame of reference of a UAV following a closed curve. An alternative approach to the problem is addressed using a chaotic camera mounted on a UAV, which follows a deterministic trajectory, in order to make the design more energy efficient [43].

4.2. Description of the Technique

The method proposed in this work is inspired by [10], but with several modifications. Its schematic is shown in Figure 17. In the designed scenario, an autonomous agent is set to follow a predefined path in the 3D space. This path is chosen as a circular one in the simulation scenario, and is denoted by the black circular curve in the figure. Instead of following this exact path, the agent performs a set of maneuvers on a toroidal area formed around the main path. The maneuvers are performed a predefined set of times to reduce redundant movement. In a realistic situation, this parameter can be set according to the given requirements.

To perform a maneuver, any of the chaotic maps proposed in the previous section can be used. So each time a maneuver must be performed, the value of the chaotic map x_i is mapped in the angle interval $\phi \in [-90, 90]$. This angle value corresponds to the amount of clockwise or counter-clockwise rotation that the agent will perform around on the circular area, defined from the frame of motion of the agent, intersecting the torus it moves on. The angle of rotation is limited to half the circular area to reduce redundant maneuvering, and it is motivated by [38], where a similar limitation is imposed to the turning of the agent. A schematic of this is shown in Figure 18. The advantage of using the proposed maps is that for longer simulations, it is possible to switch between parameter pairs (a, b) so that the chaotic time series changes its statistical behavior over time, leading to an even more unpredictable trajectory.

This process repeats any time a maneuver is set to be performed, and can be repeated for any number of times that the agent will perform a full crossing along the path of interest. The outline of this process is given in the Algorithm 1 below.

Algorithm 1: Chaotic Maneuvering Algorithm

Input. A closed surveillance path of interest.
A toroidal surface around the closed path.
A starting position on the torus, for the autonomous agent.
A choice of N, denoting the amount of maneuverings performed as the agent moves along the torus.
A chosen chaotic map from the above, with set parameters a, b, c and initial condition w_0.

Loop For $i = 1 : N$.

Step 1. Compute w_i.

Step 2. Map the value of the chaotic map into an angle as

$$\phi_i = 180 w_i - 90. \tag{7}$$

Step 3. Rotate the agent along the circular frame of reference ϕ_i angles as in Figure 18.

End of loop. If the traversing around the surveilled path needs to be repeated, then the loop is repeated.

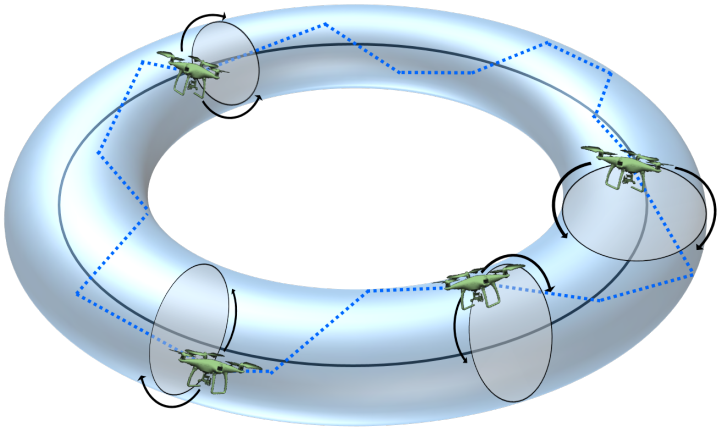

Figure 17. Outline of the surveillance path with chaotic maneuvering.

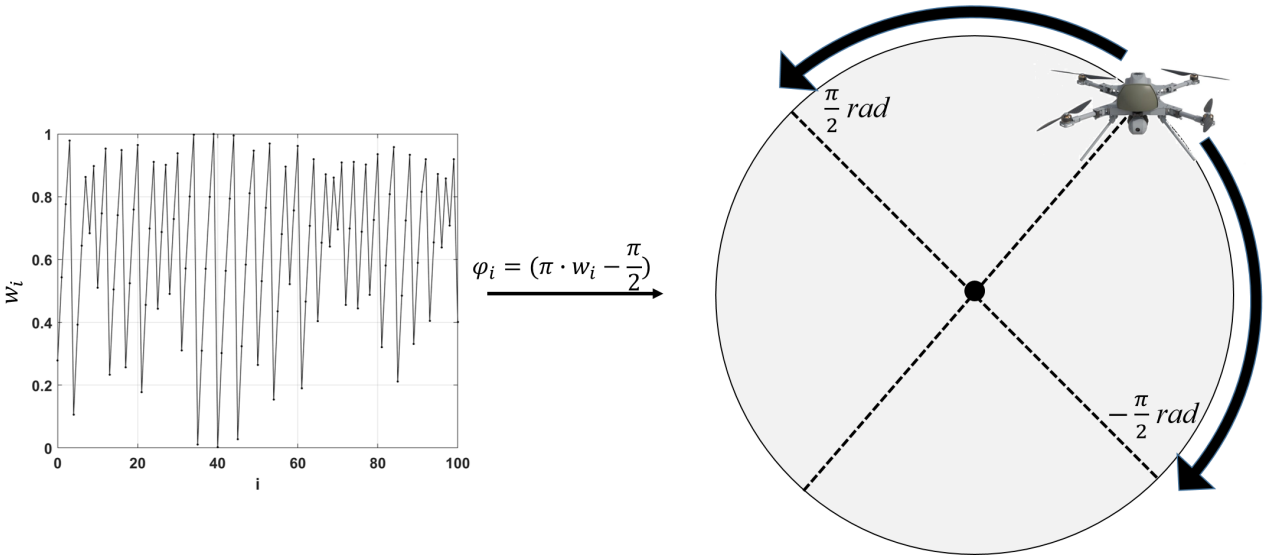

Figure 18. Frame of reference for the UAV agent. The map's values are mapped into angles in the unit circle.

4.3. Simulation Results

To showcase the proposed technique, a series of simulations are performed on a circular area of diameter 20 points, and a toroidal area of diameter 2 points around it. The points here may represent meters, or any other measure, depending on the size of the path considered. For this trajectory, a change of direction is performed at $N = 100$ equally spaced intervals. The initial position of the agent is on $(X, Y, Z) = (9, 0, 10)$. For the chaotic maps used, $w_0 = 0.111$.

4.3.1. Periodic Motion

Initially, two examples are considered, where the motion is periodic. In Figure 19a, a scenario is shown, where in each iteration the agent rotates five degrees counter-clockwise. The motion here is smooth, but also very predictable. Figure 19b also shows the coordinates of the agent, as it progresses on the torus trajectory. Similarly, Figure 20a,b show a periodic motion, where in each iteration the agent rotates 15 degrees counter-clockwise. These two examples of periodic traversing can be considered a standardized approach to surveilling maneuvers. They are smooth but predictable.

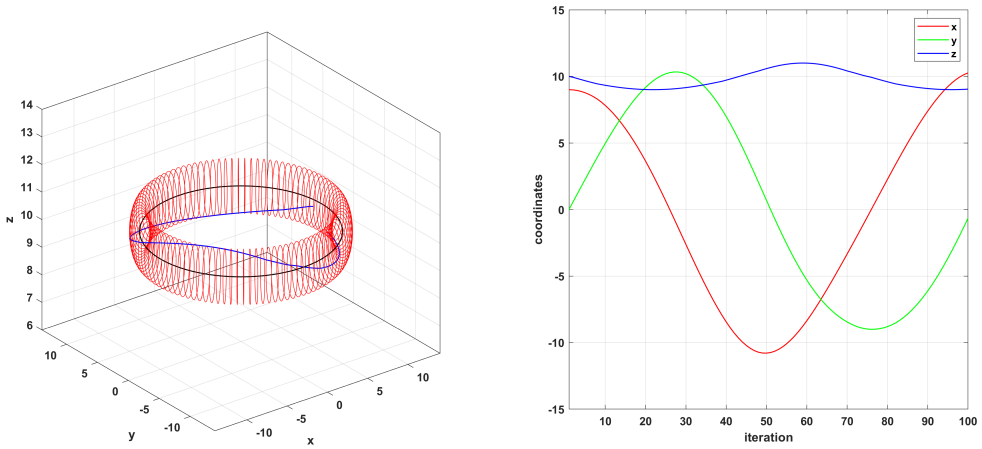

(**a**) (**b**)

Figure 19. Periodic motion of the UAV agent, with a rotation of 5 degrees per iteration. (**a**) Trajectory of the UAV agent. (**b**) Coordinates of the UAV agent.

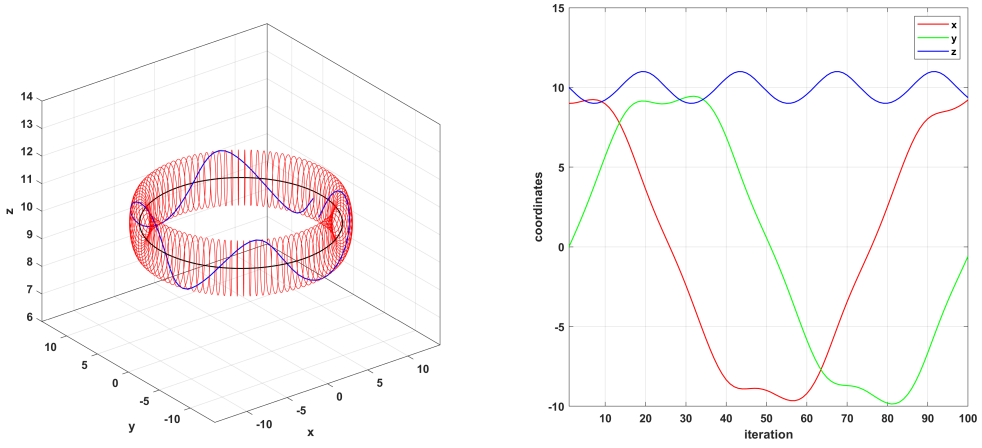

(**a**) (**b**)

Figure 20. Periodic motion of the UAV agent, with a rotation of 15 degrees per iteration. (**a**) Trajectory of the UAV agent. (**b**) Coordinates of the UAV agent.

4.3.2. Chaotic Motion

To counter this predictability, we now consider a chaotic maneuvering. The first such example is shown in Figure 21a, where the tent map (3) is used with parameters $a = c = 0$, $b = 0.5001$. The trajectory now becomes much more erratic than before. This can be seen as well from the coordinate graph of Figure 21b. The degrees of rotation fed from the chaotic map in each iteration are shown in Figure 22, where it can be seen that there is a balanced amount of positive and negative rotation commands.

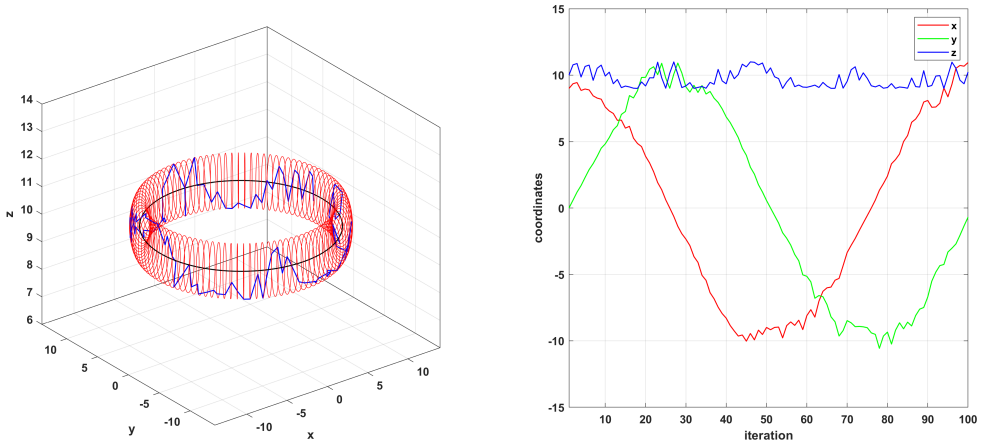

(**a**) (**b**)

Figure 21. Chaotic motion of the UAV agent, using the map (3) for $a = 0$, $b = 0.5001$, and $c = 0$. (**a**) Chaotic motion trajectory of the UAV agent. (**b**) Coordinates of the UAV agent.

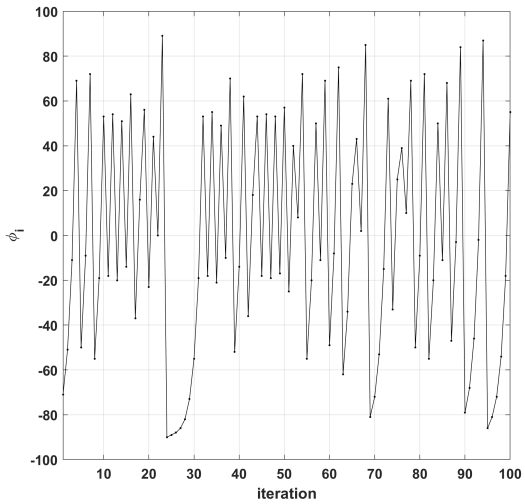

Figure 22. Rotation angles generated for the chaotic motion trajectory, using the map (3) for $a = 0$, $b = 0.5001$, and $c = 0$.

As a second example, the same map is used, this time with parameters $a = 0.4$, $b = 0.8$, and $c = 0$. The simulation result is shown in Figure 23a, and the coordinates of the agent are shown in Figure 23b. The motion is again unpredictable, with significant maneuvering. The chaotic degrees of rotation are shown in Figure 24, where it can be seen that there is an inclination towards positive rotations.

This was expected, as from the diagrams of Figures 1 and 3b, we know that the tent map becomes right-skewed for higher values of a, b. Still, this does not affect the unpredictability of the motion. More importantly, this skewness can be of advantage to the trajectory design, when the parameter pairs vary over time.

Finally, an example of two consecutive rotations is considered, shown in Figures 25a,b and 26. In Figure 25, the first rotation is shown in blue, and the second in green. Clearly, due to the inherent sensitivity of the chaotic map, the two trajectories are unrelated to each other; thus, knowledge of the first rotation points will in no way yield information about the possible future transitions performed during the second rotation.

Overall, it is clear that the use of the chaotic maps proposed can easily be adopted as computationally light sources of randomness to introduce unpredictability in the motion of an agent traversing through a predefined path. Of course, what must be noted here is that in the simulations above, the dynamics of a UAV agent were not taken into account, but rather, a series of chaotic trajectory positions around a torus were generated. These can then be followed by a UAV agent by applying appropriate control techniques. So the technique proposed here is a general architecture, which can be further adopted by specialists when considering specific UAV dynamics and limitations. For example, the amount of rotation in each iteration can be reduced from $[-90, 90]$ degrees to a smaller interval, depending on the efficiency of the agent.

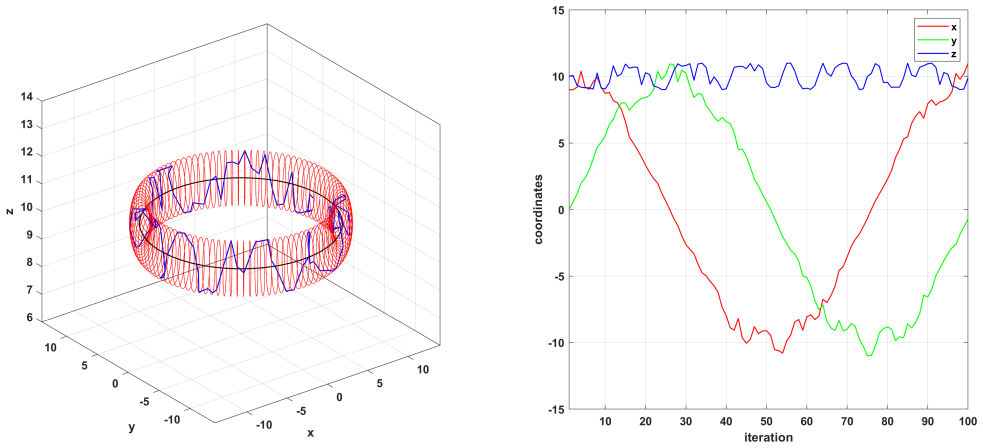

(**a**) (**b**)

Figure 23. Chaotic motion of the UAV agent, using the map (3) for $a = 0.4$, $b = 0.8$, and $c = 0$. (**a**) Chaotic motion trajectory of the UAV agent. (**b**) Coordinates of the UAV agent.

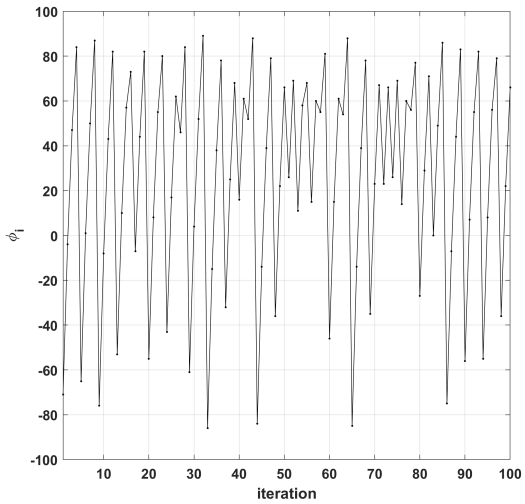

Figure 24. Rotation angles generated for the chaotic motion trajectory, using the map (3) for $a = 0.4$, $b = 0.8$, and $c = 0$.

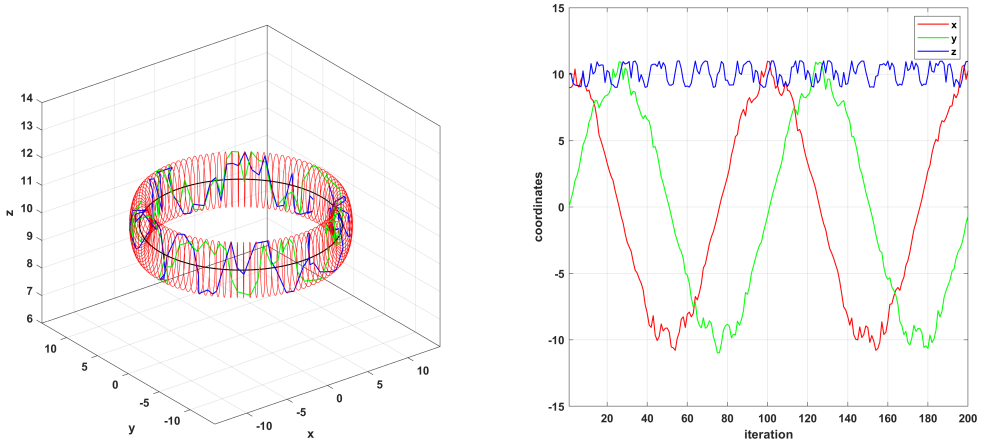

(**a**) (**b**)

Figure 25. Chaotic motion trajectory of the UAV agent, using the map (3) for $a = 0.4$, $b = 0.8$, and $c = 0$, when performing two loops around the set trajectory. (**a**) Chaotic motion trajectory of the UAV agent. (**b**) Coordinates of the UAV agent.

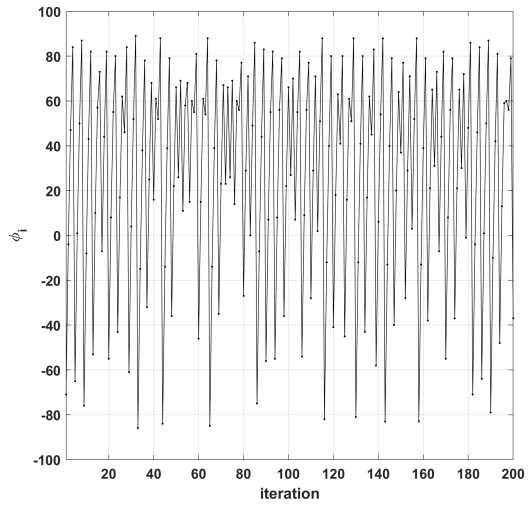

Figure 26. Rotation angles generated for the chaotic motion trajectory, using the map (3) for $a = 0.4$, $b = 0.8$ and $c = 0$, when performing two loops around the set trajectory.

5. Conclusions

This work considered a family of piecewise chaotic maps. The maps consist of three control parameters that are used to interpolate the endpoints of each subfunction at the desired positions in order to tune the distribution of the resulting time series. By considering five different chaotic maps from this family, it was deduced that it is possible to affect the statistical mean of the map's chaotic time series, by changing the control parameters, in order to affect the domain and mapping interval of each subfunction. This capability can be of use in many chaos-based applications, like optimization, secure communications, and surveillance. For that matter, the application of chaotic surveillance was considered, by proposing a strategy for maneuvering a UAV chaotically on a toroidal area around a predefined trajectory.

There are several research topics that can extend the results of the current work. Although this work considered a numerical approach for the tuning of the statistical behavior of the map based on the geometric properties of each subfunction, it is of interest to derive a theoretical proof for the effect of parameters a, b to the statistical properties of

the map. Moreover, another interesting topic is to evaluate the use of the proposed maps in chaos-based optimization algorithms. It would also be interesting to study the use of the proposed maps in chaos-based communications for hiding an information signal and transmitting it through a public channel.

In addition to the above, there have been recent developments for two families of piecewise chaotic maps. The first family is that of maps composed of functions based on fuzzy numbers [44,45]. The other family of piecewise maps is that of no equilibria maps [46,47]. It would thus be of interest to study the aforementioned families of maps, with respect to the ability to tune their statistical characteristics.

Finally, it is of interest to develop an experimental realization of the proposed chaotic trajectory using a UAV in a real environment. For the aforementioned topics, there are some undergoing studies from our research group.

Author Contributions: Conceptualization: L.M. and M.L.; methodology: L.M. and M.L.; software: L.M. and M.L.; visualization: L.M. and M.L.; writing—original draft preparation: L.M. and M.L.; writing—review and editing: L.M., M.L., C.V., M.S.B. and S.K.G.; supervision: C.V., M.S.B. and S.K.G. All authors have read and agreed to this version of the manuscript.

Funding: This research received no external funding.

Data Availability Statement: Data are contained within the article.

Acknowledgments: The authors are thankful to the anonymous reviewers for their helpful remarks.

Conflicts of Interest: The authors declare no conflict of interest.

References

1. Kaddoum, G. Wireless chaos-based communication systems: A comprehensive survey. *IEEE Access* **2016**, *4*, 2621–2648. [CrossRef]
2. Tutueva, A.V.; Nepomuceno, E.G.; Karimov, A.I.; Andreev, V.S.; Butusov, D.N. Adaptive chaotic maps and their application to pseudo-random numbers generation. *Chaos Solitons Fractals* **2020**, *133*, 109615. [CrossRef]
3. Wang, Y.; Liu, Z.; Ma, J.; He, H. A pseudorandom number generator based on piecewise logistic map. *Nonlinear Dyn.* **2016**, *83*, 2373–2391. [CrossRef]
4. Irfan, M.; Ali, A.; Khan, M.A.; Ehatisham-ul Haq, M.; Mehmood Shah, S.N.; Saboor, A.; Ahmad, W. Pseudorandom number generator (prng) design using hyper-chaotic modified robust logistic map (hc-mrlm). *Electronics* **2020**, *9*, 104. [CrossRef]
5. Lambić, D. Security analysis and improvement of the pseudo-random number generator based on piecewise logistic map. *J. Electron. Test.* **2019**, *35*, 519–527. [CrossRef]
6. Liu, W.; Sun, K.; He, S.; Wang, H. The Parallel Chaotification Map and Its Application. *IEEE Trans. Circuits Syst. I Regul. Pap.* **2023**, *70*, 3689–3698. [CrossRef]
7. Özkaynak, F. Brief review on application of nonlinear dynamics in image encryption. *Nonlinear Dyn.* **2018**, *92*, 305–313. [CrossRef]
8. Zolfaghari, B.; Koshiba, T. Chaotic image encryption: State-of-the-art, ecosystem, and future roadmap. *Appl. Syst. Innov.* **2022**, *5*, 57. [CrossRef]
9. Cetina-Denis, J.J.; Lopéz-Gutiérrez, R.M.; Cruz-Hernández, C.; Arellano-Delgado, A. Design of a Chaotic Trajectory Generator Algorithm for Mobile Robots. *Appl. Sci.* **2022**, *12*, 2587. [CrossRef]
10. Gohari, P.S.; Mohammadi, H.; Taghvaei, S. Using chaotic maps for 3D boundary surveillance by quadrotor robot. *Appl. Soft Comput.* **2019**, *76*, 68–77. [CrossRef]
11. Curiac, D.I.; Banias, O.; Volosencu, C.; Curiac, C.D. Novel bioinspired approach based on chaotic dynamics for robot patrolling missions with adversaries. *Entropy* **2018**, *20*, 378. [CrossRef] [PubMed]
12. Saremi, S.; Mirjalili, S.; Lewis, A. Biogeography-based optimisation with chaos. *Neural Comput. Appl.* **2014**, *25*, 1077–1097. [CrossRef]
13. Yang, D.; Liu, Z.; Zhou, J. Chaos optimization algorithms based on chaotic maps with different probability distribution and search speed for global optimization. *Commun. Nonlinear Sci. Numer. Simul.* **2014**, *19*, 1229–1246. [CrossRef]
14. Tawhid, M.A.; Ibrahim, A.M. Improved salp swarm algorithm combined with chaos. *Math. Comput. Simul.* **2022**, *202*, 113–148. [CrossRef]
15. Saxena, A.; Kumar, R.; Das, S. β-chaotic map enabled grey wolf optimizer. *Appl. Soft Comput.* **2019**, *75*, 84–105. [CrossRef]
16. Fiori, S.; Di Filippo, R. An improved chaotic optimization algorithm applied to a DC electrical motor modeling. *Entropy* **2017**, *19*, 665. [CrossRef]
17. Grassi, G. Chaos in the Real World: Recent Applications to Communications, Computing, Distributed Sensing, Robotic Motion, Bio-Impedance Modelling and Encryption Systems. *Symmetry* **2021**, *13*, 2151. [CrossRef]
18. Zang, H.; Yuan, Y.; Wei, X. Research on Pseudorandom Number Generator Based on Several New Types of Piecewise Chaotic Maps. *Math. Probl. Eng.* **2021**, *2021*, 1375346. [CrossRef]

19. Zhang, Z.; Wang, Y.; Zhang, L.Y.; Zhu, H. A novel chaotic map constructed by geometric operations and its application. *Nonlinear Dyn.* **2020**, *102*, 2843–2858. [CrossRef]
20. Nagaraj, N. The Unreasonable Effectiveness of the Chaotic Tent Map in Engineering Applications. *Chaos Theory Appl.* **2022**, *4*, 197–204. [CrossRef]
21. Chaves, D.P.; Souza, C.E.; Pimentel, C. A smooth chaotic map with parameterized shape and symmetry. *EURASIP J. Adv. Signal Process.* **2016**, *2016*, 122. [CrossRef]
22. Zhang, S.; Liu, L. A novel image encryption algorithm based on SPWLCM and DNA coding. *Math. Comput. Simul.* **2021**, *190*, 723–744. [CrossRef]
23. Zhao, X.; Zang, H.; Wei, X. Construction of a novel n th-order polynomial chaotic map and its application in the pseudorandom number generator. *Nonlinear Dyn.* **2022**, *110*, 821–839. [CrossRef]
24. Berliner, L.M. Statistics, probability and chaos. *Stat. Sci.* **1992**, *7*, 69–90. [CrossRef]
25. Barbosa, W.A.; Rosero, E.J.; Tredicce, J.R.; Leite, J.R.R. Statistics of chaos in a bursting laser. *Phys. Rev. A* **2019**, *99*, 053828. [CrossRef]
26. Hilliam, R.M.; Lawrance, A.J. The dynamics and statistics of bivariate chaotic maps in communications modeling. *Int. J. Bifurc. Chaos* **2004**, *14*, 1177–1194. [CrossRef]
27. Cicek, I.; Pusane, A.E.; Dundar, G. A novel design method for discrete time chaos based true random number generators. *Integration* **2014**, *47*, 38–47. [CrossRef]
28. Boyarsky, A.; Góra, P. *Laws of Chaos: Invariant Measures and Dynamical Systems in One Dimension*; Birkhäuser Boston: Boston, MA, USA , 1997.
29. McDonald, A.M.; van Wyk, M.A.; Chen, G. The inverse Frobenius-Perron problem: A survey of solutions to the original problem formulation. *AIMS Math.* **2021**, *6*, 11200–11232. [CrossRef]
30. Lai, D.; Chen, G. Generating different statistical distributions by the chaotic skew tent map. *Int. J. Bifurc. Chaos Appl. Sci. Eng.* **2000**, *10*, 1509–1512. [CrossRef]
31. Lawnik, M. Generation of pseudo-random numbers from given probabilistic distribution with the use of chaotic maps. *AIP Conf. Proc.* **2018**, *1926*, 020025. [CrossRef]
32. Nie, X.; Coca, D.; Luo, J.; Birkin, M. Solving the inverse Frobenius-Perron problem using stationary densities of dynamical systems with input perturbations. *Commun. Nonlinear Sci. Numer. Simul.* **2020**, *90*, 105302. [CrossRef]
33. Koga, S. The Inverse Problem of Flobenius-Perron Equations in 1D Difference Systems: 1D Map Idealization. *Prog. Theor. Phys.* **1991**, *86*, 991–1002. [CrossRef]
34. Fox, C.; Hsiao, L.J.; Lee, J.E.K. Solutions of the Multivariate Inverse Frobenius–Perron Problem. *Entropy* **2021**, *23*, 838. [CrossRef] [PubMed]
35. Moysis, L.; Lawnik, M.; Baptista, M.S.; Goudos, S.; Volos, C. Construction of Piecewise Chaotic Maps with Tunable Statistical Mean. In Proceedings of the 2023 12th International Conference on Modern Circuits and Systems Technologies (MOCAST), IEEE, Athens, Greece, 28–30 June 2023; pp. 1–4.
36. Sridharan, K.; Ahmadabadi, Z.N. A multi-system chaotic path planner for fast and unpredictable online coverage of terrains. *IEEE Robot. Autom. Lett.* **2020**, *5*, 5268–5275. [CrossRef]
37. Curiac, D.I.; Volosencu, C. A 2D chaotic path planning for mobile robots accomplishing boundary surveillance missions in adversarial conditions. *Commun. Nonlinear Sci. Numer. Simul.* **2014**, *19*, 3617–3627. [CrossRef]
38. Artemiou, P.; Moysis, L.; Kafetzis, I.; Bardis, N.G.; Lawnik, M.; Volos, C. Chaotic Agent Navigation: Achieving Uniform Exploration Through Area Segmentation. In Proceedings of the 2022 12th International Conference on Dependable Systems, Services and Technologies (DESSERT), IEEE, Athens, Greece, 9–11 December 2022; pp. 1–7.
39. Curiac, D.I.; Volosencu, C. Path planning algorithm based on Arnold cat map for surveillance UAVs. *Def. Sci. J.* **2015**, *65*, 483–488. [CrossRef]
40. Li, C.; Song, Y.; Wang, F.; Liang, Z.; Zhu, B. Chaotic path planner of autonomous mobile robots based on the standard map for surveillance missions. *Math. Probl. Eng.* **2015**, *2015*, 263964. [CrossRef]
41. Curiac, D.I.; Volosencu, C. Imparting protean behavior to mobile robots accomplishing patrolling tasks in the presence of adversaries. *Bioinspir. Biomim.* **2015**, *10*, 056017. [CrossRef]
42. Curiac, D.I.; Volosencu, C. Chaotic trajectory design for monitoring an arbitrary number of specified locations using points of interest. *Math. Probl. Eng.* **2012**, *2012*, 940276. [CrossRef]
43. Kafetzis, I.; Moysis, L.; Volos, C.; Stouboulos, I.; Valavanis, K. Area surveillance using a uav with mounted chaotic camera. In Proceedings of the 2021 International Conference on Unmanned Aircraft Systems (ICUAS), IEEE, Athens, Greece, 15–18 June 2021; pp. 53–62.
44. Akraam, M.; Rashid, T.; Zafar, S. An image encryption scheme proposed by modifying chaotic tent map using fuzzy numbers. *Multimed. Tools Appl.* **2023**, *82*, 16861–16879. [CrossRef]
45. Moysis, L.; Volos, C.; Jafari, S.; Munoz-Pacheco, J.M.; Kengne, J.; Rajagopal, K.; Stouboulos, I. Modification of the logistic map using fuzzy numbers with application to pseudorandom number generation and image encryption. *Entropy* **2020**, *22*, 474. [CrossRef] [PubMed]

46. Jafari, S.; Pham, V.T.; Golpayegani, S.M.R.H.; Moghtadaei, M.; Kingni, S.T. The relationship between chaotic maps and some chaotic systems with hidden attractors. *Int. J. Bifurc. Chaos* **2016**, *26*, 1650211. [CrossRef]
47. García-Grimaldo, C.; Campos-Cantón, E. Exploring a family of Bernoulli-like shift chaotic maps and its amplitude control. *Chaos, Solitons Fractals* **2023**, *175*, 113951. [CrossRef]

Disclaimer/Publisher's Note: The statements, opinions and data contained in all publications are solely those of the individual author(s) and contributor(s) and not of MDPI and/or the editor(s). MDPI and/or the editor(s) disclaim responsibility for any injury to people or property resulting from any ideas, methods, instructions or products referred to in the content.

symmetry

MDPI

Article

Assessment of Stochastic Numerical Schemes for Stochastic Differential Equations with "White Noise" Using Itô's Integral

Alina Bogoi [1,2], Cătălina-Ilinca Dan [1], Sergiu Strătilă [1,2], Grigore Cican [1,2,*] and Daniel-Eugeniu Crunteanu [1]

[1] Faculty of Aerospace Engineering, Polytechnic University of Bucharest, 1-7 Polizu Street, 011061 Bucharest, Romania; alina.bogoi@upb.ro (A.B.); catalina_ilinca.dan@stud.aero.upb.ro (C.-I.D.)
[2] National Research and Development Institute for Gas Turbines COMOTI, 220D Iuliu Maniu, 061126 Bucharest, Romania
* Correspondence: grigore.cican@upb.ro

Abstract: Stochastic Differential Equations (SDEs) model physical phenomena dominated by stochastic processes. They represent a method for studying the dynamic evolution of a physical phenomenon, like ordinary or partial differential equations, but with an additional term called "noise" that represents a perturbing factor that cannot be attached to a classical mathematical model. In this paper, we study weak and strong convergence for six numerical schemes applied to a multiplicative noise, an additive, and a system of SDEs. The Efficient Runge–Kutta (ERK) technique, however, comes out as the top performer, displaying the best convergence features in all circumstances, including in the difficult setting of multiplicative noise. This result highlights the importance of researching cutting-edge numerical techniques built especially for stochastic systems and we consider to be of good help to the MATLAB function code for the ERK method.

Keywords: stochastic; Itô; white noise; Gaussian distribution; Wiener process; convergence; Euler–Maruyama; Milshtein; Heun; Efficient Runge–Kutta

1. Introduction

Although a field that emerged in the mid-20th century [1,2], stochastic calculus is a crucial step in various domains, such as finance, meteorology, epidemiology, and engineering. Without being exhaustive, we provide examples of several authors who emphasize the role of stochastic differential equations in real-life applications. For instance, Sagirow [3] dedicates an entire course to stochastic methods in the dynamics and stability of satellite orbits. Kloeden and Platen [4] extensively present multiple areas where stochastic calculus is used, such as population dynamics, genetics, experimental psychology, seismology, and mechanics. Higham [5,6] illustrates the applicability of stochastic calculus in the probabilistic nature of chemical reactions.

Stochastic differential equations are differential equations whose solutions are influenced by boundary and initial conditions but are not solely determined by them, unlike Ordinary Differential Equations (ODEs) for which knowing the boundary and initial conditions is enough to solve these equations. The difference between the two types of differential equations is the stochastic (or probabilistic) term, which gives the integrand function a degree of uncertainty which can be associated with the uncertainty of any phenomena occurring in the real world [1,2], such as the influence of random perturbations affecting the deterministic mathematical model applied to the phenomena. Such cases involving linear and harmonic oscillators [7] and even nonlinear oscillators [8,9] have been thoroughly analyzed and are a subject of interest in present studies.

We consider that this paper is dedicated to students and researchers who want to be quickly introduced in the field of stochastic differential equations and who want to solve them numerically, but do not know what numerical scheme to choose immediately. Through this work and the provided examples, we hope to guide them as quickly as

possible towards a fair choice of the numerical method of calculation depending on the type of problem that is wanted to be solved.

2. Brownian Motion, White Noise

A stochastic process is a family $X(t), t \geq 0$ of a random variable that depends on the continuous real parameter time t, [3,10]. Thus, we can see the stochastic process like a trajectory of the system (or the sequence of values of the random variable obtained in temporal order) depending on the outcome of each probabilistic experiment.

A stochastic process with independent increments is the process in which, for arbitrary time moments $t_0 < t_1 < t_2 < \ldots < t_k$, the differences $X(t_1) - X(t_0)$, $X(t_2) - X(t_1), \ldots$, $X(t_k) - X(t_{k-1})$ are independent, and the process at any moment can be written as [6–10]:

$$X(t_k) = \sum_{i=1}^{k} (X(t_i) - X(t_{i-1})) \tag{1}$$

A Wiener process (or Brownian motion), $W(t), t \geq 0$ is a stochastic process with

$$W(0) = 0 \tag{2}$$

with probability one, the variation $W(t_2) - W(t_1) \sim N\left(0, \sqrt{t_2 - t_1}\right)$ has a normal (or Gaussian) distribution such that the expectation $\mathbb{E}$ and the variance σ^2 are:

$$\begin{aligned} &\mathbb{E}[W(t_2) - W(t_1)] = 0 \\ &\sigma^2 = Var[W(t_2) - W(t_1)] = k(t_2 - t_1), \quad k \in \mathbb{R} \end{aligned} \tag{3}$$

and the increments $W(t_2) - W(t_1)$ are independent on $[0, T]$ for any $0 \leq t_1 < t_2 \leq T$. This process is not differentiable at any point in its domain of definition. The origin of the term "noise," commonly used in SDEs, represents a generic term to describe a random variable with zero mean [11,12]. The concept of white noise can be likened to the effect of unwanted, unpredictable vibrations or unwanted interference contaminating a reference signal due to atmospheric effects or imperfections in transmitting and/or receiving equipment. White noise, denoted by $\xi(t)$, defined as the derivative of the Wiener process:

$$\xi(t) = \frac{dW}{dt} \tag{4}$$

is satisfying that the mean is $\mathbb{E}[\xi(t)] = 0$ and the covariance is $\mathbb{E}(\xi(t_1)\xi(t_2)) = \delta(t_1 - t_2)$, which is the Dirac delta function. Although we previously mentioned that the Wiener process is not differentiable, it admits, in the limit, for infinitely small-time domains, the association of the Dirac function as its derivative. White noise can be thought of as a sequence of infinitely large impulses acting in an infinitely small time [3].

3. A Brief Presentation of Stochastic Differential Equations

Given two differentiable functions $f, g : \mathbb{R} \times [0, T] \to \mathbb{R}$, we consider the stochastic initial value problem (SIVP) for the scalar Itô stochastic differential equation (SDE) given by

$$\frac{dX(t)}{dt} = f(X(t), t) + g(X(t), t)\xi(t), X(0) = X_0 \tag{5}$$

The form of a stochastic differential equation includes both the deterministic term $f(X(t), t)$ (i.e., "drift coefficient") and the probabilistic term $g(X(t), t)\xi(t)$ (i.e., "diffusion coefficient" or "stochastic term"). The equivalent relationship arises from replacing (4) in (5) and obtains:

$$dX = f(X, t)dt + g(X, t)dW(t) \tag{6}$$

where $W(t)$ is a Wiener process, f and g are known functions, at least of class $C^2(\mathbb{R})$, and $X(t)$ is the random variable to be determined. The integral solution of this stochastic differential equation is:

$$X(t) = X(t_0 = 0) + \int_{t_0}^{t} f(X(s), s)ds + \int_{t_0}^{t} g(X(s), s)dW(s) \tag{7}$$

The solution (7) of Equation (6) suggests that the knowledge of the process state at each intermediate time moment is necessary due to the integral with the integrand dW. Previously, we mentioned that the Wiener process has independent increments, so the Riemannian sense of integration is not applicable here. For this reason, a different integration concept of the Wiener process has been defined, known as the Itô integral [13]

$$\int_{t}^{t+\Delta t} g(X(s), s)dW(s) = \lim_{\Delta t \to 0} g(X(t))[W(t + \Delta t) - W(t)] \tag{8}$$

This Equation (8) represents Itô's interpretation of the integral of a Wiener stochastic process [3,14–16]. However, there is another interpretation of the integral of a stochastic process, given by the Russian mathematician Ruslan Stratonovich [3], which differs from the first one as follows (marked to avoid confusion with the previous one by the symbol ($\circ$):

$$\int_{t}^{t+\Delta t} g(X(s), s) \circ dW(s) = \lim_{\Delta t \to 0} g\left(\frac{X(t) + X(t + \Delta t)}{2}\right)[W(t + \Delta t) - W(t)] \tag{9}$$

It cannot be said that one of these definitions of the integral is correct and the other one is wrong; everything depends on the way one wants to solve an equation like the one in (6). Furthermore, if the temporal domain of computation $[t, t']$ is discretized into as many nodes as possible, we arrive at the Itô integral:

$$\int_{t}^{t'} g(X(s))dW(s) = \lim_{N \to \infty} \sum_{i=1}^{N} g(X(t_{i-1}))[W(t_i) - W(t_{i-1})] \tag{10}$$

Or to the Stratonovich integral:

$$\int_{t}^{t'} g(X(s)) \circ dW(s) = \lim_{N \to \infty} \sum_{i=1}^{N} g\left(\frac{X(t_{i-1}) + X(t_i)}{2}\right)[W(t_i) - W(t_{i-1})] \tag{11}$$

In the numerical resolution of stochastic differential equations to be analyzed, the Itô integral (10) will be used. To illustrate the differences between the two types of stochastic calculus, the integral of $WdW(t)$ will be integrated in both directions:

- In the Itô sense:

$$\int_{0}^{T} WdW = \lim_{N \to \infty} \sum_{i=1}^{N} W(t_{i-1})[W(t_i) - W(t_{i-1})] = \frac{W(T)^2 - T}{2} \tag{12}$$

- In the Stratonovich sense:

$$\int_{0}^{T} W \circ dW = \lim_{N \to \infty} \sum_{i=1}^{N} \left(\frac{W(t_{i-1}) + W(t_i)}{2}\right)[W(t_i) - W(t_{i-1})] = \frac{W(T)^2}{2} \tag{13}$$

Thus, the random variable $X(t)$ satisfies the stochastic differential equation in the Itô sense:

$$dX = f(X(t),t)dt + g(X(t),t)dW(t) \tag{14}$$

If $X(t)$ satisfies the stochastic differential equation, then to be valid in the Stratonovich sense the differential equation must be written:

$$dX = \left[f(X(t),t) - \frac{1}{2}\frac{dg(X(t),t)}{dX}g(X(t),t)\right]dt + g(X(t),t) \circ dW(t) \tag{15}$$

or

$$dX = F(X(t),t)dt + g(X(t),t) \circ dW(t) \tag{16}$$

where we denoted $F(X(t),t) = f(X(t),t) - \frac{1}{2}g'(X(t),t)g(X(t),t)$.

4. Finite Difference Schemes in Solving SDEs

Let us now consider a discretized Brownian motion by setting the time step $\Delta t = T/N$, where N is the number of intervals. The discretization of the temporal domain into a grid $t_i = i\Delta t$, $i = 0,\ N$ with a constant step is the first stage in applying a numerical scheme. In this paper, five schemes will be studied:

- *Euler–Maruyama Scheme* [2,10] of order $O\left(\Delta t^{3/2}\right)$ is given by:

$$X_{i+1} = X_i + f(X_i,t_i)\Delta t + g(X_i,t_i)\Delta W_i \tag{17}$$

where the index represents $X_i = X(t_i)$ and the difference of the Wiener process is given by $\Delta W_i = W(t_{i+1}) - W(t_i) = \sqrt{\Delta t}\ u_i$,

$$X_{i+1} = X_i + f(X_i,t_i)\Delta t + g(X_i,t_i)\sqrt{\Delta t}\ u_i \tag{18}$$

where the terms $(u_i)_{i=1,N}$ which replaced the white noise, is a set of independent Gaussian random variables with zero mean and variance 1.

- *Milstein Scheme* [2,6,10] of order $O\left(\Delta t^{3/2}\right)$ is given by:

$$X_{i+1} = X_i + f(X_i,t_i)\Delta t + g(X_i,t_i)\sqrt{\Delta t}\ u_i + \frac{1}{2}g(X_i,t_i)g'(X_i,t_i)\Delta t\left(u_i^2 - 1\right) \tag{19}$$

where $\frac{dg(X_i,t_i)}{dX} = g'(X_i,t_i)$:

- The *Stochastic Heun Scheme* [2,10,17] (or Semi-Implicit Euler Scheme) of order $O\left(\Delta t^{3/2}\right)$:

$$X_{i+1} = X_i + \frac{\Delta t}{2}\left[F(X_i,t_i) + F\left(\widetilde{X}_{i+1},t_{i+1}\right)\right] + \frac{\sqrt{\Delta t}}{2}\ u_i\left[g(X_i,t_i) + g\left(\widetilde{X}_{i+1},t_{i+1}\right)\right] \tag{20}$$

The scheme from (19) uses (16) for the notation $F(X_i,t_i)$ and requires the application of another explicit-type scheme—for example, (17) or (18)—to determine the "predicted" value $\widetilde{X}_{i+1}$ anticipated for the future time $i+1$.

- *First-order Runge–Kutta method* [13,14] involving the Itô coefficient (FRK1):

$$X_{i+1} = X_i + \sqrt{\Delta t}(F_1(X_i,t_i) + G_2(X_i,t_i)\Delta u_i) + [G_2(X_i,t_i) - G_1(X_i,t_i)]\sqrt{\Delta t} \tag{21}$$

where:

$$G_2(X_i,t_i) = g\left(X_i + \frac{1}{2}G_1(X_i,t_i)(\Delta u_i - \sqrt{\Delta t})\right). \tag{22}$$

- Improved three-stage Runge–Kutta scheme [13] (Saito and Mitsui):

$$\begin{aligned} X_{i+1} = X_i + \tfrac{1}{4}[F_1 + 3F_3]\Delta t + \tfrac{1}{4}[G_1 + 3G_3]\sqrt{\Delta t}u_i + \\ + \tfrac{1}{2\sqrt{3}}\left[f'g - g'f - \tfrac{1}{2}g''g^2\right]_i \Delta t \Delta \hat{W} \end{aligned} \tag{23}$$

where $\Delta\hat{W}_i = \sqrt{\Delta t}u'_i$ is a Wiener process with u'_i, an independent $N(0,1)$ random variables and:

$$\begin{aligned} &F_1 = F(X_i, t_i), && G_1 = g(X_i, t_i), \\ &F_2 = F\Big(X_i + \tfrac{1}{3}F_1\Delta t + \tfrac{1}{3}G_1\Delta u_i, t_i\Big), && G_2 = g(X_i + \tfrac{1}{3}F_1\Delta t + \tfrac{1}{3}G_1\Delta u_i, t_i), \\ &F_3 = F\big(X_i + \tfrac{2}{3}F_2\Delta t + \tfrac{2}{3}G_2\Delta u_i, t_i\big), && G_3 = g(X_i + \tfrac{2}{3}F_2\Delta t + \tfrac{2}{3}G_2\Delta u_i, t_i). \end{aligned} \tag{24}$$

- *Efficient Runge–Kutta method* [18,19] based on the Itô coefficient (ERKI):

$$\begin{aligned} X_{i+1} = X_i + \tfrac{1}{2}[F_1 + F_2]\Delta t + \tfrac{1}{40}[37G_1 + 30G_3 - 27G_4]\sqrt{\Delta t}u_i + \\ + \tfrac{1}{16}[8G_1 + G_2 - 9G_3]\sqrt{3\Delta t} \end{aligned} \tag{25}$$

where:

$$\begin{aligned} &F_1 = F(X_i, t_i), && G_1 = g(X_i, t_i), \\ &F_2 = F\Big(X_i + F_1\Delta t + G_1\sqrt{\Delta t}\Delta u_i, t_i\Big), && G_2 = g\Big(X_i - \tfrac{2}{3}G_1\Big(\sqrt{\Delta t}\Delta u_i + \sqrt{3\Delta t}\Big), t_i\Big), \\ &G_3 = g\Big(X_i + \tfrac{2}{9}G_1\Big(3\sqrt{\Delta t}\Delta u_i + \sqrt{3\Delta t}\Big), t_i\Big), \\ &G_4 = g\Big(X_i - \tfrac{20}{27}F_1\Delta t + \tfrac{10}{27}(G_2 - G_1)\sqrt{\Delta t}\Delta u_i - \tfrac{10}{27}G_2\sqrt{3\Delta t}, t_i\Big). \end{aligned} \tag{26}$$

The MATLAB code for the ERK method is provided in The Appendix A of this paper.

5. Convergence Analysis

In this section, we recall from the stochastic theory some relevant concepts about the strong and weak convergence of sequences of random variables. Convergence of a numerical method is measured by comparing the exact solution $X_{exact}(t_i)$ and the estimation X_i. Since $X(t_i)$ and X_i are random variables, in order to measure their difference, the expected values are used, [18]:

- A method is said to have a strong order of convergence equal to p if there exist the positive constant A such that:

$$\mathbb{E}[X_i - X_{exact}(t_i)] \leq A\Delta t^p, i = 0, N \tag{27}$$

- A method is said to have a weak order of convergence equal to q if there exist the positive constant C and an arbitrary smooth test function ϕ such that:

$$|\mathbb{E}\phi(X_i) - \mathbb{E}\phi(X(t_i))| \leq C\Delta t^q, \quad C \geq 0, i = 0, N \tag{28}$$

In this paper we will focus on the case where the test function ϕ is the identity function: $\phi(X) = X$. Strong convergence quantifies "the expected value of the error," whereas weak convergence quantifies "the error of the expected values". The strong order always satisfies $p \leq q$. The orders of convergence of the presented schemes will be studied by varying the time step [6].

6. Numerical Application

In this section, we provide a numerical study of the properties of convergence of the presented methods for two stochastic differential equations, one with additive "white" noise and the other with multiplicative "white" noise.

Benchmark Test 1: Consider the stochastic differential equation with multiplicative white noise:

$$dX(t) = \alpha X(t)dt + \beta X(t)dW(t) \tag{29}$$

with the initial condition $X(0) = X_0$. The exact solution is given by:

$$X(t) = X_0 \exp\left[\left(\alpha - \frac{\beta^2}{2}\right)t + \beta W(t)\right] \tag{30}$$

which for $\alpha = 2,\ \beta = 1, X_0 = 1, T = 1$ becomes for any $t \in [0, 1]$

$$X(t) = \exp\left[\frac{3}{2}t + W(t)\right] \tag{31}$$

The numerical strategy is the following. The time domain is initially discretized with $dt = T/2^{13}$ and then we consider seven intervals, multiple of 2, defined by $N(s) = 2^{13-s}$, $s = \overline{0,6}$.The corresponding number of time steps is $Dt = 1/N(s) = 2^s dt$. To understand how is added the white noise on each time step in the obtained results, see an example in Figure 1.

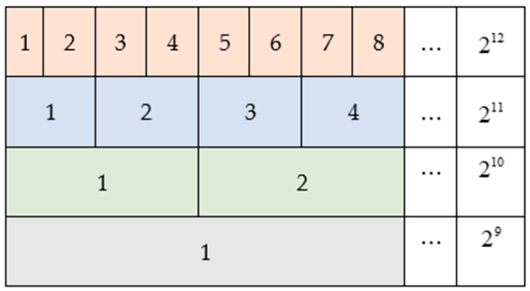

Figure 1. Contribution of the white noise. At time step $1/2^{12}$ the white noise is considered for each step. At time step $1/2^{11}$ the white noise is the sum of each two previous steps. At time step $1/2^{10}$ the white noise is the sum of each four initial steps, and the process goes on.

We compute $M = 5000$ different trajectories with white noise (Brownian paths) over the interval $[0, 1]$, following a Gaussian distribution. For each path, we have generated seven numerical solutions corresponding to each step size. To compare the numerical methods, we arbitrary choose a path from those M paths. The results are given in Figure 2 in full and detailed representations. We can notice that the Runge–Kutta classic method is practically the same as the Milshtein method.

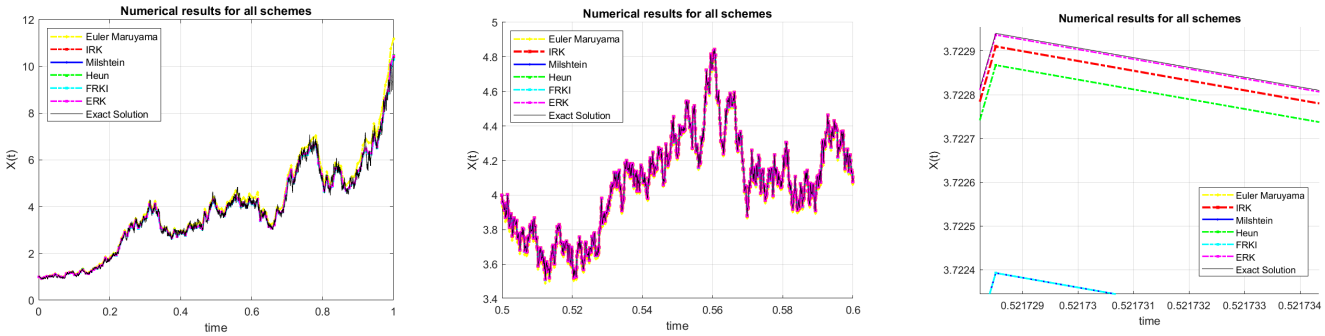

(**a**) (**b**) (**c**)

Figure 2. (**a**) Comparison of all the numerical schemes for the benchmark test 1 (**b**,**c**) Details of the comparisons.

It is evident that the Euler–Maruyama method has the worst accuracy when it is compared to the rest of the schemes. In order to observe the dependency between the size

of the time step and the accuracy of the results, the first four, smaller time steps have been considered for each scheme, as shown in Figure 3.

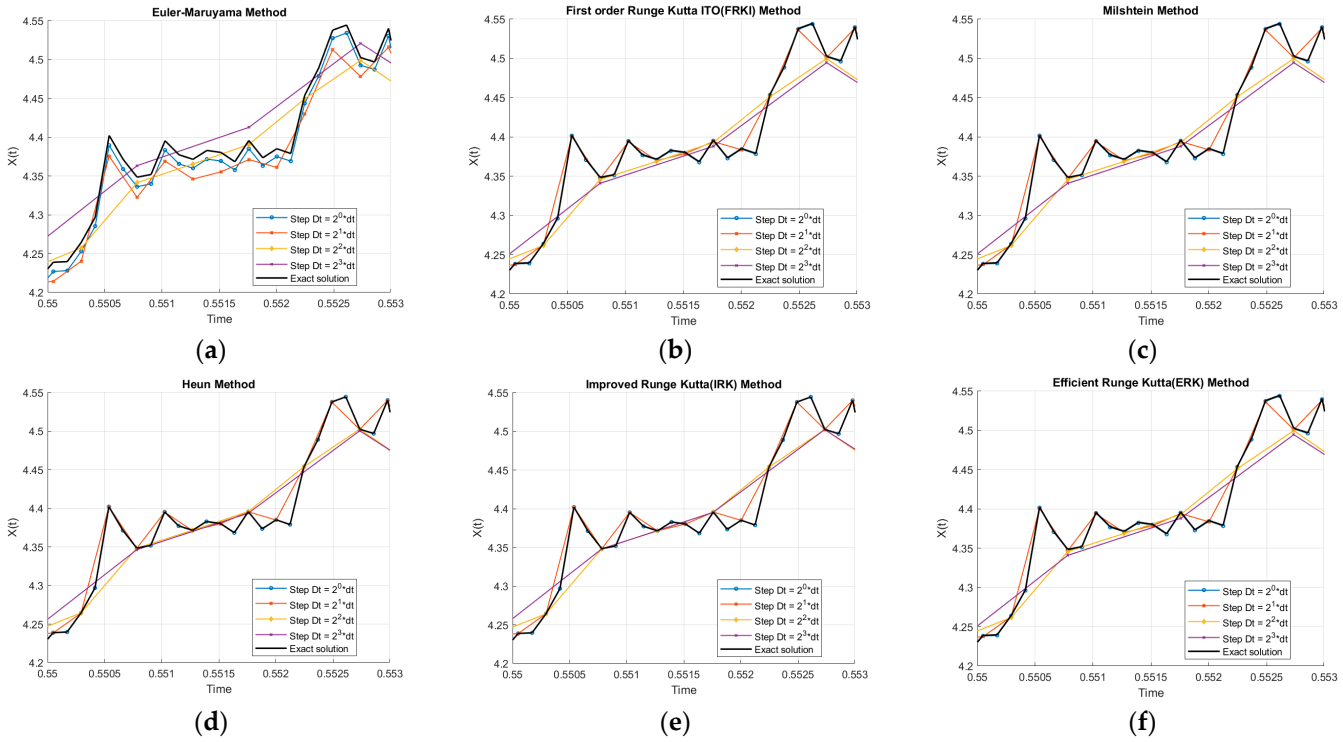

Figure 3. All methods compared for benchmark 1, varied time step: (**a**) Euler–Maruyama method, (**b**) First Order Runge–Kutta method, (**c**) Milshtein method, (**d**) Heun method, (**e**) Improved Runge–Kutta method, (**f**) Efficient Runge–Kutta method.

The Euler–Maruyama method performs well for smaller time steps and increasing the size of the time step drastically reduces the accuracy of the results. In Figure 3, the differences between the graphs considering the same range on horizontal axis are almost imperceptible ranging at the last decimal. However, out of all the schemes, the ERK method appears to have the best results (i.e., the exact solution is the closest to the line magenta in Figure 2c), not being dramatically affected by the change in time step size.

Regarding the order of convergence, we have studied the two orders of convergence for each method. According to [18] strong convergence was studied computing the expectation at the final time $t_N = T$:

$$\mathbb{E}[X_N - X_{exact}(t_N)] = \varepsilon_{\Delta t}^{strong} = A\Delta t^p, i = 0, N \tag{32}$$

where $A \in \mathbb{R}_+$ is a constant. Considering a log–log plot $\varepsilon_{\Delta t}^{strong}$ against Δt

$$\log \varepsilon_{\Delta t}^{strong} = \log A + p \log \Delta t \tag{33}$$

we expect to see a line of slope p.The absolute errors at the final time moment are taken, the averages of these errors are calculated depending on the considered time steps, and they are graphically represented in Figure 4 where the slope of the resulting line corresponds to the order of convergence, p. The numerical results confirm the orders of strong convergence of $O\left(\Delta t^{1/2}\right)$ for Euler–Maruyama and of $O(\Delta t)$ order for both Milshtein, Stochastic Heun, FRKI, and IRK schemes.

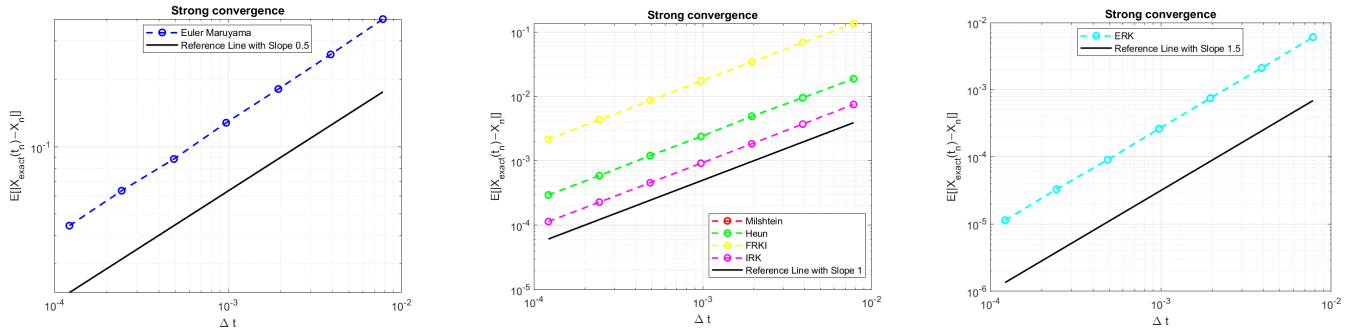

Figure 4. Study of strong convergence for all methods, graph on a logarithmic scale, multiplicative noise.

The best order of strong convergence, of $O\left(\Delta t^{3/2}\right)$ is obtained by the Efficient Runge–Kutta method. For weak convergence, we perform with a similar procedure, but the difference is that we compute at the end time the mean of the last values for all the trajectories and the mean of all the last values using a certain method:

$$|\mathbb{E}\phi(X_N) - \mathbb{E}\phi(X_{exact}(t_N))| = \varepsilon_{\Delta t}^{weak} = C\Delta t^q, \quad C \geq 0, i = 0, N \tag{34}$$

$$\log \varepsilon_{\Delta t}^{weak} = \log C + q \log \Delta t \tag{35}$$

The results are presented in Figure 5 and, with the exception of the ERK which is once again of order $O\left(\Delta t^{3/2}\right)$, and the Heun method, in which determining the type of accuracy is difficult, all the other schemes have a weak convergence of order 1.

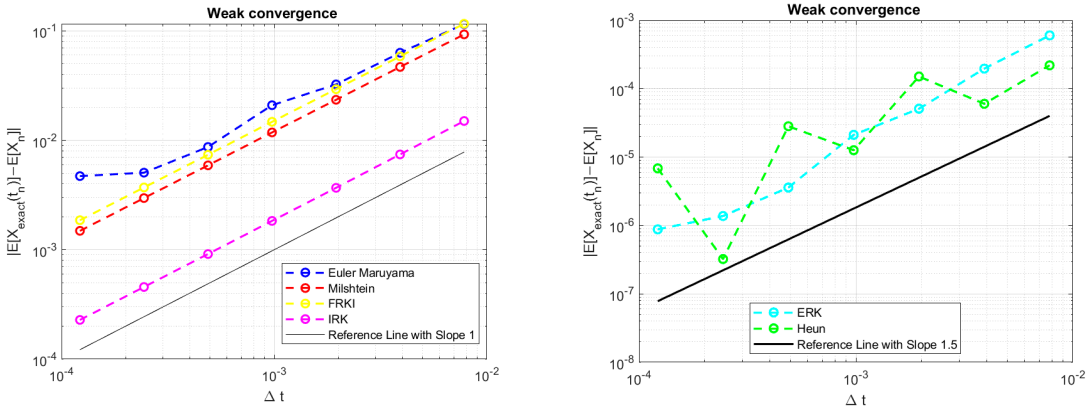

Figure 5. Study of weak convergence for all methods, logarithmic scale graph, multiplicative noise.

Benchmark Test 2: Consider the stochastic differential equation with additive white noise, discretized in the same way as in the previous example, (32):

$$dX(t) = \left[\frac{2}{1+t}X(t) + \frac{3}{2}(1+t)^2\right]dt + \frac{3}{2}(1+t)^2 dW(t) \tag{36}$$

with the initial condition $X_0 = 0.5$ and the analytical solution:

$$X(t) = (1+t)^2 X_0 + \frac{3}{2}(1+t)^2(W(t)+t) \tag{37}$$

From Figure 6, it can be observed that the values of the Milshtein method overlap with those of the Euler–Maruyama method and with those of the First Order Runge–Kutta method. This is due to the term $\frac{dg}{dX}$ which, in the case of additive noise, cancels out, and thus, the three schemes will be identical.

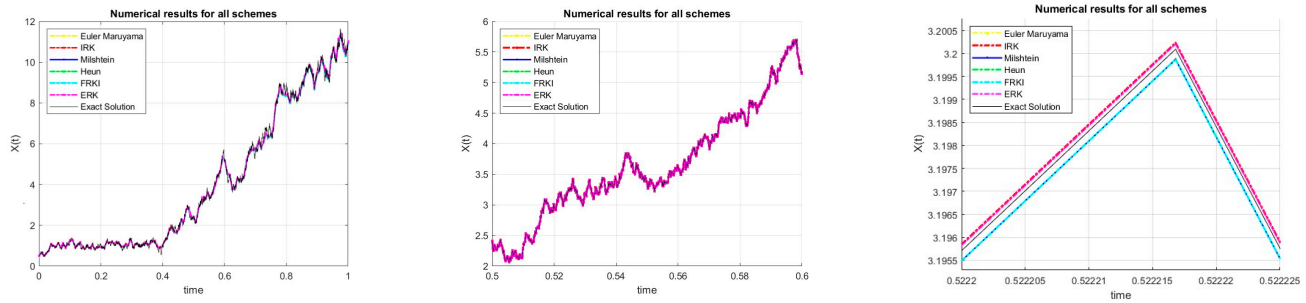

Figure 6. (**a**) Comparison of the numerical solution for all the numerical schemes used in the benchmark test 2 (**b**,**c**) Details of the comparisons.

Figure 7 shows that all schemes have very similar values, which is caused by the way the benchmark test is chosen. An interesting conclusion is that the decision to use a greater computation effort scheme is invalid since the additive noise does not allow for significant differences between the schemes.

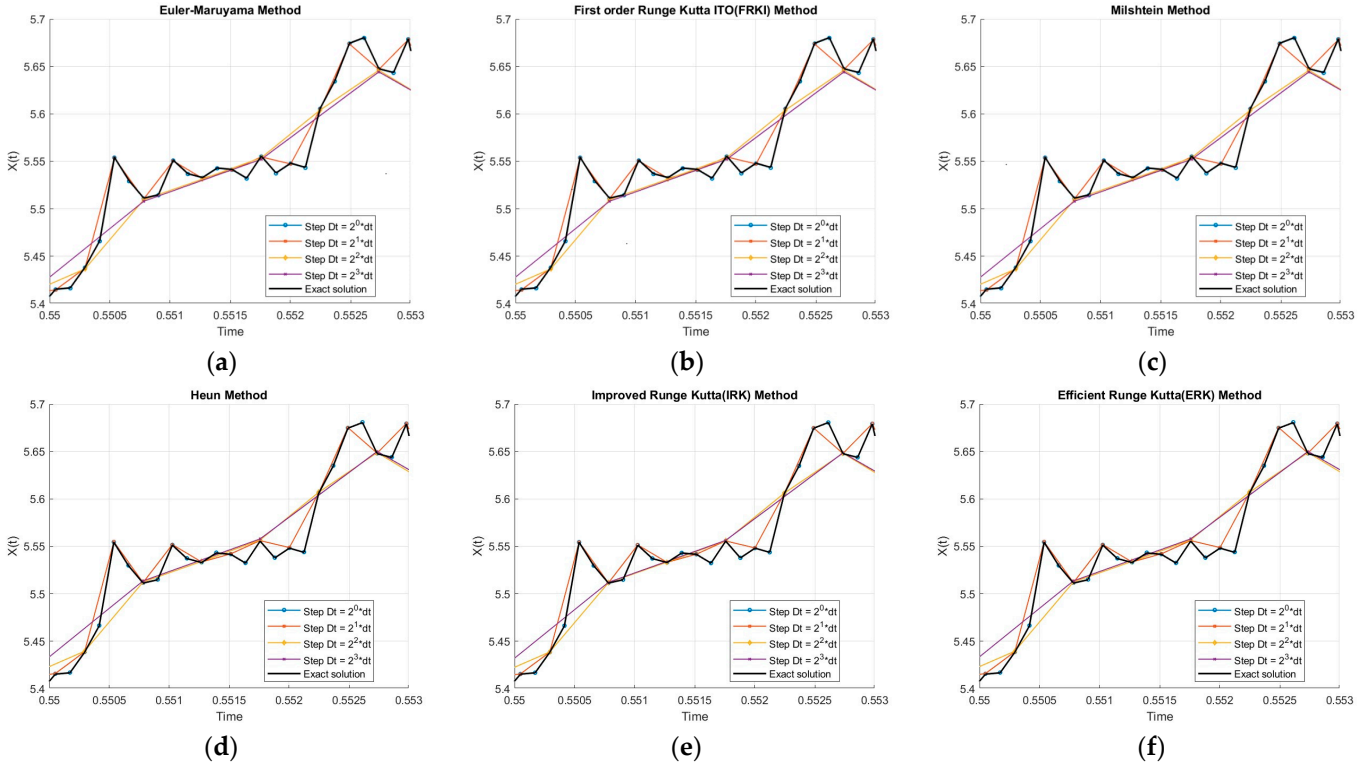

Figure 7. All methods compared for benchmark 2: (**a**) Euler–Maruyama method, (**b**) First Order Runge–Kutta method, (**c**) Milshtein method, (**d**) Heun method, (**e**) Improved Runge–Kutta method, (**f**) Efficient Runge–Kutta method.

As anticipated, Figure 8 shows the strong and weak convergence for all of the schemes, and the conclusion is that additive noise results in the same convergence $O(\Delta t)$ regardless of whether it is strong or weak. The ERK and IRK methods are still the most precise and near the exact solution among all the other numerical approaches.

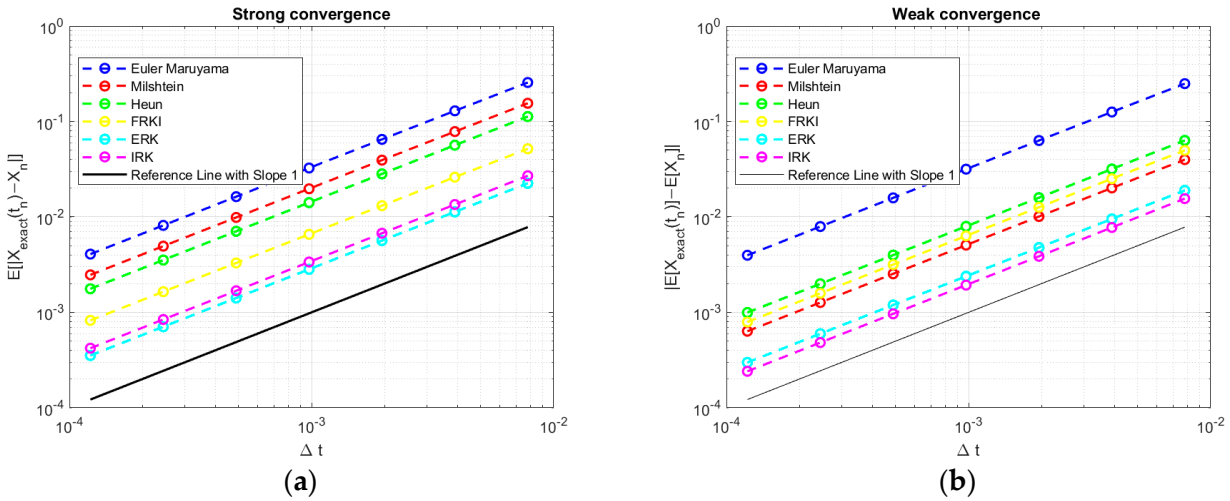

Figure 8. Study of strong (**a**) and weak (**b**) convergence for all methods, logarithmic scale graph, additive noise.

Benchmark Test 3: Solving a system of SDEs is the subject of the final test. Consider a mechanical oscillator having a negligible damping force and undamped oscillations, maintained by a harmonic force of constant amplitude and a white additive noise $\xi(t)$:

$$\ddot{x}(t) + \delta^2 x(t) = A\cos\omega t + B\xi(t) \tag{38}$$

The physics literature contains several examples of this type of stochastic oscillator (e.g., Helmholtz Resonator). It is convenient to be written in a stochastic formulation, taking into account the Wiener process by (4)

$$dX_1(t) = X_2(t)dt \tag{39}$$

$$dX_2(t) = \Big(-\delta^2 X_1(t) + A\cos\omega t\Big)dt + BdW(t) \tag{40}$$

which in matrix formulation becomes

$$d\mathbf{X} = \mathbf{F}dt + \mathbf{G}dW \tag{41}$$

where the vectors are given by:

$$\mathbf{F}(\mathbf{X},t) = \begin{pmatrix} X_2 \\ -\delta^2 X_1 + A\cos\omega t \end{pmatrix}, \mathbf{G}(\mathbf{X},t) = \begin{pmatrix} 0 \\ B \end{pmatrix} \tag{42}$$

In our example, we consider: $A = 10$, $B = 1.5$, $\delta = 10$, $\omega = 5$. For the following simulations, we chose a time step size of $\Delta t = 2^{-8}s$. For this simulation we do not take the advantage of having an exact solution to compare the results with it. However, Figure 9 shows that the evolutions in time of almost all methods are closer one to each other, which demonstrate that the methods could predict a stochastic process well.

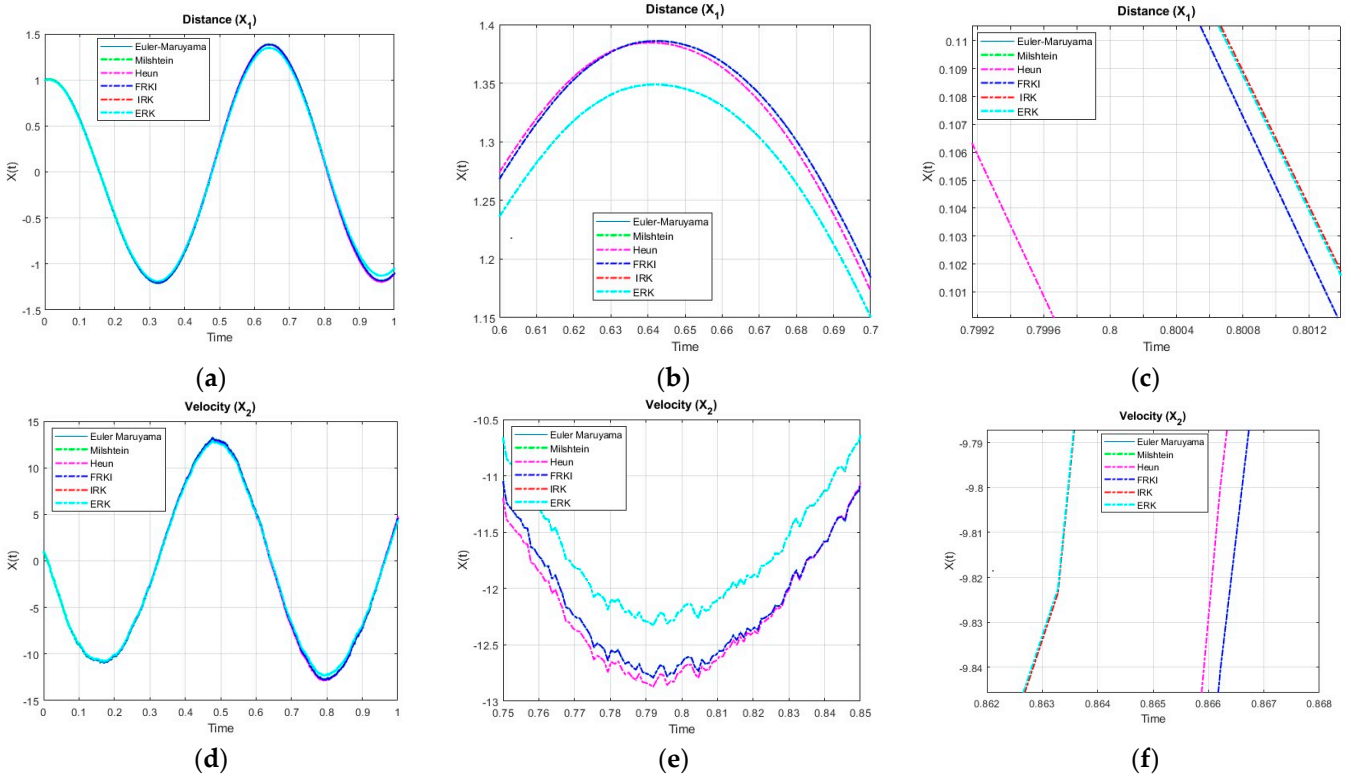

Figure 9. Time evolution of both numerical solutions of the system, (X_1, X_2), obtained in the benchmark test 3 for all the numerical schemes, (**a**) Numerical solution for the first variable (distance), (**b**,**c**) Details of the comparisons, (**d**) Numerical solution for the second variable (velocity), (**e**,**f**) Details of the comparisons.

7. Conclusions

In order to fully understand our findings, it is clear that selecting a numerical scheme requires careful consideration of the type of noise present in the system. For additive noise, the little increases in computational complexity brought on by techniques like Milshtein or Stochastic Heun do not result in an observable improvement in convergence.

The influence of multiplicative noise, however, is significant. The Efficient Runge–Kutta, which has superior convergence characteristics, appears as the best option in this case. This finding indicates us to give the MATLAB function list code, for the ERK method, in Appendix A.

Surprisingly, in the presence of multiplicative noise, the first order Runge–Kutta approach performs on par with the Milshtein method. This finding calls into question established notions on the relative accuracy of numerical techniques used in stochastic simulations.

In conclusion, our research emphasizes how crucial it is to select a suitable numerical scheme depending on the problem's noise characteristics. The nature of the noise has a significant influence on how well these strategies' function, and while computing complexity should not be completely discounted, occasionally, simpler approaches can produce unexpectedly accurate results. Additionally, when dealing with intricate stochastic dynamics, the Efficient Runge–Kutta approach proves to be a potent instrument for reaching excellent convergence.

Author Contributions: Conceptualization, A.B.; methodology, A.B., S.S. and G.C.; software A.B., S.S., C.-I.D.; validation, A.B., S.S. G.C., C.-I.D. and D.-E.C.; formal analysis A.B.; writing—original draft preparation, S.S., C.-I.D. and A.B.; writing—review and editing, C.-I.D., S.S. and A.B.; visualization, A.B.; supervision, G.C. and D.-E.C.; project administration, G.C. and D.-E.C.; funding acquisition, D.-E.C. All authors have read and agreed to the published version of the manuscript.

Funding: This work has been funded by University POLITEHNICA of Bucharest through the PubArt program.

Data Availability Statement: Data are contained within the article.

Conflicts of Interest: The authors declare no conflict of interest.

Appendix A

The function MATLAB code for the ERK method of the scalar case.

```
function [XRKE, RKE_err,WRKE_err,XRKEFull,str] = ERK(R,dW,nrTEST)
%R = [1; 16; 32; 64; 128]; % stepsizes are R*dt


global dt Dt T N M randomNumber Xzero Xtrue


     str='Efficient Runge Kutta(ERK) Method'
     disp('Efficient Runge Kutta(ERK) Method')


     Xerr = zeros(M,size(R,1)); %.  preallocate array of errors of each step time
     XRKEFull = zeros(size(R,1),N);


     for p = 1:size(R,1) % 5 different stepsizes
        Dt = R(p)*dt;
        L = N/R(p); % L Euler steps of size Dt = R*dt
        Xtemp = Xzero*ones(M,1);
        XRKE = zeros(1,L);
        for j = 1:L
           Wien = sum(dW(:,R(p)*(j-1)+1:R(p)*j),2); % sum of each row
           F1=f(Xtemp,Dt*j,nrTEST);
           G1=g(Xtemp,Dt*j,nrTEST);
           F2=f(Xtemp+F1*Dt+G1.*Wien,Dt*j,nrTEST);
           G2=g(Xtemp-2/3*G1.*(Wien+sqrt(3*Dt)),Dt*j,nrTEST);
           G3=g(Xtemp+2/9*G1.*(3*Wien+sqrt(3*Dt)),Dt*j,nrTEST);


G4=g(Xtemp-20/27*F1*Dt+10/27*(G2-G1).*Wien-10/27*G2*sqrt(3*Dt),Dt*j,nrTEST);
           Xtemp =
Xtemp+(F1+F2)*Dt/2+1/40*(37*G1+30*G3-27*G4).*Wien+1/16*(8*G1+G2-9*G3)*sqrt(3*Dt);
           XRKE(j) = Xtemp(randomNumber);
        end
        timeVector = Dt:Dt:T;
        Xerr_RKEfinal(:,p) = abs(Xtemp- Xtrue(:,end)); % store the error at t = 1
        XRKEFull(p,1:size(timeVector,2))=XRKE;
        RKE_err(:,p) = abs(Xtemp-Xtrue(:,end));
        WRKE_err(p)=sum(Xtemp)/M;


     end
end
```

References

1. Gard, T.C. *Introduction to Stochastic Differential Equations*; Marcel Dekker: New York, NY, USA, 1988.
2. Toral, P.R. *Colet: Stochastic Numerical Methods*; Wiley VCH: Weinheim, Germany, 2014.
3. Sagirow, P. Stochastic methods in the dynamics of satellites. In *International Centre for Mechanical Sciences—Courses and Lectures*; Springer: Viena, Austria, 1970; Volume 57.
4. Kloeden, P.E.; Platen, E. *Numerical Solutions of Stochastic Differential Equations*; Springer-Verlag: Berlin/Heidelberg, Germany, 1999.

5. Higham, D.J. Modeling and Simulating Chemical Reactions. *SIAM Rev.* **2008**, *50*, 347–368. [CrossRef]
6. Higham, D.J. An Algorithmic Introduction to Numerical Simulation of Stochastic Differential Equations. *SIAM Rev.* **2001**, *43*, 525–546. [CrossRef]
7. Scalone, C. A Numerical Scheme for Harmonic Stochastic Oscillators Based on Asymptotic Expansions. *Mathematics* **2022**, *10*, 3083. [CrossRef]
8. Lingala, N.; Namachchivaya, N.; Pavlyukevich, I. Random perturbations of a periodically driven nonlinear oscillator: Escape from a resonance zon. *Nonlinearity* **2017**, *30*, 1376–1404. [CrossRef]
9. D'Ambrosio, R.; Scalone, C. On the numerical structure preservation of nonlinear damped stochastic oscillators. *Numer. Algorithms* **2021**, *86*, 933–952. [CrossRef]
10. Evans, L.C. *An Introduction to Stochastic Differential Equations*; Berkeley University, Department of Mathematics: Berkeley, CA, USA, 2012.
11. Slesar, V.C. *Curs de Probabilități și Statistică Matematică*; Facultatea de Inginerie Aerospațială, UPB: Bucharest, Romania, 2022.
12. Mackevičius, V. Introduction to Stochastic Analysis. In *Integrals and Differential Equation*; ISTE: London, UK, 2011.
13. Itô, K. Stochastic integral. *Proc. Imp. Acad.* **1944**, *20*, 519–524. [CrossRef]
14. Rößler, A. Second Order Runge–Kutta Methods for Itô Stochastic Differential Equations. *Soc. Ind. Appl. Math. J.* **2009**, *47*, 1713–1738. [CrossRef]
15. Hussain, S. Numerical Solutions of Stochastic Differential Equations by using Heun's method. *Acad. J. Nawroz Univ.* **2018**, *7*, 208–215. [CrossRef]
16. Saito, Y.; Mitsui, S. Stability Analysis of Numerical Schemes for Stochastic Differential Equations. *SIAM J. on Appl. Math.* **1996**, *33*, 2254–2267. [CrossRef]
17. Newton, N.J. Asymptotically Efficient Runge-Kutta Methods for a Class of Ito and Stratonovich Equations. *SIAM J. on Appl. Math* **1991**, *51*, 542–567. [CrossRef]
18. Ieregi, X.O. *Weak Integration of Stochastic Differential Equations*; University of Bergen: Bergen, Norway, 2022.
19. Melbø, H.S.; Higham, D.J. Numerical simulation of a linear stochastic oscillator with additive noise. *Appl. Numer. Math.* **2004**, *51*, 89–99. [CrossRef]

Disclaimer/Publisher's Note: The statements, opinions and data contained in all publications are solely those of the individual author(s) and contributor(s) and not of MDPI and/or the editor(s). MDPI and/or the editor(s) disclaim responsibility for any injury to people or property resulting from any ideas, methods, instructions or products referred to in the content.

symmetry

MDPI

Article

The Numerical Solution of Nonlinear Fractional Lienard and Duffing Equations Using Orthogonal Perceptron

Akanksha Verma [1], Wojciech Sumelka [2,*] and Pramod Kumar Yadav [3]

[1] Department of Mathematics, Dyal Singh College, University of Delhi, New Delhi 110003, India; akankshaverma.maths@dsc.du.ac.in
[2] Institute of Structural Analysis, Poznan University of Technology, Piotrowo 5 Street, 60-965 Poznan, Poland
[3] Department of Mathematics, Motilal Nehru National Institute of Technology Allahabad, Prayagraj 211004, India; pramodky@mnnit.ac.in
* Correspondence: wojciech.sumelka@put.poznan.pl

Abstract: This paper proposes an approximation algorithm based on the Legendre and Chebyshev artificial neural network to explore the approximate solution of fractional Lienard and Duffing equations with a Caputo fractional derivative. These equations show the oscillating circuit and generalize the spring–mass device equation. The proposed approach transforms the given nonlinear fractional differential equation (FDE) into an unconstrained minimization problem. The simulated annealing (SA) algorithm minimizes the mean square error. The proposed techniques examine various non-integer order problems to verify the theoretical results. The numerical results show that the proposed approach yields better results than existing methods.

Keywords: orthogonal neural network; simulated annealing optimization technique; fractional differential equations; Caputo derivative

1. Introduction

In ancient times, fractional calculus was used by mathematicians due to its several applications in applied mathematics as well as mathematical physics. Recently, fractional differential equations have been used to model many real-world problems in circuit theory, fluid dynamics, physics, mathematical biology, quantum mechanics, electrochemistry, etc. Also, it is well known that non-integer-order derivatives control the models efficiently. Talebi et al. [1] explored the application of fractional calculus to filtering structures for α-stable systems, where α-stable distributions are a class of probability distributions that generalize the Gaussian distribution and can describe asymmetric and heavy-tailed behavior. These distributions are encountered in real-world scenarios, including financial time series and communication channels. Fractional-order filters and processing methods might provide better tools for dealing with such systems. Therefore, studying these equations and finding their solutions is necessary. The general form of the Lienard equation [2] is given by

$$z''(t) + f(z)z'(t) + g(z) = h(t). \tag{1}$$

Various types of selection of the functions f, g, and h give distinct models. For example, if $f(z)z'(t)$ is the damping force, $g(z)$ is the restoring force, and $h(t)$ is the external force, then it forms the damped pendulum equation. Moreover, if we have $f(z) = \epsilon(z^2 - 1)$, $g(z) = z$, and $h(t) = 0$, then Equation (1) is transferred to the Van der Pol equation [3], representing a nonlinear electronic oscillation model. However, it is well known that the exact solution of Equation (1) is a complex problem.

Kong [4] and Feng [5] investigated the exact solution of the Lienard equation in the form

$$z''(t) + Lz'(t) + Mz^3 + Nz^5 = 0, \tag{2}$$

where, L, M, and N are constant coefficients.

The general form of the Duffing oscillator equation is

$$z''(t) + Lz'(t) + Pz + Mz^3 = 0, \tag{3}$$

where, L, M, and P are constant coefficients.

Some recent works in the literature, such as [6–9], focused on generalized forms of the Lienard and Duffing equations using fractional calculus. Fractional-order derivatives can explore various physical methods that vary with time and space [10,11]. Also, using fractional calculus principles is well established in several scientific fields. Bohner and Tunç [12] conducted a qualitative analysis of Caputo fractional integro-differential equations with constant delays. This work delves into the dynamics of such equations, shedding light on their behavior and properties and contributing to the advancement of their understanding in this specialized area of mathematics. In [13], the authors dived into fractional calculus and delay integro-differential equations. Their work, which focuses on Caputo proportional fractional derivatives, presents novel solution estimation techniques. By addressing these intricate equations, the authors contributed to advancing analytical methods in the context of fractional calculus and its applications. Many real-life phenomena are represented by the fractional Lienard equation and Duffing equation, such as oscillating circuit theory [14,15], the mass damping effect [16], and pipelines and fluid dynamics [17].

The general form of the fractional order Lienard equation is given as follows:

$$D^{\nu}z(t) + LD'z(t) + Mz^3 + Nz^5 = 0, \quad 1 < \nu \leq 2, \quad t \in [0,1], \tag{4}$$

with respect to

$$z(0) = \alpha, \qquad z'(0) = \beta, \text{ where } \alpha \text{ and } \beta \text{ are constants.} \tag{5}$$

Also, the fractional Duffing equation with the damping effect is given as follows:

$$D^{\eta}z(t) + LD'z(t) + Pz(t) + Mz^3 = 0, \quad 1 < \eta \leq 2, \quad t \in [0,1], \tag{6}$$

subject to

$$z(0) = \gamma \qquad z'(0) = \delta, \text{ where } \gamma \text{ and } \delta \text{ are constants.} \tag{7}$$

In the literature, many analytical and numerical approaches exist for solving Equations (4) and (6). In 2004, Feng [18] explicitly presented the exact solution of the Lienard equation and provided some applications. In 2008, Matinfar et al. [19] used the variation iteration technique to solve the Lienard equation and compared the numerical solutions obtained with the analytic solution. Furthermore, Xu [20] acquired the eight types of explicit analytical solutions of the Lienard equation, which included periodic wave solutions and solitary wave solutions in terms of elliptic Jacobian and trigonometric functions. Janiczek [21] demonstrated the modulating functions method for all models described by fractional differential equations. Modulating functions are used to reduce the order of derivatives in an equation, generate equations without derivatives of output signals, and eliminate the need to solve differential equations. Chebyshev's operational matrix method for solving the multi-term fractional-order ordinary differential equation was proposed by Atabakzadeh et al. [22]. To apply this approach, they first converted the given problem into a system of fractional ODEs and then used the Chebyshev operational matrix method. Again, Kazem [23] analyzed fractional ODEs via an integral operational matrix approach based on Jacobi polynomials. Nourazar and Mirzabeigy [16] proposed a modified differential transform technique to deal with the fractional Duffing equation with a damping effect. In 2016, Ezz-Eldien [24] discovered a new numerical approach to solving fractional variational problems. Furthermore, Gómez-Aguilar et al. [17] used the Laplace homotopy analysis technique with a new fractional derivative without a singular kernel to solve the fractional Lienard equation that describes the fluid dynamics of the pipeline. The

homotopy analysis method was implemented in [25,26] to solve the Duffing oscillator and the Lienard problem with a fractional derivative. Recently, Singh et al. [14,15,27,28] also made several effective attempts to find the solutions to Equations (4) and (6) by using a variety of techniques. Also, Kumar et al. [29] used the Rabotnov fractional exponential kernel to solve the nonlinear Lienard equation numerically. More recently, Adel [30] demonstrated an approach based on Bernoulli collocation and shifted Chebyshev collocation points to solve Equations (4) and (6).

In recent years, neural architecture-based approximation schemes have been used to solve FDEs, ODEs, PDEs, and delay differential equations (DDEs) [31–38]. In 2013, Lefik [39] illustrated that an ANN performs the numerical representation of the inverse relation. It can be used as many times as needed in the same application, replacing traditional "ad hoc" back computation for any new piece of experimental data. Malik et al. [40] proposed a hybrid heuristic approach to solve the Lienard equation based on genetic algorithms, such as memetic computation, combining genetic algorithms, the interior-point algorithm, and the active set algorithm. Furthermore, Mall and Chakraverty [33,36] used the multilayer perceptron and functional connection neural network with regression-based parameters to solve ODEs. In [34,38], the authors also used the multilayer perceptron technique with quasi-Newton and Broyden–Fletcher–Goldfarb–Shanno (BFGS) algorithms to solve the singular initial and boundary value problems. Kumar et al. [41] presented a comparative analysis of two distinct neural modeling approaches to approximate the multidimensional poverty levels within an Indian state. This study sought to provide useful information for choosing the best modeling approaches to determine poverty levels in the Indian setting by examining their performance and precision. Sahoo and Chakraverty [42] proposed a symplectic artificial neural network to handle nonlinear systems arising in dusty plasma models. They presented the dynamics of Van der Pol–Mathieu–Duffing oscillator problems for different excitation functions using the proposed method, and numerical simulations and graphical representations were carried out to establish the accuracy of the presented algorithm.

Motivated by the above, in this manuscript, we discuss the functional link neural network architecture, which is a single-layer neural network. This article aims to find the solutions to fractional Lienard and Duffing equations using functional link neural networks. This technique offers us the following attractive features:

- The proposed technique gives us the solution in a closed analytic form.
- The functional link neural network consists of a single layer, and thus the number of network parameters is less than the traditional multilayer ANN and works with low computational complexity.
- It is capable of fast learning and is computationally efficient.
- This process does not need linearization to solve a nonlinear problem.

We have organized the present article as follows. Section 2 includes some important preliminaries and discusses the structure of the Chebyshev and Legendre neural networks. Section 3 discusses the methodology, including a well-explained algorithm and the implication protocol, while Section 4 discusses the numerical experiments and their results. Section 5 deals with the error analysis of the technique, while Section 6 concludes the work.

2. Preliminaries

This section provides some basic definitions and results related to the Chebyshev and Legendre artificial neural network models used in this paper. We begin with the following definitions:

Definition 1. *Suppose that r and s are positive integers such that $r-1 < s < r$. Then, for a continuous function $p(x)$, the Riemann–Liouville derivative and integral of a fractional order s are given by*

$$ {}_a^R D_x^s p(x) = \frac{1}{\Gamma r - s} \frac{d^r}{dx^r} \int_a^x (x-\tau)^{r-s-1} p(\tau) d\tau, $$

and

$$ {}_{a}^{R}D_{x}^{-s}p(x) = \frac{1}{\Gamma s}\int_{a}^{x}(x-\tau)^{s-1}p(\tau)d\tau, $$

respectively.

Definition 2. *Suppose that r and s are positive integers such that* $r-1 < s < r$. *Then, for a continuous function* $p(x)$, *the Caputo derivative and integral of a fractional order s are given by*

$$ {}_{a}^{C}D_{x}^{s}p(x) = \frac{1}{\Gamma(r-s)}\int_{a}^{x}\frac{p^{(r)}(\tau)}{(x-\tau)^{s+1-r}}d\tau, \qquad r-1 \le s \le r, $$

and

$$ {}_{a}^{C}D_{x}^{-s}p(x) = \frac{1}{\Gamma s}\int_{a}^{x}(x-\tau)^{s-1}p(\tau)d\tau, $$

respectively.

Remark 1. *Note that the Caputo definition has the advantage of being bound, which means that the derivative of a constant is equal to zero. It also allows for the consideration of easily understood initial conditions.*

2.1. Chebyshev and Legendre Artificial Neural Network Models

Chebyshev and Legendre artificial neural networks are functional link neural networks with one single layer. Both models can learn fast and have functional expansion blocks to enhance input patterns. In 1995, Pao and Philips [43] presented an approach based on a single-layer functional connection neural network. The architectures of the Chebyshev and Legendre neural network models are given as follows.

The architecture of the Chebyshev neural network model: The structure of the ChNN model is shown in Figure 1. It consists of a single input node, a Chebyshev polynomial function expansion block, and an output node. Assume that t is a single input node with k data; that is, $(t = t_1, t_2, \ldots, t_k)^T$. $N(t, p)$ is the output of the feedforward neural network.

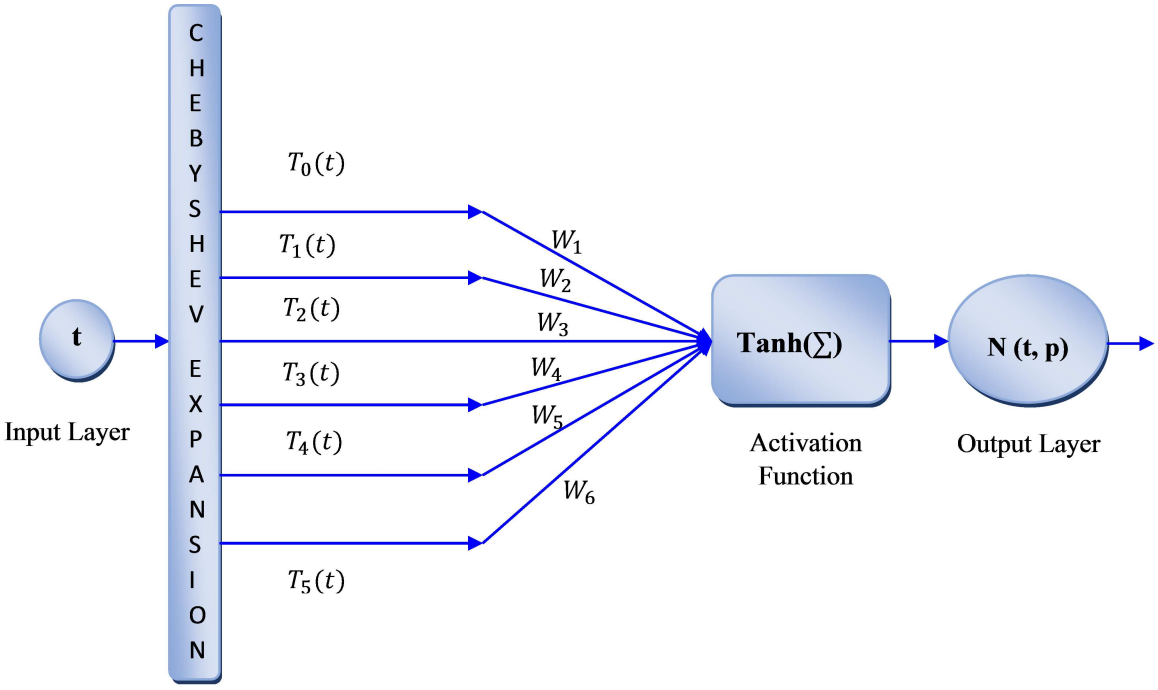

Figure 1. Structure of Chebyshev neural network.

The following are the first two Chebyshev polynomials:

$$T_0[t] = 1,$$

$$T_1[t] = t.$$

The well-known recurrence relation can be used to obtain higher-order Chebyshev polynomials:

$$T_{n+1}(t) = 2tT_n(t) - T_{n-1}(t).$$

The architecture of the Legendre neural network model: The structure of the LeNN model is depicted in Figure 2. It has a single input node, a Legendre polynomial function expansion block, and an output node. Assume that t is a single input node with l data; that is, $(t = t_1, t_2, \ldots, t_l)^T$. $N(t, p)$ is the output of the feedforward neural network.

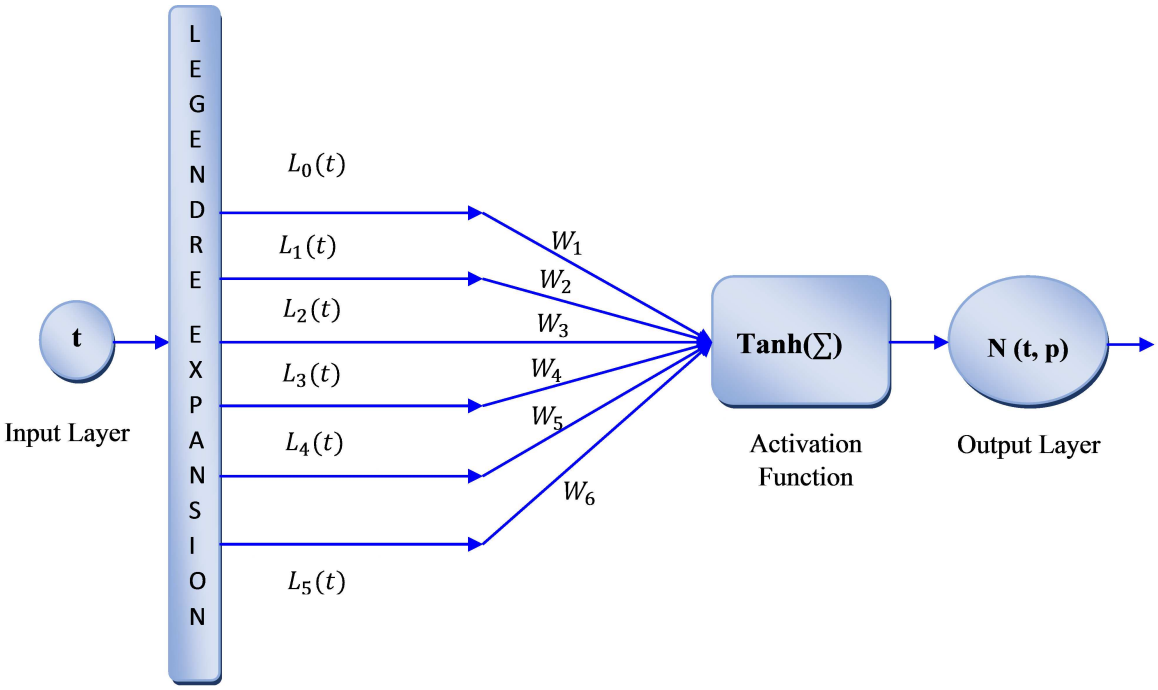

Figure 2. Structure of Legendre neural network.

Some Legendre polynomials are as follows:

$$L_0[t] = 1,$$

$$L_1[t] = t,$$

$$L_2[t] = \frac{1}{2}(3t^2 - 1).$$

The well-known recurrence relation can be used to obtain higher-order Legendre polynomials:

$$L_{n+1}(t) = \frac{1}{n+1}[(2n+1)tL_n(t) - nL_{n-1}(t)].$$

2.2. Simulated Annealing Algorithm

Simulated annealing is a straightforward stochastic function minimizer. It is inspired by the annealing process, which involves heating a metal piece to a high temperature and letting it cool gently. This process enables the metal's atomic structure to settle into a lower energy state, making it harder. Using optimization terminology, annealing enables the structure to leave a local minimum and to search for and arrive at a better, ideally global minimum. A new point is generated randomly near the present point with each iteration

of the simulated annealing technique. The radius of the neighborhood decreases with each iteration.

3. Description of the Method

3.1. General Remarks

The orthogonal perceptron expands upon the classical perceptron algorithm utilized for binary classification applications. The perceptron is a fundamental building element that accepts input values, adds weights to them, and generates output in the context of machine learning and neural networks. The orthogonal perceptron introduces a significant change: it requires orthogonality between the weight vectors connected to various classes. The weight vectors are modified in conventional perceptrons to reduce misclassification errors. However, in the orthogonal perceptron, the weight vectors for various classes are restricted to be orthogonal to one another, in addition to being modified to minimize mistakes. In higher-dimensional spaces, the orthogonal constraint provides a discriminating component that can better explain class separation. Orthogonal weight vectors can lead to better decision boundaries and enhanced generalization.

A flow chart demonstrates the proposed technique in Figure 3. We have also explained the methodology stepwise.

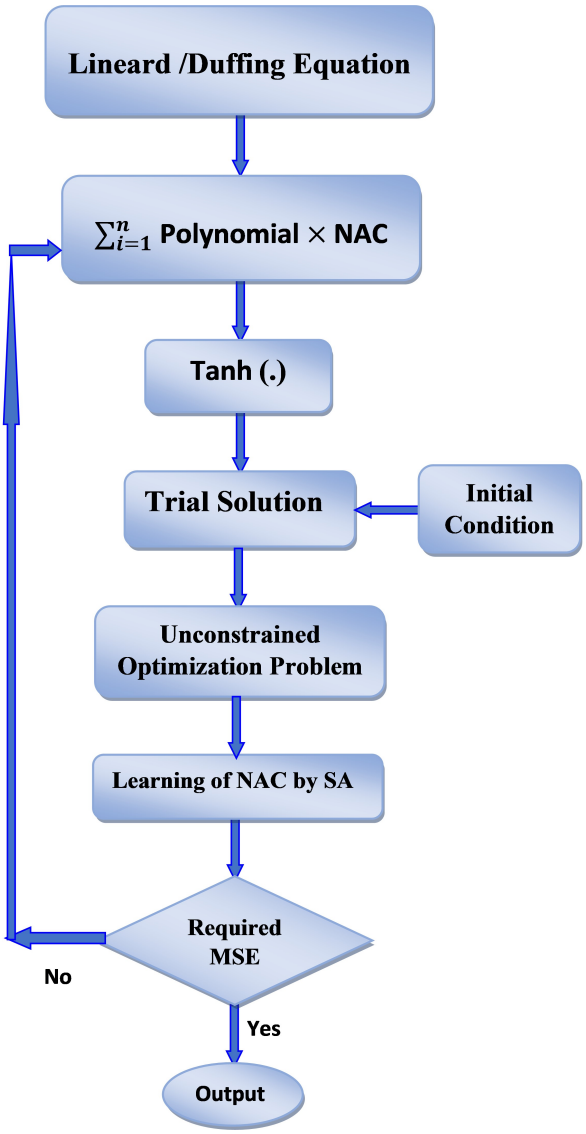

Figure 3. Pictorial presentation of the algorithm.

Due to the similarity of both techniques, we discuss the combined steps for the Chebyshev and Legendre ANN techniques. For both methods, the entire procedure is the same except for the polynomial selection

- Prepare the network by using the Chebyshev or Legendre polynomials.
- Provide the network adaptive coefficients (NACs) for each polynomial.
- Calculate and save the sum of the products of the NACs and Chebyshev polynomials or Legendre polynomials as a function μ or δ.
- Use the Taylor series extension of the activation function $tanh(.)$ to activate the function μ or δ.
- Now, construct the problem's trial solution, which satisfies the given initial or boundary conditions.
- Substitute the derivatives of the trial solution into the given situation and obtain the error function.
- To minimize the error function, use simulated annealing optimization techniques.
- If the assessment of the mean square error is in an acceptable range, then collect the value of the adaptive coefficients of the network and substitute it into the trial solution to obtain the results; otherwise, repeat the same process for various values of the NACs until the agreeable MSE is acquired.

3.2. Employment on Nonlinear FDEs

Here, we apply the proposed technique to fractional-order nonlinear differential equations of the following type:

$$D^{\nu}z(t) = F(t, z, z'(t)), \tag{8}$$

subjected to the following conditions:

$$z(0) = \alpha, \qquad z'(0) = \beta.$$

Equation (8) can be written in the following form to apply the Chebyshev and Legendre ANN techniques:

$$D^{\nu}z_{tr}(t, \psi) - F(t, z_{tr}(t, \psi), Dz_{tr}(t, \psi)) = 0, \qquad t \in [0, 1], \qquad 1 < \nu \leq 2, \tag{9}$$

where z_{tr} is the trial solution of Equation (8) which satisfies the given initial or boundary conditions and ψ is network adaptive coefficients known as bias and weight. Let us try the trial solution for Equation (8) expressed as

$$z_{tr}(t, \psi) = A + tN(t, \psi), \tag{10}$$

where N is the network output for the Chebyshev ANN. We apply the Taylor series to the $tanh(.)$ activation function to activate the sum of the product of the weights and orthogonal polynomials such that

$$N = tanh(\mu) = \mu - \frac{\mu^3}{3} + \frac{2\mu^5}{15}, \tag{11}$$

Here, μ is given by

$$\mu = \sum_{i=1}^{n} \psi_i T_{i-1}, \tag{12}$$

where T_{i-1} represents the Chebyshev polynomials, which can be characterized with the following recursive formula:

$$T_{i+1}(t) = 2tT_i(t) - T_{i-1}(t), \quad i \geq 2, \tag{13}$$

Here, $T_0(t) = 1$ and $T_1(t) = t$ are the fundamental values of the Chebyshev polynomials.

For the Legendre ANN, the activation function N is defined by

$$N = tanh(\delta) = \delta - \frac{\delta^3}{3} + \frac{2\delta^5}{15}, \tag{14}$$

Here, δ is given by

$$\delta = \sum_{i=1}^{n} \psi_i L_{i-1}, \tag{15}$$

where L_{i-1} represents the Legendre polynomials, which are defined by the following recursive formula:

$$L_{i+1}(t) = \frac{1}{(i+1)}(2i+1)tL_i(t) - \frac{1}{(i+1)}iL_{i-1}(t), \quad i \geq 2, \tag{16}$$

Here, $L_0(t) = 1$ and $L_1(t) = t$ are the fundamental values of the Legendre polynomial.

Now, we can write the trial solution in terms of μ and δ for the Chebyshev and Legendre ANNs, respectively, and obtain the following:

$$z_{tr}(t,\psi) = A + t\left(\mu - \frac{\mu^3}{3} + \frac{2\mu^5}{15}\right) \qquad \text{and} \qquad = A + t\left(\delta - \frac{\delta^3}{3} + \frac{2\delta^5}{15}\right), \tag{17}$$

Now, we put the values of μ and δ into Equation (17) for $n = 2$ and obtain

$$z_{tr}(t,\psi) = A + t\left((\psi_1 + t\psi_2) - \frac{(\psi_1 + t\psi_2)^3}{3} + \frac{2(\psi_1 + t\psi_2)^5}{15}\right). \tag{18}$$

By applying the Caputo fractional-order derivative, we obtain

$$\begin{aligned} D^{\nu} z_{tr}(t,\psi) = {} & \frac{\Gamma 2}{\Gamma(2-\nu)} t^{1-\nu}\left(\psi_1 - \frac{\psi_1^3}{3} + \frac{2\psi_1^5}{15}\right) + \frac{2}{3}\frac{\Gamma 6}{\Gamma(6-\nu)} t^{5-\nu}(\psi_1\psi_2^4) + \frac{2}{15}\frac{\Gamma 7}{\Gamma(7-\nu)} t^{6-\nu}(\psi_2^5) \\ & + \frac{\Gamma 3}{\Gamma(3-\nu)} t^{2-\nu}\left(\psi_2 - \psi_1^2\psi_2 + \frac{2}{3}\psi_1^4\psi_2\right) + \frac{\Gamma 4}{\Gamma(4-\nu)} t^{3-\nu}\left(\frac{4}{3}\psi_1^3\psi_2^2 - \psi_1\psi_2^2\right) + \\ & \frac{\Gamma 5}{\Gamma(5-\nu)} t^{4-\nu}\left(\frac{4}{3}\psi_1^2\psi_2^3 - \frac{\psi_2^3}{3}\right). \end{aligned} \tag{19}$$

Also, the mean square error for Equation (8) can be calculated as follows:

$$E(\psi) = \sum_{j=1}^{m} \frac{1}{m}\left(D^{\nu} z_{tr}(t_j,\psi_i) - F(t_j, z_{tr}(t_j,\psi_i), Dz_{tr}(t_j,\psi_i))\right)^2, \quad t \in [0,1]. \tag{20}$$

Here, we refer to Equation (20) as a fitness function and m as the number of trial points. We used a thermal minimization process known as simulated annealing to minimize the fitness function. This is a probabilistic method used to approximate the global optimum of a function. This method consists of three steps: perturb the solution, determine the consistency of the solution, and accept the solution if it is better than the improved one. The learning of NACs will be performed from Equation (18) by minimizing the MSE to the lowest possible acceptable minimum value.

3.3. Advantages of the Proposed Technique

1. To approximate the complex nonlinear interactions present in fractional differential equations, the orthogonal perceptron-based method uses the adaptability of artificial neural networks. It can capture complex behaviors that are exceedingly difficult to express using conventional numerical techniques.
2. Once trained, the orthogonal perceptron may generalize its learned patterns to fresh input data. This is extremely helpful when solving fractional differential equations with various initial conditions or parameters.

3. Traditional numerical techniques are frequently built with well-established convergence features. However, the neural network approach's convergence is determined by the quality of the data and the architecture used.

4. Numerical Implementation

In this section, two fractional-order problems are solved using the ChNN and LeNN architectures. The numerical results show that the proposed technique is highly efficient and robust. All the computations were performed on a computer with an Intel Core i3 processor (Intel Corporation, Santa Clara, CA, USA) with 8 gigabytes of RAM, and the simulation was conducted with Mathematica 11.1.0 for each problem.

Problem 1. *Consider the particular choice of the parameters* $L = -1$, $M = 4$, *and* $N = 3$ *in Equation (4). The fractional Lienard problem is given as follows [14,15,28]:*

$$D^{\nu}z(t) - D'z(t) + 4z^3 + 3z^5 = 0, \quad 1 < \nu \leq 2, \quad t \in [0,1], \tag{21}$$

$$z(0) = \alpha = \sqrt{\frac{\tau}{2+\kappa}} \quad and \quad z'(0) = \beta = 0,$$

where

$$\tau = 4\sqrt{\frac{3a^2}{3b^2 - 16ac}} \quad and \quad \kappa = -1 + \frac{\sqrt{3}b}{\sqrt{(3b^2 - 16ac)}}. \tag{22}$$

For $\nu = 2$, the exact solution is already known with the given conditions

$$z(t) = \sqrt{\frac{\tau \sec h^2\sqrt{-a}t}{2 + \kappa \sec h^2\sqrt{-a}t}} \tag{23}$$

Equation (22) presents the values of τ and κ.

As we discussed in Section 4, we constructed the trial solution as

$$z_{tr}(t, \psi) = \alpha + t^2 N(t, \psi). \tag{24}$$

The given Lienard problem was solved by ChNN and LeNN techniques for the various values of ν and employed by dividing the domain into 10 equidistant training points with 6 NACs. The acquired appropriate MSEs were 1.39515×10^{-10} and 5.27835×10^{-10}, respectively. The computational time for Problem 1 was 0.05 s and 0.09 s, respectively. Table 1 shows the accurate values of the NACs after training by the SA algorithm. In Table 2, we have listed the approximated solution by our methods (ChNN and LeNN), the methods of Singh [14,15,28], and the exact solution. Table 2 shows the good agreement with these methods.

Table 1. The ideal estimations of NAC (Problem 1).

NAC	W_1	W_2	W_3	W_4	W_5	W_6
ChNN	−0.41174	0.379264	0.463621	0.386701	0.0344511	0.0811897
LeNN	−1.53305	1.02509	−2.11092	1.1266	−0.969482	0.15995

Table 2. Comparison of numerical results at $\nu = 2$ for Problem 1.

t	Exact Solution	ChNN	LeNN	[28]	[14]	[15]
0.00	0.643594	0.643594	0.643594	0.643594	0.643594	0.643594
0.01	0.643556	0.643524	0.643524	0.643524	0.643524	0.643524
0.02	0.643443	0.643313	0.643313	0.643313	0.643313	0.643314
0.03	0.643255	0.642959	0.642959	0.642959	0.642959	0.642965
0.04	0.642991	0.642462	0.642462	0.642461	0.642461	0.642477

Table 2. *Cont.*

t	Exact Solution	ChNN	LeNN	[28]	[14]	[15]
0.05	0.642653	0.641821	0.641821	0.641818	0.641818	0.641894
0.06	0.642239	0.641033	0.641033	0.641029	0.641028	0.641082
0.07	0.641751	0.640100	0.640100	0.640093	0.640092	0.640176
0.08	0.641189	0.639019	0.639019	0.639009	0.639009	0.639130
0.09	0.640553	0.637790	0.637790	0.637777	0.637776	0.637946
0.1	0.639844	0.636413	0.636413	0.636395	0.636395	0.636623

In Figure 4, we have compared the approximate solutions by the LeNN and ChNN methods with the solutions obtained by the methods given in [14,15,28]. Figures 5 and 6 show the approximate solutions for the various values of ν.

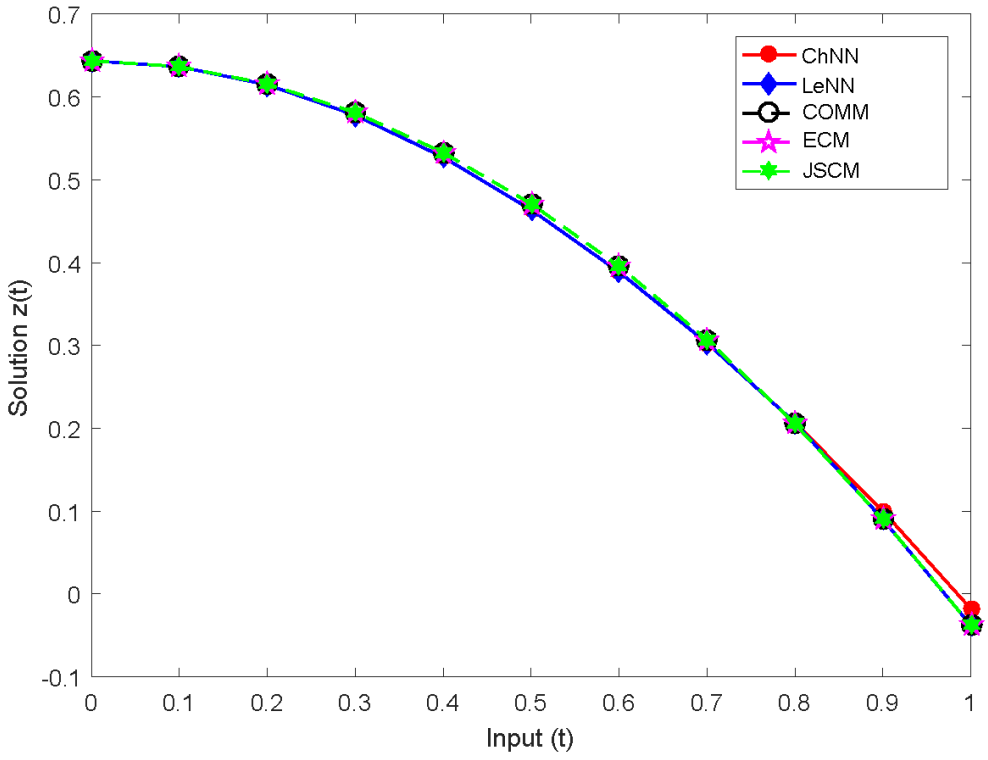

Figure 4. Comparison of approximate solutions at $\nu = 2$ by ChNN, LeNN Method with [28], [14], [15] (Problem 1).

From Figures 5 and 6, we observed that the solution varied continuously from the fractional-order solution to the integer order. Therefore, we can say that the behaviors of approximate solutions for different fractional orders converge to integer-order solutions.

Problem 2. *Consider the particular choice of the parameters* $L = 0.5$, $P = 25$, *and* $M = 25$ *in Equation (6). The fractional duffing equation is given as follows [14,15,28]:*

$$D^{\eta}z(t) + 0.5D'z(t) + 25z + 25z^3 = 0, \quad 1 < \eta \leq 2, \tag{25}$$

$$z(0) = \gamma = 0.1 \quad \textit{and} \quad z'(0) = \delta = 0.$$

The exact solution of Problem 2 at $\eta = 2$ when using the differential transform method [16] is given as follows:

$$z(t) = 0.1 - 1.2625t^2 + 0.2104t^3 + 2.6828t^4 - 0.5392t^5 - 2.6563t^6 + 0.6152t^7. \tag{26}$$

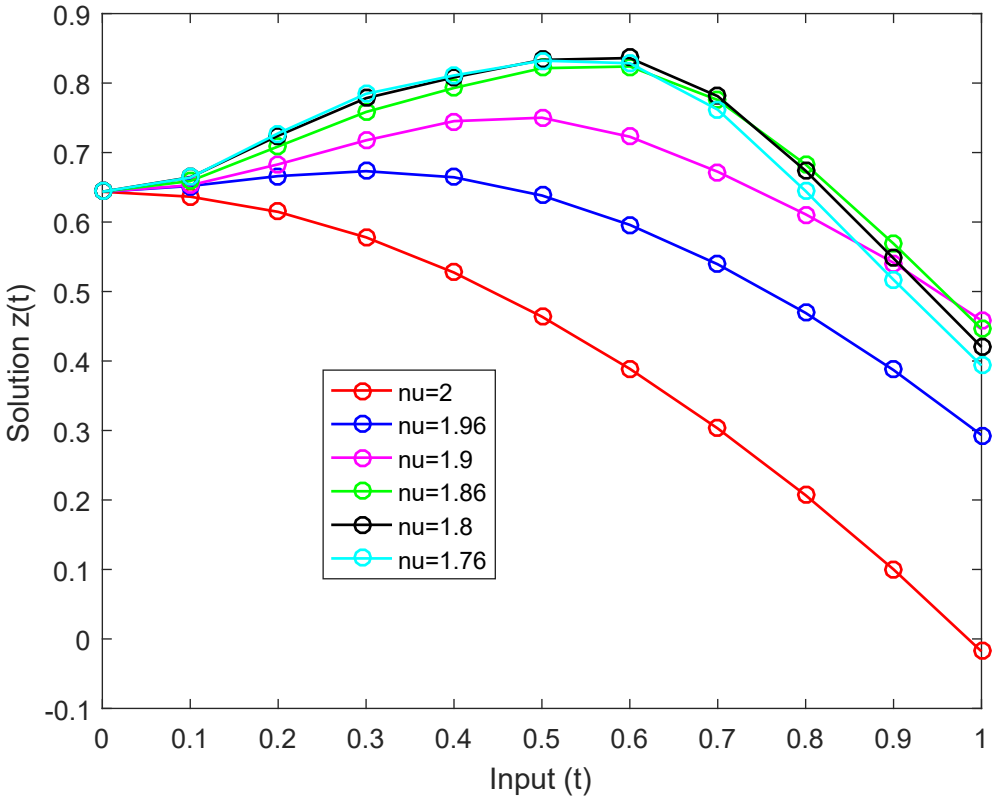

Figure 5. Nature of the approximate results with the LeNN method at $\nu = 2, 1.96, 1.9, 1.86, 1.8, 1.76$ (Problem 1).

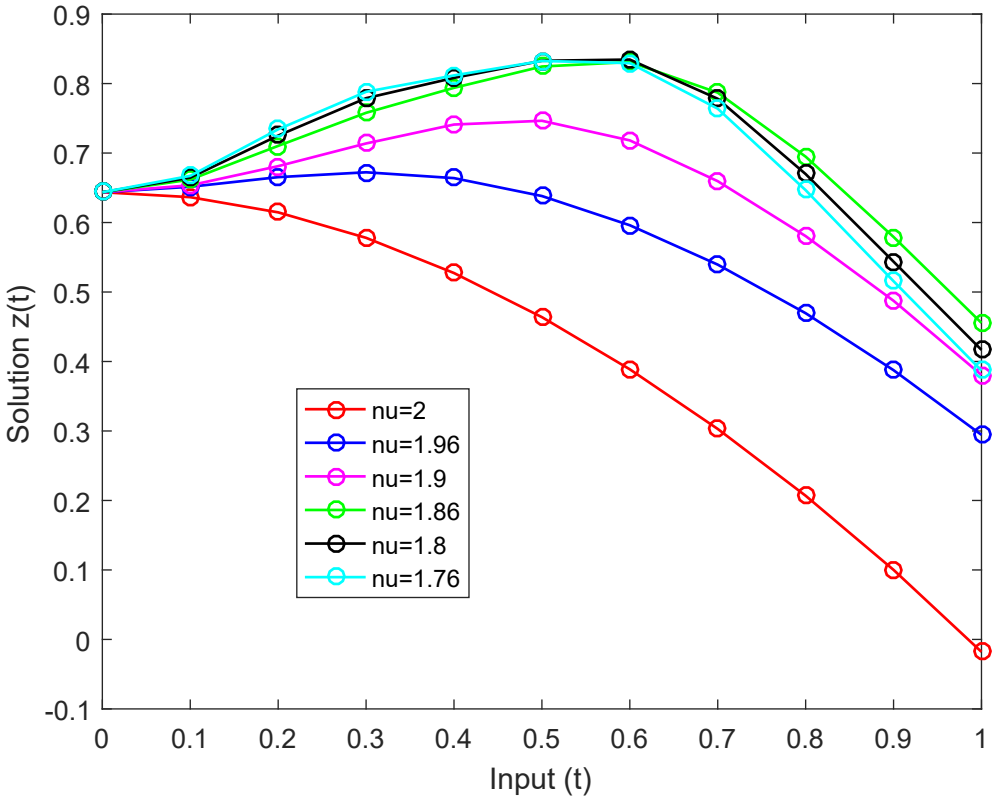

Figure 6. Nature of the approximate results with the ChNN method at $\nu = 2, 1.96, 1.9, 1.86, 1.8, 1.76$ (Problem 1).

The trial solution can be written as

$$z_{tr}(t, \psi) = 0.1 + t^2 N(t, \psi). \tag{27}$$

The Duffing equation was solved with the ChNN and LeNN techniques for the various values of η. We trained the network using 10 equidistant points in the domain $[0, 0.1]$ with 6 NACs. The obtained MSEs were 1.61568×10^{-9} and 1.73644×10^{-8}, respectively. The appropriate values of the NACs using the SA algorithm are given in Table 3. The computational time for Problem 2 was 0.05 s and 0.03 s, respectively. In Table 4, we have listed the obtained solutions by the proposed methods (ChNN and LeNN) and the existing method's solutions from [15,16,28]. Table 4 shows the good accuracy for the acquired results and the results given in [16].

Table 3. The ideal estimations of the NAC (Problem 2).

NAC	W_1	W_2	W_3	W_4	W_5	W_6
ChNN	−0.84541	2.43209	0.54458	1.04621	−0.0457733	0.165949
LeNN	−1.54176	0.143329	−0.674402	−0.433421	−0.617103	−0.35283

Table 4. Comparison of numerical results at $\eta = 2$ for Problem 2.

t	DTM [16]	ChNN	LeNN	[28]	[15]
0.00	0.100000	0.100000	0.100000	0.1000000	0.100000
0.01	0.099874	0.099874	0.099874	0.0998745	0.099874
0.02	0.099497	0.0994971	0.099497	0.0995025	0.099502
0.03	0.098871	0.0988715	0.0988715	0.0988894	0.098889
0.04	0.098002	0.0980002	0.0980001	0.0980414	0.098041
0.05	0.096886	0.0968865	0.0968864	0.0969644	0.096964
0.06	0.095534	0.0955346	0.0955344	0.0956646	0.095664
0.07	0.093949	0.093949	0.0939488	0.0941484	0.094148
0.08	0.092135	0.0921351	0.0921348	0.0924222	0.092422
0.09	0.090098	0.0900985	0.0900982	0.0904924	0.090492
0.1	0.087845	0.0878456	0.0878453	0.0883660	0.088366

In Figure 7, we have compared the approximate solutions with the proposed method and the solutions given in [15,16,28]. Figures 8 and 9 show the solutions for the different values of η.

From Figures 8 and 9, we observed that the solutions varied continuously from fractional-order solutions to integer-order solutions. Therefore, we can say that the behaviors of the approximate solutions for different fractional orders converged to an integer-order solution, and the periodic behavior of the solution can be seen.

Problem 3. *Consider the particular choice of the parameters $L = -1$, $M = 4$, and $N = -3$ in Equation (4). The fractional duffing equation is given as follows [14,44]:*

$$D^{\nu} z(t) - D' z(t) + 4z^3 - 3z^5 = 0, \quad 1 < \nu \leq 2, \tag{28}$$

$$z(0) = c_1 = \sqrt{\frac{-2L}{M}} \quad \textit{and} \quad z'(0) = c_2 = -\frac{L\sqrt{-L}}{M\sqrt{\frac{-2L}{M}}}.$$

The exact solution for the considered problem (Problem 3) for $\nu = 2$ is given as follows:

$$z(t) = \sqrt{\frac{-2L(1 + tanh\sqrt{-L}t)}{M}}. \tag{29}$$

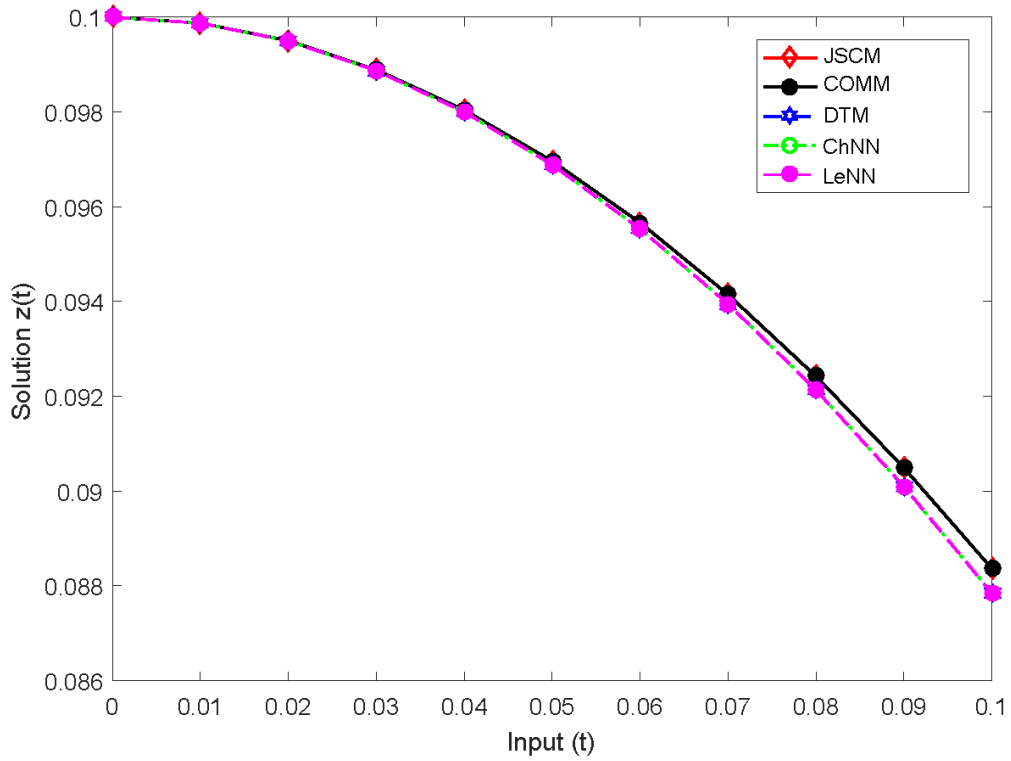

Figure 7. Comparison of approximate solutions at $\eta = 2$ by ChNN, LeNN method with [16], [28], [15] (Problem 2).

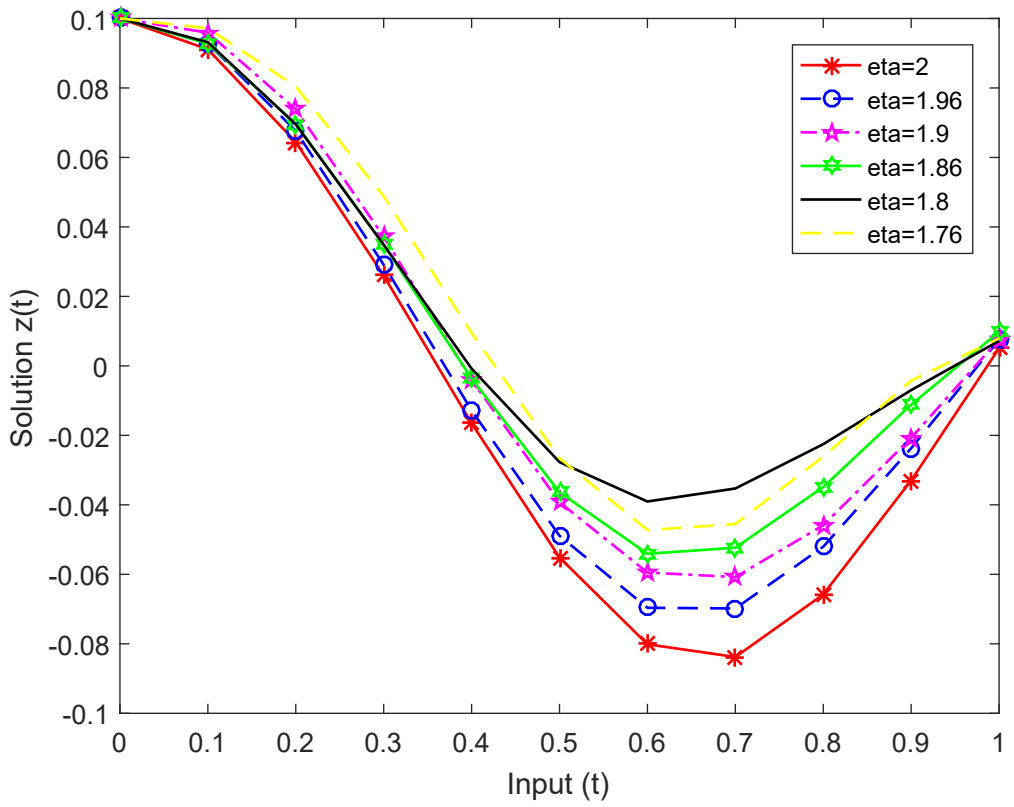

Figure 8. Nature of the approximate results with the LeNN method at $\eta = 2, 1.96, 1.9, 1.86, 1.8, 1.76$ (Problem 2).

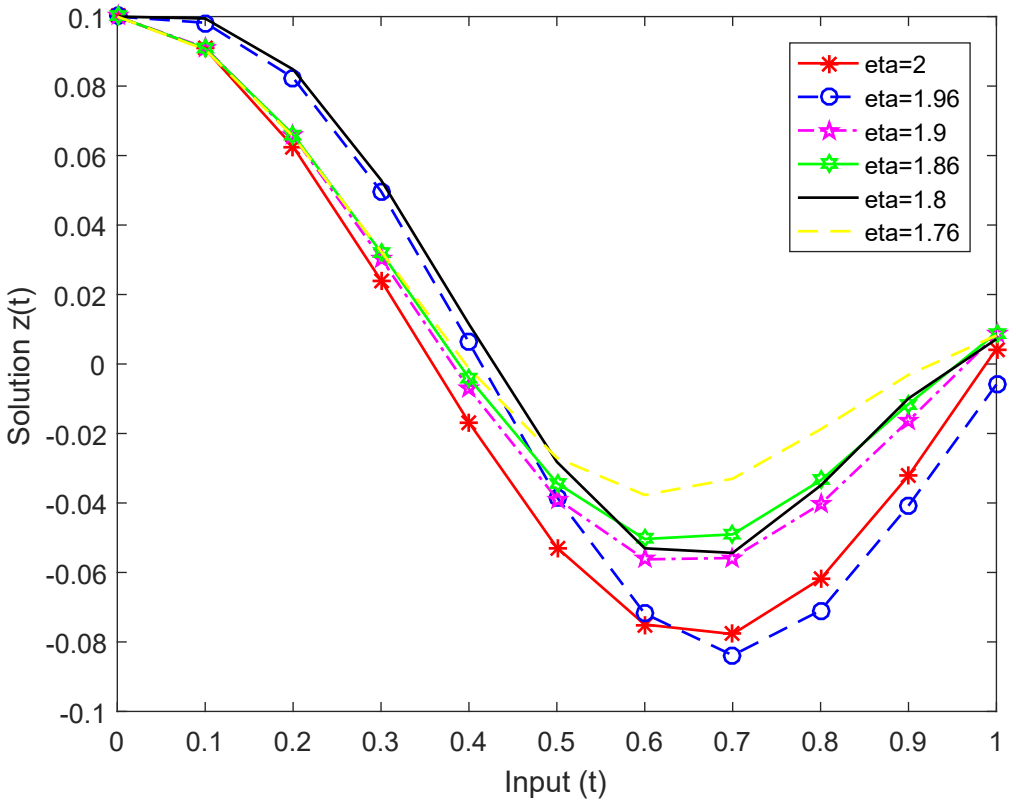

Figure 9. Nature of the approximate results with the ChNN method at $\eta = 2, 1.96, 1.9, 1.86, 1.8, 1.76$ (Problem 2).

The trial solution can be written as

$$z_{tr}(t, \psi) = c_1 + t^2 N(t, \psi). \tag{30}$$

The given Duffing equation was solved with the ChNN and LeNN techniques for the various values of ν. We trained the network by taking 10 equidistant points in the domain $[0, 0.1]$ with 6 NACs. The obtained MSEs were 5.49991×10^{-9} and 2.69692×10^{-10}, respectively. The computational time for the problem was 0.08 s and 0.09 s, respectively. The appropriate values for the NACs using the SA algorithm are given in Table 5. In Table 6, we listed the outcomes by the proposed method, analytic method and the solutions obtained by other existing numerical methods [15,44]. In Table 7, we have shown the absolute error between the exact solution and solution obtained by the proposed technique and other existing techniques.

Table 5. The ideal estimations of NAC (Problem 3).

NAC	W_1	W_2	W_3	W_4	W_5	W_6
ChNN	0.815413	1.23726	2.53108	1.03956	0.498807	0.307813
LeNN	− 1.04706	−1.33436	0.254833	−1.04073	−0.113977	−0.295584

In Figure 10, we have compared the approximate solutions with the proposed methods with the exact solution and the solutions given in [15]. In Figures 11 and 12, we have presented the solutions to Problem 3 for the various values of ν.

In Figures 11 and 12, we can see that the solution varied continuously from fractional order to integer order.

Table 6. Comparison of numerical results at $\nu = 2$ for Problem 3.

t	Exact	ChNN	LeNN	[15]	[44]
0.00	0.7071067	0.7071067	0.7071067	0.7071067	0.7071067
0.01	0.7106334	0.710811	0.710722	0.7106155	
0.02	0.7141419	0.71432	0.714231	0.7140699	0.7141419094
0.03	0.7176318	0.717811	0.717722	0.7174686	
0.04	0.7211028	0.721283	0.721193	0.7208102	0.7211028634
0.05	0.7245544	0.724736	0.724645	0.7240935	
0.06	0.7279862	0.728168	0.728077	0.7273171	0.7279862988
0.07	0.7313979	0.731581	0.731489	0.7304797	
0.08	0.7347890	0.734973	0.734881	0.7335800	0.7347890065
0.09	0.7381591	0.738344	0.738251	0.7366167	
0.1	0.7415079	0.741693	0.741601	0.7395886	0.7415079207

Table 7. Absolute error comparison from various numerical technique for Problem 3 at $\nu = 2$.

t	Abs. Error (ChNN)	Abs. Error (LeNN)	Abs. Error [15]	Abs. Error [44]
0.00	0	0	0	0
0.01	1.776×10^{-4}	8.85×10^{-5}	1.79×10^{-5}	
0.02	1.780×10^{-4}	8.90×10^{-5}	7.19×10^{-5}	1.8669×10^{-6}
0.03	1.790×10^{-4}	9.02×10^{-5}	1.63×10^{-4}	
0.04	1.801×10^{-4}	9.01×10^{-5}	2.93×10^{-4}	6.2706×10^{-6}
0.05	1.810×10^{-4}	9.06×10^{-5}	4.61×10^{-4}	
0.06	1.818×10^{-4}	9.08×10^{-5}	6.69×10^{-4}	4.94502×10^{-5}
0.07	1.831×10^{-4}	9.12×10^{-5}	9.18×10^{-4}	
0.08	1.839×10^{-4}	9.20×10^{-5}	1.21×10^{-3}	1.161249×10^{-4}
0.09	1.849×10^{-4}	9.19×10^{-5}	1.54×10^{-3}	
0.1	1.851×10^{-4}	9.31×10^{-5}	1.91×10^{-3}	2.24737×10^{-4}

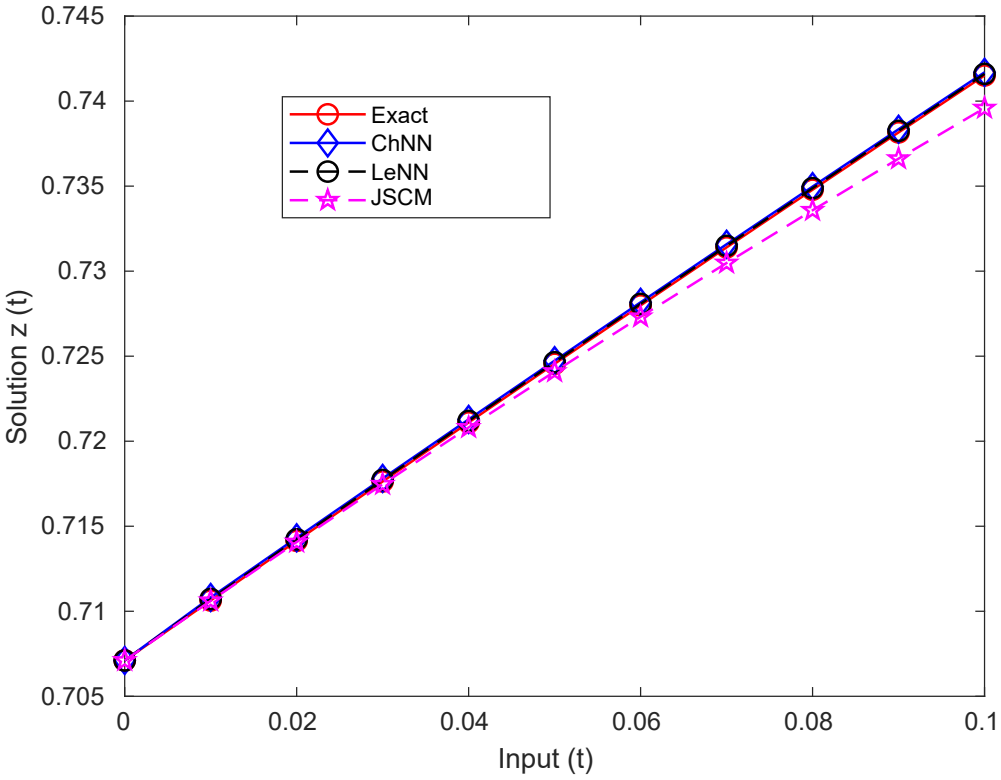

Figure 10. Comparison of approximate solutions at $\eta = 2$ by ChNN, LeNN Method with exact solution and [15] (Problem 3).

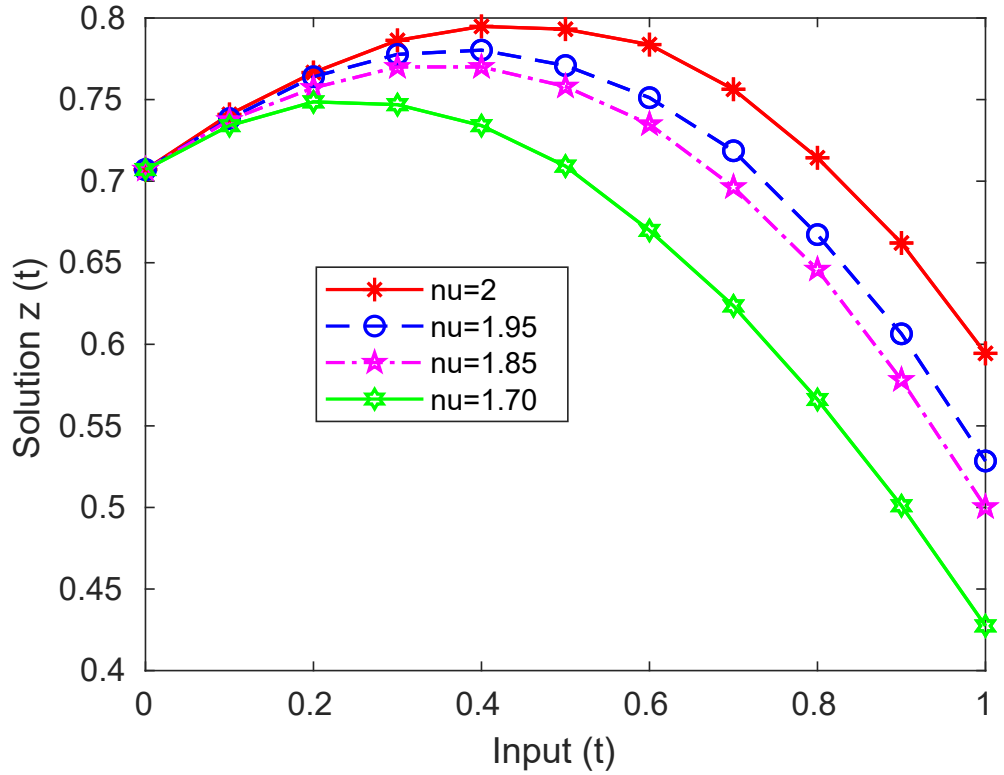

Figure 11. Nature of the approximate results with the ChNN method at $\nu = 2, 1.95, 1.85, 1.70$ (Problem 3).

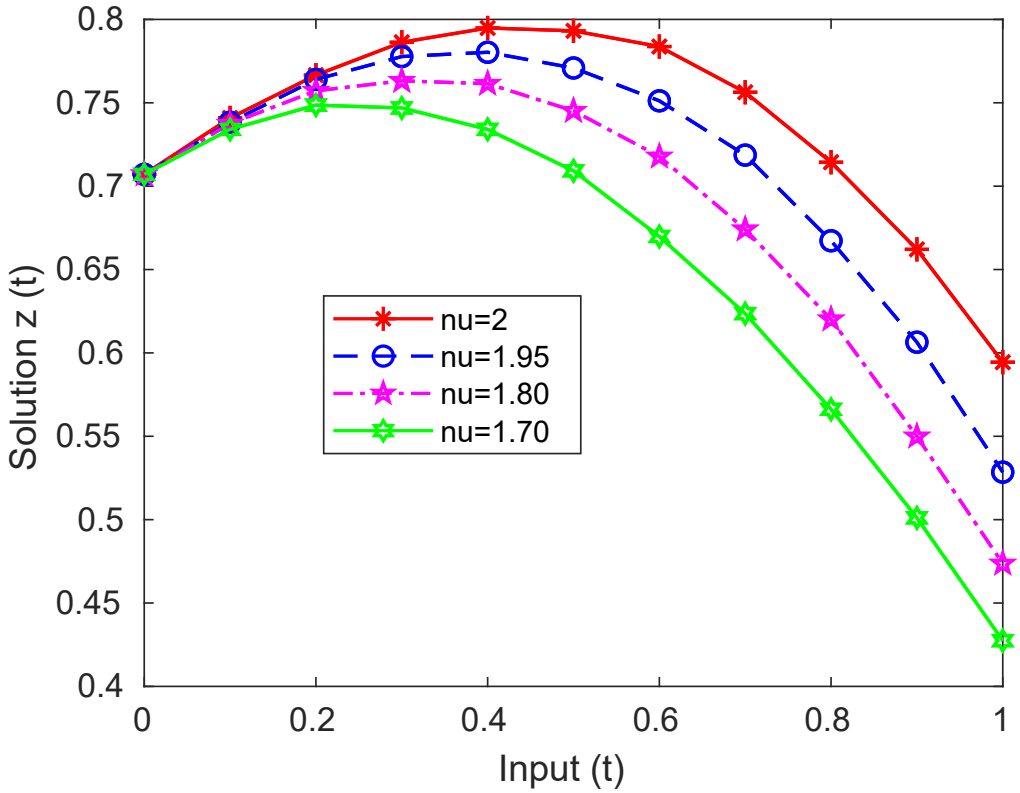

Figure 12. Nature of the approximate results with the ChNN method at $\nu = 2, 1.95, 1.80, 1.70$ (Problem 3).

5. Error Analysis

For the above problems, we have presented the error analysis of the numerical solutions of the ChNN and LeNN techniques. Initially, we trained the neural network using the SA algorithm and collected the appropriate values of the network parameters. After that, we substituted the NAC values into the trial solution and obtained the results for the ChNN or LeNN techniques (according to the polynomial). To analyze the precision of the method within the domain [0,1], we also substituted it into Equation (31):

$$E(t, \psi) = |D^{\nu} z_{tr}(t, \psi) - F(t, z_{tr}(t, \psi), Dz_{tr}(t, \psi))| \cong 0 \tag{31}$$

where we found the $z(t)$ approximated continuous results through the ChNN and LeNN techniques. $E(t)$ approached 0 as the value of the MSE acquired with the ChNN and LeNN with the SA algorithm changed. The solution's convergence depends upon the optimization algorithm, the number of network adaptive coefficients, and the neural network's architecture, which we used.

For Problem 1, the mean square errors for the ChNN and LeNN techniques at $\nu = 2$ were 1.39515×10^{-10} and 5.27835×10^{-10}, respectively, which showed that the minimum error for the ChNN and LeNN was 1.3×10^{-5}. This presents that both the strategies' precisions were inversely proportional to the mean square error value. When we exchanged the polynomials and used the SA algorithm for the network training, we observed that both techniques were strongly affected, as can be seen in Table 1.

Problem 2 is known as the fractional-order Duffing equation. For $\eta = 2$, the values of the MSE with 6 NACs by using ChNN and LeNN methods are 1.61568×10^{-9} and 1.73644×10^{-8} respectively. For the fractional value of $\eta = 1.96, 1.9$, the LeNN shows better results with minimum value for the MSE, however for $\eta = 1.86, 1.8$ and 1.76 both techniques yielded a similar MSE. Problem 3 is also a fractional Lienard equation. We solved it approximately for the various values of ν and obtained better results with less computational time than other existing numerical techniques [15,44].

6. Conclusions

This article has solved the Lienard and Duffing fractional- and integer-order equations using the ChNN and LeNN techniques with the SA algorithm. The proposed approach is easy to implement on nonlinear FDEs with simplicity of evaluation. The method's accuracy can be improved by enhancing the NAC learning methodology. The numerical results show that the proposed strategies give better results compared with other existing numerical techniques, such as DTM [16], the spectral collocation method [15], the Chebyshev operational matrix method [28], HAM [25], and the fractional homotopy analysis transform method [44]. For the solution of nonlinear problems, this technique does not require any linearization process. As a result, we can conclude that the method is exceptional and applicable to a broad range of nonlinear fractional-order differential equations that arise in engineering and science. The proposed technique can also be improved for precision in the future by improving the neural architecture and the learning technique of NACs. In the proposed technique, once the network has been trained, it allows continuous evaluation of the solution inside the domain. Also, it can be considered a powerful tool for the computation of nonlinear problems.

Author Contributions: Methodology and Simulation, A.V.; Conceptualization, W.S.; Supervision P.K.Y.; All authors have read and agreed to the published version of the manuscript.

Funding: This research was funded by the National Science Centre, Poland under Grant No. 2017/27/B/ST8/00351.

Data Availability Statement: Not Applicable

Acknowledgments: We express our sincere thanks to Late Manoj Kumar, who provided the inspiration for this research.

Conflicts of Interest: The authors declare no conflicts of interest.

Abbreviations

The following abbreviations are used in this manuscript:

FDE	Fractional differential equation
SA	Simulated annealing
ChNN	Chebyshev neural network
LeNN	Legendre neural network
NAC	Network adaptive coefficient
COMM	Chebyshev Operational Matrix Method
JSCM	Jacobi Spectral Collocation Method
DTM	Differential Transform Method
ECM	Efficient Computational Method

References

1. Talebi, S.P.; Godsill, S.J.; Mandic, D.P. Filtering Structures for α-Stable Systems. *IEEE Control Syst. Lett.* **2023**, *7*, 553–558. [CrossRef]
2. Liénard, A. Etude des oscillations entretenues. *Rev. Gen. l'Electr.* **1928**, *23*, 901–912.
3. Guckenheimer, J. Dynamics of the Van der pol equation. *IEEE Trans. Circuit Syst.* **1980**, *27*, 938–989. [CrossRef]
4. Kong, D.X. Explicit exact solutions for the Lienard equation and its applications. *Phys. Lett. A* **1995**, *196*, 301–306. [CrossRef]
5. Feng, Z. On explicit exact solutions for the Lienard equation and its applications. *Phys. Lett. A* **2002**, *293*, 50–56. [CrossRef]
6. Diethelm, K.; Walz, G. Numerical solution of fractional order differential equations by extrapolation. *Numer. Algorithms* **1997**, *16*, 231–253. [CrossRef]
7. Esmaeili, S.; Shamsi, M.; Luchko, Y. Numerical solution of fractional differential equations with a collocation method based on Müntz polynomials. *Comput. Math. Appl.* **2011**, *62*, 918–929. [CrossRef]
8. Demirci, E.; Ozalp, N. A method for solving differential equations of fractional order. *J. Comput. Appl. Math.* **2012**, *236*, 2754–2762. [CrossRef]
9. Han, W.; Chen, Y.M.; Liu, D.Y.; Boutat, D. Numerical solution for a class of multi-order fractional differential equations with error correction and convergence analysis. *Adv. Differ. Equ.* **2018**, *253*, 253. [CrossRef]
10. Sumelka, W.; Luczak, B.; Gajewski, T.; Voyiadjis, G.Z. Modelling of AAA in the framework of time-fractional damage hyperelasticity. *Int. J. Solids Struct.* **2020**, *206*, 30–42. [CrossRef]
11. Sumelka, W. Fractional calculus for continuum mechanics—Anisotropic non-locality. *Bull. Pol. Acad. Sci. Tech. Sci.* **2016**, *64*, 361–372. [CrossRef]
12. Bohner, M.; Tunç, O.; Tunç, C. Qualitative analysis of caputo fractional integro-differential equations with constant delays. *Comput. Appl. Math.* **2021**, *40*, 214. [CrossRef]
13. Tunç, O.; Tunç, C. Solution estimates to Caputo proportional fractional derivative delay integro-differential equations. *Rev. R. Acad. Cienc. Exactas Fís. Nat. Ser. A Mat.* **2023**, *117*, 12. [CrossRef]
14. Singh, H. An efficient computational method for non-linear fractional Lienard equation arising in oscillating circuits. In *Methods of Mathematical Modelling: Fractional Differential Equations*; CRC Press : London, UK; New York, NY, USA, 2019.
15. Singh, H.; Srivastava, H.M. Numerical Investigation of the Fractional-Order Liénard and Duffing Equations Arising in Oscillating Circuit Theory. *Front. Phys.* **2020**, *8*, 120. [CrossRef]
16. Nourazar, S.; Mirzabeigy, A. Approximate solution for nonlinear Duffing oscillator with damping effect using the modified differential transform method. *Sci. Iran. B* **2013**, *20*, 364–368.
17. Gómez-Aguilar, J.F.; Torres, L.; Yépez-Martínez, H.; Baleanu, D.; Reyes, J.M.; Sosa, I.O. Fractional Liénard type model of a pipeline within the fractional derivative without singular kernel. *Adv. Differ. Equ.* **2016**, *2016*, 173. [CrossRef]
18. Feng, Z. Exact solutions for the Lienard equation and its applications. *Chaos Solitons Fractals* **2004**, *21*, 343–348. [CrossRef]
19. Matinfar, M.; Hosseinzadeh, H.; Ghanbari, M. A numerical implementation of the variational iteration method for the Lienard equation. *World J. Model. Simul.* **2008**, *4*, 205–210.
20. Xu, G.Q. New explicit exact solutions for the Liénard equation and its applications. *arXiv* **2010**, arxiv:1003.2921v1.
21. Janiczek, T. Generalisation of the modulating functions method into the fractional differential equations. *Bull. Pol. Acad. Sci. Tech. Sci.* **2010**, *58*, 593–599. [CrossRef]
22. Atabakzadeh, M.H.; Akrami, M.H.; Erjaee, G.H. Chebyshev Operational Matrix Method for Solving Multi-order Fractional Ordinary Differential Equations. *Appl. Math. Model.* **2013**, *37*, 8903–8911. [CrossRef]
23. Kazem, S. An integral operational matrix based on Jacobi polynomials for solving fractional-order differential equations. *Appl. Math. Model.* **2013**, *37*, 1126–1136. [CrossRef]
24. Ezz-Eldien, S.S. New quadrature approach based on operational matrix for solving a class of fractional variational problems. *J. Comput. Phys.* **2016**, *317*, 362–381. [CrossRef]
25. Ejikeme, C.L.; Oyesanya, M.O.; Agbebaku, D.F.; Okofu, M.B. Solution to nonlinear Duffing Oscillator with fractional derivatives using Homotopy Analysis Method (HAM). *Glob. J. Pure Appl. Math.* **2018**, *14*, 1363–1388.

26. Morales-Delgado, V.F.; Gómez-Aguilar, J.F.; Torres, L.; Escobar-Jiménez, R.F.; Taneco-Hernandez, M.A. Exact Solutions for the Liénard Type Model via Fractional Homotopy Methods. In *Fractional Derivatives with Mittag-Leffler Kernel*; Springer: Cham, Switzerland, 2019; Volume 194, pp. 269–291. [CrossRef]
27. Singh, H.; Srivastava, H.M.; Kumar, D. A reliable numerical algorithm for the fractional vibration equation. *Chaos Solitons Fractals* **2017**, *103*, 131–138. [CrossRef]
28. Singh, H. Solution of fractional Lienard equation using Chebyshev operational matrix method. *Nonlinear Sci. Lett. A* **2017**, *8*, 397–404.
29. Kumar, S.; Gomez-Aguilar, J.F.; Lavın-Delgado, J.E.; Baleanu, D. Derivation of operational matrix of Rabotnov fractional-exponential kernel and its application to fractional Lienard equation. *Alex. Eng. J.* **2020**, *59*, 2991–2997. [CrossRef]
30. Adel, W. A fast and efficient scheme for solving a class of non-linear Lienard's equations. *Math. Sci.* **2020**, *14*, 167–175. [CrossRef]
31. Kumar, M.; Yadav, N. Multilayer perceptrons and radial basis function neural network methods for the solution of differential equations: A survey. *Comput. Math. Appl.* **2011**, *62*, 3796–3811. [CrossRef]
32. Khan, N.A.; Shaikh, A.; Sultan, F.; Ara, A. Numerical Simulation Using Artificial Neural Network on Fractional Differential Equations. In *Numerical Simulation—From Brain Imaging to Turbulent Flows*; IntechOpen: London, UK, 2017. [CrossRef]
33. Chakraverty, S.; Mall, S. *Artificial Neural Networks for Engineers and Scientists Solving Ordinary Differential Equations*; CRC Press: London, UK; New York, NY, USA, 2017.
34. Verma, A.; Kumar, M. Numerical solution of Lane–Emden type equations using multilayer perceptron neural network method. *Int. J. Appl. Comput. Math.* **2019**, *5*, 141. [CrossRef]
35. Shaikh, A.; Jamal, M.A.; Hanif, F.; Khan, M.S.A.; Inayatullah, S. Neural minimisation methods for solving variable order fractional delay differential equations with simulated annealing. *PLoS ONE* **2019**, *14*, e0223476. [CrossRef] [PubMed]
36. Chakraverty, S.; Mall, S. Single layer Chebyshev neural network model with regression-based weights for solving nonlinear ordinary differential equations. *Evol. Intell.* **2022**, *13*, 687–694. [CrossRef]
37. Verma, A.; Kumar, M. Numerical solution of Bagley–Torvik equations using Legendre artificial neural network method. *Evol. Intell.* **2020**, *14*, 2027–2037. [CrossRef]
38. Verma, A.; Kumar, M. Numerical solution of third-order Emden–Fowler type equations using artificial neural network technique. *Eur. Phys. J. Plus* **2020**, *135*, 751. [CrossRef]
39. Lefik, M. Some aspects of application of artificial neural network for numerical modeling in civil engineering. *Bull. Pol. Acad. Sci. Sci.* **2013**, *61*, 39–50. [CrossRef]
40. Malik, S.A.; Qureshi, I.M.; Amir, M.; Haq, I. Numerical Solution of Lienard Equation Using Hybrid Heuristic Computation. *World Appl. Sci. J.* **2013**, *28*, 636–643.
41. Kumar, S.; Sahoo, A.K.; Chakraverty, S. A Comparative study of Chebyshev and Legendre Polynomial-based Neural Models for Approximating Multidimensional Poverty for an Indian State. In *Polynomial Paradigms: Trends and Applications in Science and Engineering*; IOP Publishing: Bristol, UK, 2023. [CrossRef]
42. Sahoo, A.K.; Chakraverty, S. A neural network approach for the solution of Van der Pol-Mathieu-Duffing oscillator model. *Evol. Intell.* **2023**. [CrossRef]
43. Pao, Y.H.; Philips, S.M. The functional link net and learning optimal control. *Neurocomputing* **1995**, *9*, 149–164. [CrossRef]
44. Kumar, D.; Agarwal, R.P.; Singh, J. A modified numerical scheme and convergence analysis for fractional model of Lienard's equation. *J. Comput. Appl. Math.* **2018**, *339*, 405–413. [CrossRef]

Disclaimer/Publisher's Note: The statements, opinions and data contained in all publications are solely those of the individual author(s) and contributor(s) and not of MDPI and/or the editor(s). MDPI and/or the editor(s) disclaim responsibility for any injury to people or property resulting from any ideas, methods, instructions or products referred to in the content.

symmetry

MDPI

Article

Symmetry in a Fractional-Order Multi-Scroll Chaotic System Using the Extended Caputo Operator

A. E. Matouk [1,2,*], D. K. Almutairi [2], M. A. E. Herzallah [3,4], M. A. Abdelkawy [5,6] and T. N. Abdelhameed [1,2,5]

[1] Department of Mathematics, College of Science Al-Zulfi, Majmaah University, Al-Majmaah 11952, Saudi Arabia
[2] College of Engineering, Majmaah University, Al-Majmaah 11952, Saudi Arabia
[3] Faculty of Science, Zagazig University, Zagazig 44519, Egypt
[4] Faculty of Science and Humanities, Shaqra University, Al-Dawadmi 11911, Saudi Arabia
[5] Mathematics Department, Faculty of Science, Beni-Suef University, Beni-Suef 62514, Egypt
[6] Department of Mathematics and Statistics, Faculty of Science, Imam Mohammad Ibn Saud Islamic University (IMSIU), Riyadh 11564, Saudi Arabia
* Correspondence: ae.mohamed@mu.edu.sa or aematouk@hotmail.com

Abstract: In this work, complex dynamics are found in a fractional-order multi-scroll chaotic system based on the extended Gamma function. Firstly, the extended left and right Caputo fractional differential operators are introduced. Then, the basic features of the extended left Caputo fractional differential operator are outlined. The proposed operator is shown to have a new fractional parameter (higher degree of freedom) that increases the system's ability to display more varieties of complex dynamics than the corresponding case of the Caputo fractional differential operator. Numerical results are performed to show the effectiveness of the proposed fractional operators. Then, rich complex dynamics are obtained such as coexisting one-scroll chaotic attractors, coexisting two-scroll chaotic attractors, or approximate periodic cycles, which are shown to persist in a shorter range as compared with the corresponding states of the integer-order counterpart of the multi-scroll system. The bifurcation diagrams, basin sets of attractions, and Lyapunov spectra are used to confirm the existence of the various scenarios of complex dynamics in the proposed systems.

Keywords: the multi-scroll chaotic system; extended Caputo fractional differential operators; coexisting one-scroll chaotic attractors; coexisting two-scroll chaotic attractors; approximate periodic cycles

MSC: 45D05

1. Introduction

In the current century, many engineers, scientists, and economists have described and analyzed their related problems using the aid of fractional calculus (FC) [1–9]. The primary rationale is that using FC provides a greater level of accuracy when measuring natural phenomena. Therefore, FC demonstrated immense potential for applications in various scientific and engineering fields. Notably, it has found utility in disciplines such as engineering [6], fluid dynamics [2], thermoelasticity [4,5], mathematical biology [1,8], as well as market dynamics [9]. Additionally, the biological models that are described in terms of FC involve the memory effect which is considered to be a powerful tool in modeling the epidemiological diseases and viral dynamics. In recent times, the Caputo fractional differential operator (CFDO) has gained significant importance as a valuable tool for modeling various scientific and engineering phenomena. This is primarily due to its ability to facilitate the determination of relevant initial values [10]. Consequently, the CFDO is widely used in real-world applications. Indeed, the CFDO is the classic left Caputo fractional differential operator (LCFDO).

On the other hand, chaotic attractors, present in both fractional- and integer-order equations, have demonstrated immense potential for applications in various technological and scientific fields. Notably, they have found utility in disciplines such as meteorological systems [11], chemical systems [12], as well as engineering systems [6,13–15]. The first chaotic attractor was discovered by Lorenz when he tried to make a mathematical model that can predict the weather [11]. Afterward, many chaotic attractors were reported by scientists such as Rossler system [12], Chua system [13], Chen system [14], Liu system [15], and MAVPD system [6]. Indeed, the Chua, Chen, Liu, and MAVPD systems are realized through an electronic circuit design. Recently, chaotic attractors in fractional-order equations were shown to have great potential applications in some technological and scientific disciplines such as the fractional Lorenz system [16], the fractional Chua system [17], the fractional Chen system [18], the fractional Rossler system [19], and the fractional MAVPD system [6]. In Ref. [7], the phase transition of chaotic attractors between the integer-order system and its fractional-order counterpart is discussed. It is found that under certain conditions, the chaotic attractors that appear in the fractional-order system may not exist in its integer-order counterpart. However, the periodic orbits that exist in the integer-order system cannot exist in its fractional-order counterpart involving the CFDO [20]. The approximate periodic cycles that may appear in the case of CFDO are due to the truncation error of the solution algorithm and the observation scale.

The multi-scroll chaotic system [21] is an autonomous dynamical system (DS) that has three quadratic nonlinearities. According to Ref. [22], this system is considered to be a transition system between the Chen system and the Lorenz system. So, the multi-scroll chaotic systems have promising applications to science and engineering.

One of the effective tools to describe the complex dynamics of the DS is the plot of the Poincaré points of a component of the solution for every period T of the external forcing signal against the system's dynamical parameter. This tool is briefly termed the system's bifurcation diagram. In such diagrams, the shaded (or colored) parts refer to regions where chaotic dynamics occur.

The Lyapunov exponents (LEs) are considered to be excellent estimators to quantify chaotic dynamics. The three-dimensional DS has a maximum of three LEs (Λ_i, $i = 1, 2, 3$). In Ref. [23], Haken proved that one LE must vanish for any limit set other than an equilibrium point. Furthermore, one LE must vanish for continuous flows. When chaos exists, the system's greatest LE must be positive. In addition, the third LE is negative for dissipative three-dimensional DS. Indeed, the sum of the LEs is the divergence of the flow corresponding to the DS. One of the most efficient numerical algorithms to estimate the LEs in the integer-order DS was reported by Wolf et al. [24]. In the fractional-order case, the LEs can successfully be estimated using the numerical algorithm given by Danca and Kuznetsov [25].

The extended Gamma function is a generalization of the well-known Euler Gamma function, which was discovered in the 18th century [26]. Recently, the extended Gamma function has had useful applications in science and engineering. Indeed, the LCFDO involves the Euler Gamma function. Hence, replacing the Euler Gamma function with the extended Gamma function in the Caputo fractional operators is an interesting line for research that was initiated by Matouk and Bachioua in Ref. [27]. Furthermore, in Ref. [28], Matouk and Bachioua investigated some chaotic behaviors in two fractional-order predator–prey models that consist of the generalized Caputo fractional operators. In Ref. [8], Matouk inserted the extended Gamma function into the CFDO for investigating the complex dynamics in an antimicrobial resistance model. These references [8,27,28] assert that the CFDO involving the extended Gamma function is more suitable to handle the complex dynamics arising from the models that describe the natural phenomena due to its high adequacy in predicting the models' dynamics and also due to the existence of a higher degree of freedom that can be used to obtain more intricate dynamics that cannot present in the case of the corresponding classic fractional Caputo operators.

Here, we intend to investigate the chaotic dynamics of the multi-scroll chaotic system using the extended left Caputo fractional differential operators (ELCFDO). By introducing a new fractional parameter to the ELCFDO, more intricate dynamics can be achieved that were not present in the case of the corresponding classic LCFDO. This leads to the emergence of a diverse range of complex dynamics, including coexisting one-scroll chaotic attractors, coexisting two-scroll chaotic attractors, and approximate periodic cycles. Furthermore, advanced measures of DS such as bifurcation diagrams, basin sets of attractions (BSA), and Lyapunov spectra are utilized to validate the existence of these complex dynamics in multi-scroll chaotic systems. To summarize the main motivations in this article, we recall that the ELCFDO has a higher degree of freedom in comparison with the CFDO, which makes the multi-scroll chaotic system exhibit more scenarios of complex dynamics. In addition, the motivations of this work are clearly provided by comparing the results obtained via the ELCFDO with the results obtained via the classic integer- and fractional-order operators. Therefore, we compare the dynamics of the multi-scroll chaotic system involving the ELCFDO and the dynamics of the corresponding integer-order counterpart of the system by demonstrating the bifurcation diagrams and calculating the LEs. The outcome of this comparison asserts that the ELCFDO is a better candidate to handle the complex dynamics in the multi-scroll chaotic system since it provides varieties of complex dynamics that persist in a shorter range as compared with the corresponding states of the system's integer-order counterpart.

The rest of this article is organized as follows. The basic definitions of the ELCFDO and the extended right Caputo fractional differential operators (ERCFDO) are introduced in Section 2. The integer-order multi-scroll chaotic system is introduced in Section 3, in which we provide the system's bifurcation diagrams, the system's Lyapunov spectra, and compute the system's BSA. The fractional-order form of the multi-scroll chaotic system involving the ELCFDO is investigated in Section 4 where the system's bifurcation diagrams and Lyapunov spectra are provided to confirm the main motivations of this work. Finally, we provided the concluding statements and future studies in Section 5.

Notations: Throughout this article, the sets of positive (negative) real numbers are, respectively, represented by $R^+(R^-)$. The set of all natural numbers is represented by N. $AC([u,v])$ represents the set of all functions that are absolutely continuous on the interval $[u,v]$. The expression of the ceiling function is represented by $\lceil . \rceil$.

2. Fractional Calculus

The ELCFDO is described by

$$ {}^{E}_{C}\mathrm{O}^{q,\eta}_{u+}\kappa(t) = \mathrm{K}^{l-q,\eta}_{u+}\frac{d^{l}\kappa(t)}{dt^{l}}, \ \ q \in R^{+}, \tag{1} $$

where $l = \lceil q \rceil$, $\mathrm{K}^{\xi,\eta}_{u+}\varphi(t) = [\int_{u}^{t} \frac{\varphi(x)}{(t-x)^{1-\xi}}dx]/\Gamma_0(\xi,\eta)$, $\xi \in R^{+}$, $t > u$, represents the ξth-order extended left Riemann–Liouville (ELRL) fractional integral, where $\Gamma_0(\xi,\eta)$ is the extended Gamma function defined by

$$ \Gamma_0(\xi,\eta) = \left[\int_{0}^{+\infty} \frac{y^{\xi-1}}{e^{y}}dy\right]/\eta^{\xi}, \ \ \xi, \eta \in R^{+}. \tag{2} $$

However, the ξth-order extended right Riemann–Liouville (ERRL) fractional integral is

$$ K^{\xi,\eta}_{v-}\varphi(t) = [\int_{t}^{v} \frac{\varphi(x)}{(x-t)^{1-\xi}}dx]/\Gamma_0(\xi,\eta), \ \ \xi \in R^{+}, \ t < v. \tag{3} $$

Hence, the ERCFDO is given by

$$ {}^{E}_{C}\mathrm{O}^{q,\eta}_{v-}\kappa(t) = \mathrm{K}^{l-q,\eta}_{b-}\left(-\frac{d}{dt}\right)^{l}\kappa(t),\ \ q \in R^{+},\ l \in N. \tag{4} $$

The following relations hold for the ELCFDO

(i) Let $c \in R\backslash\{0\}$ be a constant number then ${}^{E}_{C}\mathrm{O}^{q,\eta}_{u+}c = 0$.
(ii) Let $\kappa(t) \in AC([u,v])$ and $q \in (0,1]$, then

$$ \lim_{q\to 1} {}^{E}_{C}\mathrm{O}^{q,\eta}_{u+}\kappa(t) = \frac{d\kappa(t)}{dt}. \tag{5} $$

Furthermore, the following properties for the ELRL fractional integral hold

$$ \begin{array}{ll} \text{(I)} & \mathrm{K}^{1,\eta}_{u+}\kappa(t) = \eta\int_{u}^{t}\kappa(x)dx. \\ \text{(II)} & \text{If } \kappa(t) \in L^{1}, \text{ then } \mathrm{K}^{\xi_1,\eta}_{u+}\ \mathrm{K}^{\xi_2,\eta}_{u+}\kappa(t) = \mathrm{K}^{\xi_1+\xi_2,\eta}_{u+}\kappa(t). \\ \text{(III)} & \lim_{\xi\to l}\mathrm{K}^{\xi,\eta}_{u+}\kappa(t) = \mathrm{K}^{l,\eta}_{u+}\kappa(t) \text{ uniformly on } [u,v],\ l = 1, 2, 3, \ldots. \\ \text{(IV)} & \lim_{\xi\to 0}\mathrm{K}^{\xi,\eta}_{u+}\kappa(t) = \kappa(t) \text{ weakly}. \\ \text{(V)} & \text{If } 0 < \xi < 1 \text{ and } \kappa \in C[0,v] \text{ then } \mathrm{K}^{\xi,\eta}_{0+}\kappa(t)\Big|_{t=0} = 0. \\ \text{(VI)} & \mathrm{K}^{\xi_1,\eta}_{u+}\ \mathrm{K}^{\xi_2,\eta}_{u+}\kappa(t) = \mathrm{K}^{\xi_2,\eta}_{u+}\ \mathrm{K}^{\xi_1,\eta}_{u+}\kappa(t)\ \forall\ \xi_1,\ \xi_2 \in R^{+}\cup\{0\}. \\ \text{(VII)} & \mathrm{K}^{\xi,\eta}_{0+}t^{n} = \frac{\Gamma_0(1+n,\eta)}{\Gamma_0(1+n+\xi,\eta)}t^{\xi+n}\ \forall\ n > -1. \end{array} \tag{6} $$

The relation between the ELCFDO and the classic CFDO (${}_{C}\mathrm{O}^{q}_{u+}\kappa(t)$) is given as

$$ {}^{E}_{C}\mathrm{O}^{q,\eta}_{u+}\kappa(t) = \eta^{l-q}\,{}_{C}\mathrm{O}^{q}_{u+}\kappa(t),\ \ \eta, q \in R^{+}, \tag{7} $$

where $l = \lceil q \rceil$. The parameter η acts as a higher degree of freedom for the ELCFDO. Hence, more intricate dynamics can be achieved that were not present in the case of the corresponding classic LCFDO. This leads to the emergence of a diverse range of complex dynamics.

3. Description of the Integer-Order Multi-Scroll Chaotic System

The classic multi-scroll chaotic system [21] is presented as

$$ \begin{array}{l} \frac{d\beta_1}{dt} = c - d\beta_1 - \beta_2\beta_3, \\ \frac{d\beta_2}{dt} = a\beta_2 + \beta_1\beta_3, \\ \frac{d\beta_3}{dt} = b\beta_3 + \beta_1\beta_2, \end{array} \tag{8} $$

where $d = \frac{ab}{b+a}$.

Obviously, the divergence of the system (8) is given as div(**F**) = a + b − d, where **F** represents the flow vector. Hence, the integer-order multi-scroll system (8) is dissipative if and only if the quantity div(**F**) is negative. This means that the volume element V_0 converges to zero as the time t increases to infinity at an exponential rate, a + b − d. Therefore, the motion of all the system orbits asymptotically settles onto an attractor. In addition, the integer-order multi-scroll chaotic system (8) has a highly symmetric structure that makes the system robust to different small perturbations. Thus, chaotic attractors are expected in this system when it undergoes sensitive dependence on initial data. One-scroll and two-scroll chaotic attractors in this system are obtained using the parameter sets A = $\{a, b, c\} = \{-10, -4, 18.1\}$ and $B = \{a, b, c\} = \{-10, -4, 0\}$, respectively. For, $a, b \in R^{-}$ and $c > -\frac{\gamma^{\frac{3}{2}}}{b+a}$, $\gamma = \sqrt{ab}$, the system's equilibrium points are

$$P_1 = (\frac{c}{d}, 0, 0), P_{2,3} = (\gamma, \pm\frac{\gamma}{a}\sqrt{\frac{d\gamma^2 - \gamma c}{b}}, \pm\sqrt{\frac{d\gamma^2 - \gamma c}{b}}), P_{4,5} = (-\gamma, \pm\frac{\gamma}{a}\sqrt{\frac{d\gamma^2 - \gamma c}{b}}, \pm\sqrt{\frac{d\gamma^2 - \gamma c}{b}}). \quad (9)$$

The above-mentioned equilibria are reduced to only three when using selection A of the parameter values. So, we obtain

$$P_1 = (\frac{c}{d}, 0, 0) \text{ and } P_{2,3} = (\gamma, \pm\frac{\gamma}{a}\sqrt{\frac{d\gamma^2 - \gamma c}{b}}, \pm\sqrt{\frac{d\gamma^2 - \gamma c}{b}}). \quad (10)$$

For $a, b \in R^-$ and $c = 0$, the system's equilibrium points are

$$P_0 = (0, 0, 0), P_{2,3} = (\gamma, \pm\frac{\gamma}{a}\sqrt{\frac{a\gamma^2}{b + a}}, \pm\sqrt{\frac{a\gamma^2}{b + a}}), P_{4,5} = (-\gamma, \pm\frac{\gamma}{a}\sqrt{\frac{a\gamma^2}{b + a}}, \pm\sqrt{\frac{a\gamma^2}{b + a}}). \quad (11)$$

System (8) is numerically integrated based on the MATLAB command ODE45 to obtain its bifurcation diagrams (See Figures 1–3) and the BSA. The initial states are chosen as $(\beta_{10}, \beta_{20}, \beta_{30}) = (0.1, 0.1, 0.1)$. The bifurcation diagrams confirm the existence of a rich variety of chaotic attractors in this system and different routes to chaos via period-doubling bifurcations.

The corresponding Les are calculated based on the numerical algorithm in Ref. [24]. Furthermore, the Lyapunov spectra of the system (8) are also obtained to confirm the existence of such wide regions of chaotic dynamics. The results are depicted in Figures 4–6.

The bifurcation diagrams and the Les illustrate the region of chaotic dynamics in the system (8) as follows. In Figure 1, chaotic dynamics exist when $-11 < a \leq -8.96$ (see Figure 1a) and exist when $-11 \leq a \leq -7$ (See Figure 1b). In Figure 2, chaotic dynamics exist when $-4.7 < b \leq -4$ (see Figure 2a) and exist when $-5.7 < b \leq -3$ (see Figure 2b). In Figure 3, chaotic dynamics exist when $17 < c < 19.3$ (see Figure 3a) and exist when $0 \leq c < 12$ and $15 \leq c \leq 19$ (see Figure 3b).

The BSA is given in the Figures 4 and 5 to confirm the coexistence of multi-attractors in this system. In Figure 7, the blue and the red regions refer to the coexisting two one-band chaotic attractors. In Figure 8, the yellow and the turquoise regions refer to the coexisting two double-band chaotic attractors.

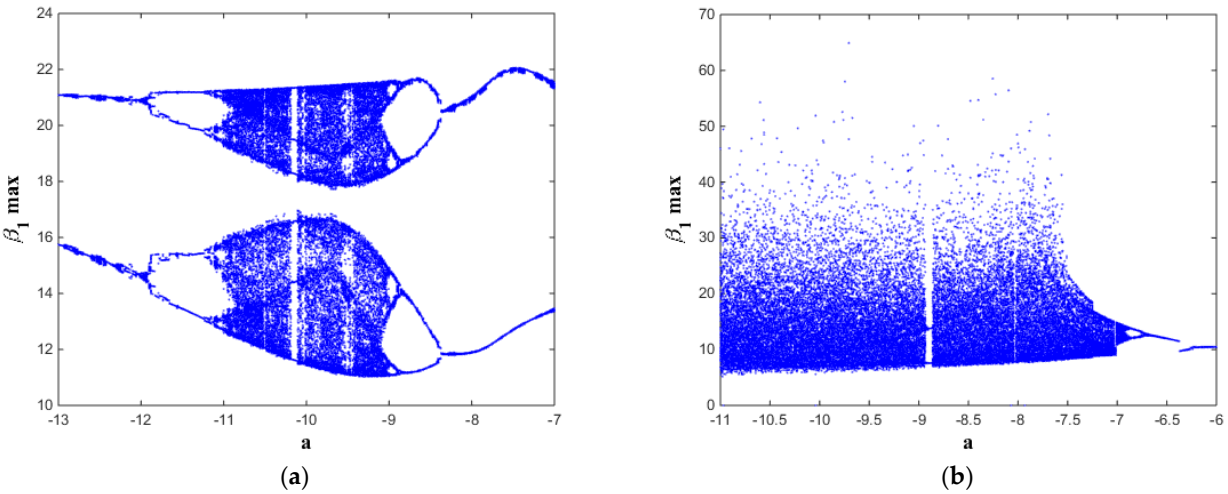

Figure 1. The bifurcation diagram of the system (8) with varying a and using (**a**) the parameter set A and (**b**) the parameter set B.

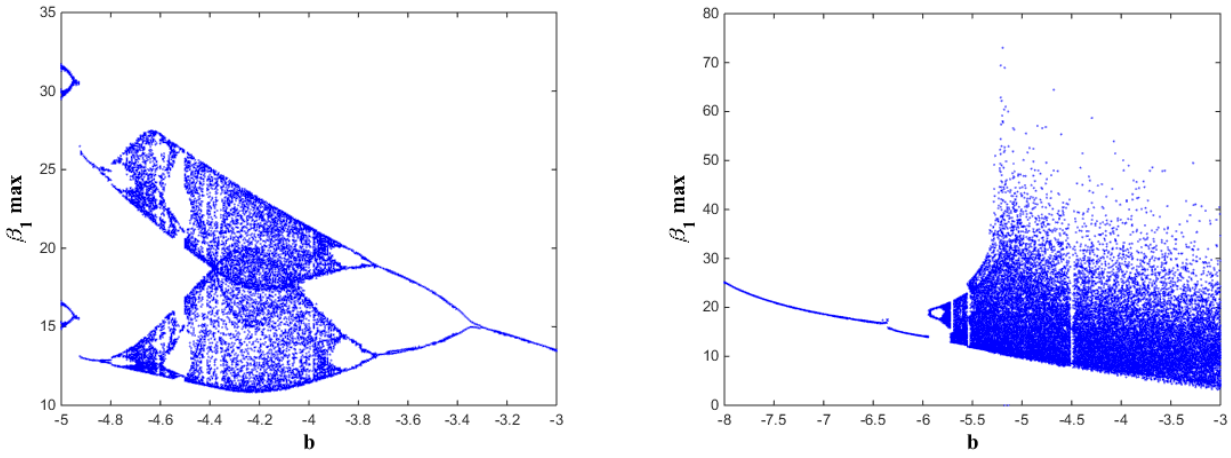

Figure 2. The bifurcation diagram of the system (8) with varying b and using (**a**) the parameter set A and (**b**) the parameter set B.

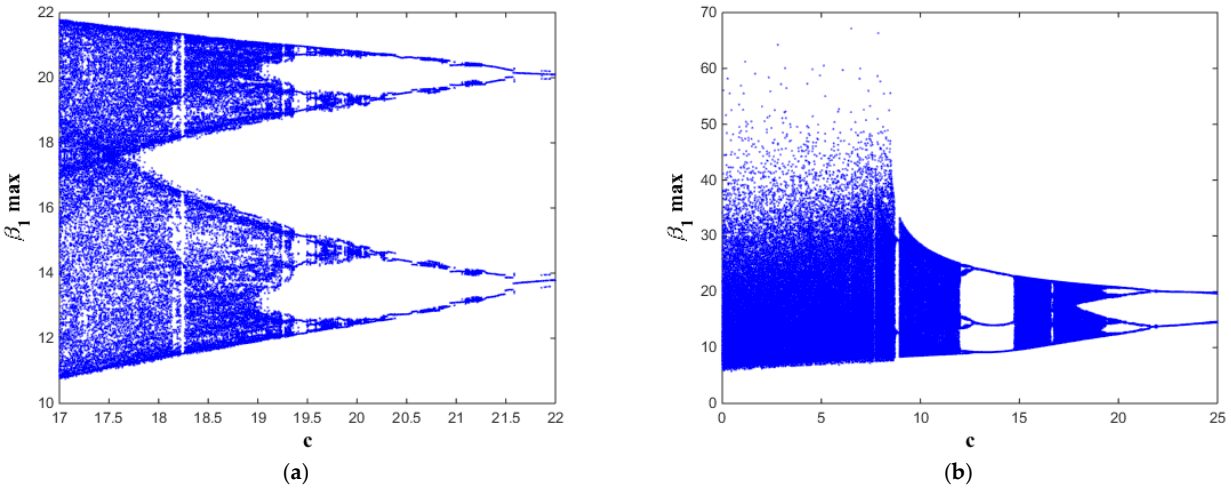

Figure 3. The bifurcation diagram of the system (8) with varying c and using (**a**) the parameter set A and (**b**) the parameter set B.

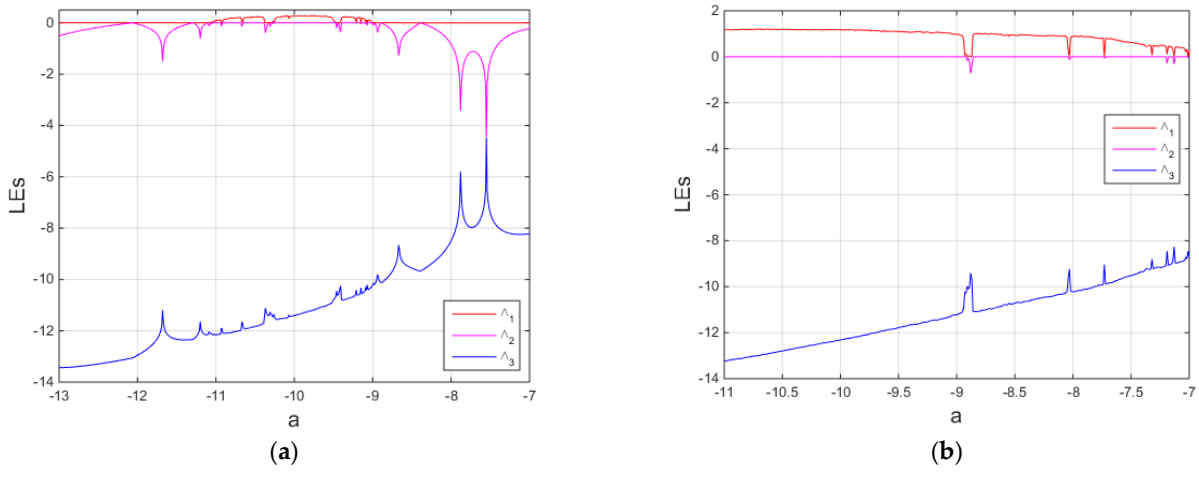

Figure 4. The Lyapunov spectrum of the system (8) with varying a and using (**a**) the parameter set A and (**b**) the parameter set B.

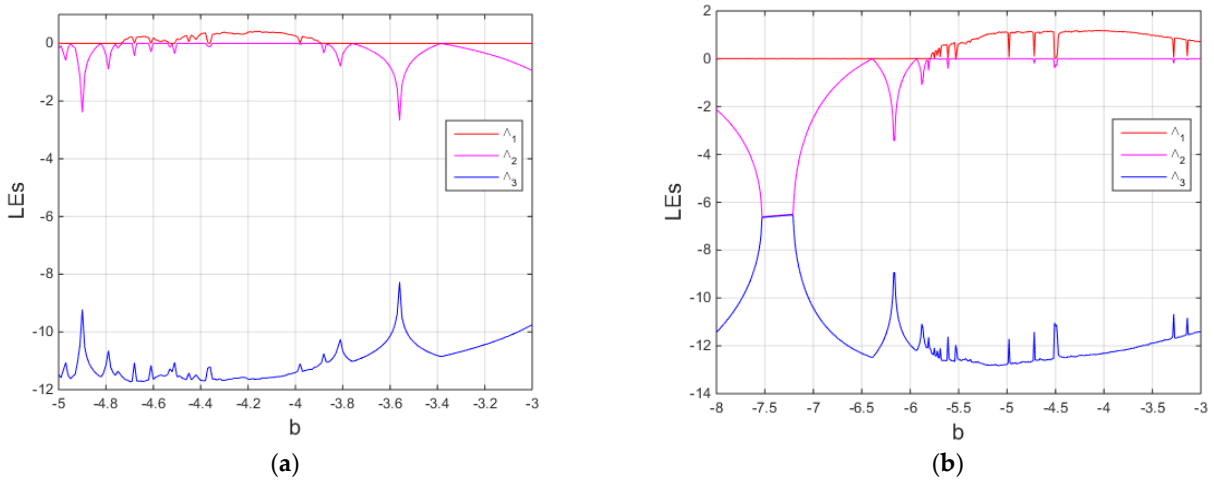

Figure 5. The Lyapunov spectrum of the system (8) with varying b and using (**a**) the parameter set A and (**b**) the parameter set B.

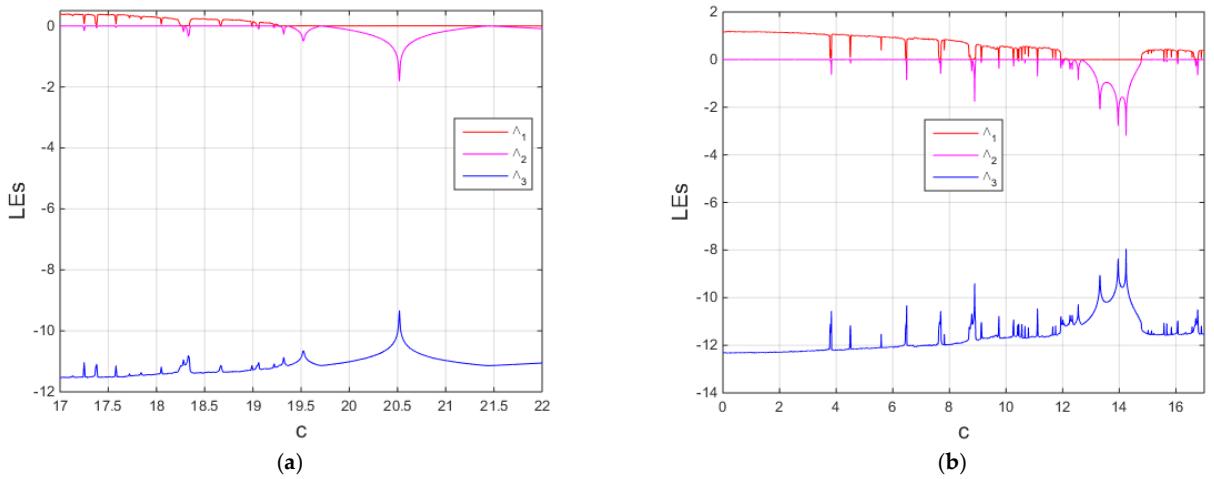

Figure 6. The Lyapunov spectrum of the system (8) with varying c and using (**a**) the parameter set A and (**b**) the parameter set B.

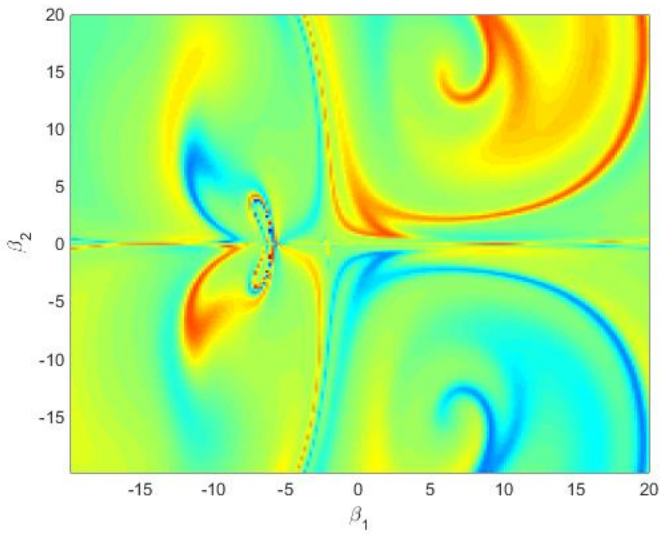

Figure 7. The BSA of the system (8) with the parameter set A.

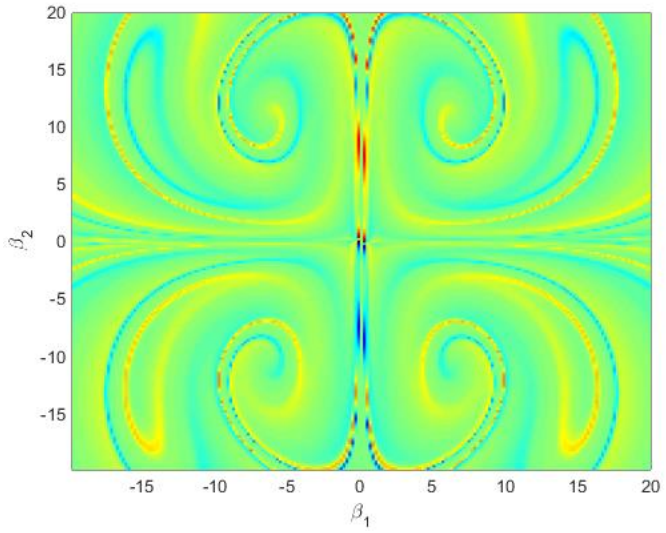

Figure 8. The BSA of the system (8) with the parameter set B.

4. The Fractional-Order Multi-Scroll Chaotic System via the ELCFDO

The fractional-order version of the system (8) via the ELCFDO is given by

$$\begin{aligned} {}_{C}^{E}O_{0+}^{q,\eta}\beta_1 &= c - d\beta_1 - \beta_2\beta_3, \\ {}_{C}^{E}O_{0+}^{q,\eta}\beta_2 &= a\beta_2 + \beta_1\beta_3, \quad q \in (0,1). \\ {}_{C}^{E}O_{0+}^{q,\eta}\beta_3 &= b\beta_3 + \beta_1\beta_2, \end{aligned} \tag{12}$$

Since the ELCFDO is a linear operator, we obtain ${}_{C}^{E}O_{0+}^{q,\eta}(-\beta_i(t)) = -{}_{C}^{E}O_{0+}^{q,\eta}(\beta_i(t))$, $i = 1,2,3$. So, the multi-scroll chaotic system (12) is symmetrical about the $\beta_i - axis$, $i = 1,2,3$ due to the invariance of this system under the transforms $(\beta_1,\beta_2,\beta_3) \to (\beta_1,-\beta_2,-\beta_3)$, $(\beta_1,\beta_2,\beta_3) \to (-\beta_1,\beta_2,-\beta_3)$, and $(\beta_1,\beta_2,\beta_3) \to (-\beta_1,-\beta_2,\beta_3)$.

Then, numerical simulations based on the modified PECE scheme [27] are carried out for the system (12) using the parameter sets A and B. Throughout the simulations, the selection of initial values $(\beta_{10},\beta_{20},\beta_{30}) = (0.1,0.1,0.1)$ and $(\beta_{10},\beta_{20},\beta_{30}) = (0.1,0.1,-0.1)$ are used for the upper attractors (red domain) and the lower attractors (blue domain), respectively. In Figure 9, coexisting upper and lower one-scroll chaotic attractors and approximate periodic cycles are shown. In Figure 10, different types of coexisting upper and lower two-scroll chaotic attractors with different intensities are depicted.

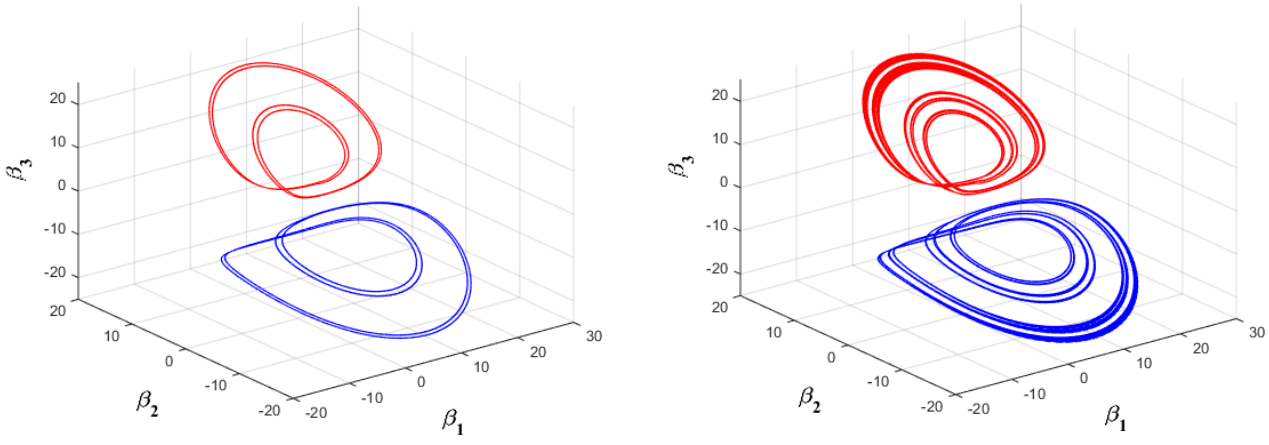

(**a**) (**b**)

Figure 9. Phase plots of the multi-scroll chaotic system (12) with the set A, q = 0.99 and (**a**) η = 1.0, and (**b**) η = 4.12.

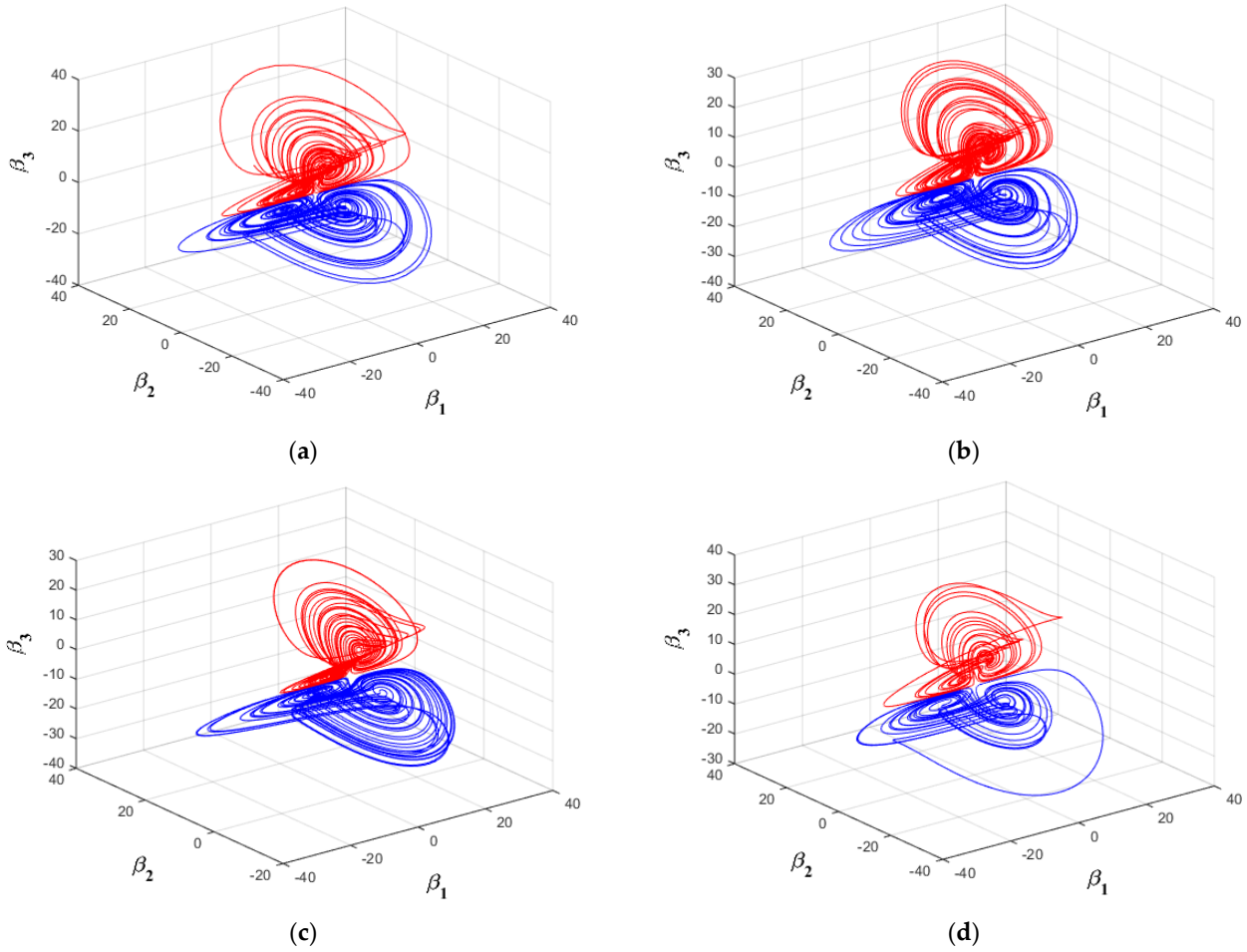

Figure 10. Phase plots of the multi-scroll chaotic system (12) with the set B, q = 0.99 and (**a**) η = 1.05, (**b**) η = 1.0, (**c**) η = 0.9, and (**d**) η = 0.5.

The bifurcation diagrams for system (12) are obtained via the local maxima algorithm to confirm the existence of a wide range of chaotic dynamics. The results are depicted in Figures 11–14.

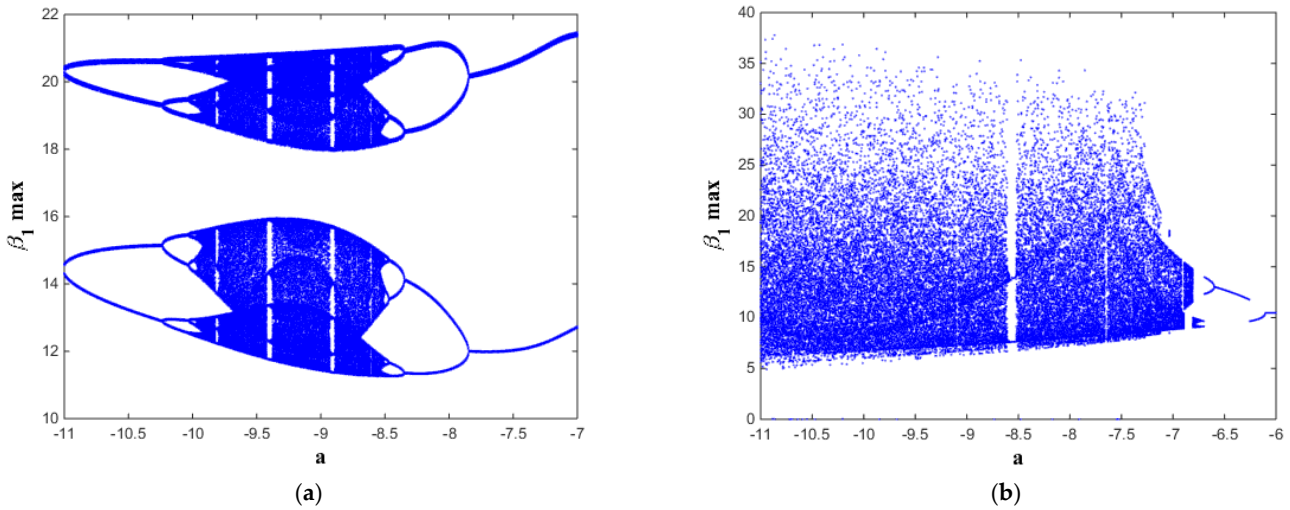

Figure 11. The bifurcation diagram of the system (12) with varying a, setting q = 0.99 and using (**a**) the parameter set A, η = 4.12, and (**b**) the parameter set B, η = 1.05.

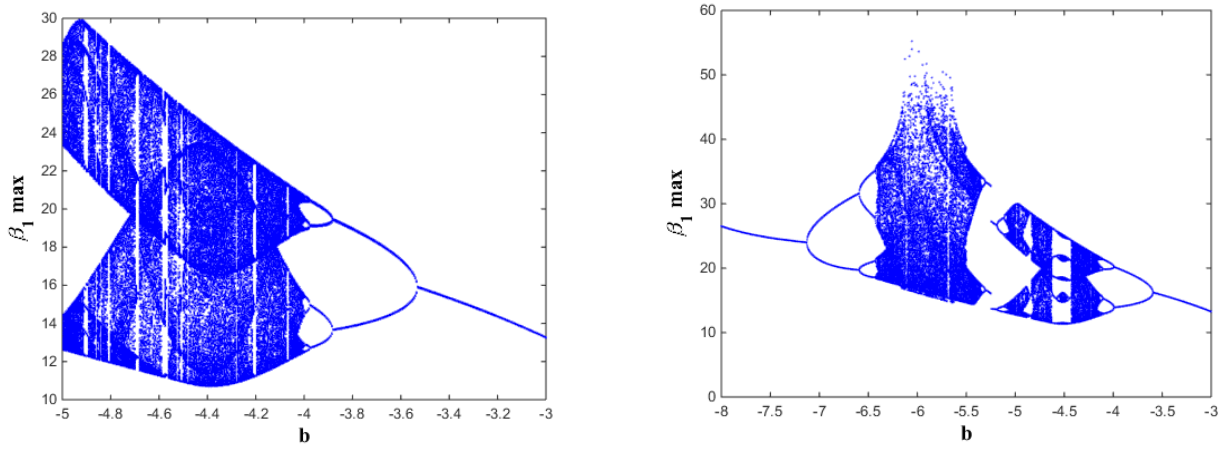

Figure 12. The bifurcation diagram of the system (12) with varying b, setting q = 0.99 and using (**a**) the parameter set A, η = 4.12, and (**b**) the parameter set B, η = 1.05.

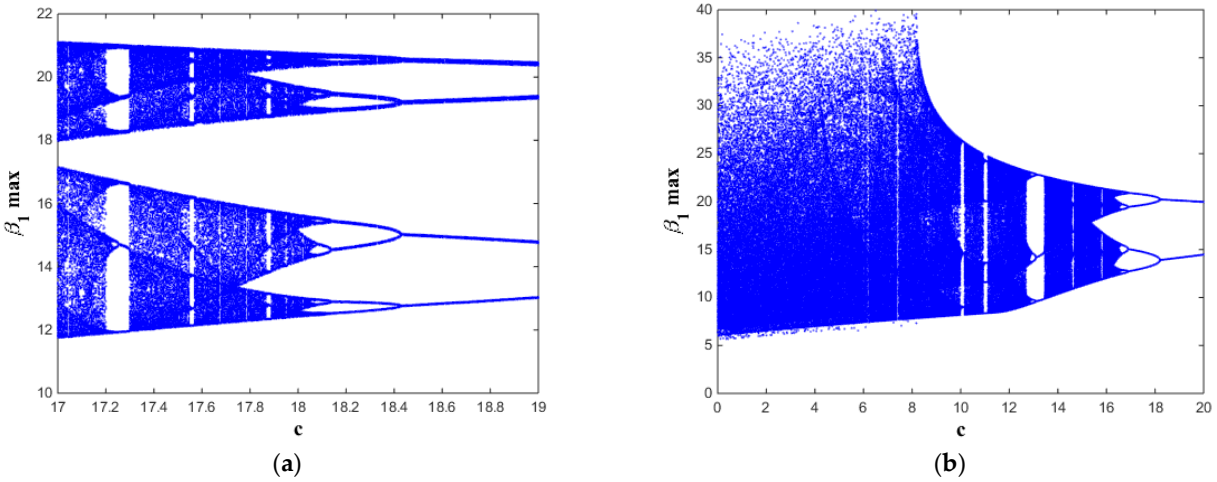

Figure 13. The bifurcation diagram of the system (12) with varying c, setting q = 0.99 and using (**a**) the parameter set A, η = 4.12, and (**b**) the parameter set B, η = 1.05.

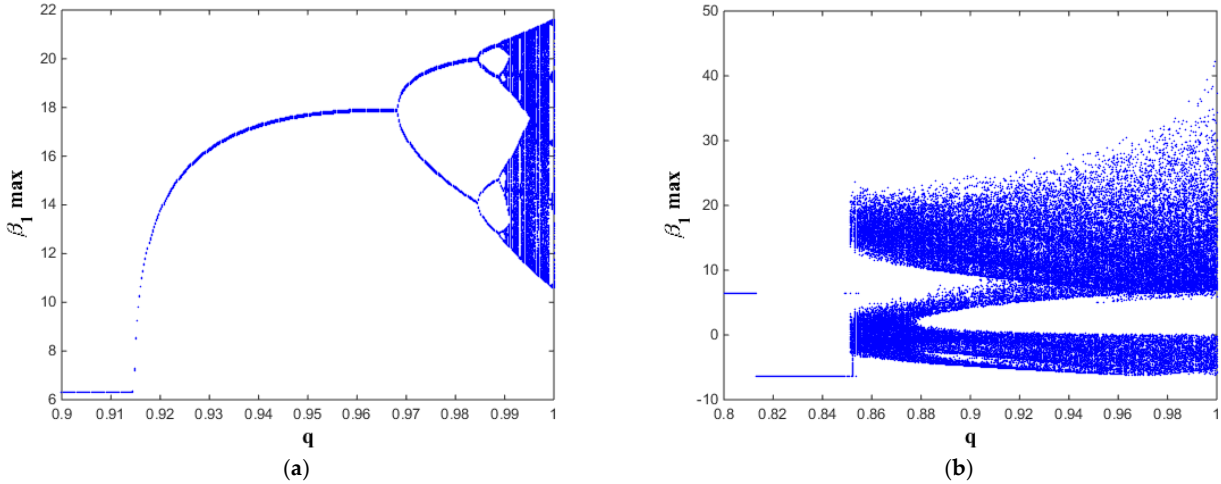

Figure 14. The bifurcation diagram of the system (12) with varying q and using (**a**) the parameter set A, η = 4.12, and (**b**) the parameter set B, η = 1.05.

On the other hand, the Les are calculated based on the numerical algorithm in Ref. [25]. Furthermore, the Lyapunov spectra of the system (12) are also obtained to confirm the existence of such wide regions of chaotic dynamics. Then, the results are depicted in Figures 15–18.

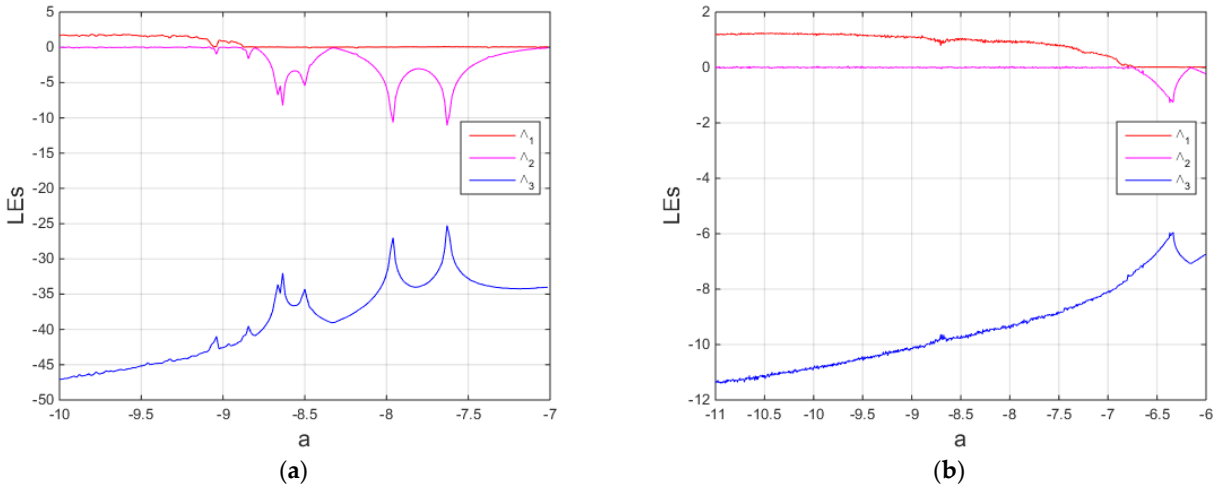

Figure 15. The Lyapunov spectrum of the system (12) with varying a, setting q = 0.99 and using (**a**) the parameter set A, η = 4.12, and (**b**) the parameter set B, η = 1.05.

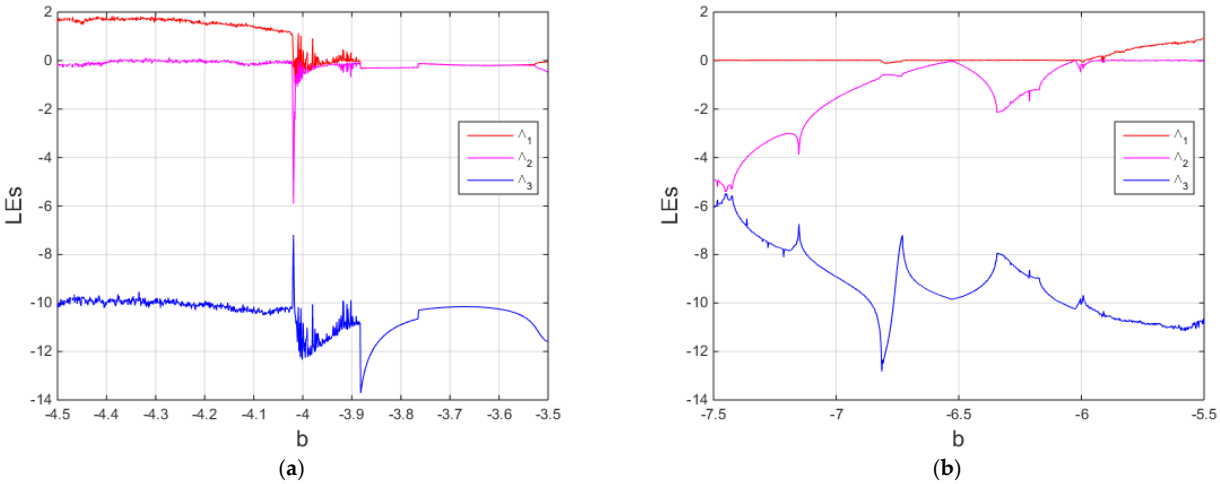

Figure 16. The Lyapunov spectrum of the system (12) with varying b, setting q = 0.99 and using (**a**) the parameter set A, η = 4.12, and (**b**) the parameter set B, η = 1.05.

The region of chaotic dynamics in the system (12) can be illustrated via the bifurcation diagrams and the Les as follows. In Figure 11, chaotic dynamics exist when $-11 < a \leq -8.9$ (see Figure 11a) and exist when $-11 \leq a \leq -7$ (see Figure 11b). In Figure 12, chaotic dynamics exist when $-5 \leq b < -4$ (see Figure 12a) and exist when $-6.5 < b < -5.7$, and $-5.7 < b < -4.1$ (see Figure 12b). In Figure 13, chaotic dynamics exist when $17 < c \leq 17.2$, and $17.3 < c \leq 18$ (see Figure 13a) and exist when $0 \leq c < 13$, and $13 < c \leq 17$ (see Figure 13b). In most corresponding cases, except Figures 2a and 12a observe that the chaotic dynamics in the multi-scroll chaotic system involving the ELCFDO are displayed in shorter ranges when compared with the system's integer-order form. Furthermore, the approximate periodic cycles in Figure 12a exist in a shorter range than the corresponding periodic orbits in Figure 2a. Thus, the ELCFDO can be implemented to shorten the complex dynamics in this system using a suitable choice of the new fractional parameter η.

Figure 19 is carried out to confirm the existence of a higher degree of unpredictability and complexity of basins' structures in the system (12). In Figure 19a, the blue and the

red regions refer to the coexisting two approximate period 4 cycles. In Figure 19b, the coexisting two approximate higher periodic cycles are characterized by the dotted line and the dotted turquoise regions.

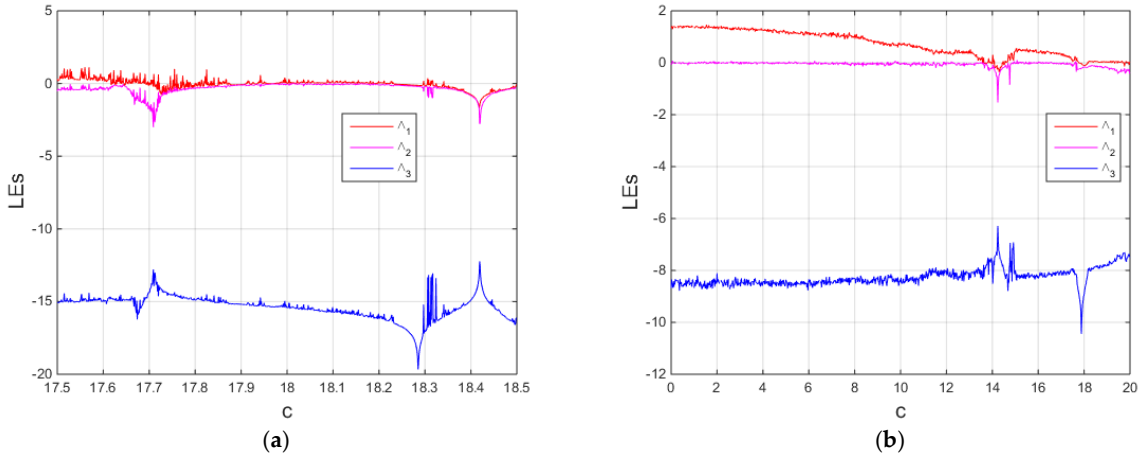

Figure 17. The Lyapunov spectrum of the system (12) with varying c, setting q = 0.99 and using (**a**) the parameter set A, η = 4.12, and (**b**) the parameter set B, η = 1.05.

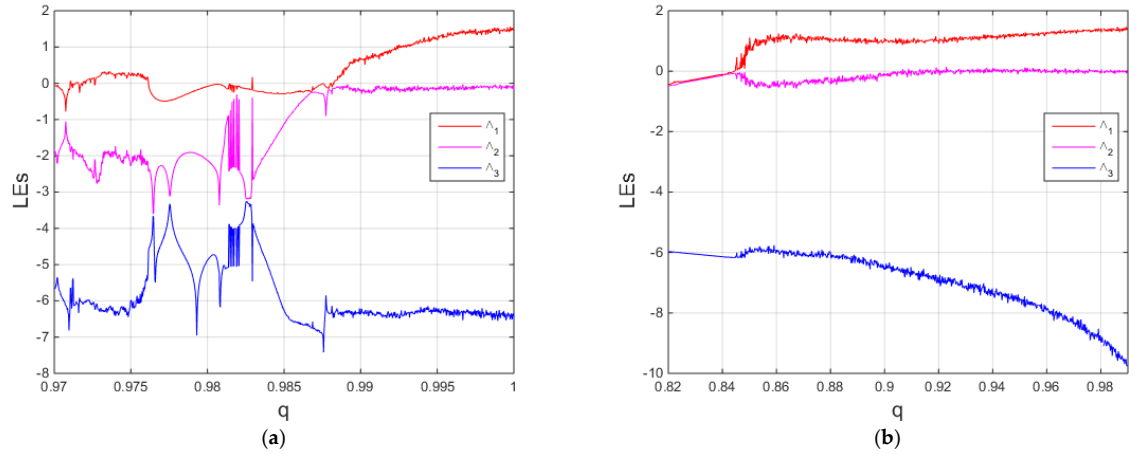

Figure 18. The Lyapunov spectrum of the system (12) with varying q and using (**a**) the parameter set A, η = 1.18, and (**b**) the parameter set B, η = 1.05.

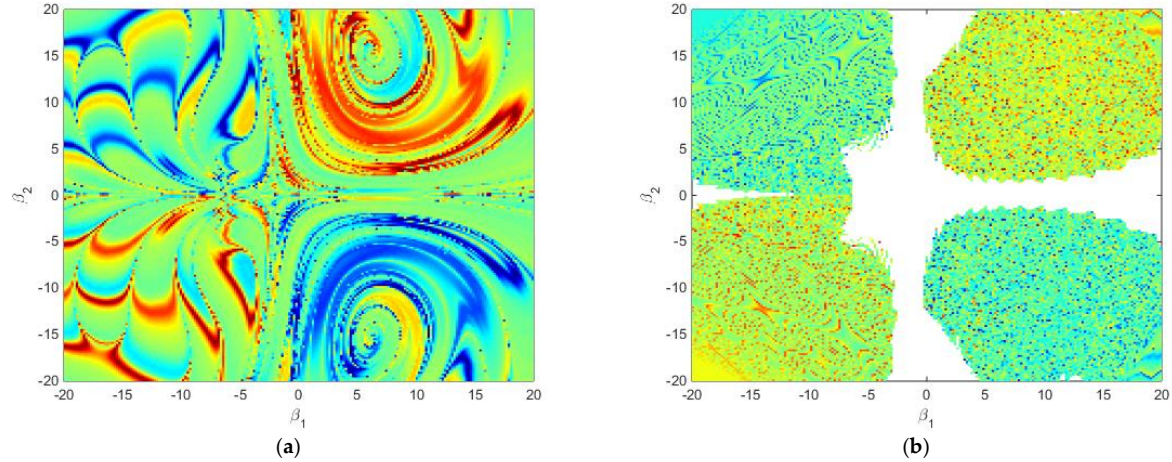

Figure 19. The BSA of the system (12) with the parameter set A q = 0.99 and using (**a**) η = 1, and (**b**) η = 4.12.

5. Conclusions

The ERCFDO and ELCFDO have been presented, and some related mathematical relations have been provided. Complex dynamics have been found in the fractional multi-scroll chaotic system using the ELCFDO. It has been found that the new parameter of the ELCFDO helps the multi-scroll chaotic system to exhibit more complex dynamics that cannot be found in its counterpart with the classic LCFDO. As an illustration, a wide array of complex dynamics are achieved, encompassing coexisting one-scroll chaotic attractors, coexisting two-scroll chaotic attractors, and approximate periodic cycles. Furthermore, advanced measures of DS such as the bifurcation diagrams, basin sets of attraction, and Lyapunov spectra have been utilized to confirm the existence of the complex dynamics in the multi-scroll chaotic systems.

Throughout this article, some comparisons have been performed by demonstrating the systems' bifurcation diagrams and calculating the systems' LEs, which illustrate that full scenarios of complex dynamics in the multi-scroll chaotic system involving the ELCFDO persist in a shorter range as compared with the corresponding states of the system's integer-order counterpart. Moreover, the higher degree of freedom in the case of the ELCFDO increases the system's ability to display more varieties of complex dynamics than the corresponding CFDO case. The summary of such results indicates that the ELCFDO is a better choice to describe the complex dynamics of the multi-scroll chaotic system.

Future studies can be extended to implement microcontroller-based circuits based on the multi-scroll chaotic system involving the ELCFDO, which may be useful in real digital engineering applications such as secure communication. Studying chaos control and synchronization in the multi-scroll chaotic system involving the ELCFDO are also two main points of interest for future works.

Author Contributions: Conceptualization, A.E.M.; Methodology, A.E.M.; Software, A.E.M.; Formal analysis, A.E.M.; Investigation, A.E.M.; Resources, A.E.M.; Data curation, A.E.M.; Writing—original draft, D.K.A., M.A.E.H., M.A.A. and T.N.A. All authors have read and agreed to the published version of the manuscript.

Funding: This research was funded by Deputyship for Research & Innovation, Ministry of Education in Saudi Arabia, grant number IFP-2022-31.

Institutional Review Board Statement: Not applicable.

Informed Consent Statement: Not applicable.

Data Availability Statement: Not applicable.

Acknowledgments: The authors extend their appreciation to the Deputyship for Research & Innovation, Ministry of Education in Saudi Arabia, for funding this research work through the project number (IFP-2022-31).

Conflicts of Interest: The authors declare no conflict of interest. The funders had no role in the design of the study; in the collection, analyses, or interpretation of data; in the writing of the manuscript; or in the decision to publish the results.

References

1. Ahmed, E.; Elgazzar, A.S. On fractional order differential equations model for non-local epidemics. *Phys. A* **2007**, *379*, 607–614. [CrossRef] [PubMed]
2. Abbas, S.; Nazar, M.; Nisa, Z.U.; Amjad, M.; El Din, S.M.; Alanzi, A.M. Heat and Mass Transfer Analysis of MHD Jeffrey Fluid over a Vertical Plate with CPC Fractional Derivative. *Symmetry* **2022**, *14*, 2491. [CrossRef]
3. Kumar, A.; Alzaid, S.S.; Alkahtani, B.S.T.; Kumar, S. Complex Dynamic Behaviour of Food Web Model with Generalized Fractional Operator. *Mathematics* **2022**, *10*, 1702. [CrossRef]
4. Zenkour, A.; Abouelregal, A. Fractional thermoelasticity model of a 2D problem of mode-I crack in a fibre-reinforced thermal environment. *J. Appl. Comput. Mech.* **2019**, *5*, 269–280. [CrossRef]
5. Abouelregal, A.; Ahmad, H. A Modified Thermoelastic Fractional Heat Conduction Model with A Single-Lag and Two Different Fractional-Orders. *J. Appl. Comput. Mech.* **2021**, *7*, 1676–1686. [CrossRef]

6. Matignon, D. Stability results for fractional differential equations with applications to control processing. In Proceedings of the Computational Engineering in Systems and Application Multi-Conference, IMACS, IEEE-SMC Proceedings, Lille, France, 9–12 July 1996; Volume 1, pp. 963–968.
7. Matouk, A.E. Chaotic attractors that exist only in fractional-order case. *J. Adv. Res.* **2023**, *45*, 183–192. [CrossRef]
8. Matouk, A.E. Applications of the generalized gamma function to a fractional-order biological system. *Heliyon* **2023**, *9*, e18645. [CrossRef]
9. Laskin, N. Fractional market dynamics. *Phys. A* **2000**, *287*, 482–492. [CrossRef]
10. Caputo, M. Linear Models of Dissipation whose Q is almost Frequency Independent—II. *Geophys. J. R. Astron. Soc.* **1967**, *13*, 529–539. [CrossRef]
11. Lorenz, E.N. Deterministic nonperiodic flow. *J. Atmos. Sci.* **1963**, *20*, 130–141. [CrossRef]
12. Rössler, O.E. An equation for continuous chaos. *Phys. Rev. A* **1976**, *57*, 397–398. [CrossRef]
13. Chua, L.O.; Lin, G.-N. Canonical realization of Chua's circuit family. *IEEE Trans. Circuits Syst.* **1990**, *37*, 885–902. [CrossRef]
14. Chen, G.; Ueta, T. Yet another chaotic attractor. *Int. J. Bifurc. Chaos* **1999**, *9*, 1465–1466. [CrossRef]
15. Liu, C.; Liu, T.; Liu, L.; Liu, K. A new chaotic attractor. *Chaos Solitons Fractals* **2004**, *22*, 1031–1038. [CrossRef]
16. Grigorenko, I.; Grigorenko, E. Chaotic Dynamics of the Fractional Lorenz System. *Phys. Rev. Lett.* **2003**, *91*, 034101. [CrossRef] [PubMed]
17. Hartley, T.T.; Lorenzo, C.F.; Qammer, H.K. Chaos in a fractional order Chua's system. *IEEE Trans. Circuits Syst. I* **1995**, *42*, 485–490. [CrossRef]
18. Li, C.P.; Peng, G.J. Chaos in Chen's system with a fractional order. *Chaos Solitons Fractals* **2004**, *22*, 443–450. [CrossRef]
19. Li, C.G.; Chen, G. Chaos and hyperchaos in the fractional-order Rössler equations. *Phys. A* **2004**, *341*, 55–61. [CrossRef]
20. Tavazoei, M.S. A note on fractional-order derivatives of periodic functions. *Automatica* **2010**, *46*, 945–948. [CrossRef]
21. Lü, J.; Chen, G.; Cheng, D. A new chaotic system and beyond: The generalized lorenz-like system. *Int. J. Bifurc. Chaos* **2004**, *14*, 1507–1537. [CrossRef]
22. Vanecek, A.; Celikovsky, S. *Control Systems: From Linear Analysis to Synthesis of Chaos*; Prentice-Hall: London, UK, 1996.
23. Haken, H. At least one Lyapunov exponent vanishes if the trajectory of an attractor does not contain a fixed point. *Phys. Lett. A* **1983**, *94*, 71–72. [CrossRef]
24. Wolf, A.; Swift, J.B.; Swinney, H.L.; Vastano, J.A. Determining Lyapunov exponents from a time series. *Phys. D Nonlinear Phenom.* **1985**, *16*, 285–317. [CrossRef]
25. Danca, M.-F.; Kuznetsov, N. Matlab Code for Lyapunov Exponents of Fractional-Order Systems. *Int. J. Bifurc. Chaos* **2018**, *28*, 1850067. [CrossRef]
26. Agarwal, S.K.; Kalla, S.L. A generalized gamma distribution and its application in reliability. *Commun. Statist. Theory Meth.* **1996**, *25*, 201–210. [CrossRef]
27. Matouk, A.E.; Bachioua, L. Rich complex dynamics in new fractional-order hyperchaotic systems using a modified Caputo operator based on the extended Gamma function. *Part. Diff. Equat. Appl. Math.* **2022**, *6*, 100458. [CrossRef]
28. Matouk, A.E.; Bachioua, L. Chaotic dynamics in some fractional predator–prey models via a new Caputo operator based on the generalised Gamma function. *Chaos Solitons Fractals* **2023**, *166*, 112946. [CrossRef]

Disclaimer/Publisher's Note: The statements, opinions and data contained in all publications are solely those of the individual author(s) and contributor(s) and not of MDPI and/or the editor(s). MDPI and/or the editor(s) disclaim responsibility for any injury to people or property resulting from any ideas, methods, instructions or products referred to in the content.

symmetry

MDPI

Article

Spontaneous Symmetry Breaking in Systems Obeying the Dynamics of On–Off Intermittency and Presenting Bimodal Amplitude Distributions

Stelios M. Potirakis [1,2,*], Pericles Papadopoulos [1], Niki-Lina Matiadou [1], Michael P. Hanias [3], Stavros G. Stavrinides [3], Georgios Balasis [2] and Yiannis Contoyiannis [1]

[1] Department of Electrical and Electronics Engineering, University of West Attica, 12244 Athens, Greece; ppapadop@uniwa.gr (P.P.); lmatiadou@uniwa.gr (N.-L.M.); yiaconto@uniwa.gr (Y.C.)
[2] Institute for Astronomy, Astrophysics, Space Applications and Remote Sensing, National Observatory of Athens, Metaxa and Vasileos Pavlou, 15236 Athens, Greece; gbalasis@noa.gr
[3] Department of Physics, International Hellenic University, 65404 Kavala, Greece; mhanias@physics.ihu.gr (M.P.H.); s.stavrinides@ihu.edu.gr (S.G.S.)
* Correspondence: spoti@uniwa.gr

Abstract: In this work, first, it is confirmed that a recently introduced symbolic time-series-analysis method based on the prime-numbers-based algorithm (PNA), referred to as the "PNA-based symbolic time-series analysis method" (PNA-STSM), can accurately determine the exponent of the distribution of waiting times in the symbolic dynamics of two symbols produced by the 3D Ising model in its critical state. After this numerical verification of the reliability of PNA-STSM, three examples of how PNA-STSM can be applied to the category of systems that obey the dynamics of the on–off intermittency are presented. Usually, such time series, with on–off intermittency, present bimodal amplitude distributions (i.e., with two lobes). As has recently been found, the phenomenon of on–off intermittency is associated with the spontaneous symmetry breaking (SSB) of the second-order phase transition. Thus, the revelation that a system is close to SSB supports a deeper understanding of its dynamics in terms of criticality, which is quite useful in applications such as the analysis of pre-earthquake fracture-induced electromagnetic emission (also known as fracture-induced electromagnetic radiation) (FEME/FEMR) signals. Beyond the case of on–off intermittency, PNA-STSM can provide credible results for the dynamics of any two-symbol symbolic dynamics, even in cases in which there is an imbalance in the probability of the appearance of the two respective symbols since the two symbols are not considered separately but, instead, simultaneously, considering the information from both branches of the symbolic dynamics.

Keywords: 3D Ising model; on–off intermittency; symbolic dynamics; dynamical systems; prime numbers; fracture-induced electromagnetic emissions/radiation (FEME/FEMR); nano-MOSFET

1. Introduction

In a series of works [1,2], it has been shown that the use of a device with circular rings carrying electric currents of the same intensity but in a random flow direction results in a symmetrical stratified magnetic field, i.e., a magnetic field that presents a zonal structure around an axis of symmetry. Furthermore, using the most recently introduced prime-numbers-based algorithm (PNA) to simulate the magnetic field of the specific device [3], the quantization of the above-mentioned stratified magnetic field is achieved, i.e., the magnetic field values' zones can be converted to quantized magnetic field values. Thus, if a two-symbol symbolic time series (using, for example, the symbols "+1", "−1") is employed to determine the flow directions of the rings' currents, a time-to-space mapping of the dynamics of the system producing the time series, is achieved [3]. This mapping enables the calculation of the exponents of the "waiting times" distributions in the space of

the magnetic field positions, "k," leading to the development of the method of symbolic time-series analysis referred to as the PNA-based symbolic-time-series-analysis method (PNA-STSM) [3]). The PNA-STSM can be applied to any two-symbol symbolic time series that is produced directly or indirectly (after coarse-graining) by any real or numerical dynamic system and presents the advantage that it can reliably expose the real dynamics of a complex system, even if a relatively short time series is available and the probabilities of the occurrence of each of the two symbols are not equal [3].

Waiting times are essential because their distribution can reveal the dynamics of the system generating the time series under analysis [3]. For example, if the distribution of the waiting times follows a power law with the exponent $p \in [1, 2)$, this is a strong indication that the system is in its critical state [4]. On the other end of the dynamical spectrum, the presence of exponential laws in these distributions suggests the complete absence of dynamics that create long scales; in such cases, long scales are truncated [5]. Between these two extremes of the dynamics spectrum, any intermediate state can be quantitatively determined from the competition of these two extreme cases (power law and exponential distributions).

Furthermore, waiting times can be defined in different ways. For example, in time series resulting from intermittent dynamics, the waiting times, also called laminar lengths [6], are defined as the time intervals between bursts, namely, the number of consecutive values of the time series that fall within specific thresholds that define the boundaries of a non-burst (laminar) values' region. In a sequence of symbols, such as the symbolic dynamics of the symbols "+1" and "-1", the waiting times are defined as the number of the same consecutive symbols (e.g., "+1"), which are interrupted by a number of consecutive appearances of the other symbol (e.g., "-1"), or vice versa. A key difference from the above-mentioned time domain (waiting-time-based) analysis approaches is that PNA-STSM introduces a space-domain analog of waiting times, called "k waiting lengths," which takes into account both symbols' dynamics.

The first part of this work shows that PNA-STSM is an analysis method capable of correctly estimating the exponents characterizing the dynamics embedded in a time series. This is proven by comparing the results obtained by PNA-STSM with the results obtained by other well-known and reliable methods, as well as with the theoretical results for the 3D Ising model in the critical state. Subsequently, the main advantages of PNA-STSM over other analysis methods are highlighted. Three examples of dynamical systems are employed to demonstrate the efficacy of PNA-STSM. The first is a numerical example and refers to a special behavior of the 3D Ising model, and the second is from the area of nano-electronics, and the third concerns earthquake (EQ)-preparation processes. The common behaviors of these three systems are that they all obey the dynamics of on–off intermittency (of various forms) and that they all present bimodal (two-lobe) amplitude distributions, which, as has recently been shown [7], appears to be connected with the spontaneous symmetry breaking (SSB) phenomenon observed in the preparation of the second-order phase transition in finite systems. Through these examples, it is shown how to apply the PNA-STSM to systems that obey the dynamics of on–off intermittency and present bimodal amplitude distributions in order to extract the information on their critical state and the SSB. Moreover, it is demonstrated that beyond on–off intermittency, PNA-STSM can provide credible results for the dynamics of any two-symbol symbolic-dynamics time series or for general two-symbol sequences because it is not affected by any imbalances in the probability of the appearance of the two symbols, since it simultaneously considers the information from both branches of the symbolic dynamics.

2. The 3D Ising Model and Its Waiting Times

The 3D Ising model is a well-known model in statistical mechanics describing specific ferromagnetic behavior [8,9]. It successfully describes the continuous phase transition in equilibrium, as well as more specialized topics, such as the SSB of the φ^4 Landau free energy [10]. According to the theory of critical phenomena, all natural systems are

classified into universality classes that are characterized by the values of the so-called critical exponents. The 1D Ising model has been analytically solved by Ernst Ising [11] and does not present phase transition for any finite temperature. Likewise, the 2D Ising model has been analytically solved by Onsager [12], and the six critical exponents of this model have been accurately calculated. Finally, the 3D Ising model has not been solved analytically yet, but only numerical solutions have been provided. However, it must be mentioned that in [13], and under suitable boundary conditions, the 3D Ising model can be described by the operator algebra and thus can be solved exactly. This theory has been studied using renormalization group methods, Monte-Carlo simulations, conformal bootstrap and other techniques [8,9,14,15].

Generally speaking, for a Z(N) spin system, spin variables are defined as: $s(a_i) = e^{i2\pi a_i/N}$ (lattice vertices $i = 1, \ldots, i_{max}$), with $a_i = 0, 1, 2, 3, \ldots, N-1$. For $N = 2$, one may derive the above-mentioned Ising models. Utilizing the Metropolis algorithm configurations at constant temperatures may be selected with Boltzmann statistical weights $e^{-\beta\mathcal{H}}$, where $\mathcal{H}$ is the Hamiltonian of the spin system for which the nearest neighbors' interactions without external field can be written as:

$$\mathcal{H} = -\sum_{<i,j>} J_{ij} s_i s_j, \;\; s_j, \; s_j = \pm 1. \tag{1}$$

It is known that this model undergoes a second-order phase transition when the temperature drops below a critical value [10,16]. Thus, for a lattice of 20^3 nodes in three dimensions (3D Ising model), the critical (or pseudocritical for finite-size lattices) temperature has been found to be $T_c = 4.545$ ($J_{ij} = 1$). Considering the sweep of the whole lattice as an algorithmic time unit, the possible values that spin can have in the model are ± 1. The quantity recorded in a numerical experiment (conducted using the Metropolis algorithm) is the mean magnetization (space averaged magnetization density) M, which plays the role of the order parameter. The trajectory generated by the numerical experiment is a "time series" of the fluctuations of the order parameter. This means that for a simulation performed for N_{iter} lattice sweeps, the generated time series of M will consist of N_{iter}-points, with a time step equal to the algorithmic time of the whole lattice sweep. Figure 1 presents the distribution of the resulting mean magnetization M values at the pseudocritical point $T_c = 4.545$ for $N_{iter} = 200{,}000$.

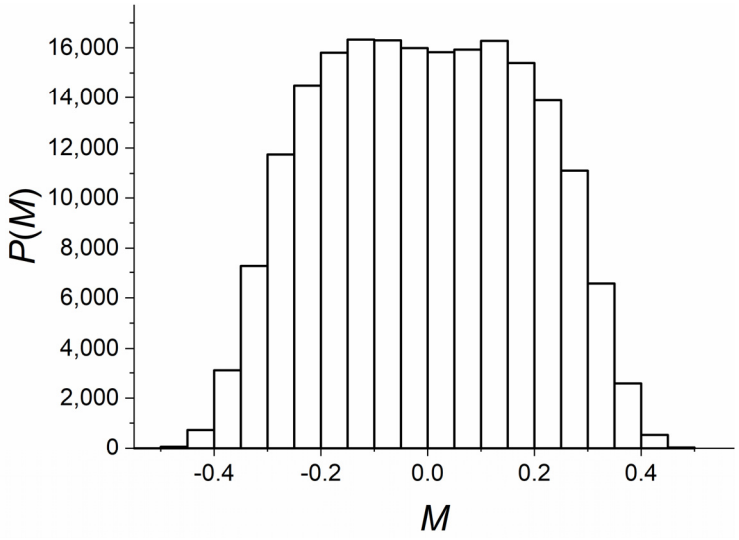

Figure 1. The distribution of the mean magnetization values obtained from 200,000 configurations of a 20^3 3D Ising lattice at the pseudocritical temperature $T_c = 4.545$.

Calculating the distribution of waiting times (see Section 1), one may extract useful and important quantitative information about the dynamics of the studied system. In

the cases that this distribution turns out to be a scale-free function (i.e., a power law), the signature of the critical state of the system could be revealed. Therefore, the correct calculation of waiting times is of great importance. As it has been shown in [4,17], the fluctuations of the order parameter at the critical point follow the dynamics of Type I intermittency, for which it is known that the distribution $P(L)$ of the appropriately defined waiting times L (laminar lengths, see Section 1) follows a power law of the form [6]:

$$P(L) \sim L^{-p} . \tag{2}$$

As shown in [4], the exponent p is related to the isothermal critical exponent δ, as:

$$p = 1' + \frac{1}{\delta} , \tag{3}$$

while it holds that $\Gamma(M) \sim M^{\delta+1}$ [4], where $\Gamma(M)$ is the effective action for the mean magnetization. It is also mentioned that the exponent p is related to other well-known exponents through the isothermal critical exponent δ (one of the six critical exponents, related one another through four relations, known as "scaling laws" [16]). Moreover, it has been shown that p is related to the spectral exponent, the Hurst exponent, and the fractal dimension [18], as well as to the exponent describing Lévy flights and the Tsallis non-extensive parameter q [19].

Since $\delta > 1$ [16], one may deduce from Equation (3) that the critical state exists when $p \in [1, 2)$. Beyond the critical point, another type of intermittency dynamics [20] that describe the dynamics of the order parameter fluctuations at the beginning of a tricritical crossover, has been found. This happens around the point where the second-order phase transition and the first-order phase transition lines meet in the parametric space of Ginzburg–Landau free energy (tricritical point according to Griffiths [16]). In this case, the exponent p of the power law distribution of laminar lengths is given as [4]:

$$p = \frac{\delta + 1}{\delta + 2} , \tag{4}$$

from which it follows that $p \in (0.66, 1)$ [21]. At this point, it should be mentioned that when the distribution of the waiting times follows a power law with an exponent $p \in (0,\ 0.66)$ it probably refers to some subcritical region without clear boundaries that can be predicted by the theory, and it does not indicate criticality (critical or tricritical point). In our analyses of dynamical systems, real and numerical, coming from different disciplines, we have not yet come across such a case.

In [4], the value of the exponent p for the critical 3D Ising model has been estimated with very good agreement with the one predicted from the theory of critical phenomena, using the notion of waiting times in a time series (see Section 1). Specifically, using the method of critical fluctuations (MCF) [4,22], which has been introduced for this purpose, it has been found that the exponent p obtains the value $p = 1.21 \pm 0.02$ for the critical 3D Ising model [4]. Exactly at the pseudocritical point, the characteristic exponent is the isothermal critical exponent δ. Notice that for the 3D Ising model this exponent has the value $\delta = 4.8$ [23]. Consequently, from Equation (4), the theoretical value of the exponent p is $p = 1.208$, and therefore, the value estimated using the MCF for the numerical experiment ($p = 1.21$) is in perfect agreement with the theoretical one.

Another way to calculate the exponent p of the distribution of the waiting times in the critical 3D Ising model is to resort to symbolic dynamics based on two symbols in the time domain. This can be achieved by appropriately converting the mean magnetization time series to a symbolic time series and then by defining the waiting times as the number of the same consecutive symbols (see Section 1). Given that the distribution of Figure 1 is almost symmetrical around $M = 0$, a straightforward way to obtain a two-state coarse-graining description of the mean magnetization value for the specific numerical experiment (as mentioned, 200,000 configurations of a 20^3 3D Ising lattice at the pseudocritical temperature

$T_c = 4.545$) is to assign positive and negative time series values to the symbols "+1" and "−1", respectively. Thus, the simulated mean magnetization time series is converted into a two-symbol symbolic time series. By calculating the waiting times of the obtained mean magnetization symbolic time series, one may create the distributions for each of the two symbols, which are shown in Figure 2. As in the MCF, one may employ the truncated power law function $g(L)$ for each symbol in order to model the distribution of waiting times $P(L)$:

$$g(L) = p_1 \cdot L^{-p_2} \cdot e^{-Lp_3}, \quad (5)$$

In the case that $p_3 = 0$, then p_2 is equal to the power law exponent p.

For the waiting times corresponding to the symbol "+1", their distribution indeed follows a power law with an exponent value $p = 1.159 \pm 0.017$ (Figure 2a); while for the waiting times corresponding to the symbol "−1", again a power law distribution holds, but this time with a different exponent value of $p = 1.182 \pm 0.026$ (Figure 2b). Apparently, these exponent values are not the same due to the small asymmetry between the two symbols, 49% ("+1"'s) vs. 51% ("−1"'s) probability of occurrence, which is reflecting the small asymmetry between the positive and negative values of the original mean magnetization time series (also 49% vs. 51%, see the distribution in Figure 1). It is also noted that considering the error limits, the "+1" branch leads to p values in the range between 1.142 and 1.176, while the "−1" branch leads to p values in the range between 1.156 and 1.208, which intersect one another. However, the resulting higher value for the "+1" branch (1.176) is close but lower than the nominal value of the "−1" branch (1.182). Thus, one cannot claim that the two nominal values (1.159 and 1.182) coincide within their error limits.

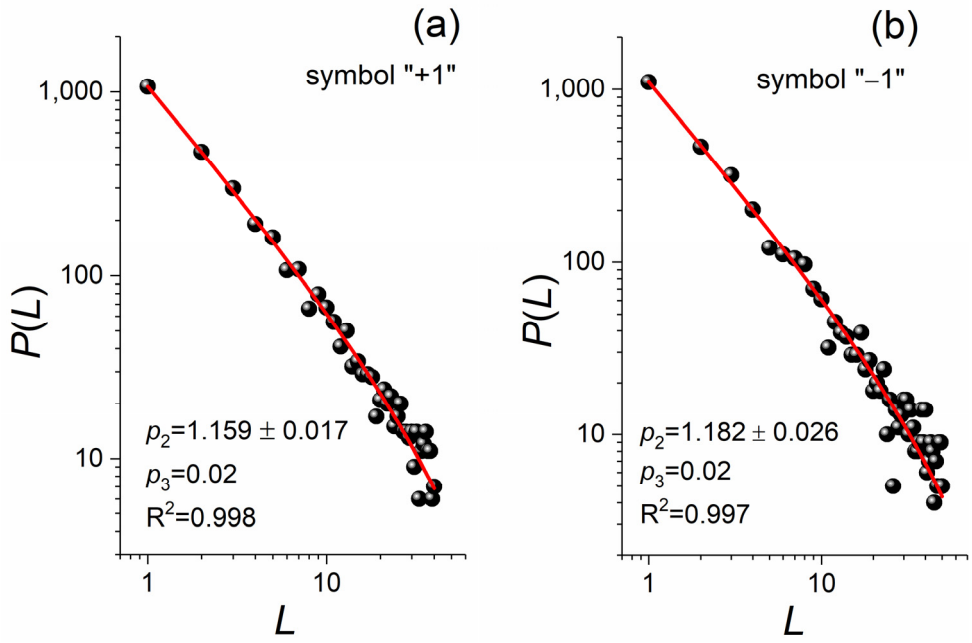

Figure 2. The distribution of the mean magnetization two-symbol symbolic sequence for waiting times at the (**a**) "+1", and (**b**) the "−1" symbol, respectively.

Summing up, based on the same numerical data of 200,000 configurations for a 20^3 lattice at the pseudocritical temperature $T_c = 4.545$, the MCF estimates for the exponent p a value of 1.21, whereas the waiting times analysis of the corresponding two-symbol symbolic time series in the time domain leads to two different exponent p values, 1.159 and 1.182, for each symbolic branch; while we know that for the 3D Ising model, the theoretically calculated value of the waiting times distribution's power law exponent is $p = 1.208$. From the above, it is clear that although the existence of dynamics in a 3D Ising two-symbol symbolic time series can be revealed in the time domain via the scaling behavior of the waiting times, the quantitative result is ambiguous, even for time series

with only a slight asymmetry in the distribution of their values, as has also been shown in [3] for the case of the 2D Ising model. Furthermore, the 3D Ising model case proves that this result is not only ambiguous but also far from the one theoretically calculated. However, it has been proven in [3] that PNA-STSM can overcome this ambiguity issue, even for time series of relatively short length, in which one of the symbols appears more often than the other. So, in Section 3, after a brief presentation of the key notions of the PNA-STSM, the case of the 3D Ising symbolic time series is analyzed using the PNA-STSM, leading not only to unambiguous but also accurate exponent p estimation.

3. Application of PNA-STSM to the Critical 3D Ising Model

3.1. The PNA-STSM Time Series Analysis Method

By briefly presenting the application of PNA-STSM in the case of a two-symbol symbolic time series, we use as an example the symbolic time series of the mean magnetization fluctuations of the critical 3D Ising model that has been presented in Section 2. For a detailed description of the PNA-STSM, one may refer to [3], while in the Appendix of [3], one may find a Fortran implementation of the main part of the method.

The block diagram depicted in Figure 3 schematically presents all stages of the PNA-STSM, which accepts as input any two-symbol symbolic time series directly or indirectly (after coarse-graining) produced by any real or numerical dynamical system.

In order to apply the PNA-STSM to the 3D Ising model at the pseudocritical temperature $T_c = 4.545$, one begins from the two-symbol symbolic time series obtained, as described in Section 2. The symbolic time series is fed to the "transformation" from the time domain (t) to the space domain (k), where k (see Figure 3) denotes the ring positions of the employed current carrying circular rings device of Figure 4. The electric currents are of the same intensity I, but their flow direction $(+I, -I)$ is determined by the corresponding symbol of the symbolic time series. Specifically, if the two-symbol symbolic time series is $\{x(t_i)\}$, $t_i = i \cdot \tau$, τ being the sampling period and $i = 1, 2, \ldots, N$, then for $i = k = 1$, if $x(t_1) = -1$, then $I_1 = -1$, while if $x(t_1) = +1$, then $I_1 = +1$, etc. This way, a mapping from the time domain (t) to the space domain (ring positions k) is achieved. Each resulting spatial pattern of the magnetic field is unique and determined by the respective symbolic dynamics of the driving time series.

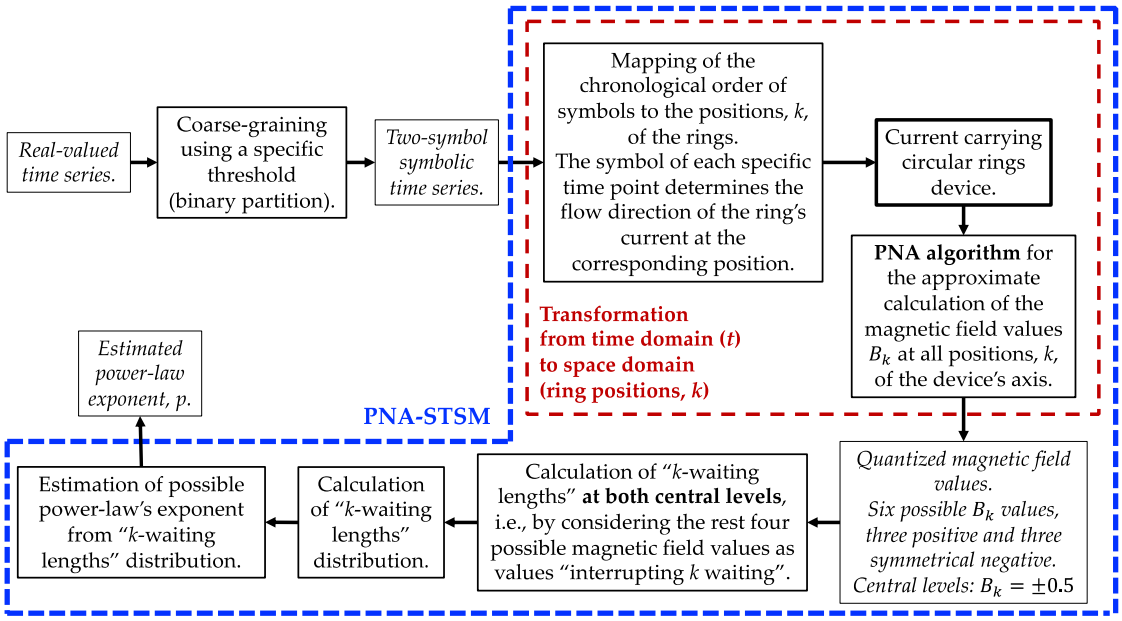

Figure 3. Block diagram schematically presenting the PNA-STSM.

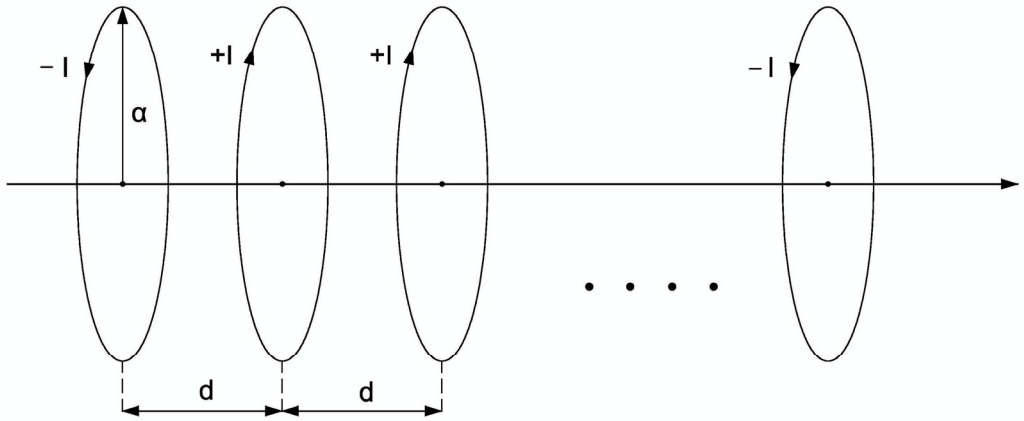

Figure 4. The device of identical rings carrying currents of the same intensity I, the flow direction of which $(+I, -I)$ is determined by the corresponding symbol of the driving time series [3]. The radius of the rings is α and the distance of two consecutive rings is d.

Each ring is circular, with radius α, d is the distance between two consecutive rings (Figure 4), while $c = a/d$ is a parameter determining the behavior of the device. Using the PNA algorithm, results in a quantized magnetic field of six values (three positive and three symmetric negative) in the case $c^2 \ll 1$, while if $c \ll 1$, only the central positive and negative ones $B_k = \pm 0.5$ remain in the pattern of the magnetic field [3]. Thus, these central values possess a special property since their existence does not depend on the value of the geometric characteristics of the device. On the other hand, as has been shown in [3], in each half-space of the quantized magnetic field (positive or negative), the probability of the appearance of a quantized magnetic field value at the central level, $B_k = +0.5$ or $B_k = -0.5$, is equal to the sum of the probabilities of the appearance of the quantized magnetic field values at the two other value levels of the corresponding half-space.

As already mentioned in Section 1, the PNA-STSM introduced a space domain analog of the waiting times called the "k waiting lengths". The latter are calculated by counting the number of consecutive ring positions for which the quantized magnetic field value remains equal to "the value of interest" [3]. The simultaneous choice of both central levels, $B_k = \pm 0.5$ as "the value of interest", respects the above-mentioned symmetry. This way, an equivalent description is obtained when ones considers either the distribution at both central levels or at the other four possible quantized magnetic field levels. This justifies the definition of the "k waiting lengths" as a representation of the dynamics of the alteration of the magnetic field between the central values $B_k = \pm 0.5$ and any of the other four (two positive and two negative) possible values (see Figure 3). Thus, when one calculates the "k waiting lengths" in the PNA-STSM, it practically counts the number of consecutive ring positions for which the quantized magnetic field value is either $B_k = +0.5$ or $B_k = -0.5$, thus taking into account the positive and the negative subspace of the symbolic dynamics in the space-domain, simultaneously [3].

The calculation of the "k waiting lengths" that considers both subspaces simultaneously is the most important choice in the PNA-STSM since it provides a single statistical representation of the inputted symbolic time series in the space domain. This way, any (even slight) asymmetry in the driving symbolic time series does not affect the obtained result. Namely, if the distribution of the "k waiting lengths" follows a power law, then the value of the power law exponent p estimated using PNA-STSM is unambiguous [3], in contrast to the time domain approach demonstrated for the 3D Ising case in Section 2.

Finally, it is mentioned that in all cases of the PNA-STSM application presented in the following sections, the following parameters have been used for the current carrying circular rings device: $a = 1$, $d = 10$, and $I = 1$. Therefore, $c = a/d = 0.1$ and $c^2 \ll 1$. Moreover, it should be mentioned that the time needed for carrying out the involved calculations appears to present a power law dependence on the length of the time series. However, the calculations are not particularly time-consuming, e.g., for a rather weak

personal computer (Intel® Core™2 Duo processor T5670, with clock speed 1.8 GHz, bus speed 800 MHz, and 4 GB DDR2 RAM @667 MHz) a 100,000-points-long time series takes only 1.25 min to be analyzed, whereas a 200,000-points-long time series takes less than 5 min to be analyzed.

3.2. Application of PNA-STSM to the Critical 3D Ising Model

In this section, we present the results obtained by the application of PNA-STSM to the two-symbol symbolic time series that was analyzed in the time domain in Section 2 ($N_{iter} = 200{,}000$ configurations in a 20^3 3D Ising lattice at the pseudocritical temperature $T_c = 4.545$). Figure 5a portrays a 1000-point segment of the 3D Ising mean magnetization time series $M(t)$ of the specific numerical experiment, while Figure 5b shows the corresponding quantized magnetic field pattern produced after the "transformation" of the corresponding two-symbol symbolic time series from the time domain (t) to the space-domain (k). Three positive and three symmetric negative magnetic field values were produced. The positive quantized values of the resulting magnetic field, calculated with an accuracy of four decimal points, are: $B_k = 0.500$, $B_k = 0.4988$, and $B_k = 0.5012$. Similarly, in the negative half-space, the corresponding negative ones appear. From Figure 5b, one can easily identify the existence of the same magnetic field value at consecutive positions (k), interrupted by gaps, during which the magnetic field gets one of the other possible quantized values.

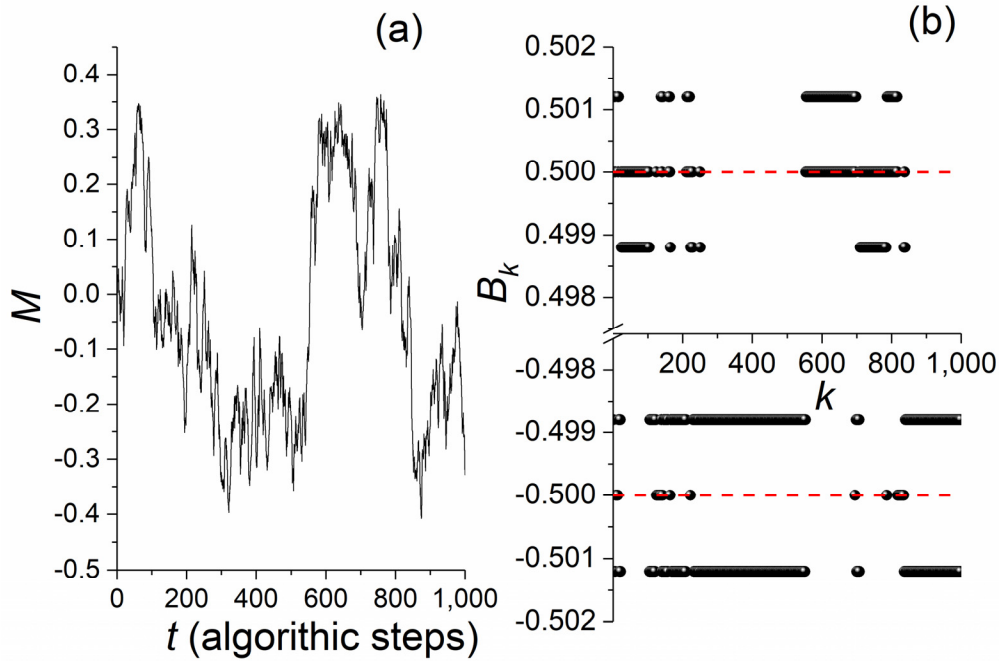

Figure 5. (**a**) Excerpt of the 3D Ising model real-valued mean magnetization time series that was analyzed using the PNA-STSM. (**b**) The corresponding quantized magnetic field values produced after the "transformation" from the time domain (t) to the space-domain (k). Red-colored dashed horizontal lines denote the central values $B_k = \pm 0.5$ at which the "k waiting lengths" are calculated according to the PNA-STSM.

For the calculation of the "k waiting lengths" distributions, the whole quantized magnetic field pattern in the space domain, i.e., for $k = 1, 2, \ldots, 200{,}000$, was used. Figure 6 presents the "k waiting lengths" distribution according to the PNA-STSM, i.e., by counting the number of consecutive ring positions for which the quantized magnetic field value is either $B_k = +0.5$ or $B_k = -0.5$, interrupted by magnetic field values at any of the other four possible levels of the produced spatial pattern. Since $p_3 \approx 0$ ($p_3 = 0.01$), the distribution of the "k waiting lengths" in Figure 6 actually follows a power law with exponent $p(= p_2) = 1.202 \pm 0.030$. Thus, by taking into account both positive and negative

branches, the PNA-STSM not only provides an unambiguous (a single power law exponent) but also an accurate result. Indeed, the estimated exponent's nominal value (1.202) is much closer to the theoretically calculated value ($p = 1.208$) of the 3D Ising model at the pseudocritical temperature than the two different power law exponent's nominal values that were calculated by analyzing the waiting times (time domain analysis) at each of the two symbols of the symbolic time series, i.e., 1.159 and 1.182 at "+1" and "−1", respectively (see Section 2). We also note that concerning the exponential factor of the fitting function of Equation (5), the time domain analysis resulted in $p_3 = 0.02$ for both symbols (see Figure 2), while the PNA-STSM led to a value for p_3 closer to zero $(p_3 = 0.01)$. It is apparent that the PNA-STSM-obtained distribution is closer to the power law.

Finally, it should be mentioned that the time domain analysis could lead to comparable results with the PNA-STSM only to the asymptotic limit $N_{iter} \to \infty$, for which the distribution of Figure 1 becomes perfectly symmetric. However, for real signals of finite length, this is impossible; there will always be, even slight, asymmetry. Thus, the time domain analysis of the waiting times at each of the symbols of such a two-symbol time series will always lead to different exponent values. On the other hand, the estimation of a single exponent as the average value of the two calculated exponents usually does not apply since the phenomena producing the symbolic dynamics may be strongly nonlinear. In such cases, the waiting times time domain analysis is generally leading to ambiguous and inaccurate results, rendering it inferior to the PNA-STSM.

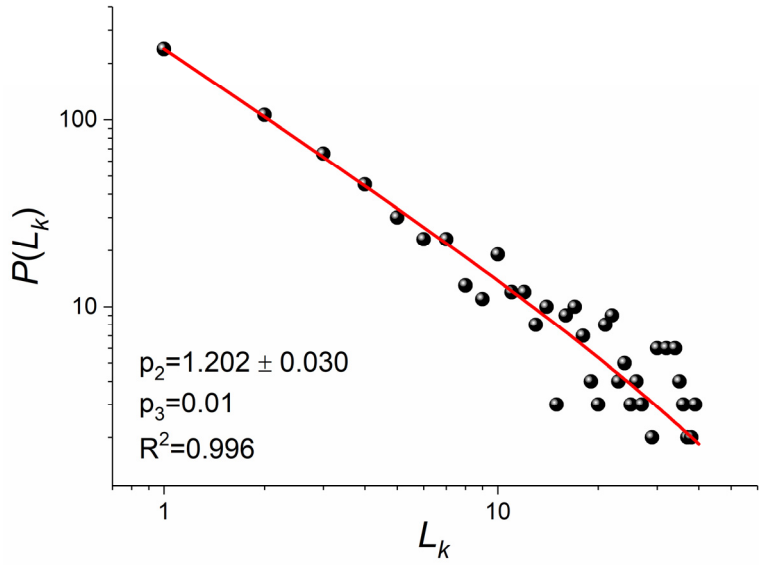

Figure 6. The distribution of the "k waiting lengths" L_k, for the central values ± 0.5 of the quantized magnetic field, according to the PNA-STSM. The fitting (red-colored line) was performed using the fitting function of Equation (5).

4. Analysis of Time Series Presenting Two-Lobes' Amplitude Distributions Using PNA-STSM

As has recently been shown [7,24] and according to the φ^4 theory, systems of finite size that undergo a second-order phase transition present a hysteresis zone between the pseudocritical point and the completion of the SSB, where the critical state continues to survive, also referred to as the "SSB-zone". Within this hysteresis zone, the single minimum of the Landau free energy, appearing at the value of the control parameter that corresponds to the symmetrical phase (pseudocritical point), is replaced by a degenerate set of minima. These minima "communicate" until the SSB is completed by appropriately changing the value of the control parameter. In terms of the distribution of the order parameter's values, this hysteresis zone is manifested by the change of the distribution form from unimodal (one lobe) to bimodal (two lobes). This happens because a fixed point (the Landau free energy minimum) attracts a high number of values of the order parameter close to it.

Thus, the appearance of the degenerate set of minima changes the form of the distribution to bimodal.

As the control parameter, which in thermal systems is the temperature, falls below the pseudocritical temperature, these lobes reduce their communication, and as soon as their complete separation is achieved, the SSB is completed. Essentially, it is a degeneration of the critical state, which continues as long as the temperature drops until the complete separation of the two lobes is completed [7].

Beyond thermal systems, the appearance of two lobes in the distribution of an observable is found in many natural systems and beyond. Then, the question raised for all these systems is whether they could be found in the conditions of the above-mentioned hysteresis zone, like the thermal systems. The answer to this question is a very important piece of information in understanding how the critical state is organized in nature, but also what the consequences of the completion of SSB are (such as the imminent occurrence of an extreme event, e.g., earthquake, geomagnetic storm, stock market crash, etc.).

The answer to the above-raised question would be positive if the examined observable is a quantity that possesses the characteristics of the order parameter and if the distribution of the waiting times or, in the case of the PNA-STSM analysis, of the "k waiting lengths" is a power law with an exponent $p \in [1, 2)$, as already explained in Section 2. Since the MCF requires a form of stationarity in the analyzed time series, it is not possible to apply it to time series that present bimodal amplitude distributions. On the other hand, in real systems, ideal conditions that allow the appearance of the two lobes with equal probabilities do not occur. This means that the solution must consider the information embedded in both lobes simultaneously, which points to the use of PNA-STSM.

As already mentioned in Section 1, in the following we present the application of PNA-STSM to three different time series, obtained from three different systems. In specific, the cases of:

(a) The 3D Ising mean magnetization time series at some temperature (below the pseudocritical one) within the hysteresis zone which confirms that the critical state survives in the SSB-zone;
(b) The time series of a nano-MOSFET noise current, and
(c) A MHz fracture-induced electromagnetic emission (also known as fracture-induced electromagnetic radiation) (FEME/FEMR) time series recorded prior to a strong earthquake event, are studied in Section 4.1, Section 4.2, and Section 4.3, respectively.

4.1. The Case of the Hysteresis Zone in 3D Ising Model

The first case studied regards the analysis of the mean magnetization time series at the temperature $T = 4.51$ ($< T_c = 4.545$), which is within the hysteresis zone for the 3D Ising model. The numerical experiment was conducted for $N_{iter} = 300,000$. As can be seen in Figure 7a, the obtained time series indicates dynamics similar to the on–off intermittency dynamics, while the corresponding distribution presents two (asymmetric) lobes. The separation point between the lobes is located at the position $M = 0$ (Figure 7b), which is the critical point according to the φ^4 critical theory. It is also noted that the two lobes are not completely separated, instead they "communicate" with one another (SSB has not been completed for $T = 4.51$).

After converting the mean magnetization time series (as in the case of the critical state in Section 2) into a two-symbol ("+1", "-1") symbolic time series, one can apply the PNA-STSM, as presented in Section 3. It is mentioned that the probabilities of appearance of the two symbols are not the same (46% "+1" vs., 54% "-1") in the analyzed symbolic time series, thus the specific symbolic time series has statistics closer to the ones of real time series. The result of the PNA-STSM analysis, is that the distribution of the "k waiting lengths" at the central values ± 0.5 of the quantized magnetic field is very close to a power law since $p_3 = 0.02$, with power law exponent $p = (p_2 =) 1.21$ (see Figure 7c). The obtained exponents' values, i.e., $p_2 \in [1, 2)$ and $p_3 \approx 0$, indicate that the critical state survives within

the hysteresis zone, which is something expected since the studied temperature $T = 4.51$ is very close to the pseudocritical temperature $T_c = 4.545$.

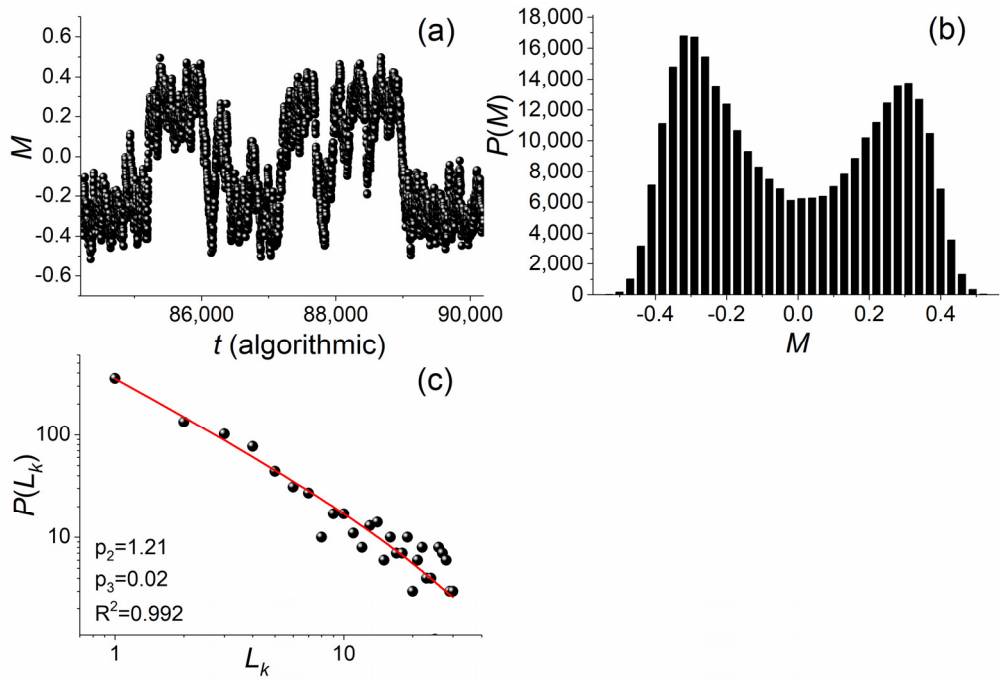

Figure 7. (**a**) A segment of the mean magnetization time series in case of the 3D Ising model at $T = 4.51$. The dynamics are similar to the on–off intermittency dynamics. (**b**) The distribution of the 300,000 values of mean magnetization presents a bimodal structure in which the two lobes communicate with one another. (**c**) The "k waiting lengths" L_k, for the central values ± 0.5 of the quantized magnetic field, according to the PNA-STSM. The fitting has been performed using the fitting function of Equation (4).

Analyzing the specific symbolic time series in the time domain, i.e., by analyzing the waiting times at each of the two symbols separately (see Section 2), one arrives at two different results: for waiting times for the "+1" symbol distribution, the estimated exponents' values are $p_2 = 1.15 \in [1, 2)$, $p_3 = 0.02$, whereas for the waiting times for the symbol "−1" distribution, the estimated values are $p_2 = 1.10 \in [1, 2)$, $p_3 = 0.04$. Both sets of exponents' values indicate that the critical state survives at $T = 4.51$, but the estimated power law exponent $p(= p_2)$ is different for each symbol.

Thus, one cannot reach a definite quantitative result by employing the time domain analysis. On the contrary, the use of the PNA-STSM, which considers both symbolic dynamics' branches simultaneously, leads to a single power law exponent ($p = 1.21$), providing a definite quantitative result. It should be finally mentioned that the value of the exponent p estimated using the PNA-STSM cannot be obtained by any linear combination of the two different power law exponent values estimated using the time domain analysis, e.g., as their mean value. This also indicates the strong nonlinearity and complexity of the examined system.

4.2. The Case of the Nano-MOSFET Electronic Device

The second case studied regards an ultrathin body and buried box (UTBB) fully depleted silicon-on-insulator (FD-SOI) nano-MOSFET. This device was fabricated with channel dimensions W = 0.5 μm and L = 30 nm, while the silicon film thickness was t_{Si} = 7 nm [25]. Finally, the box thickness was 25 nm, and the equivalent front gate oxide thickness was (EOT) t_{ox} = 1.55 nm (TiN/HfSiON stack) [25]. Fully depleted silicon-on-insulator MOSFETs [26,27] exhibit low threshold voltage and threshold voltage controllability (by the second gate bias) at the nanoscale. Because of its compatibility to the standard

planar CMOS technology, it is capable of further downscaling; therefore, the characteristics of noise currents are crucial to study. Next to typical noise analysis [25], UTBB-FD-SOI nano-MOSFET has also been studied from the point of view of nonlinear dynamics [28], critical phenomena [29], as well as Tsallis non-extensive statistics [30]. All three approaches confirmed the deterministic origin of demonstrated random telegraph noise (RTN).

In the following, we present the analysis of the above-mentioned nano-MOSFET's drain current I_d time series of a duration of 5 s, sampled at a sampling period of 5×10^{-5} s, thus consisting of 100,000 points. The drain current has been acquired for bias conditions: $V_d = 30$ V, $V_{bg} = 0$ V, and $V_g = 300$ mV, while V_g acted as a control parameter. Figure 8a portrays a small segment of the analyzed time series to illustrate that I_d values fluctuate around two current levels, hereafter referred to as "HIGH values" and "LOW values", respectively. In the case of the specific nano-MOSFET on–off intermittency occurs between HIGH and LOW values. One can easily identify the bimodal form of the corresponding time series values' histogram (Figure 8b), while the two lobes are not completely separated from each other; thus, they "communicate". If one defines as "separation point" between the two lobes of the distribution of the histogram bin of the smallest statistic ($I_d = 1.35 \times 10^{-7}$ A), a straightforward way to obtain a two-state coarse-graining description of the I_d value for the specific experiment is to assign time series values $I_d \geq 1.35 \times 10^{-7}$ A and $I_d < 1.35 \times 10^{-7}$ A to the symbols "+1" (HIGH value) and "−1" (LOW value), respectively.

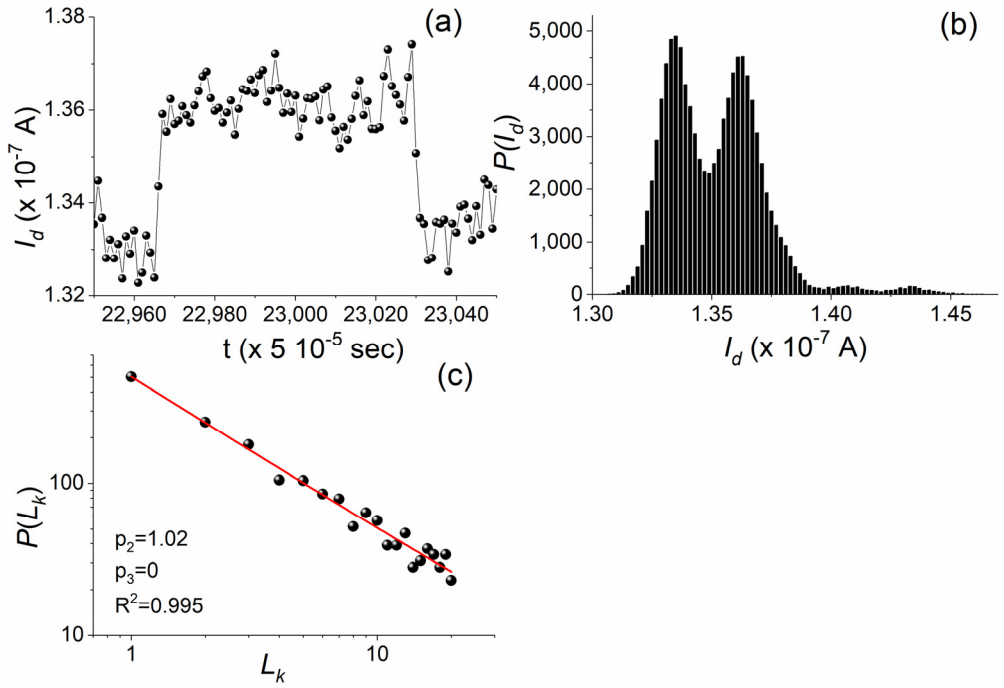

Figure 8. (**a**) A nano-MOSFET's drain current I_d, time series segment, obtained for the control parameter value $V_g = 300$ mV, presenting an on–off intermittency. (**b**) Distribution of the drain current values. The separation point between the two lobes (see text), which separates the HIGH values from the LOW values is $I_d = 1.35 \times 10^{-7}$ A. (**c**) Distribution of the "k waiting lengths" L_k, for the central values ± 0.5 of the quantized magnetic field, according to PNA-STSM. The fit has been performed using the fitting function of Equation (5). The result is $p_2 = 1.02 \pm 0.04$ and $p_3 = 0.00$, which lies at the borderline between critical and tricritical dynamics.

As soon as the original real-valued time series was converted into a two-symbol symbolic time series, PNA-STSM analysis was applied (see Section 3.1). The result is presented in Figure 8c, showing that the distribution of the "k waiting lengths" at the central values ± 0.5 of the quantized magnetic field is an exact power law ($p_3 = 0.00$) with power law exponent $p = (p_2 =) 1.02 \pm 0.04$. Since the nominal value of the estimated power law exponent is $p = 1.02 \in [1, 2)$, we confirm that the dynamics embedded in the

I_d symbolic time series are indeed critical dynamics; but notice that at the lower error limit, the tricritical dynamics appears ($p_{-error} = 1.02 - 0.04 = 0.98 \in (0.66, 1)$). This entanglement of the critical and the tricritical points is confirmed by the theory of critical phenomena. Indeed, according to the φ^6 theory in the parametric space of the Landau free energy, where the coefficients of the φ^2 and φ^4 terms of the Landau polynomial serve as the parameters, meeting of the lines of the second-order phase transition and the first-order phase transition takes place [16]. Thus, the critical point, which is the endpoint of the second-order phase transition line, meets the tricritical point, which is the starting point of the first-order phase transition line. Therefore, the result obtained by the PNA-STSM indicates exactly the above-mentioned meeting that the theory predicts.

It is also interesting to see the results obtained if one analyzes the specific symbolic time series in the time domain, i.e., by analyzing the waiting times at each of the two symbols separately (see Section 2). The time domain analysis of the waiting times for the "+1" symbol distribution leads to the set of exponents $p_2 = 0.980 \pm 0.027$, $p_3 = 0.00$; while for the distribution of the waiting times for the "-1" symbol, one obtains $p_2 = 1.100 \pm 0.032$, $p_3 = 0.00$. In both cases, an exact power law fits the waiting times distribution. However, although the probabilities of the appearance of the two symbols are very close, 49% ("+1") vs. 51% ("-1"), the two estimated power law exponents differ. Importantly, on the one hand, the nominal value of the power law exponent estimated for the "-1" symbol distribution is $p = 1.10 \in [1, 2)$, indicating a critical state; on the other hand, the nominal value of the power law exponent estimated for the "+1" symbol distribution is $p = 0.98 \in (0.66, 1)$, which denotes a tricritical state. Additionally, considering the error limits of the two estimated p values, one finds that the p value resulting from the "-1" branch is clearly in the critical state, contrary to the one resulting from the "+1" branch that is mainly in the tricritical state, but also marginally enters the critical state. Thus, by means of the time domain waiting times analysis, one cannot definitely answer the question of what are the dynamics to which the drain current fluctuations obey. On the contrary, as already shown above, the PNA-STSM analysis, which simultaneously considers the information from both symbols, provides a clear answer.

4.3. The Case of the Presismic MHz Fracto-Electromagnetic Emission

As has been shown in [31,32], earthquake (EQ) preparation processes present remarkable analogies to thermal systems, as studied through the analysis of FEME/FEMR in the MHz band. Specifically, the spin organization mechanism of the 3D Ising model presents striking similarities, both in qualitative and quantitative terms, with the pre-seismic organization of a strong EQ. As already mentioned in Section 4, in finite thermal systems, the transition from the critical state to the SSB occurs gradually as the temperature drops. The characteristic of this temperature transition zone is the communication of the two lobes of the mean magnetization distribution. As soon as this communication stops, the two lobes completely separate, signifying the completion of the SSB. In the FEME/FEMR time series recorded before the EQ occurrence in the MHz band, there can be found segments of the signal values distributions which are bimodal, while the two lobes communicate with one another, as it happens with the mean magnetization of the 3D Ising model within the zone between the critical state and the SSB.

In the following example, we refer to a shallow, very strong EQ ($M_w = 6.9$) which occurred on 14 February 2008 offshore Methoni town (South-West Peloponnese, Greece). Two days before the EQ occurrence, the 41 MHz receiver of the ELSEM-Net (hELlenic Seismo-ElectroMagnetics Network, http://elsemnet.uniwa.gr, (accessed on 8 June 2023) station located in Zakynthos (Zante) Island recorded the 40,000-sec-long time series excerpt depicted in Figure 9a (sampling period = 1 s, the receiver output voltage, V_E, is directly related to the received electric field level at 41 MHz). As shown in Figure 9b, the specific time series excerpt presents a bimodal amplitude distribution, while the two lobes are again not completely separated.

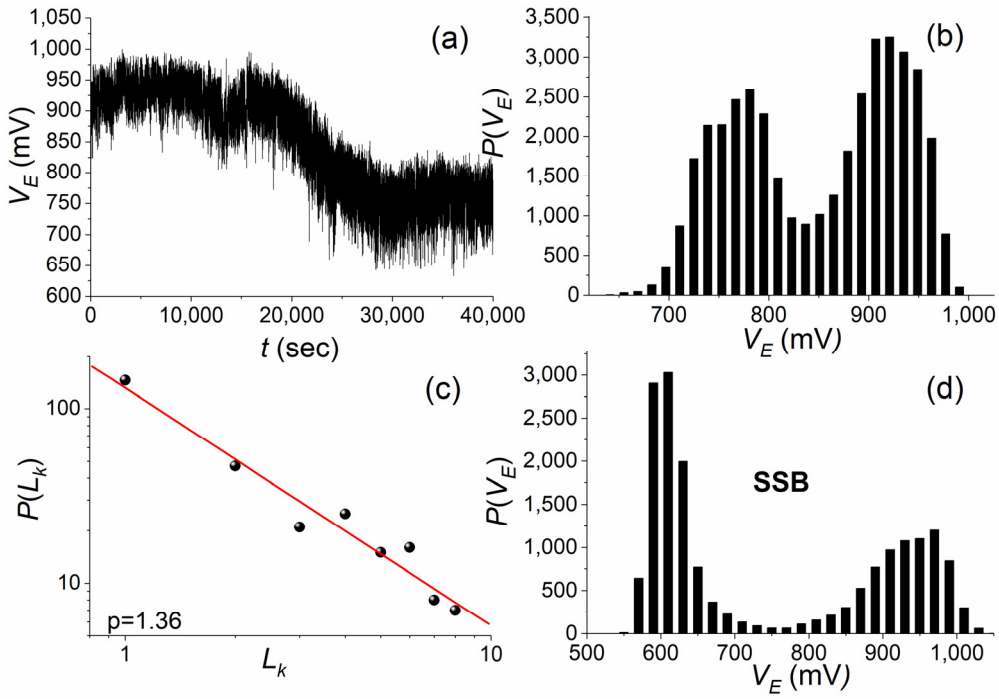

Figure 9. (**a**) A 40,000 s long segment of the 41 MHz FEME/FEMR time series recorded prior to the 14 February 2008, $M_w = 6.9$, Methoni EQ which presents two levels of values (HIGH and LOW). (**b**) The corresponding time series values distribution. The separation point between the two lobes (see text), which separates the HIGH values from the LOW values is $V_E = 837$ mV. (**c**) The distribution of the "k waiting lengths" L_k, for the central values ± 0.5 of the quantized magnetic field, according to the PNA-STSM that follows the power law $P(L_k) \sim L_k^{-1.36}$ indicating a critical state because the power law exponent bears a value of $p = 1.36 \in [1, 2)$. (**d**) The distribution of the time series values of an 18,000-sec-long excerpt of the 41 MHz FEME/FEMR recorded after the signal shown in (**a**) and 3.5 h before the Methoni EQ (see in text). It is characteristic that the communication of the two lobes has reached its end, that is, the SSB has been completed.

Although Figure 9a does not resemble the familiar structure of on–off intermittency encountered in the two previous time series of the examples utilized (Sections 4.1 and 4.2), one could consider that it presents a kind of on–off intermittency with only a single alternation between two value levels (HIGH and LOW), around which fluctuations occur. If one defines as "separation point" between the two lobes of the distribution of Figure 9b, the histogram bin of the smallest statistic ($V_E = 837$ mV), a straightforward way to obtain a two-state coarse-graining description of the V_E values could be established. For the specific recording, we assigned time series values $V_E \geq 837$ mV and $V_E < 837$ mV to the symbols "+1" (HIGH value) and "−1" (LOW value), respectively. It must be noted that the exact position of the "separation point" does not substantially affect the results.

After converting the real-valued time series of the MHz FEME/FEMR recordings into a two-symbol symbolic time series, the PNA-STSM analysis was applied (see Section 3.1). The result is presented in Figure 9c, showing that the eight first points of the distribution of the "k waiting lengths" at the central values ± 0.5 of the quantized magnetic field can be fitted by a power law with exponent $p = 1.36 \in [1, 2)$, which declares the critical state. In studying MHz FEME/FEMR precursors, it is very important to reveal the information embedded in time series excerpts, such as the presented one, that present bimodal amplitude distributions because such time series segments herald the upcoming complete separation of the two lobes. As already mentioned, the complete separation of the two lobes signifies the completion of the SSB, which leads to preferred directions in the organization of the fractures in the focal area [31,32]. In other words, it leads to ruptures that may result in seismic events. In Figure 9d, we present the values' distribution of such an SBB time series

excerpt that was recorded after the critical segment of Figure 9a. The specific SSB excerpt was 18,000-sec-long and was completed just 3.5 h before the examined EQ.

We finally mention that if one tries to analyze the same symbolic time series in the time domain, i.e., by analyzing the waiting times at each of the two symbols separately (see Section 2), a very different, in fact false, picture is drawn. As shown in [33], a power law distribution of the waiting times with exponent $p \in (1,\ 1.5)$ indicates that the critical organization is achieved by the domination of the Lévy process, which may result in the occurrence of a strong EQ, while if $p \in (1.5, 2)$, then a slow transition from the Lévy to the Gaussian process appears, which means that a strong EQ should not be expected to follow. Our "a posteriori" analysis by means of the PNA-STSM yielded a single power law exponent $p = 1.36 \in (1,\ 1.5)$, which is a result in perfect agreement with the fact that a strong EQ indeed occurred after the analyzed MHz FEME/FEMR time series excerpt of Figure 9a. On the contrary, the time domain analysis of the waiting times at the "+1" symbol distribution estimates an exponent $p = 1.64 \in (1.5, 2)$, which leads to the false conclusion that a strong EQ should not be expected to follow, whereas time domain analysis of the waiting times at the "-1" symbol results to a waiting times distribution that does not follow any power law. Therefore, PNA-STSM is the only credible way to retrieve the information embedded in MHz FEME/FEMR precursors time series excerpts that present bimodal amplitude distributions, such as the presented one.

5. Conclusions

The results emerging from this work strongly lead to the conclusion that the PNA-STSM can unambiguously and accurately estimate the power law exponent p that characterizes the waiting times of the 3D Ising model at the critical state. Having proved the accuracy of the method, three examples of the application of the PNA-STSM have been presented, demonstrating the way one may apply this method to time series, as long as these follow the dynamics of on–off intermittency and present a bimodal amplitude distribution. In all three cases, it was found that the systems producing the studied time series were in a critical state, which was further leading to an SSB of a second-order phase transition.

Finally, it was shown that, contrary to the standard time domain analysis of the waiting times, the PNA-STSM is capable of providing safe results for the dynamics of any symbolic dynamics of two symbols. This is due to the fact that the probability of the appearance of any of the two symbols is not affected by any imbalance because it simultaneously considers the information from both branches of the symbolic dynamics.

Author Contributions: Conceptualization, S.M.P. and Y.C.; methodology, S.M.P. and Y.C.; software, Y.C.; validation, P.P., N.-L.M., M.P.H. and S.G.S.; formal analysis, S.M.P. and Y.C.; investigation, M.P.H. and S.G.S.; writing, original draft preparation, S.M.P. and Y.C.; writing, review and editing, S.M.P., P.P., N.-L.M., M.P.H., S.G.S. and G.B. All authors have read and agreed to the published version of the manuscript.

Funding: This research received no external funding.

Data Availability Statement: The data that support the findings of this study are available upon request to the authors.

Acknowledgments: The authors would like to thank Dimitris Tassis and Christophoros Theodorou for providing the experimental data for the case of the UTBB-FD-SOI nano-MOSFET.

Conflicts of Interest: The authors declare no conflict of interest.

References

1. Anagiannis, V.D.; Contoyiannis, Y.F.; Diakonos, F.K. Magnetic field fluctuations in an array of randomly directed circular currents. *Eur. Phys. J. B* **2013**, *86*, 460. [CrossRef]
2. Contoyiannis, Y.; Potirakis, S.M.; Papadopoulos, P.; Kampitakis, M. Diffraction-like stratified magnetic field in a device of circular rings. *J. Appl. Phys.* **2021**, *129*, 014501. [CrossRef]

3. Contoyiannis, Y.; Papadopoulos, P.; Matiadou, N.-L.; Potirakis, S.M. A new symbolic time series analysis method based on time-to-space mapping, through a symmetric magnetic field, quantized by prime numbers. *Symmetry* **2022**, *14*, 2366. [CrossRef]
4. Contoyiannis, Y.F.; Diakonos, F.K.; Malakis, A. Intermittent dynamics of critical fluctuations. *Phys. Rev. Lett.* **2002**, *89*, 035701. [CrossRef]
5. Contoyiannis, Y.F.; Diakonos, F.K.; Papaefthimiou, C.; Theophilidis, G. Criticality in the relaxation phase of a spontaneously contracting atria isolated from a frog's heart. *Phys. Rev. Lett.* **2004**, *93*, 098101. [CrossRef] [PubMed]
6. Schuster, H.G. *Determinist Chaos: An Introduction*; Wiley-VCH: New York, NY, USA, 1989.
7. Diakonos, F.K.; Contoyiannis, Y.F.; Potirakis, S.M. Subcritical jump probability and anomalous order parameter autocorrelations. *Europhys. Lett.* **2022**, *140*, 11002. [CrossRef]
8. Pelissetto, A.; Vicari, E. Critical phenomena and renormalization-group theory. *Phys. Rep.* **2002**, *368*, 549–727. [CrossRef]
9. Kleinert, H. Critical exponents from seven-loop strong-coupling φ^4 theory in three dimensions. *Phys. Rev. D* **1999**, *60*, 085001. [CrossRef]
10. Kaku, M. *Quantum Field Theory: A Modern Introduction*; Oxford University Press: New York, NY, USA, 1993.
11. Ising, E. Beitrag zur Theorie des Ferromagnetismus. *Z. Phys.* **1925**, *31*, 253–258. [CrossRef]
12. Onsager, L. Crystal statistics. I. A two-dimensional model with an order-disorder transition. *Phys. Rev.* **1944**, *65*, 117–149. [CrossRef]
13. Zhang, D. Exact Solution for Three-Dimensional Ising Model. *Symmetry* **2021**, *13*, 1837. [CrossRef]
14. Billó, M.; Caselle, M.; Gaiotto, D.; Gliozzi, F.; Meineri, M.; Pellegrini, R. Line defects in the 3d Ising model. *J. High Energy Phys.* **2013**, *2013*, 55. [CrossRef]
15. El-Showk, S.; Paulos, M.F.; Poland, D.; Rychkov, S.; Simmons-Duffin, D.; Vichi, A. Solving the 3D Ising model with the conformal bootstrap II. *c*-Minimization and precise critical exponents. *J. Stat. Phys.* **2014**, *157*, 869–914. [CrossRef]
16. Huang, K. *Statistical Mechanics*, 2nd ed.; Wiley: New York, NY, USA, 1987.
17. Contoyiannis, Y.F.; Diakonos, F.K. Criticality and intermittency in the order parameter space. *Phys. Lett. A* **2000**, *268*, 286–292. [CrossRef]
18. Contoyiannis, Y.F.; Kapiris, P.G.; Eftaxias, K.A. Monitoring of a preseismic phase from its electromagnetic precursors. *Phys. Rev. E* **2005**, *71*, 066123. [CrossRef]
19. Contoyiannis, Y.F.; Eftaxias, K. Tsallis and Levy statistics in the preparation of an earthquake. *Nonlinear Proc. Phys.* **2008**, *15*, 379–388. [CrossRef]
20. Contoyiannis, Y.; Potirakis, S.M.; Eftaxias, K.; Contoyianni, L. Tricritical crossover in earthquake preparation by analyzing preseismic electromagnetic emissions. *J. Geodyn.* **2015**, *84*, 40–54. [CrossRef]
21. Zitis, P.I.; Contoyiannis, Y.; Potirakis, S.M. Critical dynamics related to a recent Bitcoin crash. *Int. Rev. Financ. Anal.* **2022**, *84*, 102368. [CrossRef]
22. Potirakis, S.M.; Contoyiannis, Y.; Schekotov, A.; Eftaxias, K.; Hayakawa, M. Evidence of critical dynamics in various electromagnetic precursors. *Eur. Phys. J. Spec. Top.* **2021**, *230*, 151–177. [CrossRef]
23. Campostrini, M.; Pelissetto, A.; Rossi, P.; Vicari, E. 25th-order high-temperature expansion results for three-dimensional Ising-like systems on the simple-cubic lattice. *Phys. Rev. E* **2002**, *65*, 066127. [CrossRef] [PubMed]
24. Contoyiannis, Y.; Hanias, M.P.; Papadopoulos, P.; Stavrinides, S.G.; Kampitakis, M.; Potirakis, S.M.; Balasis, G. Tachyons and solitons in spontaneous symmetry breaking in the frame of field theory. *Symmetry* **2021**, *13*, 1358. [CrossRef]
25. Karatsori, T.A.; Theodorou, C.G.; Mescot, X.; Haendler, S.; Planes, N.; Ghibaudo, G.; Dimitriadis, C.A. Study of hot-carrier-induced traps in nanoscale advanced UTBB FD-SOI MOSFETs by low frequency noise measurements. *IEEE Trans. Electron. Dev.* **2016**, *63*, 3222–3228. [CrossRef]
26. Cheung, K.P.; Wang, C.; Campbell, J.P. Nanoscale MOSFET as a potential room-temperature quantum current source. *Micromachines* **2020**, *11*, 364. [CrossRef] [PubMed]
27. Marquez, C.; Rodriguez, N.; Gamiz, F.; Ruiz, R.; Ohata, A. Electrical characterization of Random Telegraph Noise in Fully-Depleted Silicon-On-Insulator MOSFETs under extended temperature range and back-bias operation. *Solid-State Electron.* **2016**, *117*, 60–65. [CrossRef]
28. Tassis, D.H.; Stavrinides, S.G.; Hanias, M.P.; Theodorou, C.G.; Ghibaudo, G.; Dimitriadis, C.A. Chaotic behavior of random telegraph noise in nanoscale UTBB FD-SOI MOSFETs. *IEEE Electron. Device Lett.* **2017**, *38*, 517–520. [CrossRef]
29. Contoyiannis, Y.; Potirakis, S.M.; Stavrinides, S.G.; Hanias, M.P.; Tassis, D.H. Intermittency-induced criticality in the random telegraph noise of nanoscale UTBB FD-SOI MOSFETs. *Microelectron. Eng.* **2019**, *216*, 111027. [CrossRef]
30. Antoniades, I.P.; Marinos, G.; Karakatsanis, L.P.; Pavlos, E.G.; Stavrinides, S.G.; Tassis, D.; Pavlos, G.P. Tsallis nonextensive statistics and multifractal analysis of the dynamics of a fully depleted MOSFET nano device. *Physica A* **2019**, *533*, 121820. [CrossRef]
31. Contoyiannis, Y.; Potirakis, S.M. Signatures of the symmetry breaking phenomenon in pre-seismic electromagnetic emissions. *J. Stat. Mech.* **2018**, *2018*, 083208. [CrossRef]

32. Potirakis, S.M.; Contoyiannis, Y.; Eftaxias, K.; Melis, N.S.; Nomicos, C. Post-spontaneous-symmetry-breaking power-laws after a very strong earthquake: Indication for the preparation of a new strong earthquake or not? *Physica A* **2022**, *589*, 126607. [CrossRef]
33. Potirakis, S.M.; Contoyiannis, Y.; Eftaxias, K. Lévy and Gauss statistics in the preparation of an earthquake. *Physica A* **2019**, *528*, 121360. [CrossRef]

Disclaimer/Publisher's Note: The statements, opinions and data contained in all publications are solely those of the individual author(s) and contributor(s) and not of MDPI and/or the editor(s). MDPI and/or the editor(s) disclaim responsibility for any injury to people or property resulting from any ideas, methods, instructions or products referred to in the content.

symmetry

MDPI

Article

Nonlinear Dynamics of a Piecewise Modified ABC Fractional-Order Leukemia Model with Symmetric Numerical Simulations

Hasib Khan [1,2,*,†], Jehad Alzabut [1,3,†], Wafa F. Alfwzan [4,†] and Haseena Gulzar [5,†]

[1] Department of Mathematics and Sciences, Prince Sultan University, Riyadh 11586, Saudi Arabia; jalzabut@psu.edu.sa
[2] Department of Mathematics, Shaheed Benazir Bhutto Uniersity, Sheringal, Dir Upper 18000, Pakistan
[3] Department of Industrial Engineering, OSTİM Technical University, 06374 Ankara, Türkiye
[4] Department of Mathematical Sciences, College of Science, Princess Nourah bint Abdulrahman University, P.O. Box 84428, Riyadh 11671, Saudi Arabia; wfalfwzan@pnu.edu.sa
[5] Department of Biotechnology, Shaheed Benazir Bhutto Uniersity, Sheringal, Dir Upper 18000, Pakistan; haseenagulzar@sbbu.edu.pk
* Correspondence: hkhan@psu.edu.sa
† These authors contributed equally to this work.

Abstract: In this study, we introduce a nonlinear leukemia dynamical system for a piecewise modified ABC fractional-order derivative and analyze it for the theoretical as well computational works and examine the crossover effect of the model. For the crossover behavior of the operators, we presume a division of the period of study $[0, t_2]$ in two subclasses as $\mathcal{I}_1 = [0, t_1]$, $\mathcal{I}_2 = [t_1, t_2]$, for $t_1, t_2 \in \mathbb{R}$ with $t_1 < t_2$. In $\mathcal{I}_1$, the classical derivative is considered for the study of the leukemia growth while in $\mathcal{I}_2$ we presume modified ABC fractional differential operator. As a result, the study is initiated in the piecewise modified ABC sense of derivative for the dynamical systems. The novel constructed model is then studied for the solution existence and stability as well computational results. The symmetry in dynamics for all the three classes can be graphically observed in the presented six plots.

Keywords: piecewise modified ABC derivative; leukemia mathematical model; existence of solutions; Hyers–Ulam stability; crossover behavior

1. Introduction

The dynamics of real-world situations are investigated through the use of mathematical modeling and simulation in the practical areas of science, engineering, biological processes, and economics. They aid in the comprehension of the globe, the development of reliable forecasting methods, and the introduction of novel methods and apparatus. In mathematical modeling, the systems of the real world are represented by their abstract mathematical counterparts. The models can range from something as simple as a set of algebraic equations to being as complex as a set of differential or partial differential equations. Intricate system behavior can be understood and predicted with the use of mathematical models [1–3]. Simulations allow one to put mathematical models through their paces and make predictions about how a system will react in different situations. Mathematical modeling is used in computer simulations to predict the results. The results of these simulations can be used to check the veracity of a model and improve it. The tools of mathematical modeling and simulation can be used in many different contexts. They are essential for engineers to devise new ways to build things like airplanes, bridges, and chemical plants. In physics, they are used to simulate the actions of various substances and small-scale components. They are very important in the field of biology, particularly in the areas of disease research and medical care. Economists use them to predict how the market will react to proposed changes in legislation and regulation. There are, however,

limitations to mathematical modeling and simulation that must be recognized. Since they are based on assumptions and simplifications, the quality of the input data greatly affects their accuracy. In addition, the findings of simulations are not always easy to comprehend and can be computationally expensive [4–6].

The origins of leukemia, a malignancy of the blood and bone marrow, are murky and extend back hundreds of years. Rudolf Virchow, a German pathologist, originally used the term "leukemia" to describe the disease in the 1840s. The sickness, however, has a long history of written record. Leukemia-like symptoms were first described in ancient Egyptian and Greek medical books, where they were referred to as "elephantiasis" or "leucophlegmasia". Leukemia frequently manifests with spleen and lymph node swelling, which was suggested by these accounts [7,8].

The late 19th and early 20th centuries saw major developments in the study of leukemia. Chemotherapy, first introduced by a German doctor named Paul Ehrlich in the year 1900, is now an essential part of the standard treatment for leukemia. Radiation therapy was developed in the 1940s, considerably enhancing the success rate of treatments. In the middle of the 20th century, researchers identified and categorized various subtypes of leukemia. The French, American, and British (FAB) classification system for leukemia was developed in 1973 and uses cell shape and genetic factors to divide leukemia into distinct subtypes. The insights gained from this categorization system were essential in developing effective therapies [9,10].

Technological developments in fields like molecular biology and genetics have significantly contributed to our knowledge of leukemia. More targeted medicines and individualized treatment techniques have emerged as a result of the discovery of chromosomal abnormalities and genetic alterations associated with leukemia subtypes. Today, immunotherapies and targeted molecular treatments are at the forefront of ongoing research to enhance outcomes for leukemia patients. Progress in understanding and treating this complicated disease is being driven by collaboration between academics, physicians, and organizations [11]. Numerous people of various populations are affected by leukemia, making it a major global health concern. However, we can provide some background on leukemia based on data collected up until 2021, which is as recent as we have access to. It is estimated by the World Health Organization (WHO) that 2.8% of all cancer cases occur due to leukemia. Incidence rates vary widely between locations, but overall, it ranks as the eleventh most prevalent kind of cancer. According to the American Cancer Society, there will be 437,033 new cases of leukemia worldwide in 2020. This is about 3% of all cancer cases. They also calculated that around 309,006 people lost their lives to leukemia that year. Certain forms of leukemia are more common in youngsters, whereas others are more common in adults. In children, acute lymphoblastic leukemia (ALL) predominates, but in adults, chronic lymphocytic leukemia (CLL) is more frequent. The incidence of leukemia may vary among regions [7,12]. For instance, certain emerging regions have recorded greater rates compared to Western countries. However, efforts are being made to enhance data collection and reporting in a number of countries, which could lead to more precise and timely statistics in the future. Please note that since our previous training update in September 2021, some numbers may have altered. We suggest checking authoritative resources, such the World Health Organization or national cancer registries, for the latest and most reliable global data on leukemia [13,14].

Modeling leukemia spread and simulations are currently rich research-oriented areas. Leukemia is a malignancy of the blood and bone marrow that, when it progresses, can have devastating effects on the human body. Bone marrow is the site of disease initiation, since it is where abnormal white blood cells (leukemia cells) are created. These cells can travel to the brain, spinal cord, lymph nodes, spleen, and liver through the circulatory system. When leukemia cells multiply uncontrollably, they interfere with the body's ability to produce the normal amounts of several types of blood cells. Many different symptoms and consequences can arise as a result of this disruption. Leukemia is characterized by an impaired immune system. When aberrant white blood cells multiply out of control, the

body loses its ability to fight off infections. People with leukemia are more susceptible to infection, may become ill more frequently, and may be sick for longer periods of time. Anemia, characterized by a low number of red blood cells, is another complication of leukemia. This causes fatigue, weakness, shortness of breath, and a gray color to the skin. Recently, Islam et al. [15] considered a double sliding mode control for leukemia disease. Islam et al. [16] studied leukemia spread under monotonic and nonmonotonic functions and analyzed the different aspects of treatment therapy via sliding mode control. Using the literature, we are interested in the qualitative and computational studied of the following piecewise leukemia model:

$$\begin{aligned}
{}^{pmABC}\mathbb{D}^{\varrho} X_1 &= \psi_n X_1 \ln\left(\frac{N_a}{X_1}\right) - \eta_n X_1 - p X_1 X_2 - \frac{X_1 X_3}{a_1 X_3^2 + b_1 X_3 + 1}, \\
{}^{pmABC}\mathbb{D}^{\varrho} X_2 &= \psi_l X_2 \ln\left(\frac{L_a}{X_2}\right) - \eta_l X_2 - \frac{X_2 X_3}{a_2 X_3^2 + b_2 X_3 + 1} \\
{}^{pmABC}\mathbb{D}^{\varrho} X_3 &= -\eta_h X_3,
\end{aligned} \tag{1}$$

where X_1 represents the number of normal cells, X_2 represents the leukemic cells, and X_3 is the quantity of chemotherapeutic agent. $\psi_l > 0$ and $\psi_n > 0$ is the reproduction rates of leukemic cells and normal cells, respectively; $\eta_l > 0$ and $\eta_n > 0$ is the mortality rates of leukemic cells and normal cells, respectively; and $p > 0$ is the infection rate in normal cells caused by leukemic cells. $N_a > 0$ and $L_a > 0$ indicate the limits of the normal cell population and the leukemic cell population, respectively, while $\eta_h > 0$ reflects the rate at which the therapeutic agent is dissipated. The modified piecewise ABC fractional structure of the aforementioned model will be used to discuss the existence, uniqueness, stability, and numerical simulations of this model, which will overcome the gap of crossover behavior of the operator and the dynamics of the model.

Fractional calculus (FC) has been applied in almost all areas of science and engineering in theoretical, numerical, and experimental works [17–20]. Further, Atangana and Araz recently presented a new class of operators they call piecewise integrals and derivatives [21], since the exponential and Mittag–Lefler kernels do not allow for specifying the crossover time. Among the novel approaches to addressing these issues is the piecewise derivative, which is discussed in [22]. Researchers now have a new way to investigate the crossover behaviors exhibited by these operators. In the analysis of disease dynamics, extensive use has been made of the concept of piecewise operators. Dengue virus transmission within populations was studied using the fractional piecewise derivative and the piecewise operator of fractional order by Ahmad et al. [23]. The literature cites additional examples of the piecewise operator's use in problem modeling in [24–26]. Simulations of fractional differential equations rely heavily on symmetry. They take into account the harmony and correspondence existing inside the system to provide facts about its operation. Researchers can cut down on processing time and unearth previously unseen patterns by using symmetry features. The use of correct numerical methods, guaranteed by symmetry, allows for precise and efficient simulations. It also helps in finding the conservation laws and invariant values that explain the dynamics. By expanding our knowledge of symmetry in fractional differential equations, we can make strides forward in many disciplines, including physics, engineering, and finance. These simulations rely heavily on symmetry to perform in-depth analysis and make accurate predictions [27–29].

Paper organization: This paper is organized in seven sections. In Section 1, the introduction of the leukemia model and relevant literature are presented. In Section 2, the preliminary results, definitions, and results for the piecewise operators are presented, which help in the crossover behavior analysis study of the dynamical systems. In Section 3, the proposed leukemia model (1) is expressed in its equivalent piecewise-integral version, two essential assumptions are presented, and the presumed model is studied for the solution existence and uniqueness. In Section 4, the stability analysis of HU-type is defined for and proved based on certain assumptions for the system (1). A computational iterative

scheme is produced with the help of Lagrange's interpolation polynomial in Section 5. Section 6 is reserved for the numerical data of the model for the piecewise version and the crossover behavior is analyzed graphically for different fractional orders for $\tau_1 = [0, 50]$ and $\tau_2 = [50, 200]$. The work is summarized in Section 7.

2. Preliminaries

Crossover behavior is a phenomenon in dynamical models where the behavior of a system changes from one state to another. A qualitative shift in the dynamics of the system occurs when specific parameters or situations exceed a critical threshold. It is not uncommon to observe crossover phenomena in the physical, biological, and economic sciences. In physics, for instance, a system exhibiting crossover behavior is one that is changing from one state of matter to another (e.g., from a solid to a liquid or a liquid to a gas). Changes in stability, periodicity, or attractor patterns are all examples of crossover behavior in dynamical models. The system behavior can undergo rapid changes, bifurcations, or even chaos if the model's parameters are tweaked slightly. Gaining insights into the behavior of complex systems requires an understanding of crossover behavior, which can aid in locating the system's critical, threshold, or tipping points. By analyzing crossovers, scientists can learn more about the system's dynamics and forecast how it will respond to changes in input parameters [30–32]. In order to capture the crossover behavior the IS model (1), piecewise operators in the sense of modified Atangana–Baleanu derivative are presented in parts of the article.

Definition 1 ([33,34]). *For $\zeta \in (0, 1)$, and $\mathbf{w} \in L^1(0, T)$, the modified ABC derivative is given as follows:*

$$ {}^{mABC}D_0^{\zeta}\mathbf{w}(t) = \frac{B(\zeta)}{1-\zeta}\big[\mathbf{w}(t) - E_{\zeta}(-\mu_{\zeta}t^{\zeta})\mathbf{w}(0) - \mu_{\zeta}\int_0^t (t-s)^{\zeta-1}E_{\zeta,\zeta}(-\mu_{\zeta}(t-s)^{\zeta})\mathbf{w}(s)ds\big]. $$

For any constant C, we have ${}^{mABC}D_0^{\zeta}C = 0$; see in [33]. The corresponding integral is given in the following definition.

Definition 2 ([33,34]). *For $\zeta \in (0, 1)$, and $\mathbf{w} \in L^1(0, T)$, the modified AB integral is given as follows:*

$$ {}^{mAB}I_0^{\zeta}\mathbf{w}(t) = \frac{B(1-\zeta)}{B(\zeta)}\big[\mathbf{w}(t) - \mathbf{w}(0)\big] + \big[{}^{RL}I_0^{\zeta}(\mathbf{w}(t) - \mu_{\zeta}\mathbf{w}(0))\big]. \tag{2} $$

Lemma 1 ([33]). *For $\mathbf{w}' \in L^1(0, \infty)$, and $\zeta \in (0, 1)$, we have:*

$$ {}^{mAB}I_0^{\zeta}\,{}^{mABC}D_0^{\zeta}\mathbf{w}(t) = \mathbf{w}(t) - \mathbf{w}(0). \tag{3} $$

Definition 3 ([21]). *For a differentiable function $\mathbf{w}(\mathtt{t})$, the piecewise integral is:*

$$ {}_0^{PF}\mathbb{I}_{\mathtt{t}}\mathbf{w}(\mathtt{t}) = \begin{cases} \int_0^{\mathtt{t}} \mathbf{w}(s)ds, & 0 < \mathtt{t} \le \mathtt{t}_1, \\ \int_{\mathtt{t}_1}^{\mathtt{t}} \mathbf{w}(s)ds & \mathtt{t}_1 < \mathtt{t} \le \mathtt{t}_2. \end{cases}, $$

Definition 4. *Let us assume that $\mathbf{w}(\mathtt{t})$ be differentiable function, then the piecewise derivative of $\mathbf{w}(\mathtt{t})$ in the integer and fractional-order modified ABC is defined as:*

$$ {}_0^{PF}\mathbf{D}_{\mathtt{t}}^{\zeta}\mathbf{w}(\mathtt{t}) = \begin{cases} \mathbf{w}'(t), & 0 < t \le t_1, \\ {}_0^{\mathbf{mABC}}\mathbf{D}_{\mathtt{t}}^{\zeta}\mathbf{w}(\mathtt{t}) & \mathtt{t}_1 < \mathtt{t} \le \mathtt{t}_2, \end{cases}, \tag{4} $$

Definition 5. *For a differentiable function* $\mathbf{w}(\mathrm{t})$*, the piecewise integration of classical and modified AB integral is then given by:*

$$ {}_0^{PF}\mathbf{I}_{\mathrm{t}}\mathbf{w}(\mathrm{t}) = \begin{cases} \displaystyle\int_0^{\mathrm{t}} \mathbf{w}(s)ds, \ \ 0 < \mathrm{t} \leq \mathrm{t}_1, \\ \dfrac{B(1-\zeta)}{B(\zeta)}\big[\mathbf{w}(t) - \mathbf{w}(0)\big] + \big[{}^{RL}I_0^{\zeta}(\mathbf{w}(t) - \mu_{\zeta}\mathbf{w}(0))\big], \ \ \mathrm{t}_1 < \mathrm{t} \leq \mathrm{t}_2, \end{cases}, $$

where ${}_0^{PF}\mathbb{I}_{\mathrm{t}}\mathbf{w}(\mathrm{t})$ *represents integration of classical case in* $0 < \mathrm{t} \leq \mathrm{t}_1$ *and for the modified AB sense is given in* $\mathrm{t}_1 < \mathrm{t} \leq \mathrm{t}_2$*.*

Lemma 2. *The general piecewise differential equation for* $t \in (0, t_2]$*, where* $0 < t_1 \leq t_2$*:*

$$ {}_0^{PFC}\mathbf{D}_{\mathrm{t}}^{\zeta}\mathbf{w}(t) = \mathbb{S}(t, \mathbf{w}(t)), $$

has the solution given by:

$$ \mathbf{w}(\mathrm{t}) = \begin{cases} \mathbf{w}_0 + \displaystyle\int_0^{\mathrm{t}} \mathbf{w}(s)ds, & 0 < \mathrm{t} \leq \mathrm{t}_1, \\ \mathbf{w}_0 + \dfrac{1-\zeta}{B(\zeta)}\mathbb{S}(t, \mathbf{w}(t)) + \dfrac{\zeta}{\Gamma(\zeta)B(\zeta)}\displaystyle\int_0^t (t-s)^{\zeta-1}\mathbb{S}(s, \mathbf{w}(s))ds & \\ - \dfrac{1-\zeta}{B(\zeta)}\mathbb{S}(0, \mathbf{w}(0))\Big(1 + \dfrac{\gamma_{\zeta}}{\Gamma(\zeta+1)}t^{\zeta}\Big), & \mathrm{t}_1 < \mathrm{t} \leq \mathrm{t}_2. \end{cases} \tag{5} $$

Proof. By applying the Definition 5 on (4) and putting the initial value h_0, one can directly get the solution (5). □

3. Qualitative Analysis

Existence of solution and uniqueness analysis have been a trend in last few years in the theoretical results of FDES. We highlight some useful works which are related to the upcoming results in [35–44]. For simplicity in calculations, we can write the piecewise modified Leukemia therapy-model (1) as:

$$ \begin{aligned} {}_0^{pmABC}\mathbb{D}_t^{\zeta}(\mathrm{X}_1) &= \begin{cases} \mathbb{D}_t^{\zeta}(\mathrm{X}_1(t)) = \mathbb{S}_1(\mathrm{X}_1, \mathrm{X}_2, \mathrm{X}_3, t), \ 0 < t \leq t_1, \\ {}^{mABC}{}_0\mathbb{D}_t^{\zeta}(\mathrm{X}_1(t)) = \mathbb{S}_2(\mathrm{X}_1, \mathrm{X}_2, \mathrm{X}_3, t), \ t_1 < t \leq t_2, \end{cases}, \\ {}_0^{pmABC}\mathbb{D}_t^{\zeta}(\mathrm{X}_2) &= \begin{cases} \mathbb{D}_t^{\zeta}(\mathrm{X}_2(t)) = \mathbb{S}_3(\mathrm{X}_1, \mathrm{X}_2, \mathrm{X}_3, t), \ 0 < t \leq t_1, \\ {}^{mABC}{}_0\mathbb{D}_t^{\zeta}(\mathrm{X}_2(t)) = \mathbb{S}_2(\mathrm{X}_1, \mathrm{X}_2, \mathrm{X}_3, \ t_1 < t \leq t_2, \end{cases}, \\ {}_0^{pmABC}\mathbb{D}_t^{\zeta}\mathrm{X}_3 &= \begin{cases} \mathbb{D}_0^{\zeta}(\mathrm{X}_3(t)) = \mathbb{S}_3(\mathrm{X}_1, \mathrm{X}_2, \mathrm{X}_3, t), \ 0 < t \leq t_1, \\ {}^{mABC}{}_0\mathbb{D}_t^{\zeta}(\mathrm{X}_3(t)) = \mathbb{S}_3(\mathrm{X}_1, \mathrm{X}_2, \mathrm{X}_3, t), \ t_1 < t \leq t_2, \end{cases}, \end{aligned} \tag{6} $$

where $\mathbb{S}_1 = \psi_n X_1 \ln\left(\frac{N_a}{X_1}\right) - \eta_n X_1 - pX_1X_2 - \frac{X_1X_3}{a_1X_3^2 + b_1X_3 + 1}$, $\mathbb{S}_2 = \psi_l X_2 \ln\left(\frac{L_a}{X_2}\right) - \eta_l X_2 - \frac{X_2X_3}{a_2X_3^2 + b_2X_3 + 1}$, $\mathbb{S}_3 = -\eta_h X_3$. Here, the EUS results of the presumed piecewise mABC model (1) are discussed. The next thing that we need to do is determine whether or not a solution can be found for the hypothetical piecewise derivable function, as well as the particular solution characteristic that it holds. If a solution can be discovered, then we may move on to the next step.

One possible form for the solution to an equation including the piecewise mABC derivative

$$ {}_0^{pmABC}\mathbf{D}_{\mathrm{t}}^{\zeta}\mathbf{w}(\mathrm{t}) = \mathbb{S}(\mathrm{t}, \mathbf{w}(\mathrm{t})), \ \ 0 < \mathrm{t} \leq T, \tag{7} $$

is

$$\mathbf{w}(\mathrm{t}) = \begin{cases} \mathbf{w}_0 + \int_0^{\mathrm{t}} \mathbf{w}(s)ds, & 0 < \mathrm{t} \leq \mathrm{t}_1, \\ \mathbf{w}_0 + \frac{1-\zeta}{B(\zeta)}\mathbb{S}(t, \mathbf{w}(t)) + \frac{\zeta}{\Gamma(\zeta)B(\zeta)} \int_0^t (t-s)^{\zeta-1}\mathbb{S}(s, \mathbf{w}(s))ds & \\ -\frac{1-\zeta}{B(\zeta)}\mathbb{S}(0, \mathbf{w}(0))\Big(1 + \frac{\gamma_\zeta}{\Gamma(\zeta+1)}t^\zeta\Big), & \mathrm{t}_1 < \mathrm{t} \leq \mathrm{t}_2. \end{cases} \tag{8}$$

where

$$\mathbf{w}(t) = \begin{cases} \mathrm{X}_1(t) \\ \mathrm{X}_2(t), \\ \mathrm{X}_3(t) \end{cases} \quad \mathbf{w}_0 = \begin{cases} \mathrm{X}_1(0) \\ \mathrm{X}_2(0), \\ \mathrm{X}_3(0) \end{cases} \quad \mathbf{w}_{t_1} = \begin{cases} \mathrm{X}_1(t_1) \\ \mathrm{X}_2(t_1), \\ \mathrm{X}_3(t_1) \end{cases} \quad \mathbb{S}(t, \mathbf{w}(t)) = \begin{cases} \mathbb{S}_1(\mathrm{X}_1, \mathrm{X}_2, \mathrm{X}_3, t), \\ \mathbb{S}_2(\mathrm{X}_1, \mathrm{X}_2, \mathrm{X}_3, t), \\ \mathbb{S}_3(\mathrm{X}_1, \mathrm{X}_2, \mathrm{X}_3, t). \end{cases} \tag{9}$$

Consider the set $E = C[0, T]$ as a Banach space with

$$\|\mathbf{w}^*\| = \max_{t\in[0,T]} |\mathbf{w}^*(t)|.$$

The following are presumptions are made for handling the nonlinear function $\mathbb{S}$.

(C1) $\exists\ L_{\mathbf{w}^*} > 0; \forall\ g,\ \mathbf{w}^* \in E$, we arrive at:

$$|\mathbb{S}(t, g) - \mathbb{S}(t, \mathbf{w}^*)| \leq L_{\mathbb{S}}|\mathbf{w}^* - g|.$$

(C2) $\exists\ C_{\mathbb{S}} > 0$ & $M_{\mathbb{S}} > 0$;

$$|\mathbb{S}(t, \mathbf{w}^*(t))| \leq C_{\mathbb{S}}|\mathbf{w}^*| + M_{\mathbb{S}}.$$

Theorem 1. *For the presumed function* $\mathbb{S}$*, which is a piecewise continuous on* $0 < t \leq t_1$ *and* $t_1 < t \leq t_2$ *as subintervals of* $[0, T]$*, with the assumption of* $(C2)$*, the IS model* (7) *has a solution.*

Proof. We presume the following closed subset $\mathfrak{B}$ of E,

$$\mathfrak{B} = \{\mathbf{w} \in E :\ \|\mathbf{w}\| \leq R,\ R > 0\}.$$

Let $\mathbb{F} : \mathfrak{B} \to \mathfrak{B}$ and by the help of (8), such that

$$\mathbb{F}(\mathrm{g})(t) = \begin{cases} \mathbf{w}_0 + \int_0^{\mathrm{t}} \mathbf{w}(s)ds, & 0 < \mathrm{t} \leq \mathrm{t}_1, \\ \mathbf{w}_0 + \frac{1-\zeta}{B(\zeta)}\mathbb{S}(t, \mathbf{w}(t)) + \frac{\zeta}{\Gamma(\zeta)B(\zeta)} \int_0^t (t-s)^{\zeta-1}\mathbb{S}(s, \mathbf{w}(s))ds & \\ -\frac{1-\zeta}{B(\zeta)}\mathbb{S}(0, \mathbf{w}(0))\Big(1 + \frac{\gamma_\zeta}{\Gamma(\zeta+1)}t^\zeta\Big), & \mathrm{t}_1 < \mathrm{t} \leq \mathrm{t}_2. \end{cases}$$

For the $\mathbf{w}^* \in B$, we have

$$
\begin{aligned}
|\mathbb{F}(g)(t)| &\leq \begin{cases} |\mathbf{w}_0^*| + \int_0^{t_1} |\mathbb{S}(\bar{\delta}, g(\bar{\delta}))| d\bar{\delta}, & 0 < \mathrm{t} \leq \mathrm{t}_1, \\ |\mathbf{w}_{t_1}| + \frac{1-\zeta}{B(\zeta)} |\mathbb{S}(t, \mathbf{g}(t))| + \frac{\zeta}{\Gamma(\zeta) B(\zeta)} \int_0^t (t-s)^{\zeta-1} |\mathbb{S}(s, \mathbf{w}(s))| ds \\ + \frac{1-\zeta}{B(\zeta)} |\mathbb{S}(0, \mathbf{w}(0))| \Big(1 + \frac{\gamma_\zeta}{\Gamma(\zeta+1)} t^\zeta\Big), & t_1 < t \leq t_2, \end{cases} \\
&\leq \begin{cases} |\mathbf{w}_0^*| + t_1 (C_{\mathbb{S}} |\mathbf{w}^*| + M_{\mathbb{S}}), & 0 < \mathrm{t} \leq \mathrm{t}_1, \\ |\mathbf{w}_{t_1}| + \frac{1-\zeta}{B(\zeta)} (C_{\mathbb{S}} |\mathbf{w}^*| + M_{\mathbb{S}}) + \frac{1}{\Gamma(\zeta) B(\zeta)} t_2^\zeta (C_{\mathbb{S}} |\mathbf{w}^*| + M_{\mathbb{S}})| \\ + \frac{1-\zeta}{B(\zeta)} |(C_{\mathbb{S}} |\mathbf{w}^*| + M_{\mathbb{S}}) \Big(1 + \frac{\gamma_\zeta}{\Gamma(\zeta+1)} t_2^\zeta\Big), & t_1 < t \leq t_2, \end{cases} \\
&\leq \begin{cases} \beta_1, & 0 < t \leq t_1, \\ \beta_2, & t_1 < t \leq t_2. \end{cases} \qquad (10)
\end{aligned}
$$

For $\beta_1 = \max_{t \in [0, t_1]} \{|\mathbf{w}_0^*| + t_1 (C_{\mathbb{S}} |\mathbf{w}^*| + M_{\mathbb{S}})\}$, $\beta_2 = \max_{t \in [t_1, t_2]} \{|\mathbf{w}_{t_1}| + \frac{1-\zeta}{B(\zeta)} (C_{\mathbb{S}} |\mathbf{w}^*| + M_{\mathbb{S}}) + \frac{1}{\Gamma(\zeta) B(\zeta)} t_2^\zeta (C_{\mathbb{S}} |\mathbf{w}^*| + M_{\mathbb{S}}) + \frac{1-\zeta}{B(\zeta)} |(C_{\mathbb{S}} |\mathbf{w}^*| + M_{\mathbb{S}}) \Big(1 + \frac{\gamma_\zeta}{\Gamma(\zeta+1)} t_2^\zeta\Big)\}$. This implies that $\mathbb{F}(\mathfrak{B}) \subset \mathfrak{B}$. Thus, it shows that $\mathbb{F}$ is closed and complete operator. Now, for the completely continuity of $\mathbb{F}$, we consider $t_n > t_m \in [0, t_1]$, which gives us:

$$
\begin{aligned}
|\mathbb{F}(\mathbf{w}^*)(t_n) - \mathbb{F}(\mathbf{w})(t_m)| &= \Big| \int_0^{t_n} \mathbb{S}(s, \mathbf{w}^*(s)) ds - \int_0^{t_m} \mathbb{S}(s, \mathbf{w}(s)) ds \Big| \\
&\leq \int_0^{t_n} |\mathbb{S}(s, \mathbf{w}^*(s))| ds + \int_0^{t_m} |\mathbb{S}(s, \mathbf{w}(s))| ds \\
&\leq \int_0^{t_n} (C_{\mathbb{S}} |\mathbf{w}^*| + M_{\mathbb{S}}) ds - \int_0^{t_m} (C_{\mathbb{S}} |\mathbf{w}| + M_G) ds \\
&\leq (C_{\mathbb{S}} \mathbf{w}^* + M_{\mathbb{S}}) t_n + (C_{\mathbb{S}} \mathbf{w} + M_{\mathbb{S}}) t_m. \qquad (11)
\end{aligned}
$$

Thanks to (11), when $t_m \to t_n$, then

$$|\mathbb{F}(\mathbf{w}^*)(t_n) - \mathbb{F}(\mathbf{w})(t_m)| \to 0, \text{ as } t_m \to t_n.$$

Thus, $\mathbb{F}$ is equicontinuous in $[0, t_1]$. Consider $t_m, t_n \in [t_1, T]$ in the sense of modified ABC as

$$
\begin{aligned}
|\mathbb{F}(\mathbf{w}^*)(t_n) - \mathbb{F}(\mathbf{w}^*)(t_m)| &= \Big|\mathbf{w}_0 + \frac{1-\zeta}{B(\zeta)}\mathbb{S}(t_n, \mathbf{w}(t_n)) \\
&+ \frac{\zeta}{\Gamma(\zeta)B(\zeta)}\int_0^{t_n}(t_n - s)^{\zeta-1}\mathbb{S}(s, \mathbf{w}(s))ds \\
&- \frac{1-\zeta}{B(\zeta)}\mathbb{S}(0, \mathbf{w}(0))\Big(1 + \frac{\gamma_\zeta}{\Gamma(\zeta+1)}t_n^\zeta\Big) \\
&- \Big[\mathbf{w}_0 + \frac{1-\zeta}{B(\zeta)}\mathbb{S}(t_m, \mathbf{w}(t_m)) \\
&+ \frac{\zeta}{\Gamma(\zeta)B(\zeta)}\int_0^{t_m}(t_m - s)^{\zeta-1}\mathbb{S}(s, \mathbf{w}(s))ds \\
&- \frac{1-\zeta}{B(\zeta)}\mathbb{S}(0, \mathbf{w}(0))\Big(1 + \frac{\gamma_\zeta}{\Gamma(\zeta+1)}t_m^\zeta\Big)\Big]\Big| \\
&\leq \frac{1-\zeta}{B(\zeta)}|\mathbb{S}(t_n, \mathbf{w}(t_n)) - \mathbb{S}(t_m, \mathbf{w}(t_m))| \\
&+ \frac{\zeta}{\Gamma(\zeta)B(\zeta)}\Big[\int_0^{t_n}(t_n - s)^{\zeta-1} - \int_0^{t_m}(t_m - s)^{\zeta-1}\Big]|\mathbb{S}(s, \mathbf{w}(s))|ds \\
&+ \frac{1-\zeta}{B(\zeta)}\mathbb{S}(0, \mathbf{w}(0))\Big(1 + \frac{\gamma_\zeta}{\Gamma(\zeta+1)}|t_n^\zeta - t_m^\zeta|\Big) \\
&\leq \frac{1-\zeta}{B(\zeta)}|\mathbb{S}(t_n, \mathbf{w}(t_n)) - \mathbb{S}(t_m, \mathbf{w}(t_m))| + \frac{|t_n^\zeta - t_m^\zeta|}{\Gamma(\zeta)B(\zeta)}(C_\mathbb{S}\mathbf{w}^* + M_\mathbb{S}) \\
&+ \frac{1-\zeta}{B(\zeta)}\mathbb{S}(0, \mathbf{w}(0))\Big(1 + \frac{\gamma_\zeta}{\Gamma(\zeta+1)}|t_n^\zeta - t_m^\zeta|\Big).
\end{aligned} \tag{12}
$$

If $t_n \to \mathrm{t}_m$, then

$$|\mathbb{F}(\mathbf{w}^*)(t_n) - \mathbb{F}(\mathbf{w}^*)(t_m)| \to 0, \text{ as } t_m \to t_n.$$

This demonstrates that $\mathbb{F}$ is equally continuous over the interval $[t_1, t_2]$. As a result, the map T is equicontinuous. Completely and uniformly continuous and bounded, T is the operator of interest due to the Arzel'a-Ascoli and Schauder theorems implying that the piecewise TB model under consideration has a solution. □

Theorem 2. *Let* $(C1)$ *hold true and* $\mathbb{L}_g\big(\frac{1-\zeta}{B(\zeta)} + \frac{1}{B(\zeta)}\frac{(t_2-t_1)^\zeta}{\Gamma(\zeta)}\big) < 1$*; if so, then the proposed piecewise mABC IS model has a unique solution.*

Proof. As in the above proof, we have the piecewise continuity of $\mathbb{F} : \mathfrak{B} \to \mathfrak{B}$ that, furthermore, for g, $\bar{\mathbf{w}}^* \in \mathfrak{B}$ on $[0, t_1]$ implies

$$
\begin{aligned}
\|\mathbb{F}(\mathbf{w}^*) - \mathbb{F}(\bar{\mathbf{w}}^*)\| &= \max_{t\in[0,t_1]}\Big|\int_0^{t_1}\mathbb{S}(s, \mathbf{w}^*(s))ds - \int_0^{t_1}\mathbb{S}(s, \bar{\mathbf{w}}^*(s))ds\Big| \\
&\leq \mathbf{t_1}L_\mathbb{S}\|\mathbf{w}^* - \bar{\mathbf{w}}^*\|.
\end{aligned} \tag{13}
$$

From (13), we have

$$\|\mathbb{F}(\mathbf{w}^*) - \mathbb{F}(\bar{\mathbf{w}}^*)\| \leq \mathbf{t_1}L_\mathbb{S}\|\mathbf{w}^* - \bar{\mathbf{w}}^*\|. \tag{14}$$

Therefore, we have $\mathbb{F}$ is a contraction. By Banach's result, the presumed TB system has a unique solution in the given subinterval. Moreover, we have for $t \in [t_1, t_2]$

$$
\begin{aligned}
\|\mathbb{F}(\mathbf{w}^*) - \mathbb{F}(\bar{\mathbf{w}}^*)\| &= \max_{t\in[t_1,t_2]} \Big| \mathbf{w}_0 + \frac{1-\zeta}{B(\zeta)}\mathbb{S}(t_n, \mathbf{w}(t_n)) + \frac{\zeta}{\Gamma(\zeta)B(\zeta)} \int_{t_1}^{t_2} (t_2 - s)^{\zeta-1}\mathbb{S}(s, \mathbf{w}(s))ds \\
&- \frac{1-\zeta}{B(\zeta)}\mathbb{S}(0, \mathbf{w}(0))\Big(1 + \frac{\gamma_\zeta}{\Gamma(\zeta+1)}t^\zeta\Big) \\
&- \Big[\bar{\mathbf{w}}_0 + \frac{1-\zeta}{B(\zeta)}\mathbb{S}(t, \bar{\mathbf{w}}(t)) + \frac{\zeta}{\Gamma(\zeta)B(\zeta)} \int_{t_1}^{t_2} (t_2 - s)^{\zeta-1}\mathbb{S}(s, \bar{\mathbf{w}}(s))ds \\
&- \frac{1-\zeta}{B(\zeta)}\mathbb{S}(0, \mathbf{w}(0))\Big(1 + \frac{\gamma_\zeta}{\Gamma(\zeta+1)}t^\zeta\Big)\Big]\Big| \\
&\leq \frac{1-\zeta}{B(\zeta)}\mathbb{L}_g|g - \bar{g}| + \frac{1}{B(\zeta)}\mathbb{L}_g|g - \bar{g}|\frac{(t_2 - t_1)^\zeta}{\Gamma(\zeta)} \\
&= \mathbb{L}_g\big(\frac{1-\zeta}{B(\zeta)} + \frac{1}{B(\zeta)}\frac{(t_2 - t_1)^\zeta}{\Gamma(\zeta)}\big)|g - \bar{g}|.
\end{aligned} \tag{15}
$$

From (15), we have

$$
\|\mathbb{F}(\mathbf{w}^*) - \mathbb{F}(\bar{\mathbf{w}}^*)\| \leq \mathbb{L}_g\big(\frac{1-\zeta}{B(\zeta)} + \frac{1}{B(\zeta)}\frac{(t_2 - t_1)^\zeta}{\Gamma(\zeta)}\big)|g - \bar{g}|. \tag{16}
$$

Hence, $\mathbb{F}$ is a contraction. According to the Banach result, this means that there is exactly unique solution to the considered model in the given subinterval. Accordingly, (14) and (16), and the TB model in the piecewise nature has a unique solution for each subinterval. □

4. Stability Analysis

Here, the proof of HU stability is the aim of the section. For this, we assume the interval $\mathrm{B} = [0, T]$.

Definition 6. *The piecewise model in the classical and modified ABC derivatives for the TB* (1) *is HU stable if for each* $\alpha > 0$ *and*

$$
\Big|{}^{PCC}\mathbb{D}_t^\zeta \mathbf{w}^*(t) - \mathbb{F}(t, \mathbf{w}^*(t), {}^{PCC}\mathrm{D}_t^\zeta \mathbf{w}^*(t))\Big| < \alpha, \ for\ all, t \in \mathrm{B}, \tag{17}
$$

there is a unique solution $\overline{\mathbf{w}^*} \in Z$ *with* $\mathcal{H} > 0$*, a constant, such that*

$$
\big|\big|\mathbf{w}^* - \overline{\mathbf{w}^*}\big|\big|_Z \leq \mathcal{H}\alpha, for\ \ all, t \in \mathrm{B}. \tag{18}
$$

Also, if we possess a nondecreasing function $\Phi : [0, \infty) \to R^+$*, satisfying that*

$$
\big|\big|\mathbf{w}^* - \overline{\mathbf{w}^*}\big|\big|_Z \leq \mathcal{H}\Phi(\alpha), at\ every, t \in \mathrm{B}, \tag{19}
$$

where $\Phi(0) = 0$*, then the solution of the proposed piecewise model for the TB* (1) *is generally HU stable.*

Lemma 3. *Consider the function*

$$
{}_0^{PCC}\mathrm{D}_t^\zeta \mathbf{w}^*(t) = \mathbb{F}(t, \mathbf{w}^*(t)), \ \ 0 < \zeta \leq 1. \tag{20}
$$

The solution of (20) is:

$$\mathbf{w}^*(t) = \begin{cases} \mathbf{w}_0^* + \Phi(\mathbf{w}^*) + \int_0^{t_1} \mathcal{F}(s, \mathbf{w}^*(s))ds + \int_0^{t_1} \phi(s)ds, \ 0 < t \leq t_1, \\ \mathbf{w}_0 + \frac{1-\zeta}{B(\zeta)}\mathbb{S}(t, \mathbf{w}^*(t)) + \frac{\zeta}{\Gamma(\zeta)B(\zeta)} \int_0^t (t-s)^{\zeta-1}\mathbb{S}(s, \mathbf{w}^*(s))ds \\ - \frac{1-\zeta}{B(\zeta)}\mathbb{S}(0, \mathbf{w}^*(0))\Big(1 + \frac{\gamma_\zeta}{\Gamma(\zeta+1)}t^\zeta\Big), \qquad\qquad \mathtt{t}_1 < \mathtt{t} \leq \mathtt{t}_2 \end{cases}$$

It is simple for us to derive the inequality that is presented below.

$$\big|\big|\mathbb{F}(\mathbf{w}^*) - \mathbb{F}(\overline{\mathbf{w}^*})\big|\big| \leq \begin{cases} \left(\frac{t_1}{1 - \frac{L_\mathbb{F}}{1-M_\mathbb{F}}}\right)\alpha, t \in \mathrm{B}_1, \\ \left[\frac{L_g}{\alpha}\left(\frac{1-\zeta}{B(\zeta)} + \frac{1}{\Gamma(\zeta)B(\zeta)}\right)\right]\alpha = \Lambda\alpha, t \in \mathrm{B}_2. \end{cases} \tag{21}$$

Theorem 3. *Based on the lemma 3, if we have* $\frac{L_\mathbb{F}}{1-M_f} < 1$*, is the case, then the solution to our considered model, which is denoted by* (1) *, will be HU stable as well as generalized HU stable.*

Proof. Assume that $\mathbf{w}^* \in Z$ be a solution of the piecewise TB system (1) and $\overline{\mathbf{w}^*} \in Z$ be an approximation of (1), then
Case 1: for $t \in \mathrm{B}$, we have

$$\begin{aligned} \big|\big|\mathbf{w}^* - \overline{\mathbf{w}^*}\big|\big| &= \sup_{t\in\mathrm{B}}\left|\mathbf{w}^* - \left(\mathbf{w}_\circ^* + \Phi(\overline{\mathbf{w}^*}) + \int_0^{t_1}\mathbb{F}\big(s, \overline{\mathbf{w}^*}(s)\big)d\bar{s} + \int_0^{t_1}\mathbf{w}^*(s)ds\right)\right| \\ &\leq \sup_{t\in\mathrm{B}}\left|\mathbf{w}^* - \left(\mathbf{w}_\circ^* + \Phi(\overline{\mathbf{w}^*}) + \int_0^{t_1}\mathbb{F}\big(s, \overline{\mathbf{w}^*}(s)\big)ds\right)\right| \\ &+ \sup_{t\in\mathrm{B}}\left|\Phi(\mathbf{w}^*) - \Phi(\overline{\mathbf{w}^*}) + \int_0^{t_1}\mathbb{F}(s, \mathbf{w}^*(s))d\bar{s} + \int_0^{t_1}\mathbb{F}\big(s, \overline{\mathbf{w}^*}(s)\big)ds\right| \\ &\leq t_1\alpha + \frac{L_\mathbb{F}}{1-M_f}\big|\big|\mathbf{w}^* - \overline{\mathbf{w}^*}\big|\big|_Z. \end{aligned}$$

On further simplification:

$$\big|\big|\mathbf{w}^* - \overline{\mathbf{w}^*}\big|\big| \leq \left(\frac{t_1}{1 - \frac{L_\mathbb{F}}{1-M_\mathbb{F}}}\right)\alpha. \tag{22}$$

Case 2: for $t \in \mathrm{B}$, we have

$$\begin{aligned} \big|\big|\mathbf{w}^* - \overline{\mathbf{w}^*}\big|\big| &= \sup_{t\in\mathrm{B}}\big|\mathbf{w}_0^* + \frac{1-\zeta}{B(\zeta)}\mathbb{S}(t, \mathbf{w}^*(t)) + \frac{\zeta}{\Gamma(\zeta)B(\zeta)}\int_0^{t_2}(t_2-s)^{\zeta-1}\mathbb{S}(s, \mathbf{w}^*(s))ds \\ &- \frac{1-\zeta}{B(\zeta)}\mathbb{S}(0, \mathbf{w}^*(0))\Big(1 + \frac{\gamma_\zeta}{\Gamma(\zeta+1)}t^\zeta\Big) \\ &- \big[\mathbf{w}_0^* + \frac{1-\zeta}{B(\zeta)}\mathbb{S}(t, \bar{\mathbf{w}}^*(t)) + \frac{\zeta}{\Gamma(\zeta)B(\zeta)}\int_0^{t_2}(t_2-s)^{\zeta-1}\mathbb{S}(s, \bar{\mathbf{w}}^*(s))ds \\ &- \frac{1-\zeta}{B(\zeta)}\mathbb{S}(0, \mathbf{w}^*(0))\Big(1 + \frac{\gamma_\zeta}{\Gamma(\zeta+1)}t^\zeta\Big)\big]\big| \\ &\leq \sup_{t\in\mathrm{B}}\left|\frac{1-\zeta}{B(\zeta)}L_g\|\mathbf{w}^* - \bar{\mathbf{w}}^*\|\right| + \frac{\zeta}{\Gamma(\zeta)B(\zeta)}\int_0^{t_2}(t_2-s)^{\zeta-1}\|\mathbb{S}(s, \mathbf{w}^*(s) - \mathbb{S}(s, \bar{\mathbf{w}}^*(s)\|ds \\ &g\left(\frac{1-\zeta}{B(\zeta)} + \frac{1}{\Gamma(\zeta)B(\zeta)}\right)\|\mathbf{w}^* - \bar{\mathbf{w}}^*\| \\ &= \bar{\delta}_g\|\mathbf{w}^* - \bar{\mathbf{w}}^*\|\alpha, \end{aligned} \tag{23}$$

for $\bar{\delta}_g = \frac{L_g}{\alpha}\left(\frac{1-\zeta}{B(\zeta)} + \frac{1}{\Gamma(\zeta)B(\zeta)}\right)$. Since, we have assume $\mathbf{w}^*$, $\bar{\mathbf{w}}^*$ solutions of the piecewise TB model (1), this implies, these are the fixed points of the operator $\mathbb{F}$, or mathematically, $\mathbb{F}(\mathbf{w}^*) = g$, and $\mathbb{F}(\bar{\mathbf{w}}^*) = \bar{\mathbf{w}}^*$. Thus, from (23), we proceed to the following relation

$$\|\mathbb{F}(\mathbf{w}^*) - \mathbb{F}(\bar{\mathbf{w}}^*)\| \leq \bar{\delta}_g \|\mathbf{w}^* - \bar{\mathbf{w}}^*\|. \tag{24}$$

Also, we have

$$\begin{aligned} |\mathbf{w}^* - \overline{\mathbf{w}^*}| &= \|\mathbf{w}^* - \mathbb{F}(\mathbf{w}^*) + \mathbb{F}(\bar{\mathbf{w}}^*) - \overline{\mathbf{w}^*}\| \\ &\leq \|\mathbf{w}^* - \mathbb{F}(\mathbf{w}^*)\| + \|\mathbb{F}(\mathbf{w}^*) - \mathbb{F}(\overline{\mathbf{w}^*})\|. \end{aligned} \tag{25}$$

By the help of (23), (24), and (25), we have

$$\|\mathbf{w}^* - \overline{\mathbf{w}^*}\| \leq \frac{\alpha^*}{1-\bar{\delta}_g} = \mathcal{H}\alpha^*. \tag{26}$$

For $\mathcal{H} = \frac{1}{1-\bar{\delta}_g}$. Thus, the presumed model is Hyers–Ulam stable. Furthermore, replacing α by $\Phi(\alpha)$ the system (20) implies

$$\left|\left|\mathbf{w}^* - \overline{\mathbf{w}^*}\right|\right|_Z \leq \mathcal{H}\Phi(\alpha), at \ \ each \ t \in \mathrm{B}.$$

Now $\Phi(0) = 0$, this implies the solution of the piecewise TB model (1) is generalized HU stable. □

5. Numerical Scheme

In this part of the article, we will derive a numerical scheme for the model that we proposed in (1), and we will proceed to implement it. We were able to obtain the piecewise integral by employing it on (6), which allowed us to reach our objective.

$$\mathrm{X}_1(t) = \begin{cases} \mathrm{X}_1(0) + \displaystyle\int_0^{t_1} \mathbb{S}_1(s, \mathrm{X}_1)ds, \ \ 0 < t \leq t_1, \\ \mathrm{X}_1(t_1) + \dfrac{1-\zeta}{B(\zeta)}\mathbb{S}_1(t, \mathrm{X}_1(t)) + \dfrac{\zeta}{\Gamma(\zeta)B(\zeta)}\displaystyle\int_0^{t_2}(t_2 - s)^{\zeta-1}\mathbb{S}_1(s, \mathrm{X}_1(s))ds \\ - \dfrac{1-\zeta}{B(\zeta)}\mathbb{S}_1(0, \mathrm{X}_1(0))\left(1 + \dfrac{\gamma_\zeta}{\Gamma(\zeta+1)}t^\zeta\right), \ \ t_1 < t \leq t_2, \end{cases}$$

$$\mathrm{X}_2(t) = \begin{cases} \mathrm{X}_2(0) + \displaystyle\int_0^{t_1} \mathbb{S}_2(s, C)ds, \ \ 0 < t \leq t_1, \\ \mathrm{X}_2(t_1) + \dfrac{1-\zeta}{B(\zeta)}\mathbb{S}_2(t, \mathrm{X}_2(t)) + \dfrac{\zeta}{\Gamma(\zeta)B(\zeta)}\displaystyle\int_0^{t_2}(t_2 - s)^{\zeta-1}\mathbb{S}_2(s, \mathrm{X}_2(s))ds \\ - \dfrac{1-\zeta}{B(\zeta)}\mathbb{S}_2(0, \mathrm{X}_2(0))\left(1 + \dfrac{\gamma_\zeta}{\Gamma(\zeta+1)}t^\zeta\right), \ \ t_1 < t \leq t_2, \end{cases}$$

$$\mathrm{X}_3(t) = \begin{cases} \mathrm{X}_3(0) + \displaystyle\int_0^{t_1} \mathbb{S}_3(s, \mathrm{X}_3)ds, \ \ 0 < t \leq t_1, \\ \mathrm{X}_3(t_1) + \dfrac{1-\zeta}{B(\zeta)}\mathbb{S}_1(t, \mathrm{X}_3(t)) + \dfrac{\zeta}{\Gamma(\zeta)B(\zeta)}\displaystyle\int_0^{t_2}(t_2 - s)^{\zeta-1}\mathbb{S}_3(s, \mathrm{X}_3(s))ds \\ - \dfrac{1-\zeta}{B(\zeta)}\mathbb{S}_3(0, \mathrm{X}_3(0))\left(1 + \dfrac{\gamma_\zeta}{\Gamma(\zeta+1)}t^\zeta\right) \ t_1 < t \leq t_2. \end{cases}$$

At $t = t_{n+1}$, we deduce it for the system (27), as under:

$$\mathrm{X}_1(t_{n+1})) = \begin{cases} \mathrm{X}_1(0) + \int_0^{t_1} \mathbb{S}_1(s, \mathrm{X}_1)ds, 0 < t_{n+1} \leq t_1, \\ \mathrm{X}_1(t_1) + \frac{1}{\Gamma(\zeta)} \int_{t_1}^{t_{n+1}} (t-s)^{\zeta-1} \mathbb{S}_1(s, \mathrm{X}_1)ds, \ t_1 < t_{n+1} \leq t_2. \end{cases} . \tag{27}$$

Now, the equation (27) can be expressed by using Lagrange's interpolation polynomial for the modified ABC part of the piecewise operator, we presume $k \in \{1, 2, \ldots, n\}$ in the following scheme:

$$\mathrm{X}_1(t_{n+1}) = \begin{cases} \mathrm{X}_1(0) + \left\{ \sum_{\mathbf{K}=2}^{i} \left[\frac{5}{12} \mathbb{S}_1(t_{\mathbf{K}-2}, \mathrm{X}_1) - \frac{4}{3} \mathbb{S}_1(\mathbb{U}_1, t_{\mathbf{K}-1}) \bar{\delta} t + \mathbb{S}_1(\mathbb{U}, t_{\mathbf{K}}) \right], \quad 0 < t_{n+1} \leq t_1, \right. \\ \mathrm{X}_1(t_1) + \left\{ \begin{array}{l} + \frac{1-\zeta}{B(\zeta)} \mathbb{S}_1(t_k, \mathrm{X}_1(t_k)) \\ + \frac{\zeta_1 h^\zeta}{\Gamma(\zeta+2)} \Sigma_{k=1}^{n} \left[\mathbb{S}_1(t_k, \mathrm{X}_1(t_k)) \left((n+1-k)^\zeta (n-k+\zeta+2) \right. \right. \\ \left. - (n-k)^\zeta (n+2-k+2\zeta) \right) - \mathbb{S}_1(t_{k-1}, \mathrm{X}_{1k-1}) \left((n-k+1)^{\zeta+1} \right. \\ \left. \left. - (n-k)^\zeta (n-k+1+\zeta) \right) \right] - \frac{1-\zeta}{B(\zeta)} \mathbb{S}_1(0, \mathrm{X}_1(0)) \left(1 + \frac{\gamma_\zeta (kh)^\zeta}{\Gamma(\zeta+1)} \right), \\ t_1 < t_{n+1} \leq t_2. \end{array} \right\} \end{cases} \tag{28}$$

$$\mathrm{X}_2(t_{n+1}) = \begin{cases} \mathrm{X}_2(0) + \left\{ \begin{array}{l} \sum_{\mathbf{K}=2}^{i} \left[\frac{5}{12} \mathbb{S}_2(t_{\mathbf{K}-2}, \mathrm{X}_2) \bar{\delta} t \right. \\ \left. - \frac{4}{3} \mathbb{S}_2(t_{\mathbf{K}-1}, \mathrm{X}_2) \bar{\delta} t + \mathbb{S}_2(t_{\mathbf{K}}, \mathrm{X}_2) \right], \quad 0 < t \leq t_1, \end{array} \right. \\ \mathrm{X}_2(t_1) + \left\{ \begin{array}{l} + \frac{1-\zeta}{B(\zeta)} \mathbb{S}_2(t_k, \mathrm{X}_2(t_k)) \\ + \frac{\zeta_1 h^\zeta}{\Gamma(\zeta+2)} \Sigma_{k=1}^{n} \left[\mathbb{S}_2(t_k, \mathrm{X}_2(t_k)) \left((n-k+1)^\zeta (n+2-k+\zeta) \right. \right. \\ \left. - (n-k)^\zeta (n+2-k+2\zeta) \right) - \mathbb{S}_2(t_{k-1}, \mathrm{X}_{2k-1}) \left((n-k+1)^{\zeta+1} \right. \\ \left. \left. - (n-k)^\zeta (n-k+1+\zeta) \right) \right] - \frac{1-\zeta}{B(\zeta)} \mathbb{S}_2(0, \mathrm{X}_2(0)) \left(1 + \frac{\gamma_\zeta (kh)^\zeta}{\Gamma(\zeta+1)} \right), \\ t_1 < t_{n+1} \leq t_2, \end{array} \right\} \end{cases} \tag{29}$$

$$\mathrm{X}_3(t_{n+1}) = \begin{cases} \mathrm{X}_3(0) + \begin{cases} \sum_{\mathbf{K}=2}^{i} \left[\frac{5}{12}\mathbb{S}_3(t_{\mathbf{K}-2}, \mathrm{X}_3)\bar{\delta}t \right. \\ \left. - \frac{4}{3}\mathbb{S}_3(t_{\mathbf{K}-1}, \mathrm{X}_3)\bar{\delta}t + \mathbb{S}_3(t_{\mathbf{K}}, \mathrm{X}_3) \right], \quad 0 < t \leq t_1, \end{cases} \\ \mathrm{X}_3(t_1) + \begin{cases} + \frac{1-\zeta}{B(\zeta)}\mathbb{S}_3(t_k, \mathrm{X}_3(t_k)) \\ + \frac{\zeta_1 h^{\zeta}}{\Gamma(\zeta+2)}\Sigma_{k=1}^{n} \left[\mathbb{S}_3(t_k, \mathrm{X}_3(t_k)) \left((n+1-k)^{\zeta}(n+2-k+\zeta) \right. \right. \\ \left. - (n-k)^{\zeta}(n+2-k+2\zeta) \right) - \mathbb{S}_3(t_{k-1}, \mathrm{X}_{3k-1}) \left((n-k+1)^{\zeta+1} \right. \\ \left. \left. - (n-k)^{\zeta}(n+1+\zeta-k) \right) \right] - \frac{1-\zeta}{B(\zeta)}\mathbb{S}_3(0, \mathrm{X}_3(0)) \left(1 + \frac{\gamma_{\zeta}(kh)^{\zeta}}{\Gamma(\zeta+1)} \right), \\ t_1 < t_{n+1} \leq t_2. \end{cases} \end{cases} \tag{30}$$

In the next section, this scheme for the leukemia dynamics are applied for assumptions from the available literature. For other numerical techniques, the authors may refer to the work in [45–50].

6. Computational Discussion for the Leukemia Model

Because of recent developments in genomic profiling and molecular characterization, distinct genetic abnormalities in leukemia cells have been identified. Tyrosine kinase inhibitors (TKIs) and monoclonal antibodies are two examples of targeted medicines that have greatly improved the treatment of some types of leukemia. Rituximab is used to treat B-cell acute lymphoblastic leukemia (B-ALL), whereas imatinib is used to treat chronic myeloid leukemia (CML). Increased response rates and increased survival times are the results of these medicines' ability to selectively block abnormal signaling pathways.

Here, we present the application of the numerical scheme for the simulation of the fractional-order IS model (1) with the parametric values given $X_1 = 1.8 \times 10^8$, $X_2 = 1.8 \times 10^8$, $X_3 = 0$, $\psi_n = 0.15$, $\eta_n = 0.04$, $\eta_l = 0.04$, $Na = 10^{10}, La = 10^{10}, a_1 = 2.5$, $a_2 = 1.4$, $b_1 = b_2 = 0.01$. For details, see [15,16].

Figure 1 shows the simulation results for the presumed piecewise mABC model for the classical case or integer order as a joint solution.

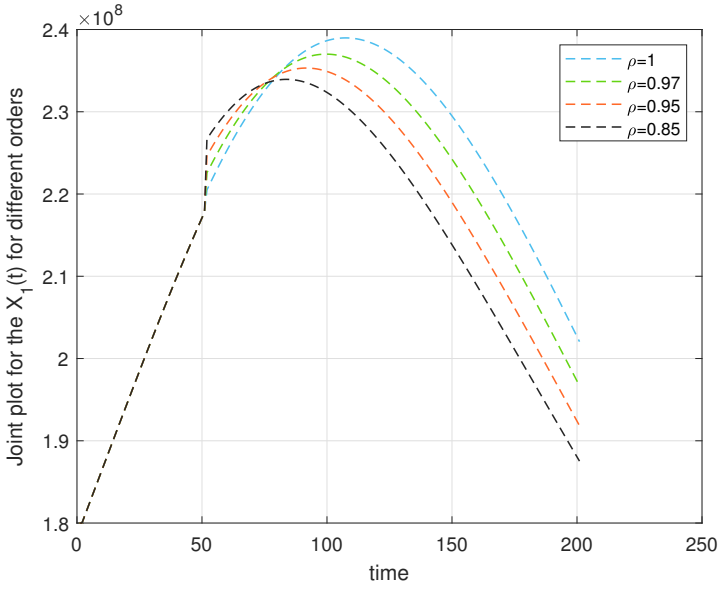

Figure 1. Graphical representation of X_1 in piecewise model (1) with $t_1 = 50$ keeping $\psi_n = \psi_l = 0.04$.

The simulations are carried out in the figures and explained here. Our proposed differential operator and integral operator are in the piecewise combination of the classical and the modified ABC operators. For this, we have considered the interval of study as for two hundred units; that is, $I = [0, 200]$. This interval is divided into two subintervals. The first is $I_1 = [0, 50]$ and the second is $[50, 200]$. Thus, $t_1 = 50$ while $t_2 = 200$. The first graph is for $X_1(t)$, in which we can see the simulations for the dynamics are representing the crossover behavior given in the Figure 1. This class shows a sudden fall in its population after 100 days. The fractional orders are considered in the second subinterval $[50, 200]$. Crossover behavior is apparently observed in the simulations. In Figure 2 that follows, we have dynamics for the X_2, which is described in two intervals $\mathcal{I}_1$ and $\mathcal{I}_2$. In the $\mathcal{I}_1$, the dynamics are presented for the classical derivative of order 1, while in the second interval $\mathcal{I}_2$, the modified ABC fractional derivative is considered. A clear crossover behavior of the X_2 is observed at the time 50. The fractional orders are considered as 1, 0.95, 0.90, 0.85. There is initially an increase in leukemic cells. In Figure 3, the chemotherapeutic agents are presented, which are decreasing with respect to the time. In these three figures, we have considered the reproduction of normal cells and leukemic cells identical as $\psi_n = \psi_l = 0.04$ and per the references [15,16]. In the next three figures, we have presumed that $\psi_n = \psi_l = 0.08$, which affects the fall in the accumulation of normal cells, and there is a comparatively rapid increase in leukemic cells, which can be observed in the Figures 4 and 5, respectively.

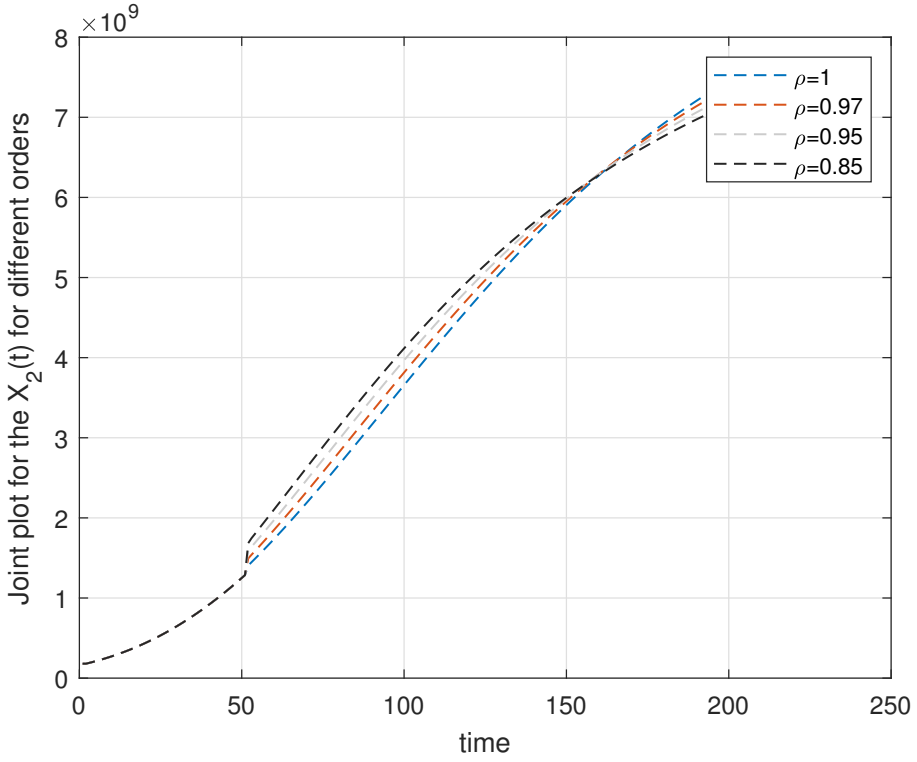

Figure 2. Graphical representation of X_2 in piecewise model (1) with $t_1 = 50$ keeping $\psi_n = \psi_l = 0.04$.

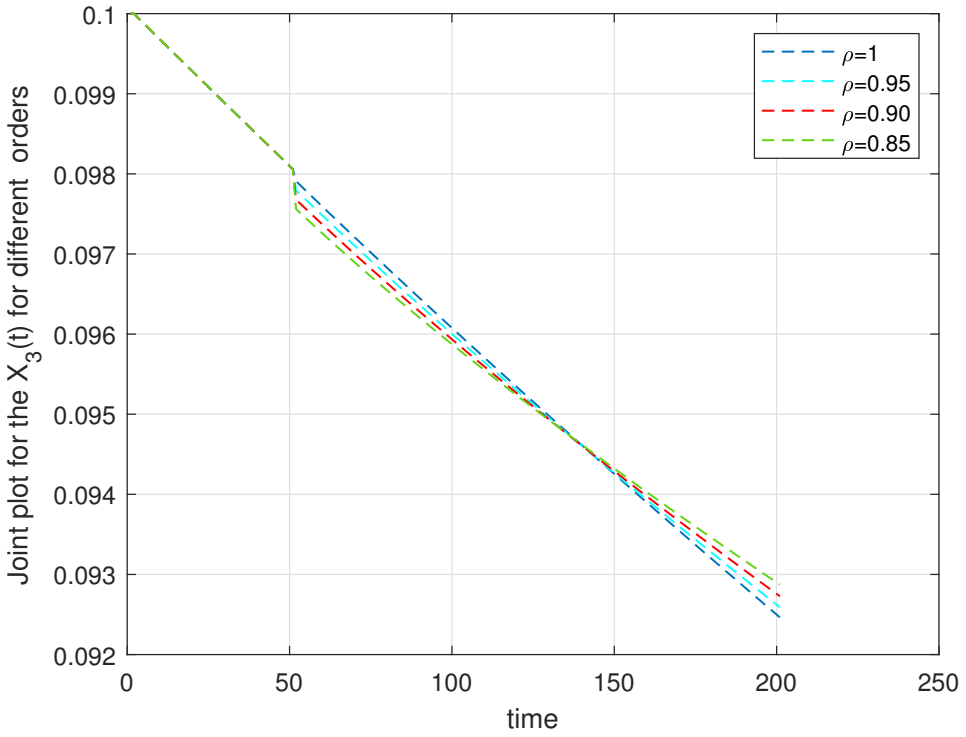

Figure 3. Graphical representation of X_3 in piecewise model (1) with $t_1 = 50$ keeping $\psi_n = \psi_l = 0.04$.

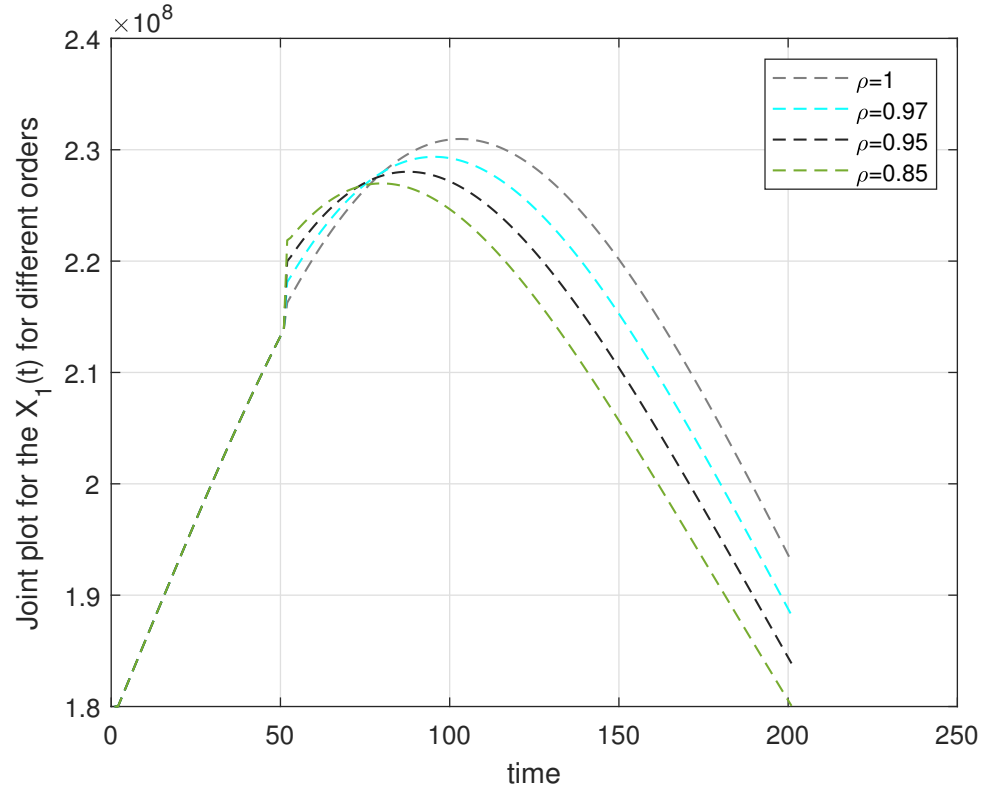

Figure 4. Graphical representation of X_1 in piecewise model (1) with $t_1 = 50$ keeping $\psi_n = \psi_l = 0.08$.

In Figure 1, we have given results for the X_1, which represents the class of normal cells.

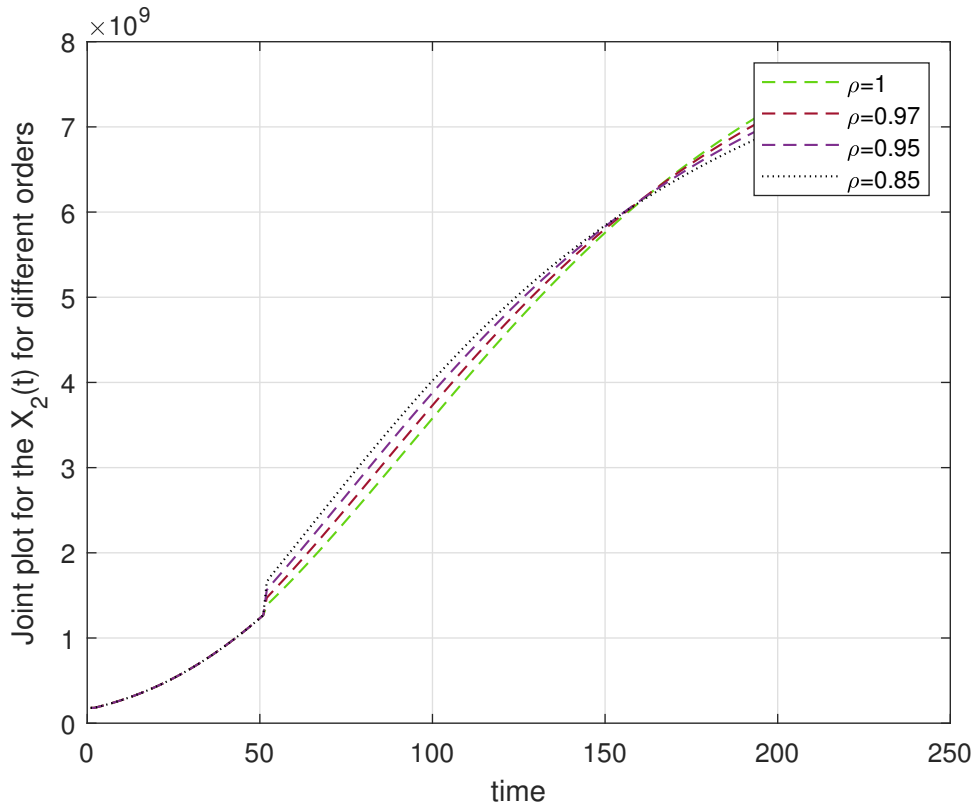

Figure 5. Graphical representation of X_2 in piecewise model (1) with $t_1 = 50$ keeping $\psi_n = \psi_l = 0.08$.

7. Conclusions

In this article, a leukemia piecewise fractional-order model is constructed and presented for theoretical as well computational works. In theoretical works, the theory of fixed points is considered for the solution existence, and solution uniqueness and stability are obtained with the classical notions. The numerical work is based on our computational scheme carried out with the help of Lagrange's polynomial. The model is studied for two different cases. In the first case, we have considered the values of $\psi_n = \psi_l = 0.04$, as per classical case. And the computational results are presented in three graphs as Figures 1–3. Then, the values are modified to $\psi_n = \psi_l = 0.08$, and further new computations are presented in Figures 4–6. With the increase in these values, we observe the loss in the normal cells with a further increase and the shift to leukemia growth, which even falls under the role of chemotherapy. Recent chemotherapeutic developments in leukemia have opened up promising new treatment options for patients. Due to their remarkable effectiveness, targeted treatments, immunotherapies, and combination regimens are gradually displacing conventional chemotherapy in some patient populations. Drug resistance and toxicity are two problems that still need to be addressed. To further improve the efficacy and safety of leukemia chemotherapy, future studies should concentrate on improving treatment regimens, discovering predictive biomarkers, and generating novel drugs. One can extend the work in the stochastic version with the help of [50].

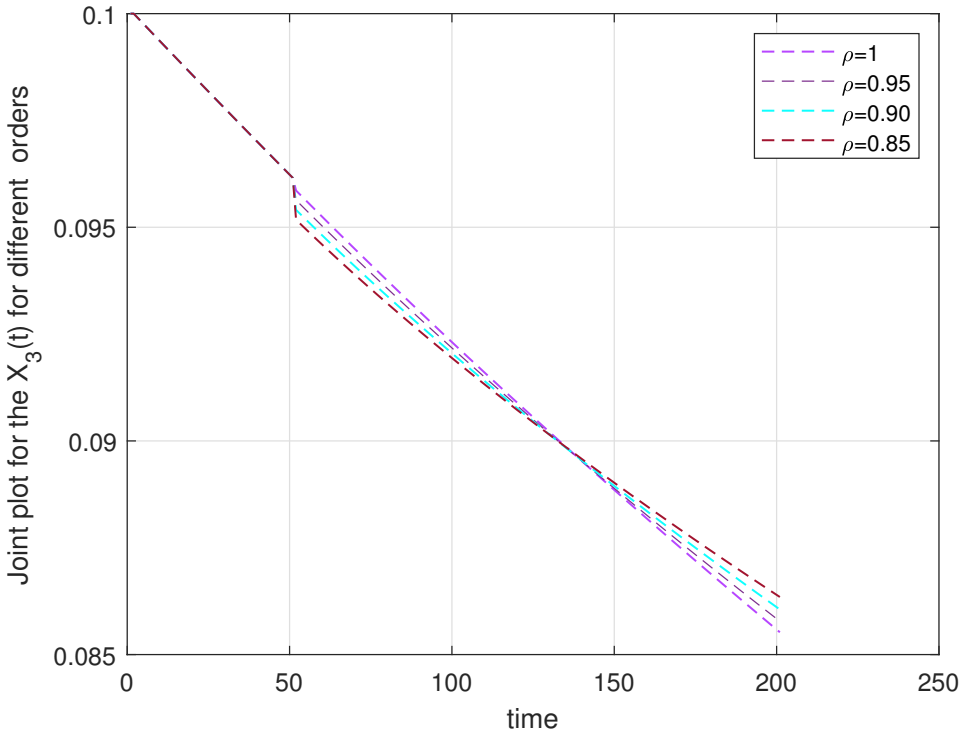

Figure 6. Graphical representation of X_3 in piecewise model (1) with $t_1 = 50$ keeping $\psi_n = \psi_l = 0.08$.

Author Contributions: H.K. contributed to the conceptualization, J.A. to the methodology, W.F.A. to the formal analysis, and H.G. helped with the introduction of the biological literature of leukemia disease and its scientific role. All authors have read and agreed to the published version of the manuscript.

Funding: W.F.A. is funded by Princess Nourah bint Abdulrahman University Researchers Supporting Project number (PNURSP2023R 371), Princess Nourah bint Abdulrahman University, Riyadh, Saudi Arabia.

Data Availability Statement: No data are available.

Acknowledgments: H.K. and J.A. are thankful to Prince Sultan University for their endless support under the SEED Project (SEED-CHS-2023-126). J.A. is also thankful to OSTIM Technical University. W.F.A. is thankful to the Princess Nourah bint Abdulrahman University Researchers Supporting Project number (PNURSP2023R 371), Princess Nourah bint Abdulrahman University, Riyadh, Saudi Arabia.

Conflicts of Interest: There are no conflicts of interest among the authors.

Abbreviations

The following abbreviations are used in this manuscript:

ABC	Atangana–Baleanu in Caputo's sense
FDEs	fractional differential equations
FPT	fixed-point theorems

References

1. Doebelin, E. *System Dynamics: Modeling, Analysis, Simulation, Design*; CRC Press: Boca Raton, FL, USA, 1998.
2. Castillo-Chavez, C.; Song, B. Dynamical models of tuberculosis and their applications. *Math. Biosci. Eng.* **2004**, *1*, 361–404. [CrossRef]
3. Velten, K. *Mathematical Modeling and Simulation: Introduction for Scientists and Engineers*; John Wiley & Sons: Hoboken, NJ, USA, 2009.

4. Formaggia, L.; Quarteroni, A.; Veneziani, A. *Cardiovascular Mathematics: Modeling and Simulation of the Circulatory System*; Springer Science & Business Media: Berlin/Heidelberg, Germany, 2010.
5. Bunimovich-Mendrazitsky, S.; Kronik, N.; Vainstein, V. Optimization of Interferon–Alpha and Imatinib Combination Therapy for Chronic Myeloid Leukemia: A Modeling Approach. *Adv. Theory Simul.* **2019**, *2*, 1800081. [CrossRef]
6. Khatun, M.S.; Biswas, M.H. Modeling the effect of adoptive T cell therapy for the treatment of leukemia. *Comput. Math. Methods* **2020**, *2*, e1069. [CrossRef]
7. Piller, G. The history of leukemia: A personal perspective. *Blood Cells* **1993**, *19*, 521–529. [PubMed]
8. Drexler, H.G.; Minowada, J. History and classification of human leukemia-lymphoma cell lines. *Leuk. Lymphoma* **1998**, *31*, 305–316. [CrossRef] [PubMed]
9. Thomas, X. First contributors in the history of leukemia. *World J. Hematol.* **2013**, *2*, 62–70. [CrossRef]
10. Mehranfar, S.; Zeinali, S.; Hosseini, R.; Mohammadian, M.; Akbarzadeh, A.; Feizi, A.H. History of leukemia: Diagnosis and treatment from beginning to now. *Galen Med. J.* **2017**, *6*, 12–22. [CrossRef]
11. Afenya, E. Acute leukemia and chemotherapy: A modeling viewpoint. *Math. Biosci.* **1996**, *138*, 79–100. [CrossRef] [PubMed]
12. Khatun, M.S.; Biswas, M.H. Mathematical analysis and optimal control applied to the treatment of leukemia. *J. Appl. Math. Comput.* **2020**, *64*, 331–353. [CrossRef]
13. Nobile, M.S.; Vlachou, T.; Spolaor, S.; Bossi, D.; Cazzaniga, P.; Lanfrancone, L.; Mauri, G.; Pelicci, P.G.; Besozzi, D. Modeling cell proliferation in human acute myeloid leukemia xenografts. *Bioinformatics* **2019**, *35*, 3378–3386. [CrossRef]
14. Li, Y.F.; Combes, F.P.; Hoch, M.; Lorenzo, S.; Sy, S.K.; Ho, Y.Y. Population pharmacokinetics of asciminib in tyrosine kinase inhibitor-treated patients with Philadelphia chromosome-positive chronic myeloid leukemia in chronic and acute phases. *Clin. Pharmacokinet.* **2022**, *61*, 1393–1403. [CrossRef] [PubMed]
15. Islam, Y.; Ahmad, I.; Zubair, M.; Shahzad, K. Double integral sliding mode control of leukemia therapy. *Biomed. Signal Process. Control* **2020**, *61*, 102046. [CrossRef]
16. Islam, Y.; Ahmad, I.; Zubair, M.; Islam, A. Adaptive terminal and supertwisting sliding mode controllers for acute Leukemia therapy. *Biomed. Signal Process. Control* **2022**, *71*, 103121. [CrossRef]
17. Awadalla, M.; Subramanian, M.; Abuasbeh, K. Existence and Ulam–Hyers Stability Results for a System of Coupled Generalized Liouville–Caputo Fractional Langevin Equations with Multipoint Boundary Conditions. *Symmetry* **2023**, *15*, 198. [CrossRef]
18. Alesemi, M.; Shahrani, J.S.; Iqbal, N.; Shah, R.; Nonlaopon, K. Analysis and Numerical Simulation of System of Fractional Partial Differential Equations with Non-Singular Kernel Operators. *Symmetry* **2023**, *15*, 233. [CrossRef]
19. Baitiche, Z.; Benchohra, C.D.C.M.; Zhou, Y. A New Class of Coupled Systems of Nonlinear Hyperbolic Partial Fractional Differential Equations in Generalized Banach Spaces Involving the ψ–Caputo Fractional Derivative. *Symmetry* **2021**, *13*, 2412. [CrossRef]
20. Srinivasa, K.; Baskonus, H.M.; Sanchez, Y.G. Numerical solutions of the mathematical models on the digestive system and COVID-19 pandemic by hermite wavelet technique. *Symmetry* **2021**, *13*, 2428. [CrossRef]
21. Atangana, A.; Araz, S.I. New concept in calculus:Piecewise differential and integral operators. *Chaos Solitons Fractals* **2021**, *145*, 110638. [CrossRef]
22. Ahmad, S.; Yassen, M.F.; Alam, M.M.; Alkhati, S.; Jarad, F.; Riaz, M.B. A numerical study of dengue internal transmission model with fractional piecewise derivative. *Results Phys.* **2022**, *39*, 105798. [CrossRef]
23. Heydari, M.H.; Razzaghi, M.; Baleanu, D. A numerical method based on the piecewise Jacobi functions for distributed-order fractional Schrödinger equation. *Commun. Nonlinear Sci. Numer. Simul.* **2023**, *116*, 106873. [CrossRef]
24. Kafle, R.C.; Kim, D.Y.; Holt, M.M. Gender-specific trends in cigarette smoking and lung cancer incidence: A two-stage age-stratified Bayesian joinpoint model. *Cancer Epidemiol.* **2023**, *84*, 102364. [CrossRef]
25. Abdelmohsen, S.A.M.; Yassen, M.F.; Ahmad, S.; Abdelbacki, A.M.M.; Khan, J. Theoretical and numerical study of the rumours spreading model in the framework of piecewise derivative. *Eur. Phys. J. Plus* **2022**, *137*, 738. [CrossRef]
26. Xu, C.; Liu, Z.; Pang, Y.; Akgul, A.; Baleanu, D. Dynamics of HIV-TB coinfection model using classical and Caputo piecewise operator: A dynamic approach with real data from South-East Asia, European and American regions. *Chaos Solitons Fractals* **2022**, *165*, 112879. [CrossRef]
27. Hasan, A.; Akgul, A.; Farman, M.; Chaudhry, F.; Sultan, M.; De la Sen, M. Epidemiological Analysis of Symmetry in Transmission of the Ebola Virus with Power Law Kernel. *Symmetry* **2023**, *15*, 665. [CrossRef]
28. Shah, A.; Khan, H.; De la Sen, M.; Alzabut, J.; Etemad, S.; Deressa, C.T.; Rezapour, S. On Non-Symmetric Fractal-Fractional Modeling for Ice Smoking: Mathematical Analysis of Solutions. *Symmetry* **2022**, *15*, 87. [CrossRef]
29. Feng, Y.; Yu, J. Lie symmetry analysis of fractional ordinary differential equation with neutral delay. *AIMS Math.* **2021**, *6*, 3592–3605. [CrossRef]
30. Liu, Y. On piecewise continuous solutions of higher order impulsive fractional differential equations and applications. *Appl. Math. Comput.* **2016**, *287*, 38–49. [CrossRef]
31. Ansari, K.J.; Asma; Ilyas, F.; Shah, K.; Khan, A.; Abdeljawad, T. On new updated concept for delay differential equations with piecewise Caputo fractional-order derivative. *Waves Random Complex Media* **2023**, 1–20. [CrossRef]
32. Angstmann, C.N.; Henry, B.I.; Jacobs, B.A.; McGann, A.V. Discretization of fractional differential equations by a piecewise constant approximation. *Math. Model. Nat. Phenom.* **2017**, *12*, 23–36. [CrossRef]
33. Al-Refai, M.; Baleanu, D. On an Extension of the Operator with Mittag-Leffler Kernel. *Fractals* **2022**, *30*, 1–7. [CrossRef]

34. Al-Refai, M. Proper inverse operators of fractional derivatives with nonsingular kernels. *Rend. Del Circ. Mat. Palermo Ser.* **2022**, *71*, 525–535. [CrossRef]
35. Khan, A.; Abdeljawad, T.; Gomez-Aguilar, J.F.; Khan, H. Dynamical study of fractional order mutualism parasitism food web module. *Chaos Solitons Fractals* **2020**, *134*, 109685. [CrossRef]
36. Khan, H.; Alzabut, J.; Gulzar, H. Existence of solutions for hybrid modified ABC-fractional differential equations with *p*-Laplacian operator and an application to a waterborne disease model. *Alex. Eng. J.* **2023**, *70*, 665–672. [CrossRef]
37. Boutiara, A.; Matar, M.M.; Alzabut, J.; Samei, M.E.; Khan, H. On ABC coupled Langevin fractional differential equations constrained by Perov's fixed point in generalized Banach spaces. *AIMS Math.* **2023**, *8*, 12109–12132. [CrossRef]
38. Khan, H.; Alzabut, J.; Baleanu, D.; Alobaidi, G.; Rehman, M.U. Existence of solutions and a numerical scheme for a generalized hybrid class of n-coupled modified ABC-fractional differential equations with an application. *AIMS Math.* **2023**, *8*, 6609–6625. [CrossRef]
39. Khan, A.; Ain, Q.T.; Abdeljawad, T.; Nisar, K.S. Exact Controllability of Hilfer Fractional Differential System with Non-instantaneous Impluleses and State Dependent Delay. *Qual. Theory Dyn. Syst.* **2023**, *22*, 62. [CrossRef]
40. Djaout, A.; Benbachir, M.; Lakrib, M.; Matar, M.M.; Khan, A.; Abdeljawad, T. Solvability and stability analysis of a coupled system involving generalized fractional derivatives. *AIMS Math.* **2023**, *8*, 7817–7839. [CrossRef]
41. Thirthar, A.A.; Abboubakar, H.; Khan, A.; Abdeljawad, T. Mathematical modeling of the COVID-19 epidemic with fear impact. *AIMS Math.* **2023**, *8*, 6447–6465. [CrossRef]
42. Houas, M.; Kaushik, K.; Kumar, A.; Khan, A.; Abdeljawad, T. Existence and stability results of pantograph equation with three sequential fractional derivatives. *AIMS Math.* **2023**, *8*, 5216–5232. [CrossRef]
43. Khan, A.; Shah, K.; Abdeljawad, T.; Alqudah, M.A. Existence of results and computational analysis of a fractional order two strain epidemic model. *Results Phys.* **2022**, *39*, 105649. [CrossRef]
44. Scholtes, S. *Introduction to Piecewise Differentiable Equations*; Springer Science & Business Media: Berlin/Heidelberg, Germany, 2012.
45. Tanvi, A.; Aggarwal, R.; Raj, Y.A. A fractional order TB co-infection model in the presence of exogenous reinfection and recurrent TB. *Nonlinear Dyn.* **2021**, *104*, 4701–4725.
46. Zeb, A.; Alzahrani, A. Non-standard finite difference scheme and analysis of smoking model with reversion class. *Res. Phys.* **2021**, *21*, 103785. [CrossRef]
47. Srivastava, H.M.; Gusu, D.M.; Mohammed, P.O.; Wedajo, G.; Nonlaopon, K.; Hamed, Y.S. Solutions of general fractional-order differential equations by using the spectral Tau method. *Fractal Fract.* **2022**, *6*, 7. [CrossRef]
48. Youssri, Y.H.; Abd-Elhameed, W.M.; Ahmed, H.M. New fractional derivative expression of the shifted third-kind Chebyshev polynomials: Application to a type of nonlinear fractional pantograph differential equations. *J. Funct. Spaces* **2022**, *2022*, 3966135. [CrossRef]
49. Doha, E.; Abd-Elhameed, W.M.; Ahmed, H. The coefficients of differentiated expansions of double and triple Jacobi polynomials. *Bull. Iran. Math. Soc.* **2012**, *38*, 739–765.
50. Ain, Q.T.; Nadeem, M.; Akgul, A.; De la Sen, M. Controllability of Impulsive Neutral Fractional Stochastic Systems. *Symmetry* **2022**, *14*, 2612. [CrossRef]

Disclaimer/Publisher's Note: The statements, opinions and data contained in all publications are solely those of the individual author(s) and contributor(s) and not of MDPI and/or the editor(s). MDPI and/or the editor(s) disclaim responsibility for any injury to people or property resulting from any ideas, methods, instructions or products referred to in the content.

symmetry

MDPI

Article

A Family of 1D Chaotic Maps without Equilibria

Marcin Lawnik [1,*], Lazaros Moysis [2,3,*] and Christos Volos [2]

[1] Department of Mathematics Applications and Methods for Artificial Intelligence, Faculty of Applied Mathematics, Silesian University of Technology, Kaszubska 23, 44-100 Gliwice, Poland
[2] Laboratory of Nonlinear Systems-Circuits & Complexity, Physics Department, Aristotle University of Thessaloniki, 54124 Thessaloniki, Greece; volos@physics.auth.gr
[3] Department of Mechanical Engineering, University of Western Macedonia, 50100 Kozani, Greece
* Correspondence: marcin.lawnik@polsl.pl (M.L.); lmousis@physics.auth.gr (L.M.)

Abstract: In this work, a family of piecewise chaotic maps is proposed. This family of maps is parameterized by the nonlinear functions used for each piece of the mapping, which can be either symmetric or non-symmetric. Applying a constraint on the shape of each piece, the generated maps have no equilibria and can showcase chaotic behavior. This family thus belongs to the category of systems with hidden attractors. Numerous examples of chaotic maps are provided, showcasing fractal-like, symmetrical patterns at the interchange between chaotic and non-chaotic behavior. Moreover, the application of the proposed maps to a pseudorandom bit generator is successfully performed.

Keywords: chaos; discrete map; hidden attractor; fixed point; equilibrium; chaotification

1. Introduction

Chaos theory is one of the great discoveries of the 20th century. Deterministic chaos as a physical phenomenon is present in many different aspects of nature [1,2]. The field of chaos theory encompasses numerous applications in the natural sciences [3], with contributing research groups from all over the world [4]. One such aspect is chaos-based cryptography. This type of cryptography uses chaotic dynamical systems as a randomness source to perform actions relevant to confusion and diffusion, which are common operations used to encrypt a signal. Due to the determinism of chaos, every action performed on the information signal in order to encrypt it can be reversed at the receiver end to re-obtain the original message.

However, despite the effective use of chaos in encryption, many authors have pointed out some weaknesses in the design of chaotic encryption setups [5,6]. One of the weak points is the chosen chaotic dynamical system, which usually does not have decent properties from the point of view of cryptography. These properties include, among others: a sufficiently large space of possible parameters and initial conditions for which the system is chaotic, appropriate sensitivity to the change of initial conditions and parameters expressed in the form of the Lyapunov exponent, acceptable computational complexity of the algorithm itself, or acceptable complexity of the chaotic dynamical system. Unfortunately, the chaotic systems used in the literature often do not meet all the above-mentioned assumptions.

Currently, chaos-based cryptography is a field of great interest. The interests of researchers include text [7] or image encryption [8], pseudorandom number generators [9,10], methods of generating S-boxes [11], or even asymmetric algorithms [12]. However, chaotic cryptography is not the only application of dynamical systems with chaotic behavior. Other areas where chaotic systems play an important role include secure communications [13], chaotic navigation [14], or optimization [15]. In all these applications, the chaotic systems used should satisfy a certain set of requirements relevant to the application at hand, for example a high key space, uninterrupted chaotic behavior with respect to parameter changes, resistance to parameter estimation attacks, and more.

There are many works on chaotic dynamical systems in the literature. They concern classical systems, such as the logistic map or tent map, and new systems created for the needs of a specific algorithm. However, the newly created systems are often computationally complicated (e.g., they require the use of appropriate numerical methods to generate solutions), or it is difficult to precisely determine for which parameters chaos occurs. Furthermore, in the literature, works on the so-called chaotification can be found, that is, methods of constructing new systems or improving the properties of already existing chaotic systems [16–18].

However, many of the new chaotic systems and the chaotification methods do not address the problem of the existence of the fixed points. Fixed points, which are also termed equilibrium points, are problematic because choosing one such point as an initial condition for the system will lead to non-chaotic behavior and thus ruin the design. Moreover, if a fixed point is stable, it will have an attracting region around it, meaning that trajectories starting around a region of the fixed point will also converge to it, again ruining the application performance. Hence, in such situations, the fixed point, along with its basin of attraction, must be excluded from the acceptable set of key values, so as not to ruin the application. A similar situation applies to periodic orbits, which, like fixed points, are not desirable from the point of view of applications. This paper deals with chaotic mappings without fixed points.

Thus, from the point of view of applications, the ideal chaotification method ensures that the system is chaotic, but at the same time, there are no fixed points. The works dealing with this problem concern continuous systems for which the above-mentioned problems occur [19–25], or for discrete maps, mainly piecewise linear ones [26–32]. Thus, in work [19], the authors presented a 3D dynamical system, which, apart from the lack of fixed points, is characterized by the coexistence of a limit cycle and torus. In [20], a simple no-equilibrium chaotic system with only one signum function is presented. This system is also characterized by the so-called hidden attractors, which can be distributed in a 1D line, a 2D lattice, or even a 3D grid. In turn, work [21] presents a fractional chaotic system, which is described by equations with few terms and parameters with a minimum of digits. A chaotic fractional dynamical system without fixed points is also shown in [22]. Another chaotic fractional system is also discussed in [23], where apart from the new dynamical system, its synchronization was also presented. In [24], a continuous 3D chaotic dynamical system with no equilibrium and its chaos anti-synchronization was presented. In turn, in [25], the authors present a novel continuous chaotic system without equilibrium. The work shows the dynamics, synchronization, and circuit realization of the proposed system.

Discrete chaotic systems may also not have fixed points. These systems are divided into one-dimensional (1D) systems, usually representing piecewise maps [26–29] or multi-dimensional systems [30–32]. In [26], a family of 1D piecewise linear maps is proposed, and necessary and sufficient conditions for the absence of equilibria are provided. The mapping region is also tunable by an appropriate parameter choice. In [28], a 1D map from [26] was implemented in an FPGA device. In [29], a new family of 1D maps termed Vertigo was proposed, with a tunable starting period and a period doubling transition to chaos. In [30], two 2D maps with quadratic nonlinearities were proposed, which were not in piecewise form. In [31], a 2D map inspired by the Arnold's cat map was proposed. In [32], a 2D map was developed combining cosine nonlinearity and a memristor. Finally, work [27] presents a comparative study of recent 1D and 2D maps with and without fixed points. Overall, following the development of continuous time systems, discrete maps without fixed points are receiving more attention in recent years, as more researchers are studying methods of efficiently constructing and studying such systems.

The aim and contribution of this work is the construction of chaotic discrete maps that do not have fixed points. The resulting dynamic systems can be either piecewise linear or nonlinear. The family of maps has three parameters, which are aimed at controlling the shape of each nonlinear piece, so that the map exhibits no fixed points. Three such maps are presented and studied. All maps showcase interesting patterns of transitioning in and

out of chaotic behavior, in the space of parameter values. The proposed family of maps has a general form, and thus, numerous maps without equilibria can be generated, meaning that further modifications can be developed in the future. The article also discusses the usefulness of such systems in the area of chaos-based cryptography.

The rest of the work is structured as follows. In Section 2, some fundamental preliminaries are provided regarding discrete maps. Section 3 presents a method for constructing a family of chaotic maps without fixed points. In turn, Section 4 presents examples of maps resulting from the proposed construction along with their analysis. In Section 5, the applications of the obtained chaotic mappings in the context of chaotic cryptography are presented. Section 6 then discusses the conclusions.

2. Preliminaries

In this work, we consider one-dimensional (1D) discrete dynamical systems, described by:

$$x_{k+1} = f(x_k), \tag{1}$$

where k denotes the iteration number, $x(k)$ is the state of the map, and $f(\cdot)$ the mapping function. In this paper, we will consider discrete dynamical systems for which f: $[0,1] \to [0,1]$.

A fixed point, or equilibrium, of a discrete dynamical system Equation (1) is a state value of x^* for which the following relation holds

$$f(x^*) = x^*. \tag{2}$$

Graphically, Equation (2) means that the plot of the function $f(x)$ intersects the bisector line at the point (x^*, x^*).

The necessary condition for the occurrence of chaos for mapping Equation (1) is the positive value of the Lyapunov exponent λ. The value of λ for the system Equation (1) is calculated according to the formula

$$\lambda = \lim_{n\to\infty} \frac{1}{n} \sum_{i=0}^{n-1} \ln |f'(x_i)|. \tag{3}$$

3. The Proposed Family of Maps

Let us consider the following discrete piecewise map

$$x_{k+1} = f(x_k) = \begin{cases} (a-1)f_1(x_k) + 1, & 0 \le x \le b \\ cf_2(x_k), & b < x \le 1 \end{cases}, \tag{4}$$

where $a, b, c \in (0,1)$ are control parameters. Furthermore, f_1: $[0,b] \to [0,1]$ and f_2: $[b,1] \to [0,1]$ are monotonic continuous functions with boundary values

$$f_1(0) = 1,\ f_1(b) = 0, \tag{5}$$

$$f_2(b) = 0,\ f_2(1) = 1. \tag{6}$$

The goal is to appropriately select the functions f_1, f_2 and parameters a, b and c so that Equation (4) has no fixed points.

Examples of functions f_1 and f_2 and the corresponding dynamical system of the form Equation (4) are shown in Figure 1. Furthermore, this figure clearly shows that each function f_1 and f_2 has exactly one fixed point (for the function f_2, it is the point $x^* = 1$). In turn, the mapping constructed on their basis does not have such fixed points.

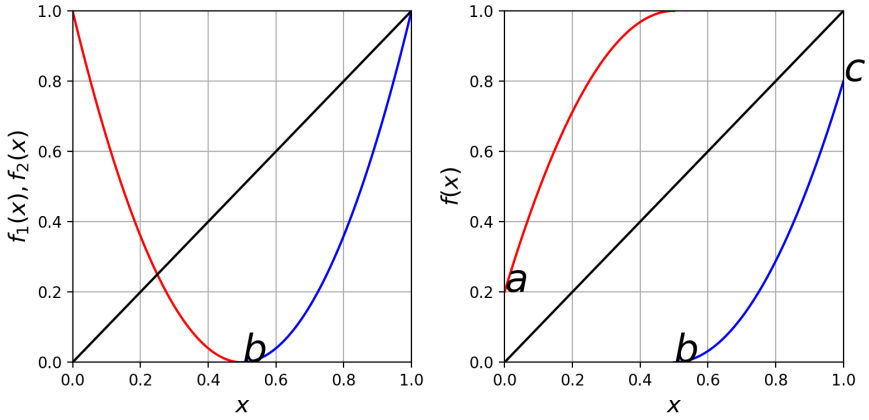

Figure 1. Left: Example of f_1 (red) and f_2 (blue) functions, where $f_1(x) = 4\left(x - \frac{1}{2}\right)^2$ for $x \in \left[0, \frac{1}{2}\right]$ and $f_2(x) = 4\left(x - \frac{1}{2}\right)^2$ for $x \in \left[\frac{1}{2}, 1\right]$. **Right**: map in form Equation (4) with the example functions f_1 and f_2.

Remark 1. *Map Equation* (4) *does not have equilibria if none of the functions* $f_1(x)$, $f_2(x)$ *have graphs that intersect with the bisector in the interval* $x \in [0,1]$. *Equivalently, setting* $x_{k+1} = x_k = x^*$, *the following equations*

$$(a-1)f_1(x^*) + 1 - x^* = 0, \quad 0 \le x^* \le b \tag{7}$$

$$cf_2(x^*) - x^* = 0, \quad b < x^* \le 1 \tag{8}$$

should not have a solution in the specified intervals.

Remark 2. *Note that the same result can be obtained if the functions* $f_1(x)$ *and* $f_2(x)$ *are replaced by the functions* $g_1(x) = -f_1(x) + 1$ *and* $g_2(x) = -f_2(x) + 1$. *Then, the dynamical system takes the form*

$$x_{k+1} = g(x_k) = \begin{cases} (1-a)g_1(x_k) + a, & 0 \le x \le b \\ -cg_2(x_k) + c, & b < x \le 1 \end{cases}, \tag{9}$$

where as before, $a, b, c \in (0,1)$ *are control parameters, and* g_1*:* $[0,b] \to [0,1]$, g_2*:* $[b,1] \to [0,1]$. *Furthermore,* g_1 *and* g_2 *are continuous monotonic functions with boundary values*

$$g_1(0) = 0, \; g_1(b) = 1, \tag{10}$$

$$g_2(b) = 1, \; g_2(1) = 0. \tag{11}$$

Examples of g_1 *and* g_2 *and the corresponding dynamical system of the form Equation* (9) *are shown in Figure 2.*

Remark 3. *The given construction of mappings without fixed points can be defined in yet another way. Instead of specifying the functions* f_1 *and* f_1, *(or* g_1 *and* g_2*) as shown in the case of mapping Equation* (4) *(or Equation* (9)*), it is possible to use the given boundary conditions directly. Then, the construction of mappings will be of the form:*

$$x_{k+1} = h(x_k) = \begin{cases} h_1(x_k), & 0 \le x \le b \\ h_2(x_k), & b < x \le 1 \end{cases}, \tag{12}$$

where $h_1 : [0,b] \to [a,1]$ $h_2 : [b,1] \to [0,c]$, $a, b, c \in (0,1)$.

Furthermore, functions h_1 *and* h_2 *should satisfy the conditions*

$$h_1(x) > x, \quad \forall x \in [0,b] \tag{13}$$

$$h_2(x) < x, \quad \forall x \in [b, 1]. \tag{14}$$

The construction of form Equation (12) *is more general than the constructions Equation* (4) *or Equation* (9). *However, determining functions* h_1 *and* h_2 *may be more difficult in practice. Furthermore, the mappings Equations* (4) *and* (9) *can be obtained by using other chaotic systems that are defined in the unit square.*

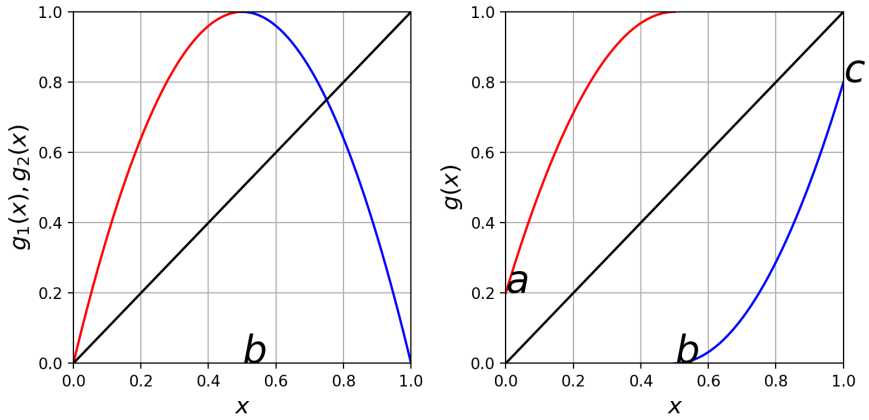

Figure 2. Left: Example of g_1 (red) and g_2 (blue) functions, where $g_1(x) = 4x(1-x)$ for $x \in \left[0, \frac{1}{2}\right]$ and $g_2(x) = 4x(1-x)$ for $x \in \left[\frac{1}{2}, 1\right]$. **Right**: map in form Equation (9) with the example functions g_1 and g_2.

4. Chaotic Map Examples

This section presents three examples illustrating the proposed method for constructing mappings without fixed points. When constructing such maps, the chosen subfunctions of the piecewise mapping can either have symmetry with respect to the family of nonlinear functions they belong, such as polynomial or trigonometric, graphical symmetry with respect to the bisector, or no symmetry at all.

4.1. Example 1—Polynomial Piecewise Map

Let us take the power functions as f_1 and f_2. Then, the chaotic mapping Equation (4) takes the form:

$$x_{k+1} = \begin{cases} (a-1)\left(\frac{b-x_k}{b}\right)^d + 1, & 0 \le x \le b \\ c\left(\frac{x_k - b}{1-b}\right)^d, & b < x \le 1 \end{cases}, \tag{15}$$

where $a, b, c \in (0, 1)$, $d \in \mathbb{R}_+$.

Recursion Equation (15) represents a whole family of chaotic maps. Using Remark 2, the asymmetric tent map (then $d = 1$ in Equation (15)) or the logistic map (then $d = 2$ and $b = 0.5$ in Equation (15)—this case is also shown in Figure 2)) can be used as basis functions g_1 and g_2 to obtain the dynamical system of form Equation (15). Thus, one of the most popular chaotic mappings in the literature can be used to create new dynamical systems.

Lemma 1. *For* $d \ge 1$, *map Equation* (15) *has no fixed points.*

Proof. First, consider the case $d = 1$. Then, the recursion functions are linear functions that pass through the points $(0, a)$ and $(b, 1)$ for $x \in [0, b]$ and $(b, 0)$ and $(1, c)$ for $x \in [b, 1]$, respectively. Thus, none of the functions intersect the line $y = x$. This means that for $d = 1$, system Equation (15) has no fixed points.

Now consider the case $d > 1$. Then, the left function is an increasing continuous concave function that passes through the points $(0, a)$ and $(b, 1)$ for $x \in [0, b]$. This conclusion follows directly from the analysis of the properties of the first derivative

$$f'(x) = \frac{-d(a-1)}{b}\left(\frac{b-x}{b}\right)^{d-1}, \tag{16}$$

which is positive in the domain, and the second derivative

$$f''(x) = \frac{d(d-1)(a-1)}{b^2}\left(\frac{b-x}{b}\right)^{d-2}, \tag{17}$$

which in this case is negative for $x \in (0, b)$.

In turn, the right function is an increasing continuous convex function that passes through points $(b, 0)$ and $(1, c)$ for $x \in (b, 1]$. This conclusion also follows directly from the analysis of the properties of the first derivative

$$f'(x) = \frac{dc}{(1-b)}\left(\frac{x-b}{1-b}\right)^{d-1}, \tag{18}$$

which is positive in the domain, and the second derivative

$$f''(x) = \frac{d(d-1)c}{(1-b)^2}\left(\frac{x-b}{1-b}\right)^{d-2}, \tag{19}$$

which in this case is also positive for $x \in (b, 1)$. Thus, none of the functions intersect the line $y = x$. This means that for $d > 1$, system Equation (15) has no fixed points. □

Examples of mappings for selected parameter values that meet the assumptions of Lemma 1 are presented, among others, in Figure 3a,b. Figure 3a shows a situation in which different values of parameter b are considered. In turn, Figure 3b shows a situation in which different values of the d parameter were used in Equation (15). Moreover, these mappings are symmetrical.

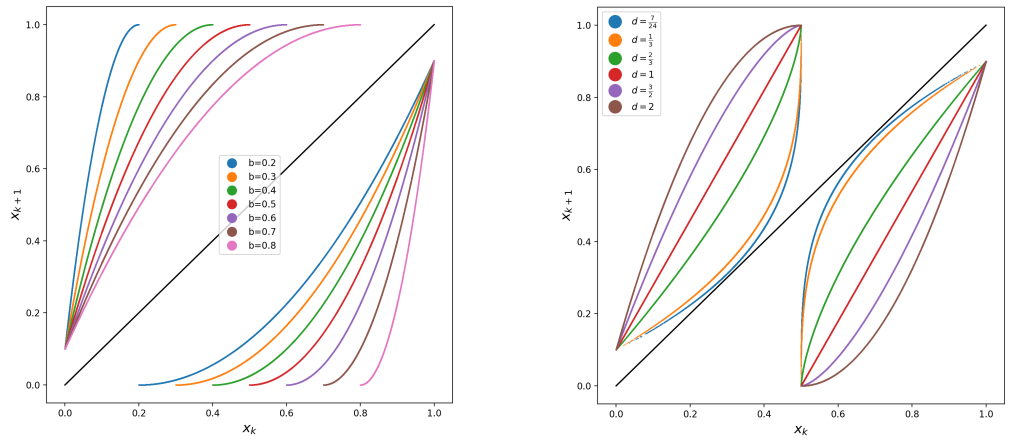

(**a**) (**b**)

Figure 3. Phase diagrams of map Equation (15). (**a**) Phase diagrams of map Equation (15) for different b parameter values $(a = 0.1, c = 0.9, d = 2)$. (**b**) Phase diagrams of map Equation (15) for different d parameter values $(a = 0.1, b = 0.5, c = 0.9)$.

Remark 4. *For $d < 1$, whether map Equation* (15) *has fixed points or not is determined by the relationships between the parameters a, b and c. This situation is illustrated, among others, in Figure 3b, where for $d = 2/3$ or $d = 1/3$, the map Equation* (15) *has no fixed points.*

Indicating the relationship when the system has no fixed points analytically can be difficult and, sometimes, even impossible due to the non-linear nature of the mapping. For this purpose, a numerical confirmation of Lemma 1 is shown in Figure 4. The black

color shows for which parameter values map Equation (15) has no fixed points. These plots are obtained as follows: the coordinates show whether the functions of map Equation (15) intersect the line $y = x$. If so, such values are marked in white, and if not, in black.

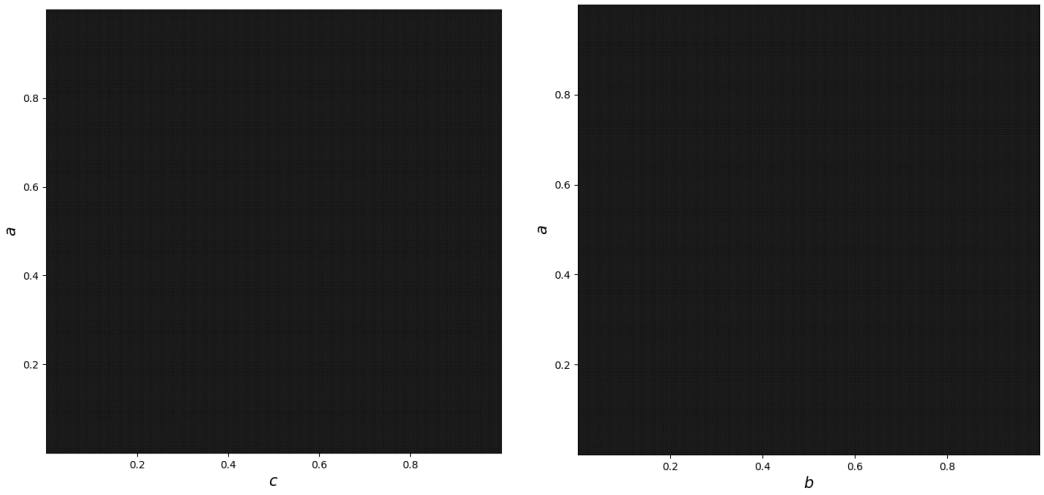

(**a**) (**b**)

Figure 4. Areas without fixed points of map Equation (15) with different parameter relations. (**a**) Areas (black) without fixed points of map Equation (15) for different a and c parameter values $(b = 0.5, d = 2)$. (**b**) Areas (black) without fixed points of map Equation (15) for different a and b parameter values $(c = 0.9, d = 2)$.

The above remarks refer to the situation in which system Equation (15) has no fixed points. However, this does not mean that its dynamics are chaotic. To check whether map Equation (15) is chaotic, the value of the Lyapunov exponent λ should be determined using formula (3). The results obtained are presented in Figure 5. The black color in these plots is the area where the value of the Lyapunov exponent λ is not positive. In turn, the other colors show that system Equation (15) is chaotic, and its sensitivity to changes in initial conditions is a fact. In addition, these graphs have a fractal nature, i.e., they are self-similar. This means that it is challenging (if even possible) to give some closed formula to specify when mapping Equation (15) is chaotic and when it is not. Moreover, it can be observed that the graph in Figure 5a is symmetrical.

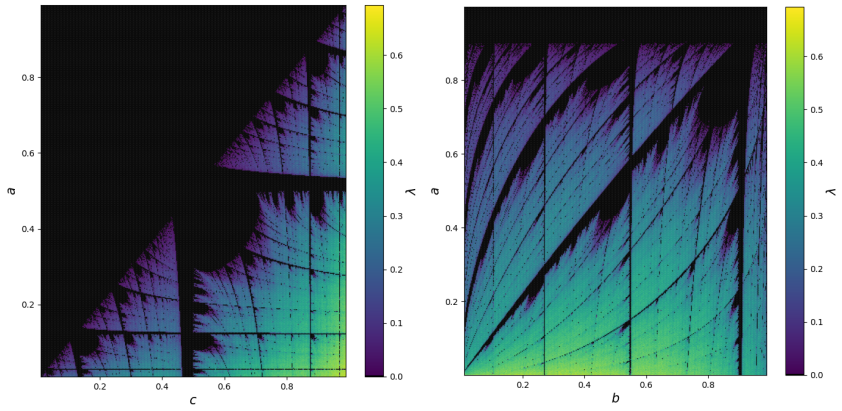

(**a**) (**b**)

Figure 5. Lyapunov exponent of map Equation (15) with different parameter relations (black color denotes nonchaotic region). (**a**) Lyapunov exponent of map Equation (15) for different a and c parameter values ($b = 0.5$, $d = 2$). (**b**) Lyapunov exponent of map Equation (15) for different a and b parameter values $(c = 0.9, d = 2)$.

4.2. Example 2—Cosine Piecewise Map

Let us take the *cosine* functions as f_1 and f_2. Then, chaotic mapping Equation (4) takes the form:

$$x_{k+1} = \begin{cases} (a-1)\cos\left(\frac{\pi x_k}{2b}\right) + 1, & 0 \le x \le b \\ c\cos\left(\frac{\pi(x_k-1)}{2-2b}\right), & b < x \le 1 \end{cases}, \tag{20}$$

where $a, b, c \in (0, 1)$.

As in the first example, recursion Equation (20) represents a whole family of chaotic maps. Examples of recursion Equation (20) are shown in Figure 6. The plots of Figure 6 also show that the left and right subfunction of recursion Equation (20) are convex and concave, respectively.

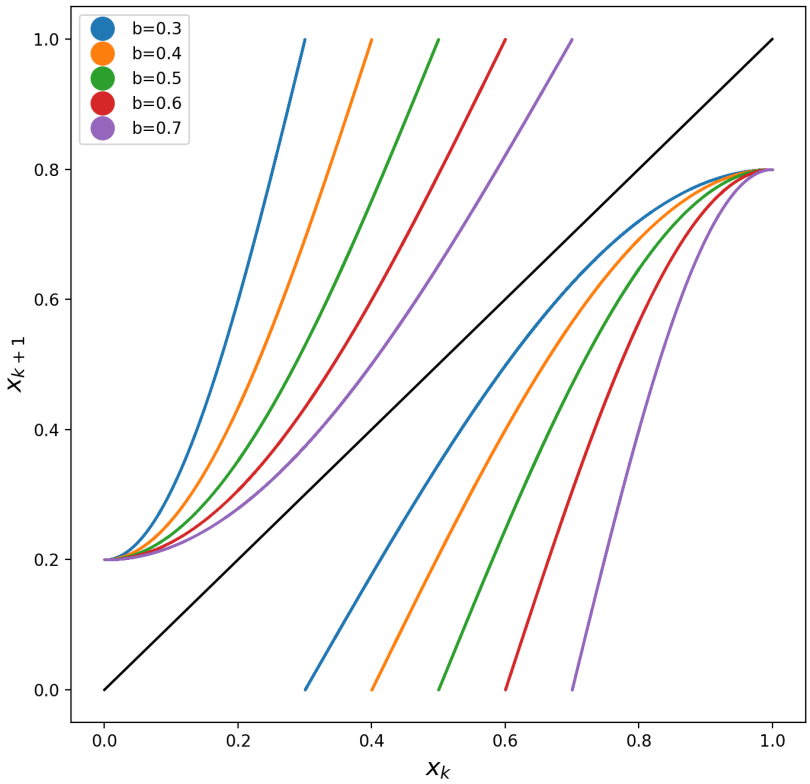

Figure 6. Phase diagram of map Equation (20).

As in the first example, indicating the relationship when the system has no fixed points analytically can be difficult and, sometimes, even impossible due to the non-linear nature of the mapping. Therefore, a numerical analysis of this problem for selected parameter values is shown in Figure 7a,b. The black color shows for which parameter values map Equation (20) has no fixed points. These plots are obtained as in the first example.

By analogy with the first example, the above remarks refer to the situation in which system Equation (20) has no fixed points. However, this does not mean that its dynamics are chaotic. To check whether map Equation (20) is chaotic, the value of the Lyapunov exponent λ should be determined using formula (3). The results obtained are presented in Figure 8a,b. The black color in these plots is the area where the value of the Lyapunov exponent λ is not positive. In turn, the other colors show that the system Equation (20) is unstable, and its sensitivity to changes in initial conditions is a fact. In addition, these graphs have a fractal nature, i.e., they are self-similar. This means that it is challenging (if even possible) to give some rules when mapping Equation (20) is chaotic and when it is not. Moreover, it can be observed that the graph in Figure 8a is symmetrical.

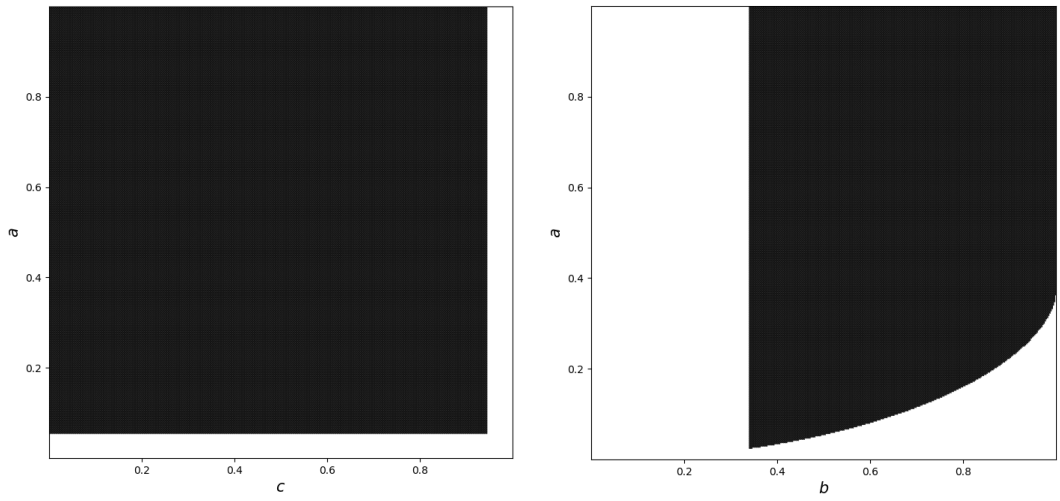

(**a**) (**b**)

Figure 7. Areas without fixed points of map Equation (20) with different parameter relations. (**a**) Areas (black) without fixed points of Equation (20) for different a and c parameters $(b = 0.5)$. (**b**) Areas (black) without fixed points of Equation (20) for different a and b parameters $(c = 0.9)$.

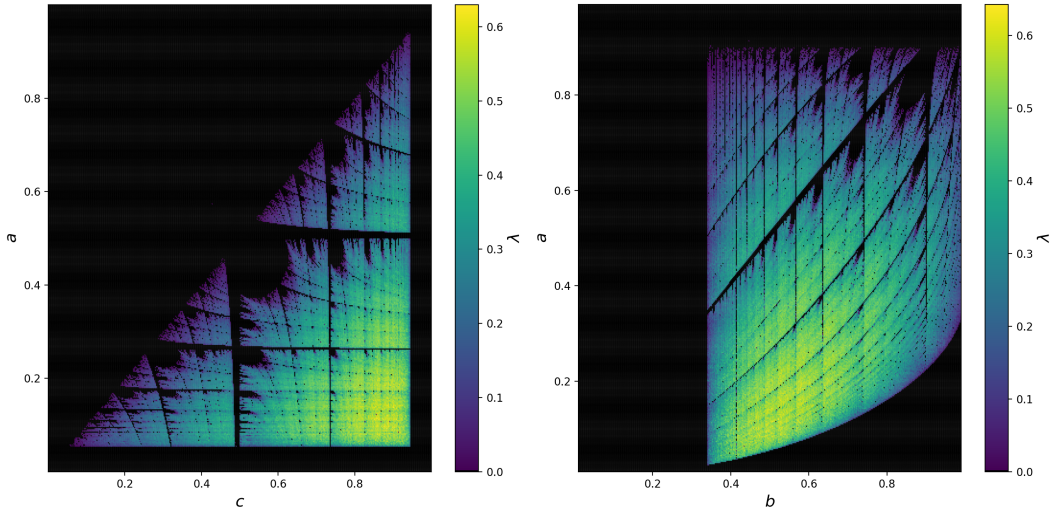

(**a**) (**b**)

Figure 8. Lyapunov exponent of map Equation (20) with different parameter relations (black color denotes nonchaotic region). (**a**) Lyapunov exponent of map Equation (20) for different a and c parameters $(b = 0.5)$. (**b**) Lyapunov exponent of map Equation (20) for different a and b parameters $(c = 0.9)$.

4.3. Example 3—Sine-Exponential Piecewise Map

As a final example, let us take two different functions f_1 and f_2. Let f_1 be the square of the *sine* function, and let f_2 be the *exponential* function. Then, chaotic mapping Equation (4) takes the form:

$$x_{k+1} = \begin{cases} (a-1)\sin^2\left(\frac{\pi x_k - \pi b}{2b}\right) + 1, & 0 \le x \le b \\ \frac{c}{\exp(1)-1}\left(\exp\left(\frac{x_k - b}{1-b}\right) - 1\right), & b < x \le 1 \end{cases}, \tag{21}$$

where $a, b, c \in (0, 1)$.

As in the previous examples, recursions Equation (21) represent a whole family of chaotic maps. Examples of recursions Equation (21) are shown in Figure 9. Figure 9 also shows, unlike in the previous examples, that the left subfunction is neither convex nor

concave over its entire domain. However, the left subfunction changes its behavior from convex to concave (there is an inflection point). In turn, the right subfunction is convex over its entire domain.

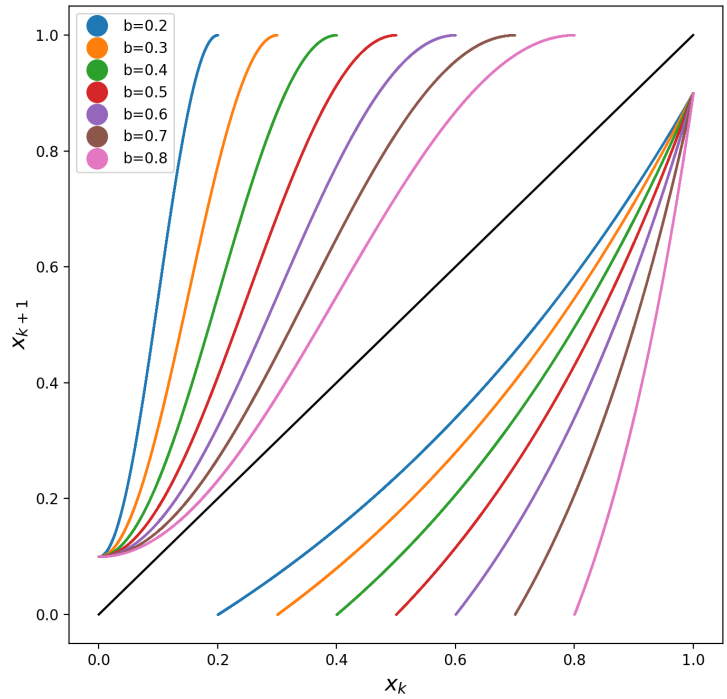

Figure 9. Phase diagram of map Equation (21).

As in the previous examples, indicating the relationship when the system has no fixed points analytically can be difficult and, sometimes, even impossible due to the non-linear nature of the mapping. Therefore, a numerical analysis of this problem for selected parameter values is shown in Figure 10a,b. The black color shows for which parameter values map Equation (21) has no fixed points. These plots are obtained as in the first example.

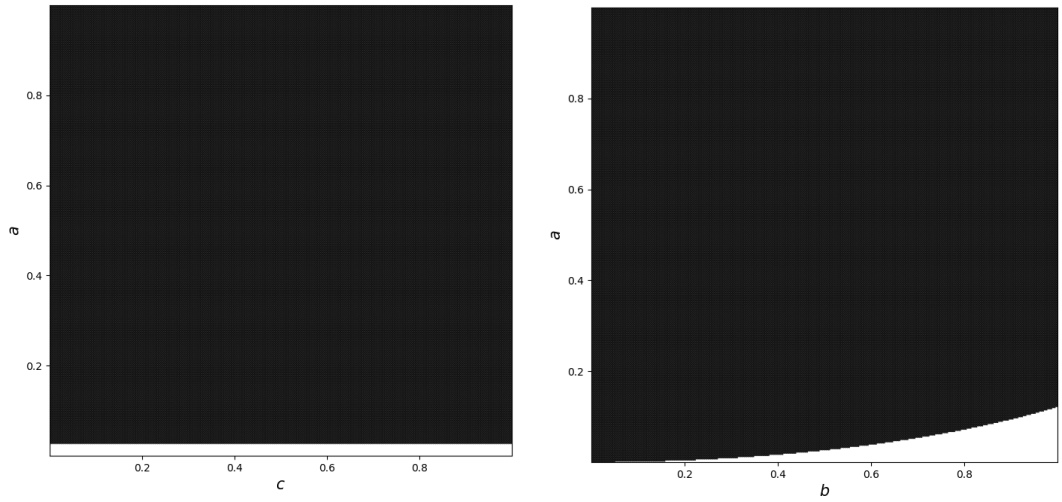

(**a**) (**b**)

Figure 10. Areas without fixed points on map Equation (21) with different parameter relations. (**a**) Areas (black) without fixed points of Equation (21) for different a and c parameters ($b = 0.5$). (**b**) Areas (black) without fixed points of Equation (21) for different a and b parameters ($c = 0.9$).

By analogy with the previous examples, the above remarks refer to the situation in which system Equation (21) has no fixed points. However, this does not mean that its dynamics are chaotic. To check whether map Equation (21) is chaotic, the value of the Lyapunov exponent λ should be determined using formula (3). The results obtained are presented in Figure 11a,b. The black color in these plots is the area where the value of the Lyapunov exponent λ is not positive. In turn, the other colors show that system Equation (21) is unstable, and its sensitivity to changes in initial conditions is a fact. In addition, these graphs have a fractal nature, i.e., they are self-similar. This means that it is challenging (if even possible) to give some rules when mapping Equation (21) is chaotic and when it is not.

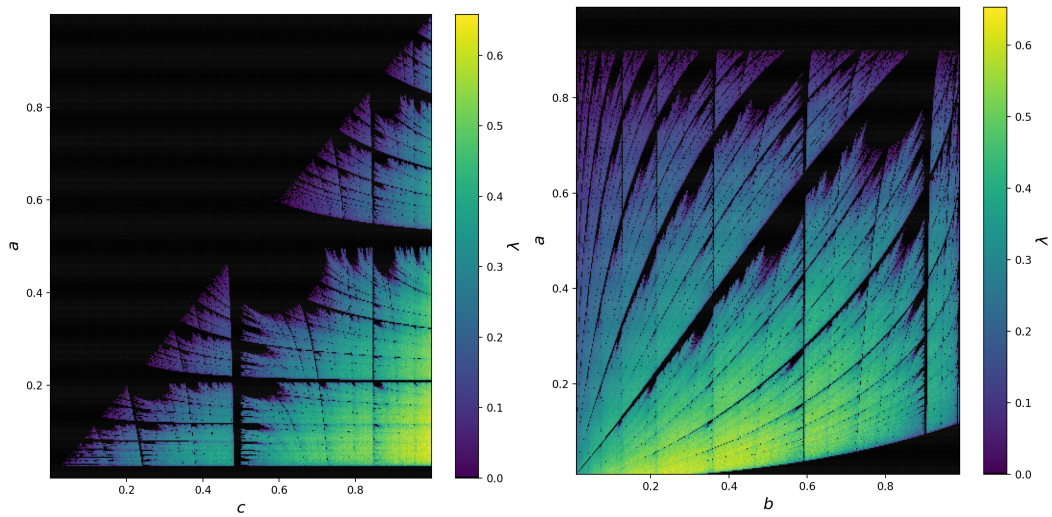

(**a**) (**b**)

Figure 11. Lyapunov exponent of map Equation (21) with different parameter relations (black color denotes nonchaotic region). (**a**) Lyapunov exponent of map Equation (21) for different a and c parameters $(b = 0.5)$. (**b**) Lyapunov exponent of map Equation (21) for different a and b parameters $(c = 0.9)$.

5. Applications of the Proposed Mappings

Chaotic systems find many applications in various engineering areas. One of them is chaotic cryptography. In this area, they can be used as sources in pseudorandom number/bit generators. However, many publications in this area choose continuous multidimensional systems for which chaos occurs with at least three equations describing the system's dynamics [33,34]. However, such systems in this application area have many disadvantages, for example, the need to use integration methods to obtain solutions, computational complexity, or the difficulty in determining the space of parameter values and initial conditions for which the system behaves chaotically. This makes discrete, one-dimensional systems a better choice in chaotic cryptography. The presented constructions of chaotic mappings Equations (4) and (12) fit perfectly into this application area. The specific presented examples of new mappings do not have the disadvantages mentioned above of multidimensional systems. In turn, their lack of fixed points is undoubtedly a very desirable feature of such dynamical systems. For this reason, the representations of forms Equations (4) and (12) can be used in encryption-related applications.

However, despite the obvious advantages, not all one-dimensional discrete systems are equally good from the point of view of applications. Thus, taking into account the most frequently chosen one-dimensional model in scientific publications, the logistic map, it has many disadvantages from the point of view of applications. One of them is the very limited range of parameter values for which chaos occurs. This disadvantage also applies to many other discrete systems. However, the proposed maps, as can be seen from the Lyapunov exponent graphs, have a fairly large area where the Lyapunov exponent takes a positive

value. Furthermore, the proposed construction of mappings, as well as the presented map examples, use at least three parameters (a, b, and c), for which the possibility of chaos occurring is much greater than for mappings with only one parameter.

A Proposed PseudoRandom Bit Generator

As an illustrative example, a pseudorandom bit generator (PRBG) will be designed and tested on all of the considered maps. The PRBG generates 16 bits in each iteration, by hashing the value of the chaotic map through a multiplication and a modulo function. The bit generation in each iteration is given as

$$\mathfrak{B}_k = \text{de2bi}(\lfloor(\text{rem}(10^{12}x_k, 2^{16})\rfloor, 16), \tag{22}$$

where de2bi denotes the binary representation of the obtained decimal number, rem is the remainder operator, and $\mathcal{B} = \{\mathfrak{B}_1, \mathfrak{B}_2, \dots\}$ is the resulting bitstream. The PRBG generates 16 bits per iteration; thus, in order to generate N bits, the chaotic map must be iterated $\lceil \frac{N}{16} \rceil$ times.

To test the PRBG, the proposed polynomial piecewise map Equation (15), the cosine piecewise map Equation (20), and the sine-exponential piecewise map Equation (21) are considered, with parameters $d = 2$, $a = 0.1$, $b = 0.5$, $c = 0.8$ for the first two maps and $a = 0.1$, $b = 0.5$, $c = 0.9$ for the third. For each map, a set of 1000×10^6 bits are generated, for random initial conditions. Thus, the seed map is initiated for a random $x_0 \in (0, 1)$, and 10^6 bits are generated using PRBG Equation (22). This process is repeated 1000 times, and the resulting bits are all appended into a single file of 1000×10^6 digits.

The resulting bitstream is tested through the NIST standard test suite, which consists of 15 statistical tests [35]. The results are shown in Table 1 and are successful, meaning that the PRBG Equation (22) with Equation (15), Equation (20) or Equation (21) as a source of randomness can generate sequences that can be considered statistically random. For tests with multiple runs, the last result value is printed.

Table 1. NIST test results for PRBG Equation (22) using different maps.

		Map Equation (15)		**Map Equation** (20)		**Map Equation** (21)	
No.	**Test**	**Ratio**	**Result**	**Ratio**	**Result**	**Ratio**	**Result**
1	Frequency	990/1000	Pass	990/1000	Pass	987/1000	Pass
2	BlockFrequency	988/1000	Pass	993/1000	Pass	992/1000	Pass
3	CumulativeSums	990/1000	Pass	991/1000	Pass	984/1000	Pass
4	Runs	989/1000	Pass	992/1000	Pass	989/1000	Pass
5	LongestRun	991/1000	Pass	989/1000	Pass	993/1000	Pass
6	Rank	992/1000	Pass	991/1000	Pass	992/1000	Pass
7	FFT	995/1000	Pass	990/1000	Pass	986/1000	Pass
8	NonOverlappingTemplate	990/1000	Pass	988/1000	Pass	990/1000	Pass
9	OverlappingTemplate	990/1000	Pass	994/1000	Pass	990/1000	Pass
10	Universal	987/1000	Pass	986/1000	Pass	987/1000	Pass
11	ApproximateEntropy	985/1000	Pass	983/1000	Pass	995/1000	Pass
12	RandomExcursions	628/634	Pass	626/636	Pass	616/623	Pass
13	RandomExcursionsVariant	626/634	Pass	632/636	Pass	615/623	Pass
14	Serial	987/1000	Pass	988/1000	Pass	989/1000	Pass
15	LinearComplexity	993/1000	Pass	987/1000	Pass	987/1000	Pass

Note that since the proposed PRBGs used chaotic maps as a source of randomness, the bitstreams will remain aperiodic. Of course, as with all chaotic systems, and digital systems for that matter, the aperiodicity is only limited by the floating point accuracy, which can guarantee sufficiently long aperiodic behavior for the applications in mind. If longer aperiodicity is required, however, the proposed PRBGs can easily be improved by considering available techniques such as parameter perturbation. This technique involves slightly perturbing the map's parameter after a number of iterations, which can diminish

any chance of falling into periodic behavior. Since the maps showcase parameter windows of uninterrupted chaotic behavior, such a technique is applicable.

6. Conclusions

This work considered the construction of piecewise maps without any fixed points. In the numerical examples, polynomial, trigonometrical, and exponential terms were considered, all yielding maps without fixed points, that showcased wide ranges of chaotic behavior and interesting fractal-like patterns in the space of parameters that differentiate between chaotic and nonchaotic behavior.

A major advantage for the proposed family of maps is that it is highly receptive to modifications. The candidate functions $f_1(x)$, $f_2(x)$ that can be considered in Equation (4) that satisfy the conditions in Remark 1 are numerous; thus, in addition to the maps already proposed in the Examples section, a plethora of new maps can be constructed. These can be explored in future studies. Moreover, by using the approach proposed in, e.g., Ref. [36], it will be possible to construct new successive chaotic maps without fixed points. In addition, piecewise maps with more than two subfunctions can be constructed, for example by considering techniques similar to the ones developed in [29], in an effort to create robust chaotic maps without fixed points, and with absence of N-periodic behavior.

The methodology proposed in this work can be generalized to a wider family of multi-dimensional maps. The design constraint for the absence of fixed points is the same and has to be satisfied by each individual state of the map. This is currently under development.

Author Contributions: Conceptualization, M.L. and L.M.; methodology, M.L.; software, M.L. and L.M.; visualization, M.L.; writing—original draft preparation, M.L. and L.M.; writing—review and editing, M.L., L.M. and C.V.; supervision, C.V. All authors have read and agreed to the published version of the manuscript.

Funding: This research received no external funding.

Data Availability Statement: There are no data associated with this work.

Acknowledgments: The authors are thankful to the anonymous reviewers for their helpful remarks.

Conflicts of Interest: The authors declare no conflict of interest.

References

1. Strogatz, S.H. *Nonlinear Dynamics and Chaos: With Applications to Physics, Biology, Chemistry, and Engineering*; CRC Press: Boca Raton, FL, USA, 2018.
2. Oestreicher, C. A history of chaos theory. *Dialogues Clin. Neurosci.* **2007**, *9*, 279–289. [CrossRef] [PubMed]
3. Grassi, G. Chaos in the real world: Recent applications to communications, computing, distributed sensing, robotic motion, bio-impedance modelling and encryption systems. *Symmetry* **2021**, *13*, 2151. [CrossRef]
4. Akmeşe, Ö.F. Bibliometric Analysis of Publications on Chaos Theory and Applications during 1987–2021. *Chaos Theory Appl.* **2022**, *4*, 169–178. [CrossRef]
5. Baptista, M.S. Chaos for communication. *Nonlinear Dyn.* **2021**, *105*, 1821–1841. [CrossRef]
6. Teh, J.S.; Alawida, M.; Sii, Y.C. Implementation and practical problems of chaos-based cryptography revisited. *J. Inf. Secur. Appl.* **2020**, *50*, 102421. [CrossRef]
7. Lawnik, M.; Moysis, L.; Volos, C. Chaos-Based Cryptography: Text Encryption Using Image Algorithms. *Electronics* **2022**, *11*, 3156. [CrossRef]
8. Kumar, M.; Saxena, A.; Vuppala, S.S. A survey on chaos based image encryption techniques. In *Multimedia Security Using Chaotic Maps: Principles and Methodologies*; Springer: Berlin/Heidelberg, Germany, 2020; pp. 1–26.
9. Tutueva, A.V.; Nepomuceno, E.G.; Karimov, A.I.; Andreev, V.S.; Butusov, D.N. Adaptive chaotic maps and their application to pseudo-random numbers generation. *Chaos Solitons Fractals* **2020**, *133*, 109615. [CrossRef]
10. Murillo-Escobar, M.; Cruz-Hernández, C.; Cardoza-Avendaño, L.; Méndez-Ramírez, R. A novel pseudorandom number generator based on pseudorandomly enhanced logistic map. *Nonlinear Dyn.* **2017**, *87*, 407–425. [CrossRef]
11. Bin Faheem, Z.; Ali, A.; Khan, M.A.; Ul-Haq, M.E.; Ahmad, W. Highly dispersive substitution box (S-box) design using chaos. *ETRI J.* **2020**, *42*, 619–632. [CrossRef]
12. Shakiba, A. A randomized CPA-secure asymmetric-key chaotic color image encryption scheme based on the Chebyshev mappings and one-time pad. *J. King Saud Univ. Comput. Inf. Sci.* **2021**, *33*, 562–571. [CrossRef]

13. Rybin, V.; Karimov, T.; Bayazitov, O.; Kvitko, D.; Babkin, I.; Shirnin, K.; Kolev, G.; Butusov, D. Prototyping the Symmetry-Based Chaotic Communication System Using Microcontroller Unit. *Appl. Sci.* **2023**, *13*, 936. [CrossRef]
14. Artemiou, P.; Moysis, L.; Kafetzis, I.; Bardis, N.G.; Lawnik, M.; Volos, C. Chaotic Agent Navigation: Achieving Uniform Exploration Through Area Segmentation. In Proceedings of the 2022 12th International Conference on Dependable Systems, Services and Technologies (DESSERT), Athens, Greece, 9–11 December 2022; pp. 1–7. [CrossRef]
15. Saremi, S.; Mirjalili, S.; Lewis, A. Biogeography-based optimisation with chaos. *Neural Comput. Appl.* **2014**, *25*, 1077–1097. [CrossRef]
16. Moysis, L.; Lawnik, M.; Antoniades, I.P.; Kafetzis, I.; Baptista, M.S.; Volos, C. Chaotification of 1D Maps by Multiple Remainder Operator Additions—Application to B-Spline Curve Encryption. *Symmetry* **2023**, *15*, 726. [CrossRef]
17. Natiq, H.; Banerjee, S.; Said, M. Cosine chaotification technique to enhance chaos and complexity of discrete systems. *Eur. Phys. J. Spec. Top.* **2019**, *228*, 185–194. [CrossRef]
18. Ablay, G. Lyapunov exponent enhancement in chaotic maps with uniform distribution modulo one transformation. *Chaos Theory Appl.* **2022**, *4*, 45–58. [CrossRef]
19. Wang, Z.; Akgul, A.; Pham, V.T.; Jafari, S. Chaos-based application of a novel no-equilibrium chaotic system with coexisting attractors. *Nonlinear Dyn.* **2017**, *89*, 1877–1887. [CrossRef]
20. Zhang, S.; Wang, X.; Zeng, Z. A simple no-equilibrium chaotic system with only one signum function for generating multi-directional variable hidden attractors and its hardware implementation. *Chaos Interdiscip. J. Nonlinear Sci.* **2020**, *30*, 053129. [CrossRef]
21. Cafagna, D.; Grassi, G. Chaos in a new fractional-order system without equilibrium points. *Commun. Nonlinear Sci. Numer. Simul.* **2014**, *19*, 2919–2927. [CrossRef]
22. Rahman, Z.A.S.A.; Jasim, B.H.; Al-Yasir, Y.I.A.; Abd-Alhameed, R.A.; Alhasnawi, B.N. A New No Equilibrium Fractional Order Chaotic System, Dynamical Investigation, Synchronization, and Its Digital Implementation. *Inventions* **2021**, *6*, 49. [CrossRef]
23. Ouannas, A.; Khennaoui, A.A.; Momani, S.; Grassi, G.; Pham, V.T. Chaos and control of a three-dimensional fractional order discrete-time system with no equilibrium and its synchronization. *AIP Adv.* **2020**, *10*, 045310. [CrossRef]
24. Tamba, V.K.; Pham, V.T.; Hoang, D.V.; Jafari, S.; Alsaadi, F.E.; Alsaadi, F.E. Dynamic system with no equilibrium and its chaos anti-synchronization. *Automatika* **2018**, *59*, 35–42. [CrossRef]
25. Azar, A.T.; Volos, C.; Gerodimos, N.A.; Tombras, G.S.; Pham, V.T.; Radwan, A.G.; Vaidyanathan, S.; Ouannas, A.; Munoz-Pacheco, J.M. A Novel Chaotic System without Equilibrium: Dynamics, Synchronization, and Circuit Realization. *Complexity* **2017**, *2017*, 7871467. [CrossRef]
26. García-Grimaldo, C.; Campos, E. Chaotic Features of a Class of Discrete Maps without Fixed Points. *Int. J. Bifurc. Chaos* **2021**, *31*, 2150200. [CrossRef]
27. García-Grimaldo, C.; Campos-Cantón, E. Comparative Analysis of Chaotic Features of Maps Without Fixed Points. In *Complex Systems and Their Applications*; Huerta Cuéllar, G., Campos Cantón, E., Tlelo-Cuautle, E., Eds.; Springer: Cham, Switzerland, 2022; pp. 151–176.
28. García-Grimaldo, C.; Bermudez-Marquez, C.F.; Tlelo-Cuautle, E.; Campos-Cantón, E. FPGA Implementation of a Chaotic Map with No Fixed Point. *Electronics* **2023**, *12*, 444. [CrossRef]
29. Jafari, S.; Pham, V.T.; Golpayegani, S.M.R.H.; Moghtadaei, M.; Kingni, S.T. The relationship between chaotic maps and some chaotic systems with hidden attractors. *Int. J. Bifurc. Chaos* **2016**, *26*, 1650211. [CrossRef]
30. Panahi, S.; Sprott, J.C.; Jafari, S. Two simplest quadratic chaotic maps without equilibrium. *Int. J. Bifurc. Chaos* **2018**, *28*, 1850144. [CrossRef]
31. Wang, C.; Ding, Q. A New Two-Dimensional Map with Hidden Attractors. *Entropy* **2018**, *20*, 322. [CrossRef]
32. Almatroud, O.A.; Pham, V.T. Building Fixed Point-Free Maps with Memristor. *Mathematics* **2023**, *11*, 1319. [CrossRef]
33. Nestor, T.; De Dieu, N.J.; Jacques, K.; Yves, E.J.; Iliyasu, A.M.; Abd El-Latif, A.A. A multidimensional hyperjerk oscillator: Dynamics analysis, analogue and embedded systems implementation, and its application as a cryptosystem. *Sensors* **2019**, *20*, 83. [CrossRef]
34. Zou, C.; Zhang, Q.; Wei, X.; Liu, C. Image encryption based on improved Lorenz system. *IEEE Access* **2020**, *8*, 75728–75740. [CrossRef]
35. Bassham, L.E.; Rukhin, A.L.; Soto J.; Nechvatal J.R.; Smid M.E.; Barker E.B.; Leigh S.D.; Levenson M.; Vangel M.; Banks D.L.; et al. *A Statistical Test Suite for Random and Pseudorandom Number Generators for Cryptographic Applications*; Sp 800-22 Rev. 1a; National Institute of Standards & Technology: Gaithersburg, MD, USA, 2010.
36. Rand, D.; Ostlund, S.; Sethna, J.; Siggia, E.D. Universal transition from quasiperiodicity to chaos in dissipative systems. *Phys. Rev. Lett.* **1982**, *49*, 132. [CrossRef]

Disclaimer/Publisher's Note: The statements, opinions and data contained in all publications are solely those of the individual author(s) and contributor(s) and not of MDPI and/or the editor(s). MDPI and/or the editor(s) disclaim responsibility for any injury to people or property resulting from any ideas, methods, instructions or products referred to in the content.

symmetry

MDPI

Article

Chaotification of 1D Maps by Multiple Remainder Operator Additions—Application to B-Spline Curve Encryption

Lazaros Moysis [1,2,*], Marcin Lawnik [3,*], Ioannis P. Antoniades [1], Ioannis Kafetzis [1], Murilo S. Baptista [4] and Christos Volos [1]

[1] Laboratory of Nonlinear Systems-Circuits & Complexity, Physics Department, Aristotle University of Thessaloniki, 54124 Thessaloniki, Greece
[2] Department of Mechanical Engineering, University of Western Macedonia, 50100 Kozani, Greece
[3] Department of Mathematics Applications and Methods for Artificial Intelligence, Faculty of Applied Mathematics, Silesian University of Technology, Kaszubska 23, 44-100 Gliwice, Poland
[4] Institute for Complex Systems and Mathematical Biology, SUPA, University of Aberdeen, Aberdeen AB24 3UX, UK
* Correspondence: lmousis@physics.auth.gr (L.M.); marcin.lawnik@polsl.pl (M.L.)

Abstract: In this work, a chaotification technique is proposed for increasing the complexity of chaotic maps. The technique consists of adding the remainder of multiple scalings of the map's value for the next iteration, so that the most- and least-significant digits are combined. By appropriate parameter tuning, the resulting map can achieve a higher Lyapunov exponent value, a result that was first proven theoretically and then showcased through numerical simulations for a collection of chaotic maps. As a proposed application of the transformed maps, the encryption of B-spline curves and patches was considered. The symmetric encryption consisted of two steps: a shuffling of the control point coordinates and an additive modulation. A transformed chaotic map was utilised to perform both steps. The resulting ciphertext curves and patches were visually unrecognisable compared to the plaintext ones and performed well on several statistical tests. The proposed work gives an insight into the potential of the remainder operator for chaotification, as well as the chaos-based encryption of curves and computer graphics.

Keywords: chaos; chaotification technique; Lyapunov exponent; B-splines; encryption

1. Introduction

1.1. Applications of Chaos and Chaotification

The applications of chaos in the digital world have been reported in multiple works [1–4] and span the areas of computing, encryption, surveillance, communications, fingerprinting, and many more. Within the broad range of these applications, both continuous and discrete chaotic systems are considered, depending on the application at hand.

Continuous chaotic systems have many merits, such as more degrees of freedom and a higher state space. However, this comes at the cost of computational time, which may pose problems in applications where execution time is of the essence. They are also heavily dependent on the numerical method used to compute their solution, which creates issues of reproducibility across different computers and digital devices.

This is why it is more suitable to consider discrete-time chaotic systems, or chaotic maps as they are also termed. Discrete maps can achieve chaotic behaviour even in a single dimension, have a much lighter computational cost, and are solved iteratively, so they are not dependent on numerical integration methods.

Still, for both continuous and discrete systems, there are several features that need to be present, in order to make a chaotic system suitable for use in security-related applications, such as encryption, watermarking, surveillance, and others. Desirable features include the absence of parameter ranges that lead to periodic behaviour and an increased sensitivity

to the initial conditions, indicated by high Lyapunov exponent values, a high key space, and an unrecognisable phase diagram with no visual structure. These are all attributes of maps with increased complexity. The pursuit of finding such maps led to the field of study known as *chaotification*, which in general refers to the problem of constructing novel chaotic maps or devising methods to modify known maps in order to satisfy the above properties. Since there is already an abundance of chaotic maps in the literature, chaotification usually does not involve the generation of novel maps, but techniques that can be applied to any known map to improve its performance in cryptographic and similar tasks.

The field of chaotification is very active at the moment, with numerous contributions. Popular techniques include the use of sinusoidal functions [5–12], exponential terms [13], piecewise maps [14,15], the modulo operator [7,16–19], the coupling of maps [20], the composition through internal perturbation [21], and others [22,23].

In [18], the authors proposed a chaotification technique that consisted of adding a remainder term to any 1D map, in order to mix the most- and least-significant digits in each iteration and boost the chaotic behaviour of the seed map. Indeed, it was shown that, by the appropriate parameter choice, the Lyapunov exponent of the modified map can be larger than that of the seed map. Moreover, the modified map showed wide areas of uninterrupted chaotic behaviour in its parameter space. The present work is a straightforward extension of the chaotification technique in [18] by using a summation of remainder operators. The transformed maps are then considered for the encryption of B-spline curves and patches.

1.2. Encryption

The principles of chaos-based encryption are applicable to any type of data and, so far, have indeed been applied to the encryption of images [11,12,24,25], text [25], and continuous signals [26]. Image encryption seems to be the most-popular application, mainly due to its visual aspect, which makes it easier to depict and compare plaintext and ciphertext data and interpret the results of the various statistical tests performed on them.

In addition to the above, recently, there has been an increasing interest in encrypting 3D objects. Three-dimensional graphics can represent any type of data, from mechanical and biological objects, to video game graphics, [27–29]. The format used to represent such graphics is the stereolithography (STL) format. In this work, in order to complement the work on computer graphics encryption, B-spline curves and patches will be chosen as the plaintext data.

B-spline curves, and their simpler form, Bézier curves, are a well-established family of parametric curves, which are extensively used for modelling 2D and 3D graphics [30–36]. Their use originated in the automotive industry, but currently, their usage has been expanded to a plethora of applications, most notably graphic design, robotics, and navigation, as they can be used to effectively generate motion trajectories for a robotic manipulator, a UVG, or a UAV.

There are several properties that make B-spline curves so useful. First is the ease of their implementation, as they are simply described by a closed-form formula. That formula requires only the specification of a set of control points characterising the shape of the curve. These points also define the convex hull of the curve, so it is easy to specify its boundaries, making it easier to avoid intersections with obstacles. Another property is that they are locally controllable, meaning that changing a single control point of the B-spline will affect only a part of the curve. Finally, their smoothness can also be controlled by choosing the appropriate curve order and control point placement.

In this work, a symmetric encryption technique of B-spline curves and patches was considered, which consists of two separate steps. The first step involves the shuffling of the control points, by the application of a chaotic pseudorandom rule. The second consists of combining the control points with the values of a transformed chaotic map, to mask their value. The resulting ciphertext curves were visually unrecognisable and also performed well on several statistical tests. This technique complements previous

works that considered the encryption of 3D objects and proposes a setup for encrypting parametric curves.

The main contributions of this work is the construction and analysis of mappings using multiple remainder operators and the presentation of a new B-spline encryption algorithm. The use of multiple remainder operators can efficiently mix the least- and most-significant digits between iterative mappings and can be further explored and modified in the future. The encryption of B-spline curves using a two-step process can be a starting point for further experimentation into encrypting geometrical data structures in general.

The rest of the work is structured as follows. In Section 2, the proposed chaotification technique is introduced. In Section 3, the technique is applied to several known maps. In Section 4, the effect of the proposed chaotification technique in expanding the key space of the resulting encryption protocol is discussed. In Section 5, the computational cost of applying the technique is presented. In Sections 6 and 7, the symmetric encryption of B-spline curves and surfaces is considered. The simulation results of encryption are shown in Section 8. Finally, Section 9 concludes the present work and discusses topics for future research.

2. The Proposed Chaotification Technique

Consider a one-dimensional discrete time map described by the iterative formula:

$$x_i = \mathcal{F}(x_{i-1}). \tag{1}$$

The proposed chaotification technique is an extension of [18] and consists of using the remainder operator to add multiple scalings of the map's value x_{i-1} into the next iteration x_i as follows:

$$x_i = \mathcal{H}_m(x_{i-1}) = \mathcal{F}(x_{i-1}) + \sum_{j=1}^{m} \text{rem}(a_j x_{i-1}, N_j), \tag{2}$$

where $a_j > 0$ are the control parameters, $N_j \in \mathbb{R}_*^+$ map the remainder result on the interval $(-N_j, N_j)$, and $m \in \mathbb{N}$. The technique is also illustrated in Figure 1.

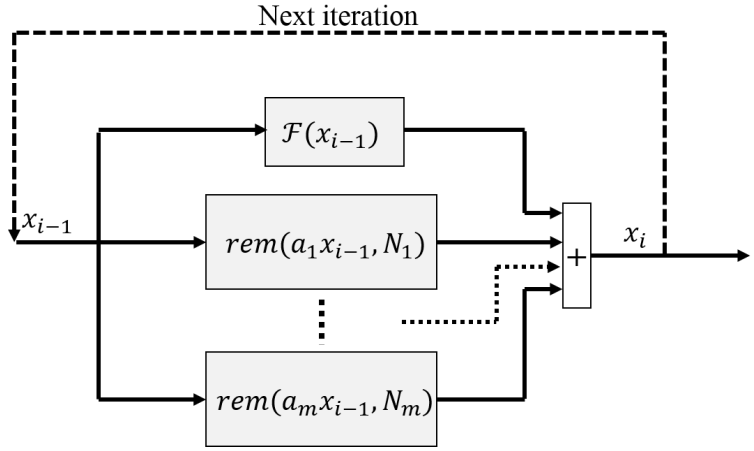

Figure 1. The proposed chaotification technique (2).

Theorem 1. *Let*

$$\mathcal{H}_m(x_i) = \mathcal{F}(x_i) + \sum_{j=1}^{m} rem(a_j x_i, N_j). \tag{3}$$

Then, the following hold:

1. *The map $\mathcal{H}_m(x_i)$ has a higher Lyapunov exponent if*

$$\left| \sum_{j=1}^{m} a_j \right| > 2 \sup_{x_i \in \mathbb{D}_m} \left| \dot{\mathcal{F}}(x_i) \right|, \tag{4}$$

where $\mathbb{D}_m$ is the domain of $\mathcal{F}$.

2. *Let λ_μ denote the Lyapunov exponent of* (3)*. If a_{m+1} is selected, so that*

$$|a_{m+1}| > 2 \sup_{x_i \in \mathbb{D}_m} \left|\dot{\mathcal{H}}_m(x_i)\right|, \tag{5}$$

then $\left(\lambda_\mu\right)_{\mu\in\mathbb{N}}$ is increasing.

Proof. We begin by considering the derivative of the remainder operation, which is

$$\frac{d}{dx} rem(a \cdot x, N) = a \tag{6}$$

for almost all x. Using (6), the derivative of $\mathcal{H}_m(x_i)$ as in (3) for almost all x_i is

$$\dot{\mathcal{H}}_m(x_i) = \dot{\mathcal{F}}_m(x_i) + \sum_{j=1}^{m} a_j. \tag{7}$$

Observe that $\sum_{j=1}^{m} a_j$ is independent of x_i, and thus, if we denote it as

$$\widetilde{A_m} := \sum_{j=1}^{m} a_j, \tag{8}$$

then

$$\dot{\mathcal{H}}_m(x_i) = \dot{\mathcal{F}}_m(x_i) + \widetilde{A_m} \tag{9}$$

which is exactly the case studied in [18], from which the conclusion is that, selecting

$$\widetilde{A_m} > 2 \sup_{x_i \in \mathbb{D}_m} \left|\dot{\mathcal{F}}(x_i)\right| \tag{10}$$

results in a system with a greater Lyapunov exponent. Hence, in our case, the terms a_j must be chosen so that $\sum\limits_{j=1}^{m} a_j > 2\sup_{x_i\in\mathbb{D}_m}\left|\dot{\mathcal{F}}(x_i)\right|$. We can extend the proof in that work by observing that a selection of

$$\widetilde{A_m} < -2 \sup_{x_i \in \mathbb{D}_m} \left|\dot{\mathcal{F}}(x_i)\right| \tag{11}$$

yields the same result. Thus, combining (10) and (11) yields that, selecting

$$\left|\sum_{j=1}^{m} a_j\right| > 2 \sup_{x_i \in \mathbb{D}_m} \left|\dot{\mathcal{F}}(x_i)\right| \tag{12}$$

results in a system that has a higher Lyapunov exponent than that of the original system.

Observe that, until this point, no specific assumption has been made for each of the coefficients a_j individually, only for their sum.

Next, we are interested in determining conditions such that the sequence of Lyapunov exponents created by adding extra terms in (3) is increasing. First of all, we observe that for every $m \in \mathbb{N}$, the domains of $\mathcal{F}$ and $\mathcal{H}_m$ coincide. With that in mind, we can then write

$$\mathcal{H}_{m+1}(x_i) = \mathcal{F}(x_i) + \sum_{j=1}^{m+1} rem(a_j x_i, N_j) \tag{13}$$

$$= \mathcal{F}(x_i) + \sum_{j=1}^{m} rem(a_j x_i, N_j) + rem(a_{m+1} x_i, N_{m+1}) \tag{14}$$

$$= \mathcal{H}_m(x_i) + rem(a_{m+1} x_i, N_{m+1}). \tag{15}$$

Combining (15) with the first part of the proof and the fact that the domains of $\mathcal{F}$ and $\mathcal{H}$ coincide yields that selecting a_{m+1} as

$$|a_{m+1}| > 2 \sup_{x_i \in \mathbb{D}_m} \left|\dot{\mathcal{H}}_m(x_i)\right| \tag{16}$$

guarantees that $\lambda_{m+1} > \lambda_m$ for any m, which concludes the proof. □

Remark 1. *Note that the choice of the remainder operator is made over the more common modulo operator, as the remainder operator does not change the sign of its input. This results in a more uniform distribution of the map's values, compared to the use of the modulo. Figure 2 illustrates this difference using a modified version of the Sine Map. In addition, it is worth noting that the remainder operator results in a symmetric distribution in this case. In contrast, the map distribution with the modulo operator does not have such symmetry.*

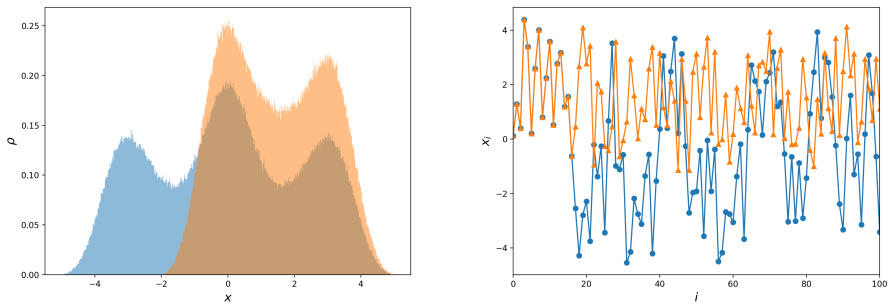

(**a**) (**b**)

Figure 2. Difference between the map (18) $x_i = 2\sin(\pi x_{i-1}) + rem(10x_{i-1}), 1) + rem(100x_{i-1}), 1) + rem(1000x_{i-1}), 1)$, (blue), when replacing the $rem(\cdot, 1)$ operators with $mod(\cdot, 1)$ (orange). (**a**) Density of the same map showing the difference between modulo and remainder operators. (**b**) Orbits of Sine Map (17) with modulo and remainder operators, ($x_0 = 0.123$).

3. Chaotification Examples for Different Chaotic Maps

In this section, we apply the above chaotification technique to several well-known maps as shown below.

3.1. Sine Map

Consider the well-known Sine Map [37,38]:

$$x_i = k\sin(\pi x_{i-1}). \tag{17}$$

Using the Sine Map (17) as the base function $\mathcal{F}(x)$, two cases of mappings of the form (2) are further analysed, for $m = 2$ and $m = 3$:

$$x_i = k\sin(\pi x_{i-1}) + rem(10x_{i-1}, 1) + rem(100x_{i-1}, 1), \tag{18}$$

$$x_i = k\sin(\pi x_{i-1}) + rem(10x_{i-1}, 1) + rem(100x_{i-1}, 1) + rem(1000x_{i-1}, 1). \tag{19}$$

The first map (18), apart from the base function (17), consists of two additional components: $rem(10x_{i-1}, 1)$ and $rem(100x_{i-1}, 1)$. In turn, the second map (19) modifies the first with an additional component: $rem(1000x_{i-1}, 1)$.

One of the tools for analysing dynamical systems is to present the so-called phase diagrams that show the system's relationship (x_{i-1}, x_i). The phase diagrams of all three cases (Sine Map (17) and its two modifications (18) and (19)) for fixed parameter values are presented in Figure 3a. These graphs show that adding multiple $rem(\cdot)$ operators causes a significant increase in the complexity of the base mapping. In turn, Figure 3b presents bifurcation diagrams of the analysed mappings. This figure depicts the existence

of the so-called periodic windows for the Sine Map (17) and their respective absence for the modified mappings (18) and (19). This means that, in the case of mappings (18) and (19), there is no worry about choosing the proper mapping parameters, as any choice will always result in chaotic behaviour.

The increased complexity of the resulting maps is also confirmed by the three-dimensional phase diagrams, which show the relation of points (x_i, x_{i-1}, x_{i-2}). These charts are presented in Figure 4. In the case of the Sine Map (17), the graph in Figure 4a shows that points fall on a curve, while for the modified maps (19) (Figure 4b), they fill up a 3D region, forming a cloud of points. Therefore, the mapping with the $rem(\cdot)$ operators is much more complex than the base mapping.

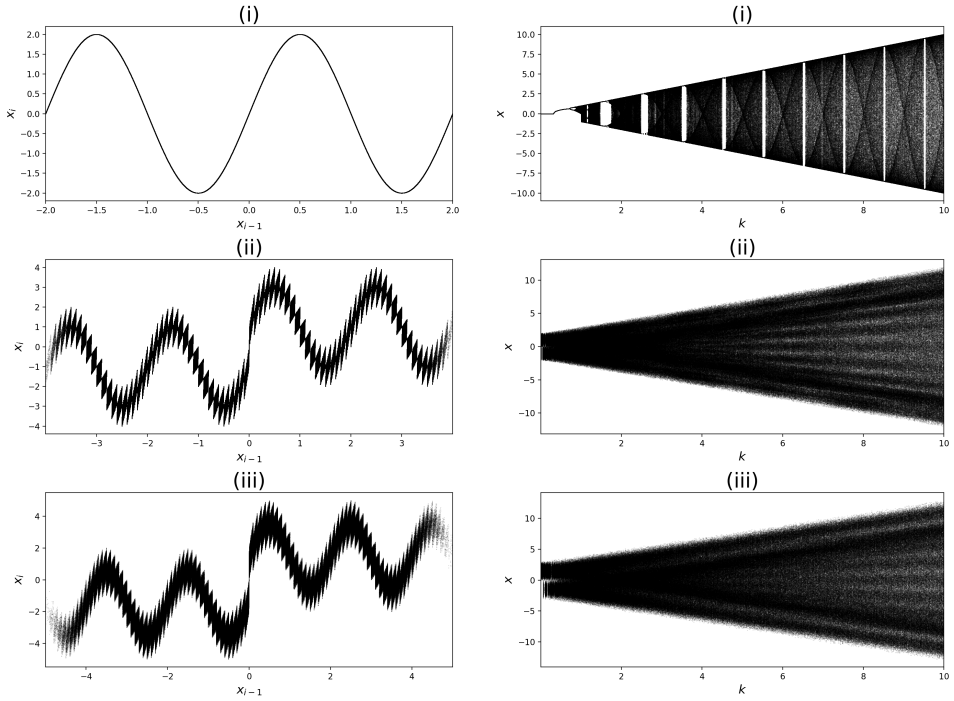

(**a**) (**b**)

Figure 3. Phase and bifurcation diagrams. (**a**) Phase diagrams of: (**i**) Sine Map (17), (**ii**) map (18), (**iii**) map (19), ($k = 2, N = 1$). (**b**) Bifurcation diagrams of: (**i**) Sine Map (17), (**ii**) map (18), (**iii**) map (19),

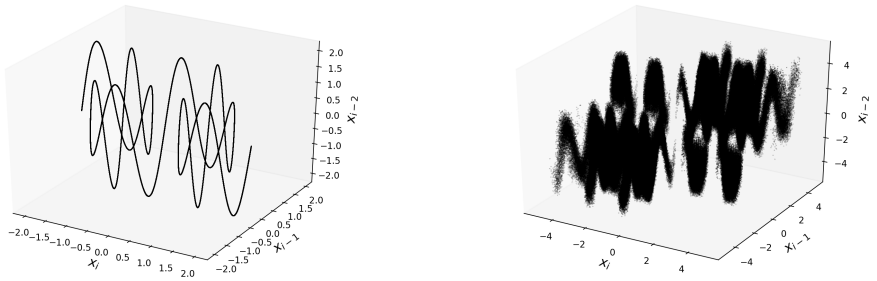

(**a**) (**b**)

Figure 4. Three-dimensional phase diagrams. (**a**) Three-dimensional phase diagram of the Sine Map (17), ($k = 2$). (**b**) Three-dimensional phase diagram of the map (19), ($k = 2, N = 1$).

Chaotic systems are characterised by the system's sensitivity to a change in initial conditions, which is measured using the Lyapunov exponent λ given by the formula:

$$\lambda = \lim_{n\to\infty} \frac{1}{n} \sum_{i=0}^{n-1} \ln |\mathcal{F}'(x_i)|. \tag{20}$$

The plot of the Lyapunov exponent is shown in Figure 5a. This figure clearly shows the presence of stable/periodic regions for the Sine Map (17) and their absence for mappings with the $rem(\cdot)$ operator. This figure also shows that the sensitivity to the change of initial conditions for the mappings (18) and (19) is roughly constant for the entire range of the parameter k. Thus, after the same number of iterations, the system will lose information about the initial conditions.

Moreover, to better illustrate the chaotic nature of the analysed dynamical systems, the Lyapunov exponent value λ's dependence on (k, N) is calculated. The results are shown in Figure 5b. The obtained values show that $\lambda > 0$ for the entire analysed parameter range for the mapping (19). Moreover, the λ value is roughly constant for the whole range of parameter values. These results are consistent with the value of the Lyapunov exponent from Figure 5a. They also confirm that the mapping (19) is characterised by interrupted chaotic behaviour for large ranges of parameter changes and, thus, has a much more complex behaviour than the base function Sine Map (17).

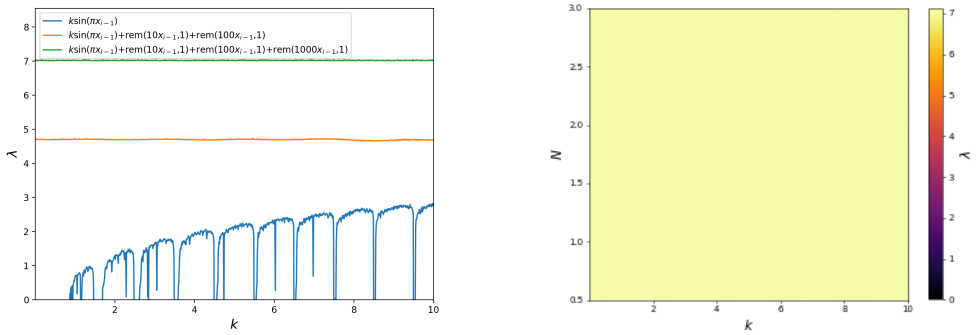

(**a**) (**b**)

Figure 5. Lyapunov exponent. (**a**) Lyapunov exponent of Sine Map (17) (blue) and its modifications (18) and (19) (orange and green). (**b**) Colour-coded Lyapunov exponent diagram in relation to (k, N) for the map (19). The colour bar corresponds to the value of the exponent.

3.2. Sine-Sine Map

In [6] a sine chaotification was proposed. As an example of this method, consider the Sine-Sine Map:

$$x_i = \sin(\pi k \sin(\pi x_{i-1})). \tag{21}$$

As in the case of the Sine Map (17), the Sine-Sine Map (21) was also used as the base function $\mathcal{F}(x)$, and two new maps are defined, which will be analysed further in the paper:

$$x_i = \sin(\pi k \sin(\pi x_{i-1})) + rem(10x_{i-1}, 1) + rem(100x_{i-1}, 1), \tag{22}$$

$$x_i = \sin(\pi k \sin(\pi x_{i-1})) + rem(10x_{i-1}, 1) + rem(100x_{i-1}, 1) + rem(1000x_{i-1}, 1). \tag{23}$$

Their design is very similar to the previous case, i.e., the first one, apart from the base function having two additional components $rem(10x_{i-1}, 1)$ and $rem(100x_{i-1}, 1)$. In turn, the second one has one more component equal to $rem(1000x_{i-1}, 1)$.

As previously, the phase diagrams of all three cases (Sine—Sine Map (21) and its two modified versions (22) and (23)) for various fixed parameter values are presented in

Figure 6a. These graphs confirm that adding multiple $rem(\cdot)$ operators causes a significant increase in the complexity of the base mapping. In addition, Figure 6b presents bifurcation diagrams of the analysed mappings. This figure also demonstrates that, although there are visible periodic windows for the Sine-Sine Map (21), they are absent for the modified mappings (22) and (23). Similar to the Sine Map, this means that any choice of mapping parameters in (22) or (23) will always result in chaotic behaviour.

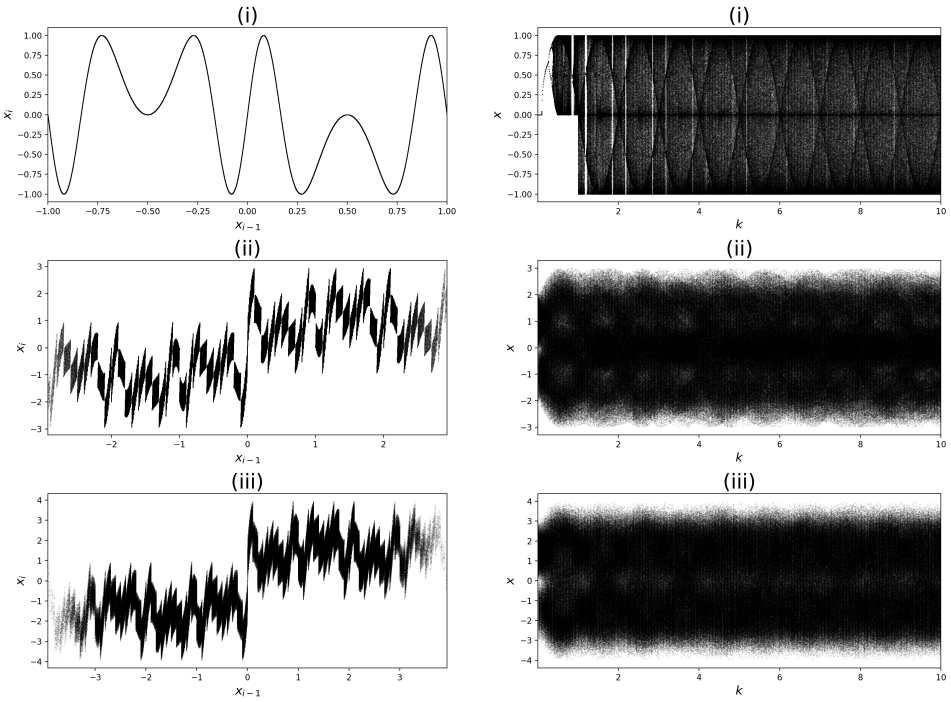

Figure 6. Phase and bifurcation diagrams. (**a**) Phase diagrams of: (**i**) Sine–Sine Map (21), (**ii**) map (22), (**iii**) map (23), ($k = 2, N = 1$). (**b**) Bifurcation diagrams of: (**i**) Sine–Sine Map (21), (**ii**) map (22), (**iii**) map (23), ($N = 1$).

The three-dimensional phase diagram confirms the increase of complexity also in this case. These relevant plots are presented in Figure 7. In the case of the Sine—Sine Map (21), the graph in Figure 7a consists of points forming a curve, while for the map (23) (Figure 7b), points fill up a 3D region indicating that the mapping with the $rem(\cdot)$ operators is much more complex than the base mapping.

Similar to the sine map analysis, the Lyapunov exponent was also calculated, showing the significant increase of the system's sensitivity to initial conditions after the chaotification is applied. The plot of the Lyapunov exponent is shown in Figure 8a. The results are very similar to the Sine Map case. This figure clearly shows the presence of stable regions for the Sine—Sine Map (21) and their absence for mappings with the $rem(\cdot)$ operator. This figure also shows that the sensitivity to the change of initial conditions for the mappings (22) and (23) is roughly constant for the entire range of the parameter k. Thus, after the same number of iterations, the system will lose information about the initial conditions.

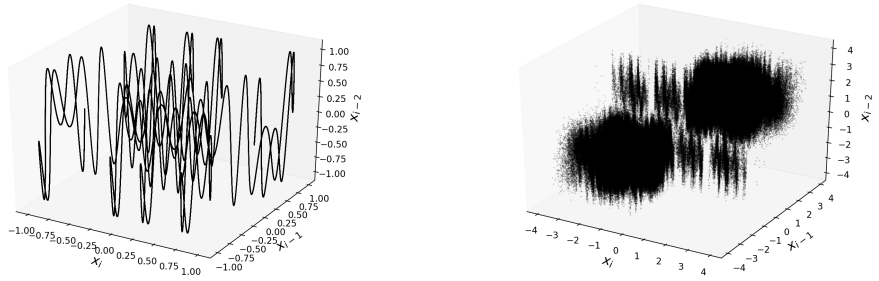

(**a**) (**b**)

Figure 7. Three-dimensional phase diagrams. (**a**) Three-dimensional phase diagram of the Sine—Sine Map (21), ($k = 2$). (**b**) Three-dimensional phase diagram of the map (23), ($k = 2, N = 1$).

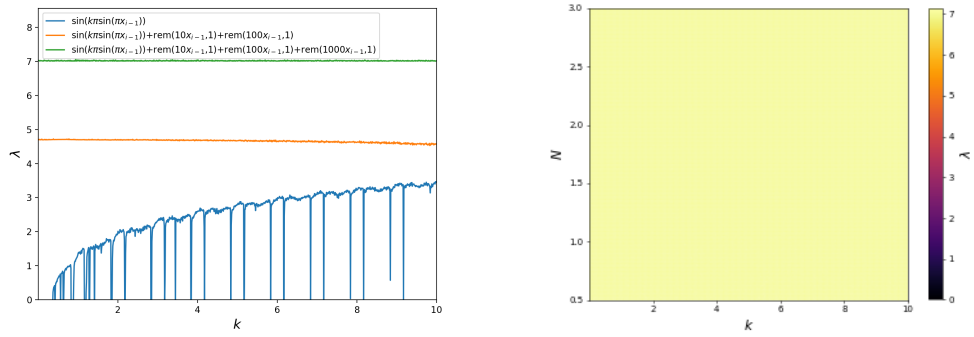

(**a**) (**b**)

Figure 8. Lyapunov exponent. (**a**) Lyapunov exponent of Sine–Sine Map (21) (blue) and its modifications (22) and (23) (orange and green). (**b**) Colour-coded Lyapunov exponent diagram in relation to (k, N) for the map (23). The colour bar corresponds to the value of the exponent.

Moreover, for these mappings, the Lyapunov exponent value λ was also determined as a function of parameters (k, N). The results are shown in Figure 8b. The obtained values show that $\lambda > 0$ for the entire analysed parameter range for the mapping (23). Moreover, λ is roughly constant for the whole range of parameter values. These results are consistent with the value of the Lyapunov exponent from Figure 8a. The obtained results confirmed that the mapping (23) is characterised by interrupted chaotic behaviour for large ranges of parameter changes and, therefore, has a much more complex behaviour than the base function Sine–Sine Map (21).

3.3. Cosine–Logistic Map

In [5] a cosine chaotification was proposed. As an example of this method, consider the Cosine—Logistic Map:

$$x_i = k\cos(rx_{i-1}(1 - x_{i-1})). \tag{24}$$

As in the case of the analysed previous maps, the Cosine—Logistic Map (24) was also used as the base function $\mathcal{F}(x)$, and two new maps are defined, which will be analysed further in the paper:

$$x_i = k\cos(4x_{i-1}(1 - x_{i-1})) + rem(10x_{i-1}, 1) + rem(100x_{i-1}, 1), \tag{25}$$

$$x_i = k\cos(4x_{i-1}(1 - x_{i-1})) + rem(10x_{i-1}, 1) + rem(100x_{i-1}, 1) + rem(1000x_{i-1}, 1). \tag{26}$$

Their design is very similar to the previous cases, i.e., the first one, apart from the base function, has two additional components $rem(10x_{i-1}, 1)$ and $rem(100x_{i-1}, 1)$. In turn, the second one has one more component equal to $rem(1000x_{i-1}, 1)$.

As before, phase diagrams of all three cases (the base Cosine—Logistic Map (24) and its two modifications (25) and (26))) for fixed parameter values are presented in Figure 9a. These graphs confirm that adding multiple $rem(\cdot)$ operators causes a significant increase in the complexity of the base mapping. Figure 9b presents bifurcation diagrams of the analysed mappings. This figure shows that the behaviour of the Cosine—Logistic Map (24) is more complex than the behaviour of the previous base functions, i.e., after some value of the k parameter, there are no visible periodic windows. However, the mappings (25) and (26) also do not have visible periodic windows. Similar to the previous cases, this means that the choice of the mapping parameters in (25) or (26) will always result in chaotic behaviour.

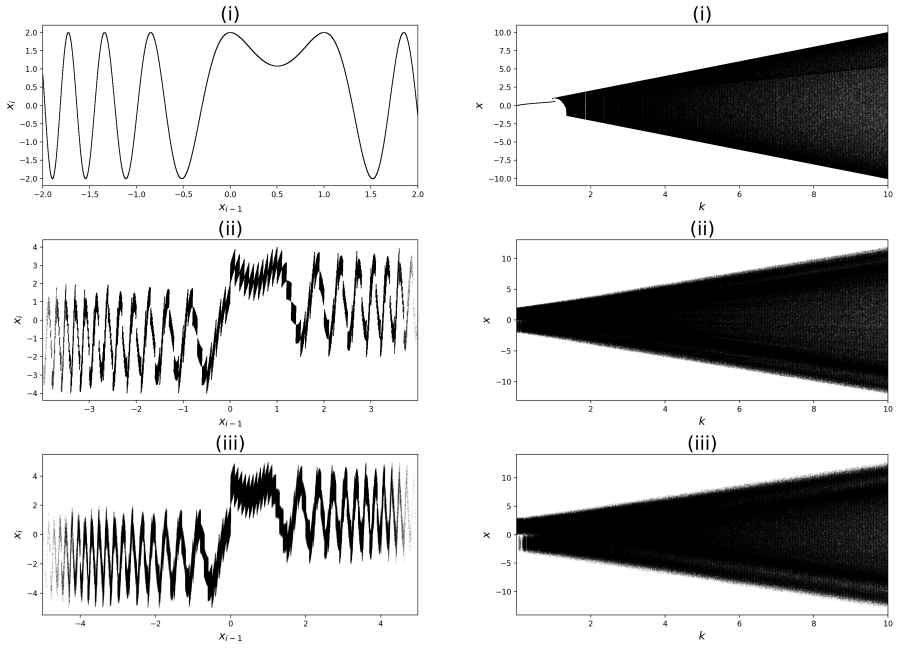

(**a**) (**b**)

Figure 9. Phase and bifurcation diagrams. (**a**) Phase diagrams of: (**i**) Cosine—Logistic Map (24), (**ii**) map (25), (**iii**) map (26), ($k = 2, N = 1$). (**b**) Bifurcation diagrams of: (**i**) Cosine–Logistic Map (24), (**ii**) map (25), (**iii**) map (26), ($N = 1$).

Figure 10a,b also depict the difference between the three-dimensional phase diagrams of the Cosine—Logistic Map (24) and the map (26). The original map has a curve diagram, but the modified map fills a wide 3D region.

The respective plots of the Lyapunov exponent are shown in Figure 11a. The results are very similar to the Sine—Sine Map. This figure clearly shows the presence of stable regions for the Cosine—Logistic Map (24) and their absence for the respective modified mappings with the $rem(\cdot)$ operator. This figure also shows that the sensitivity to the change of initial conditions for the mappings (25) and (26) is roughly constant for the entire range of the parameter k. Thus, after the same number of iterations, the system will lose information about the initial conditions.

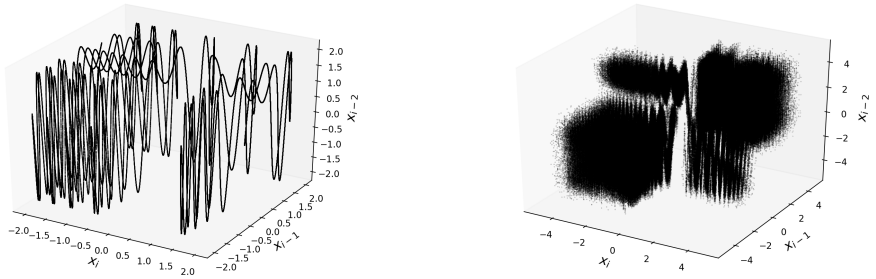

(**a**) (**b**)

Figure 10. Three-dimensional phase diagrams. (**a**) Three-dimensional phase diagram of the Cosine—Logistic Map (24), ($k = 2$). (**b**) Three-dimensional phase diagram of the map (26), ($k = 2, N = 1$).

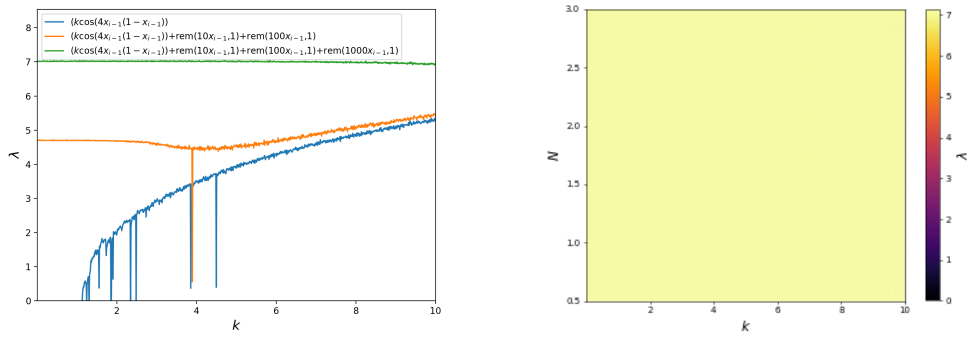

(**a**) (**b**)

Figure 11. Lyapunov exponent. (**a**) Lyapunov exponent of Cosine–Logistic Map (24) (blue) and some cosine-logistic maps with the remainder operator (orange and green). (**b**) Colour-coded Lyapunov exponent diagram in relation to (k, N) for the map (26). The colour bar corresponds to the value of the exponent.

Moreover, for these mappings, the Lyapunov exponent value λ was determined as a function of (k, N). The results are shown in Figure 11b. The obtained values show that $\lambda > 0$ for the entire analysed parameter range for the mapping (26). Moreover, the λ value is roughly constant for the whole range of parameter values. These results are consistent with the value of the Lyapunov exponent from Figure 11a. Again, the obtained results confirm that the mapping (26) is characterised by interrupted chaotic behaviour for large ranges of parameter changes and, thus, has a much more complex behaviour than the base function Cosine—Logistic Map (24).

3.4. Renyi Map

Consider the Renyi Map [39]:

$$x_i = \mathrm{mod}(kx_{i-1}, 1). \tag{27}$$

Finally, the Renyi Map (27) was also used as the base function $\mathcal{F}(x)$, and two new maps are defined, which will be analysed further in the paper:

$$x_i = \mathrm{mod}(kx_{i-1}, 1) + rem(10x_{i-1}, 1) + rem(100x_{i-1}, 1), \tag{28}$$

$$x_i = \mathrm{mod}(kx_{i-1}, 1) + rem(10x_{i-1}, 1) + rem(100x_{i-1}, 1) + rem(1000x_{i-1}, 1). \tag{29}$$

The design is very similar to the previous cases, i.e., the first one, apart from the base function, has two additional components $rem(10x_{i-1}, 1)$ and $rem(100x_{i-1}, 1)$. In turn, the second one has one more component equal to $rem(1000x_{i-1}, 1)$.

As in the earlier analysis, the phase diagrams of all three cases (Renyi Map (27) and its two modifications (28) and (29)) for fixed parameter values are presented in Figure 12a. These graphs confirm that adding multiple $rem(\cdot)$ operators causes a significant complication in the base mapping. In turn, Figure 12b presents bifurcation diagrams of the analysed mappings. This figure shows that the behaviour of the Renyi Map (27) is also very complicated, with no visible periodic windows (the stable states occur in this map for $k \in \mathbb{N}$). However, the mappings (28) and (29) also do not have visible periodic windows. As in the previous cases, this situation means that choosing the mapping parameters in (28) or (29) will always result in a chaotic behaviour of the system.

The three-dimensional phase diagrams are shown in Figure 13 for the Renyi Map (27) and the map (29). The Renyi Map diagram consists of piecewise linear parts, while the modified map has a phase diagram that is more dense and covers a 3D area.

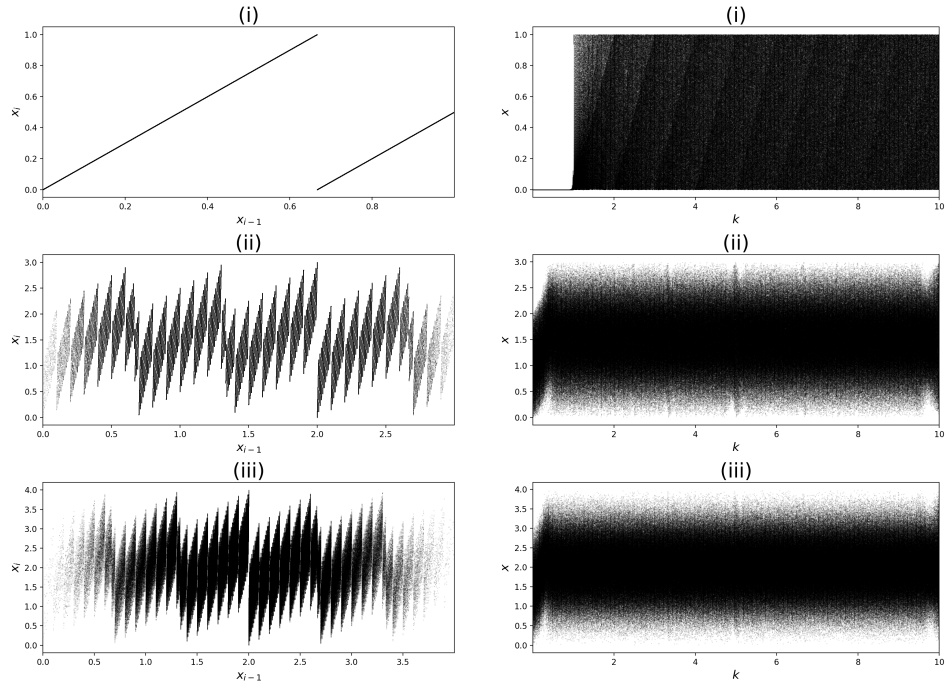

Figure 12. Phase and bifurcation diagrams. (**a**) Phase diagrams of: (**i**) Renyi Map (27), (**ii**) map (28), (**iii**) map (29), ($k = 1.5, N = 1$). (**b**) Bifurcation diagrams of: (**i**) Renyi Map (27), (**ii**) map (28), (**iii**) map (29), ($N = 1$).

Similar to the analysis of the previous maps, plots of the Lyapunov exponent were also determined in this case, showing the system's sensitivity to the change of the initial conditions. The plot of the Lyapunov exponent is shown in Figure 14a. The obtained results are very similar to the previous case. This figure clearly shows the presence of stable regions for the Renyi Map (27) and their absence for mappings with the $rem(\cdot)$ operator. This figure also shows that the sensitivity to the change of initial conditions for the mappings (28) and (29) is roughly constant for the entire range of the parameter k. Thus, after the same number of iterations, the system will lose information about the initial conditions.

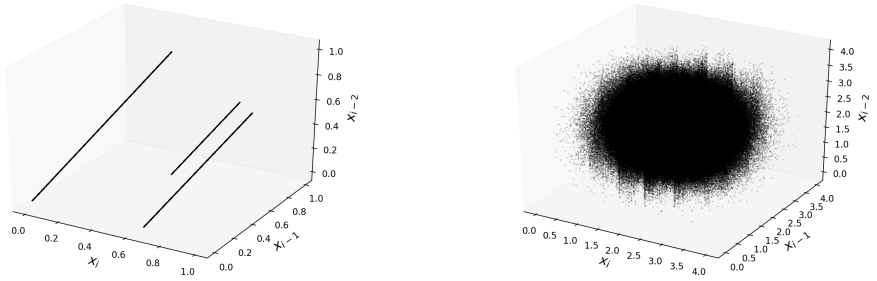

(**a**) (**b**)

Figure 13. Three-dimensional phase diagrams. (**a**) Three-dimensional phase diagram of the Renyi Map (27), ($k = 1.5$). (**b**) Three-dimensional phase diagram of the map (29), ($k = 1.5, N = 1$).

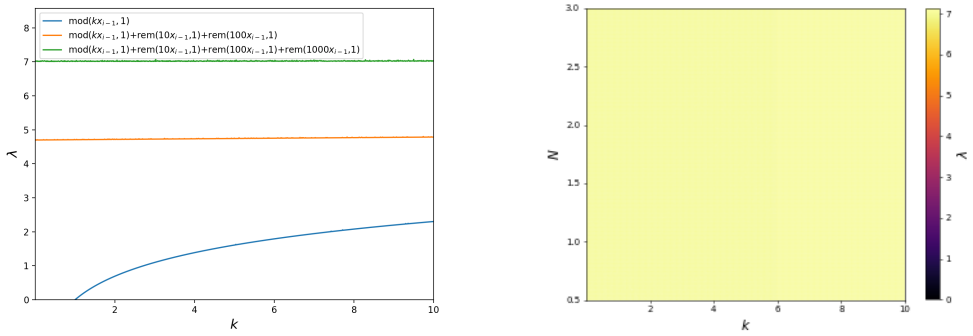

(**a**) (**b**)

Figure 14. Lyapunov exponent. (**a**) Lyapunov exponent of Renyi Map (27) (blue) and some modified maps with the remainder operator (orange and green). (**b**) Colour-coded Lyapunov exponent diagram in relation to (k, N) for the map (29). The colour bar corresponds to the value of the exponent.

Again, the Lyapunov exponent value λ was also determined with respect to (k, N). The results are shown in Figure 14b. The obtained values show that $\lambda > 0$ for the entire analysed parameter range for the mapping (29). Moreover, λ is roughly constant for the whole range of parameter values. These results are consistent with the value of the Lyapunov exponent from Figure 14a. The obtained results confirm that the mapping (29) is characterised by interrupted chaotic behaviour for large ranges of parameter changes and, thus, has a much more complex behaviour than the base function Renyi Map (27).

4. Effect on Key Space

Let $\mathcal{K}$ denote the key space of a seed map, that is the sum of all possible key parameter combinations for that map, which can result in unique solution trajectories. The proposed chaotification technique (2) introduces $2m$ additional parameters, a_j, N_j, $j = 1, \ldots, m$. Assuming a D digit accuracy, this results in a multiplicative increase of the key space by 10^{2mD}. If we let $D = 16$, the key space increase is $10^{32m} \approx (10^3)^{10.6m} \approx (2^{10})^{10.6m} = 2^{106m}$. In the proposed examples, there are three added terms, so $m = 3$, and the increase is approximately 2^{318}. Table 1 lists the key spaces for all the considered maps.

Table 1. Key space of the considered maps.

	Chaotic System			
	Sine (17)	Sine–Sine (21)	Cosine–Logistic (24)	Renyi (27)
Seed	2^{53}	2^{53}	2^{106}	2^{53}
Modified	2^{373}	2^{373}	2^{426}	2^{373}

5. Operations per Iteration

Here, the number of operations that the technique introduces in a single iteration is counted. The results are summarised in Table 2. For m remainder terms, the chaotification technique requires 3 m additional operations, so the computational complexity of the chaotification technique increases linearly with the number of remainder operators.

Note that, in Table 2, operations that can be precomputed only once are not counted. For example, the term πk in the Sine—Sine Map (21) only needs to be computed once and not repeated in every iteration.

Table 2. Number of operations per iteration for the modified maps.

		Chaotic System			
Operation	(2) ($m = 3$)	Mod. Sine (19)	Mod. Sine–Sine (23)	Mod. Cos.–Logistic (26)	Mod. Renyi (29)
Addition	m (3)	3	3	4	3
Multiplication	m (3)	5	5	6	4
Sinusoidal	0	1	2	1	0
Remainder	m (3)	3	3	3	4
Overall	3m (9)	12	13	14	11

6. Application to Symmetric Encryption of B-Spline Curves

6.1. B-Spline Basics

A B-spline curve of degree n is characterised by its control points. Given $p+1$ control points $P_i \in \mathbb{R}^d$ in the d-dimensional space, the curve is described by

$$x(t) = \sum_{i=0}^{p} N_i^n(t) P_i, \tag{30}$$

where $N_i^n(t)$ are the B-spline basis polynomials of degree n. The curve is defined over a knot sequence T in the interval $t \in [0, 1]$, which we assumed here as uniform, described by

$$T = [t_0, \ldots, t_{p+n+1}] = \left[\underbrace{0, \ldots, 0}_{n+1}, t_{n+1}, \ldots, t_p, \underbrace{1, \ldots, 1}_{n+1}\right]. \tag{31}$$

The repetition of the first and last knots is performed so that the curve interpolates the first and last control points and is also tangent to the control polygon.

6.2. Encryption of a B-Spline Curve

As described in the previous section, the information required to completely describe a B-Spline curve is its control points $P_0, \ldots, P_p$ arranged in order, the polynomial degree n, and a knot sequence. Thus, the encryption of a curve should aim at masking these characteristics. As changing the polynomial order would effect the proper definition of the knot sequence, here we assumed that the encryption process will not affect the degree of the curve. The same holds for the knot sequence. The proposed encryption will not affect it, as it is fairly common to assume a uniform knot sequence. If required though, an optional step can be added, encrypting the knot sequence as well.

The procedure is described in the steps below. There are two main steps involved: a shuffling of the plaintext values and a modulation through addition. The purpose of the

shuffling step is to disperse the information regarding the sequence of control points, for all their coordinates. The second step hides this information, by combining it with the values of a chaotic map. For both steps, a chaotic map is used, chosen from the ones presented in the previous section. Here, the modified Sine Map (19) is considered as an example.

Here, it is worth noting that a common, and very effective substitution action is the exclusive or (XOR) operation, which is performed on the binary level of the plaintext. Here, since the plaintext consists of rational numbers, the application of the XOR operation is possible only after transforming to binary format, for example using the IEEE-754 standard. However, as this is deemed time-consuming, the more computationally efficient option of additive modulation was chosen:

Input. A plaintext B-spline curve described by its control points $P_0, \ldots, P_p \in \mathbb{R}^d$ arranged in a matrix $\Pi = (P_0, \ldots, P_p) \in \mathbb{R}^{d\times(p+1)}$, the polynomial degree n, and a knot sequence U. It is assumed that all the control point coordinates lie in the interval $[-B, B]$.
A chaotic map of the form (19), with key parameters $k, a_1, a_2, a_3, N_1, N_2, N_3$, to be computed below.

Data setup. First, the entries of Π are concatenated in a single vector Π_{row} of size $1 \times d \cdot (p+1)$ as follows:

$$\Pi_{row} = \begin{pmatrix} P_{0,1} & P_{0,2} & \cdots P_{0,d} & \cdots P_{1,1} & \cdots P_{1,d} & \cdots & P_{p,d} \end{pmatrix} \tag{32}$$

where $P_{i,j}$ represents the j-th coordinate of the P_i control point.

Key setup. To make the design resistant to plaintext attacks, the map keys should be plaintext-dependent. This achieves the confusion task in encryption. They are initialised as

$$\begin{aligned} x_0 &= mean(\Pi_{row})/||\Pi_{row}|| && (33)\\ k &= B + \text{entropy}(\Pi_{row}) && (34)\\ a_1 &= 10 + \text{mean}(\Pi_{row}) && (35)\\ a_2 &= 100 + \text{var}(\Pi_{row}) && (36)\\ a_3 &= 1000 && (37)\\ N_1 &= 1 && (38)\\ N_2 &= 1 && (39)\\ N_3 &= 1 && (40) \end{aligned}$$

where $||\cdot||$ denotes the Euclidean norm.

Step 1. The first step is to shuffle the sequence of the control points. This is also part of the usual confusion step in encryption, which disperses the plaintext information. For the shuffling operation, the following pseudo-random number generator (PRNG) is utilised:

$$p_i = \lfloor \text{mod}(10^8 x_i, d \cdot (p+1)) \rfloor + 1, \tag{41}$$

which generates integers in the interval $[1, d \cdot (p+1)]$, until $d \cdot (p+1)$ discrete values are generated. If an integer is generated twice, it is discarded the second time. The result is a list of $d \cdot (p+1)$ non-repeating integers, denoted as $S = (s_0, \ldots, s_{d\cdot(p+1)-1})$. These integers represent the new order of the elements of the vector Π_{row}. Therefore, the s_0 element of Π_{row} is moved to the first position, the s_1 element of Π_{row} is moved to the second position, and so on. The resulting matrix, which contains the re-arranged elements of Π_{row}, is denoted as Σ_{row}:

$$\Sigma_{row} = \begin{pmatrix} \Sigma_{row,0} & \Sigma_{row,1} & \cdots & \Sigma_{row,d\cdot(p+1)-1} \end{pmatrix} \tag{42}$$

Step 2. The next step is the diffusion of the shuffled plaintext. The values of the vector Σ_{row} are masked using the values of the chaotic map used in Step 1. Continuing the iteration of the map from Step 2 (without making use of the PRNG), the elements of Σ_{row} are masked as follows:

$$\begin{aligned} C_0 &= \Sigma_{row,0} + x_i && (43)\\ C_1 &= \Sigma_{row,1} + x_{i+1} && (44)\\ &\vdots \\ C_{d\cdot(p+1)-1} &= \Sigma_{row,d\cdot(p+1)-1} + x_{i+d\cdot(p+1)-1} && (45) \end{aligned}$$

where the i index in x_i is used to denote that the map is being iterated, continuing from the previous Step 1. The resulting values are arranged in a vector:

$$\Psi_{row} = \begin{pmatrix} C_0 & C_1 & \cdots & C_{d\cdot(p+1)-1} \end{pmatrix} \quad (46)$$

Step 3. After the substitution step is finished, the elements of Ψ_{row} are reshaped into an $d \times (p+1)$ matrix $\Psi = (E_0, \ldots, E_p)$, where each column represents a ciphertext control point, similar to the matrix Π.

Output. A ciphertext B-spline curve described by its control points $E_0, \ldots, E_p$, the polynomial degree n, and a knot sequence U.

6.3. Decryption Process

The decryption process follows the exact same steps, in reverse order. These are described below:

Input. A ciphertext B-spline curve described by its control points $E_0, \ldots, E_p$, the polynomial degree n, and a knot sequence U.
A chaotic map of the form (19), with key parameters $k, a_1, a_2, a_3, N_1, N_2, N_3$.

Step 1. The first step is to arrange the elements of the ciphertext control points $E_0, \ldots, E_p$ in a $1 \times d \cdot (p+1)$ vector, as Equation (46):

Step 2 The PRNG (41) is initialised. The PRNG generates integers in the interval $[1, d \cdot (p+1)]$, until $d \cdot (p+1)$ discrete values are generated. Therefore, if an integer is generated twice, it is discarded the second time. The result is a list of $d \cdot (p+1)$ non-repeating integers, denoted as $S = (s_0, \ldots, s_{d\cdot(p+1)-1})$.

After this process is finished, the map is iterated again $d \times (p+1)$ times, to generate the values $x_i, \ldots, x_{i+d\cdot(p+1)-1}$. The i index here denotes that the map is iterated consecutively from the previous process of generating S.

Step 3. The confusion is reversed as

$$\begin{aligned} \Sigma_{row,0} &= C_0 - x_i && (47)\\ \Sigma_{row,1} &= C_1 - x_{i+1} && (48)\\ &\vdots \\ \Sigma_{row,d\cdot(p+1)-1} &= C_{d\cdot(p+1)-1} - x_{i+d\cdot(p+1)-1} && (49) \end{aligned}$$

The resulting elements are combined in a vector as Eqauiton (42):

Step 4. The next step is to reverse the shuffling of the elements of Σ_{row}.

The elements of S from Step 2 indicate the shuffling that was originally performed in the encryption process. The procedure is reversed, by moving the first element into the s_0 position, the second element into the s_1 position, and so on, until the last element is moved into the $s_{d\cdot(p+1)-1}$ position. The new matrix is denoted as Π_{row}.

Step 5. Finally, the elements of Π_{row} are reshaped into an $m \times (p+1)$ matrix $\Pi = (P_0, \ldots, P_p)$, where each column represents the plaintext control point.

Output. A plaintext B-spline curve described by its control points $P_0, \ldots, P_p \in \mathbb{R}^d$ arranged in a matrix $\Pi = (P_0, \ldots, P_p) \in \mathbb{R}^{d \times (p+1)}$, the polynomial degree n, and a knot sequence U.

7. Patch Encryption

B-spline patches are obtained by considering a net of control points $P_{i,j} \in \mathbb{R}^3$, $i = 0, \ldots, P$, $j = 0, \ldots, Q$, and two B-spline polynomial bases $N_i^n(u)$, $N_j^m(v)$ of degrees n, m, defined over knot sequences U, V as in (31). The B-spline patch is defined as

$$x(u,v) = \sum_{i=0}^{P} \sum_{j=0}^{Q} N_i^n(u) N_j^m(v) P_{i,j} \tag{50}$$

or in matrix form:

$$x(u,v) = \begin{pmatrix} N_0^n(u) & \cdots & N_P^n(u) \end{pmatrix} \begin{pmatrix} P_{0,0} & \cdots & P_{0,Q} \\ \vdots & \ldots & \vdots \\ P_{P,0} & \cdots & P_{P,Q} \end{pmatrix} \begin{pmatrix} N_0^m(v) \\ \vdots \\ N_Q^m(v) \end{pmatrix}. \tag{51}$$

To encrypt a B-spline patch, the procedure followed is a direct extension of Section 6.2. The idea is again to encrypt the control points of the patch, and this is performed following the exact same steps. To do so, the only modification required is to concatenate all the control points in a single row vector. This can be performed by arranging the coordinates of all points in a row Π_{row} similar to (32) as follows:

$$\Pi_{row} = \begin{pmatrix} P_{0,0,1} & P_{0,0,2} & P_{0,0,3} & P_{1,0,1} & \cdots & P_{P,Q,3} \end{pmatrix}, \tag{52}$$

where the third index in $P_{i,j,1}$, $P_{i,j,2}$, $P_{i,j,3}$ denotes the x, y, z coordinates, respectively. With this modification and the appropriate reshaping of Ψ_{row}, Section 6.2 can be applied to encrypt a B-spline patch.

The same process can be performed when there is a collection of curves or patches to be encrypted. Since in (33), the encryption keys are plaintext-dependent, repeating the process of key generation for a collection of curves or patches would be impractical. This can be easily resolved, by arranging first all of the given control points into a single vector Π_{row}, as in (32) or (52), and then, performing the encryption on the single vector Π_{row}, which carries the plaintext information on all the curves. Of course, the appropriate reverse reshaping would have to be performed during the decryption stage.

8. Simulation Results

The encryption design is tested on a collection of several 2D and 3D cubic B-splines. Here, $B = 5$. Figures 15–17 show a collection of cubic B-spline curves to be used for encryption, along with their convex hulls, and the corresponding encrypted curves. The encrypted curves have no visual similarity to the corresponding plaintext ones. The curves in Figure 16 are taken from [31]. The curves were generated using the algorithms described in [30,40].

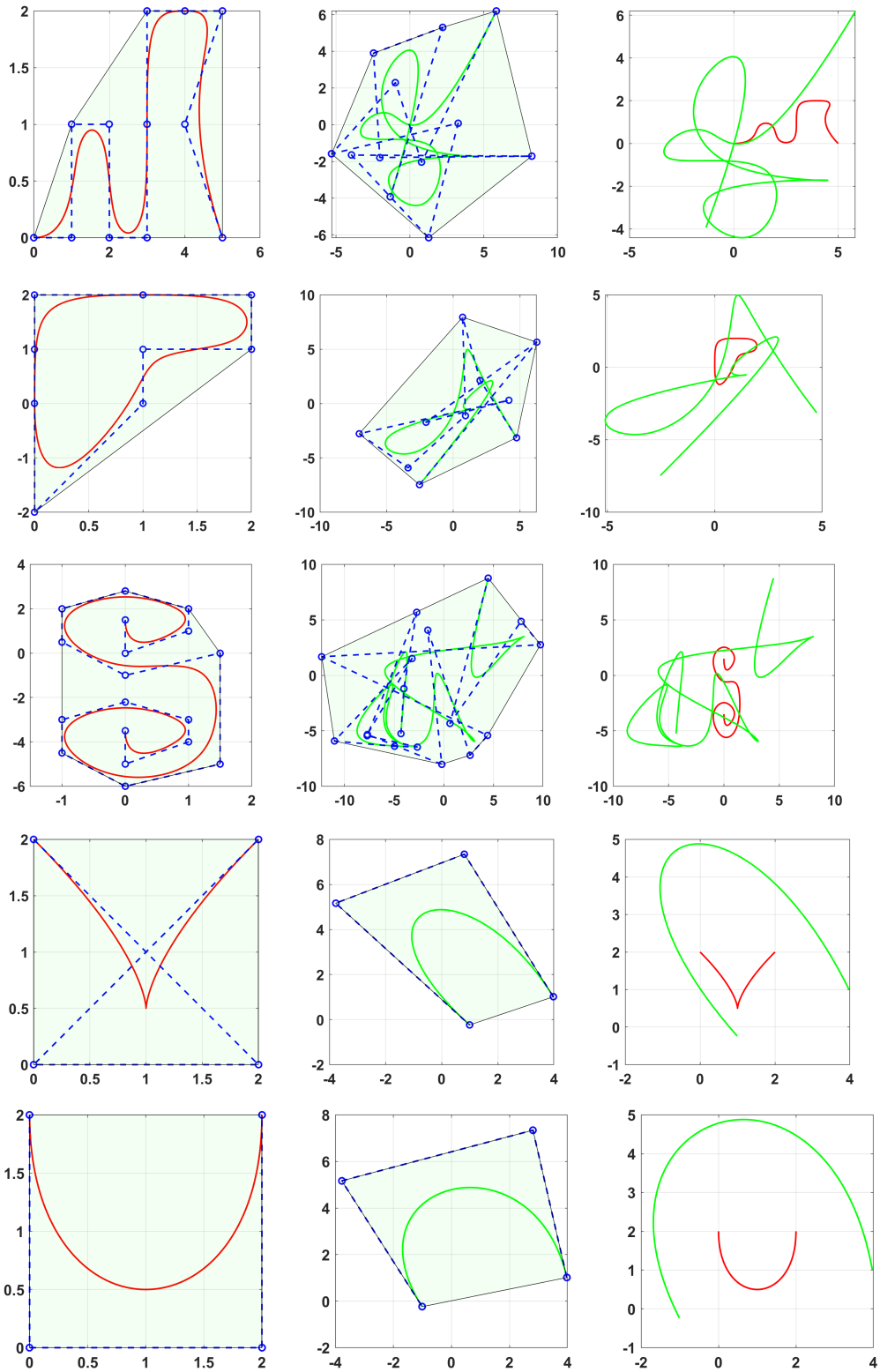

Figure 15. Examples of cubic B-spline curves (**left**), along with their convex hull, the encrypted curve (**middle**), and both curves (**right**).

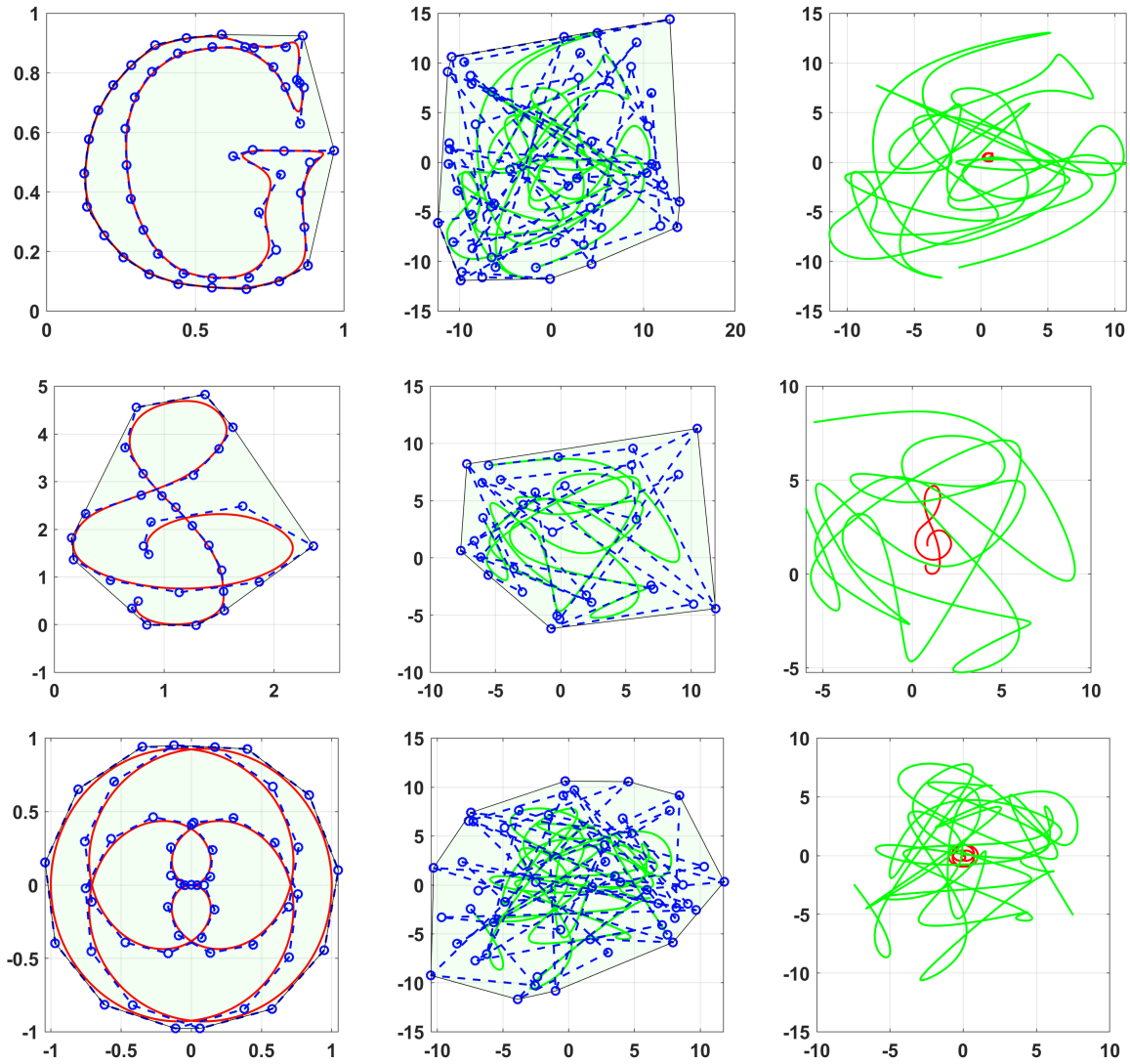

Figure 16. Examples of cubic B-spline curves (**left**) [31], along with their convex hull, the encrypted curve (**middle**), and both curves (**right**).

Figure 18 shows a collection of three patches and the respective encrypted ones. The encrypted patches are again visually dissimilar from the corresponding plaintext patch. Moreover, the encryption of the Utah teapot, teacup, and teaspoon is considered, with data taken from [41]. The data available consist of a .txt file of control points and a secondary .txt file indicating the control point indexes in the first file, for each patch. The results are shown in Figure 19. The teapot consists of 32 patches; the cup is 26 patches; the spoon is 16 patches. The resulting ciphertext collection of patches clearly has no distinguishable shape. Note that, for the ease of implementation, the reshaping of the control points into a single vector Π_{row} (52) is performed directly to the .txt file provided in [41].

In the following subsections, a series of statistical tests were performed on the plaintext and ciphertext curves. For this, the curves in Figure 16 and the shapes in Figure 19 were chosen, due to having the most control points. The "G" curve consists of 50 control points; the music key consists of 30 control points; the sinusoidal curve consists of 50 control points. For the teapot, all 32 patches have overall 306 control points; the teacup has 251 points; the teaspoon 251 control points.

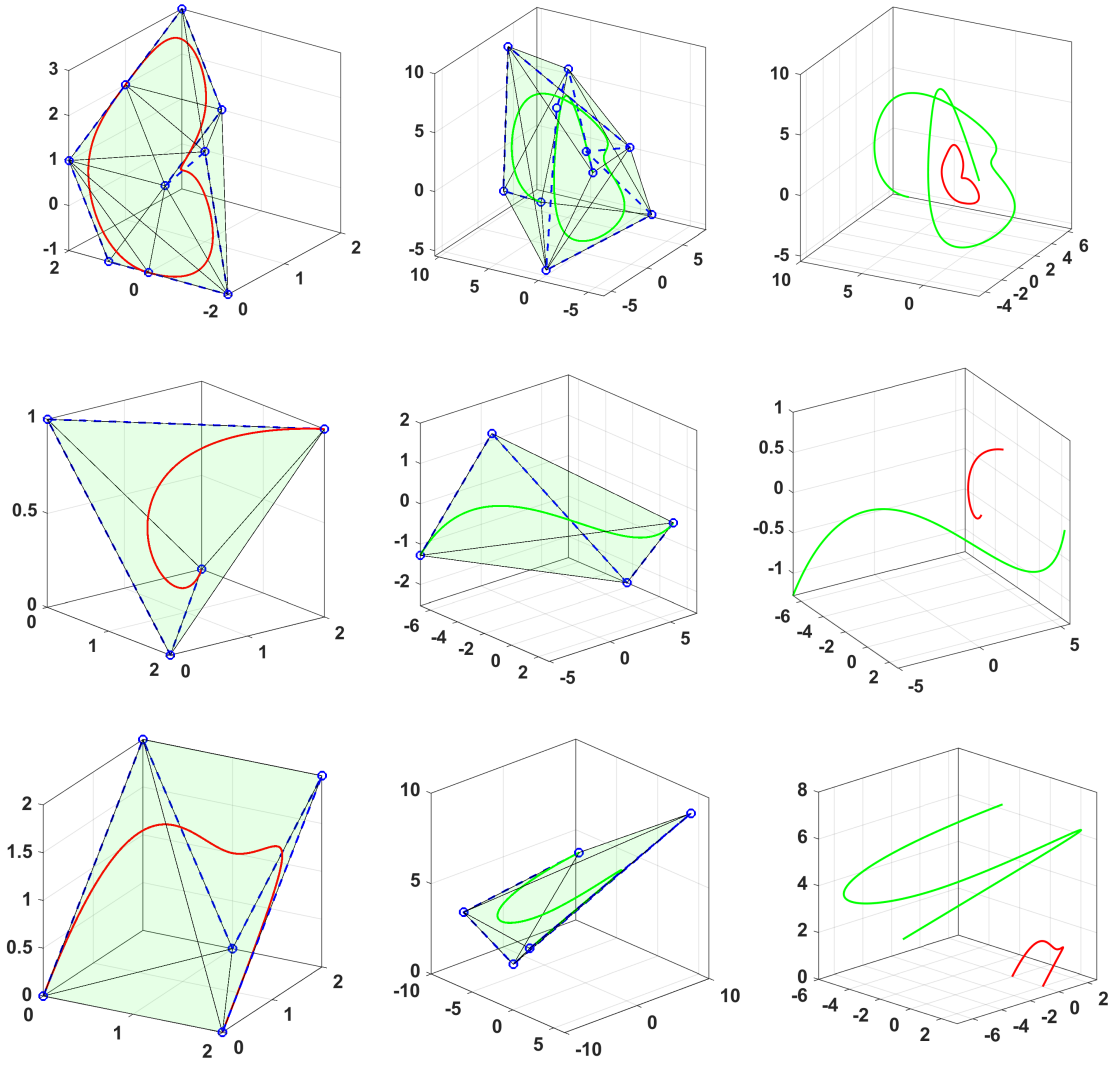

Figure 17. Examples of 3D cubic B-spline curves (**left**), along with their convex hull, the encrypted curve (**middle**), and both curves (**right**).

8.1. Map Choice

In (34), the map parameter k is chosen based on the value where the curve lies. Depending on the map, the choice of k can affect the map's range. This is the case for the sine map (19) and the Cosine—Logistic Map (24). Having a map with a wider range will affect how wide the resulting curve will be, after the modulation step. Naturally, the map's range should be wide enough to hide the plaintext curve's range after the modulation. See, for example, Figures 15 and 16, where the encrypted curves lie on a much wider area in the plane, effectively hiding the range of the plaintext control points.

If a map's control parameter k cannot affect its mapping range, as for example in the sine–sine (21) and Renyi (27) maps, then before the additive modulation step, the chaotic values can be scaled by an appropriate factor.

8.2. Histogram Analysis

Any statistically unbiased random time series should have a histogram that is uniform, indicating that there is no bias in the average values that occur over a specific subinterval of the state space. Here, the histograms were computed for the concatenated coordinate vectors Π_{row}, Ψ_{row}. The row Σ_{row}, being a shuffling of Π_{row}, has the exact same histogram, so it is not shown here. The histograms are displayed in Figure 20. For the curves, the

histogram consists of 10 groups, while for the surfaces, there are 30 groups. The ones corresponding to the ciphertext curves/patches are clearly more uniform compared to the plaintext ones. Table 3 also displays the histogram variance for three curves and shapes. The variance is much lower for the ciphertext points, indicating a more uniform histogram. Notice, however, that this analysis was performed in a very small ciphertext and, therefore, should only be interpreted as a measure of improved confusion in the ciphertext.

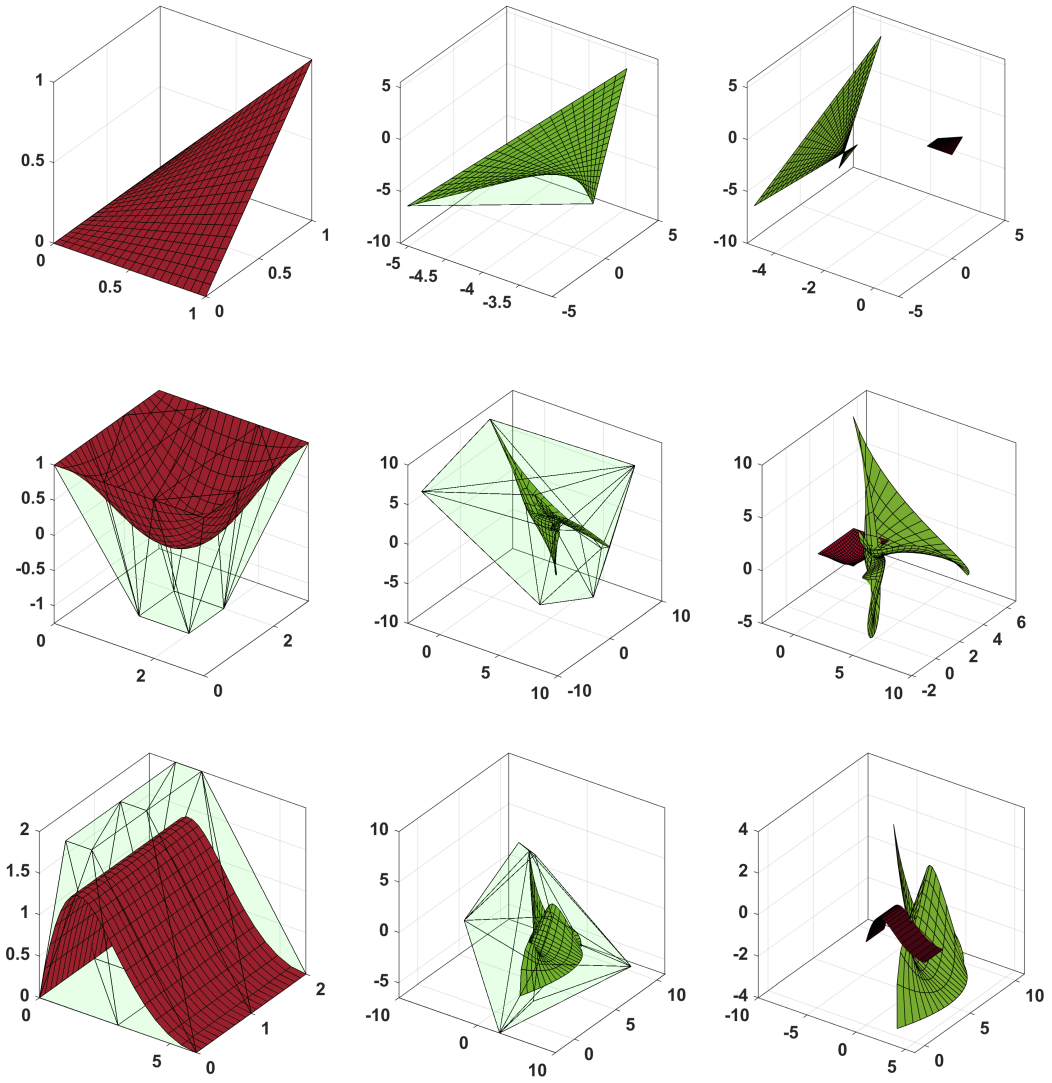

Figure 18. Examples of B-spline patches (**left**), the encrypted patch (**middle**), and both patches (**right**).

Table 3. Histogram variance of the curves shown in Figures 16 and 19.

	Original	**Shuffled**	**Modulated**
Curve 1 (G)	7.3333	7.3333	11.3333
Curve 2 (music key)	0.9290	0.9290	0.0572
Curve 3 (sinusoidal)	26.2222	26.2222	6.6667
Teapot	814.17	814.17	244.66
Teacup	646.78	646.78	88.6448
Teaspoon	2707.6	2707.6	70.593

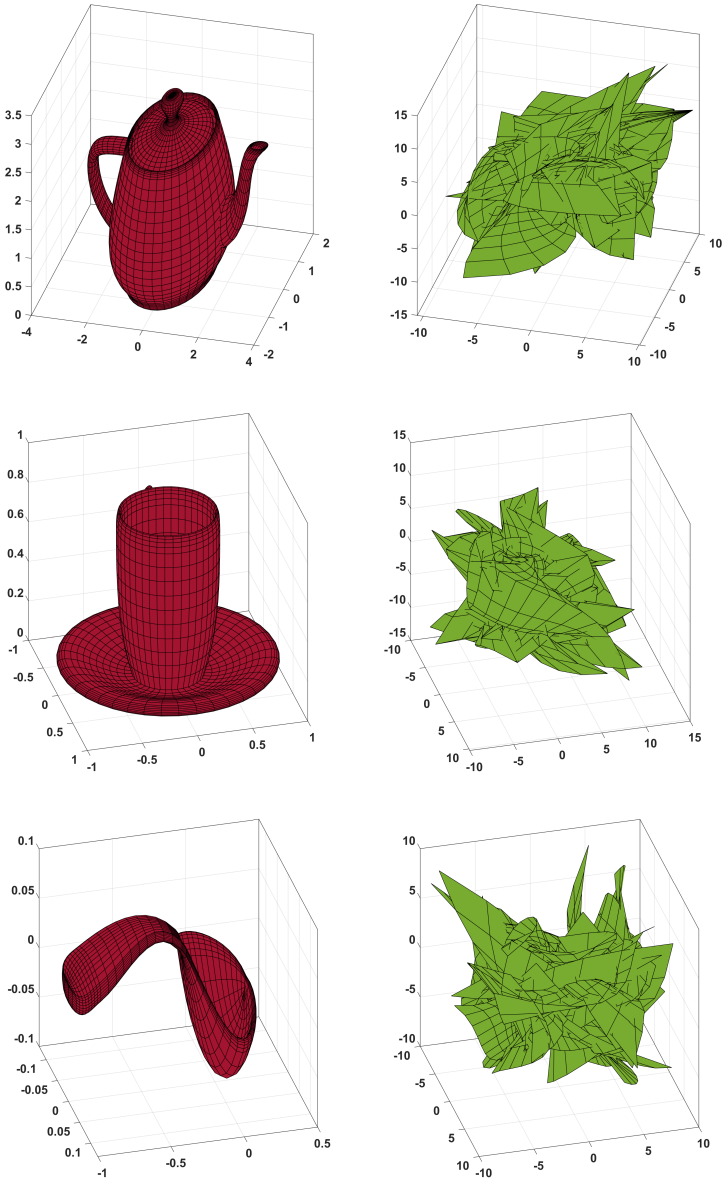

Figure 19. Examples of the teapot (32 patches), cup (26 patches), and spoon (16 patches) and the corresponding encrypted patches (right).

8.3. Correlation

Correlation indicates whether there is any linear relationship between two datasets. For two independent datasets, their correlation should be very close to zero, indicating that their values are linearly independent. Here, the correlation was measured between consecutive control points in the plaintext and ciphertext curves. Note here that, as a plaintext curve can have any form or shape, it is possible that the consecutive control points of the plaintext curve may also showcase low correlation. However, even in this case, it is expected that the correlation of the ciphertext control points will be even lower. The results are shown in Table 4.

Table 4. Correlation of consecutive points for the curves shown in Figure 16 and 19.

	Original	**Shuffled**	**Modulated**
Curve 1 (G)	0.9573	−0.1049	−0.0361
Curve 2 (music key)	0.9290	0.0812	0.0572
Curve 3 (sinusoidal)	0.8523	−0.0142	−0.1371
Teapot	0.9144	−0.0420	0.2114
Teacup	0.8356	0.0049	0.1822
Teaspoon	0.9788	0.0330	0.2180

Figure 20. Histogram of plaintext (red) and encrypted (green) coordinates in vectors Π_{row}, Ψ_{row} for the curves and patches in Figures 16 and 19.

8.4. Noise

The process of decryption described in Section 6.3 can be performed even if the ciphertext $\hat{\Psi} = \Psi + \mathcal{W}$ has been corrupted by noise $\mathcal{W}$ during transmission. The noise will still be present in the decrypted set of control points though. When the channel noise is too intense, the decryption process can be independently complemented by a suitable filtering process to reduce the noise.

Figure 21 shows the result of decryption from a ciphertext set $\hat{\Psi}$ of control points under different noise intensities. The noise was modelled as uniform random numbers in the interval $[-z, z]$, where $z = 0.001, 0.01, 0.1$ for the "G" curve and $z = 0.01, 0.1, 0.5$ for the teapot. The error norms between the plaintext and decrypted control points are 0.0041, 0.0380, and 0.4505, respectively, for the "G" curve and 0.1043, 1.0768, 5.1801 for the teapot.

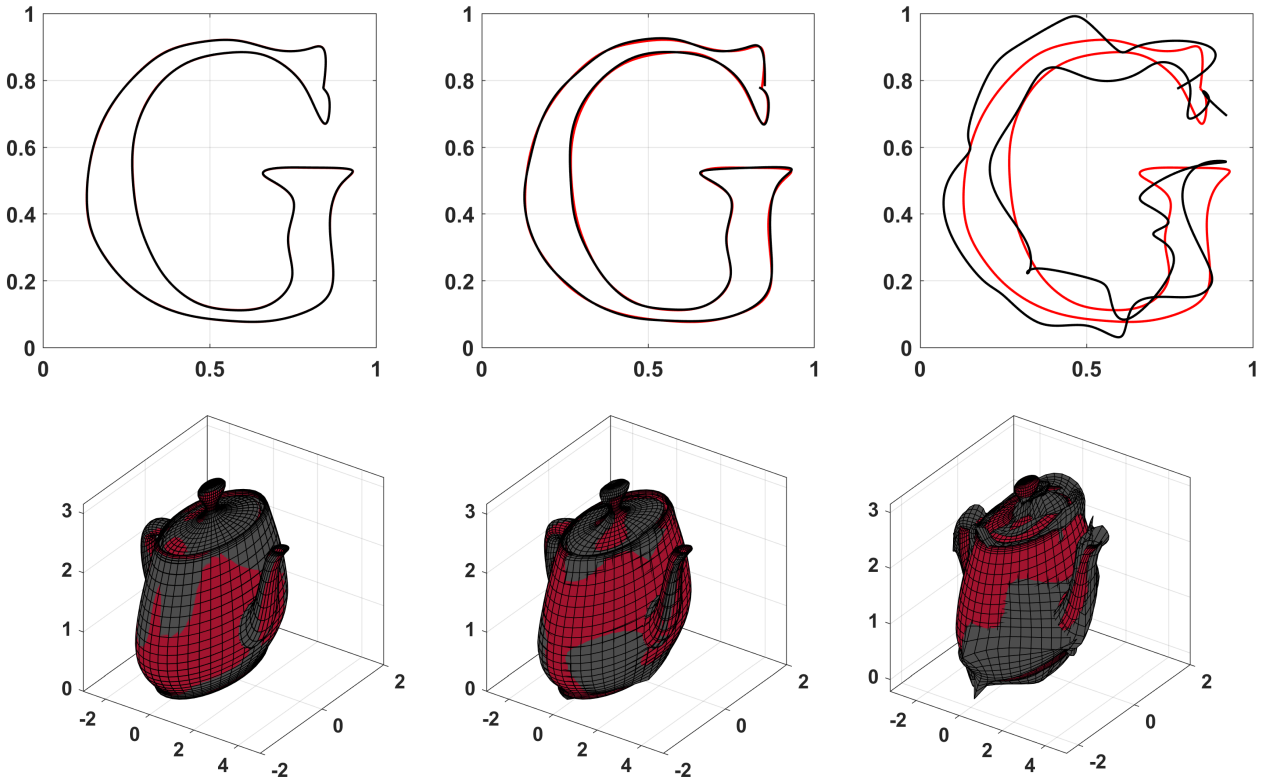

Figure 21. Examples of plaintext (red) and decrypted (black) curve, where noise is added in the encrypted data. The noise is added as a uniform random series in the interval $[-z, z]$. For the "G" curve, $z = 0.001$ (**left**), $z = 0.01$ (**middle**), $z = 0.1$ (**right**). For the teapot, $z = 0.01$ (**left**), $z = 0.1$ (**middle**), $z = 0.5$ (**right**).

8.5. Key Space

The key space of the encryption (Section 6.2) is the same as the key space of the source map. As shown in Table 1, all the maps have the required key space to resist brute force attacks.

8.6. Key Sensitivity

The encryption process inherits the avalanche property of the chaotic map it uses as its source of randomness. As any chaotic map showcases sensitivity to parameter changes, perturbing any key value in (33) in the decryption process will result in the failure of the decryption. Figure 22 shows two such examples, were it can be observed that, indeed, the decryption fails to recreate the original plaintext curve and patch.

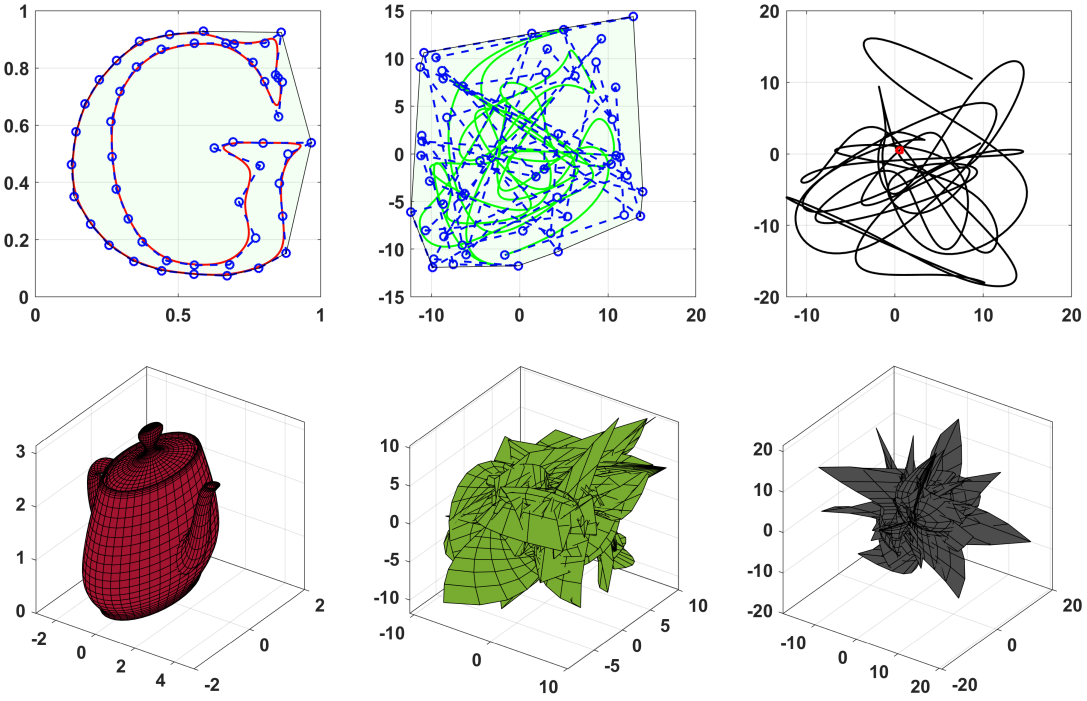

Figure 22. Examples of plaintext (red, left), encrypted (green, middle), and decrypted (black, right) curve/patch, where the key value x_0 is perturbed as $\hat{x}_0 = x_0 + 10^{-9}$ during the decryption.

9. Conclusions and Future Goals

This work studied a chaotification technique, which is an extension of [18] and consists of combining the remainder of multiple scalings of the map's value for the next iteration. The resulting maps can achieve a high Lyapunov exponent value, which can be controlled by appropriate parameter tuning.

An application of the proposed maps to the encryption of B-spline curves and patches was considered. The encryption consists of two steps: the first is the shuffling of the control points, and the second is an addition modulation step.

Future studies will be directed towards two main research areas. The first is the problem of chaotification. The use of the remainder operator will be explored for the creation of chaotic maps with a controllable mapping domain and without any equilibria. The control of the mapping interval will be of use in developing maps with modifiable statistical characteristics, which is desirable in various applications. The absence of equilibria is also desirable for achieving robust chaotic behaviour, as the Period 1 behaviour completely vanishes. Moreover, maps and systems without equilibria are themselves a distinct topic of study in dynamical systems' analysis.

A second extension of this work is to generalise the encryption for rational B-spline curves and patches [30]. Here, the process should include the encryption of the control points along with the corresponding weights. Moreover, other types of geometric data structures can be considered, for example 3D objects. Finally, apart from the additive modulation, which is a linear operator, other operations can be considered for increased complexity, such as multiplication or cosine transformation. It must be noted though that highly nonlinear operations may introduce numerical errors during the decryption, so their choice must be carefully made. Any additional encryption steps can be considered either directly on the floating point plaintext data or in their binary representation. It would also be interesting to study if chaotic maps can be used for watermarking B-spline curves.

Author Contributions: Conceptualisation, L.M. and M.L.; methodology, L.M. and M.L.; software, L.M. and M.L.; formal analysis, L.M., M.L., I.P.A., and I.K.; writing—original draft preparation, L.M. and M.L.; writing—review and editing, I.P.A. and I.K.; visualisation, L.M. and M.L.; supervision, M.S.B. and C.V. All authors have read and agreed to the published version of the manuscript.

Funding: This research received no external funding.

Data Availability Statement: No new data were created or analyzed in this study. Data sharing is not applicable to this article.

Acknowledgments: The authors are thankful to Chongyang Deng for providing the control points for the three curves used for encryption. The authors are thankful to the anonymous Reviewers for their comments.

Conflicts of Interest: The authors declare no conflict of interest.

References

1. Grassi, G. Chaos in the Real World: Recent Applications to Communications, Computing, Distributed Sensing, Robotic Motion, Bio-Impedance Modelling and Encryption Systems. *Symmetry* **2021**, *13*, 2151. [CrossRef]
2. Moysis, L.; Butusov, D.N.; Tutueva, A.; Ostrovskii, V.; Kafetzis, I.; Volos, C. Introducing Chaos and Chaos Based Encryption Applications to University Students-Case Report of a Seminar. In Proceedings of the 2022 11th International Conference on Modern Circuits and Systems Technologies (MOCAST), Bremen, Germany, 8–10 June 2022; pp. 1–6.
3. Özkaynak, F. Brief review on application of nonlinear dynamics in image encryption. *Nonlinear Dyn.* **2018**, *92*, 305–313. [CrossRef]
4. Akmeşe, Ö.F. Bibliometric Analysis of Publications on Chaos Theory and Applications during 1987–2021. *Chaos Theory Appl.* **2022**, *4*, 169–178. [CrossRef]
5. Natiq, H.; Banerjee, S.; Said, M. Cosine chaotification technique to enhance chaos and complexity of discrete systems. *Eur. Phys. J. Spec. Top.* **2019**, *228*, 185–194. [CrossRef]
6. Hua, Z.; Zhou, B.; Zhou, Y. Sine chaotification model for enhancing chaos and its hardware implementation. *IEEE Trans. Ind. Electron.* **2018**, *66*, 1273–1284. [CrossRef]
7. Hua, Z.; Zhang, Y.; Zhou, Y. Two-dimensional modular chaotification system for improving chaos complexity. *IEEE Trans. Signal Process.* **2020**, *68*, 1937–1949. [CrossRef]
8. Mansouri, A.; Wang, X. A novel one-dimensional chaotic map generator and its application in a new index representation-based image encryption scheme. *Inf. Sci.* **2021**, *563*, 91–110. [CrossRef]
9. Wu, Q. Cascade-sine chaotification model for producing chaos. *Nonlinear Dyn.* **2021**, *106*, 2607–2620. [CrossRef]
10. Belazi, A.; Kharbech, S.; Aslam, M.N.; Talha, M.; Xiang, W.; Iliyasu, A.M.; Abd El-Latif, A.A. Improved Sine-Tangent chaotic map with application in medical images encryption. *J. Inf. Secur. Appl.* **2022**, *66*, 103131. [CrossRef]
11. Lu, Q.; Yu, L.; Zhu, C. Symmetric Image Encryption Algorithm Based on a New Product Trigonometric Chaotic Map. *Symmetry* **2022**, *14*, 373. [CrossRef]
12. Zhu, H.; Ge, J.; Qi, W.; Zhang, X.; Lu, X. Dynamic analysis and image encryption application of a sinusoidal-polynomial composite chaotic system. *Math. Comput. Simul.* **2022**, *198*, 188–210. [CrossRef]
13. Hua, Z.; Zhou, Y. Exponential chaotic model for generating robust chaos. *IEEE Trans. Syst. Man Cybern. Syst.* **2019**, *51*, 3713–3724. [CrossRef]
14. Zang, H.; Yuan, Y.; Wei, X. Research on Pseudorandom Number Generator Based on Several New Types of Piecewise Chaotic Maps. *Math. Probl. Eng.* **2021**, *2021*, 1375346. [CrossRef]
15. Zhang, S.; Liu, L. A novel image encryption algorithm based on SPWLCM and DNA coding. *Math. Comput. Simul.* **2021**, *190*, 723–744. [CrossRef]
16. Ablay, G. Lyapunov Exponent Enhancement in Chaotic Maps with Uniform Distribution Modulo One Transformation. *Chaos Theory Appl.* **2022**, *4*, 45–58. [CrossRef]
17. Khairullah, M.K.; Alkahtani, A.A.; Bin Baharuddin, M.Z.; Al-Jubari, A.M. Designing 1D Chaotic Maps for Fast Chaotic Image Encryption. *Electronics* **2021**, *10*, 2116. [CrossRef]
18. Moysis, L.; Kafetzis, I.; Baptista, M.S.; Volos, C. Chaotification of One-Dimensional Maps Based on Remainder Operator Addition. *Mathematics* **2022**, *10*, 2801. [CrossRef]
19. Zhang, Z.; Zhu, H.; Ban, P.; Wang, Y.; Zhang, L.Y. Buffeting Chaotification Model for Enhancing Chaos and Its Hardware Implementation. *IEEE Trans. Ind. Electron.* **2022**, *70*, 2916–2926. [CrossRef]
20. Zhu, M.; Wang, C. A novel parallel chaotic system with greatly improved Lyapunov exponent and chaotic range. *Int. J. Mod. Phys. B* **2020**, *34*, 2050048. [CrossRef]
21. Dong, C.; Rajagopal, K.; He, S.; Jafari, S.; Sun, K. Chaotification of Sine-series maps based on the internal perturbation model. *Results Phys.* **2021**, *31*, 105010. [CrossRef]
22. Lawnik, M.; Berezowski, M. New Chaotic System: M-Map and Its Application in Chaos-Based Cryptography. *Symmetry* **2022**, *14*, 895. [CrossRef]

23. Ablay, G. Chaotic map construction from common nonlinearities and microcontroller implementations. *Int. J. Bifurc. Chaos* **2016**, *26*, 1650121. [CrossRef]
24. Liu, L.; Wang, J. A cluster of 1D quadratic chaotic map and its applications in image encryption. *Math. Comput. Simul.* **2023**, *204*, 89–114. [CrossRef]
25. Akgul, A.; Kacar, S.; Pehlivan, I.; Aricioglu, B. Chaos-based encryption of multimedia data and design of security analysis interface as an educational tool. *Comput. Appl. Eng. Educ.* **2018**, *26*, 1336–1349. [CrossRef]
26. Abdallah, H.A.; Meshoul, S. A Multilayered Audio Signal Encryption Approach for Secure Voice Communication. *Electronics* **2023**, *12*, 2. [CrossRef]
27. Wang, X.; Xu, M.; Li, Y. Fast encryption scheme for 3D models based on chaos system. *Multimed. Tools Appl.* **2019**, *78*, 33865–33884. [CrossRef]
28. Gao, S.; Wu, R.; Wang, X.; Wang, J.; Li, Q.; Wang, C.; Tang, X. A 3D model encryption scheme based on a cascaded chaotic system. *Signal Process.* **2023**, *202*, 108745. [CrossRef]
29. Gao, X.; Miao, M.; Chen, X. Multi-image encryption algorithm for 2D and 3D images based on chaotic system. *Front. Phys.* **2022**, *10*, 498. [CrossRef]
30. Piegl, L.; Tiller, W. *The NURBS Book*; Springer Science & Business Media: Berlin/Heidelberg, Germany, 2012.
31. Deng, C.; Lin, H. Progressive and iterative approximation for least squares B-spline curve and surface fitting. *Comput.-Aided Des.* **2014**, *47*, 32–44. [CrossRef]
32. Hu, H.; Beck, J.; Lauer, M.; Stiller, C. Continuous Fusion of Motion Data Using an Axis-Angle Rotation Representation with Uniform B-spline. *Sensors* **2021**, *21*, 5004. [CrossRef]
33. Majeed, A.; Abbas, M.; Qayyum, F.; Miura, K.T.; Misro, M.Y.; Nazir, T. Geometric modeling using new Cubic trigonometric B-spline functions with shape parameter. *Mathematics* **2020**, *8*, 2102. [CrossRef]
34. Noreen, I. Collision free smooth path for mobile robots in cluttered environment using an economical clamped cubic B-spline. *Symmetry* **2020**, *12*, 1567. [CrossRef]
35. Marinić-Kragić, I.; Perišić, S.; Vučina, D.; Ćurković, M. Superimposed RBF and B-spline parametric surface for reverse engineering applications. *Integr.-Comput.-Aided Eng.* **2020**, *27*, 17–35. [CrossRef]
36. Zachariadis, O.; Teatini, A.; Satpute, N.; Gómez-Luna, J.; Mutlu, O.; Elle, O.J.; Olivares, J. Accelerating B-spline interpolation on GPUs: Application to medical image registration. *Comput. Methods Programs Biomed.* **2020**, *193*, 105431. [CrossRef] [PubMed]
37. Hua, Z.; Zhou, Y. Image encryption using 2D Logistic-adjusted-Sine map. *Inf. Sci.* **2016**, *339*, 237–253. [CrossRef]
38. Pareek, N.; Patidar, V.; Sud, K. Cryptography using multiple one-dimensional chaotic maps. *Commun. Nonlinear Sci. Numer. Simul.* **2005**, *10*, 715–723. [CrossRef]
39. Alzaidi, A.A.; Ahmad, M.; Doja, M.N.; Al Solami, E.; Beg, M.S. A New 1D Chaotic Map and β-Hill Climbing for Generating Substitution-Boxes. *IEEE Access* **2018**, *6*, 55405–55418. [CrossRef]
40. Moysis, L. *Introduction to Computer Aided Geometric Design—A Student's Companion with Matlab Examples*. 2019. Available online: https://www.researchgate.net/profile/Lazaros-Moysis/publication/329337381_Introduction_to_Computer_Aided_Geometric_Design_-_A_student's_companion_with_Matlab_examples_2nd_Edition/links/5c66dcfb4585156b57ffdffb/Introduction-to-Computer-Aided-Geometric-Design-A-students-companion-with-Matlab-examples-2nd-Edition.pdf (accessed on 30 January 2023).
41. Burkardt, J. Teapot, Teacup, Teaspoon Data Files. 2006. Available online: https://people.sc.fsu.edu/~jburkardt/data/bezier_surface/bezier_surface.html (accessed on 30 January 2023).

Disclaimer/Publisher's Note: The statements, opinions and data contained in all publications are solely those of the individual author(s) and contributor(s) and not of MDPI and/or the editor(s). MDPI and/or the editor(s) disclaim responsibility for any injury to people or property resulting from any ideas, methods, instructions or products referred to in the content.

symmetry

MDPI

Article

Towards a Holographic-Type Perspective in the Analysis of Complex-System Dynamics

Ștefana Agop [1], Dumitru Filipeanu [2], Claudiu-Gabriel Țigănaș [3], Claudia-Elena Grigoraș-Ichim [4], Lucia Moroșan-Dănilă [4], Alina Gavriluț [5,*], Maricel Agop [6,7] and Gavril Ștefan [1]

[1] Department of Agroeconomy, University of Life Sciences, 700490 Iasi, Romania; stefanaagop@yahoo.com (Ș.A.); stefang@uaiasi.ro (G.Ș.)
[2] Faculty of Civil Engineering and Buildings Services, Gheorghe Asachi Technical University, 700050 Iasi, Romania; dumitru.filipeanu@academic.tuiasi.ro
[3] Faculty of Economics and Business Administration, Alexandru Ioan Cuza University of Iasi, 700505 Iasi, Romania; claudiu.tiganas@uaic.ro
[4] Department of Accounting Audit and Financing, Stefan cel Mare University, 720229 Suceava, Romania; claudiag@seap.usv.ro (C.-E.G.-I.); lucia.danila@usm.ro (L.M.-D.)
[5] Department of Mathematics, "Al. I. Cuza" University of Iasi, 700506 Iasi, Romania
[6] Department of Physics, "Gh. Asachi" Technical University of Iasi, 700050 Iasi, Romania; m.agop@tuiasi.ro
[7] Romanian Scientists Academy, 54 Splaiul Independentei, 050094 Bucharest, Romania
* Correspondence: gavrilut@uaic.ro

Abstract: By operating with the Scale Relativity Theory by means of two scenarios (Schrödinger and Madelung-type scenarios) in the dynamics of complex systems, we can achieve a description of these complex systems through a holographic-type perspective. Then, a gauge invariance of the Riccati type becomes functional in complex-system dynamics, which implies several consequences: conservation laws (in particular, for dynamics, the kinetic momentum conservation law), simultaneity and synchronization among the structural units' (belonging to a complex system) dynamics, and temporal patterns through harmonic mappings. Finally, an economic case analysis is highlighted.

Keywords: Scale Relativity Theory; Schrödinger-type scenario; Madelung-type scenario; SL(2R) group; harmonic mappings; fractal; multi-fractal; Riccati-type gauge

1. Introduction

Determinism is not an indicator of regular (periodic motions, self-structures, etc.) or predictable behaviors in the dynamics of complex systems (for example, gene networks which interact through activation and inhibition, and a set of activated genes defines a tissue; the dynamics of a cell is made up of proteins which are in chemical reactions, and its evolution allows an adaptation to the environment; the brain is a collection of neurons that transmit electrical and chemical impulses to each other; the stock market implies brokers making trades that create global phenomena such as bubbles or crashes; a company is a set of people and organizations that interact with each other and which also interacts with its environment through stakeholders, etc.) [1,2]. In linear analysis, on which a complex system relies almost exclusively, unbounded predictability has been an intrinsic characteristic of complex-system dynamics. The evolution of non-linear analysis and the explaining of the laws governing chaos have shown that the reductionist method of analysis, which is applicable to complex systems, has been hitherto restricted, but its applicability has also been restricted. Unrestricted predictability is not a feature of complex systems; rather, it is a fundamental effect of their reduction by the linear approach. Only a handful of such behaviors—where non-linearity and chaos emphasize regular behaviors (superstructure, flammability, etc.), specifically, a generality in the laws dictating the dynamics of complex systems [3,4]—can be found.

The behaviors of complex systems are determined by the conditions in which they function and the restrictions to which they are subjected. The non-linearity and chaoticity of any complex system are determined by the interactions between its structural units. In such a situation, the generality of the dynamic laws of complex systems becomes functional and must be found in the employed mathematical procedures. There are authors who progressively discuss the holographic implementation involved in the description of complex-system dynamics (fractal/multifractal paradigm of nature) [5–9].

On the other hand, the standard physical models applied in the characterization of the dynamics of complex systems are founded on an otherwise unbased hypothesis of the differentiability of the physical quantities utilized to explain their evolution. Then, the positive outcome of these models must be understood progressively [5]. Differentiable and integrable mathematical procedures fail when they are intended to illustrate the dynamics of complex systems involving only non-linearity and chaoticity. For the purpose of describing the dynamics of these systems, it is required to expressly introduce the scale resolution concept in the physical variables and, moreover, into the fundamental equations of these dynamics [7–9].

It can be inferred that any physical variable, dependent on the usual mathematical procedures on space–time co-ordinates, will also depend on a scale resolution. As a consequence, any physical variable used to characterize the dynamics of complex systems will function as the limit of a family of mathematical functions, the function being non-differentiable for a zero-scale resolution and differentiable for a non-zero-scale resolution [7–9].

Therefore, there is a need for the evolution of both new geometric structures and physical theories, for which the laws of motion, invariant to time co-ordinate transformations, are also invariant to transformations with respect to the scale resolution. In our opinion, such an approach can be one based on the concept of the fractal/multifractal and the corresponding physical model depicted in the Scale Relativity Theory (SRT) [7–9]. From this perspective, the holographic implementation in the portrayal of complex-system dynamics will be made explicit based on the depiction of the dynamics of the structural units of any complex-system fractal/multifractal curves.

Some consequences are evident:

(i) Motions with constraints on the continuous and differentiable curves in a Euclidean space are replaced by free motions on the fractal/multifractal curves in a fractal/multifractal space;
(ii) Motion curves act both as the geodesics of a fractal/multifractal space and as the flow lines of a fractal/multifractal fluid;
(iii) The structural units of any complex system are replaced by their own geodesics, any external constraint being rendered as a choice of geodesics on the basis of local–global/whole–part compatibility, etc.;
(iv) For large time scales, relative to the inverse of the largest value of the Lyapunov exponent, deterministic trajectories can be substituted by families of potential trajectories, so that the concept of position will be replaced by that of probability density [3,4];
(v) Taking into account that the portrayal of complex-system dynamics is given by fractal/multifractal curves and that these curves have the self-similarity property, the "holographic" description of the complex-system dynamics become functional.

Then, two scenarios in the portrayal of complex-system dynamics become operational: one scenario is explained through the multifractal Schrödinger equation (Schrödinger-type scenario) and another through the multifractal hydrodynamic equation system (Madelung-type scenario). The two scenarios for describing complex-system dynamics are not mutually exclusive; moreover, they are complementary. For more details regarding the various mathematical procedures in complex-system descriptions, see [10–16].

Taking into account the fact that, in any of the scenarios, the symmetries are highlighted, in the current paper, several symmetries will be explained and their consequences will be discussed.

2. Gauge Invariances of the Riccati Type and Conservation Laws in Complex-System Dynamics

It is well-known that the dynamics of complex systems in the SRT [7–9] can be described through a Schrödinger-type scenario explained through the differential equation (multifractal Schrödinger equation)

$$\lambda^2 (dt)^{[\frac{4}{f(\alpha)}]-2} \partial_l \partial^l \Psi + i\lambda (dt)^{[\frac{2}{f(\alpha)}]-1} \partial_t \Psi = 0, \tag{1}$$

where

$$\partial_t = \frac{\partial}{\partial t},\ \partial_l = \frac{\partial}{\partial x^l}\ ,\ \partial_l \partial^l = \frac{\partial^2}{\partial x_l^2} \tag{2}$$

In the above relations:

- Ψ is the states function;
- dt is the scale resolution;
- x^l is the multifractal spatial co-ordinate;
- t is the non-multifractal temporal co-ordinate with the role of an affine parameter;
- λ is a parameter associated with the fractal/multifractal-non-fractal/non-multifractal scale transition;
- $f(\alpha)$ is the singularity spectrum with a singularity index of order $\alpha = \alpha(D_F)$;
- D_F is the fractal dimension of the motion curves [3,4,6].

There are many modes of the definition of fractal dimensions: the Kolmogorov fractal dimension, the Hausdorff–Besikovitch fractal dimension, etc. [3,4,6]. It is noted that, by selecting one of these definitions and operating with it, the fractal dimension must be constant and arbitrary for the entirety of the dynamical analysis. Moreover, operating with $f(\alpha)$, the following possibilities emerge in the complex-system dynamics:

- It is possible to identify the "areas" of the complex-system dynamics that are characterized by a certain fractal dimension (monofractal complex-system dynamics);
- It is possible to identify the number of "areas" whose fractal dimensions are situated within an interval of values (multifractal complex-system dynamics);
- It is possible to identify the classes of universality in the complex-system dynamic laws, even when the regular or strange attractors have different aspects.

In such a context, through a convenient choice of the singularity spectrum $f(\alpha)$, concerted with the scale resolution, various functional dynamics regimes can be highlighted—period-doubling regimes, damping-oscillation regimes, intermittence regimes, and quasi-periodicity regimes, as we will show in the following (in particular, a specific pattern will be given).

The multifractal Schrödinger equation admits, by an extension of [10], an extra set of symmetries, such as a SL(2,R)-type group [11]. A general discussion on the SL(2,R)-type groups and their implications in quantum mechanics and general relativity can be found in [3,4,10]. It is mentioned that, in the standard Schrödinger equation, special symmetries and their implications are given in [12–14].

For what follows, it is necessary to construct the finite equations of the specific SL(2,R) group, according to [15,16]. Operating with the variables (t, r) as above, the finite equations are given by:

$$t \to \frac{\alpha t + \beta}{\gamma t + \delta};\ r \to \frac{r}{\gamma t + \delta} \tag{3}$$

Then, the infinitesimal generators are given by:

$$X_1 = \frac{\partial}{\partial t},\ \ X_2 = t\frac{\partial}{\partial t} + \frac{r}{2}\frac{\partial}{\partial r},\ \ X_3 = t^2\frac{\partial}{\partial t} + tr\frac{\partial}{\partial r} \tag{4}$$

and satisfy the structural equations:

$$[X_1, X_2] = X_1, \ \ [X_2, X_3] = X_3, \ \ [X_3, X_1] = -2X_2 \tag{5}$$

The group possesses an invariant function, extracted as the solution of a partial differential equation:

$$\begin{gathered}(cX_1 + 2bX_2 + aX_3)f(t,r) = 0 \\ \left(at^2 + 2bt + c\right)\frac{\partial f}{\partial t} + (at + b)r\frac{\partial f}{\partial r} = 0\end{gathered} \tag{6}$$

The general solution of this equation is

$$\frac{r^2}{at^2 + 2bt + c} \tag{7}$$

The ratio found in relation (7) is constant and, moreover, it depicts the various paths of transitivity of the action given by (4).

We must notice that the content of time in Equation (3) is not classical anymore, at least not in general, being a ratio of co-ordinates representing two uniform motions. The second Equation (3) can be taken as representing the content of a spatial co-ordinate of the motion in terms of the classical co-ordinate of the uniform motion. For more details, see [10,15,16].

On the other hand, by choosing Ψ of the form (the Madelung's choosing)

$$\Psi = \sqrt{\rho}e^{is} \tag{8}$$

where $\sqrt{\rho}$ is the amplitude and s is the phase, and introducing the real velocity fields (V_D^i—differentiable velocity field, V_F^i—non-differentiable velocity field):

$$V_D^i = 2\lambda(dt)^{[\frac{2}{f(\alpha)}]-1}\partial^i s \tag{9}$$

$$V_F^i = i\lambda(dt)^{[\frac{2}{f(\alpha)}]-1}\partial^i \ln\rho \tag{10}$$

The multifractal Schrödinger equation is reduced to the multifractal hydrodynamic equation system:

$$\partial_t V_D^i + V_D^l \partial_l V_D^i = -\partial^i Q \tag{11}$$

$$\partial_t \rho + \partial_l\left(\rho V_D^l\right) = 0 \tag{12}$$

with Q as the multifractal-specific potential:

$$Q = -2\lambda^2(dt)^{[\frac{4}{f(\alpha)}]-2}\frac{\partial^l\partial_l\sqrt{\rho}}{\sqrt{\rho}} = -V_F^i V_F^i - \frac{1}{2}\lambda(dt)^{[\frac{2}{f(\alpha)}]-1}\partial_l V_F^l \tag{13}$$

Equation (11) defines the multifractal-specific momentum conservation law, while Equation (12) defines the multifractal-state density conservation law. The multifractal-specific potential (13) induces the multifractal-specific force:

$$F^i = -\partial^i Q = -2\lambda^2(dt)^{[\frac{4}{f(\alpha)}]-2}\partial^i\frac{\partial^l\partial_l\sqrt{\rho}}{\sqrt{\rho}} \tag{14}$$

Relation (14) is a measure of the multifractality of the motion curves of the dynamics.

The main conclusions which result from Equations (11)–(13) are given in [8,9]. Now, using the tensor:

$$\hat{\tau}^{il} = 2\lambda^2(dt)^{[\frac{4}{f(\alpha)}]-2}\rho\partial^i\partial^l \ln\rho \tag{15}$$

Equation (14) takes the form:

$$\rho\partial^i Q = \partial_l\hat{\tau}^{il} \tag{16}$$

Moreover, since the tensor $\hat{\tau}^{il}$ can also be expressed as:

$$\hat{\tau}^{il} = \eta\left(\partial_l V_F^i + \partial_i V_F^l\right) \tag{17}$$

with

$$\eta = \lambda(dt)^{\left[\frac{2}{f(\alpha)}\right]-1}\rho \tag{18}$$

In these conditions, a multifractal linear constitutive equation for a multifractal "viscous fluid" becomes functional, offering, at the same time, the reason for an original interpretation of the coefficient η as a multifractal dynamic viscosity of the multifractal fluid.

In order to have a better grasp of these mathematical facts, it is necessary to return to the transformation (3) and approach it from the point of view of multifractal physics.

Firstly, let us observe that the multifractal-specific force (14) is defined with the help of a gradient. As an immediate consequence, if 'r' denotes the distance of the moving complex-system structural unit from the center of the multifractal-specific force, then

$$r^2 d\theta = \dot{a}dt \qquad \dot{a}\frac{dt}{d\theta} = r^2 \qquad \dot{a} = const. \tag{19}$$

where θ is the central angle of the position vector of the moving complex-system structural unit with respect to the center of the multifractal-specific force and $\dot{a}$ is the constant of the multifractal kinetic moment.

Now, since according to (7),

$$\frac{r^2}{at^2 + 2bt + c} = L = const.\,, \tag{20}$$

Then, from (20) and (19), through the substitutions

$$\frac{dt}{d\theta} = \dot{w}, \;\; \frac{Lat^2}{\dot{a}} = \frac{1}{M}w^2, \;\; \frac{2Lbt}{\dot{a}} = -2\frac{R}{M}w, \;\; \frac{Lc}{\dot{a}} = K \tag{21}$$

the following Riccati-type differential equation is satisfied (i.e., we operate here with a Riccati-type gauge):

$$\dot{w} - \frac{1}{M}w^2 + 2\frac{R}{M}w - K = 0. \tag{22}$$

For obviously physical reasons, it is necessary to seek out the most general solution of that equation. José Carineña et al. offer us a pass in a short but modern and pertinent review of the integrability of Riccati's equation [17]. For the current needs, it should be noted that the complex numbers

$$w_0 \equiv R + iM\Omega, \;\; w_0^* \equiv R - iM\Omega; \; \Omega^2 = \frac{K}{M} - \left(\frac{R}{M}\right)^2 \tag{23}$$

The roots of the quadratic polynomial on the right side of Equation (22) are the two solutions (constants) of the equation: being constants, their derivative is zero; being roots of the right-hand polynomial, they cancel. Therefore, first, we perform the homographic transformation:

$$z = \frac{w - w_0}{w - w_0^*} \tag{24}$$

and now it can easily be seen by a direct calculation that z is a solution of the linear and homogeneous equation of the first order:

$$\dot{z} = 2i\Omega z \therefore z(t) = z(0)e^{2i\Omega t} \tag{25}$$

Therefore, if we conveniently express the initial condition $z(0)$, we can give the general solution of Equation (22) by simply inverting the transformation (24), with the result

$$w = \frac{w_0 + re^{2i\Omega(t-t_r)}w_0^*}{1 + re^{2i\Omega(t-t_r)}} \tag{26}$$

where r and t_r are the two real constants that characterize the solution. Using Equation (23), we can put this solution in real terms, i.e.,

$$\begin{array}{rl} z = & R + M\Omega\Big(\frac{2r\sin[2\Omega(t-t_r)]}{1+r^2+2r\cos[2\Omega(t-t_r)]} \\ & +i\frac{1-r^2}{1+r^2+2r\cos[2\Omega(t-t_r)]}\Big) \end{array} \tag{27}$$

which highlights a frequency modulation through what we would call a Stoler transformation [15,16] which leads us to a complex form of this parameter. More than that, if we make the notation

$$r \equiv \cot \mathrm{h}\tau, \tag{28}$$

Equation (27) becomes

$$z = R + M\Omega h \tag{29}$$

where h is given by

$$h = -i\frac{\cos \mathrm{h}\tau - e^{-2i\Omega(t-t_m)}\sin \mathrm{h}\tau}{\cos \mathrm{h}\tau + e^{-2i\Omega(t-t_m)}\sin \mathrm{h}\tau}. \tag{30}$$

The meaning of this complex parameter will be clear a little later. For the moment, let us note that any dynamic process appears here as a frequency-modulation process by means of a gauge invariance of the Riccati type, imposed through the multifractal kinetic momentum conservation law.

3. Gauge Invariances of the Riccati Type and Simultaneity in Complex-System Dynamics

Consider a complex system revolving in the multifractal-specific force. It can be viewed as a swarm of structural units, such as a swarm highlighting multifractal laws (for a classical case, see [18]), as long as it is viewed as a swarm of free structural units. In the first part of Equation (3), this means that the structural units are considered simultaneously. Then, each structural unit can be identified in the swarm by α, β, γ, δ, or by three non-homogeneous co-ordinates, according to [9]. The simultaneity in the motion of the swarm of structural units can be differentially characterized, giving a Riccati-type equation:

$$d\frac{\alpha t + \beta}{\gamma t + \delta} = 0, \;\; dt = \omega^1 t^2 + \omega^2 t + \omega^3 \tag{31}$$

Thus, it is sufficient to define a coframe of the SL(2R) algebra:

$$\omega^1 = \frac{\alpha d\gamma - \gamma d\alpha}{\alpha\delta - \beta\gamma};\; \omega^2 = \frac{\alpha d\delta - \delta d\alpha + \beta d\gamma - \gamma d\beta}{\alpha\delta - \beta\gamma};\; \omega^3 = \frac{\beta d\delta - \delta d\beta}{\alpha\delta - \beta\gamma} \tag{32}$$

Such an algebra can be verified through the Maurer–Cartan equations:

$$\begin{array}{c} d \wedge \omega^1 - \omega^1 \wedge \omega^2 = 0 \\ d \wedge \omega^2 + 2\big(\omega^3 \wedge \omega^1\big) = 0 \\ d \wedge \omega^3 - \omega^2 \wedge \omega^3 = 0 \end{array} \tag{33}$$

which describe the coframe.

According to [19], the right member of (31) is an integral. The Cartan–Killing metric of this coframe is given by the quadratic form $(\omega^2/2)^2 - \omega^1\omega^3$, which defines a Riemannian three-dimensional space. The geodesics of such a space are:

$$\omega^1 = a^1(d\theta);\ \omega^2 = 2a^2(d\theta);\ \omega^3 = a^3(d\theta) \tag{34}$$

where $a^{1,2,3}$ are constants and θ is the affine parameter of the geodesics. Taking into account the geodesics, (31) is an ordinary differential equation of the Riccati type:

$$\frac{dt}{d\theta} = a^1 t^2 + 2a^2 t + a^3 \tag{35}$$

This equation can be identified with (19). Mathematically, this requires an ensemble generated by a harmonic mapping between the positions in space and the structural units. Following the same line of thought previously presented, a solution of the same type as (30) can be highlighted.

4. Gauge Invariances of the Riccati Type and Synchronizations in Complex-System Dynamics

According to the meanings of the state function Ψ from the SRT, a physical significance is only attached to the density of the state $\rho = \Psi\,\overline{\Psi}$. In such a context, if $\Psi = a + ib$, then the constant density of states can be localized inside the unity radius circle

$$x^2 + y^2 = 1 \tag{36}$$

where

$$\frac{a^2}{\rho} = x^2,\ \frac{b^2}{\rho} = y^2 \tag{37}$$

Now, the Lobachevsky plane metric can be generated as a Caylean metric of a Euclidean plane, for which the absoluteness is the circle (36). In such a context, by following the method described in [15,16], the following is obtained:

$$-\frac{ds^2}{k^2} = \frac{\Omega(dX, dX)}{\Omega(X, X)} - \frac{\Omega^2(X, dX)}{\Omega^2(X, X)}, \tag{38}$$

In the above relation, $\Omega(X, Y)$ is the duplication of $\Omega(X, X)$ and k is a constant connected to the space curvature. Therefore:

$$\frac{ds^2}{k^2} = \frac{(1-y^2)dx^2 + 2xydxdy + (1-x^2)dy^2}{(1-x^2-y^2)^2}, \tag{39}$$

where

$$\begin{aligned} \Omega(X, X) &= 1 - x^2 - y^2 \\ \Omega(X, dX) &= -xdx - ydy \\ \Omega(dX, dX) &= -dx^2 - dy^2 \end{aligned} \tag{40}$$

Now, by means of substitutions:

$$x = \frac{h\overline{h} - 1}{h\overline{h} + 1}, \qquad y = \frac{h + \overline{h}}{h\overline{h} + 1} \tag{41}$$

with

$$h = u + iv, \qquad \overline{h} = u - iv \tag{42}$$

The metric (39) takes the form of a Poincaré metric of the superior complex plane:

$$\frac{ds^2}{k^2} = 4\frac{dhd\overline{h}}{\left(h-\overline{h}\right)^2} = \frac{du^2+dv^2}{v^2}, \tag{43}$$

The metric (43) induces the simply transitive group in the quantities h and $\overline{h}$, whose actions are:

$$\begin{array}{c} h \leftrightarrow \frac{ah+b}{ch+d}, \\ \overline{h} \leftrightarrow \frac{a\overline{h}+b}{c\overline{h}+d}, \end{array} \tag{44}$$

The structure of this group is typical of SL(2R), i.e.,

$$\begin{array}{c} \left[B^1, B^2\right] = B^1, \\ \left[B^2, B^3\right] = B^3, \\ \left[B^3, B^1\right] = -2B^2 \end{array} \tag{45}$$

where B^l are the infinitesimal generators of the group:

$$\begin{array}{c} B^1 = \frac{\partial}{\partial h} + \frac{\partial}{\partial \overline{h}} \\ B^2 = h\frac{\partial}{\partial h} + \overline{h}\frac{\partial}{\partial \overline{h}} \\ B^3 = h^2\frac{\partial}{\partial h} + \overline{h}^2\frac{\partial}{\partial \overline{h}} \end{array} \tag{46}$$

and admits the two-form (43).

Since (43) is invariant with respect to the group $SL(2R)$ [9,15,16], this group can be assimilated with a "synchronization" group between the different structural units of the complex system.

5. Harmonic Mappings and Working Regimes in Complex-System Dynamics

In what follows, complex-system dynamics will be generated through harmonic mappings. Let it be assumed that the complex-system dynamics can be depicted through the variables $\left(Y^j\right)$ for which the multifractal metric below applies:

$$h_{ij}dY^i dY^j \tag{47}$$

In a usual space of the multifractal metric:

$$\gamma_{\alpha\beta}dX^\alpha dX^\beta \tag{48}$$

In these conditions, the field equations are generated by the multifractal Lagrangian:

$$L = \gamma^{\alpha\beta}h_{ij}\frac{dY^i dY^j}{\partial X^\alpha \partial X^\beta} \tag{49}$$

In the present case, (47) is defined through (43). Therefore, if the variational principle

$$\delta \int L\sqrt{\gamma}d^3x = 0 \tag{50}$$

holds true for $\gamma = \left|\gamma_{\alpha\beta}\right|$, then the multifractal Euler equations corresponding to the variational principle (45) become:

$$\begin{array}{c} \left(h-\overline{h}\right)\nabla(\nabla h) = 2(\nabla h)^2 \\ \left(h-\overline{h}\right)\nabla\left(\nabla\overline{h}\right) = 2\left(\nabla\overline{h}\right)^2 \end{array} \tag{51}$$

with the solution:

$$h = \frac{\cosh(\Phi/2) - \sinh(\Phi/2)e^{-i\alpha}}{\cosh(\Phi/2) + \sinh(\Phi/2)e^{-i\alpha}},\ \alpha \in \mathbb{R} \tag{52}$$

In the above relation, α is real and arbitrary, as long as $(\Phi/2)$ is the solution of a multifractal Laplace equation for the free space, such that

$$\nabla^2(\Phi/2) = 0 \tag{53}$$

It should be noted that, up to the factor $(-i)$, (30) can be identified with (52) through the identifications

$$\Phi/2 \equiv \tau,\ \alpha = -2i\Omega(t - t_m)$$

Now, the significance of this complex parameter must be linked to the harmonic mappings between the Euclidean space (i.e., measurement space) and the hyperbolic space (i.e., phase space, in which the "self-structuring" manifests). In Figure 1a–h, the natural transition of the complex-system dynamics is to progress from the normal period-doubling state towards the damped oscillating and a strong modulated dynamics. The complex-system dynamics never reach a chaotic state but they permanently evolve towards that state.

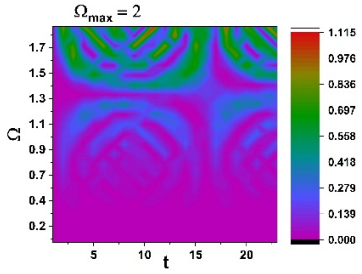

(**a**) contour plot—period-doubling regimes

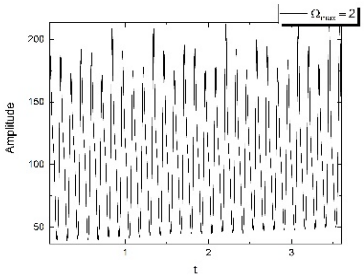

(**b**) time series—period-doubling regimes

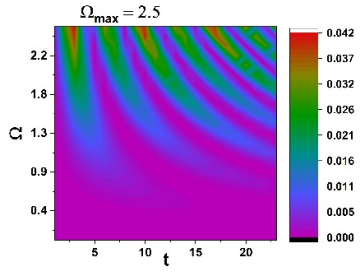

(**c**) contour plot—damping-oscillation regimes

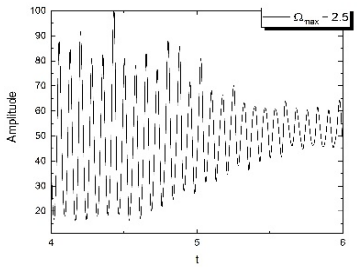

(**d**) time series—damping-oscillation regimes

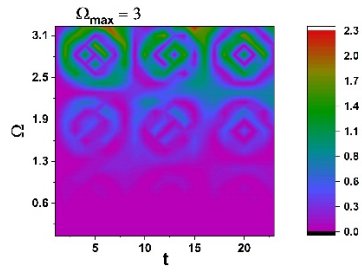

(**e**) contour plot—quasi-periodicity regimes

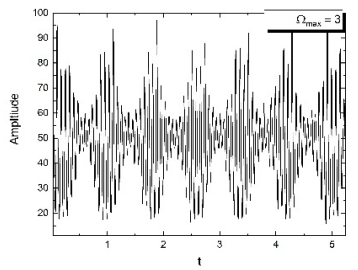

(**f**) time series—quasi-periodicity regimes

Figure 1. *Cont.*

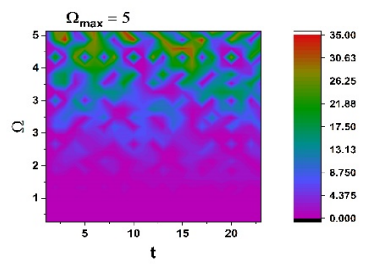

(**g**) contour plot—intermittence regimes

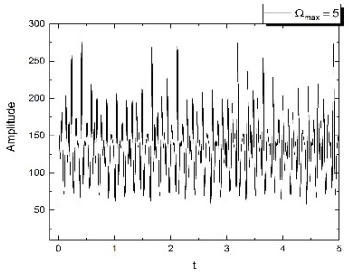

(**h**) time series—intermittence regimes

Figure 1. (**a**–**h**)—Various work regimes of complex-system dynamics (contour plot and time series) as a function of scale resolution chosen by Ω_{max}: period-doubling regimes for $\Omega_{max} = 2$ (**a**,**b**); damping-oscillation regimes for $\Omega_{max} = 2.5$ (**c**,**d**); quasi-periodicity regimes for $\Omega_{max} = 3$ (**e**,**f**); and intermittence regimes for $\Omega_{max} = 5$ (**g**,**h**).

A periodicity can be identified, regarding the entire series of transitions. The evolution of the complex systems sees a "jump" into a period-doubling oscillation state and the transition resumes towards a quasi-chaotic state.

We present in Figure 2 a specific pattern (reconstituted attractor) for the period-doubling regimen.

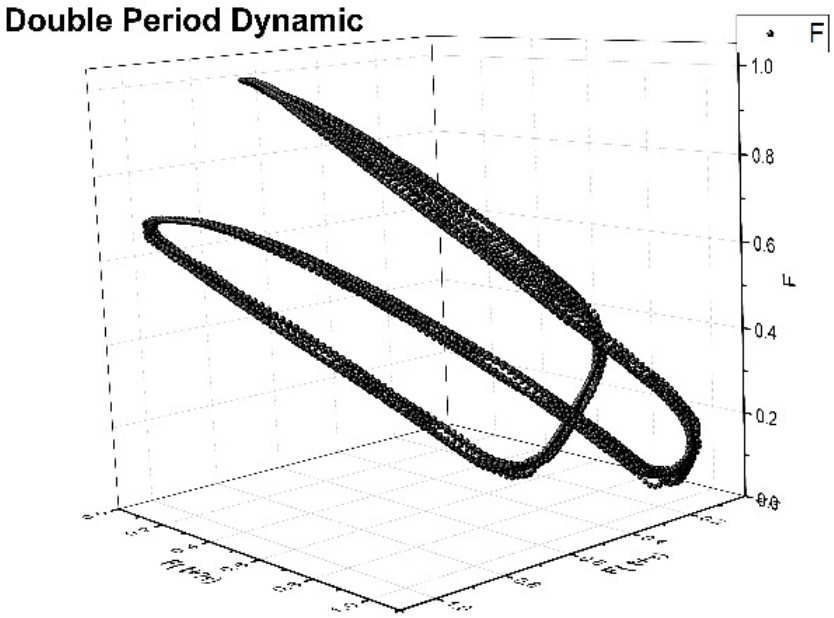

Figure 2. A specific pattern (reconstituted attractor) for the period-doubling regimen.

The bifurcation map is presented in Figure 3 where it is observed that the complex-system dynamics start from a steady state (period-doubling regimes) and evolve towards a chaotic one ($\Omega_{max} = 2, 2.5, 3, 5$), but they never reach that state. We note that such work regimes are manifested both in biological and biocompatible material structures (period-doubling regimes [20–23], damping-oscillation regimes [24–27], quasi-periodicity regimes [28,29], and intermittence regimes [30–32]).

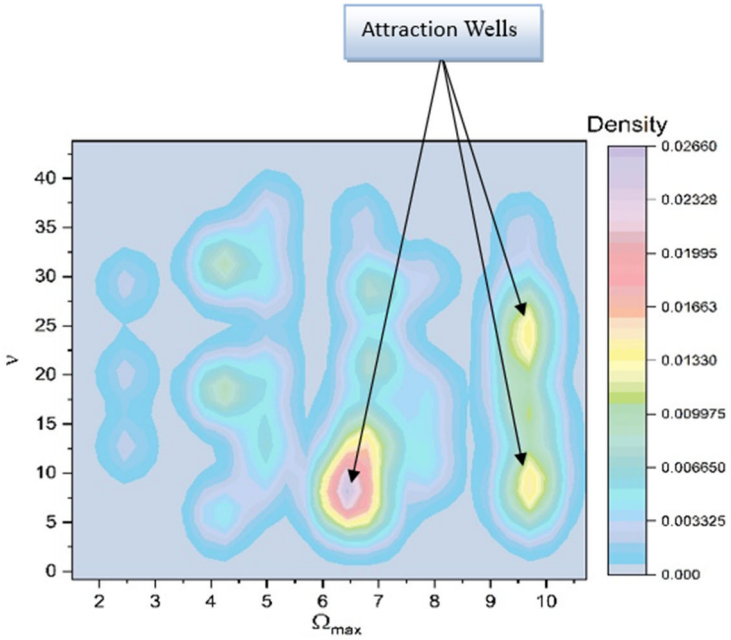

Figure 3. Bifurcation map by means of oscillation frequency of the complex-system dynamics as a function of scale resolution chosen by Ω_{max}.

6. An Economic Case Analysis

Initially applied in the consumer goods market, the fractal/multi-fractal theory has encompassed other economics domains such as: price changes in the open market, the distribution of income of the companies and the scaling relation of thet company's size fluctuations [33,34].

The financial markets, through their inherently speculative character, can constitute a trans- and interdisciplinary domain. The globalization of financial markets and the application of new informational technologies emphasize the complexity degree of these markets.

The 2008 economic crisis has challenged the mainstream economic theory. In such a context, speculative bubbles, an increasing phenomenon encountered in these markets, are the result of the individual reaction to market signals through the price at that particular moment (an aspect which can be assimilated into the digital signals) in the context of an optimistic state induced by the behaviors of large investors and of the State through banking or monetary policies (analogical signals) [35,36]. The results of contemporary empirical studies prove that the market dynamics and the evolution of economic indicators are not a random phenomenon.

The markets have a fractal/multi-fractal structure in the long term, being characterized by a self-memory. In such a context, the individual reaction to the market signal can be associated with period doubling, damping oscillations, quasi-periodicity, and intermittences (i.e., to the digital signals), while the behaviors of large investors and of the State through banking or monetary policies can be associated with the "world finite effect" [6] (i.e., analogical signals). The economical structures emphasize the fluctuations but they never reach the chaos state (see Figure 2).

7. Conclusions

In the Schrödinger-type and Madelung-type scenarios for the description of complex-system dynamics, the SL(2R) symmetries are highlighted. The existence of such symmetries has several consequences for the aforementioned dynamics: conservation laws as gauge invariances of the Riccati type (in particular, for SRT dynamics, the kinetic momentum conservation law); simultaneity as gauge invariances of the Riccati type; synchronization as gauge invariances of the Riccati type; and working regimes through harmonic mappings.

Moreover, the existence of such symmetries implies, through a Poincaré-type metric of the hyperbolic space, that holography can be associated with deep learning.

Author Contributions: Conceptualization, M.A., Ș.A. and A.G.; methodology, D.F., Ș.A. and A.G.; validation, G.Ș.; writing—original draft preparation, M.A., Ș.A. and A.G.; writing—review and editing, M.A., Ș.A. and A.G.; visualization, C.-G.Ț., C.-E.G.-I. and L.M.-D. All authors have read and agreed to the published version of the manuscript.

Funding: This research received no external funding.

Data Availability Statement: Not applicable.

Conflicts of Interest: The authors declare no conflict of interest.

References

1. Mitchell, M. *Complexity: A Guided Tour*; Oxford University Press: Oxford, UK, 2009.
2. Badii, R. *Complexity: Hierarchial Structures and Scaling in Physics*; Cambridge University Press: Cambridge, UK, 1997.
3. Jackson, E.A. *Perspectives of Nonlinear Dynamics*; Cambridge University Press: New York, NY, USA, 1993; Volumes 1–2.
4. Cristescu, C.P. *Nonlinear Dynamics and Chaos. Theoretical Fundaments and Applications*; Romanian Academy Publishing House: Bucharest, Romania, 2008.
5. Bar-Yam, Y. *Dynamics of Complex Systems*; The Advanced Book Program; Addison-Wesley: Reading, MA, USA, 1997.
6. Mandelbrot, B.B. *The Fractal Geometry of Nature*; W.H. Freeman and Co.: San Francisco, CA, USA, 1982.
7. Nottale, L. *Scale Relativity and Fractal Space-Time: A New Approach to Unifying Relativity and Quantum Mechanics*; Imperial College Press: London, UK, 2011.
8. Merches, I.; Agop, M. *Differentiability and Fractality in Dynamics of Physical Systems*; World Scientific: Hackensack, NJ, USA, 2016.
9. Agop, M.; Paun, V.-P. *On the New Perspectives of Fractal Theory. Fundaments and Applications*; Romanian Academy Publishing House: Bucharest, Romania, 2017.
10. Niederer, U. The Maximal Kinematical Invariance Group of the Free Schrödinger Equation. *Helv. Phys. Acta* **1972**, *45*, 802–810.
11. de Alfaro, V.; Fubini, S.; Furlan, G. Conformal Invariance in Quantum Mechanics. *Il Nuovo Cim. A* **1976**, *34*, 569–611. [CrossRef]
12. Herrero, A.; Morales, J.A. Radial Conformal Motions in Minkowski Space-Time. *J. Math. Phys.* **1999**, *40*, 3499–3508. [CrossRef]
13. Herrero, A.; Morales, J.A. Painlevé-Gullstrand Synchronizations in Spherical Symmetry. *Class. Quantum Gravity* **2010**, *27*, 175007. [CrossRef]
14. Bianchi, L. On Three-Dimensional Spaces Which Admit a Continuous Group of Motions. *Gen. Relativ. Gravit.* **2001**, *33*, 2171–2253. [CrossRef]
15. Mazilu, N.; Agop, M. *At the Crossroads of Theories. Between Newton and Einstein—The Barbilian Universe (in Romanian)*; ArsLonga Publishing House: Iasi, Romania, 2010.
16. Mazilu, N.; Agop, M. *Skyrmions: A Great Finishing Touch to Classical Newtonian Philosophy*; World Philosophy Series; Nova: New York, NY, USA, 2012.
17. Carinena, J.F.; Clemente-Gallardo, J.; Marmo, G. Reduction Procedures in Classical and Quantum Mechanics. *Int. J. Geom. Methods Mod. Phys.* **2007**, *4*, 1363–1403. [CrossRef]
18. Larmor, J.W. On the Statistical Dynamics of Gas Theory as Illustrated by Meteor Swarms and Optical Rays. *Nature* **1900**, *63*, 168–169.
19. Cartan, E. *La Theorie des Groupes Finis et Continus et la Geometrie Differentielle Traitees par la Methode du Repere Mobile*; GauthierVillars: Paris, France, 1951.
20. Cimpoeşu, N.; Stanciu, S.; Tesloianu, D.; Cimpoeşu, R.; Popa, R.F.; Moraru, E. A study of the damping capacity of mechanically processed cu–9.2 Al–5.3 Mn–0.6 Fe shape memory alloys. *Met. Sci. Heat Treat.* **2017**, *58*, 729–733. [CrossRef]
21. Iovan, G.; Stoleriu, S.; Pancu, G.; Nica, I.; Sandu, A.V.; Andrian, S.; Tanculescu, O. Effect of finishing techniques on the junction between the composite restoration and the dental enamel. *Mater. Plast.* **2017**, *54*, 375–379. [CrossRef]
22. Nica, I.; Cimpoesu, N.; Rusu, V.; Andronache, M.; Stefanescu, C. Structural properties of nanofilled and microfillled restorative composites. *Mater. Plast.* **2012**, *49*, 176–180.
23. Tărăboanță, I.; Stoleriu, S.; Nica, I.; Georgescu, A.; Gamen, A.G.; Maftei, G.A.; Andrian, S. Roughness variation of a nannohbrid composite resin submitted to acid and abrasive challenges. *Int. J. Med. Dent.* **2020**, *24*, 182–187.
24. Iovan, G.; Stoleriu, S.; Nica, I.; Solomon, S.; Munteanu, A.; Andrian, S. Surface characteristics of restorative composite resins after polishing with Profine Lamineer tips. *Mater. Plast.* **2016**, *53*, 755–758.
25. Tofan, N.; Andrian, S.; Nica, I.; Stoleriu, S.; Topoliceanu, C.; Chelariu, R.; Bolat, M.; Pancu, G. The assessment of erosive potential of some acid beverages on indirect-restorative materials. *Rev. Chim.* **2016**, *67*, 1144–1149.
26. Pancu, G.; Iovan, G.; Ghiorghe, A.; Topoliceanu, C.; Nica, I.; Tofan, N.; Stoleriu, S.; Sandu, A.V.; Andrian, S. The assessment of biological parameters and remineralisation potential of saliva in pregnancy. *Rev. Chim.* **2015**, *66*, 2051–2056.
27. Stoleriu, S.; Iovan, G.; Pancu, G.; Nica, I.; Andrian, S. Study concerning the influence of the finishing and polishing systems on the surface state of various types of composite resins. *Rom. J. Oral Rehabilit.* **2013**, *5*, 78–83.

28. Nica, I.; Rusu, V.; Paun, M.A.; Stefanescu, C.; Vizureanu, P.; Aluculesei, A. Thermal properties of nanofilled and microfilled restorative composites. *Mater. Plast.* **2009**, *46*, 431–434.
29. Balmus, I.M.; Ciobica, A.; Cojocariu, R.; Luca, A.C.; Gorgan, L. Irritable Bowel Syndrome and Neurological Deficiencies: Is There A Relationship? The Possible Relevance of the Oxidative Stress Status. *Medicina* **2020**, *56*, 175. [CrossRef]
30. Morariu, S.I.; Duceac, L.D.; Luca, A.C.; Popescu, F.; Pavel, L.; Gavrilescu, C.M. Soil Chemical Pollution and Aggressive Pathologies. *Rev. Chim.* **2018**, *69*, 2278–2282. [CrossRef]
31. Duceac, L.D.; Stafie, L.; Valeanu, I.P.; Mitrea, G.; Baciu, G.; Banu, E.A.; Romila, L.; Luca, A.C. Sepsis in paediatrics—A special form of infection associated to medical assistance. *Int. J. Med. Dent.* **2018**, *22*, 229–235.
32. Luca, F.A.; Ioan, C.A.; Sasu, C.; Luca, A.C. The Impact of Public Health Care Services on the Patients' Perception as Regards the Health Institutions Brand on the Background of the Health Reform in Romania. *Rev. De Cercet. Si Interv. Soc.* **2015**, *49*, 80–97.
33. Battiston, S.; Farmer, J.D.; Flache, A.; Garlaschelli, D.; Haldane, A.G.; Heesterbeek, H.; Hommes, C.; Jaeger, C.; May, R.; Scheffer, M. Complexity Theory and Financial Regulation. *Science* **2016**, *351*, 818–819. [CrossRef] [PubMed]
34. Takayasu, H. *Empirical Science of Financial Fluctuations–The Advent of Econophysics*; Springer: Tokyo, Japan, 2002.
35. Takayasu, H. *Application of Econophysics*; Springer: Tokyo, Japan, 2003.
36. Sviridov, O.Y.; Nekrasova, I.V. Fractal analysis of financial markets. *Международный научно-Исследовательскийжурна* **2016**, *10*, 74–80. [CrossRef]

Disclaimer/Publisher's Note: The statements, opinions and data contained in all publications are solely those of the individual author(s) and contributor(s) and not of MDPI and/or the editor(s). MDPI and/or the editor(s) disclaim responsibility for any injury to people or property resulting from any ideas, methods, instructions or products referred to in the content.

symmetry

MDPI

Article

Analysis of the Type V Intermittency Using the Perron-Frobenius Operator

Sergio Elaskar [1,*], Ezequiel del Rio [2] and Walkiria Schulz [3]

[1] Departamento de Aeronáutica, Instituto de Estudios Avanzados en Ingeniería y Tecnología (IDIT), FCEFyN, Universidad Nacional de Córdoba and CONICET, Córdoba 5000, Argentina
[2] Departamento de Física Aplicada, ETSI de Aeronáutica y Espacio, Universidad Politécnica de Madrid, 28040 Madrid, Spain
[3] Departamento de Aeronáutica, FCEFyN, Universidad Nacional de Córdoba, Córdoba 5000, Argentina
* Correspondence: selaskar@unc.edu.ar or sergio.elaskar@gmail.com

Abstract: A methodology to study the reinjection process in type V intermittency is introduced. The reinjection probability density function (RPD), and the probability density of the laminar lengths (RPDL) for type V intermittency are calculated. A family of maps with discontinuous and continuous RPD functions is analyzed. Several tests were performed, in which the proposed technique was compared with the classical theory of intermittency, the *M* function methodology, and numerical data. The analysis exposed that the new technique can accurately capture the numerical data. Therefore, the scheme presented herein is a useful tool to theoretically evaluate the statistical variables for type V intermittency.

Keywords: reinjection process; type V intermittency; one-dimensional maps

1. Introduction

Dynamical systems model numerous phenomena, processes, and mechanisms, that can evolve into chaos using different routes. One of these routes is chaotic intermittency, where a dynamical system solution alternates chaotic bursts with laminar or regular phases. The regular phases correspond with pseudo-equilibrium regions or pseudo-periodic solutions, but at the bursts the evolution is chaotic [1–4].

Classic chaotic intermittency was grouped into three types, I, II and III, according to the periodic orbit stability loss evaluated by the Floquet multipliers, or to the fixed point loss of stability evaluated by the eigenvalues of the map. Subsequent papers introduced other types of intermittencies: on–off (in–out), V, X, eyelet, and ring [5–10].

We emphasize that a more complete understanding of chaotic intermittency could expand its application to various fields of study, due to previous experiences observed in physics, chemistry, medicine, and economics [11–21].

One-dimensional maps are widely utilized to analyze chaotic intermittency [1–4,22]. Maps with intermittency are characterized by a local map that determines the intermittency type, and a non-linear map that generates the reinjection process. The reinjection probability density function (RPD) is utilized to describe the reinjection process, and establishes the probability of the trajectories to be reinjected in the laminar interval [1,4]. Accordingly, the proper calculation of the RPD function is fundamental to accurately outline the chaotic intermittency phenomenon. There was no universal methodology to determine the RPD, and distinct methods were used of which the uniform reinjection mechanism (constant RPD function) was the most utilized [1–3,22]. However, a more extensive methodology to calculate the RPD function, the *M* function, has been developed over the last decade. It has accurately worked for different maps with types I, II, III, and V intermittencies [23–27].

Type V intermittency was previously described in the literature by [28–30], and occurs when a fixed point loses its stability via a collision with a non-differentiable point (NDP)

forming a channel between the bisector line and the map. However, at this point, the local map is non-differentiable or discontinuous and there is no tangent bifurcation. More recent studies to calculate the RPD in type V intermittency are presented in Refs. [26,27]. Applications of type V intermittency can be found in neuronal activity studies [31–33]. For example, in the Hindmarsh–Rose model, there is an intermittent behavior between irregular bursting and laminar phases close to a period-3 bursting [32].

In this paper, we utilize the Perron–Frobenius operator to elaborate a methodology to compute the reinjection probability density function and the probability density of the laminar lengths (RPDL) for type V intermittency [34,35]. Hereafter, this methodology is referred to as the continuity technique. To validate the continuity technique in order to evaluate the RPD and RPDL functions for type V intermittency, a family of maps is analyzed. Comparisons between analytical results calculated using this technique, the classical theory of intermittency, the M function methodology, and numerical data are carried out. Finally, the advantages and drawbacks of the continuity technique are described.

2. Study of Type V Intermittency

Prior to discussing the application to type V intermittency, a short description about the evolution of densities is necessary (the Perron–Frobenius operator). A more complete and deeper explanation of this subject can be found in Refs. [36,37]. We consider a family of evolution operators $F^t(x) : D \to D$, such as $F^{t_1+t_2} = F^{t_1} \circ F^{t_2}$ and $F^0 =$ identity, $x \in D$, being D a compact manifold, and t the evolution variable. If t varies over the real numbers ($t \in \mathbb{R}$), $F^t(x)$ represents a dynamical system. Nevertheless, if t acquires exclusively discrete values, the operator $F^t(x)$ is a map. There are, at least, two formulations to explain the functioning of $F^t(x)$. One alternative is to analyze the trajectories evolution, the other considers the density and the probability measure concepts.

Let us introduce a map $y = F(x)$, that transforms some interval $\Delta \subset \mathbb{R}$ into another interval $\Delta_a \subset \mathbb{R}$. Hence, $x \in \Delta$ and $y \in \Delta_a$. In Δ, the density of trajectories can be defined as $\rho(x)$, while in Δ_a the trajectories density is $\rho_a(y)$. We can transform the density ρ in ρ_a, and we write $\rho_a = \mathcal{L} \circ \rho$. If we consider $\Delta = [y_0, y]$, where the upper limit y is variable, the density $\rho_a(y)$ results

$$\rho_a(y) = \frac{d}{dy} \int_{F^{-1}[y_0,y]} \rho(x)\, \mathrm{d}x = \rho(F^{-1}(y)) \left| \frac{dF^{-1}(y)}{dy} \right|. \tag{1}$$

This equation assumes that $F(x)$ is piecewise differentiable and invertible. Furthermore, the derivative $\frac{d\,F^{-1}(x)}{d\,x}$ is piecewise continuous [36].

To apply Equation (1) in type V intermittency, we introduce the following family of maps

$$F(x) = \begin{cases} F_1(x) = \lambda_1\, x + \varepsilon & \hat{x} \le x < 0, \\ F_2(x) = \varepsilon + x + \lambda_2\, x^2 & 0 \le x < x_m, \\ F_3(x) = \hat{x} + \frac{(y_m - \hat{x})(y_m - x)^\gamma}{(y_m - x_m)^\gamma} & x_m \le x \le y_m\,, \end{cases} \tag{2}$$

where $y_m = F(x_m) = 1$, ε is the control parameter, λ_1 is the slope of the straight line ($0 < \lambda_1 < 1$), λ_2 is the quadratic term coefficient in $F_2(x)$, γ is the exponent in $F_3(x)$, and $\hat{x}$ is the lower boundary of reinjection [4]. For $\varepsilon = 0$, $x_0 = 0$ is a fixed point of the map, and for $0 < \varepsilon \ll 1$ type V intermittency occurs. To carry out a more general study, this family of maps does not have symmetry around the fixed point, and it can generate type V intermittency with continuous and discontinuous RPD functions.

If we apply Equation (1) to the map given by Equation (2), for the sub-interval $[\hat{x}, F_1(\hat{x}))$ we obtain

$$\mathcal{L} \circ \rho\,(x) = \rho(F_3^{-1}(x)) \left| \frac{dF_3^{-1}(x)}{dx} \right|, \tag{3}$$

for the sub-interval $[F_1(\hat{x}), 0)$ results

$$\mathcal{L} \circ \rho\,(x) = \rho(F_1^{-1}(x)) \left| \frac{dF_1^{-1}(x)}{dx} \right| + \rho(F_3^{-1}(x)) \left| \frac{dF_3^{-1}(x)}{dx} \right|, \tag{4}$$

and for the sub-interval $[0, y_m]$ we have

$$\mathcal{L} \circ \rho\,(x) = \rho(F_2^{-1}(x)) \left| \frac{dF_2^{-1}(x)}{dx} \right| + \rho(F_3^{-1}(x)) \left| \frac{dF_3^{-1}(x)}{dx} \right|. \tag{5}$$

Figure 1 shows how the intervals are mapped to obtain Equations (3)–(5). Blue, red, and green arrows correspond to Equations (3)–(5), respectively. Furthermore, Figure 1 and Equations (4) and (5) show that there is symmetry in the process of density evolution.

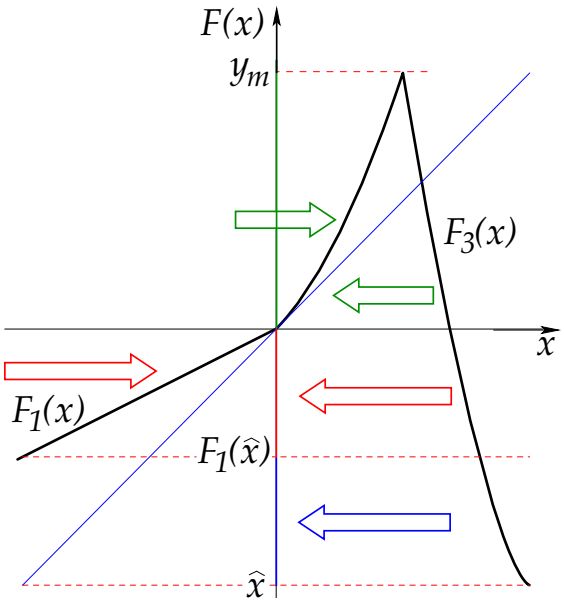

Figure 1. Density evolution. Blue arrow: Equation (3). Red arrows: Equation (4). Green arrows: Equation (5).

On the other hand, for a map $F(x_n) : H \to H$ where $H \subset \mathbb{R}$, the probability measure of an interval $S \subset H$ can be written as

$$P(S) = \lim_{N\to\infty} \frac{1}{N} \sum_{n=0}^{N} I_S(x_n)\,, \tag{6}$$

where $I_S(x)$ is the characteristic function of the interval S

$$I_S(x) = \begin{cases} 1, & \text{if} \quad x \in S \\ 0, & \text{if} \quad x \notin S\,. \end{cases} \tag{7}$$

Consequently, the probability measure indicates the frequency that the trajectory reaches the corresponding interval, and is related to the invariant density $\rho(x)$ by

$$P(S) = \int_S \rho(x)dx\,. \tag{8}$$

Let $L \equiv S$ be the laminar region. Before considering the probability $P(L)$ given by Equation (6), we divide the whole data series into three subsets

$$\{x_n\} = \{x_{n'}\} \cup \{x_{n''}\} \cup \{x_{n'''}\}\,. \tag{9}$$

First, we choose $x_{n'} \in L$, and in the preceding iteration it has already been there, that is $I_L(x_{n'}) = 1$ and $I_L(x_{n'-1}) = 1$. Furthermore, we have $x_{n''} \in L$ but in the preceding iteration it has not been there, that is $I_L(x_{n''}) = 1$ and $I_L(x_{n''-1}) = 0$. Finally, $x_{n'''} \notin L$. It is notable that there exists no intersection between them

$$\{x_{n'}\} \cap \{x_{n''}\} = \{x_{n''}\} \cap \{x_{n'''}\} = \{x_{n'''}\} \cap \{x_{n'}\} = \emptyset\,. \tag{10}$$

Therefore, $P(L)$ is

$$P(L) = \lim_{N\to\infty} \frac{1}{N} \sum_{n'=0}^{N} I_L(x_{n'}) + \lim_{N\to\infty} \frac{1}{N} \sum_{n''=0}^{N} I_L(x_{n''})\,, \tag{11}$$

The first term in Equation (11) is the probability for the trajectory to be in L when in the preceding iteration it has already been there. Subsequently, only the second term in the RHS of Equation (11) defines the RPD function, denoted here by $\phi(x)$, by means of the following relation

$$\lim_{N\to\infty} \frac{1}{N} \sum_{n''=0}^{N} I_L(x_{n''}) = w \int_L \phi(x)\mathrm{d}x\,, \tag{12}$$

where the weight w is introduced because it is common to normalize the function $\phi(x)$ over the whole laminar interval L as $\int_L \phi(x)dx = 1$. Next, to evaluate the RPD function the sums in Equation (3)–(5) have to exclude the contributions that do not produce reinjection inside of the laminar interval [4,35]

$$\phi(x) = \sum_{j\neq l}^{n} \left| \frac{dF_j^{-1}(x)}{dx} \right| \rho(F_j^{-1}(x))\,, \tag{13}$$

where l indicates the integrals that do not generate reinjection and $\rho(F_j^{-1}(x))$ is the density in the preceding iteration to reinjection. The normalization condition is

$$\sum_{j\neq l}^{n} \int_{F_j^{-1}(x_0-c)}^{F_j^{-1}(x_0+c)} \rho(F_j^{-1}(x))\,\mathrm{d}x = 1\,, \tag{14}$$

where c is the semi-amplitude of the laminar interval, and x_0 is the fixed point, $L = [x_0 - c, x_0 + c]$.

2.1. Continuous RPD

Let us consider the lower boundary of reinjection in the family of maps described by Equation (2) with $\hat{x} = x_0 - c$, $x_0 = 0$, and $y_m = 1$. Therefore, there is no reinjection from points $x < x_0 - c$ because the lower limit of the laminar interval is the lower boundary of reinjection. To obtain the RPD function we use Equations (13) and (14). Note that $F_1(x)$ and $F_2(x)$ do not produce reinjection, and the RPD can then be calculated as

$$\phi(x) = \rho(F_3^{-1}(x)) \left| \frac{dF_3^{-1}(x)}{dx} \right|, \tag{15}$$

where

$$\left| \frac{dF_3^{-1}(x)}{dx} \right| = \frac{(1 - x_m)\,(x + c)^{1/\gamma - 1}}{\gamma\,(1 + c)^{1/\gamma}}\,. \tag{16}$$

To apply Equation (15) we have to evaluate the density at pre-reinjection points, $\rho(F_3^{-1}(x))$. Let us expand ρ by a Taylor series around the pre-image of the lower boundary of the reinjection $F_3^{-1}(-c)$. Using the notation $y = F_3^{-1}(x)$ and $y_{-c} = F_3^{-1}(-c)$ we get

$$\rho(y) = \rho(y_{-c}) + \left.\frac{d\,\rho(y)}{d\,y}\right|_{y=y_{-c}} (y - y_{-c}) + \frac{1}{2}\left.\frac{d^2\,\rho(y)}{d\,y^2}\right|_{y=y_{-c}} (y - y_{-c})^2 + \dots . \tag{17}$$

Using the normalization condition, Equation (14), we obtain

$$\begin{aligned} \rho(y) \cong \; & \tfrac{1}{\Delta y(c)} + \left.\tfrac{d\,\rho(y)}{d\,y}\right|_{y=y_{-c}} \left(\Delta y(x) - \tfrac{\Delta y(c)}{2}\right) \\ & + \left.\tfrac{d^2\,\rho(y)}{d\,y^2}\right|_{y=y_{-c}} \left(\tfrac{\Delta y^2(x) - \frac{\Delta y^2(c)}{3}}{2}\right), \end{aligned} \tag{18}$$

where we define $\Delta y(x) = F_3^{-1}(-c) - F_3^{-1}(x)$, hence we have $\Delta y(c) = F_3^{-1}(-c) - F_3^{-1}(c)$.

As $c << 1$, the family of maps described by Equation (2) verifies that $\Delta y(x) < \Delta y(c) << 1$. Note that for $c = 0.05$, the linear term has the same magnitude as the first one in the Taylor series if the derivative $\left.\frac{d\,\rho(y)}{d\,y}\right|_{y=y_{-c}}$ is approximately one order of magnitude greater than the first term, $\frac{1}{\Delta y(c)}$. Following a similar analysis, the second derivative, $\left.\frac{d^2\,\rho(y)}{d\,y^2}\right|_{y=y_{-c}}$ has to be approximately two orders of magnitude greater than the first term in the series. Furthermore, from Equations (15) and (18) the RPD can be written as

$$\begin{aligned} \phi(x) \cong \; & \left(\tfrac{1}{\Delta y(c)} + \left.\tfrac{d\,\rho(y)}{d\,y}\right|_{y=y_{-c}} \left(\Delta y(x) - \tfrac{\Delta y(c)}{2}\right)\right) \left|\tfrac{dy}{dx}\right| \\ & + \left(\left.\tfrac{d^2\,\rho(y)}{d\,y^2}\right|_{y=y_{-c}} \left(\tfrac{\Delta y^2(x) - \frac{\Delta y^2(c)}{3}}{2}\right)\right) \left|\tfrac{dy}{dx}\right| . \end{aligned} \tag{19}$$

If the derivative $\left|\frac{dy}{dx}\right| = \left|\frac{dF_3^{-1}(x)}{dx}\right|$ has very high or close to zero values, and the variation generated by the linear and quadratic terms in Equation (18) is not really significant in comparison with the first term, $\frac{1}{\Delta y(c)}$, they do not significantly modify the RPD. Therefore, the first term in Equation (18) can be considered the most important, and we can assume that

$$\rho(F_3^{-1}(x)) \cong \frac{1}{F_3^{-1}(-c) - F_3^{-1}(c)} = \frac{1}{1 - x_m}\left(\frac{1+c}{2\,c}\right)^{1/\gamma}, \tag{20}$$

then the RPD results

$$\phi(x) = \frac{(x+c)^{1/\gamma - 1}}{\gamma\,(2c)^{1/\gamma}}\,. \tag{21}$$

This is a power function with exponent $\alpha = \frac{1}{\gamma} - 1$. This same result was calculated using the M function methodology [27].

To validate the new theoretical evaluations, we perform a comparison between the RPDs here obtained with numerical data, with those calculated by the M function methodology and with the classical theory of intermittency. A detailed explanation of the M function methodology can be found in Refs. [4,23–25], and is not described here. On the other hand, the classical theory uses a constant RPD to describe the reinjection process, i.e., uniform reinjection (see Refs. [1,3,4,22]). To obtain the numerical data, we produce an iterative process for the map and also split the laminar interval into N_s sub-intervals. After that, we calculate the histogram of reinjections and the numerical RPD. To obtain the histogram we consider at least $10\,N_s$ reinjections, which indicates millions of iterations.

For all tests in this section, the following parameters are used $a_1 = 0.9$, $a_2 = 1$, and $\hat{x} = -c$. Thus, the reinjection process is driven only by $F_3(x)$. The reinjected points in the

laminar interval, $L = [x_0 - c, x_0 + c]$, are mapped only by $F_3(x)$ from points in the interval $I_3(x) = [F_3^{-1}(x_0 - c), F_3^{-1}(x_0 + c)]$. For the first test, we also use $\gamma = 1$, $\varepsilon = 0.001$, and $c = 0.05$. To obtain the RPD function, we consider Equation (21), and it results

$$\phi(x) = \frac{1}{2\,c}\,. \tag{22}$$

To validate this result, we conduct a complete set of numerical simulations for a different number of reinjected points N, and we divide the laminar interval into N_s sub-intervals, where the RPDs are evaluated. To analyze the difference between numerical data and the theoretical RPD given by Equation (22), we calculate

$$D_r = \sqrt{\frac{\sum_{j=1}^{j=N_s} \frac{(\phi_t(j)-\phi_n(j))^2}{(\phi_t(j))^2}}{N_s^2}}\,, \qquad E_r = \frac{\sum_{j=1}^{j=N_s} \frac{|\phi_t(j)-\phi_n(j)|}{\phi_t(j)}}{N_s}\,, \tag{23}$$

where $\phi_n(j)$ and $\phi_t(j)$ are the numerical and theoretical values of the RPD in the sub-interval j. Note that $D_r, E_r \geq 0$.

Figure 2a,b show $\ln(D_r)$ and $\ln(E_r)$ for a different number of reinjected points, N from 5×10^4 to 25×10^5 with $N_s = 100$. We highlight that as the number of reinjected points grows, the differences between the theoretical formulations and the numerical data decrease. Notice that the M function methodology calculates $\alpha \approx 0$. This result coincides with Equation (22). Numerical and theoretical RPDs are shown in Figure 3. From Figures 2a,b and 3 we observe a good agreement between the RPD functions.

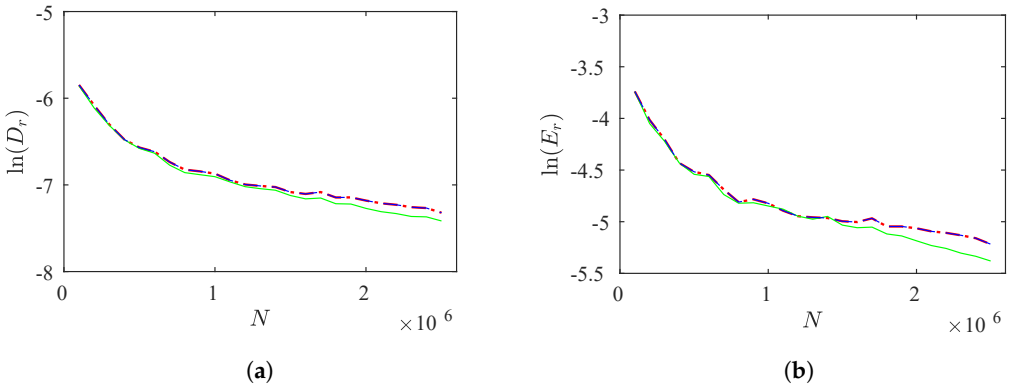

Figure 2. (**a**) $\ln(D_r)$, and (**b**) $\ln(E_r)$ vs. N for $\gamma = 1$, $\varepsilon = 0.001$, $c = 0.05$, and $N_s = 100$. Blue line: continuity technique. Red line: classical theory. Green line: M function methodology.

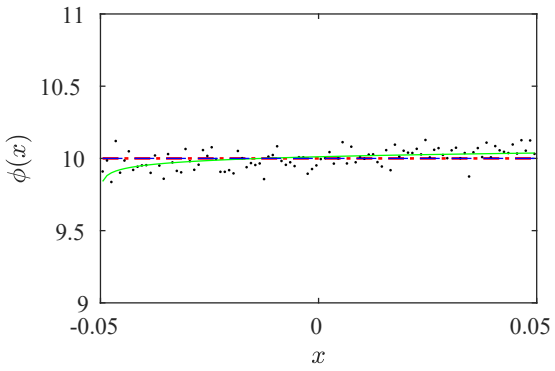

Figure 3. Continuous RPD function for $\gamma = 1$, $\varepsilon = 0.001$, $c = 0.05$, $N_s = 100$, and $N = 25 \times 10^5$. Blue line: continuity technique. Red line: classical theory. Green line: M function methodology. Black points: numerical data.

To evaluate the rate of convergence, we utilize the sequence $\{\frac{1}{N^p}\}_{N=1}^{\infty}$ that converges to zero for $p > 0$ (N are positive integer numbers), and we must verify

$$D_r \leq K_d \frac{1}{N^{p_d}}, \qquad E_r \leq K_e \frac{1}{N^{p_e}}, \tag{24}$$

for K_d, K_e, p_d and p_e fixed positive real numbers. Therefore, $\{D_r\}_{N=1}^{\infty}$ and $\{E_r\}_{N=1}^{\infty}$ converge to zero with order, or rate, of convergence $O(\frac{1}{N^{p_d}})$ and $O(\frac{1}{N^{p_e}})$, respectively, [38]. For this test we obtain $p_d \approx p_e \approx 0.45$. Subsequently, D_r and E_r converge to zero for $N \to \infty$.

The parameters $\gamma = 0.5$, $\varepsilon = 0.005$, and $c = 0.15$ are utilized for the second test. By Equation (21) we obtain

$$\phi(x) = \frac{(x+c)}{2\,c^2} = 50\,(x+0.1)\,. \tag{25}$$

The calculated RPD using the M function methodology is [27]

$$\phi(x) = 48.99\,(x+0.1)^{0.9999}\,. \tag{26}$$

Figure 4a,b show $\ln(D_r)$ and $\ln(E_r)$ for a number of reinjected points, respectively. For these figures, we use N from 5×10^4 to 25×10^5 and $N_s = 1500$. We can observe that the differences between RPDs calculated with the continuity technique and the M function methodology with numerical data decrease while N increases. However, this behavior is not verified by the classical RPD.

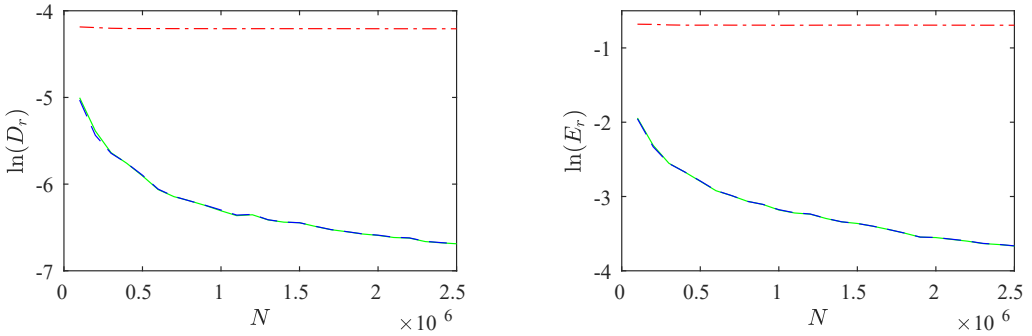

(**a**) (**b**)

Figure 4. (**a**) $\ln(D_r)$, and (**b**) $\ln(E_r)$ vs. N for $\gamma = 0.5$, $\varepsilon = 0.005$, $c = 0.15$, and $N_s = 1500$. Blue line: continuity technique. Red line: classical theory. Green line: M function methodology.

Figure 5 shows the comparison between theoretical and numerical RPDs. From this figure, and Figure 4a,b we note that the classical theory does not obtain correct results for this test. However, we observe that both methodologies, M function, and continuity, work better than classical theory, capture the numerical data, and D_r and E_r decrease while N increases. For the continuity technique, we find that $p_d \approx p_e \approx 0.45$; therefore, D_r and E_r converge to zero for $N \to \infty$.

For the third test, we use $\gamma = 0.8$, $\varepsilon = 0.01$, $c = 0.1$, N from 5×10^4 to 30×10^5 and $N_s = 1000$. From Equation (21) we calculate

$$\phi(x) = 9.346\,(x+0.1)^{0.25}\,. \tag{27}$$

The M function methodology obtains

$$\phi(x) = 9.414\,(x+0.1)^{0.253}\,. \tag{28}$$

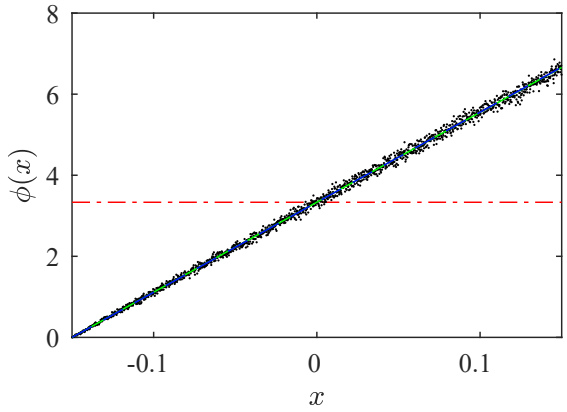

Figure 5. Continuous RPD function for $\gamma = 0.5$, $\varepsilon = 0.005$, $c = 0.15$, $N_s = 1500$ and $N = 25 \times 10^5$. Blue line: continuity technique. Red line: classical theory. Green line: M function methodology. Black points: numerical data.

Figure 6a,b show $\ln(D_r)$ and $\ln(E_r)$ vs. the number of reinjected points for N from 5×10^4 to 3×10^6. We observe that the D_r and E_r calculated with continuity and M function methodologies decrease while N increases. Again, this behavior is not obtained for the classical RPD.

The RPD functions are shown in Figure 7. We note that the RPDs calculated with the continuity and M function methodologies adequately represent the numerical data. However, the classical RPD function cannot accurately reproduce the numerical data. If we use Equation (24) for the continuity technique, we obtain $p_d \approx 0.5$ and $p_e \approx 0.45$, i.e., D_r and E_r converge to zero for $N \to \infty$.

The fourth test uses $\gamma = 1.5$, $\varepsilon = 0.0001$, $c = 0.015$, N from 5×10^4 to 25×10^5 and $N_s = 1000$. From Equation (21) we calculate

$$\phi(x) = 6.905\,(x + 0.015)^{-1/3}. \tag{29}$$

The M function methodology obtains

$$\phi(x) = 7.091\,(x + 0.015)^{-0.328}. \tag{30}$$

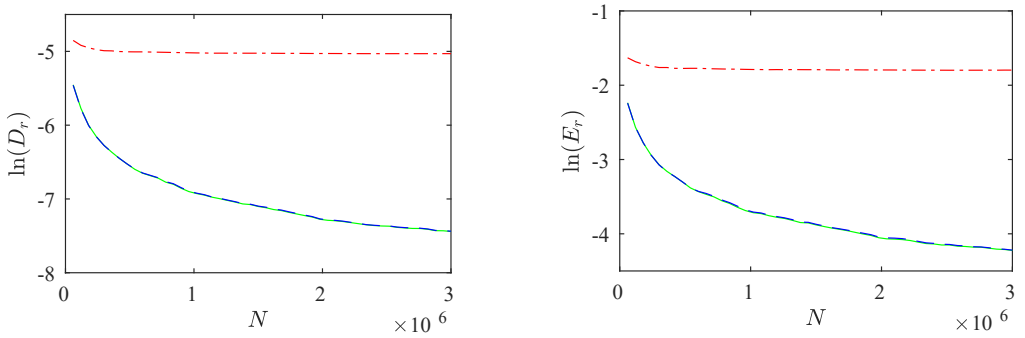

(**a**) (**b**)

Figure 6. (**a**) $\ln(D_r)$, and (**b**) $\ln(E_r)$ vs. N for $\gamma = 0.8$, $\varepsilon = 0.01$, $c = 0.1$, and $N_s = 1000$. Blue line: continuity technique. Red line: classical theory. Green line: M function methodology.

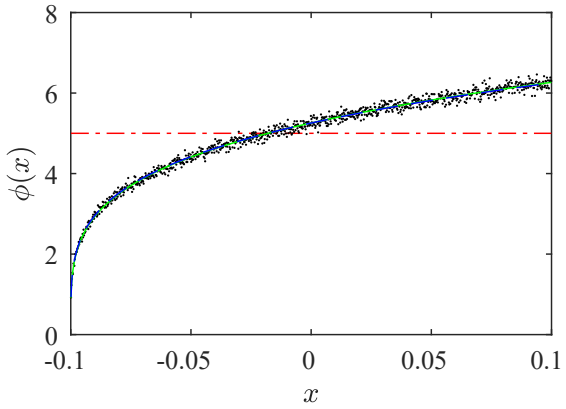

Figure 7. Continuous RPD function for $\varepsilon = 0.01$, $\gamma = 0.8$, $N = 30 \times 10^5$, $c = 0.1$. Blue line: continuity technique. Red line: classical theory. Green line: M function methodology. Black points: numerical data.

The $\ln(D_r)$ and $\ln(E_r)$ are shown in Figure 8a,b for N from 5×10^4 to 25×10^5 and $N_s = 1000$. We observe that the D_r and E_r calculated with continuity and M function methodologies decrease for increasing N. Similar to the previous tests, the classical theory obtains poor results. For the RPD function calculated by the continuity methodology, we obtain $p_d \approx 0.4$ and $p_e \approx 0.45$, then D_r and E_r converge to zero for $N \to \infty$ (see Equation (24)).

Figure 9 shows the RPDs functions. The RPDs calculated using the continuity and M function methodologies can describe the numerical data behavior. On the other hand, the classical RPD function cannot accurately reproduce the numerical data.

For the fifth test, we consider $\gamma = 2$, $\varepsilon = 0.0005$, $c = 0.02$, and $N_s = 2000$. If we use the continuity technique, Equation (21), we obtain

$$\phi(x) = 2.5\,(x + 0.02)^{-0.5}\,. \tag{31}$$

The RPD calculated using the M function methodology is

$$\phi(x) = 2.474\,(x + 0.02)^{-0.502}\,. \tag{32}$$

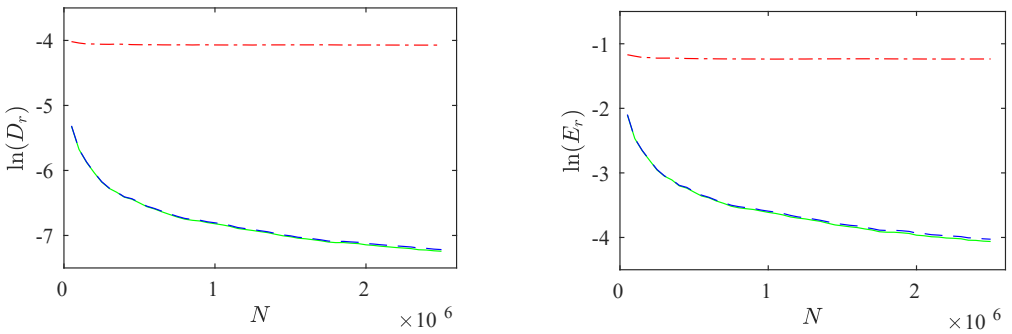

(**a**) (**b**)

Figure 8. (**a**) $\ln(D_r)$, and (**b**) $\ln(E_r)$ vs. N for $\gamma = 1.5$, $\varepsilon = 0.0001$, $c = 0.015$ and $N_s = 1000$. Blue line: continuity technique. Red line: classical theory. Green line: M function methodology.

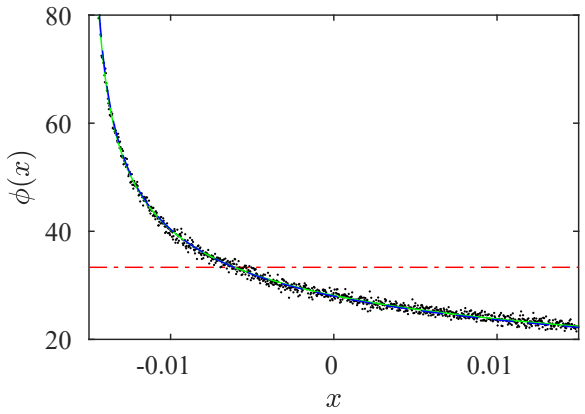

Figure 9. Continuous RPD function for $\gamma = 1.5$, $\varepsilon = 0.0001$, $c = 0.015$ and $N = 25 \times 10^5$. Blue line: continuity technique. Red line: classical theory. Green line: M function methodology. Black points: numerical data.

For $N = 5 \times 10^4 - 25 \times 10^5$, Figure 10a,b show $\ln(D_r)$ and $\ln(E_r)$. From these figures, we observe that for the continuity technique and the M function methodology D_r and E_r decrease whereas N increases. However, D_r and E_r are approximately constant for the classical theory. For the RPD given by Equation (31), we obtain that $p_d \approx 0.35$ and $p_e \approx 0.4$, accordingly D_r , $E_r \to 0$ for $N \to \infty$.

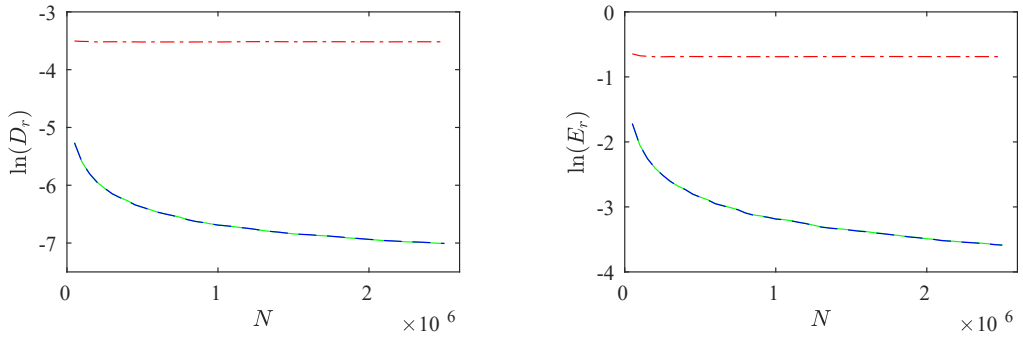

(**a**) (**b**)

Figure 10. (**a**) $\ln(D_r)$, and (**b**) $\ln(E_r)$ vs. N for $\gamma = 2$, $\varepsilon = 0.0005$, $c = 0.02$, and $N_s = 2000$. Blue line: continuity technique. Red line: classical theory. Green line: M function methodology.

The RPD functions are shown in Figure 11. The RPDs calculated by the M function methodology and continuity technique reproduce the numerical results whereas classical theory does not.

The results for the five sets of tests are summarized in Table 1. In these tests, we use different values of the exponent γ, the length of the laminar interval c, the parameter ε, and the number of sub-intervals N_s, despite that in all these tests for the continuity technique D_r and E_r diminish as the number of re-injected points increases, showing that the theoretical evaluation given by Equation (21) approximates with more accuracy the numerical RPD as the number of reinjected points increases. For all tests, the convergence process verifies $0.35 < p_d < 0.5$ and $0.4 < p_e < 0.45$. Furthermore, from the tests we highlight that the continuity technique works better than the classical theory, and obtains RPD functions with approximately the same accuracy as the M function methodology. In addition, the continuity technique has the advantage of being able to predict analytic RPD functions knowing only the map without using numerical or experimental data.

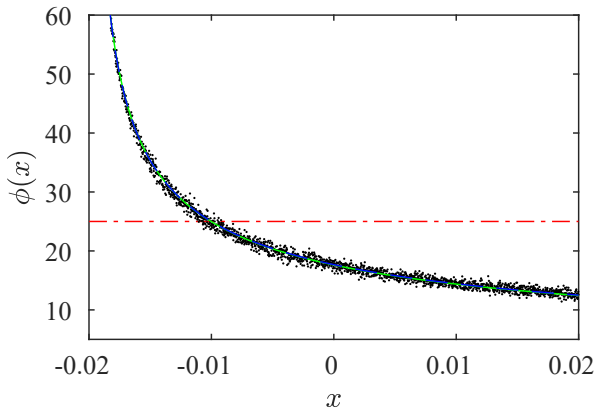

Figure 11. Continuous RPD function for $\gamma = 2$, $\varepsilon = 0.0005$, $c = 0.02$, $N = 25 \times 10^5$, and $N_s = 2000$. Blue line: continuity technique. Red line: classical theory. Green line: M function methodology. Black points: numerical data.

Table 1. Results for the five sets of tests with continuous RPD functions.

ε	γ	c	N_s	p_e	p_d
0.001	1.0	0.05	100	0.45	0.45
0.005	0.5	0.15	1500	0.45	0.45
0.010	0.8	0.10	1000	0.45	0.50
0.0001	1.5	0.015	1000	0.45	0.40
0.0005	2.0	0.02	2000	0.40	0.35

Only the first and second tests produce symmetric RPD functions around the fixed point. For $\gamma \neq 0.5$ and $\gamma \neq 1$ the symmetry is lost.

Note that to obtain the previous results, we have assumed a constant density at pre-reinjection points. This assumption is based on two concepts. The first one is, when the density can be approximated by a Taylor series because the laminar interval is small, large values of the first and second derivatives are needed to affect the density (see Equation (18)). The second one is related with Equation (15), from this equation the RPD function is calculated as the product of two factors, one is the density at pre-reinjection points and the other is $\left|\frac{dF_3^{-1}(x)}{dx}\right|$, which can reach very high or close to zero values. Therefore, this factor has a greater influence in determining the RPD than first and second derivatives in the Taylor series.

2.2. Discontinuous RPD

If the lower boundary of reinjection verifies $\hat{x} < x_0 - c$, type V intermittency shows discontinuous RPD functions. These RPDs occur because there are two different processes of reinjection, one is generated by $F_3(x)$ and the other one by $F_1(x)$. To obtain the RPDs, we use Equation (13) with $j \neq 2$

$$\phi(x) \quad = \phi_1(x) + \phi_3(x) = \left|\frac{dF_1^{-1}(x)}{dx}\right| \rho_1^1(F_1^{-1}(x)) + \left|\frac{dF_3^{-1}(x)}{dx}\right| \rho_3(F_3^{-1}(x)), \tag{33}$$

where $\rho_1^1(x)$ and $\rho_3(x)$ are the trajectory densities inside the intervals $I_1^1 = [F_1^{-1}(x_0 - c), x_0 - c)$ and $I_3 = [F_3^{-1}(x_0 - c), F_3^{-1}(x_0 + c)]$, respectively. Hence

$$\phi_1(x) = \left|\frac{dF_1^{-1}(x)}{dx}\right| \rho_1^1(F_1^{-1}(x)), \tag{34}$$

is only defined in the interval $[x_0 - c, F_1(x_0 - c))$. However, $\phi_3(x)$ is defined in the complete laminar interval $L = [x_0 - c, x_0 + c]$

$$\phi_3(x) = \left| \frac{dF_3^{-1}(x)}{dx} \right| \rho_3(F_3^{-1}(x)) \,. \tag{35}$$

Accordingly, the RPD is

$$\phi(x) = \begin{cases} \phi_I(x) = \phi_1(x) + \phi_3(x) & x < F_1(x_0 - c), \\ \phi_{II}(x) = \phi_3(x) & x \geq F_1(x_0 - c) \,. \end{cases} \tag{36}$$

Following the previous subsection, we use $\rho_3(x) = k =$ constant in the interval $I_3^s = [F_3^{-1}(\hat{x}), F_3^{-1}(x_0 + c)]$. As I_3 is included in I_3^s ($I_3 \subset I_3^s$), the density $\rho_3(F_3^{-1}(x))$ is constant in Equations (33) and (35). To evaluate $\rho_1^1(x)$, which is defined inside the interval $I_1^1 = [F_1^{-1}(x_0 - c), x_0 - c)$, we must consider the iteration procedure for Equation (2) because $\rho_1^1(x)$ depends on the density at the preceding iteration.

The interval $I_3^a = [F_3^{-1}(F_1^{-1}(x_0 - c), F_3^{-1}(x_0 - c)))$ maps on the interval I_1^1

$$I_3^a \;\longrightarrow\; I_1^1 : [F_3^{-1}(F_1^{-1}(x_0 - c)), F_3^{-1}(x_0 - c)) \to [F_1^{-1}(x_0 - c), x_0 - c) \,. \tag{37}$$

Moreover, points in the interval $I_1^2 = [F_1^{-1}(F_1^{-1}(x_0 - c)), F_1^{-1}(x_0 - c))$ map on the interval $I_1^1 = [F_1^{-1}(x_0 - c), x_0 - c)$

$$I_1^2 \;\longrightarrow\; I_1^1 : [F_1^{-1}(F_1^{-1}(x_0 - c)), F_1^{-1}(x_0 - c)) \to [F_1^{-1}(x_0 - c), x_0 - c) \,, \tag{38}$$

consequently, the density $\rho_1^1(x)$ in the interval I_1^1 receives two contributions (see Equations (37) and (38)), one is generated by $\rho_3(x)$ from the interval I_3^a and the other is given by $\rho_1^2(x)$ from the interval I_1^2

$$\rho_1^1(x) = \left| \frac{dF_1^{-1}(x)}{dx} \right| \rho_1^2(F_1^{-1}(x)) + \left| \frac{dF_3^{-1}(x)}{dx} \right| \rho_3(F_3^{-1}(x)) \,. \tag{39}$$

As $\rho_3(x) = k$ in $I_3^s = [F_3^{-1}(\hat{x}), F_3^{-1}(x_0 + c)]$, Equation (39) simplifies

$$\rho_1^1(x) = \left| \frac{dF_1^{-1}(x)}{dx} \right| \rho_1^2(F_1^{-1}(x)) + \left| \frac{dF_3^{-1}(x)}{dx} \right| k \,, \tag{40}$$

where k is obtained from the normalization condition

$$\int_{F_3^{-1}(\hat{x})}^{F_3^{-1}(x_0+c)} -k \, dx = 1 \;\;\Rightarrow\;\; k = \frac{(y_m - \hat{x})^{1/\gamma}}{(x_m - y_m)\,(x_0 + c - \hat{x})^{1/\gamma}} \,. \tag{41}$$

Now, we must calculate $\rho_1^2(x)$ in the interval I_1^2. Let us consider that points in the interval $I_1^n = [\hat{x}, F_1(\hat{x}))$ need n iterations to reinject. The density ρ_1^n in I_1^n is determined only by $\rho_3 = k$

$$\rho_1^n(x) = k \left| \frac{dF_3^{-1}(x)}{dx} \right| . \tag{42}$$

The density $\rho_1^{n-1}(x)$ in $I_1^{n-1} = [F_1(\hat{x}), F_1(F_1(\hat{x})))$ can then be calculated as

$$\rho_1^{n-1}(x) = \left| \frac{dF_1^{-1}(x)}{dx} \right| \rho_1^n(F_1^{-1}(x)) + k \left| \frac{dF_3^{-1}(x)}{dx} \right| . \tag{43}$$

In the interval $I_1^{n-2} = [F_1(F_1(\hat{x})), F_1(F_1(F_1(\hat{x}))))$, the density $\rho_1^{n-2}(x)$ results

$$\rho_1^{n-2}(x) = \left|\frac{dF_1^{-1}(x)}{dx}\right| \rho_1^{n-1}(F_1^{-1}(x)) + k\left|\frac{dF_3^{-1}(x)}{dx}\right|, \tag{44}$$

where

$$F_1^{-1}(x) = \frac{x-\varepsilon}{a_1}; \quad \frac{dF_1^{-1}(x)}{dx} = 1/a_1\,, \tag{45}$$

and

$$F_3^{-1}(x) = y_m - \frac{y_m - x_m}{(y_m - \hat{x})^{1/\gamma}}(x-\hat{x})^{1/\gamma}, \quad \frac{dF_3^{-1}(x)}{dx} = \frac{x_m - y_m}{\gamma(y_m-\hat{x})^{1/\gamma}}(x-\hat{x})^{-1+1/\gamma}\,. \tag{46}$$

If we introduce Equations (41), (45) and (46) into Equations (42)–(44), we find

$$\rho_1^{n}(x) = \frac{(x-\hat{x})^{-1+1/\gamma}}{\gamma\,(x_0+c-\hat{x})^{1/\gamma}}\,, \tag{47}$$

$$\rho_1^{n-1}(x) = \frac{(x-\hat{x})^{-1+1/\gamma}}{\gamma\,(x_0+c-\hat{x})^{1/\gamma}} + \frac{(F_1^{-1}(x)-\hat{x})^{-1+1/\gamma}}{a_1\,\gamma\,(x_0+c-\hat{x})^{1/\gamma}}\,, \tag{48}$$

$$\rho_1^{n-2}(x) = \frac{(x-\hat{x})^{-1+1/\gamma}}{\gamma\,(x_0+c-\hat{x})^{1/\gamma}} + \frac{(F_1^{-1}(x)-\hat{x})^{-1+1/\gamma}}{a_1\,\gamma\,(x_0+c-\hat{x})^{1/\gamma}} + \frac{(F_1^{-2}(x)-\hat{x})^{-1+1/\gamma}}{a_1^2\,\gamma\,(x_0+c-\hat{x})^{1/\gamma}}\,. \tag{49}$$

In consequence, we can generalize the previous equations as

$$\rho_1^{n-h}(x) = \frac{\sum_{l=0}^{l=h} \frac{(F_1^{-l}(x)-\hat{x})^{-1+1/\gamma}}{a_1^l}}{\gamma\,(x_0+c-\hat{x})^{1/\gamma}}\,, \tag{50}$$

where $h = 0, 1, 2, ..., n$. For $h = n$, $\phi_I(x)$ is calculated (see Equation (36))

$$\phi_I(x) = \frac{\sum_{l=0}^{l=n} \frac{(F_1^{-l}(x)-\hat{x})^{-1+1/\gamma}}{a_1^l}}{\gamma\,(x_0+c-\hat{x})^{1/\gamma}}\,. \tag{51}$$

The second RPD in Equation (36), $\phi_{II}(x)$, results

$$\phi_{II}(x) = k\left|\frac{dF_3^{-1}(x)}{dx}\right| = \frac{(x-\hat{x})^{-1+1/\gamma}}{\gamma\,(x_0+c-\hat{x})^{1/\gamma}}\,. \tag{52}$$

We highlight that $\phi_{II}(x_n)$ considers only points coming from $F_3(x_{n-1})$, where $x_n = F_3(x_{n-1})$. Figure 12 shows the reinjection process governed by $F_1(x)$ and $F_3(x)$. In the larger figure, the evolution of the density generated by $F_3(x)$ is indicated with thick arrows and the red discontinuous lines show the laminar interval. In the smaller box, the evolution produced by $F_1(x)$ is shown with thin blue arrows. In this figure, a trajectory needs three iterations to move from $\hat{x}$ to $x_0 - c$.

To validate the previous theoretical equations, we performed four sets of tests. The first one used $\varepsilon = 0.001$, $\gamma = 0.5$, $y_m = 1$, $x_0 = 0$, $c = 0.1128$, $\hat{x} = -0.158449931412894$, $N = 1 \times 10^5 - 15 \times 10^5$, and $N_s = 300$. For this set of tests, a trajectory took three iterations to displace from $\hat{x}$ to $x_0 - c$. We calculated the RPD function using the continuity technique, the M function methodology, and numerically. Figure 13a shows the comparison between the three RPDs. Black points are the numerical data, the green line is the RPD calculated using the M function methodology, and the RPD obtained by the continuity technique is the dashed blue line. We can observe that both methodologies, M function and continuity technique, capture the behavior of the numerical RPD. However, the continuity

technique captures the numerical results more accurately. The rates of convergence using the continuity technique for D_r and E_r are $O(\frac{1}{N^{0.1}})$ and $O(\frac{1}{N^{0.37}})$, respectively. The values of D_r and E_r for $N = 15 \times 10^5$ are 2.314×10^{-3} and 1.426×10^{-2}, respectively.

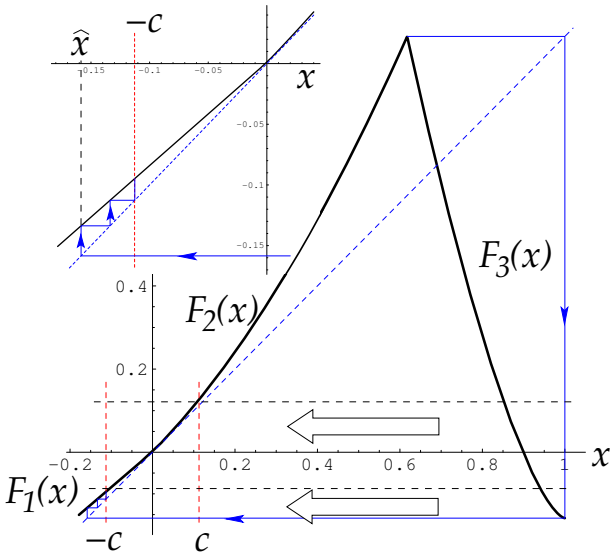

Figure 12. Reinjection process governed by $F_1(x)$ and $F_3(x)$ functions.

The parameters for the second set of tests were the same but $\gamma = 1.5$. Again, the trajectories took three iterations from $\hat{x}$ to $x_0 - c$. Results are shown in Figure 13b. Again, both methodologies capture the behavior of the numerical data. We have calculated the rates of convergence for the continuity technique: for D_r it is approximately $O(\frac{1}{N^{0.06}})$, and for E_r is $O(\frac{1}{N^{0.15}})$. For $N = 15 \times 10^5$, we obtained $D_r = 5.497 \times 10^{-3}$ and $E_r = 3.925 \times 10^{-2}$.

The parameters for the third and fourth sets of tests were $\varepsilon = 0.001$, $y_m = 1$, $x_0 = 0$, $c = 0.1128$, $\hat{x} = -0.12644444444$, $N = 1 \times 10^5 - 15 \times 10^5$, and $N_s = 300$. However, $\gamma = 0.5$ for the third set of tests, and $\gamma = 1.5$ for the fourth one. For both sets of tests, a trajectory needed only one iteration to move from $\hat{x}$ to $x_0 - c$. The theoretical and numerical results are shown in Figure 14a,b. The continuity technique and the M function methodology reproduce the behavior of the numerical RPD. However, from Figure 14a we can observe that the density technique approximates the numerical data more accurately. For the third set of tests, we have obtained $O(\frac{1}{N^{0.35}})$ for D_r, and E_r, and for the fourth set of tests we have calculated $O(\frac{1}{N^{0.15}})$ for D_r, and E_r.

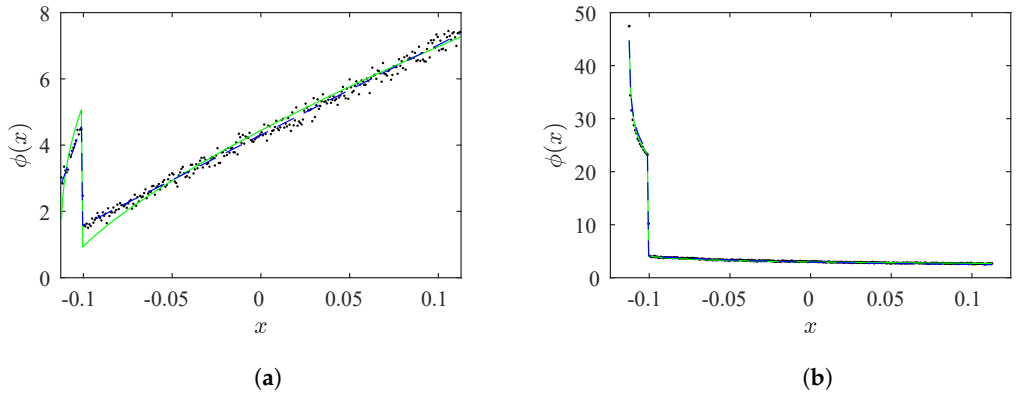

(**a**) (**b**)

Figure 13. Discontinuous RPD function for, $\varepsilon = 0.001$, $N = 15 \times 10^5$, $c = 0.1128$, $\hat{x} = -0.158449931412894$. (**a**) $\gamma = 0.5$. (**b**) $\gamma = 1.5$. Green line: M function methodology. Blue line: continuity technique. Black points: numerical data.

The results of these four sets of tests are summarized in Table 2. The first column is the lower boundary of reinjection $\hat{x}$, the second one gives the exponent γ, the third and fourth columns are the order of convergence exponents for E_r and D_r, respectively, and the last two columns show the calculated values of E_r and D_r for $N = 15 \times 10^5$. We note that the rate of convergence and the values of D_r and E_r display a better behavior for $\gamma = 0.5$ than for $\gamma = 1.5$. This occurs mainly because for $\gamma = 1.5$, the value of the numerical RPD in the first sub-interval is slightly larger than predicted by the continuity technique (see Figures 13a and 14b).

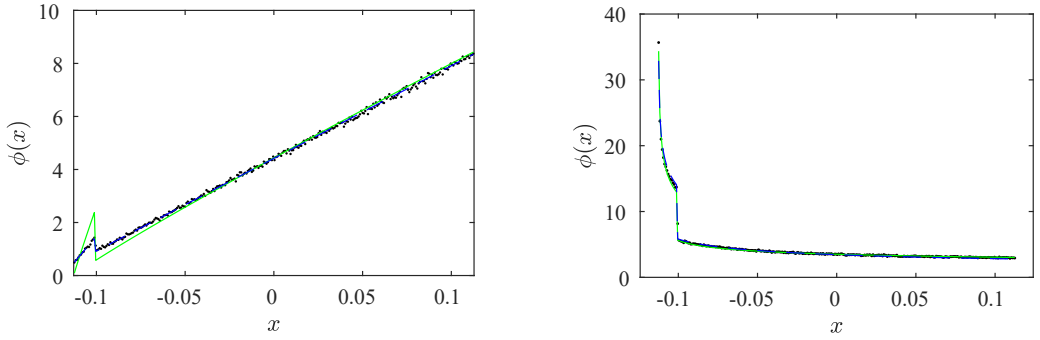

(**a**) (**b**)

Figure 14. Discontinuous RPD function for $\varepsilon = 0.001$, $N = 15 \times 10^5$, $c = 0.1128$, $\hat{x} = -0.12644444444$. (**a**) $\gamma = 0.5$. (**b**) $\gamma = 1.5$. Green line: M function methodology. Blue line: continuity technique. Black points: numerical data.

Table 2. Results for the four tests. p_e and p_d are the order of convergence exponents for E_r, and D_r, respectively.

$\hat{x}$	γ	p_e	p_d	E_r	D_r
-0.158449931412894	0.5	0.37	0.10	1.426×10^{-2}	2.314×10^{-3}
-0.158449931412894	1.5	0.15	0.06	3.925×10^{-2}	5.497×10^{-3}
-0.12644444444	0.5	0.35	0.35	1.424×10^{-2}	1.255×10^{-3}
-0.12644444444	1.5	0.15	0.15	3.185×10^{-2}	2.559×10^{-3}

From Figures 13 and 14 and Table 2, we can notice that the theoretical evaluations obtained using the continuity technique and the M function methodology capture the numerical RPD behavior. In addition, we can observe that the continuity technique displays a better behavior than the M function methodology.

Probability Density of the Laminar Lengths

Once the RPD function is evaluated, we are able to calculate the probability density of the laminar lengths, $\psi(l)$, which determines the probability of finding laminar lengths between l and $l + dl$ [4]

$$\psi(l, c) = \phi[X(l, c)] \left| \frac{dX(l, c)}{dl} \right|, \tag{53}$$

$X(l, c)$ is the inverse of $l(x, c)$, which is the laminar length for each reinjected point x. For the maps described by Equation (2), $\frac{dX(l,c)}{dl}$ is approximated by

$$\frac{dX(l, c)}{dl} = \begin{cases} \varepsilon + x\,(\lambda_1 - 1) & x < 0\,, \\ \varepsilon + \lambda_2\, x^2 & x \geq 0\,. \end{cases} \tag{54}$$

We calculated the RPDL functions for the four sets of tests previously presented. The results are shown in Figures 15 and 16. We can observe a good accuracy between the continuity technique, the M function methodology, and the numerical data.

From Figures 13 and 14, we can observe the different behaviors of the RPD functions. For $\gamma < 1$, the number of trajectories that return close to the lower limit of the laminar interval is low, and the RPDs are increasing functions. For $\gamma > 1$, the number of trajectories that return close to the lower limit of the laminar interval is high, and the RPDs are decreasing functions. These behaviors are also observed for the probability density of the laminar lengths (see Figures 15 and 16). However, in all tests, we can observe two sub-intervals $[x_0 - c, F_1(x_0 - c))$ and $[F_1(x_0 - c), x_0 + c]$ with different behaviors described by Equation (36).

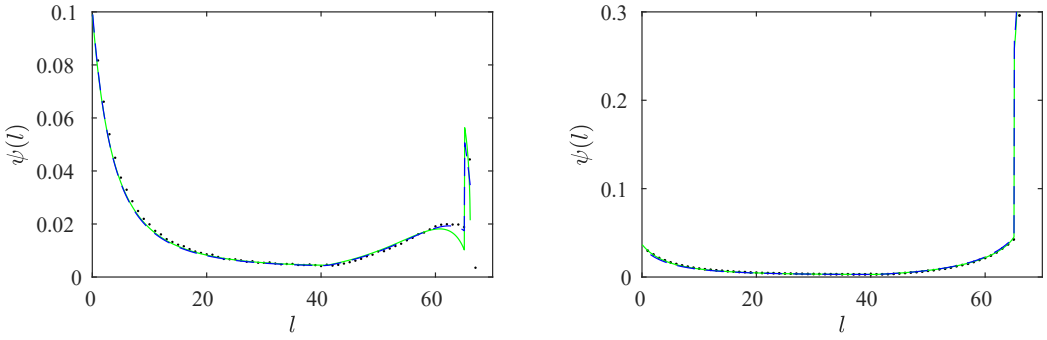

(**a**) (**b**)

Figure 15. RPDL function for $\varepsilon = 0.001$, $N = 15 \times 10^5$, $c = 0.1128$, $\hat{x} = -0.158449931412894$. (**a**) $\gamma = 0.5$. (**b**) $\gamma = 1.5$. Green line: M function methodology. Blue line: continuity technique. Black points: numerical data.

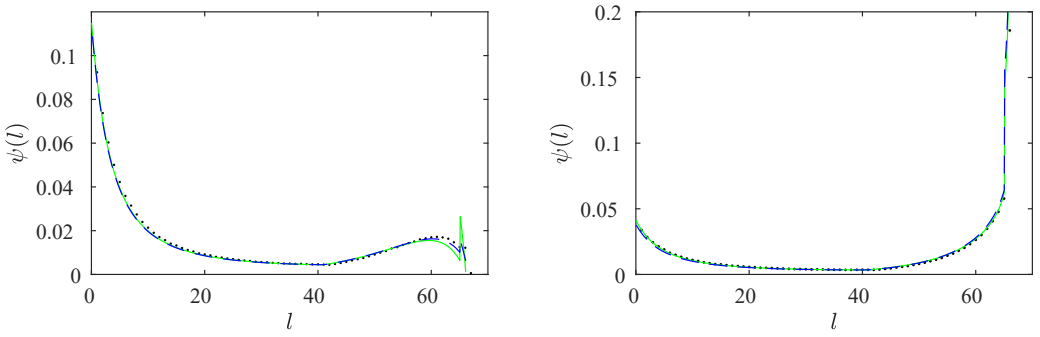

(**a**) (**b**)

Figure 16. RPDL function for $\varepsilon = 0.001$, $N = 15 \times 10^5$, $c = 0.1128$, $\hat{x} = -0.12644444444$. (**a**) $\gamma = 0.5$. (**b**) $\gamma = 1.5$. Green line: M function methodology. Blue line: continuity technique. Black points: numerical data.

3. Conclusions

In this paper, we presented a new methodology to calculate the statistical properties of type V intermittency. This methodology is obtained from the evolution of densities (Perron–Frobenius operator), and we refer to it as the continuity technique. We introduced and utilized this technique to obtain the reinjection probability density function (RPD), $\phi(x)$, and the probability density of the laminar lengths (RPDL), $\psi(l)$, for the family of maps described by Equation (2).

To the authors' best knowledge, this is the first time that the continuity technique has been used to calculate the RPD and RPDL functions in type V intermittency. Furthermore, it is the first time that this technique is implemented where multiple iterations are needed to obtain the RPD and where the reinjection is generated simultaneously by two different processes.

We performed comparisons between the theoretical results obtained by the continuity technique with those calculated by the classical theory of intermittency, the M function methodology, and with numerical data. We found that both methodologies, continuity and M function, produce similar $\phi(x)$ and $\psi(l)$ functions for different parameters, either with continuous or discontinuous RPD functions and with one or two functions governing the reinjection process. Furthermore, the theoretical results for the continuity technique accurately capture the numerical data. In addition, the results obtained with the continuity technique are more accurate than those calculated by the classical theory. We highlight that $\phi(x)$ and $\psi(l)$ functions, calculated with the continuity technique, exhibit a wider range of behaviors than those expected by uniform reinjection.

The classical studies on type V intermittency use the assumption that the RPD is uniform [28–30]. More recent studies consider a less restrictive hypothesis of a constant density at pre-reinjection points, i.e., points that govern the reinjection process [26,27,35]. Here, the assumption of constant density at pre-reinjection points was analyzed for the family of maps described by Equation (2). The classic formulation of chaotic intermittency used a constant RPD. In this work, this condition was relaxed, allowing the RPD to be a more complex function. However, the hypothesis of constant density at pre-reinjection points was assumed. This assumption works accurately because the length of the laminar interval is small, and the RPD function depends, in addition to the density, on the derivative of the function at pre-reinjection points, which can take very large or close to zero values.

For continuous RPD functions, we have conducted several tests using different values of the exponent γ, the length of the laminar interval c, the parameter ε, the number of reinjected points N, and the number of sub-intervals N_s. In all these tests for the continuity technique, the values of D_r and E_r decrease as the number of re-injected points grows, showing that the theoretical evaluation given by Equation (21) approximates the numerical RPD more accurately as the number of reinjected points increases. Furthermore, we have computed the rate of convergence of D_r and E_r for all tests, and detected that the process is convergent with a rate of convergence $O(\frac{1}{N^p})$ within $0.35 < p < 0.5$. We emphasize that the continuity technique converges better than classical theory, and obtains RPDs with similar accuracy to the M function methodology.

A similar study was developed for discontinuous RPD functions using different values of γ and the lower boundary of reinjection $\hat{x}$. For all tests, we observe that the continuity technique captures the behavior of the numerical data. Furthermore, the RPDs calculated using the continuity technique are more accurate for several tests than those obtained with the M function methodology. For all tests performed with the continuity technique, D_r and E_r decrease as the number of re-injected points increases. The exponents to evaluate the order of convergence, p_e and p_d were always positive. In addition, the continuity technique has the advantage of allowing the prediction of analytic RPD functions, continuous or discontinuous, only knowing the map without the need for using numerical or experimental data. If the assumption of constant density at the pre-reinjection points can be used, the RPD function mainly depends on the map derivative at the pre-reinjection points (see Equation (13)).

We can conclude that the continuity technique has the ability to accurately calculate the RPD and RPDL functions for type V intermittency.

Author Contributions: Conceptualization, S.E. and E.d.R.; methodology, S.E. and E.d.R.; software, S.E.; validation, S.E. and W.S.; formal analysis, S.E. and E.d.R.; investigation, S.E., E.d.R. and W.S; resources, S.E., E.d.R. and W.S.; writing—original draft preparation, S.E.; writing—review and editing, S.E., W.S. and E.d.R.; visualization, S.E. and W.S.; supervision, S.E. project administration, S.E. and E.d.R.; funding acquisition, S.E. and E.d.R. All authors have read and agreed to the published version of the manuscript.

Funding: This work was supported by SECyT of Universidad Nacional de Córdoba, Universidad Politécnica de Madrid, and Ministerio de Ciencia, Innovación y Universidades of Spain under grand No RTI2018-094409-B-I00.

Institutional Review Board Statement: Not applicable.

Informed Consent Statement: Not applicable.

Data Availability Statement: Not applicable.

Acknowledgments: The authors thank the Department of Aeronautics, FCEFyN of Universidad Nacional de Córdoba and Department of Applied Physics, ETSIAE of Universidad Politécnica de Madrid.

Conflicts of Interest: The authors declare no conflict of interest.

References

1. Schuster, H.; Just, W. *Deterministic Chaos*; Wiley VCH: Mörlenbach, Germany, 2005.
2. Nayfeh, A.; Balachandran, B. *Applied Nonlinear Dynamics*; Wiley: New York, NY, USA, 1995.
3. Marek, M.; Schreiber, I. *Chaotic Behaviour of Deterministic Dissipative Systems*; Cambridge University Press: Cambridge, UK, 1995.
4. Elaskar, S.; del Rio, E. *New Advances on Chaotic Intermittency and Its Applications*; Springer: New York, NY, USA, 2017.
5. Kaplan, H. Return to type I intermittency. *Phys. Rev. Lett.* **1992**, 68, 553–557. [CrossRef] [PubMed]
6. Price, T.; Mullin, P. An experimental observation of a new type of intermittency. *Physica D* **1991**, 48, 29–52. [CrossRef]
7. Platt, N.; Spiegel, E.; Tresser, C. On-off intermittency: A mechanism for bursting. *Phys. Rev. Lett.* **1993**, 70, 279–282. [CrossRef] [PubMed]
8. Pikovsky, A.; Osipov, G.; Rosenblum, M.; Zaks, M.; Kurths, J. Attractor–repeller collision and eyelet intermittency at the transition to phase synchronization. *Phys. Rev. Lett.* **1997**, 79, 47–50. [CrossRef]
9. Lee, K.; Kwak, Y.; Lim, T. Phase jumps near a phase synchronization transition in systems of two coupled chaotic oscillators. *Phys. Rev. Lett.* **1998**, 81, 321–324. [CrossRef]
10. Hramov, A.; Koronovskii, A.; Kurovskaya, M.; Boccaletti, S. Ring intermittency in coupled chaotic oscillators at the boundary of phase synchronization. *Phys. Rev. Lett.* **2006**, *97*, 114101. [CrossRef] [PubMed]
11. Dubois, M.; Rubio, M.; Berge, P. Experimental evidence of intermittencies associated with a subharmonic bifurcation. *Phys. Rev. Lett.* **1983**, *16*, 1446–1449. [CrossRef]
12. Stavrinides, S.; Miliou, A.; Laopoulos, T.; Anagnostopoulos, A. The intermittency route to chaos of an electronic digital oscillator. *Int. J. Bifurcation Chaos* **2008**, *18*, 1561–1566. [CrossRef]
13. Sanchez-Arriaga, G.; Sanmartin, J.; Elaskar, S. Damping models in the truncated derivative nonlinear Schrödinger equation. *Phys. Plasmas* **2007**, *14*, 082108. [CrossRef]
14. Zambrano, S.; Mariño, I.P.; Sanjuan, M. Controlling crisis-induced intermittency using its relation with a boundary crisis. *New J. Phys.* **2009**, *11*, 023025. [CrossRef]
15. Pizza, G.; Frouzakis, C.; Mantzaras, J. Chaotic dynamics in premixed Hydrogen/air channel flow combustion. *Combust. Theor. Model* **2012**, *16*, 275–299. [CrossRef]
16. Nishiura, Y.; Ueyama, D.; Yanagita, T. Chaotic pulses for discrete reaction diffusion systems. *SIAM J. App. Dyn. Syst.* **2005**, *4*, 723–754. [CrossRef]
17. de Anna, P.; Le Borgne, T.; Dentz, M.; Tartakovsky, A.; Bolster, D.; Davy, P. Flow intermittency, dispersion and correlated continuous time random walks in porous media. *Phys. Rev. Lett.* **2013**, *110*, 184502. [CrossRef]
18. Stan, C.; Cristescu, C.; Dimitriu, D. Analysis of the intermittency behavior in a low-temperature discharge plasma by recurrence plot quantification. *Phys. Plasmas* **2010**, *17*, 042115. [CrossRef]
19. Chian, A. *Complex System Approach to Economic Dynamics*; Lecture Notes in Economics and Mathematical Systems; Springer: Berlin, Germany, 2007.
20. Zebrowski, J.; Baranowski, R. Type I intermittency in nonstationary systems: Models and human heart-rate variability. *Physica A* **2004**, *336*, 74–86. [CrossRef]
21. Paradisi, P.; Allegrini, P.; Gemignani, A.; Laurino, M.; Menicucci, D.; Piarulli, A. Scaling and intermittency of brains events as a manifestation of consciousness. *AIP Conf. Proc.* **2013**, *1510*, 151–161. [CrossRef]
22. Hirsch, J.; Huberman, B.; Scalapino, D. Theory of intermittency. *Phys. Rev. Lett.* **1982**, *25*, 519–532. RevA.25.519. [CrossRef]
23. del Rio, E.; Elaskar, S. New characteristic relation in type II intermittency. *Int. J. Bifurcation Chaos* **2010**, *20*, 1185–1191. [CrossRef]
24. Elaskar, S.; del Rio, E.; Donoso, J. Reinjection probability density in type III intermittency. *Physica A* **2011**, *390*, 2759–2768. [CrossRef]
25. Elaskar, S.; del Rio, E.; Elaskar, S. Intermittency Reinjection in the Logistic Map. *Symmetry* **2022**, *14*, 481. 14030481. [CrossRef]
26. Elaskar, S.; del Rio, E. Discontinuous reinjection probability density function in type V intermittency. *J. Comp. Nonlinear Dynam.* **2018**, *13*, 121001–121010. [CrossRef]
27. Elaskar, S.; del Rio, E.; Gutierrez Marcantoni, L. Non-uniform reinjection probability density function in type V intermittency. *Nonlinear Dynam.* **2018**, *92*, 683–697. [CrossRef]

28. Bauer, M.; Habip, S.; He, D.; Martiessen, W. New type of intermittency in discontinuous maps. *Phys. Rev. Lett.* **1992**, *68*, 1625–1628. [CrossRef] [PubMed]
29. He, D.; Bauer, M.; Habip, S.; Kruger, U.; Martiessen, W.; Christiansen, B.; Wang, B. Type V intermittency. *Phys. Lett. A* **1992**, *171*, 61–65. [CrossRef]
30. Fan, J.; Ji, F.; Guan, S.; Wang, B.; He, D. The distribution of laminar lengths in type V intermittency. *Phys. Lett. A* **1993**, *182*, 232–237. [CrossRef]
31. Wu, S.; He, D. Characteristics of period-doubling bifurcation cascades in quasi-discontinuous systems. *Commun. Theor. Phys.* **2001**, *35*, 275–282. [CrossRef]
32. Wang, D.; Mo, J.; Zhao, X.; Gu, H.; Qu, S.; Ren, W. Intermittent chaotic neural firing characterized by non-smooth like features. *Chin. Phys. Lett.* **2010**, *27*, 070503. [CrossRef]
33. Gu, H.; Xiao, W. Difference Between Intermittent chaotic bursting and spiking of neural firing patterns. *Int. J. Bifurcation Chaos* **2014**, *24*, 1450082. [CrossRef]
34. Sternberg, S. *Dynamical Systems*; Dover Publications: New York, NY, USA, 2010.
35. Elaskar, S.; del Rio, E.; Zapico, E. Evaluation of the statistical properties for type-II intermittency using the Perron-Frobenius operator. *Nonlinear Dynam.* **2016**, *86*, 1107–1116. [CrossRef]
36. Lasota, A.; Mackey, M. *Chaos, Fractals, and Noise: Stochastic Aspects of Dynamics*; Springer Science & Business Media: New York, NY, USA, 1998; Volume 97.
37. Beck, C.; Schogl, F. *Thermodynamics of Chaotic Systems*; Cambridge University Press: Cambridge, UK, 1993.
38. Burden, R.; Faires, J.; Burden, A. *Numerical Analysis*; Cengage Learning: Boston, MA, USA, 2014.

MDPI AG
Grosspeteranlage 5
4052 Basel
Switzerland
Tel.: +41 61 683 77 34

Symmetry Editorial Office
E-mail: symmetry@mdpi.com
www.mdpi.com/journal/symmetry

Disclaimer/Publisher's Note: The title and front matter of this reprint are at the discretion of the Guest Editor. The publisher is not responsible for their content or any associated concerns. The statements, opinions and data contained in all individual articles are solely those of the individual Editor and contributors and not of MDPI. MDPI disclaims responsibility for any injury to people or property resulting from any ideas, methods, instructions or products referred to in the content.

Academic Open
Access Publishing

mdpi.com

ISBN 978-3-7258-4443-2